



**Files are in or Adobe format.
Download the newest version from [Adobe](#).**

24th International Symposium on BALLISTICS

New Orleans, LA

September 22-26, 2008

Conference Agenda

TUESDAY, SEPTEMBER 23, 2008

GENERAL SESSION

- *"IBC Presentation 2008"*, Bo Janzon, IBC Chairman, SECRA, Sweden
- *"GS009 A Brief History of Shaped Charges"*, William Walters, USA
- *"GS104 Numerical Simulation of Muzzle Exit and Separation Process for Sabot-Guided Projectiles at $M > 1$ "*, Jorn van Keuk, Germany; Arno Klomfass, Germany

TERMINAL BALLISTICS

- *"TB068 Performance and Production of Jacketed Penetrators having Different Jacket Thickness"*, B.J. van der Meer, The Netherlands; Mark Dijkstra, The Netherlands; Erik Carton, The Netherlands
- *"TB227 Loading Mechanisms on a Target from Detonation of a Buried Charge"*, Leslie Taylor, USA; William Fournay, USA; Ulrich Leiste, USA; Bryan Cheesman, USA
- *"TB167 Predicting the Onset of Lateral Instability of Long Rod Penetrators in a Particulate Target"*, Melissa Hankins, USA; S. E. Jones, USA; Karen L. Torres, USA
- *"TB135 A Comparative Study of Penetration Codes for Brittle Materials"*, Sikhanda Satapathy, USA; Anthony Dawson, USA; Gregory Rodin, USA
- *"TB200 Radial Jet Dispersion Due to Current Interaction in an Electric Armour Application"*, Patrik Lundberg, Sweden; Patrik Appelgren, Sweden; Melker Skoglund, Sweden; Lars Westerling, Sweden; Tomas Hurtig, Sweden; Anders Larsson, Sweden

WARHEAD MECHANISMS

- “*WM056 Munitions Effects: A Schematic Overview of Munitions and Warheads, Trends for the Future*”, Andre Diederer, The Netherlands
- “*WM097 Initiation Controlled Multimode Warheads*”, Thomas Falter, Germany
- “*WM203 Combined Effects Aluminized Explosives*”, Ernest Baker, USA; Leonard Stiel, USA; Christos Capellos, USA; Wendy Balas, USA; Jack Pincay, USA
- “*WM134 Multiple Effects Warheads for Defeat of Urban Structures and Armour*”, Anthony Whelan, UK
- “*WM161 Development of the NLOS-LS PAM Warhead*”, Melissa Hobbs, USA; Christopher English, USA; David Hunter, USA; Jim Strom, USA; William Zarr, USA

EXTERIOR BALLISTICS & LAUNCH DYNAMICS

- “EB113 Range Extension of Gun-Launched Smart Munitions”, Frank Fresconi, USA
- “EB166 Numerical Prediction of Magnus of Spin-Stabilized Projectiles”, James DeSpirito, USA; Sidra Silton, USA
- “EB206 Mine Countermeasure Dart Dispense Modeling & Simulation”, Gary Prybyla, USA; Michael Dean Neaves, USA; Kevin Losser, USA; James Baltar, USA; William Dietz, USA
- “EB178 Trajectory Deflection of Fin- and Spin-Stabilized Projectiles using Paired Lateral Impulses”, Pierre Wey, France; Daniel Corriveau, Canada
- “LD011 Numerical Analysis of Bi-Metallic Explosive Shock-Loading and Release Experiments”, Jeremy Kleiser, USA; Brian Plunkett, USA; Lalit Chhabildas, USA

WEDNESDAY SEPTEMBER 24, 2008

ARMOUR & PERSONAL PROTECTION

- “APP032 Assessment and Measurement of Potential Blunt Trauma Under Ballistic Helmets”, Celia Watson, UK; Annette Webb, Australia; Ian Horsfall, UK
- “APP171 Ballistic Performance Assessment of Lightweight Body Armour Material Systems Against IED Threat”, Gilles Pageau, Canada; Kevin Williams, Canada; Daniel Bourget, Canada; Ming Cheng, Canada; Clint Hedge, Canada; Benoit Anctil, Canada
- “APP001 Experimental Validation of the Origin of the Bodywork Effect (K-Effect) in the Up-Armouring of Civil and Military Vehicles”, Frederik Coghe, Belgium; Bernard Kestelyn, Belgium; Marc Pirlot, Belgium
- “APP075 Half Scale Experiments with Rig for Measuring Structural Deformation and Impulse Transfer from Land Mines”, Björn Zakrisson, Sweden; Bo Johansson, Sweden; Bengt Wikman, Sweden
- “APP062 A Computational Study of the Energy Dissipation through an Acrylic Target Impacted by Various Size FSP”, Costas Fountzoulas, USA; Peter Dehmer, USA; Jian Yu, USA; James Sands, USA

TERMINAL BALLISTICS

- “TB035 High Speed Penetration into Low Strength Concrete Target”, Vincent Luk, USA; James Dykes, USA; Joseph Bishop, USA; John Ludwigsen, USA; Douglas Dederman, USA; P. A. Taylor, USA
- “TB168 Fragment Penetration Modeling of Anthropometric Ballistic Mannequins”, William Bruchey, USA; Amy Tank, USA
- “TB230 Effects of Small Caliber Ammunition Through Intermediate Barriers”, Jeremy Lucid, USA; Chris Gandy, USA

THURSDAY SEPTEMBER 25, 2008

GENERAL SESSION

- *“EB139 Numerical Computations of Dynamic Pitch-Damping Derivatives using Time-Accurate CFD Techniques”*, Jubaraj Sahu, USA
- *“GS137 Consideration of the Ignition Delay of Gun Propellants”*, Clive Woodley, UK; Michael Taylor, UK; Steve Fuller, UK; Steve Gilbert, UK; Joseph Gransden, UK
- *“GS232 U.S. Army Tactical Wheeled Vehicle Vulnerability Test & Evaluation Methodology”*, Stephanie Koch, USA
- *“The Effect of Velocity on Jacketed Rod Efficiency”*, Brad Pederson, Stephan Bless, Robert Fromm

WARHEAD MECHANISMS

- *“WM085 The Appendix”*, Eitan Hirsch, Israel; Meir Mayseless, Israel
- *“WM256 Behind Armour Effects at Shaped Charge Attacks”*, Manfred Held, Germany
- *“WM016 Warhead Filling and Casing Interactions Affect the Blast Field Performance”*, Paul Locking, UK; Dennis Flynn, UK; J. Dunnett, UK
- *“WM234 Reaction of Metal Fragments from Cased Explosive Charges”*, Laura Donahue, Canada; Robert Ripley, Canada; Jeff Leadbetter, Canada; Yasuyuki Horie, USA; Fan Zhang, Canada

INTERIOR BALLISTICS & LAUNCH DYNAMICS

- *“IB098 Numerical Simulation of Projectile Acceleration Process Using Solid/Gas Two-Phase Reacting Flow Model”*, Hiroaki Miura, Japan; Akiko Matsuo, Japan; Yuichi Nakamura, Japan
- *“IB015 Two-Dimensional Modelling of Modular Charge Gun Firings”*, Clive Woodley, UK; Steve Fuller, UK
- *“LD027 Launch Dynamics Environment of a Water Piercing Missile Launcher”*, Jon Yagla, USA; John Basic, USA; Samuel Koski, USA; Chris Weiland, USA
- *“LD065 Experiments with Gun Launched Penetrators into Gelatin Target Materials”*, John Stubberfield, UK; Nicholas Lynch, UK; Clive Woodley, UK; Alan Hepper, UK

WOUND BALLISTICS & VULNERABILITY

- *“WB053 The Validation of a Thoracic and Abdominal Test Rig for BABT Soft Body Armour Testing”*, Kate Hewins, UK; Ian Horsfall, UK; Celia Watson, UK
- *“WB242 Survivability Measures for Evaluation of Personnel in Military Systems”*, Natalie Eberius, USA; Patricia Frounfelker, USA; Kelly Benjamin, USA
- *“WB144 Diagnostic Techniques for Multiphase Blast Fields”*, Richard Ames, USA; Michael Murphy, USA

FRIDAY SEPTEMBER 26, 2008

GENERAL SESSION

- *“GS023 Predicting Hazard Response Scenarios in Weapon Systems”*, Ian Cullis, UK; I.H. Brown, UK; P.D. Church, UK; P. Gould, UK; V.E. Ingamells, UK
- *“GS130 Experimental Validation of a Kevlar Fabric Model for Ballistic Impact”*, Chian Yen, USA; Tusit Weerasooriya, USA; Paul Moy, USA; Brian Scott, USA; Bryan Cheeseman, USA
- *“GS205 Shaped Charge Penetration of Gas Saturated Sandstone”*, Brenden Grove, USA; Jeremy Harvey, USA

TERMINAL BALLISTICS

- “*TB025 Penetration Resistance of Glass and a Glass Ceramic*”, Stephan Bless, USA; Don Berry, USA
- “*TB111 Long-Rod Penetration into Intact and Pre-Damaged SiC Ceramic*”, Charles Anderson, USA; Thilo Behner, Germany; Dennis Orphal, USA; Arthur Nicholls, USA; Timothy Holmquist, USA; Matthias Wickert, Germany
- “*TB058 The Shock Response Of a Cemented Tungsten Carbide*”, Koen Herlaar, The Netherlands; Andre Diederer, The Netherlands; Gareth Appleby-Thomas, UK; Paul J Hazell, UK
- “*TB038 GRC’s Impact Behavior*”, Alejandro Enfedaque Diaz, Spain; David Cendón Franco, Spain; Francisco Gálvez Díaz-Rubio, Spain; Vicente Sánchez Gálvez, Spain
- “*TB248 The Mechanics of Projectile Arrest for Compliant Cross Plied Unidirectional Laminates*”, Brian Scott, USA; Bryan Cheeseman, USA



24th International Symposium on **BALLISTICS**

New Orleans, Louisiana, USA

Sponsored by the Ballistics
Division of NDIA in
association with the
International Ballistics
Committee



CONFERENCE AGENDA

SHERATON NEW ORLEANS ► NEW ORLEANS, LA

SEPTEMBER 22-26, 2008
WWW.NDIA.ORG/MEETINGS/8210

The 24th International Symposium on Ballistics is jointly organized and supported by the National Defense Industrial Association, USA in conjunction with the International Ballistics Committee

Symposium Co-Chairmen:

Dr. Stephan Bless

Dr. James Walker

PREVIOUS INTERNATIONAL SYMPOSIA ON BALLISTICS

Orlando, Florida, USA	1974
Daytona, Florida, USA	1976
Karlsruhe, Germany	1977
Monterey, California, USA	1978
Toulouse, France	1980
Orlando, Florida, USA	1981
The Hague, The Netherlands	1983
Orlando, Florida, USA	1984
Shrivenham, UK	1986
San Diego, California, USA	1987
Brussels, Belgium	1989
San Antonio, Texas, USA	1990
Stockholm, Sweden	1992
Quebec City, Canada	1993
Jerusalem, Israel	1995
San Francisco, California, USA	1996
Midrand, South Africa	1998
San Antonio, Texas, USA	1999
Interlaken, Switzerland	2001
Orlando, Florida, USA	2002
Adelaide, South Australia	2004
Vancouver, BC, Canada	2005
Tarragona, Spain	2007

24TH INTERNATIONAL SYMPOSIUM ON BALLISTICS:

SEPTEMBER 22-26, 2008 ► SHERATON NEW ORLEANS
NEW ORLEANS, LA

SYMPOSIUM ATTIRE

Appropriate dress for this symposium is business for civilians (coat and tie) and class A uniform or uniform of the day for military.

PAPER SELECTION COMMITTEE

Dr. Charles E. Anderson, Jr., USA

Mr. Joseph Backofen, USA

Dr. Dennis Baum, USA

Dr. Stephan Bless, USA

Mme. Manon Bolduc, Canada

Dr. Donald Carlucci, USA

Dr. James Cazamias, USA

Mr. Pierre Chanteret, France

Dr. Sidney Chocron, USA

Dr. Ian Cullis, UK

Mr. Philip Cunliff, USA

Dr. Andre Diederer, Netherlands

Dr. Eric Fahrenthold, USA

Dr. William Flis, USA

Dr. Richard Fong, USA

Dr. Francisco Galvez, Spain

Dr. Marc Giraud, France

Dr. Manfred Held, Germany

Dr. Bo Janson, Sweden

Dr. Valeriy Kartuzov, Ukraine

Dr. Michael Murphy, USA

Dr. Dennis Nandall, Canada

Mr. Dennis Orphal, USA

Dr. Ake Persson, Sweden

Dr. Xiangyang Quan, USA

Mr. Jack P. Riegel, III, USA

Mr. Erick Sagebiel, USA

Dr. Sikhanda Satapathy, USA

Dr. Douglas Templeton, USA

Dr. James Walker, USA

Dr. Paul Weinacht, USA

Mr. Carl Weiss, USA

Dr. Joe Wells, USA

INTERNATIONAL BALLISTICS COMMITTEE

Executive Committee

Dr. Bo Janson, Sweden

Chairman

Mr. Jack Riegel, USA

Vice-Chairman

Dr. Ian Cullis, UK

Secretary

Prof. Ron Brown, USA

Bursar #1

Dr. Richard Fong, USA

Bursar #2

Dr. Pieter Nel, South Africa

Immediate Past Chairman

Dr. Roxan Cayzac, France

POC Europe

Dr. Meir Mayseless, Israel

POC Other Nations

Dr. Joe Carleone, USA

POC North America

Members

Dr. Charles Anderson, Jr., USA

Mr. Joe Backofen, USA

Dr. Dennis Baum, USA

Dr. Ronald Brown, USA

Dr. Norbert Burman, Australia

Dr. Joseph Carleone, USA

Dr. Roxan Cayzac, France

Mr. Pierre Chanteret, France

Dr. Sidney Chocron, USA

Dr. Ian Cullis, UK

Dr. Andre Diederer, The Netherlands

Dr. William Flis, USA

Mr. Richard Fong, USA

Dr. Francisco Galvez, Spain

Dr. Marc Giraud, France

Prof. Dr. Manfred Held, Germany

Dr. Dieter Hensel, France

Dr. Eitan Hirsch, Israel

Dr. Bo Janson, Sweden

Dr. Hanspeter Kaufmann, Switzerland

Dr. Eva Liden, Sweden

Dr. Meir Mayseless, Israel

Dr. Frederick Mostert, South Africa

Dr. Michael Murphy, USA

Dr. Dennis Nandall, Canada

Dr. Pieter Nel, South Africa

Dr. Ake Persson, Sweden

Dr. Moshe Ravid, Israel

Dr. William Reinecke, USA

Mr. Jack Riegel, USA

Dr. Brian Scott, USA

Prof. Dr. Klaus Thoma, Germany

Prof. Zhongyuan Wang, China

Dr. Paul Weinacht, USA

Emeritus Members

Dr. Bruce Burns

Prof. Eduard Celens, Belgium

Dr. Pei Chi Chou, USA

Dr. Rudi Heiser, Germany

Dr. Albert Horst, USA

Dr. Gunther Krauth, Germany

Dr. Ir. Hans Pasman, The Netherlands

Dr. E. Schmidt, USA

Dr. Gustav-Adolf Schroeder, Germany

Mr. David Scott, UK

Dr. Alois Stilp, Germany

Dr. Louis Zernow, USA

Guest Members

Mr. P. U. Deshpande, India

Professor Tan Hua, China

Dr. Carlos Navarro, Spain

Acad. Victor S. Soloviev, Russia

MONDAY, SEPTEMBER 22, 2008

7:00 am - 7:00 pm Registration Open

9:00 am - 4:30 pm Independent Tutorials
Additional Registration Fee Applies
Presented by Professor Dr. Manfred Held

AM SESSION

9:00 am	Warhead Mechanism <ul style="list-style-type: none">1.1 Blast Charges1.2 Shaped Charges1.3 Flat Cone Charges
10:45 am	Coffee Break
11:00 am	Warhead Mechanism Continued <ul style="list-style-type: none">1.4 EFP Charges1.5 Fragment Charges (Anti-AC/Anti-TBM)

PM SESSION

1:30 pm	Overview on Armour for MBT's and APC's <ul style="list-style-type: none">2.1 RHA2.2 Ceramics2.3 Glass
3:00 pm	Coffee Break
3:15 pm	Overview on Armour for MBT's and APC's Cont. <ul style="list-style-type: none">2.4 Composites2.5 ERA2.6 NERA or Bulging2.7 Active Defence Concepts

10:00 am - 4:00 pm Exhibitor Move In

5:00 pm Exhibit Hall Open

5:00 pm - 7:00 pm Opening Reception - Exhibit Hall
Featuring the New Orleans Spice Jazz Band

These tutorials will provide attendees with a better understanding of the many very specialized papers in the 24th International Symposium on Ballistics. Every course attendee will receive a handout of the slides used in the lectures.

Prof. Dr. Held is one of the foremost experts in the world in ballistics. The material in this course is drawn from his lectures at the Military University in Munich.

TUESDAY, SEPTEMBER 23, 2008

7:00 am Continental Breakfast & Registration

8:00 am Welcome & Administrative Remarks

8:10 am - 9:50 am General Session
Chaired by Pieter Nel & Marc Giraud

8:10 am *GS009 A Brief History of Shaped Charges*
William Walters, USA

8:50 am *GS109 Interface Defeat for Unconfined SiC Ceramics*
Thilo Behner, Germany; Charles Anderson, USA; Timothy Holmquist, USA; Matthias Wickert, Germany; Doug Templeton, USA

9:10 am *GS104 Numerical Simulation of Muzzle Exit and Separation Process for Sabot-Guided Projectiles at $M > 1$*
Jorn van Keuk, Germany; Arno Klomfass, Germany

9:30 am *GS117 Origin and Magnitude of the Pressure and Temperature Increase Behind Defeated Armor*
Andreas Heine, Germany; Matthias Wickert, Germany

9:30 am - 5:30 pm Exhibit Hall Open

9:50 am - 10:10 am Coffee Break in Exhibit Hall

10:10 am - 10:30 am Presentation on Proposed International Ballistics Society

10:30 am - 12:10 pm Terminal Ballistics
Chaired by Dennis Nandlall & Sikhanda Satapathy

10:30 am *TB068 Performance and Production of Jacketed Penetrators having Different Jacket Thickness*
B.J. van der Meer, The Netherlands; Mark Dijkstra, The Netherlands; Erik Carton, The Netherlands

10:50 am *TB227 Loading Mechanisms on a Target from Detonation of a Buried Charge*
Leslie Taylor, USA; William Fourny, USA; Ulrich Leiste, USA; Bryan Cheesman, USA

11:10 am *TB167 Predicting the Onset of Lateral Instability of Long Rod Penetrators in a Particulate Target*
Melissa Hankins, USA; S. E. Jones, USA; Karen L. Torres, USA

11:30 am *TB135 A Comparative Study of Penetration Codes for Brittle Materials*
Sikhanda Satapathy, USA; Anthony Dawson, USA; Gregory Rodin, USA

11:50 am *TB200 Radial Jet Dispersion Due to Current Interaction in an Electric Armour Application*
Patrik Lundberg, Sweden; Patrik Appelgren, Sweden; Melker Skoglund, Sweden; Lars Westerling, Sweden; Tomas Hurtig, Sweden; Anders Larsson, Sweden

12:10 pm - 12:30 pm Introduction to Poster Sessions

12:30 pm - 2:00 pm Lunch - Armstrong Ballroom; 8th Floor

2:00 pm - 3:40 pm Warhead Mechanisms
Chaired by Pierre Chanteret & Richard Fong

2:00 pm *WM056 Munitions Effects: A Schematic Overview of Munitions and Warheads, Trends for the Future*
Andre Diederens, The Netherlands

2:20 pm *WM097 Initiation Controlled Multimode Warheads*
Thomas Falter, Germany

2:40 pm *WM203 Combined Effects Aluminized Explosives*
Ernest Baker, USA; Leonard Stiel, USA; Christos Capellos, USA; Wendy Balas, USA; Jack Pincay, USA

3:00 pm *WM134 Multiple Effects Warheads for Defeat of Urban Structures and Armour*
Anthony Whelan, UK

3:20 pm *WM161 Development of the NLOS-LS PAM Warhead*
Melissa Hobbs, USA; Christopher English, USA; David Hunter, USA; Jim Strom, USA; William Zarr, USA

3:40 pm - 5:30 pm Terminal Ballistics Poster Session

3:40 pm Coffee Break in Exhibit Hall

4:00 pm - 5:40 pm Exterior Ballistics & Launch Dynamics
Chaired by Paul Weinacht & Roxan Gayzac

- 4:00 pm** *EB113 Range Extension of Gun-Launched Smart Munitions*
Frank Fresconi, USA
- 4:20 pm** *EB166 Numerical Prediction of Magnus of Spin-Stabilized Projectiles*
James DeSpirito, USA; Sidra Siltan, USA
- 4:40 pm** *EB206 Mine Countermeasure Dart Dispense Modeling & Simulation*
Gary Prybyla, USA; Michael Dean Neaves, USA; Kevin Losser, USA; James Baltar, USA; William Dietz, USA
- 5:00 pm** *EB178 Trajectory Deflection of Fin- and Spin-Stabilized Projectiles using Paired Lateral Impulses*
Pierre Wey, France; Daniel Corriveau, Canada
- 5:20 pm** *LD011 Numerical Analysis of Bi-Metallic Explosive Shock-Loading and Release Experiments*
Jeremy Kleiser, USA; Brian Plunkett, USA; Lalit Chhabildas, USA

TERMINAL BALLISTICS POSTER SESSION

3:40 pm - 5:30 pm

CHAIRMEN: JACK RIEGEL, CARL WEISS & KOEN HERLAAR

TB002 Ballistic Performance of Protective Liners

Moshe Ravid, Israel; Shlomo Birger, Israel; Nimi Shapira, Israel; Avi Ya'akovovith, Israel; Yoav Hirschberg, Israel

TB008 Non-Invasive Ballistic Impact Damage Diagnostics Capabilities with XCT: Now and in the Future

Joe Wells, USA

TB018 Protection Capability of Steel Armor with Liquid Filled Cavities Against Shaped Charge Jets

Andreas Holzwarth, Germany

TB020 Deformation and Breakup of Tungsten Alloy Cubes, Cylinders and Spheres on Aluminum Plates

Karl Weber, Germany

TB030 Penetration of Tube-Like Projectiles into Metal Targets

Vladislav Veldanov, Russia; Sergey Fedorov, Russia; Victor Kozlov, Russia; Mikhail Maximov, Russia

TB031 Penetration Model Taking in Mind Viscosity Properties of the Impacted Body Materials. Comparison with Test.

Vladislav Veldanov, Russia; Victor Kozlov, Russia

TB045 The Effect of a Copper Buffer on Interface Defeat

Timothy Holmquist, USA; Charles Anderson, USA; Thilo Behner, Germany

TB050 On Penetration/Perforation of Concretes Struck by Rigid Projectiles

Xiaowei Chen, China

TB052 Study on the Effect of Reinforcement of Concrete Targets upon the Penetration Performance of a Projectile

Hak Jun Kim, Korea; Leeju Park, Korea; Hyungwon Kim, Korea

TB057 Ballistic Impact Experiments of Tungsten Carbide Projectiles onto Tungsten Carbide Targets

Koen Herlaar, The Netherlands; Andre Diederer, The Netherlands; Gareth Appleby-Thomas, UK; Paul Hazell, UK

TB058 The Shock Response Of a Cemented Tungsten Carbide

Koen Herlaar, The Netherlands; Andre Diederer, The Netherlands; Gareth Appleby-Thomas, UK; Paul J Hazell, UK

TB060 Modeling of Defects in Transparent Ceramics for Improving Military Armor

Costas Fountzoulas, USA; James Sands, USA; Gary Glide, USA; Parimal Patel, USA

TB064 Modeling the Influence of Damage in Compression on the Spall Strength of Alumina

Zvi Cooper, Israel; Miles Rubin, Israel

TB067 New Analytical Model of Expansion of Spherical Cavity in Porous Plastic Material and Penetration into Such Materials

Boris Galanov, Ukraine; Valeriy Kartuzov, Ukraine; Sergei Ivanov, Ukraine

TB080 An Experimental Study of Penetration Behavior of Shaped Charge Jet in Water Filled Targets

Dev Raj Saroha, India; Gurmit Singh, India; Virendra Kumar Mahala, India

TB083 Ricochet of AP Projectiles from Hard Concrete Targets

Meir Mayseless, Israel; Yehiel Reifen, Israel; David Touati, Israel; Dan Yaziv, Israel; G. Tibon, Israel

TB089 Numerical Study or the Relations between Material Properties of Tungsten-Alloy Rod and its Ballistic Performance

Lou Jianfeng, China; He Changjiang, China; Hong Tao, China; Wang Zheng, China; Hang Yihong, China

TB106 Numerical and Experimental Study of the Defeating the RPG-7

Stanislav Rolc, Czech Republic; Jaroslav Buchar, Czech Republic; Zbynek Akstein, Czech Republic; Giovanni Cozzani, Italy; C. De Giorgi, Italy

TB128 New Lightweight Metals for Armors

Frans van Wegen, The Netherlands; Erik Carton, The Netherlands

TB132 An Analytical Investigation of the Energy-Volume Relationship Observed in Concrete Targets Penetrated by Shaped Charge Jets

Milton Frick Maritz, South Africa; Frikkie Mostert, South Africa; Cornelis Tereblanche, South Africa

TB138 The Effect of Velocity on Jacketed Rod Efficiency

Brad Pedersen, USA; Stephan Bless, USA; Robert Fromm, USA

TB141 Preliminary Results From Firings of Glass Shaped Charge Jets into Steel Targets

Michael Edwards, UK; Rhydian Harries, UK; Euan Henderson, UK

TB146 An Accuracy and Efficiency Assessment of Beanbags

Alexandre Papy, Belgium; Fatiha Id-Boufker, Belgium

TB148 A Comparison of the Ballistic Performance between Rolled Plate in AZ31B-H24 Magnesium & 5083-H131 Aluminum

Tyrone Jones, USA; Matthew Burkins, USA; Rick DeLorme, USA

TB149 In Situ Penetration Testing of Darts with 15-Inch Mobile Gas Gun

Douglas Dederman, USA; James Dykes, USA; John Foster, USA; Damon Burnett, USA

TB190 How to Model Fracture Behaviour in Long Rod Projectile

Ewa Lidén, Sweden

TB192 Concept Analysis and Impact Performance of Kinetic Energy Penetrators against Composite Hard Targets

A. K. Sharma, India

TB197 Multiple Hit Performance of 7.62 mm Hardened Steel and 30 mm APFSDS Projectiles in Brick and Reinforced Concrete Walls

Stephan Lampert, Switzerland; Hanspeter Kaufmann, Switzerland; Dieter Hoffmann, Germany

TB201 Supersonic Penetration by Wedges and Cones into Dry Sand

William Flis, USA; David Jann, USA; Lucia Shan, USA

TB207 Constitutive Properties of Transparent Nylon during High Velocity Impact

Nicholas Tsantinis, USA; John Song, USA; Jason Parker, USA; Phillip Cuniff, USA

TB217 Penetration Performance of Geopenetrators in the High Velocity Regime

Norbert Heider, Germany; Arno Klomfass, Germany; Makfred Salk, Germany

TB229 Simple Explicit Analysis for the Effect of Ceramic Thickness on the Dwell/ Penetration Transition

Jerry LaSalvia, USA

WEDNESDAY, SEPTEMBER 24, 2008

7:00 am Continental Breakfast & Registration

8:00 am Administrative Remarks

8:00 am - 1:30 pm Exhibit Hall Open

**8:10 am - 10:10 am Armour & Personal Protection
Chaired by Doug Templeton & Eric Fahrenthold**

8:10 am APP032 Assessment and Measurement of Potential Blunt Trauma Under Ballistic Helmets
Celia Watson, UK; Annette Webb, Australia; Ian Horsfall, UK

8:30 am APP171 Ballistic Performance Assessment of Lightweight Body Armour Material Systems Against IED Threat
Gilles Pageau, Canada; Kevin Williams, Canada; Daniel Bourget, Canada; Ming Cheng, Canada; Clint Hedge, Canada; Benoit Anctil, Canada

8:50 am APP001 Experimental Validation of the Origin of the Bodywork Effect (K-Effect) in the Up-Armouring of Civil and Military Vehicles
Frederik Coghe, Belgium; Bernard Kestelyn, Belgium; Marc Pirlot, Belgium

9:10 am APP075 Half Scale Experiments with Rig for Measuring Structural Deformation and Impulse Transfer from Land Mines
Björn Zakrisson, Sweden; Bo Johansson, Sweden; Bengt Wikman, Sweden

9:30 am APP062 A Computational Study of the Energy Dissipation through an Acrylic Target Impacted by Various Size FSP
Costas Fountzoulas, USA; Peter Dehmer, USA; Jian Yu, USA; James Sands, USA

9:50 am APP163 Simulation of Damage to a Vehicle by Explosion of an Improvised Explosive Device
Chris Quan, USA; John Paxon, USA

8:10 am - 10:30 am Warhead Mechanisms Poster Session

10:10 am - 10:30 am Coffee Break in Exhibit Hall

10:30 am - 12:00 pm Terminal Ballistics
Chaired by Klaus Thoma & Ake Persson

10:30 am *TB035 High Speed Penetration into Low Strength Concrete Target*
Vincent Luk, USA; James Dykes, USA; Joseph Bishop, USA; John Ludwigsen, USA; Douglas Dederman, USA; P. A. Taylor, USA

10:50 am *TB168 Fragment Penetration Modeling of Anthropometric Ballistic Mannequins*
William Bruchey, USA; Amy Tank, USA

11:10 am *TB230 Effects of Small Caliber Ammunition Through Intermediate Barriers*
Jeremy Lucid, USA; Chris Gandy, USA

11:30 am *TB222 Protecting the New Horizons Spacecraft's Radioisotope Thermoelectric Generator from Potential Fragment Impacts during Launch Self Destruct*
James Walker, USA; Walt Gray, USA

12:00 am - 1:30 pm Lunch - Armstrong Ballroom; 8th Floor

1:30 pm - 5:30 pm Tour of the French Quarter (included in attendee registration)

Conference attendees will be split into 4 groups, determined by bead theme and color given at registration. Groups will convene in the lobby of the Sheraton before taking off for Bourbon Street! Stay with your group to enjoy New Orleans' famous bars and restaurants!

WARHEAD MECHANISMS POSTER SESSION

8:10 am - 10:30 am

CHAIRMEN: EITAN HIRSCH, FRIKKIE MOSTERT, DAVE LAMBERT

WM003 *Experimental, Numerical and Analytical Studies on Two Linear Demolition Shape Charges for Two Initiation Modes*

Shakeel Abbas Rofi, China; Huang Fenglei, China

WM004 *Experimental and Numerical Investigations on the Formation and Penetration of Jet Projectile Charges against Concrete Targets*

Shakeel Abbas Rofi, China; Huang Fenglei, China; Zhang Leilei, China

WM010 *Softening of Shaped Charge Jet Particles While Penetrating Air*

Joe Backofen, USA

WM019 *Lethality Enhancer Against TBMs with Demanding Submunition Payloads*

Werner Arnold, Germany; Ernst Rottenkolber, Germany

WM022 *Optimisation of Fragmentation Warheads*

Lawrence Davey, UK; John Curtis, UK; Andrew Bowden, UK

WM029 *Near Field Impulse Loading Measurement Techniques for Evaluating Explosive Blast Performance*

Thuvan Piehler, USA; Avi Birk, USA; Richard Benjamin, USA; Vincent Boyle, USA; Eugene Summers, USA; Stephen Aubert, USA

WM040 *Study on Virtual Prototyping Design Method for Conventional Warhead*

Yang Yunbin, China; Qian Lixin, China; Sun Chuanjie, China; Zhou Yan, China

WM094 *Influence of Peripheral Frame Parameters on Fragments Dispersion*

Alex Zlatkis, Israel; Natanel Korin, Israel; Ilan Azulay, Israel; David Touati, Israel; Evgeny Gofman, Israel

WM101 *Multi-Purpose Projectile Concept to Balance the Conflicting Requirements for Peace Support Operations*

Gawie De la Bat, South Africa; Jean Louis Du Plessis, South Africa; Donovan Wilson, South Africa; Dieter Peters, South Africa; Johan Mare, South Africa

WM155 *Development of the M982 Excalibur Unitary Warhead*

Richard Szczepanski, USA; Terry Young, USA

WM156 *Development of Fielding of the Guided Multi-Launch Rocket System (GMRLS) Unitary Warhead*

Renita Friese, USA; Richard Tuznik, USA; Tracey Westmoreland, USA

WM164 *Small EFP Charge for Armor Development*

David Davison, USA; Dan Pratt, USA; James Bustamante, USA

WM185 *The Effect of Corner Turning on Wave Shaper Performance*

Andreas Helte, Sweden; Jonas Lundgren, Sweden; Håkan Örnhed, Sweden

WM189 *SDSC – A Structure Destroying Shaped Charge*

Lippe Sadwin, Israel; Eitan Hirsch, Israel

WM193 *The Jetting Cavity Test – A Multi Parameter Material Properties Measurement Tool*

Sergi Chanukaev, Israel; Eitan Hirsch, Israel

WM202 *Warhead Venting Design Technology Development*

Timothy Madsen, USA; Ernest Baker, USA; Stanley DeFisher, USA; Nausheen Al-Shehab, USA; Daniel Suarez, USA; Brian Fuchs, USA

WM204 *PIMS: Particle Impact Mitigation Sleeves*

James Pham, USA; Arthur Daniels, USA; Ernest Baker, USA; Koon-Wing Ng, USA; David Pfau, USA

WM212 *Effects of Computational Zoning on Resolving Partitioning and Jet Formation from Small Caliber Nitromethane Shaped Charges*

Ronald Brown, USA; Hung Cao, USA; Richard Zamberlan, USA; Dave Gerace, USA; Pedro Freitas, USA; Jose O. Sinibaldi, USA; Andreas Holzwarth, Germany

WM214 *Frangible Munitions for Reduced Collateral Damage*

Michael Minnicino, USA; Ryan Emerson, USA

THURSDAY, SEPTEMBER 25, 2008

7:00 am Continental Breakfast & Registration

8:00 am Administrative Remarks

8:10 am - 9:50 am General Session
Chaired by Zhongyuan Wang & Ed Schmidt

8:10 am *EB139 Numerical Computations of Dynamic Pitch-Damping Derivatives using Time-Accurate CFD Techniques*
Jubaraj Sahu, USA

8:30 am *GS195 Impact Effects of Light Shaped Charge Rockets with Ignition Failure on Thin Metal Armour Plates*
Hanspeter Kaufmann, Switzerland; Stephan Lampert, Switzerland

8:50 am *GS137 Consideration of the Ignition Delay of Gun Propellants*
Clive Woodley, UK; Michael Taylor, UK; Steve Fuller, UK; Steve Gilbert, UK; Joseph Gransden, UK

9:10 am *GS046 Electromagnetic Artillery*
Jerome Tzeng, USA; Ed Schmidt, USA

9:30 am *GS232 U.S. Army Tactical Wheeled Vehicle Vulnerability Test & Evaluation Methodology*
Stephanie Koch, USA

9:30 am - 3:30 pm Exhibit Hall Open

9:50 am - 10:10 am Coffee Break in Exhibit Hall

9:50 am - 11:50 am Exterior Ballistics; Interior Ballistics; Launch Dynamics Poster Sessions

10:10 am - 12:00 pm Warhead Mechanisms
Chaired by Chris Quan & Michael Murphy

10:10 am *WM085 The Appendix*
Eitan Hirsch, Israel; Meir Mayseless, Israel

10:30 am *WM256 Behind Armour Effects at Shaped Charge Attacks*
Manfred Held, Germany

10:50 am *WM211 Effect of Detonation Front Inversion on Directed Energy Output*
Ronald Brown, USA; Dimitrios Fanaras, USA; David Amondson, USA; Ronald Williams, USA; James Stork, USA; John Gamble, USA; Jose O. Sinibaldi, USA

11:10 am *WM016 Warhead Filling and Casing Interactions Affect the Blast Field Performance*
Paul Locking, UK; Dennis Flynn, UK; J. Dunnett, UK

11:30 am *WM234 Reaction of Metal Fragments from Cased Explosive Charges*
Laura Donahue, Canada; Robert Ripley, Canada; Jeff Leadbetter, Canada; Yasuyuki Horie, USA; Fan Zhang, Canada

12:00 pm - 1:30 pm Lunch - Armstrong Ballroom; 8th Floor

1:30 pm - 3:30 pm Armour & Personal Protection; Wound Ballistics & Vulnerability Poster Sessions

1:30 pm - 3:10 pm Interior Ballistics & Launch Dynamics
Chaired by Don Carlucci & Ken Kuo

1:30 pm *IB098 Numerical Simulation of Projectile Acceleration Process Using Solid/Gas Two-Phase Reacting Flow Model*
Hiroaki Miura, Japan; Akiko Matsuo, Japan; Yuichi Nakamura, Japan

1:50 pm *IB015 Two-Dimensional Modelling of Modular Charge Gun Firings*
Clive Woodley, UK; Steve Fuller, UK

2:10 pm *IB110 Numerical Simulation of Interior Ballistics Processes of a High Speed Counter-Mass Propelling Gun*
Xiaobing Zhang, China; Weiping Zhou, China; Haiqing Li, China

2:30 pm *LD027 Launch Dynamics Environment of a Water Piercing Missile Launcher*
Jon Yagla, USA; John Busic, USA; Samuel Koski, USA; Chris Weiland, USA

2:50 pm *LD065 Experiments with Gun Launched Penetrators into Gelatin Target Materials*
John Stubberfield, UK; Nicholas Lynch, UK; Clive Woodley, UK; Alan Hepper, UK

- 3:10 pm - 3:30 pm** Coffee Break in Exhibit Hall
- 3:30 pm - 8:30 pm** Exhibitor Move Out (Exhibit Hall CLOSED)
- 3:30 pm - 5:10 pm** Wound Ballistics & Vulnerability
Chaired by Phil Cunniff & Joe Backofen

- 3:30 pm** *WB053 The Validation of a Thoracic and Abdominal Test Rig for BABT Soft Body Armour Testing*
Kate Hewins, UK; Ian Horsfall, UK; Celia Watson, UK
- 3:50 pm** *WB005 Using LS-Dyna to Estimate After-barrier-effectiveness of Small Arms Projectiles*
Mark Minisi, USA
- 4:10 pm** *WB240 An Overview of the Operational Requirement-based Casualty Assessment (ORCA) Model and its Military Applications*
William Mermagen, USA; Patrick Gillich, USA
- 4:30 pm** *WB242 Survivability Measures for Evaluation of Personnel in Military Systems*
Natalie Eberius, USA; Patricia Frounfelker, USA; Kelly Benjamin, USA
- 4:50 pm** *WB144 Diagnostic Techniques for Multiphase Blast Fields*
Richard Ames, USA; Michael Murphy, USA

7:00 pm - 9:00 pm Symposium Banquet - Armstrong Ballroom; 8th Floor (included in attendee registration)

Join us for an evening of New Orleans-inspired food, traditional jazz music, and dancing!

INTERIOR BALLISTICS POSTER SESSION

LAUNCH DYNAMICS POSTER SESSION

EXTERIOR BALLISTICS POSTER SESSION

9:50 am - 11:50 am

CHAIRMAN: CHRIS VAN DRIEL

IB049 Effects of Condensed Phases in Primer Output on Charge Ignition in Small Ammunition

Lang-Mann Chang, USA; Anthony Williams, USA

IB051 A Study on the Erosion Characteristics of K9 Thunder 155mm 52Cal. SPH (Self Propelled Howitzer)

Jae Kab Kim, Korea; Byung Doo Choi, Korea; Seong Ho Park, Korea; No Seok Park, Korea; Yeon-Sik Cho, Korea

IB054 The Effect of a Balanced Breech 120 mm Tank Gun System on Gun Dynamics and Firing Accuracy

Eugene Adamovski, Israel; Ilan Azulay, Israel; Yoav Gur, Israel; Davis Touati, Israel; Boris Manilov, Israel

IB074 Ignition Behaviour of LOVA Propellant

Chris Van Driel, The Netherlands

IB078 Linking Ignition and Transient Loading on a Medium Caliber Projectile

Richard Beyer, USA; Albert Horst, USA

IB090 Medium Caliber Lead Free Electric Primer

Robert Brewer, USA; Sarah Ford, USA; Kelvin Higa, USA

IB098 Numerical Simulation of Projectile Acceleration Process Using Solid/Gas Two-Phase Reacting Flow Model

Hiroaki Miura, Japan; Akiko Matsuo, Japan; Yuichi Nakamura, Japan

IB131 Interior Ballistics Characterization of a 40-mm Cartridge

Andrew Brant, USA; Joseph Colburn, USA; Anthony Williams, USA

IB147 Combustion Model for TAGzT and TAGzT Mixtures

Clint Conner, USA; William Anderson, USA

IB151 Revised Model for RDX Combustion

William Anderson, USA; Gabriel da Silva, USA; Clint Conner, USA; Rubik Asatryan, USA; Joseph Bozzelli, USA

IB169 The Effects of Igniter Design on the Interior Ballistic Performance of Deterrent Coated Propellants

Thelma Manning, USA; Kelly Moran, USA; Steven Ritchie, USA; Joseph Colburn, USA; Barrie Homan, USA; Carlton Adam, USA; Michael Ellis, USA; D. Park, USA; E. Rozumov, USA; S. M. Gilbert, USA; C.R. McMurray, USA

IB196 Experimental and Numerical Study of Reduction of Pressure Wave in Large Caliber Gun Chamber

Yuichi Nakamura, Japan; Hiroaki Miura, Japan; Akiko Matsuo, Japan

IB219 Matching Internal Ballistics Code Fidelity to Gun System and Analysis Complexity

Martin Pocock, UK; T. Melvin, UK; I. Robertson, UK; C. Woodley, UK; Chris Guyott, UK

IB223 Collection and Modelling of 155mm Artillery Projectile In-Bore Ballistic Data

George Yorke, USA; Don Carlucci, USA

IB249 Study for the Bore Resistance Factors Due to Friction and Engraving in NATO STANAG 4367, Edition 3

James Matts, USA; Ari Tuomainen, Finland

LD013 A Case Study on Flight Failure of a Supersonic Spinning Rocket and Successful Problem Solving through Modal Analysis & Testing

K M Rajan, India; Anil Datar, India; Surendra Kumar, India

LD024 Balloting in a Frenet Frame

Satoru Shoji, Japan

LD081 3D Unsteady Intermediate Ballistics Modelling: Muzzle Brake and Sabot Separation

Roxan Cayzac, France; T. Alziary de Roquefort, France; E. Carette, France

LD165 Occasion-to-Occasion Tank Gun Error Sources

Mark Bundy, USA; Jim Garner, USA; Dave Webb, USA; Paul Durkin, USA

EB039 Miss to Hit

Petrus Karsten, South Africa; Chris Botha, South Africa

EB059 Mathematical Modeling of Lift Sabot Separation Process

Ravindra Shriram Acharya, India; Smita D. Naik, India

EB076 Dual Mode Mortar Munition System

Yanina Rubenchik, Israel; Haim Yahia, Israel; Boris Manilov, Israel; Aron Pila, Israel; David Touati, Israel; Albert Mamane, Israel; Yuval Levy, Israel

EB082 Computational Fluid Dynamics Modeling of a Course Corrected Artillery Projectile at Transonic Speeds

Jubaraj Sahu, USA; Karen Heavey, USA; Richard Buretta, USA

EB086 NATO Shareable Software Developing into True Suite Supporting National Operational, Fire Control Systems

André Sowa, USA

EB087 NATO Testing in Turkey Shows Benefit of Meteorological Forecast Data to Indirect Fire Support

André Sowa, USA; Birger Hansen, Denmark; Sevsay Aytar Ortaç, Turkey

EB088 Liquid Payloads Impact on the Trajectory of Spinning Projectiles

Gene Cooper, USA; Mark Costello, USA

EB096 Aerodynamic and Ballistic Analysis of Rifled Mortar Munition

Hyunsung Jung, Korea; Ui Chang Hwang, Korea; Joo-Sung Kim, Korea

EB118 Research of Aerodynamic Structure and Correctional Ability for One-Dimensional Trajectory Correction Projectile

Zhongyuan Wang, China; Xiaobing Zhang, China; Jinguang Shi, China; Wenjun Yi, China; Zhiming Qiu, China

EB120 Algorithm Scheme for Tightly Integrated GPS/INS Navigation System in Large Dynamic Occasions

Lee Being, China

EB194 Fast Safety Checks for Numerical Trajectory Calculations

Alexander Kuhrt, Germany; Hendrik Rothe, Germany

EB255 On The Stagnation Point Reynolds Number of Supersonic Projectiles

William Reinecke, USA

ARMOR & PERSONAL PROTECTION POSTER SESSION

1:30 pm - 3:30 pm

CHAIRMEN: EWA LIDEN, ERICK SAGEBIEL & VELERIY KARTUZOV

APP007 On the XCT Diagnostics of Ballistic Impact Damage in a B₄C Ceramic Body Armor Plate

Joe Wells, USA; Nevin Rupert, USA

APP012 Numerical Simulation of Mine Detonation Beneath a Generalized Add-On Armor Structure

Sharon Peles, Israel; David Touati, Israel; Avi Neuberger, Israel; Ilan Azulay, Israel

APP034 Nondestructive Damage Assessment of Alumina Structural Ceramics

Raymond Brennan, USA; William Green, USA; James Sands, USA; Jian H. Yu, USA

APP044 Advances in Ballistic Performance of Commercially Available Saint-Gobain Sapphire Transparent Armor Composites

Christopher Jones, USA; Jeff Rioux, USA; John Locher, USA

APP055 Armour Materials: A Preview into a Resource-Poor Future, Implications for the Development of Armour Materials

Andre Diederer, The Netherlands

APP062 A Computational Study of the Energy Dissipation through an Acrylic Target Impacted by Various Size FSP

Costas Fountzoulas, USA; Peter Dehmer, USA; Jian Yu, USA; James Sands, USA

APP066 Analysis of Terminal Metallic Armor Plate Free-Surface Bulging

Edward Rapacki, USA

APP099 Collateral Damage Caused by Reactive Armour Protection Against PG-7-Like Threats

Martin van de Voorde, The Netherlands; Koen Bakker, The Netherlands; Frans van Wegen, The Netherlands

APP105 Response of the Plate to the Buried Blast Mine Explosion

Stanislav Rolc, Czech Republic; Jaroslav Buchar, Czech Republic; Josef Kratky, Czech Republic; Rolf Graeber, Czech Republic; Jaroslav Pechacek, Czech Republic; M.Havlicek, Czech Republic

APP121 Effect of Ceramics, Fibre Reinforced Plastics and Aluminium Used as Confinement Plates for Explosive Reactive Armours

Stefano Bianchi, Switzerland; Hanspeter Kaufmann, Switzerland; André Koch, Switzerland

APP122 Ballistic Protection of Fragment Vests Against IED Threat

Hans Broos, The Netherlands; M.J. van der Jagt-Deutekom, The Netherlands; M.J. van de Voorde, The Netherlands

APP126 Experimental Tests and Numerical Calculations using ALE and SPH Approaches on Mine Blast Effects on Structure

Geneviève Toussaint, Canada; Amal Bouamoul, Canada

APP140 Investigation of a Methodology for Producing Variable Damage in Structural Armor Ceramics

William Green, USA; Jian Yu, USA; Raymond Brennan, USA; James Sands, USA

APP153 High-Speed Photographic Study of Wave Propagation and Impact Damage in Novel Glass Laminates

James McCauley, USA; Elmar Strassburger, Germany; Parimal Patel, USA; Doug Templeton, USA; Arun Varshneya, USA

APP160 Structure, Properties and Dynamic Response of Polypropylene Fibers and Textiles

Michael Sennett, USA; Elizabeth Welsh, USA; Peter Stenhouse, USA; Philip Cunliffe, USA; Thomas Godfrey, USA; Deana Archambault, USA

APP163 Simulation of Damage to a Vehicle by Explosion of an Improvised Explosive Device

Chris Quan, USA; John Pavon, USA

APP170 Hybrid Particle-Element Simulation of Body Armor Impact Physics

Kwon Joong Son, USA; Eric Fahrenthold, USA

APP172 A Possible Approach in Support of the Characterization of Body Armors

Nevin Rupert, USA

APP183 Ballistic Impact Performance of Clothing Items Under Impact by Munition Fragments

Phillip Cunliffe, USA

APP184 Variability in Ballistic Impact Performance due to Projectile Physical Properties and Dimensions

Phillip Cunniff, USA

APP186 The Importance of Off-Normal Obliquity Impact Performance to the Casualty Reduction Potential of Ballistic Protective Helmets

Phillip Cunniff, USA

APP187 Assessment of the Ballistic Impact Performance of Variable Response Armor Systems

Phillip Cunniff, USA

APP188 The Effect of Preform Shape on Ballistic Impact Performance, Coverage and Seam Density in Combat Helmets

Jason Parker, USA; Phillip Cunniff, USA

APP198 Developing Simulation Capabilities to Link Textile Manufacturing to Ballistic Performance

Bryan Cheeseman, USA; Chian Yen, USA; Brian Scott, USA; Bruce LaMattina, USA; Yuyang Miao, USA; Youqi Wang, USA

APP199 Ballistic Testing of SSAB Ultra-High Hardness Steel for Armor Applications

Matthew Burkins, USA; William Gooch, USA; Dwight Showalter, USA; Rosmari Stockman Koch, Sweden

APP209 Ballistic Properties of Hybrid Systems for Transparent Armor Applications

John Song, USA; Nicholas Tsantinis, USA; Roy Paulson, USA

APP220 Characterizing Collateral Damage to Dismounted Troops and Other Personnel located near Active Counter Measures

Patricia Frounfelker, USA; Kathleen Doonan, USA

APP236 Ballistic Evaluation of Aluminum 2139-T8

Bryan Cheeseman, USA; Matthew Burkins, USA; William Gooch, USA

APP244 Impact of Soldier Helmet Configuration on Survivability

Natalie Eberius, USA; Patrick Gillich, USA

WOUND BALLISTICS & VULNERABILITY POSTER SESSION

1:30 pm - 3:30 pm

CHAIRMEN: BO JANZON & JOE WELLS

V041 V/L TARVAC BBN Based Understanding of Combat Damage and Operational Readiness Consequences to Assess Proportional Fire Power (Lethality)

Theo Verhagen, The Netherlands; M.F.G. van der Wurff, The Netherlands; Th.P.J. Van Rijn, The Netherlands; L.J. van Peteghem, The Netherlands

V042 (In)Sensitive Ammunition Impact on V/L TARVAC Modelling

Theo Verhagen, The Netherlands; R.H.B. Bouma, The Netherlands; R. Boeschoten, The Netherlands

V043 Munition – MOUT Effects Modelling: Embedding Experimental Research in V/L TARVAC Assessment

Theo Verhagen, The Netherlands; M.J. van de Voorde, The Netherlands; E. van Meerten, The Netherlands; Th.P.J. van Rijn, The Netherlands

V123 Comparison of Methods to Measure the Blast Impulse Loading of an Explosive Charge

Pieter Smith, South Africa; Frikkie Mostert, South Africa; Izak Snyman, South Africa

V124 Terminal Ballistics of HE Ammunition for Counter-RAM Systems

Markus Graswald, Germany; Hendrik Rothe, Germany

V142 Perspectives on the Requirements, Development, and Outputs of an X-Ray Computed Tomography Image Processing Application for Ballistic Impact Analysis in Armor Samples

Jeffrey Wheeler, USA; Nevin Rupert, USA; Joe Wells, USA

V173 Damage Assessment Method of Complex Shape Surface Target Based on Image Manipulation

Lu Yonggang, China

V245 Lethality of Bursting Munitions and Their Effect on Survivability

Natalie Eberius, USA; Kathleen Doonan, USA

V254 The Measurements of Overpressure of Thermobaric Grenade and Analysis of its Power

Chen Hao, China; Tao Gang, China

WB005 Using LS-Dyna to Estimate After-barrier-effectiveness of Small Arms Projectiles

Mark Minisi, USA

WB006 Simulating Ordinance Gelatin Impacts Using LSDyna; Correlations and Challenges

Mark Minisi, USA

WB069 Computational and Experimental Study of Paintball Impact Ocular Trauma

Walt Gray, USA; James Walker, USA; William Sponsel, USA; Carl Weiss, USA

WB071 Theoretical Study of the Motion of a Rigid Gyro-Stabilized Projectile into Homogeneous Dense Medium

Nestor Nsiampa, UK; Gunther Dyckmans, UK

WB114 Ensemble Effect for the Penetration by Non-Metallic Particles

Matthias Wickert, Germany

WB116 How to Quantify the Effects of Non-lethal Kinetic Weapons

Philippe Drapela, Switzerland; Stephan Lampert, Switzerland; R. Lorenzo, Switzerland

WB218 U.S. Army Research Laboratory Support to the Small Arms Capabilities Based Assessment

Gregory Dietrich, USA; James Newill, USA; William McLaughlin, USA

WB241 A New Small Caliber Evaluation Methodology Using Operational Requirement-based Casualty Assessment (ORCA)

Patrick Gillich, USA; Timothy Myers, USA

FRIDAY, SEPTEMBER 26, 2008

7:00 am Continental Breakfast & Registration

8:00 am Administrative Remarks

8:10 am - 9:30 am General Session

Chaired by Francisco Galvez & Dennis Baum

8:10 am *TB020 Deformation and Breakup of Tungsten Alloy Cubes, Cylinders and Spheres on Aluminum Plates*
Karl Weber, Germany

8:30 am *GS023 Predicting Hazard Response Scenarios in Weapon Systems*
Ian Cullis, UK; I.H. Brown, UK; P.D. Church, UK; P. Gould, UK; V.E. Ingamells, UK

8:50 am *GS130 Experimental Validation of a Kevlar Fabric Model for Ballistic Impact*
Chian Yen, USA; Tusit Weerasooriya, USA; Paul Moy, USA; Brian Scott, USA; Bryan Cheeseman, USA

9:10 am *GS205 Shaped Charge Penetration of Gas Saturated Sandstone*
Brenden Grove, USA; Jeremy Harvey, USA

9:30 am - 9:50 am Coffee Break

9:50 am - 12:00pm Terminal Ballistics

Chaired by James Cazamias & Patrik Lundberg

9:50 am *TB025 Penetration Resistance of Glass and a Glass Ceramic*
Stephan Bless, USA; Don Berry, USA

10:10 am *TB111 Long-Rod Penetration into Intact and Pre-Damaged SiC Ceramic*
Charles Anderson, USA; Thilo Behner, Germany; Dennis Orphal, USA; Arthur Nicholls, USA; Timothy Holmquist, USA; Matthias Wickert, Germany

10:30 am *TB058 The Shock Response Of a Cemented Tungsten Carbide*
Koen Herlaar, The Netherlands; Andre Diederer, The Netherlands; Gareth Appleby-Thomas, UK; Paul J Hazell, UK

10:50 am *TB038 GRC's Impact Behavior*
Alejandro Enfedaque Diaz, Spain; David Cendón Franco, Spain; Francisco Gálvez Díaz-Rubio, Spain; Vicente Sánchez Gálvez, Spain

11:10 am *TB237 Experimental Determination of Strain in Fabrics under Ballistic Impact*
Sidney Chocron, USA; K. Samant, USA; Arthur Nicholls, USA; Carl Weiss, USA; James Walker, USA; Charles Anderson, USA

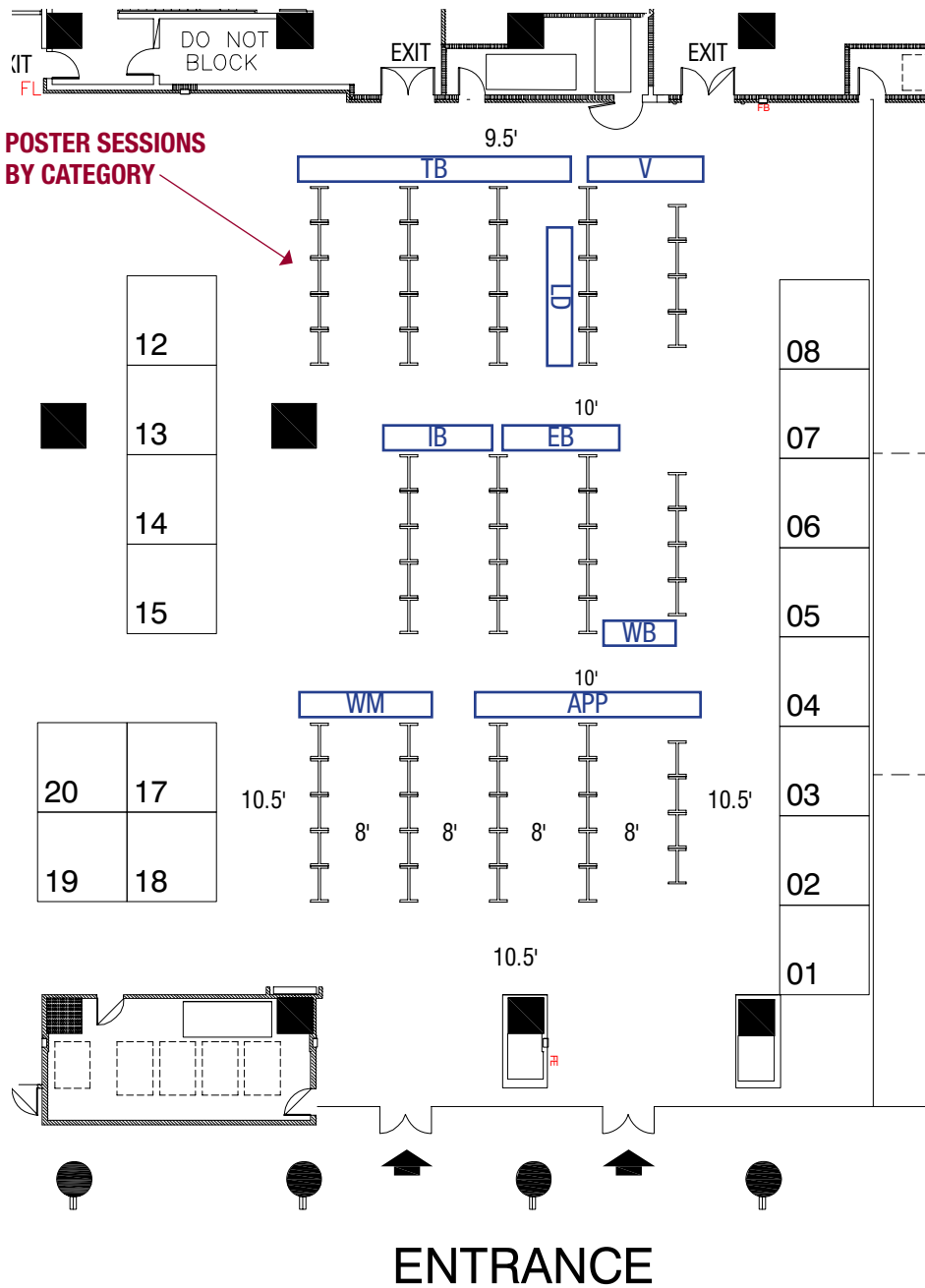
11:30 am *TB248 The Mechanics of Projectile Arrest for Compliant Cross Plied Unidirectional Laminates*
Brian Scott, USA; Bryan Cheeseman, USA

12:00 pm - 12:30 pm Presentation of Awards

12:30 pm - 12:45 pm Future Symposia Announcements

- ▶ 25th International Symposium on Ballistics - China
- ▶ 26th International Symposium on Ballistics - USA

12:45 pm Symposium Adjourns



ANSYS, INC.....	4
ARROW TECH ASSOCIATES.....	14
DRS DATA & IMAGING SYSTEMS.....	6
FRAZER-NASH CONSULTANCY.....	5
KISTLER INSTRUMENTS.....	3
MS INSTRUMENTS PLC.....	7
25 TH IBC - BEIJING.....	8
NATIONAL TECHNICAL SYSTEMS CORP.....	15
NEW LENOX MACHINE CO. INC.....	13
PHOTO-SONICS, INC.....	1
SAINT-GOBAIN CERAMICS & PLASTICS, INC.....	12
UTRON, INC.....	2
WEIBEL.....	17

PROMOTIONAL PARTNERS

Arrow Tech

Formed in 1987 Arrow Tech Associates Inc. has been providing world-class support in ammunition design and analysis including structural analysis, dynamic analysis, weapons system simulation.

Throughout history there has been a need for rapid, accurate analysis of ammunition performance. With strong skills in both engineering analysis and software development, we have been able to answer this need for our customers. Arrow Tech has been a crucial and integral team member on many weapon system design teams in both civilian and government industry ranging from Olympic Archery to Artillery Systems and everything in between.

In 1992 Arrow Tech decided to make available our internal engineering software tools that we used to accomplish our design and analysis tasks and thus the first commercially available comprehensive ammunition design package came into being. PRODAS, (Projectile Rocket Ordnance Design and Analysis Software) is now one of the most widely used and advanced ammunition design toolkits available, with over 500 users worldwide and continual development and improvements.

Analysis modules help the user estimate mass properties, predict aerodynamics and stability, fly trajectories including guided projectiles and simulate interior ballistics, in bore balloting, or rocket motors. The latest release of PRODAS captures over 45 years of experience within the industry.

Arrow Tech is proud to be a co-sponsor of this year's International Ballistics Symposium with the NDIA in New Orleans. Please feel free to stop by our booth (#14) as we look forward to talking to our current and future customers.

Foster-Miller, Inc.

LAST® Armor, the largest approved supplier of armor for fixed-wing aircraft in the United States, supports C-130s, C-17s and C-5s with add-on armor. LAST® Armor also makes a unique add-on armor appliqué system for armored vehicles and rotary-wing aircraft that installs without any cutting, welding or drilling on the base vehicle. LAST® tactical vehicle armor kits can be sent forward to deployed vehicles and the simple installation can be performed by the vehicle crew itself. It is most often affixed using a patented, high-strength Velcro® hook-and-loop fastening system.

LAST® Armor is a division of QinetiQ North America's Technology Solutions Group (TSG). Headquartered in Waltham, MA, TSG includes the businesses of Foster-Miller, Inc., and its subsidiaries Planning Systems Incorporated, Automatika, Applied Perception, Spectro, Inc., and the research and development activities of Apogen Technologies, Inc. It is a technology and product development group with an international reputation for delivering innovative products and systems that perform under the most demanding conditions.

Weibel

Weibel Scientific A/S is a designer and manufacturer of scientific measurement equipment for testing and experimental applications. Its customers include armies, navies, and air forces; test ranges; research and development establishments; ordnance industries; and security forces. Weibel's products include Doppler radar-based equipment ranging from small compact Doppler radar systems to high-performance, on-line, 3-D Doppler radar tracking systems for long-range (>1,000 km) flight analysis. Weibel Doppler radar systems are based on the most up-to-date radar, computer, and software technologies, and incorporate such unique features as self-calibration and multi-object tracking. Weibel Scientific manufactures all mechanical parts, electronics and software in house in its company owned facility just outside of Copenhagen, Denmark.

THANK YOU TO OUR PROMOTIONAL PARTNERS





Diagnostic Techniques for Multiphase Blast Fields

Richard Ames
Raytheon Missile Systems

Michael Murphy
Lawrence Livermore National Laboratory

With Contributions from

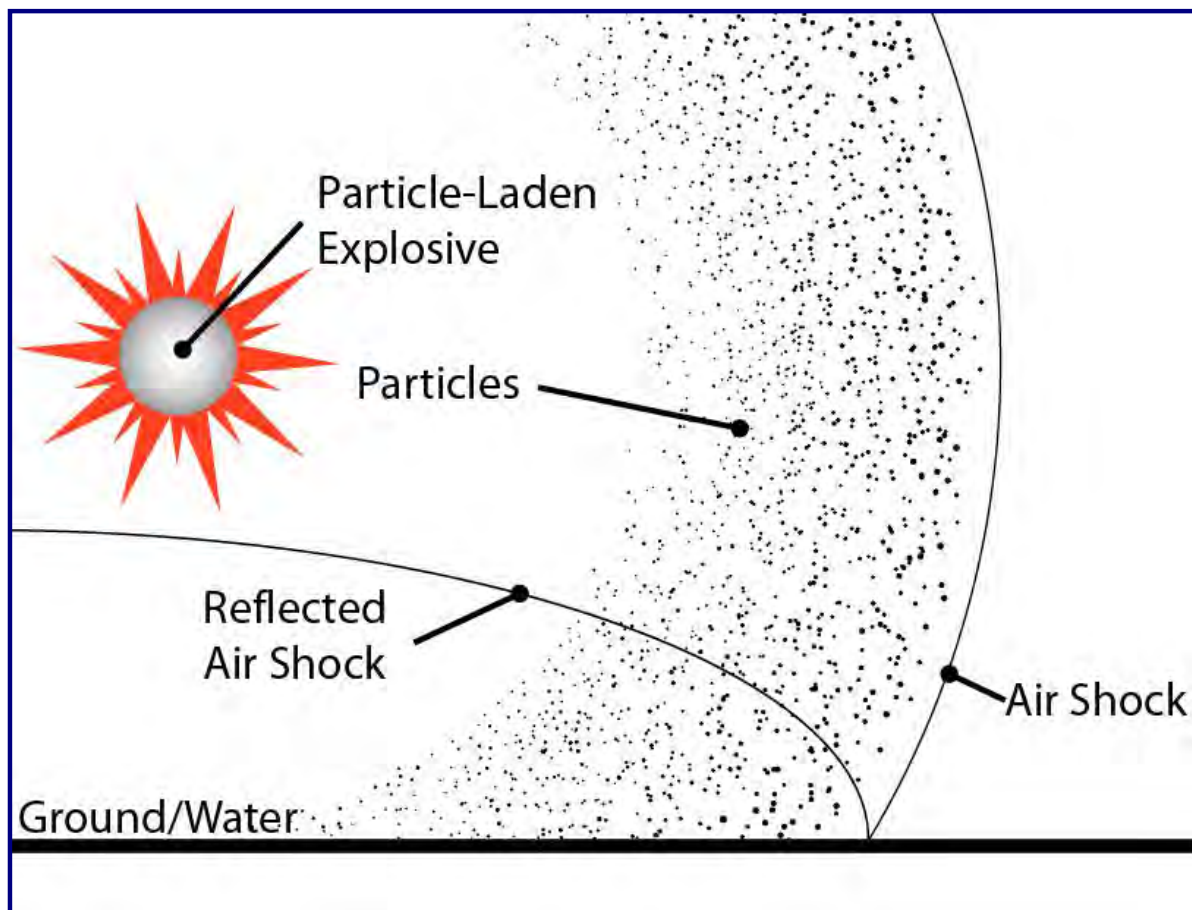
Scott Groves, Mitch Moffett
LLNL

Don Cunard, Alan Orht
AFRL Eglin

Jason Drotar
NSWC Dahlgren

Multi-Phase Blast Flows

- “ Multi-Phase Blast Flows are produced by particle-laden explosives
- “ Can also be produced when a standard explosive entrains dust and debris
- “ A key unknown is how much energy/momentum is transported in each phase within the blast field

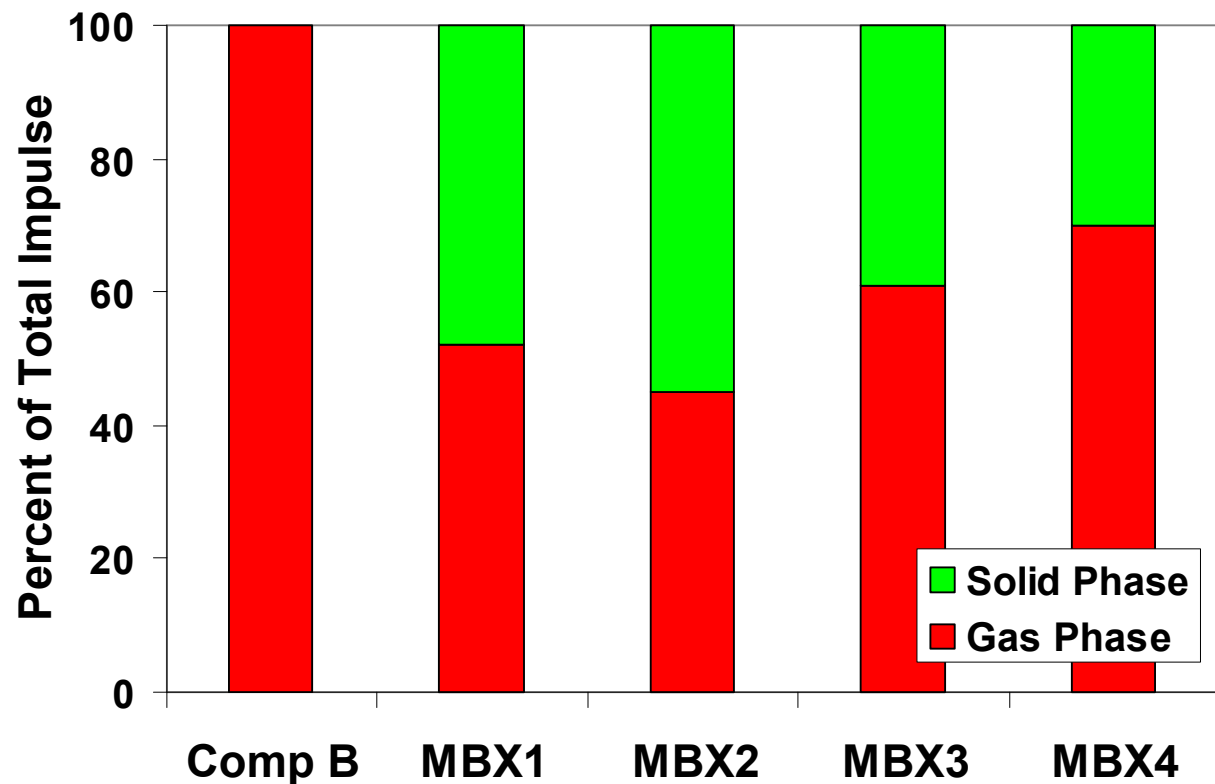


Typical MBX Blast Field

Relative Amounts of Momentum Mix in MBX Blast Flows



*Measurements of
Momentum
Transfer Against
a Flat-Plate
Target for Four
Types of
Multiphase Blast
Explosives (MBX)*



- “ The solid-phase component of MBX blast fields carries a substantial amount of momentum and energy
 - . Can be as much as 50% for some blast flows
- “ As a consequence, characterization of this class of multiphase flows must accurately account for the solid phase

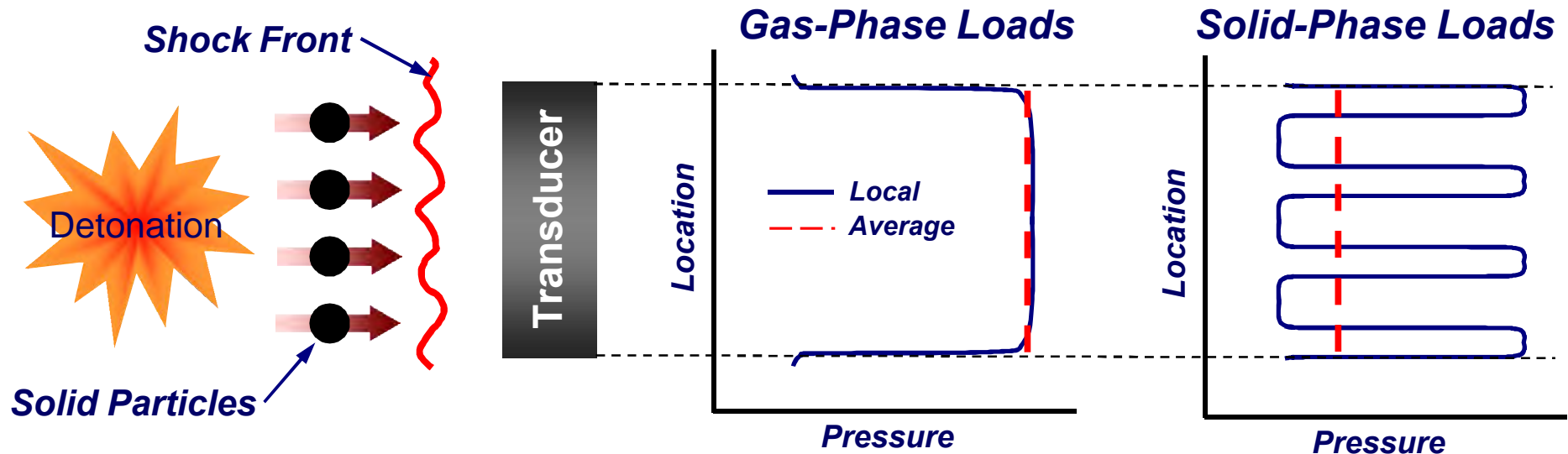


Your complimentary
use period has ended.
Thank you for using
PDF Complete.

[Click Here to upgrade to
Unlimited Pages and Expanded Features](#)

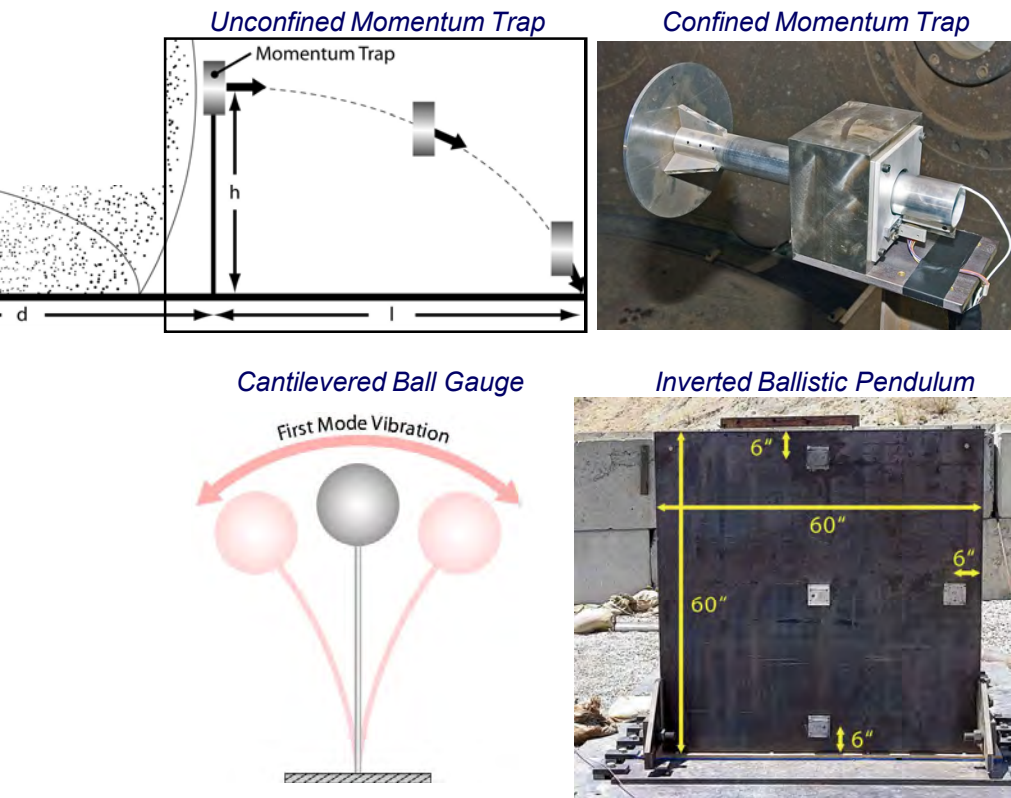
Diagnostic Techniques

Measurement Problem for Multi-Phase Blast Flows



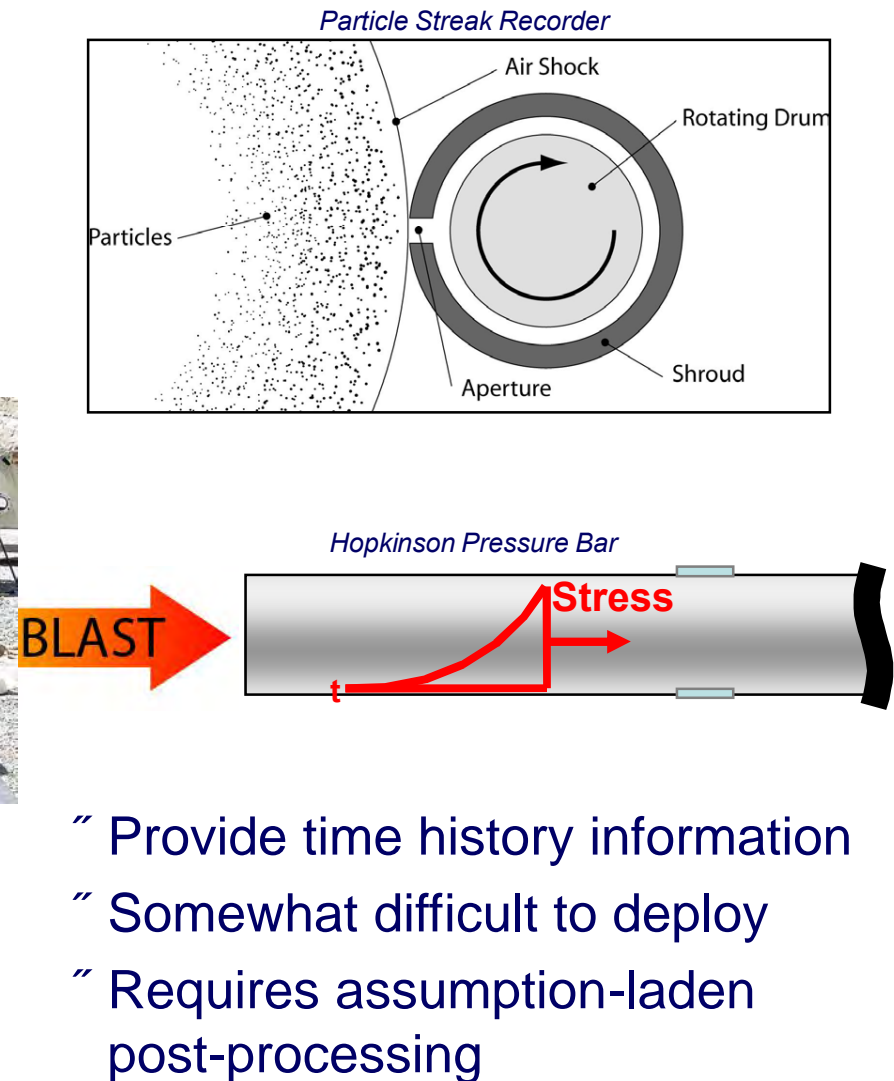
- “ Most pressure transducers are designed under the assumption of rough equivalence between small-scale, local loads and global, average loads
 - “ Good assumption for gas-phase loads because the impulse associated with individual molecular impacts is extremely small
- “ Not valid for distributed solid-phase loads
 - “ Local loads much larger than global average

Impulse Traps



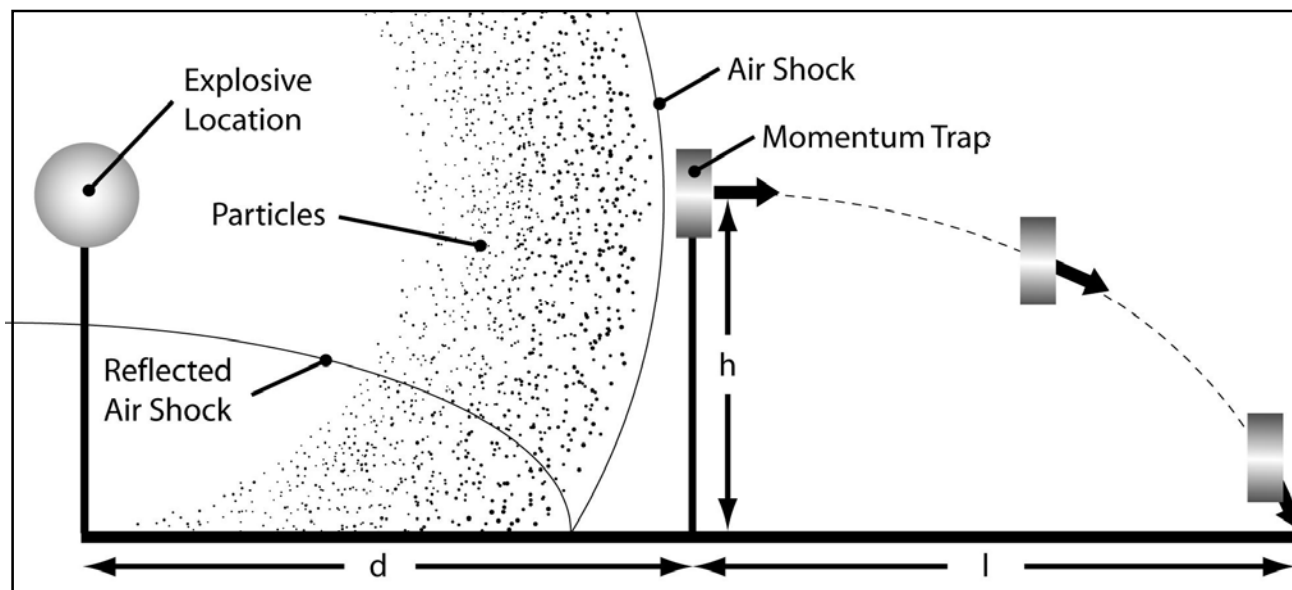
- " No time history information available
- " Easy to deploy
- " Simple physics

Time-Varying Diagnostics



- " Provide time history information
- " Somewhat difficult to deploy
- " Requires assumption-laden post-processing

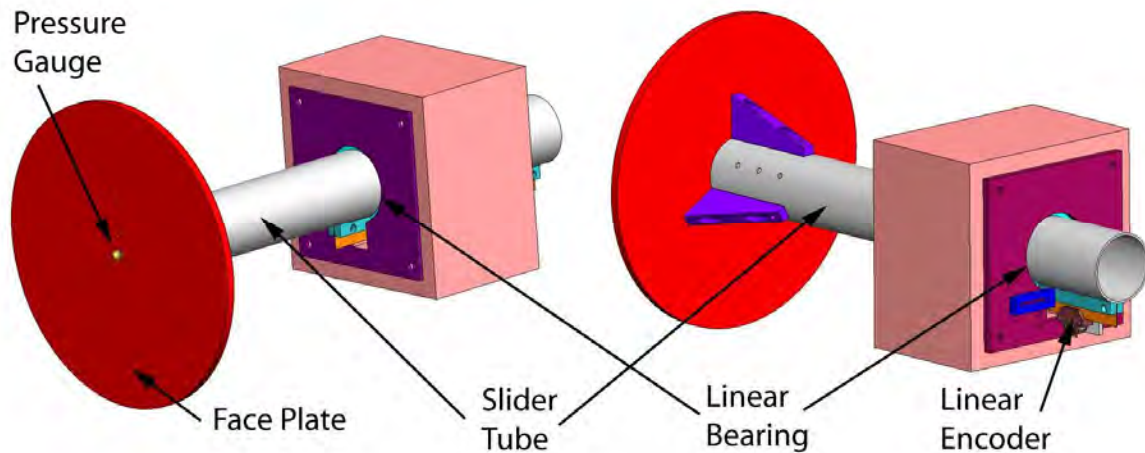
Unconfined Momentum Trap (UMT)



$$I = \frac{m_b l}{\sqrt{2h/g}}$$

- “ The Unconfined Momentum Trap (UMT) is a disk placed normal to the charge at some height
- “ The distance the trap is thrown is proportional to the impulse delivered to the face
 - . Assumes time scales associated with loads are much less than time scales associated with loading
 - . Neglects drag
- “ Different shapes can be used to provide information regarding target geometry effects

Confined Momentum Trap

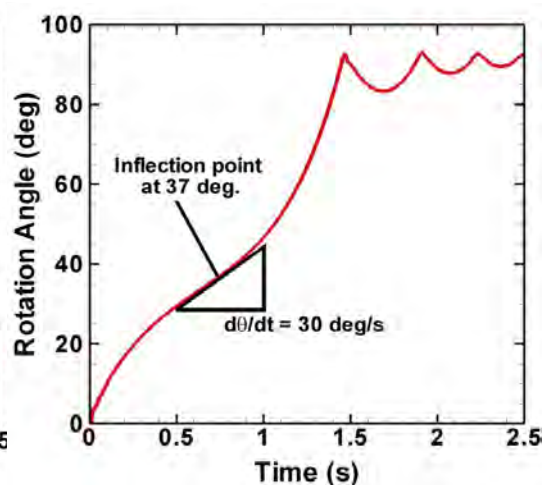
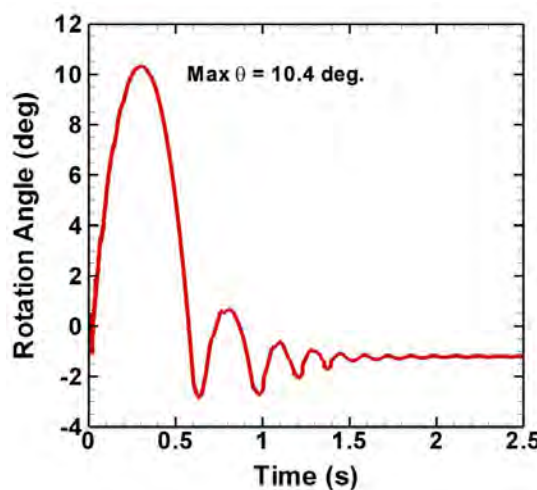
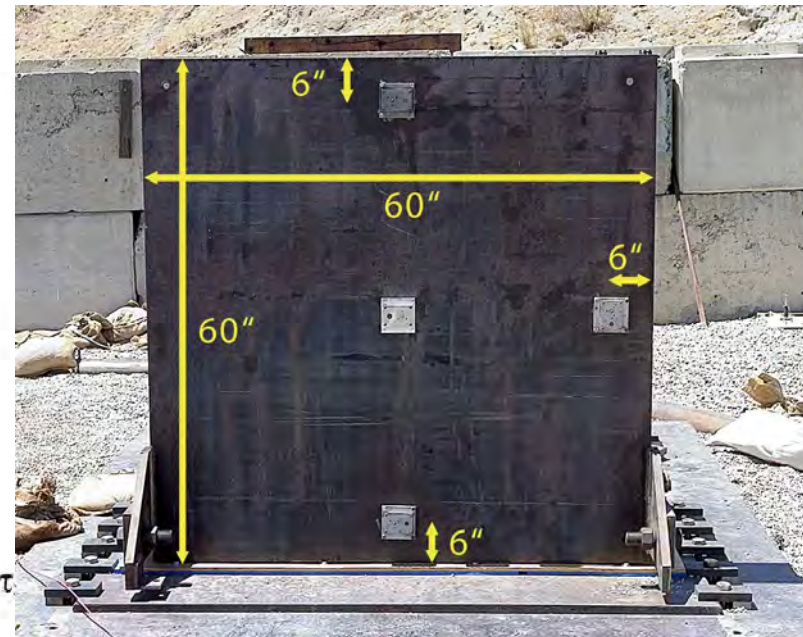
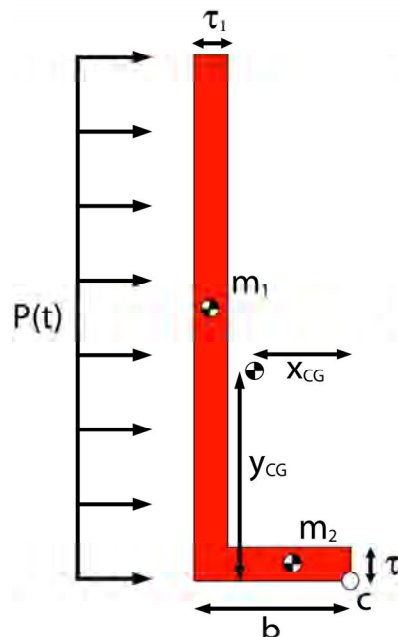


- “ Uses a disc on a slider tube with optical position encoder
- “ The time-history of the motion provides a measure of the impulse delivered to the Face Plate
- “ Face plate also includes a pressure gauge so that gas-phase loads may be measured

Inverted Ballistic Pendulum (IBP)

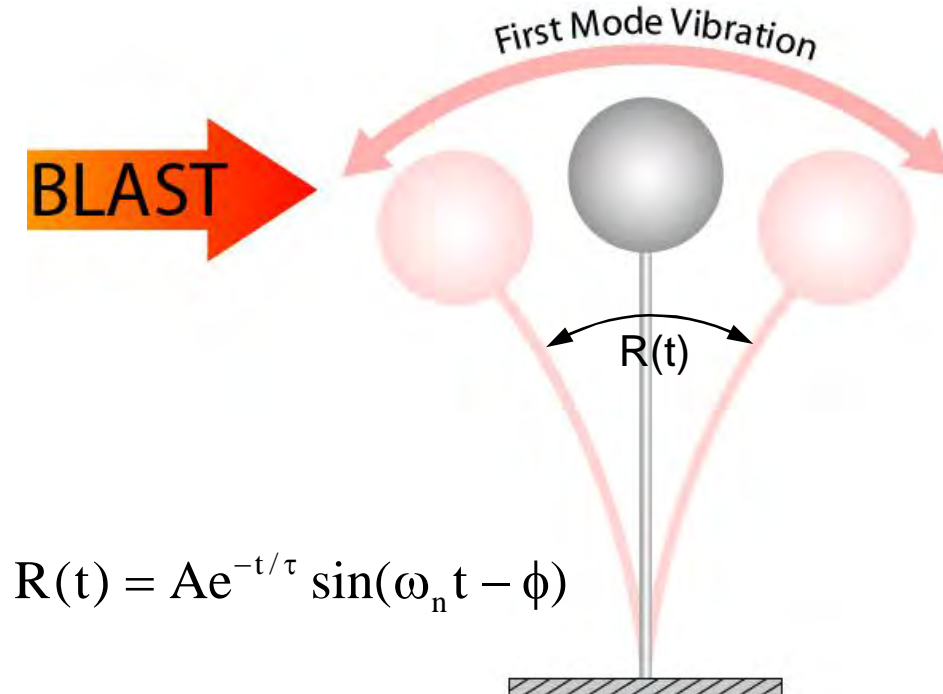


- “ The IBP is a large flat plate on a pivoting base
- “ Tip angle is proportional to impulse
- “ If the wall tips over the impulse is measured by the angular speed as the CG passes vertically over the pivot

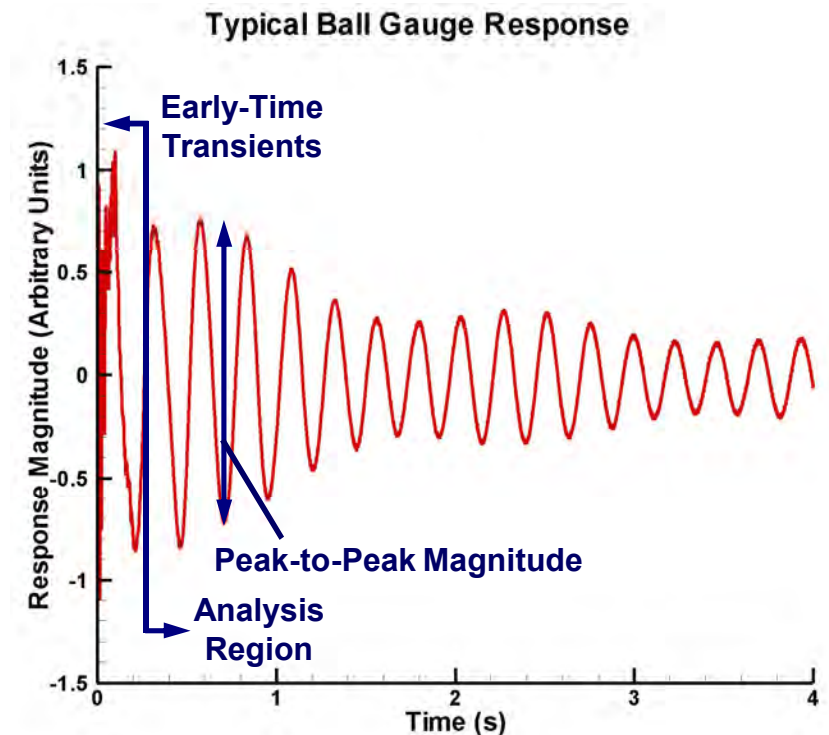


$$\begin{aligned} \theta < \theta_{\text{tip}} \quad I &= \left[\frac{8(m_1 + m_2)gJ_c (\sqrt{x_{\text{cg}}^2 + y_{\text{cg}}^2} \sin(\theta + \theta_0) - y_{\text{cg}})}{h^4 w^2} \right]^{\frac{1}{2}} \\ \theta > \theta_{\text{tip}} \quad I &= \left[\frac{8J_c}{h^4 w^2} \left[(m_1 + m_2)g(\sqrt{x_{\text{cg}}^2 + y_{\text{cg}}^2} - y_{\text{cg}}) + \frac{1}{2}J_c \dot{\theta}_{\text{IP}}^2 \right] \right]^{\frac{1}{2}} \\ \theta = \theta_{\text{tip}} \quad I_{\text{min}} &= \left[\frac{8(m_1 + m_2)gJ_c (\sqrt{x_{\text{cg}}^2 + y_{\text{cg}}^2} - y_{\text{cg}})}{h^4 w^2} \right]^{\frac{1}{2}} \end{aligned}$$

The Cantilevered Ball Gauge

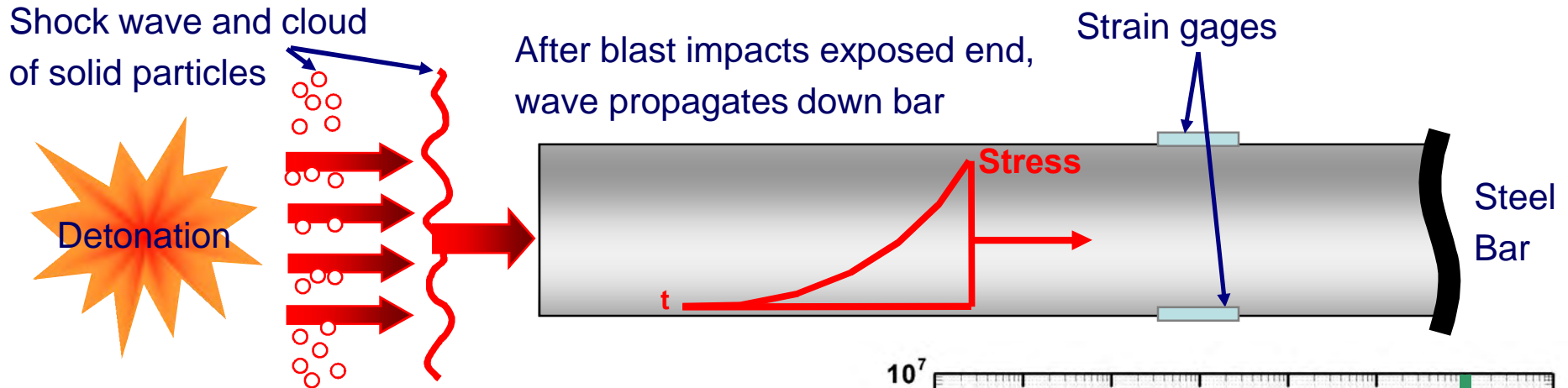


$$R(t) = Ae^{-t/\tau} \sin(\omega_n t - \phi)$$



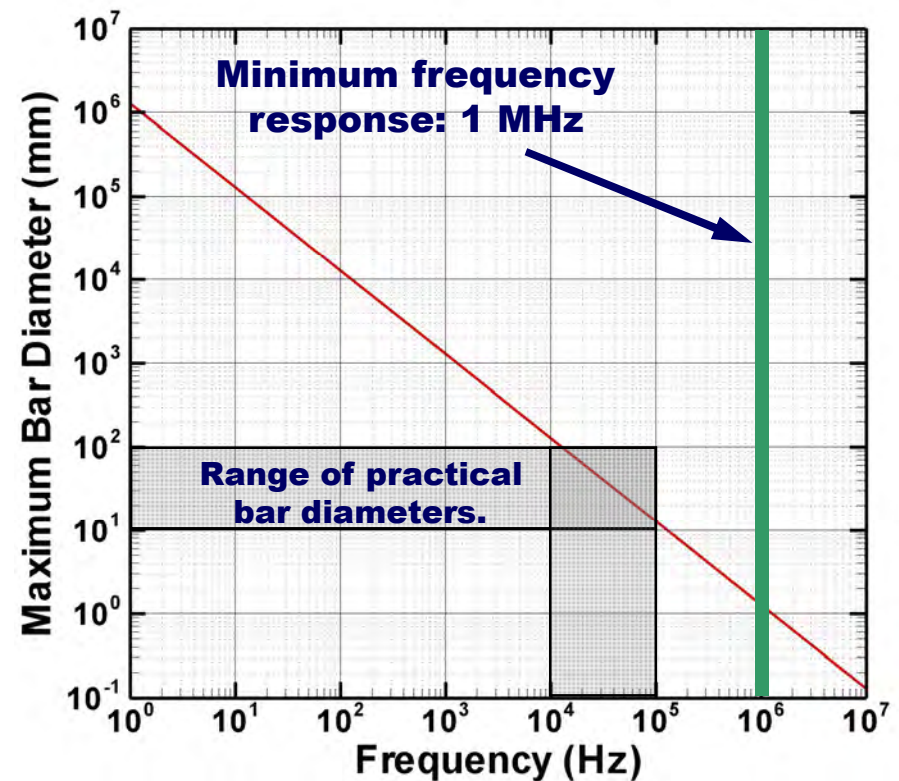
- “ Measures the total impulse delivered to a sphere on a slender rod via strain measurements that capture the vibratory motion
- “ Measurements taken in orthogonal directions in order to compute total loading in a plane normal to the sting mount
- “ Under the assumption that the loading time scales \ll structural response time scales, total impulse is proportional to the magnitude of the structural response in the first bending mode

The Hopkinson Bar

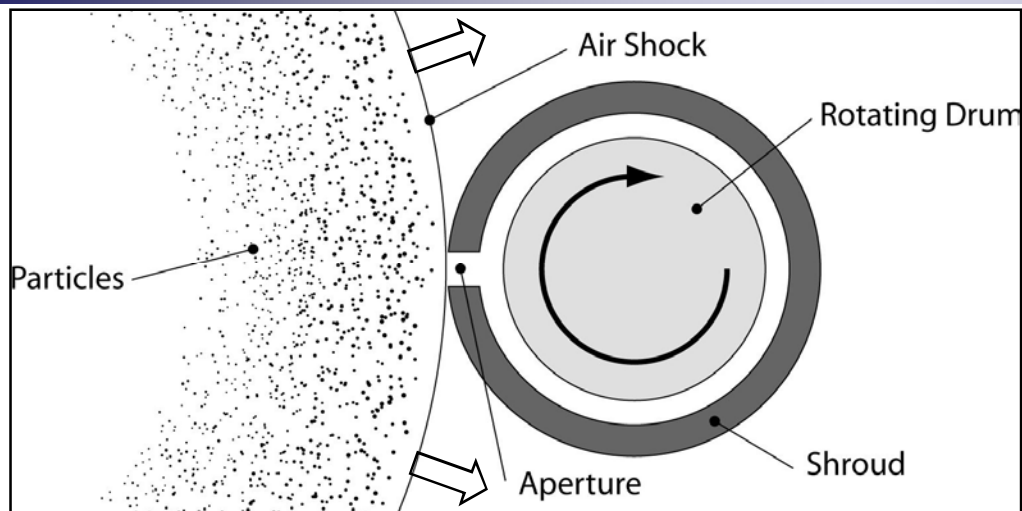


$$r < \frac{0.465c_0}{2\pi\nu f} \quad \text{For less than 5\% dispersion.}$$

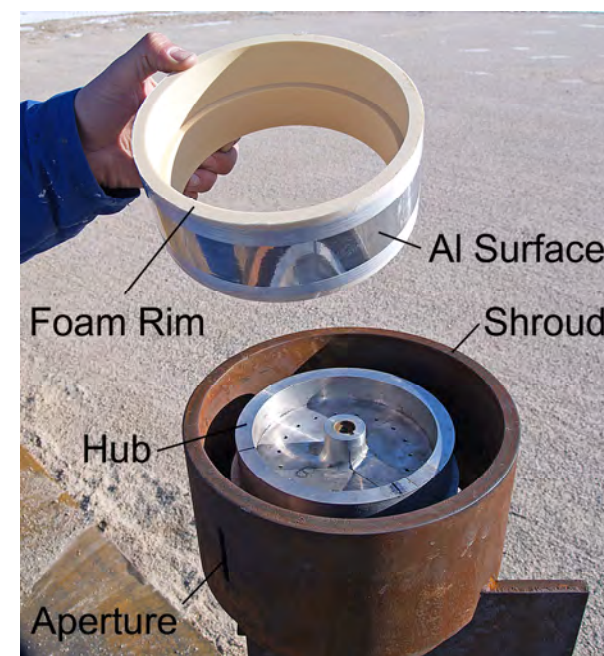
“ High Frequency components of the load move more slowly through the bar, altering the signal



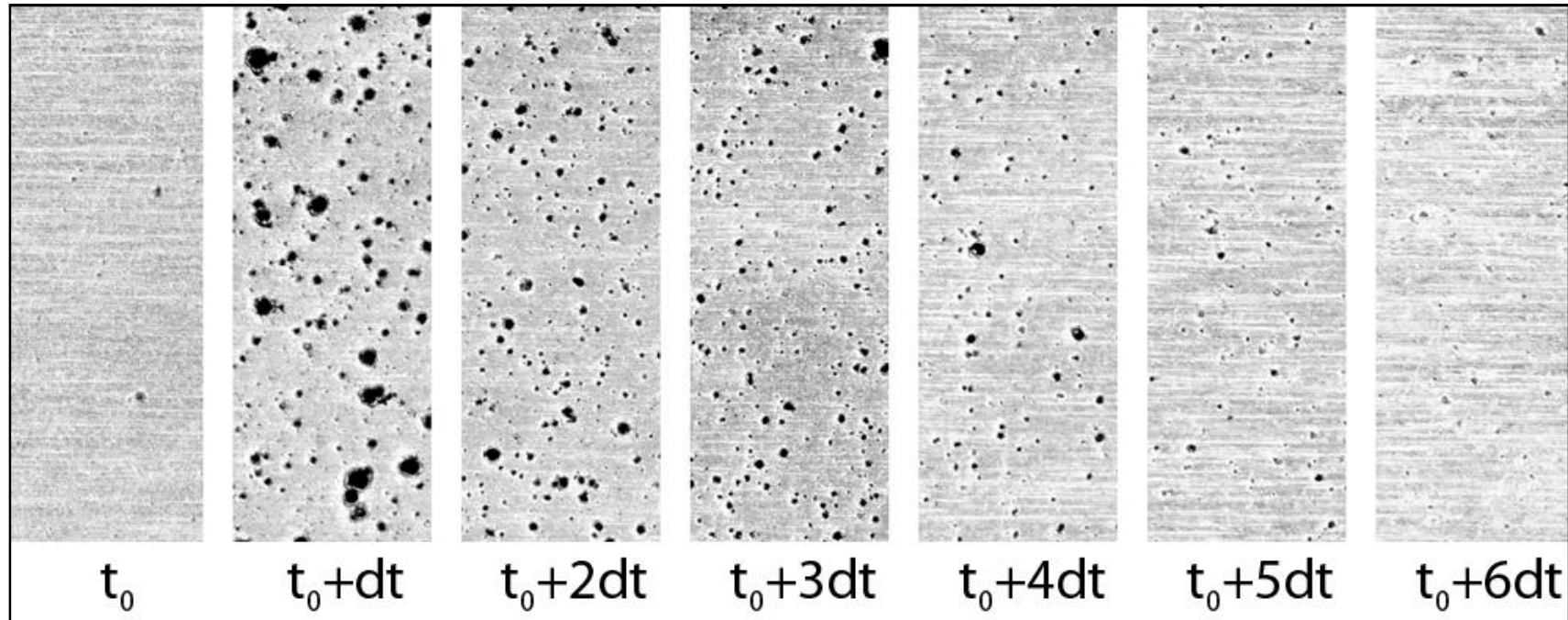
Particle Streak Recorder (PSR)



- “ Uses a rotating disc behind a thin aperture
 - Thin aluminum on a high-density foam core attached to an aluminum hub
 - Different RPMs used at different standoffs to account for differences in blast duration
- ” Provides a measure of the time history of the number density of particles
 - Can be used to estimate momentum flux given assumptions about the time dependence

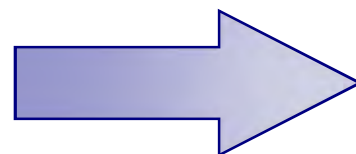
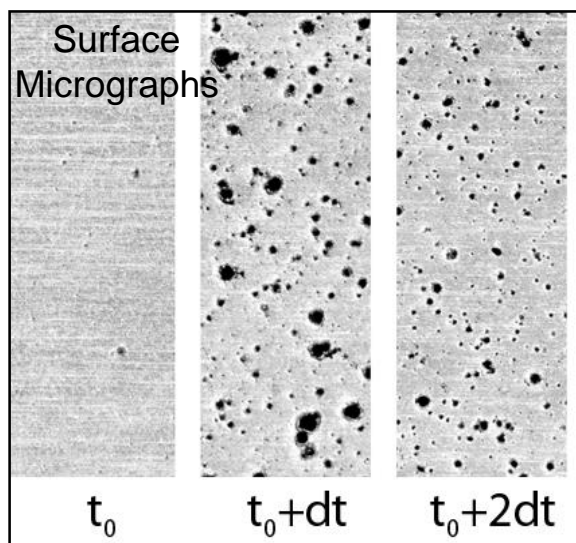


Raw Data from Particle Streak Recorders

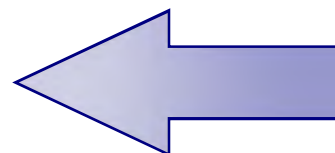
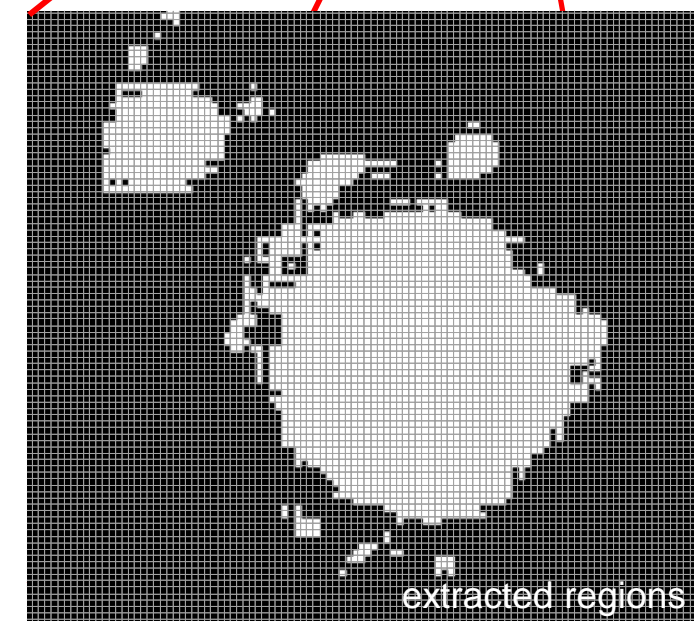
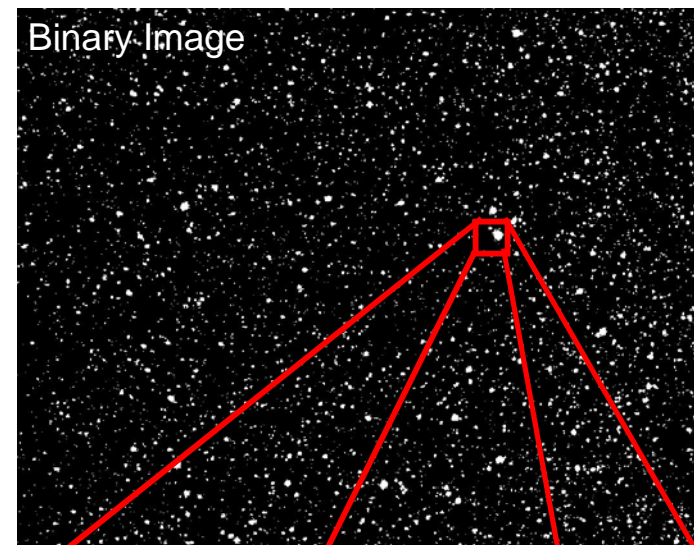


- ” The PSR data records give a measure of the time history of particle number density passing through the aperture
 - . Normally expressed as number of particles per unit area
 - . Errors arise when multiple particles produce a single hole
- ” Also provides statistics on hole sizes
 - . Relationship to actual particle sizes is difficult to define

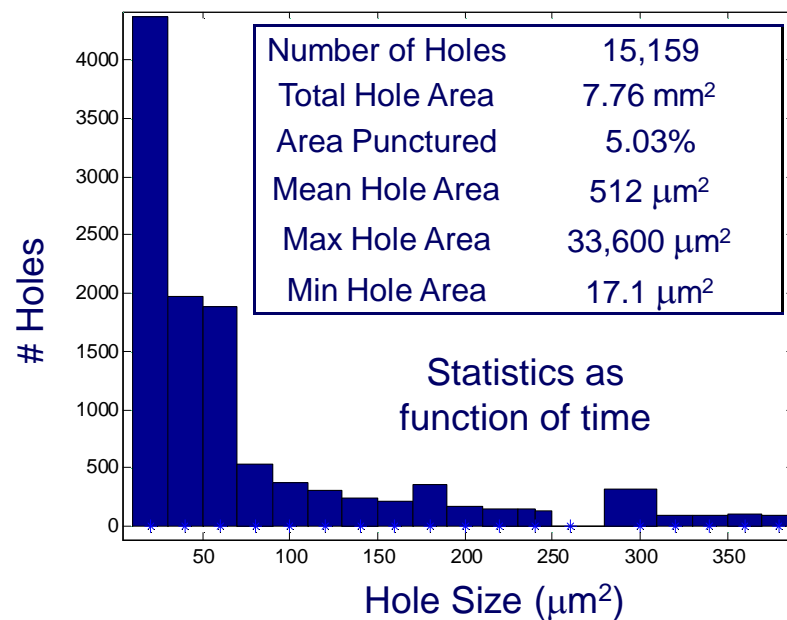
R Impact Surface Analysis Technique



**Image processing
algorithm
implemented in
Matlab**



**Connectivity
algorithm
implemented
in Matlab**



Data Analysis Procedure

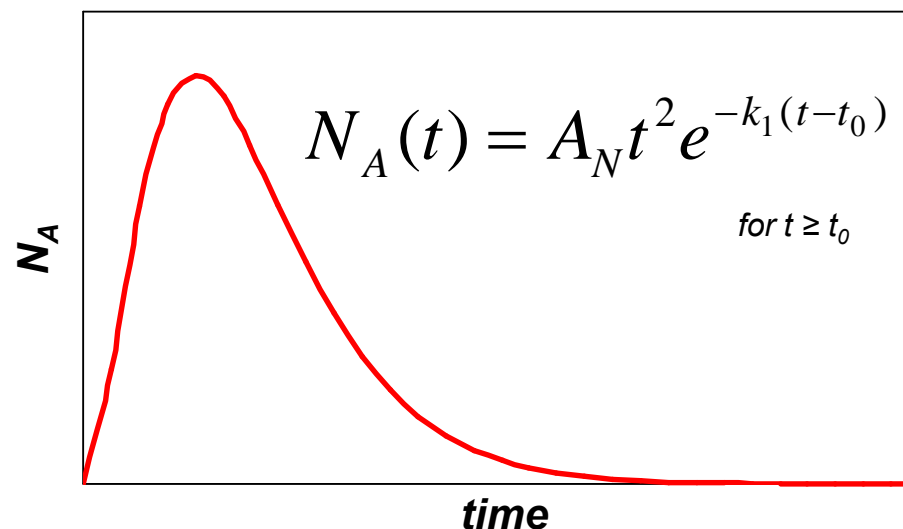


“ Momentum flux rate is simply the mass per particle times the average particle speed times number density flux rate

$$\frac{dp_A}{dt} = m_p V_p \frac{dN_A}{dt}$$

“ Data from a number of tests show that the number density flux has a modified decaying exponential behavior

- t^2 term accounts for behavior at the front of the particle wave



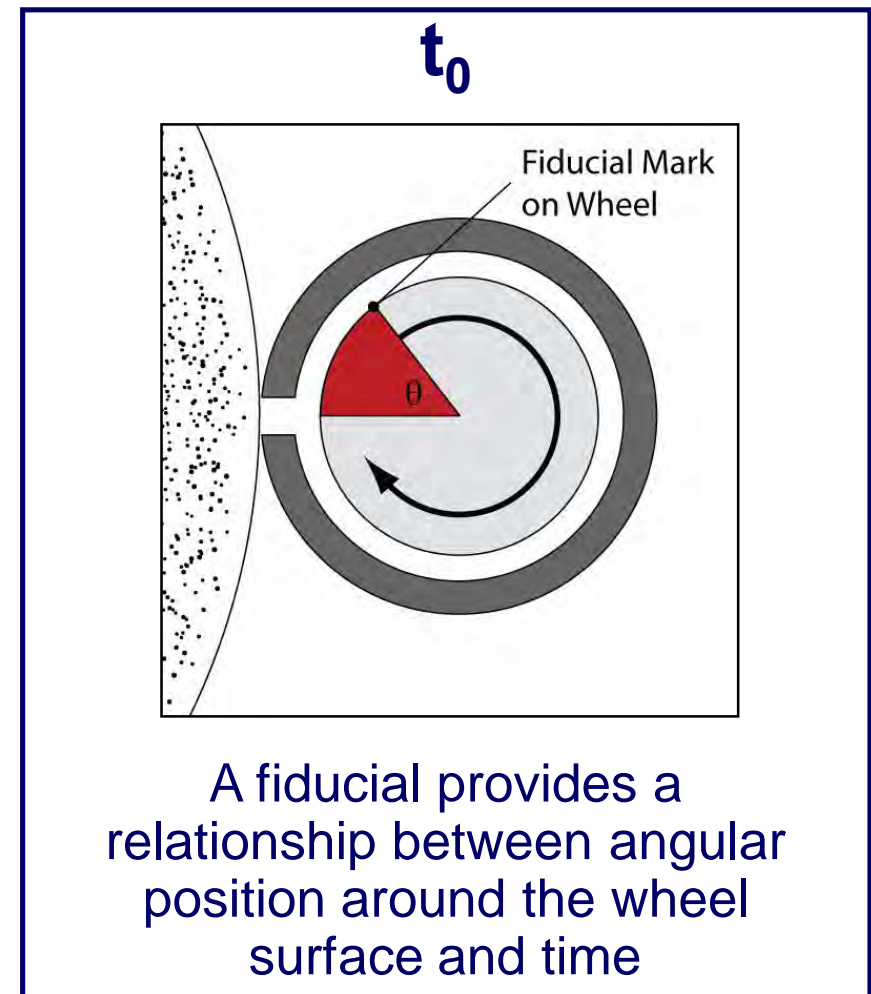
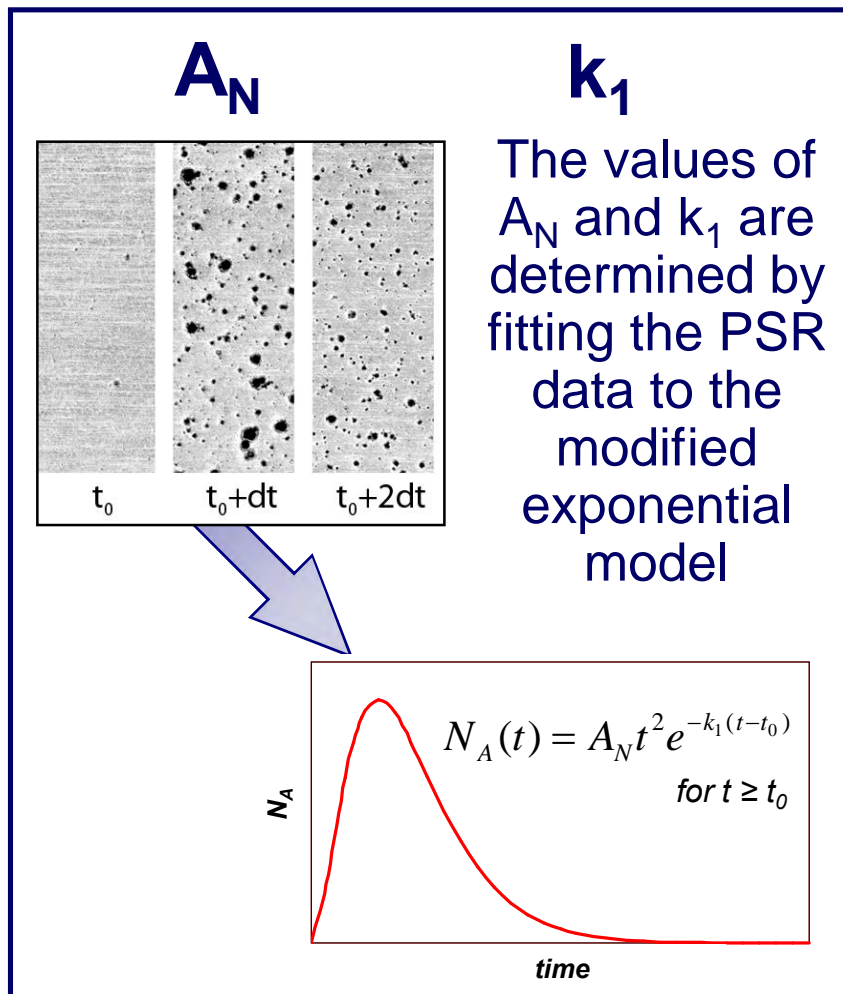
“ Particle speed is calculated based on arrival time and allowed to decay exponentially

$$V_p = \frac{d}{t} e^{-k_2(t-t_0)} \quad \text{for } t \geq t_0$$

Data Analysis Procedure

The data analysis procedure then reduces to finding four parameters:

A_N , k_1 , k_2 , and t_0



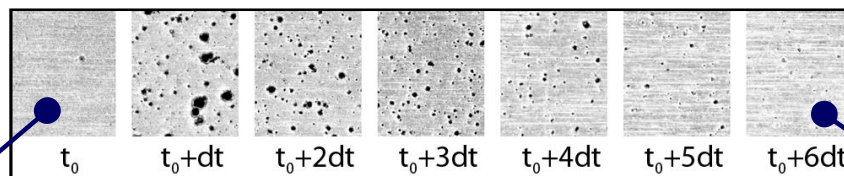
Data Analysis Procedure

The data analysis procedure then reduces to finding four parameters:

A_N , k_1 , k_2 , and t_0

k_2

For a given particle material and PSR surface material, the minimum marking speed V_{min} can be estimated.



**First appearance
of particles: t_0**

**Last evidence of
particles: t_1**

The estimate for V_{min} along with measurements of t_0 and t_1 will give the particle velocity decay constant k_2 .

$$V_p = \frac{d}{t} e^{-k_2(t-t_0)} \Rightarrow V_{min} = \frac{d}{t_1} e^{-k_2(t_1-t_0)} \Rightarrow k_2 = \frac{1}{t_0 - t_1} \ln \left(\frac{V_{min} t_1}{d} \right)$$

Finding the Impulse from the PSR Data

- “ Once the constants A_N , k_1 , k_2 , and t_0 are determined, the solid-phase impulse can be computed
- “ The impulse (per unit area) is the time integral of the momentum flux rate
 - . Assumes particle impacts are perfectly plastic
- “ Given the total impulse measurement from the Unconfined Momentum Trap, the difference between the two is the gas-phase impulse
 - . Note that these values are usually normalized to surface area

$$I_{A,SP} = \int_{t_0}^{\infty} \frac{dp_A}{dt} dt$$



$$I_{A,SP} = \frac{m_p dA_N [1 + (k_1 + k_2)t_0]}{(k_1 + k_2)^2}$$

$$I_{A,tot} = I_{A,GP} + I_{A,SP}$$


 From momentum
 trap


 From PSR



*Your complimentary
use period has ended.
Thank you for using
PDF Complete.*

[Click Here to upgrade to
Unlimited Pages and Expanded Features](#)

Wrap-Up and Summary

Review of Techniques

Diagnostic Technique	Time varying?	Separates loads by phase?	Measurement Fidelity
Unconfined Momentum Trap	No	No . total only	High
Confined Momentum Trap	No	Yes	Moderate
Inverted Ballistic Pendulum	No	Yes	Moderate
Cantilevered Ball Gauge	No	No . total only	Low
Hopkinson Pressure Bar	Yes	No . total only	Moderate
Particle Streak Recorder	Yes	No . solid phase only	Low

- “ This presentation has given an introduction to the state-of-the-art in multiphase blast diagnostic techniques
- “ These techniques are generally time-integrated
 - . Time-varying measurement techniques for solid-phase loads are relatively immature
- “ Improvements in hole detection will allow increases in the fidelity of the Particle Streak Recorder Technique
 - . Currently investigating alternate impact surface configurations to enable higher signal-to-noise ratio

Long-Rod Penetration into Intact and Pre-Damaged SiC Ceramic

Charles E. Anderson, Jr.

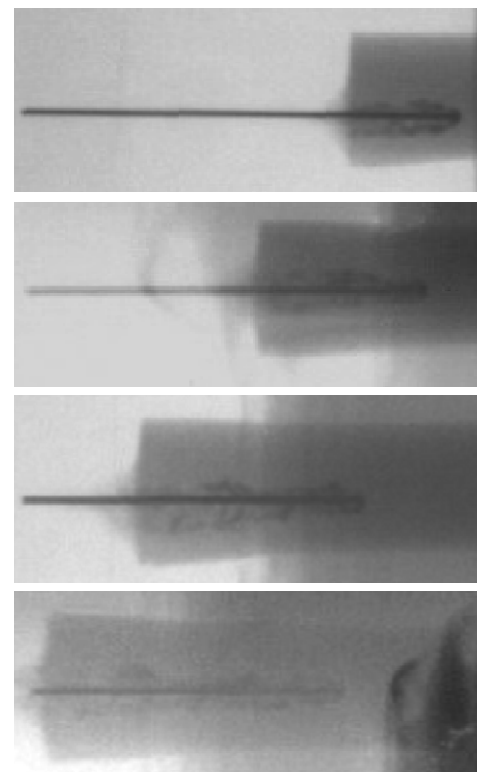
Thilo Behner

Dennis L. Orphal

Arthur E. Nicholls

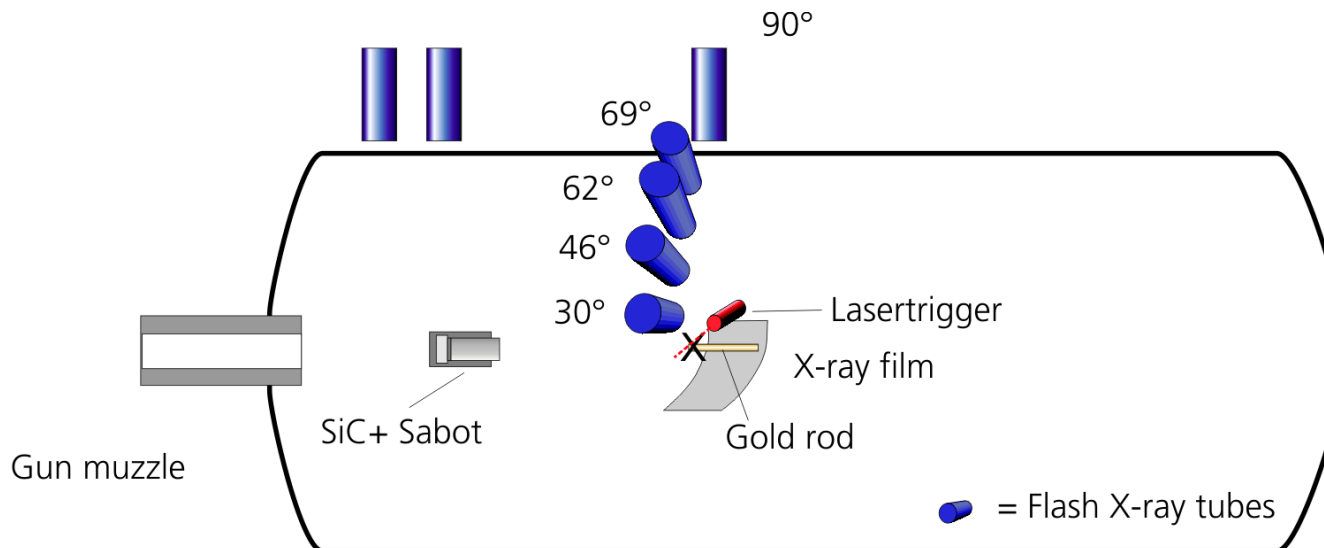
Timothy J. Holmquist

Matthias Wickert



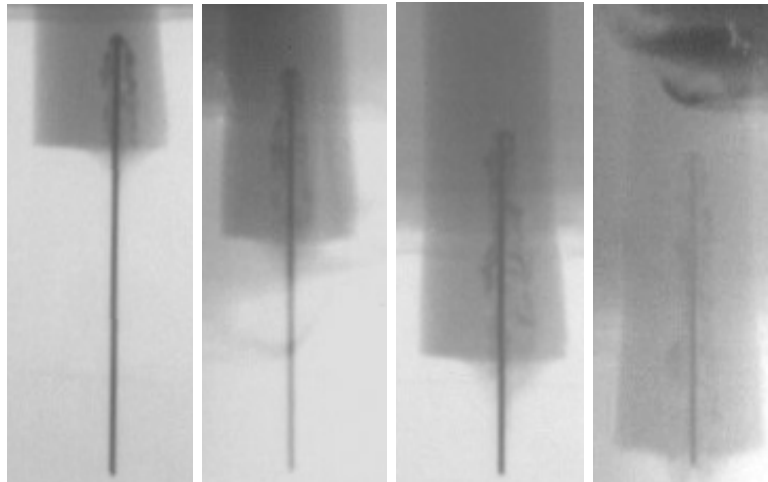
September 2008

Experimental Set-up

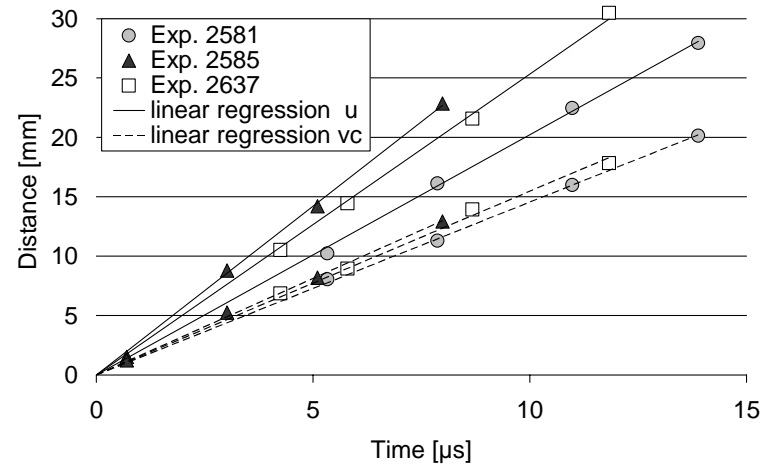


- *Reverse ballistics experiments*
- *Flash radiography used to measure position of nose and tail of rod versus time*

Penetration Experiments



Expt 2581



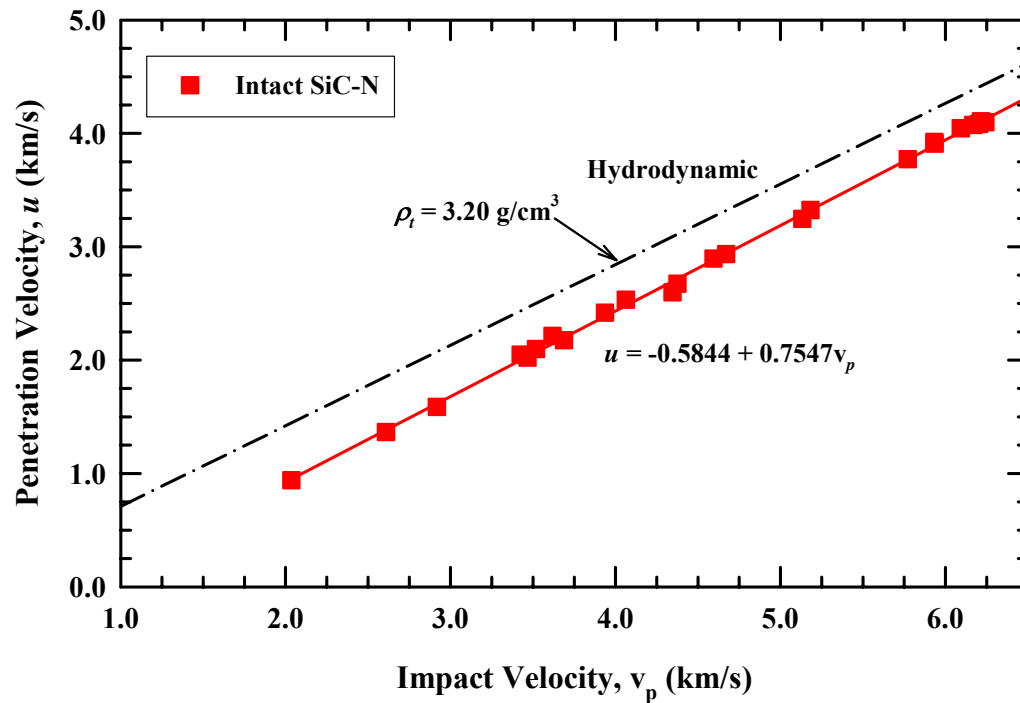
■ Regression fits

- Penetration vs. time
- Rod length vs. time

■ Slopes of regression fits

- Penetration velocity
- Consumption velocity

Penetration Velocity vs. Impact Velocity



Experiments & Analysis: 2002 - 2005

Experiments to Explore Penetration of Damaged Ceramic



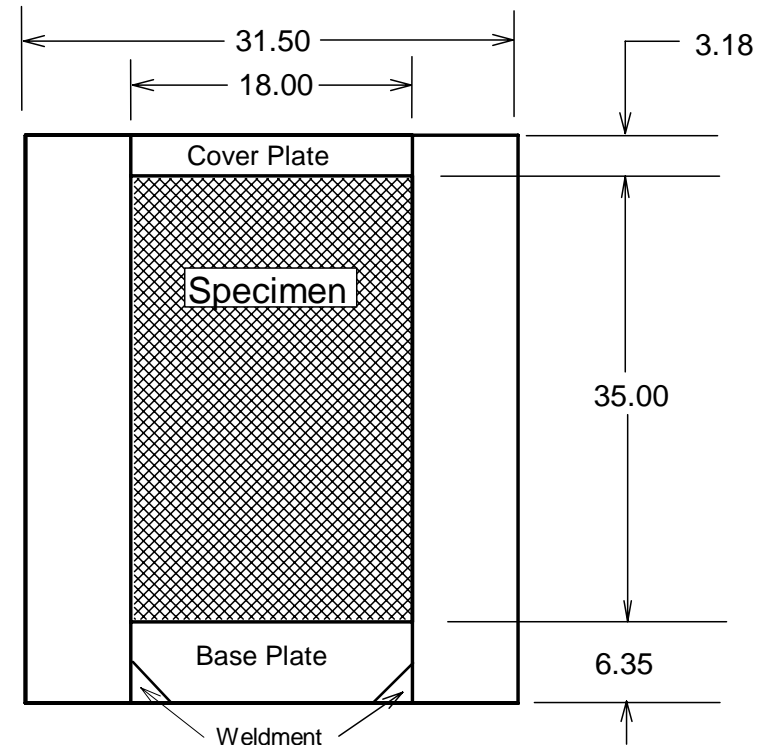
- *Conflicting interpretations for strength of damaged ceramic*
- *Designed experiments to investigate penetration response of various “damaged” SiC*
 - *Pre-damaged (thermal cycles that induced cracks)*
 - *In-situ comminuted (thermal cycle plus load/reload cycles in a MTS machine)*
 - *Compacted powder*

Experiments & Analysis: 2006 - 2007

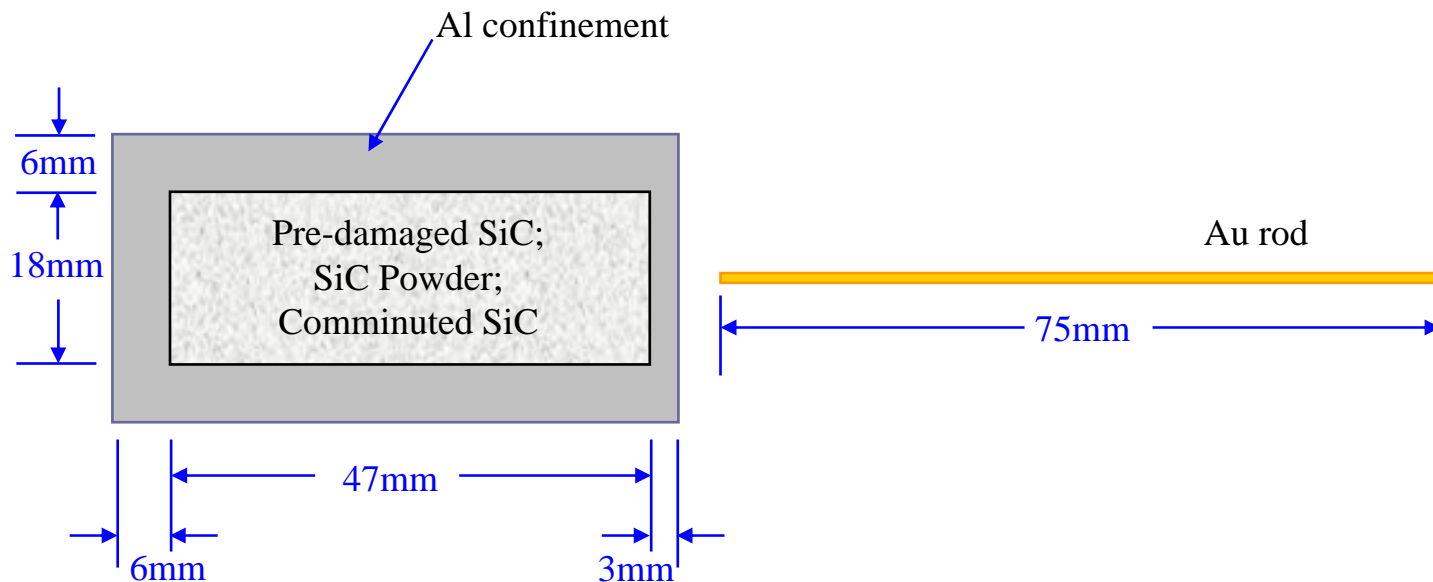
Target Design



- *7075-T6 aluminum sleeve*
- *Base plate welded*
- *Cover plate press-fit w/superglue*

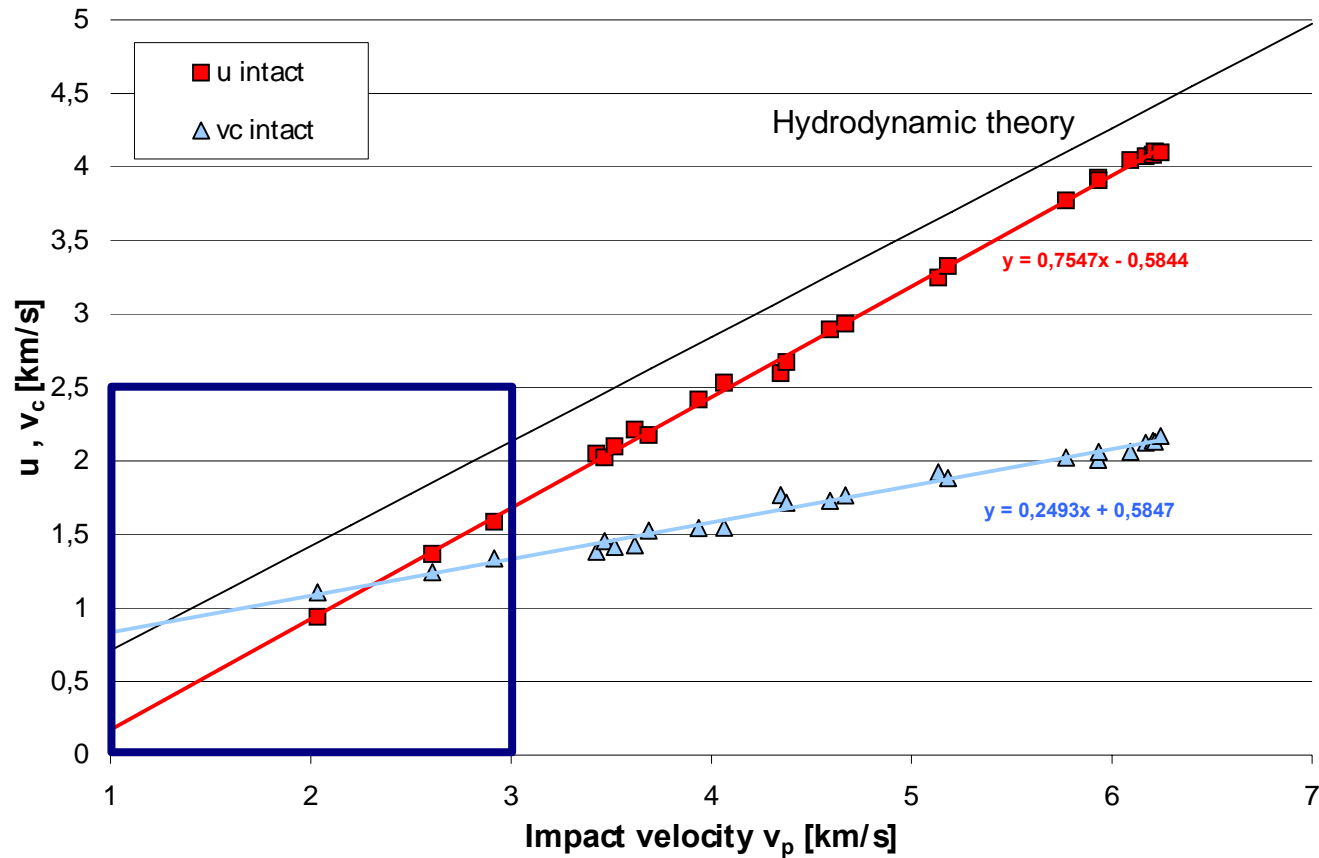


Schematic of EMI Experiments

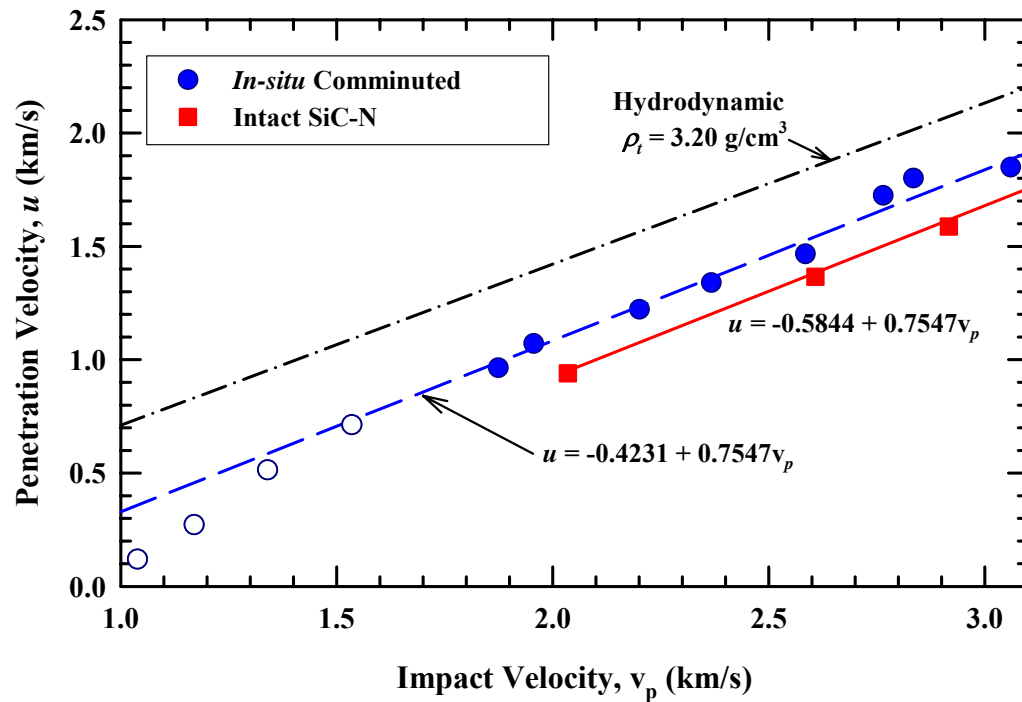


- *Differences in experiments relative to previous experiments*
 - *Aluminum confinement w/cover plate*
 - *1.00-mm diameter Au rod instead of 0.75-mm diameter rod*

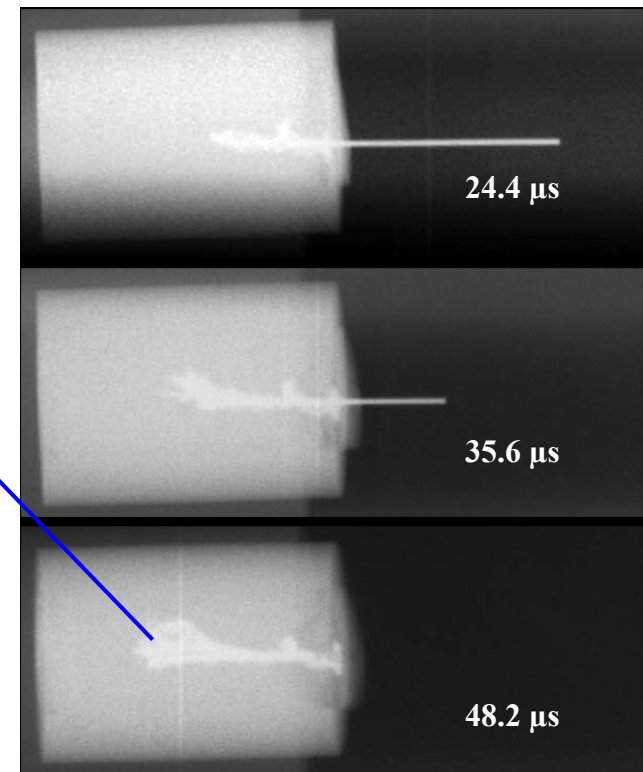
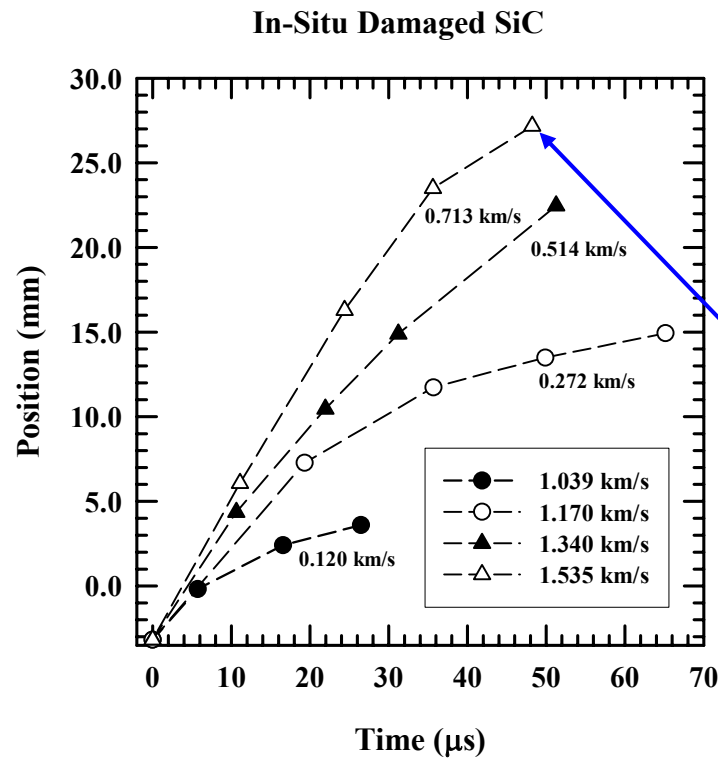
Velocity Range



In-Situ Comminuted SiC



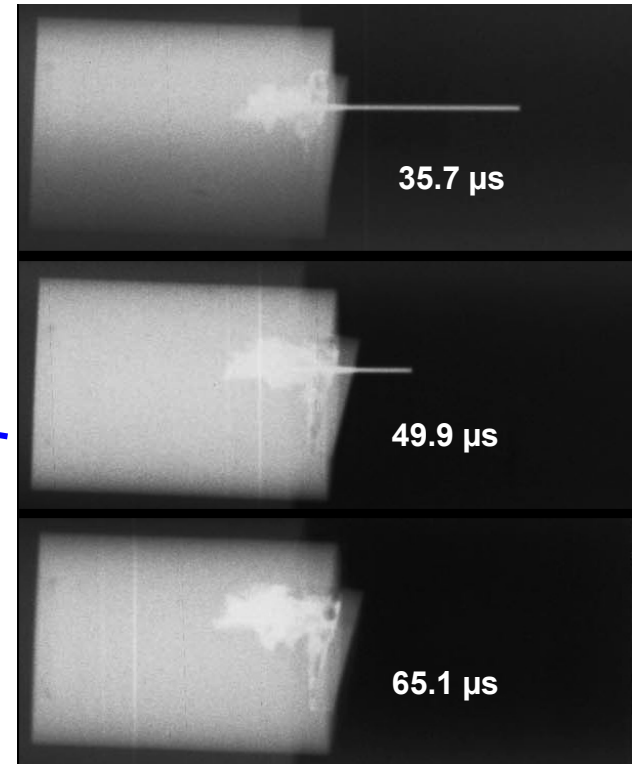
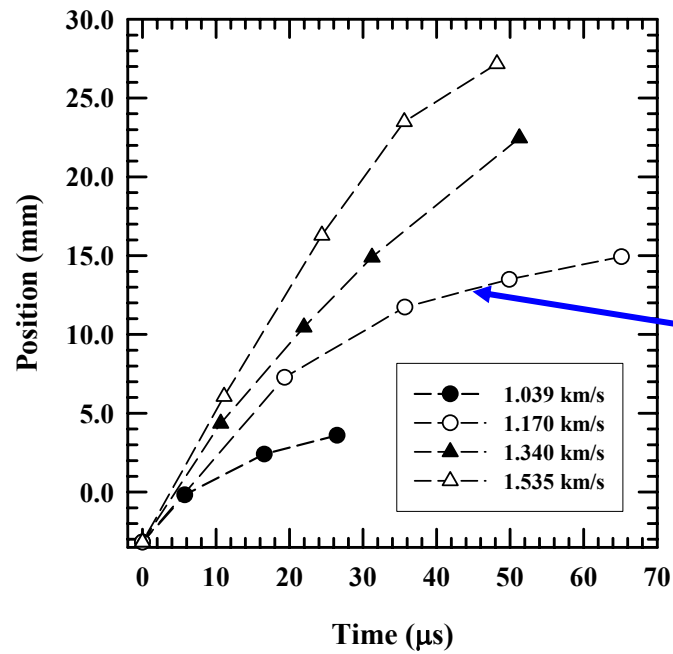
Lowest Impact Velocities



$$v_p = 1.535 \text{ km/s}$$

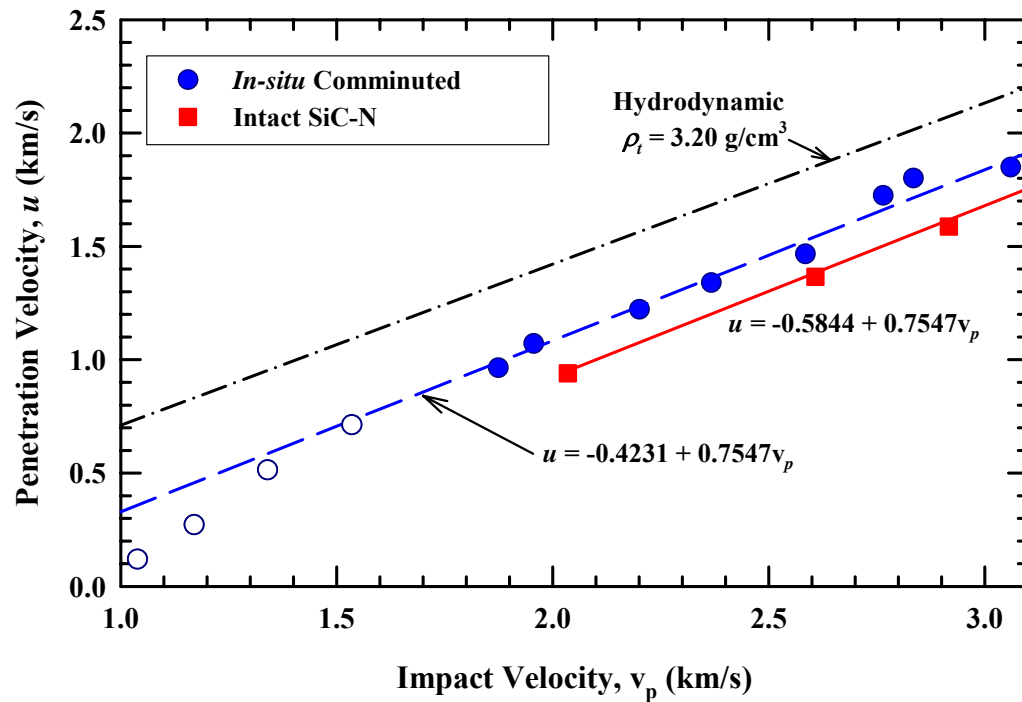
■ When $u \leq v_c$, nonlinear penetration response

Dwell-Like Behavior

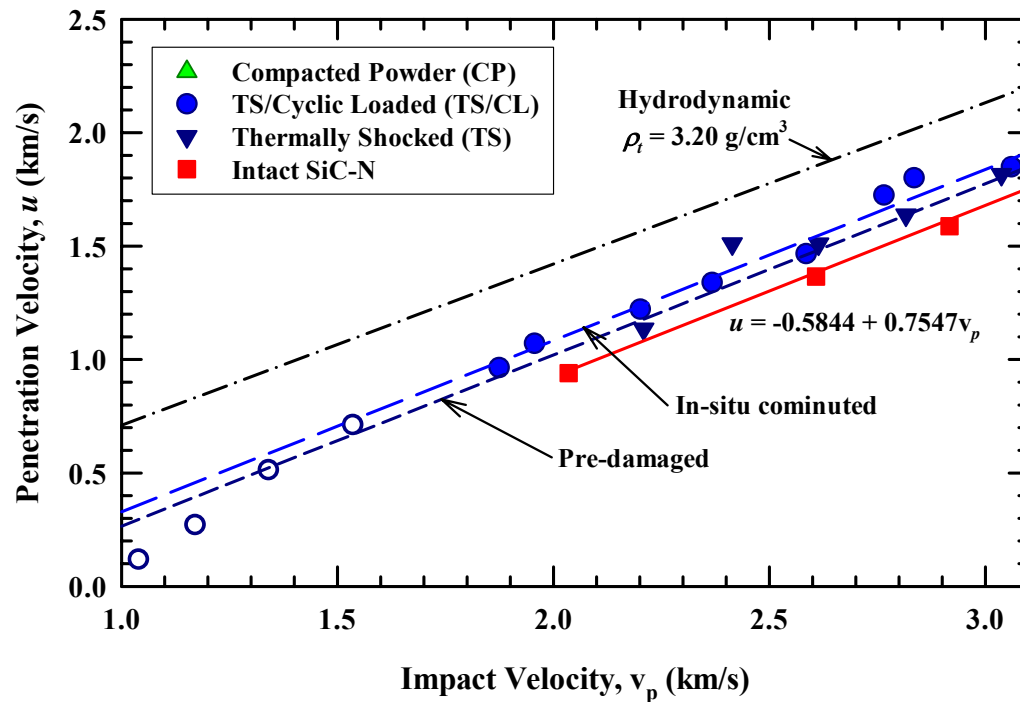


$$v_p = 1.170 \text{ km/s}$$

In-Situ Comminuted SiC

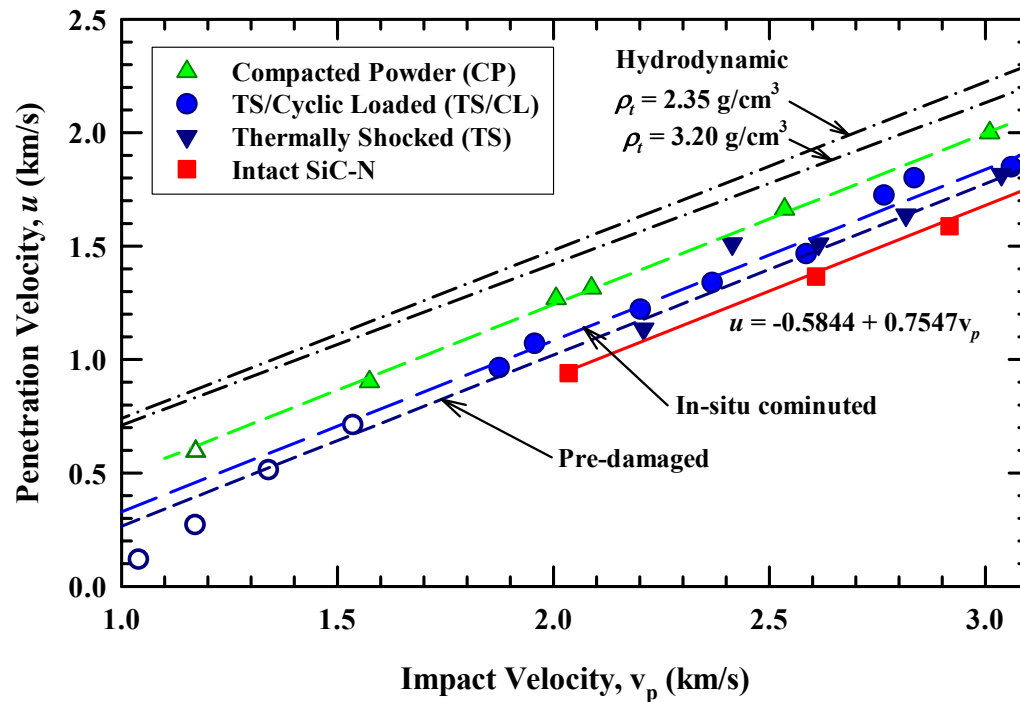


Thermally Shocked SiC



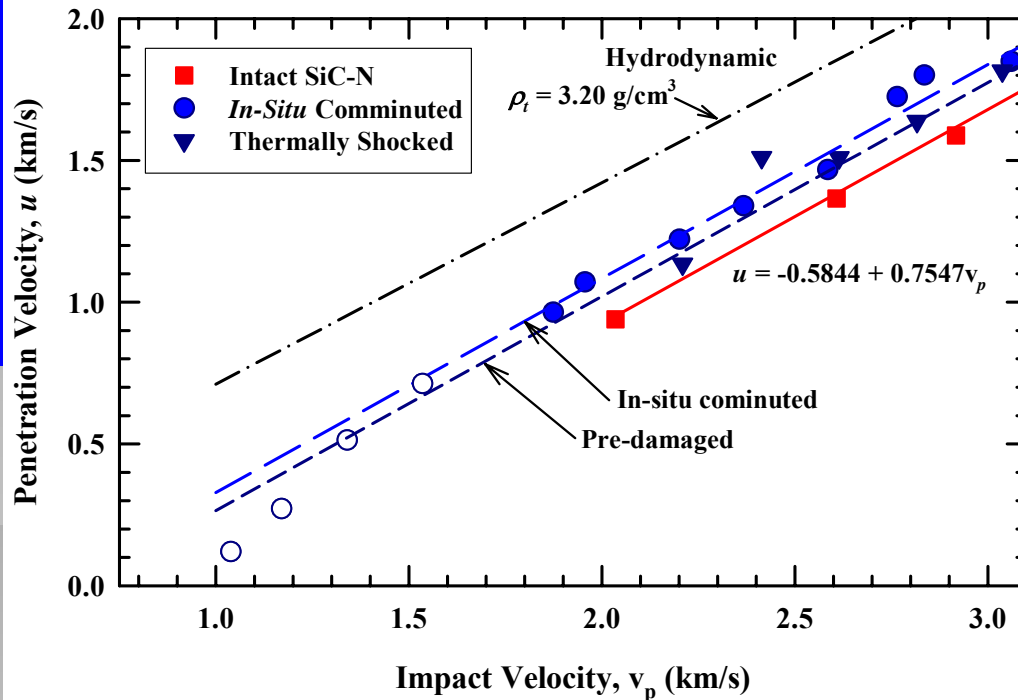
- Regression fit through pre-damaged results ignored the datum point at 2.4 km/s

Compacted SiC Powder



■ $U_{\text{intact}} < U_{\text{predamaged}} < U_{\text{comminuted}} < U_{\text{powder}} < U_{\text{hydro}}$

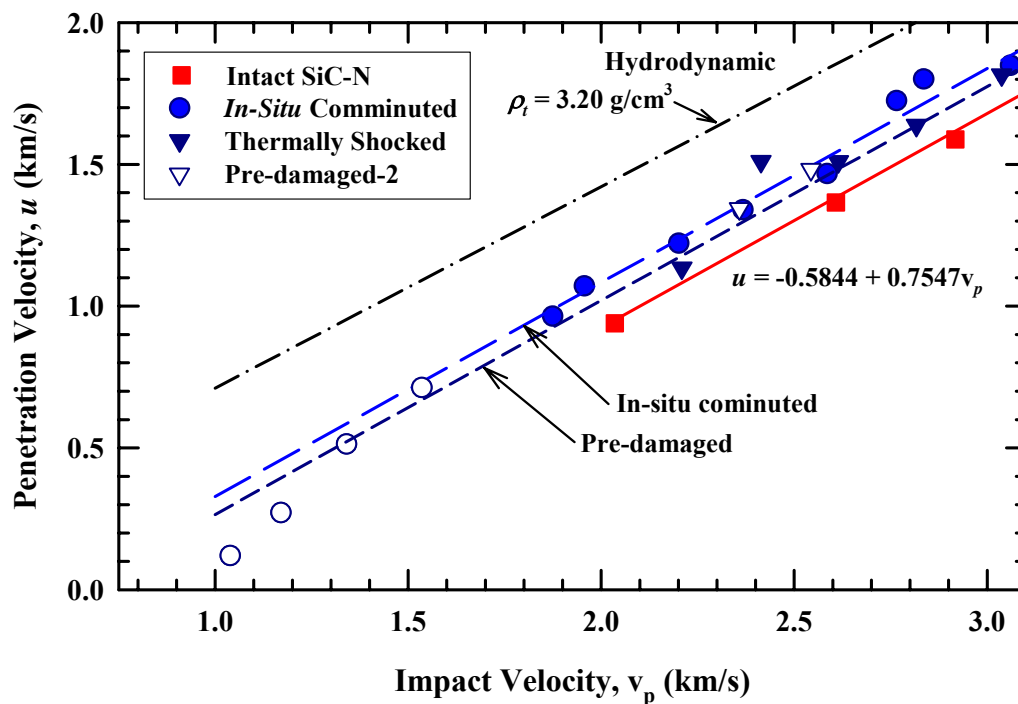
New Experiments



- *Extend pre-damaged sleeved data to lower impact velocities*
- *Check to see if data point at 2.4 km/s is an outlier*
- *Demonstrate that bare and sleeved intact ceramic have the same penetration response*
- *Extend intact data to lower impact velocities*

Pre-Damaged SiC Results

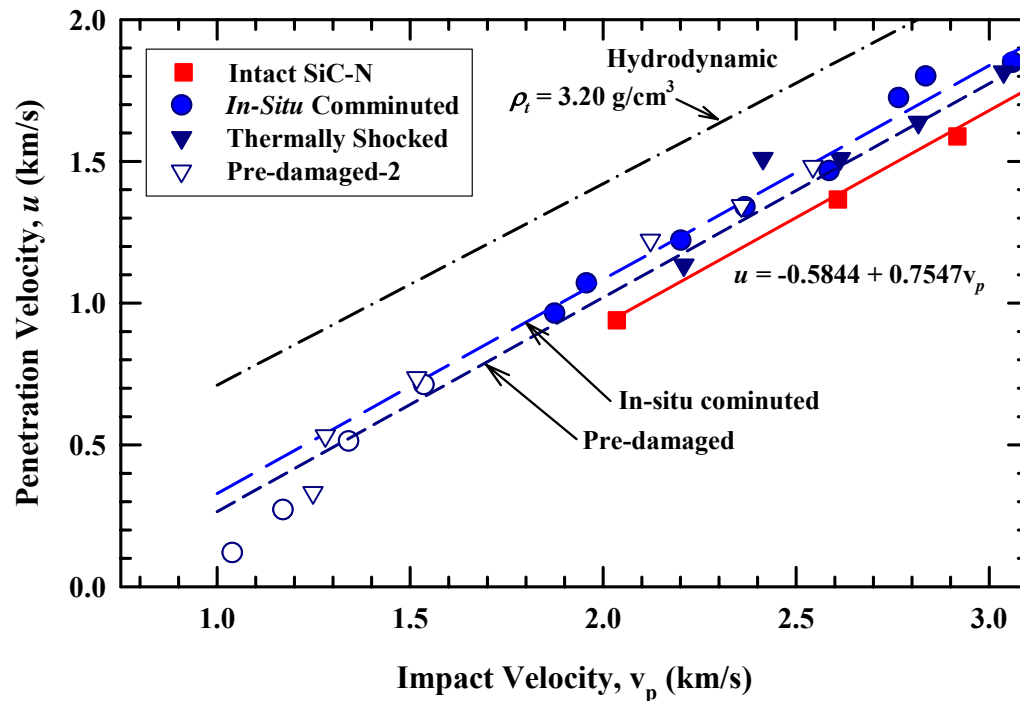
- *Was datum at 2.4 km/s anomalously high?*



- *Yes, it appears to be!*

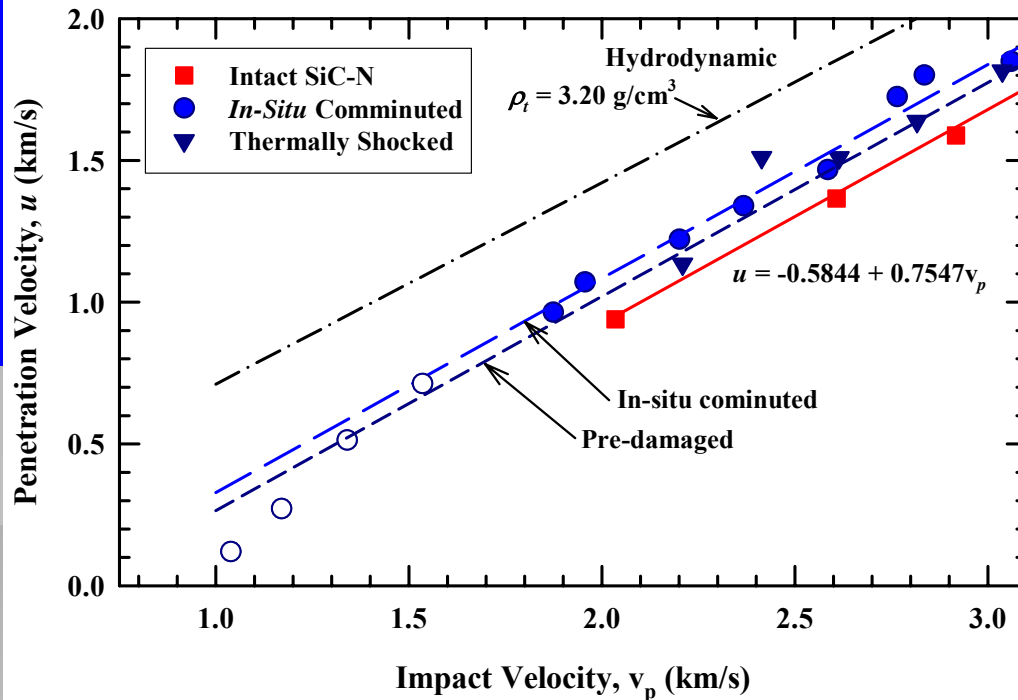
Pre-Damaged Results

- *Extend results to lower impact velocities*



- *Cannot differentiate between pre-damaged and in-situ comminuted experiments (within data scatter)*

New Experiments

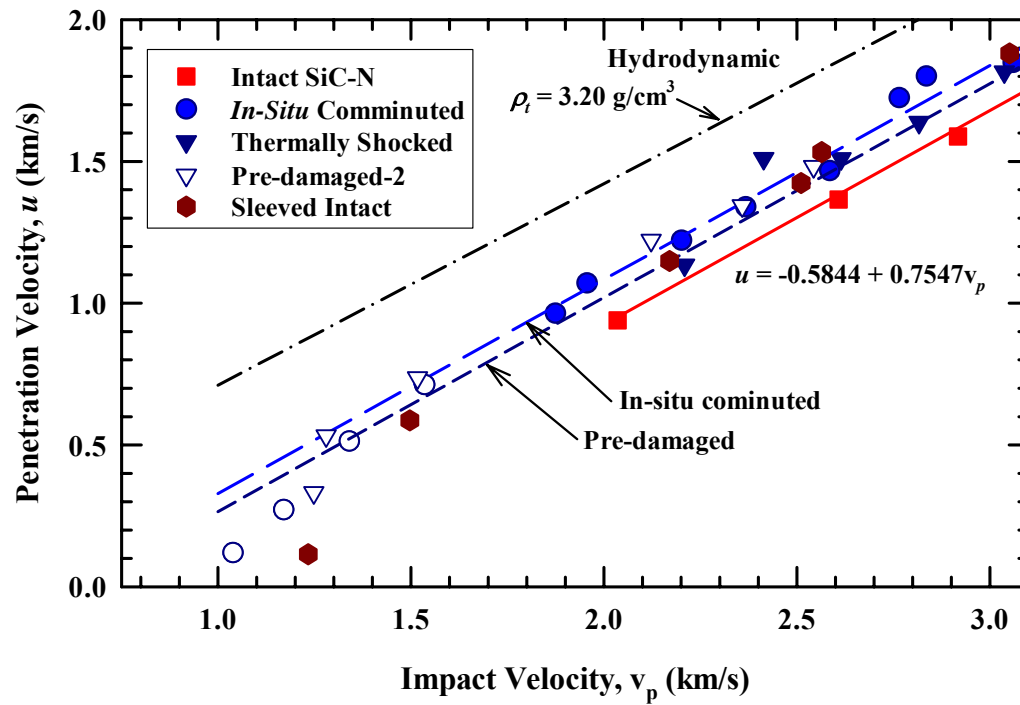


- *Extend pre-damaged sleeved data to lower impact velocities*
- *Check to see if data point at 2.4 km/s is an outlier*
- *Demonstrate that bare and sleeved intact ceramic have the same penetration response*
- *Extend intact data to lower impact velocities*

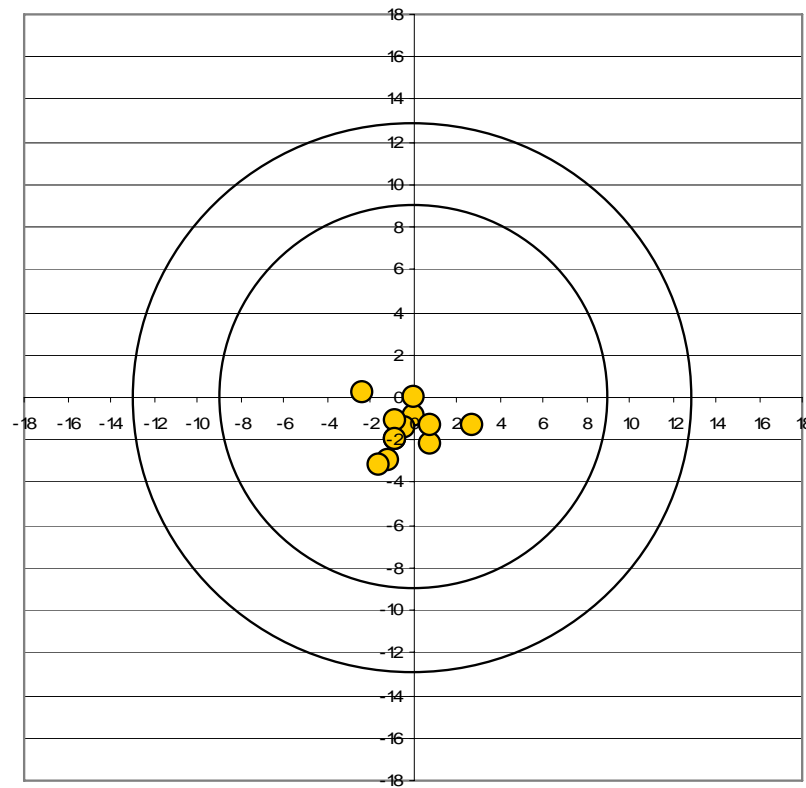
Sleeved Intact SiC



- *Begin experiments at high impact velocity (results should be independent of confinement)*



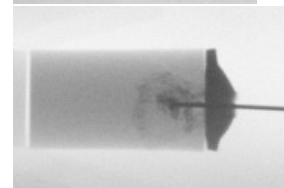
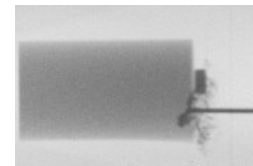
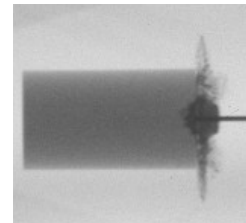
Good Impacts



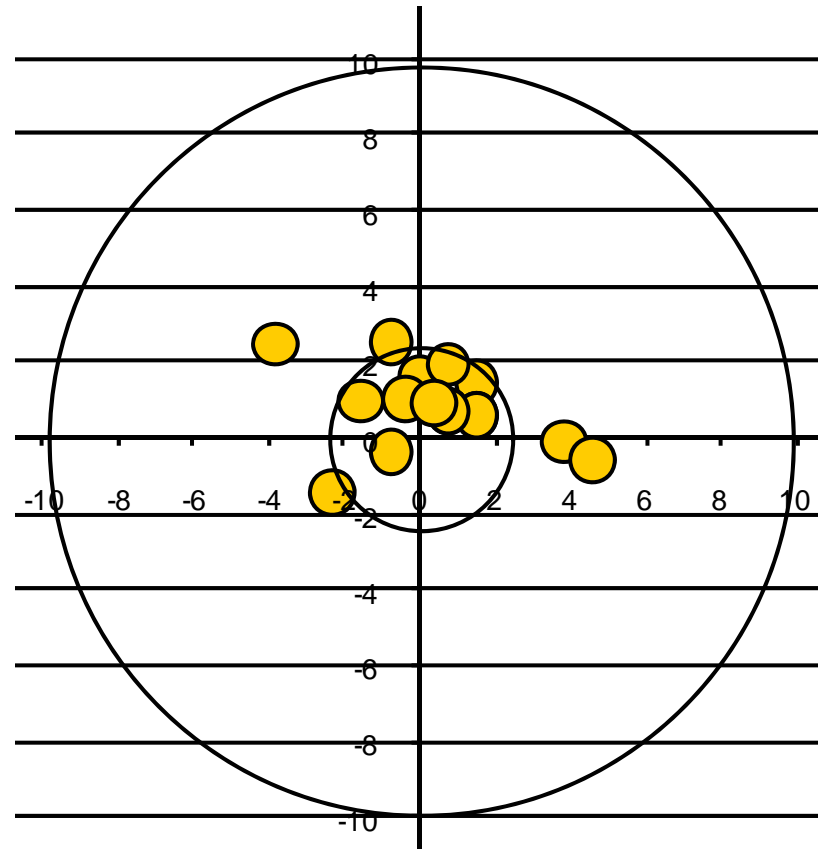
Results



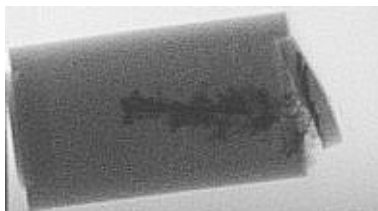
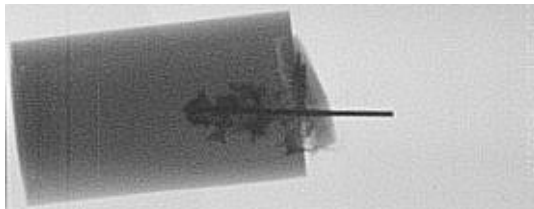
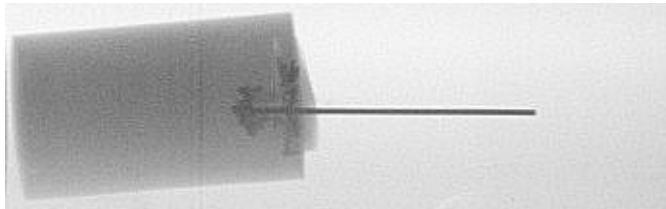
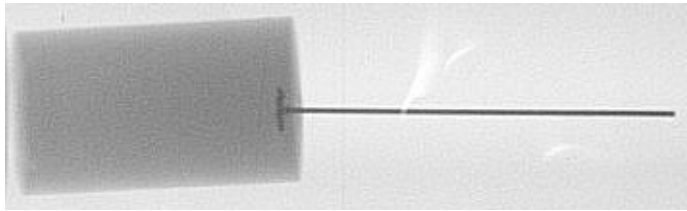
- *Cannot differentiate intact data from pre-damaged and in-situ comminuted data*
- *The new experiments were encased in the aluminum sleeve*
- *Had additional experiments to investigate interface defeat*
 - *Unconfined ceramic*
 - *With and w/o Cu buffer*
 - ❖ *Cu nub*
 - ❖ *Cu plate*



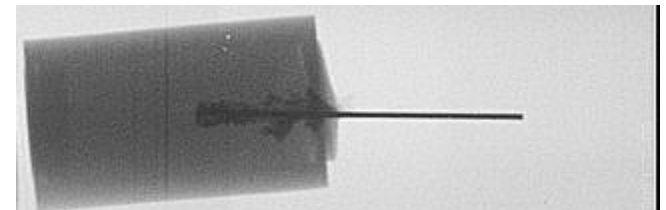
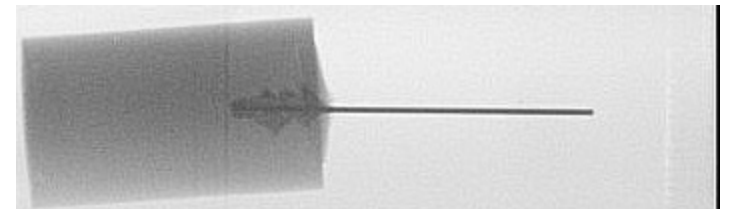
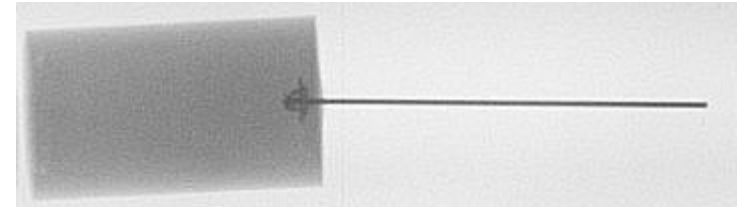
Impact Locations



Incipient Dwell w/Cover

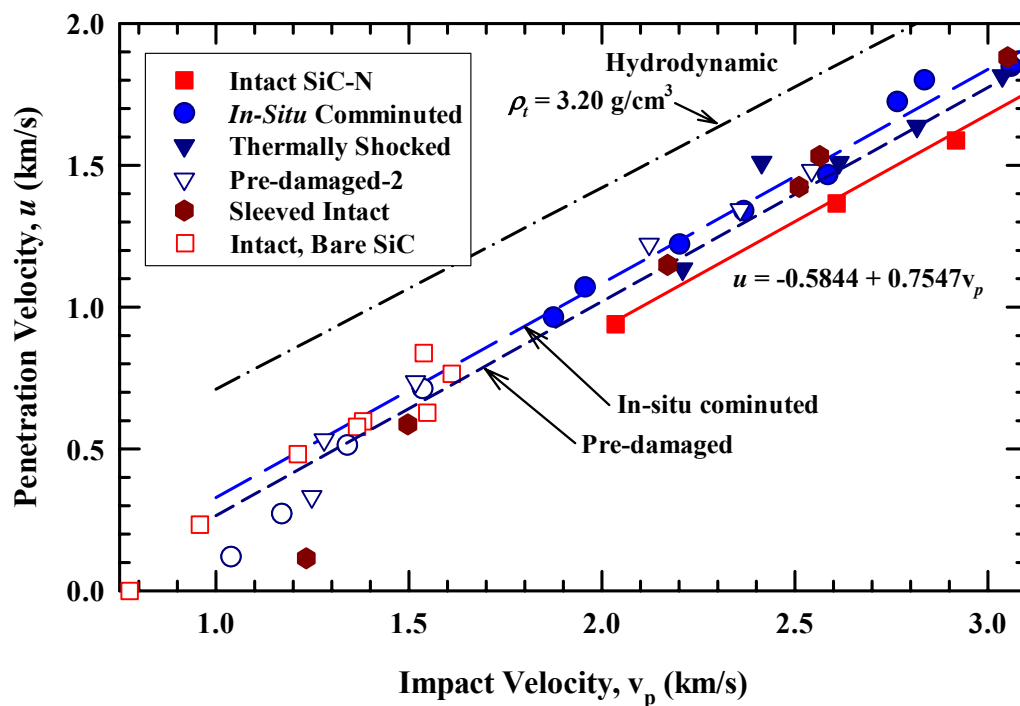


Test 11340
 $v_p = 1.497 \text{ km/s}$

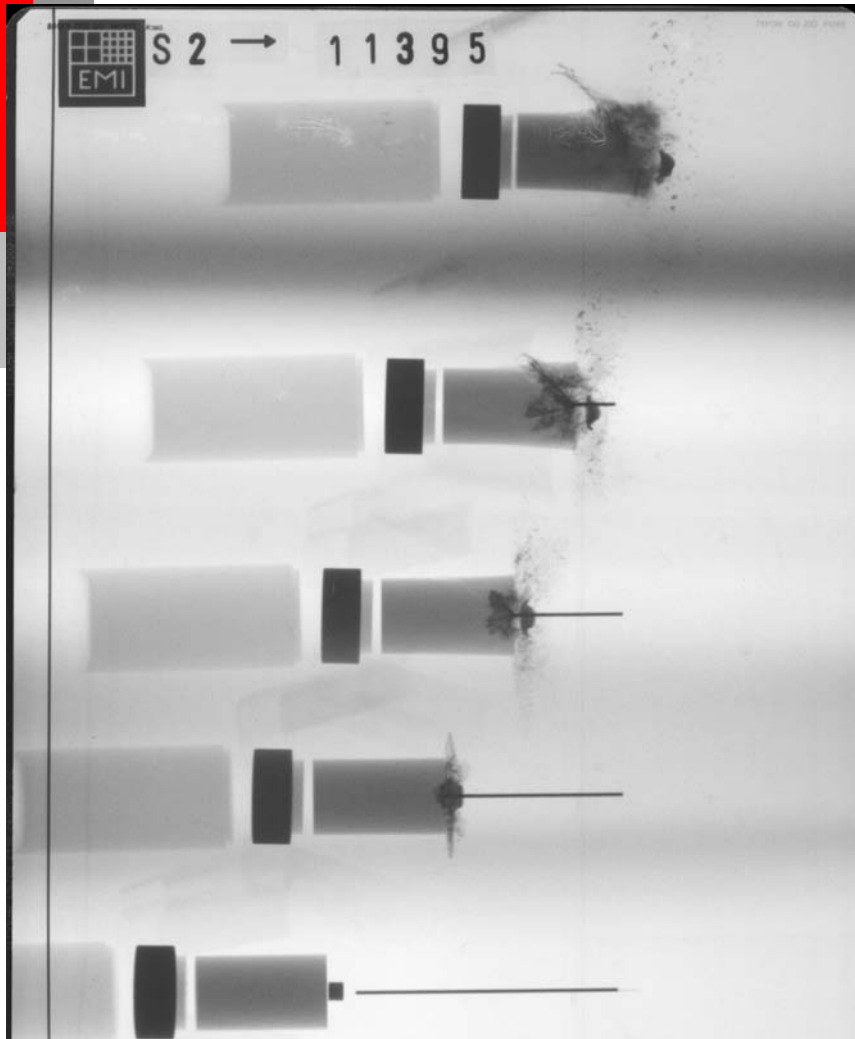


Test 11342
 $v_p = 2.170 \text{ km/s}$

Interface Defeat Expts.



Dwell Experiment



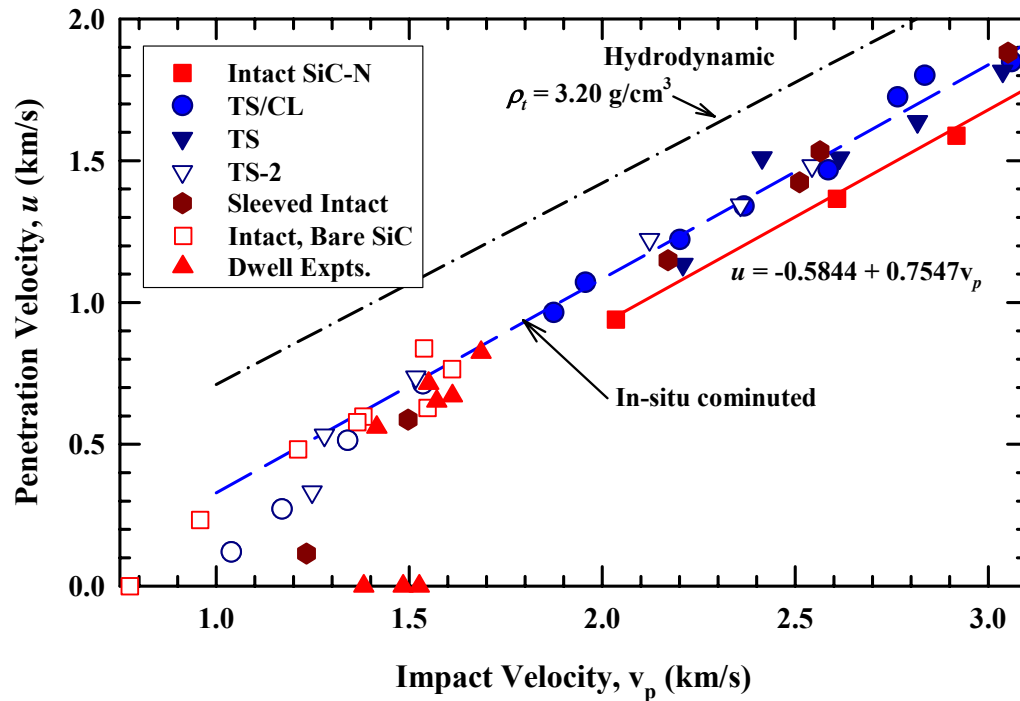
- *Test 11395*
- *Cu buffer*
- *Impact velocity: 1.526 km/s*
- *Dwelled for $\sim 10.4 \mu\text{s}$*

Dwell Experiment



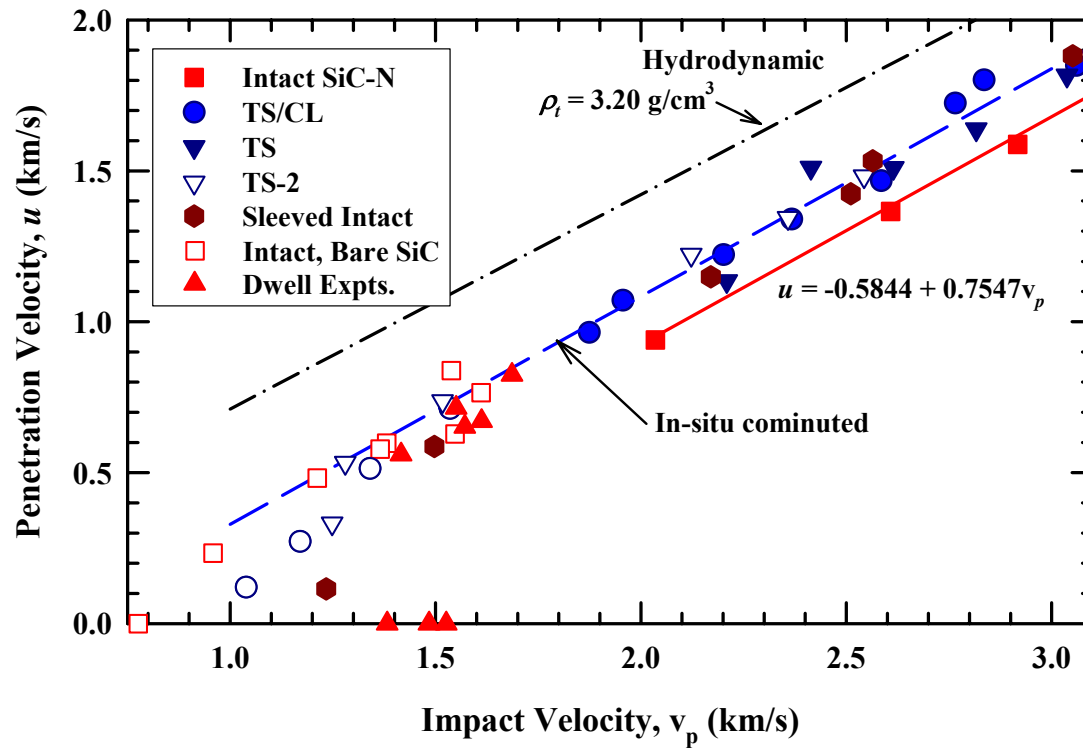
- *Test 11389*
- *Cu plate*
- *Impact velocity: 1.571 km/s*
- *Dwelled for $\sim 11 \mu\text{s}$*

Transition from Dwell to Penetration



- Within data scatter, $u_{1.00}$ for intact, pre-damaged, and in-situ comminuted are the same (sleeved or bare)
- $u_{1.00} > u_{0.75}$
- Once begin penetrating, experimental data and high-speed photography imply penetrating failed material

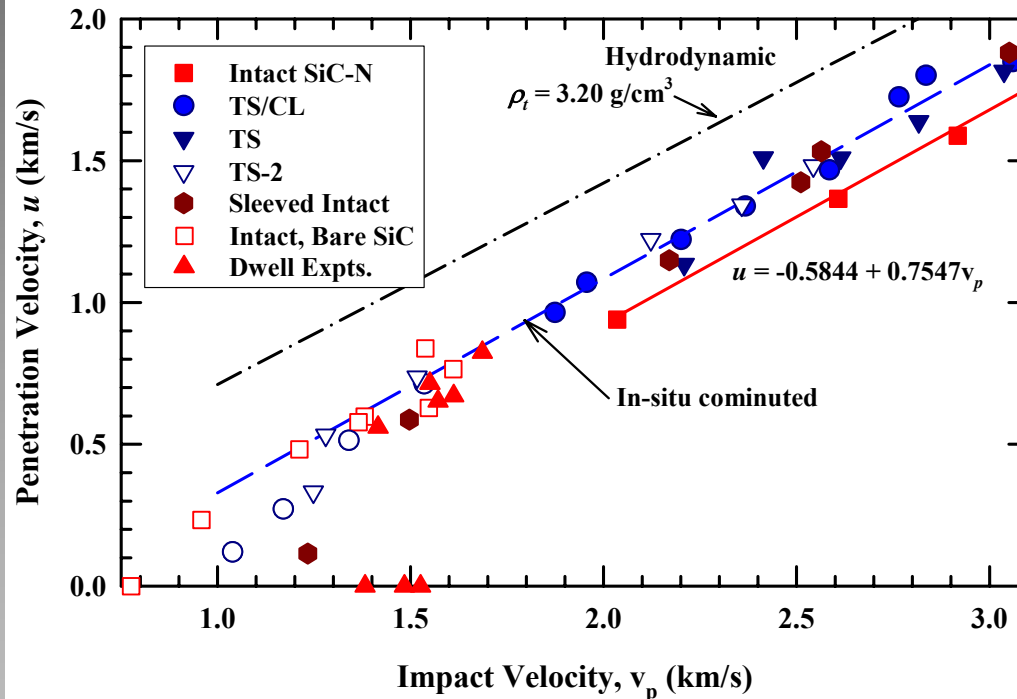
Summary of Data



~~$u_{\text{intact}} < u_{\text{predamaged}} < u_{\text{comminuted}} < u_{\text{powder}} < u_{\text{hydro}}$~~

$u_{\text{intact}} = u_{\text{predamaged}} = u_{\text{comminuted}} < u_{\text{powder}} < u_{\text{hydro}}$

Further Experiments



- 20-mm diameter, bare, SiC-N cylinders
- Impact velocity: $\sim 2.2 - 3.0 \text{ km/s}$
- Conduct ~ 5 experiments with 0.75-mm diameter Au rods
- Conduct ~ 5 experiments with 1.00-mm diameter Au rods



*In physics, you don't have to go around
making trouble for yourself—*

Nature does it for you

- Frank Wilczek

Radial jet dispersion due to current interaction in an electric armour application

Authors

- ✦ Patrik Appelgren
- ✦ Lars Westerling
- ✦ Melker Skoglund
- ✦ Patrik Lundberg*
- ✦ Tomas Hurtig
- ✦ Anders Larsson

Contents

- Introduction – electric armour (electromagnetic armour)
- Shaped charge experiments
 - Observations - results
- Modelling of jet - current interaction
 - results
- Conclusions

Electric armour

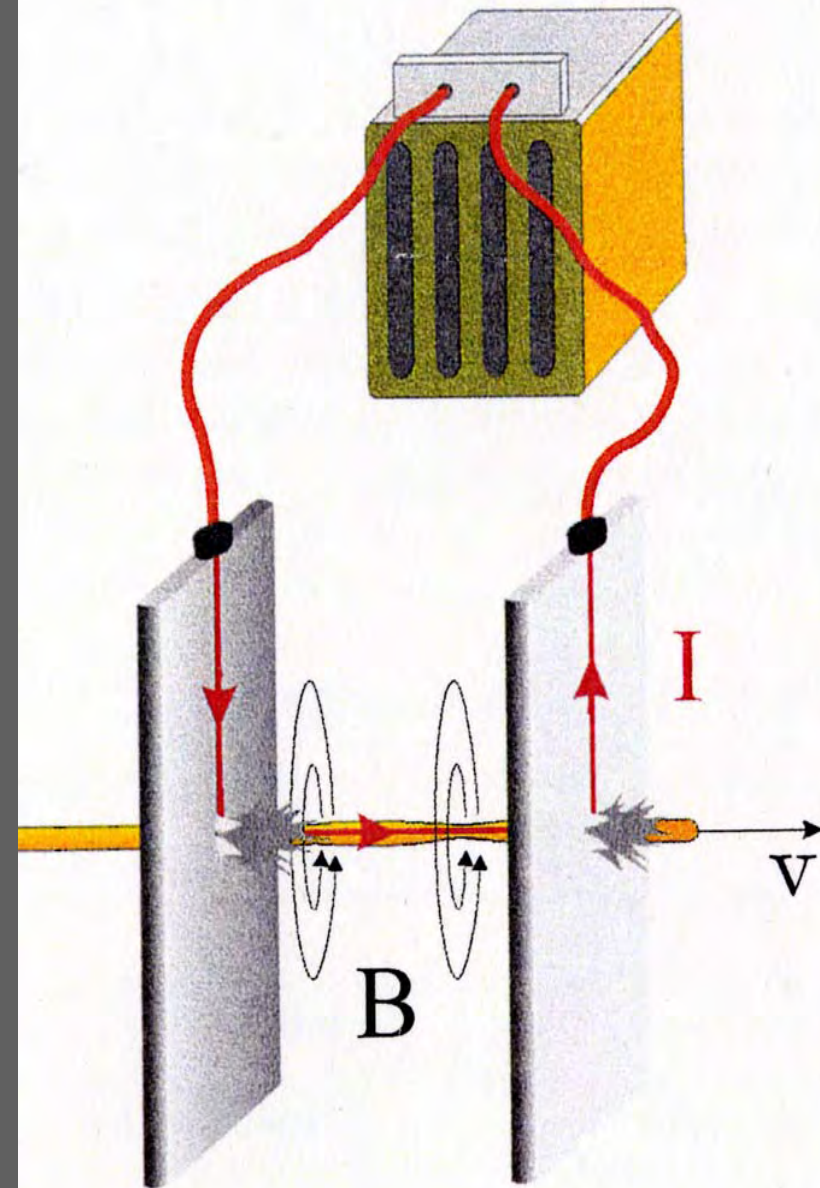
Effects on jet by:

••• Joule heating

- Heating, melting
- Local vaporisation

••• Lorentz forces

- Local instability growth
- Fragmentation, disintegration



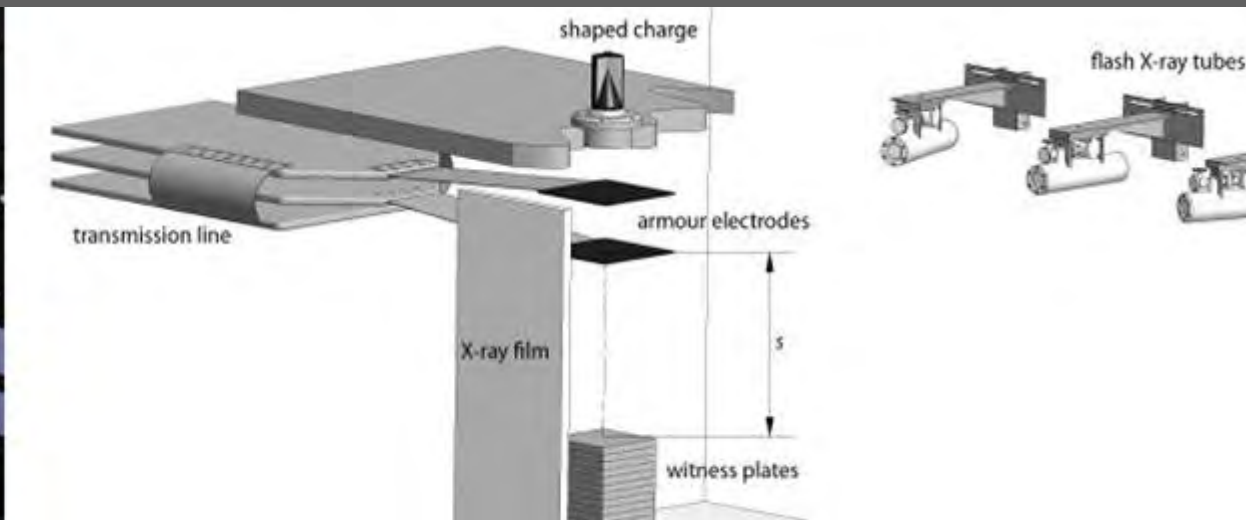
Electric armour – protective mechanism

- ❖ Magnetic forces transforms the jet from a cylindrical shape (axial coherence) to ring- or disc shaped structures



Experimental test setup

- ❖ A 1.7 mF, 400 kJ pulsed power supply
 - ❖ Two-plate electrode arrangement
 - ❖ Current and voltage diagnostics
 - ❖ Three X-rays to depict the jet

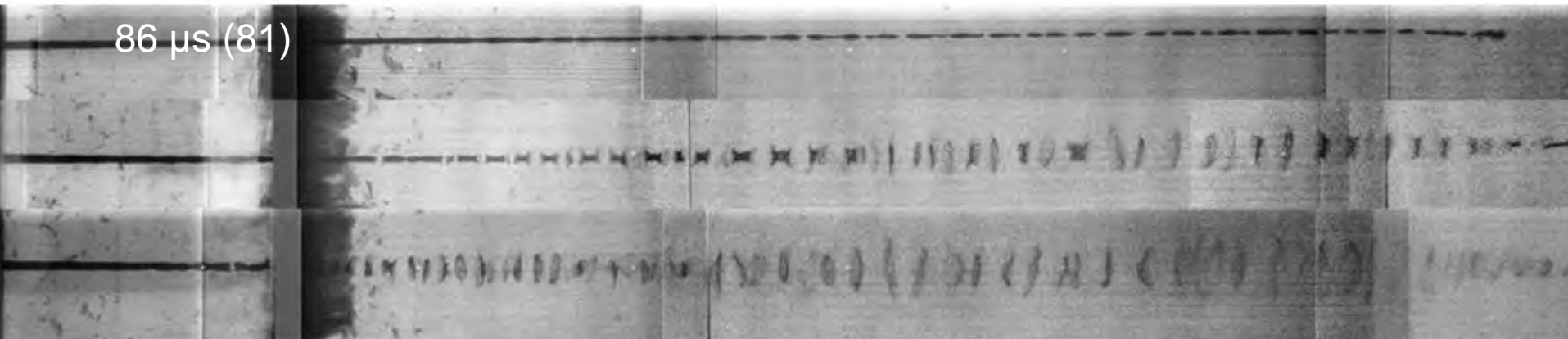


Experimental results (0, 39 kJ, 96 kJ)

36 μ s (31)

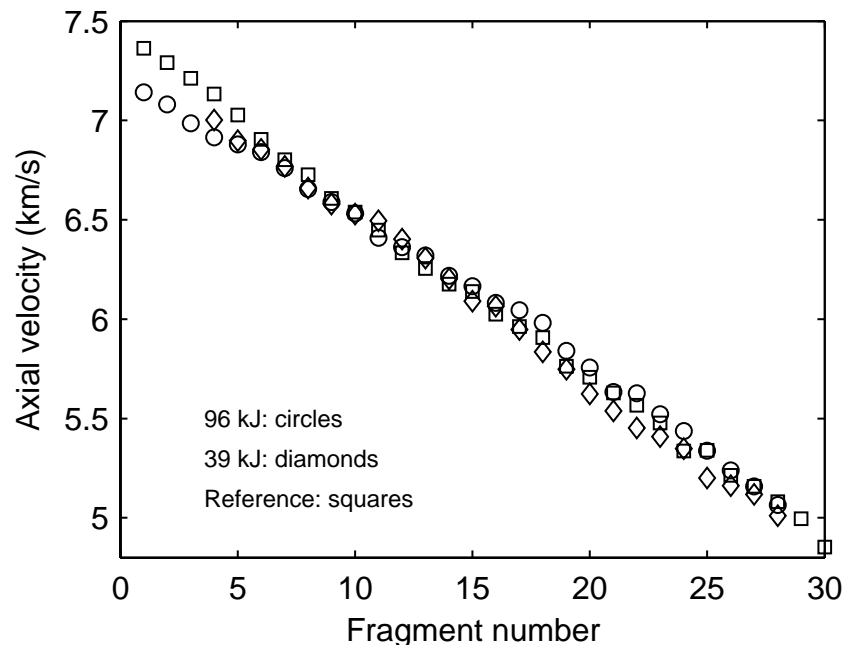


86 μ s (81)



Experimental results 39 and 96 kJ

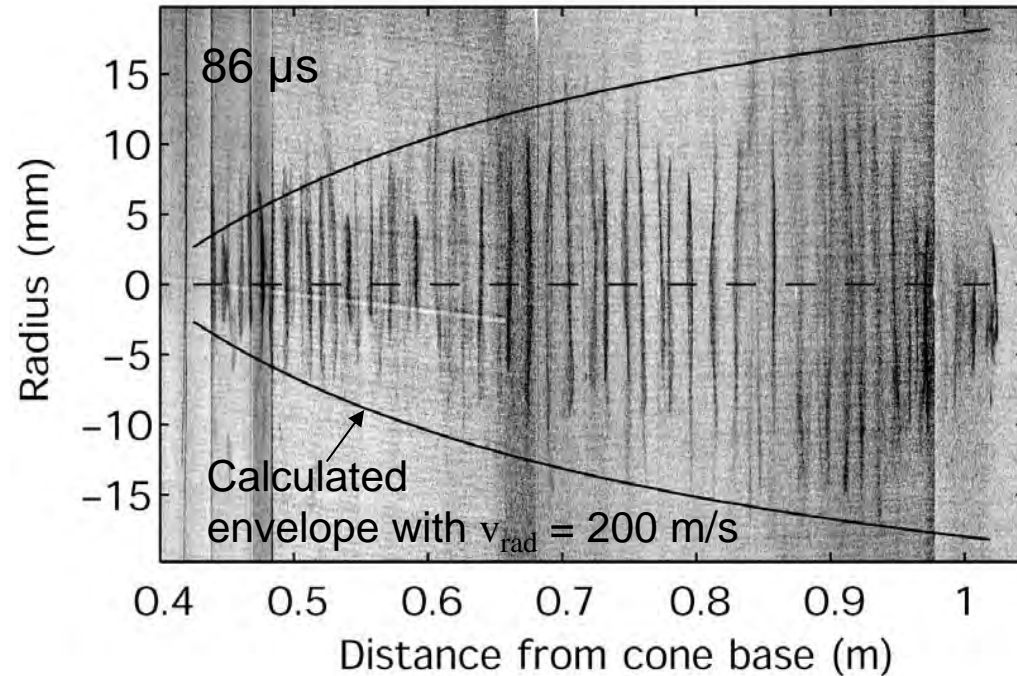
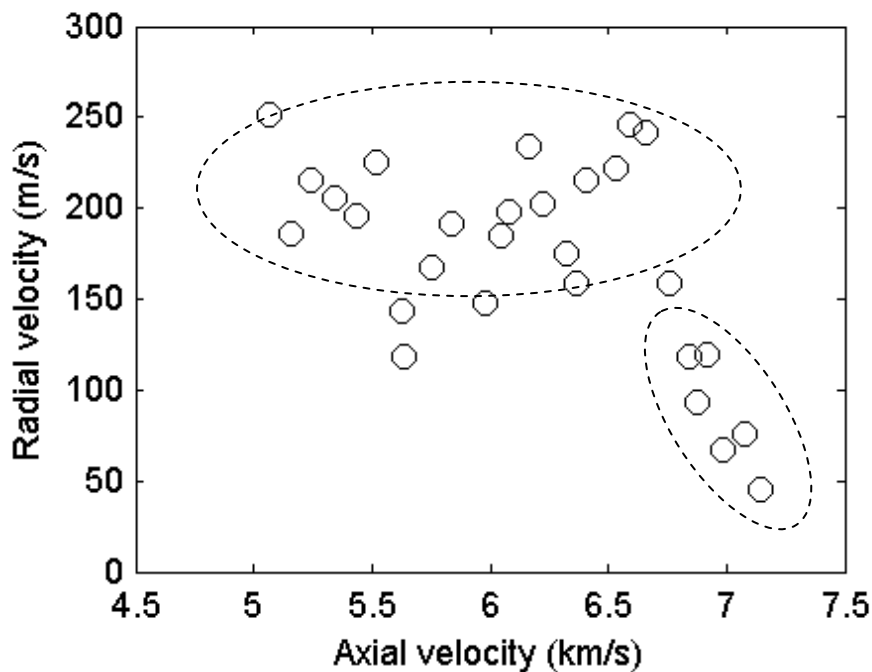
- Number of fragments independent of electric energy
- Same fragmentation behaviour but more rapid



Experimental results 96 kJ

Radial expansion velocity of jet elements:

Around 200 m/s ($3 < v_{axial} < 6.6$ km/s)

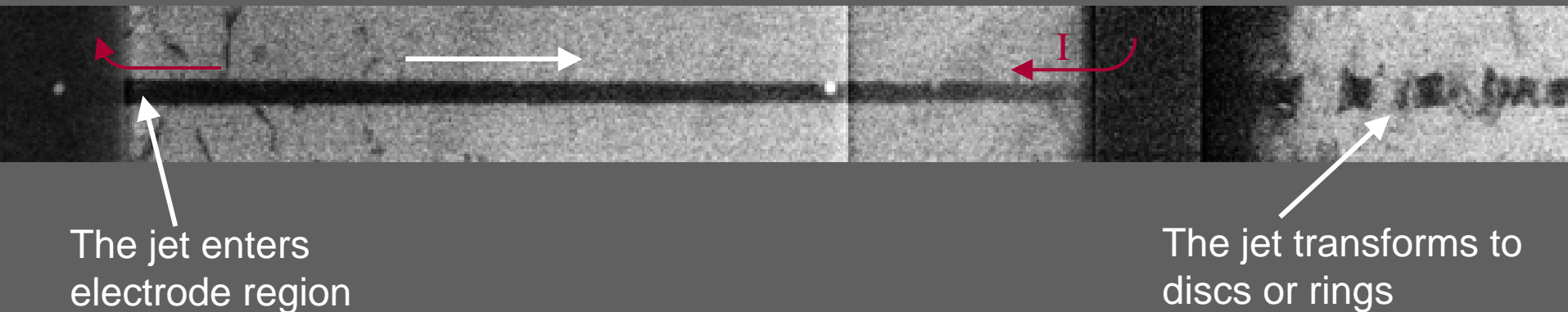


Experimental results 96 kJ

- ✦ No clear mechanical effect in-between the electrodes
- ✦ Rapid transformation at exit of electrode region
 - ✦ Fragmentation
 - ✦ Disk- and ring formation

Electrode 1

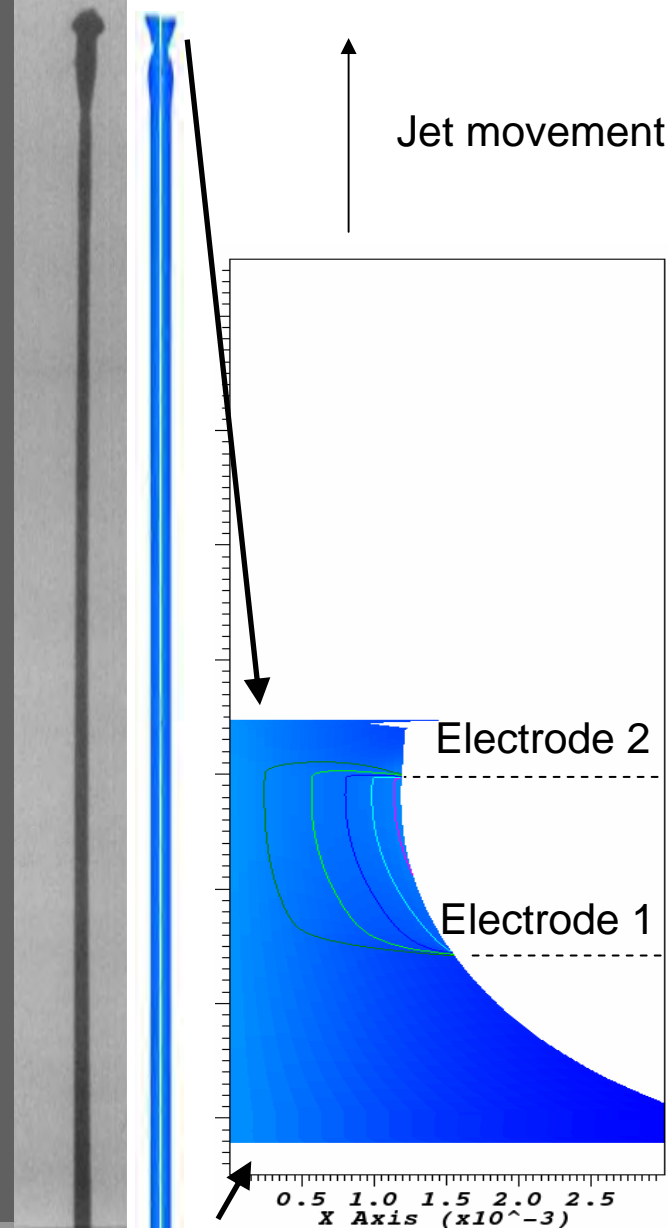
Electrode 2



Modelling of jet – current interaction

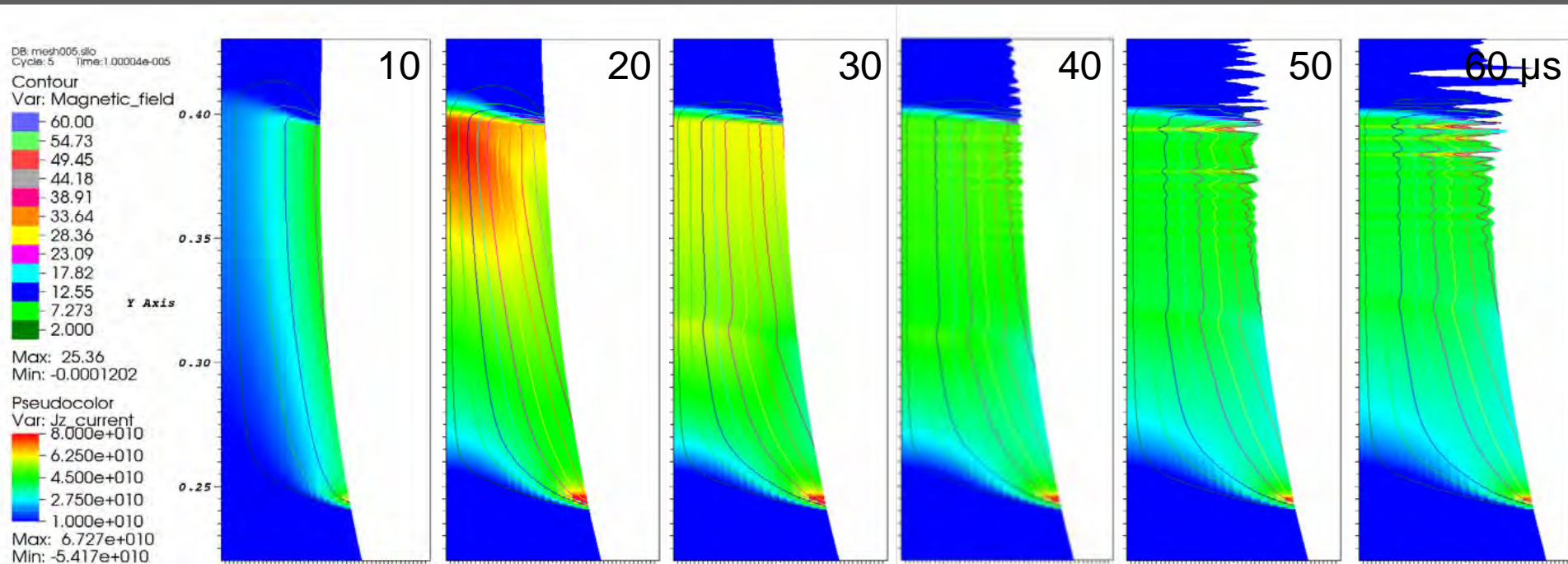
GRALE

- Hydrodynamic 2D ALE code
 - Axial symmetry and plane problems
- Magnetohydrodynamic (MDH) capability included
 - Only Lagrange-coordinates for the MHD-module
 - Pulsed power supply included as current source
- Material model includes:
 - Thermal softening
 - Temperature dependent resistivity
 - Melt (vaporisation) energies



Current density and magnetic field (96 kJ)

- Diffusion of magnetic field and current into the jet (skin effect)
- Homogeneous current distribution at times $>30 \mu\text{s}$



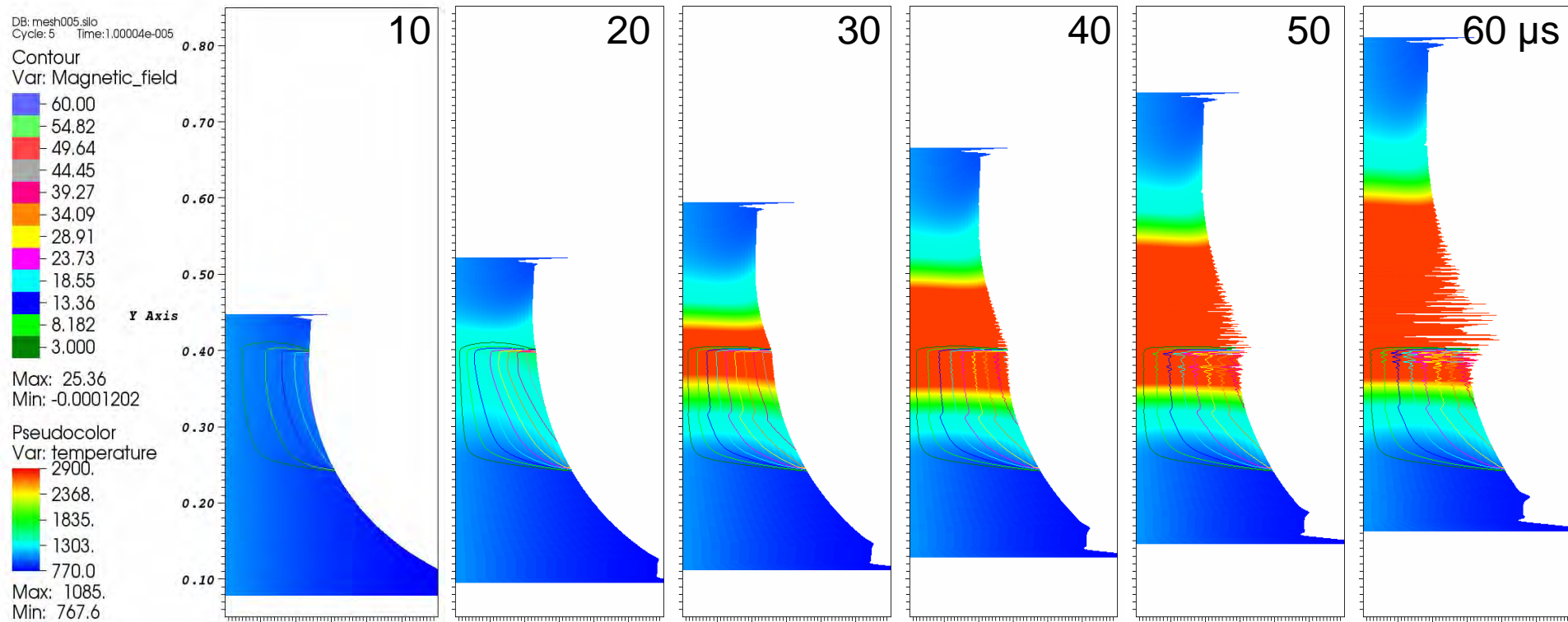
Temperature and magnetic field (96 kJ)



Temperature distribution homogenous radially

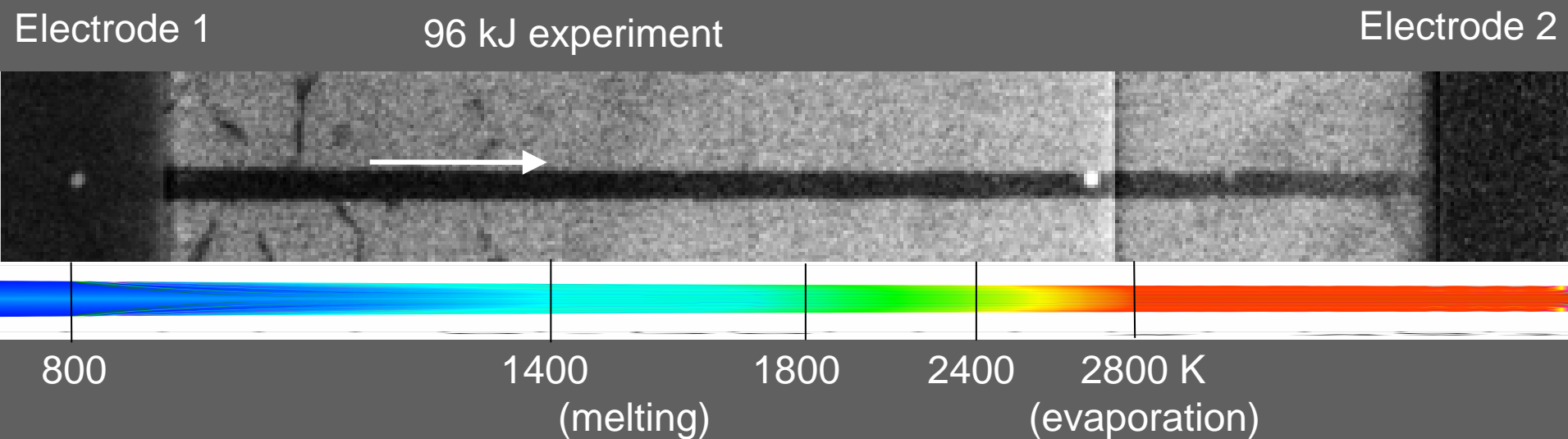


Reaches melting- and evaporation temperatures rapidly



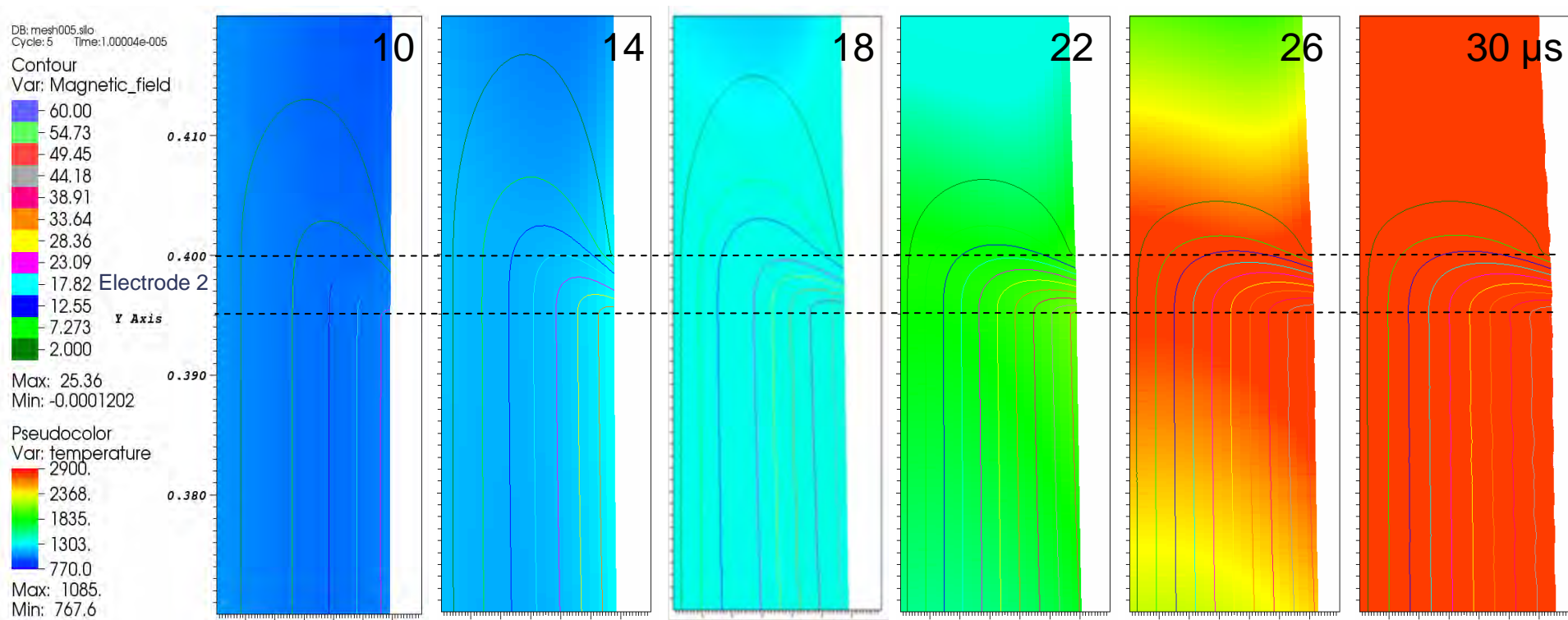
Temperature distribution (96 kJ)

- ✚ Temperature distribution homogenous radially
 - ✚ Reaches melting- and evaporation temperatures rapidly



Magnetic field

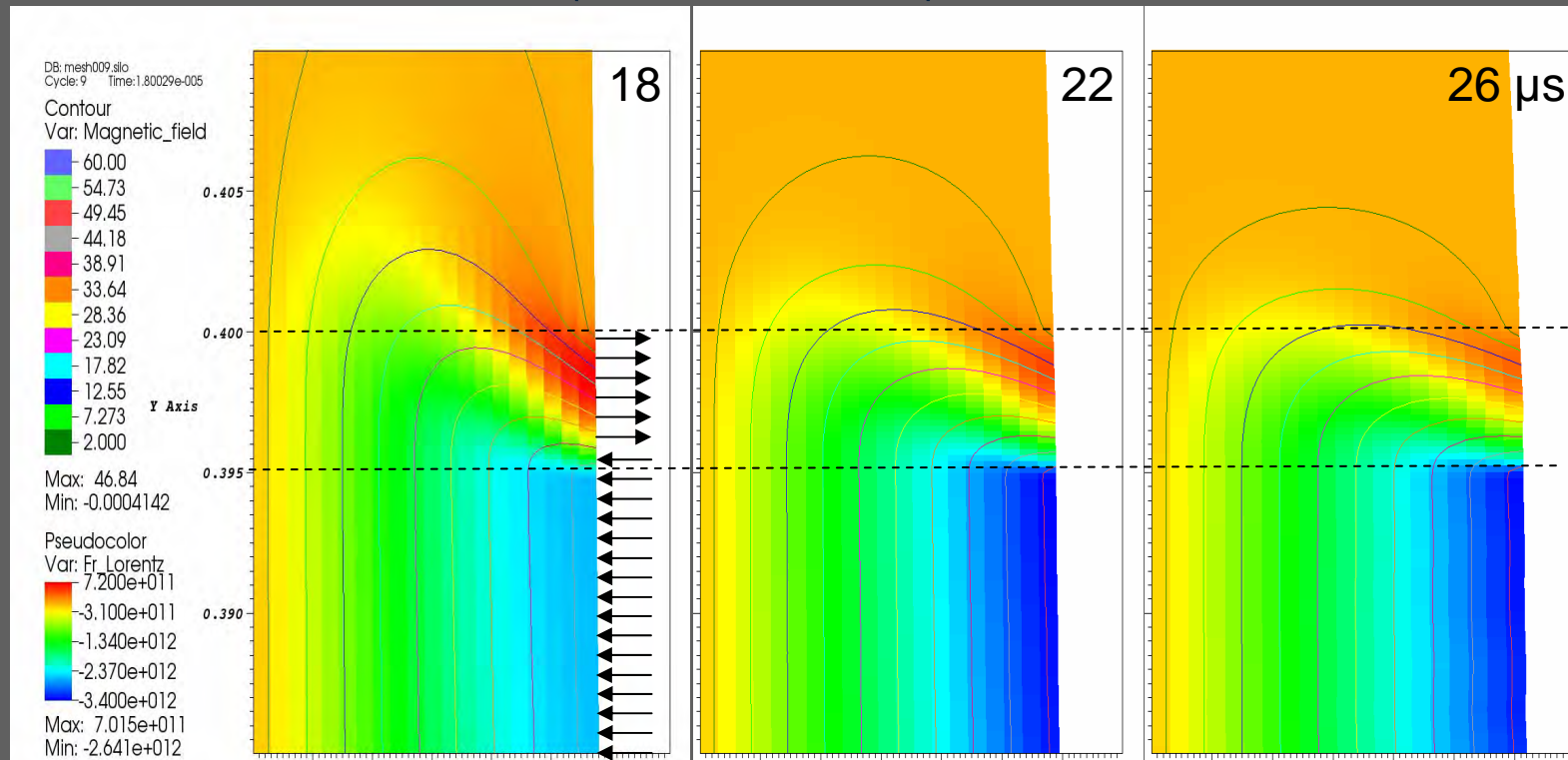
- Magnetic field frozen in when conductivity is high (low temperature)
- Diffusion velocity increases with temperature (low conductivity)



Lorentz force

- Radial component of the Lorentz' force is:
 - Compressible in-between electrodes ($\approx 3 \text{ KN/mm}^3$)
 - Tensile at electrode 2 ($\approx 0.7 \text{ KN/mm}^3$)

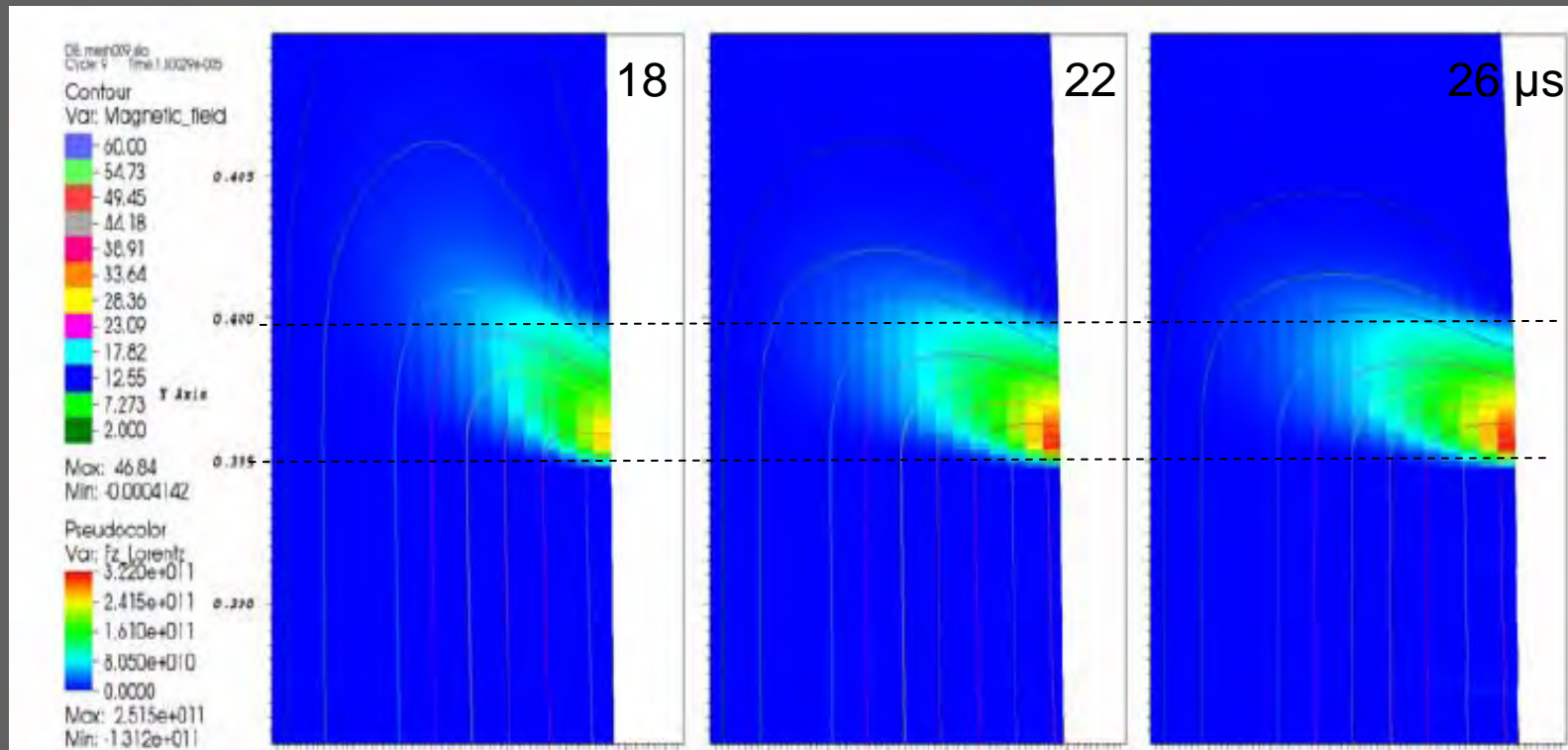
Electrode 2



Lorentz force

✦ Axial component of the Lorentz' force is:

- ✦ Zero in-between electrodes
- ✦ Tensile at electrode 2 ($\approx 0.3 \text{ KN/mm}^3$)



Conclusions

- ✦ The experiments shows:
 - ✦ Jet fragmentation (particulation) accelerates with increasing electric energy
 - ✦ Similar number of fragments (disks- or rings).
 - ✦ Close to exit of the electrode region, the jet is rapidly transformed into discs or rings
 - ✦ Radial velocity of around 200 m/s for the 96 kJ experiment

Conclusions

❖ Modelling shows:

- ❖ The jet is homogenously heated radially
 - ❖ Temperature reaches vaporisation temperatures
- ❖ Magnetic field is compressive in-between the electrodes
 - ❖ May enhance the natural necking of the stretching jet
- ❖ Magnetic field is pulled out of the electrode region causing a rapid change in direction of magnetic forces
 - ❖ From compressive to tensile in radial direction
 - ❖ From zero to tensile in axial direction

❖ These tensile forces may contribute to the rapid disc- or ring formation after current interaction ends



RDECOM



TECHNOLOGY DRIVEN. WARFIGHTER FOCUSED.

Combined Effects Aluminized Explosives

Dr. Ernest L. Baker

L.I. Stiel, W. Balas, C. Capellos and J. Pincay

23 SEP 2008

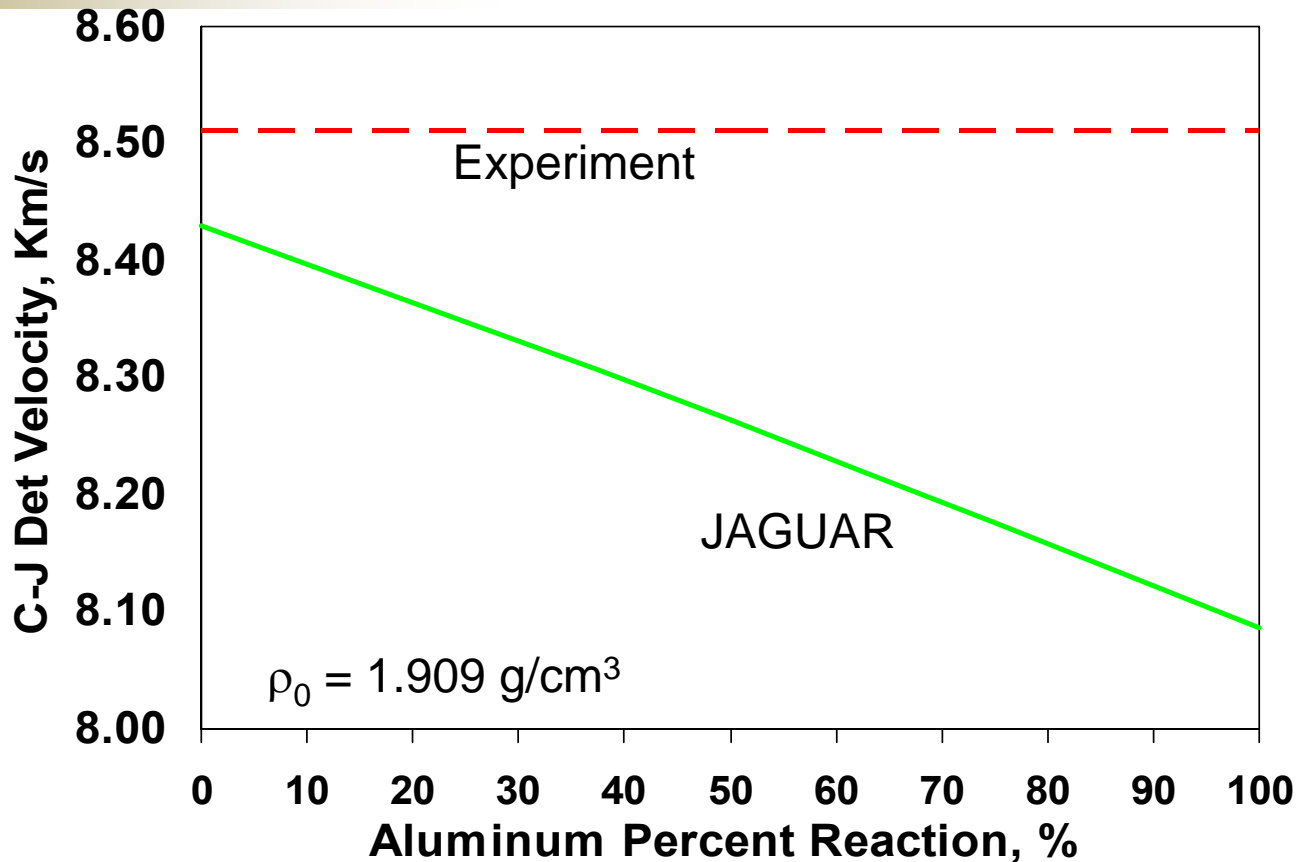
- Combined Effects Explosives
- Eigenvalue Detonation
- Detonation Velocities
- Cylinder Velocities
- Equations of State
- Conclusions

- High Energy Explosive
 - High nitramine content
 - High early work output (before 7V/V0)
- High Blast Explosive
 - Typically aluminum and additional oxidizer
 - Later work output (after 7V/V0)
- Combined Effects Explosive
 - Nitramine with fine aluminum: micron & submicron
 - Aluminum reaction occurs very early and contributes to early work

PAX-29: 77/15 CI-20/Al

PAX-30: 77/15 HMX/Al

PAX-42 77/15 RDX/Al



- **C-J Detonation velocity decreases with extent of Al reaction**
 - **Experiments:**
 - **Detonation velocity agrees with 0% Al reaction**
 - **Cylinder velocity agrees with 100% Al reaction @ 7V/V0**
- 0%: 1.69Km/s, 100%: 1.90Km/s, Experiment: 1.88Km/s

Rayleigh line (momentum) **larger D**

$$R = \rho_0^2 D^2 - P/(V_0 - V) = 0$$

smaller D

Pressure

Specific Volume

- Unreacted Hugoniot
- Reacted Hugoniot
- Rayleigh line

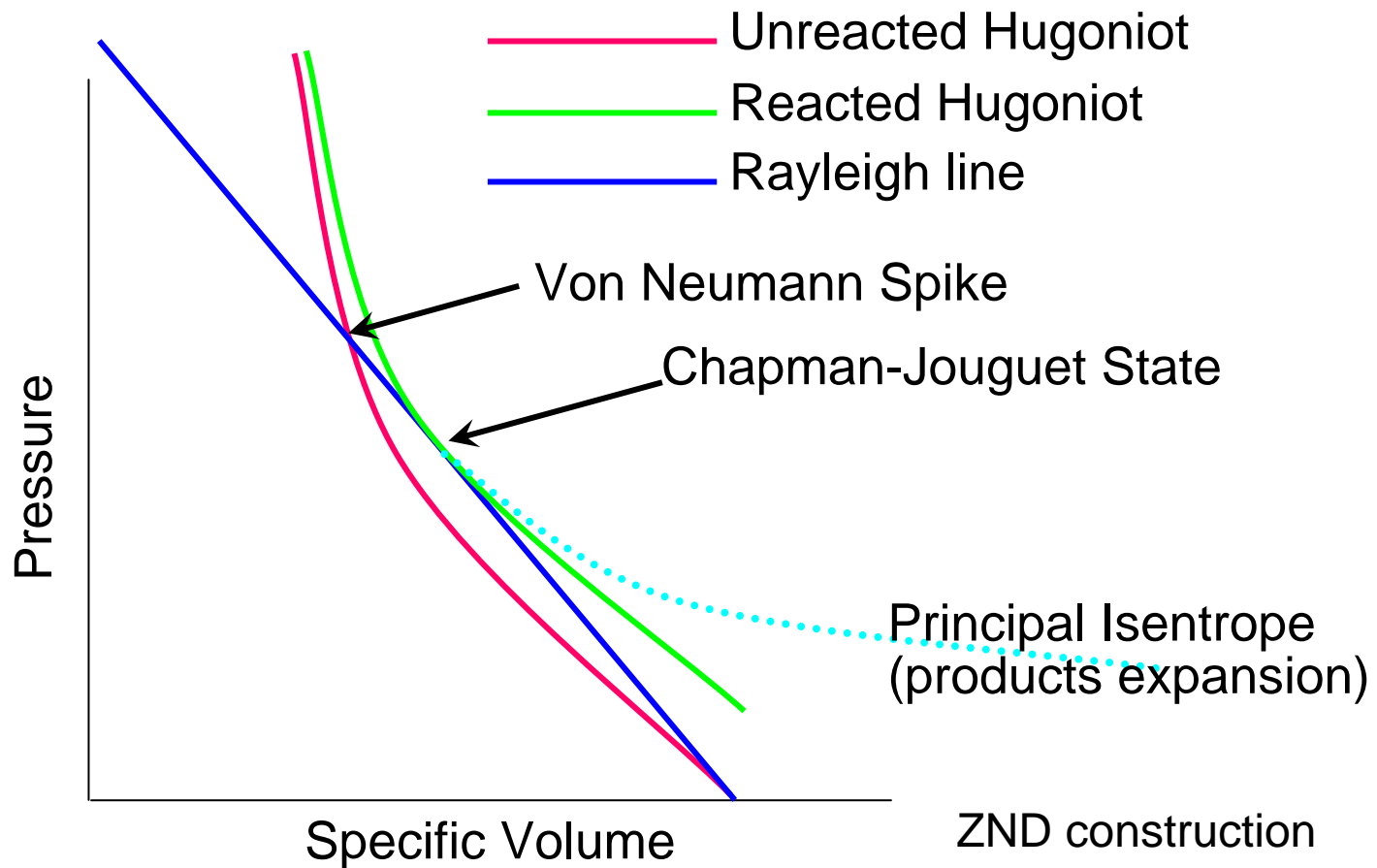
Chapman-Jouguet State

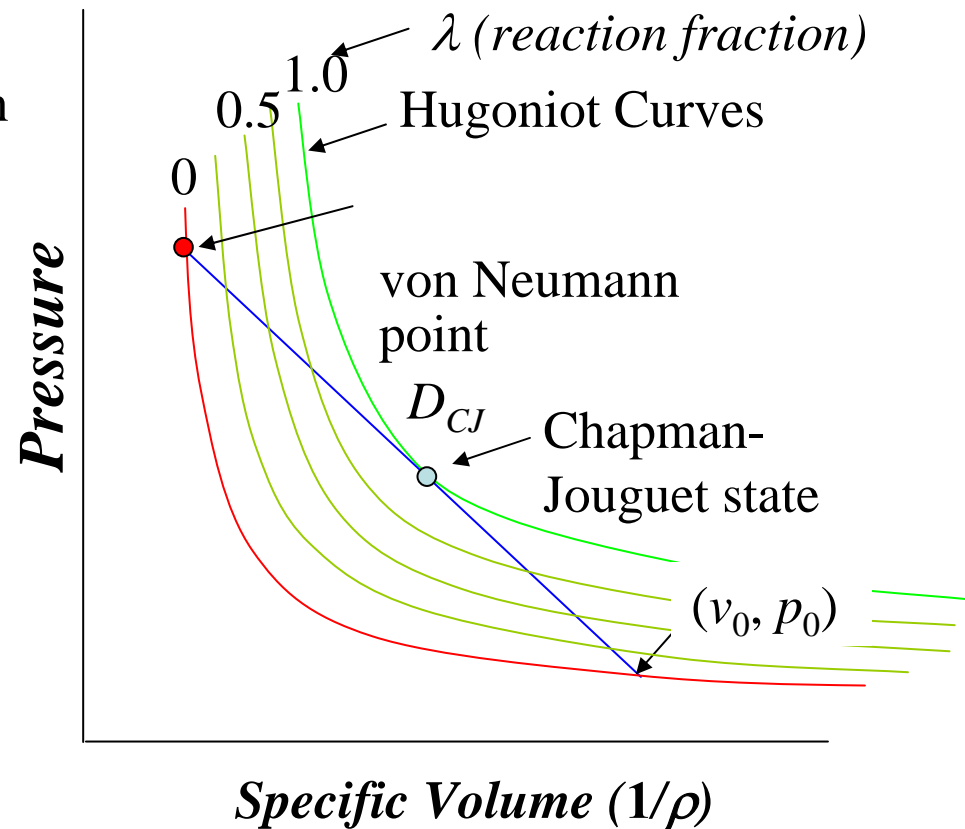
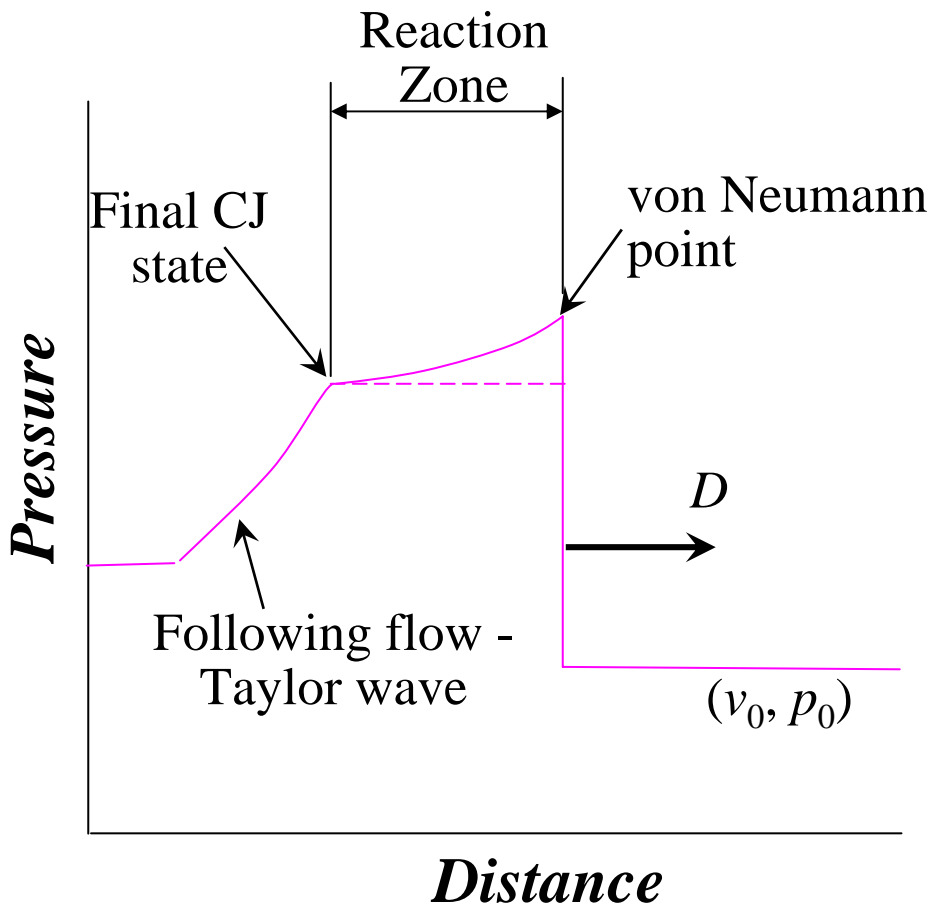
Hugoniot (energy)

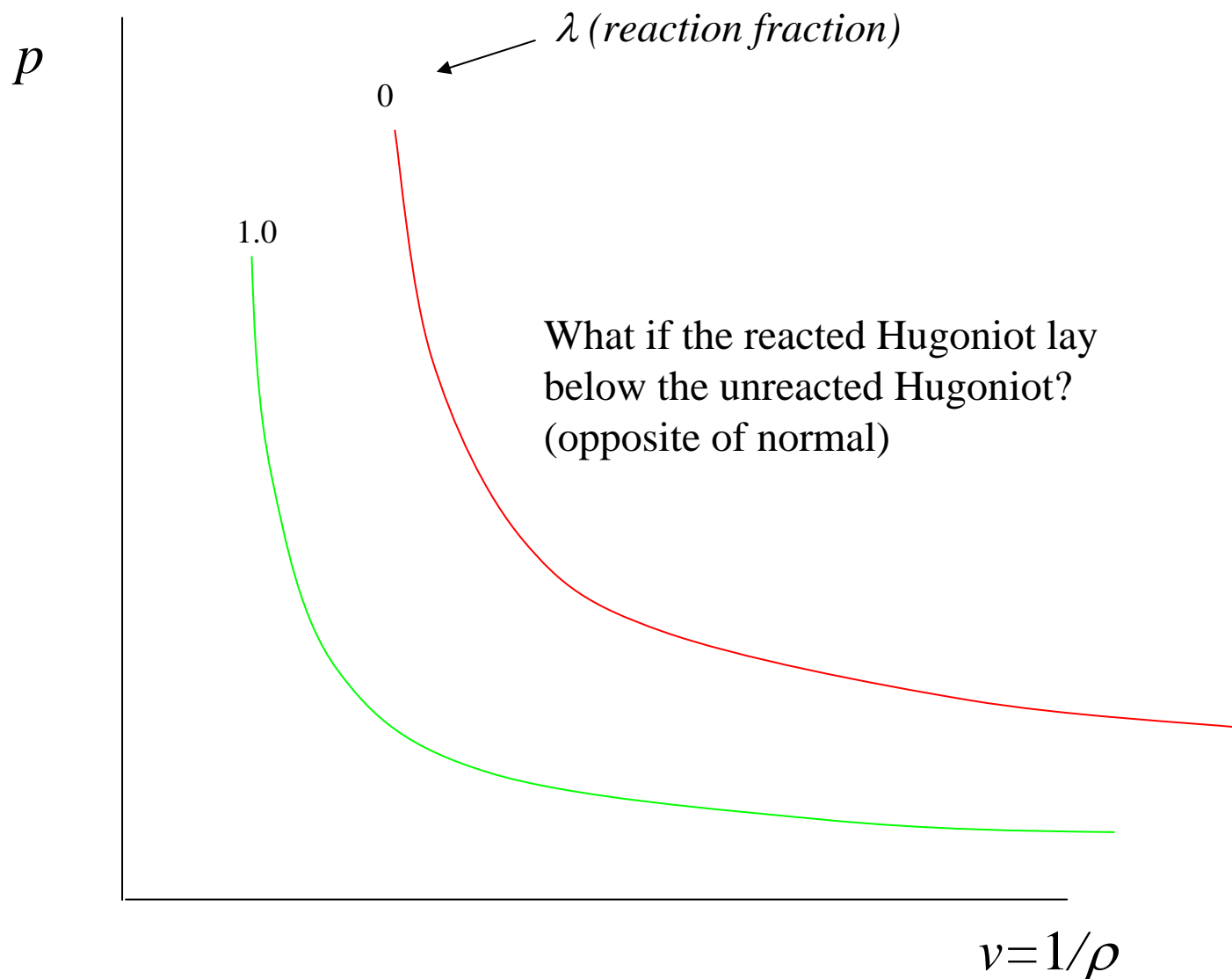
$$H = E - E_0 - 1/2 P(V_0 - V) = 0$$

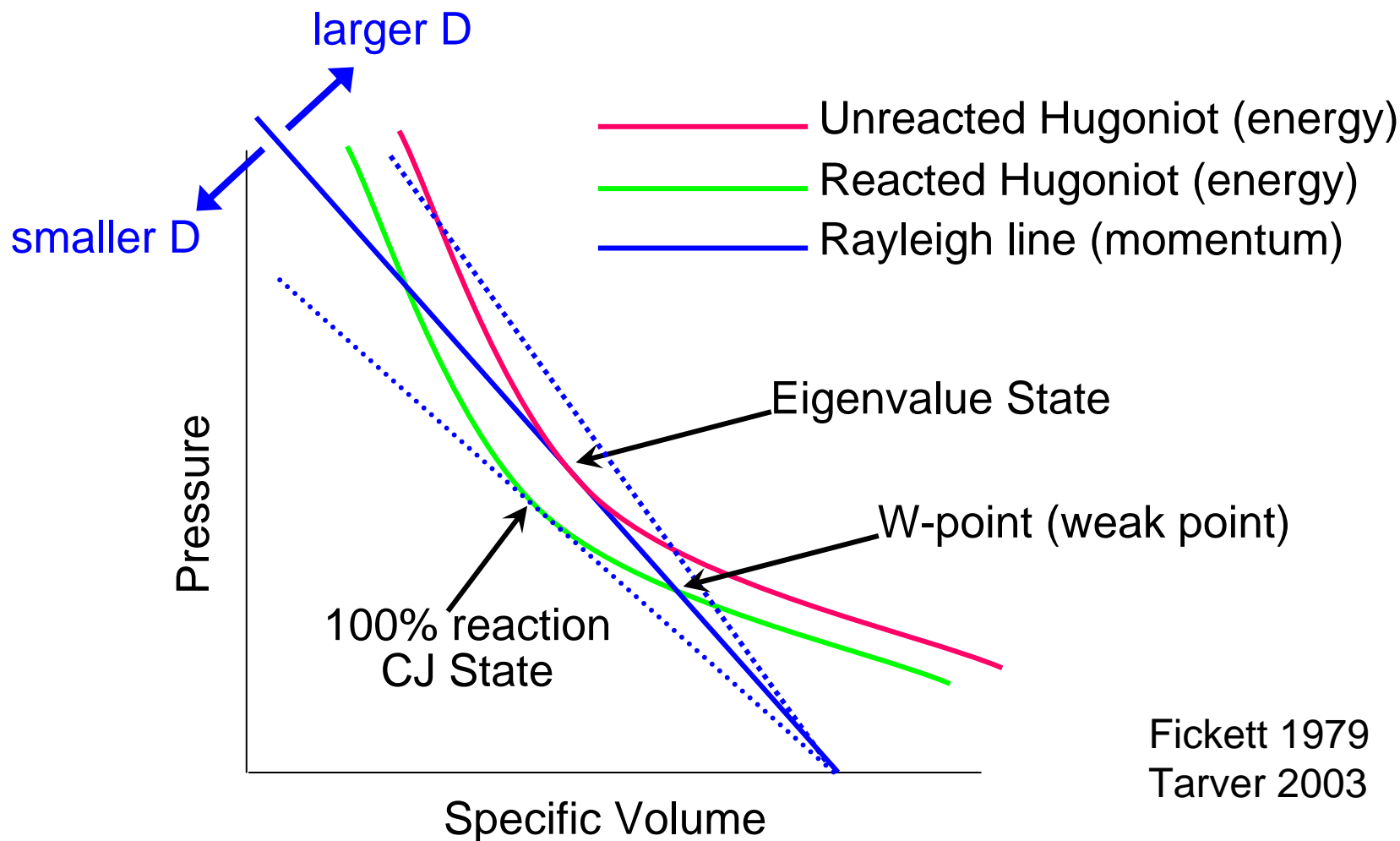
ZND construction

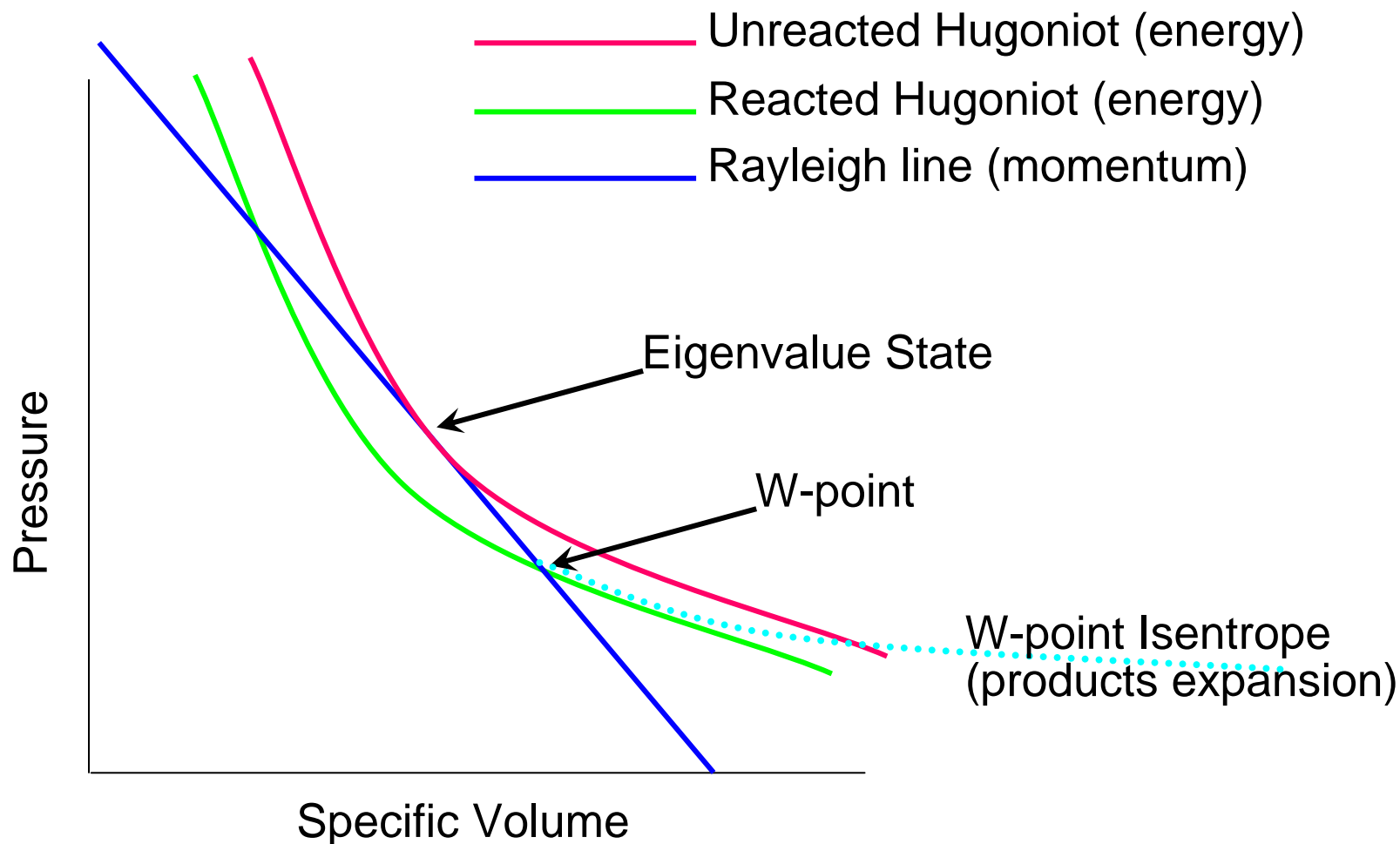
TECHNOLOGY DRIVEN. **WARFIGHTER FOCUSED.**

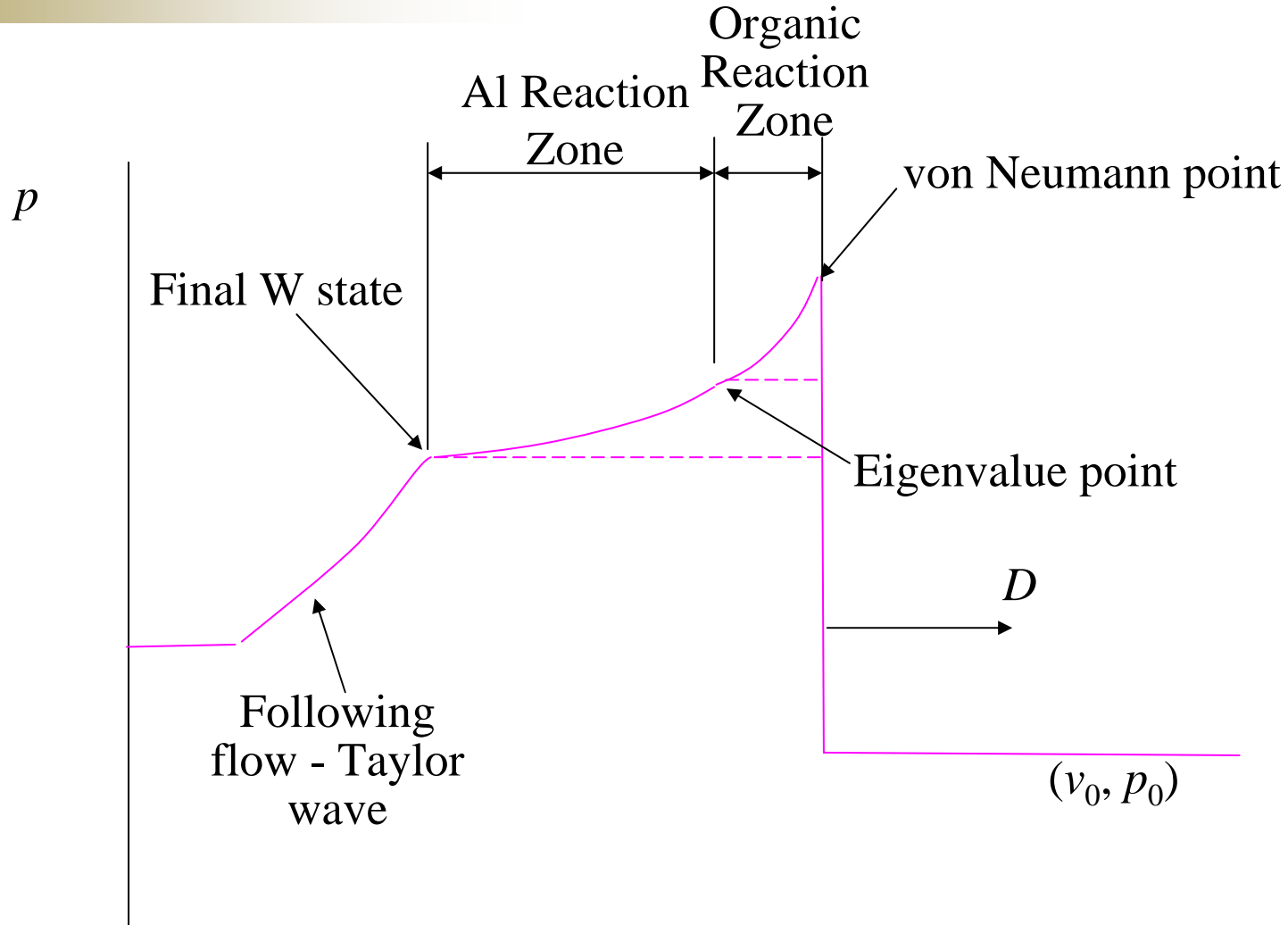


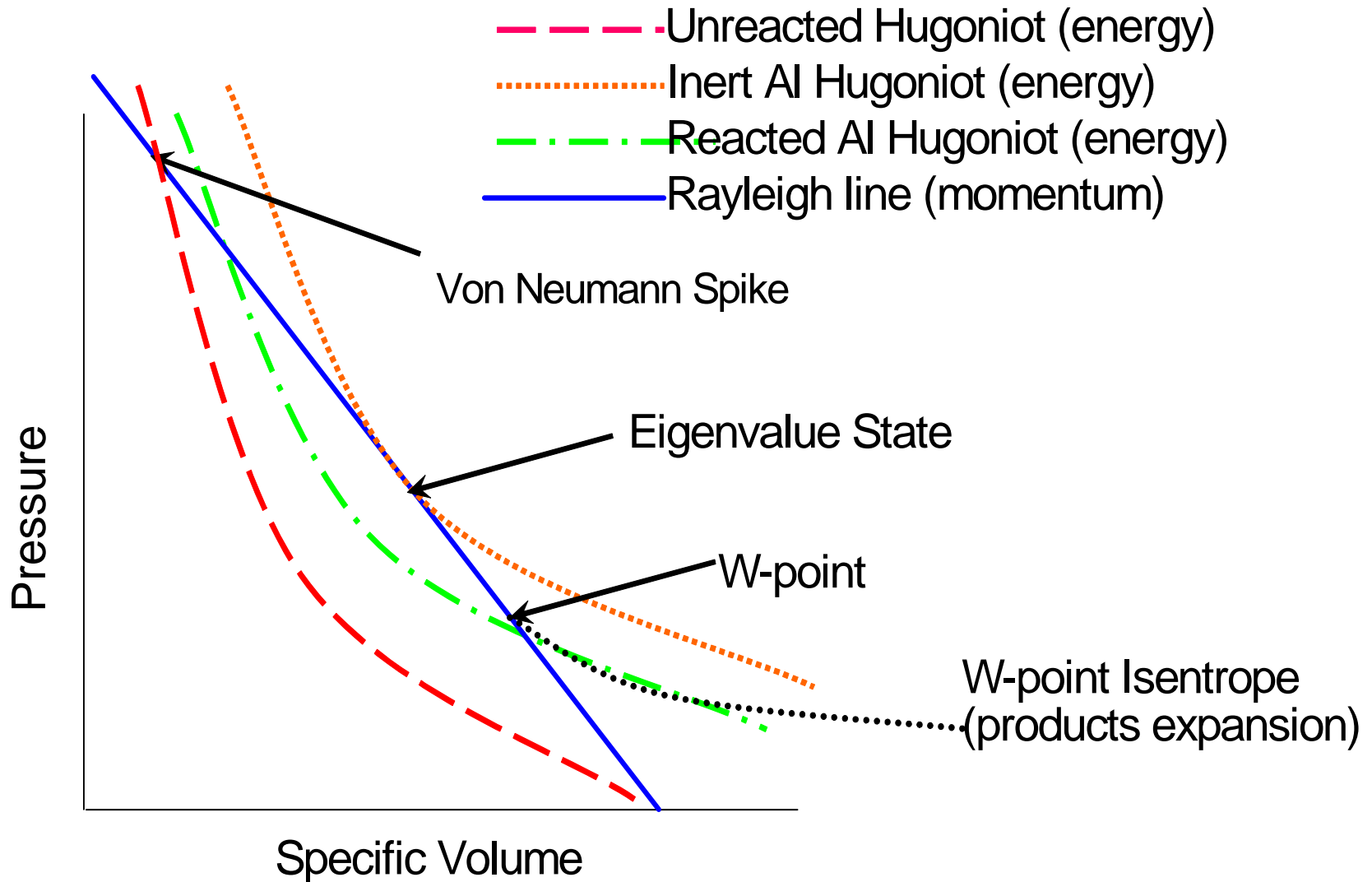




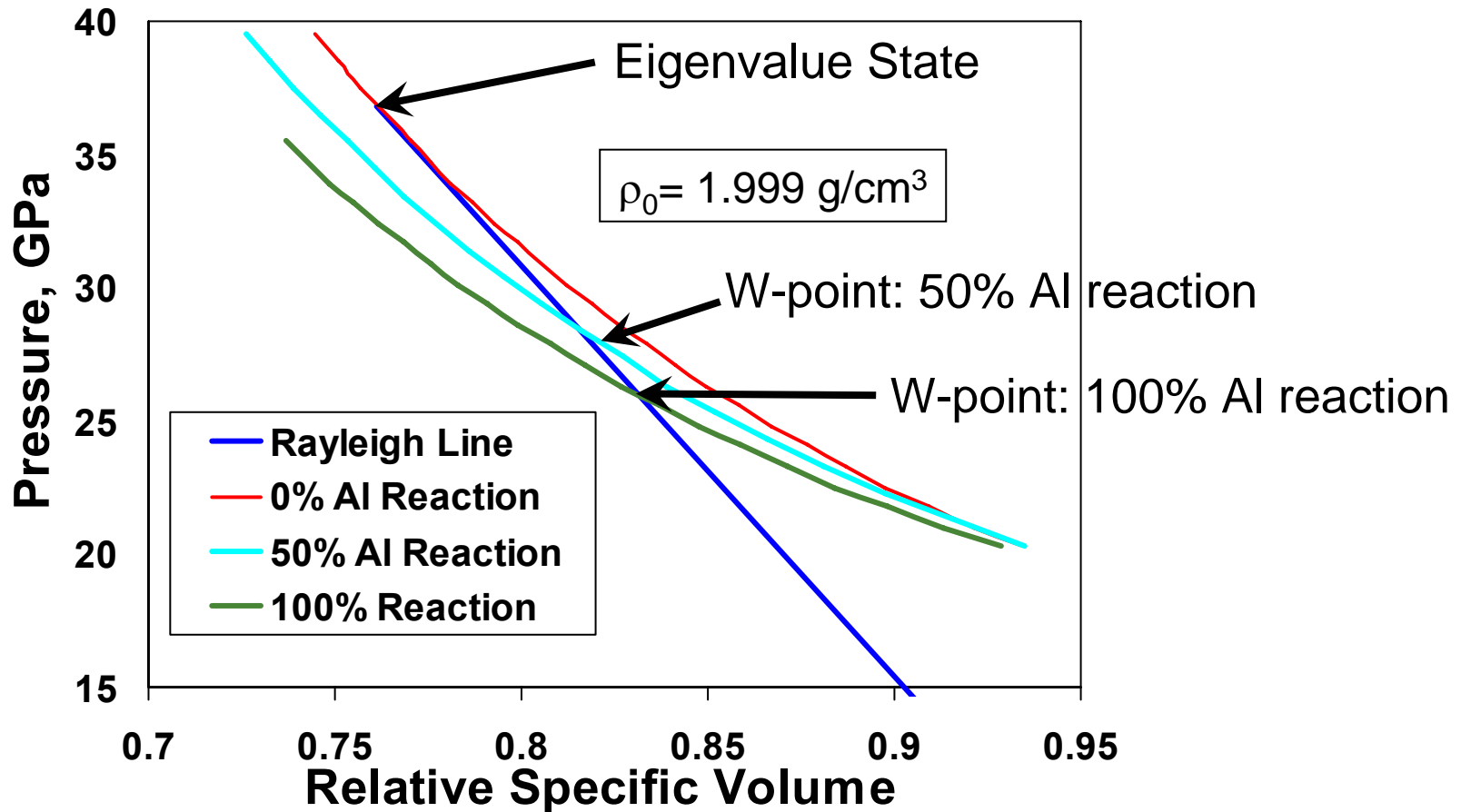






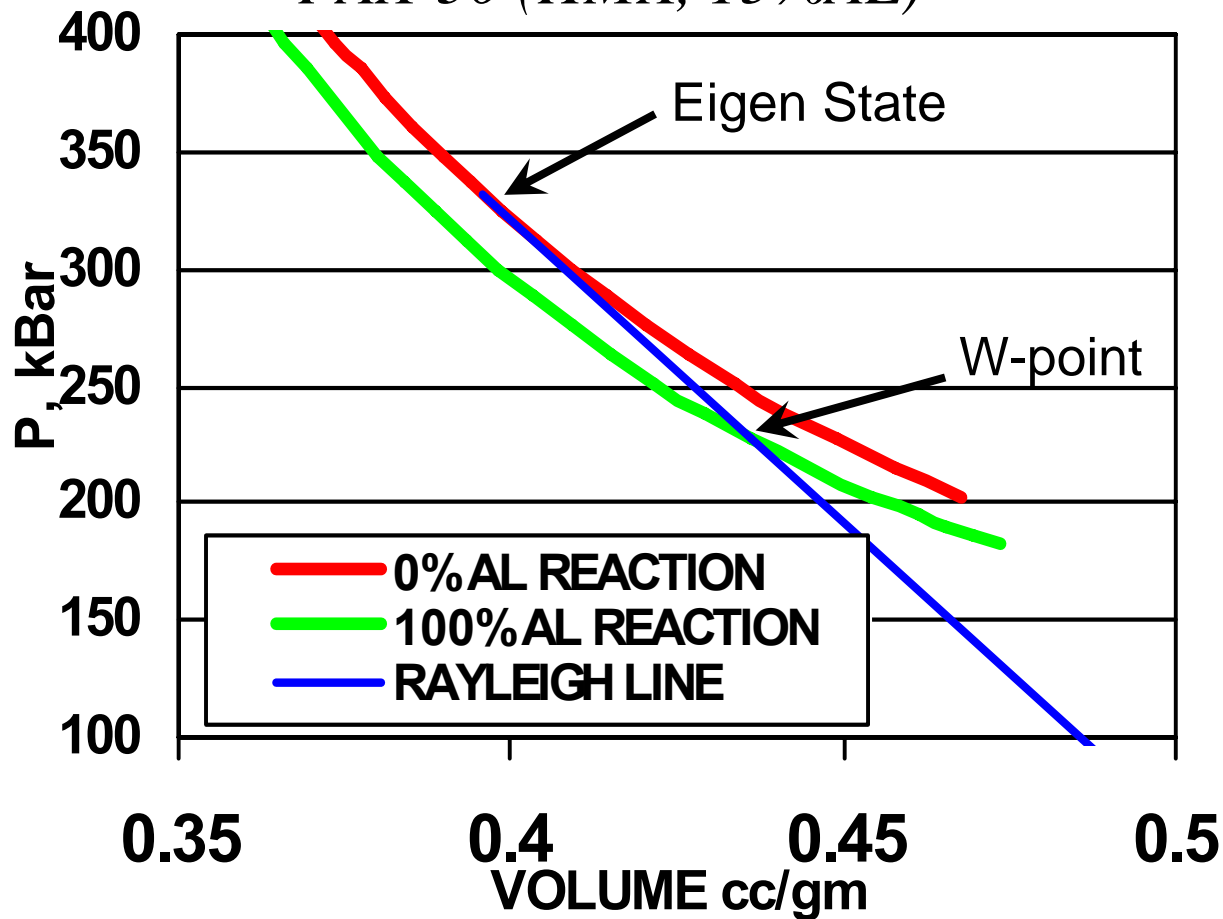


JAGUAR Calculations PAX-29 (CL-20, 15%Al)



Aluminum reaction produces lower Hugoniots

JAGUAR Calculations PAX-30 (HMX, 15%AL)



Detonation velocity controlled by 0% AL reaction Hugoniot!

Detonation Velocity Aluminized Explosives Data

EXPLOSIVE	Al%	ρ_0 (gm/cc)	Experiment D (Km/s)	JAGUAR Calculations	
				Inert Al D (Km/s)	Reacting Al D (Km/s)
HMX	5	1.84	8.71	8.66	8.53
HMX	15	1.87	8.45	8.42	7.95
HMX	25	1.95	8.55	8.35	7.32
BTNEN	15	1.96	8.29	8.38	7.45
BTNEN	15	1.91	8.06	8.16	7.24
NG	15	1.74	7.94	8.07	7.93
TNT	20	1.64	6.41	6.38	5.77
TNT	30	1.84	6.74	6.63	4.92
TNT	10	1.67	6.51	6.68	6.52
PAX-3	18	1.87	7.96	8.05	7.65
PAX-29	15	2.0	8.95	8.79	8.16
PAX-30	15	1.91	8.51	8.43	8.09
PAX-42	15	1.83	8.25	8.14	7.75
AVERAGE ERROR %				1.22	7.52

Detonation velocities agree with little or no aluminum reaction

JWLB Equation of State:

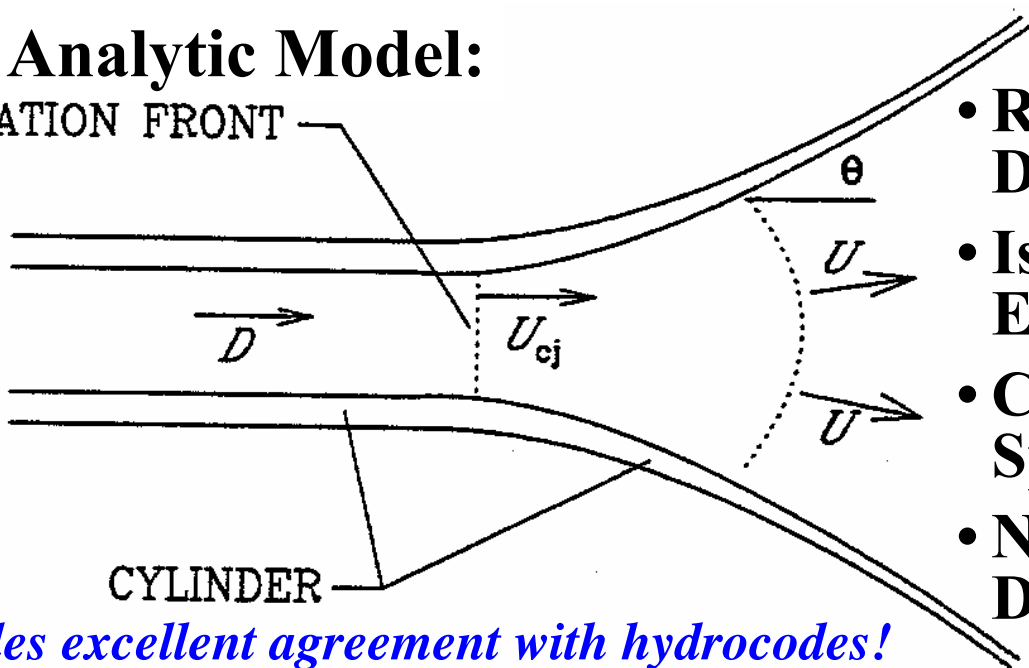
$$P = \sum_i A_i \left(1 - \frac{\lambda}{R_i V^*} \right) e^{-R_i V^*} + \frac{\lambda E}{V^*} + C \left(1 - \frac{\lambda}{\omega} \right) V^{*-(\omega+1)}$$

Gruneisen Parameter:

$$\lambda \equiv \sum (A_{\lambda i} V^* + B_{\lambda i}) e^{-R_{\lambda i} V^*} + \omega$$

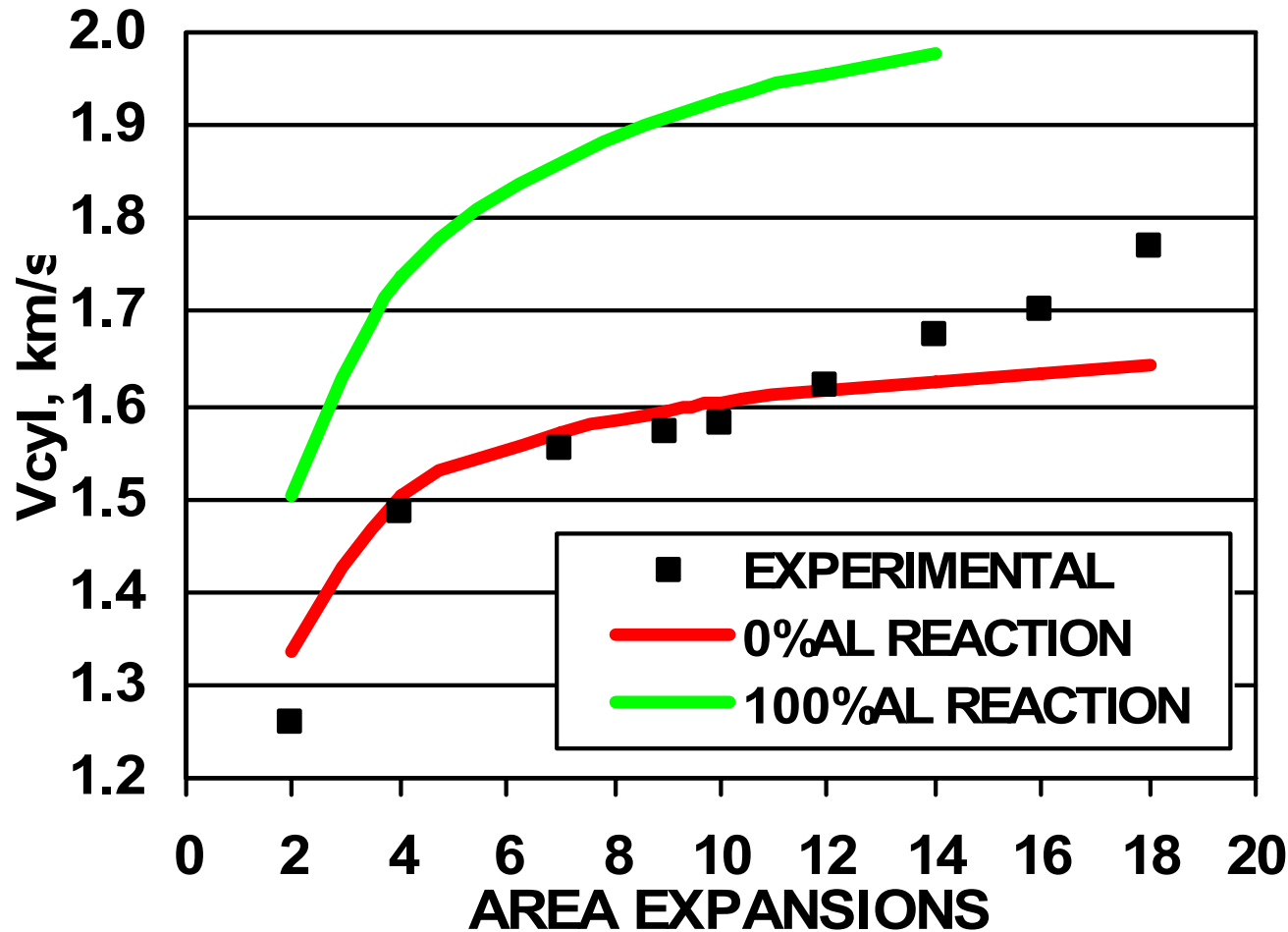
Analytic Model:

DETONATION FRONT

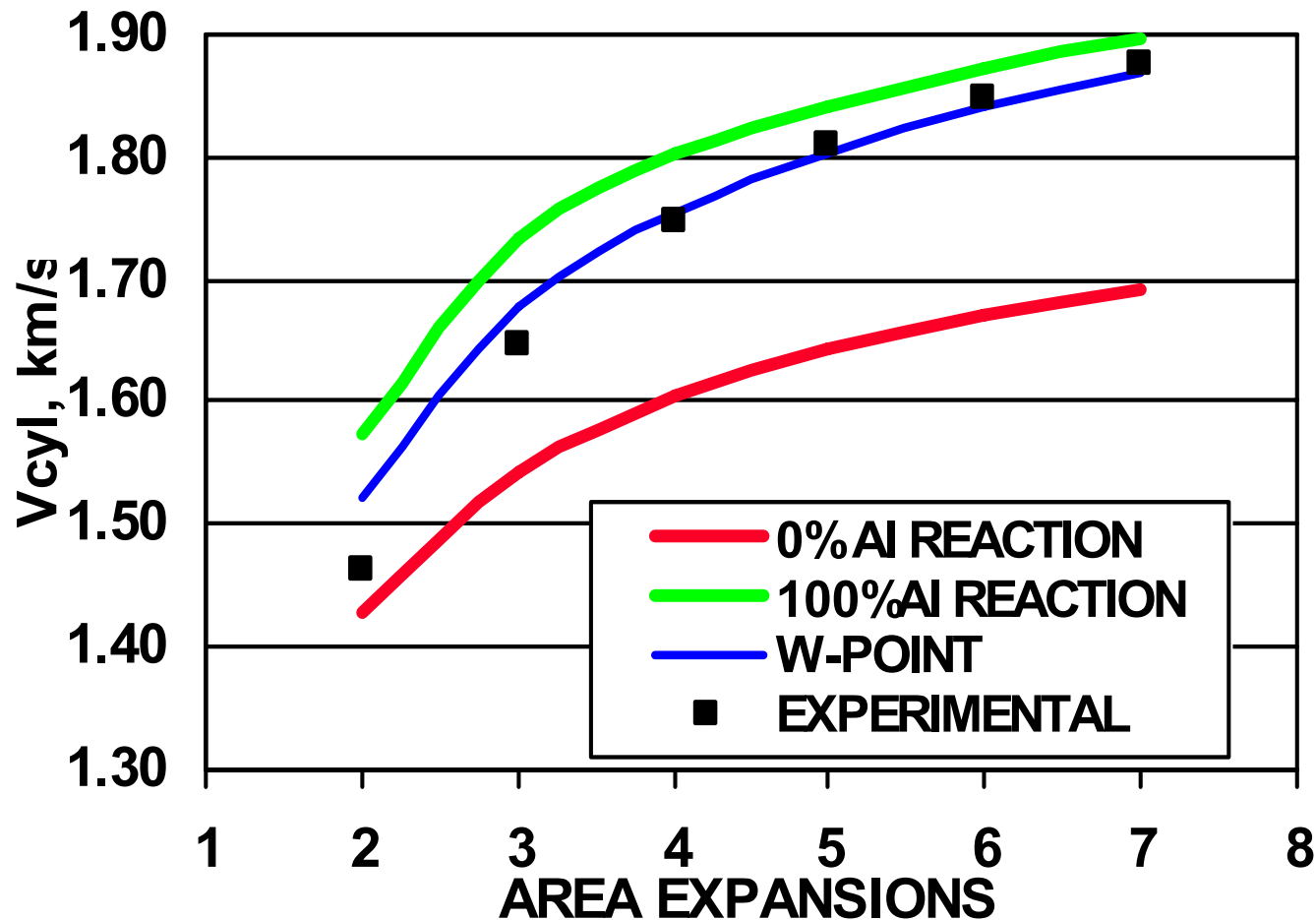


- Reference Frame at Detonation Velocity
- Isentropic Products Expansion
- Constant Properties Along Spherical Surfaces
- New: Modified for Eigen Detonation W-point

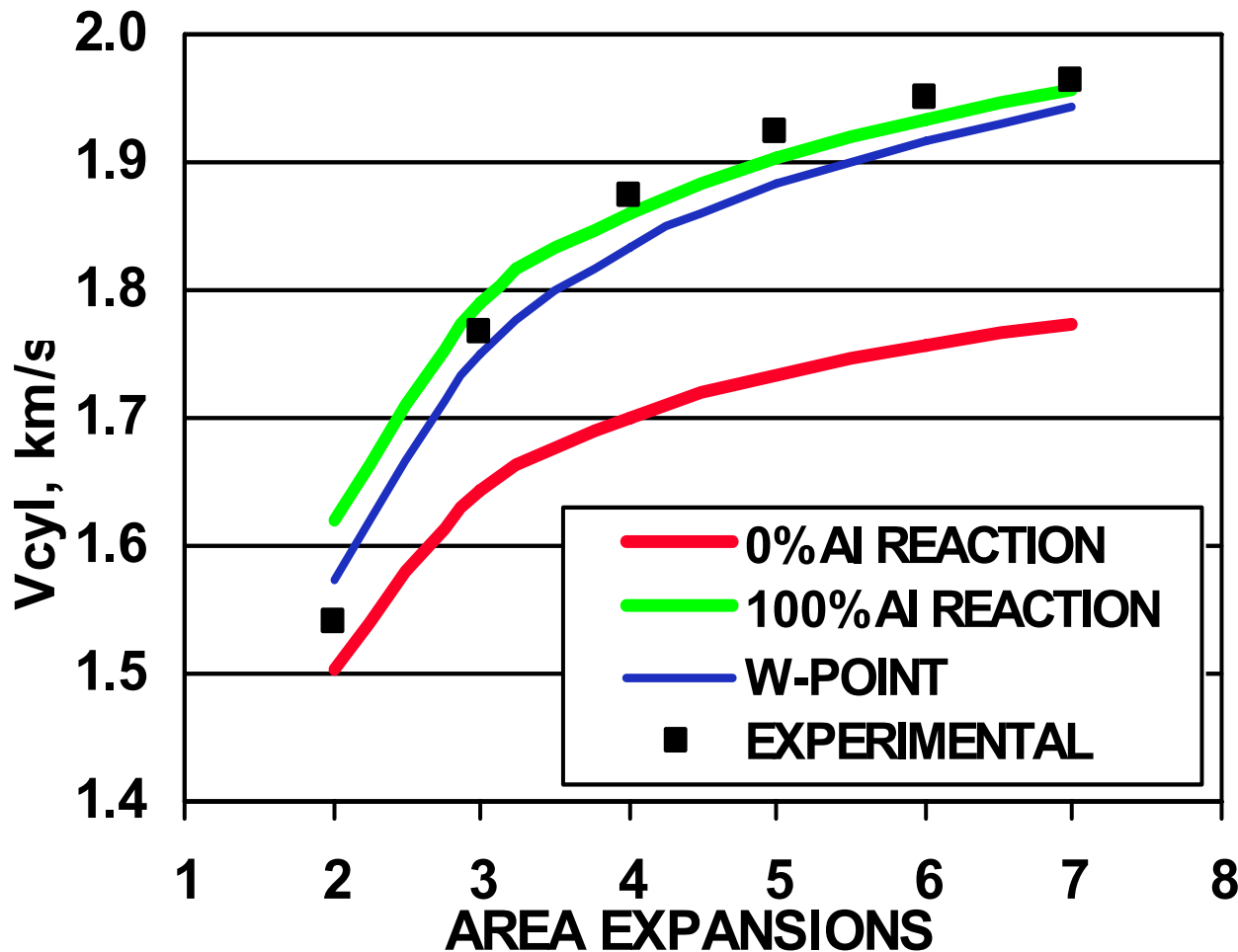
Provides excellent agreement with hydrocodes!



HMX with large particle size Aluminum: AL reacts late!



HMX with small particle size aluminum: AL reacts early!



CL-20 with small particle size Aluminum: AL reacts early!

	PAX-3 (Al INERT)	PAX-29	PAX-30	PAX-42
ρ_0 (g/cc)	1.866	1.999	1.885	1.827
E0 (Mbar)	0.08223	0.14611	0.13568	0.13109
D (cm/ μ s)	0.8023	0.8784	0.8342	0.8137
P (Mbar)	0.2937	0.2599	0.2419	0.2339
A1 (Mbar)	601.643	400.407	406.224	400.717
A2 (Mbar)	3.9482	82.630	135.309	16.5445
A3 (Mbar)	0.9403	1.5507	1.311	1.45169
A4 (Mbar)	0.049688	0.006126	0.006772	0.006103
R1	13.6055	20.9887	26.9788	13.6945
R2	3.69901	9.6288	10.6592	8.67402
R3	24.9093	24.2441	2.52342	2.5320
R4	1.04285	0.328128	0.335585	0.33570
C (Mbar)	0.007691	0.014626	0.013561	0.014057
ω	0.27780	0.24286	.234742	0.242371

D and P are from
W-Point
(not C-J values)

	LX14	PAX-2A	PAX-29	PAX-30	PAX-42
ρ_0 (g/cc)	1.819	1.770	1.999	1.885	1.827
E_0 (Mbar)	0.10213	0.09953	0.14714	0.135755	0.12994
D (cm/ μ s)	0.8630	0.8391	0.8784	0.8342	0.8137
P (Mbar)	0.3349	0.3124	0.2599	0.2419	0.2339
A_1 (Mbar)	26.1406	27.0134	8.58373	7.19151	13.8484
A_2 (Mbar)	.763619	.762675	0.168261	0.097112	0.145102
R_1	6.93245	7.22237	4.7726	4.59098	5.74864
R_2	1.94159	1.95979	1.03613	0.84089	0.99404
C (Mbar)	0.010994	0.010919	0.014556	0.013492	0.015193
ω	0.384193	0.375812	0.242252	0.233665	0.253095

Combined effects explosives: note large blast energies!

- New combined effects explosives produce both high metal pushing (early) and high blast (late) work output.
- Detonation velocities agree with little or no Al reaction even with sub-micron particles
- However, with small particles, complete Al reaction is indicated during early products expansion
- Eigen detonation theory used for EOS development

Interface Defeat for Unconfined SiC Ceramics

Th. Behner¹, Ch. E. Anderson Jr.², T. J. Holmquist³
M. Wickert¹, and D. W. Templeton⁴

¹ Fraunhofer Institut für Kurzzeitdynamik (EMI), Eckerstr. 4, 79104 Freiburg, Germany

² Southwest Research Institute, P.O. Drawer 28510, San Antonio, TX 78228, USA

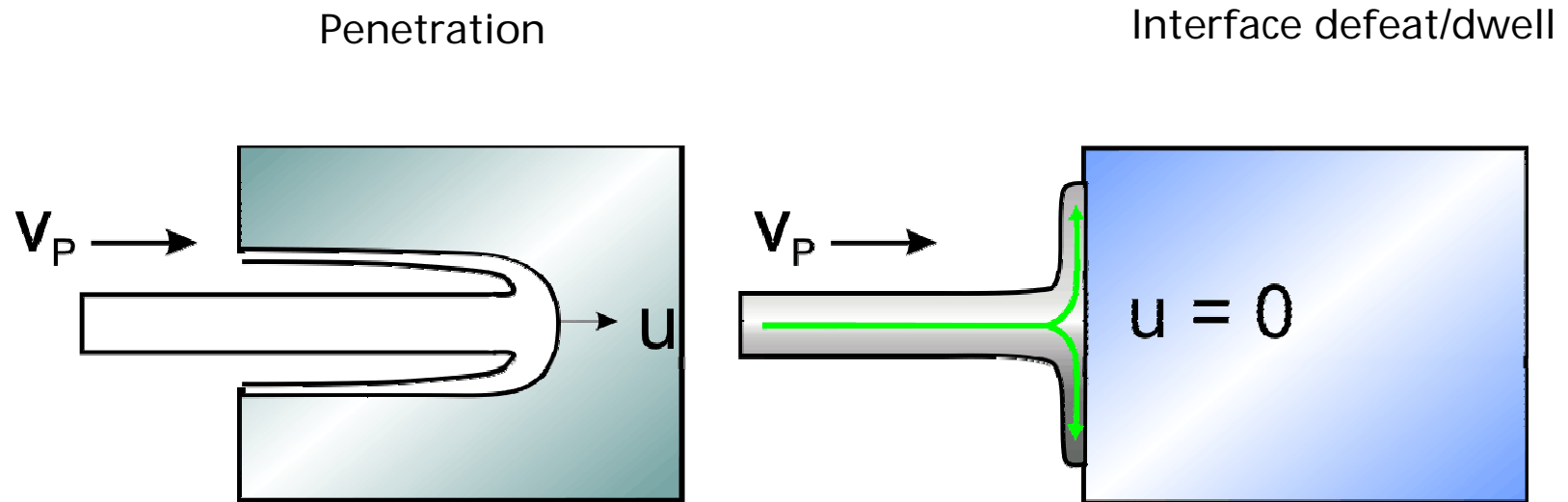
³ Southwest Research Institute, 5353 W. Yazata Blvd., Minneapolis, MN 55416, USA

⁴ U.S. Army TARDEC-RDECOM, AMSRD-TAR-R, Warren, MI 48397, USA



Motivation - Objectives

- Interface defeat/dwell on ceramics
 - ➔ ideal mechanism for an passive armor system



Behmer 09/2008

© 2008 Fraunhofer EMI

IBS 2008 - Slide 2



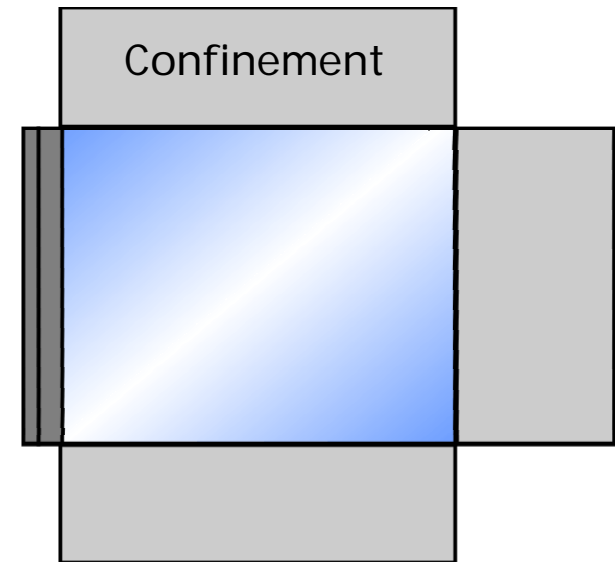
Motivation - Objectives

- Experimental study with an unconfined target design
 - ➔ focuses on dwell potential of the material and not on target arrangement
 - ➔ input for numerical model



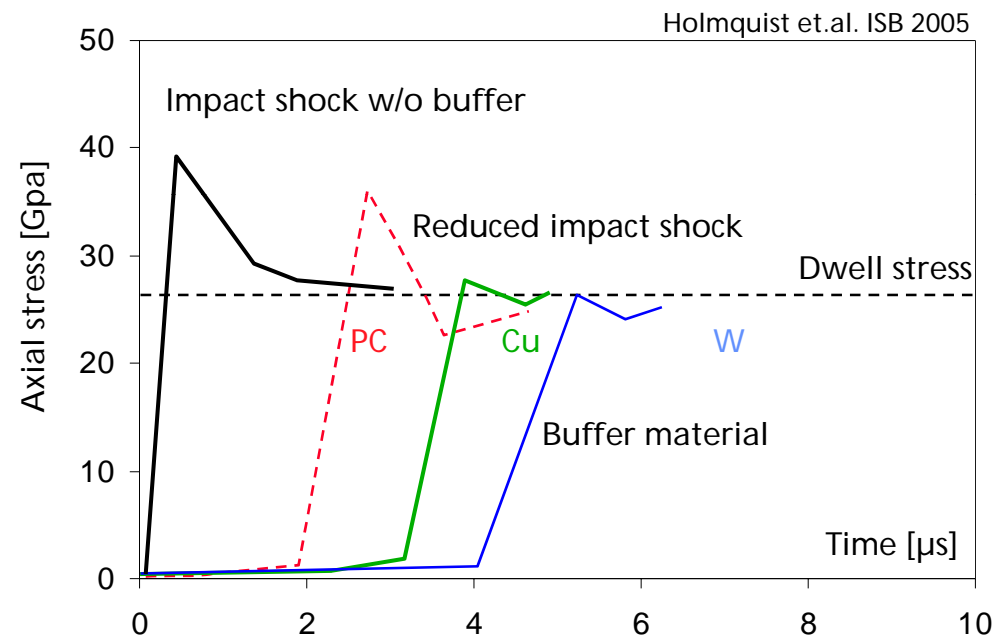
Unconfined

Coverplate
system



Motivation - Objectives

- Buffering the impact shock
 - ➔ increase transition velocity for interface defeat substantially



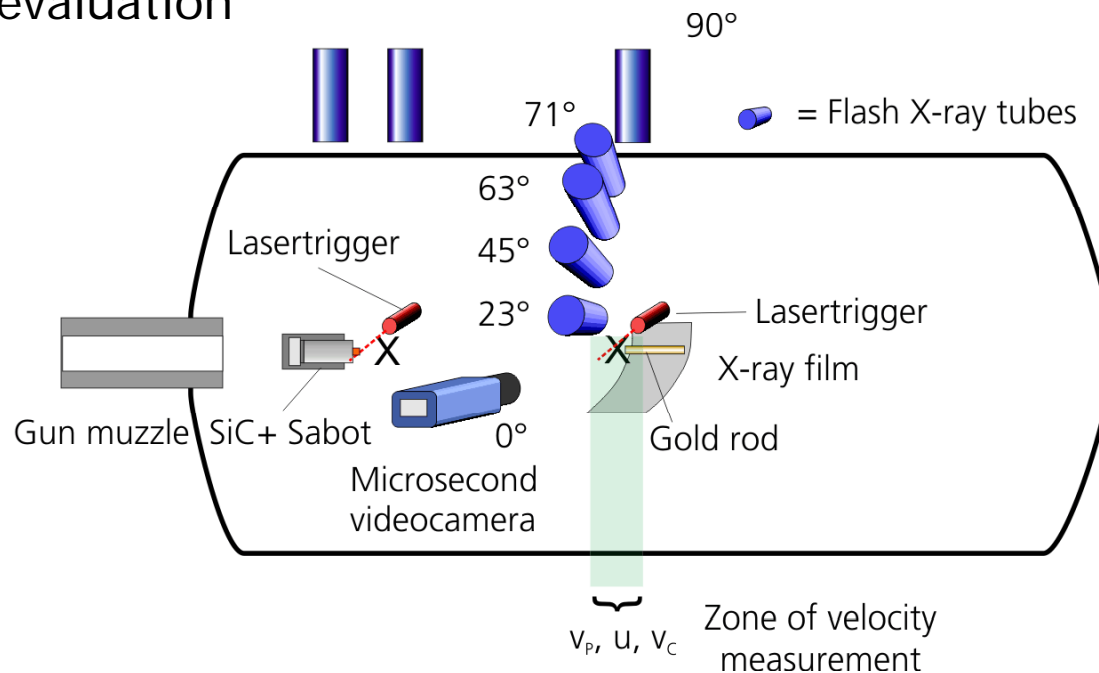
Experimental Set-Up

- Target: SiC-N cylinders, 35 mm long , Ø 20 mm
 - 3 types: ➔ bare
 - ➔ small Cu-buffer (Ø 5 mm, 4 mm height)
 - ➔ 20 mm Ø Cu-plate with 2 mm height
- Penetrator: pure gold rods (70 mm with Ø 1 mm)
 - ➔ low strength but high density
 - ➔ @ 1.6 km/s pressure/stress at target interface same as for WSA
- Reverse ballistic method
 - ➔ target launched at stationary rod
- Impact velocity v_p from 750 to 1700 m/s



Experimental Set-Up

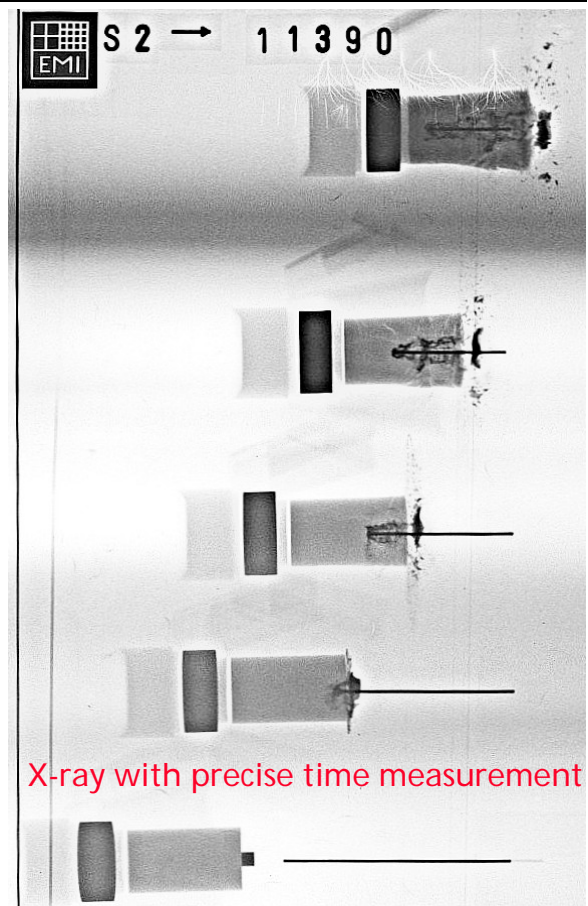
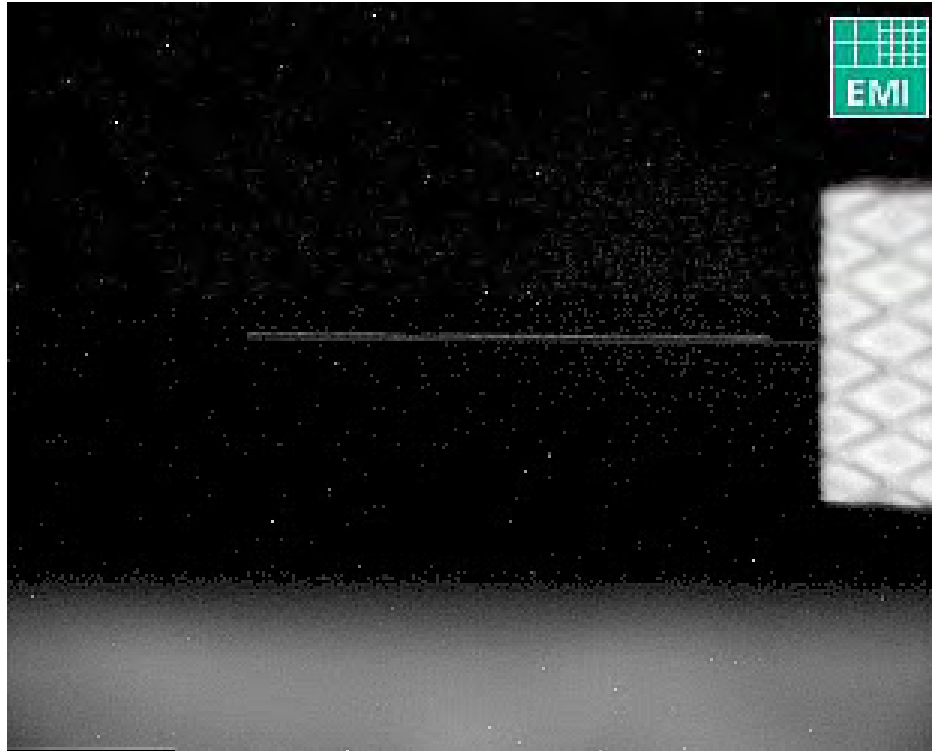
- 5 X-ray tubes in a single plane to monitor impact
- Optional a Microsecond video camera (up to 1 MFps) for optical evaluation
- All velocities measured in zone of impact
➔ high accuracy necessary



Observation of Dwell/Penetration

Exp. 11390, $v_p = 1550$ m/s

Video: 2 μ s interframe time / 500 ns exposure



Behmer 09/2008

© 2008 Fraunhofer EMI

IBS 2008 - Slide 7



Results – Bare SiC Experiments

Time after impact

$v_p = 776 \text{ m/s}$

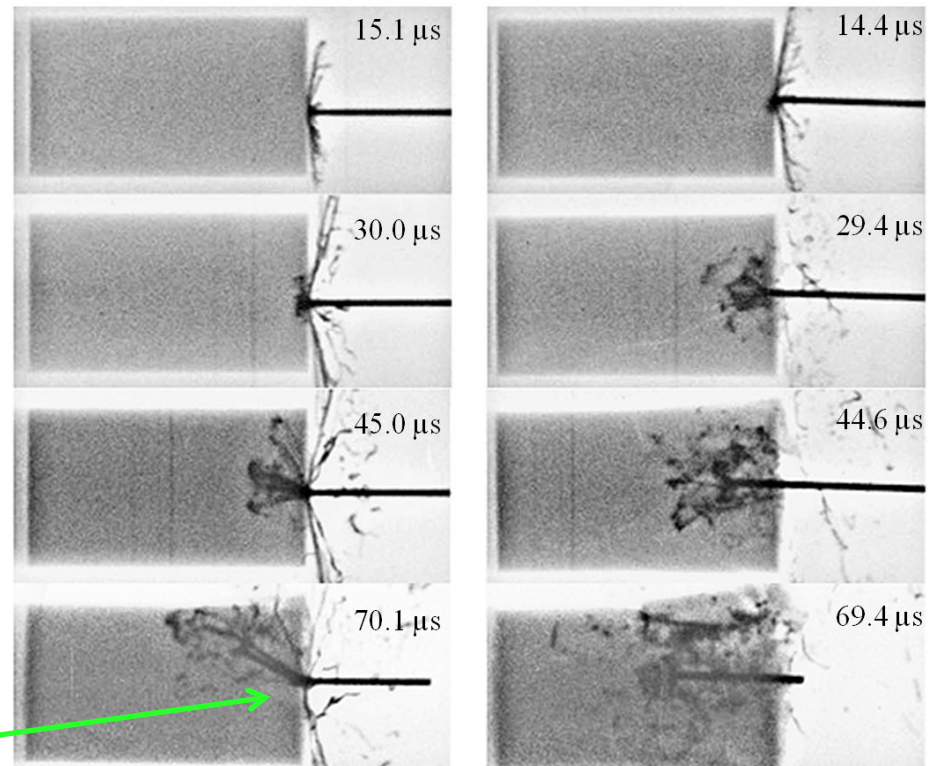
$v_p = 956 \text{ m/s}$

Left: sustained dwell

Right: short dwell phase with penetration

➔ Dwell possible up to 800 m/s impact velocity

Diversion of rod
at front surface



Results – Buffered SiC Experiments

Cu-buffer (Ø 5 mm, 4 mm height)

$v_p = 1484 \text{ m/s}$

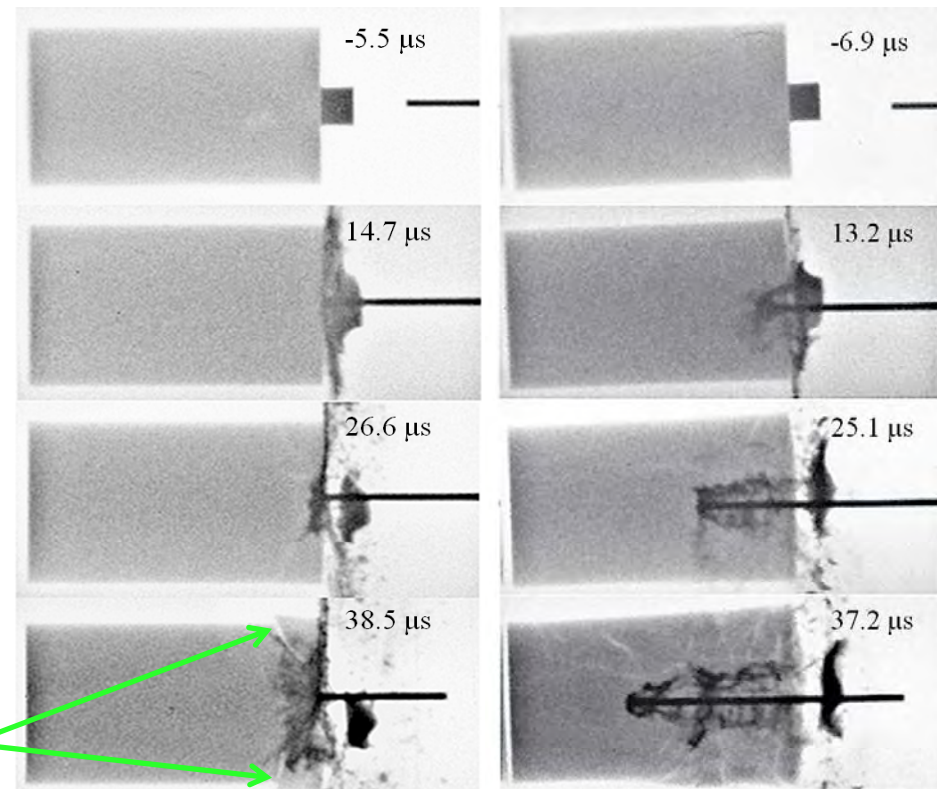
$v_p = 1550 \text{ m/s}$

Left: sustained dwell

Right: short dwell phase with penetration

➔ Dwell velocity substantially higher with buffer ($\approx 1530 \text{ m/s}$)

Conical shaped crack



Results – Buffered SiC Experiments

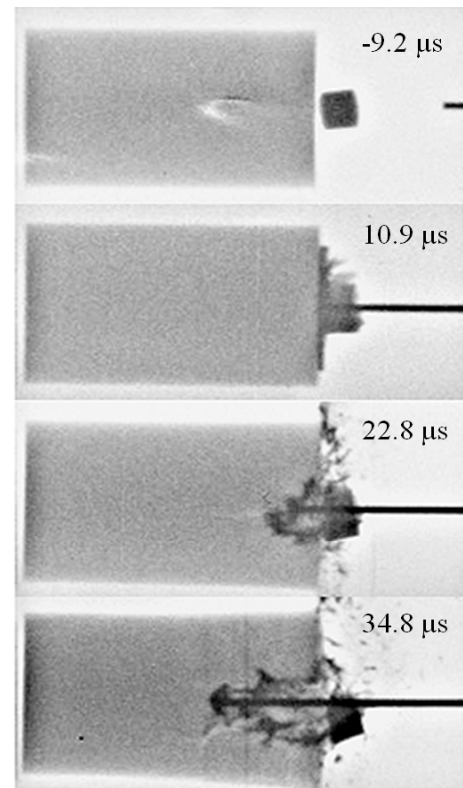
Separation of buffer before impact (accidental)

Left: large gap – short dwell

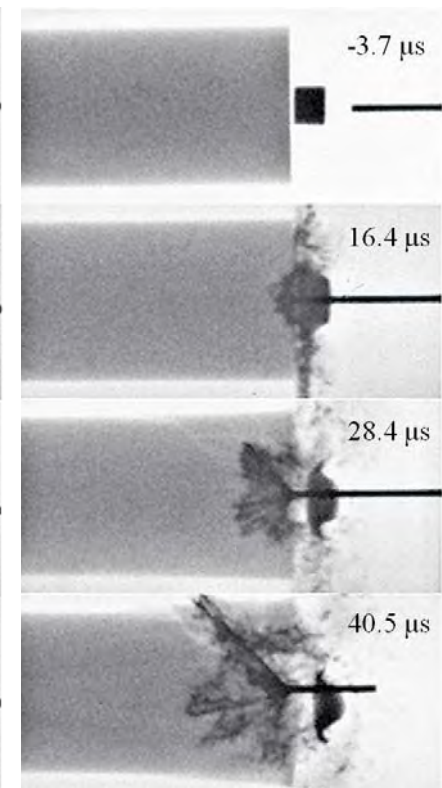
Right: short gap – sust. dwell

➔ Buffer separation influences dwell behavior
(Holmquist et. al. TB045
Poster session)

$v_p = 1416 \text{ m/s}$



$v_p = 1526 \text{ m/s}$



Results – Coverplate SiC Experiments

Cu-plate (Ø 20 mm, 2 mm height)

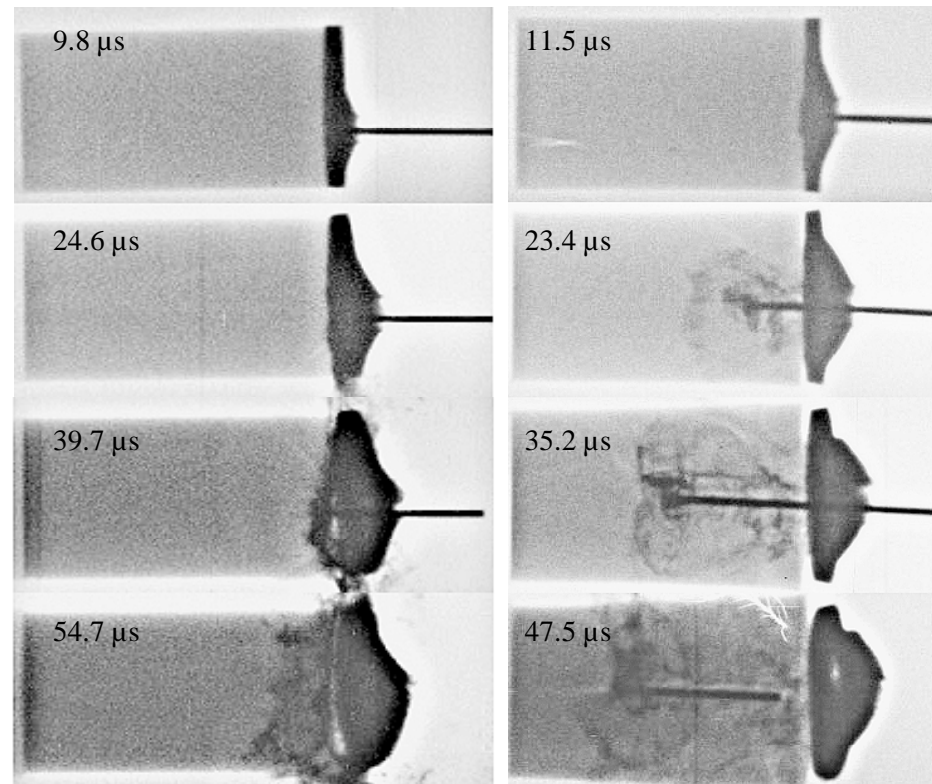
$v_p = 1382 \text{ m/s}$

$v_p = 1571 \text{ m/s}$

Left: sustained dwell

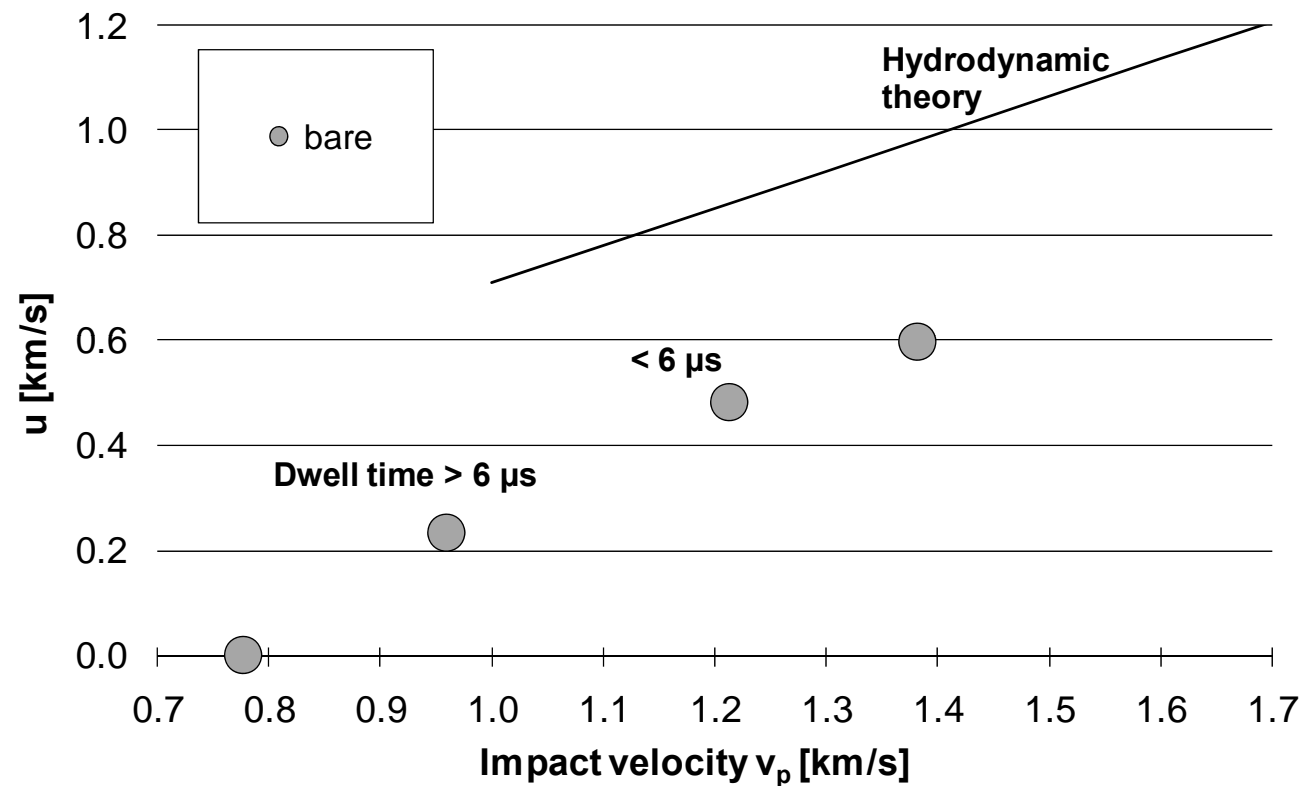
Right: short dwell phase with penetration

➔ Similar behavior as small buffer



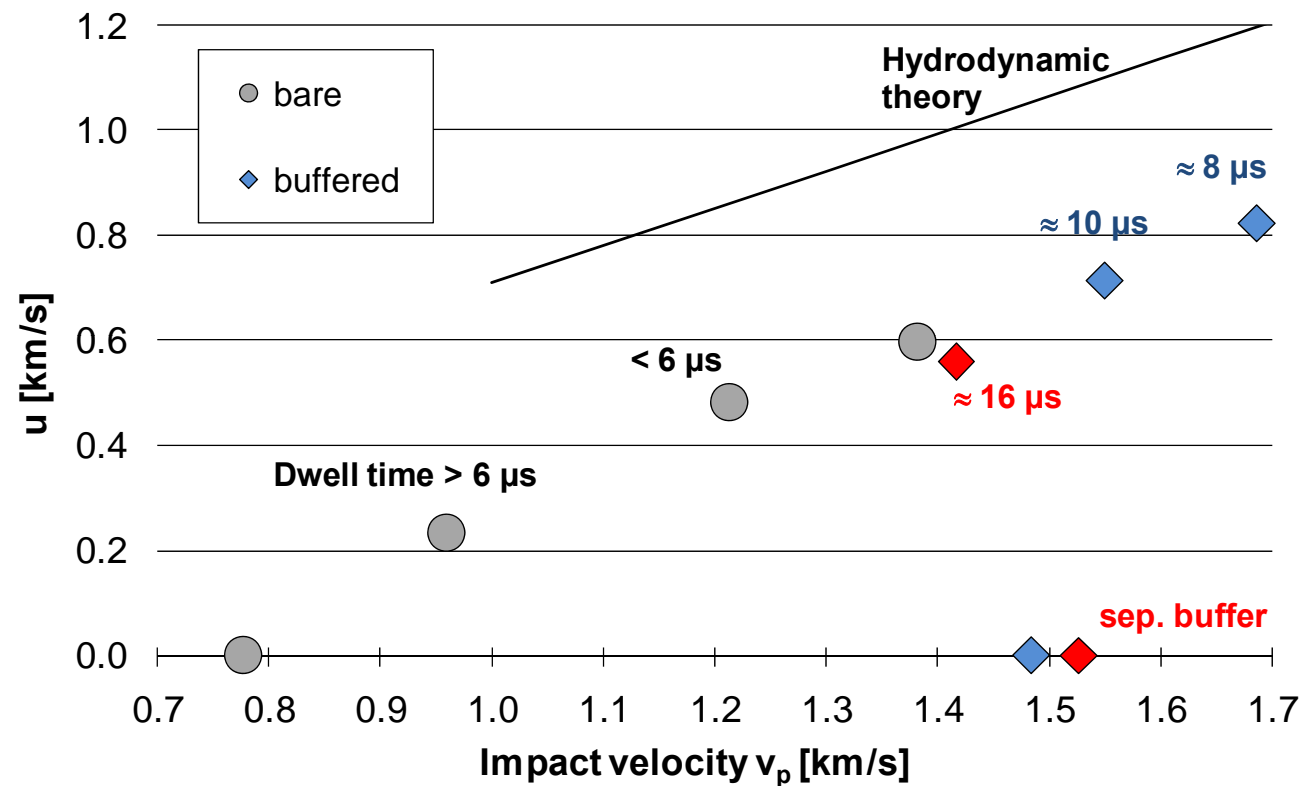
Transition from Dwell to Penetration

Penetration velocity vs. Impact velocity



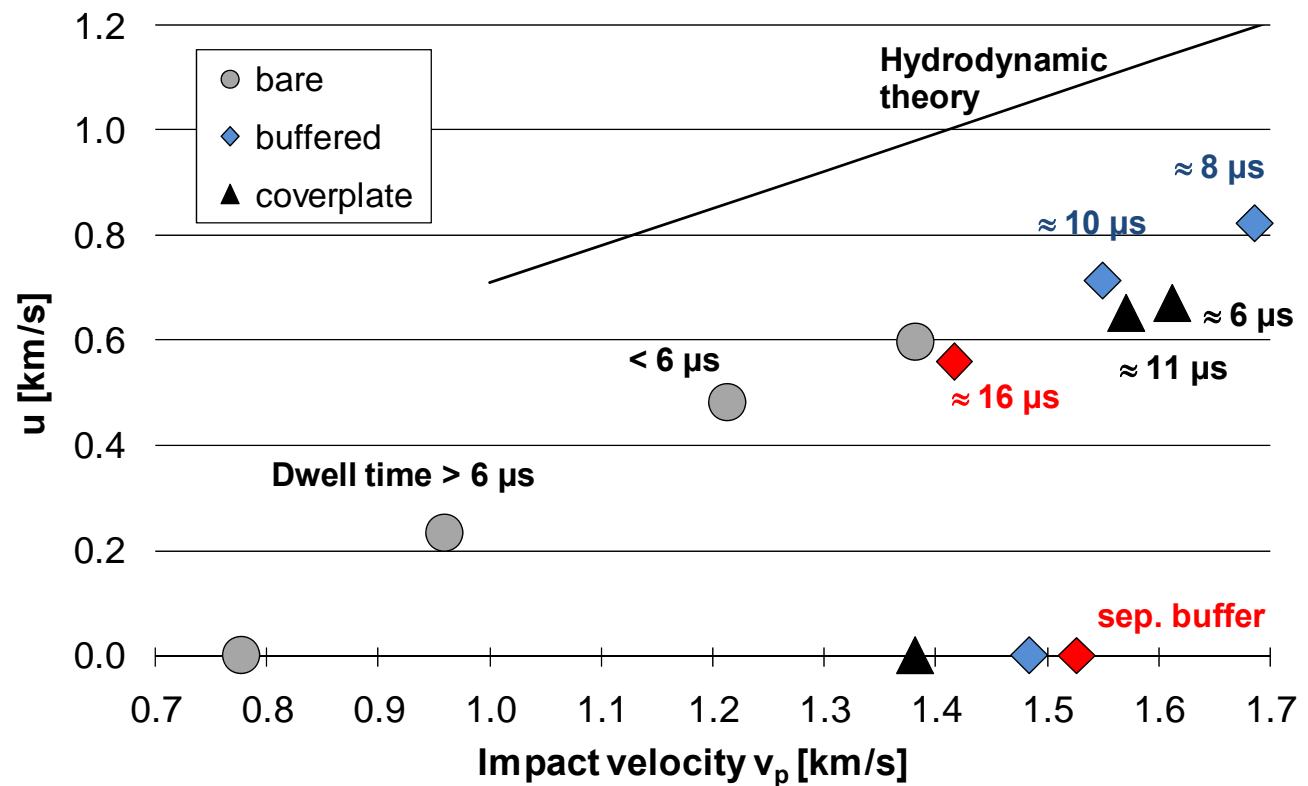
Transition from Dwell to Penetration

Penetration velocity vs. Impact velocity



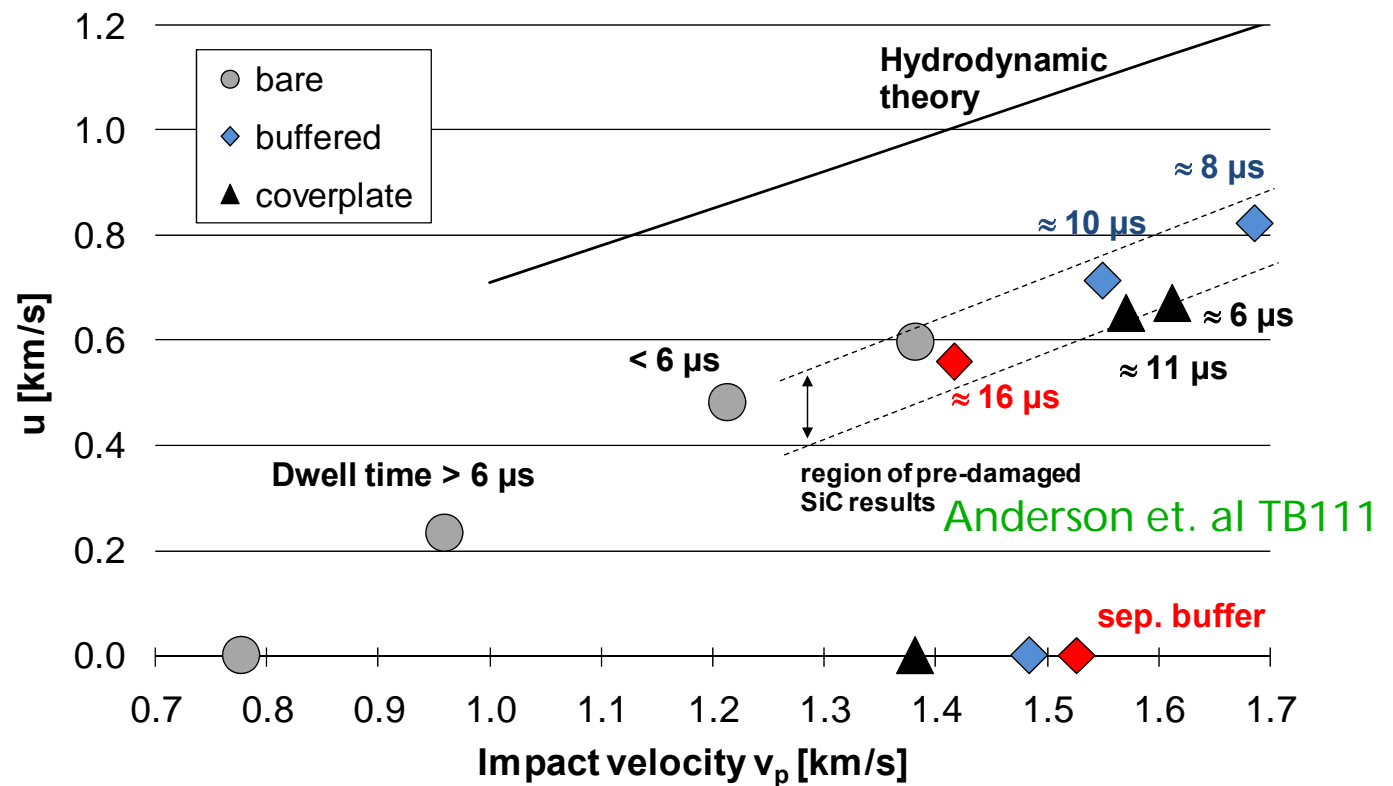
Transition from Dwell to Penetration

Penetration velocity vs. Impact velocity



Transition from Dwell to Penetration

Penetration velocity vs. Impact velocity



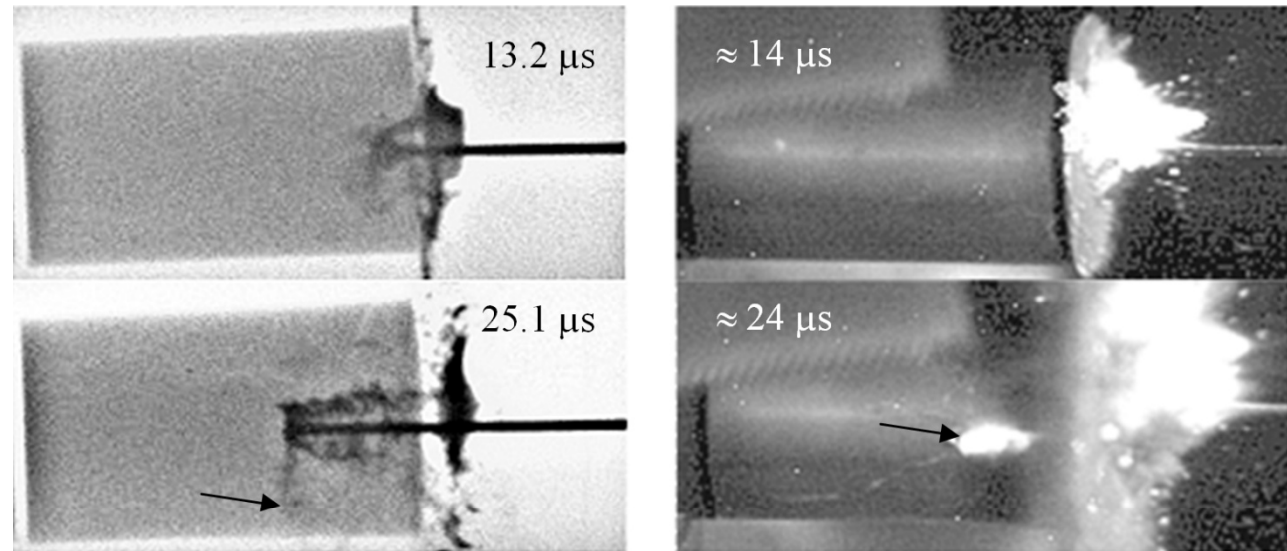
Comparing X-ray with Video still image

At nearly same time after impact

Upper section: diverted rod is forming into disc shape

Lower section: during penetration material emerges from cracks

$$v_p = 1550 \text{ m/s}$$

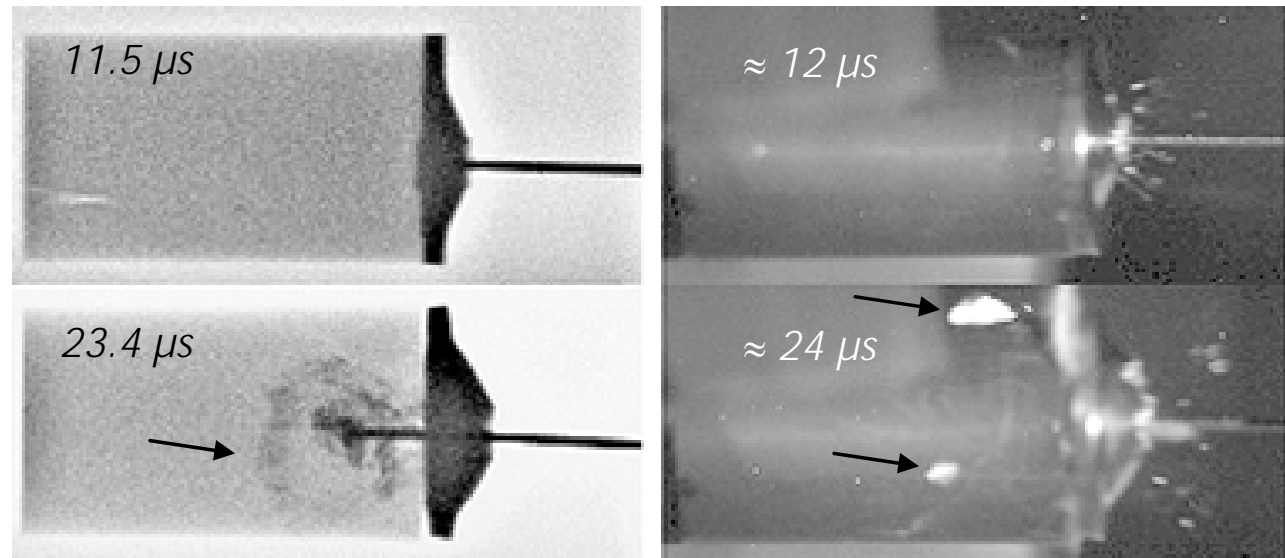


Comparing X-ray with Video still image

At nearly same time after impact

Upper section: Cover plate starts to bulge

Lower section: during penetration material emerges from cracks



$v_p = 1571 \text{ m/s}$

Behmer 09/2008

© 2008 Fraunhofer EMI

IBS 2008 - Slide 17



Summary and Conclusions

- Bare SiC samples dwell up to 800 m/s impact velocity
- A small Cu-buffer attached to front increase transition velocity to ≈ 1530 m/s
- A coverplate performs similar to a (smaller) buffer
- Microsecond video camera can reveal additional information during impact
- Further Experiments are planned to “pin down” on transition velocity



 **PDF Complete**
Your complimentary
use period has ended.
Thank you for using
PDF Complete.
[Click Here to upgrade to
Unlimited Pages and Expanded Features](#)



RDECOM



Survivability Measures for Evaluation of Personnel in Military Systems

24th International Symposium on Ballistics
22 - 26 September 2008



TECHNOLOGY DRIVEN. WARFIGHTER FOCUSED.

Kelly Benjamin
Natalie Eberius
Patricia Frounfelker

U.S. Army Research Laboratory
Survivability/Lethality Analysis Directorate

Outline

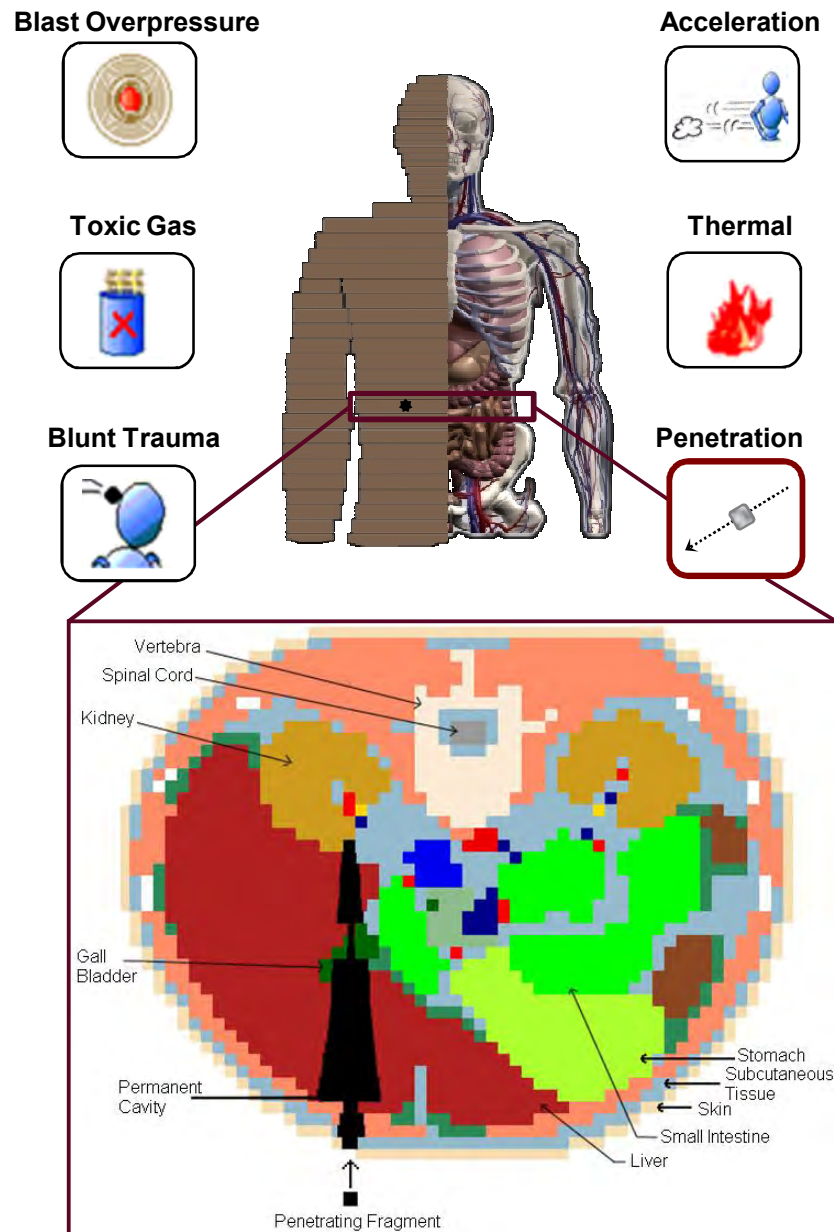


- ” ORCA overview
- ” Survivability and lethality discussion and metrics
- ” Crew casualty assessment
- ” Predictive personnel analysis of vehicle crew
- ” Sample analysis

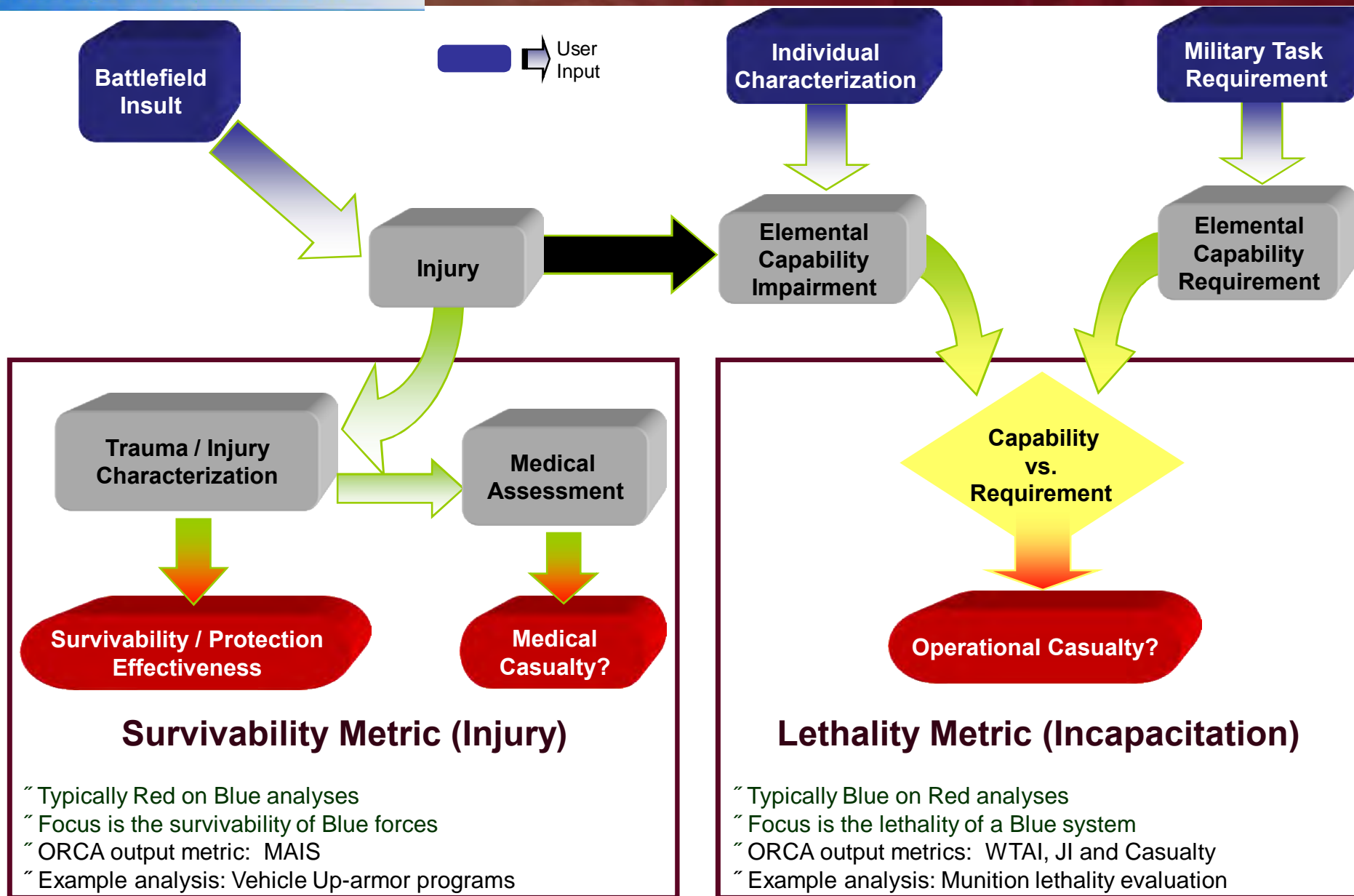
Operational Requirement-based Casualty Assessment (ORCA)



- “ ORCA is a high-resolution computerized human vulnerability model that is used to assess the impact of various casualty-causing insults on personnel.
- “ ORCA calculates several injury severity trauma metrics that may be used to characterize both an individual injury as well as multiple injuries to a single person.
- “ ORCA is used to assess the impact of various casualty-causing mechanisms on the ability of military personnel to perform battlefield tasks.
 - “ It considers the operational tasks that personnel must perform, and determines the extent to which penetration and other battlefield insults degrade the ability to perform these tasks.
 - “ The model can be applied to personnel occupying any crew position and posture on any combat platform.
 - “ Based on a given insult or set of insults, ORCA assesses whether personnel becomes impaired to the extent that the personnel is incapacitated based on his specific job/military occupational specialty (MOS).



ORCA Methodology



ORCA Metrics



SURVIVABILITY (Injury Metric): ORCA utilizes the Abbreviated Injury Scale (AIS). AIS is an anatomically-based, consensus-derived, international severity scoring system that classifies each injury by body region according to its relative importance on a 6-point ordinal scale. AIS values provide information on the type, location, and severity of anatomical injuries. AIS scores each single injury.

“ **MAIS** . Maximum Abbreviated Injury Score (MAIS) is an anatomical measure of injury severity. This score classifies injury severity on the basis of the single injury having the greatest AIS severity value. The MAIS is between 0 and 6.

MAIS	Injury Level	Head Injury Example	Type of Injury
1	Minor	Minor laceration of scalp	Superficial
2	Moderate	Major laceration of scalp, blood loss < 20%	Reversible injuries; medical attention required
3	Serious	Fracture of skull, penetration < 2 cm	Reversible injuries; hospitalization required
4	Severe	Depressed skull fracture, penetration > 2 cm	Non-reversible injuries; not fully recoverable without care
5	Critical	Depressed skull fracture, laceration of spinal artery	Non-reversible injuries; not fully recoverable even with care
6	Maximal	Massive brain stem crush	Nearly Unsurvivable

LETHALITY (Incapacitation Metric): ORCA provides operational metrics derived from evaluating the impact of injuries from one or more insults on the capabilities that humans use to accomplish tasks for a particular set of operational requirements.

“ **WTAI** . Weighted Task Average Impairment metric provides an average characterization of an individual's post-injury capability. ORCA examines the reduction in capability to perform individual tasks for a given job with respect to a minimum performance level. WTAI makes use of all task capability information by computing the average level of impairment over all of the task elements that constitute the job under consideration.

Crew Casualty Assessment



Survivability Assessment

- “ Injury/Medical metrics:
 - . Severity of Injuries
 - . Are the injuries treatable?
 - . Are there medical casualties?
 - . Trauma scoring metrics
- “ Operational Metrics (secondary questions):
 - . Are there operational casualties?
 - . Is our mission intact?

Example:

Effectiveness of Added Vehicle Protection

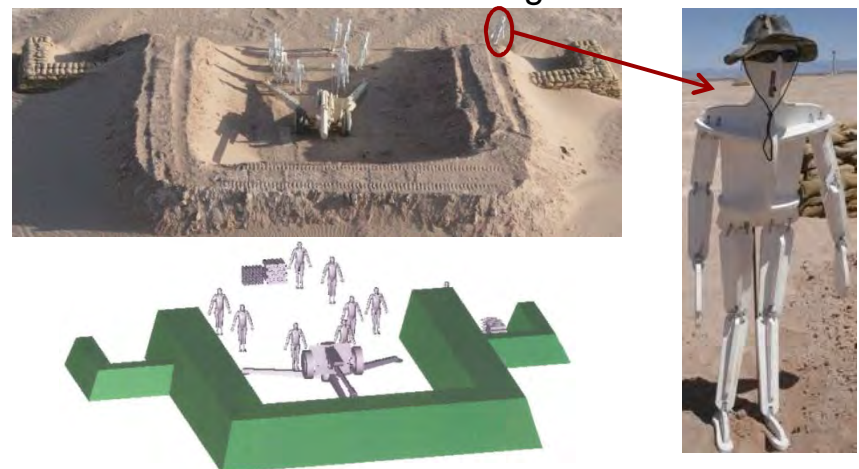


Lethality Assessment

- “ Operational Metrics:
 - . Quantitative measure of weapon performance
 - . Can soldier perform certain military tasks?
 - » Dependent on soldier's tactical role and time after wounding
 - . Has the threat been neutralized?
 - . Is the enemy's mission intact?

Example:

Effectiveness of an Air-bursting Munition



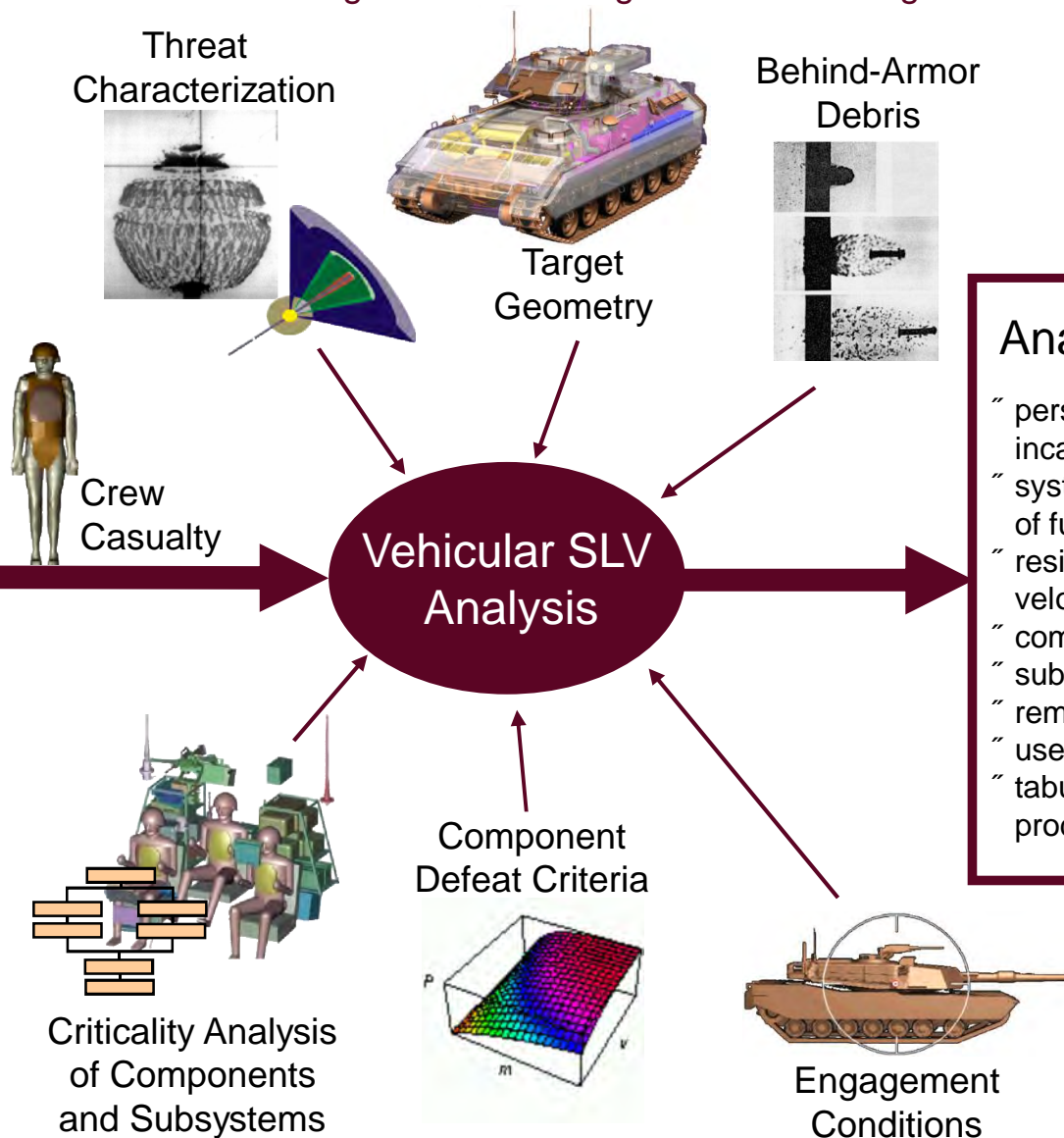
MUVES-S2 and ORCA



A Survivability/Lethality/Vulnerability (SLV) computer model capable of analyzing the effects of one or more munitions against aircraft or ground-mobile targets.

ORCA Methodology allows for:

- " discrete shot lines through anatomy based on orientation of threat trajectory to personnel
- " projectile penetration mechanics through various anatomic structures
- " velocity retardation of threat through wound track
- " injury description by type, severity, and frequency
- " in-depth description of operational effectiveness



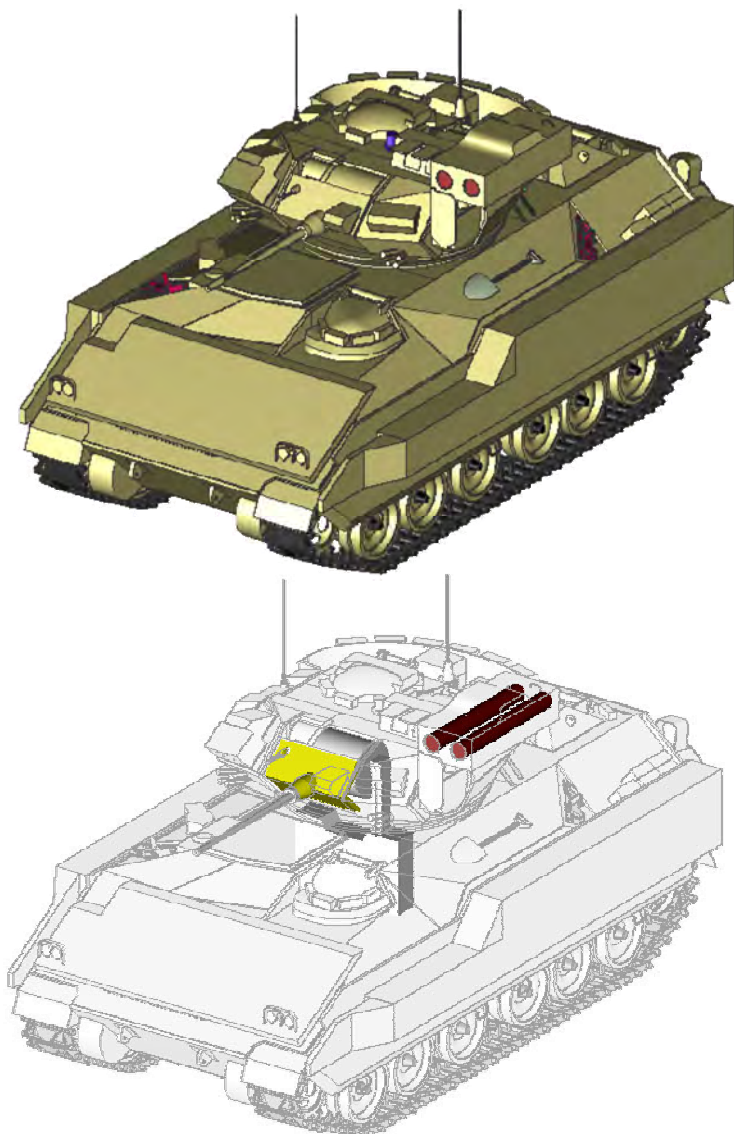
Analysis Outputs

- " personnel injury and incapacitation
- " system-level kills / loss of function
- " residual penetration & velocity
- " component damage
- " subsystem capabilities
- " remaining system utility
- " user-defined criteria
- " tabular & graphical products

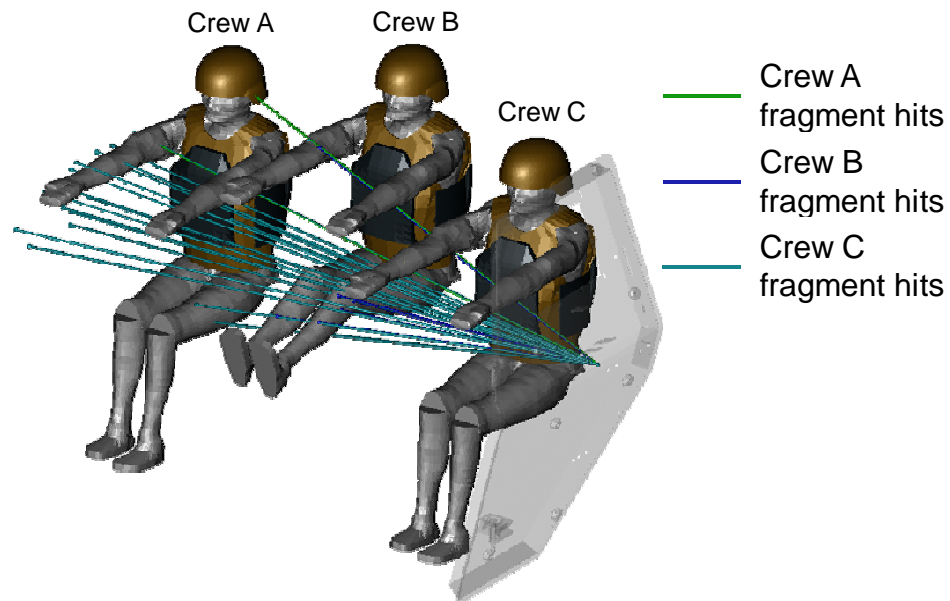
Target and Threat Characterizations




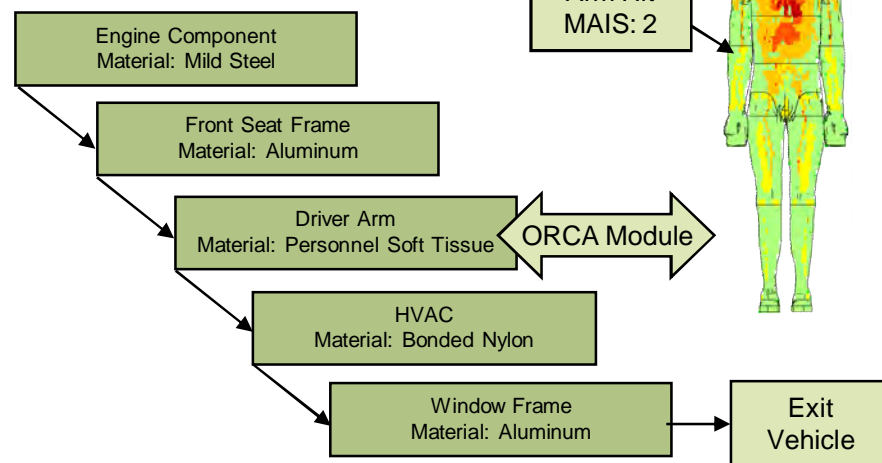
Target Description



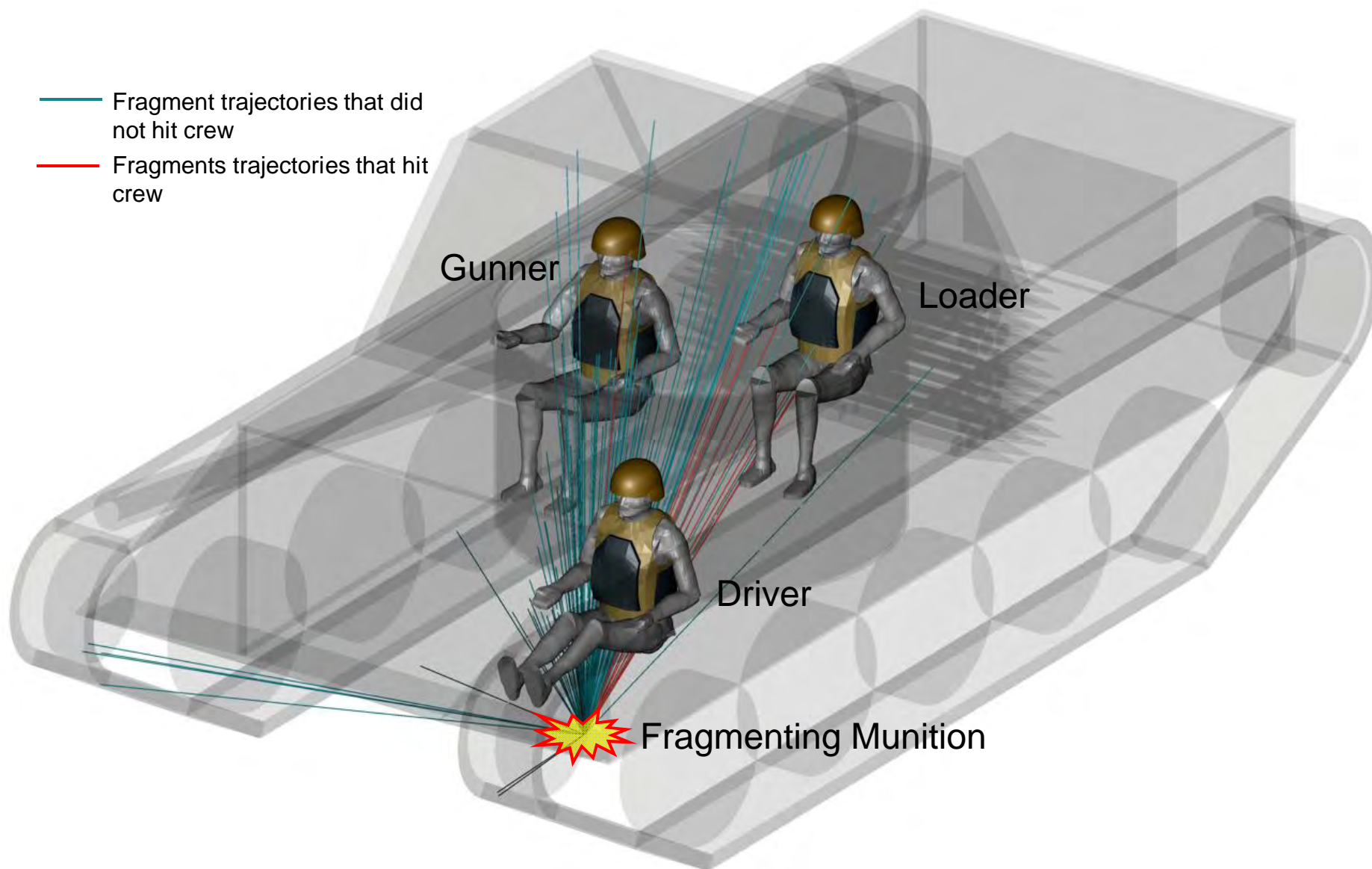
Threat Interaction



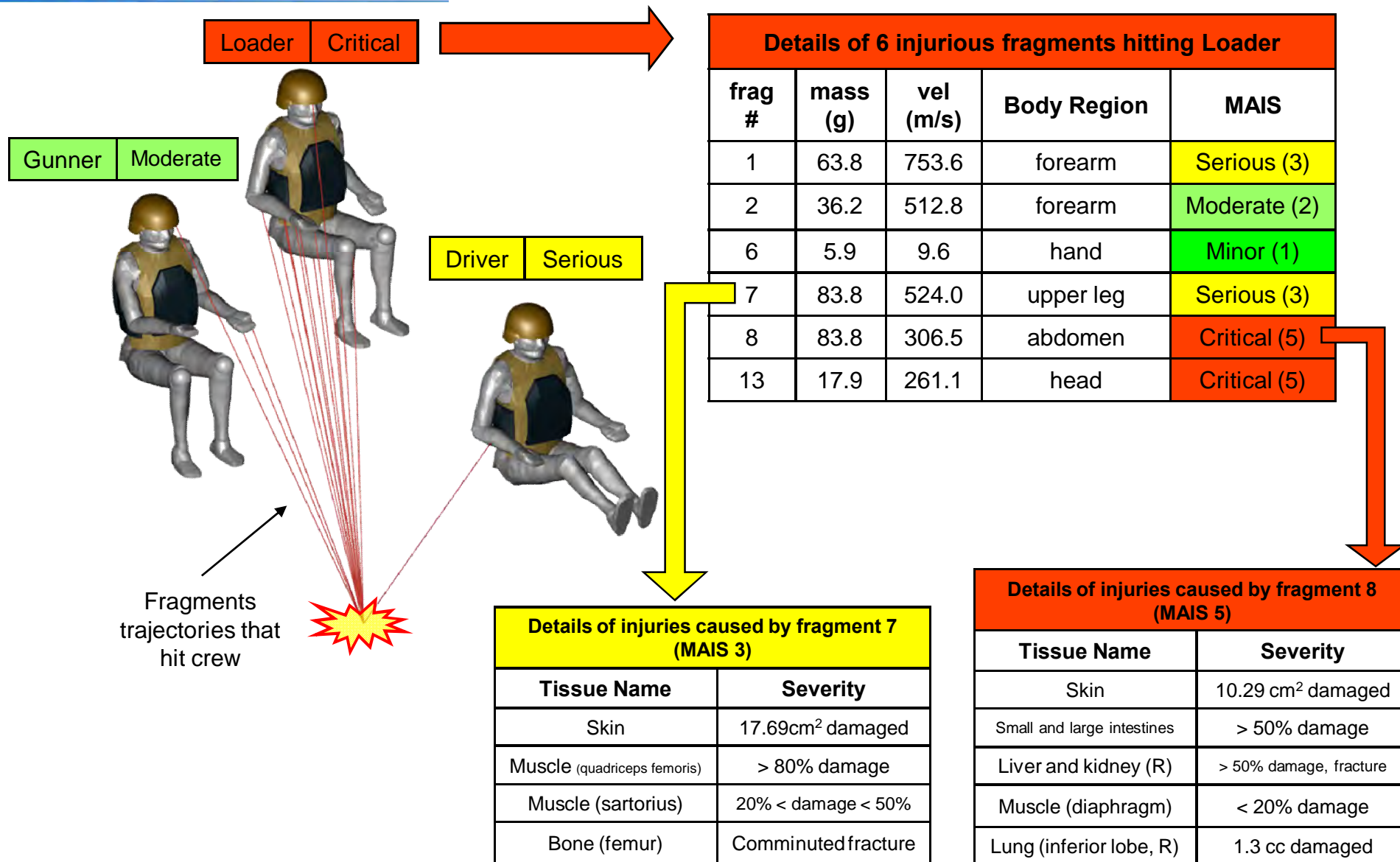

 Copper Fragment Threat
 vs.
 Modeled Vehicle



Fragmenting Munition vs. Tank Crew (1 of 4)



Injury Details (2 of 4)



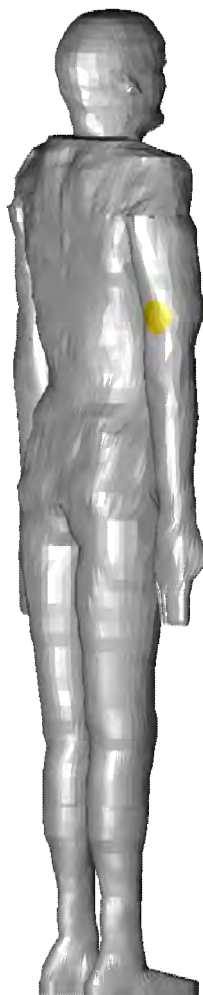
Surface Injury Mapping (3 of 4)



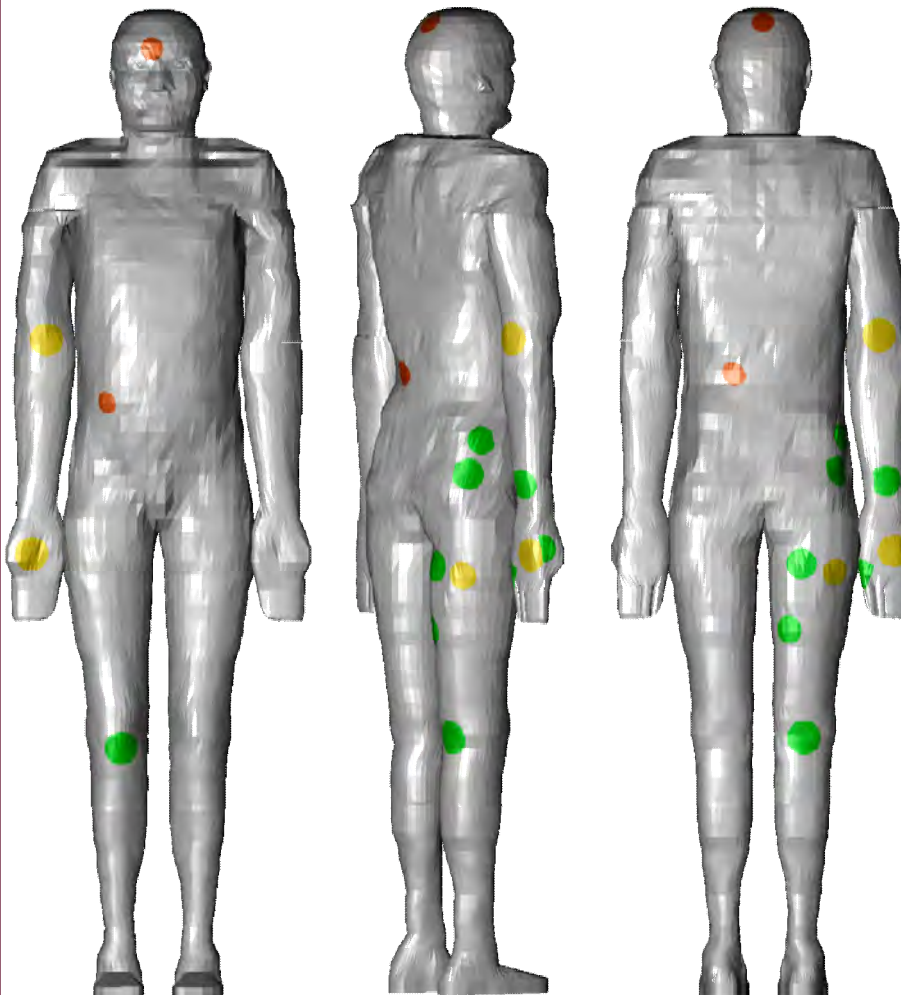
MAIS	Injury Level
1	Minor
2	Moderate
3	Serious
4	Severe
5	Critical
6	Maximal

Size of the surface damage reflects the size of damaged skin tissue and the color indicates the severity of the wound track.

Driver
 1 fragment hit
 MAIS 3
Serious



Loader
 15 fragment hits
 MAIS 5
Critical

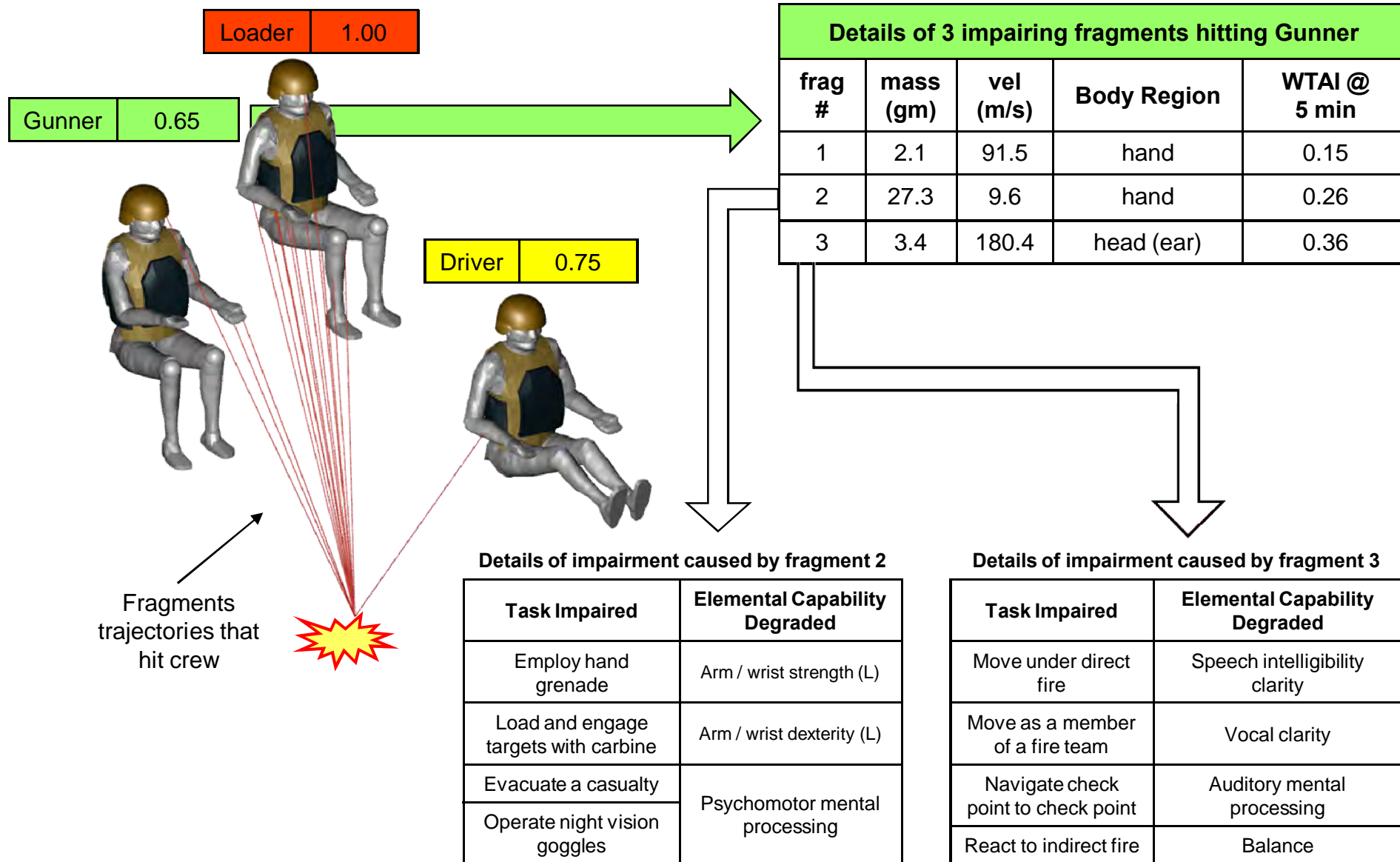


Gunner
 3 fragment hits
 MAIS 2
Moderate



Impairment Details (4 of 4)

capacitation For a Given Tactical Role and Time Period



Conclusion



- “ MUVES-S2 with ORCA improves personnel casualty assessment for SLV analysis of combat systems.
- “ ORCA provides improvements for all phases of the casualty assessment process from operational casualty assessment needed to address lethality questions to survivability-based metrics.
- “ These new survivability metrics provide injury type and severity leading to higher resolution outputs to better serve survivability assessments.
- “ This new and unique capability in MUVES-S2 allows careful analysis and design of vehicle and body armor systems and configurations.

Surface Injury Mapping (3 of 4)



MAIS	Injury Level
1	Minor
2	Moderate
3	Serious
4	Severe
5	Critical
6	Maximal

Size of the surface damage reflects the size of damaged skin tissue and the color indicates the severity of the wound track.

Driver
 1 fragment hit
 MAIS 3
Serious



Crew 1
 15 fragment hits
 MAIS 5
Critical



Crew 2
 3 fragment hits
 MAIS 2
Moderate



Resistance to FSP Penetration of Some Transparent Materials

24th International Ballistics
Symposium

22-26 September 2008

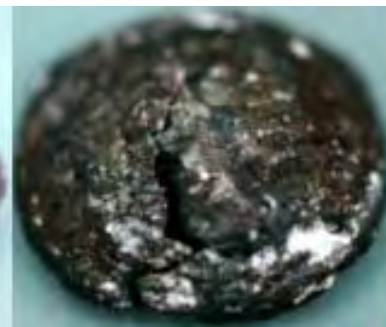
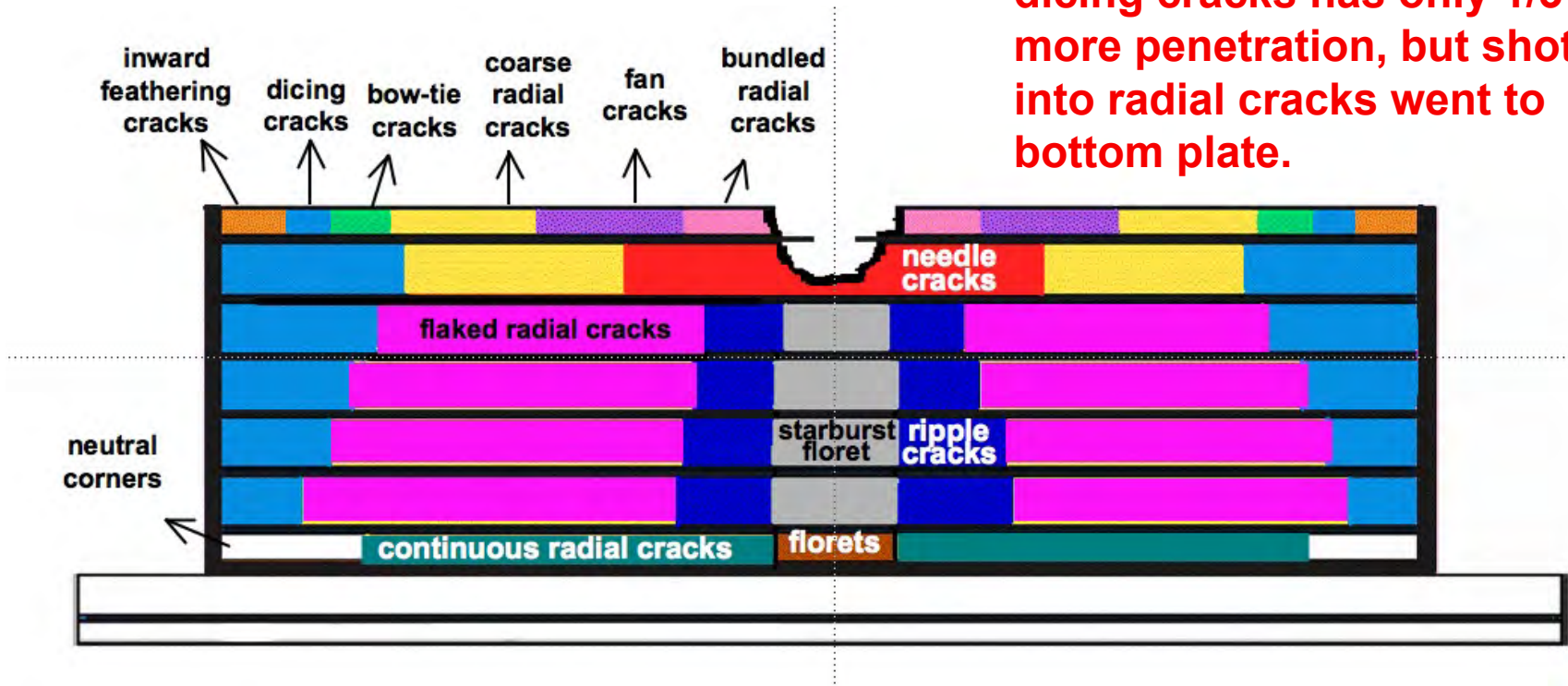


S.Bless, D.Berry
sbless@iat.utexas.edu



Last ISB: Experiments with .50 FSP into 7-layer glass targets.

Subsequent shots into dicing cracks has only 1/3 more penetration, but shots into radial cracks went to bottom plate.



Experiments with 4-layer targets turned out to give very similar results.

Four-layer targets was tested. First 4 layers same as 7 layer target.

Damage patterns were the same as 7-layer target.

1st shot: $P = 24\text{mm}$. No bulge.

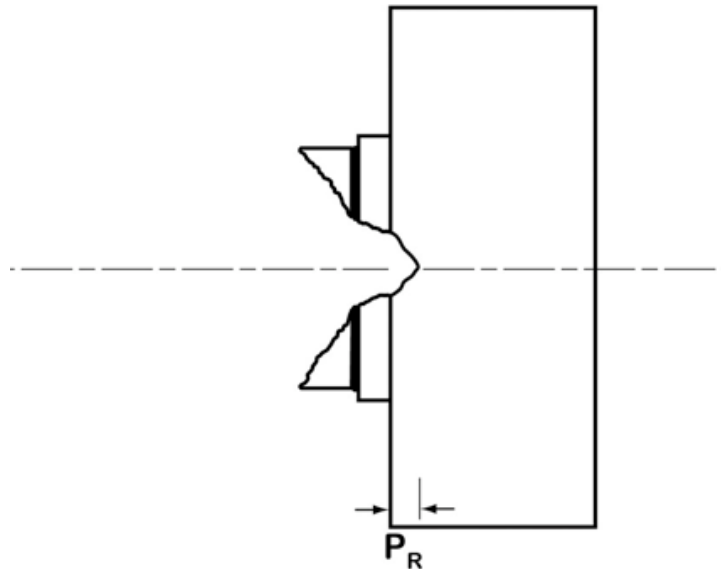
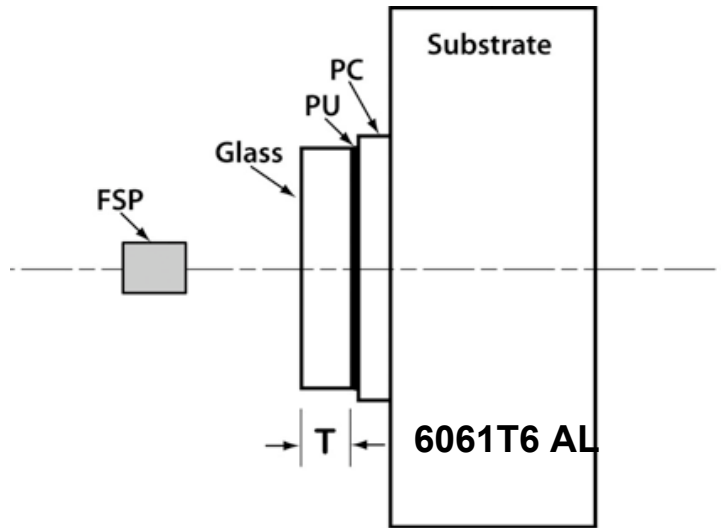
2nd shot into dicing cracks: No change in damage distribution except at impact point. $P = 42\text{mm}$. Slight bulge.

3rd shot into bundled radial cracks (surrounding first impact site): Result was complete penetration.

4th shot into dicing cracks: $P=45\text{mm}$, slight bulge.



DOP testing also gave same result



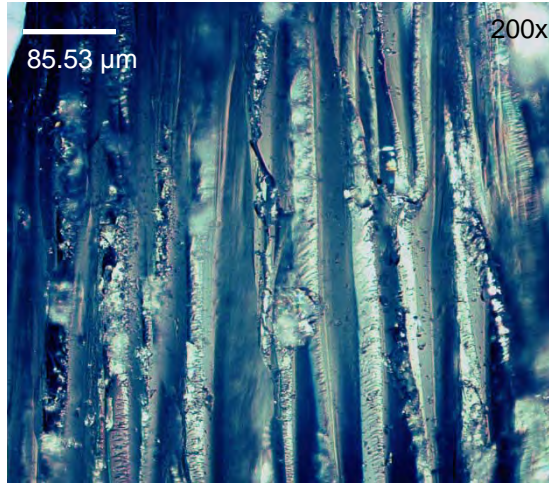
20-shot series.

Mass efficiency (rel. to aluminum) was 1.2-1.4. Did not depend on thickness. Edge proximity had little effect.

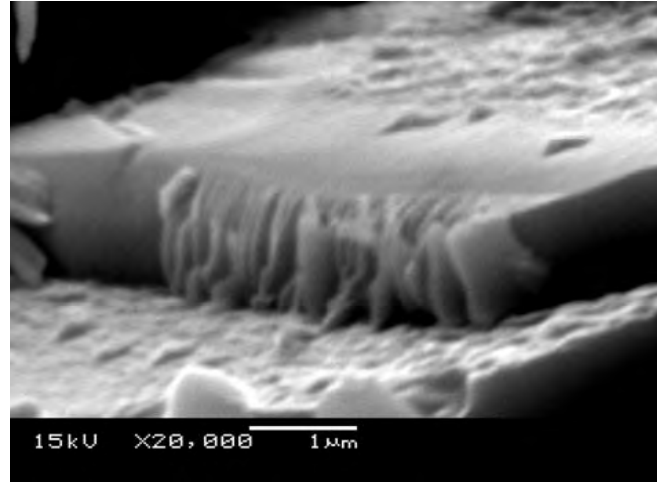
Performance for 1st and 2nd hits very similar to what was seen in multilayer target.

Recovered particles show fast communiton

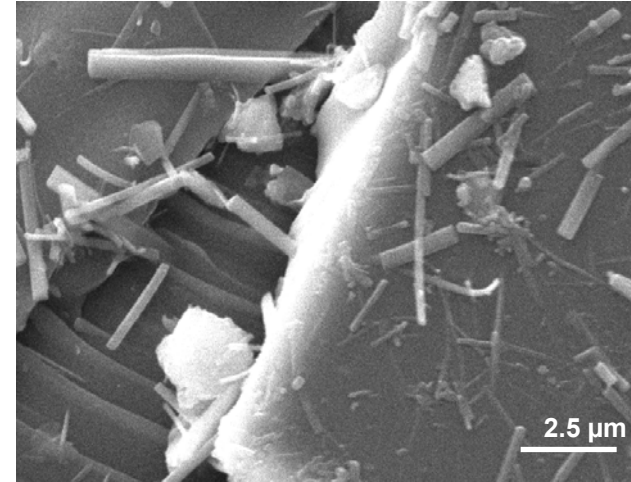
This material exhibited many features indicating very fast fracture, but very few grains showed the FW structure: e.g. conventional elastic-brittle cavity expansion.



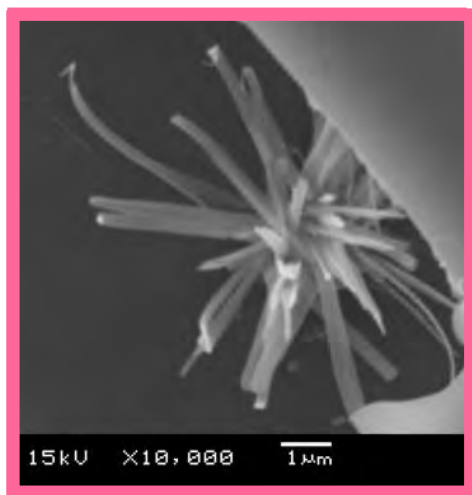
Long parallel hackles



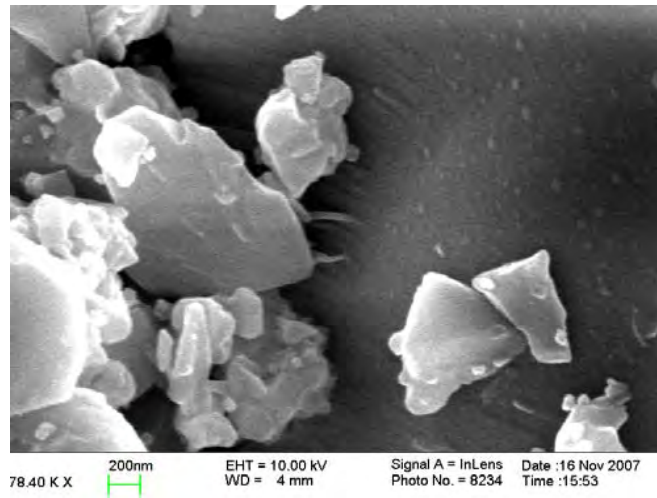
Nano “stairsteps” with hackle on steps.



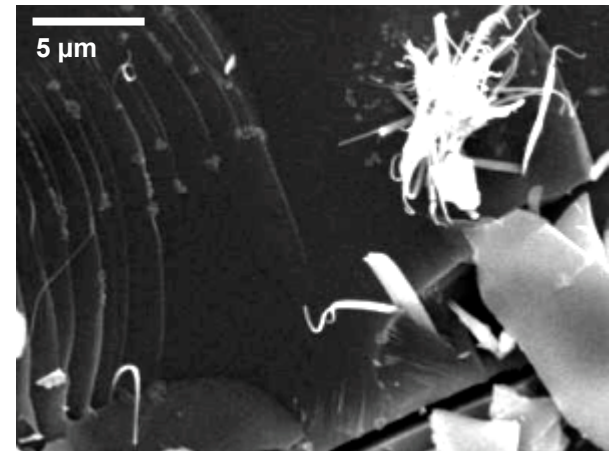
Fields of nano whiskers
*Note that whiskers may be associated with adjacent hackles



Agglomerated whiskers



Rounded nano particles

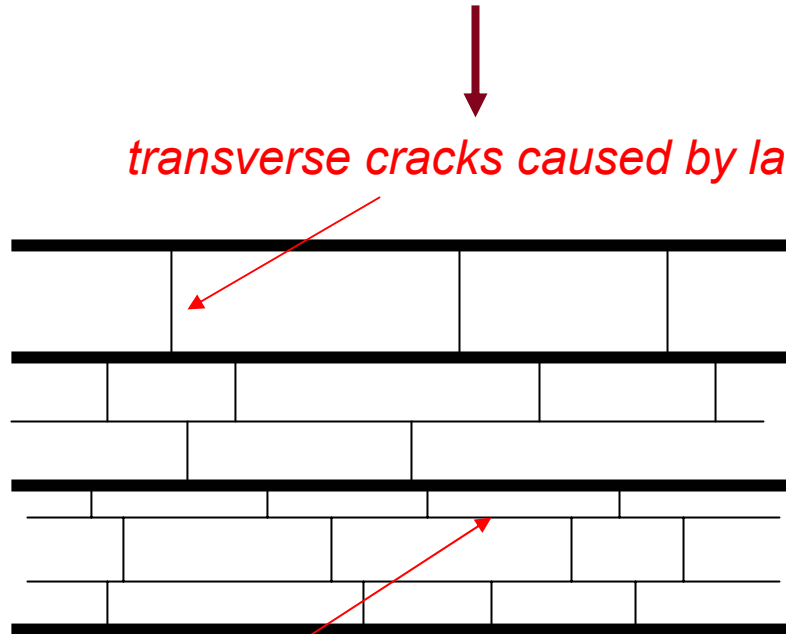


Curvature of whiskers

Hypothesis for radial crack structure within the targets

radial cracks
driven by
cavity
expansion

transverse cracks caused by late time heaving



penetration depth

radial cracks
due to flexural
stress

*slicing cracks caused by flexing driven by
momentum transfer*

Summary of results concerning how damage degrades multi-layer glass targets

Close in cavity expansion transitions to far-reaching radial crack pattern.

First shot sets up damage pattern. Two basic kinds of crack damage: dicing cracks and radial cracks, which are flaked in inner layers and pie-sections in outer layers. This pattern does not change significantly in subsequent shots.

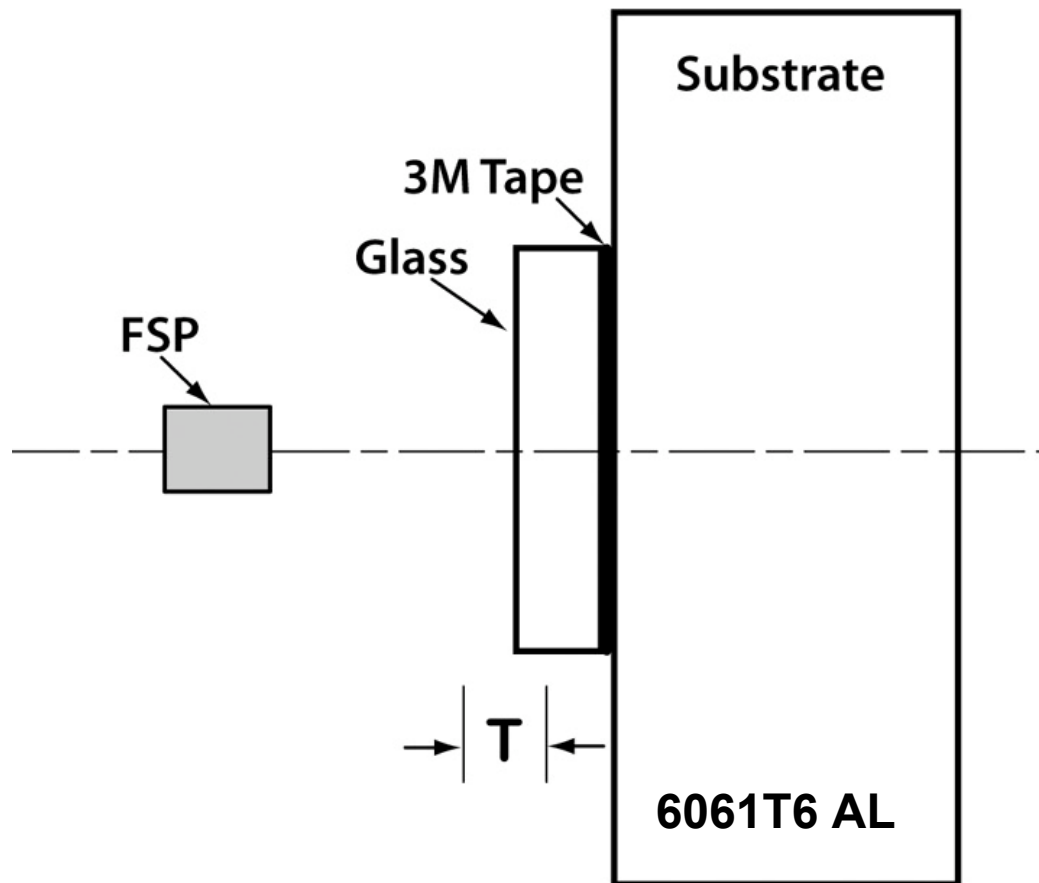
The radial cracks very seriously degrade ballistic performance. The dicing cracks do not.



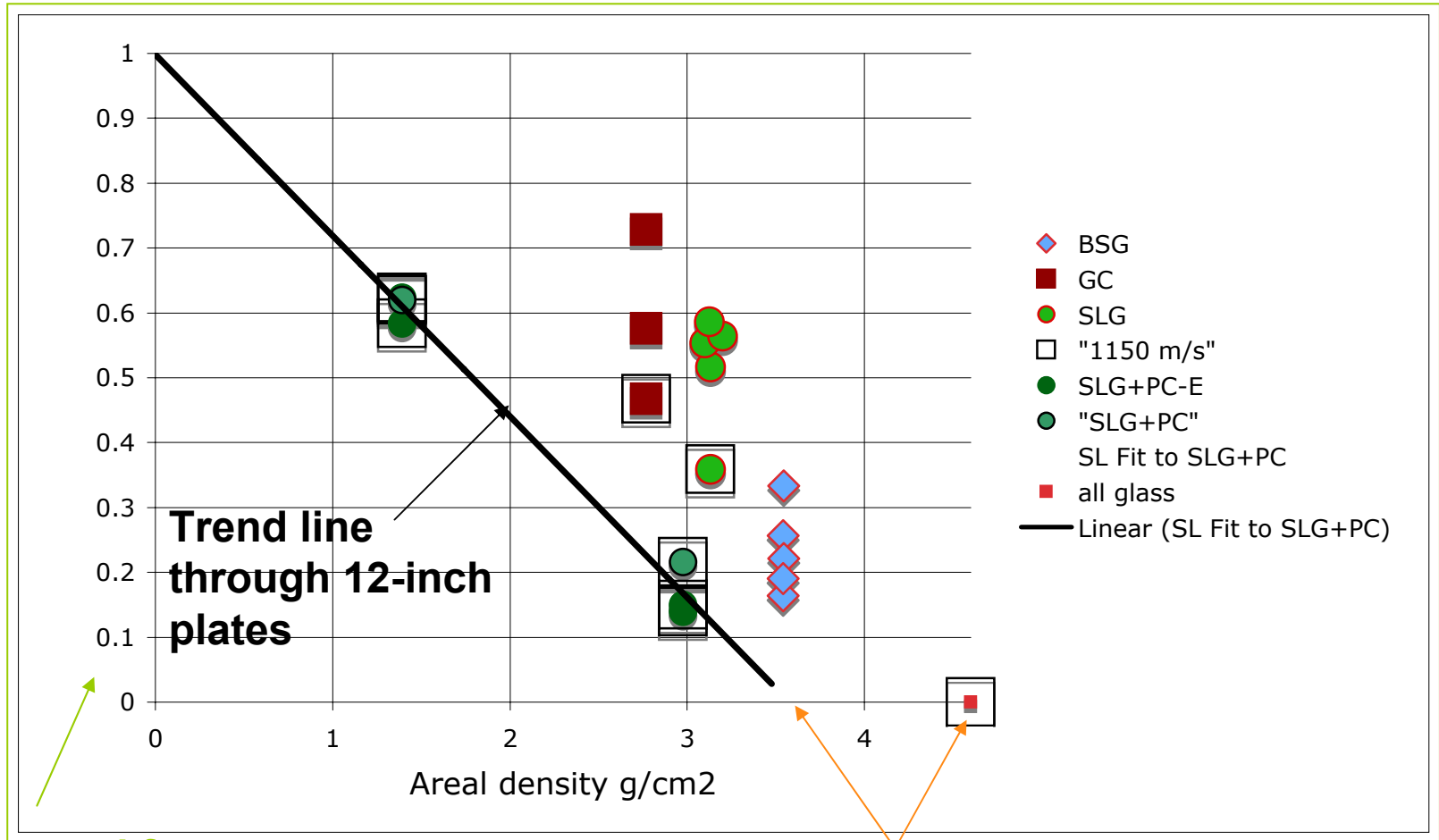
3 Materials compared to investigate effect of properties

Parameter	Soda lime glass	Boro-silicate glass	Glass ceramic (Corning)
Density (g/cm ³)	2.5	2.2	2.78
E (GPa)	72	61	72

Modified DOP test geometry for 4-inch test coupons



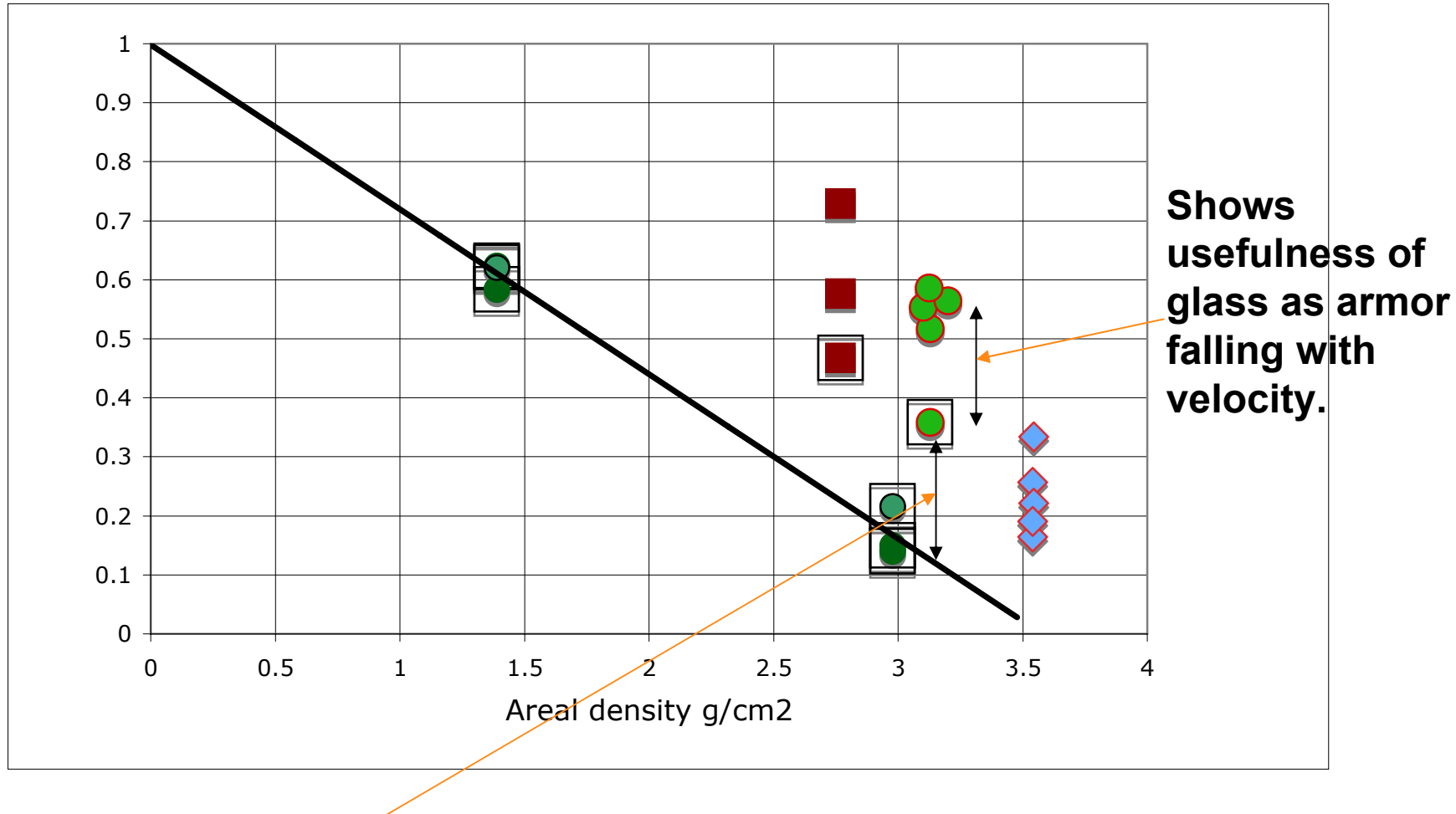
Connection of DOP tests and laminate target tests



Corrected for effect of PC.

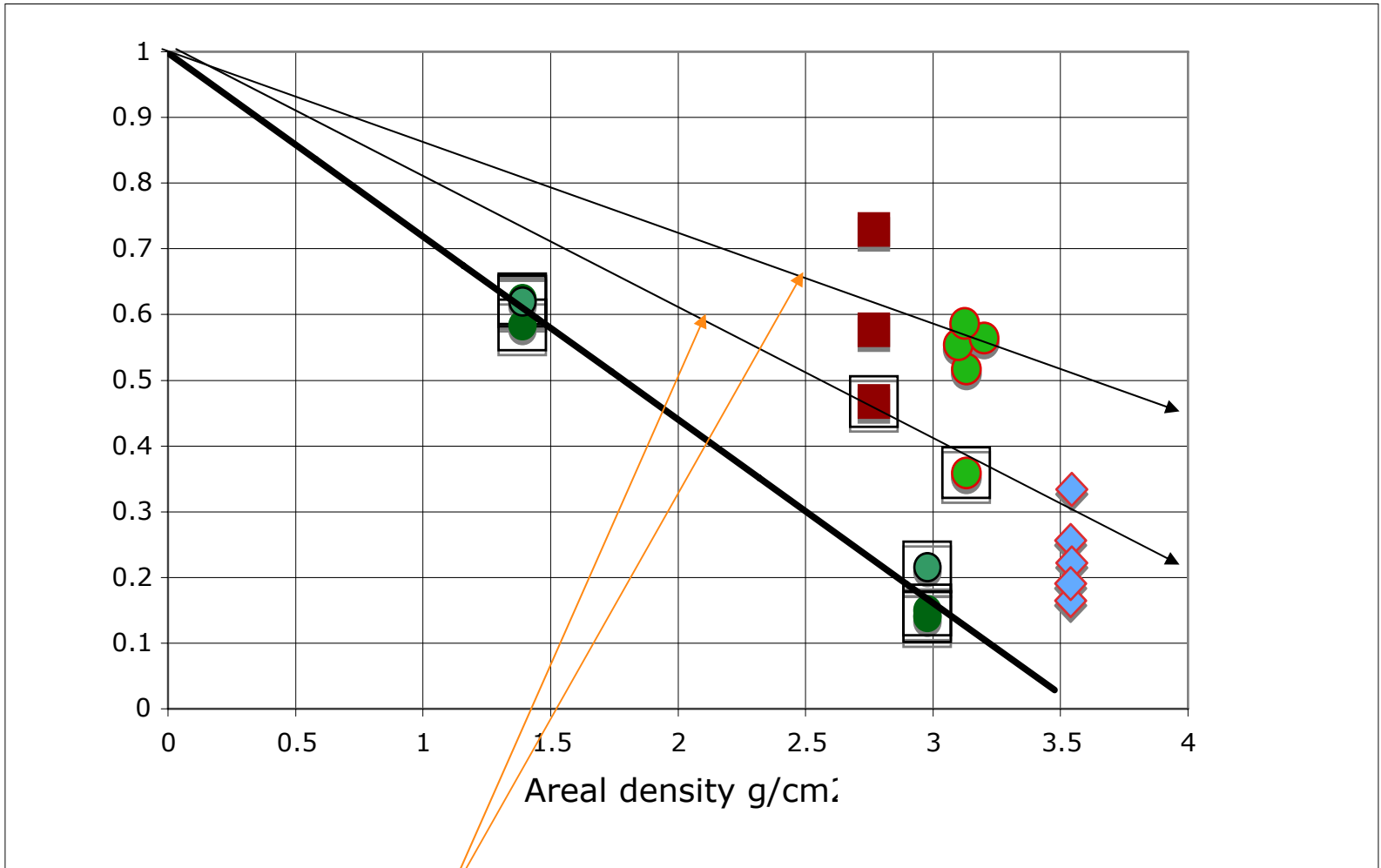
Penetration is more in an all glass target than would be predicted from DOP trend. This is probably due to loss of strength which allows projectile to "coast" to stop in glass.

Effects of Mounting and Velocity



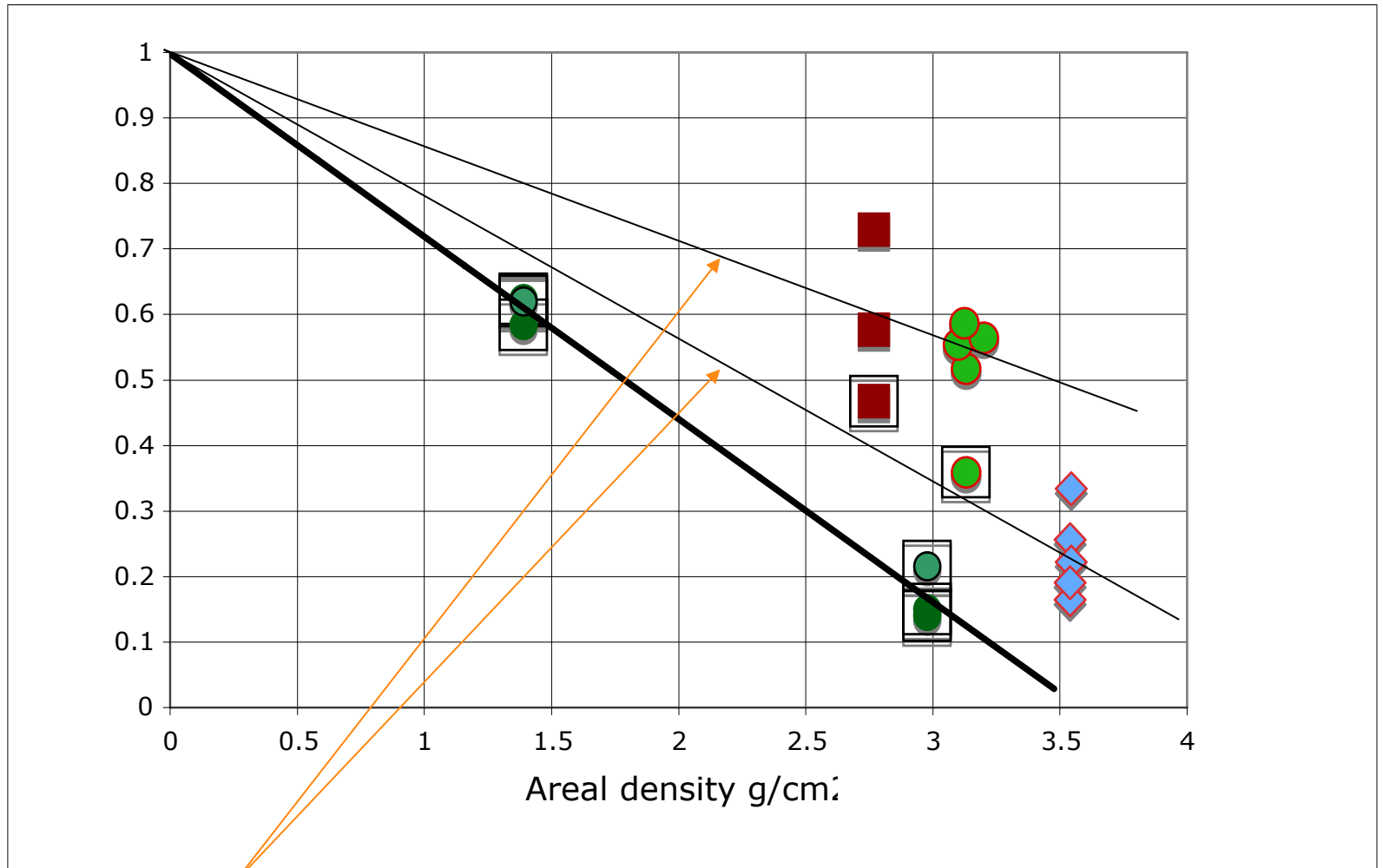
Shows SLG with 3M tape was about 34% less effective than with PU/PC mounting.

Comparison SLG and GC



Shows the efficiencies of SLG and GC are very similar.

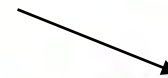
Comparison BSG and SLG



Shows that BSG is much better than SLG. Probably due to the importance of density.

Goal: Develop technique to measure strength of glasses

Stress gage here



As used in past

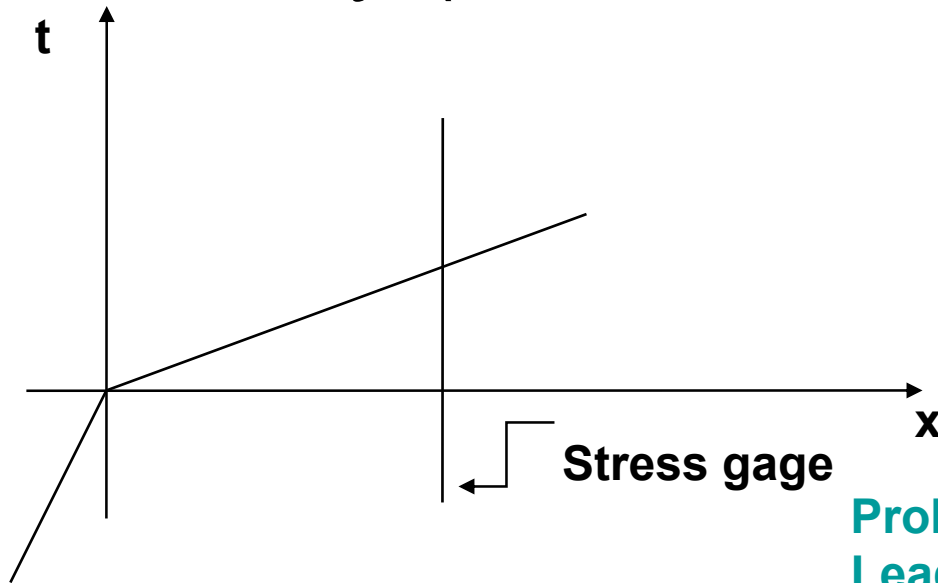
PDV view



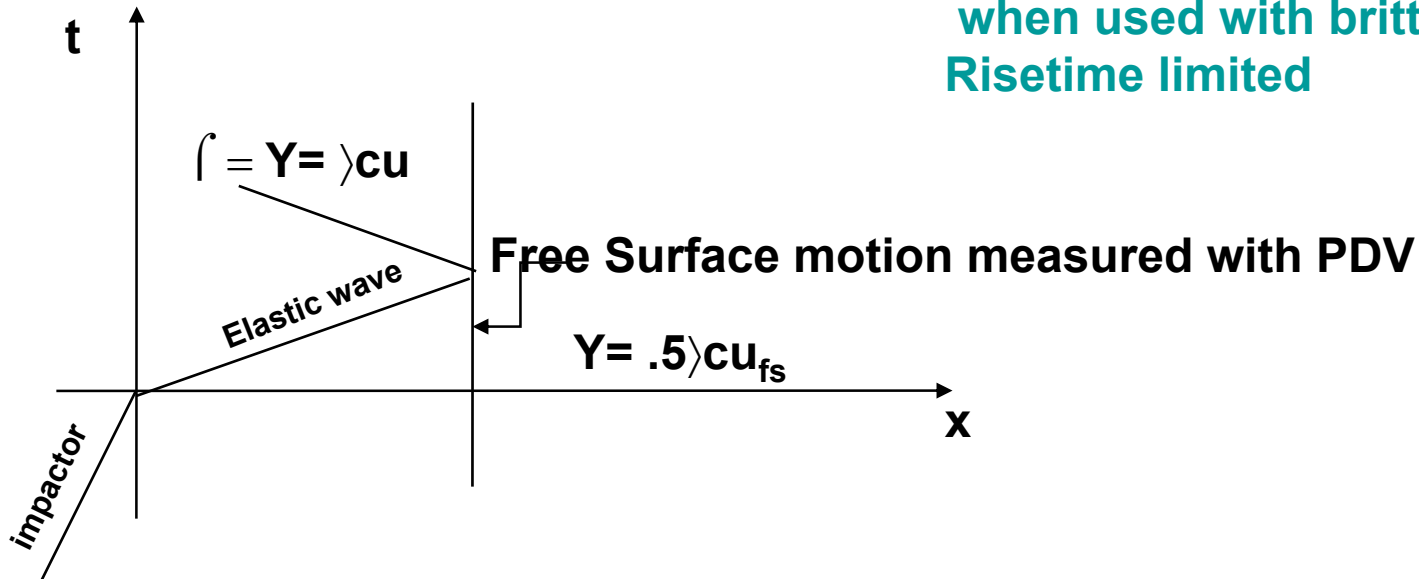
As used here

These experiments: observe free surface motion with hi speed camera and PDV.

Theory (for ductile materials)

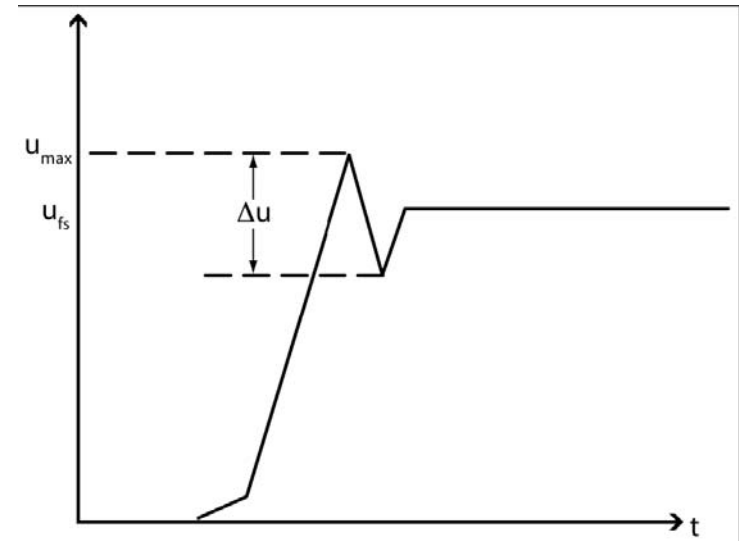
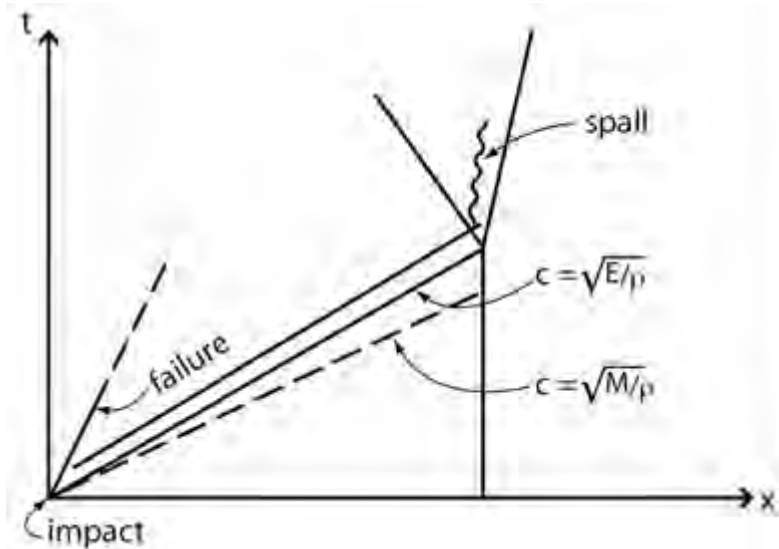


Problems with gauge –
 Leads break
 Very short lifetime
 when used with brittle materials
 Risetime limited



Theory for brittle materials

Spall equation

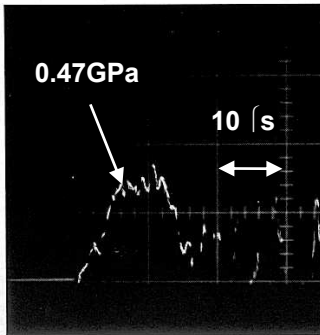


Failure causes release near impact, resulting in triangular instead of square pulse. For many brittle materials, spall strength is less than compressive strength, resulting in a “spall signal” at free surface.

($M=K+4G/3$. K, G, E are elastic moduli)

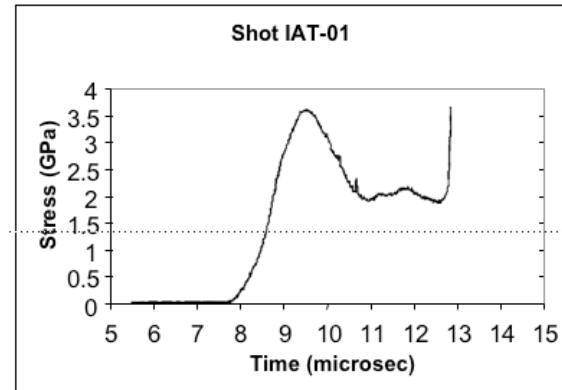
Examples of Previous work

Strength of a Mild Steel



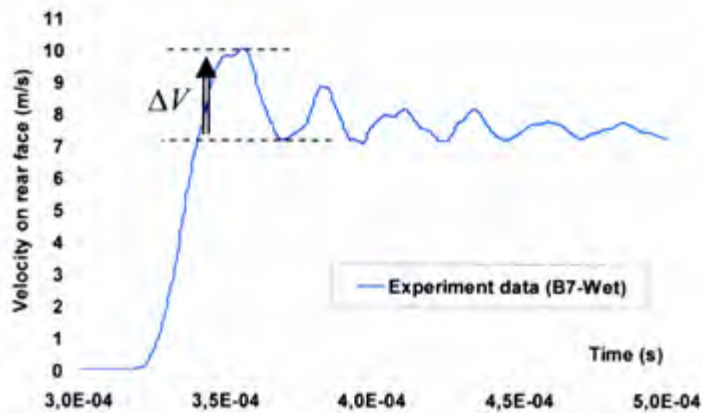
Rosenberg & Bless, 1986

Strength of Alumina



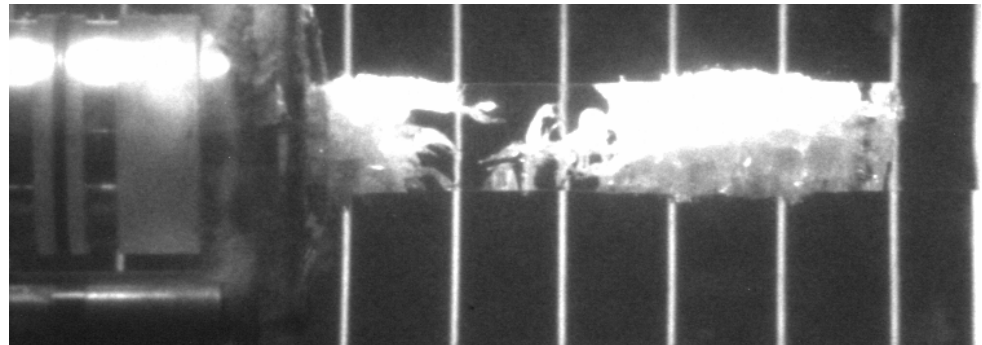
T. Beno at al, 2006, strength of alumina = 3.6 GPa

Spall in Concrete



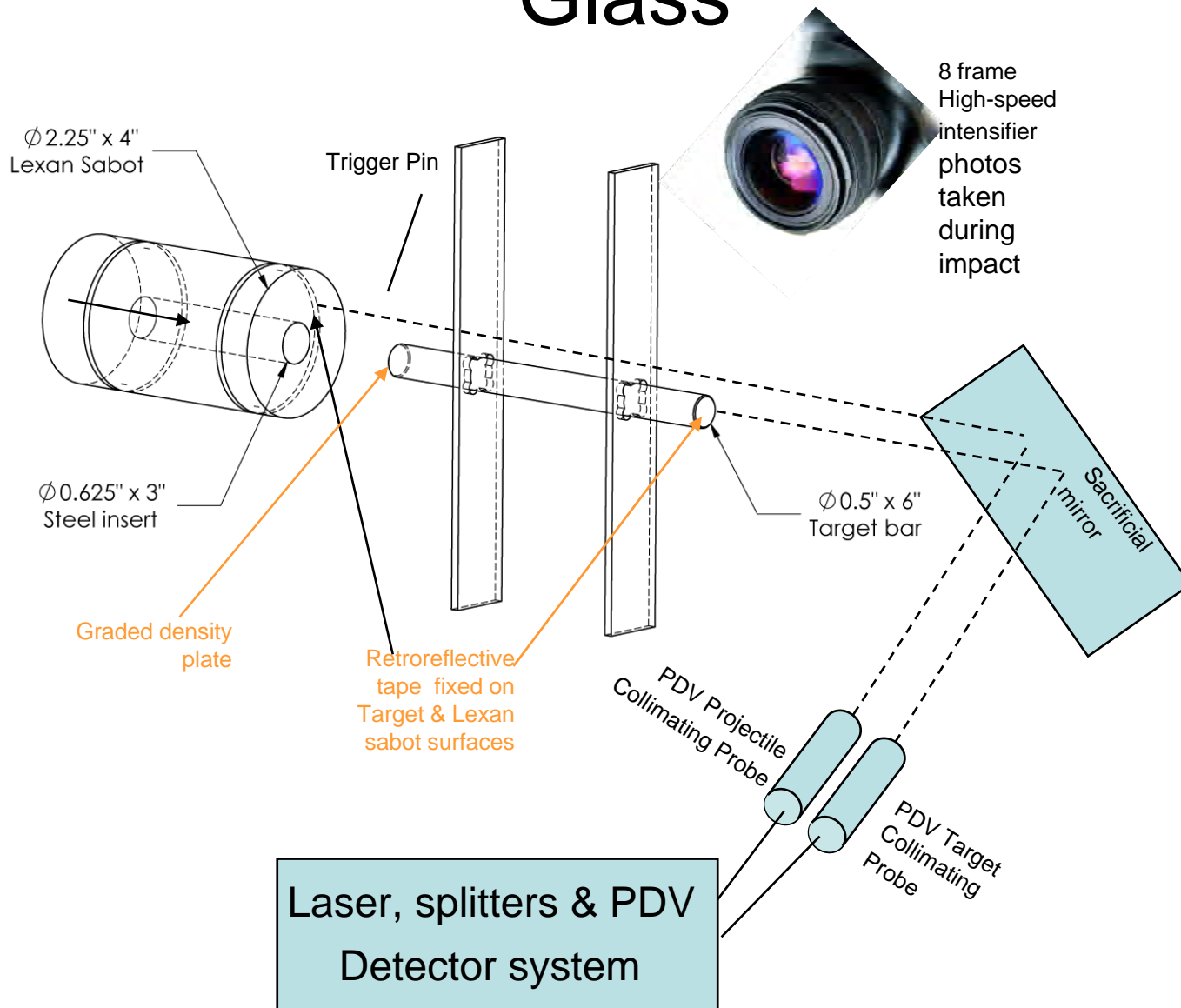
P. Forquin, & Erzan, 2008

Failure in homalite bar



Bless, 2003

Experimental Setup for Glass

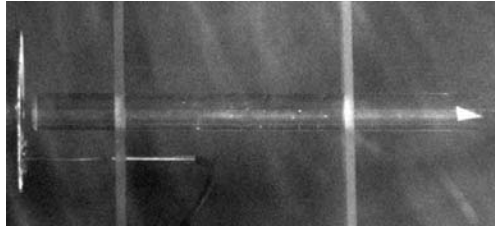


Failure process in BSG

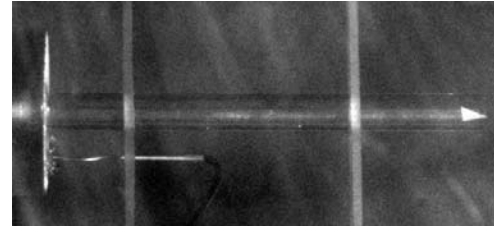
Direction of travel



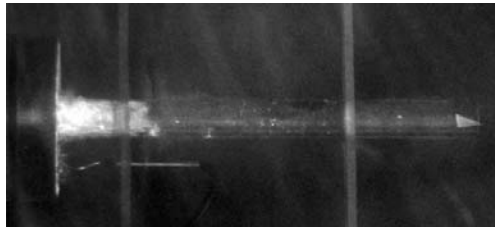
shot A1008
borosilicate glass



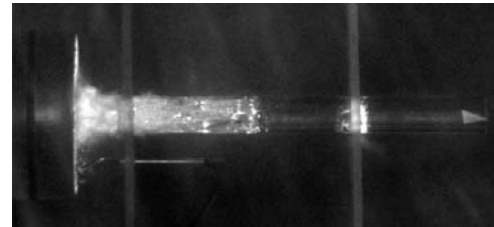
150 ☆s



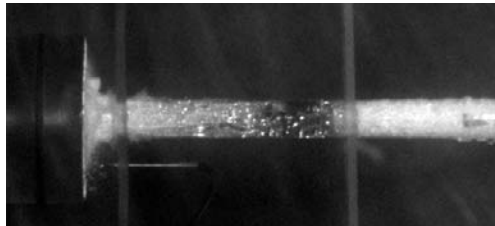
160 ☆s



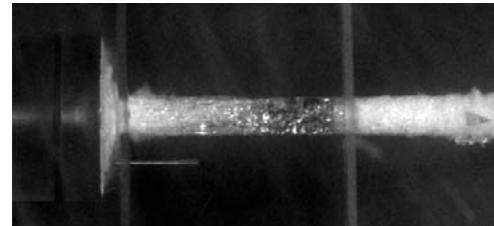
170 ☆s



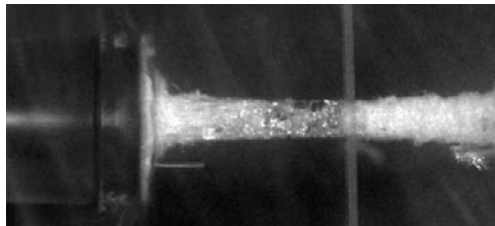
175 ☆s



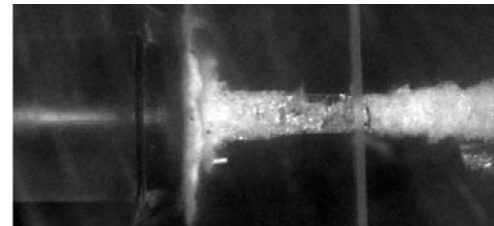
180 ☆s



200 ☆s



250 ☆s



300 ☆s

explosive tensile
failure

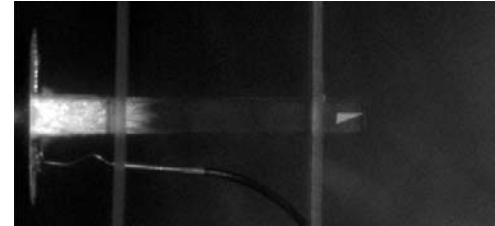
Failure of GC rod generally very similar to glass rod

Direction of travel

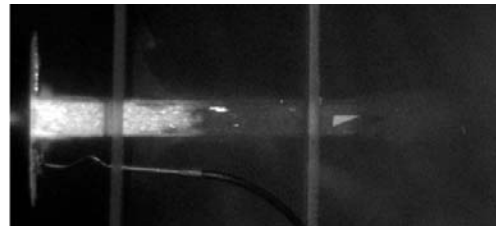
shot A1011
glass ceramic



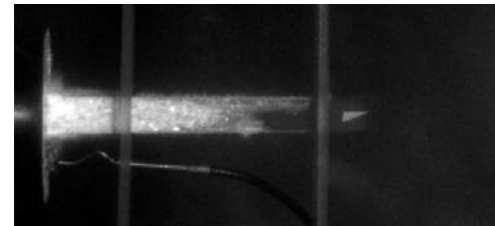
145 ☆s



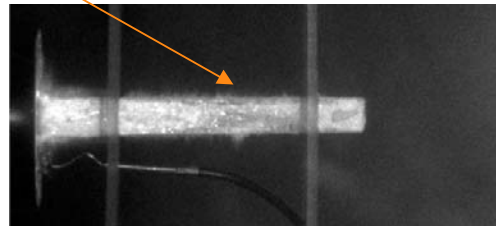
150 ☆s



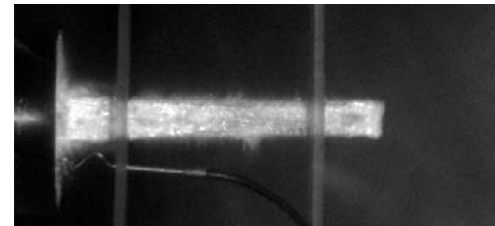
153 ☆s



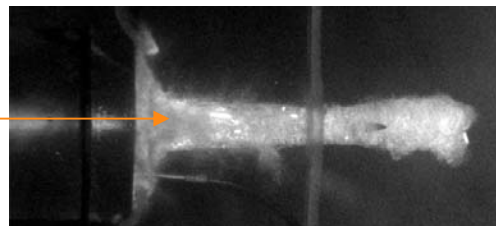
175 ☆s



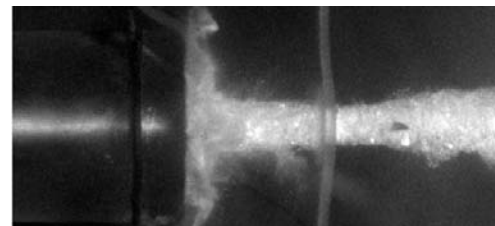
180 ☆s



200 ☆s

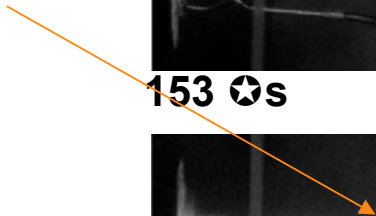


250 ☆s



300 ☆s

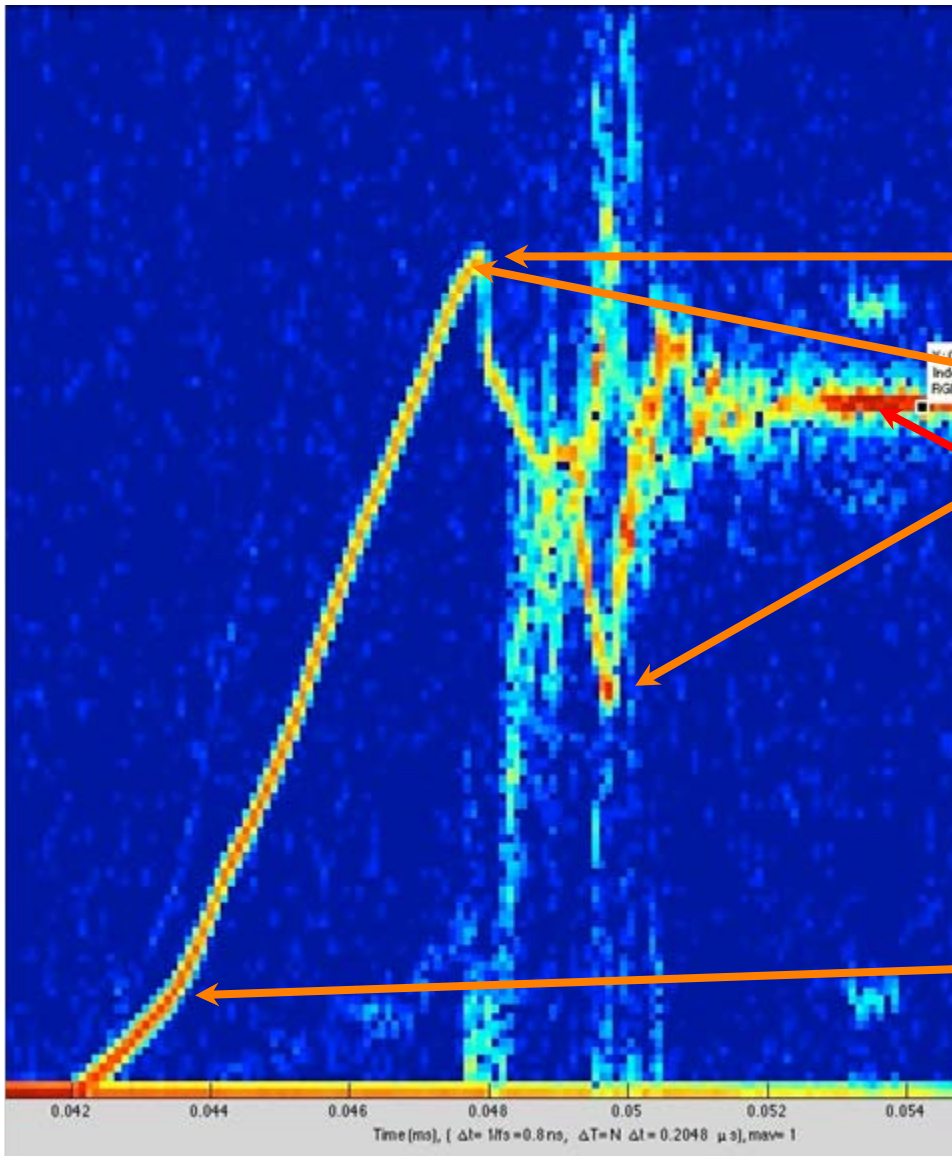
No damage-free zone in middle



More expansion in compressive zone



Free surface velocity data



Borosilicate glass

Peak stress = 2.2 GPa

spall pull back? = 187 m/s
spall stress = 1.1 GPa

final velocity = 307 m/s

**Break between 1-D strain
and 1-D stress waves.**

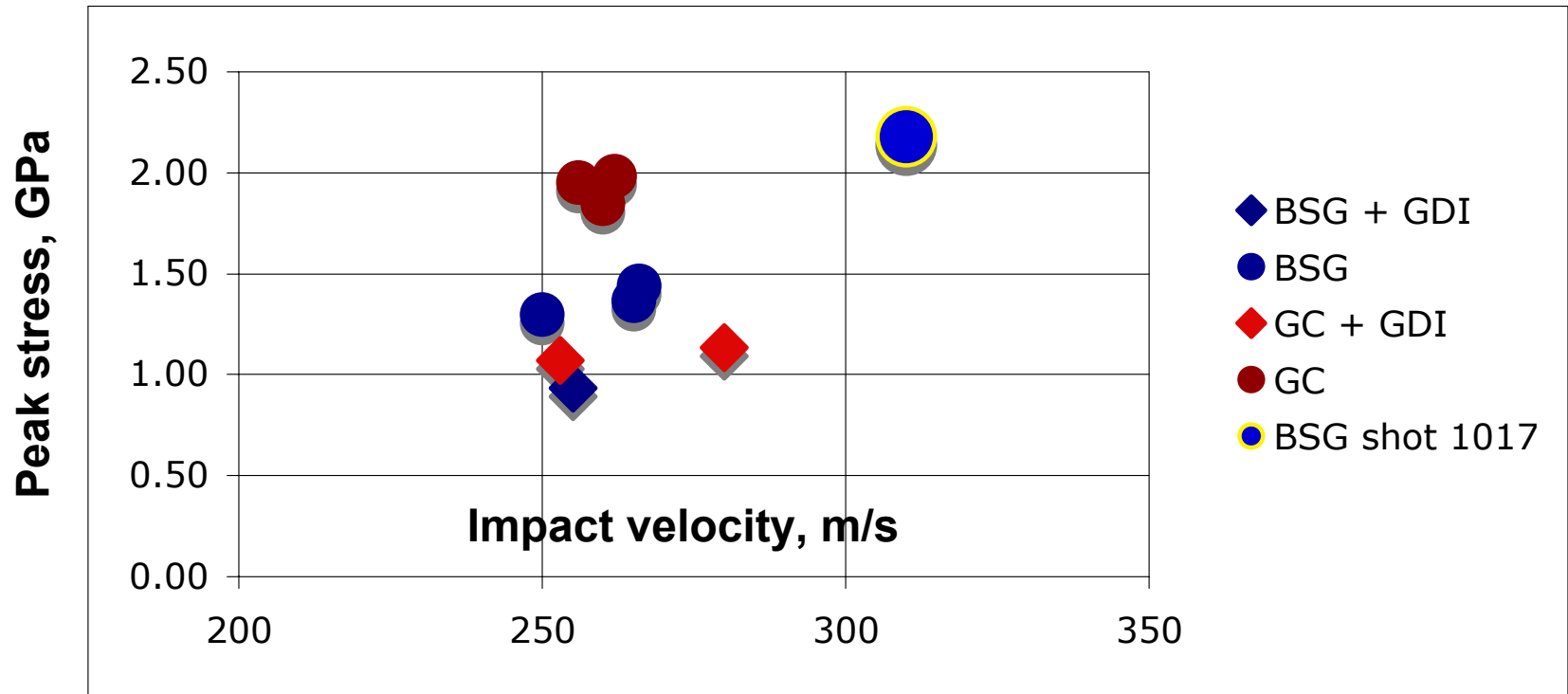
Values of stress plateau (after spall), from photos or PDV.

Test	Material	Impact Velocity (m/s)	Free Surface Velocity (m/s)	Stres (Gpa)
a1004	GC	260	287	1.84
a1007	GC	256	275	1.95
a1011	GC	262	280	1.99
a1013	GC+GDI	280	160	1.13
a1014	GC+GDI	253	151	0.84
a1015	BSG+GDI	255	160	0.93
a1003	BSG	266	247	1.44
a1008	BSG	250	223	1.30
a1012	BSG	265	235	1.37
a1017	BSG w/o Retro	310	374	2.18

GC = Glass Ceramic, BSG = Borosilicate glass

GDI=graded density impactor

Peak stress data (from PDV records)



For both materials, adding the GDI reduces measured stress.

GC is 30% stronger than BSG.

There appears to be a strong rate effect of measured peak stress.

Summary of what we learned

FSPs produce characteristic damage patterns in glass single sheets or laminates: generally radial cracks (many species) and dicing cracks.

Dicing cracks are relatively benign; not so radial cracks.

Density is much more important than strength in defeating FSP projectiles.

.



*Experimental validation of
the origin of the bodywork
effect (K-effect) in the up-
armouring of civil and
military vehicles*

F. Coghe¹, B. Kestelyn² and M. Pirlot¹

¹ Dept. Weapon Systems & Ballistics, Royal Military Academy

² DG Material Resources, Belgian Defence

Overview



- Introduction
- Experimental setup, results and discussion
- Conclusion

Introduction



VIP vehicles



- Small calibre ammunition
- Fragments
- IED
- ...

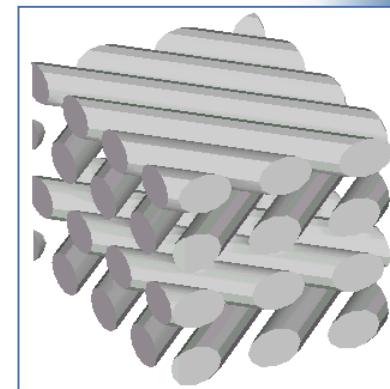
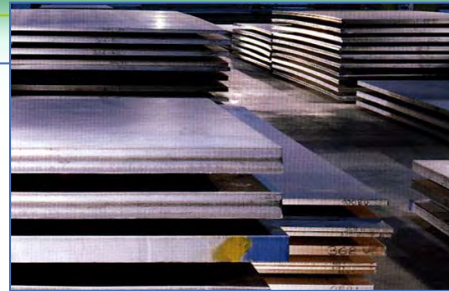
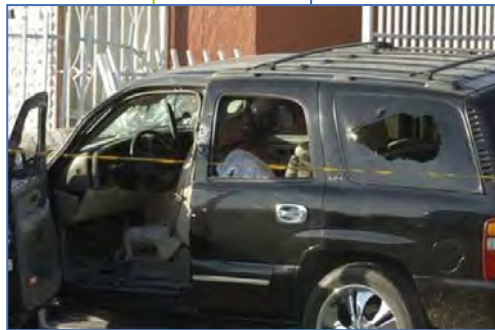


Light armoured vehicles



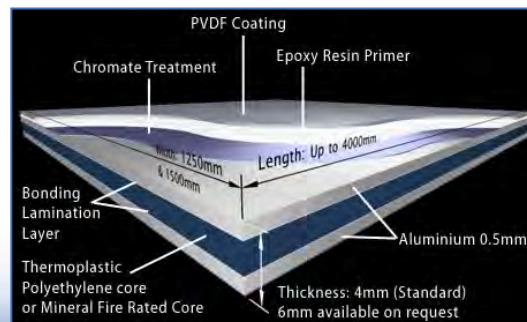
Logistic vehicles

Introduction

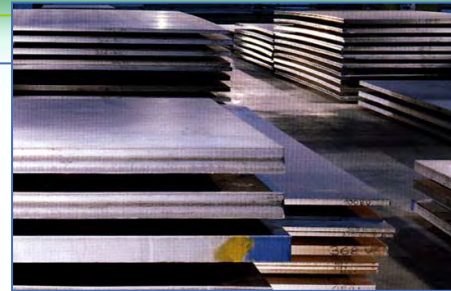
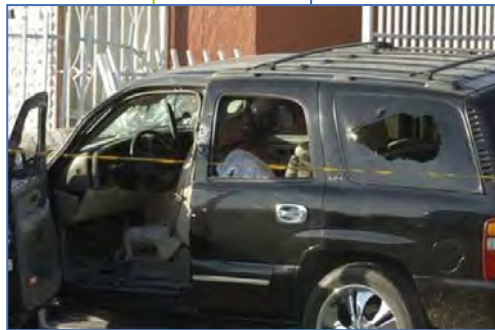


Armour materials:

- Metals
- Ceramics
- Fibre
- Composites
- ...



Introduction



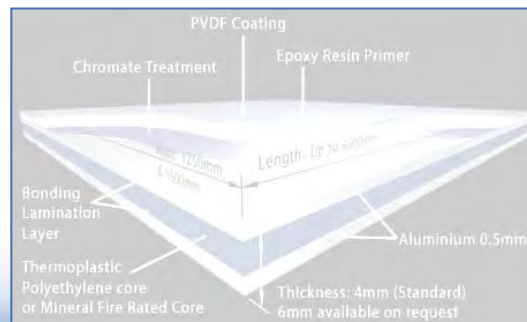
STANAG 4569 Level 1

High hardness steel plates:

- Moderate cost
- Known processing path
- Not weight-inefficient

Armour materials:

- Metals
- Ceramics
- Fibre
- Composites
- ...

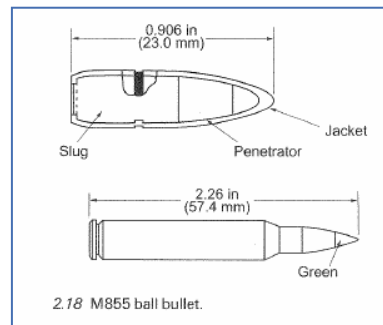


Introduction



Threat

5.56 x 45 NATO Ball (M855, SS109,...)



Protection

Thyssen-Krupp Secure 500

(high hardness ballistic armour plate, 480-530 HB)

Classification	Weapon		Bullet		Test Conditions		SECURE 500 (480-530 HB)
EN 1063 / EN 1522	Type	Calibre	Type	Mass [g]	Test range [m]	Bullet velocity ¹⁾ [m·s ⁻¹]	Minimum thickness for bullet resistance [mm]
BR / FB 3	hand-gun	.357 Magnum	FJ/CB/SC	10.2	5	430 ± 10	3.0 ²⁾
BR / FB 4		.44 Magnum	FJ/FN/SC	15.6	5	440 ± 10	3.0
BR / FB 5	rifle	5.56 mm x 45 (SS 109) <i>twist length: 178 ± 10 mm</i>	FJ/PB/SCP1	4.0	10	950 ± 10	6.5
BR / FB 6		7.62 mm x 51	FJ/PB/SC	9.5	10	830 ± 10	6.5
BR / FB 7		7.62 mm x 51 (AP) <i>twist length: 254 ± 10 mm</i>	FJ/PB/HC1	9.8	10	820 ± 10	15.5
no classification	hand-gun	.44 Magnum	FJ/FN/SC	15.6	3	435 - 455	3.0
	rifle	7.62 mm x 39	FJ/PB/SC	7.9	25	710 ± 15	4.0
		(Kalashnikov)	API	7.7	25	730 ± 15	12.0
		7.62 mm x 51	FJ/PB/SC	9.5	10	785 - 795	5.5
		7.62 mm x 51 (AP)	FJ/PB/HC1	9.8	25	800 - 810	14.5
		5.56 mm x 45 (SS 92)	FJ/PB/SC	3.6	25	965 - 975	9.0

Introduction



Single armour plate

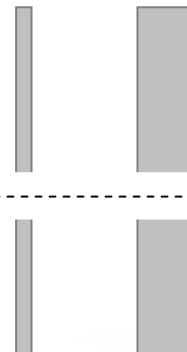


V_{50} OK



More material, less protection!!!

Armour plate behind car door panel



V_{50} not OK!!!



Experimental setup, results & discussion



Explanation

Bodywork effect



Explanation 1:

Steel penetrator loses jacket after penetration of first plate.

Steel penetrator penetrates second (armour) plate due to increased energy density.

Experimental setup, results & discussion



Validation

Analytically*:

Case 1: complete projectile

$$ED = \frac{\text{mass}_{\text{projectile}} \cdot (\text{speed}_{\text{projectile}})^2}{2 \cdot \left(\frac{\text{diameter}_{\text{projectile}}}{2} \right)^2 \cdot \pi} = \frac{0,004\text{kg} \cdot (1000\text{m/s})^2}{2 \cdot \left(\frac{0,889 \cdot 10^{-3}\text{m}}{2} \right)^2 \cdot \pi} = 3222\text{kJ/m}^2$$

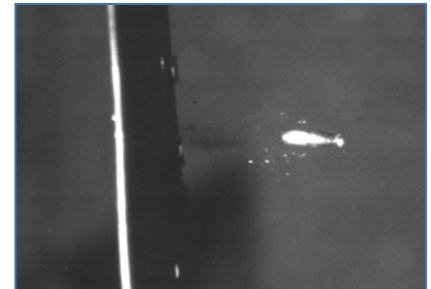
Case 2: steel penetrator and lead slug

$$ED = \frac{\text{mass}_{\text{projectile}} \cdot (\text{speed}_{\text{projectile}})^2}{2 \cdot \left(\frac{\text{diameter}_{\text{projectile}}}{2} \right)^2 \cdot \pi} = \frac{0,00324\text{kg} \cdot (1000\text{m/s})^2}{2 \cdot \left(\frac{2,68210^{-3}\text{m}}{2} \right)^2 \cdot \pi} = 457\text{kJ/m}^2$$

+ Nsiampa et al. (23rd ISB)

Experimentally:

High speed photography
(1mm mild steel plate)



Soft recovery



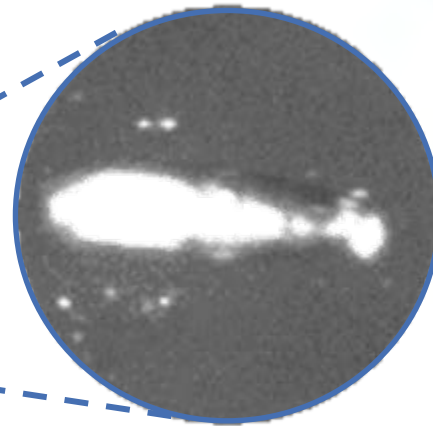
Experimental setup, results & discussion



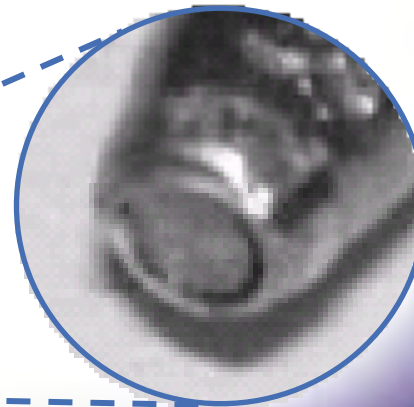
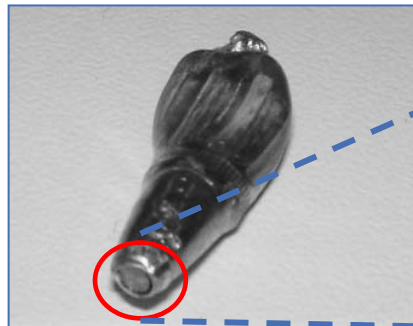
Validation

Experimentally:

High speed photography
(1mm mild steel plate)



Soft recovery



Experimental setup, results & discussion



Explanation

Bodywork effect



Steel penetrator loses jacket after
penetration of first plate

Steel penetrator penetrates second
(armour plate due to increased energy
density.

Experimental setup, results & discussion



Explanation

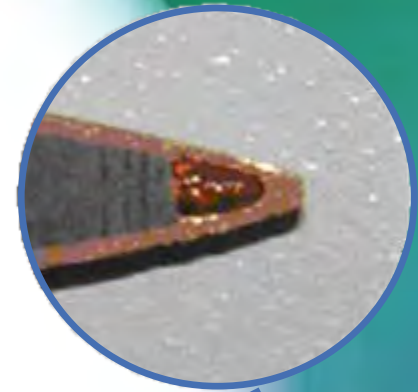
Bodywork effect



Explanation 2:

Penetration through first plate changes geometry of projectile nose (flattening).

Changed geometry changes penetration mechanism during impact on the second (armour) plate.

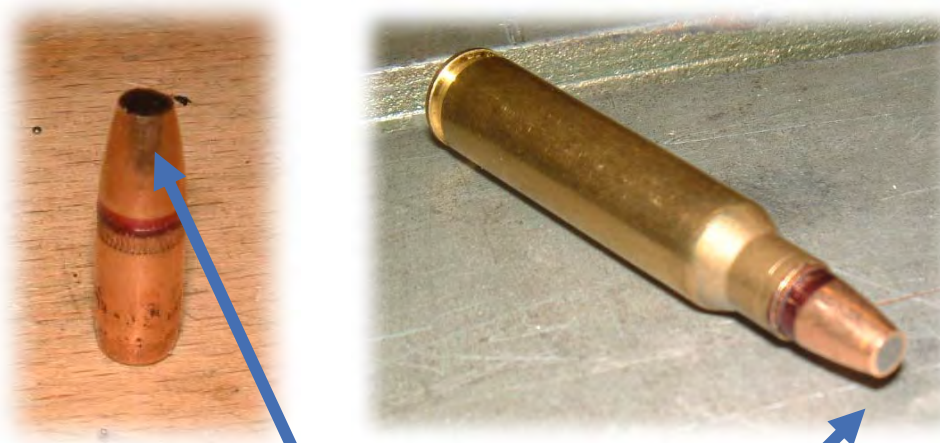


Experimental setup, results & discussion



Validation

- Adapted projectile geometry:



Truncated nose



Experimental setup, results & discussion



Validation





4 different projectile – target combinations:



Experimental setup, results & discussion



Validation

Test	Projectile	Thickness bodywork plate (mm)	Thickness armour plate (mm)	V_{50} (m/s)
1		/	6.5	1002.5
2		1	/	40.2**
3*		1	6.5	963.9
4		/	6.5	910.2





* 10 mm air gap

** Residual velocity measurement

Experimental setup, results & discussion



Validation

Test	Projectile	Thickness bodywork plate (mm)	Thickness armour plate (mm)	V ₅₀ (m/s)
1		/	6.5	1002.5
2		1	/	40.2**
3*		1	6.5	963.9
4		/	6.5	910.2

±40m/s





* 10 mm air gap

** Residual velocity measurement

Experimental setup, results & discussion



Validation

Test	Projectile	Thickness bodywork plate (mm)	Thickness armour plate (mm)	V ₅₀ (m/s)
1		/	6.5	1002.5
2		1	/	40.2**
3*		1	6.5	963.9
4		/	6.5	910.2

±90m/s

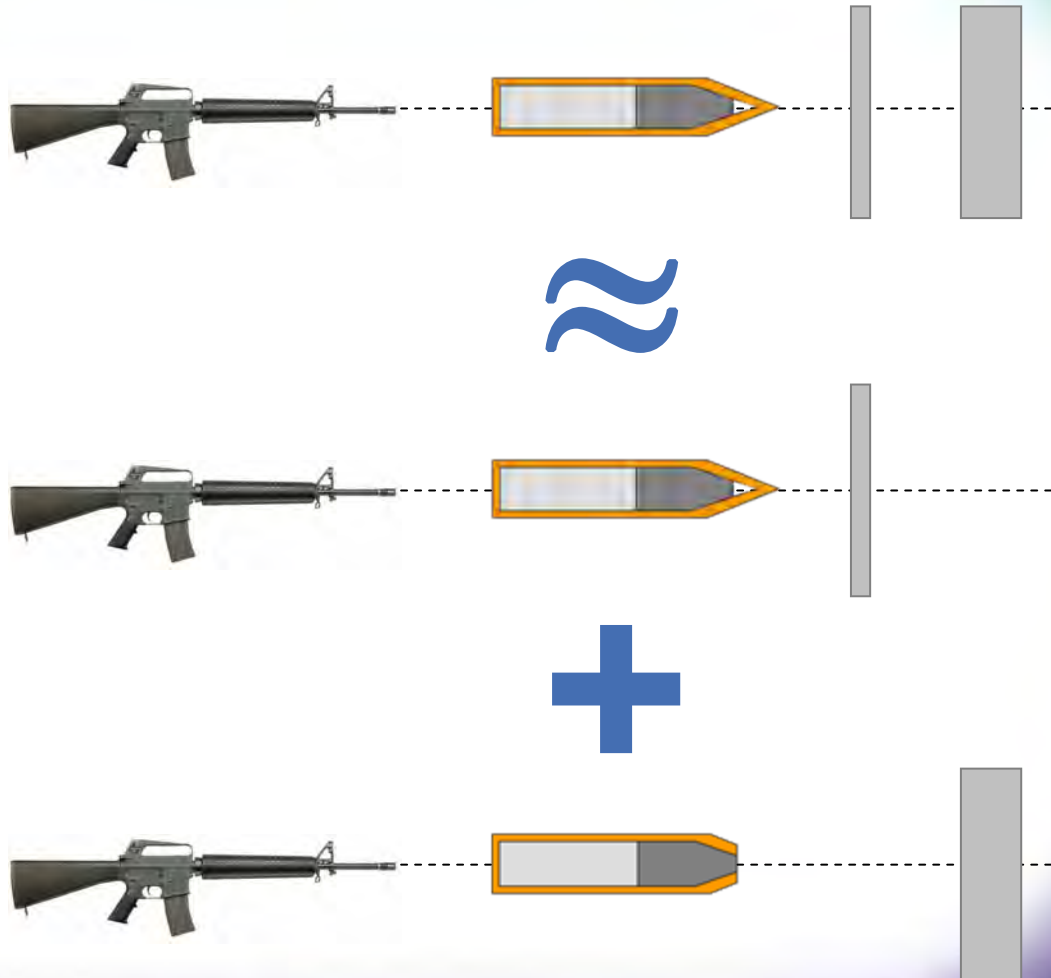
* 10 mm air gap

** Residual velocity measurement

Experimental setup, results & discussion



Validation



V_{50}

963 m/s

\approx

\approx

40 m/s

+

+

910 m/s

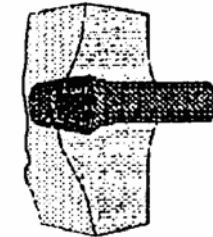
Experimental setup, results & discussion



Failure mechanism

Limited ductility even further reduced due to shear localization

Plugging



PLUGGING

Adapted projectile



Standard projectile

Conclusion



Summary

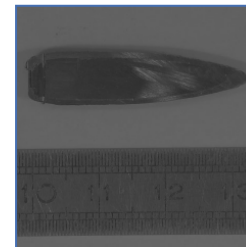
- Bodywork effect caused by changed projectile shape, which leads to enhanced plugging failure.
- Importance of in-situ testing!!!
- Be careful with norms and standards!!! Check real value.

Conclusion



Further work

- Numerical simulation
 - Dynamic material characterization
- Other projectiles
 - 7.62 x 39 M1943 Soviet
 - AP (hard core)





Questions

Predicting Hazard Response Scenarios in Weapon Systems

Ian Cullis, I Brown, P Church, P Gould, V Ingamells
A presentation to: 24th International Symposium on Ballistics

Date: 22nd - 25th September 2008



Contents

- 01 Background
- 02 Material Models: EOS
- 03 Material Models: Constitutive Response
- 04 CHARM
- 05 Munition System Application
- 06 Conclusions
- 07 Acknowledgements



01 Background

The changes in the way the UK armed forces are being asked to deploy as part of Rapid Reaction peacekeeping forces and their long-term evolution into the Balanced Force concept demands the transport and store in forward ammunition dumps of different mixes of weapon systems and ammunition. An understanding of the associated hazard would allow this to be achieved with a minimum and well-defined risk factor.

It is an essential element of the MoD's Duty of Care to the Armed Forces.

01 Background

Camp Falcon: US Army Ammunition Holding Area Iraq.

- 10th October 2006 Insurgent attack with 82mm mortars.
- Struck storage area for flares & illumination munitions. Started fire which spread to other stores.
- 7 EOD teams fully committed dawn to dusk
- Needed to secure area 1000ft radius.
- FIRE is an important hazard!



01 Background

Hazard Responses.

- Type 1: Detonation, characterised by a supersonic decomposition reaction.
- Type II: Partial detonation.
- Type III: Fast combustion of confined material (explosion) with a local pressure build up.
- Type IV: Combustion/deflagration characterised by a non-violent pressure release.
- Type V: Combustion.

Research Context.

- Need a fundamental understanding of the controlling physics and chemistry within energetic materials.
- This applies to ALL systems that contain an energetic material component.
- It provides a key component in establishing Through Life Cost of any munition procurement.

01 Background

Building Blocks

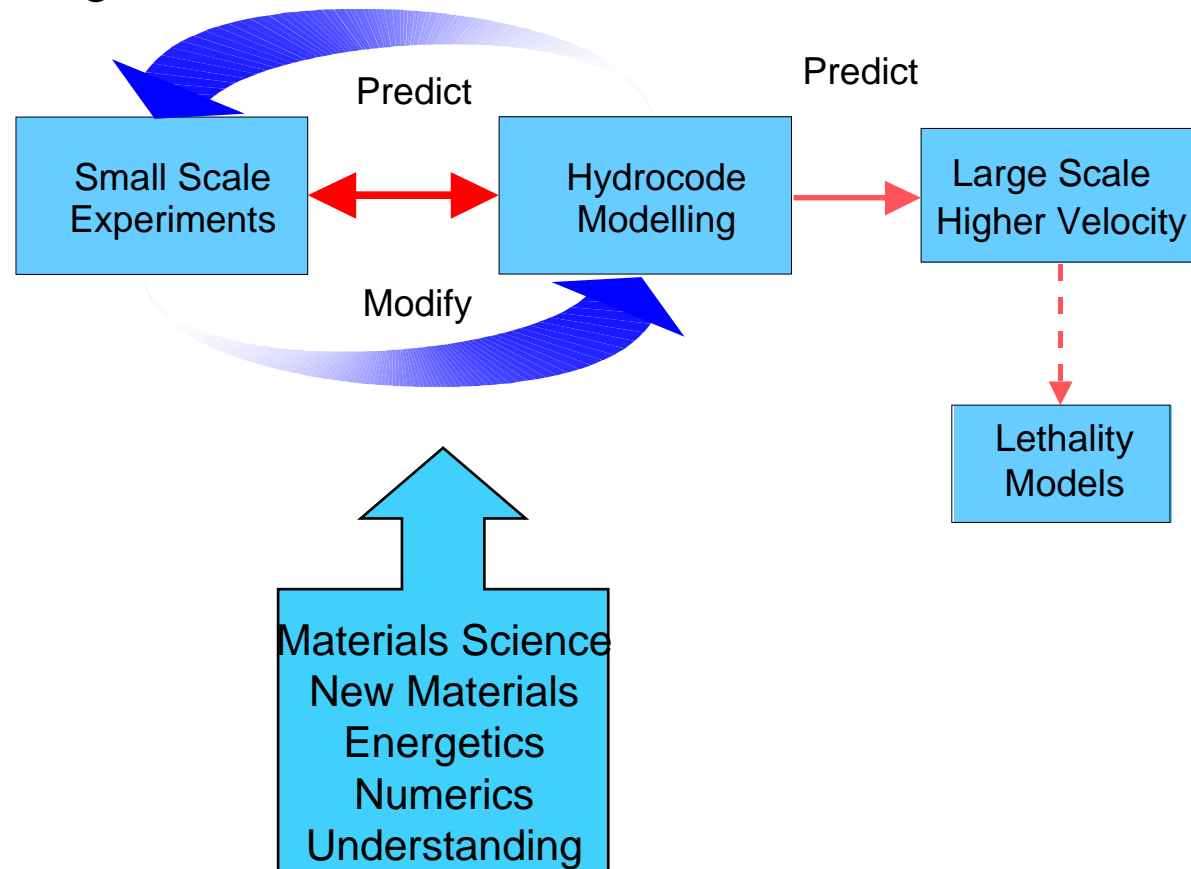
- Constitutive Response: deformation heating
- Chemical Response: ignition & growth
- Burning Response: deflagration, detonation

Needs

- Material models: EoS, constitutive, damage, fracture
- Ignition mechanisms and their description
- Link between constitutive response (damage) and ignition source term
- Burning models
- Experiments: characterisation, validation

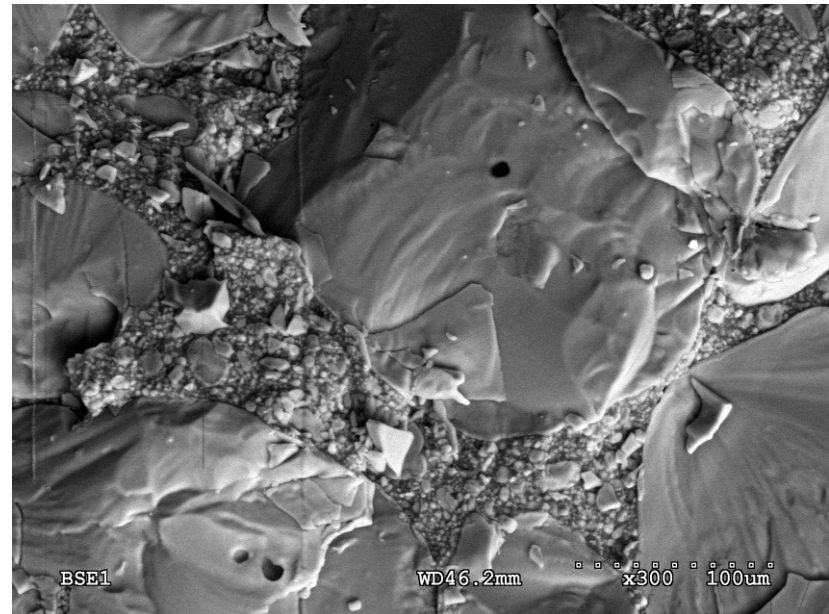
01 Background

Integrated Modelling



02

Material Model: Equation of State



02 Materials Models

Objective

To develop predictive Equations of State based on materials science with as few fitting parameters as possible – ideally none. Porter-Gould methodology, based on Group Interaction Modelling.

To develop predictive continuum based deformation and failure algorithms. These attempt to link the meso-macro scale and deal with anisotropic plastic deformation, failure and fracture.

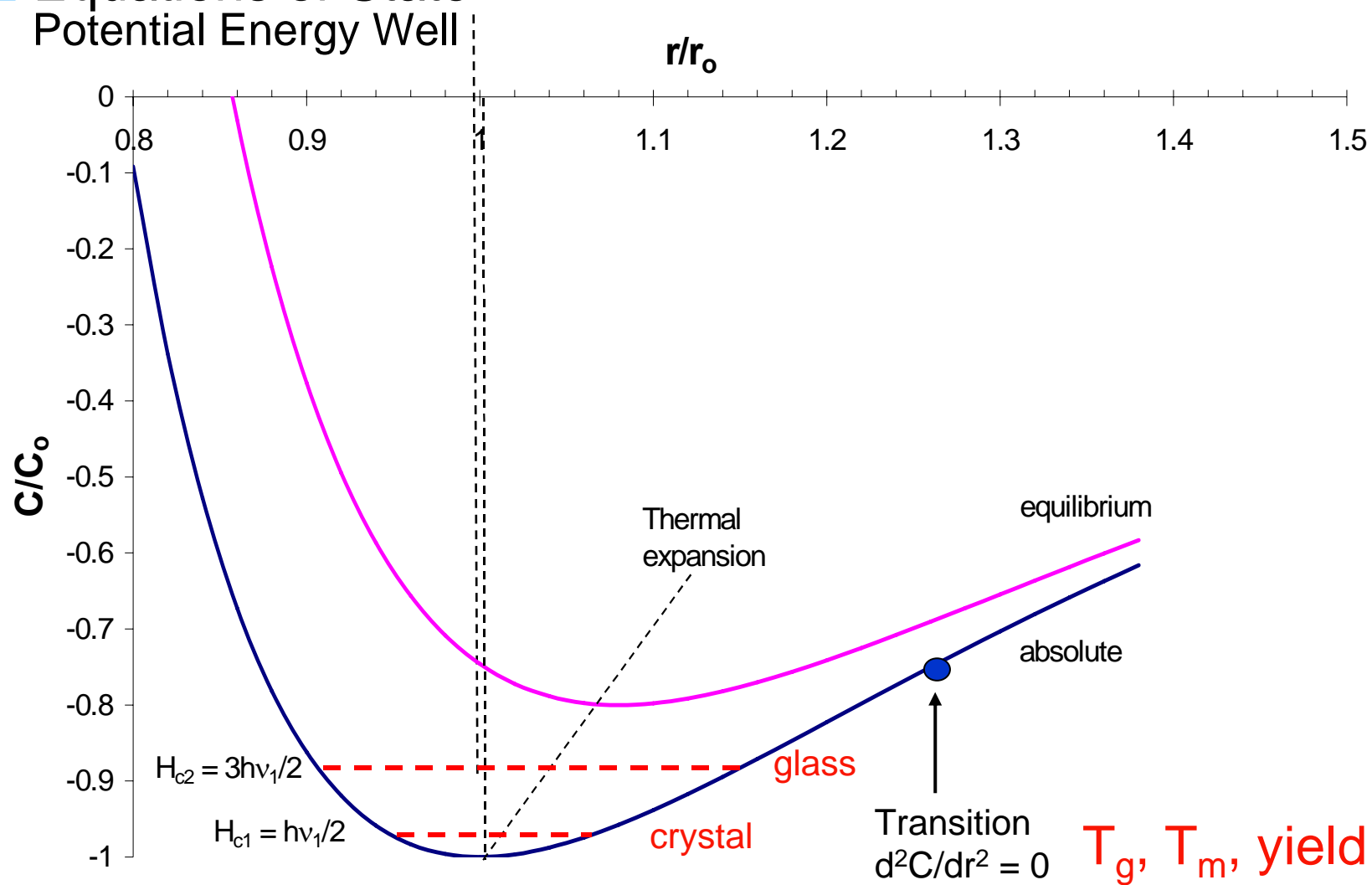
Active strategy for the past 25 years – pioneered by Barry Goldthorpe, Philip Church.

Different approach to materials tests and models.

Predictive - within 5% of experiment or within experimental error.

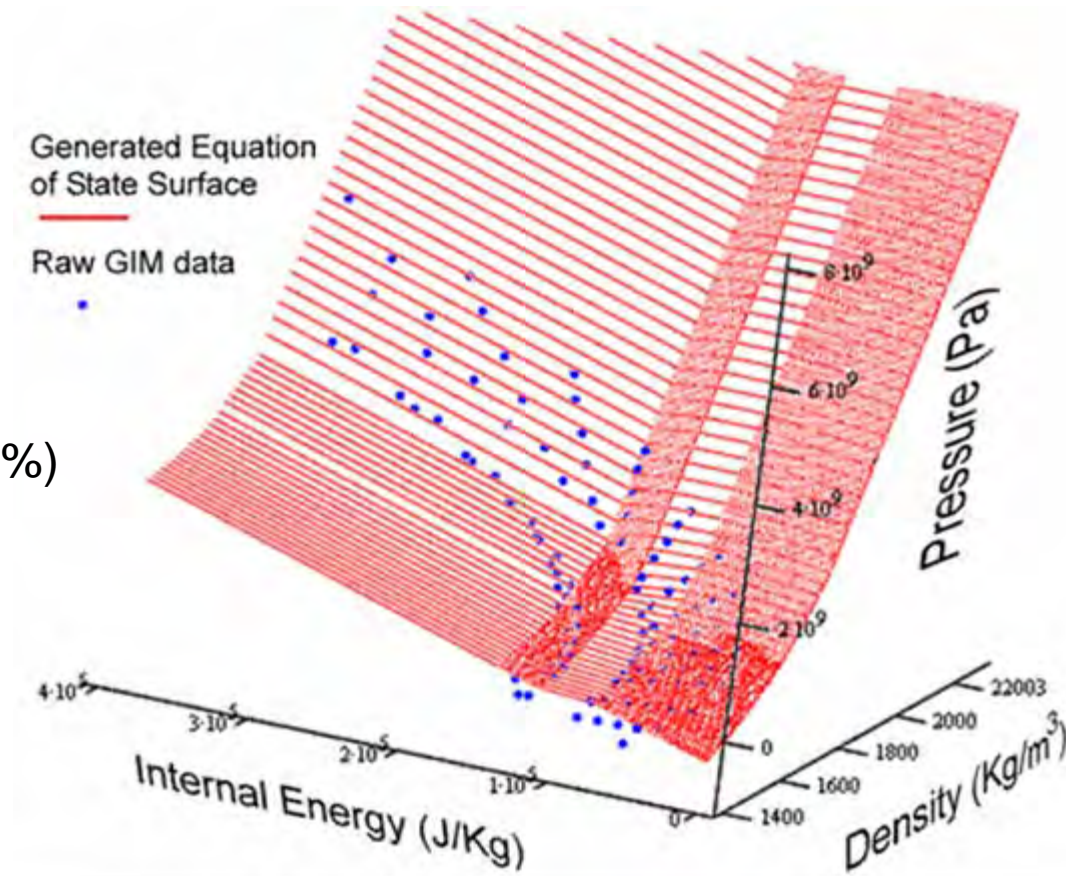
02 Equations of State

Potential Energy Well



02 Equations of State

RX1100
(RDX:HTPB :: 88%:12%)



02 Equations of State

Specific Heat

Activation Model

Prediction of reaction properties:
HTPB

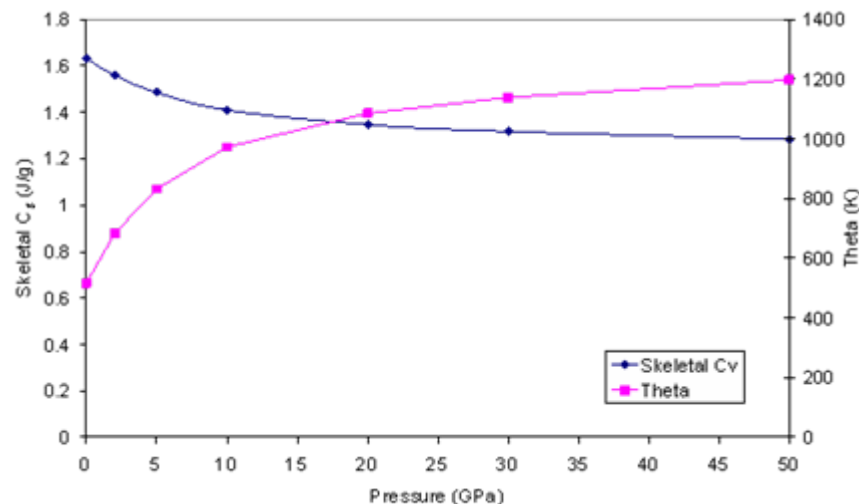
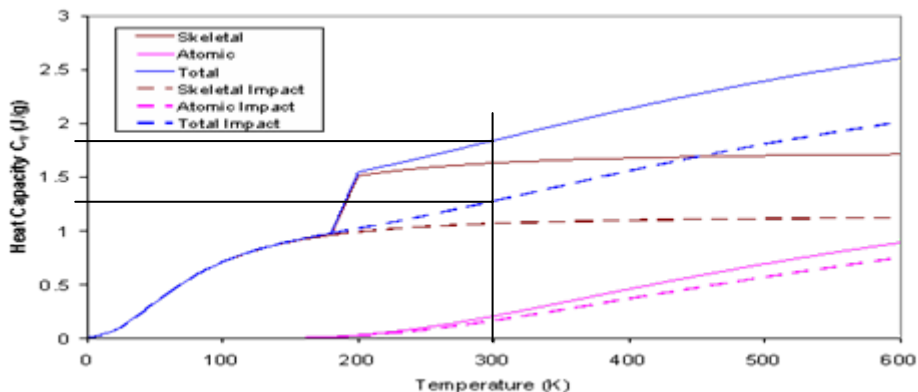
Experimental: $C_p = 1.95 \text{ Jg}^{-1}$ at 300K

Model: $C_v = 1.86 \text{ Jg}^{-1}$ at 300K

Menikoff: C_p and C_v differ by only 5%
for these materials

RDX: $C_v = 0.96 \text{ Jg}^{-1}$ compared with
experimental $C_p = 1.0 \text{ Jg}^{-1}$

Can also predict the dependency
with pressure, a significant effect and
crucial for hazard studies



03

Material Model: Constitutive Response



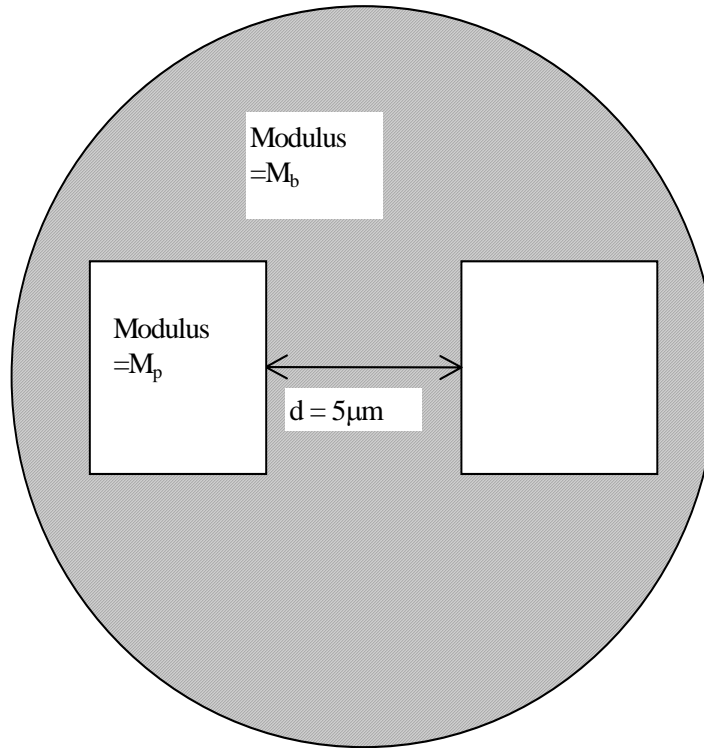
03 Constitutive Response

Binder properties

- Predicted from chemistry via Group Interaction Modelling
- Particle size distribution magnifies the binder effects
- Hierarchical model built up through multiple length scales
- Elastic material with an elastic limit
- Unique approach

03 Constitutive Response

Hierarchical model

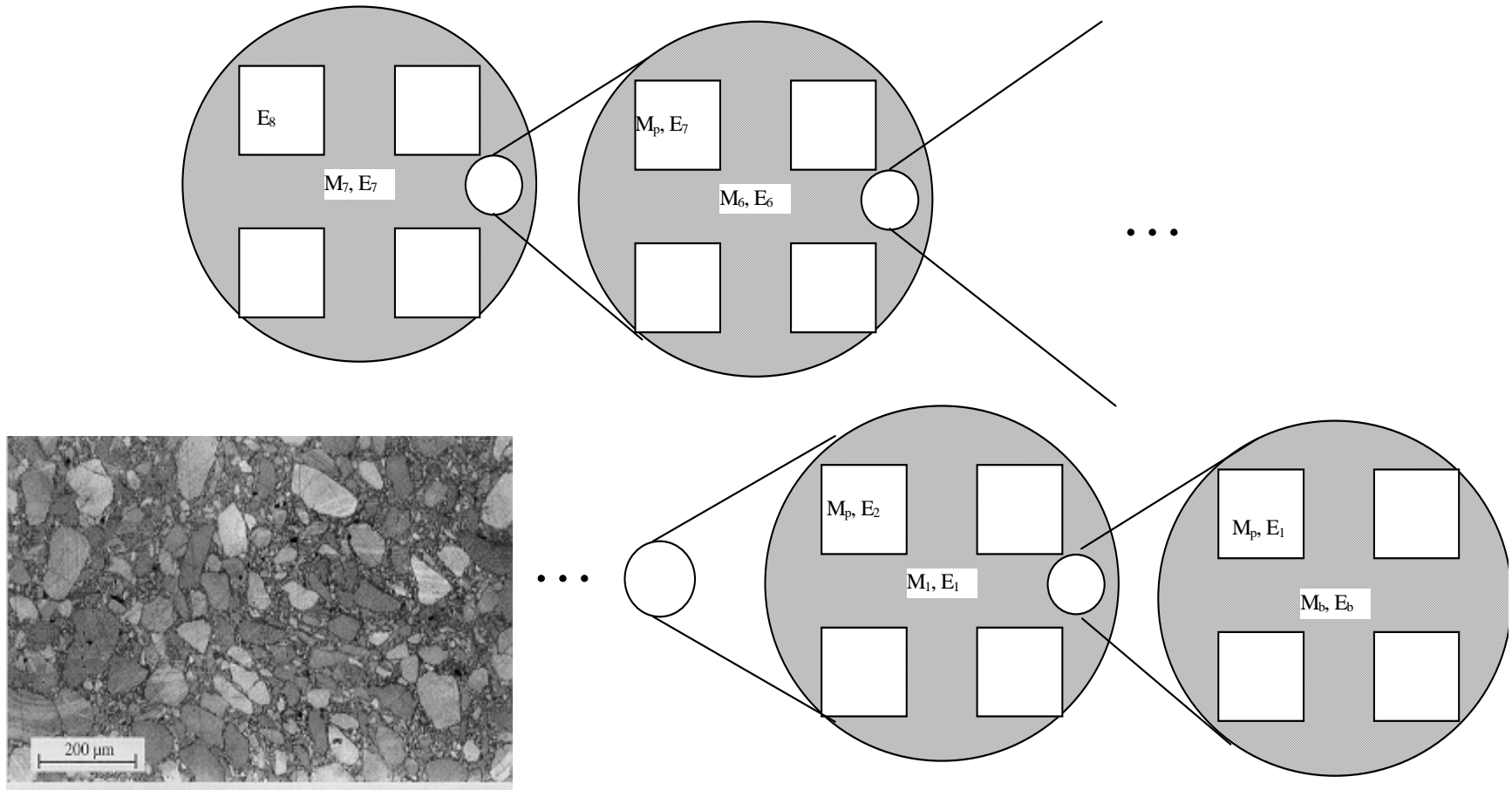


Local composite modulus

$$\frac{1}{M_{local}} = \frac{f_{V,particle}}{M_{particle}} + \frac{f_{V,binder}}{M_{binder}}$$

Schematic of smallest length scale within composite

03 Constitutive Response

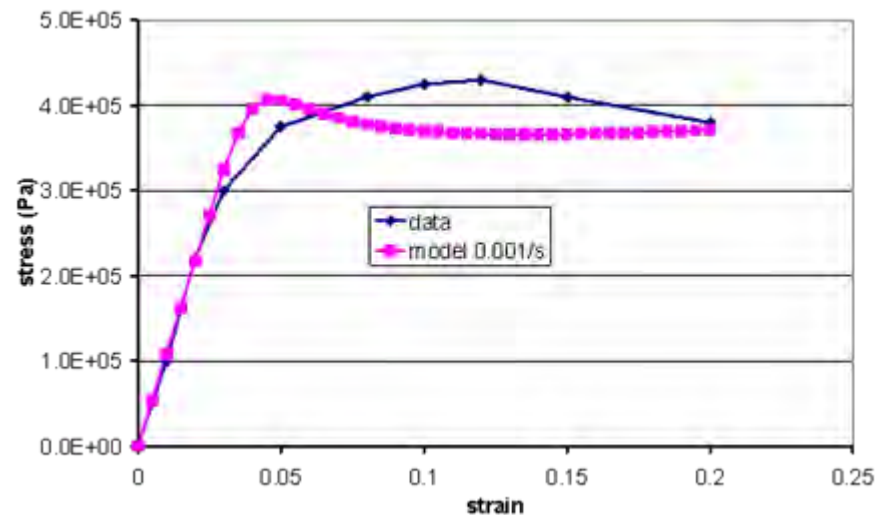
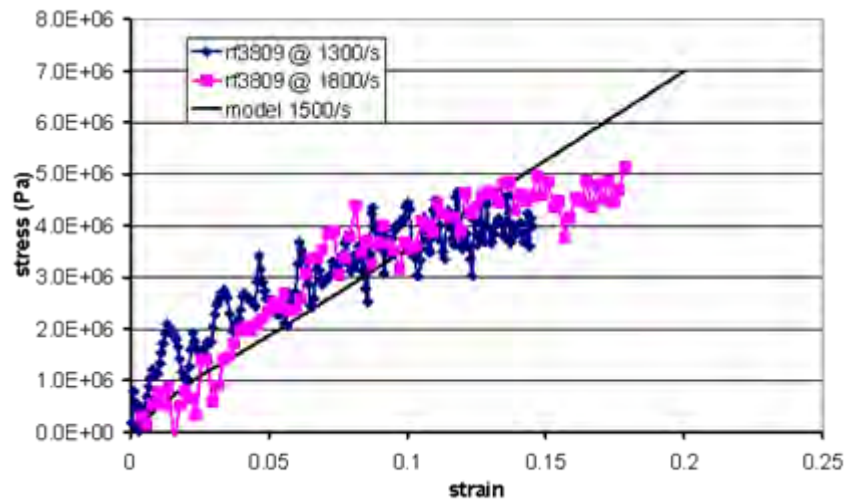


Micrograph from: PJ Rae, HT Goldrein, SJP Palmer, JE Field, AL Lewis,
Proc. Roy. Soc. Lond. A**458** (2002) pp743-762

03 Constitutive Response

Basic Model

- Can predict stress – strain behaviour over a range of strain rates.



03 Constitutive Response

Two types of failure:

- damage
- fracture

Damage is local failure and may lead to hazard response

Fracture is complete failure - material can no longer support load

Need to quantify the effect upon deformation and upon hazard response
addressing specific microstructural events

03 Constitutive Response

Energy segregation gives most deformation energy in binder.

Work to fracture the binder is significantly lower than for interface or for filler particles.

Most likely damage is local brittle failure of binder leading to voids and removal of constraint.

Fracture of filler particles will lead to increased hazard.

03 Constitutive Response

Polymer properties calculated by considering the separation distance of polymer chains. (GIM)

Chain separation beyond a certain distance breaks the weak bond between chains on one side.

This relaxes any constraint on the polymer chain but still allows it to support load via bonds with chains on other sides.

On a continuum level we can introduce the concept of a “failed” state – a polymer chain that has been separated from some of its neighbours by a cavitation event. As crazing is a general nucleation of cavitation sites then in any particular volume, there will be a fraction of “failed” states that do not contribute to constraint – although they will contribute to modulus.

Crazes link to form planes.

03 Constitutive Response

Evolution of binder modulus can be determined as a function of damage.

$$M_b = 2.5 - 1.9 * f_f$$

$$f_f = \frac{2 * \exp\left(-\frac{E_0}{E}\right)}{1 + \exp\left(-\frac{E_0}{E}\right)}$$

We can predict:

- spacing of craze planes and thus surface area
- craze size and number of voids in each craze
- void size
- Craze planes close up on unloading
- Can predict conditions under which particles will crack

03 Constitutive Response

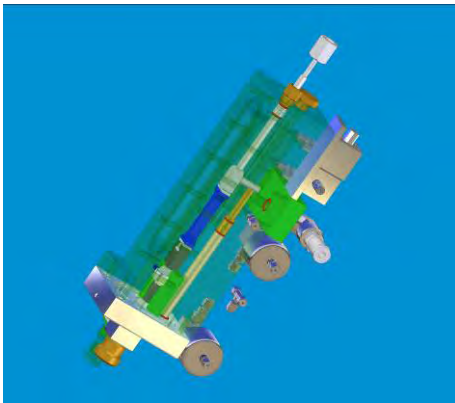
Material Damage

- Extensive research in polymers on this subject.
- Damage in composite due to debonding.
- Tomography provided validation. Can estimate created surface area caused by debonding.
- Implemented in GRIM and tested on different insults to ROWANEX1100.
- Basis for a variable hotspot density model in ignition and growth models.
- Ideas successfully being developed to describe cement composites.

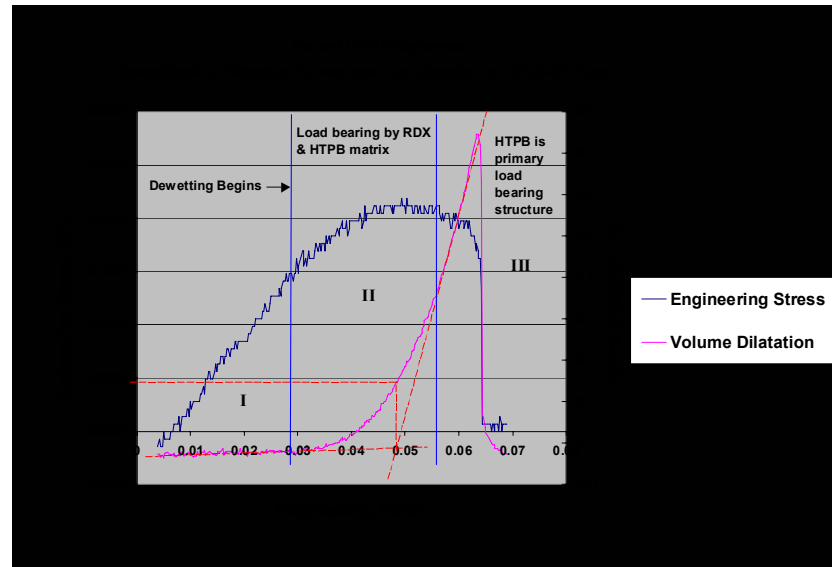
03 Constitutive Response

Gas Dilatometer

- Direct measurement of porosity and Poisson's ratio.
- Direct measurement of damage as a function of tensile strain.



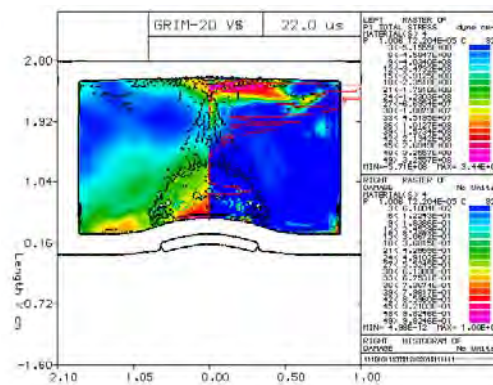
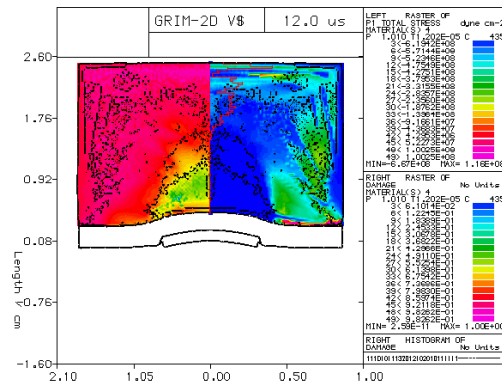
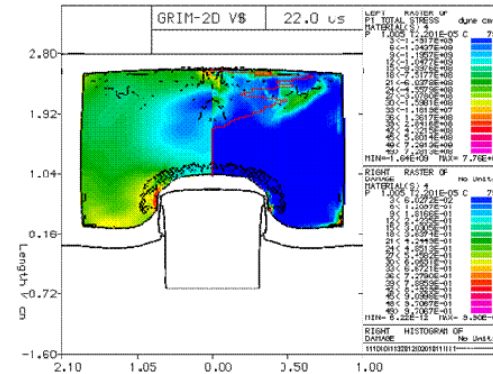
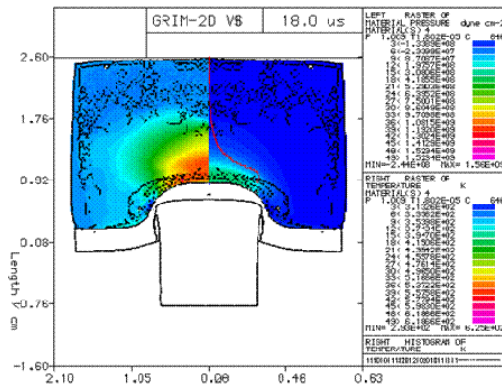
Dilatometer



Damage and stress histories

03 Constitutive Response

Material Damage



Fragment attack $v=450\text{m/s}$

04 CHARM



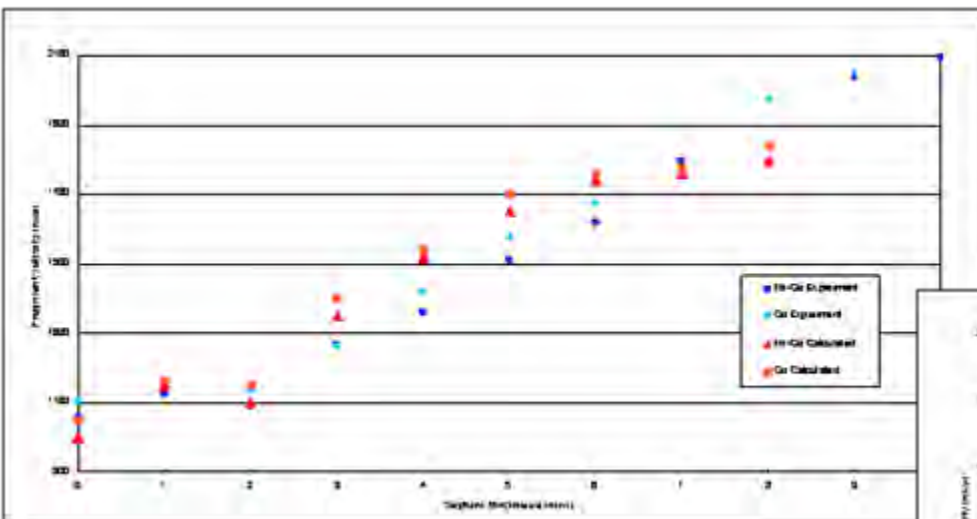
04 CHARM

CHARM Modelling

- Temperature driven 3-step Arrhenius chemistry to describe chemical reaction in solid to produce gaseous products and release of energy.
- Ideally fit the chemistry to ODTX.
- Predict fragment impact experiments (13.15mm diameter projectiles etc.)
- Adjust model to obtain best fit.
- Predict other diameter fragments
- Predict response of weapon.
- BUT, needs material data, needs 'chemistry' of explosive, often has to use literature data of 'similar' explosives.

04 CHARM

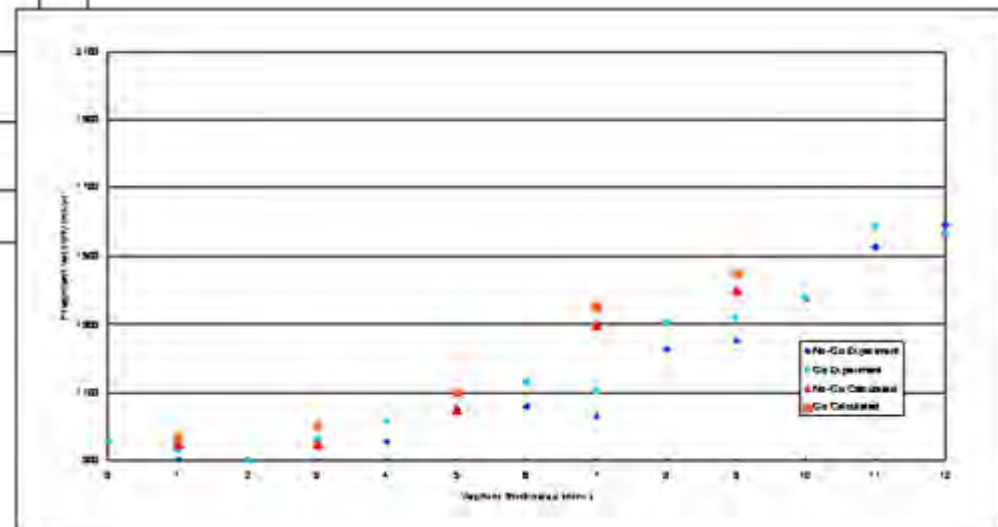
CHARM: Rowanex 1001 fragment impact SDT Threshold data



13.15mm diameter projectile

Experimental point: blue
Calculated: red

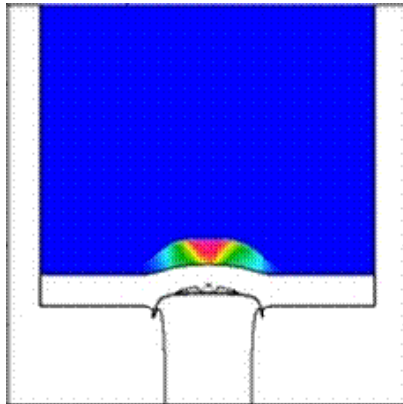
20mm diameter projectile



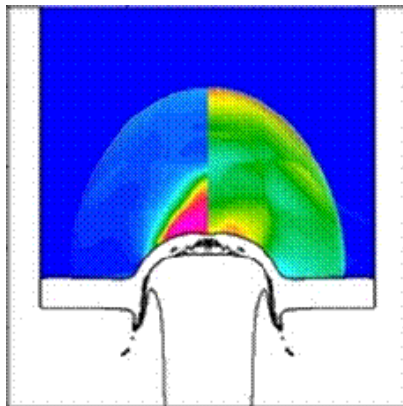
04 CHARM

CHARM: Rowanex 1001 fragment impact SDT Threshold data

Pressure - Energy

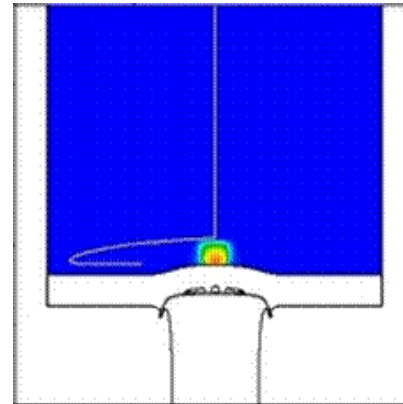


1.5 μ s

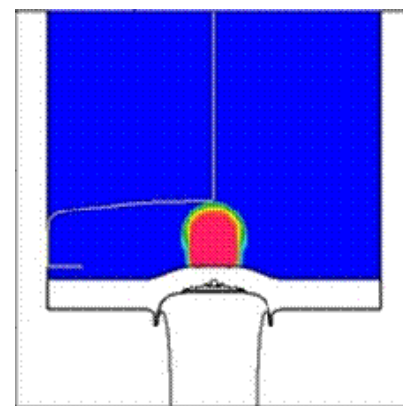


6.0 μ s

Gas Evolution



1.5 μ s



2.25 μ s

04 CHARM

Rowanex 1100 fragment impact SDT Threshold data

PG EOS

PG Constitutive Model

Pore number (size $5\mu\text{m}$)

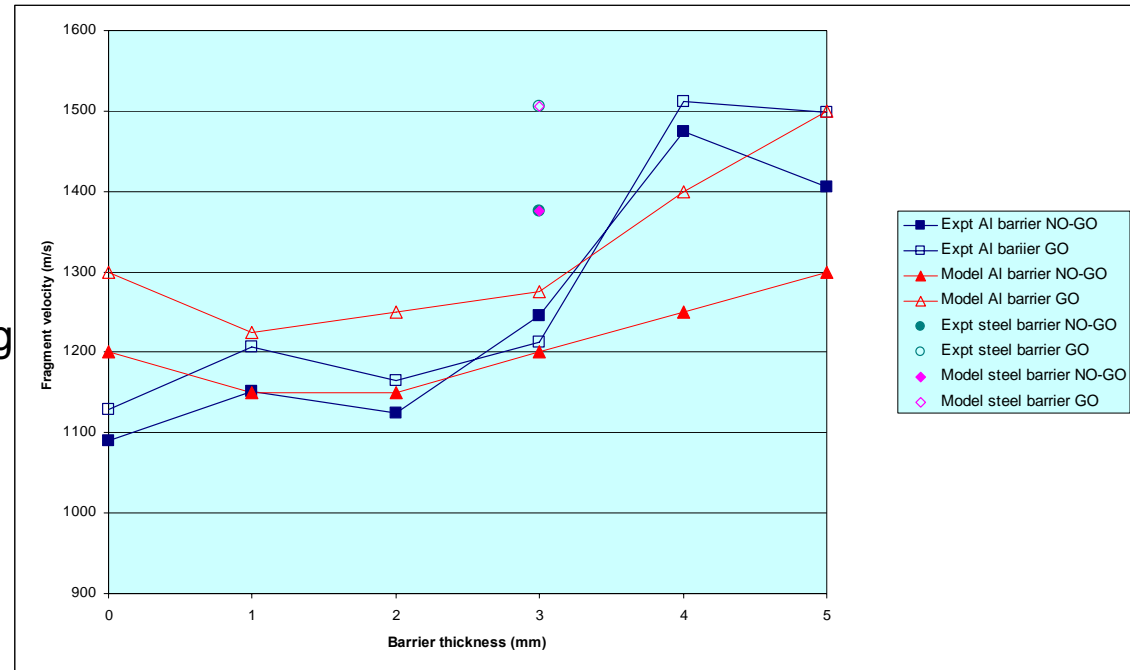
- 5.10^{10}m^{-3} in crystals
- 5.10^{10}m^{-3} due to debonding
- Porosity $6.5.10^{-6}$

Chemistry

- -1st step adjusted

Experimental point: blue

Calculated: red



13.15mm diameter projectile

05

Munition System



05 Munition System

Tube Test Explosiveness Levels



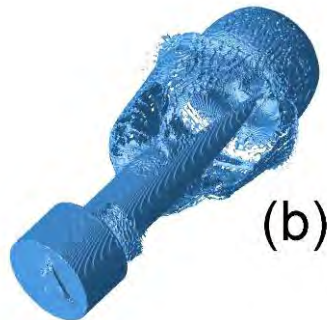
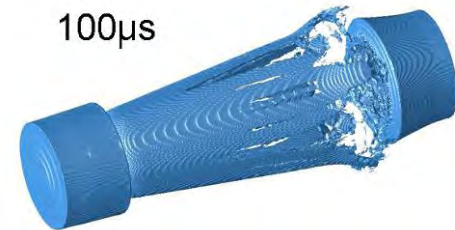
I – Pressure Burst



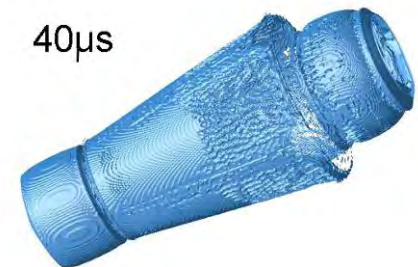
III - Explosion



II - Deflagration



IV - Detonation

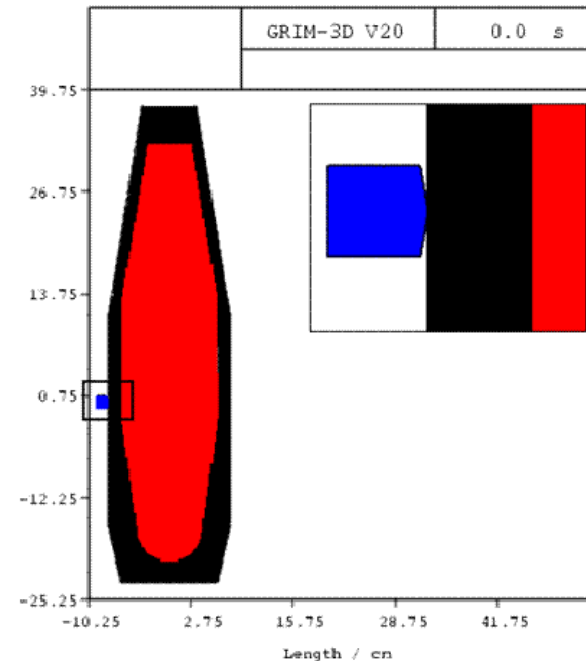


05 Munition System

Artillery Shell Fragment Attack Hazard

- CHARM, employing the advanced Equations of State (EOS), the Porter-Gould constitutive model and a physically based hotspot density distribution to predict the fragment attack experiments of an artillery shell.

STANAG Fragment $v=2536\text{m.s}^{-1}$

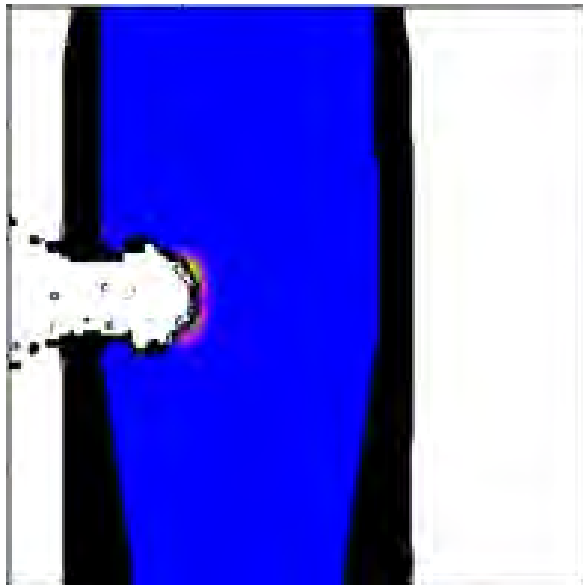


05 Munition System

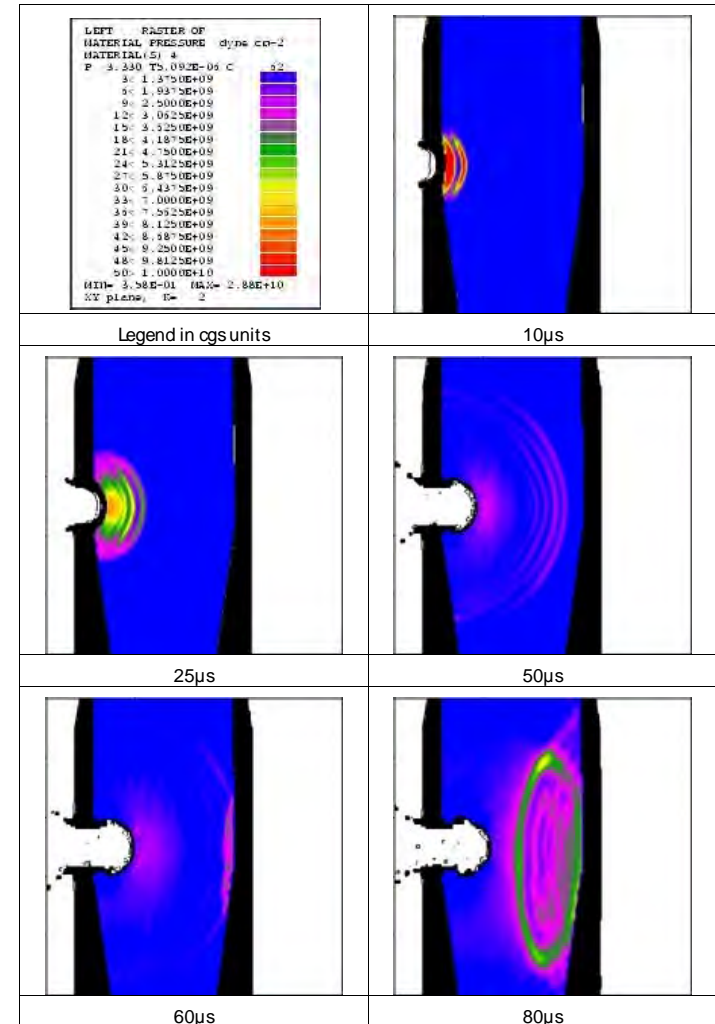
Artillery Shell Fragment Attack Hazard

Pressure field shows SDT not a mechanism

Gas evolution suggests low level BVR



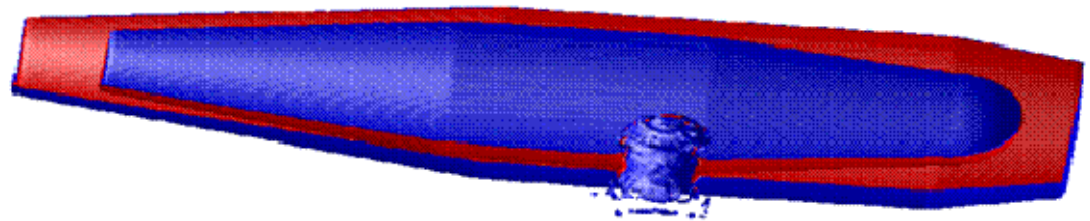
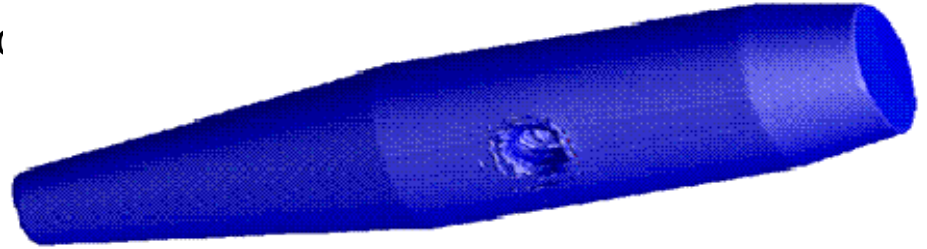
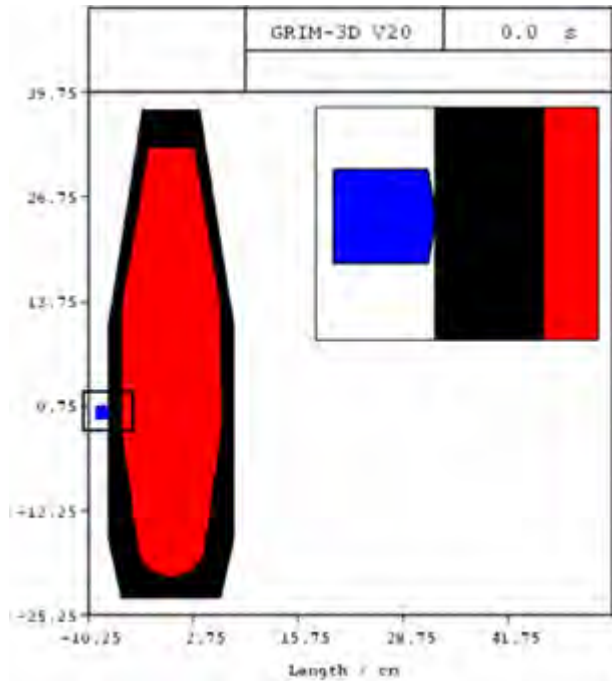
Gas evolution 80 μ s



05 Munition System

Artillery Shell Fragment Attack Hazard

Comparison with experiment



STANNAG Fragment $v=2536\text{m.s}^{-1}$

05 Munition System

Comparison with experiment.

- Modelling, in good agreement with the experiments, predicted that fragment attack of the artillery shell would not lead to an SDT event and that any subsequent reaction would be a BVR event.
- The size of the hole in the shell case and the destruction of the fragment were in excellent agreement with the experiment
- The model was able to show the generation of a small amount of gaseous reaction products around the cavity produced by the fragment in the shell filling.
- However, it was unable to predict how any subsequent reactions would grow.

06

Conclusions



06 Conclusions

The ability to predict the hazard response of a munition is an important requirement for the IM certification process of a munition.

Materials science can predict the basic behaviour of the mechanical response of a PBX:-

- Equation of State
- Constitutive response
- Damage and failure

Integration with an ignition and growth model can predict the SDT hazard response of munitions subjected to fragment attack.

A BVR model is required to predict non-SDT events and their resulting violence.

The long term UK objective is 'Certification by Simulation'

07 Acknowledgments

- Hazard UK II Consortium:
 - QinetiQ
 - BAESYSTEMS
 - Fluid Gravity Engineering
 - Cranfield University
- Defence Technology Innovation Centre, MOD for providing financial support.



Independent expertise where it matters most.



Numerical Predictions of Magnus of Spin-Stabilized Projectiles

*James DeSpirito and Sidra I. Siltan
U.S. Army Research Laboratory
Aberdeen Proving Ground, Maryland*



TECHNOLOGY DRIVEN. WARFIGHTER FOCUSED.

24th International Symposium on Ballistics

New Orleans, Louisiana

22–26 September 2008

- Nonlinear Magnus moments
 - Observed for nearly all spin-stabilized projectiles in subsonic and transonic flight.
 - Accurate prediction important to predict dynamic stability and trim angles.
- Prediction capabilities
 - Steady-state RANS provides accurate results in supersonic and high transonic flight regimes, as demonstrated in 1980s.
 - Recent work found issues in subsonic and transonic flight regimes for some projectile configurations.
 - Predictions too high at these flight speeds.
 - Time-accurate hybrid RANS/LES simulations can lead to more accurate results.



Steady-State RANS

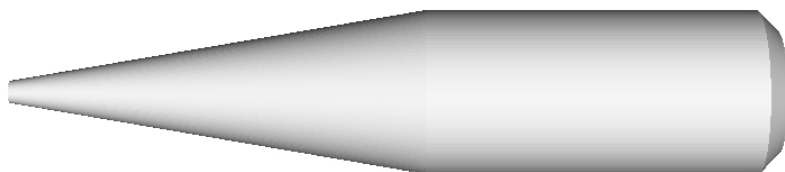
M910 Projectile
Mach 0.6



Unsteady RANS/LES

- Full 3-D Navier-Stokes calculations
- CFD++, Metacomp Technologies, Inc.
 - Implicit, dual time-stepping
 - Unstructured, finite-volume discretization
- Second order space/time accuracy
- Steady-state RANS simulations
 - Goldberg's three-equation k - ε - R turbulence model
 - Two-equation realizable k - ε turbulence model
 - Two-equation cubic k - ε turbulence model
- Unsteady hybrid RANS/LES
 - Batten-Goldberg turbulence model
 - Cubic k - ε in RANS region (handles anisotropy)
 - Anisotropic form of the Smagorinsky model in LES regions
- y^+ values < 0.5

M910 Target Practice Round



D=16.2 mm
L=4.7 cal.

*DeSpirito and Heavey, 2004
*DeSpirito, 2007

0.50-caliber round



D=12.7 mm
L=4.55 cal.

*Silton, 2005

U.S. Army-Navy Spinner Rocket (ANSR)

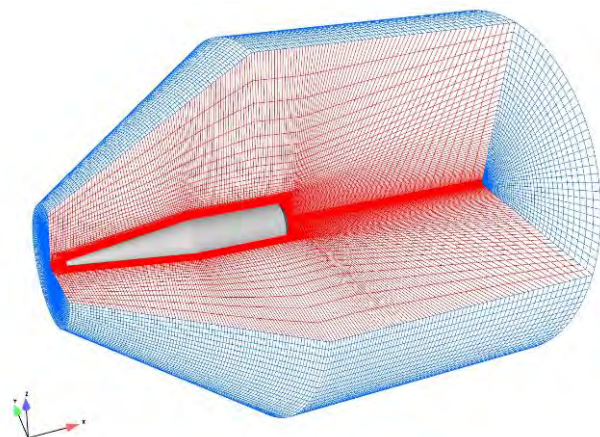


D=20.0 mm
L=7 cal.

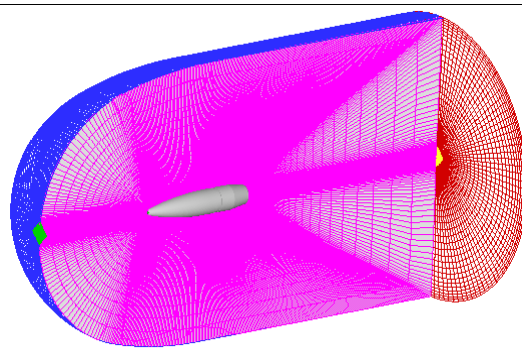


*DeSpirito, 2008

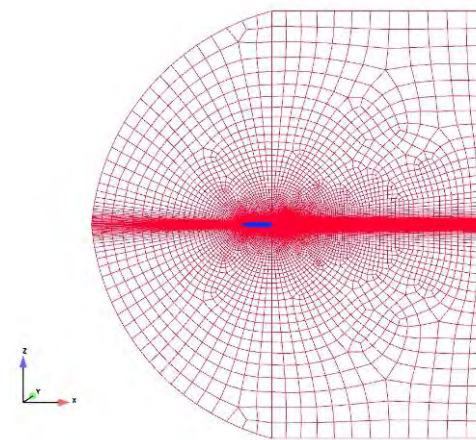
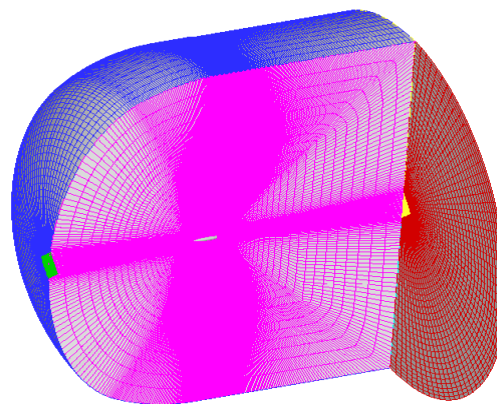
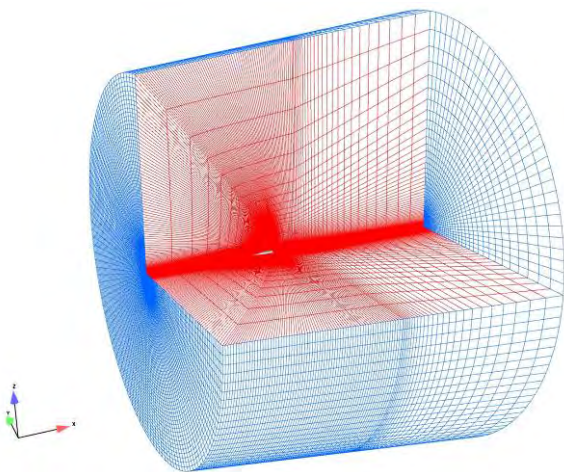
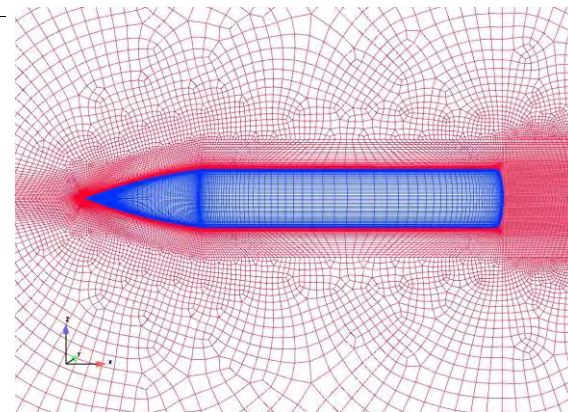
M910



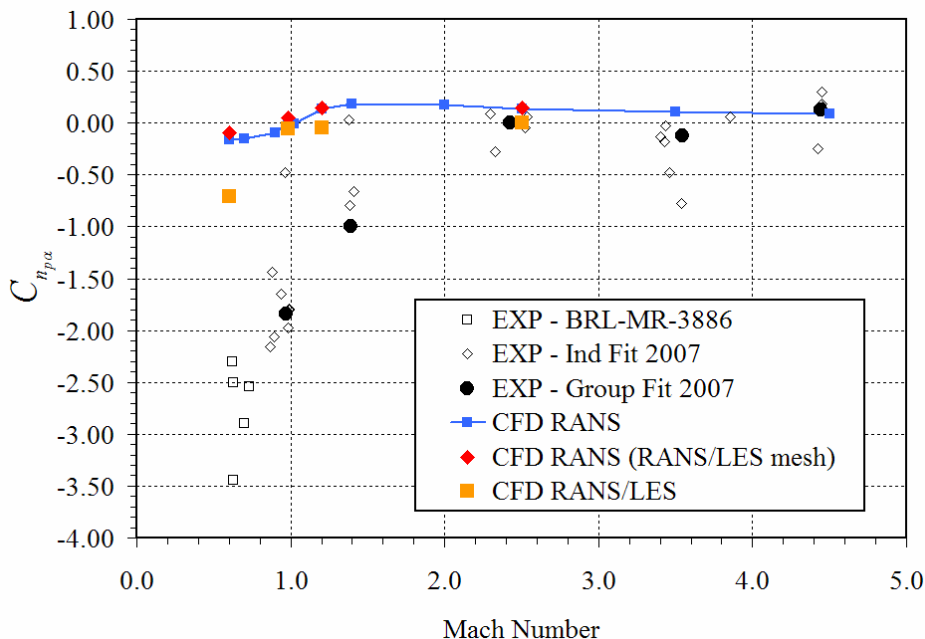
0.05-cal



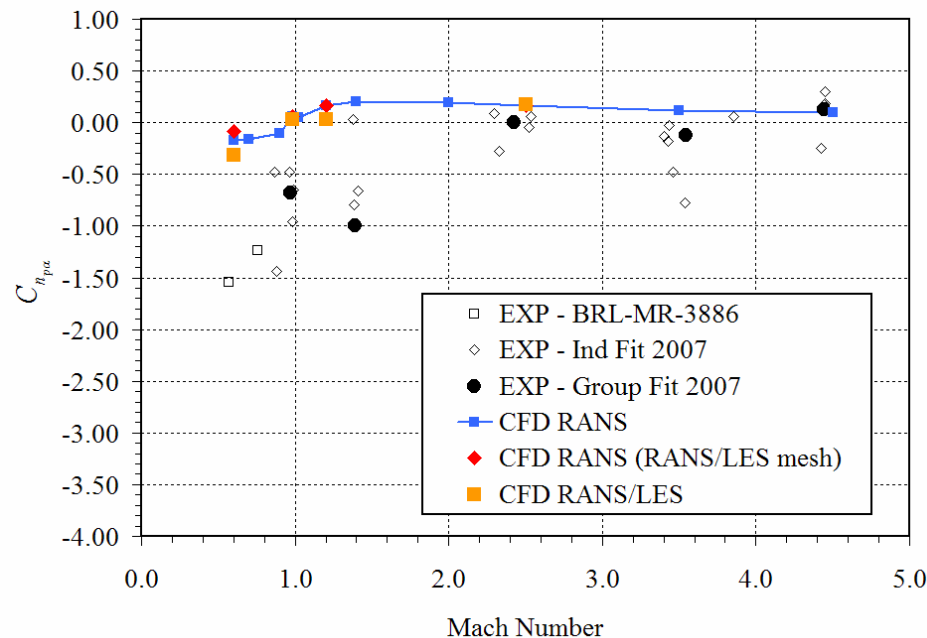
ANSR



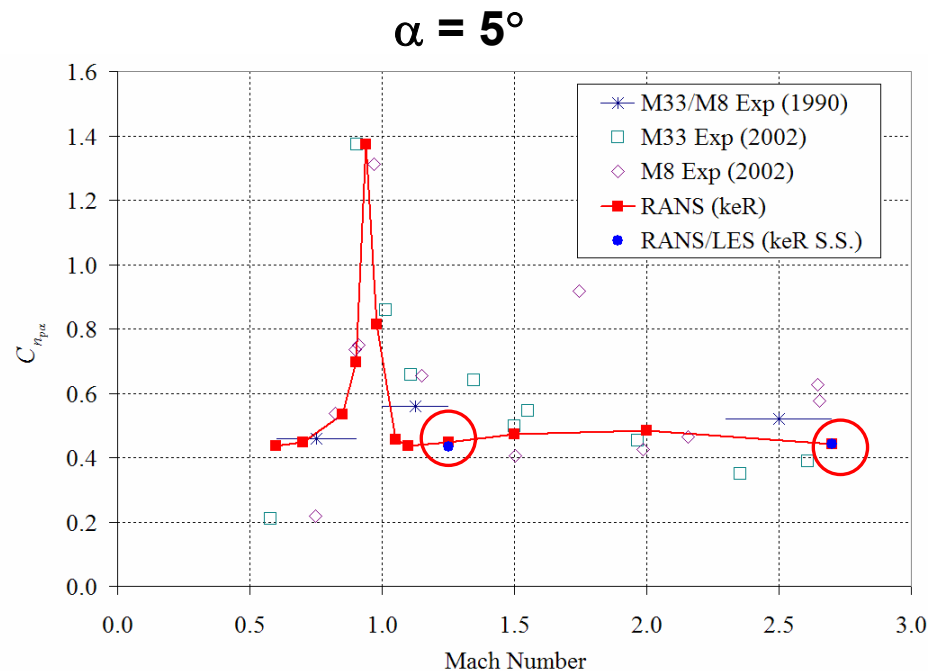
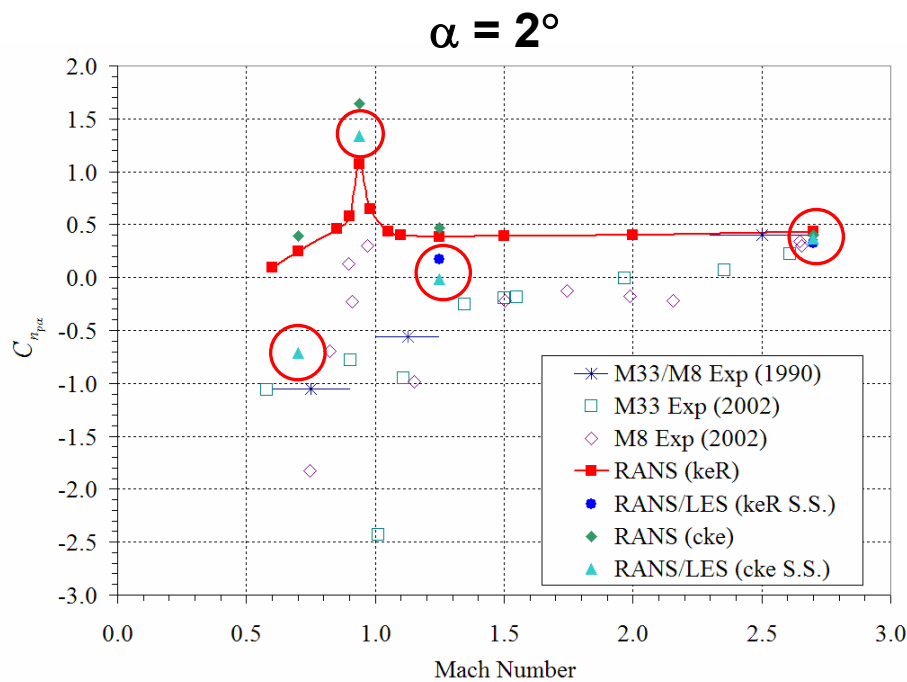
$\alpha = 3^\circ$



$\alpha = 5^\circ$

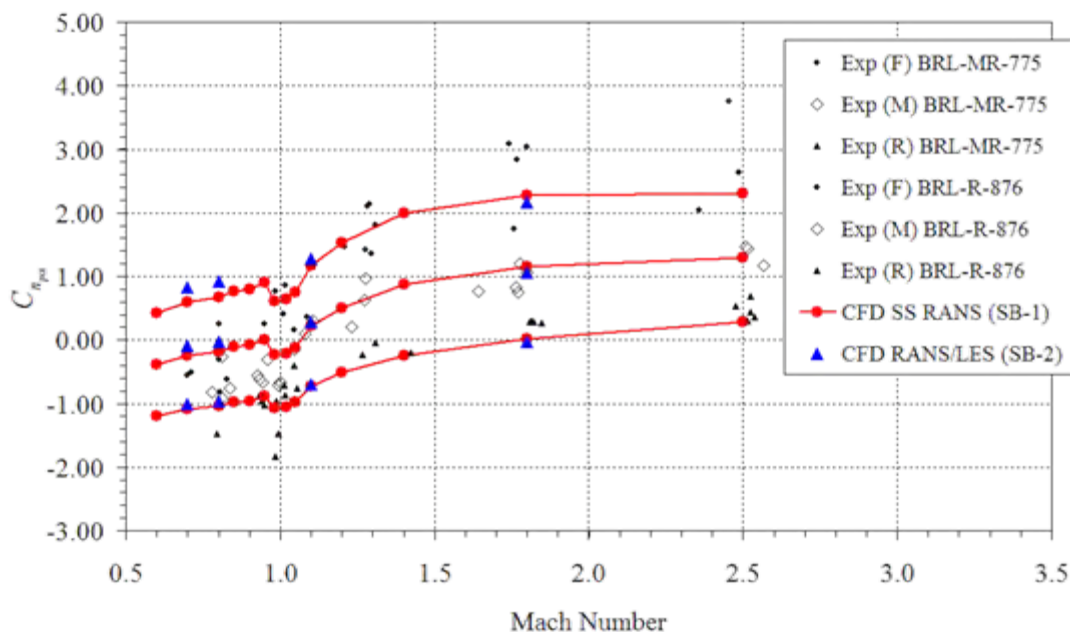


- Steady-state RANS accurate in supersonic regime.
- Time-accurate RANS/LES
 - More accurately predict negative trend at lower Mach numbers (though not as sharp a decrease).
 - Predicts nonlinearity with α , not observed in steady-state RANS simulations.



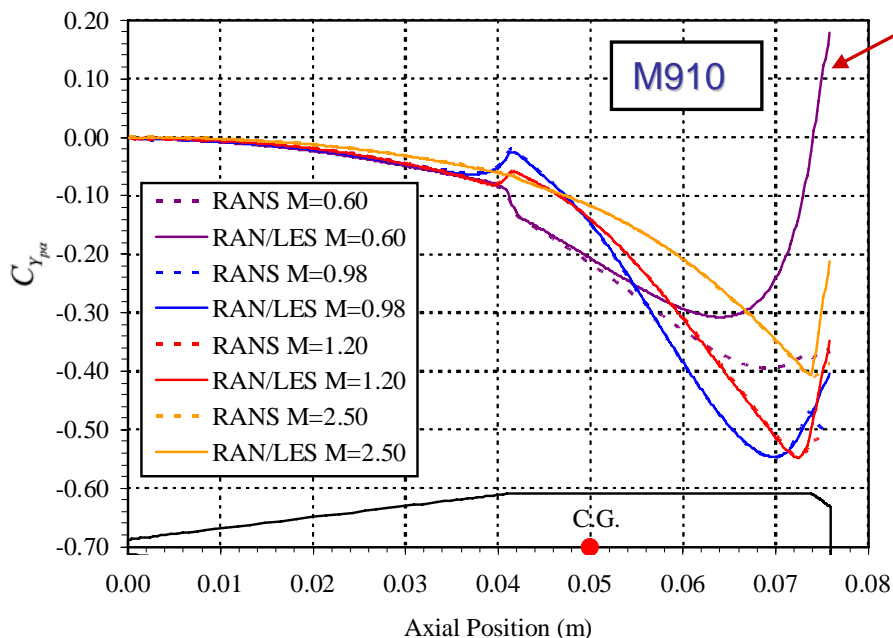
- Critical behavior in transonic region predicted by both solution methods.
- At $\alpha=5^\circ$ RANS predictions compare well with experimental data.
 - Magnus moment under predicted as Mach 1 approached from above.
 - Over predicted in subsonic range.
- At $\alpha=2^\circ$ time-accurate RANS/LES (circled) more accurate.
- RANS turbulence model has small effect on Magnus moment but did not improve prediction in subsonic range.

$$\alpha = 2^\circ$$



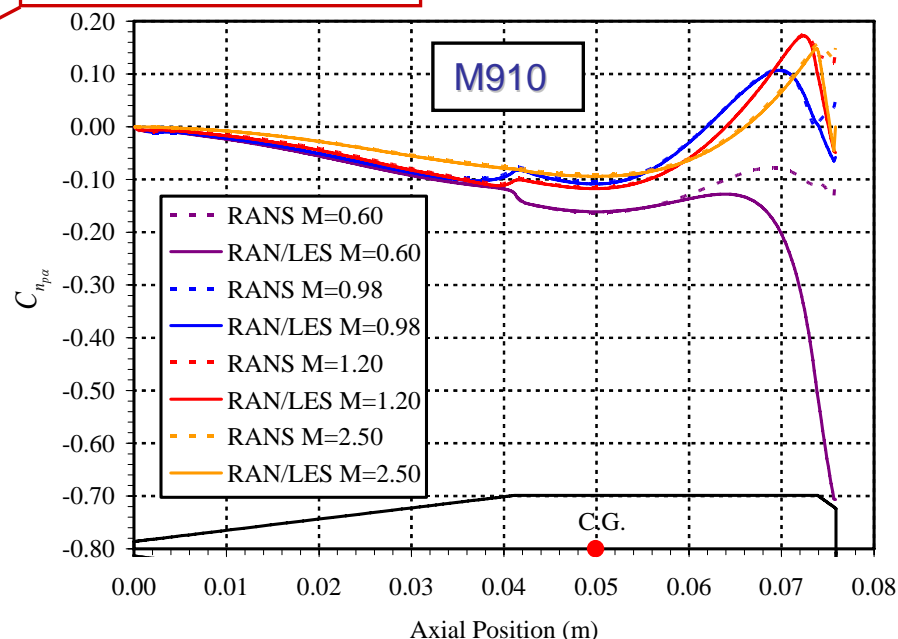
- Sharp edge on base, unlike rounded 0.50-cal. and chamfered M910.
- 3 c.g. locations.
- Little difference between RANS and RANS/LES (regardless of Mach number or c.g. location).
 - Excellent agreement for $M \geq 0.98$.
 - Slightly over predicted in subsonic range but not as great as 0.50-cal or M910.
- Similar result for 0.5-cal, 7° boattail ANSR configuration.
- Results indicates that a sharp edge (corner) on base of projectile may inhibit impact of unsteady flow phenomena on accuracy of steady-state RANS solution.
 - Weinacht (2007) previously found sharp edge reduces nonlinear Magnus effect.

Magnus Force

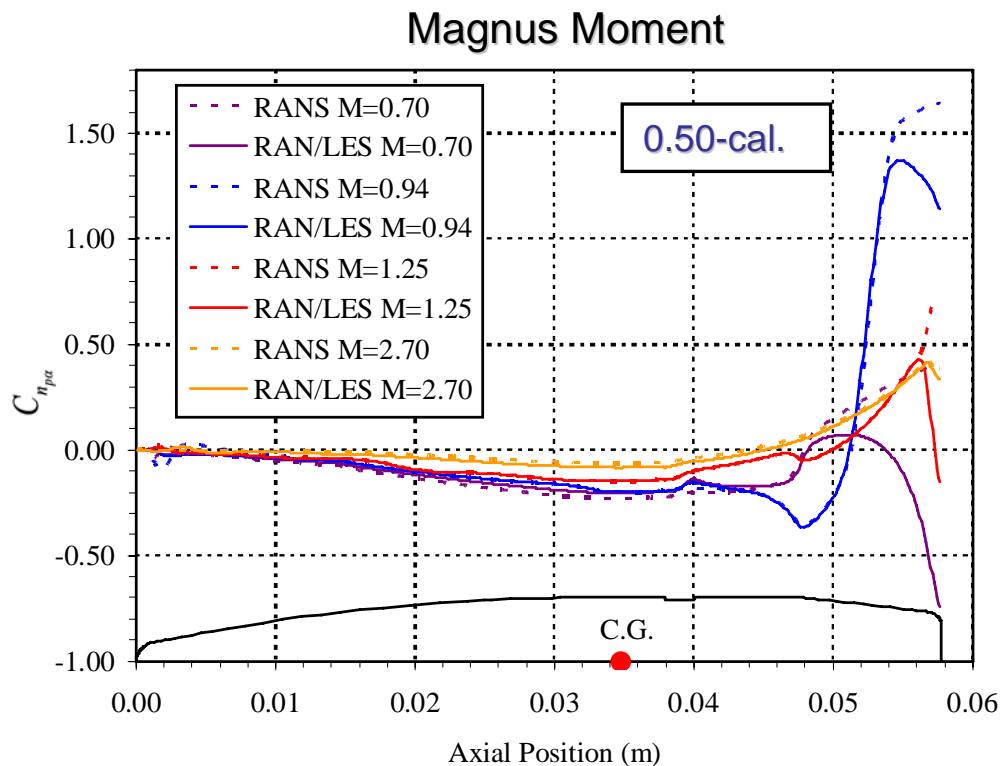


Force opposite that due to Magnus.

Magnus Moment



- Effects of Magnus confined to rear end of projectile.
- RANS vs. RANS/LES differences
 - Small for transonic and supersonic Mach numbers and confined to chamfer region.
 - Large difference at Mach 0.6 and begins farther forward on projectile.
- Subsonic (Mach 0.6) Magnus
 - Positive force indicates flow interactions have overtaken Magnus effects.
 - Magnus force usually negative (normal pointing to port side for right hand spin).
 - Magnus force center of pressure has moved rear of c.g.



- Virtually no difference between RANS and RANS/LES at Mach 2.7.
 - As Mach number decreases
 - Difference between simulation methods increases.
 - Difference between the two distributions diverge farther forward.
- (ANSR results showed only minor differences in Magnus distributions for the two simulation methods.)

Mach 0.6

Instantaneous RANS/LES



Time-averaged RANS/LES



Steady-state RANS



Mach 0.98

Instantaneous RANS/LES



Time-averaged RANS/LES



Steady-state RANS



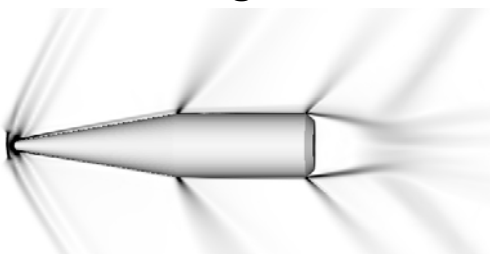
Numerical Schlieren Visualizations, $\|\nabla\rho\|$

Mach 1.2

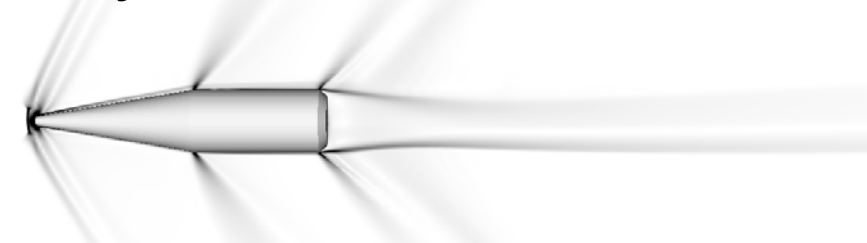
Instantaneous RANS/LES



Time-averaged RANS/LES



Steady-state RANS



Numerical Schlieren Visualizations, $\|\nabla \rho\|$

Mach 2.5

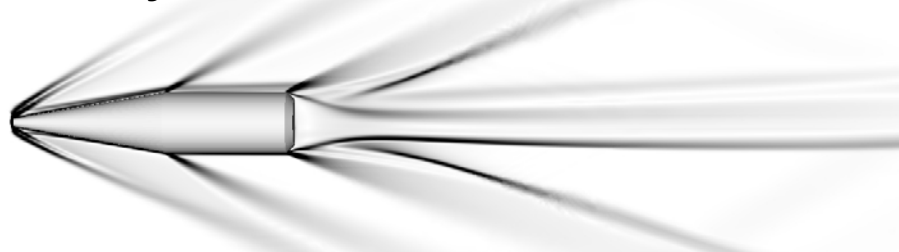
Instantaneous RANS/LES



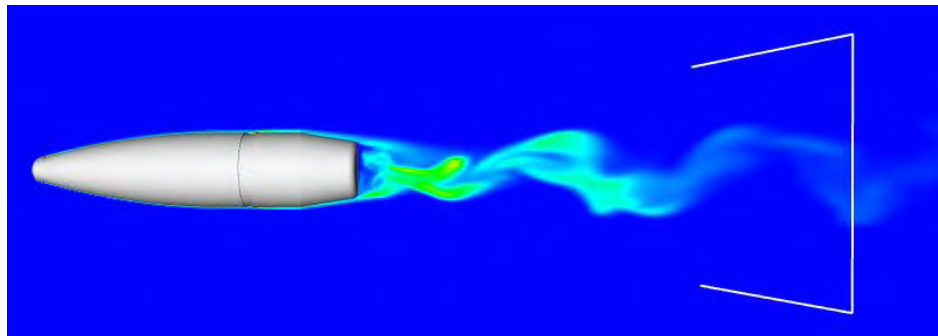
Time-averaged RANS/LES



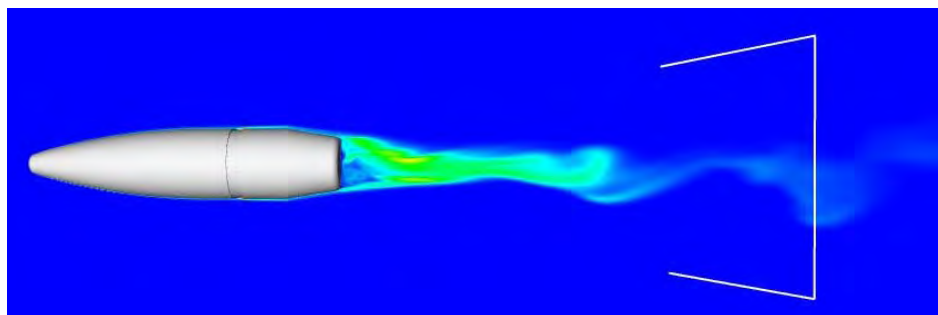
Steady-state RANS



Mach 0.7



Mach 1.25



- Similar flow field results for 0.50-cal. and ANSR (not shown).

- Projectile base shape is an important parameter.
 - Rounded or chamfered bases
 - Time-accurate RANS/LES simulations improve the Magnus moment prediction.
 - Higher nonlinear Magnus effects (Weinacht, 2007).
 - Sharp cornered base leads to less nonlinear Magnus and improved steady-state RANS predictions.
- Turbulent eddies resolved in RANS/LES simulations impact the pressure distribution on projectile at lower Mach numbers.
- Future work
 - More detailed analysis of unsteady flow field.
 - Separation
 - Pressure distribution
 - Higher angle of attack simulations ($5^\circ \leq \alpha \leq 15^\circ$).

This work was supported in part by a grant of high-performance computing time from the U.S. Department of Defense High Performance Computing Modernization program at the ARL Major Shared Resource Center, Aberdeen Proving Ground, Maryland.

Dr. James DeSpirito
U.S. Army Research Laboratory
Aberdeen Proving Ground, MD 21005-5069
410-306-0778
james.despirito@us.army.mil

Munitions effects: a schematic overview of munitions and warheads, trends for the future

24th International Symposium on Ballistics
New Orleans, LA, September 22–26, 2008

TNO | Knowledge for business



Dr. A.M. Diederer
andre.diederer@tno.nl



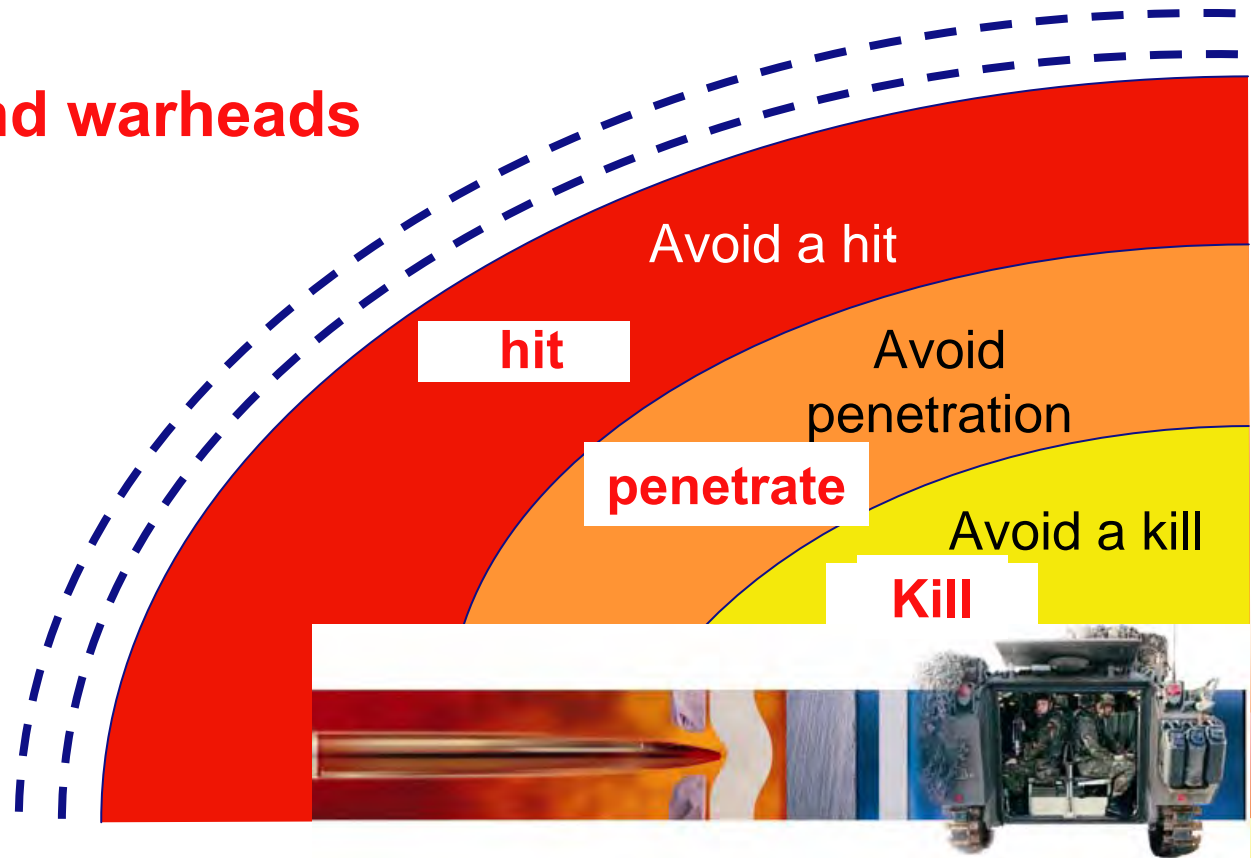
Outline

- Types of energy transfer media
atoms, electrons and photons
- Classification scheme of munitions and weapons effects
examples for kinetic energy, blast and heat, electric current
and electromagnetic radiation
- Trends
 - adaptive effects and enhanced lethality

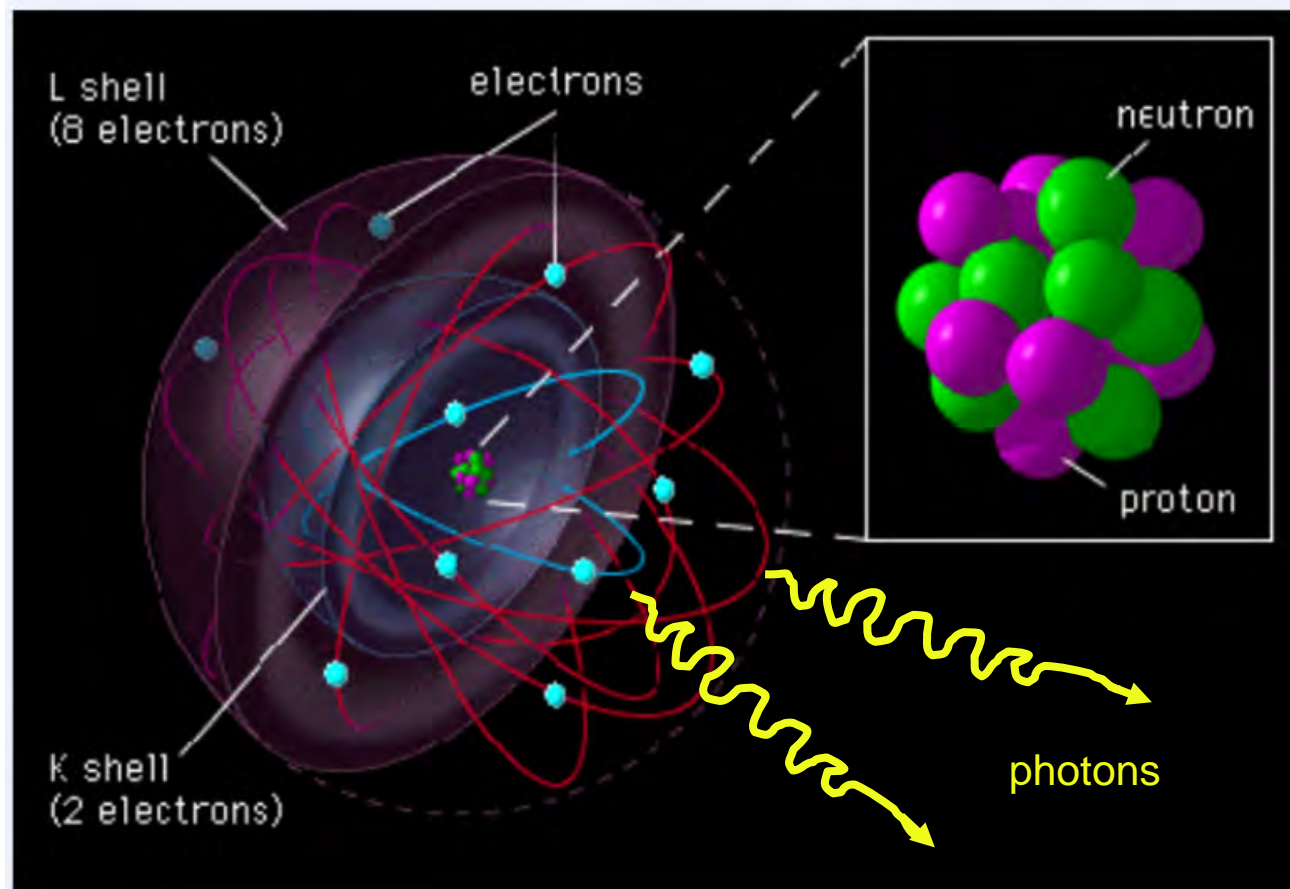
Layers of { protection **attack**

Passive, reactive and hard-kill active armour

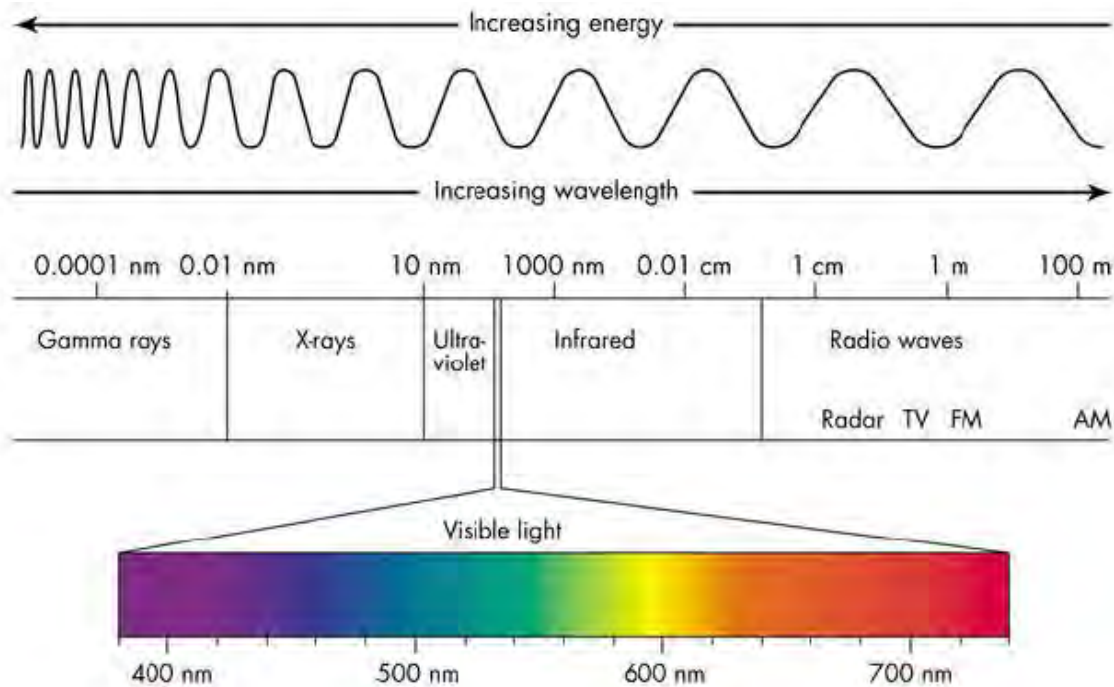
Projectiles and warheads



Munitions effects: atoms, electrons and photons as energy transfer medium

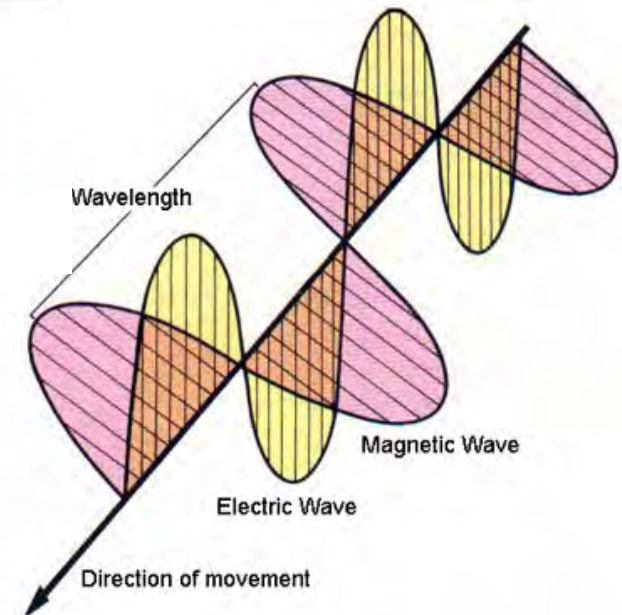


Photons as energy transfer medium: wave behaviour

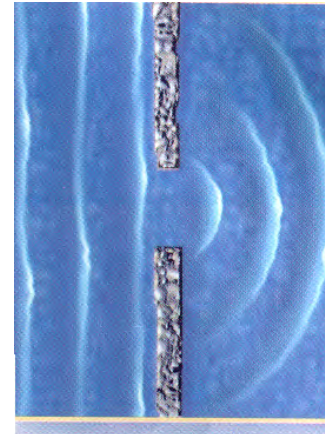
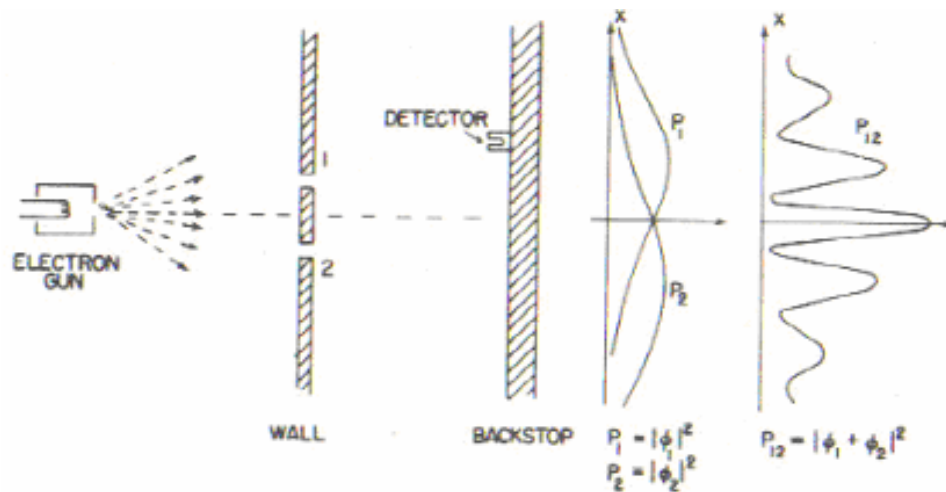


energy per photon:
Planck constant x frequency

oscillating
electromagnetic
field



Wave aspects:
besides photons, also electrons and atoms exhibit
diffraction and interference



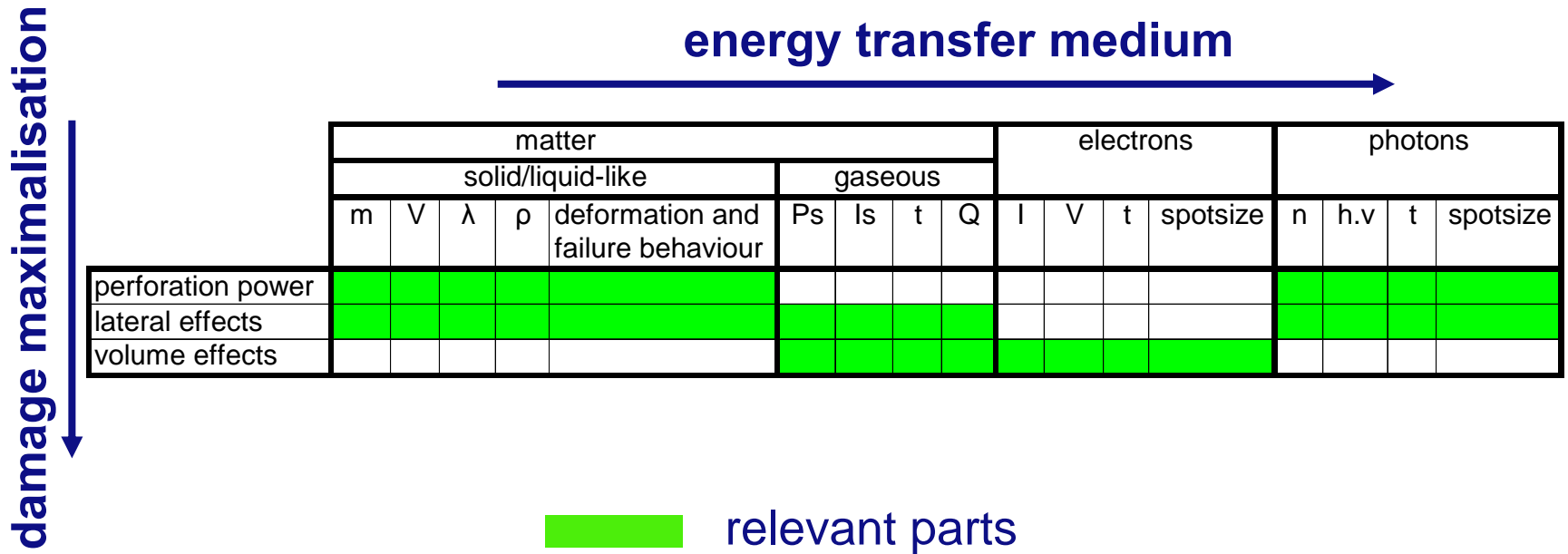
particles of matter: pressure waves and
shock waves could be interpreted as
“waves of excess density”

Atoms, electrons and photons: strength in numbers

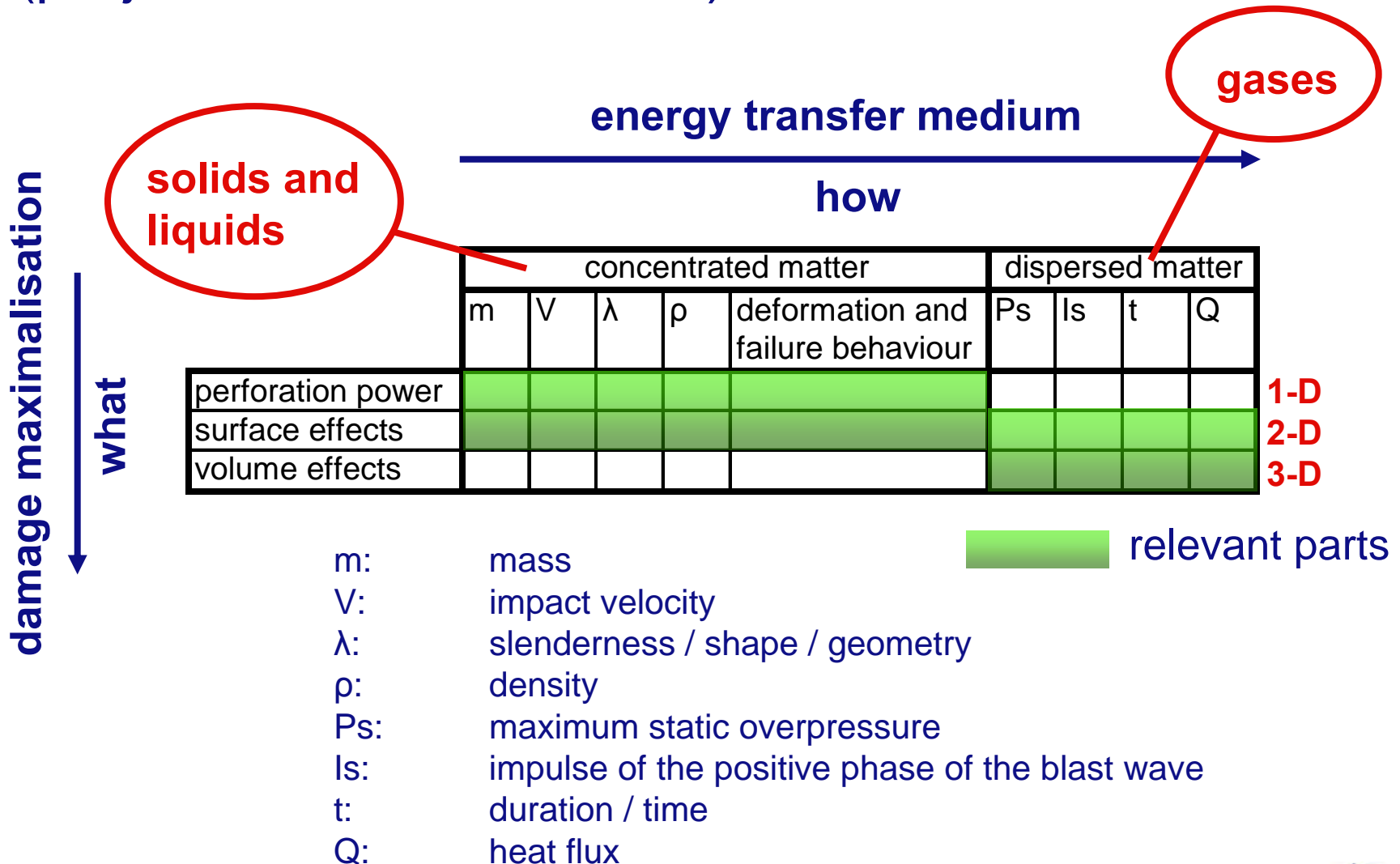
Example: energy transfer of 100 KJ

- Burning a hole in a metal target:
 10^{24} photons (at typical wavelength)
- Shortcutting a shaped charge jet (electric armour):
 10^{19} electrons (at typical high voltage)
- 200 g steel penetrator at 1000 m/s:
 10^{24} atoms

Classification scheme of munitions and weapons effects



Classification scheme: particles of matter (projectiles and warheads)



Desired effects determine parameter choices

Example:
highly lethal versus non-lethal

	concentrated matter					dispersed matter			
	m	V	λ	ρ	deformation and failure behaviour	Ps	Is	t	Q
perforation power									
surface effects									
volume effects									

M1028



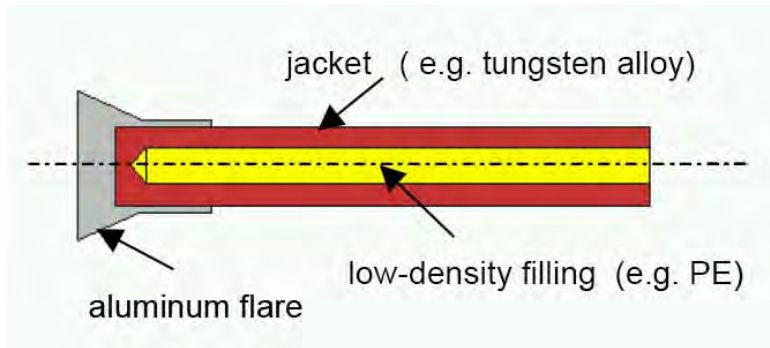
tungsten
spheres

rubber
projectiles



Example: penetrators with enhanced / advanced lateral efficiency (PELE[®], ALP[®])

longitudinal section of a typical PELE projectile:



	concentrated matter					dispersed matter			
	m	V	λ	ρ	deformation and failure behaviour	Ps	Is	t	Q
perforation power									
surface effects									
volume effects									



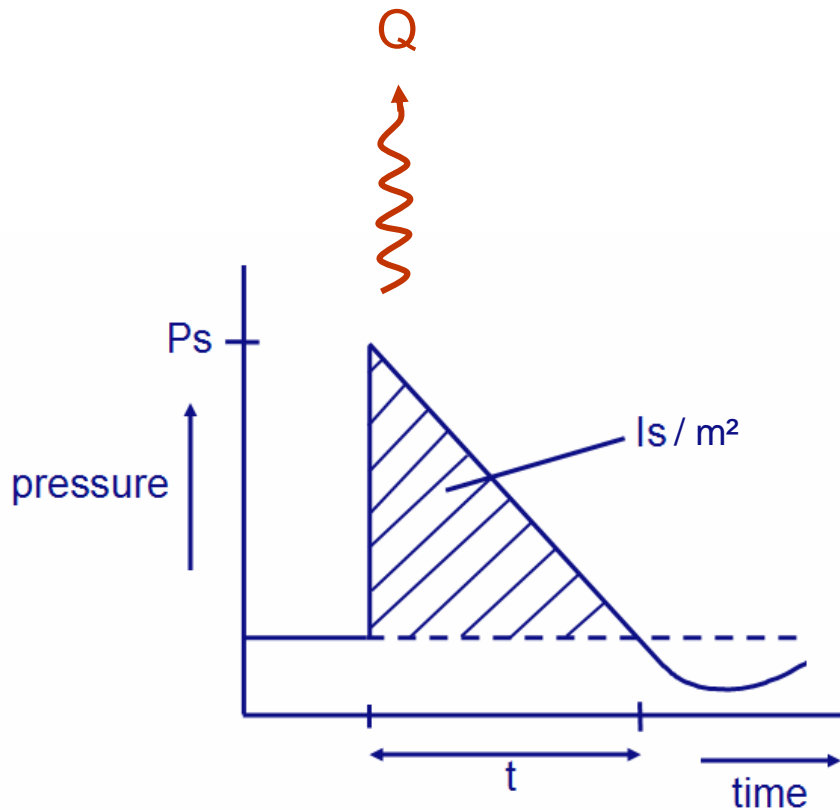
wall breach after 3 hits of large calibre PELE



(source: ISL/ Diehl/ Rheinmetall)

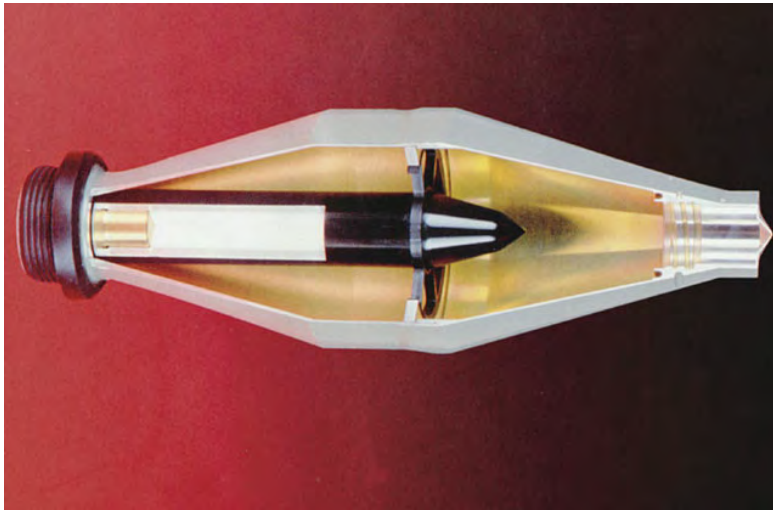
Blast (and heat)

	concentrated matter					dispersed matter			
	m	V	λ	ρ	deformation and failure behaviour	Ps	Is	t	Q
perforation power									
surface effects									
volume effects									



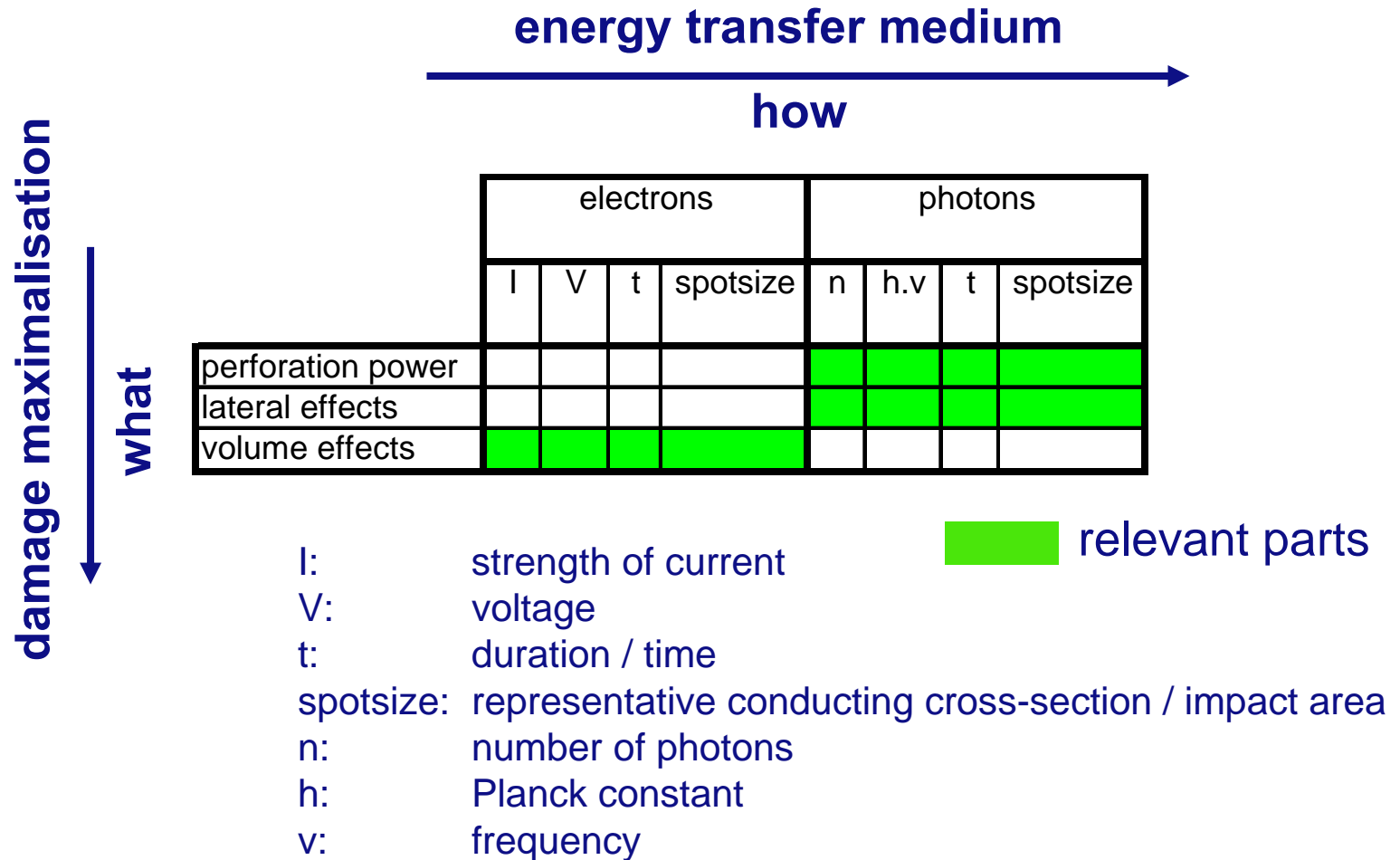
Combination of penetration/ perforation and blast

Example: Modular Explosive Penetrator (RUAG)



	concentrated matter					dispersed matter			
	m	V	λ	ρ	deformation and failure behaviour	Ps	Is	t	Q
perforation power									
surface effects									
volume effects									

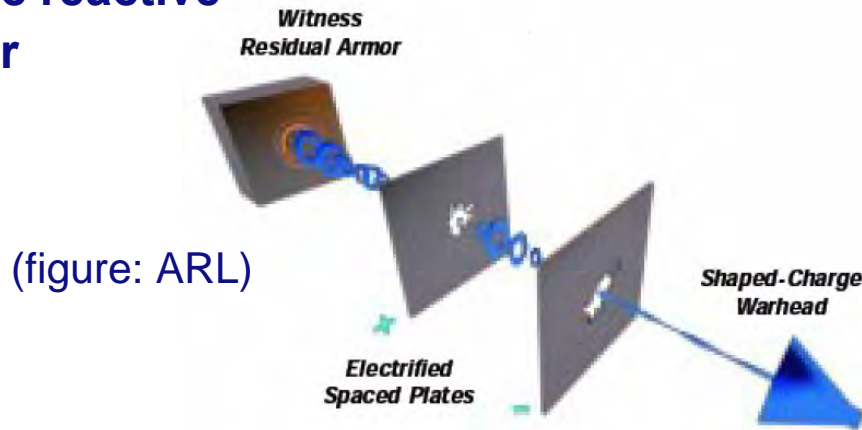
Classification scheme: electrons and photons



Electrons as transfer medium

	electrons				photons			
	I	V	t	spotsizes	n	h.v	t	spotsizes
perforation power								
lateral effects								
volume effects								

- **Electric reactive armour**



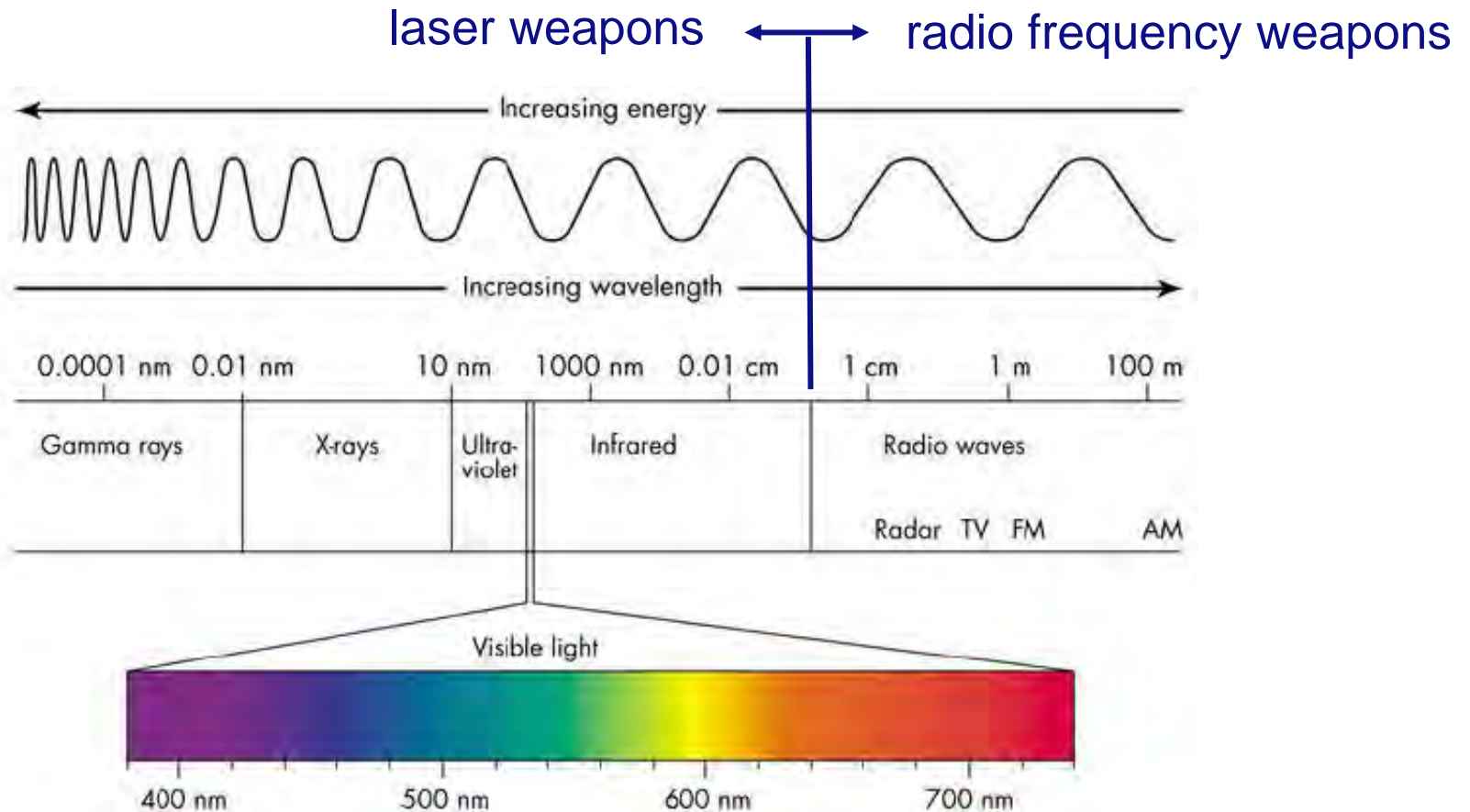
disturbance of the shaped charge jet due to magnetohydrodynamic instabilities

- **Taser**



less lethal:
incapacitation by electric current through body

Photons as energy transfer medium: EM spectrum



Photons as transfer medium

	electrons				photons			
	I	V	t	spotsize	n	h.v	t	spotsize
perforation power								
lateral effects								
volume effects								

- Radio frequency weapons



95 GHz

Effective beam volume:
1m x 1m x 250m

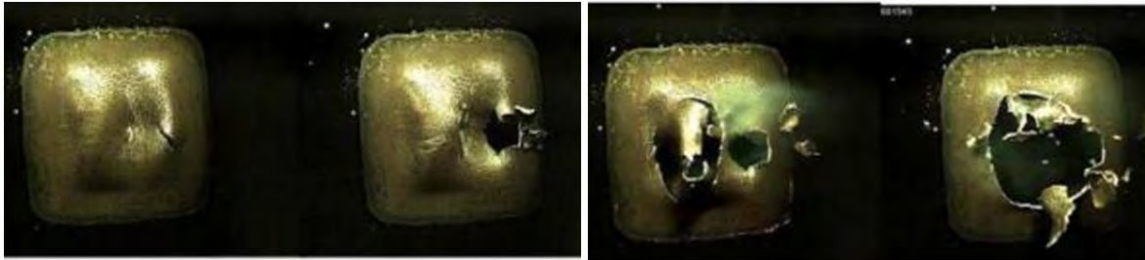
Silent Guardian (30 KW, left),
formerly known as Area Denial System (100 KW, right)

(source: Raytheon)

Photons as transfer medium

	electrons				photons			
	I	V	t	spotsize	n	h.v	t	spotsize
perforation power								
lateral effects								
volume effects								

- **Laser weapons**



(photo: Lawrence Livermore National Laboratory)



melting, 'erosive' heating or
'explosive' heating
of (armour) material

Laser Area Defence System (50 KW),
to be mounted alongside the Phalanx guns
(source: Raytheon/ Air Force Research Lab.)

Combining photons and electrons as transfer medium: “directed lightning”

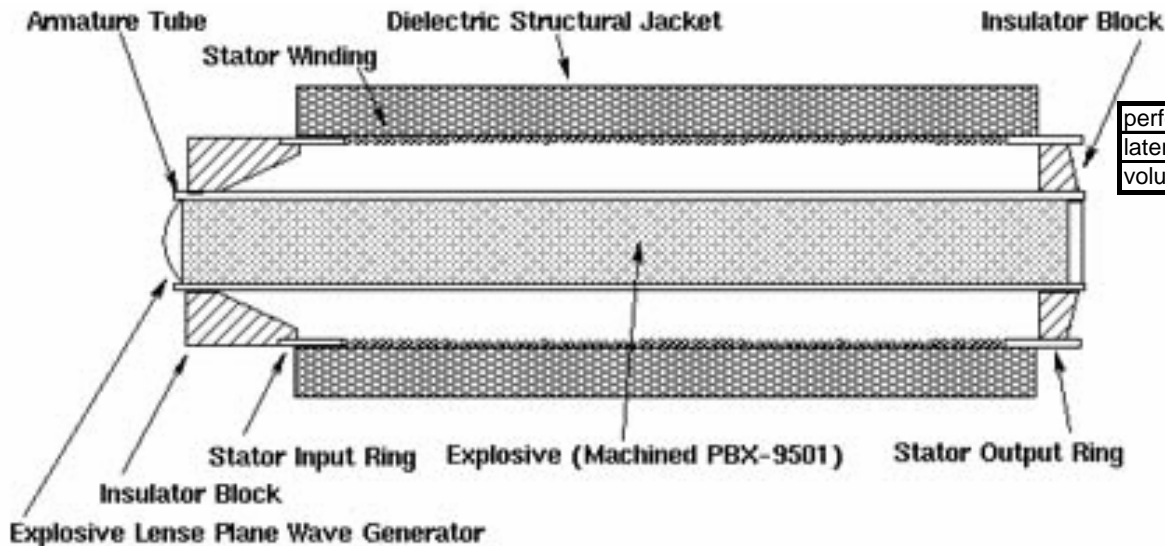


	electrons				photons			
	I	V	t	spotsize	n	h.v	t	spotsize
perforation power								
lateral effects								
volume effects								

 facilitating

use lasers (or other EM radiation) to ionize the air in the path of the subsequent electric current

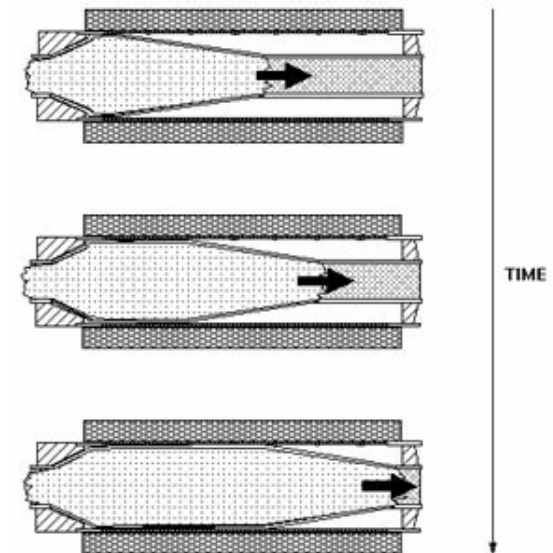
Using the high energy density of energetic materials: “E-bomb”, electromagnetic pulse



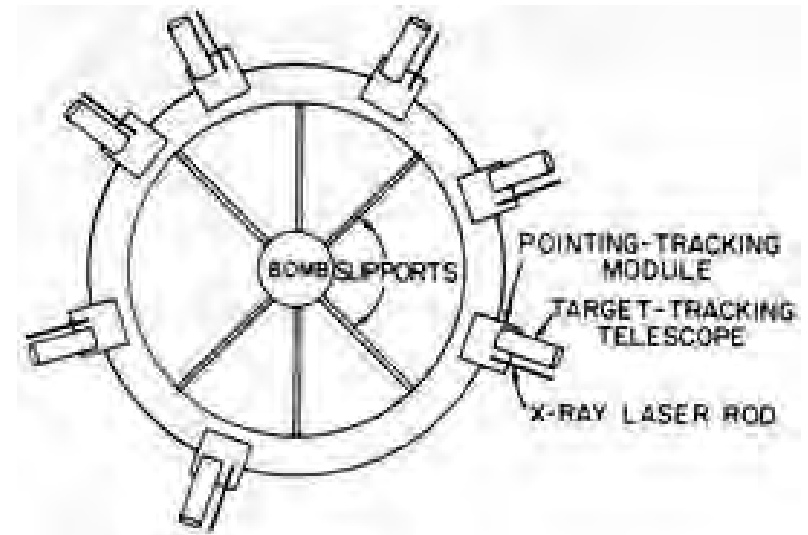
electrons				photons			
I	V	t	spotsizes	n	h.v	t	spotsizes
perforation power							
lateral effects							
volume effects							

 future

explosively pumped coaxial flux
compression generator



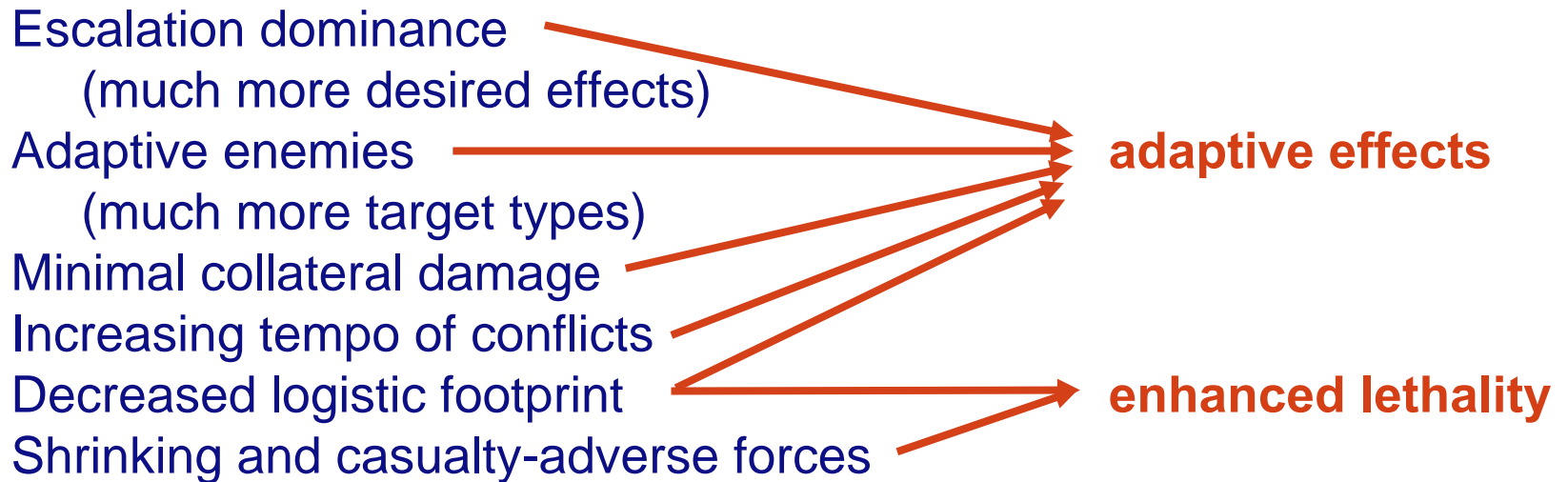
Using the high energy density of energetic materials: detonation-pumped laser?



SDI: nuclear explosion pumped X-ray laser (5MJ per laser)

Current and future munitions drivers

Starting conditions: pinpoint accuracy, insensitive energetic materials



Adaptive and enhanced lethal effects: enhanced blast

Chemical energy released by detonation



Kinetic energy of
reaction products, surrounding air and liner or casing material

(near field) blast, heat

(mid/far field) blast

SCJ, FCJ, EFP, (preformed) fragments



**can be enhanced
by reactions with
metals**

Deformation energy
in the target

anaerobic

aerobic



HE

enhanced blast

thermobaric

FAE

Examples of enhancement by reactions with metals



	concentrated matter					dispersed matter			
	m	V	λ	ρ	deformation and failure behaviour	Ps	Is	t	Q
perforation power									
surface effects									
volume effects									

(Source: US Air Force Research Laboratory)



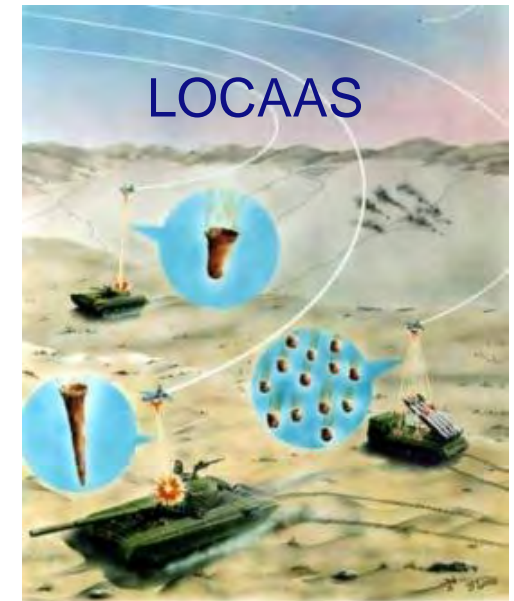
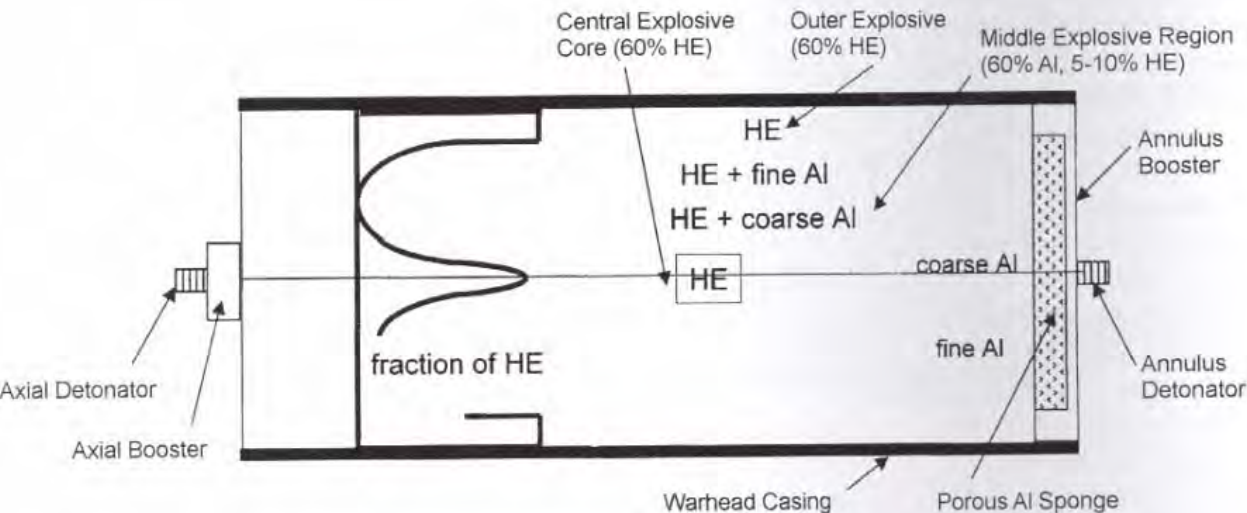
	concentrated matter					dispersed matter			
	m	V	λ	ρ	deformation and failure behaviour	Ps	Is	t	Q
perforation power									
surface effects									
volume effects									

(Source: US Office of Naval Research)

Multimode or adaptive effects

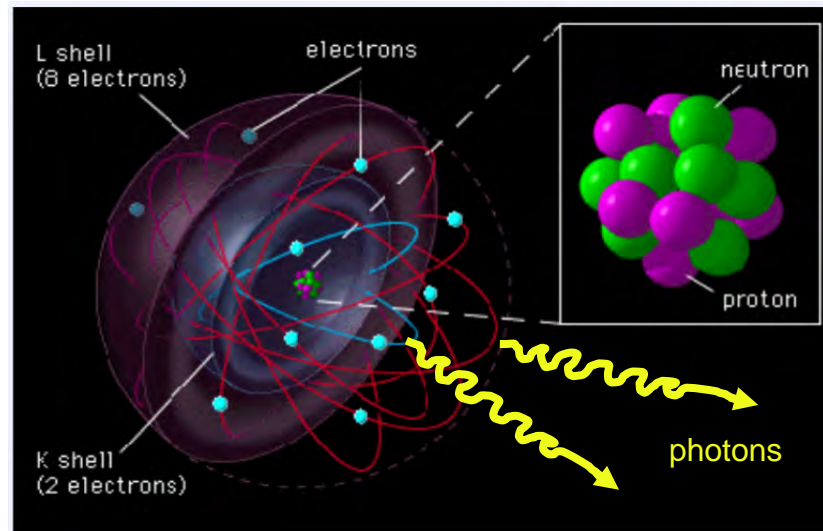
	concentrated matter					dispersed matter			
	m	V	λ	ρ	deformation and failure behaviour	Ps	Is	t	Q
perforation power									
surface effects									
volume effects									

graded explosives (US Navy)



Ultimate multimode or adaptive effects

	matter										electrons				photons			
	solid/liquid-like					gaseous												
	m	V	λ	ρ	deformation and failure behaviour	Ps	Is	t	Q		I	V	t	spotsizes	n	h.v	t	spotsizes
perforation power																		
lateral effects																		
volume effects																		



Questions?

**“If everyone thinks the same,
someone isn’t thinking”**

Contact information

Dr. A.M. Diederer

andre.diederer@tno.nl

TNO Defence, Security and Safety
Business Unit Protection, Munitions and Weapons
Research Group Explosions, Ballistics and Protection
PO Box 45, 2280 AA Rijswijk, The Netherlands

Phone +31 15 284 3509

Mobile +31 6 5184 5221

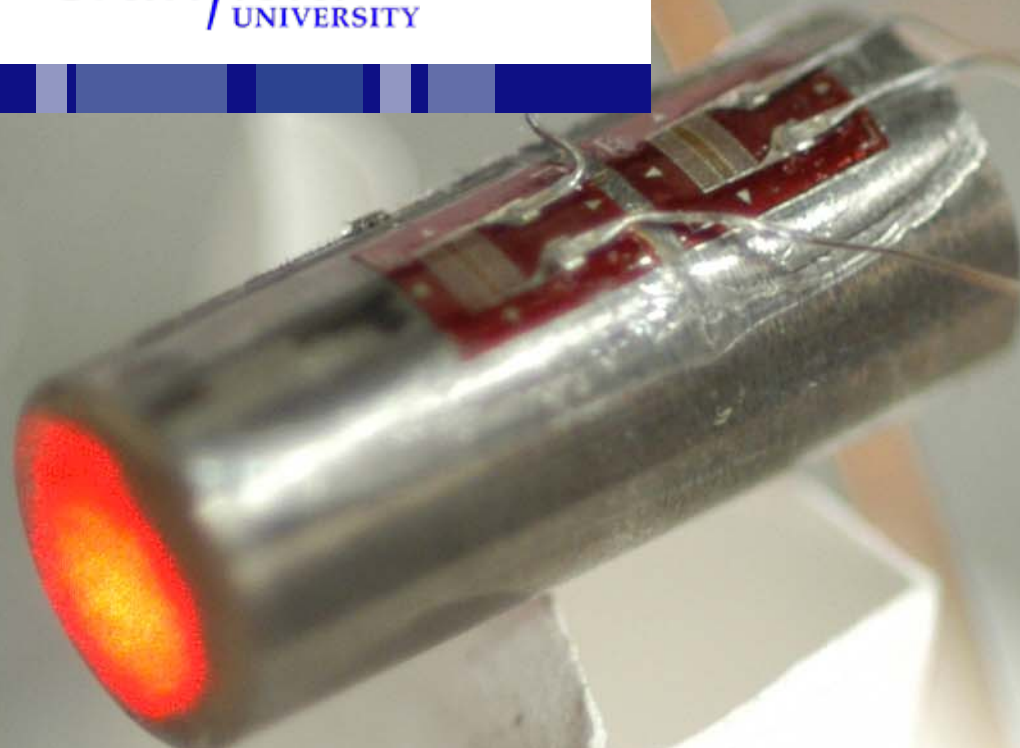
Fax: +31 15 284 3939

Tungsten carbide projectiles impacting tungsten carbide targets

Dynamic characterisation of materials



Cranfield
UNIVERSITY



Acknowledgements



- Co-author:
 - Dr. André Diederén
- Laboratory for Ballistic Research (Ypenburg, NL)

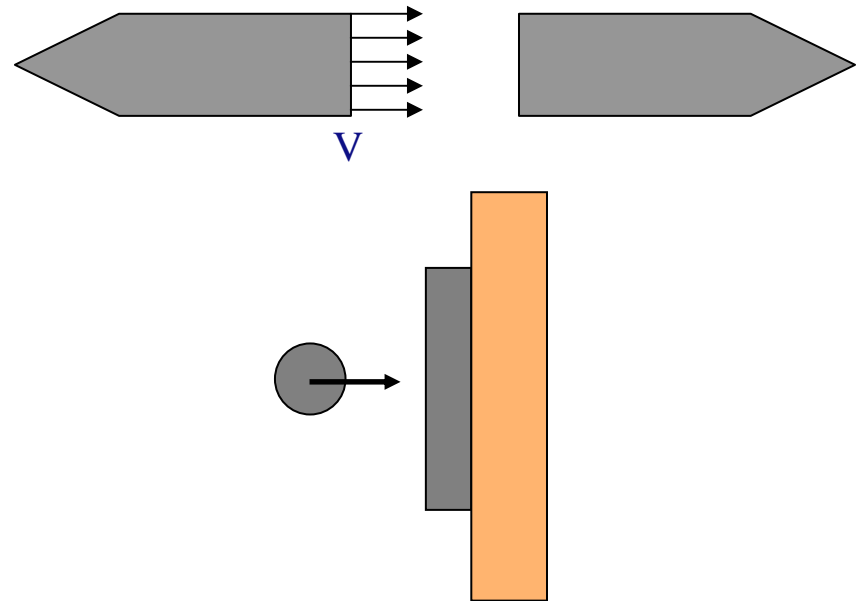


- Co-author:
 - Dr. Paul Hazell
 - Mr. Gareth Appleby-Thomas
- Material Characterisation Lab (Shrivenham, UK)

- Funded by the Dutch Ministry of Defense, partly through the research program “Munition and weapons effects”

Contents

- Introduction:
 - Overview of total research project
- Two specialized experiments:
 - Core to Core impact
 - Sphere to Disc impact
- Core to Core impact
 - Set-up
 - Results
- Summarizing
- Further research



Introduction

- In ballistic impacts events → strong interaction between dynamic behaviour of projectile and armour
- Lots of work is done in characterising and modelling armour materials
- However, characterising the dynamic behaviour of Armour Piercing (AP) projectiles is equally important
- Problems:
 - **dynamic** material testing is difficult
 - only small samples of material are available (projectile cores)
 - validation experiments for FE modelling with AP projectiles often involve 'complex' armour systems (incl. ceramics)

Overview of total research program

EOS,
hardening

- Analysing the composition of AP core material (SEM)
- ‘Standard’ dynamic material tests with material, closely resembling real AP core material: Flyer plate impact testing (*poster TB058*)

1

Failure
behaviour

- Special designed dynamic experiments with real AP cores
- Special designed dynamic experiments with simulant material
- Goal: well defined, ‘simple’, experiments (*this presentation*)

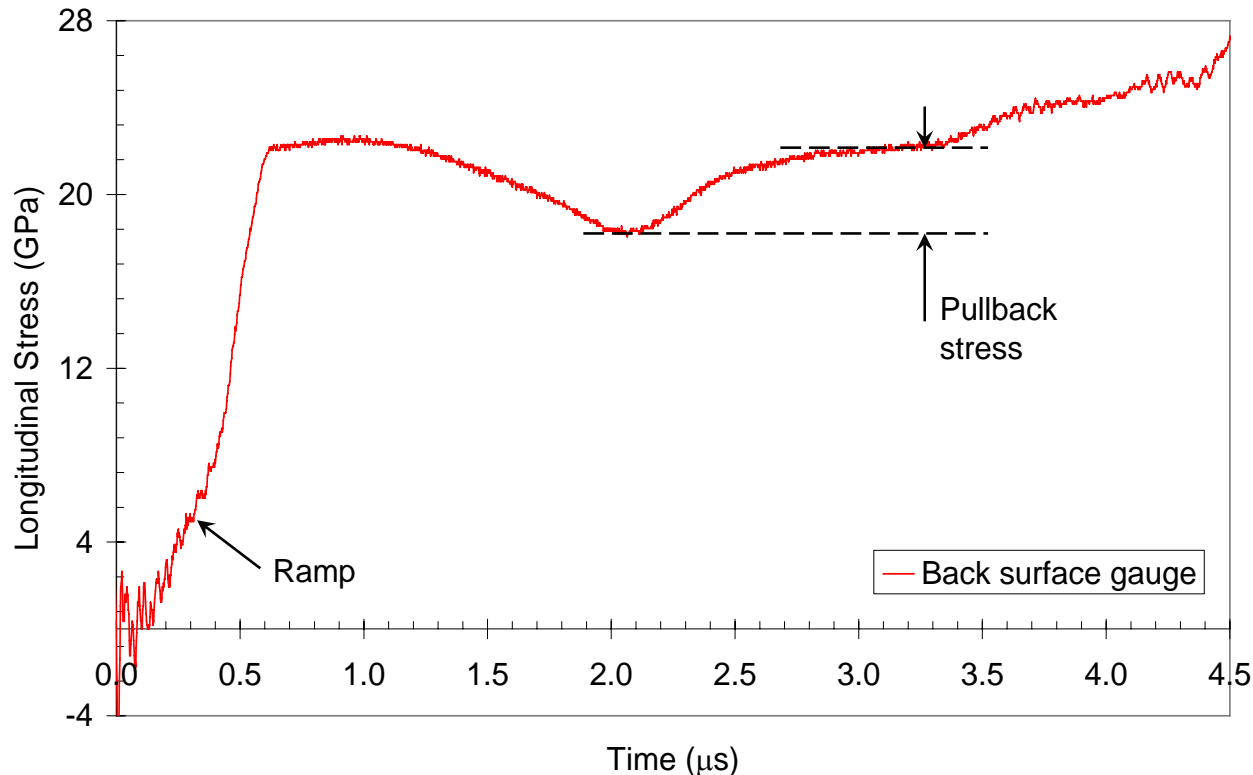
2

Total material
model

- Use the results of step 1 (direct engineering) together with the results of step 2 in order to reverse engineer the dynamic material model for the AP core material (*ongoing research*)

3

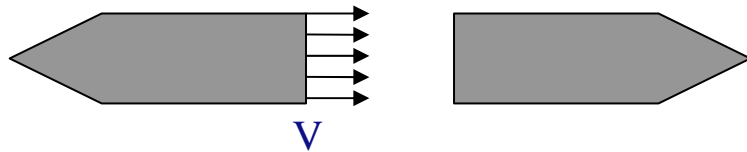
Step 1: flyer plate testing



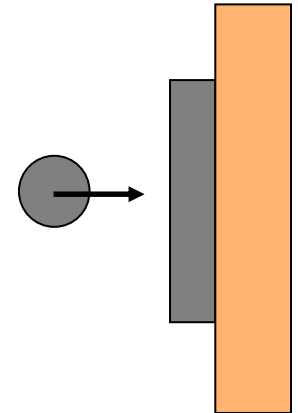
- “Shock response of a cemented Tungsten Carbide” (poster TB058)
- Measured: EOS (shock), Hugoniot Elastic Limit, Dynamic Spall Strength

Step 2: Specialized experiments

- Core to core experiments
- Acceleration of a AP core (in reverse orientation) onto an identical stationary core



- Sphere to disc experiments
- Sphere of 'simulant' AP core (WC) material impacting 'simulant' (WC) target
- Target: 6 mm WC with 12 mm polycarbonate backing

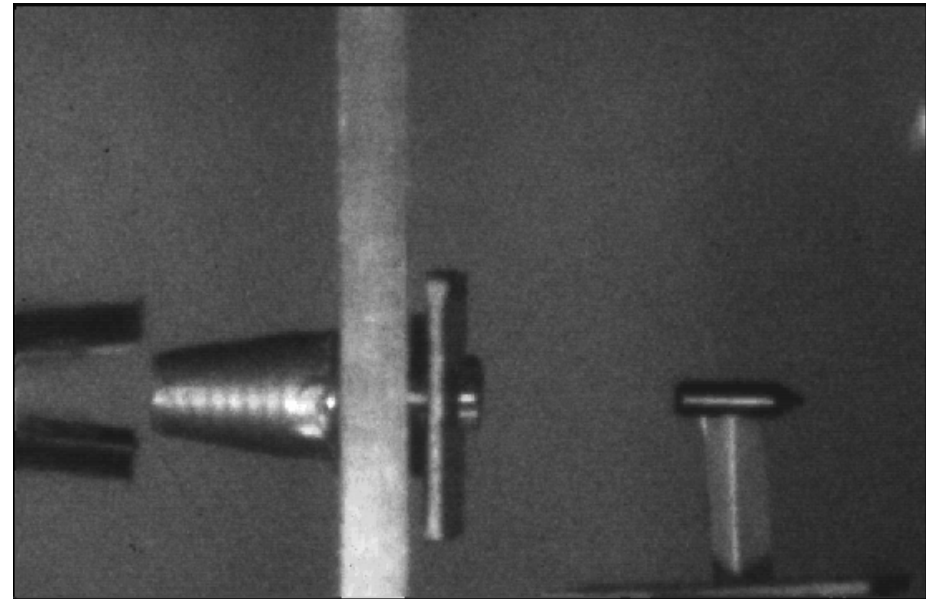
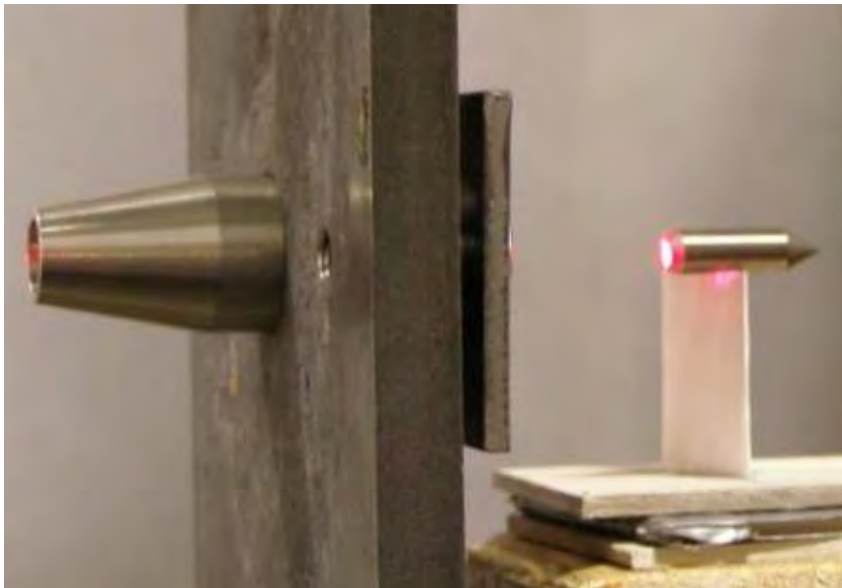


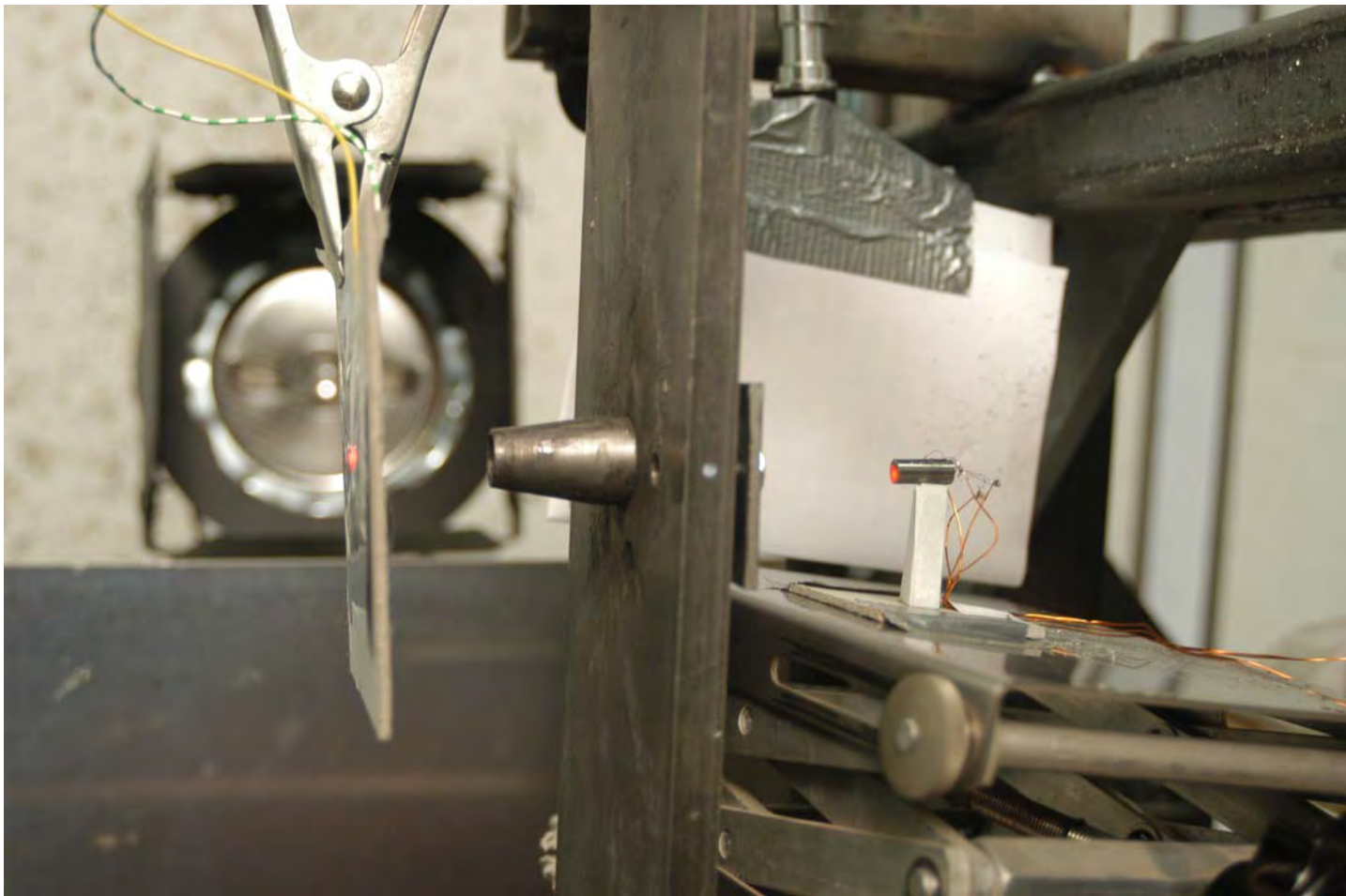
Goal: break-up of WC material with a 'simple' experimental set-up

Use the results of the experiments to reverse engineer the failure model

Step 2: Specialized experiments: Core to Core

- Acceleration of a AP core (in reverse orientation) onto an identical stationary core
- Acceleration in a sabot
- Velocity regime: 250 - 500 m/s
- Fragments are captured and collected afterwards for SEM analysis
- Occasionally strain measurements are performed on the stationary core



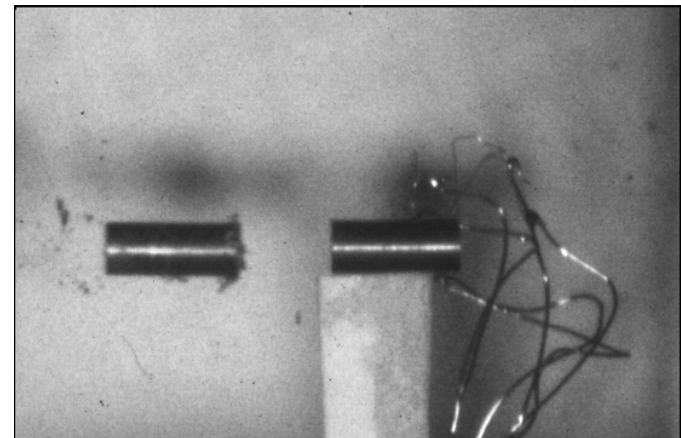
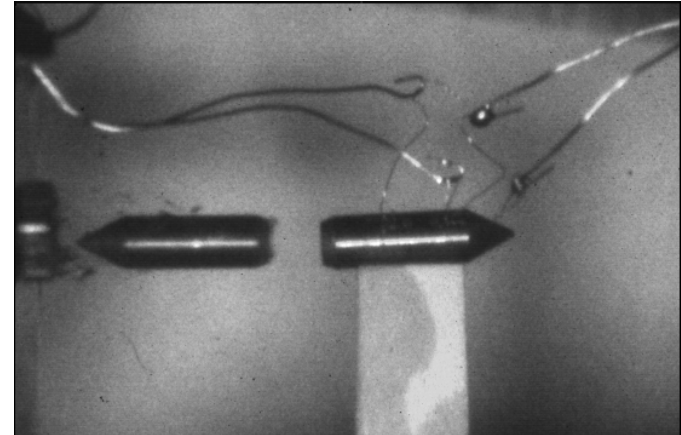


11-09-2007 -000010 0.000 94500 fps

Specialized experiments: Core to Core

- Benefits:
 - Experiments with real core material
 - Only one material is used → only one material needs to be modelled
 - Highly dynamic event (impact velocity up to 500 m/s)
 - Simple small geometry → FE models small and quick

(straight cylinders from AP cores with the use of spark erosion)



Specialized experiments: Core to Core

- Results:
 - Projectiles rapidly erode at impact surface followed by fragmentation along length



$v = 250 \text{ m/s}$



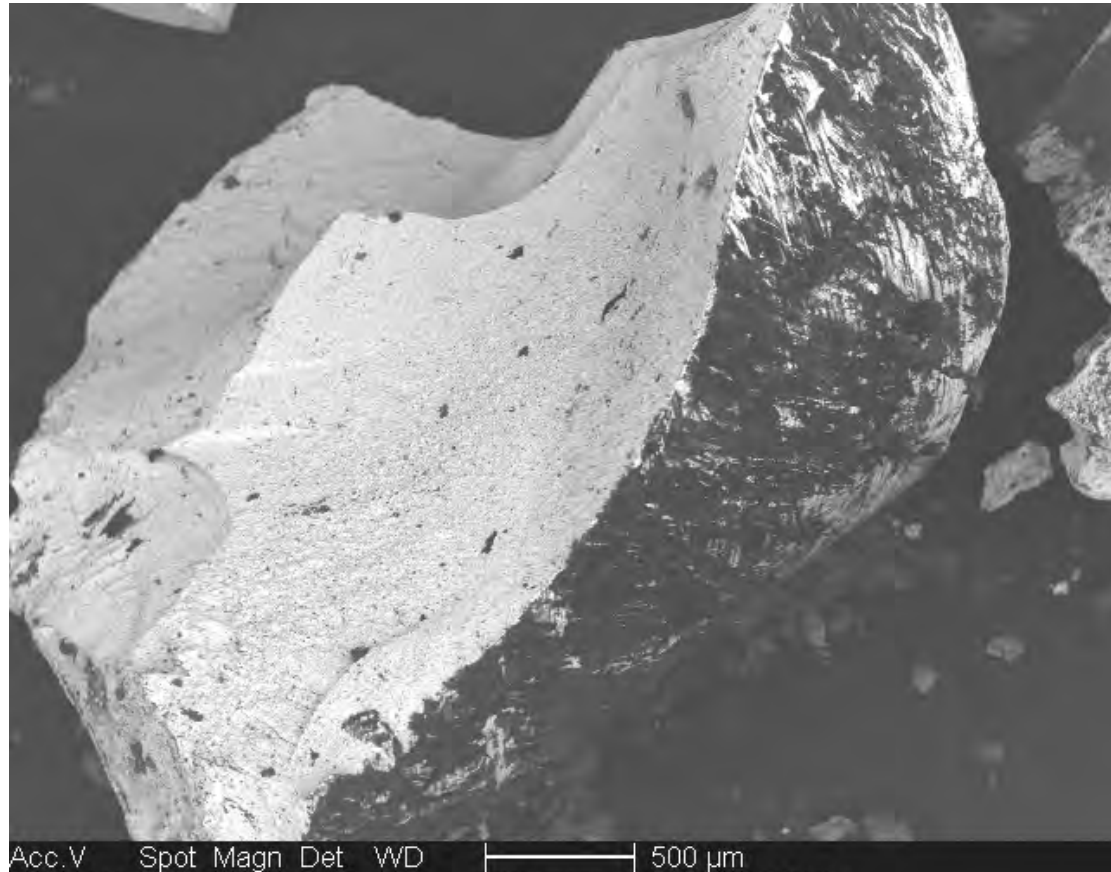
$v = 370 \text{ m/s}$



$v = 500 \text{ m/s}$

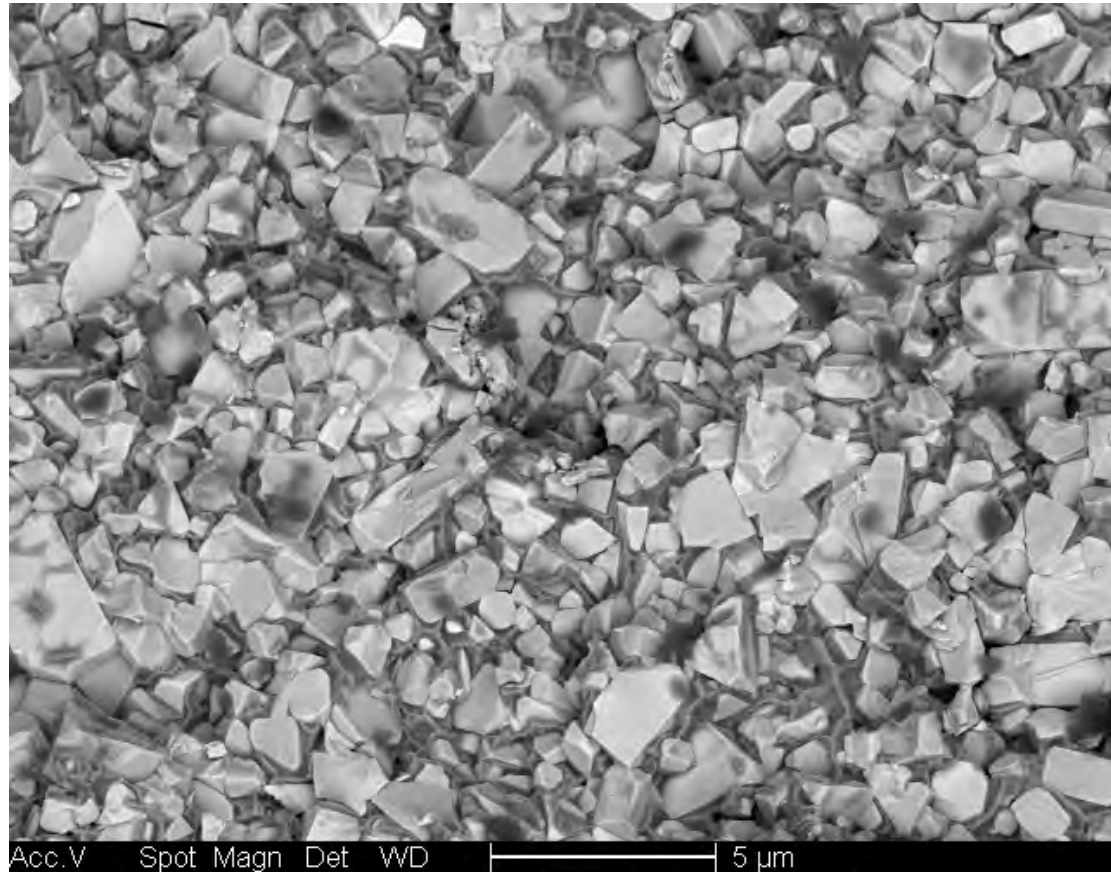
- Comminution of material increases with impact velocity
- Complete fragmentation of cores with $v = 500 \text{ m/s}$

SEM pictures recovered fragments after impact



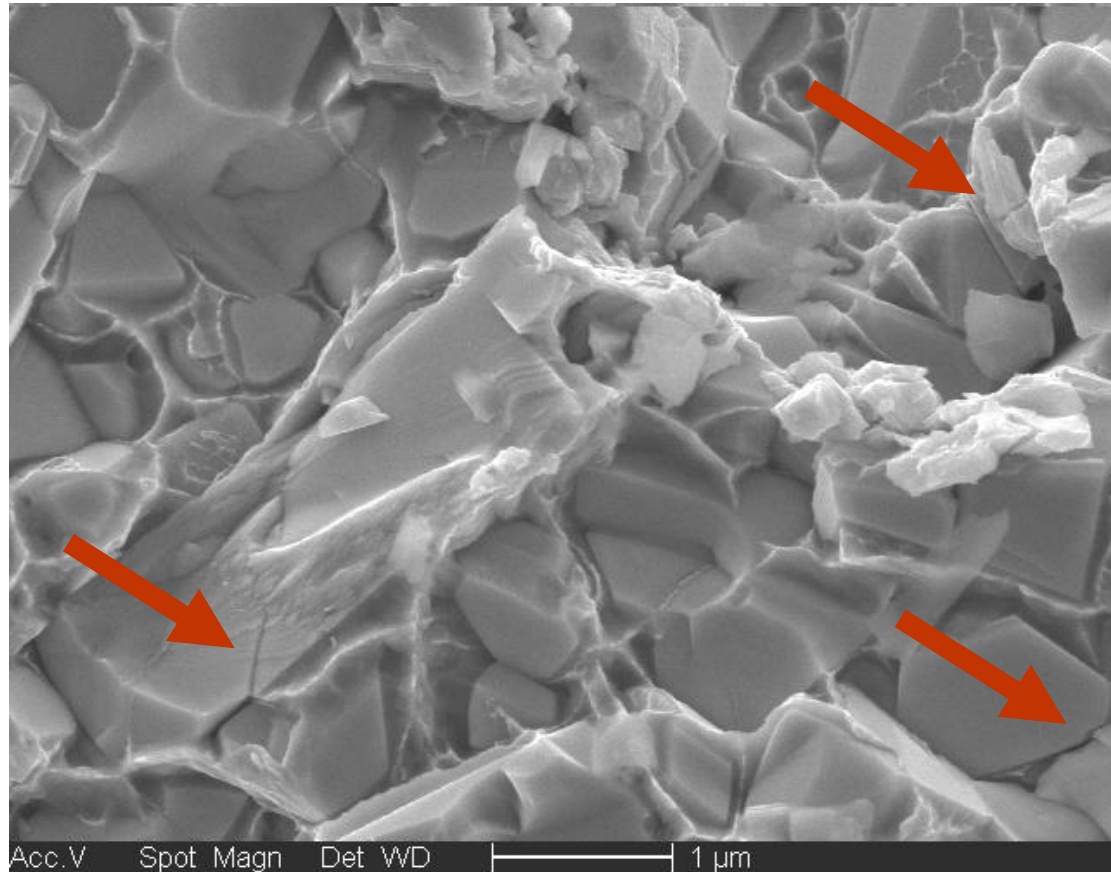
33 x magnification

SEM pictures recovered fragments after impact



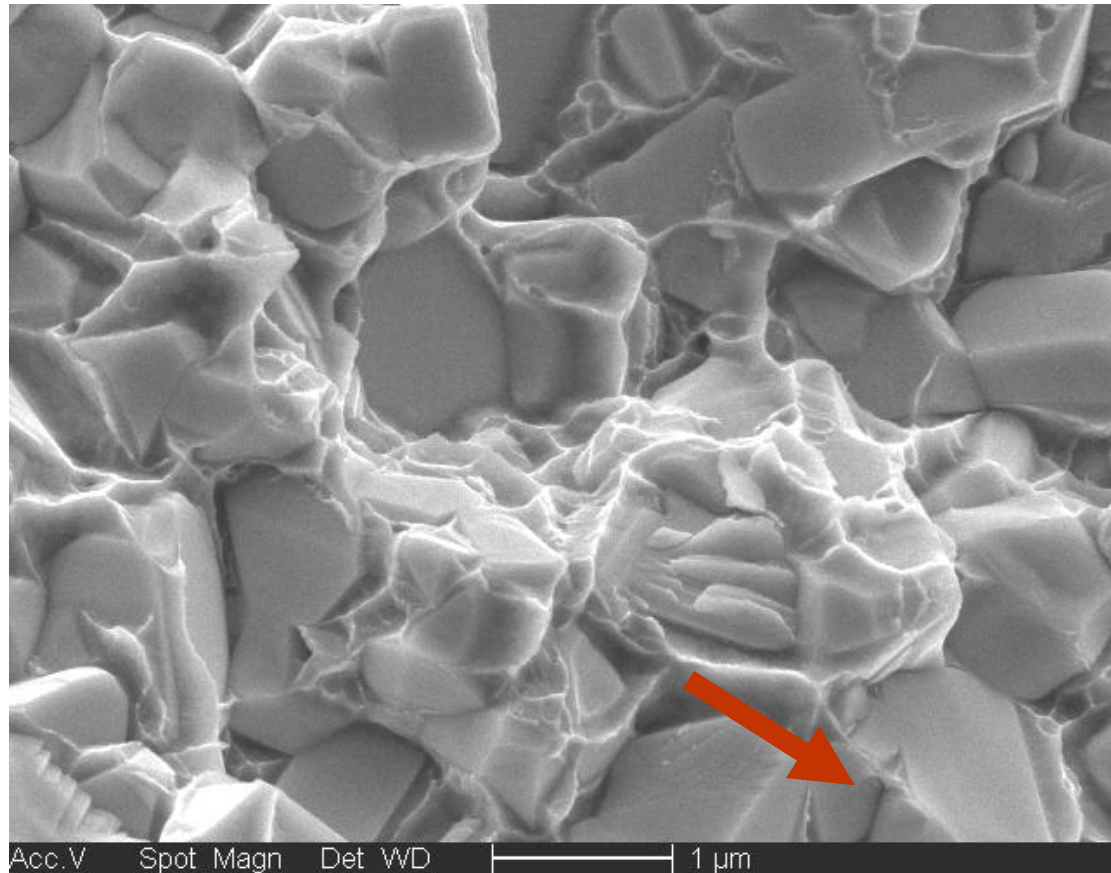
5.000 x magnification

SEM pictures recovered fragments after impact



20.000 x magnification, $v = 500$ m/s

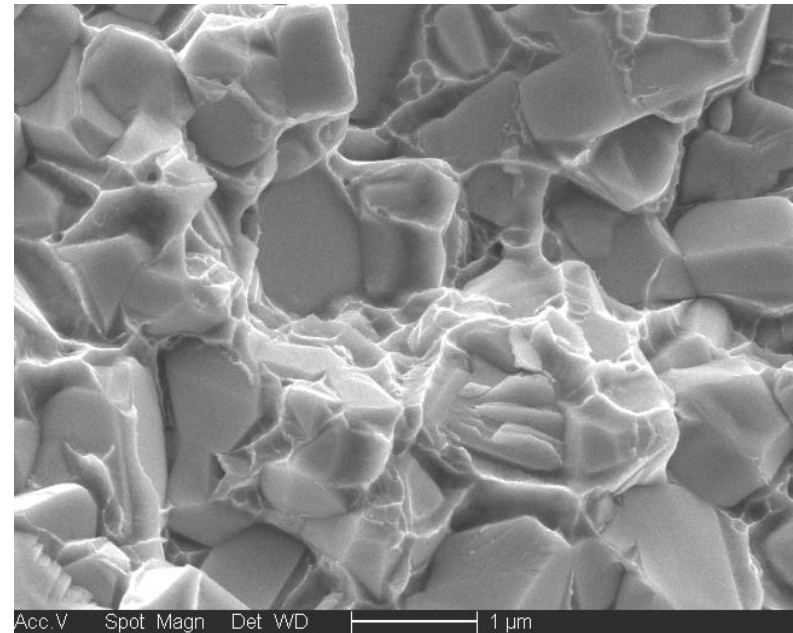
SEM pictures recovered fragments after impact



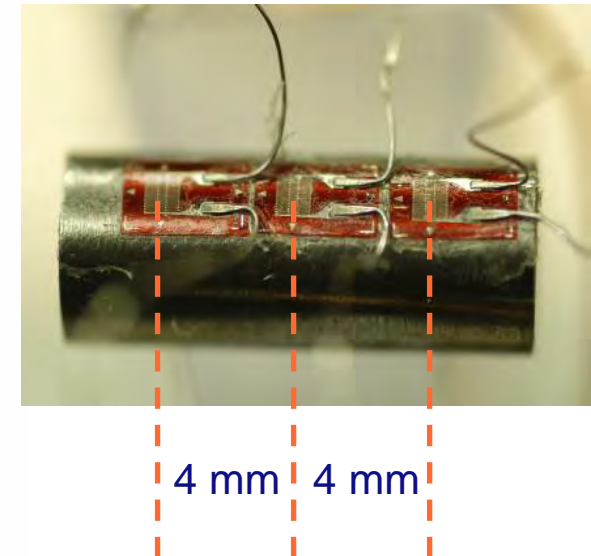
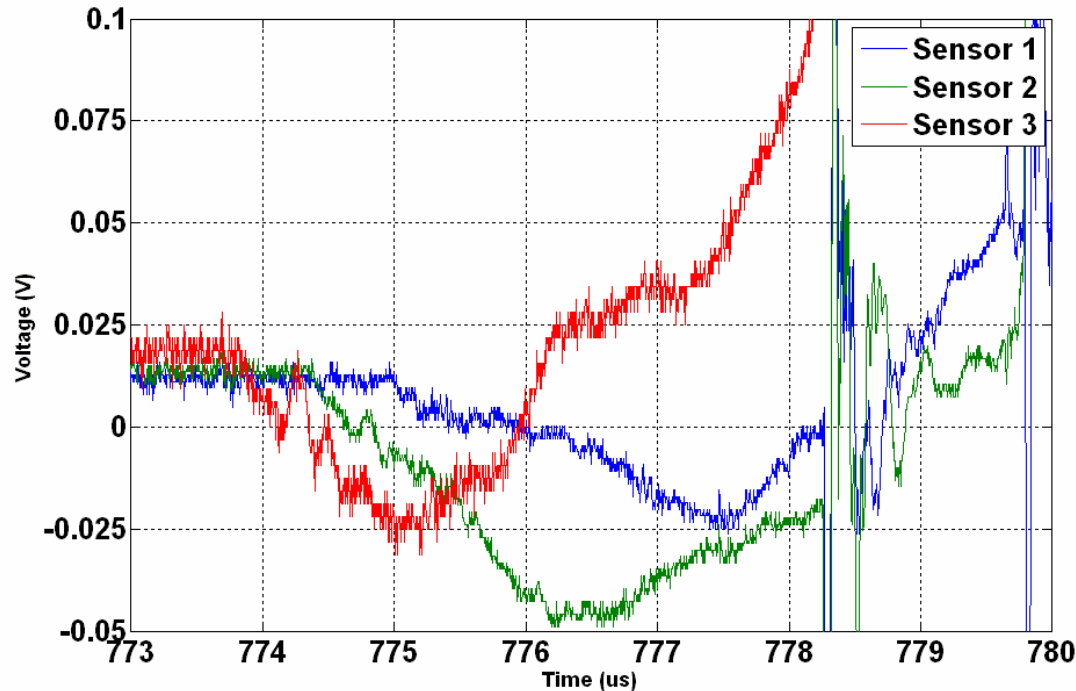
20.000 x magnification, $v = 250$ m/s

SEM pictures recovered fragments after impact

- Failure dominated by trans-granular failure in Co-matrix
- Trans-granular failure seems to be more brittle at higher impact velocities
- Inter-granular failure is rare



Results strain gauges



- Successful measurements of strain for approximately 4 μ s
- Measured wave velocity corresponds well with measured EOS

Summarizing

EOS,
hardening

- Analysing the composition of AP core material (SEM)
- ‘Standard’ dynamic material tests with material, closely resembling real AP core material: Flyer plate impact testing (*poster TB058*)

1

Failure
behaviour

- Special designed dynamic experiments with real AP cores
- Special designed dynamic experiments with simulant material
- Goal: well defined, ‘simple’, experiments (*this presentation*)

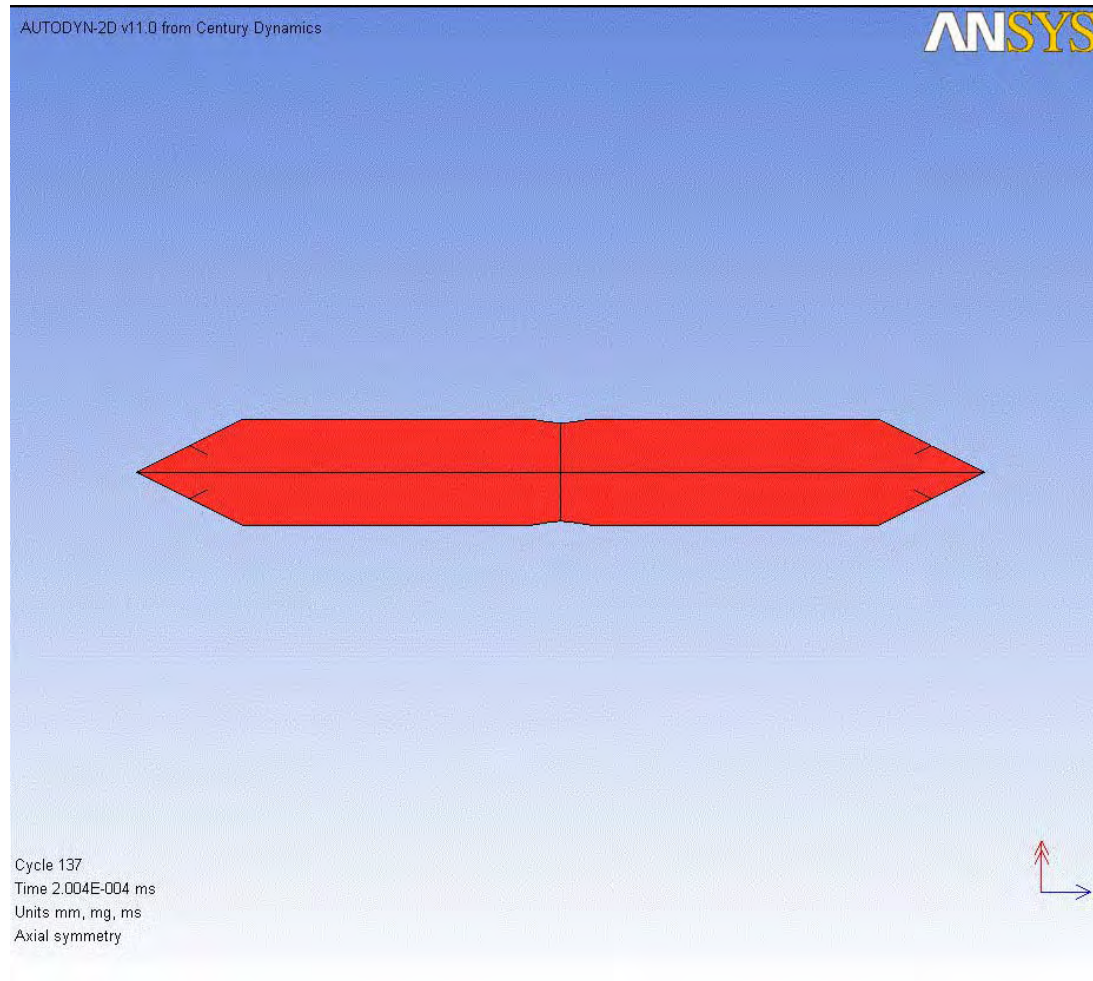
2

Total material
model

- Use the results of step 1 (direct engineering) together with the results of step 2 in order to reverse engineer the dynamic material model for the AP core material (*ongoing research*)

3

Step 3, *in progress*



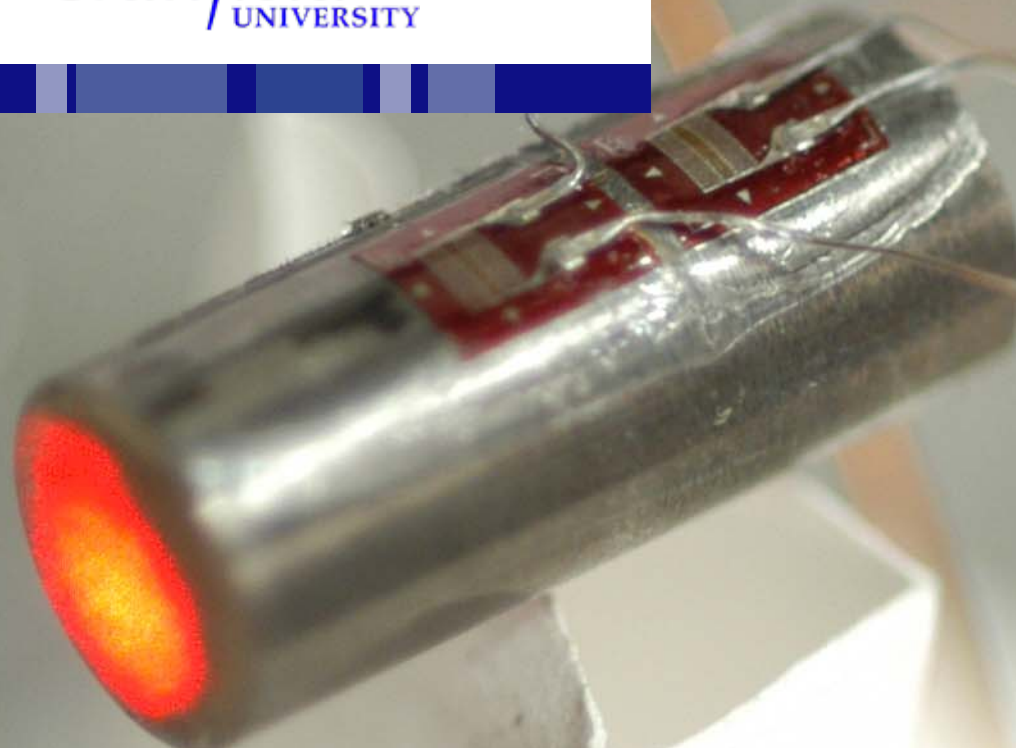
Thank you for your attention

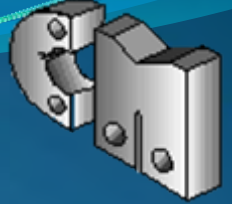
Questions ... ??

Dynamic characterisation of materials



Cranfield
UNIVERSITY

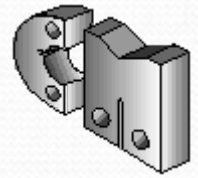




GRC's impact behavior

A. Enfedaque, F. Gálvez, D. Cendón, V. Sánchez Gálvez
Material Science Department
Polytechnic University of Madrid

Contents



1. Introduction

What is GRC?

GRC's mechanical properties

2. GRC production and tests

GRC formulation

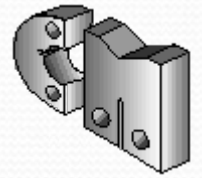
Testing facilities and projectiles

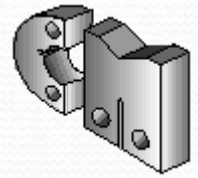
Velocity measuring systems

3. Numerical simulations

4. Conclusions

Introduction

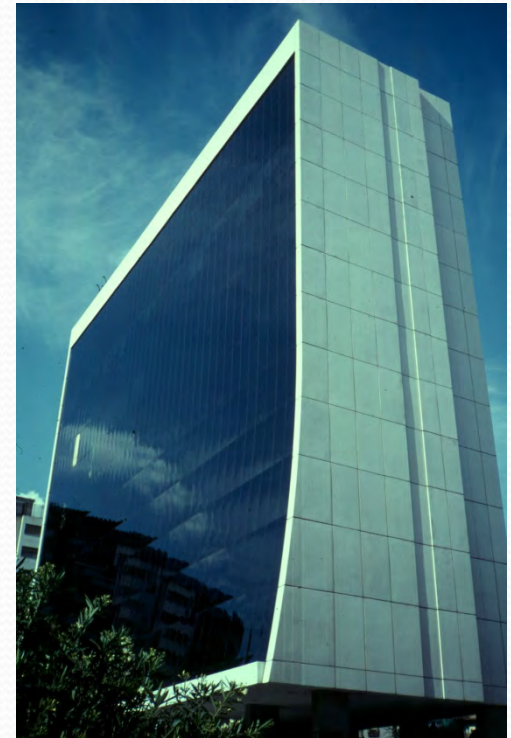


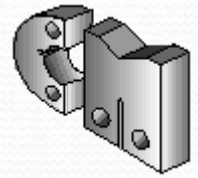


What is GRC?

¿What does GRC stand for?

GRC stands for Glass Fiber Reinforced Cement. This material is produced by spraying chopped glass fibers simultaneously with cement mortar.



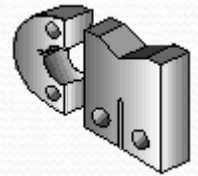


What is GRC?

Why are glass fibers added to cement mortar?

Glass fibers increase cement mortar's ductility and prevent cracking caused by shrinkening.

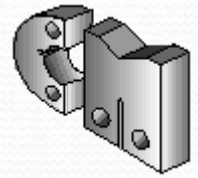




GRC's mechanical properties

GRC static mechanical properties

Density	1.900 – 2.250 Kg/m ³
Compressive strength	48 – 83 MPa.
Young modulus	10 – 20 GPa.
Flexural strength	
-First cracking	6 – 10 MPa.
-Rupture	17 – 25 MPa.
Tensile strength	
-First cracking	4,8 – 7 MPa.
-Rupture	7 – 11 MPa
Failure strain	0,6 – 1,2 %



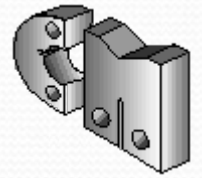
GRC's mechanical properties

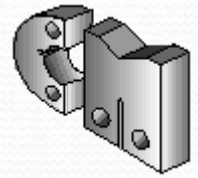
What about GRC's behavior under high strain rates?

Strain rates over 10^1 s^{-1} have not been studied.



GRC production and tests



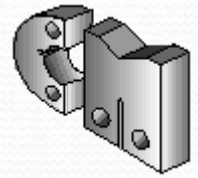


Material production

GRC was produced using a 10% metakolin addition.

Cement	Sand	Water	Plasticizer	Metakaolin
50 Kg.	50 Kg.	22 l.	0.5 liters	5 Kg.

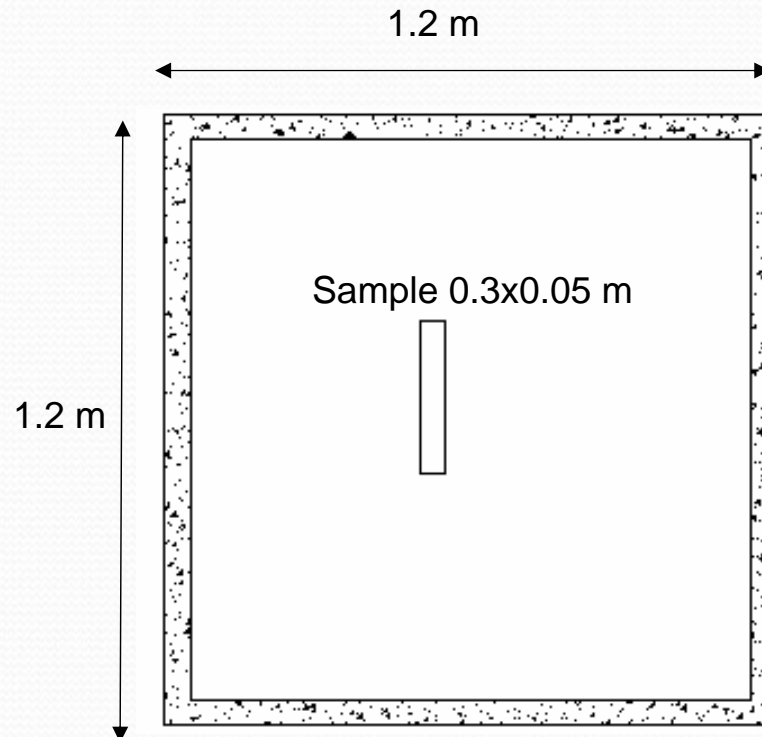




Material production

GRC tensile tested samples were cut from 1.2x1.2m test boards

Samples dimensions were 0.3x0.05 m.

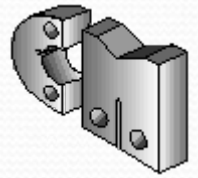


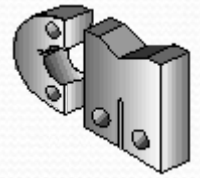
Test set up

Gas gun



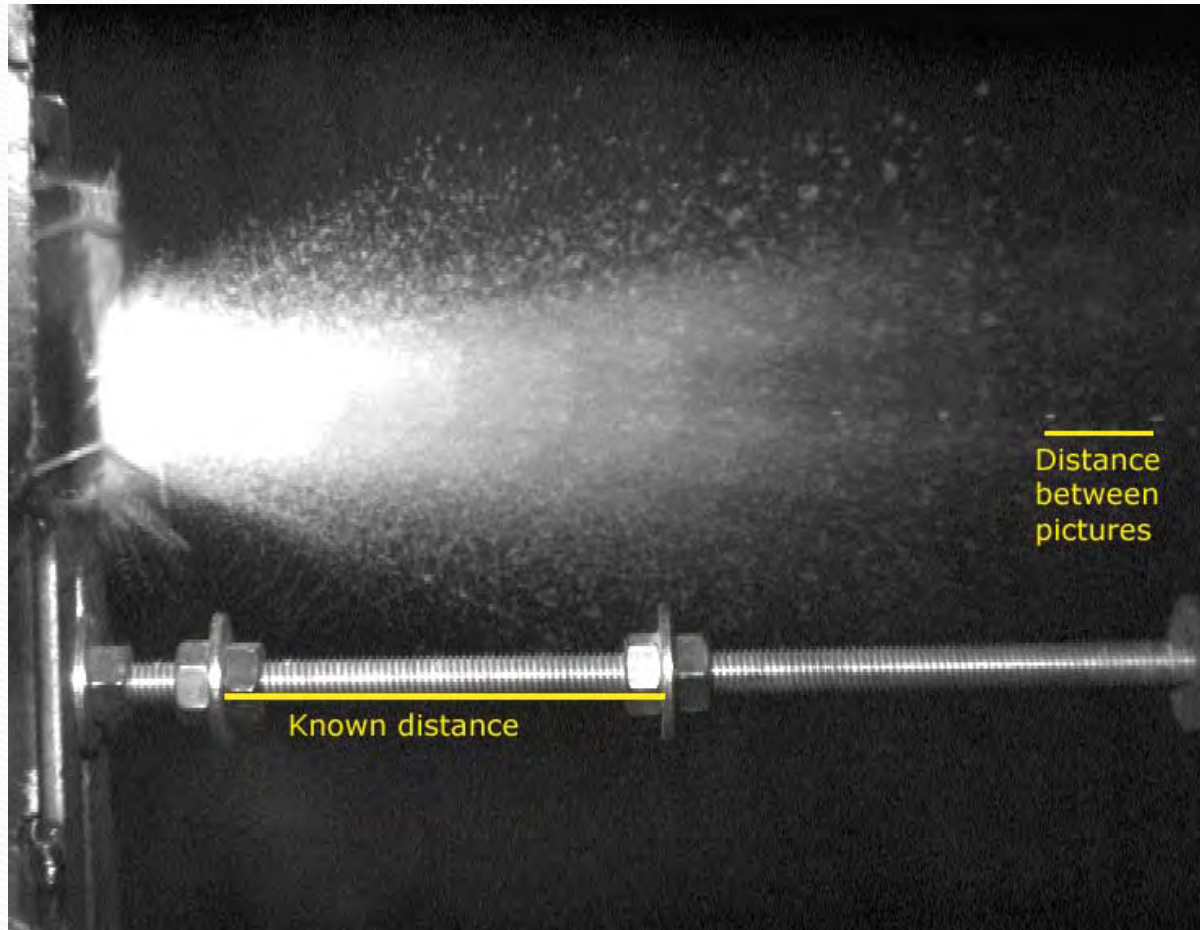
5.5 mm diameter steel spheres and sabot





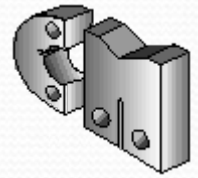
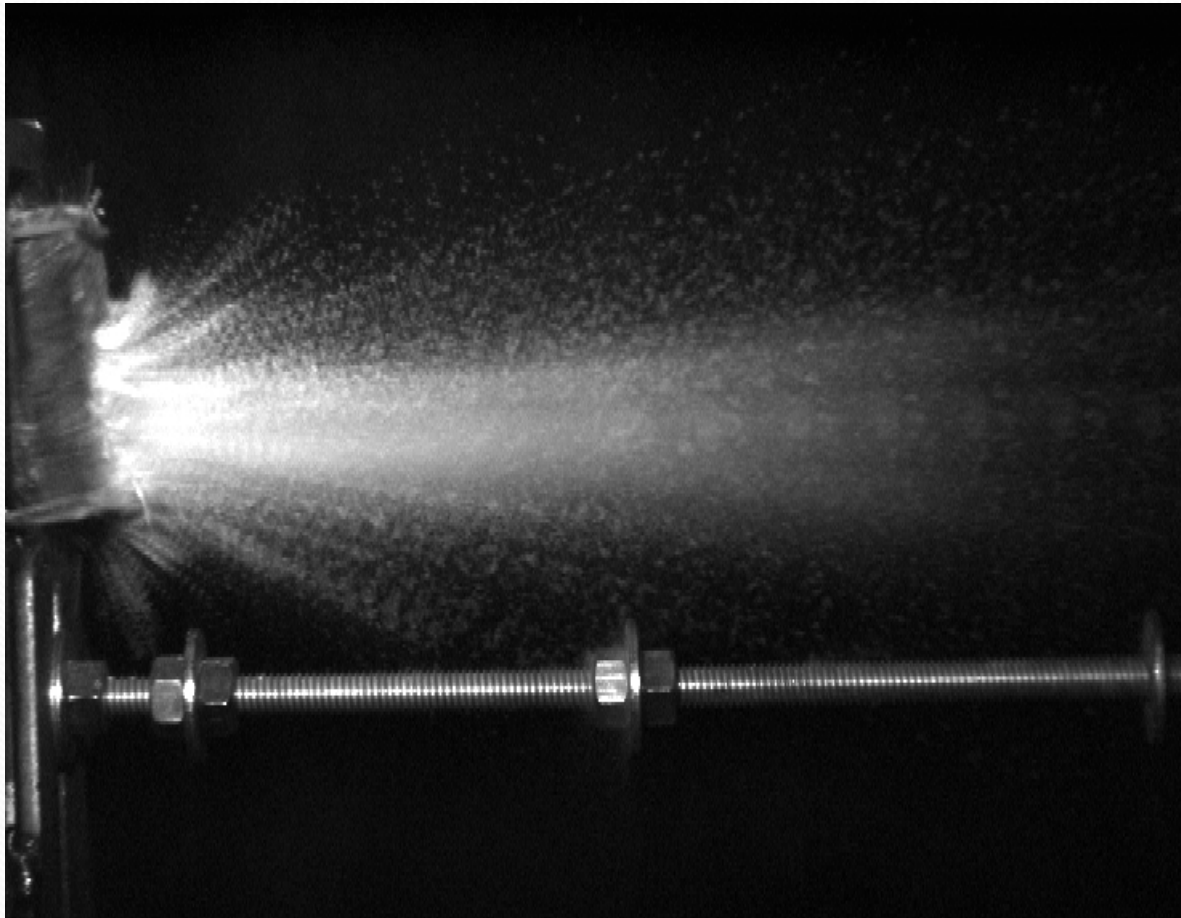
Velocity measuring systems

High speed rate pictures for high speeds (>400 m/s)

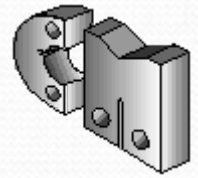


Velocity measuring systems

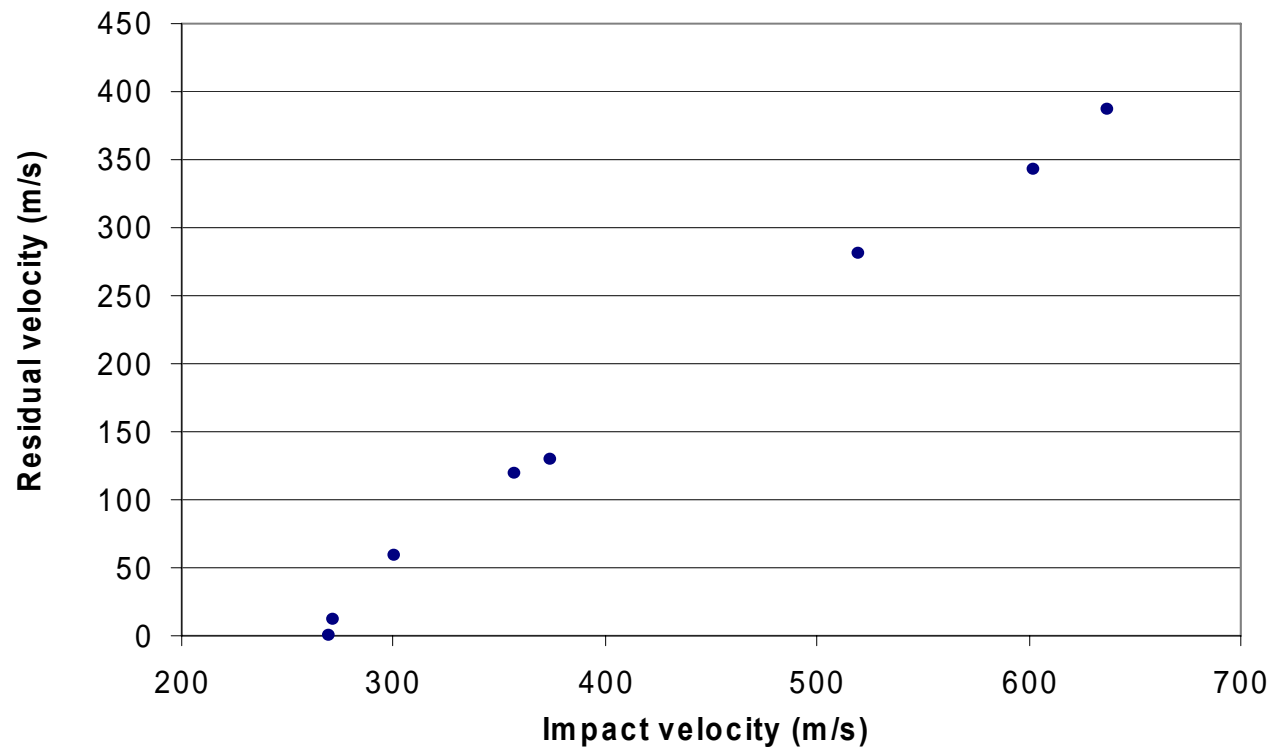
For low speeds a calibrated molding clay was used (< 400 m/s)

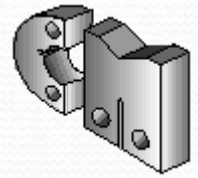


Test results



Ballistic impact tests





Numerical simulations

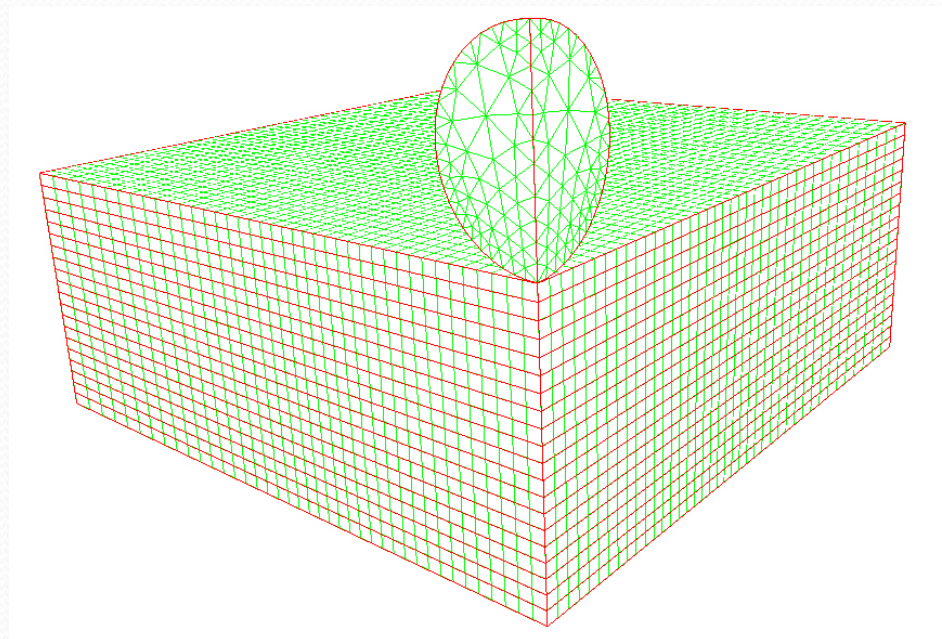
Autodyn v6 was used for calculations

GRC samples idealized as 10 mm thick plates

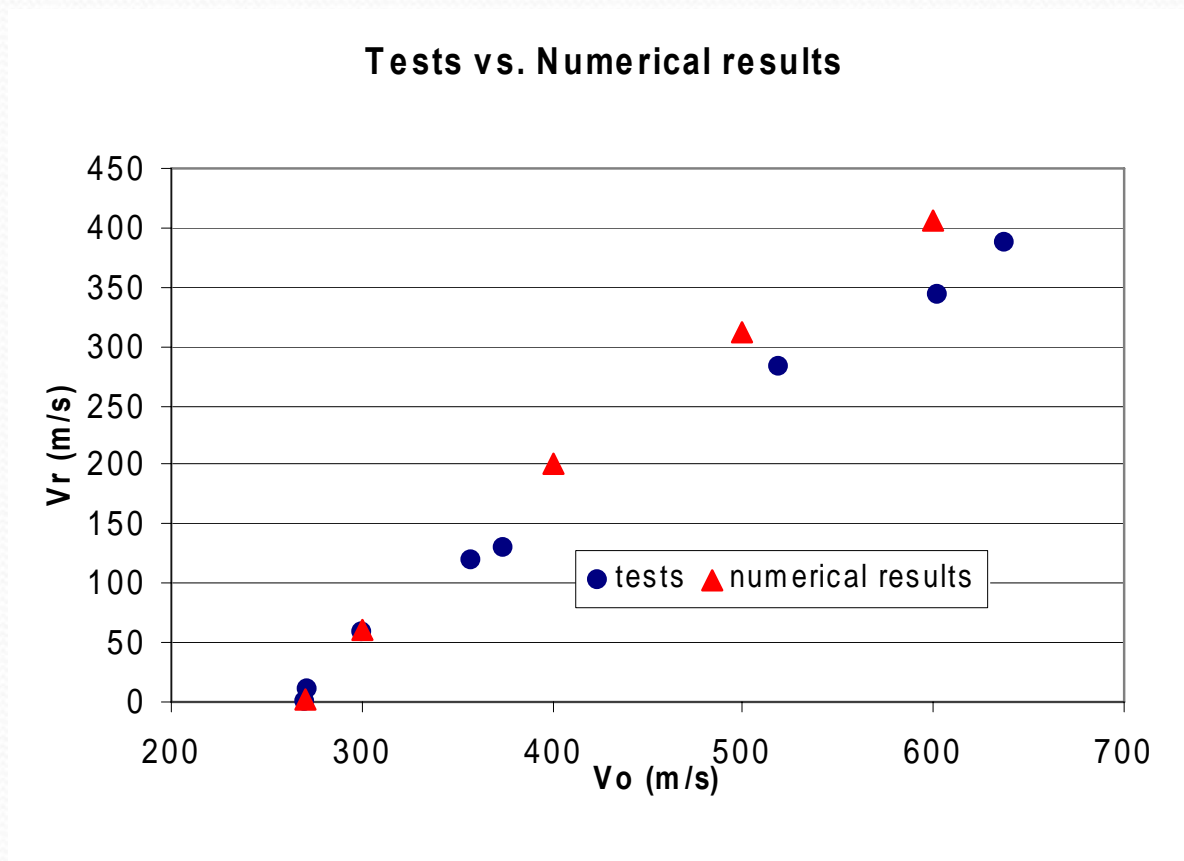
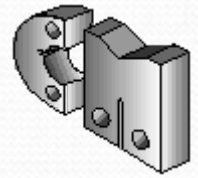
Cement simulated as Concrete-L Autodyn library material

Glass fibers introduced in the model as membrane layers between cement ones

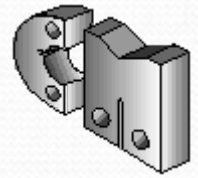
Spheres simulated as a rigid body



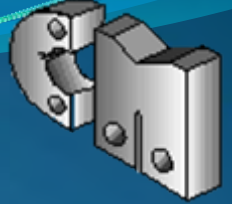
Testing vs. Numerical simulations



Conclusions



1. A complete residual velocity vs. impact velocity curve for GRC panels has been achieved.
2. Velocity measurement through high velocity photographs and indirect measurement using molding clay have been proved to be consistent.
3. Numerical simulations using Autodyn 3-D v6. are able to predict GRC's impact behavior accurately.



GRC's impact behavior

A. Enfedaque, F. Gálvez, D. Cendón, V. Sánchez Gálvez
Material Science Department
Polytechnic University of Madrid

Initiation Controlled Multimode Warheads



Dr. Thomas Falter
DBD E-MK
09/23/2008

Outline

- Introduction & Motivation
 - Multimode warhead
- Theory
 - Computational tool: ANSYS AUTODYN®
 - Underlying physics
- Simulation of an Initiation Controlled Multimode Warhead
 - EFP Mode
 - Jetting Mode
 - Fragmentation Mode
- Summary

Motivation

- Conventional HE warhead types (examples)

Warhead	Penetration performance	Standoff	Focus
SC	High (≥ 10 CD)	Low (~ 6 CD)	Directed
EFP	Medium (≥ 1 CD)	High (≥ 150 m)	Directed
Fragmentation	Low	Medium	Omnidirectional

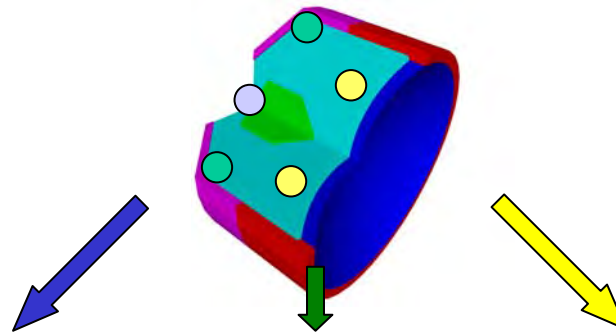
Objective

1 single multimode warhead that can switch between the three different modes

Motivation

single charge
(e.g. EFP)

multiple points of
initiation



EFP Mode



hard targets
large standoff



e.g. (main battle) tank

Jetting (SC) Mode

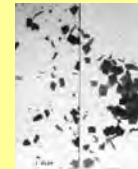


hard targets
small standoff



e.g. main battle tank

Fragmentation Mode



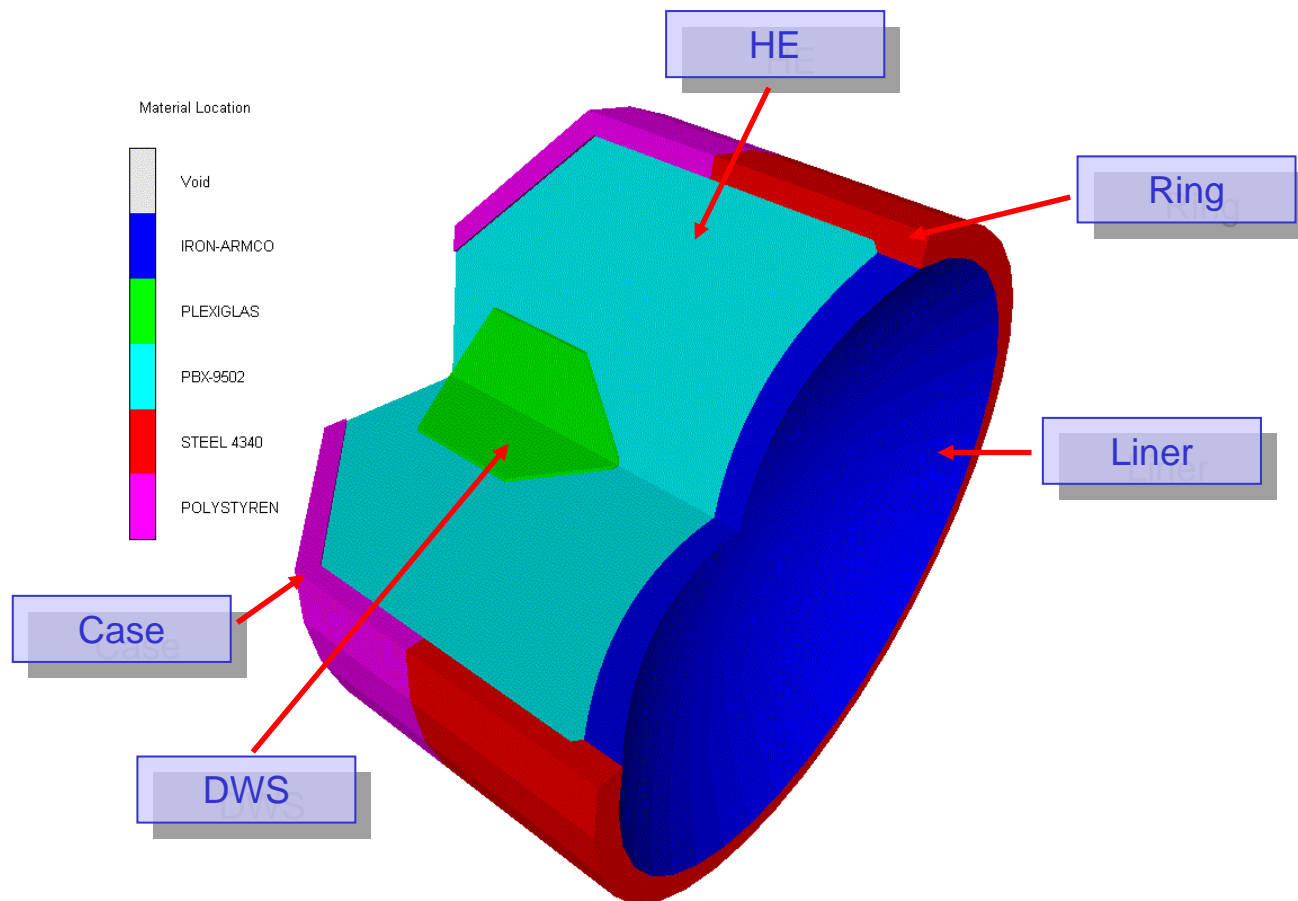
semi hard /
soft targets
medium
standoff



e.g. truck, radar, etc.

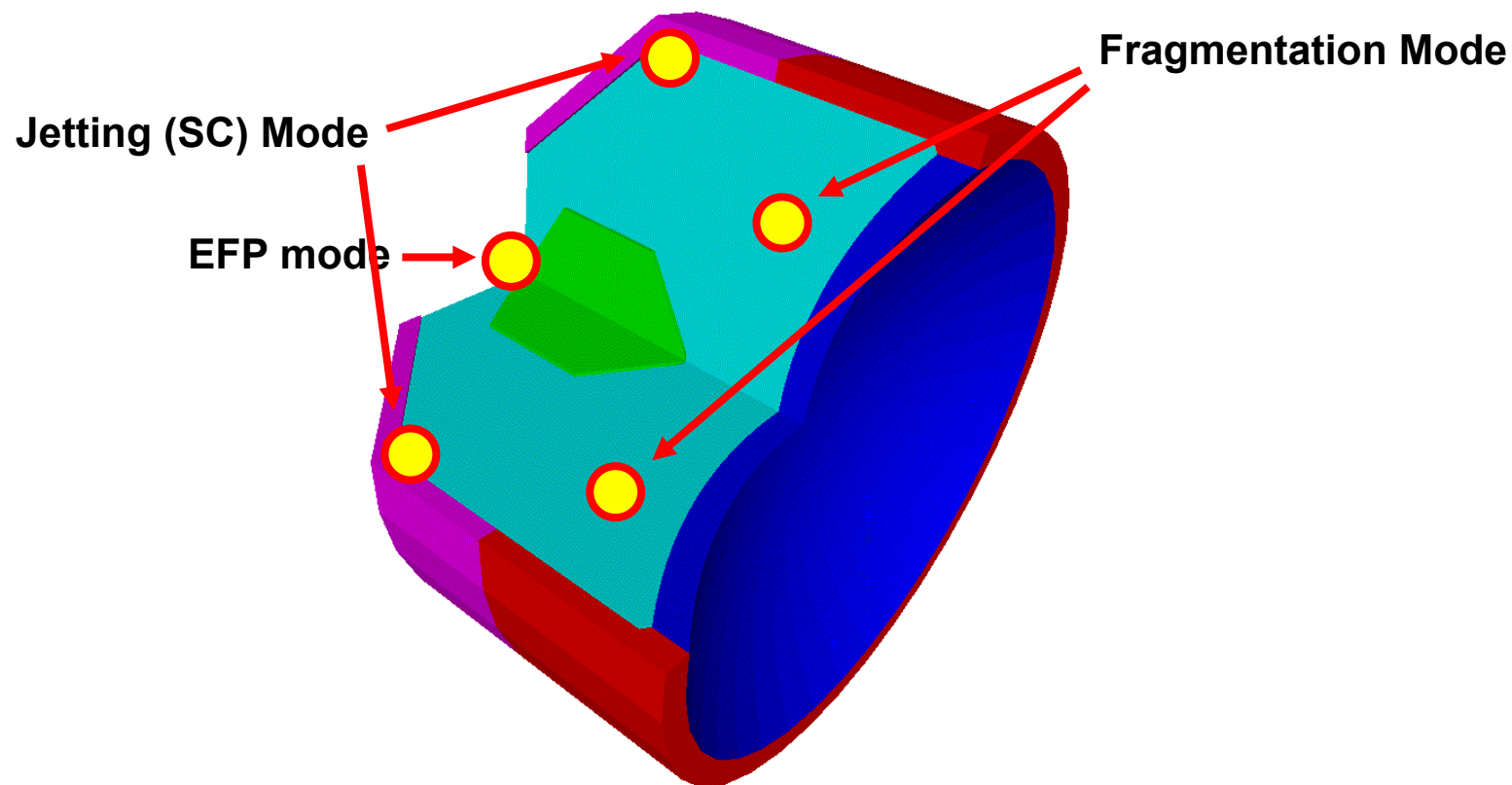
Multimode Warhead

- Basis: EFP warhead



Multimode Warhead

- Choose warhead mode by means of initiation with EFI



AUTODYN®

- Hydrocode simulation with ANSYS AUTODYN®
 - Explicit analysis tool for simulating non-linear short time dynamics of
 - solids, fluids, gases
 - fluid-structure interactions
 - Combined method of
 - finite differences
 - finite elements
 - finite volumes
 - (mesh free SPH)

Underlying Physics

■ Conservation laws

■ Mass

$$\frac{D\rho}{dt} + \rho \sum_{i=1}^3 \frac{\partial v_i}{\partial x_i} = 0$$

■ Momentum

$$\rho \frac{Dv_i}{Dt} = \sum_{j=1}^3 \frac{\partial \sigma_{ji}}{\partial x_j} + f_i \quad (i = 1, 2, 3)$$

■ Angular Momentum

$$\sigma_{ij} = \sigma_{ji} \quad (i, j = 1, 2, 3)$$

■ Energy

$$\rho \frac{Dw_{\text{int}}}{Dt} = \sum_{i,j=1}^3 \frac{\partial v_i}{\partial x_j} \sigma_{ij} - \sum_{i=1}^3 \frac{\partial q_i}{\partial x_i} + \rho s$$

t : time

x_i : position

v_i : velocity

ρ : local density

σ_{ij} : stress tensor

f_i : external force density

w_{int} : specific internal energy

s : heat sources

q_i : heat flux

■ Material laws

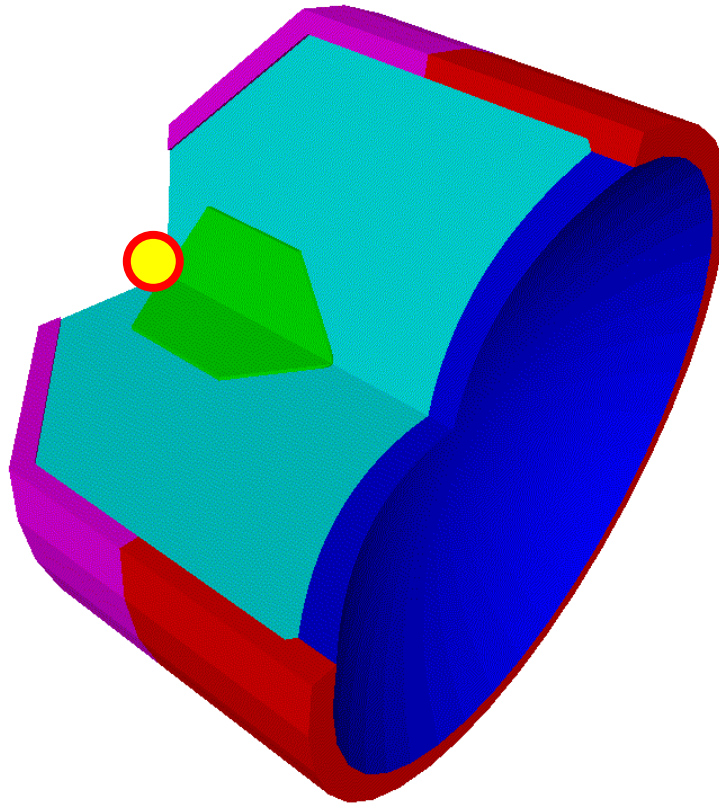
■ Equation of State

■ Material strength

■ Material Failure

EFP Mode

- Initiation point in front of DWS



Initiation Controlled Multimode Warheads

EFP Mode

AUTODYN2D v11.0 from Century Dynamics

ANSYS

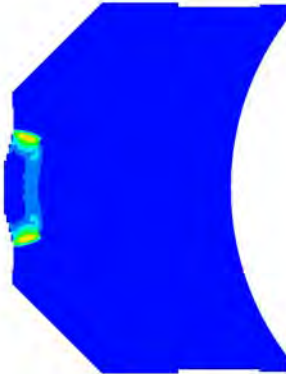
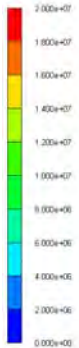
AUTODYN2D v11.0 from Century Dynamics

ANSYS

AUTODYN2D v11.0 from Century Dynamics

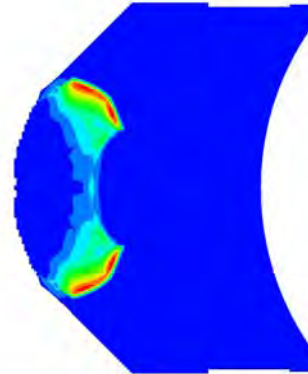
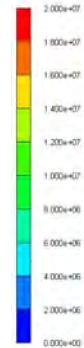
ANSYS

PRESSURE (Pa)



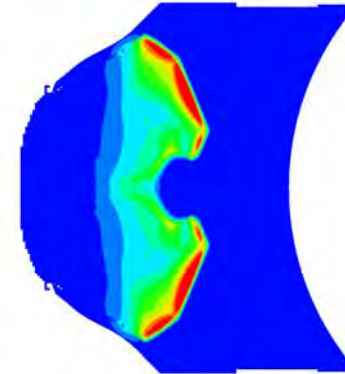
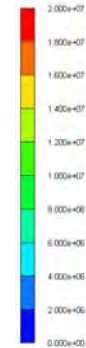
p07
Cycle 137
Time 2.000E-003 ms
Units mm, mg, ms
Axial symmetry

PRESSURE (Pa)



p07
Cycle 362
Time 4.001E-003 ms
Units mm, mg, ms
Axial symmetry

PRESSURE (Pa)



p07
Cycle 762
Time 6.000E-003 ms
Units mm, mg, ms
Axial symmetry

AUTODYN2D v11.0 from Century Dynamics

ANSYS

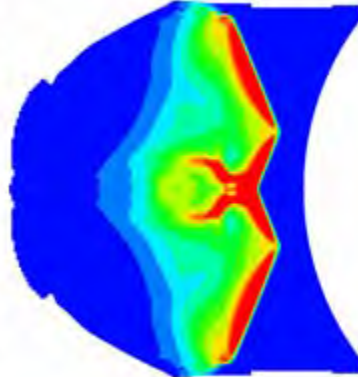
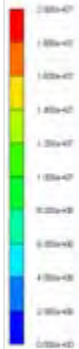
AUTODYN2D v11.0 from Century Dynamics

ANSYS

AUTODYN2D v11.0 from Century Dynamics

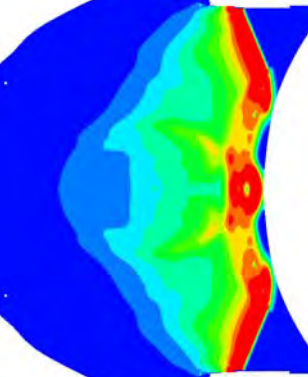
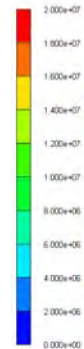
ANSYS

PRESSURE (Pa)



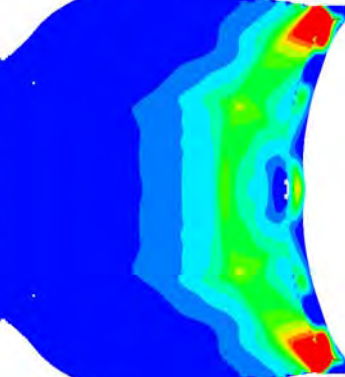
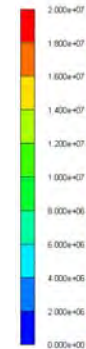
p07
Cycle 1127
Time 9.000E-003 ms
Units mm, mg, ms
Axial symmetry

PRESSURE (Pa)



p07
Cycle 1773
Time 1.000E-002 ms
Units mm, mg, ms
Axial symmetry

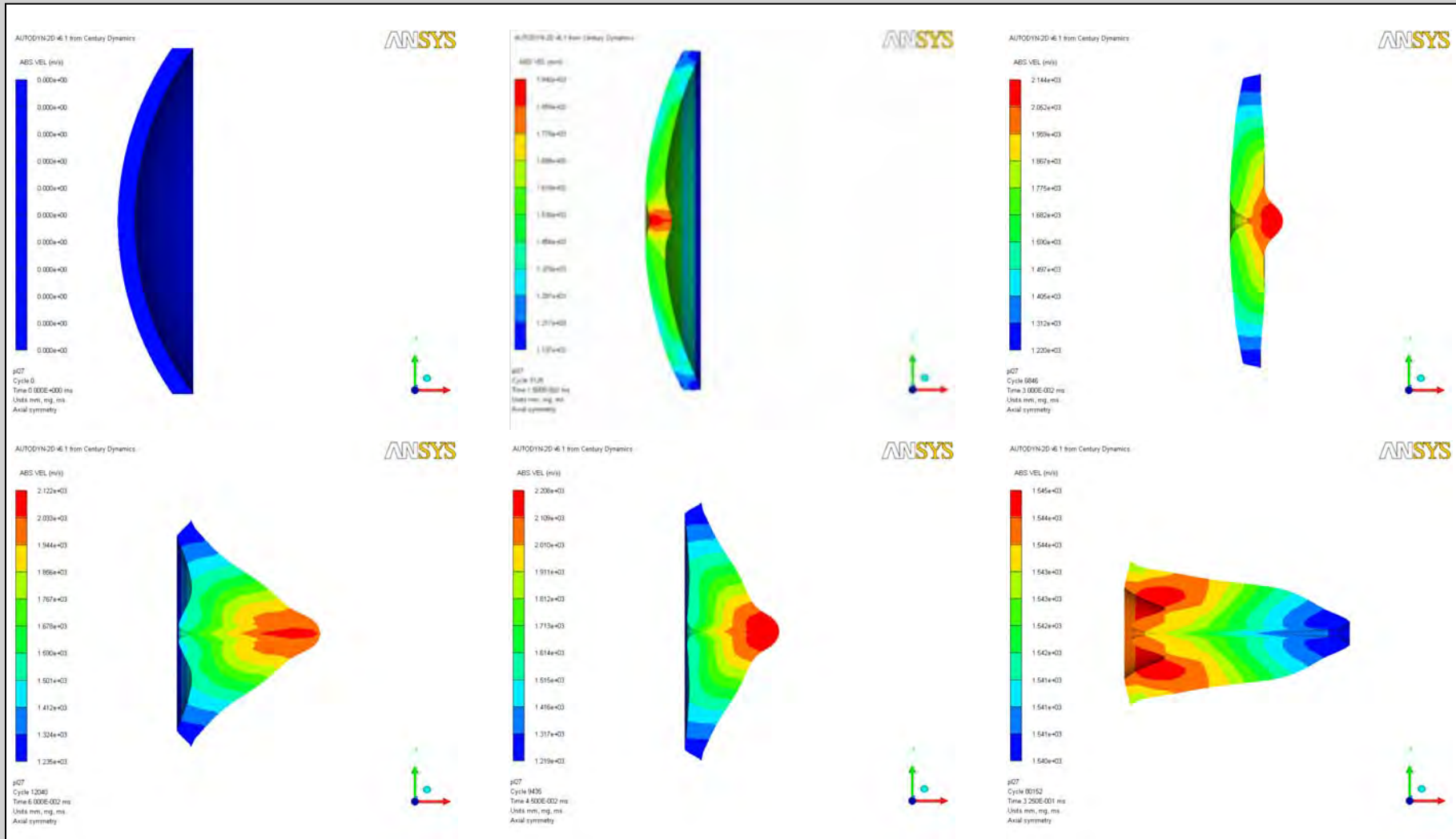
PRESSURE (Pa)



p07
Cycle 2307
Time 1.000E-002 ms
Units mm, mg, ms
Axial symmetry

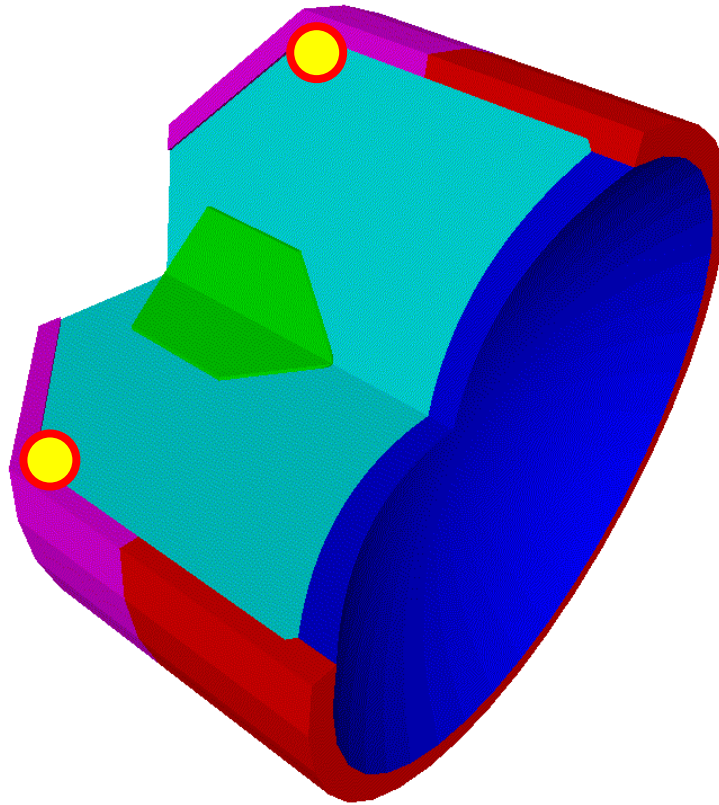
Initiation Controlled Multimode Warheads

EFP Mode

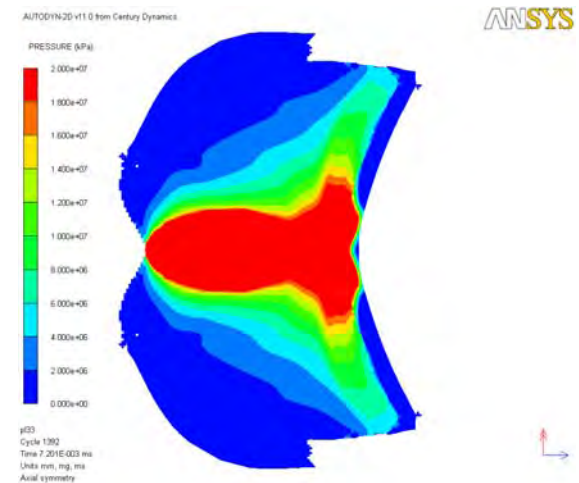
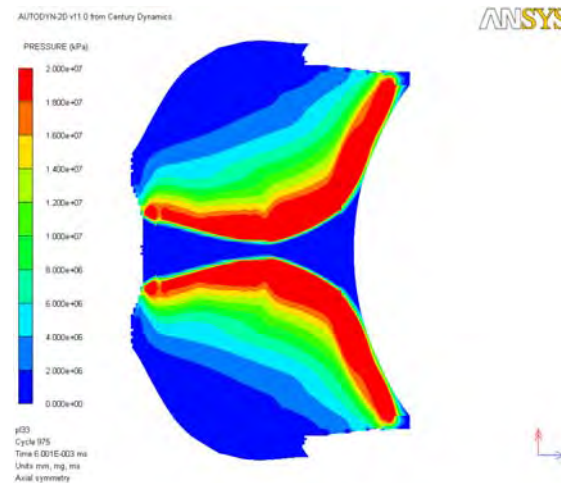
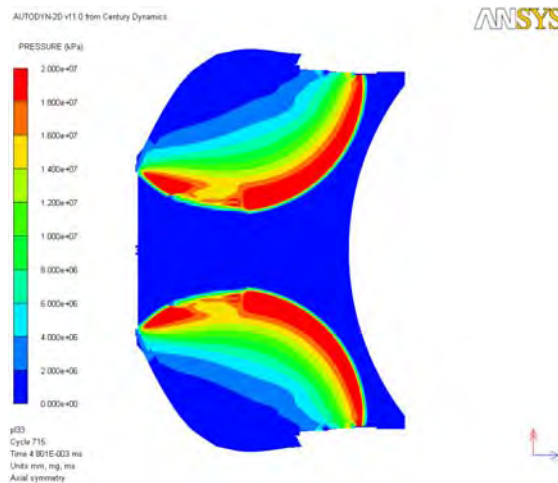
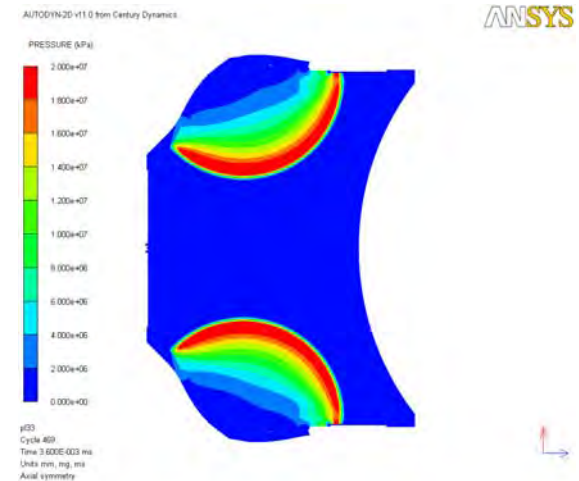
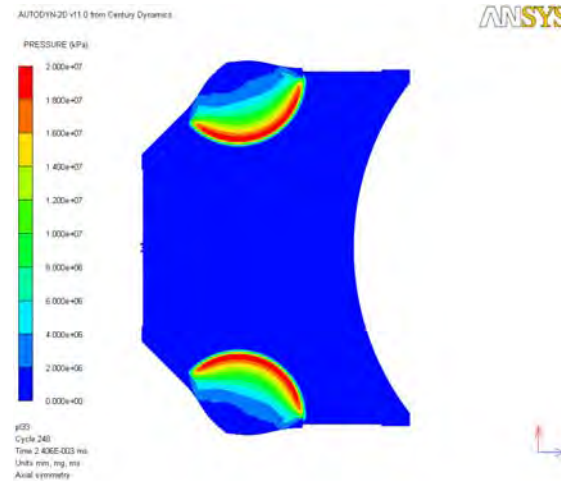
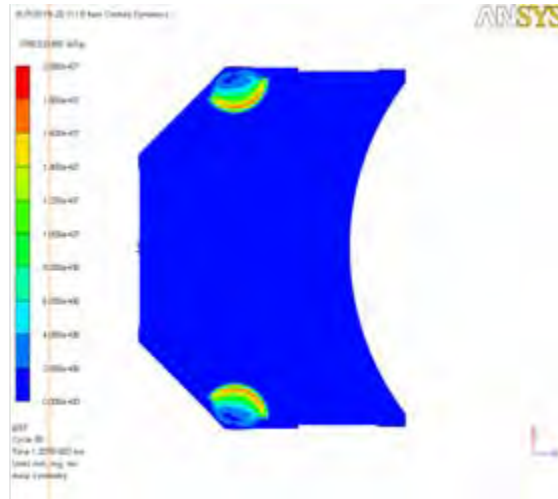


Jetting (SC) Mode

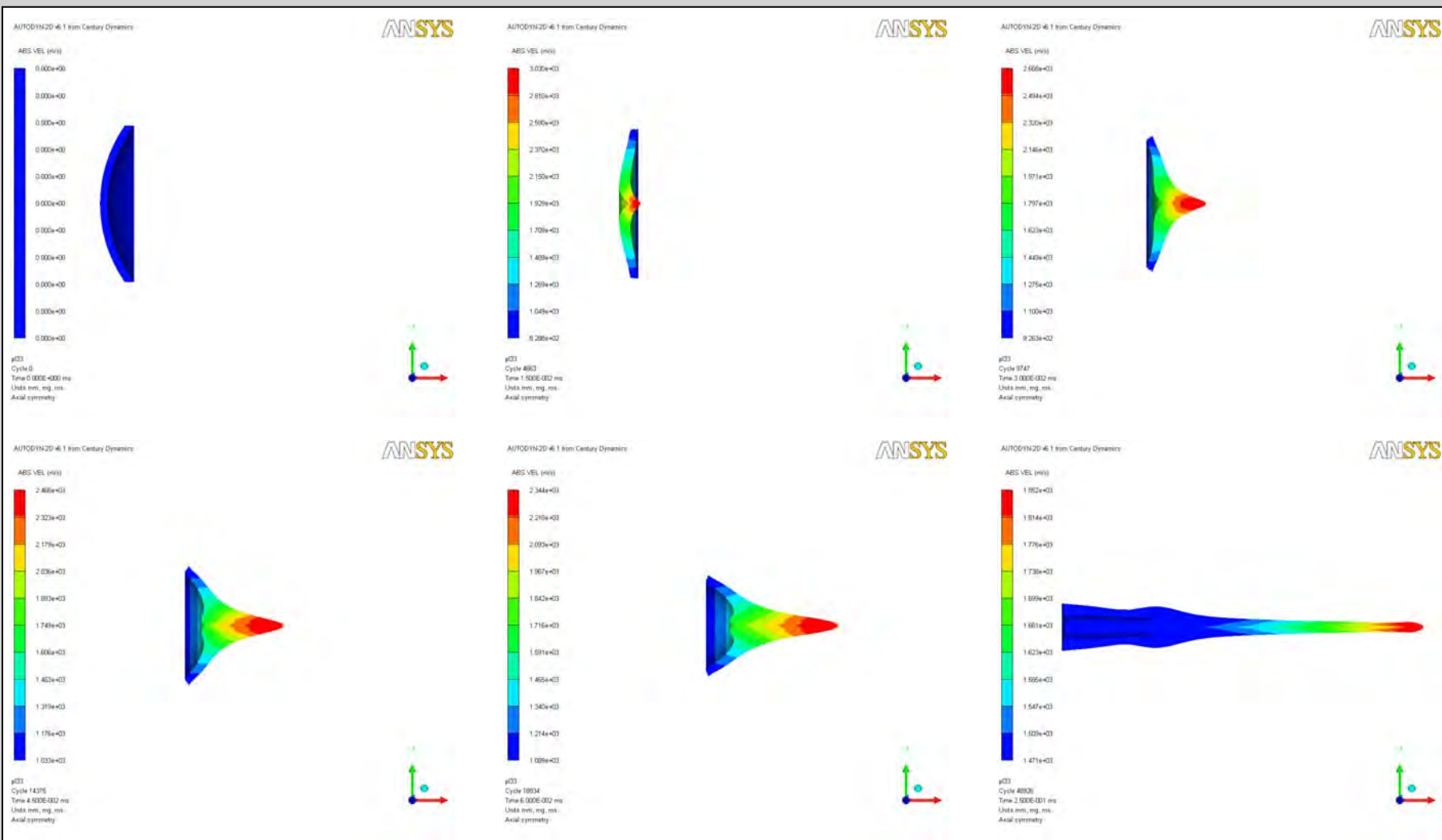
- Multiple initiation points around circumference of warhead case



Jetting (SC) Mode



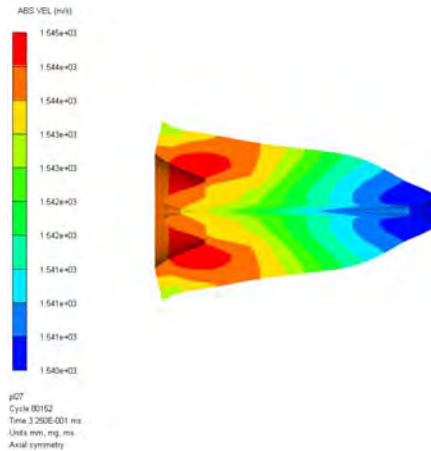
Jetting (SC) Mode



Comparison of EFP and SC Modes

AUTODYN2D v6.1 from Century Dynamics

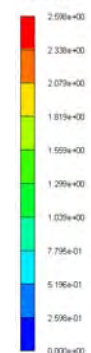
ANSYS



$v = 1540 \text{ m/s}$
 $L/D = 1.6$
 $P_{\text{Steel}} = 0.4 \text{ CD}$

AUTODYN2D v11.0 from Century Dynamics

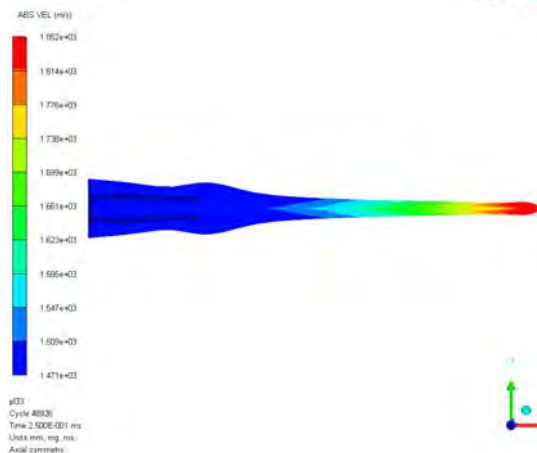
EFF PL STN



p07 penetration super
Cycle 81933
Time 4.040E-001 ms
Units mm, mg, ms
Axial symmetry

AUTODYN2D v6.1 from Century Dynamics

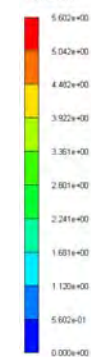
ANSYS



$v = 1850\text{-}1470 \text{ m/s}$
 $L/D = 7.6 \text{ (}t=250\mu\text{s)}$
 $P_{\text{Steel}} = 0.7 \text{ CD}$

AUTODYN2D v11.0 from Century Dynamics

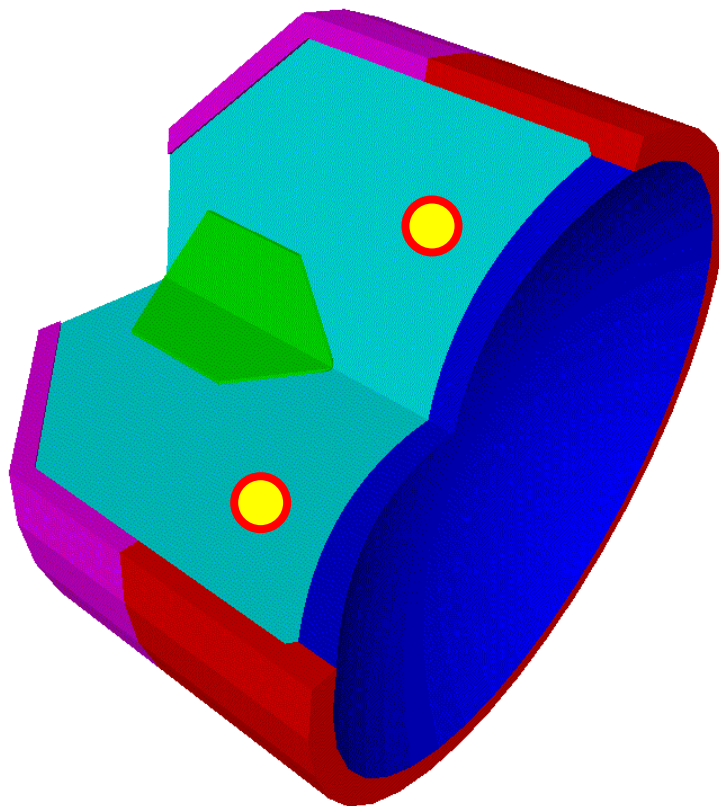
EFF PL STN



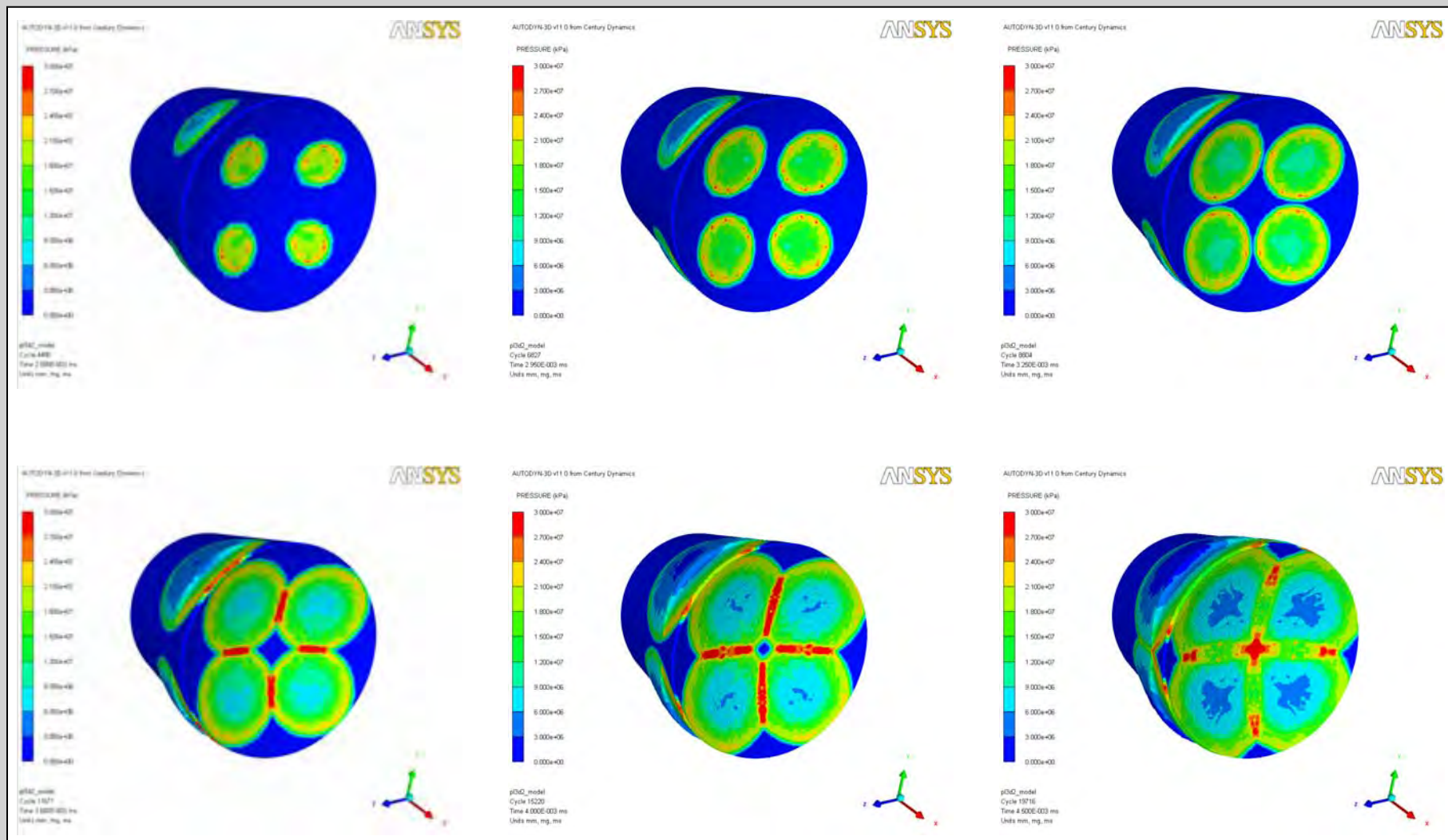
p03 penetration
Cycle 53272
Time 4.500E-001 ms
Units mm, mg, ms
Axial symmetry

Fragmentation Mode

- Few initiation points in front of liner

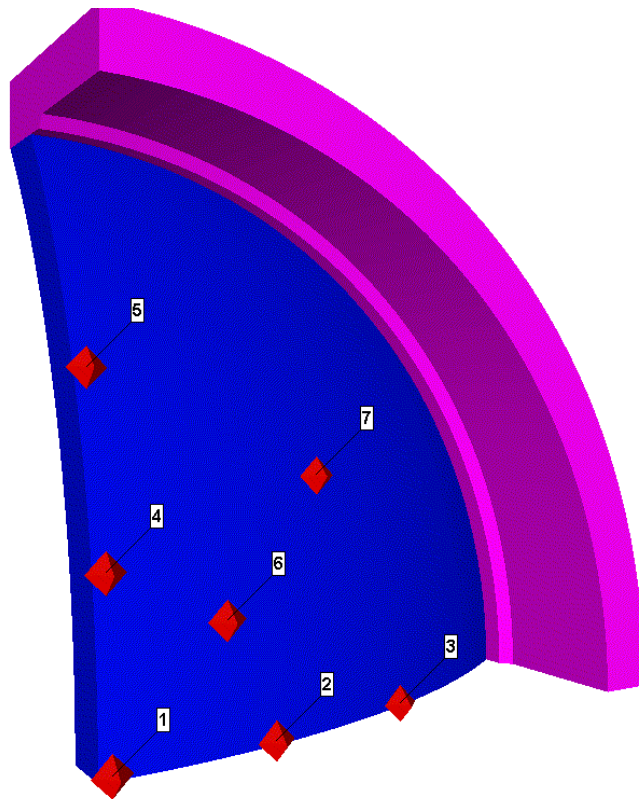


Fragmentation Mode with 4 Initiation Points



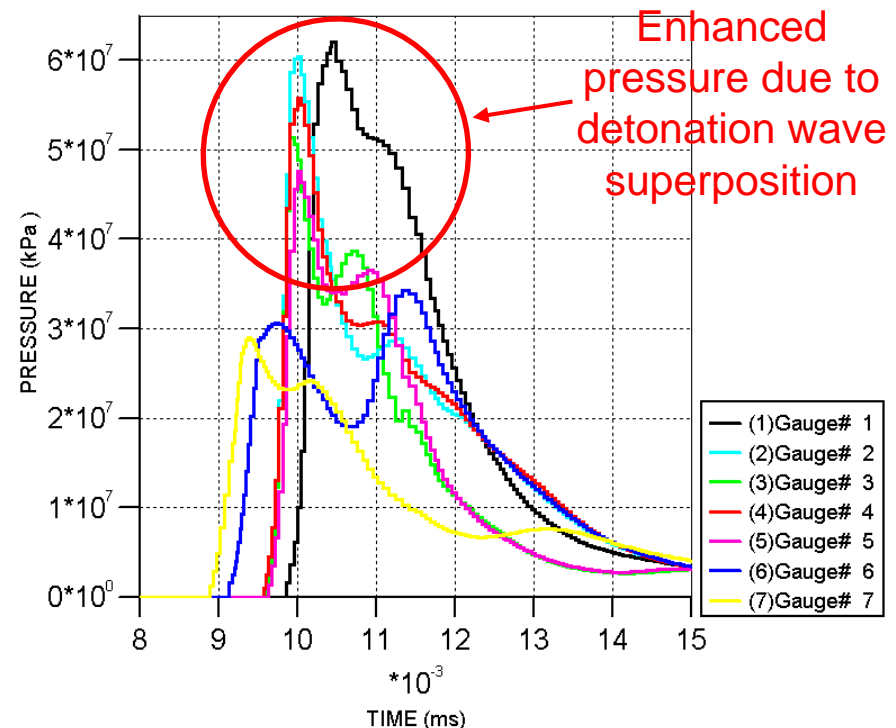
Fragmentation Mode

- Fragmentation of liner due to detonation wave superposition
 - Superposition of detonation waves lead to high local impulse densities
→ local failure of liner material



Fragmentation Mode with 4 Initiation Points

*) different initiation points than in previous figure



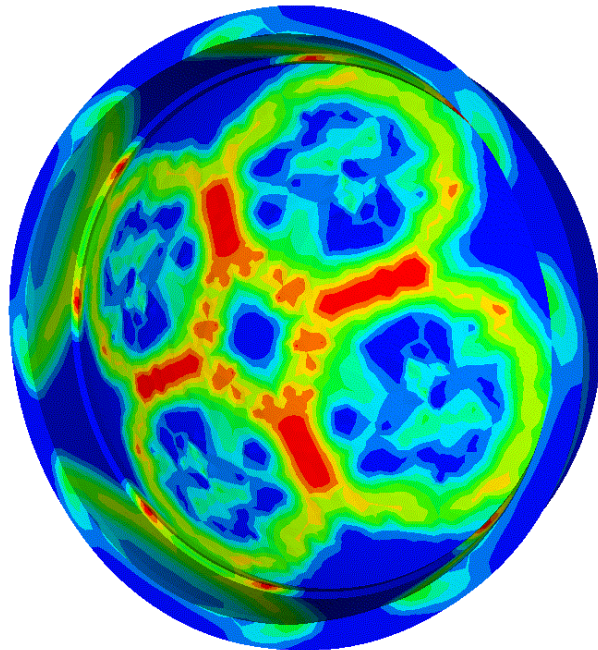
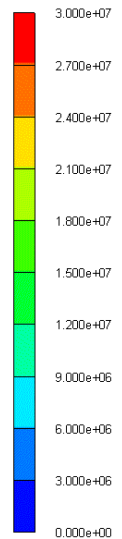
Fragmentation Mode

■ Formation of liner fragments

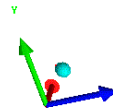
AUTODYN-3D v11.0 from Century Dynamics

ANSYS

PRESSURE (kPa)



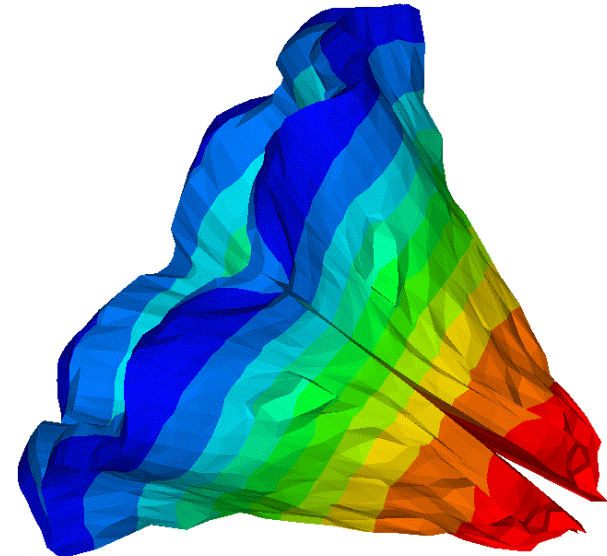
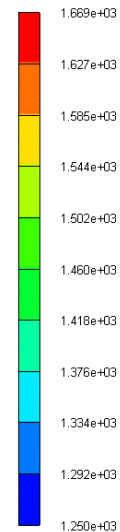
pl3d4
Cycle 2859
Time 4.000E-003 ms
Units mm, mg, ms



AUTODYN-3D v11.0 from Century Dynamics

ANSYS

ABS VEL. (m/s)



pl3d11
Cycle 51629
Time 8.236E-002 ms
Units mm, mg, ms

Limits of Initiation Controlled Multimode Warheads

- Optimum performance only for original warhead mode, i.e.
 - EFP mode for EFP based multimode warhead
 - SC mode for SC based multimode warhead
- EFP basis
 - Thick liner → low collapse velocity → no high velocity SC jet
- SC basis
 - Low liner mass, small opening angle → no EFP
 - Low liner mass → only low mass fragments

Summary

- Operating modes of initiation controlled multimode warhead demonstrated by simulation
- EFP charge with multiple initiation points
 - EFP mode: Single initiation point in front of DWL
 - Aerodynamically stable projectile → hard target defeat at long standoffs
 - Jetting (SC) mode: multipoint initiation along warhead circumference
 - Stretched projectile → enhanced penetration performance at small standoffs
 - Fragmentation mode: few initiation points in front of liner
 - Fragments → defeat of semi-hard and soft targets at medium standoffs
- Functionality of EFP and Jetting (SC) mode verified by experimental tests
- Fragmentation mode under current experimental investigation

Contact

Dr. Thomas Falter

Diehl BGT Defence GmbH & Co. KG

Phone: +49-(0)911-957-2522

Email: Thomas.Falter@diehl-bgt-defence.de

A Computational Study of the Energy Dissipation Through an Acrylic Target Impacted by Various Size FSP

C. G. Fountzoulas, P. G. Dehmer, J. M. Sands, and
J. H. Yu

U.S. Army Research Laboratory
Aberdeen Proving Ground, MD 21005-5069

cfount@arl.army.mil, pdehmer@arl.army.mil, jsands@arl.army.mil, jian.h.yu@arl.army.mil

OUTLINE



- " Objective**
- " Background**
- " Experimental Details**
- " Numerical Simulations**
- " Regression Analysis**
- " Summary**
- " Future Plans**

Knowledge of the energy absorption by an impacted material is a necessary requirement for the successful design of an armor

Objective



- ” To study the energy dissipation through acrylic targets of varying thickness and architecture impacted by various size Fragmented Simulated Projectiles (FSPs)
- ” To produce analytical expressions of the velocity profiles by using regression analysis tools in an effort
 - . to produce a general equation of energy absorption of a projectile through a PMMA target

et Penetration Factors



- “ According to M. L. Wilkins et al* %The important projectile parameters for target penetration are geometry, material strength, density, and velocity.
- . Geometry refers to the sharp point used in the design of armor piercing projectiles.
 - . Material strength is the parameter that permits the projectile to maintain the designed armor-piercing shape during the penetration process.
 - . The projectile material strength is important until a target that is stronger than the projectile is encountered.
 - “ Then, the penetration process is governed by the projectile mass and velocity.
 - . For example, ball and armor piercing, and projectiles with the same mass have about the same ballistic limit for ceramic targets strong enough to destroy the tip of the armor piercing projectile.+

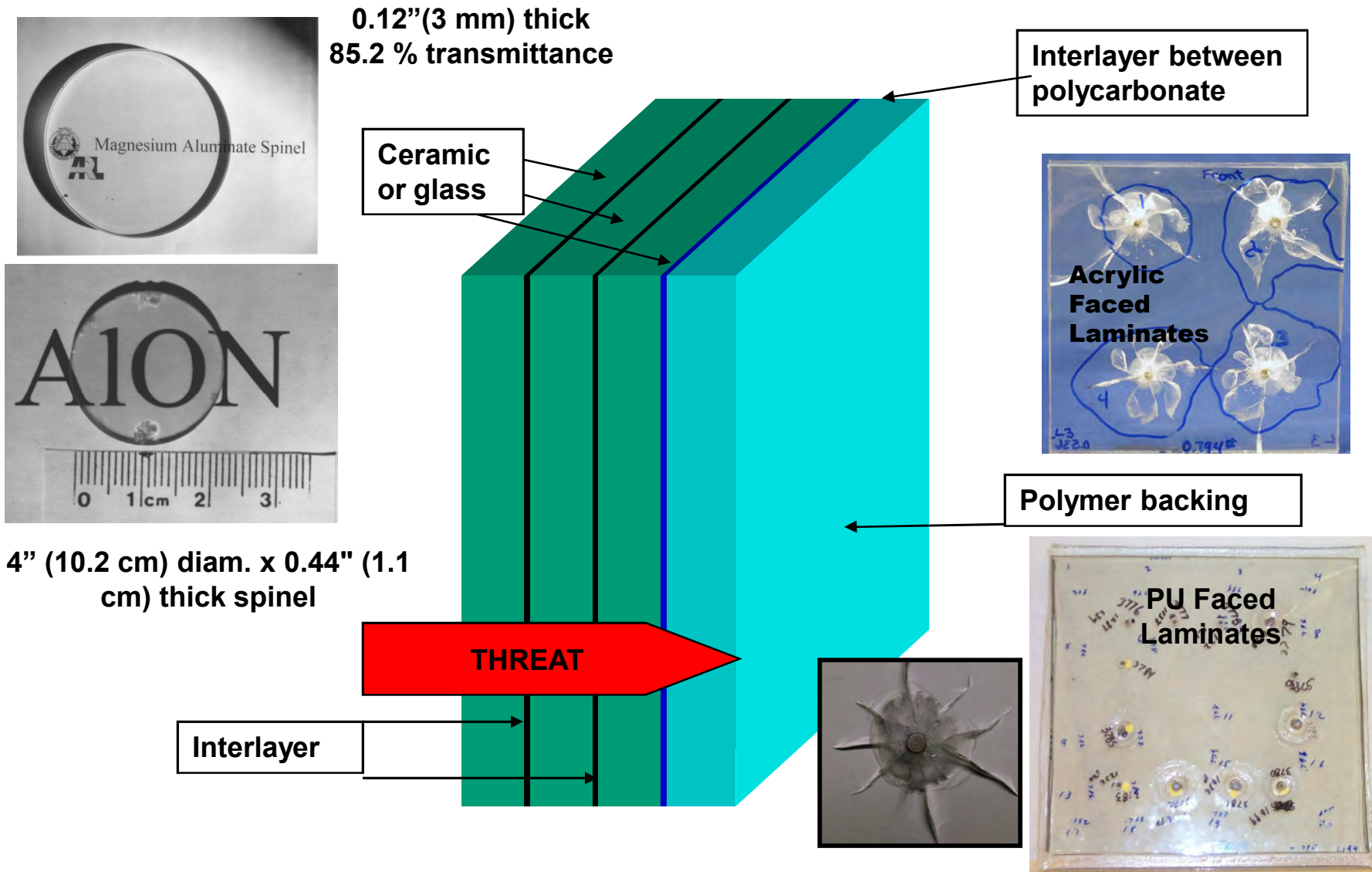
*M: L. Wilkins, R. L. Lamdingham, C. A. Honodel, Fifth Progress Report of Light Armor Program, UCRL-50980, University of California, Livermore.

Background



- “ Commercially available transparent armor systems are used in a variety of military and civilian applications including
 - face shields, goggles, vehicle vision blocks, windshields and windows, blast shields, and aircraft canopies
- “ High performance transparent armor systems typically consist of several different materials, such as
 - PMMA, float or soda lime glass, sapphire, ALON, spinel, and polycarbonate bonded together with a rubbery interlayer such as polyurethane (PU) or polyvinylbutyral (PVB),
- “ The lamination sequence, material thicknesses and bonding between layers has been shown to drastically affect system performance and it has been observed that each material serves an important function.

Transparent Armor Design



TECHNOLOGY DRIVEN. WARFIGHTER FOCUSED.

Modeling Efforts



- “ Numerical simulations coupled with experiments provide a more cost-effective way of studying the ballistic performance of monolithic and laminated transparent armor systems
- “ Accurately simulating polymeric transparent armor material over a range of strain rates has proven challenging
 - . Nandlall and Livingstone established that by adjusting the element erosion strain, the constitutive model was capable of accurately simulating the experimental ballistic limits
- “ Recent development of constitutive equations combining nonlinear viscoelasticity and viscoplasticity capture most of the time-dependent, nonlinear response observed for glassy polymers

Experimental Details

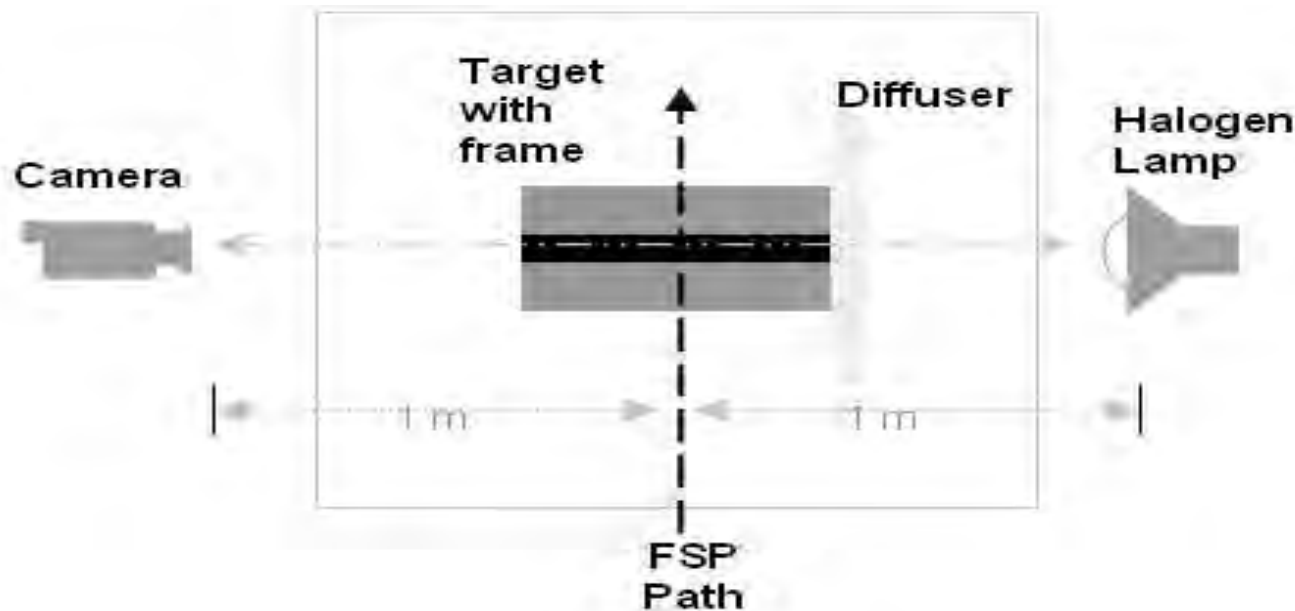


- “ Ballistic measurements were carried out at the Experimental Facility of Aberdeen Proving Ground, MD, using a 17-gr (1.1-g weight) .22-cal FSP, and a 5.85-gr (0.37 g weight) .15-cal FSP
- “ The cross-section area of all the acrylic targets was 152.4-mm x 152.4-mm. The target architecture was
 - . Monolithic targets of thickness 11.82-mm and 5.92-mm
 - “ They were impacted by .22-cal and .15-cal FSP respectively
 - . A third target, which was consisted of two 5.92-mm thick plates of acrylic without any adhesive between them-total thickness of the set 11.84-mm-
 - “ It was impacted by a .22-cal FSP.
- “ All targets were sandwiched in a transparent frame
- “ All shots were conducted with the target normal to the projectile line of flight, i.e., 0° obliquity.

Experimental Details-cont.

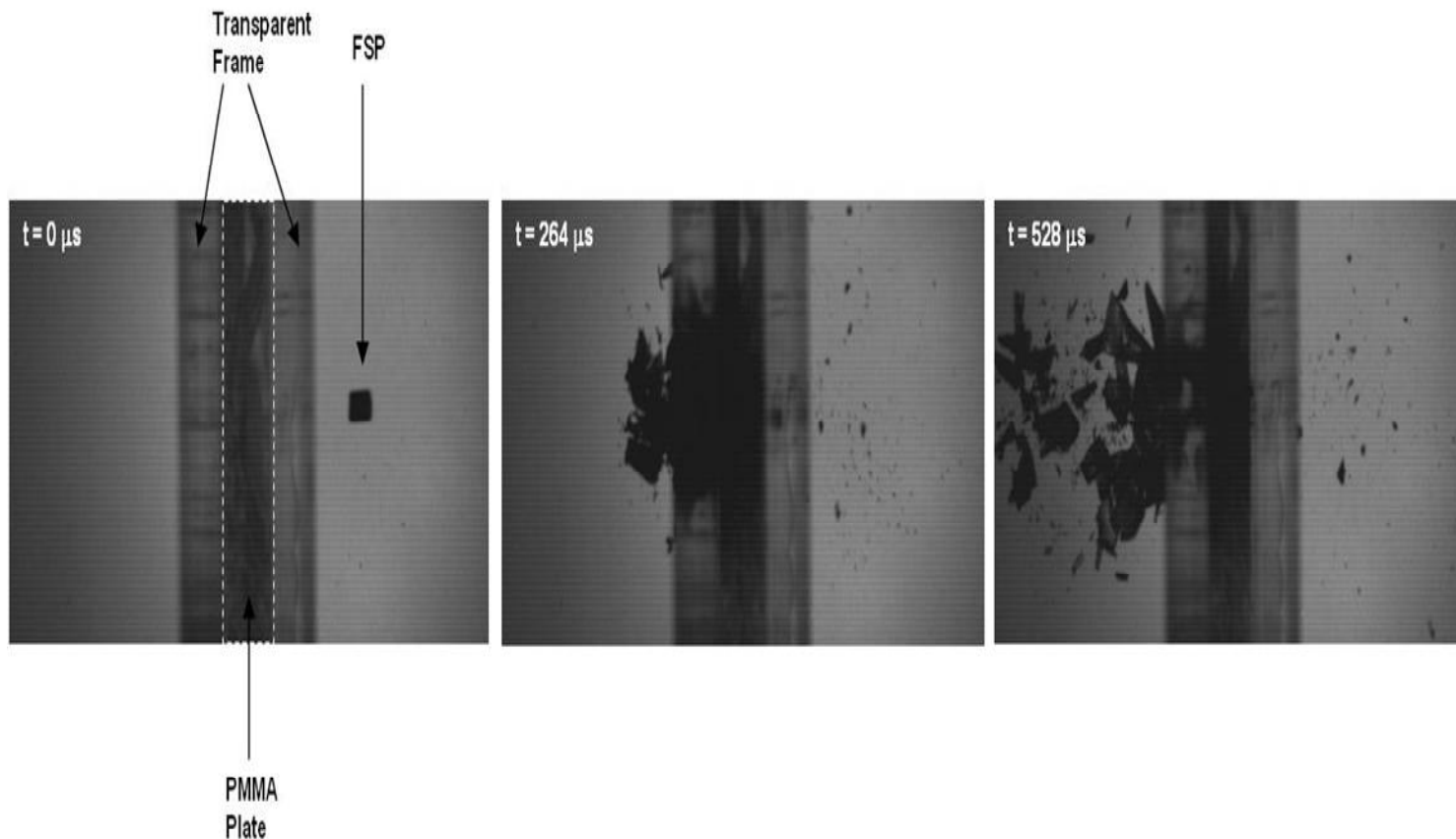


- “ The impact on the PMMA target was recorded by a Phantom v7, Vision Research, high-speed camera aiming at 90° to the path of the FSP.
- “ The targeting area was illuminated by backlighting using a high intensity halogen lamp and a diffuser was used to spread out the light intensity.



High-speed camera setup

Impact Penetration through a PMMA Plate



- “ The numerical modeling was carried out by using the nonlinear analysis commercial software ANSYS/AUTODYN using
 - . 3D axisymmetric models and smooth particle hydrodynamics (SPH) solver
 - . The particle size used for SPH solver was 0.5-mm
- “ The dimensions of the model were equal to the dimensions of the actual size target
- “ Results were obtained by simulating projectiles impacting the targets at the experimental V50 velocities of
 - . 350 m/s for the 11.84-mm thick targets and
 - . 210 m/s for the 5.92-mm thick target, respectively.

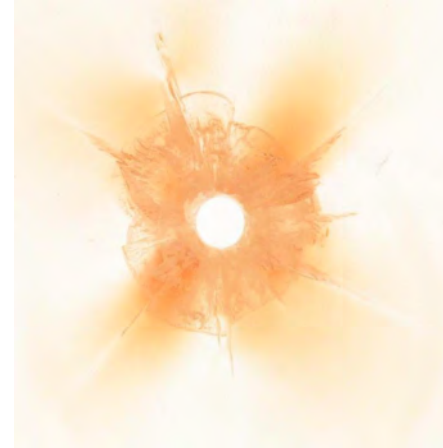
Material Models and Simulation Validation



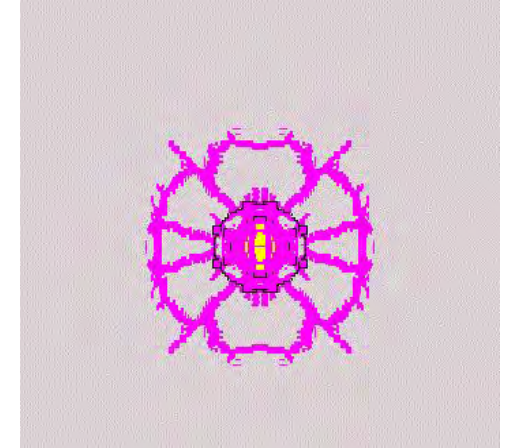
- “ **Steel** was modeled using
 - . shock EOS
 - . JC strength model.
- “ **PMMA** was modeled using
 - . shock EOS
 - . von Mises strength model
 - . principle stress failure criterion with crack softening criterion
 - “ PMMA Material Model in the Autodyn Library has No Strength and No Failure Criterion.



**Simulated
Impact before
material
models
modification,
.22-cal FSP
@350m/s**



Actual impact



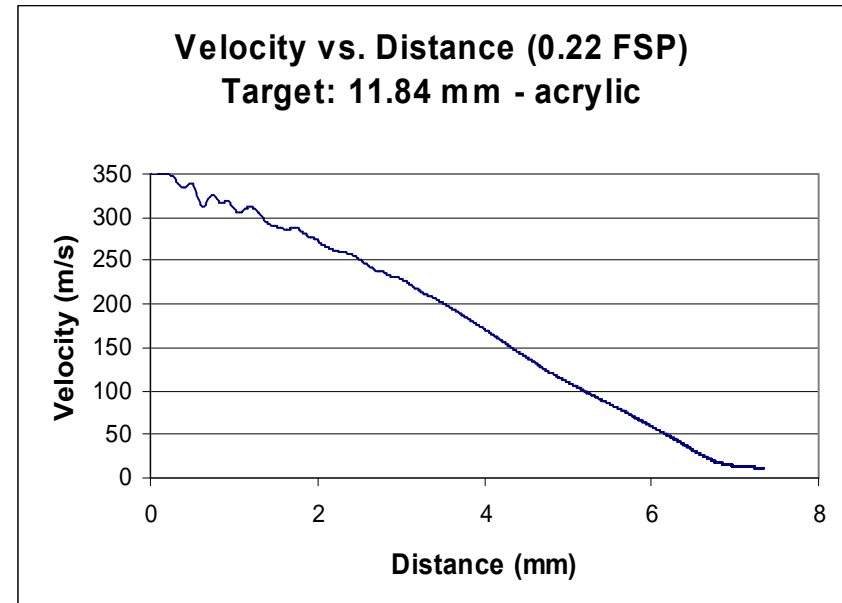
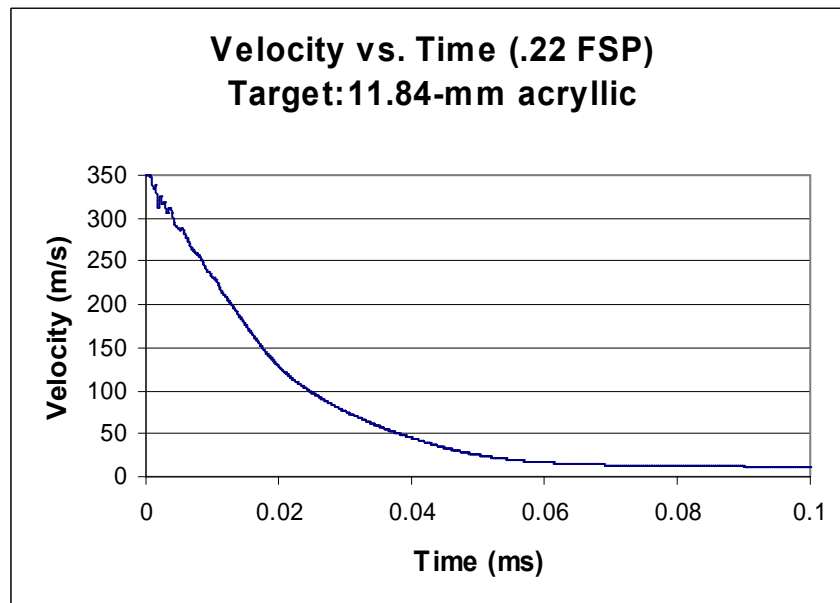
Simulated impact

**Actual and simulated target were
impacted by .22-cal FSP @ 350 m/s**

Simulation Results



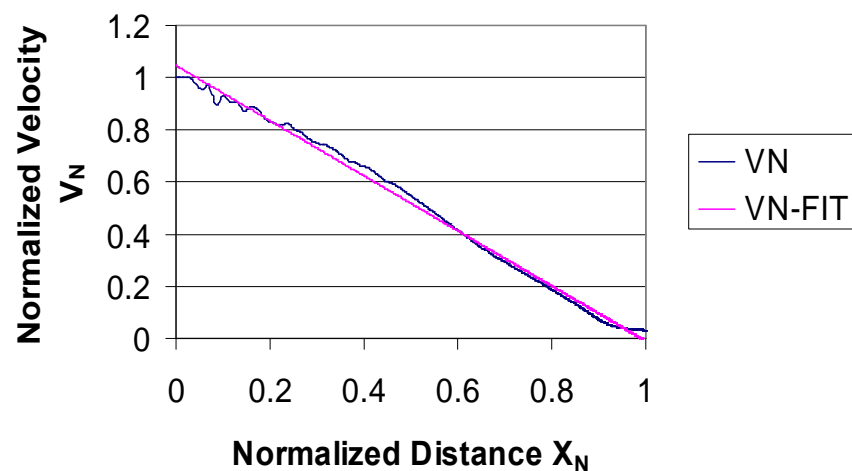
- “ All simulated exit velocities were within a few meters from the experimental exit velocities
- “ The analytical expression of the velocity profiles of all impacts was determined by using the LINEST statistical function of the Microsoft Excel



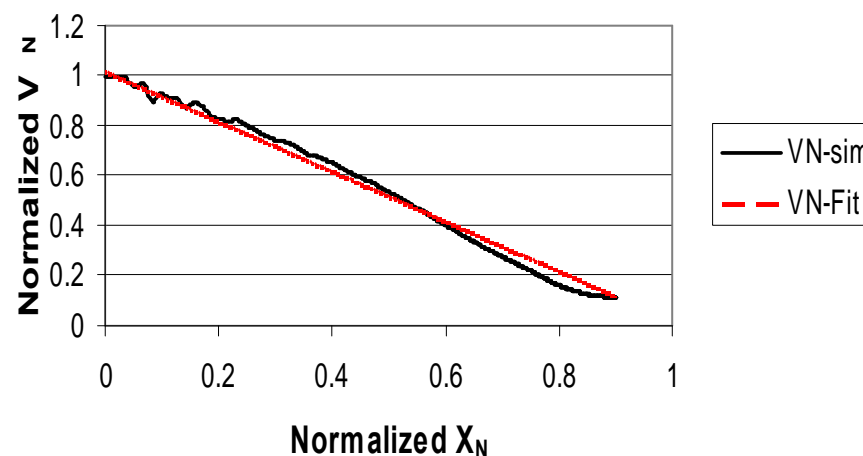
Regression Analysis



**Acrylic 11.84 mm (FSP022) Velocity
Profile vs. Distance Travelled**



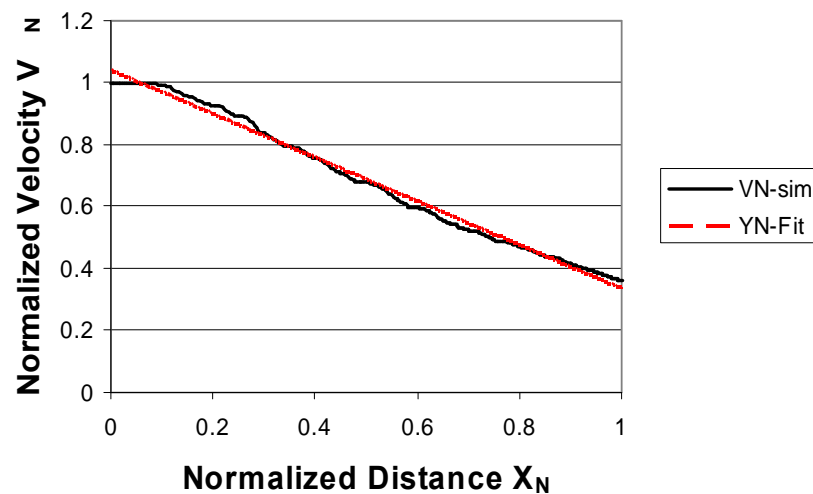
**Acrylic 2x592 (FSP022)
Velocity Profile vs. Distance**



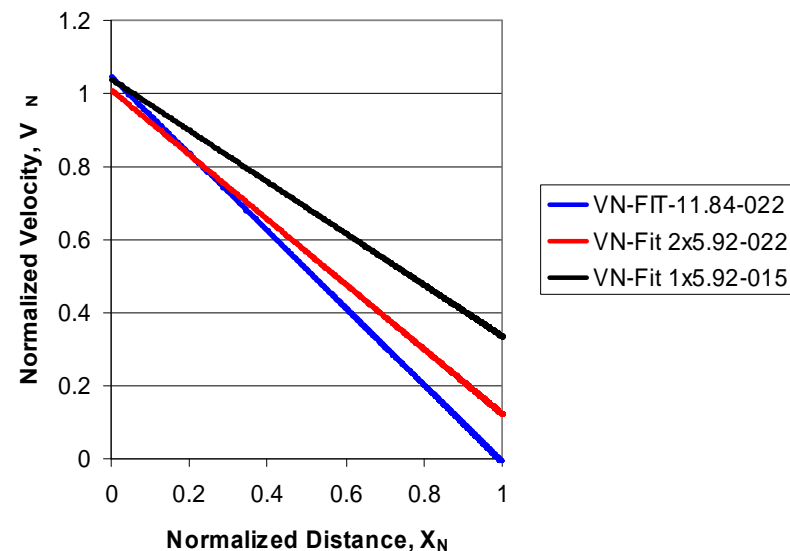
Regression Analysis



**Acrylic 1 x 5.92 mm (FSP 015)
Velocity Profile vs. Distance**



Curves of Fit-Data



EQUATIONS OF THE BEST-FIT CURVE FOR ALL SIMULATED IMPACTS



Target	Projectile	Velocity	Equation
1x11.84-mm	.22-cal FSP	350 m/s	$V/V_{MAX} = 1.046 - 1.056X_N$
2x5.92-mm (Laminated)	.22-cal FSP	350 m/s	$V/V_{MAX} = 1.010 - 0.888X_N$
1x5.92-mm	.15-cal FSP	210 m/s	$V/V_{MAX} = 1.039 - 0.7045X_N$

V = Instantaneous Projectile Velocity

V_{MAX} = Initial Impact Velocity

CONCLUSIONS



- “ The current paper has demonstrated the powerful use of computational modeling to produce analytical expressions for the prediction of the energy absorption by an acrylic target, which is impacted by various size FSPs.
- “ The results of the current study verified, the already known experimentally, that the resistance of an acrylic target to impact by FSP projectiles is affected by the
 - . Size of the FSP
 - . Impact velocity
 - . Target architecture.
- “ The experimental cracking pattern and the exit velocity of 0.22-cal and 0.15-cal FSPs through monolithic and laminated without intermediate adhesive layer PMMA targets were successfully substantiated by our modified existing strength and failure models of PMMA
 - . The PMMA material model was modified by introducing a von-Mises strength model
 - . a principal tensile strength criterion using published parameters

Conclusions



- “ The equations of the velocity profiles of the various cal FSPs traveling through the PMMA target were produced by regression analysis of the simulated velocity profile using the existing Microsoft Excel software
- “ An effort was made to produce an energy loss equation which is not only a mathematical expression, i.e. polynomial equation, but to be related to the physical parameters of the impact, such as impact velocity
- “ The **ideal equation** of the energy absorption profile is expected to be

$$(V/V_{MAX})^2 = [1 - (\text{slope}) \cdot (X/X_{MAX})]^2$$

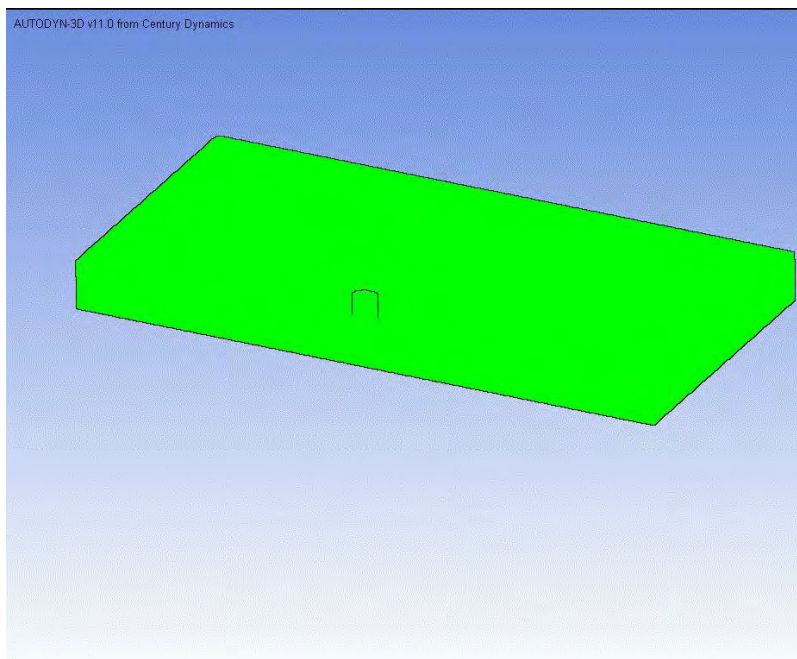
Where: V is the projectile instantaneous velocity and X distance travelled by the projectile within the PMMA target

- “ Future studies will attempt to
 - Connect the slope of the equation to the FSP mass and target architecture
 - Improve the prediction of the failure of the PMMA by simulation for various loading rates of PMMA and laminate geometries
 - Produce analytical energy absorption expression for a laminate target with more PMMA layers with and without adhesive layer between them.

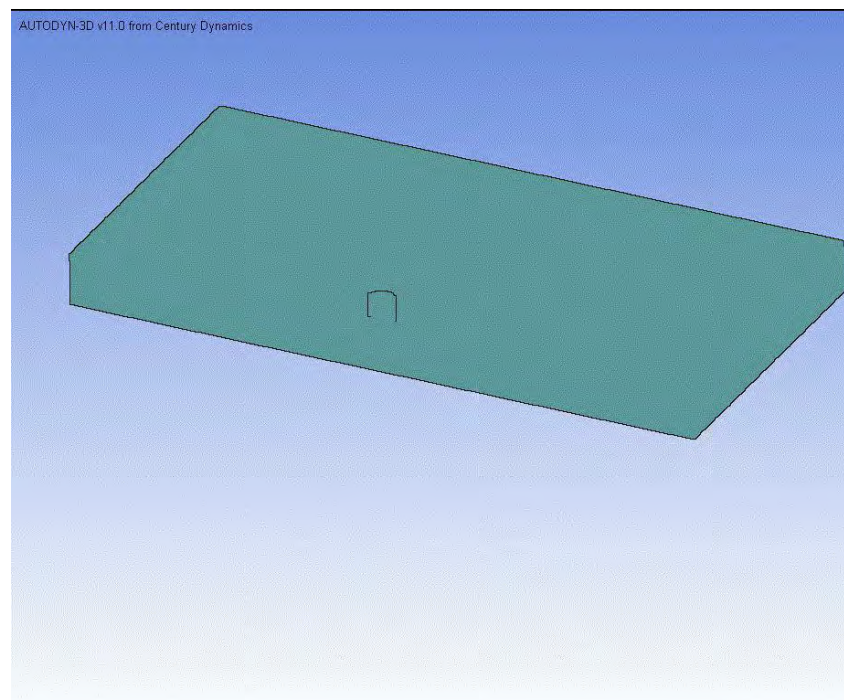
MOVIES



1 X 11.84-mm PMMA



2 X 5.92-mm PMMA



TECHNOLOGY DRIVEN. WARFIGHTER FOCUSED.



Range Extension of Gun-Launched Smart Munitions



TECHNOLOGY DRIVEN. WARFIGHTER FOCUSED.

*Dr. Frank Fresconi
Army Research Laboratory
23 September 2008*

Motivation

- Extending the range of gun-launched smart munitions enables larger area of influence, more timely fires, enhanced effectiveness, and improved urban operations.

Goal

- Identify the critical technical drivers for extended range of precision munitions

Approach

- 105-mm fin-stabilized projectile with rocket motor and general control mechanism studied in six degree-of-freedom simulation
- Guidance, navigation, and control (GNC) techniques
- Optimization of quadrant elevation, ignition time of rocket motor, start time of glide actuation
- Trade-offs in aerodynamic/control mechanism strategies

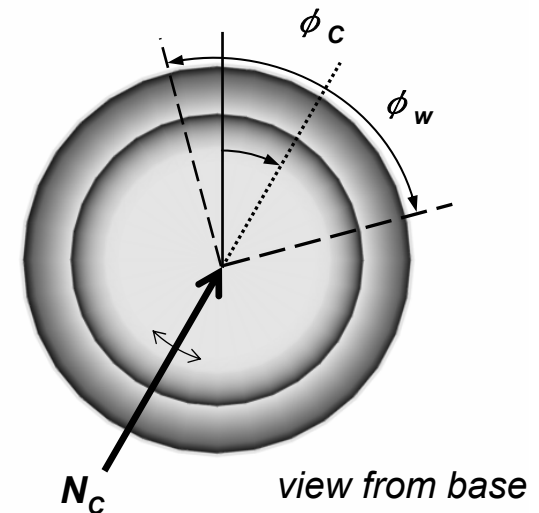
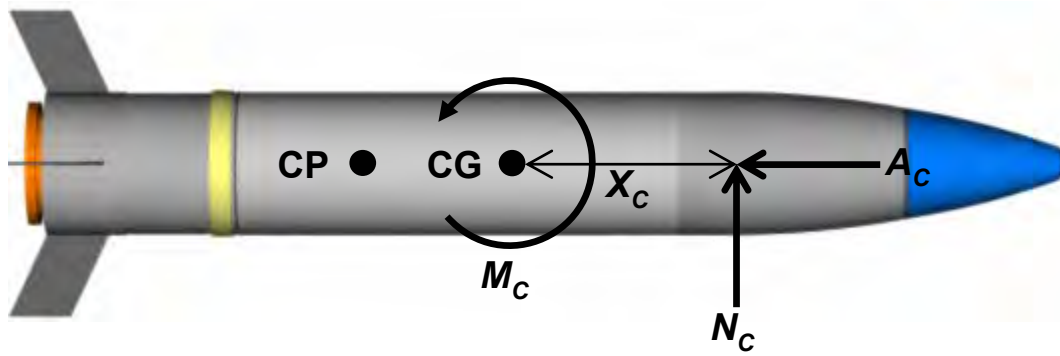
- 105-mm fin-stabilized projectile

Mass (kg)	Axial Inertia (kg-m ²)	Transverse Inertia (kg-m ²)	Center of Gravity From Nose (mm)	Diameter (mm)	Overall Length (mm)
18.40	0.03199	0.5607	422.7	104.7	762.0

- Generalized control mechanism
- Solid grain rocket motor
 - 3.6 sec burn time
 - 491.8 N thrust
 - Variable ignition time



- Control mechanism (canards, thrusters, etc.) modeled as axial control force (A_c), normal control force (N_c) with control moment arm (X_c), producing control moment (M_c).
- Maneuver direction of given control mechanism prescribed by commanded roll orientation (ϕ_c) and duration of roll cycle (ϕ_w).



- Fire control (max charge)
 - quadrant elevation (QE)
 - rocket ignition time (T_R)
 - glide start time (T_G)
- Projectile configuration
 - control normal force
 - control normal-to-axial force ratio
 - control axial location
 - static margin
 - roll window
- Metrics
 - extended range
 - total angle of attack (α_T)

- Common sense: control normal force direction (ϕ_c) should be opposite gravity to maximize range.
- Problem: Projectile drift (interaction of gravity, spin, and pitching moment) can significantly bend the trajectory in the crossrange direction and reduce range.
- Solution: develop flight control system to maximize range while minimizing drift.

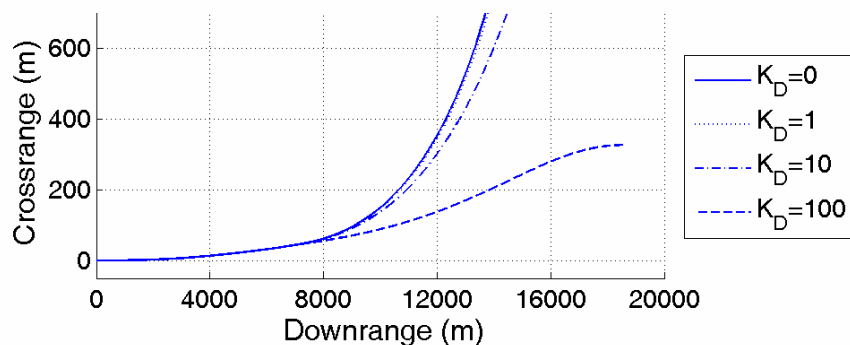
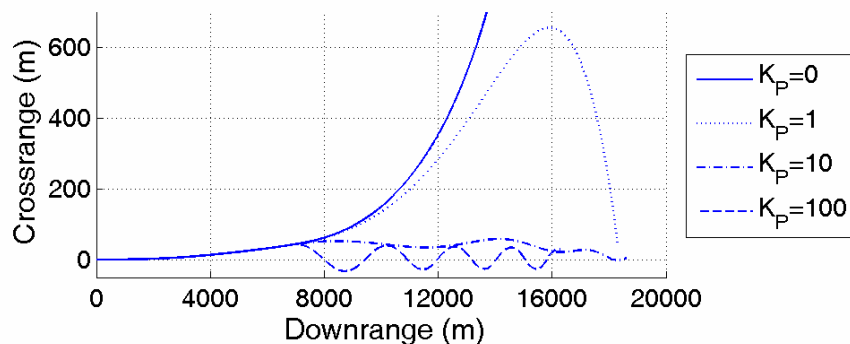
$$\varphi_C = \arctan\left(\frac{K_P e_y + K_D \dot{e}_y}{e_z}\right)$$

$$e_y = y_p - y_t$$

$$\dot{e}_y = \dot{y}_p - \dot{y}_t$$

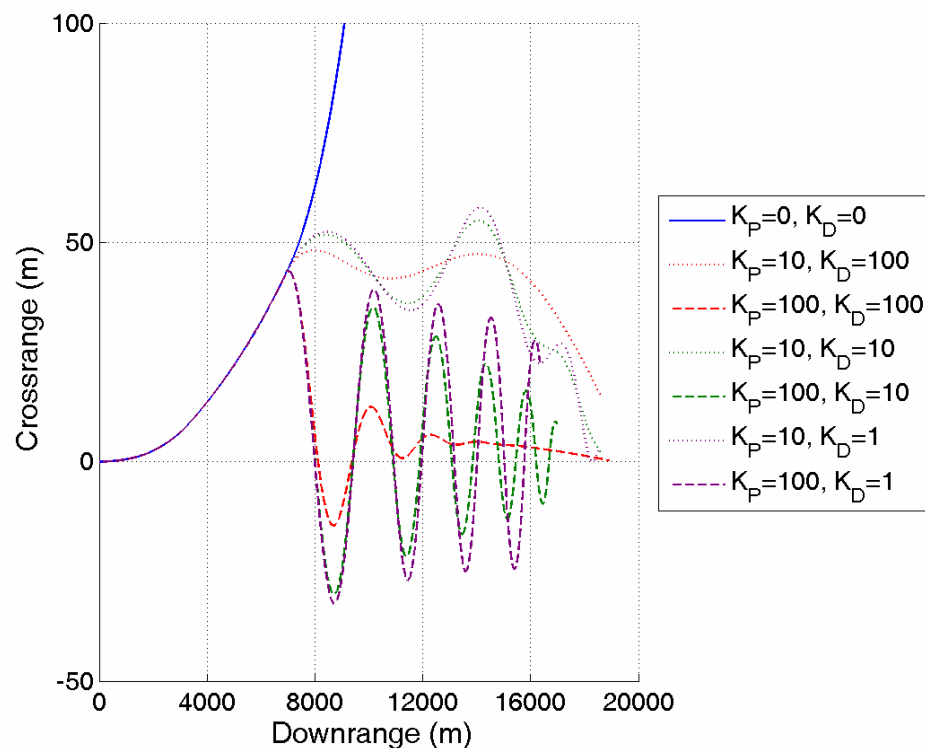
$$e_z = z_p - z_t$$

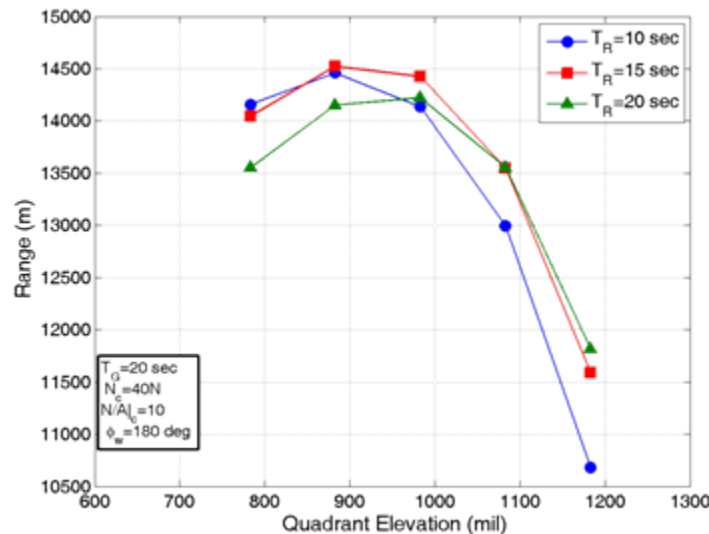
- Projectile inertial position (y_p, z_p) and velocity (\dot{y}_p) input from GPS, IMU, etc.
- Target inertial position (y_t, z_t) and velocity (\dot{y}_t) provided from fire control
- Proportional (K_P) and derivative (K_D) gains
- Flight controller seeks to maximize pitch angle of attack, minimize yaw angle of attack



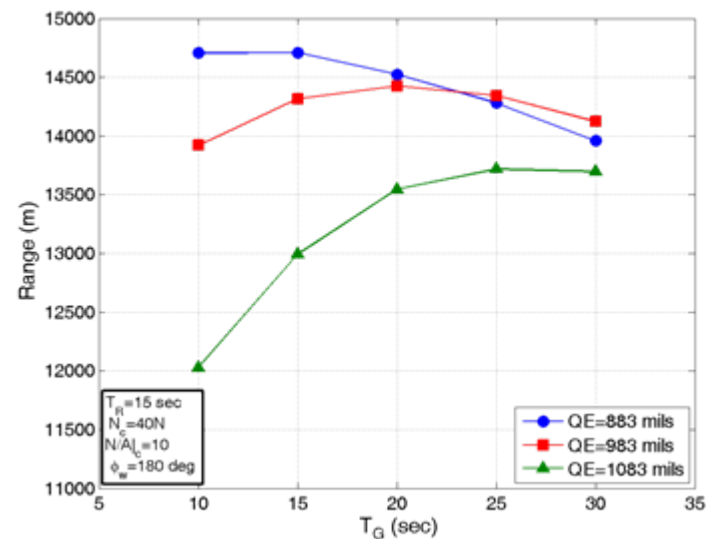
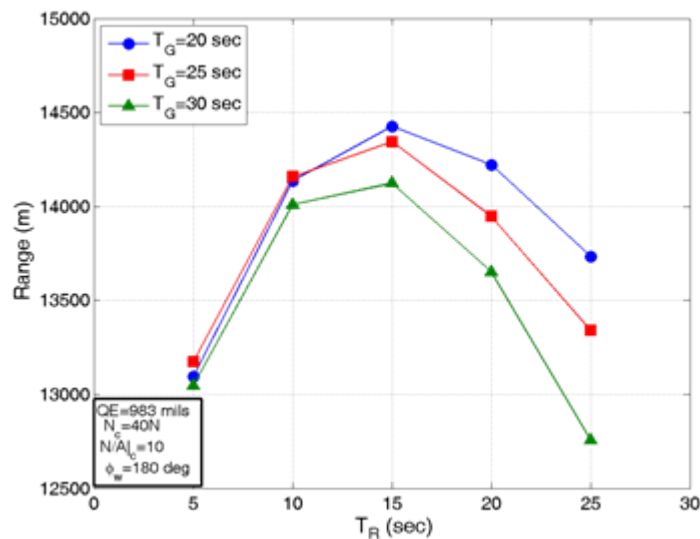
- 3000 m drift without GNC
- best combination of gains gets crossrange to zero without overcorrection and velocity heading along downrange axis ($K_p=50$, $K_D=50$).

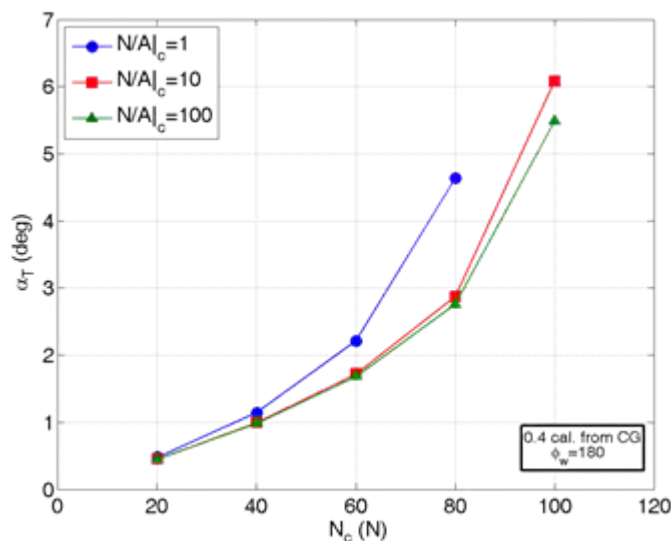
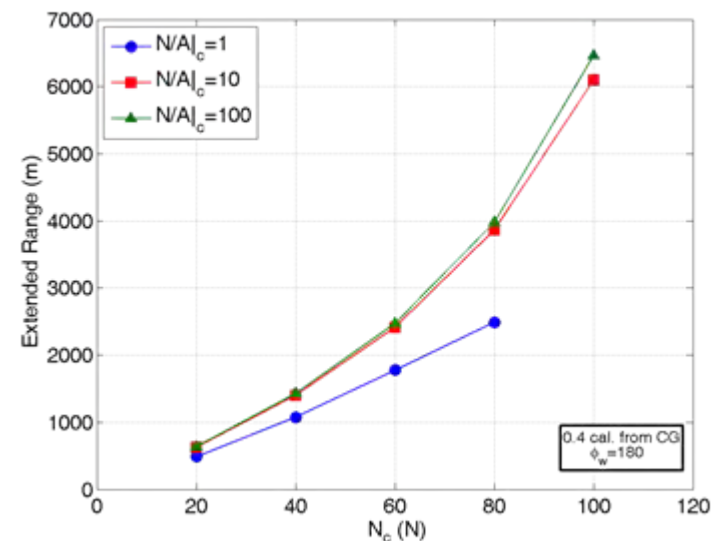
$QE = 883 \text{ mils}$
 $T_R = 13 \text{ sec}$
 $T_G = 29 \text{ sec}$
 $N_c = 40 \text{ N}$
 $N_c / A_c = 10$
 $X_c = 0.4 \text{ cal from CG}$
 $\phi_w = 180 \text{ deg}$
 $\text{static margin} = 0.96$



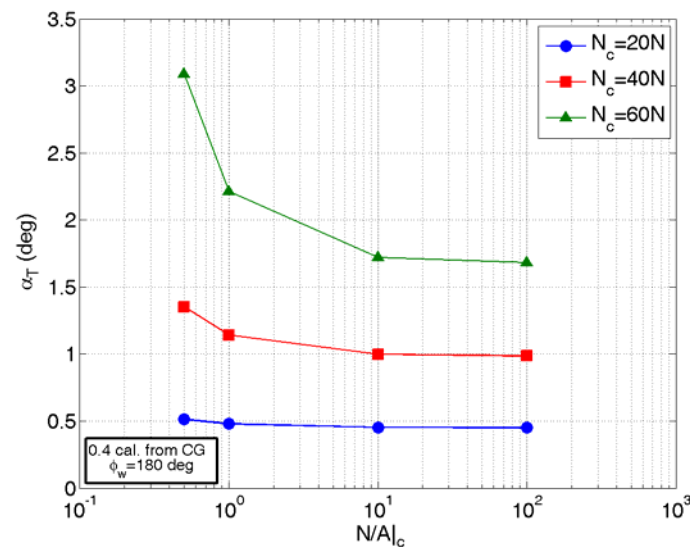
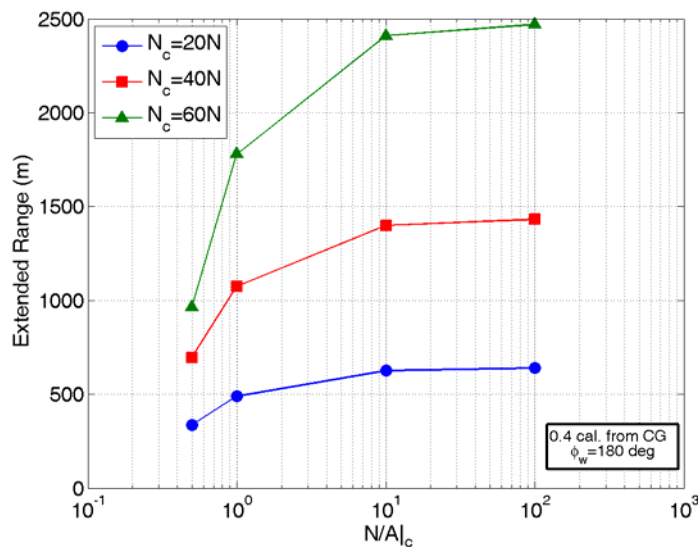


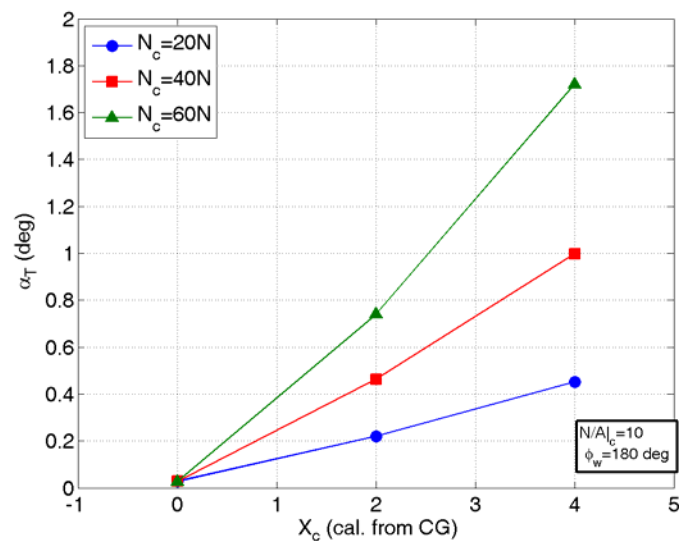
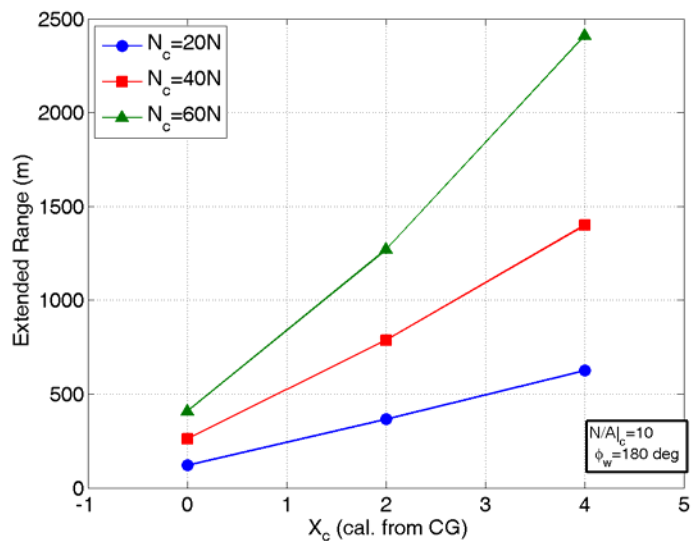
- optimize in parallel
- thrust/drag variation with atmospheric density for rocket ignition time
- lift/drag ratio of control mechanism for glide start time





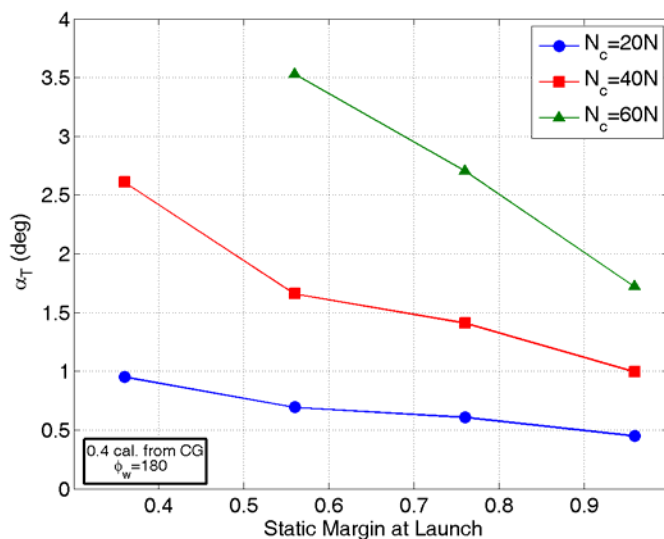
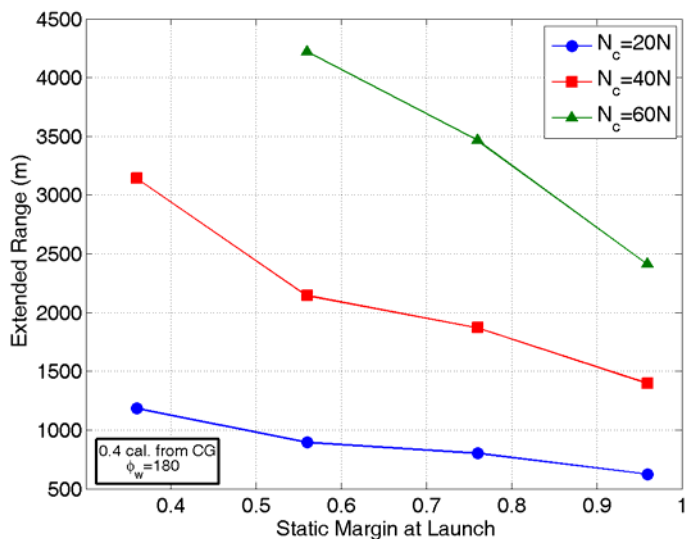
- asymptotic behavior for range increase
- more drag results in lower dynamic pressure which induces higher angle of attack to balance control moment



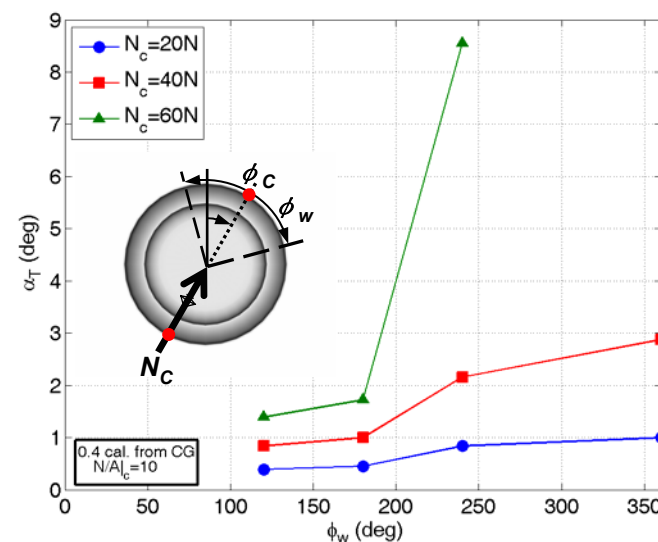
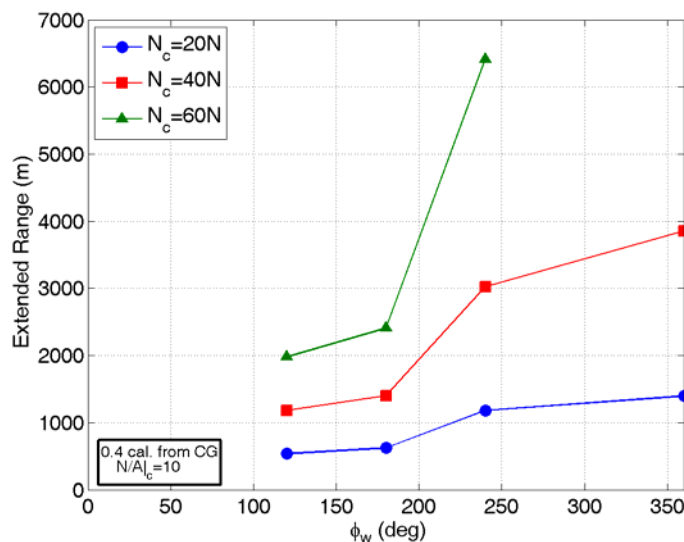


- range increases linearly with control moment arm

- lower static margin equals shorter moment arm for pitching moment to balance control moment



- adding more than one control element can significantly increase range



- Examined technical drivers to extending range of gun-launched precision munitions
 - fin-stabilized projectile with rocket motor and general control mechanism studied in six degree-of-freedom environment
 - Flight dynamics (projectile drift) required GNC algorithm development
 - maximize pitch angle and minimize yaw angle
 - Fire control parameters (QE, rocket ignition time, glide start time) must be optimized in parallel
 - Projectile configuration for maximum range: low static margin, large control normal force, control normal-to-axial force ratio of at least 10, control axial location at the nose, and large roll window

- Frank Fresconi, PhD
- U.S. Army Research Laboratory
- AMSRD-ARL-WM-BC, APG, MD 21005
- 410-306-0794



Malcolm Baldrige
National
Quality
Award
2007 Award
Recipient



TECHNOLOGY DRIVEN. WARFIGHTER FOCUSED.

Effects of Small Caliber Munitions Through Intermediate Barriers

September 2008

Chris Gandy & Jeremy Lucid – US Army - ARDEC

- Can fielded ammunition meet the needs of the war fighter?
- How well do 5.56mm projectiles penetrate automobiles?
- What are the penetration capabilities of small caliber ammunition against intermediate barriers?

Concrete Wall



Insurgent Vehicle



**This vehicle ran a checkpoint.
Could this have been prevented?**

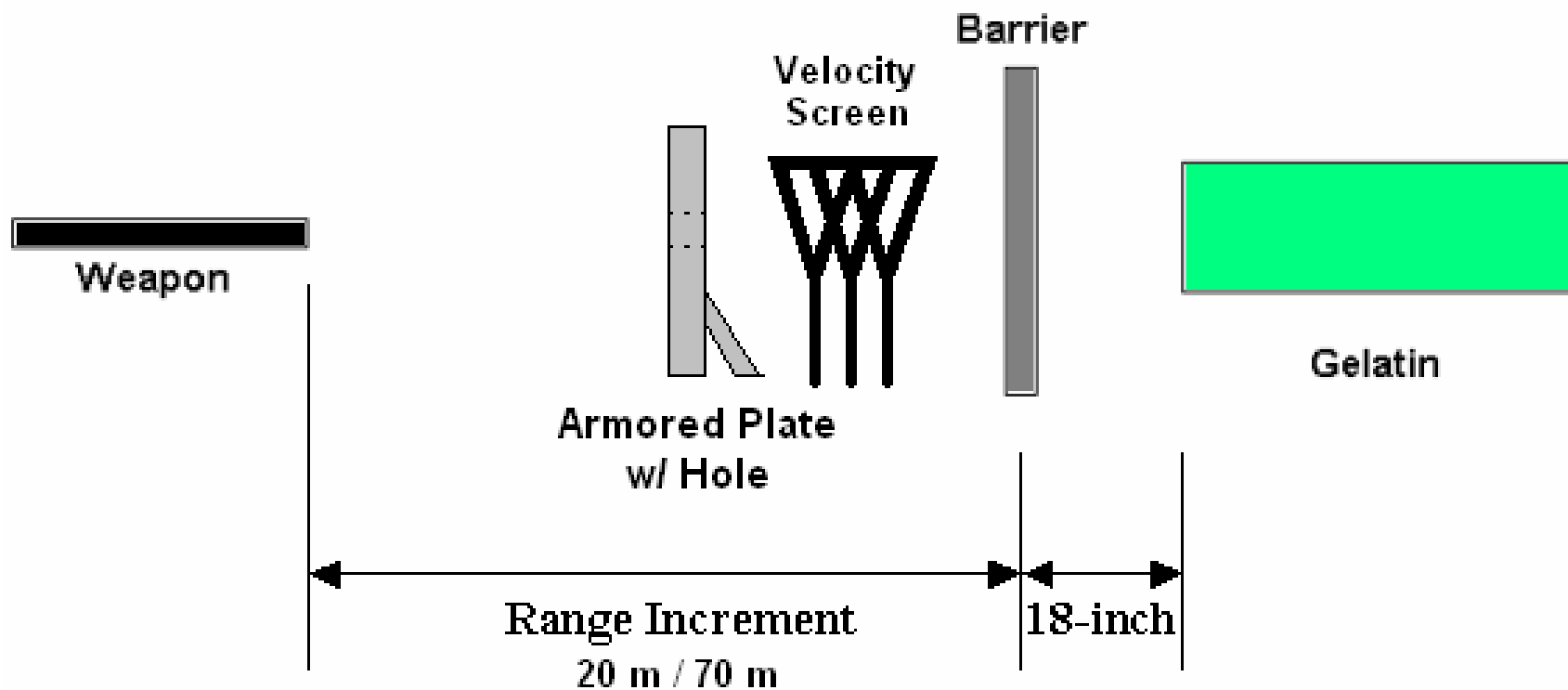
Vehicle Checkpoint



Lab Setup



Weapons → <u>Ammunition</u>	M16 (5.56mm)	M4 (5.56mm)	M240 (7.62mm)
M193 (5.56mm)	<u>Intermediate Barriers</u> <ul style="list-style-type: none"> • No Barrier (Baseline) • Windshields • Simulated Car Doors 		
M855 (5.56mm)			
MK262 (5.56mm)			
M80 (7.62mm)			



90° Steel Plates



45° Steel Plates



90° Windshield



45° Windshield

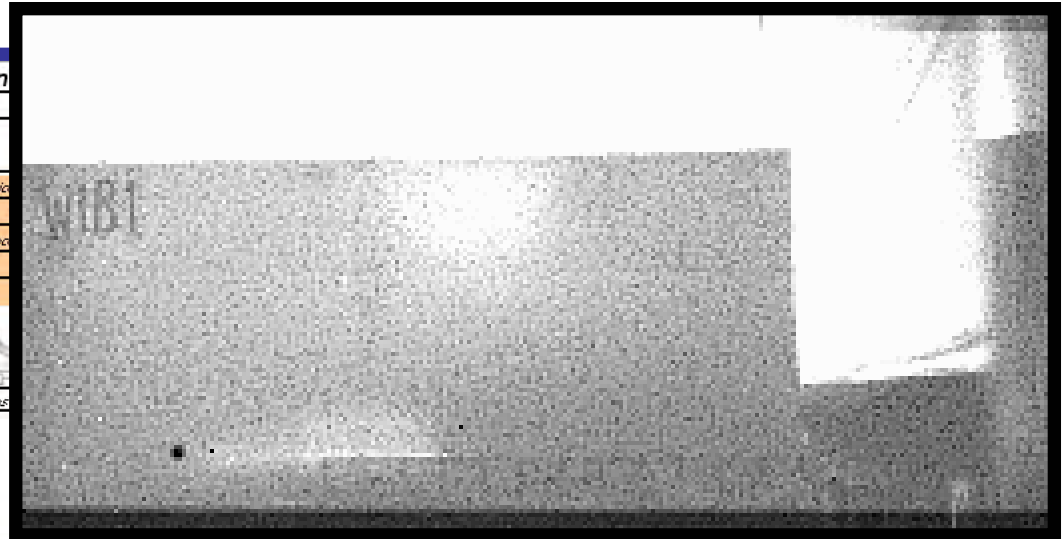


Ballistic Gelatin Test Data Collection			
Date of Manufacture	4-Jan-05	Personnel	Eli / Herb / Fred
Gelatin Block #	WIC-1	Block Density	11.0 %
Date of Shoot	11-Jan-05	Personnel	Jeremy / Chris
BB Validation Velocity	586 fps	Projectile Weight	62 grns
BB Validation Depth	3.25 in	Range	20.0 m
BB Validation Block Temp	39.1 degF	Impact Velocity	2723 fps
Date of Dissection	*****	Temp of Shot Block	*****
Block Weight	75 lb	Personnel	
Maximum Penetration Depth (1)	9. in	Dynamic MTCD*	
Penetration Depth to Largest (2)	7.5 in	Location of D-MTCD*	
Size of Largest Fragment (3)	0.46 in	Angle of attack at Impact*	
Weight of Largest (4)	8.8 grns		
Neck Length (5)	. in		
Significant Fracture Length (6)	7.25 in		
Fracture Profile Max Diam (7)	6. in		
FP Max Diam Location (8)	3.25 in		
Tot. Project. Wt. Recovered (9)	50.2 grns		

Note 1: Desired Depth Range for BB validation (10% mixing density) is 7.5 to 9.5cm (2-15/16 to 3-3/4in) @ 575 to 605 fps

Note 2: Items designated with an * are regarded as OPTIONAL characteristics to record.

Additional Notations:



➡ Recovered Projectile Parameters

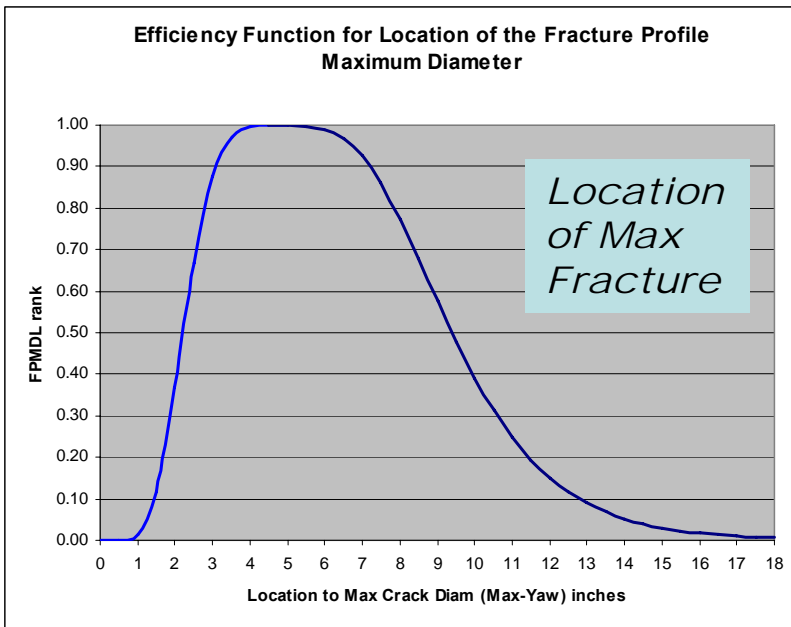
➡ High Speed Video

➡ Gelatin Damage Parameters

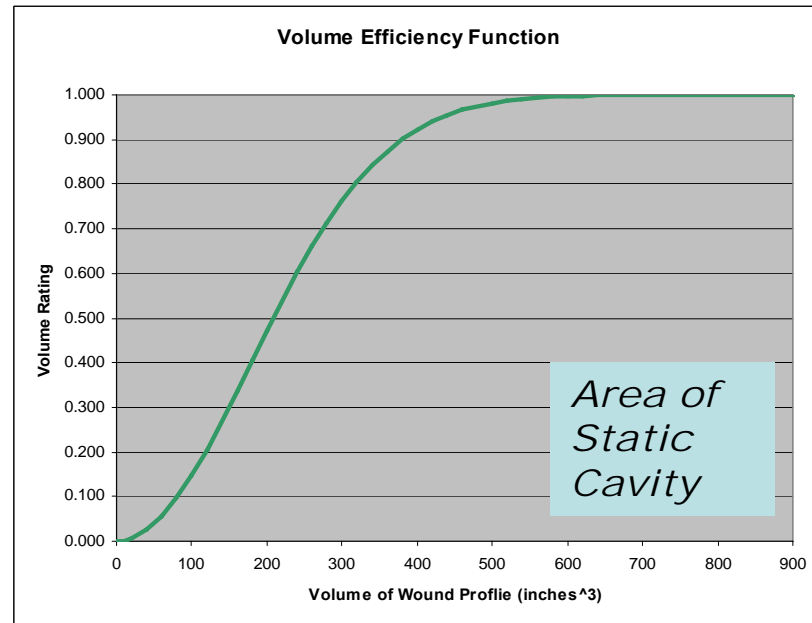
- Effective Damage Rating (EDR) is an abbreviated ranking system designed to quickly estimate the terminal performance of small caliber ammunition against human threats.
- Methodology is defined in Technical Report ARAET-TR-06013

- EDR values range from zero to one
 - (1) One is Good
 - (0) Zero is Bad
- There are four different EDR rankings
 - EDR-1 *Rapid Effects/ Location of Damage*
 - EDR-2 *Quantity of Potential Damage*
 - EDR-3 *Adequate Penetration*
 - EDR-4 *Potential Engagements of Vital Organs*
- Average of all four EDR values was used

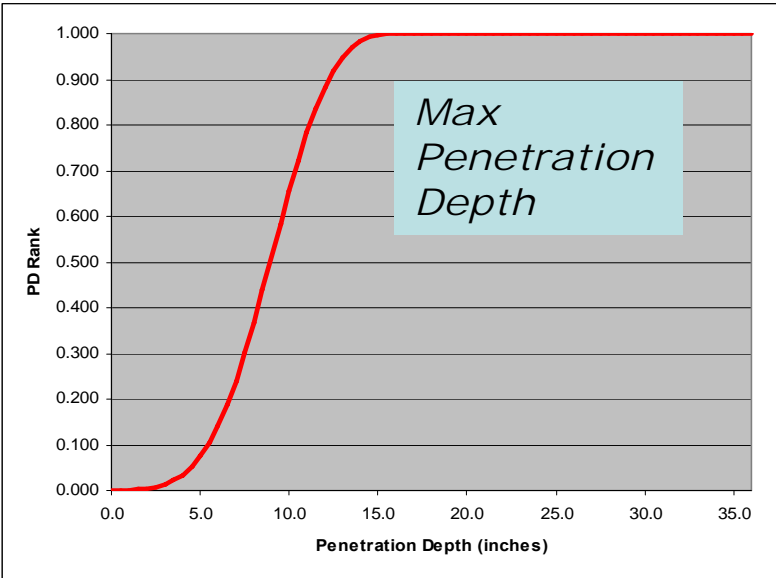
EDR-1 Rapid Effects/ Location of Damage ➡ **25%**



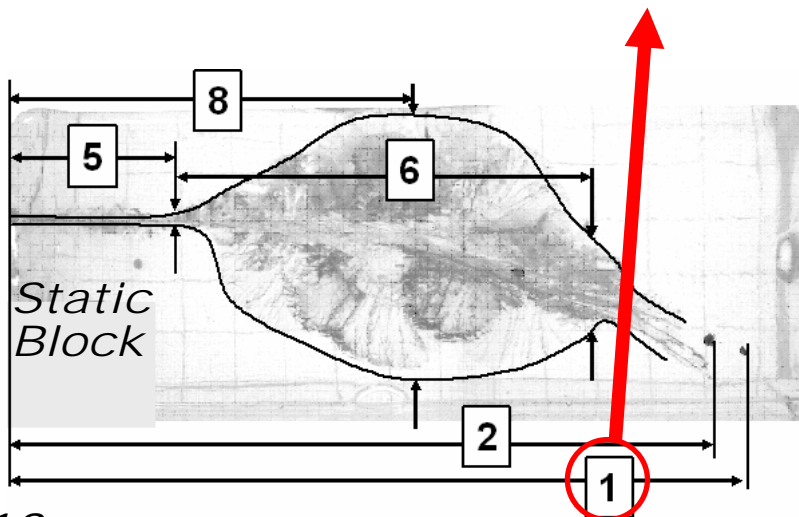
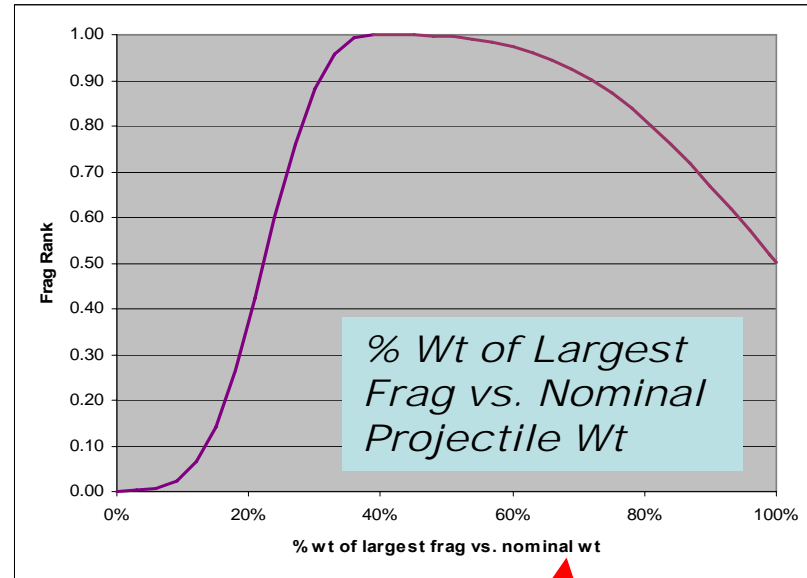
EDR-2 Quantity of Potential Damage ➡ **25%**



EDR-3 Adequate Penetration ➡ **25%**

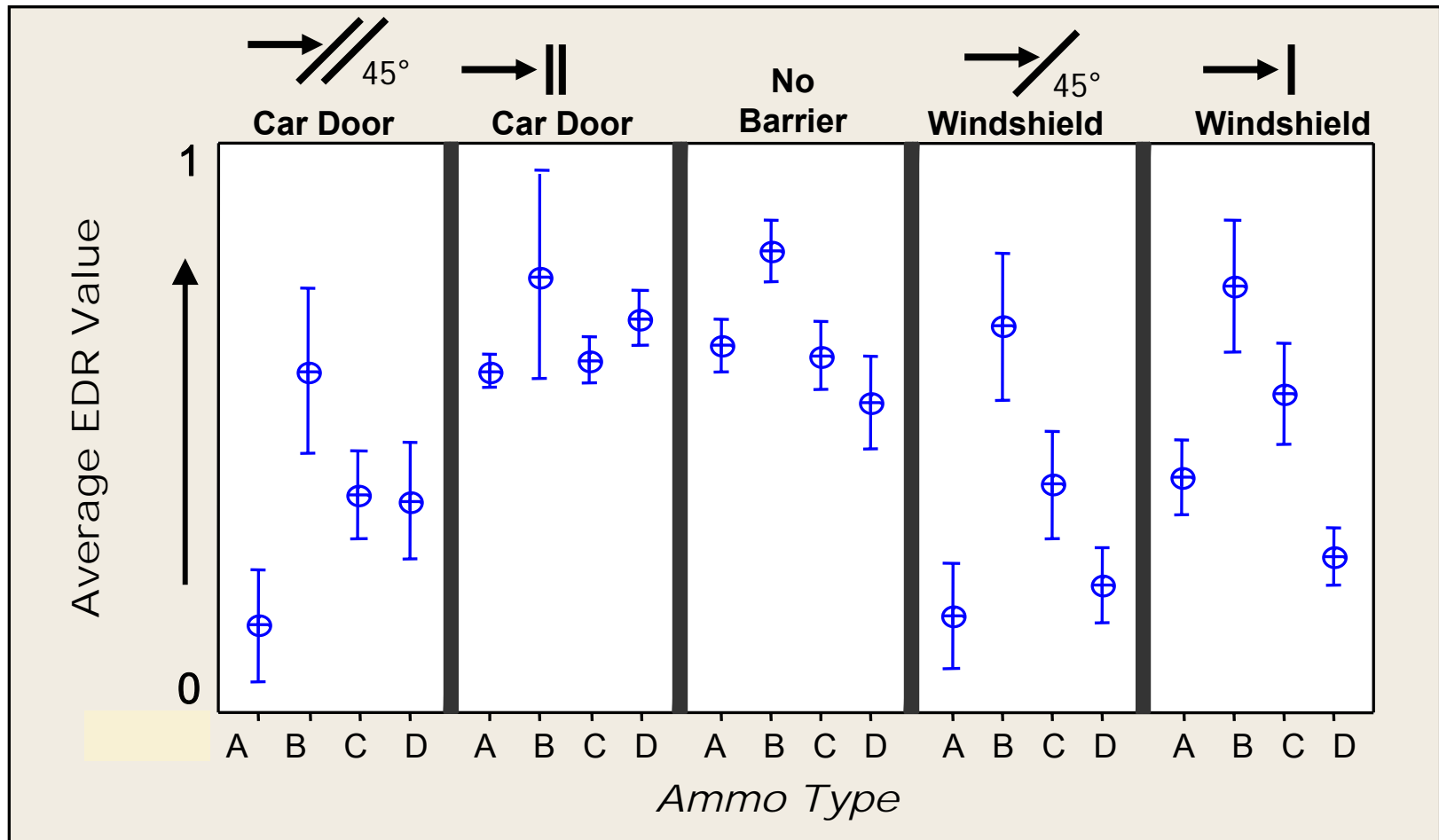


EDR-4 Potential Engagements of Vital Organs ➡ **25%**



Bullet Fragments

Average XYZ (Range: 20 m - 70 m)
95% CI for the Mean



Higher Average EDR Value = Better Post-Barrier Effectiveness

- Evaluate terminal effects of 1,600 rounds of 5.56mm & 7.62mm ammunition through:
 - Automobile windshields at steeper angles
 - Simulated truck doors w/ increased shell thickness
 - Concrete blocks
- Establish quick go/no gages for intermediate barriers to assist in assessing the threat



Weapons:

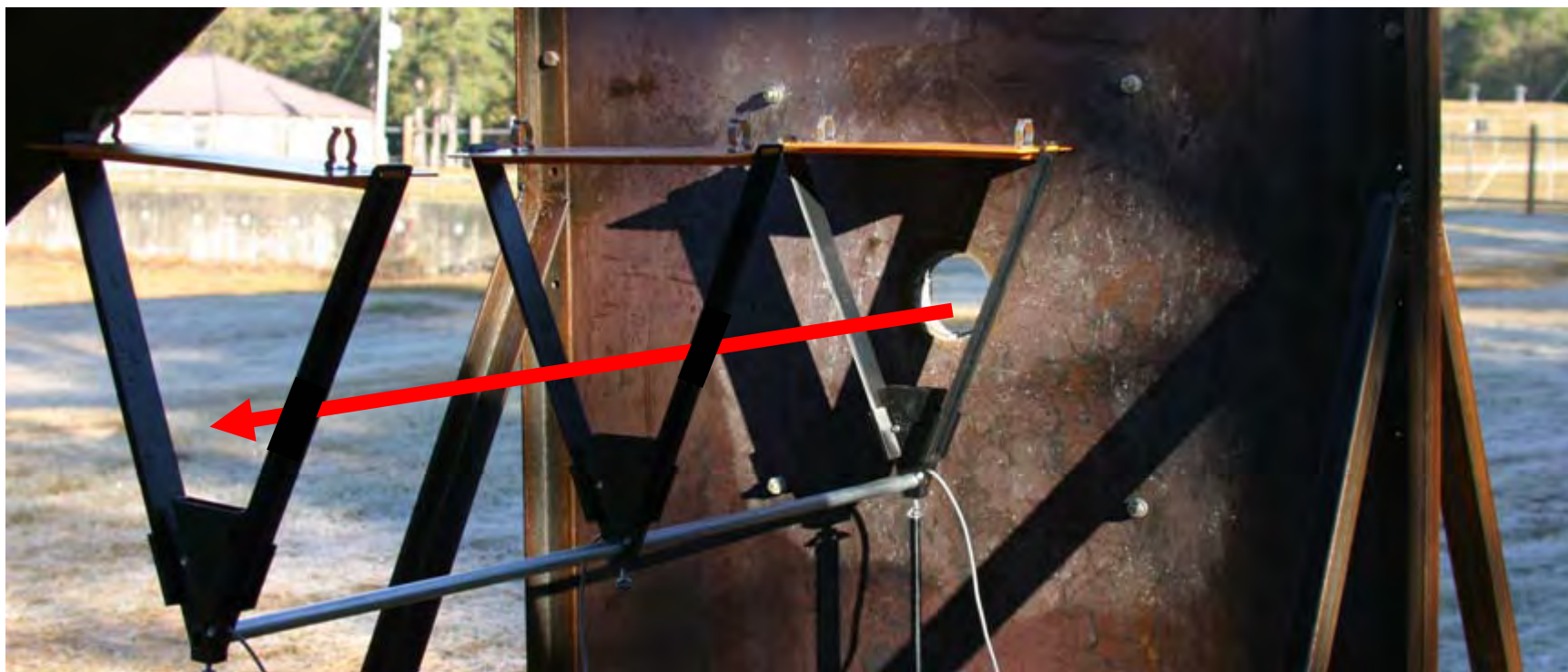
- M4
- M16
- M249
- M24
- M240

Ranges:

- 75m
- 200m

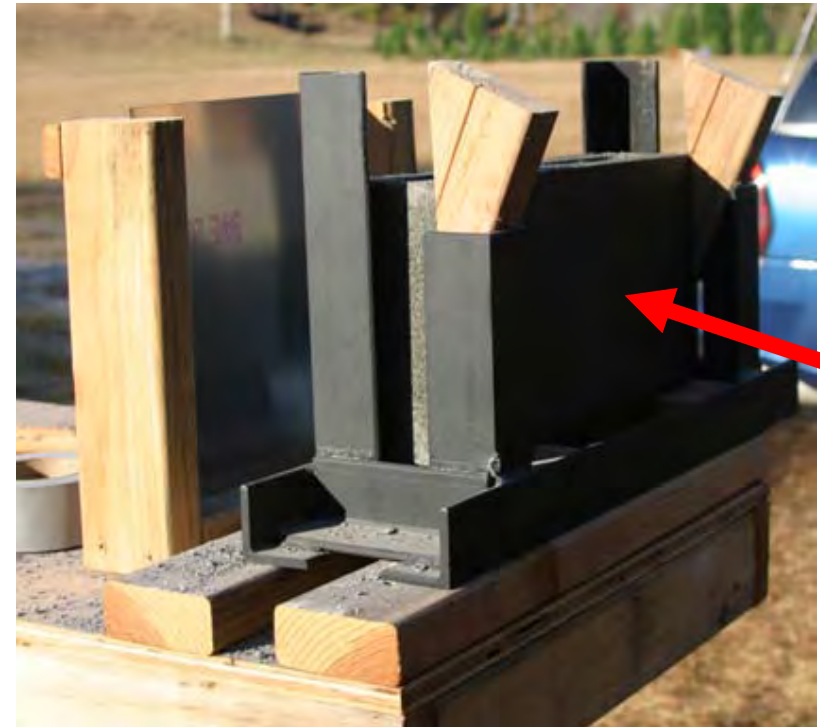
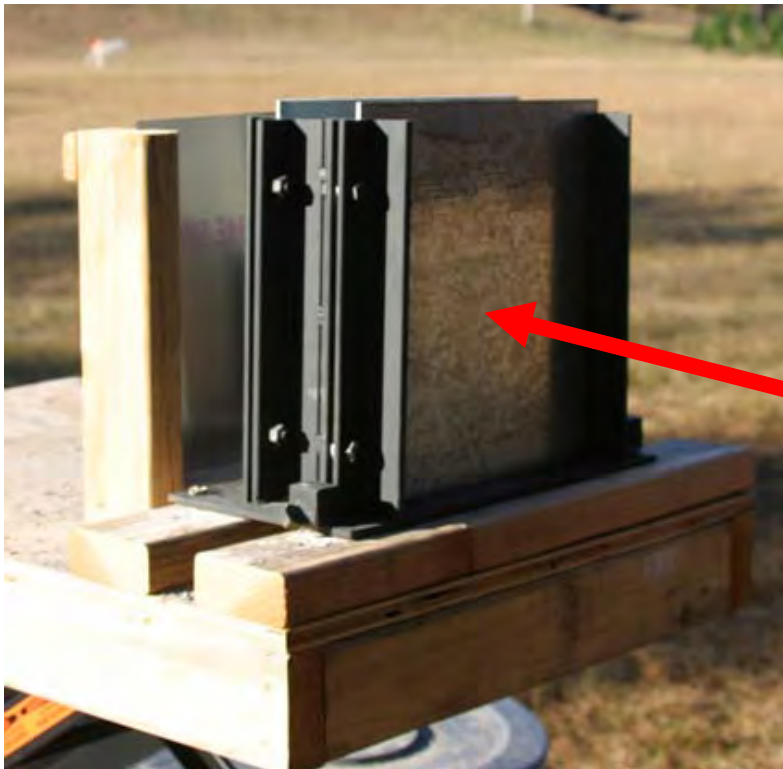
USAMU – Ft Benning

5.56mm Ammo	7.62mm Ammo
M193 M855 MK262 M995	M118LR M80

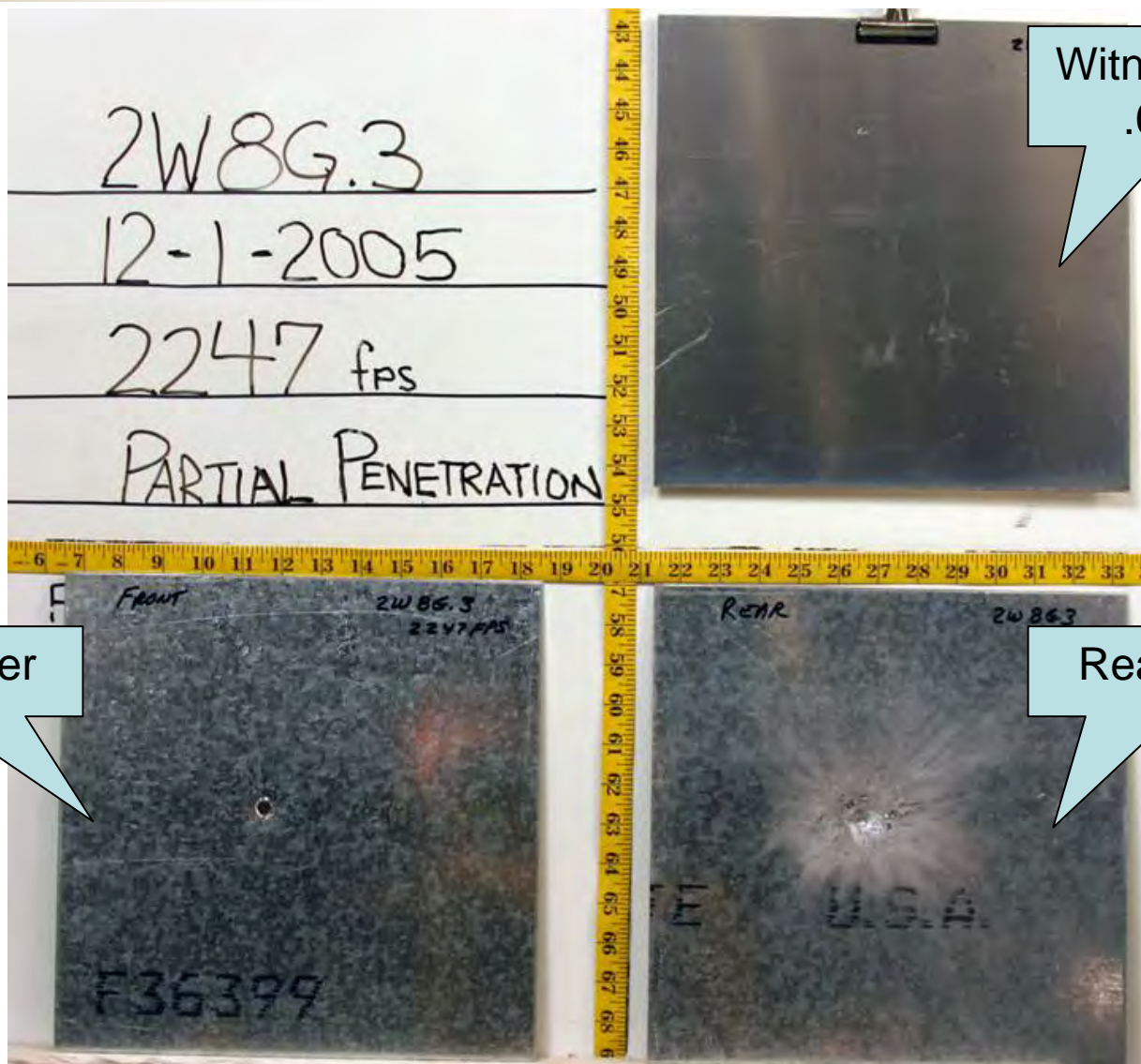




Concrete →



← *Steel*

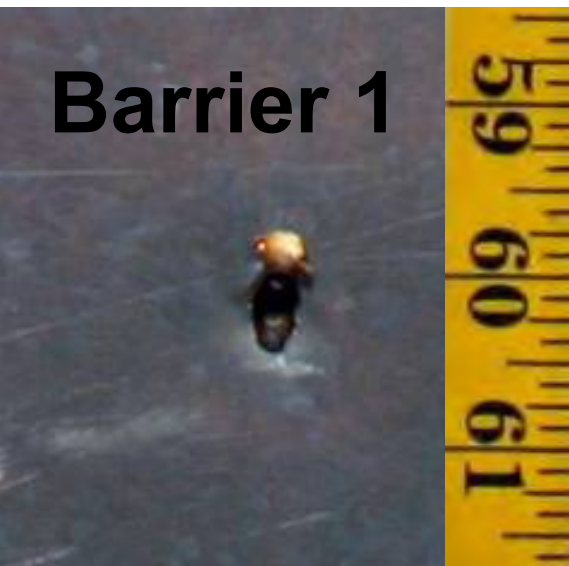


Witness Sheet
.020" Al

Front Barrier

Rear Barrier

Barrier 1



**Partial
Penetration**

**Witness
Plate 1**



Barrier 2

**Full
Penetration**

**Witness
Plate 2**



RND XYZ - XX grain

Weapon/ Range	Windshield	Heavy Truck Door		Concrete Façade	
	Worst Case	Head On	Angle	4" Hollow	4" Filled
Gun 1 - Range 1	1	1	2	1	2
Gun 1 - Range 2	1	2	2	2	3
Gun 2 - Range 1	1	2	2	1	2
Gun 2 - Range 2	1	2	2	1	3

1

Full Penetration - Minimum # of Shots Required to Penetrate Barrier
(80% of the rounds fired were able to penetrate the barrier on the first shot)

2

Partial Penetration - Multiple Shots Required To Penetrate Barrier

3

No Penetration - Maximum # of Shots Required To Penetrate Barrier
(80% of the rounds fired were unable to penetrate the barrier on the first shot)

*Quick assessment of penetration capability
across multiple barriers and ranges.*

- Provided a quick assessment of currently fielded ammunition
- Determined effectiveness through light intermediate barriers found in field
- Compiled all data for future testing and modeling efforts
- Technical Report ARAET-TR-07030

Requests for this document:

U.S. Army ARDEC

ATTN: AMSRD-AAR-EMK

Picatinny Arsenal, NJ 07806-5000

Questions?

Chris Gandy – chris.gandy@us.army.mil

Jeremy Lucid – jeremy.lucid@us.army.mil



Fragment Penetration Modeling of Anthropometric Ballistic Mannequins

24th International Symposium on Ballistics
22 - 26 September 2008

Presented by: Patrick Gillich

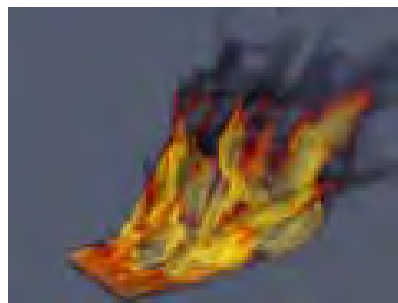


TECHNOLOGY DRIVEN. WARFIGHTER FOCUSED.

William Bruchey
Survive Engineering Company, Belcamp, MD

Amy Tank
U.S. Army Research Laboratory, APG, MD

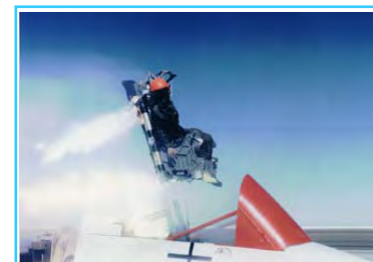
ORCA Model An Integrated Methodology for Survivability Assessment



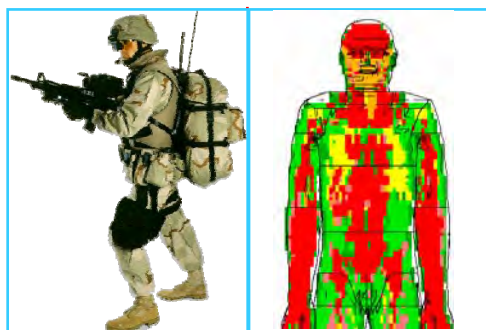
BURNSIM - THERMAL
(U.S. Air Force Research Laboratory)



INJURY - BLAST OVERPRESSURE
(U.S. Army Medical Research and Materiel Command)

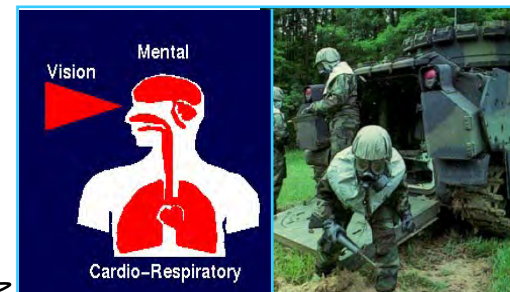


AMANDA - ACCELERATION
(U.S. Army Aeromedical Research Laboratory)



COMPUTERMAN
(U.S. Army Research Laboratory)

**Operational
Requirement-based
Casualty
Assessment**



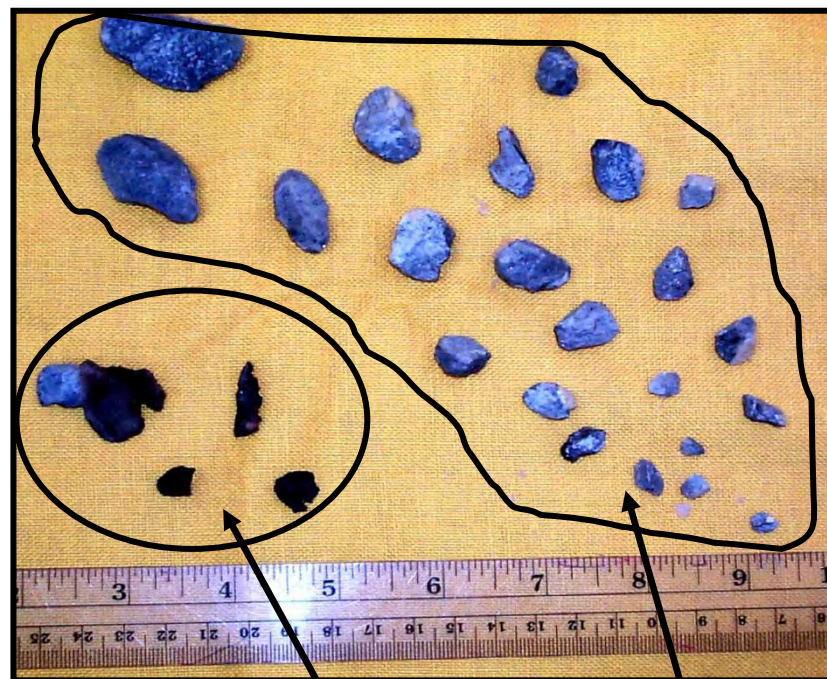
CHEMICAL MAN
(U.S. Army Research Laboratory)

- **Standard Injury Description**
- **Standard Military Task Inputs**
- **Common Integrated Crew Casualty Assessment Methodology**

Debris cloud from warhead impact



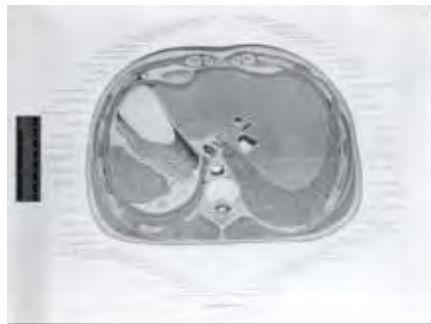
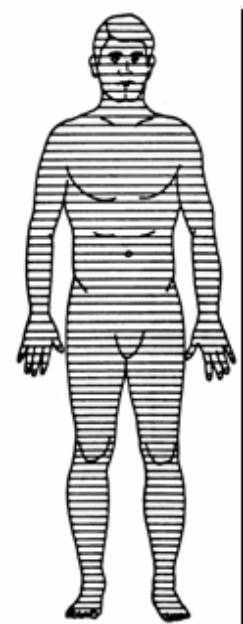
Recovered steel warhead fragments and aggregate debris



Steel fragments
Mass: 0.13g - 8g

Aggregate (stone)
Mass: 0.05g - 9g

3-D Anatomical Man



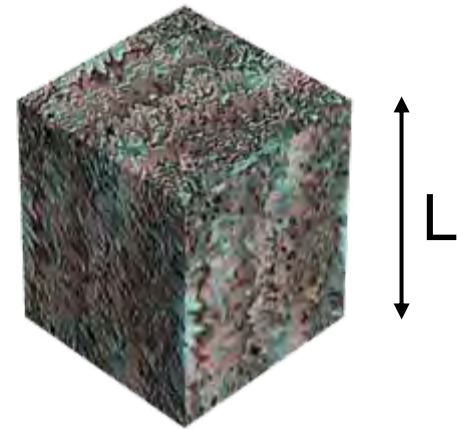
Plywood Mannequin



Wound Ballistics Modeling:

- Input : Mass, Velocity, Shape Factor , Entry & Exit Points
- Data Source: Plywood Penetration & Ballistic Gel Retardation
- Output : Expected Incapacitation (EI) of a Soldier

- Shape: Cube, Natural Aggregate
- Mass: 0.1g – 41g
- Size (Length): 0.22cm – 1.75cm
- Materials**
 - Steel
 - Aluminum
 - Aggregate
 - Granite
- Velocity: 150m/s – 1000m/s

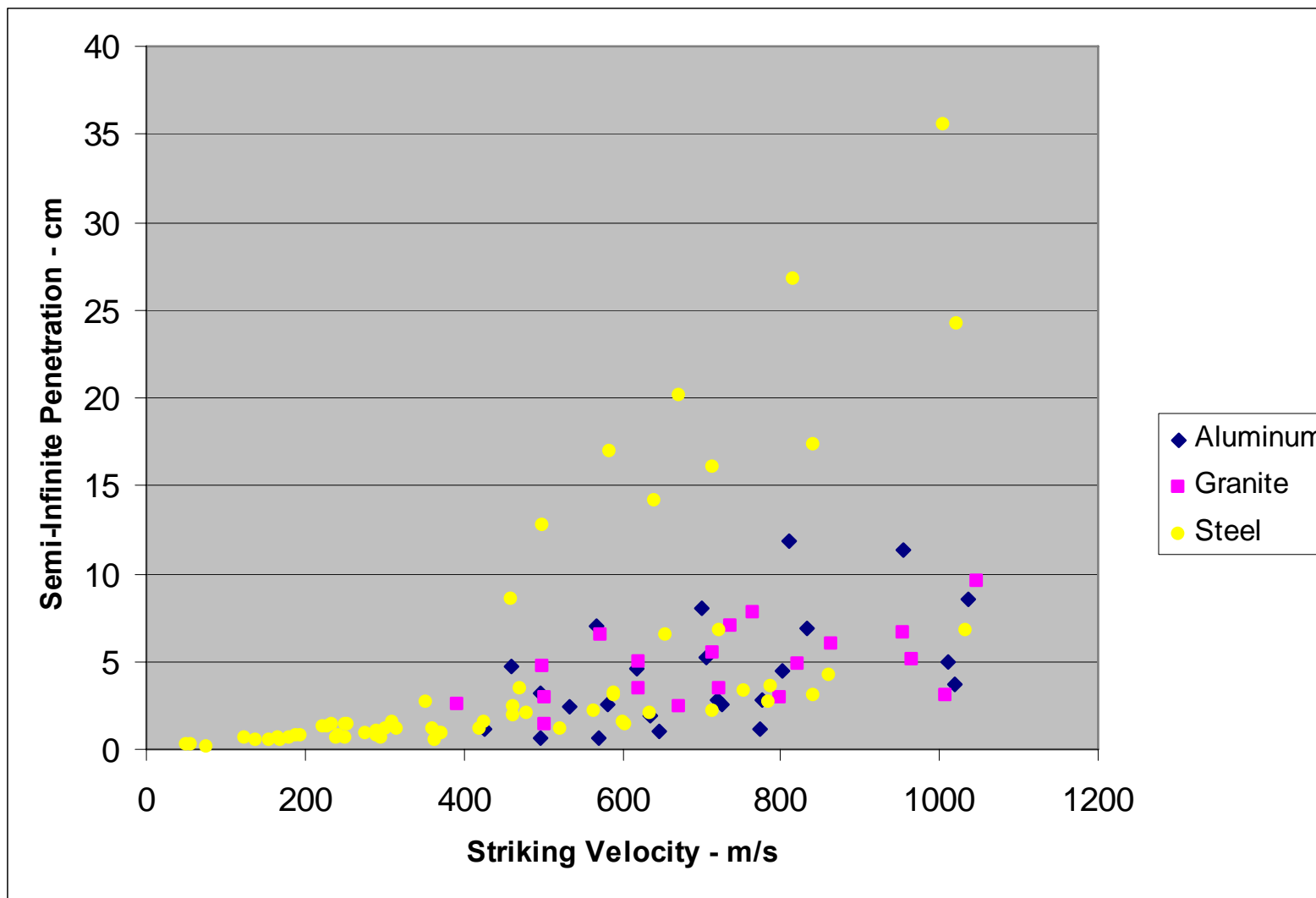


**Note: All projectiles penetrated as rigid bodies

- Material: $\frac{3}{4}$ in Marine Grade Plywood
- Density: 0.35 g/cc
- Configuration
 - Semi-infinite stack, i.e. semi-infinite target
 - Single layer, i.e. finite target
- Obliquity
 - Semi-infinite, 0° obliquity
 - Finite, 0° and 60° obliquity

Semi-Infinite Penetration (All Cubes)

Raw Data – Aluminum, Granite, and Steel



After Tate and Alekseevskii:

$$\dot{L} = V - U \quad (\text{erosion kinematics})$$

$$L \dot{U} = -Y/r_r \quad (\text{rod deceleration})$$

$$\frac{1}{2} r_r (U - V)^2 + Y = \frac{1}{2} r_t + R \quad (\text{interface stress balance})$$

“Approaches to Penetration Problems”, T. Wright, K. Frank, U.S. Army Ballistic Research Laboratory, TR-2957, December 1988

For Fragment Penetration of Plywood:

- $V - U = 0$
- $R > Y$

Differential Form of Penetration Equation:

$$-mv(dv/dx) = \frac{1}{2} rbAv^2 + sA$$

where: $r = 0.35 \text{ g/cc}$

$s = \text{strength of plywood, dynes/cm}^2$

$A = \text{Average Presented Area of Fragment, (cm}^2\text{)}$

$v = \text{striking velocity, cm/sec}$

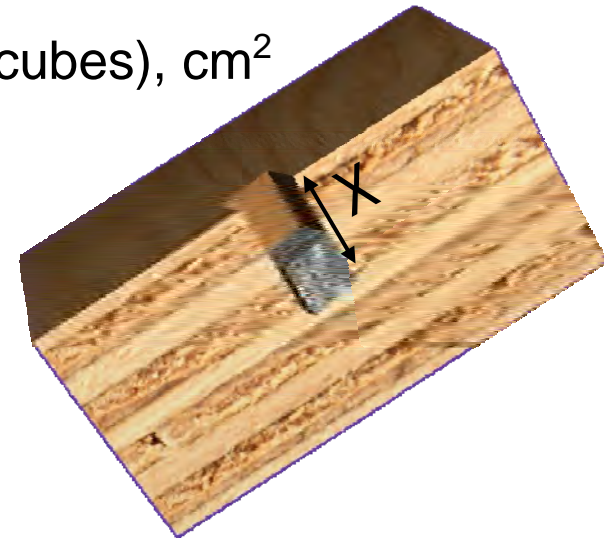
$m = \text{fragment mass, g}$

$X = \text{plywood penetration depth, cm}$

$a = A/m$

$g = \frac{1}{2} r$

$b = \text{Shape Factor}$



Integrating the above equation for v and x :

$$X = \frac{-1}{2} \cdot \frac{\ln(\sigma) - \ln(v_0^2 \cdot \gamma \cdot \beta + \sigma)}{\alpha \cdot \gamma \cdot \beta}$$

Solution requires determination of two unknowns: b, s (optimized over all fragment masses, areas, and densities => NLLS solution for b, s)

Number of Data Points: 105

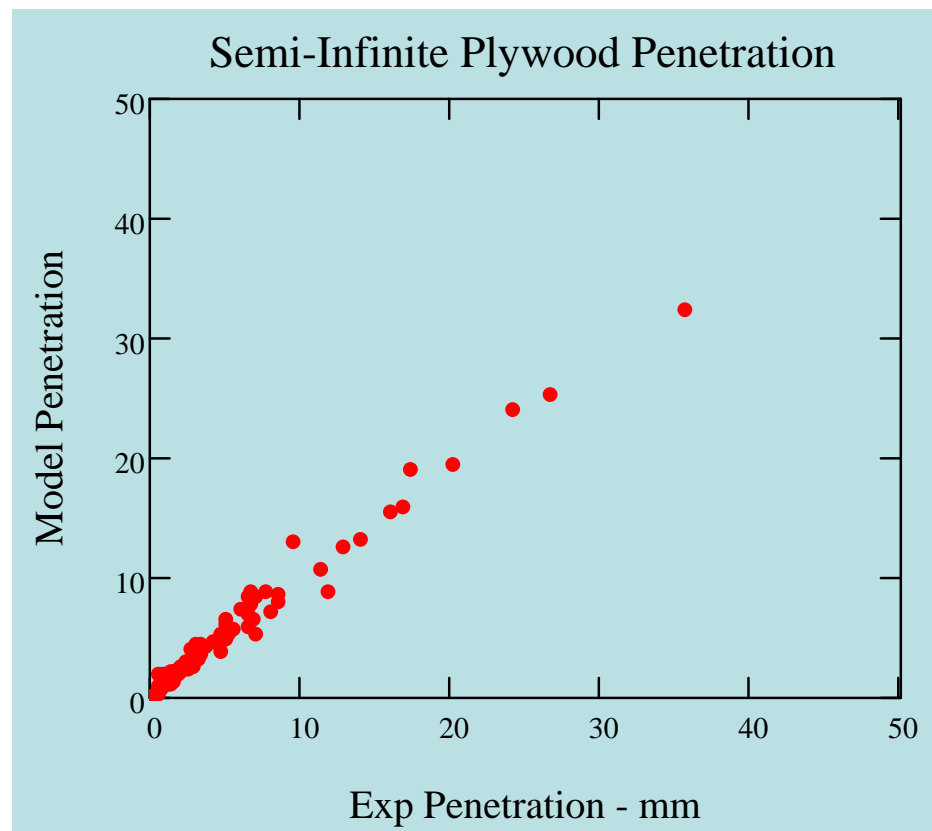
Average Miss Distance (average of all $(x_{\text{pred}} - x_{\text{obs}})$): -0.253 mm

$b = 1.014$

$s = 7.007 \times 10^8 \text{ dynes/cm}^2$

$$X = \frac{-1}{2} \cdot \frac{\ln(\sigma) - \ln(v_0^2 \cdot \gamma \cdot \beta + \sigma)}{\alpha \cdot \gamma \cdot \beta}$$

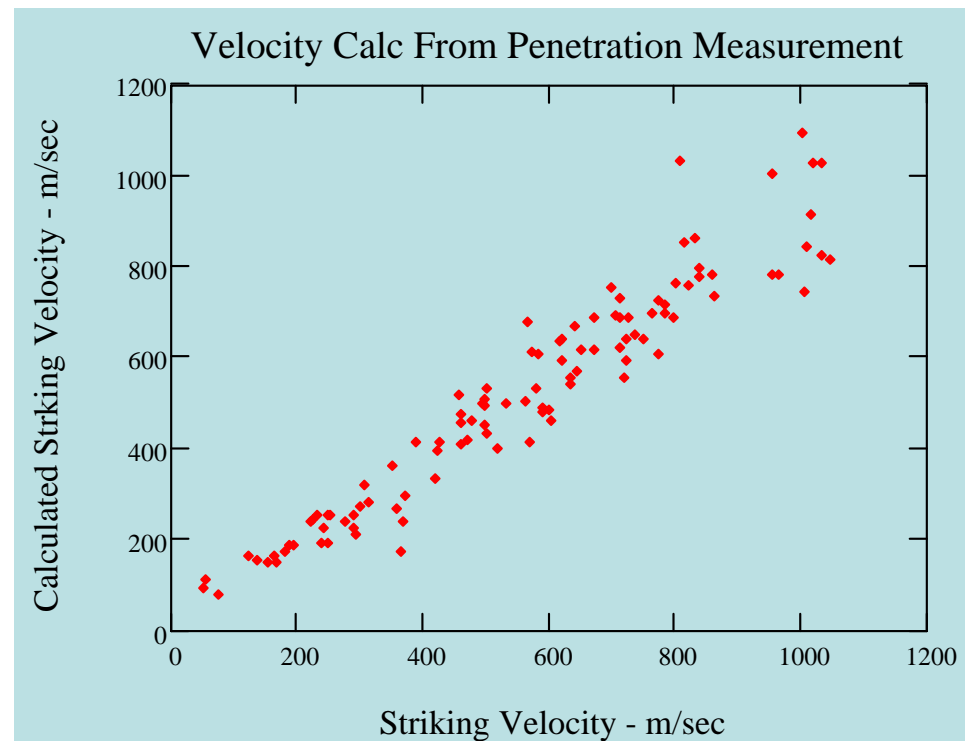
Indicates how well penetration is predicted for any fragment at a given striking velocity.



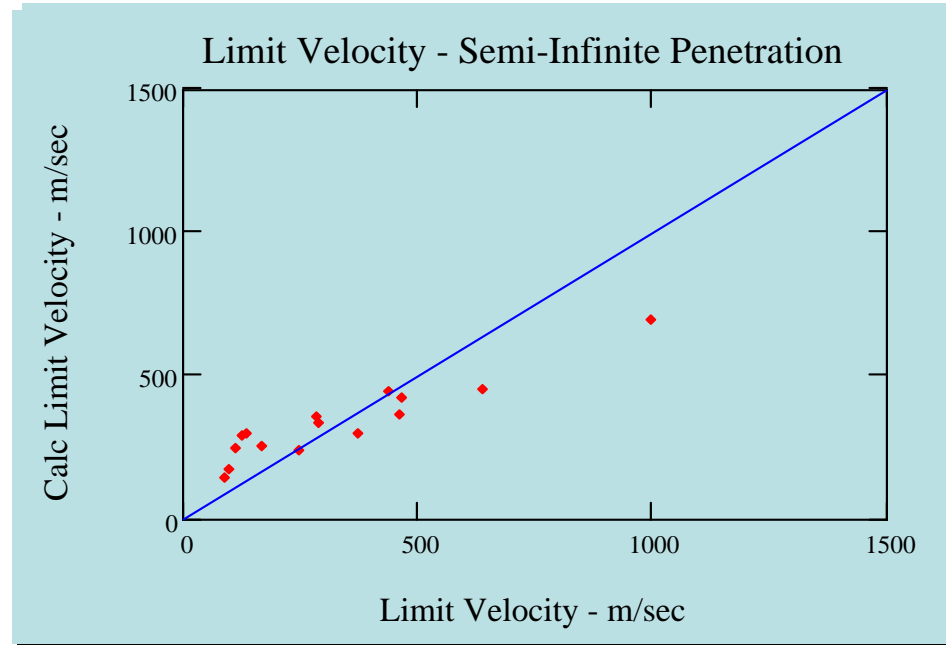
$$V_s = \frac{1}{e^{(-2) \cdot x \cdot \alpha \cdot \gamma \cdot \beta} \cdot \gamma \cdot \beta} \cdot \left[\left[-e^{(-2) \cdot x \cdot \alpha \cdot \gamma \cdot \beta} \right] \cdot \gamma \cdot \beta \cdot \sigma \cdot \left[e^{(-2) \cdot x \cdot \alpha \cdot \gamma \cdot \beta} - 1 \right] \right]^{\frac{1}{2}}$$

$$b = 1.014$$

$$s = 7.007 \times 10^8 \text{ dynes/cm}^2$$

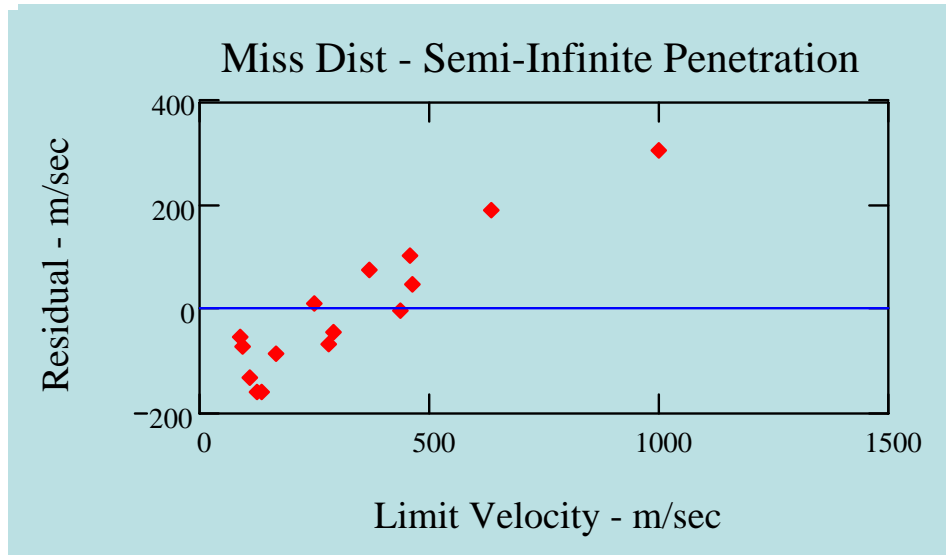


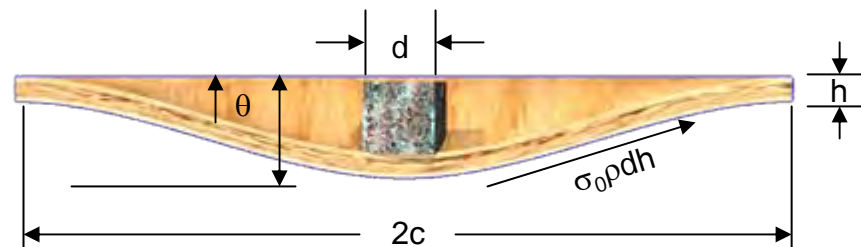
- Assume no finite target effect, i.e. limit velocity equals velocity needed to penetrate 3/4-in into semi-infinite plywood



- Analysis of residuals show linear trend → finite thickness effect

$$* \text{Residual} = (X_{\text{observed}} - X_{\text{predicted}})$$





$$mv \cdot \frac{dv}{dx} = \sigma_0 \cdot \pi \cdot d \cdot h \cdot \frac{x}{c}$$

$$\int_{v_f}^0 v \, dv = \int_0^x -\sigma_0 \cdot \pi \cdot d \cdot h \cdot \frac{x}{c \cdot m} \, dx$$

$$v_f^2 = x^2 \cdot \sigma_0 \cdot \pi \cdot d \cdot \frac{h}{c \cdot m}$$

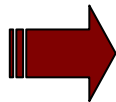
$$\rightarrow v_f \sim (A_p/m)^{1/2}$$

"The Limit Velocity of Fragments Impacting Lightweight Armor Materials: An Ad Hoc Model", W. Bruchey, BRL MR-2677, Sep 1976

Assume:

- Initial penetration is given by semi-infinite penetration analysis
- At some thickness $< \frac{3}{4}$ -in, the plywood fails and acts as if it is a membrane
- Membrane analysis shows that the failure velocity is proportional to $(A_p/m)^{1/2}$

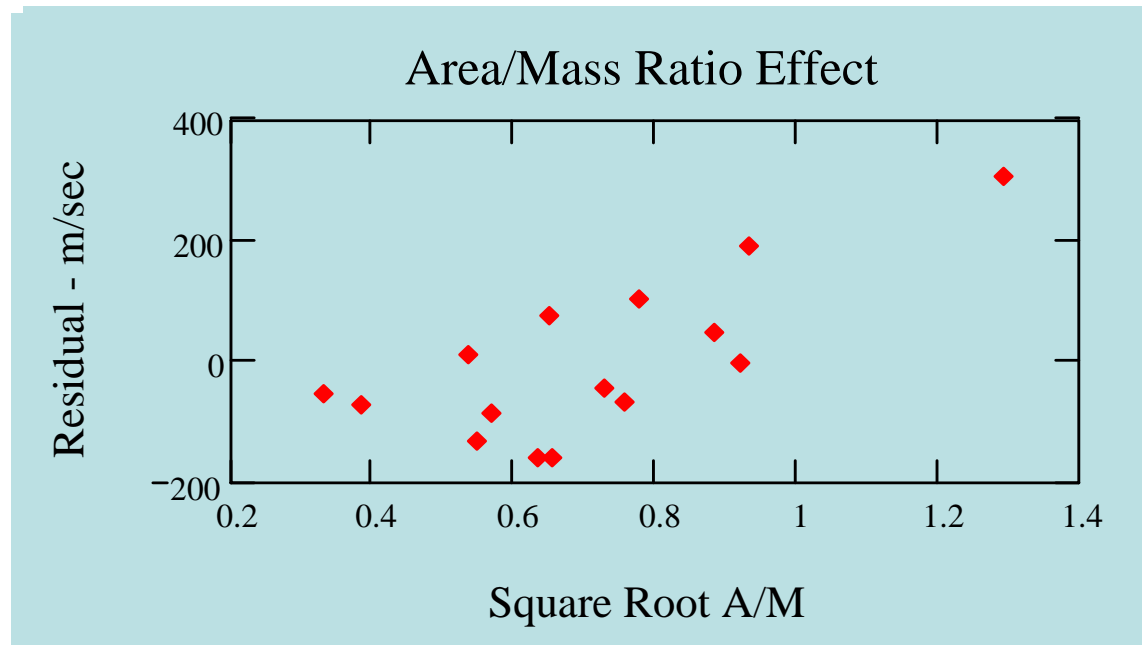
Linear relationship



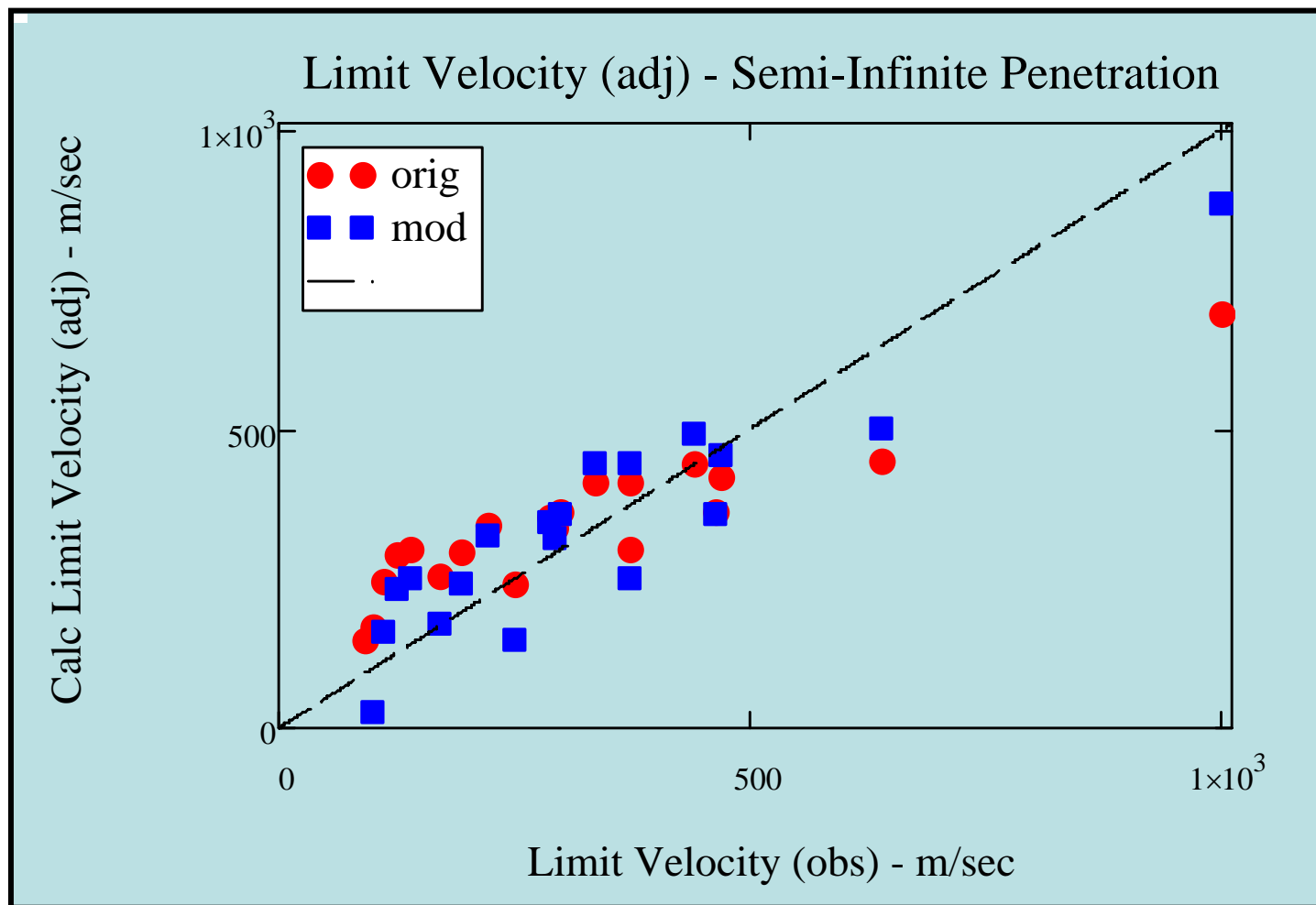
$$\text{Residual} = a + b(A_p/m)^{1/2}$$

$$a = -2.846 * 10^4$$

$$b = 3.601 * 10^4$$



Calculated Limit Velocity with Adjustment for finite thickness
versus the Observed Limit Velocity



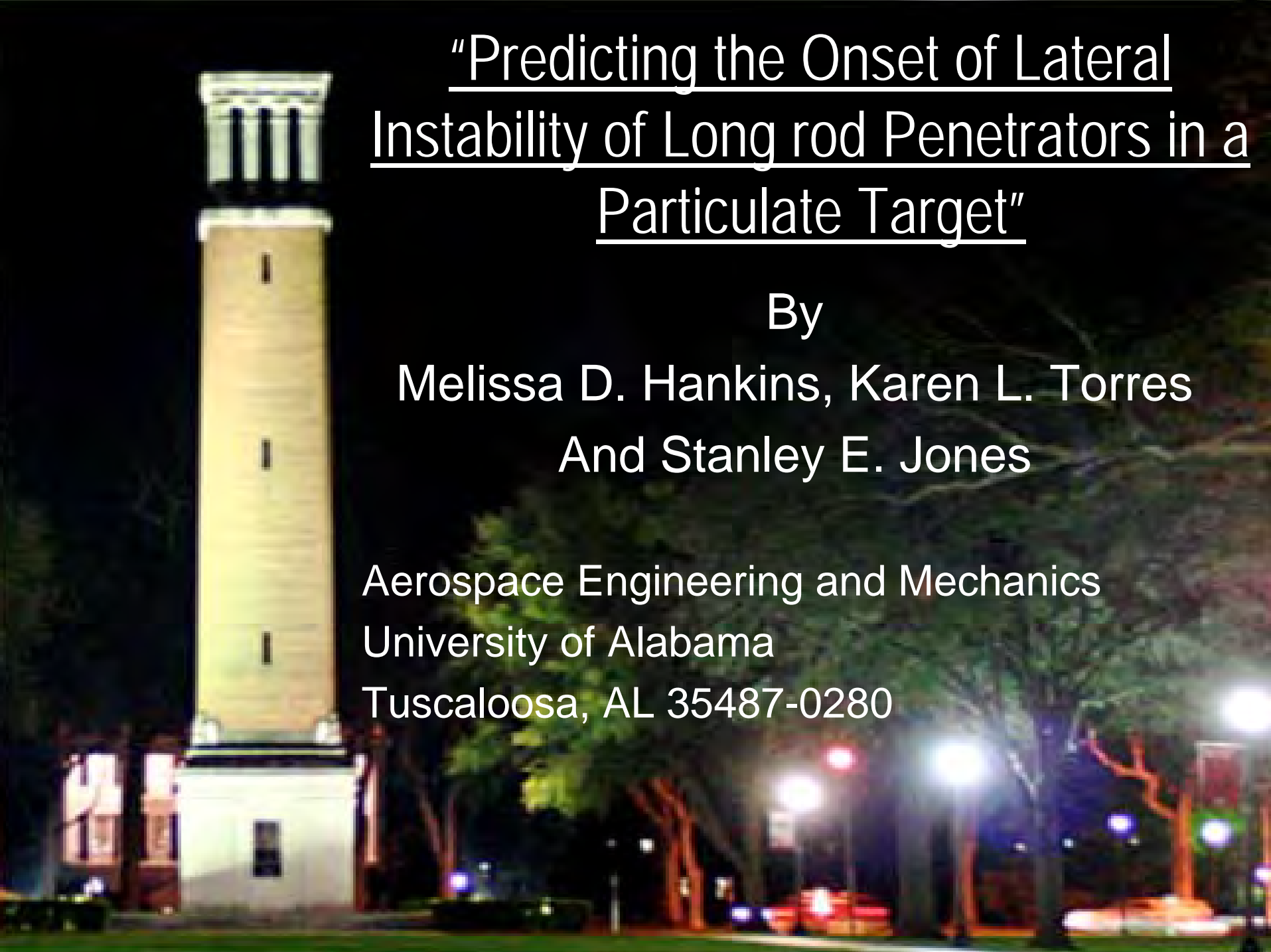
This model provides an estimate of fragment penetration into semi-infinite stacks of marine-grade plywood. Limit velocities can be estimated from semi-infinite penetration utilizing a correction factor for finite target breakout effects.

Resulting Equations:

- Semi- Infinite

$$V_s = \frac{1}{e^{(-2) \cdot x \cdot \alpha \cdot \gamma \cdot \beta} \cdot \gamma \cdot \beta} \cdot \left[\left[-e^{(-2) \cdot x \cdot \alpha \cdot \gamma \cdot \beta} \right] \cdot \gamma \cdot \beta \cdot \sigma \cdot \left[e^{(-2) \cdot x \cdot \alpha \cdot \gamma \cdot \beta} - 1 \right] \right]^{\frac{1}{2}}$$

- Finite (3/4-in Marine Plywood)
Semi- Infinite solution plus breakout correction
 $a + b(A_p/m)^{1/2}$

The background of the slide is a photograph of a tall, white, cylindrical tower with a classical-style top, illuminated at night. The tower is part of a larger building complex, with other structures and trees visible in the background under city lights.

"Predicting the Onset of Lateral Instability of Long rod Penetrators in a Particulate Target"

By

Melissa D. Hankins, Karen L. Torres
And Stanley E. Jones

Aerospace Engineering and Mechanics
University of Alabama
Tuscaloosa, AL 35487-0280



Topics

- The Instability Problem
- Laboratory Scale Testing
- Normal Penetration of Particulate Targets
- Formulation and Solution of the Problem
- Results
- Conclusions and Future Work

The Instability Problem

Penetrator Material: High Strength Steel

Penetrator Material: 12.7 mm

Target: Remolded Eglin Sand

Impact Velocity: 1525 m/sec



As recovered

Unfired

Penetrator Material: 6061-T6 Aluminum

Penetrator Material: 4.17 mm

Target: Alumina Powder

Impact Velocity: 696 m/sec

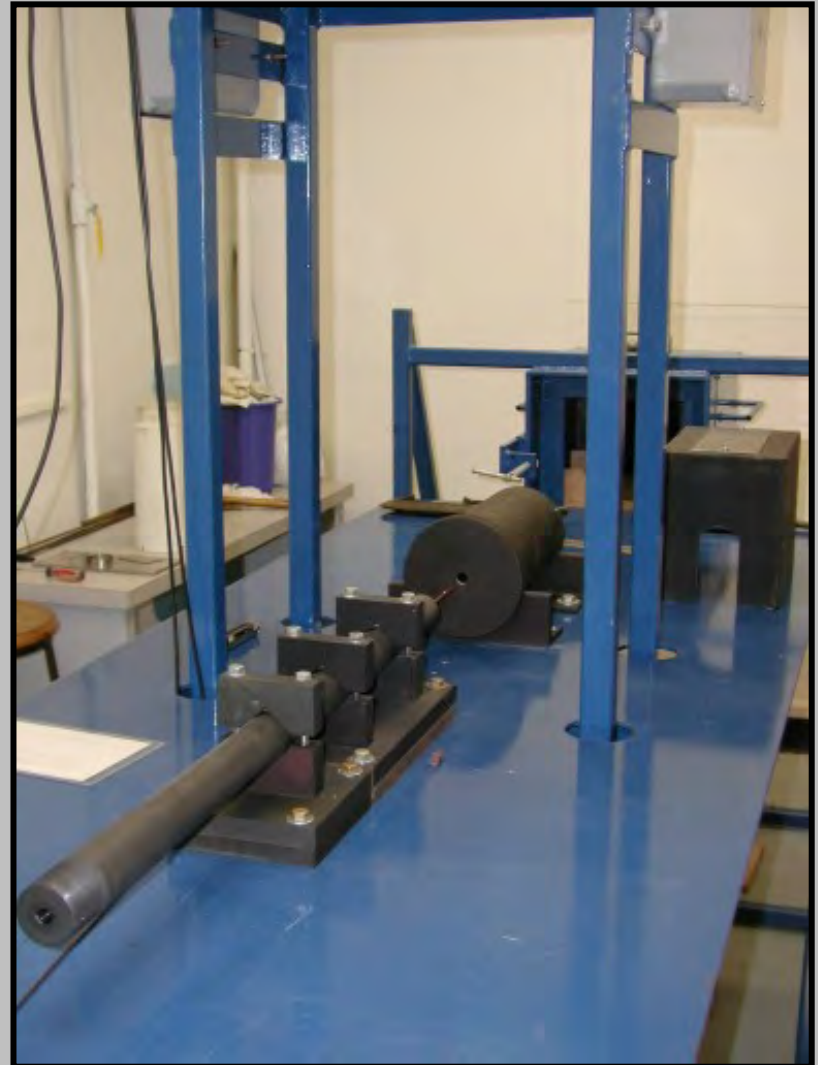
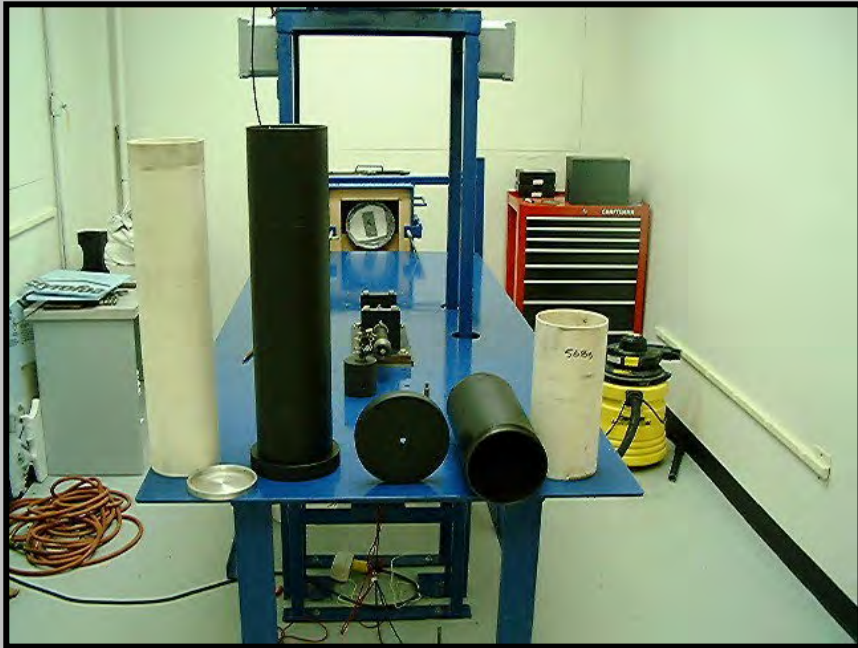


As recovered

Unfired

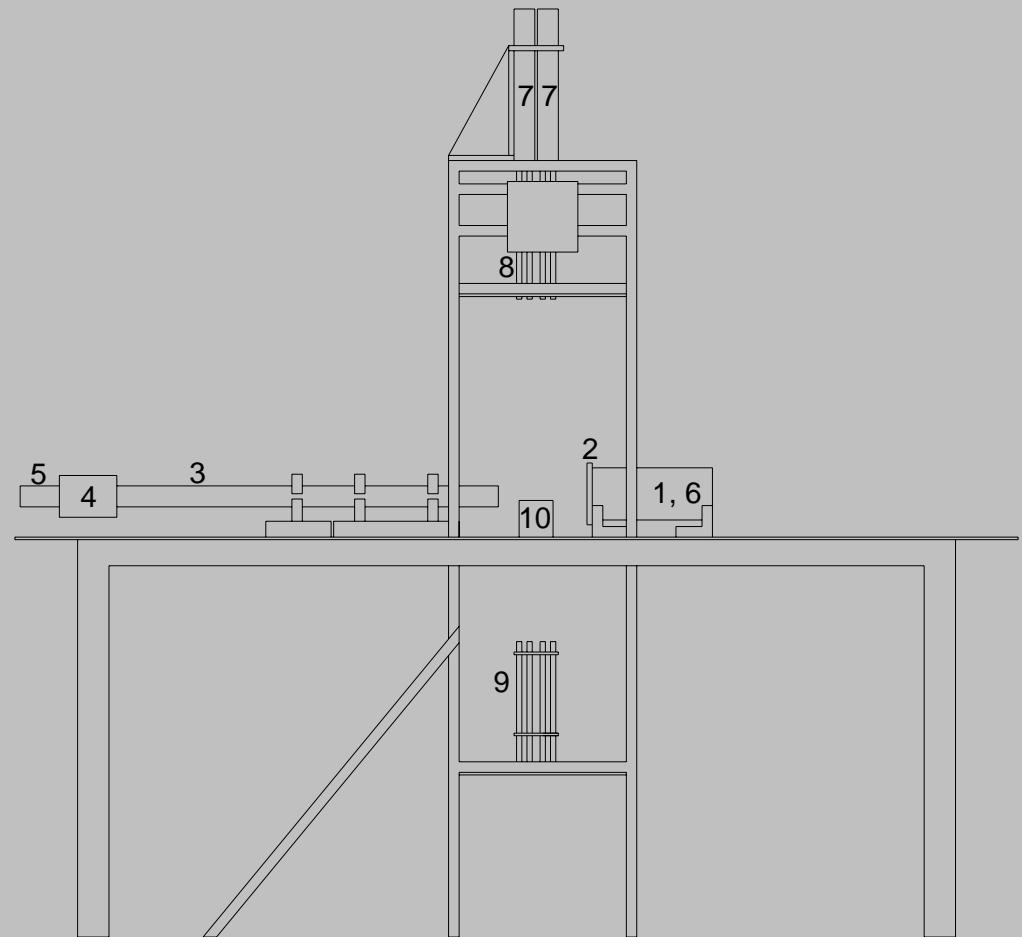
Experimental Data:

University of Alabama Ballistics Facility



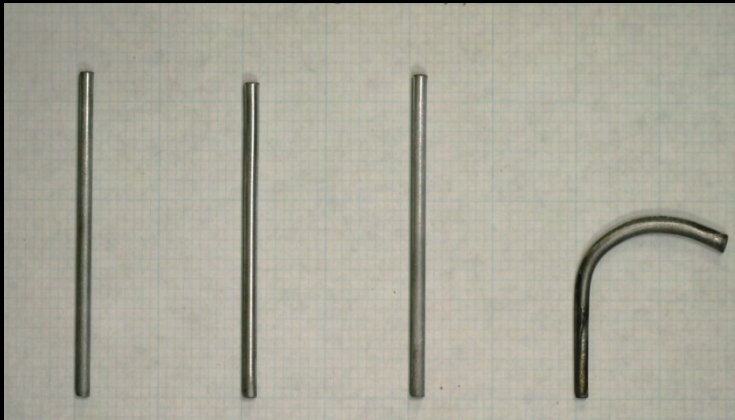
Schematic of Laboratory Penetration Test

1. Steel target canister
2. Steel target face
3. Smooth-bore gun tube (167 caliber, 0.167 inch inside diameter bore)
4. Breech
5. Solenoid driver
6. Target sleeve in canister
7. Class 3A laser heads
8. Lenses which focus the laser beams on the projectile flight path
9. Receiving unit for laser beams with photomultiplier tubes
10. Small riser to prevent target material from spilling onto the photomultiplier tubes



Laboratory Scale Penetration Testing

7075-T6 20:1 Cylindrical Projectiles in Coarse Foundry Sand



508 m/s 543 m/s 564 m/s 664 m/s

These figures demonstrate the progression of failure occurring after the critical velocity.

6061-T6 CRH 3.0 20:1 Projectiles in Coarse Foundry Sand



475 m/s 513 m/s 574 m/s 639 m/s

Normal Penetration Into Sand

$$P = \gamma \rho_t v_n^2 + R \quad \text{(Pressure)}$$

$$f = \mu P \quad \text{(Friction)}$$

Neglecting friction on the penetrator nose, the total penetration depth $>L$ is

Normal Penetration Into Sand

$$z_f = L + \frac{1}{k} \ln \left[\frac{e^{-kL_0} \left(v_0^2 + \frac{2\pi a^2 R}{mk} - \frac{4\pi\mu Ra}{mk^2} \right) + \frac{4\pi\mu Ra}{mk^2}}{\frac{2\pi a^2 R}{mk} + \frac{4\pi\mu Ra L_0}{mk}} \right]$$

L = overall penetrator length

a = shank radius

L_0 = shank length

b = nose length

μ = friction coefficient

$$k = \frac{2\pi a^2 \gamma \rho_t N}{m}$$

R = target strength factor

m = penetrator mass

$$N = \frac{2}{a^2} \int_0^b \frac{rr'^3}{1+r'^2} dx$$

p_1 = target density

Y = dimensionless drag coefficient

EVALUATION of γ

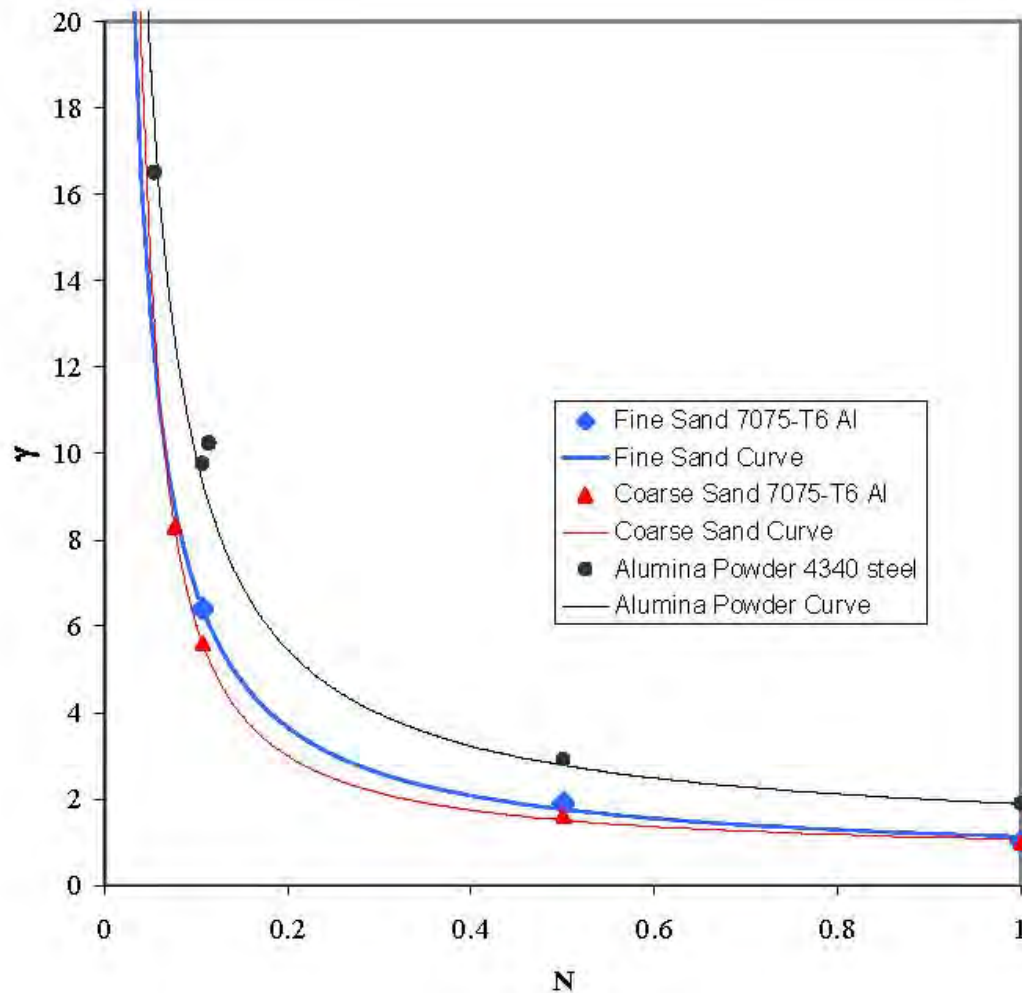
$$\gamma = \gamma_0 + \gamma_1 \left(\frac{1}{N} \right) + \gamma_2 \left(\frac{1}{N^2} \right) + \dots$$

$\gamma = \gamma_0 + \gamma_1 \left(\frac{1}{N} \right) + \gamma_2 \left(\frac{1}{N^2} \right) + \gamma_3 \left(\frac{1}{N^3} \right)$				
	γ_0	γ_1	γ_2	γ_3
Coarse Foundry Sand	0.660	0.397	0.140	0
Fine Foundry Sand	0.500	0.630	0	0
Alumina Powder	1.000	0.891	0	0

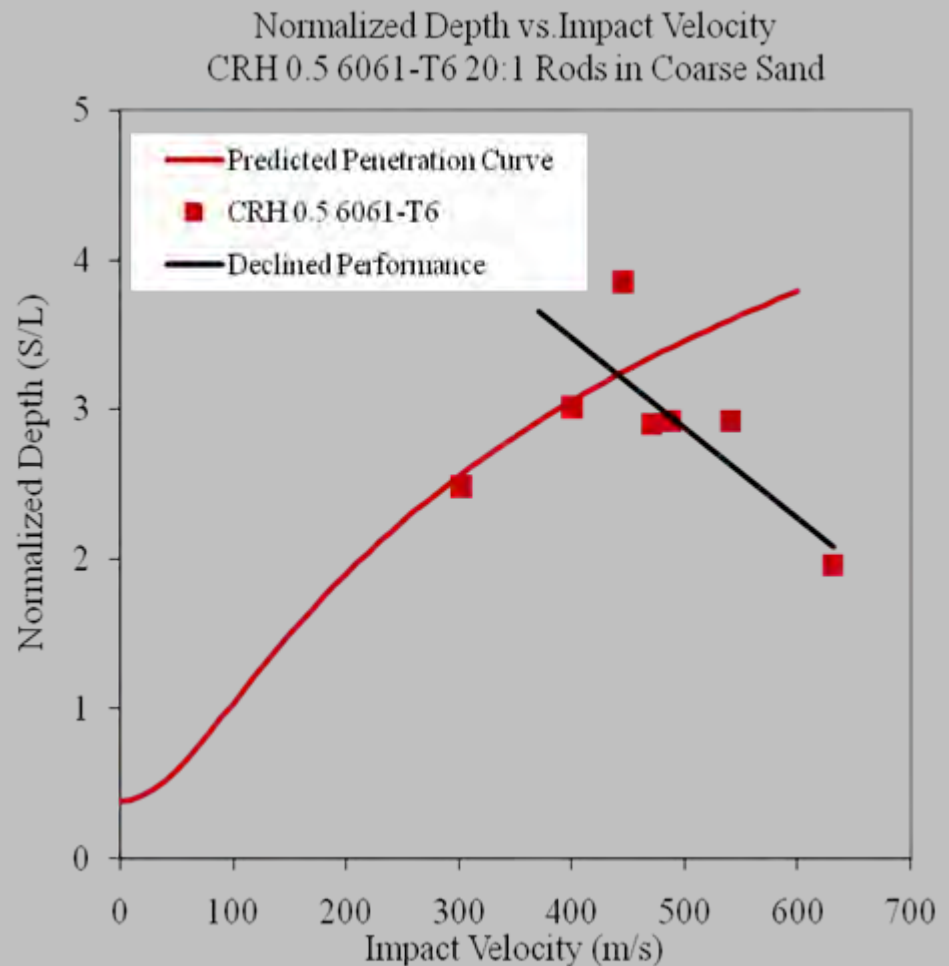
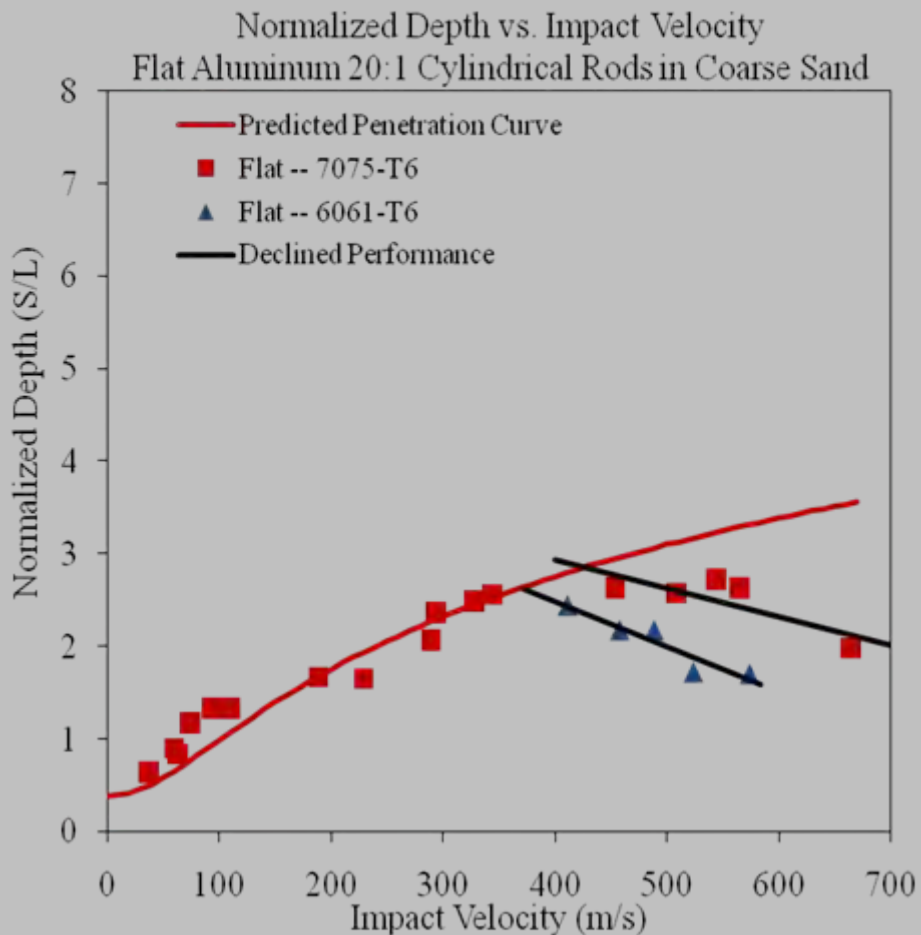
Summary of γ coefficients for three target media

EVALUATION of γ

Graph of γ vs. N for each target medium

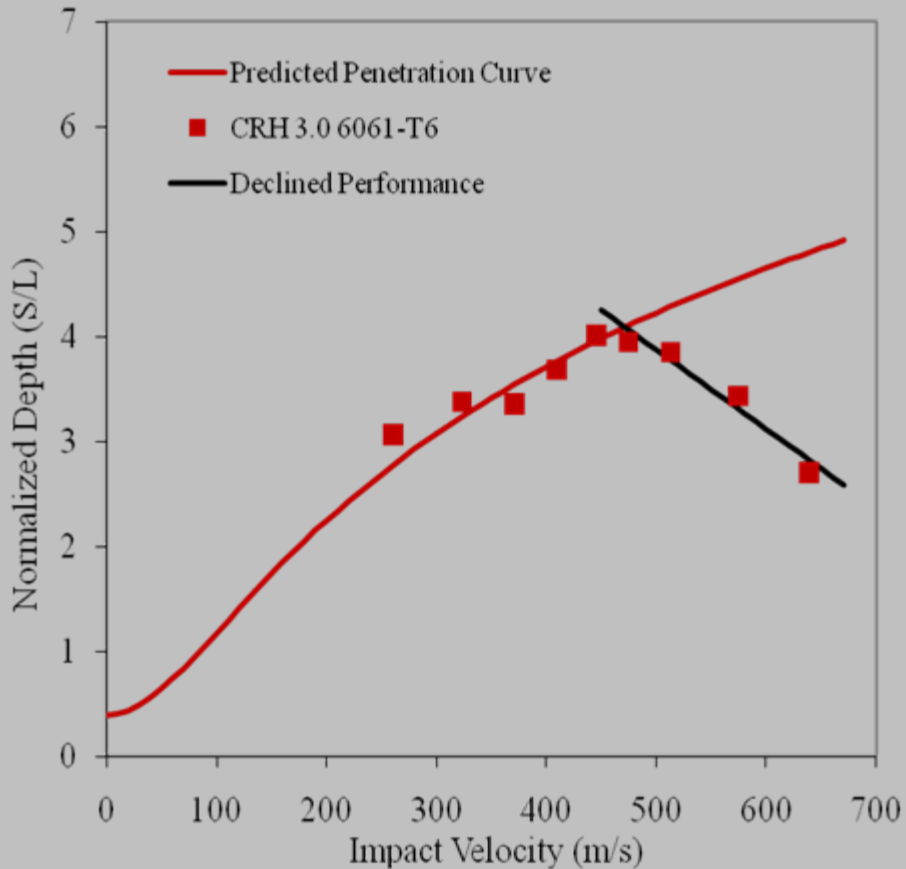


EVALUATION of γ

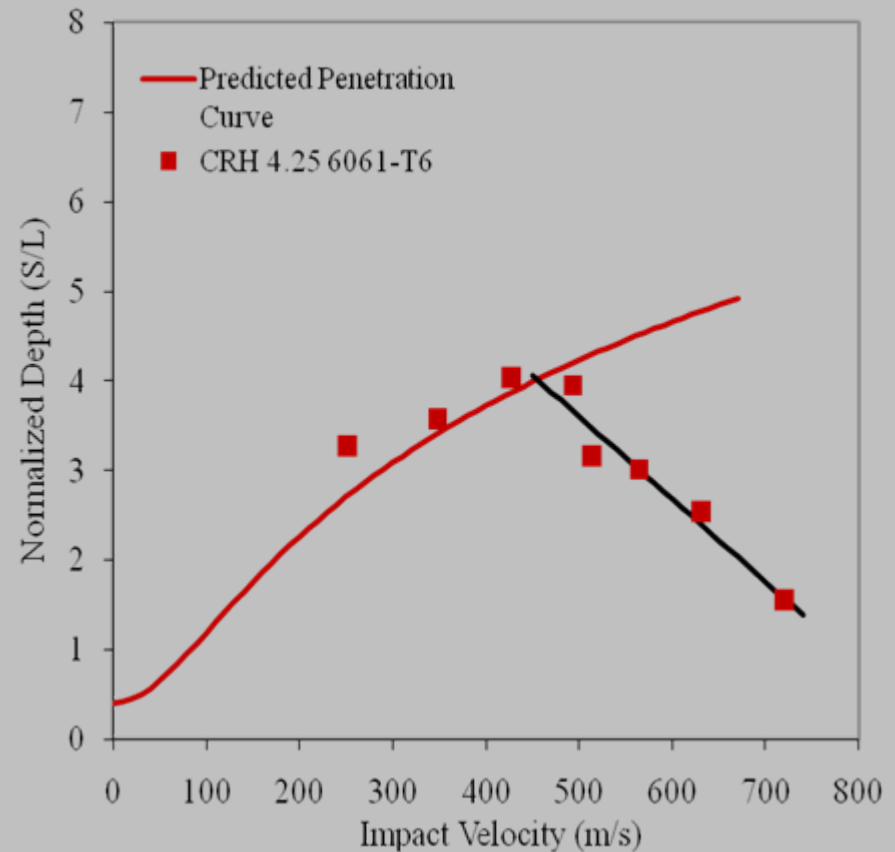


EVALUATION of γ

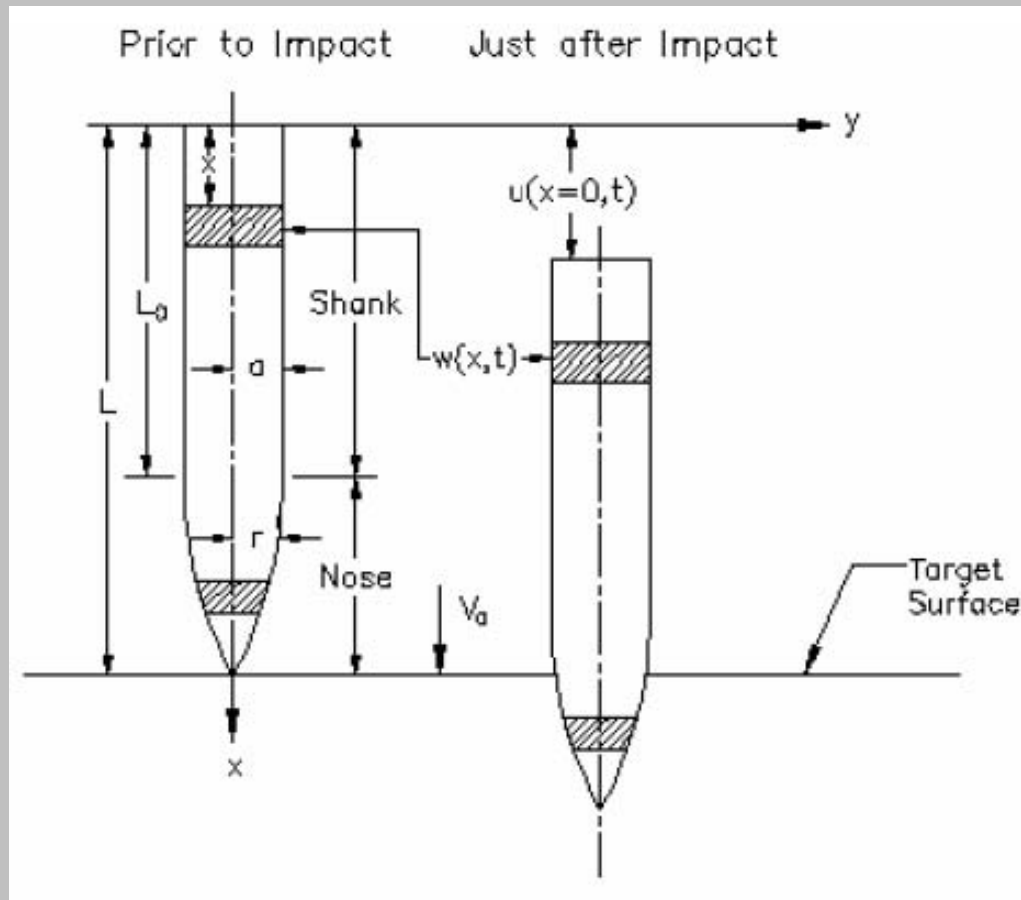
Normalized Depth vs. Impact Velocity
CRH 3.0 6061-T6 20:1 Rods in Coarse Sand



Normalized Depth vs. Impact Velocity
CRH 4.25 6061-T6 20:1 Rods in Coarse Sand



Formulation and Solution of the Problem



The Lagrangian
coordinate
system

Formulation and Solution of the Problem

$$\rho\pi r^2 \frac{\partial^2 u}{\partial t^2} = \frac{\partial P}{\partial x}$$

$$\rho\pi r^2 \frac{\partial^2 w}{\partial t^2} = \frac{\partial Q}{\partial x}$$

$$\rho\pi r^2 \frac{\partial^2 w}{\partial t^2} + \frac{\partial^2}{\partial x^2} \left(EI \frac{\partial^2 w}{\partial x^2} \right) - \frac{\partial}{\partial x} \left(P \frac{\partial w}{\partial x} \right) = 0$$

Longitudinal Force

$$m\dot{v}_G = -F(v_G(t))$$

$$\frac{\partial^2 u}{\partial t^2} = \dot{v}_G$$

$$\frac{\partial P}{\partial x} = \rho\pi r^2 \dot{v}_G \qquad 0 < x < L$$

Longitudinal Force

$$P(x, t) = \rho \pi a^2 \dot{v}_G x$$

$$0 < x < L_0$$

$$P(L_0, t) = \rho \pi a^2 \dot{v}_G L_0$$

$$P(x, t) = \rho \pi a^2 \dot{v}_G L_0 + \rho \pi \dot{v}_G \int_{L_0}^x r^2(x) dx$$

$$L_0 < x < L$$

Lateral Motion

$$\rho\pi a^2 \frac{\partial^2 w}{\partial t^2} + \frac{\partial^2}{\partial x^2} \left(EI \frac{\partial^2 w}{\partial x^2} \right) - \frac{\partial}{\partial x} \left(\rho\pi a^2 \dot{v}_G x \frac{\partial w}{\partial x} \right) = 0$$

$$0 < x < L_0$$

$$\rho\pi r^2 \frac{\partial^2 w}{\partial t^2} + \frac{\partial^2}{\partial x^2} \left(EI \frac{\partial^2 w}{\partial x^2} \right) - \frac{\partial}{\partial x} \left(\rho\pi \dot{v}_G (a^2 L_0 + \int_{L_0}^x r^2(x) dx) \frac{\partial w}{\partial x} \right) = 0$$

$$L_0 < x < L$$

Homogeneous Boundary Conditions

$$\frac{\partial^2 w}{\partial x^2}(0, t) = \frac{\partial^3 w}{\partial x^3}(0, t) = 0$$

$$w(L, t) = 0$$

$$\frac{\partial^2 w}{\partial x^2}(L, t) = 0$$

Dimensionless Variables

$$\xi = \frac{x}{L} \quad \beta = \frac{r(x)}{a} \quad z = \frac{w}{a} \quad \tau = \frac{v_0 t}{L}$$

$$\frac{EI}{\rho \pi a^2 v_0^2 L^2} \frac{\partial^4 z}{\partial \xi^2} + \frac{\partial^2 z}{\partial \tau^2} - \frac{L \dot{v}_G}{v_0^2} \frac{\partial}{\partial \xi} \left(\xi \frac{\partial z}{\partial \xi} \right) = 0$$

$$0 < \xi < \xi_0$$

$$\frac{Ea^2}{\rho \pi v_0^2 L^2 \beta^2} \frac{\partial^2}{\partial \xi^2} \left(\frac{I}{a^4} \frac{\partial^2 z}{\partial \xi^2} \right) + \frac{\partial^2 z}{\partial \tau^2} - \frac{L \dot{v}_G}{\beta^2 v_0^2} \frac{\partial}{\partial \xi} \left(\left(\xi_0 + \int_{\xi_0}^{\xi} \beta^2 d\xi \right) \frac{\partial z}{\partial \xi} \right) = 0$$

$$\xi_0 < \xi < 1$$

Deceleration Approximation

$$\dot{v}_G = -\frac{F}{m} \cong -\frac{\pi a^2 \gamma \rho_t N v_0^2}{m}$$

Separation of Variables

$$z = \Phi(\xi)T(\tau) \quad \ddot{T} + \omega T = 0$$

$$\frac{EI}{\rho\pi a^2 v_0^2 L^2} \frac{d^4 \Phi}{d\xi^4} - \omega \Phi + \frac{L\pi a^2 \gamma \rho_t N}{m} \frac{d}{d\xi} \left(\xi \frac{d\Phi}{d\xi} \right) = 0$$

$$0 < \xi < \xi_0$$

$$\frac{Ea^2}{\rho\pi v_0^2 L^2 \beta^2} \frac{d^2}{d\xi^2} \left(\frac{I}{a^4} \frac{d^2 \Phi}{d\xi^2} \right) - \omega \Phi + \frac{L\pi a^2 \gamma \rho_t N}{m\beta^2} \frac{d}{d\xi} \left(\left(\xi_0 + \int_{\xi_0}^{\xi} \beta^2 d\xi \right) \frac{d\Phi}{d\xi} \right) = 0$$

$$\xi_0 < \xi < 1$$

Boundary Conditions

$$\frac{d^2\Phi}{d\xi^2}(0) = \frac{d^3\Phi}{d\xi^3}(0) = 0$$

$$\Phi(1) = \frac{d^2\Phi}{d\xi^2}(1) = 0$$

Separation of Variables

$$\lambda \frac{d^4 \Phi}{d\xi^4} - \omega \Phi + \eta \frac{d}{d\xi} \left(\xi \frac{d\Phi}{d\xi} \right) = 0$$

$$0 < \xi < \xi_0$$

$$\lambda \frac{d^2}{d\xi^2} \left(\beta^4 \frac{d^2 \Phi}{d\xi^2} \right) - \omega \beta^2 \Phi + \eta \frac{d}{d\xi} \left(\left(\xi_0 + \int_{\xi_0}^{\xi} \beta^2 d\xi \right) \frac{d\Phi}{d\xi} \right) = 0$$

$$\xi_0 < \xi < 1$$

$$\lambda = \frac{EI_s}{\rho \pi a^2 v_0^2 L^2}$$

$$\eta = \frac{\pi L a^2 \gamma \rho_t N}{m}$$

Orthogonality of the Eigenfunctions

Consider, for simplicity, the case for a flat-ended cylinder.

$$\lambda \frac{d^4 \Phi_n}{d\xi^4} + \eta \frac{d}{d\xi} \left(\xi \frac{d\Phi_n}{d\xi} \right) - \omega_n \Phi_n = 0$$

It is not difficult to show that

$$\int_0^1 \Phi_m \Phi_n d\xi = 0 \quad m \neq n$$

$$\omega_n = \frac{\lambda \int_0^1 \left(\frac{d^2 \Phi_n}{d\xi^2} \right)^2 d\xi - \eta \int_0^1 \xi \left(\frac{d\Phi_n}{d\xi} \right)^2 d\xi}{\int_0^1 \Phi_n^2 d\xi}$$

Orthogonality of the Eigenfunctions

Consider

$$\omega = \frac{\lambda \int_0^1 \left(\frac{d^2 \Phi}{d\xi^2} \right)^2 d\xi - \eta \int_0^1 \xi \left(\frac{d\Phi}{d\xi} \right)^2 d\xi}{\int_0^1 \Phi^2 d\xi}$$

$$\Phi = k_1 \Phi_1 + k_2 \Phi_2 + \dots$$

Orthogonality of the Eigenfunctions

$$\omega = \frac{\omega_1 k_1^2 \int_0^1 \Phi_1^2 d\xi + \omega_2 k_2^2 \int_0^1 \Phi_2^2 d\xi + \dots + \omega_n k_n^2 \int_0^1 \Phi_n^2 d\xi + \dots}{k_1^2 \int_0^1 \Phi_1^2 d\xi + k_2^2 \int_0^1 \Phi_2^2 d\xi + \dots + k_n^2 \int_0^1 \Phi_n^2 d\xi + \dots}$$

The Stationary Values achieved by this quotient are the Eigenvalues $\omega_1, \omega_2, \dots$

Ogive Noses

$$\omega_n = \frac{\lambda \left[\int_0^{\xi_0} \left(\frac{d^2 \Phi_n}{d\xi^2} \right)^2 d\xi + \int_0^1 \beta^4 \left(\frac{d^2 \Phi_n}{d\xi^2} \right)^2 d\xi \right] - \eta \left[\int_0^{\xi_0} \xi \left(\frac{d\Phi_n}{d\xi} \right)^2 d\xi + \int_{\xi_0}^1 \left(\xi_0 + \int_{\psi_0}^{\xi} \beta^2 d\xi \right) \left(\frac{d\Phi_n}{d\xi} \right)^2 d\xi \right]}{\int_0^{\xi_0} \Phi_n^2 d\xi + \int_{\xi_0}^1 \beta^2 \Phi_n^2 d\xi}$$

$$\beta'(\xi_0) = 0$$

Stability Criterion

$$\omega_1 = \frac{\lambda \left[\int_0^{\xi_0} \left(\frac{d^2 \Phi_1}{d\xi^2} \right)^2 d\xi + \int_{\xi_0}^1 \beta^4 \left(\frac{d^2 \Phi_1}{d\xi^2} \right)^2 d\xi \right] - \eta \left[\int_0^{\xi_0} \xi \left(\frac{d\Phi_1}{d\xi} \right)^2 d\xi + \int_{\xi_0}^1 \left(\xi_0 + \int_{\xi_0}^{\xi} \beta^2 d\xi \right) \left(\frac{d\Phi_1}{d\xi} \right)^2 d\xi \right]}{\int_0^{\xi_0} \Phi_1^2 d\xi + \int_{\xi_0}^1 \beta^2 \Phi_1^2 d\xi} > 0$$

where ω_1 is the lowest eigenvalue and Φ_1 is the corresponding eigenfunction

Trial Functions

$$\Phi = 1 - \frac{5}{2}\xi^4 + \frac{3}{2}\xi^5 + \left(\xi - \frac{5}{2}\xi^4 + \frac{3}{2}\xi^5\right)C_1 + \left(1 - \frac{20}{3}\xi^4 + 9\xi^5 - \frac{10}{3}\xi^6\right)C_2$$

Choose C_1 and C_2 so that a minimum in the quotient is achieved.

Results

Critical Velocity of 20:1 6061 T-6 Aluminum into Course Foundry Sand				
	Flat	CRH 0.5	CRH 3.0	CRH 4.25
Two Constant Estimate	384.03 (m/s)	405 (m/s)	452 (m/s)	450.2 (m/s)
Experimental	375 (m/s)	435 (m/s)	475 (m/s)	445 (m/s)

Critical Velocity Comparisons

Critical Velocity of 20:1 6061 T-6 Aluminum into Course Foundry Sand				
	Flat	CRH 0.5	CRH 3.0	CRH 4.25
One Constant Estimate	495.25 (m/s)	522.32 (m/s)	589.265 (m/s)	613.934 (m/s)
Two Constant Estimate	384.03 (m/s)	405 (m/s)	452 (m/s)	450.2 (m/s)
Torres Estimate	406 (m/s)	421 (m/s)	472 (m/s)	468 (m/s)

Theory Comparisons

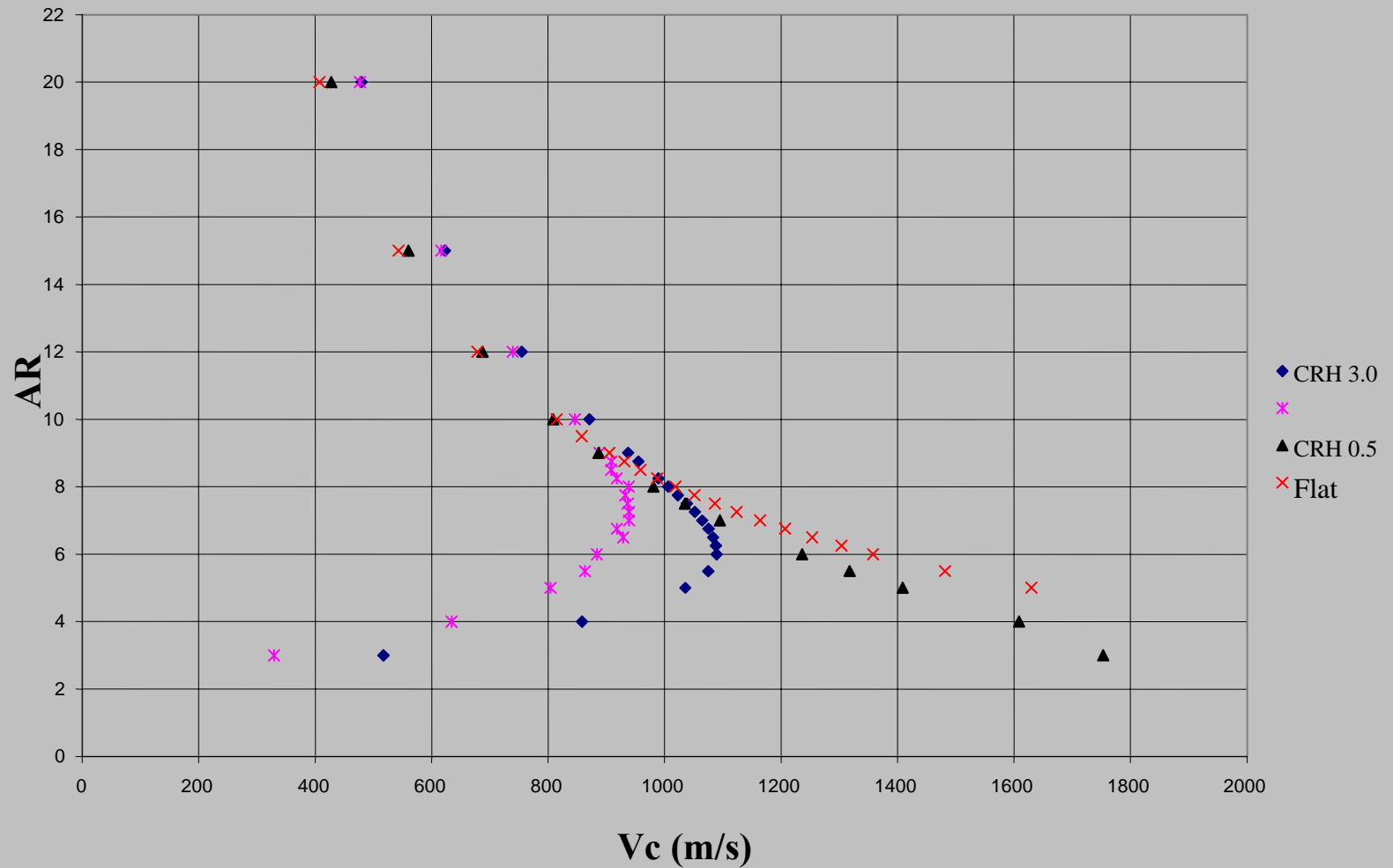
Results

7075- T6 Aluminum CRH 12 into Course Foundry Sand		
	8:1	12:1
One Constant Estimate	819.13 (m/s)	822.76 (m/s)
Two Constant Estimate	679.17 (m/s)	683.14 (m/s)
Torres Estimate	680 (m/s)	680 (m/s)
Experimental Result	700 (m/s)	690 (m/s)

More Theory Comparisons

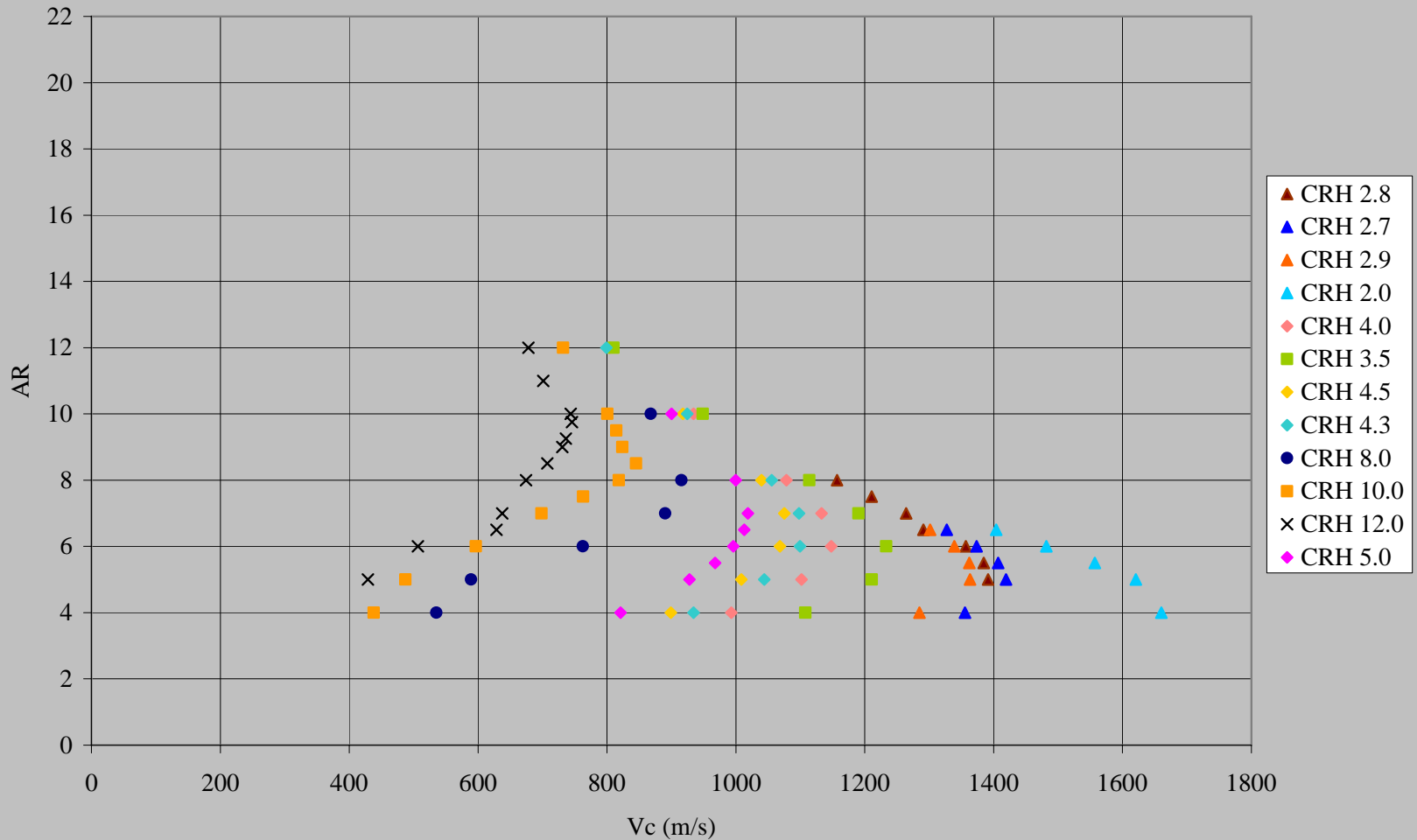
Results

Aspect Ratio vs. Critical Velocity



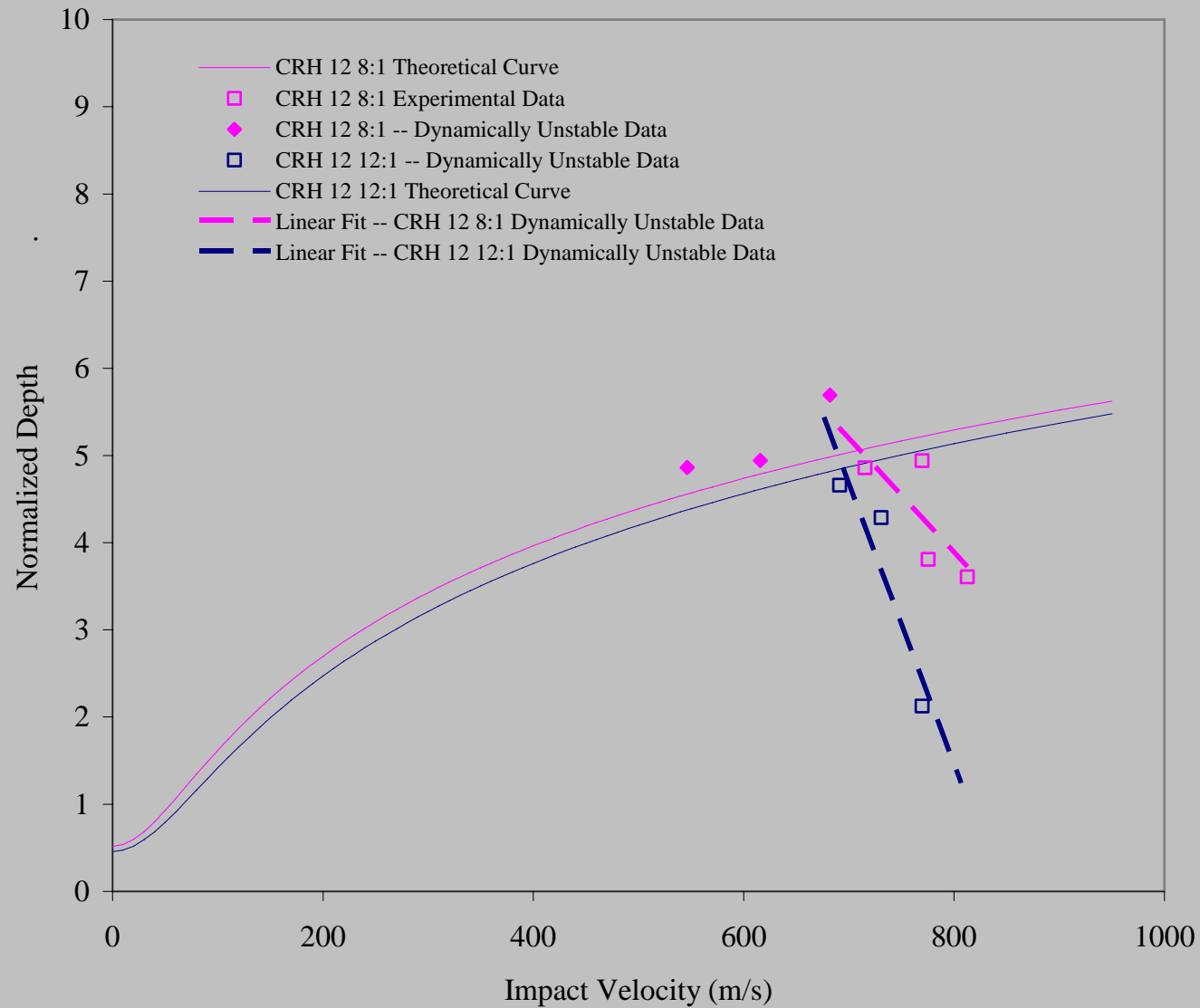
Results

Aspect Ratio vs. Critical Velocity

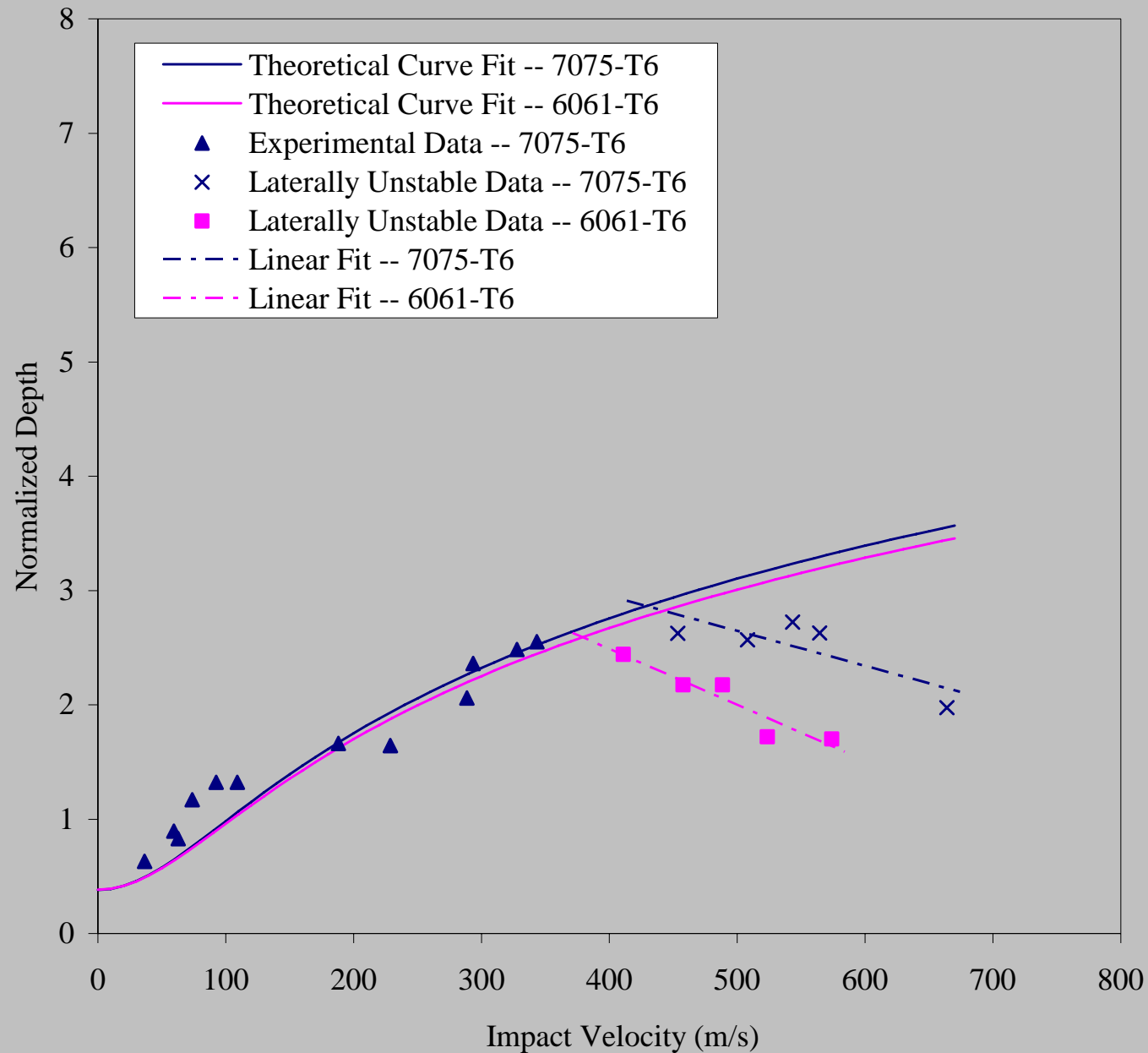


Normalized Depth vs Impact Velocity

CRH 12 7075-T6 in Coarse Sand



Normalized Depth vs. Impact Velocity
7075-T6 and 6061-T6 20:1 Cylindrical Rods in Coarse Sand





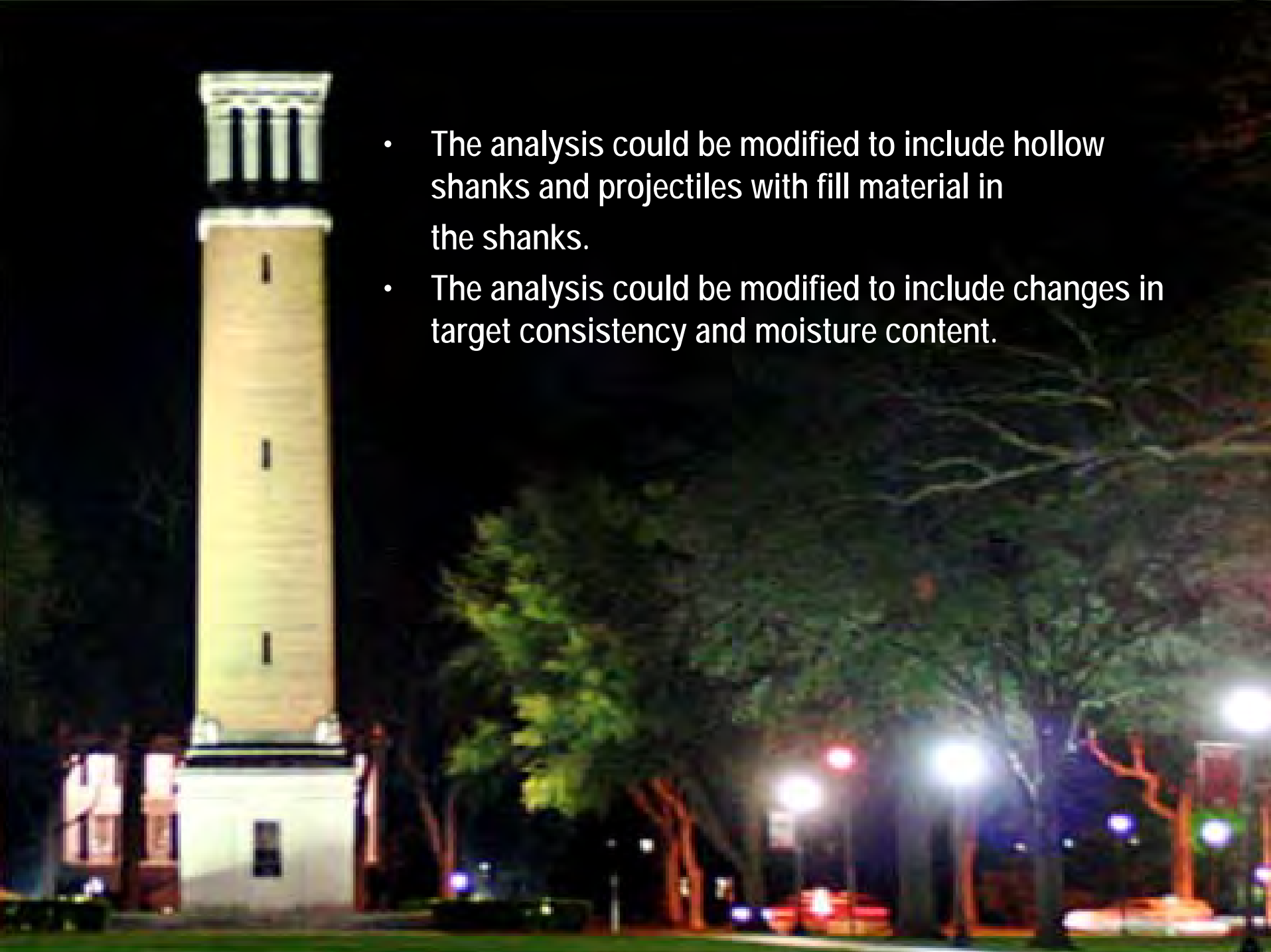
Conclusions

- An analysis of lateral motion of a cylindrical projectile normally impacting a particulate target has been presented.
- The results correlate very well to laboratory scale penetration tests for aluminum projectiles impacting foundry sand or alumina targets.
- Aspect ratios of the projectiles were chosen to permit the lateral instability to manifest itself within the velocity limits of the equipment.



Topics for Future Consideration

- Data from larger scale experiments should be used to test the theory.
- Materials with higher elastic modulus must be considered.
- The theory should be extended to more general noses than ogives.
- Different target materials should be tested and a correlation between particle size, Mohs hardness, and other properties should be made.



- The analysis could be modified to include hollow shanks and projectiles with fill material in the shanks.
- The analysis could be modified to include changes in target consistency and moisture content.



SHAPED CHARGE PENETRATION INTO GAS SATURATED SANDSTONE

Jeremy Harvey, Brenden Grove

24th International Symposium on Ballistics

New Orleans, LA

September 26, 2008

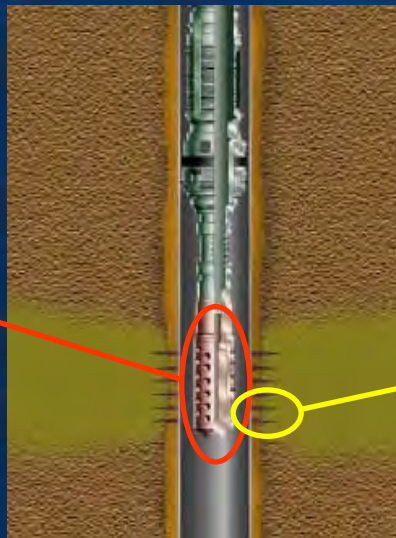
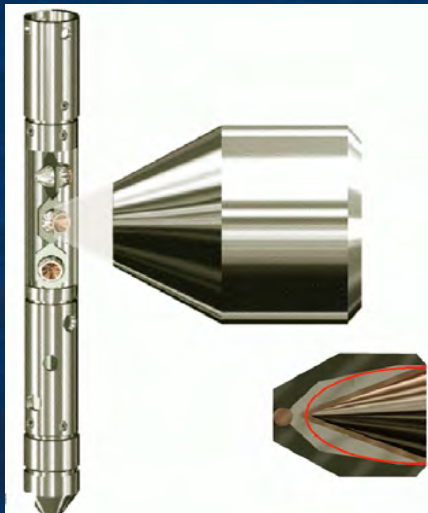
Schlumberger

Overview

- Introduction / Background
- Recent Experiments
- Conclusions & Future Work

Introduction

- Oilwell perforators
 - small caliber shaped charges
 - create the pathway for oil or gas to flow from the reservoir rock into the wellbore
- Deep, clean perforations required for well productivity



Schlumberger

Introduction

- Reservoir properties influencing perforation depth:
 - Rock strength
 - In-situ stresses (overburden, tectonic)
 - Pore fluid pressure
 - Pore fluid type (liquid vs. gas)

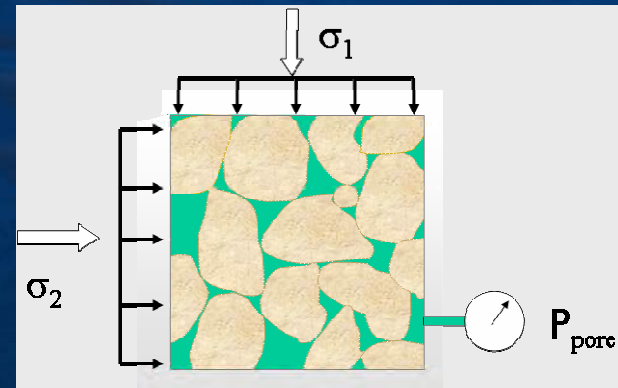
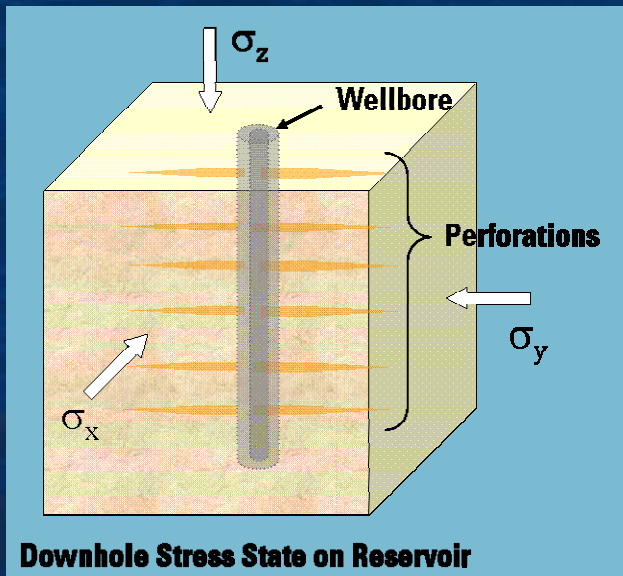
Background

■ Geomechanics considerations:

- In-situ stresses ("total" stress)
- Pore fluid pressure

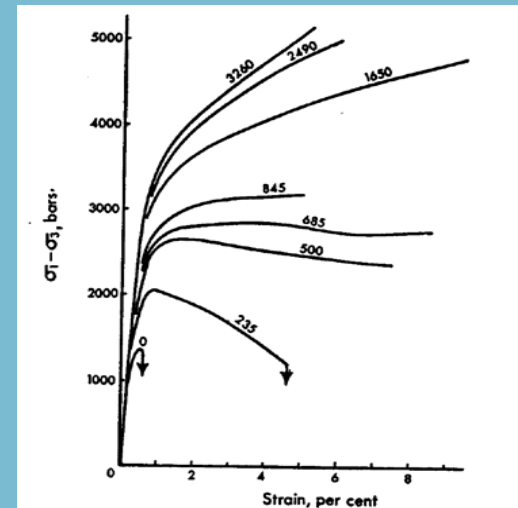
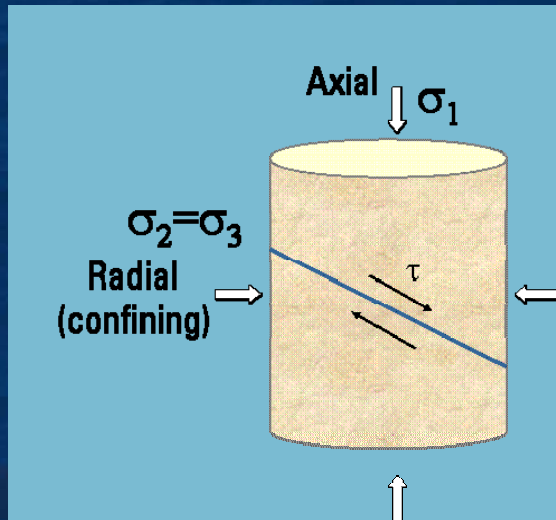
Effective stress

$$\sigma_{eff} = (\sigma_{mean} - a * P_p)$$



Background

- Why is in-situ stress important to SC penetration?
 - Rocks are stronger under increasing applied stress

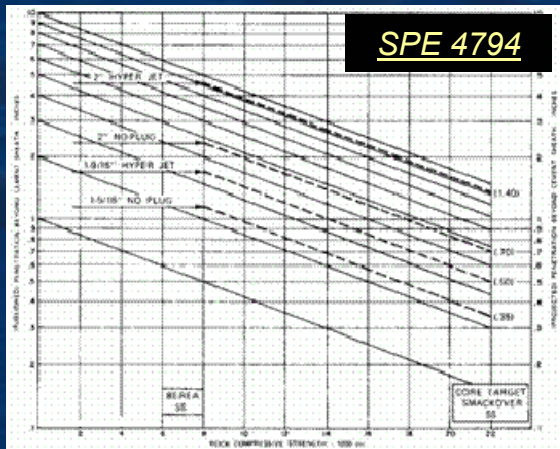


$$\tau = f(\sigma_{mean})$$

Background

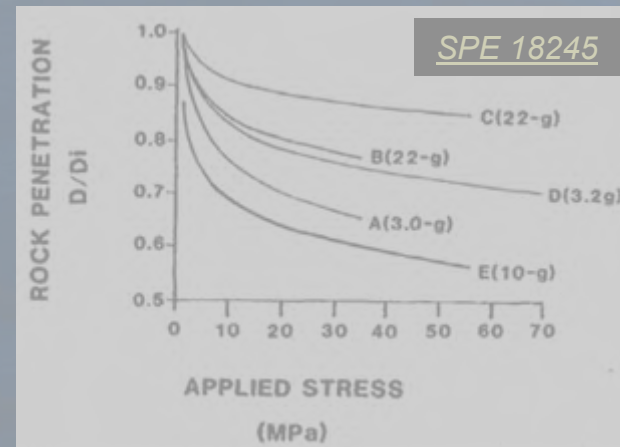
Perforation depth depends on:

a = “ballistic pore pressure coefficient”



Formation
Strength (UCS)

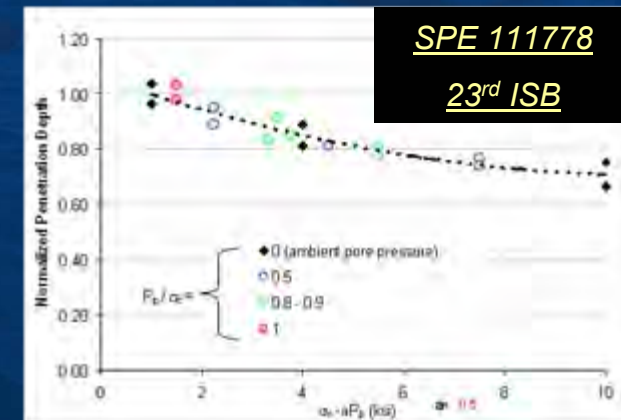
$$\sigma_{eff} = (\sigma_{mean} - P_p)$$



Formation
Effective Stress

$$\sigma_{eff} = (\sigma_{mean} - a * P_p)$$

$$a \sim 0.5$$



Schlumberger

Background

- Historical and recent laboratory work consistently demonstrated that perforation depth decreases with...
 - increasing rock strength
 - increasing effective stress
- Recent laboratory work demonstrated
 - pore pressure's influence is less significant than previously thought (i.e. $a < 1$)
 - a new definition of effective stress*

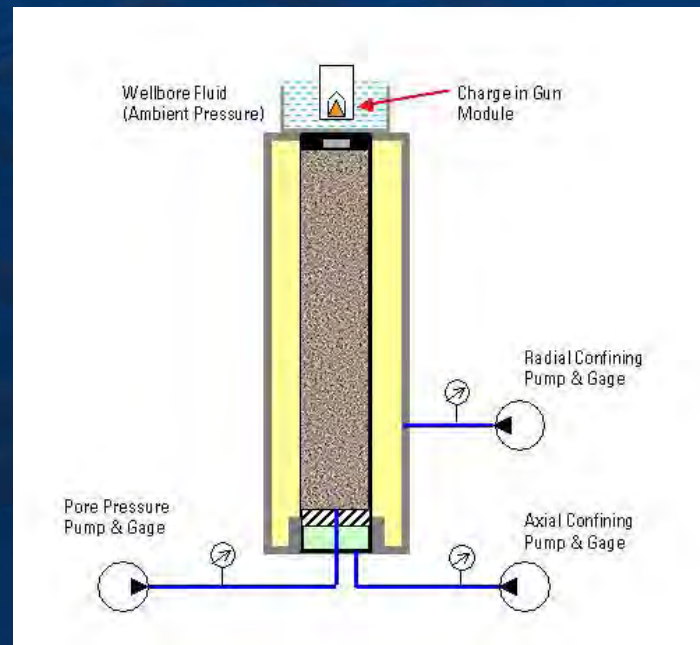
** for purposes of SC penetration depth*

Background

- Motivation for current work
 - All previous laboratory work (especially into stressed targets) addressed liquid-filled rock
 - Reasonably valid for oil reservoirs, but not necessarily for gas reservoirs
- Focus on perforation depth; tunnel diameter is another variable not addressed here

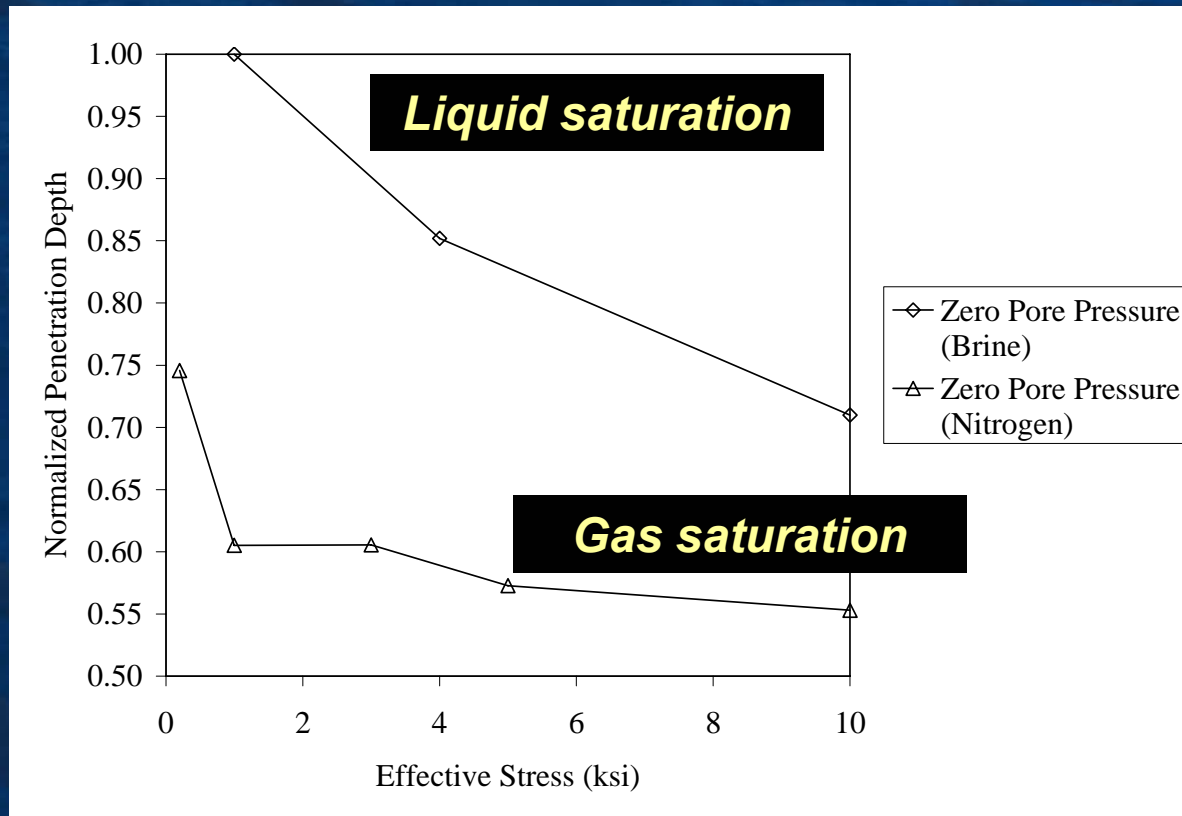
Current Work

- Penetration experiments into stressed rock targets
 - independent confining and pore pressures, up to 10,000 psi
 - simulates stress levels representative of depths up to 10,000'
 - does not mimic downhole temperature or wellbore fluid pressure
- Berea sandstone
- Pore fluid is dry N_2



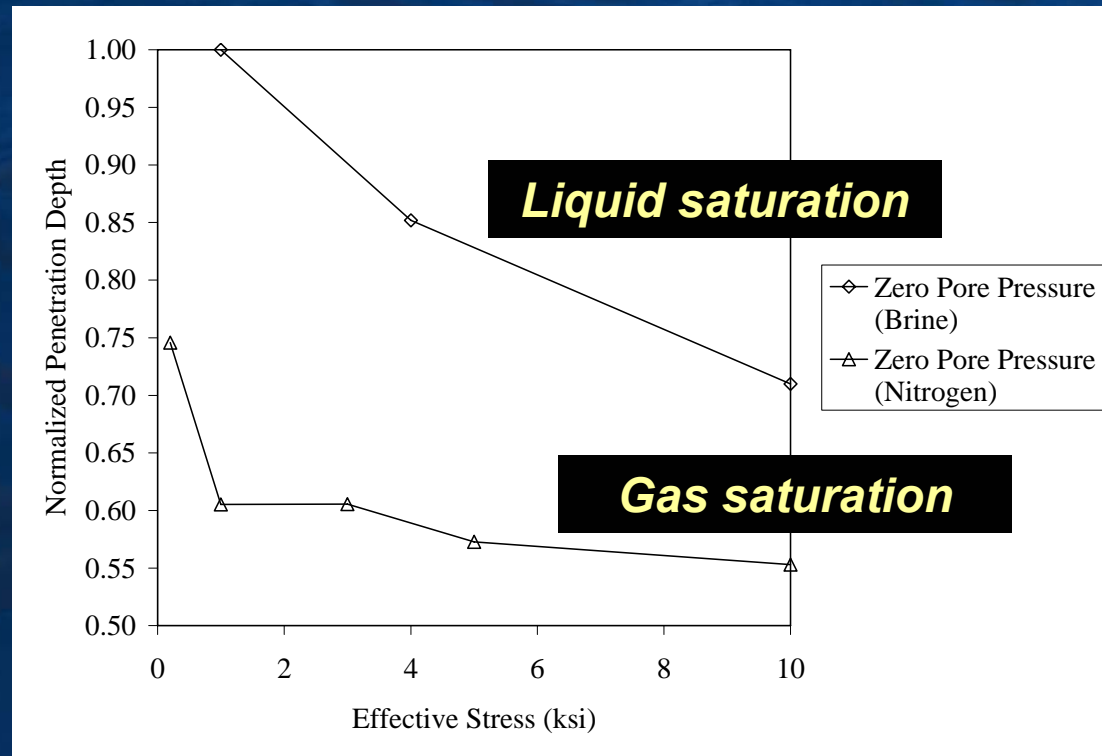
Results: Ambient Pore Pressure

- Perforation depth vs. confining stress
 - for both liquid- and gas-saturated sandstone



Results: Ambient Pore Pressure

- Two primary observations
 - PD significantly reduced in gas saturated target
 - Stress influence on PD
 - high for liquid
 - minimal for gas
(above ~1 ksi)

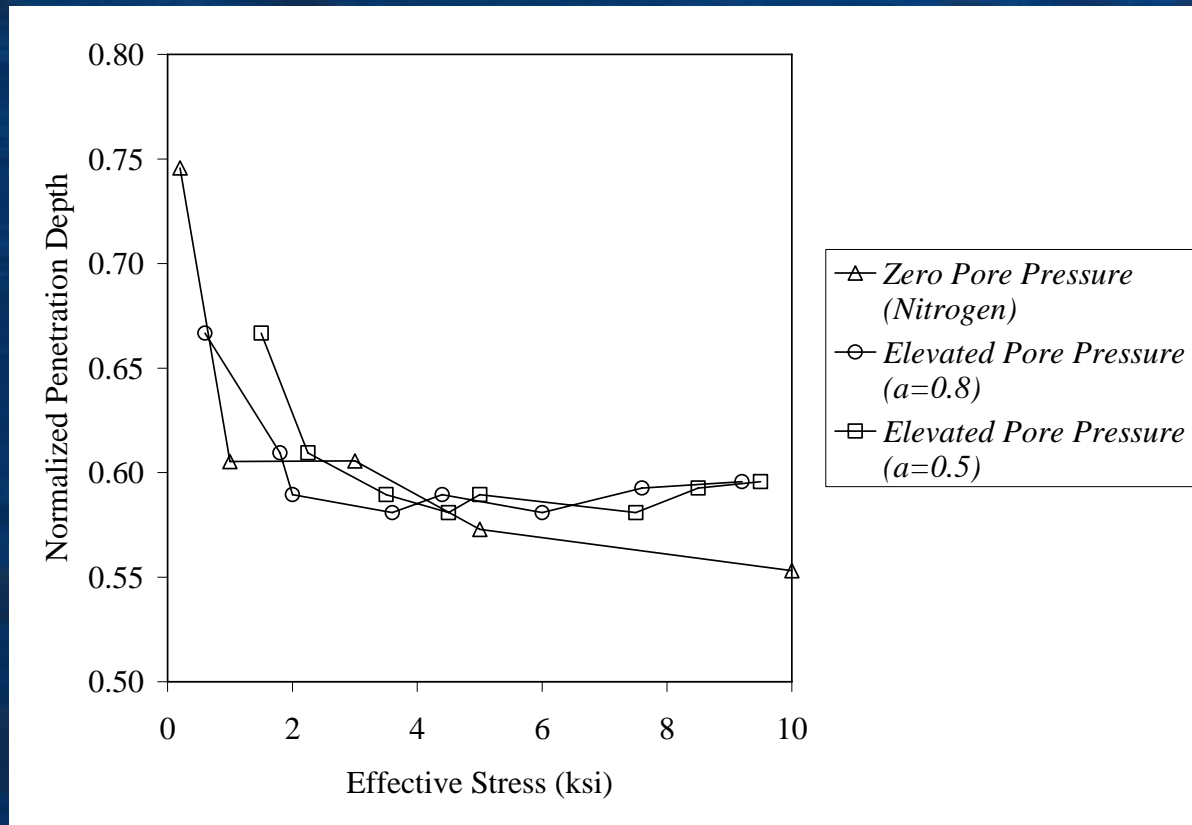


Results: Elevated Pore Pressure

■ Perforation depth vs. effective stress

$$\sigma_{eff} = (\sigma_{mean} - a * P_p)$$

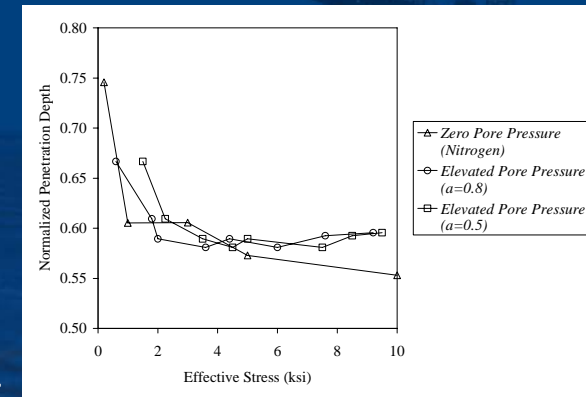
- gas saturation only; both elevated and ambient pore pressure



Results: Elevated Pore Pressure

■ Primary observations

- Pore pressure influence
 - For stress > 2ksi, $a=0.5$ gives reasonable fit
 - For stress < 2ksi, fit is improved with $a=0.8$
- Strictly speaking, BPC is not a constant rock property, but $f(\text{stress}, \text{pore fluid})$
- For elevated pore pressure, penetration into gas saturated rock is even less stress dependant



Practically speaking, both stress and pore pressure may be irrelevant to perforation depth for dry gas saturated rock (above some threshold stress value)

Summary

- Laboratory experiments were conducted
 - shaped charge penetration
 - dry nitrogen-saturated sandstone targets
 - stressed to simulate downhole conditions
- Results:
 - penetration depth into dry gas saturated sandstone is...
 - considerably shallower than into liquid-saturated sandstone
 - essentially independent of effective stress (above 2 ksi)
 - confining stress (and also pore pressure): only important at very low stress levels

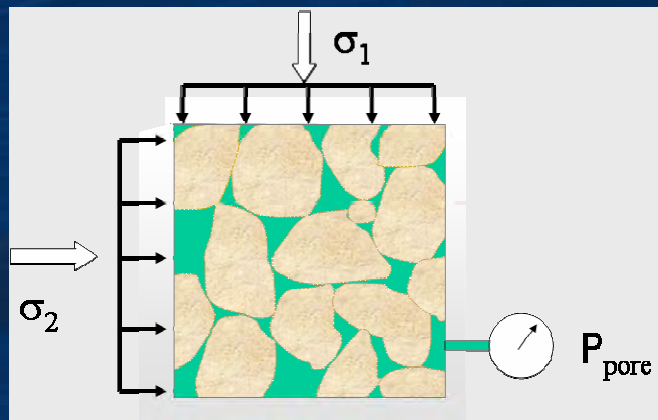
Possible Mechanisms

■ reduced penetration depth

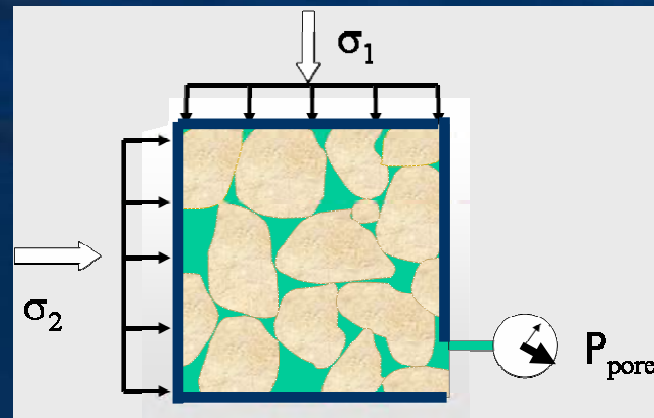
- dry sandstone is stronger than brine-saturated (surface tension and cementation weakening)
- energy absorption of pore collapse in target
- “active target” effect (Aseltine, 1985)

■ stress independence

- shallow penetration = high jet cutoff velocity ~ hydrodynamic penetration
- for liquid saturation, rapid “undrained” loading may limit the increase in the target’s “dynamic effective stress” (and, therefore, strength)



drained



Undrained, or rapid loading

Future Work

■ Future Work

- Understand the mechanisms responsible for these fundamental differences in ballistic response of liquid and gas saturated sandstones
- Design of shaped charges optimized for gas saturated reservoirs

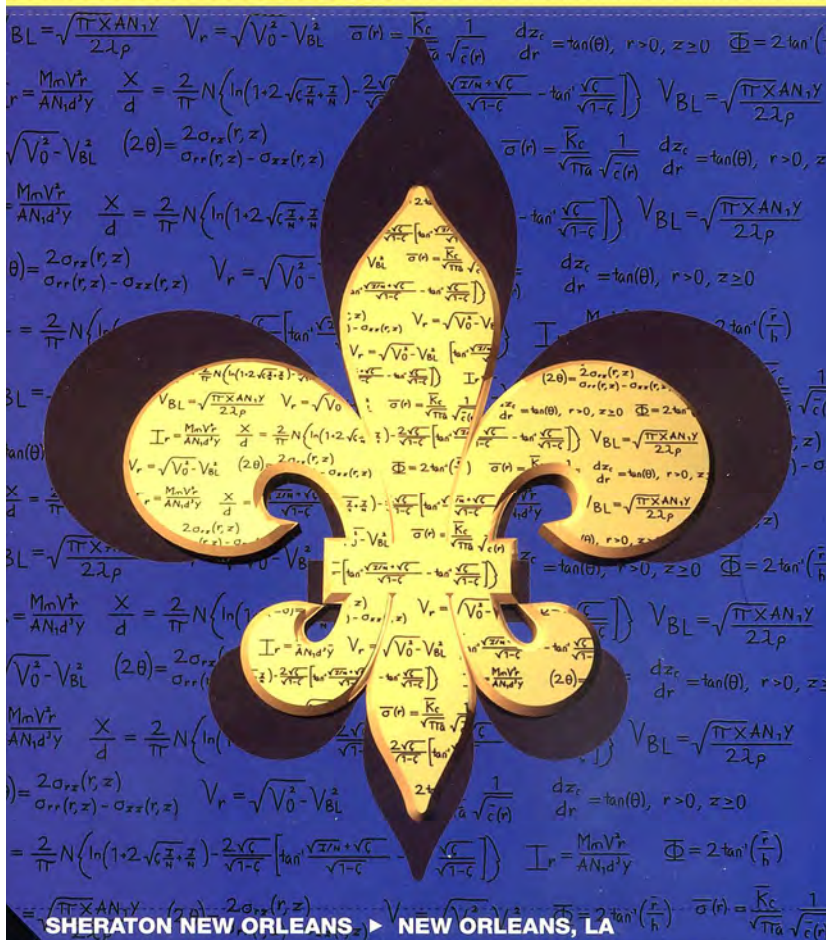
Thank You



Schlumberger

Symposium on BALLISTICS

Sponsored by the Ballistics Division of NDIA in association with the International Ballistics Committee



Behind Armour Effects at Shaped Charge Attacks

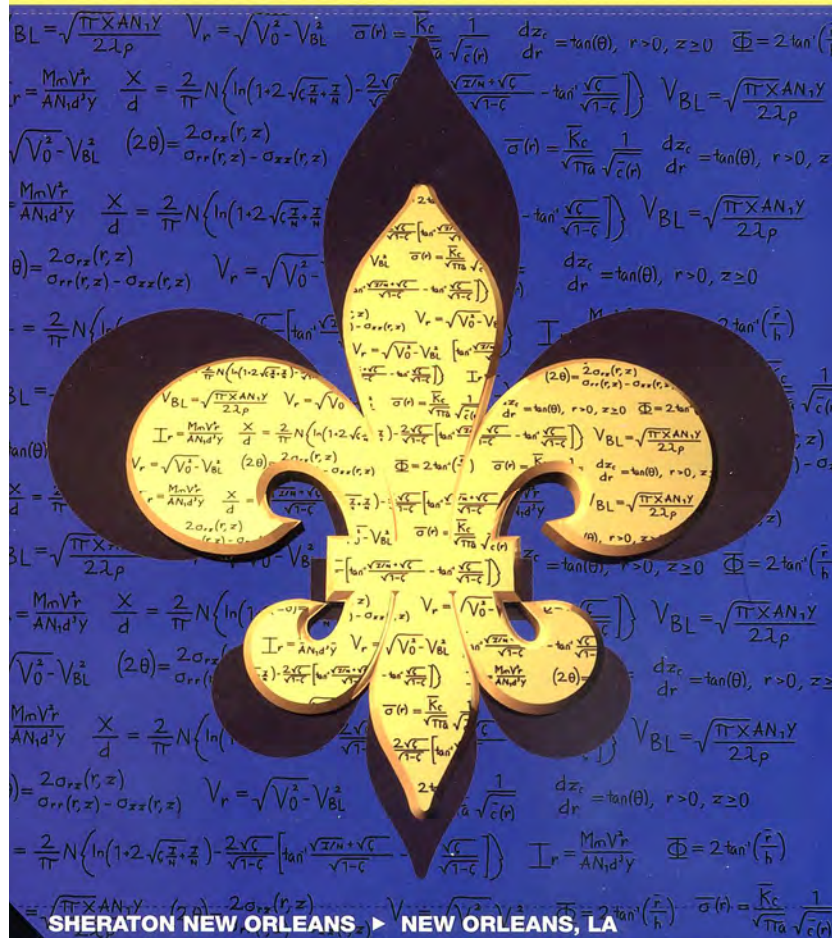
Prof. Dr. M. Held



Schrobenhausen, Germany

International Symposium on BALLISTICS

Sponsored by the Ballistics Division of NDIA in
association with the International Ballistics Committee



Content

Introduction

Diagnostic vessel

Light effects

Gaseous products

Temperature

Spall fragments

Blast effects &

HE equivalence

Incendiary effects

Ignition & Initiation

Summary



*Your complimentary
use period has ended.
Thank you for using
PDF Complete.*

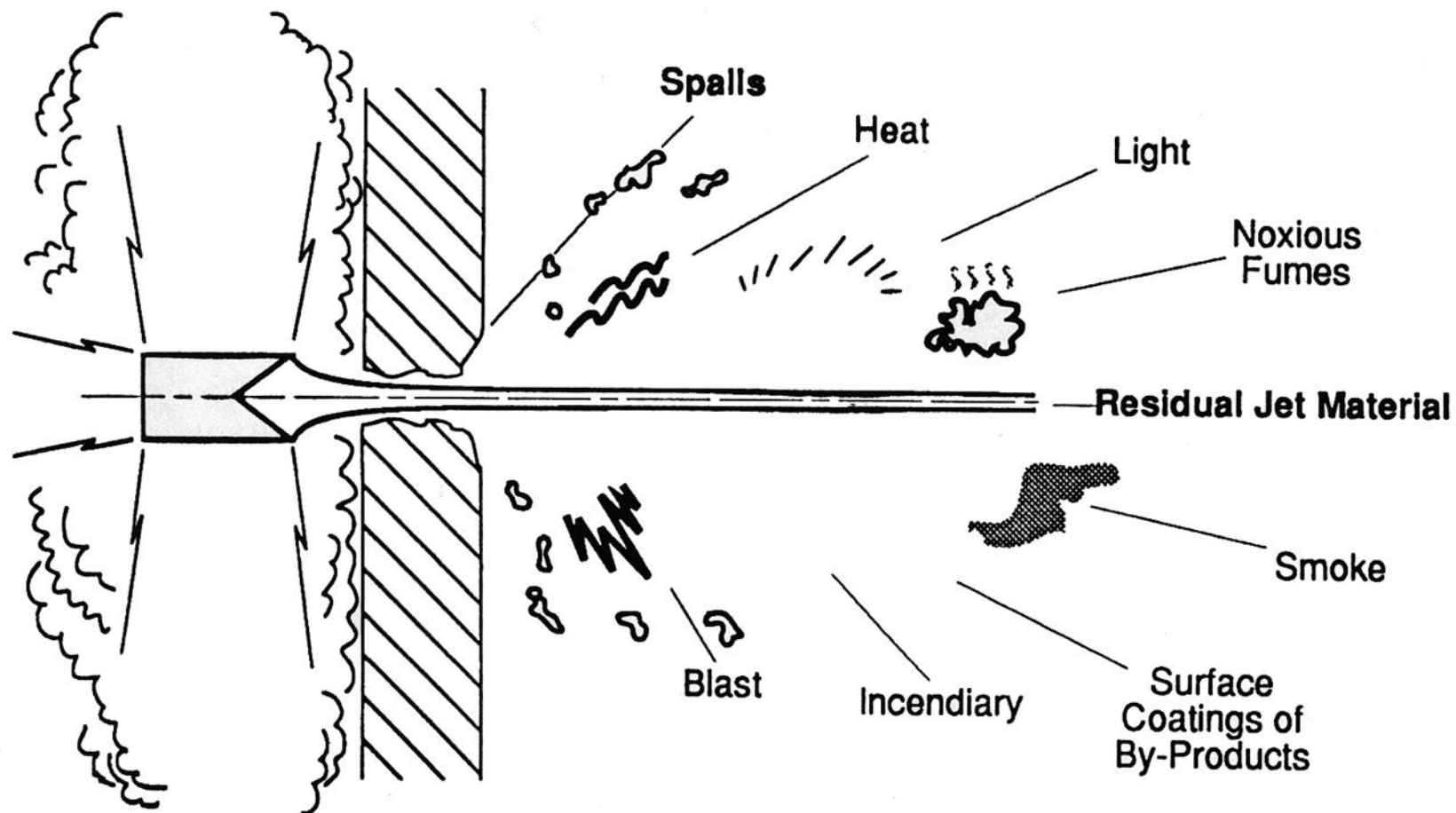
[Click Here to upgrade to
Unlimited Pages and Expanded Features](#)

Introduction

ed Charge Effects

Location	Phenomena	Efficiency Carrier	Percentage
Internal	Mechanical	<ul style="list-style-type: none"> • Residual Jet • Fragments 	
	Blast	Pressure history	
	Thermic	Heat	
	Optical	Dazzle Dust	
	Chemical	Gaseous (HE-Products)	
External	Mechanical	<ul style="list-style-type: none"> • Fragments • Blast 	

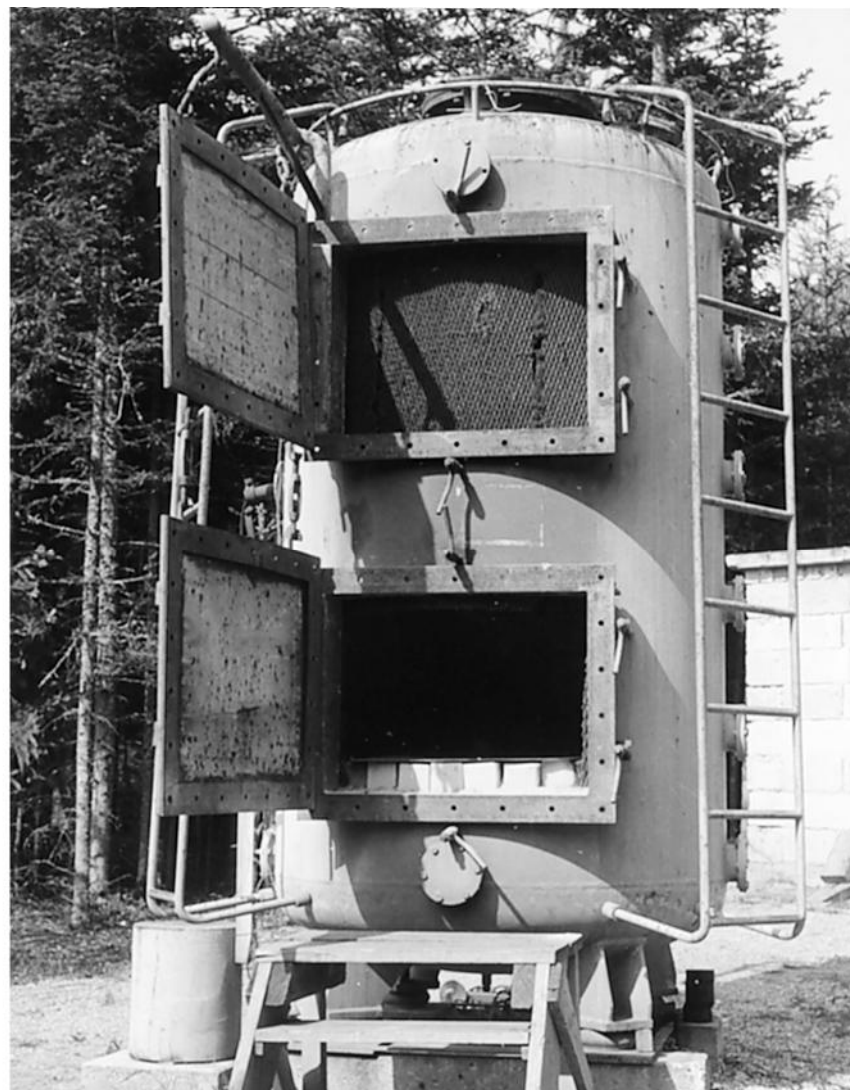
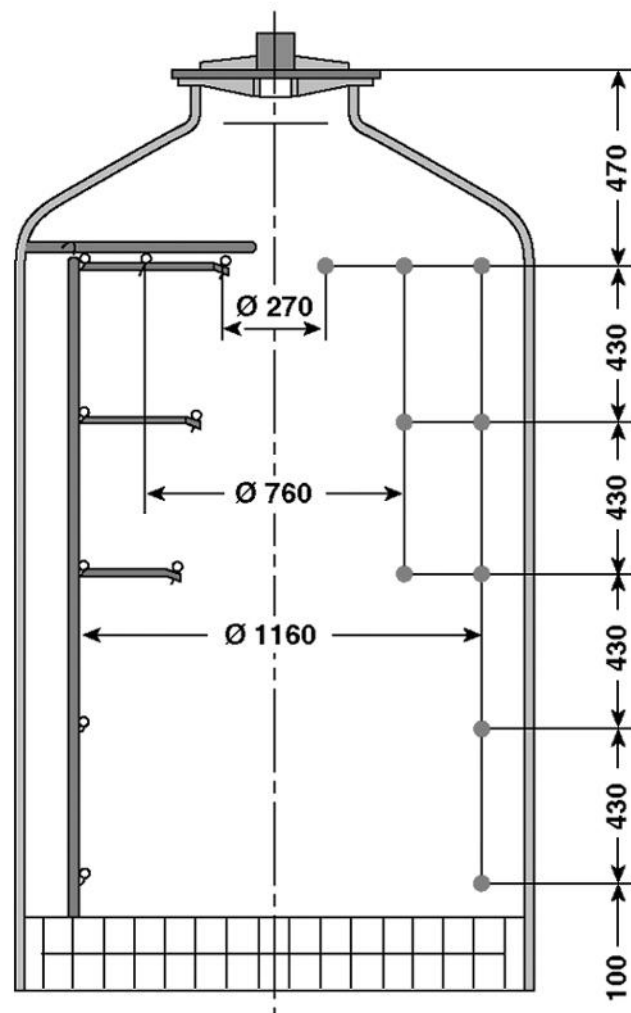
Armour Effects after Shaped Charge Jets Perforations

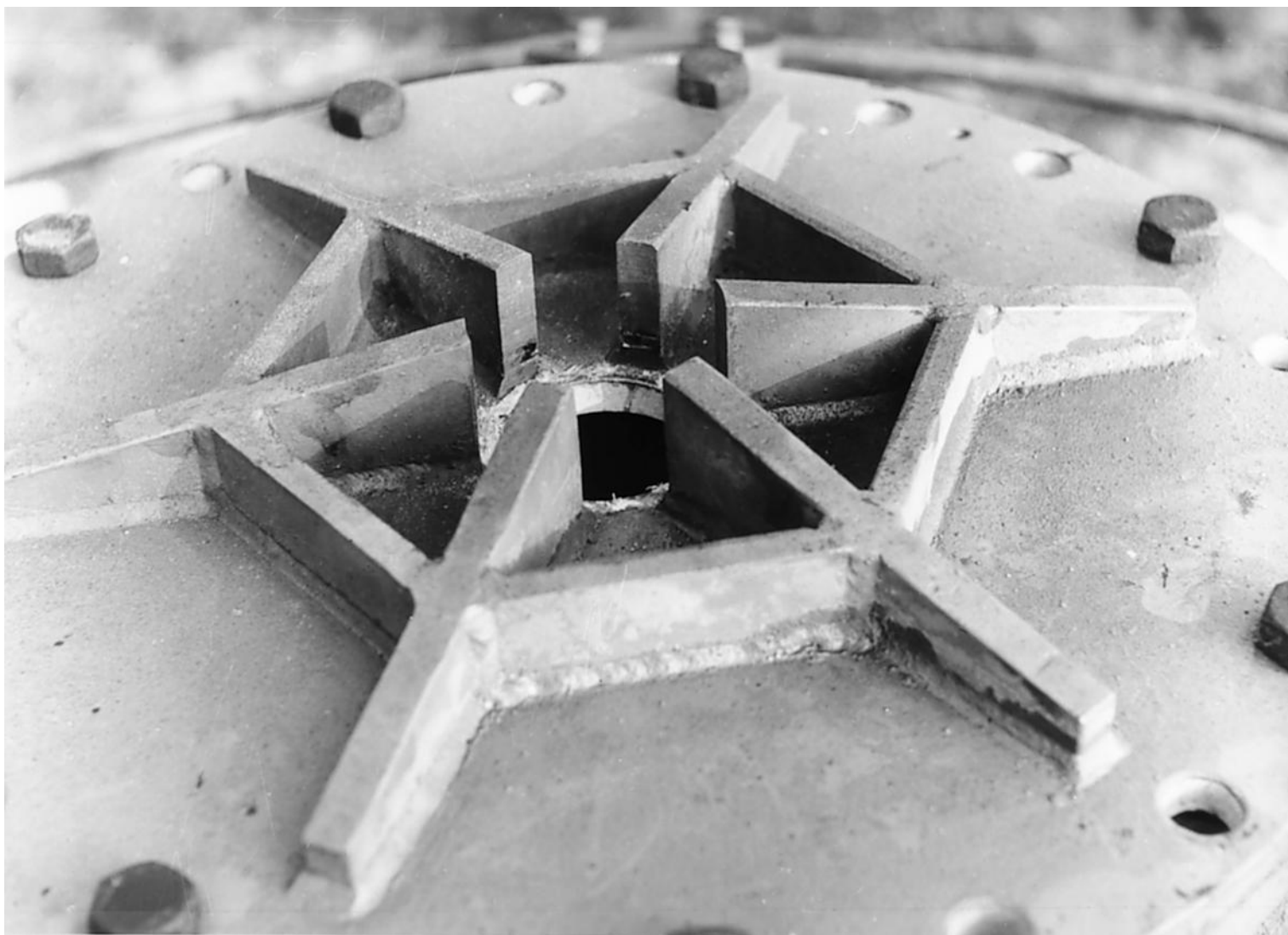


Don Kennedy

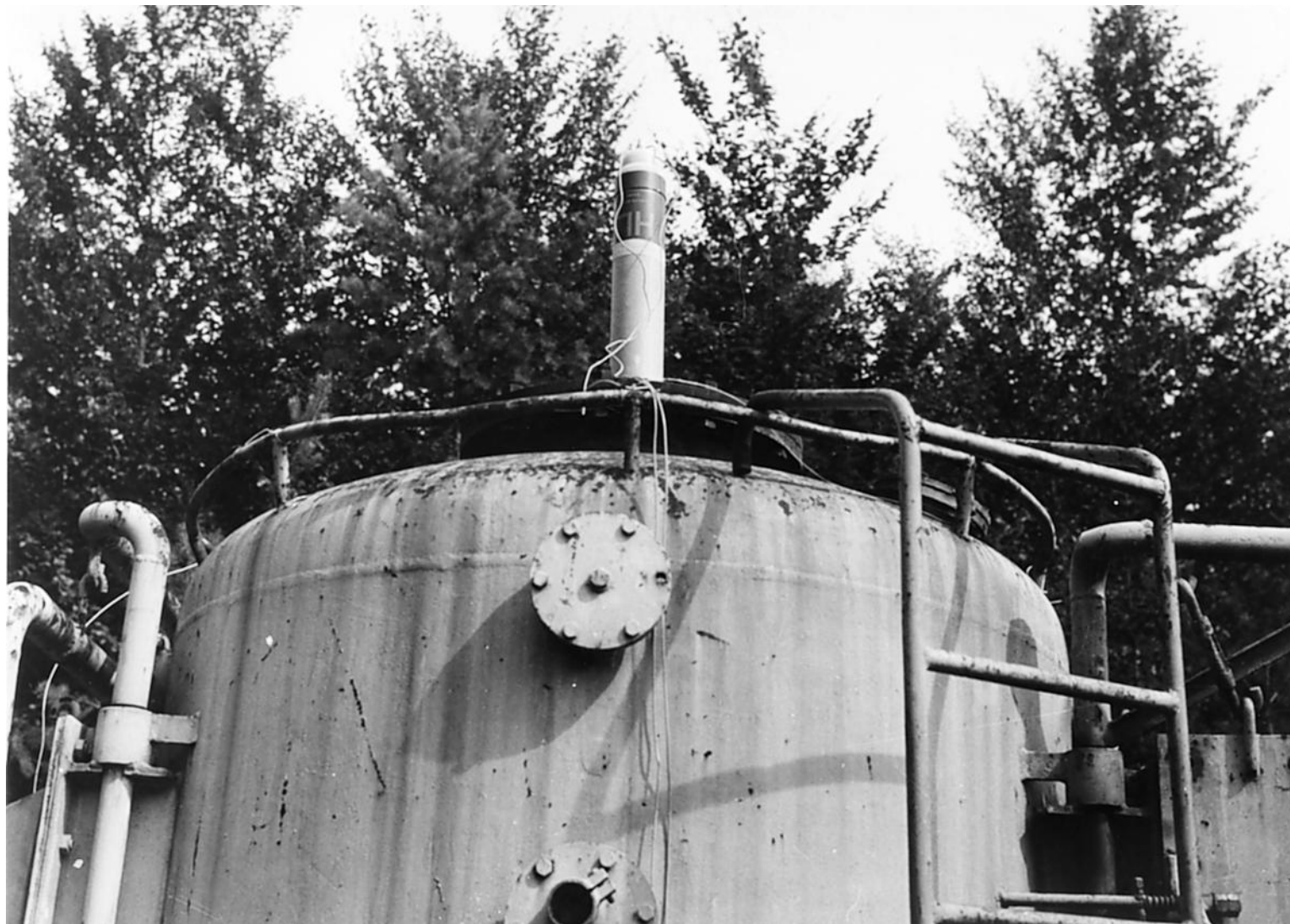
Diagnostic Vessel

with 2.4 m³ Volume



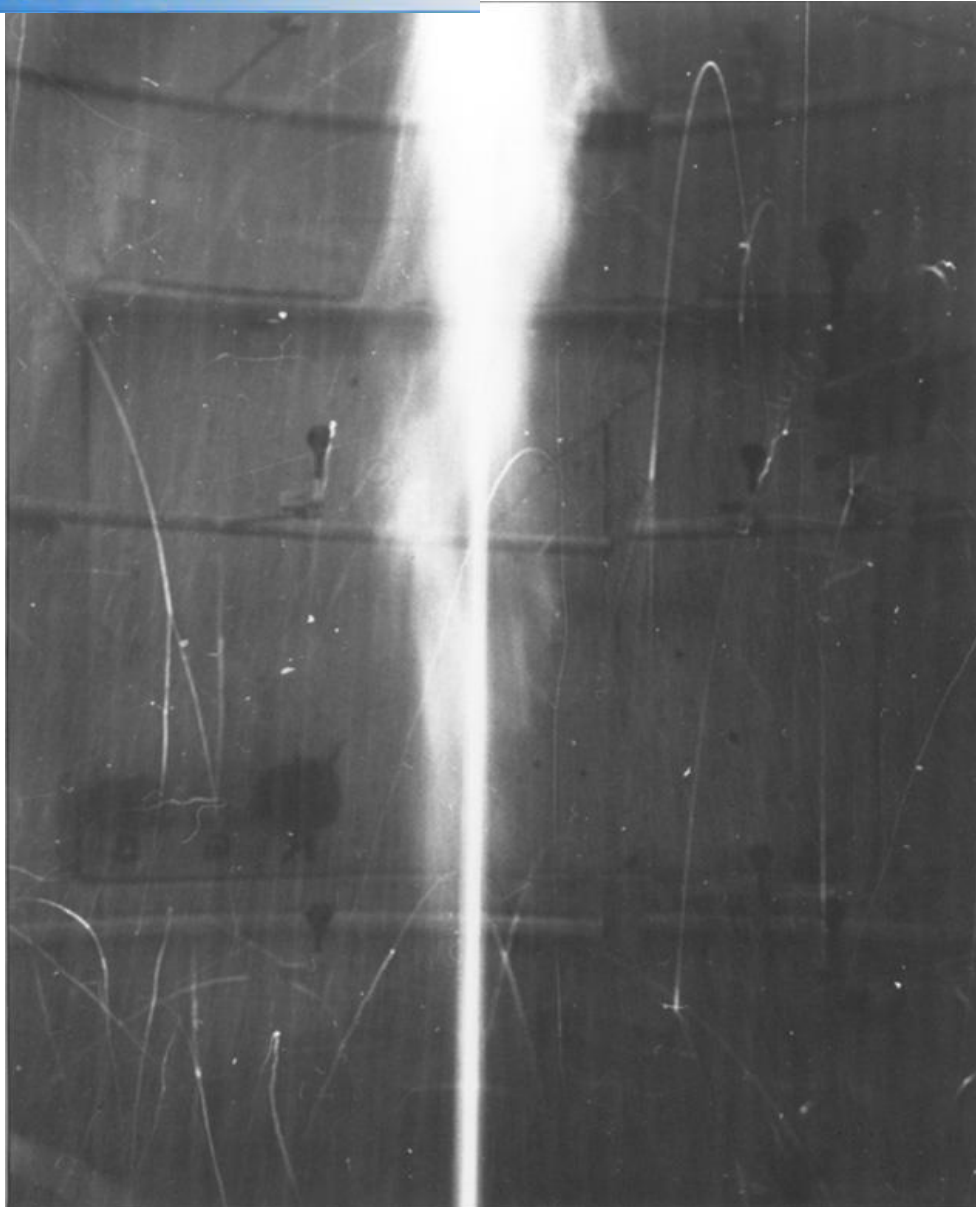


arge on Top





Pictures



Cobra with Cu liner in
the diagnostic vessel

 **PDF Complete**

*Your complimentary
use period has ended.
Thank you for using
PDF Complete.*

[Click Here to upgrade to
Unlimited Pages and Expanded Features](#)

ictures



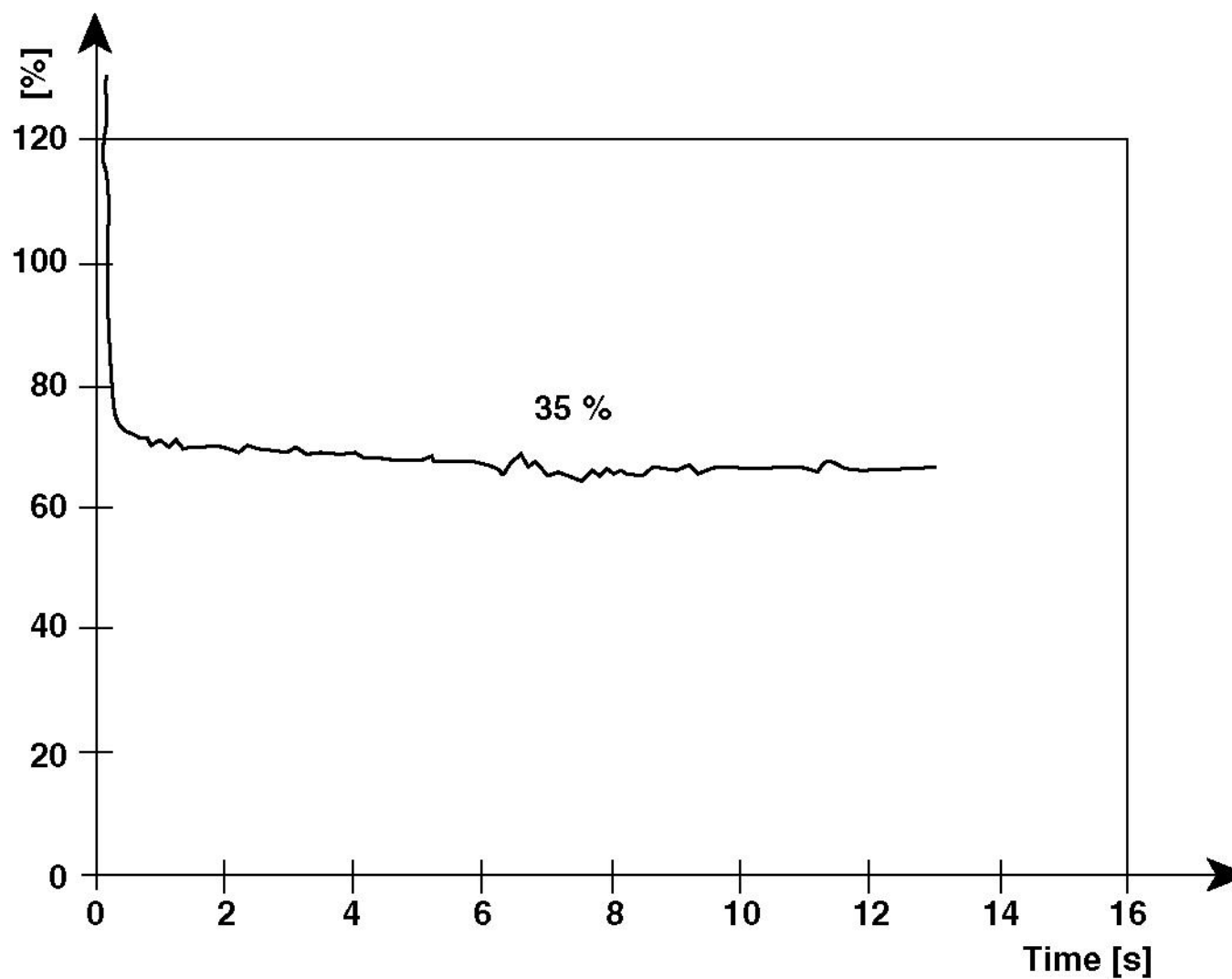
 **PDF Complete**

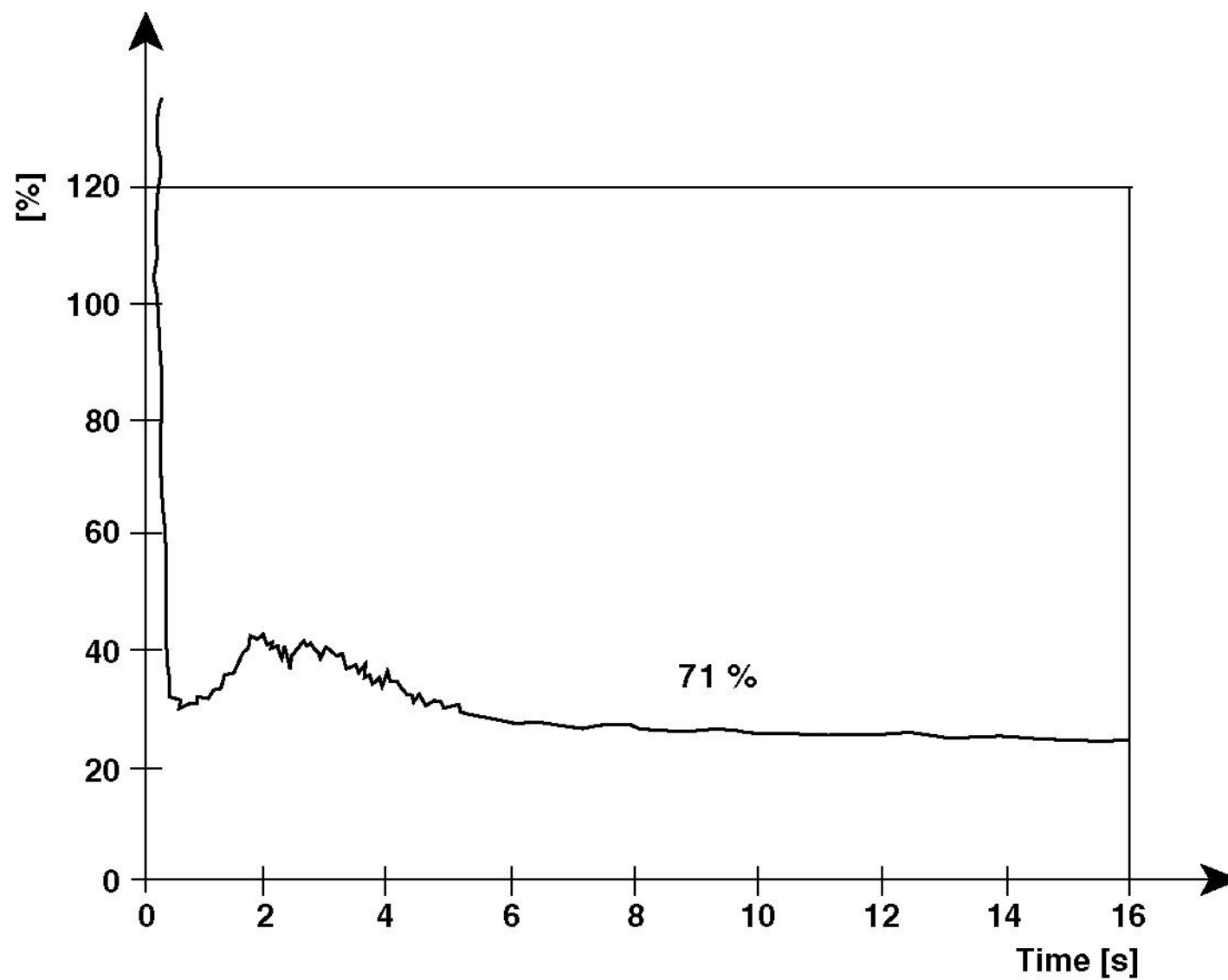
*Your complimentary
use period has ended.
Thank you for using
PDF Complete.*

[Click Here to upgrade to
Unlimited Pages and Expanded Features](#)

ictures







with Gaseous Analysis and Piezoelectric Pressure Gauges



Measuring Tank No.

Shaped Charge	:	Orig. Cobra
HE - Weight	:	1480 g
Cu liner - Weight	:	250 g
Standoff	:	300 mm
Barrier	:	300 mm

Gaseous Analysis

(Oxygen Absorption in Pyrogallol)

Oxygen before Firing : 20.9 %

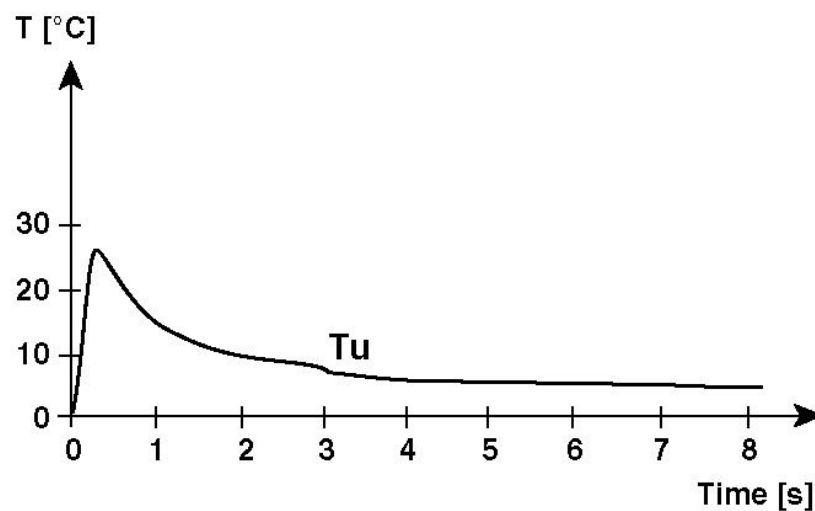
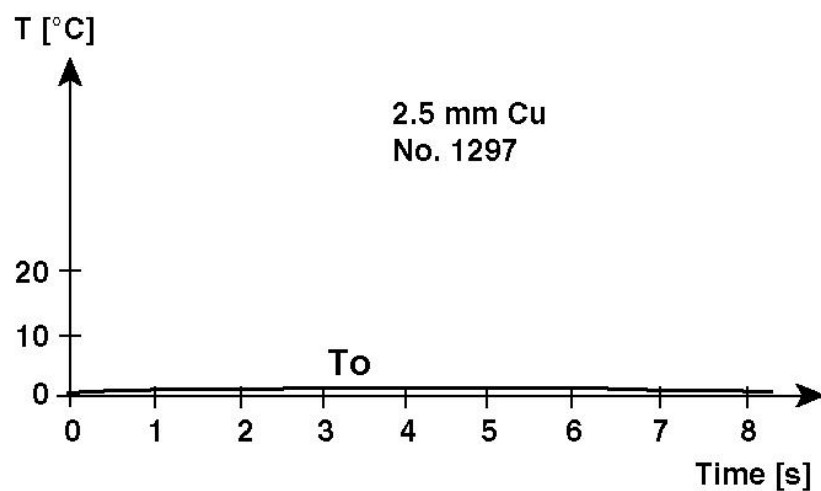
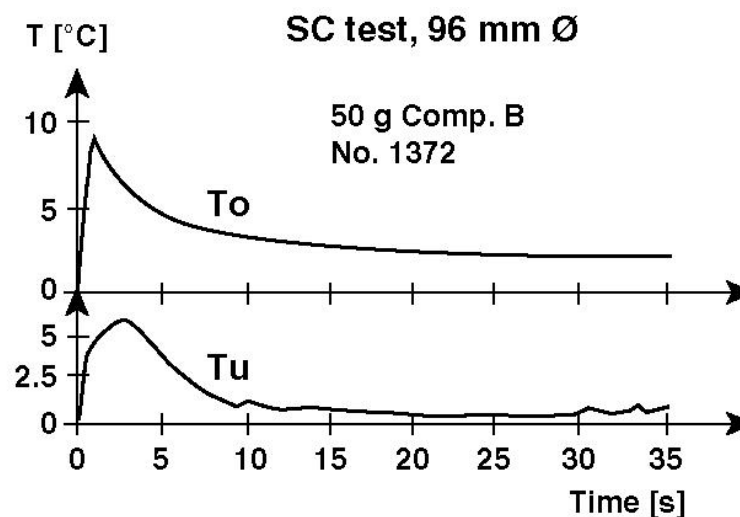
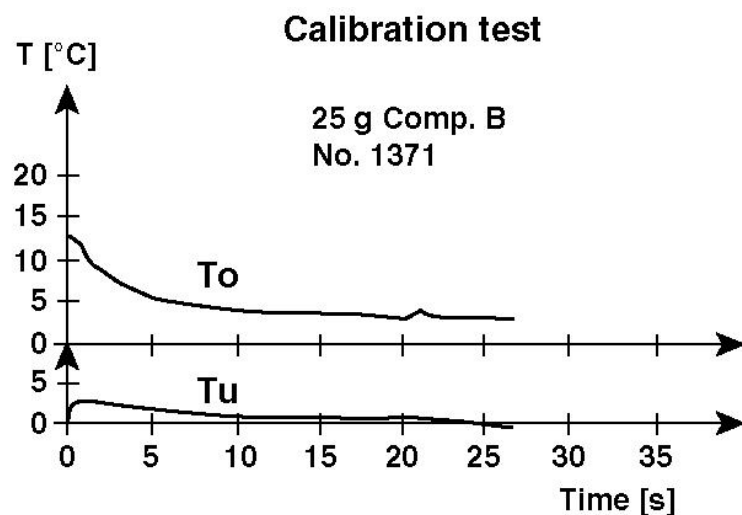
Oxygen after Firing : 20.6 %

Found in Water after 50 Liter Gas:

Iron	Fe	0.70 mg
------	----	---------

Copper	Cu	1.40 mg
--------	----	---------

Nitropenoxia	NO	Shows
--------------	----	-------

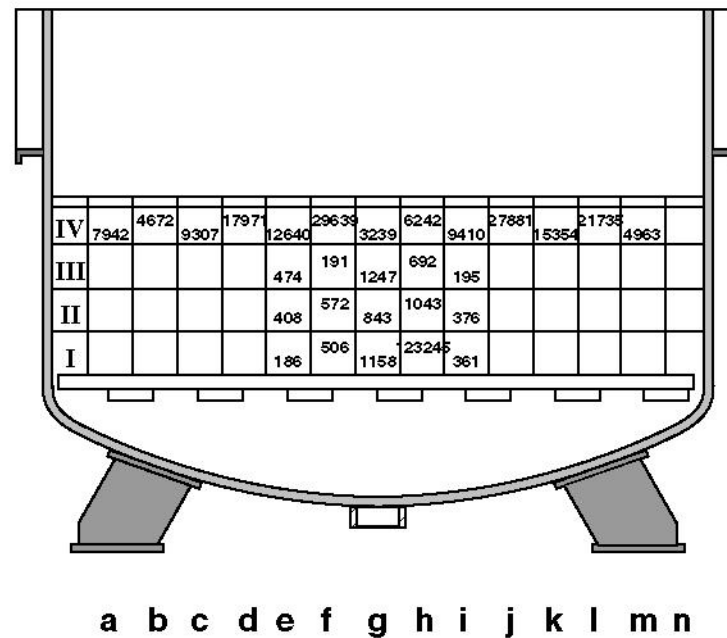
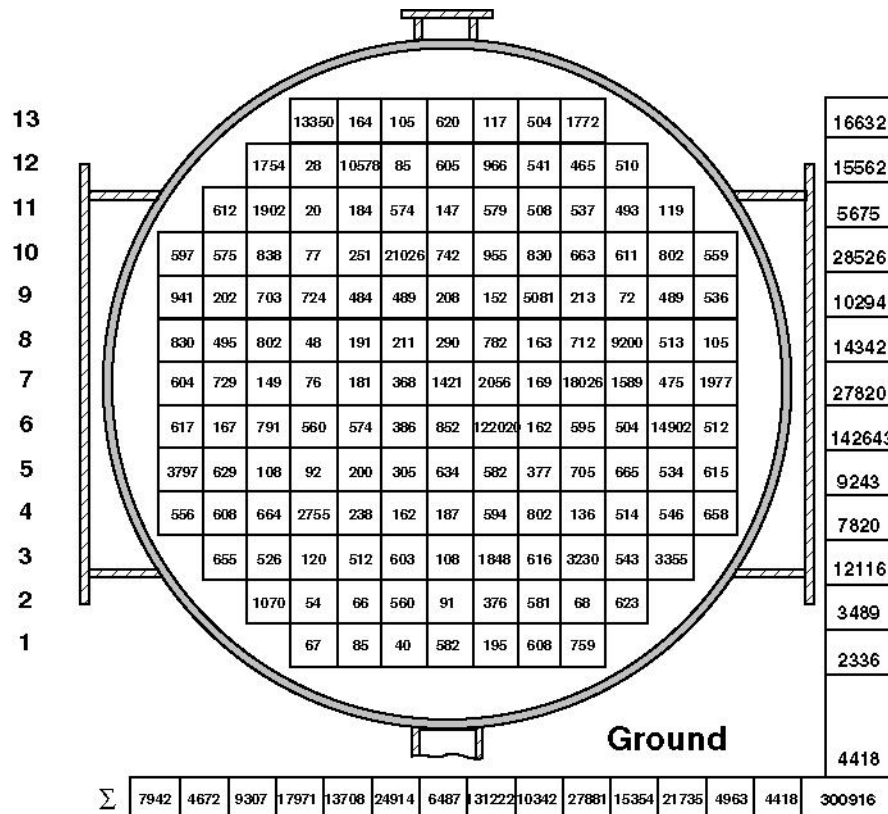


Spall Fragments



Bottom



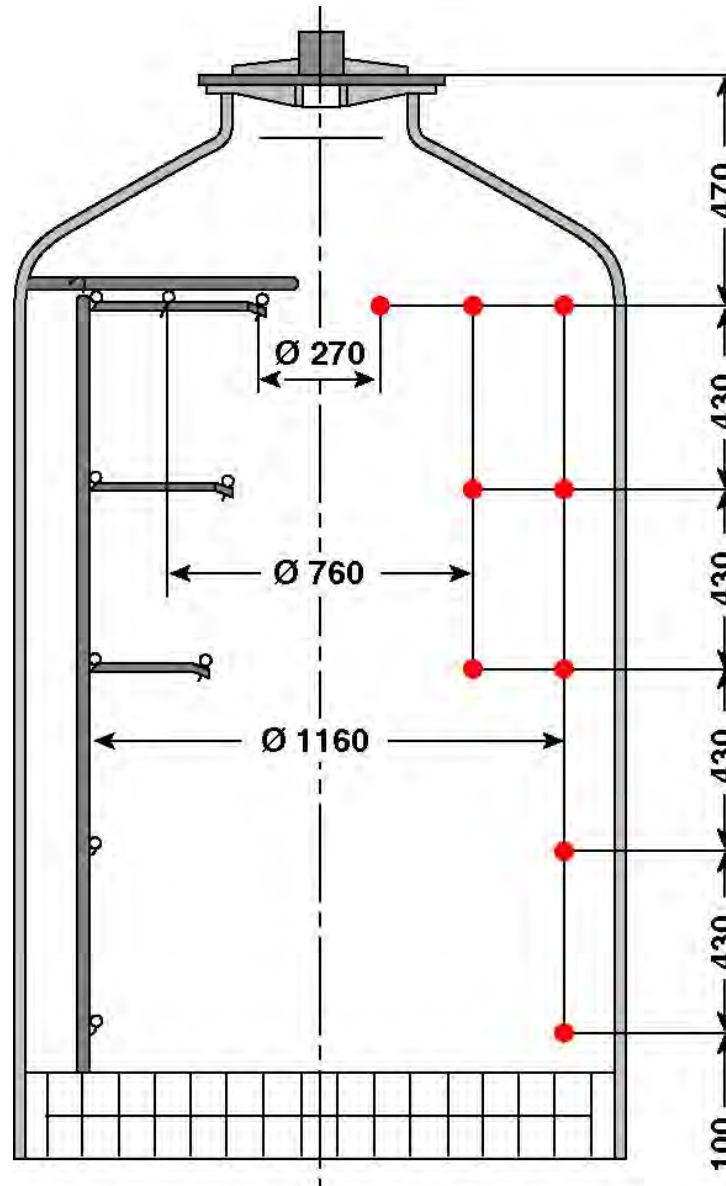


Blast Load Measurements

Gauges

6 pictures
 x 9 locations =
 = 54 diagnostic points

54 dodecahedra
 x 11 diaframa =
 594 measurements,
 distributed over the
 radius and height
 of the diagnostic vessel

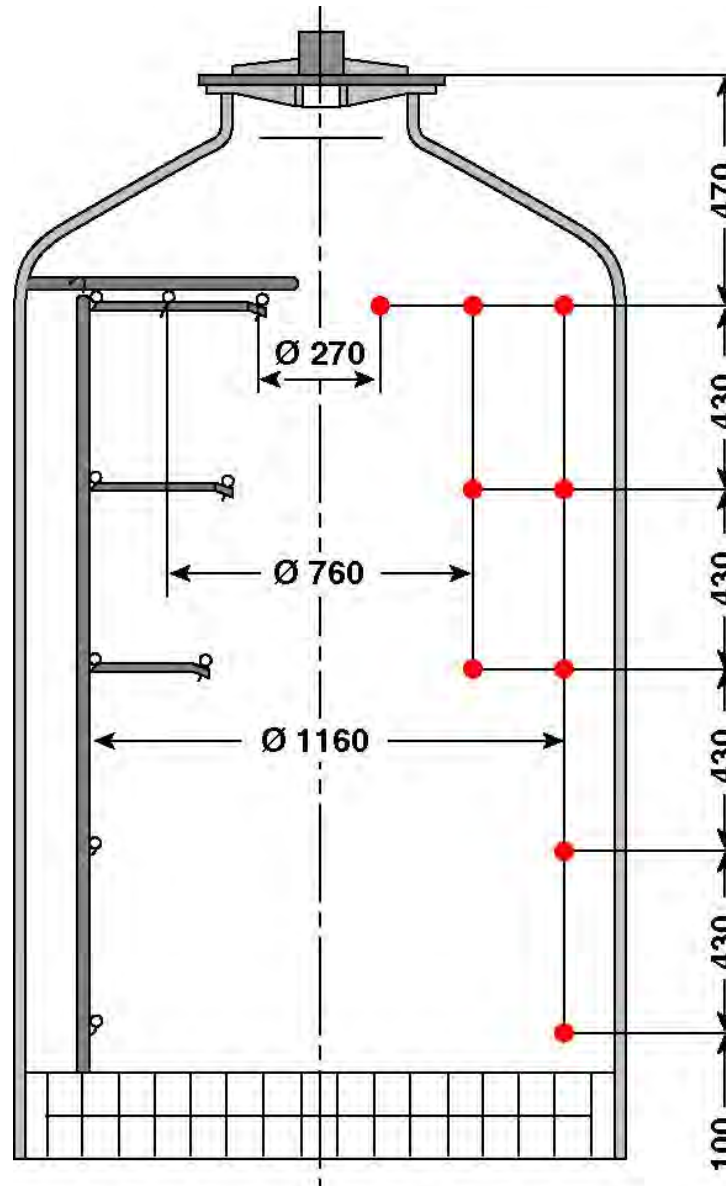


Gauges

6 pictures
 x 9 locations =
 = 54 diagnostic points

54 dodecahedra
 x 11 diafragma =
 594 measurements,
 distributed over the
 radius and height
 of the diagnostic vessel

Dodecahedra



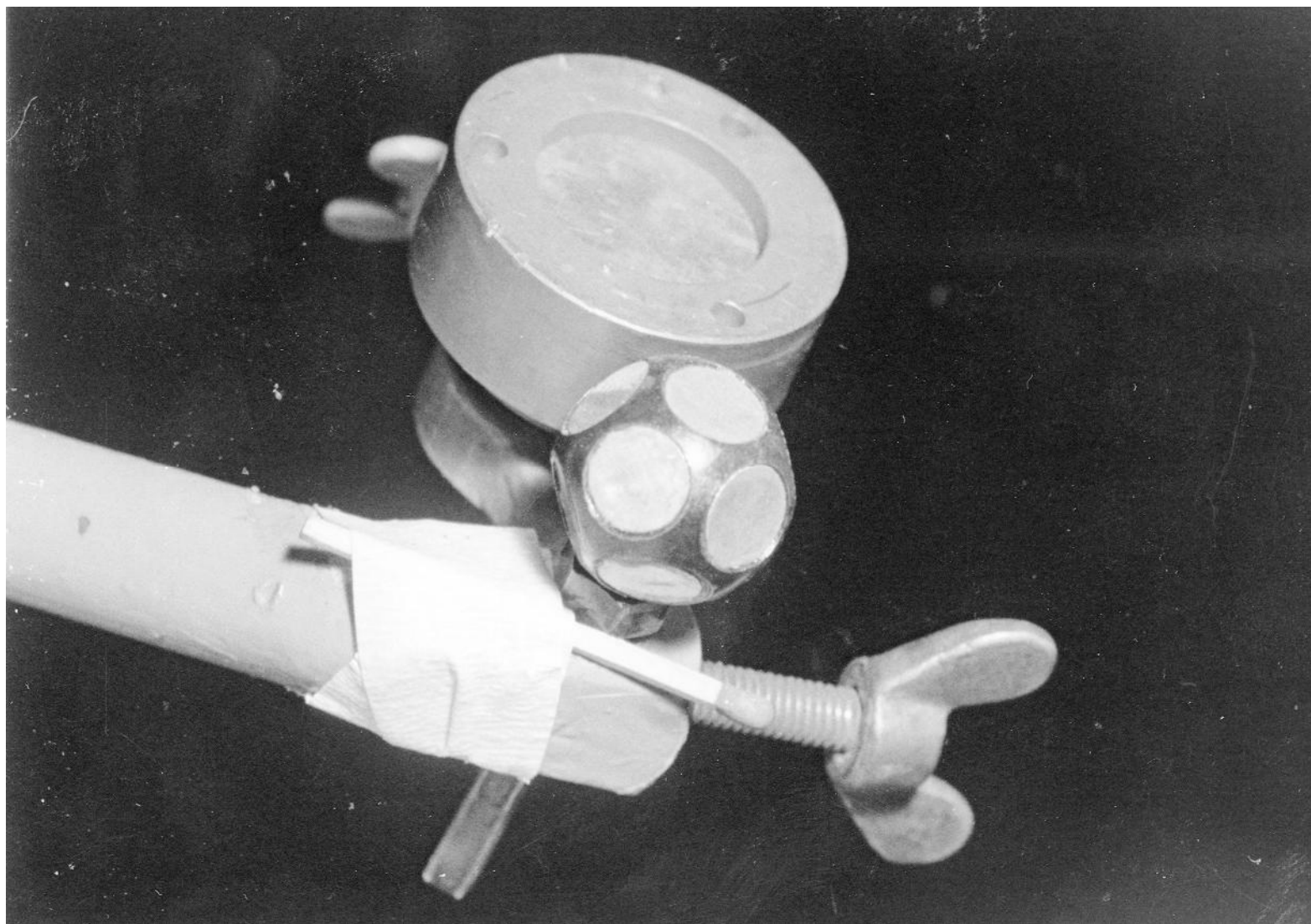
Top of diagnostic vessel



Fictitures

Expanded metal mesh

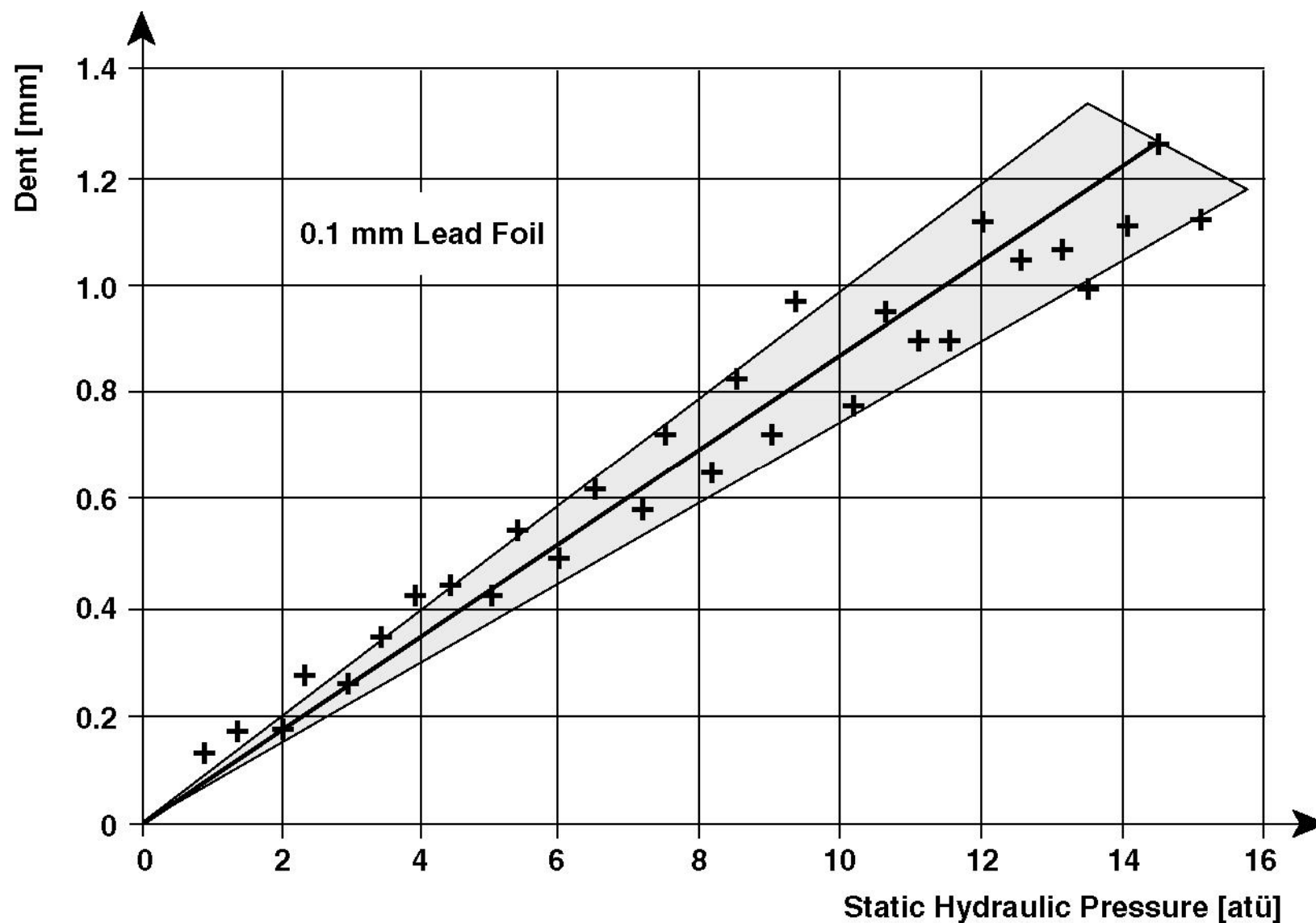
Caeder, Matches



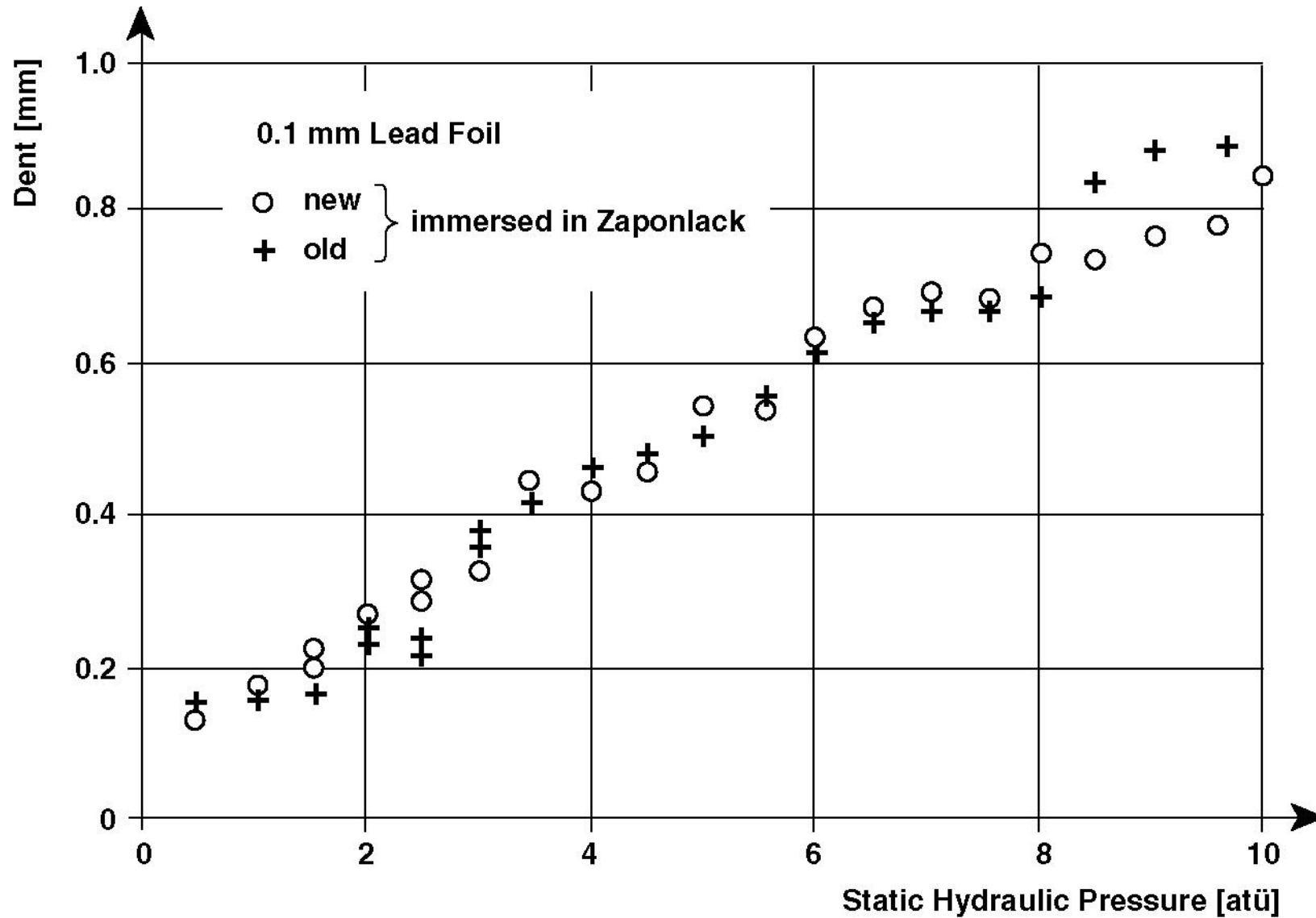
körper“

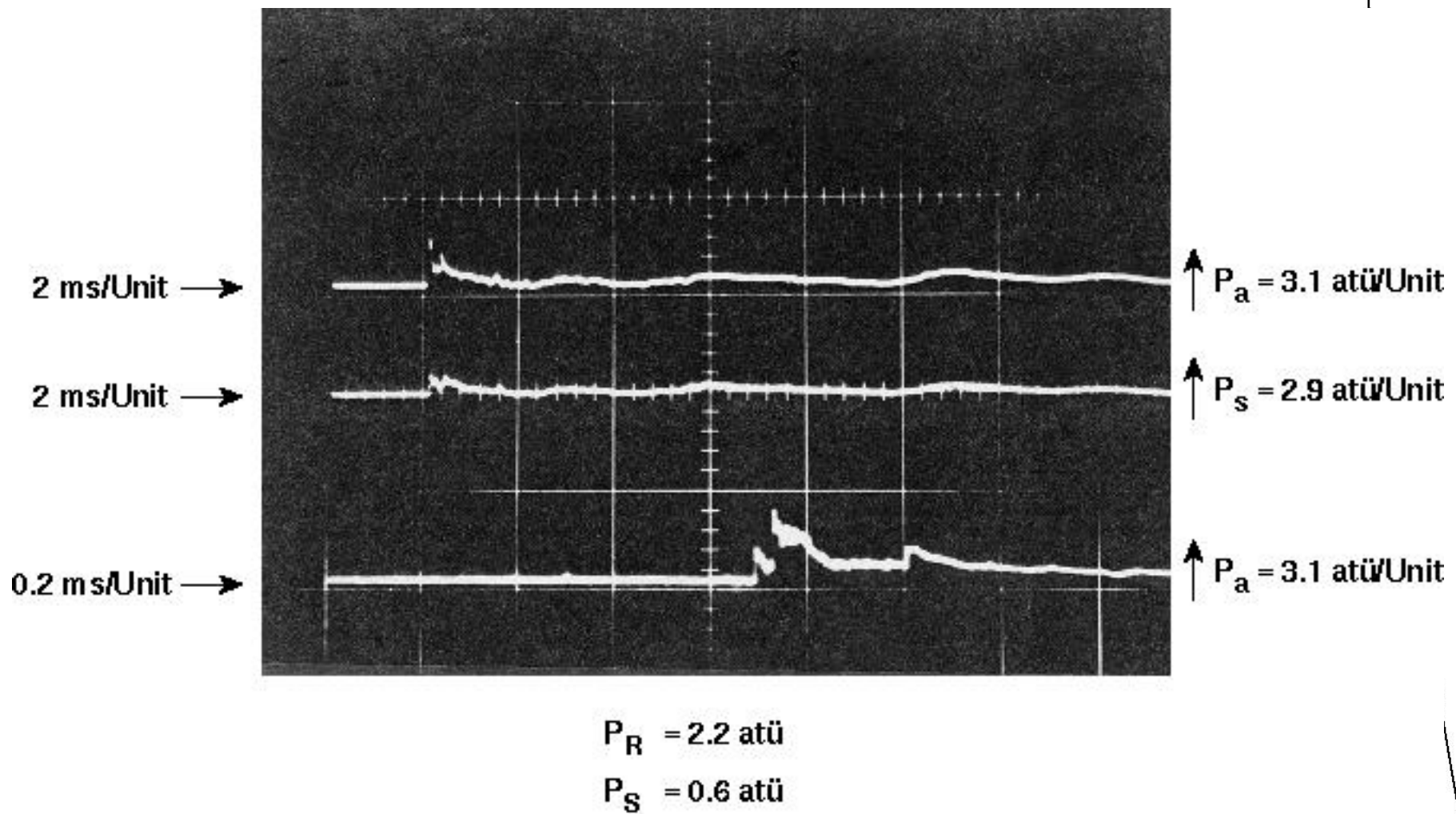


Measuring Device

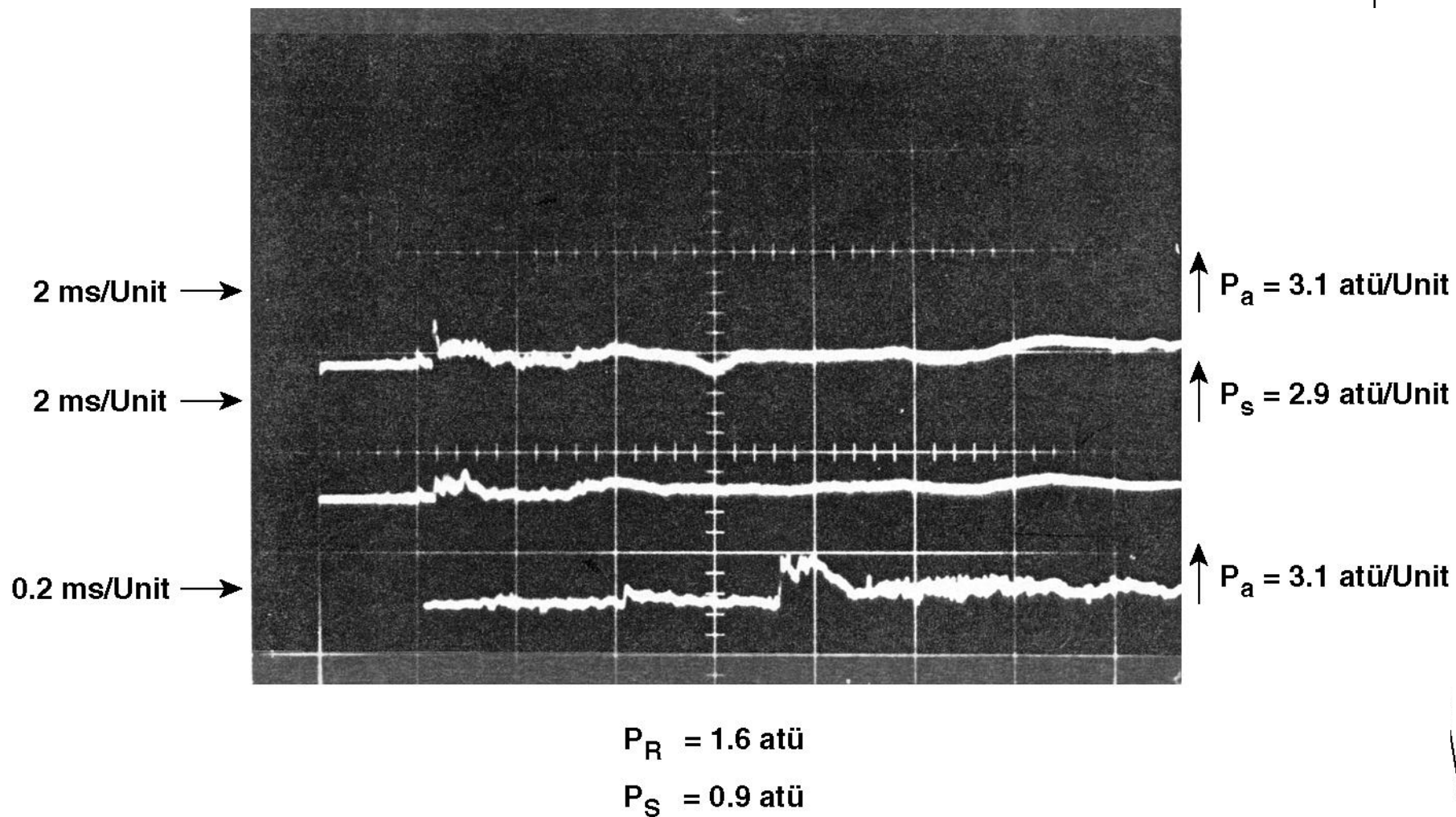


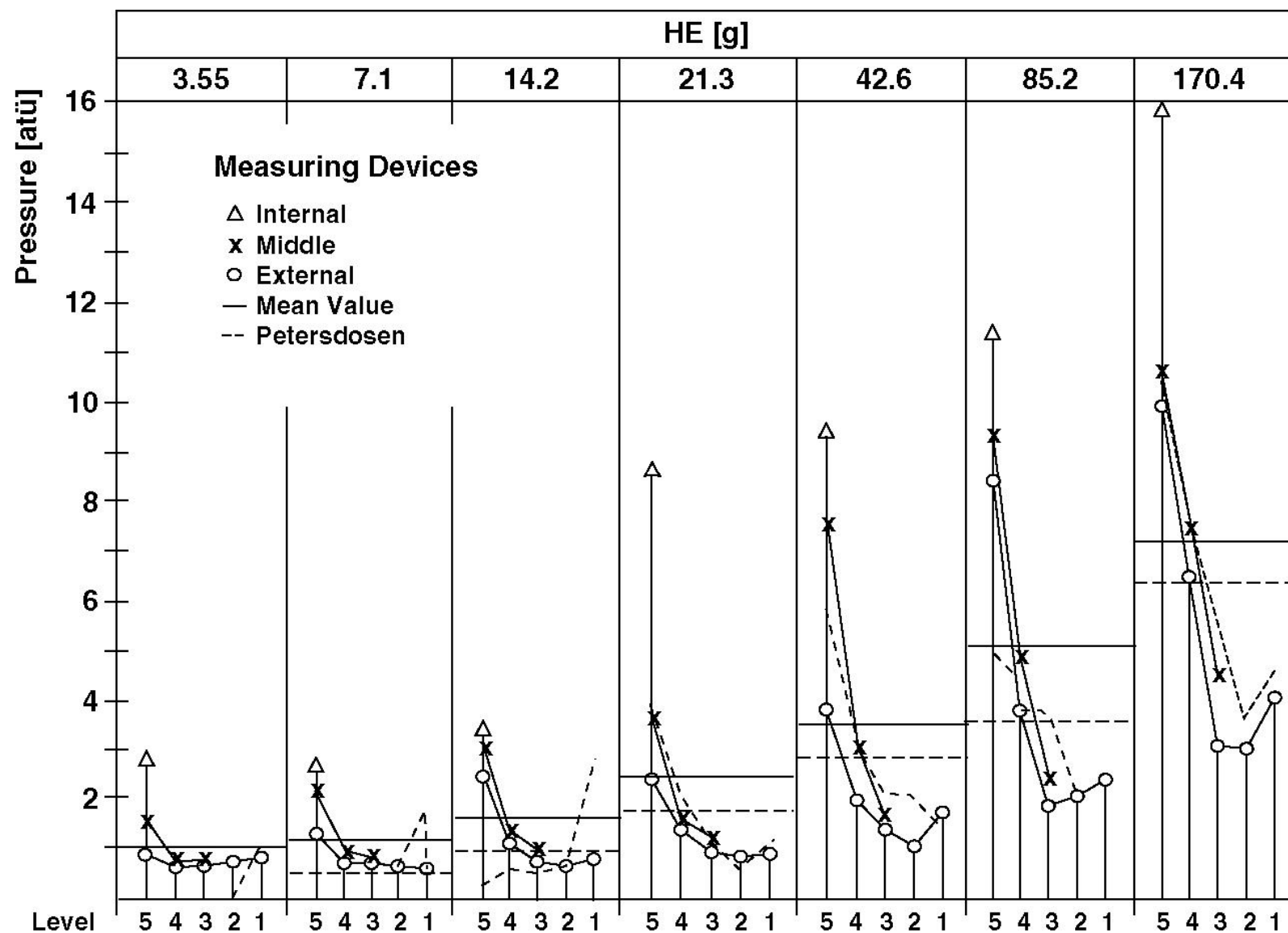
Measuring Device

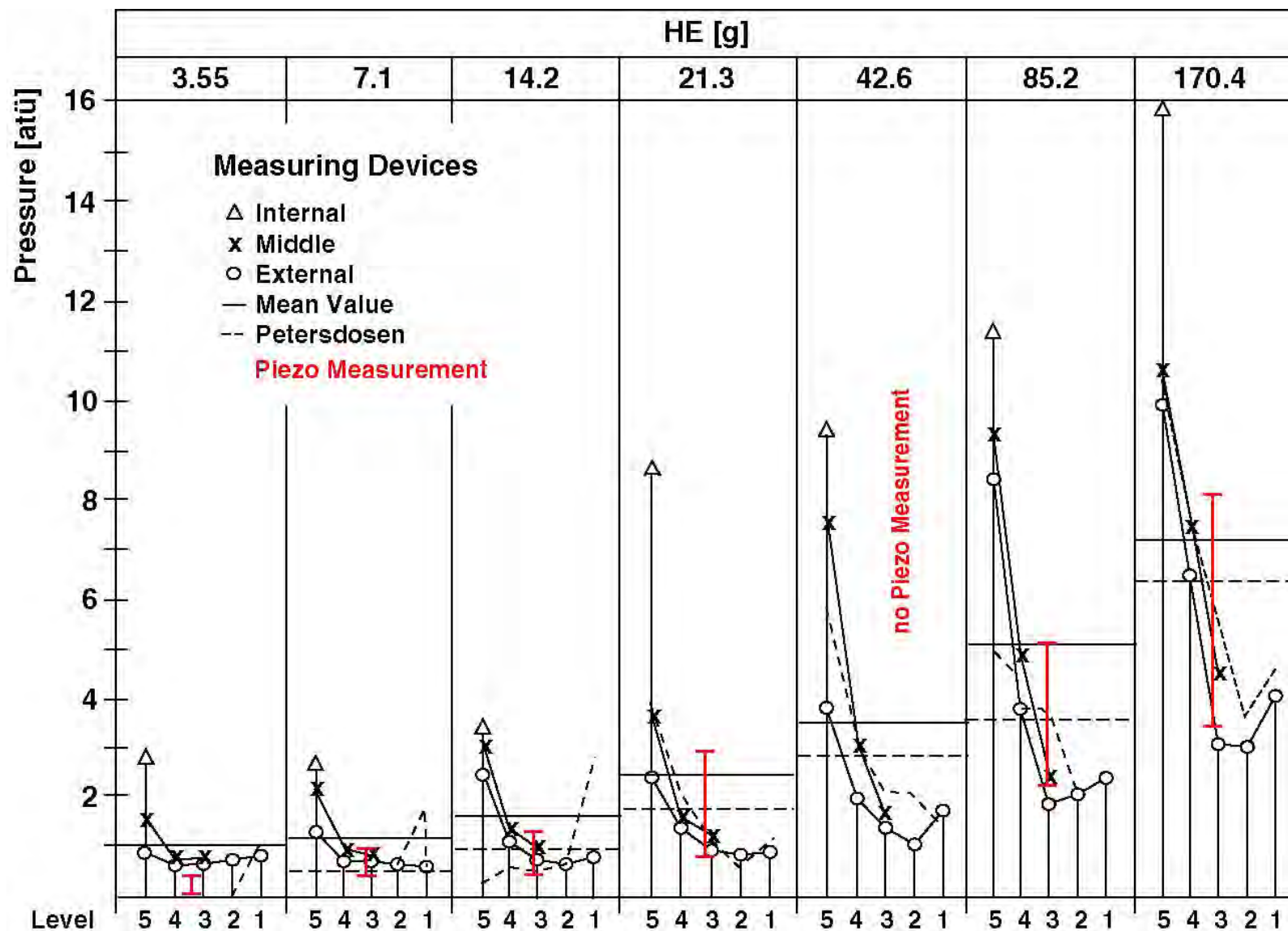


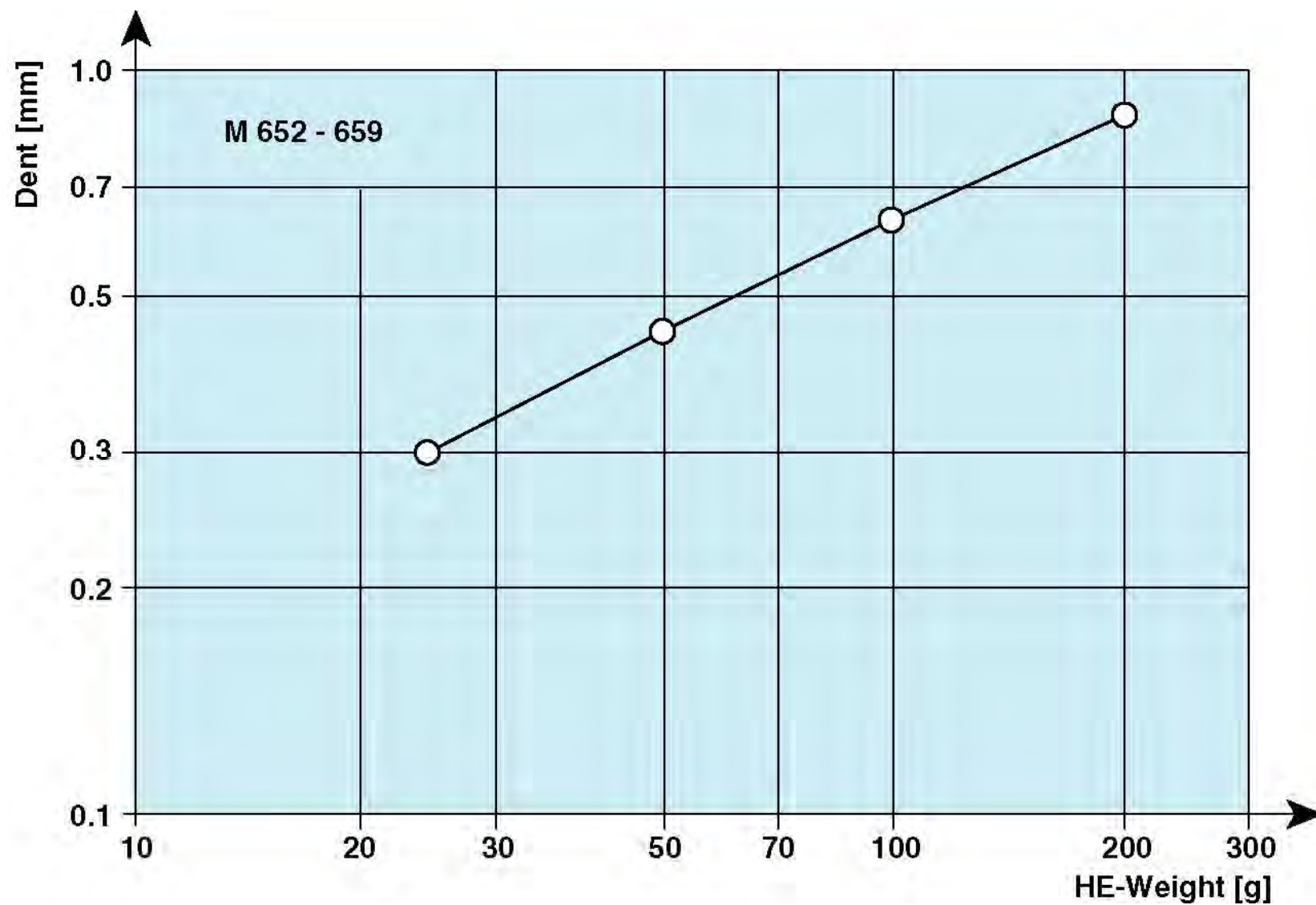


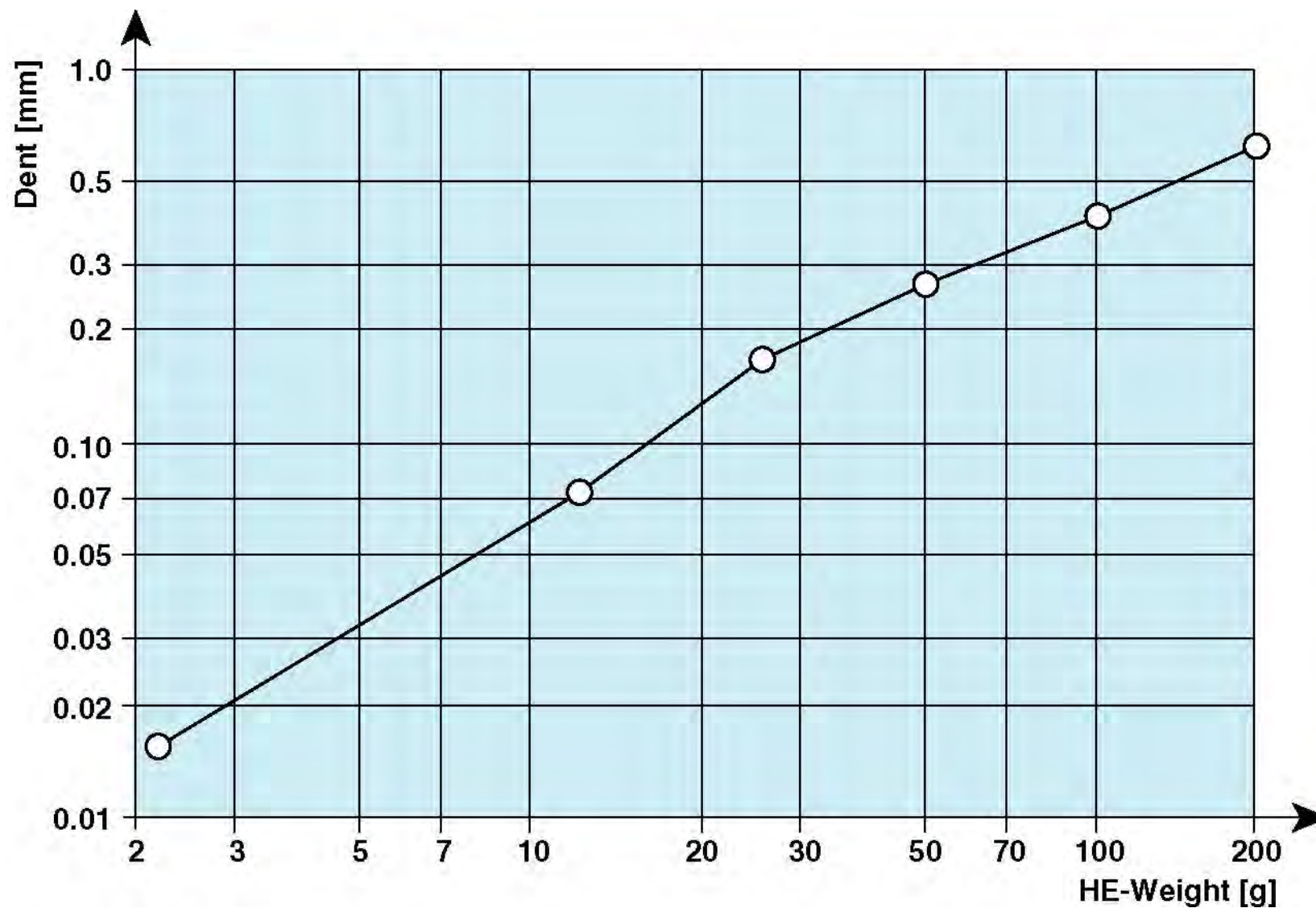
00 mm Barrier



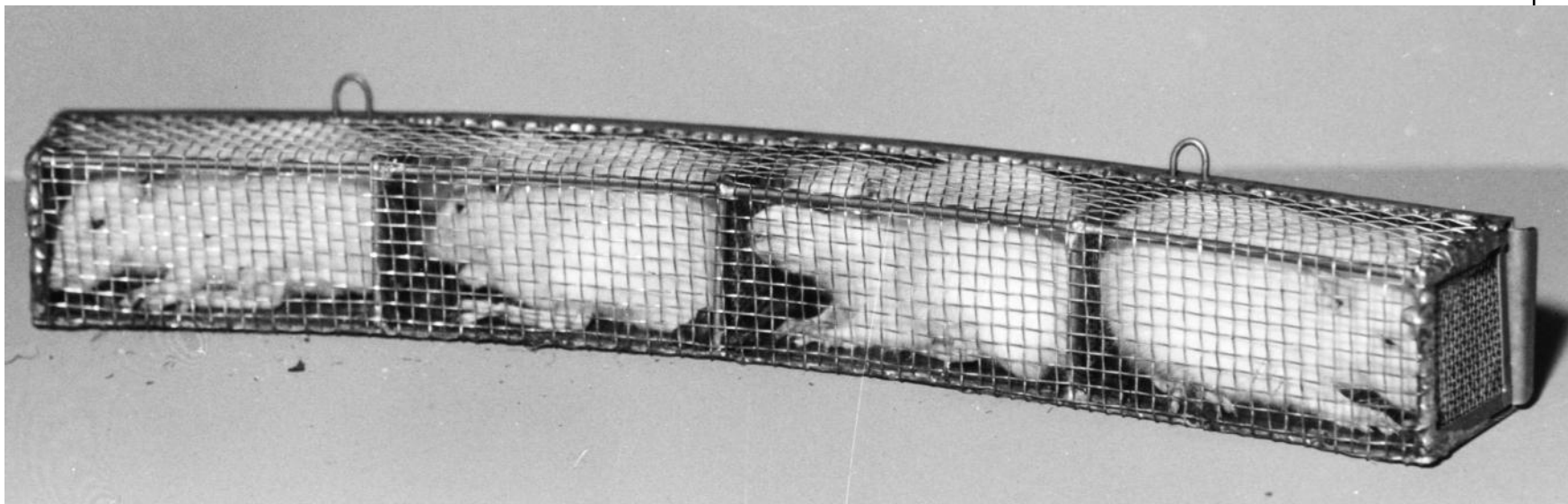




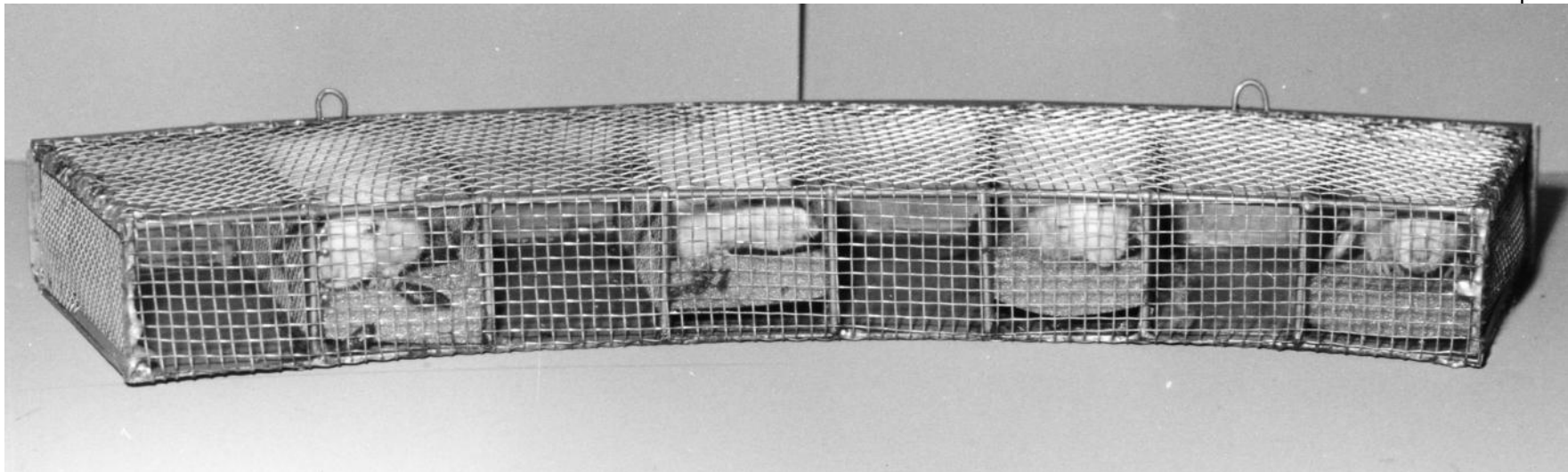




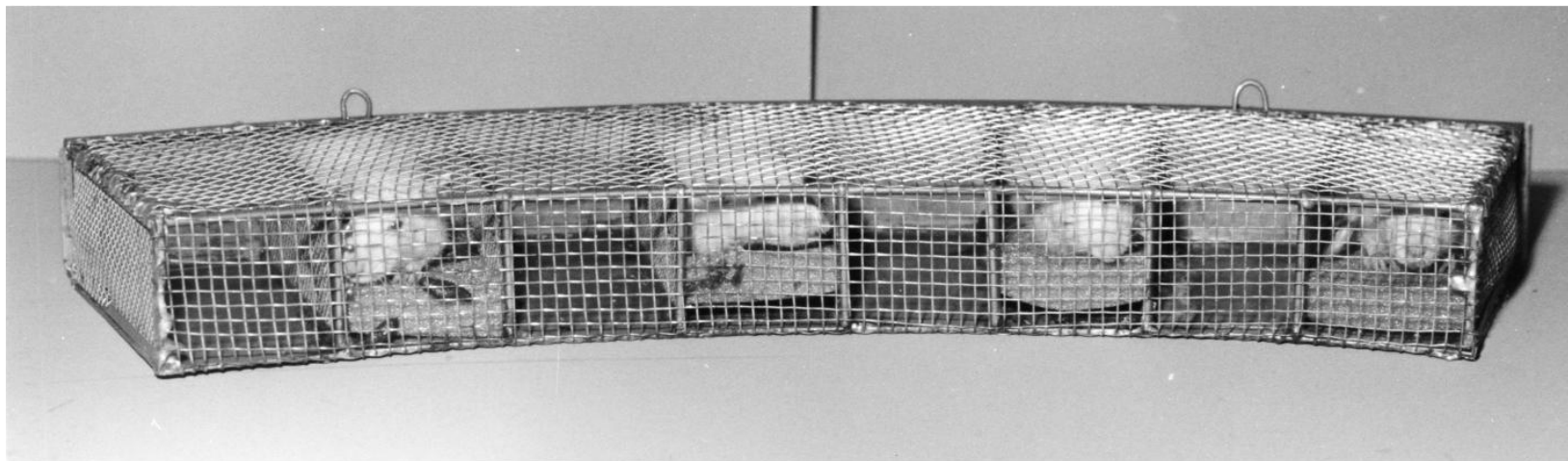
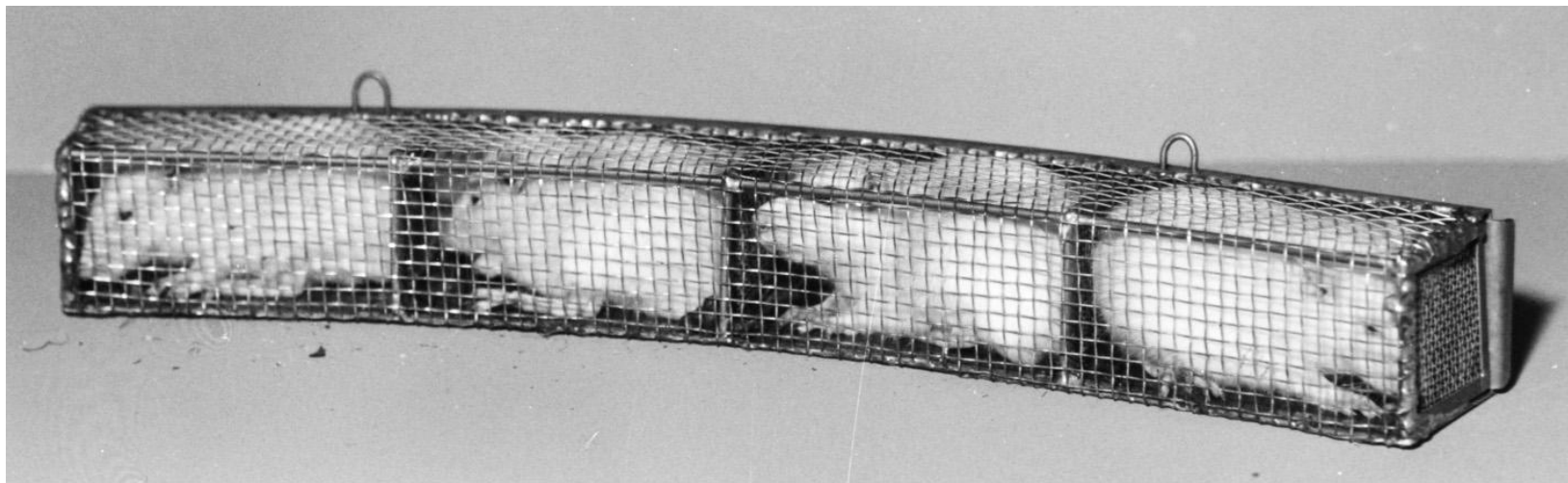
Albino Rats



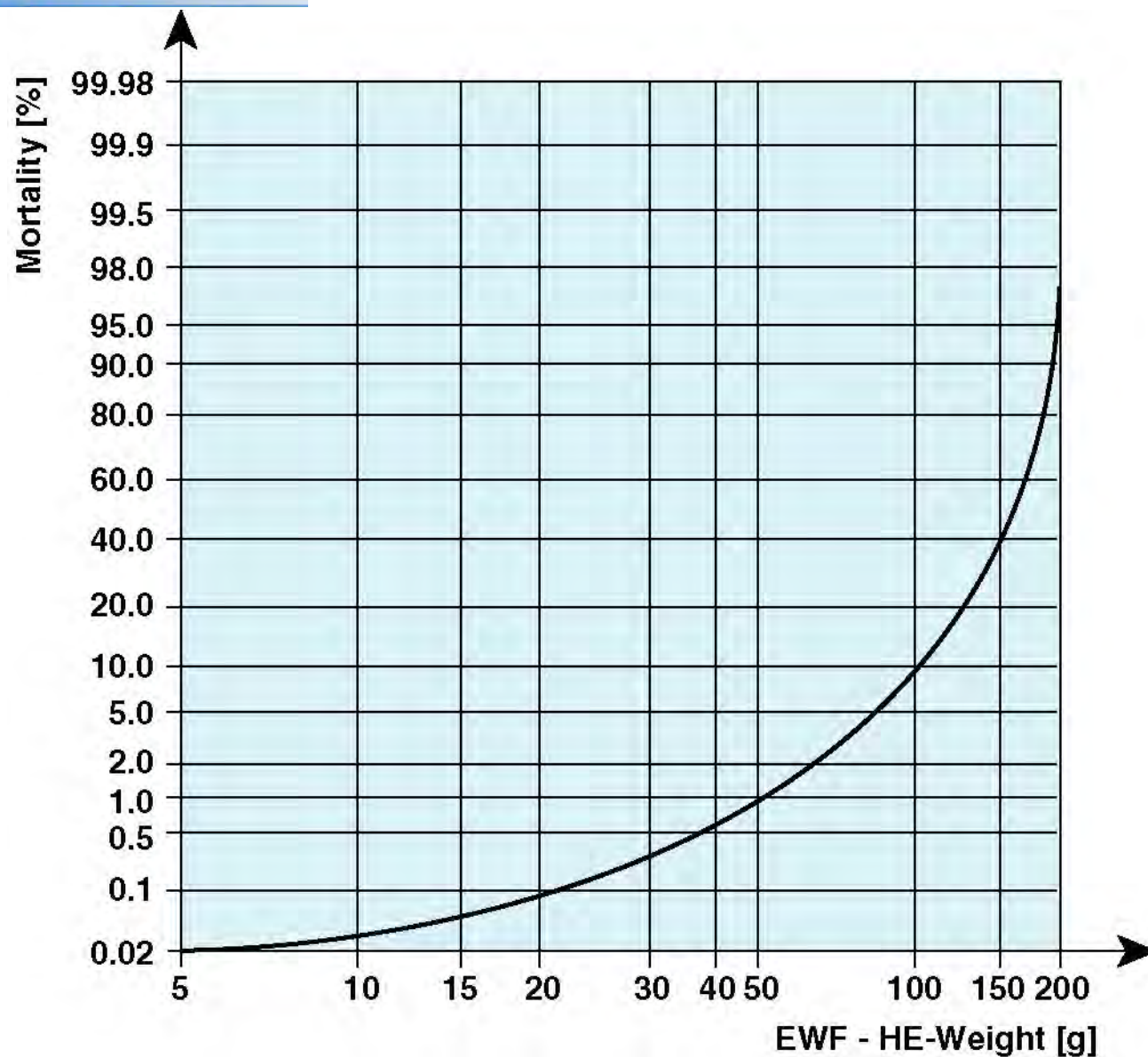
bino Rats



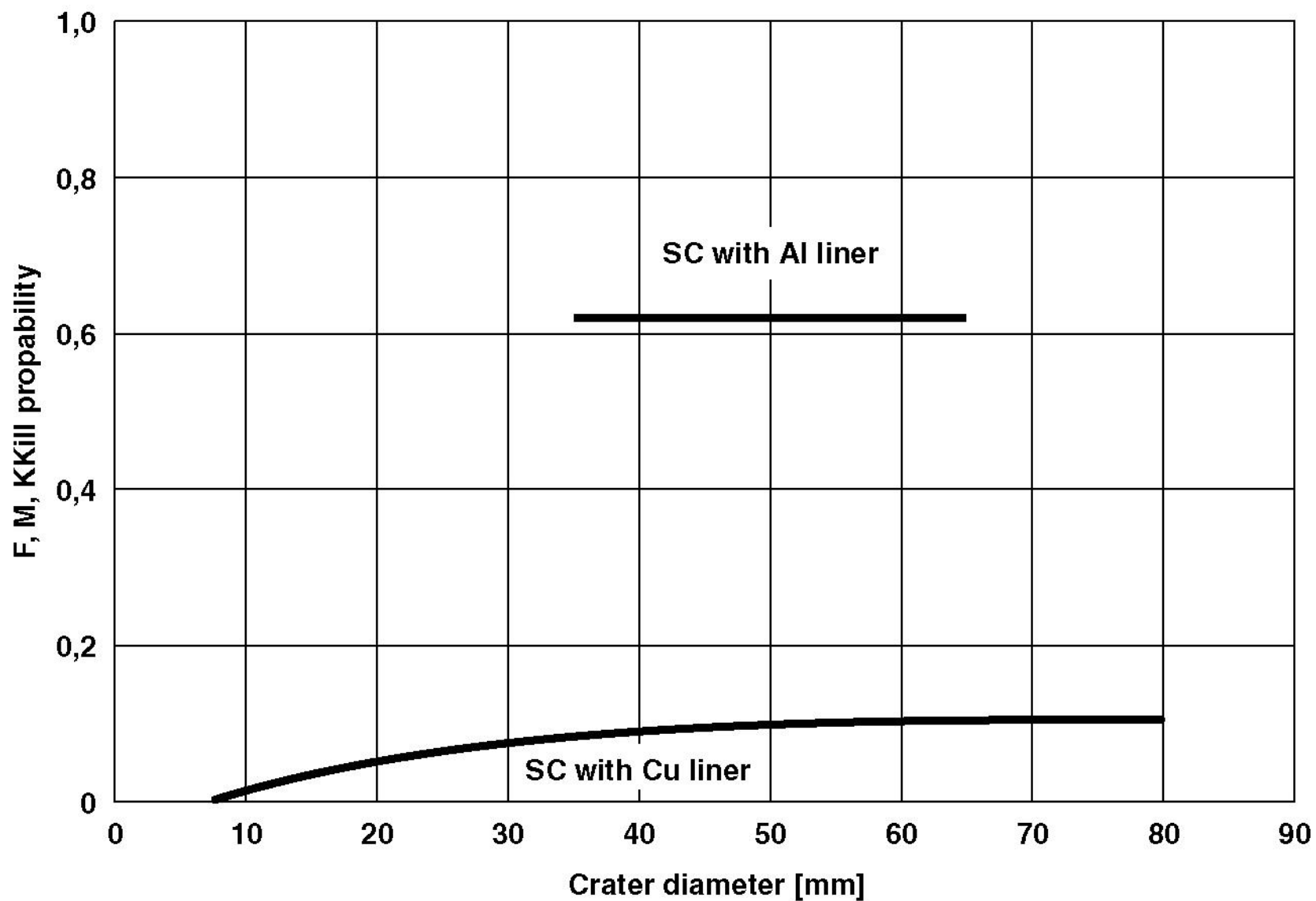
bino Rats



Rats 200g

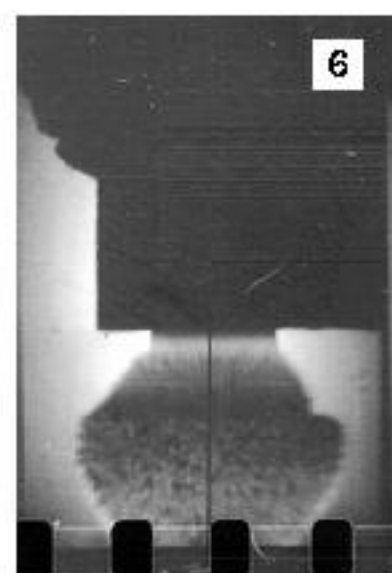
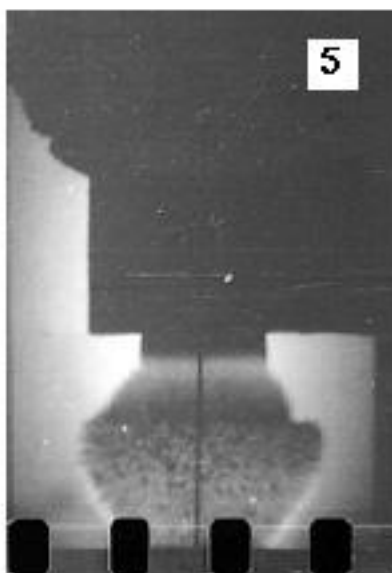
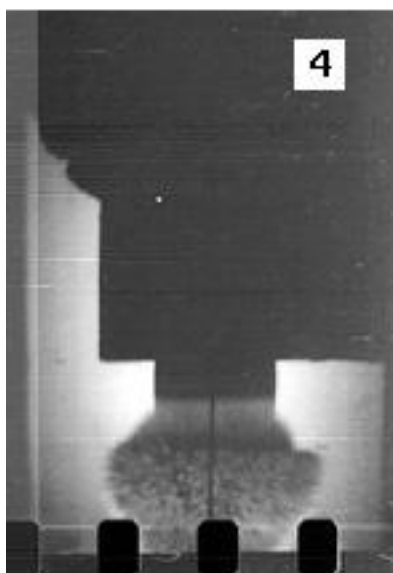
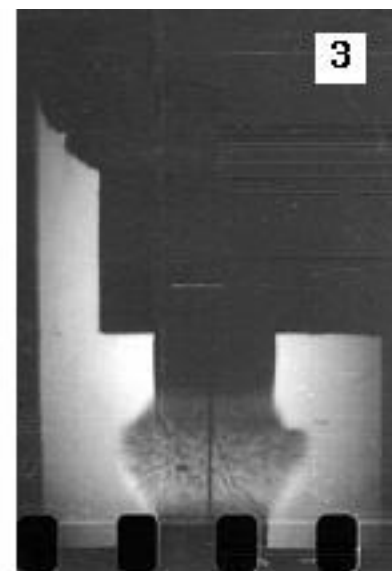
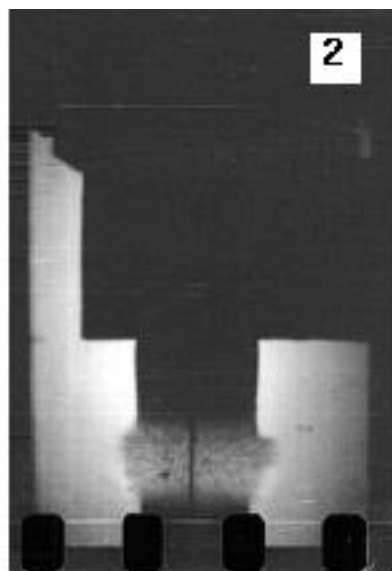
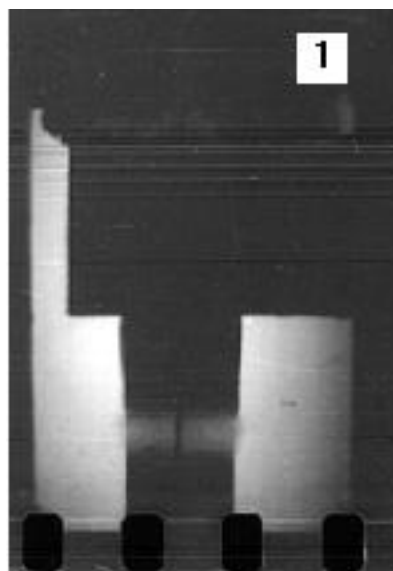


Incendiary Effects

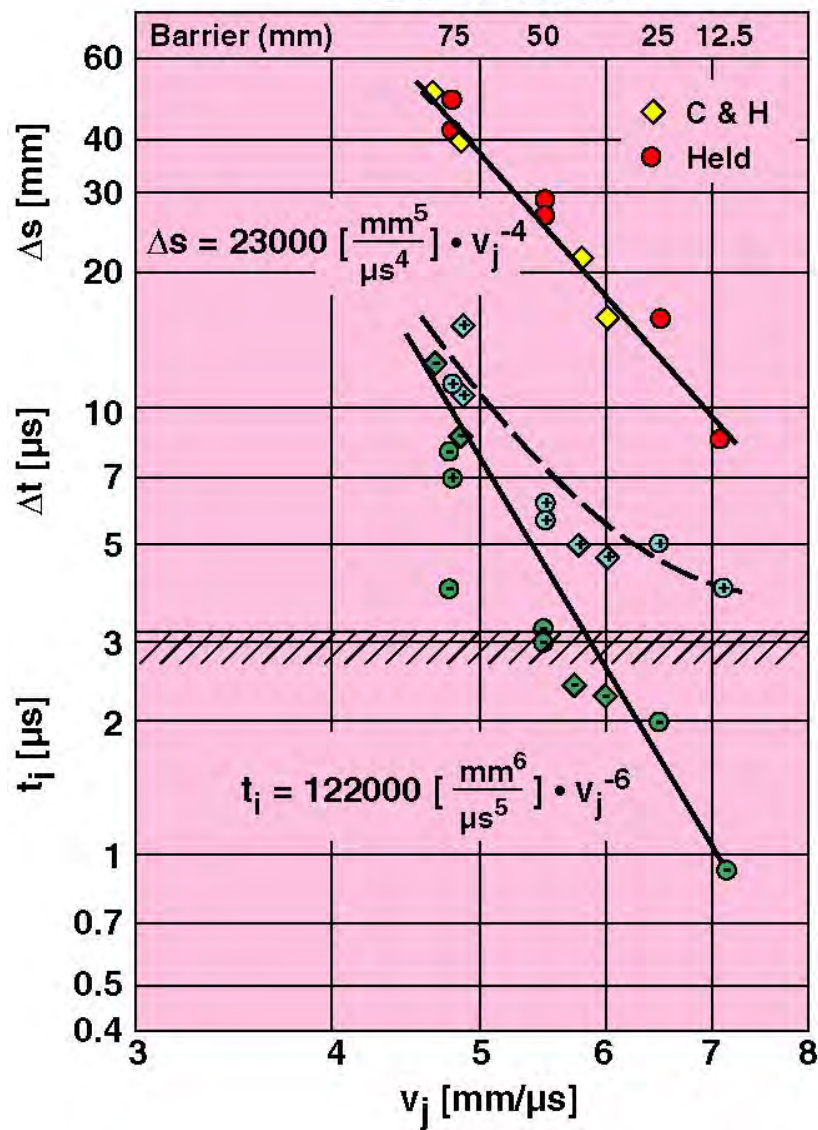




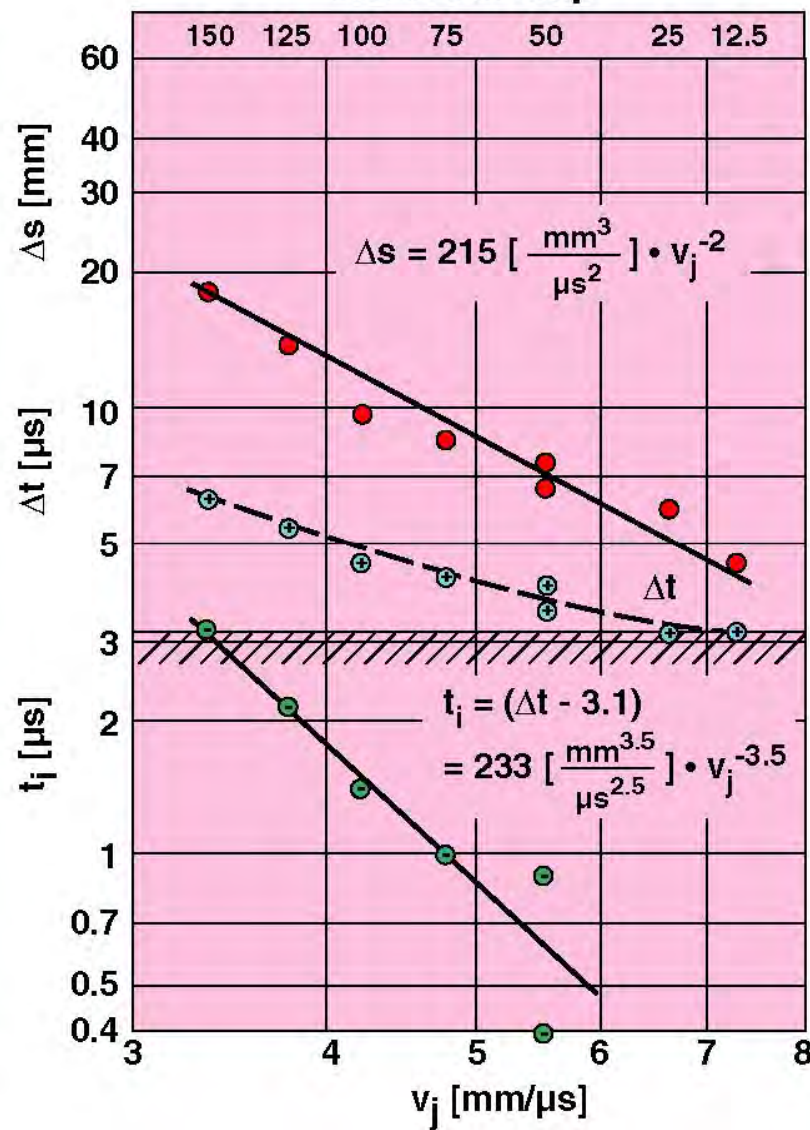
Ignition & Initiation Effects



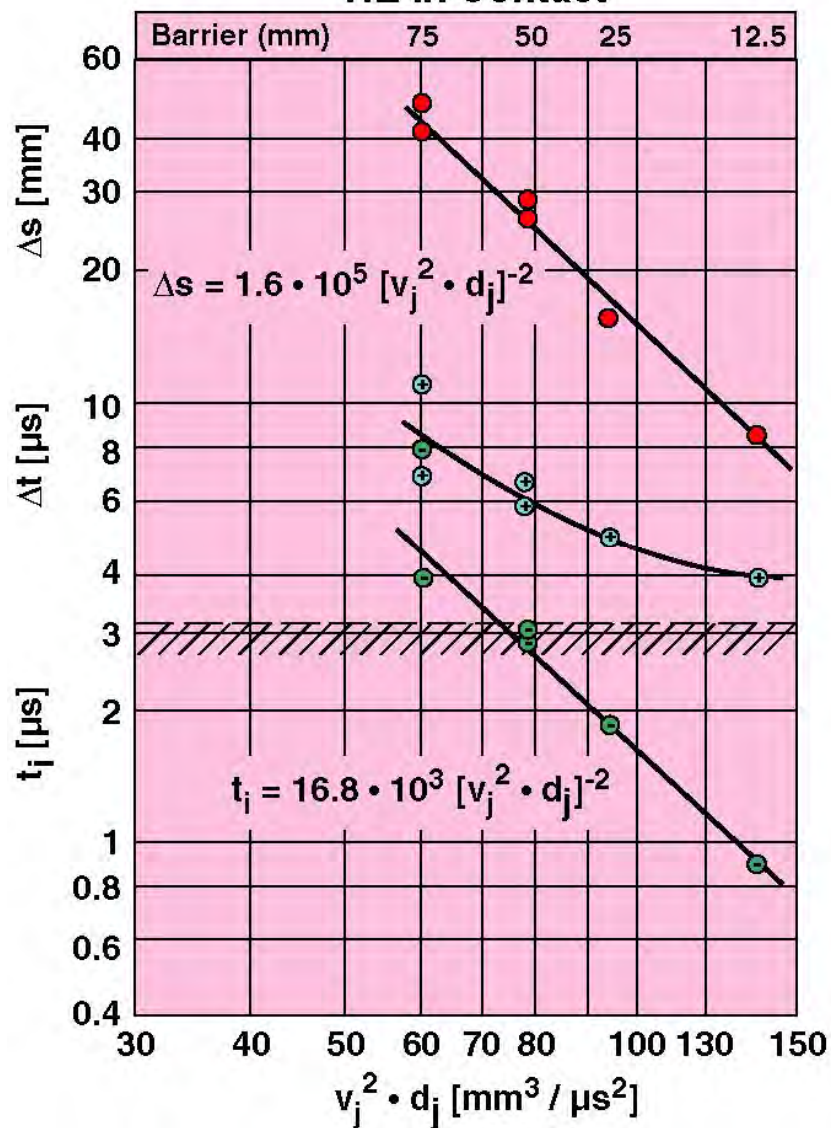
HE in Contact



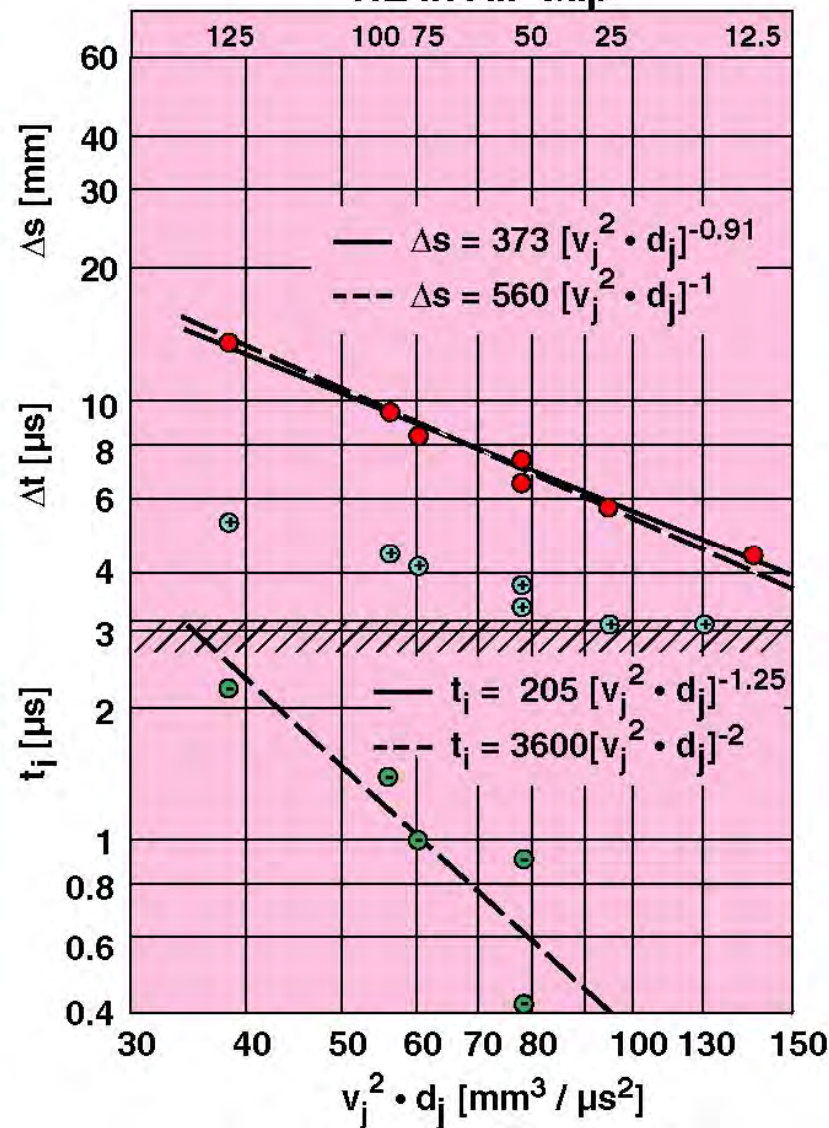
HE in Air Gap

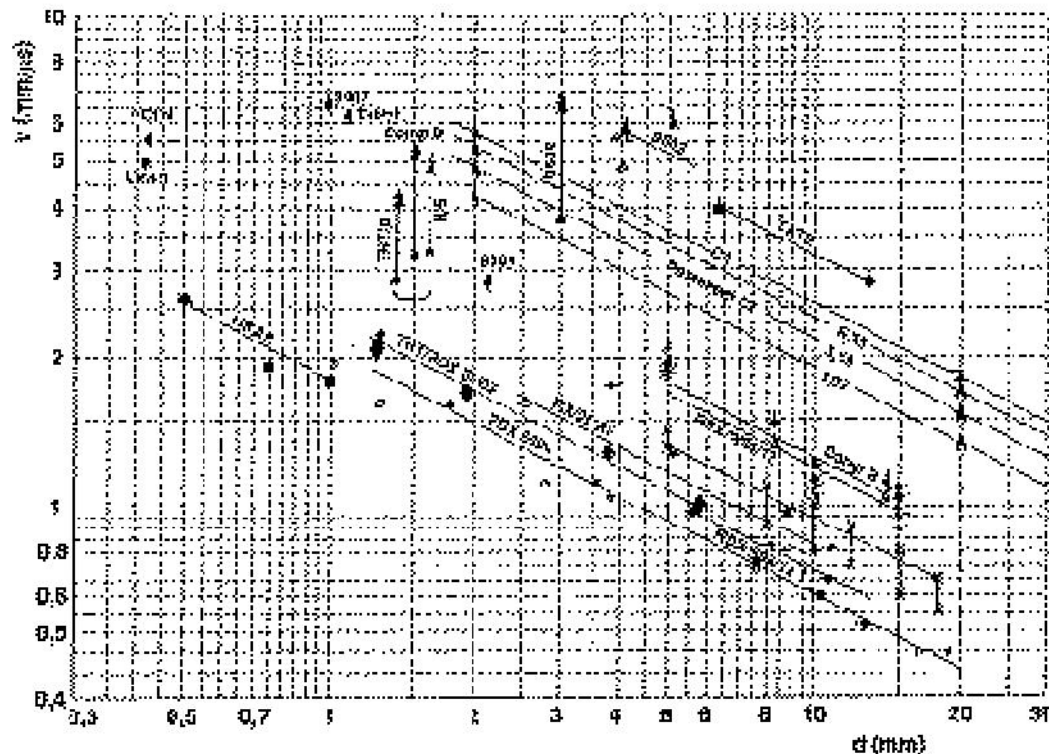


HE in Contact



HE in Air Gap





Type of HE	v^2d (mm ³ /μs ²)	Sign in Figure
HNAB	3	■
PBX 9404	4	●
RDX/Wax 88/12	5	●
TNT/RDX 15/65	6	◆
PETN (1.77)	13	▲
Comp. B	16	▲
H6	16.5	▲
Detasheet C3	36 - 53	▲
PBX 9407	40	▲
Tetryl	44	▲
C4	64	▲
TATB	108	■
PBX 9502	128	▲

△ □ ○ - no Initiation ▲ ■ ● - Initiation

The above diagram of the threshold impact velocities as functions of the diameters of the shaped charge jet (▲), projectile (●), flyer foil (■) and from FEM-calculations (x) for different high explosive charges gives a clear indication of the validity of the v^2d -criterion.

M. Held 9th Symposium (int.) on Detonation 1416 - 1426 + 1432 - 1440, 1989

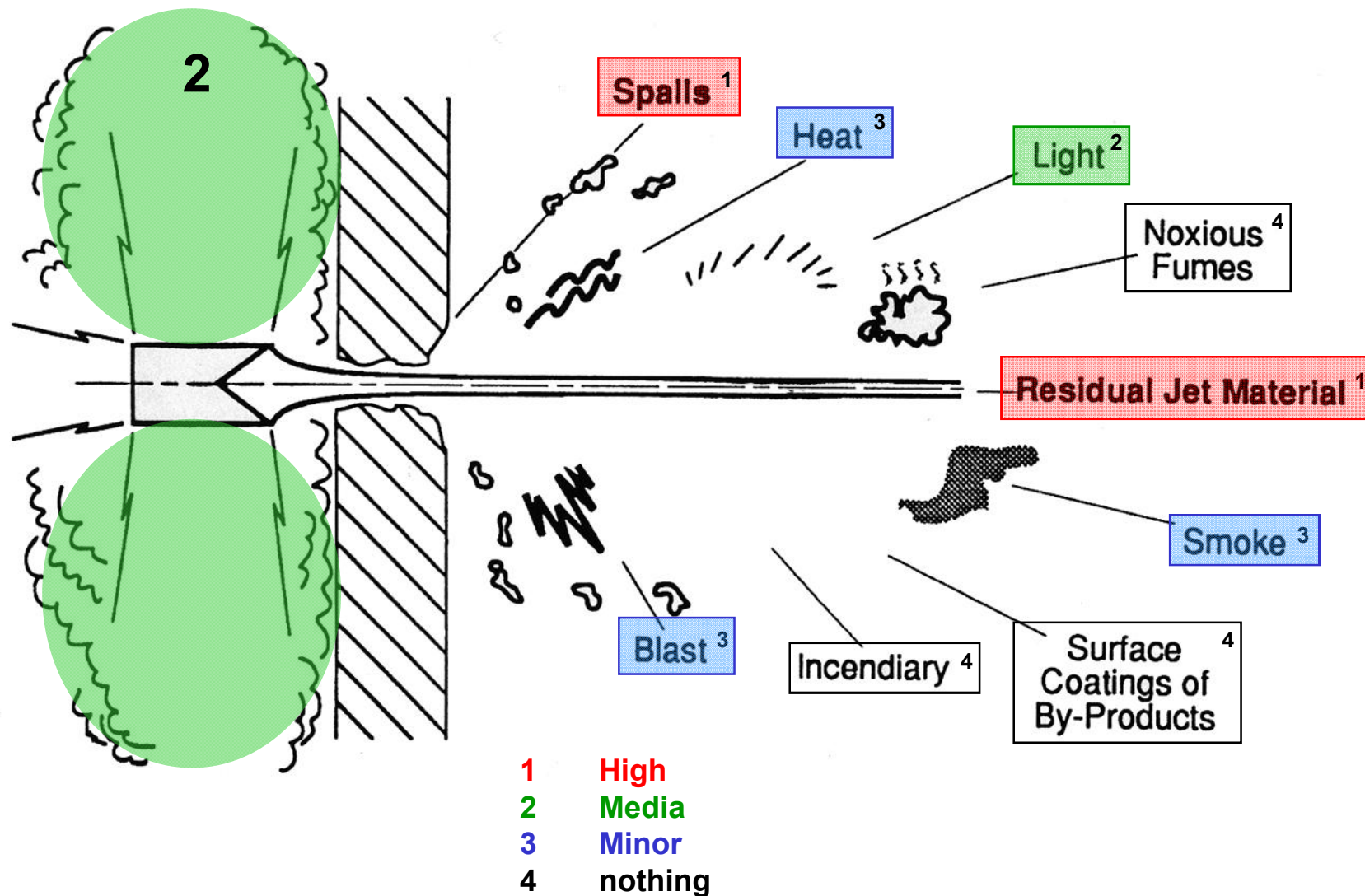
Reactions of Propellants and High Explosives

v^2d or u^2d criterion gives the ignition and initiation threshold values at shaped charge jet impacts

Less sensitive explosives are now not available against shaped charge jet loads

Take no explosives in the crew compartment, if you want to increase the survivability of the crew

and Armour Effects after Shaped Charge Jets Perforations



THE VALIDATION OF A THORACIC AND ABDOMINAL TEST RIG FOR BABT SOFT BODY ARMOUR TESTING.

K.Hewins
I.Horsfall
C.Watson

Cranfield University, Shrivenham, UK.

khewins.cu@defenceacademy.mod.uk

+00 (44) 1793 785 330

+00 (44) 7533038677



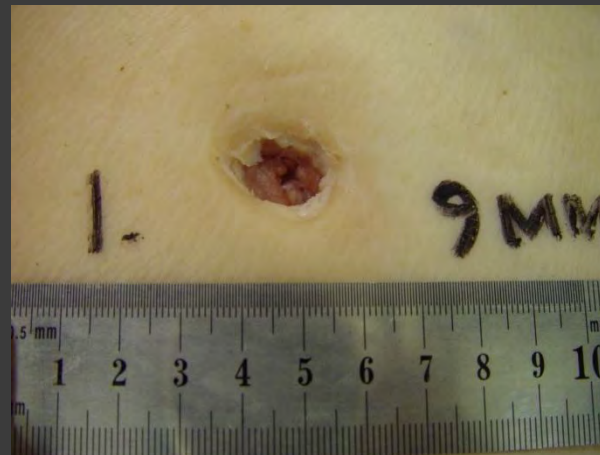
AIMS

- ⦿ Define BABT.
- ⦿ Mechanism of BABT.
- ⦿ Standards currently in place.
- ⦿ Problems with current methods.
- ⦿ The use of a Test rig
- ⦿ Further Research.

ARMOUR BLUNT TRAUMA

BABT.

- Law enforcement personal armour.
- High velocity projectile impact.
- Deformation of soft body armour
- Stress waves by initial displacement.
- Shear deformation to viscera.
- Minor and major injuries.



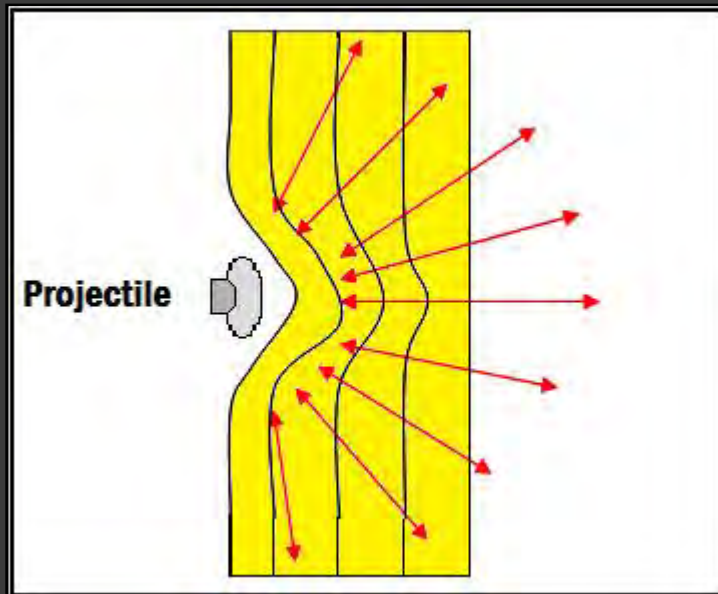


PDF
Complete

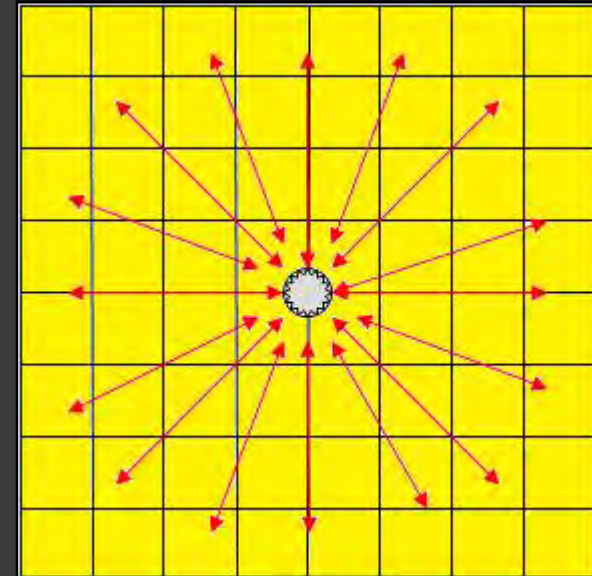
Your complimentary
use period has ended.
Thank you for using
PDF Complete.

[Click Here to upgrade to
Unlimited Pages and Expanded Features](#)

MECHANISM OF BABT.



LATERAL ABSORPTION



RADIAL ABSORPTION



CURRENT STANDARDS

- ◉ Uniform level of resistance to BABT
- ◉ UK Home Office . HOSDB
- ◉ US Government . NIJ
- ◉ Plastilina ®
- ◉ HG1/A level
- ◉ 9mm rounds
- ◉ 365 +/- 10m/s
- ◉ 44mm



PROBLEMS WITH BABT TESTING

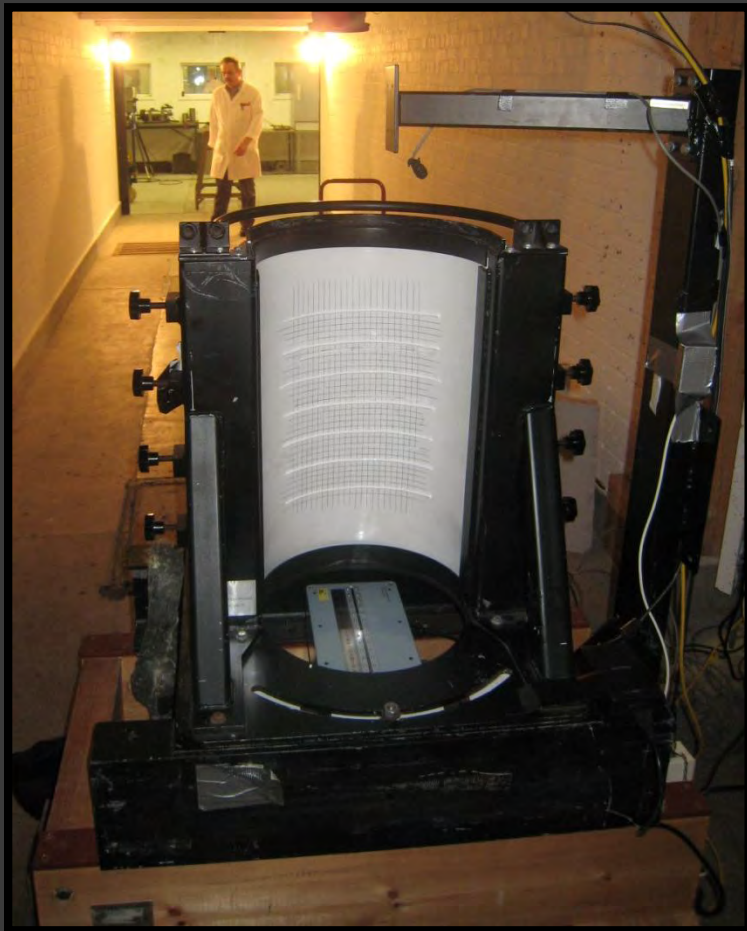
- ◎ Biofidelity of Plastilina ®
- ◎ Cadaver . Ethical Issues
- ◎ Animal - Ethical Issues
- ◎ Hybrid III . Costly

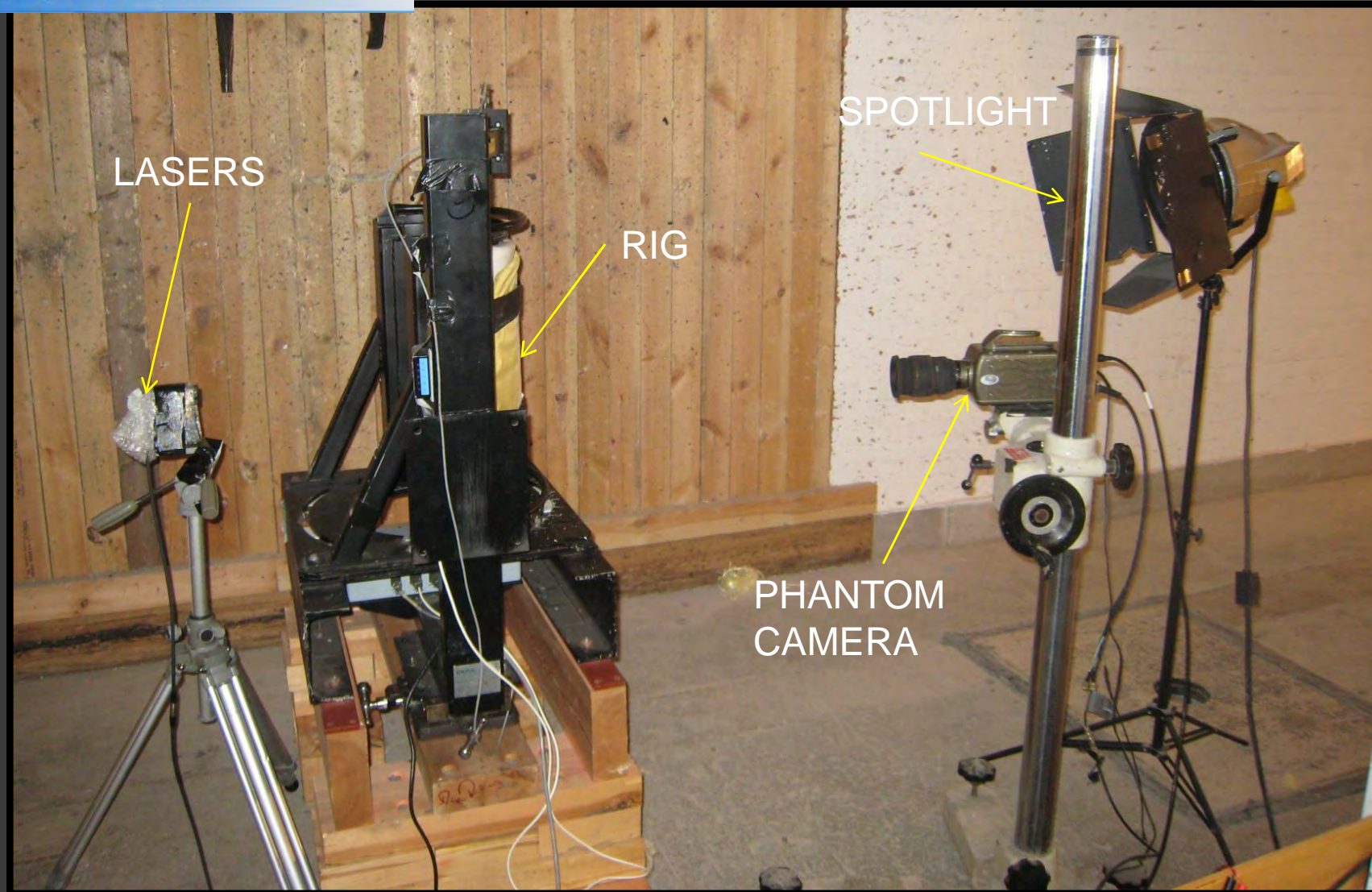
BABT TEST RIG



- Three Main Components.
- Response Element
- Lasers
- Framework

DISPLACEMENT LASERS





INJURY CRITERIA

- The Viscous Injury Criterion VC (Lau and Viano 86).
- Severity of Injury.
- Viscous tolerance = risk of soft tissue injury associated with a specific-induced viscous response, VC.
- VC_{\max} . maximum risk.

BALLISTIC TEST PROCEDURE

- HOSDB HG1/A Level
- 9x19mm Nobel Dynamit FMJ
DM11A1B2
- 5m Range
- Abdominal and Thoracic

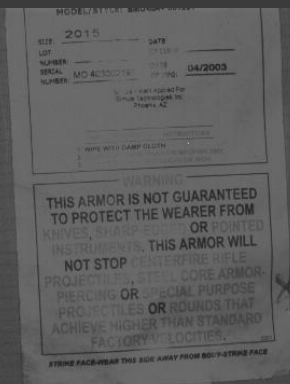
- 30 ply Kevlar ® 49
- 30 ply Teijin Twaron ®
- 30ply Zylon ®



*Your complimentary
use period has ended.
Thank you for using
PDF Complete.*

[Click Here to upgrade to Unlimited Pages and Expanded Features](#)

FRONT IMPACT



THORACIC SIMULANT



ABDOMINAL SIMULANT

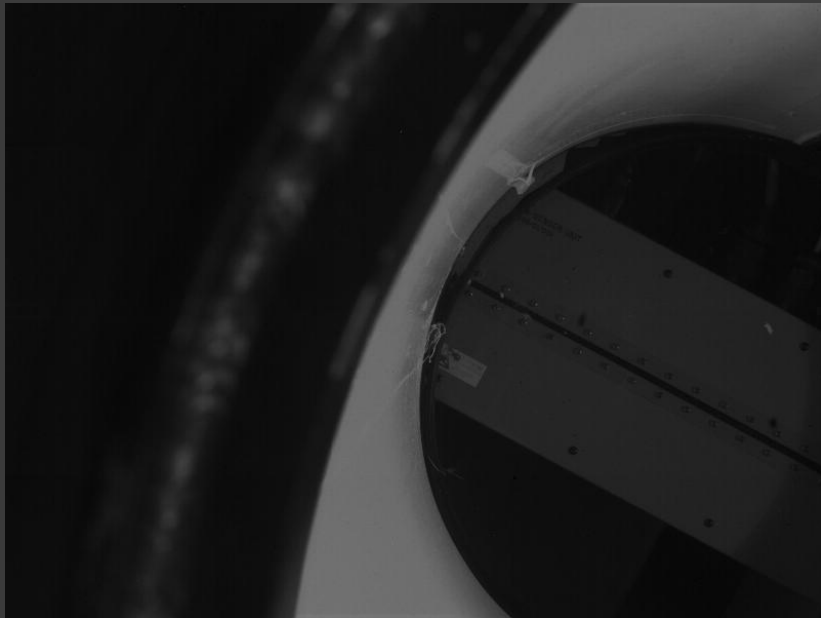


PDF
Complete

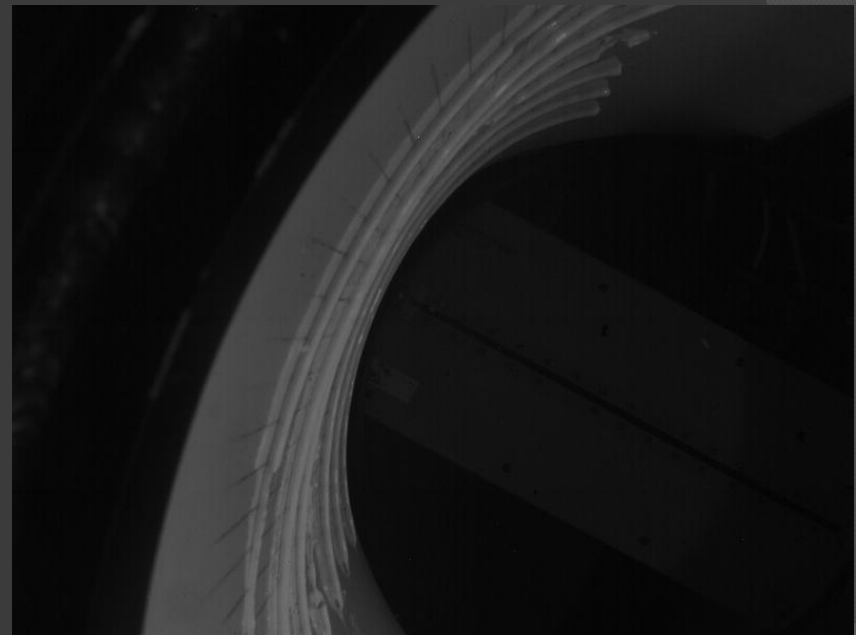
*Your complimentary
use period has ended.
Thank you for using
PDF Complete.*

[Click Here to upgrade to
Unlimited Pages and Expanded Features](#)

TOP IMPACT

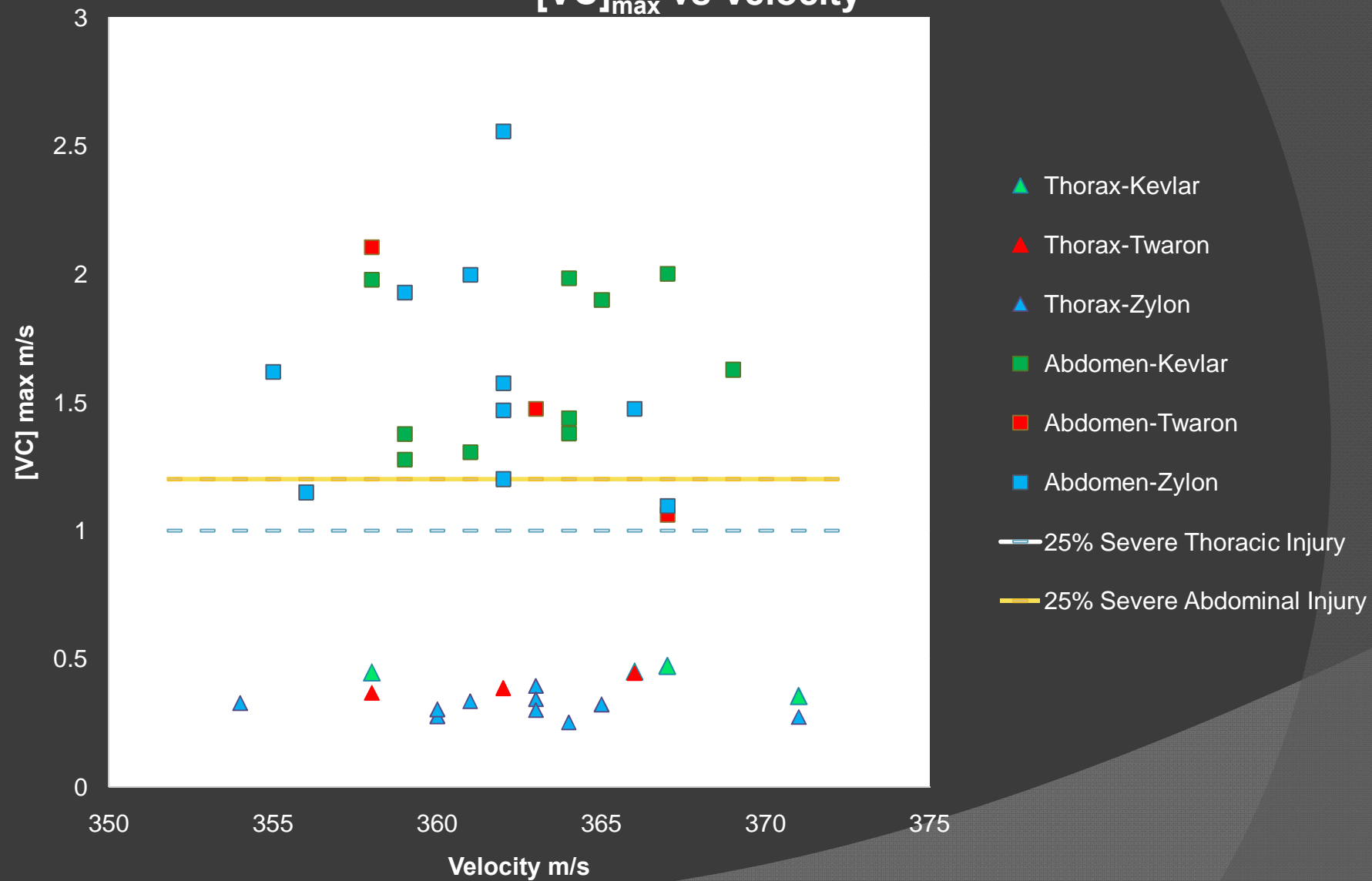


THORACIC SIMULANT

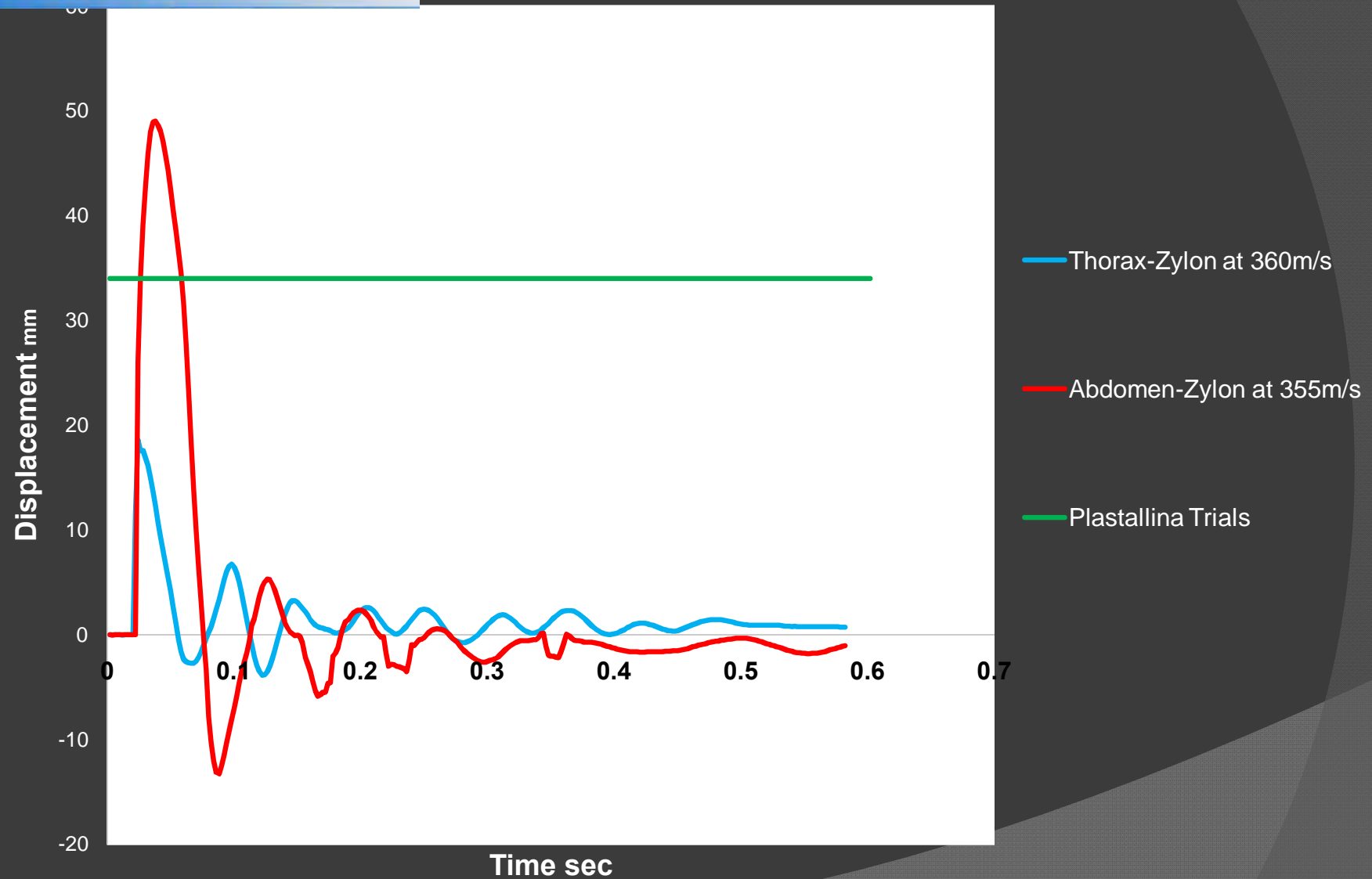


ABDOMINAL SIMULANT

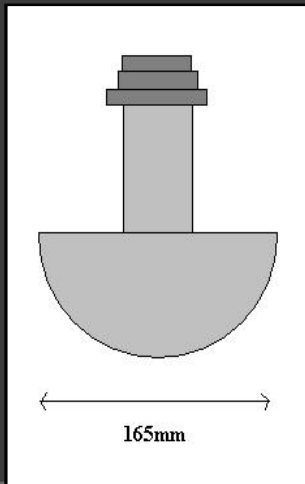
Ballistic Testing. [VC]_{max} vs Velocity



Displacement vs Time

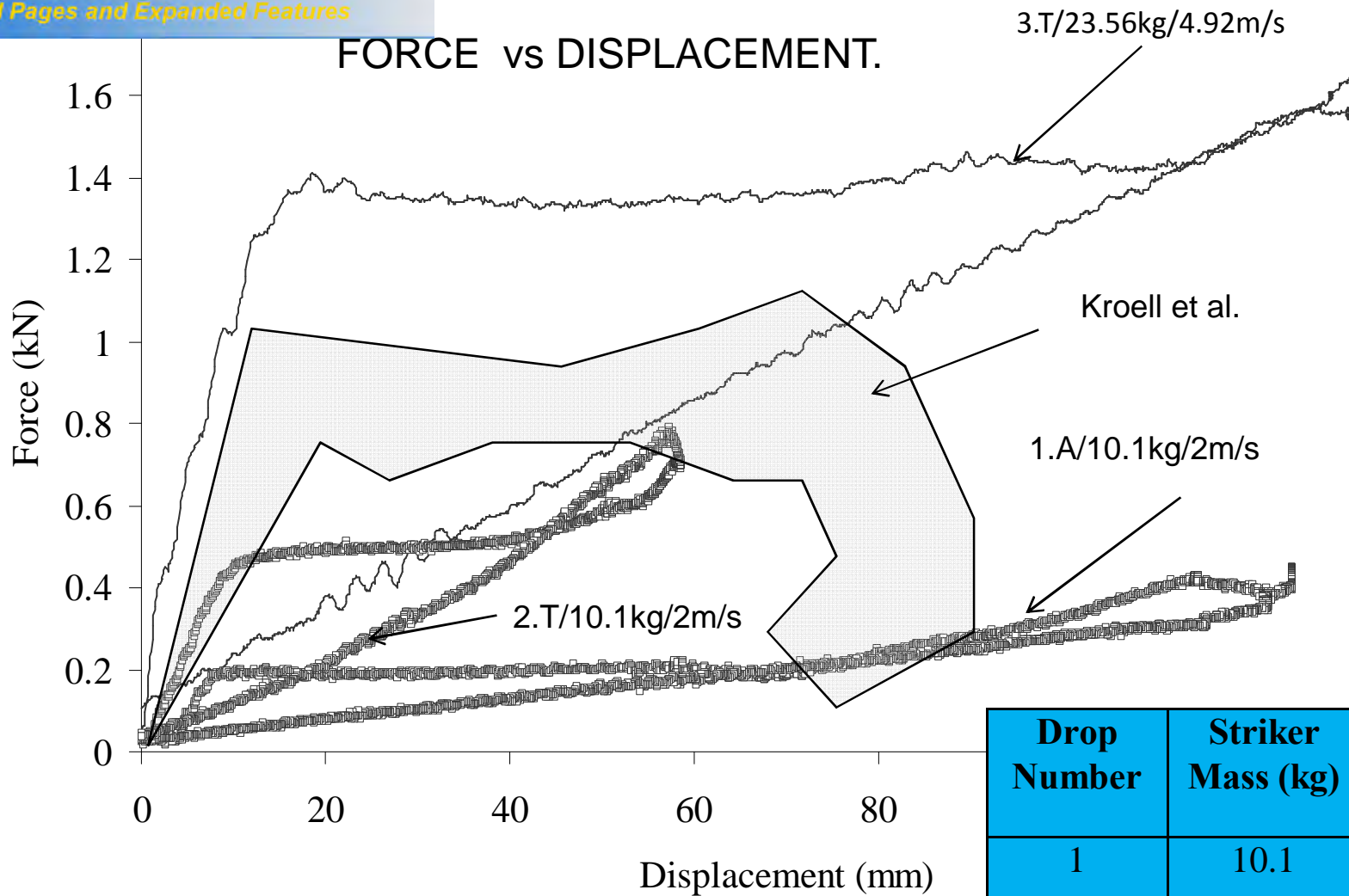


M 10 INSTRUMENTED DROP TOWER



- Displacement/Force/Striker Mass
- Abdomen . 1.8m/s and 2m/s.
Striker Mass 10.1kg
- Thorax . 1.8m/s and 5m/s
Striker Mass 10.1kg and 23.656kg
- Kroell et al 1974

FORCE vs DISPLACEMENT.



Drop Number	Striker Mass (kg)	Velocity (m/s)
1	10.1	2
2	10.1	2
3	23.56	4.92
Kroell et al	~23	~4.92

CONCLUSION

- ⦿ Positive drop tower results.
- ⦿ Ability to determine Injury severity.
- ⦿ New abdominal simulant work.
- ⦿ Further work to determine ideal thickness.
- ⦿ Advantages over previous techniques.

QUESTIONS?

Thankyou.....

Kate Hewins, Ian Horsfall, Celia Watson.

Cranfield University, Shrivenham, UK.

khewins.cu@defenceacademy.mod.uk

+00 (44) 1793 785 330

+00 (44) 7533038677



IBC Presentation 2008

Bo Janzon
IBC Chairman
(SECRAB, Sweden)
23 September 2008



Tarragona '07 - results of questionnaire

Question	YES [%]	NO [%]	Nil [%]
IBC organisation to remain as is	28	59	13
IBC to become a Society	75	19	6
Will become member of IBS	81	12	7
Be more actively involved?	67	25	8
Publishing in refereed Journal	94	1	5
Full proceedings only on a CD	56	44	1



108 answers out of 333 delegates
at 23rd ISB, Tarragona

Publication

- ❖ Will occur in the Journal of Applied Mechanics (JAM”)
- ❖ Abstracts for Journal articles due on 1 March 2009
- ❖ Manuscripts due 1 August 2009
- ❖ Authors notified by 15 November
- ❖ Final Manuscripts due 15 February 2010
- ❖ Symposium 17-21 May 2010
- ❖ Publication of JAM special ISB issue September 2010



Publication, 2

- ❖ Abstracts to be submitted to ISB '10 Organiser's website
- ❖ Manuscripts (for Journal) to be submitted to JAM's website
- ❖ Acceptance rate of order of 35 % expected
- ❖ Space for 22-25 papers in special issue
- ❖ Good papers for which there will be no space can be published later by the JAM



Publication, 3

- ❖ Papers for Journal will have extended abstract in Symposium Proceedings
- ❖ Other papers will be printed, as usual, in Symposium Proceedings
- ❖ See 25th ISB Organiser's website:

www.ISB2010.com

or link from www.ballistics.org



Future Symposia



2010

Beijing, China

2011

Miami, FL, USA

2013 Freiburg i. B., Germany

IBC 2005 – 2008 – What have we achieved?

- Organisation of future Symposia is stable, planned 4 1/2 years ahead!
- We have achieved scientific review and publication in a Journal, to be implemented in 2010
- We have started preparations for a "Ballistic Society", to be carried on by the new board.



The new IBC Executive



Chairman:	Jack Riegel, US
Vice Chairman:	Ian Cullis, UK
Secretary:	Sidney Chocron, US
Bursar #1:	Richard Fong, US
Bursar #2:	Bill Flis, US
POC Americas:	Michael Murphy, US
POC Europe:	Roxan Cayzac, France
POC OC:	Meir Mayseless, Israel
Past Chairman:	Bo Janzon, Sweden

Contact



www.ballistics.org



See you all at
Beijing!
in 2010

A BRIEF HISTORY OF SHAPED CHARGES

24TH International Symposium on Ballistics
New Orleans, LA
September 2008

BILL WALTERS
US ARMY RESEARCH
LABORATORY
AMSRD-ARL-WM-TC
Aberdeen Proving Ground, MD
410-278-6062
walters@arl.army.mil

 **PDF**
Complete

*Your complimentary
use period has ended.
Thank you for using
PDF Complete.*

[Click Here to upgrade to
Unlimited Pages and Expanded Features](#)



MISNOMERS

TECHNOLOGY DRIVEN. WARFIGHTER FOCUSED.

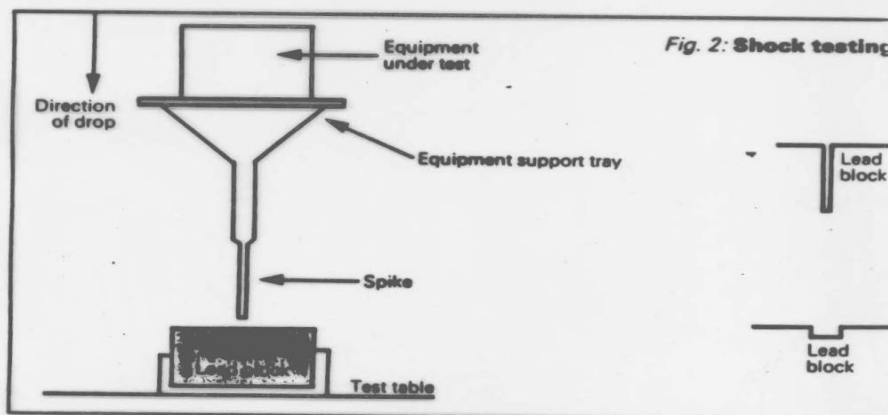


nating impulse upon striking the tough armour surface of the target. The detonator(s) fire the main body of explosive which, because of its shape, produces a narrow, high temperature plasma jet. The temperature is so high (about 20,000° Celsius) and the pressures developed are so great that even the toughest of alloy armour steels are penetrated. (The material forming the jet reaches a density several times that of steel, and the armour becomes plastic and yields whilst the jet torch assists by melting and burning the armour metal.)

It will be seen that most of the above is entirely under the control of the anti-tank

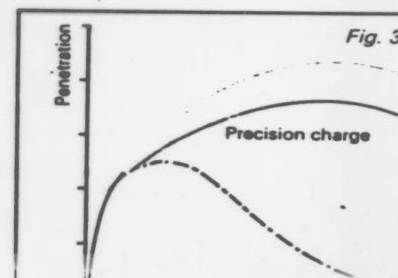
Since a top attack is often delivered by a near vertically falling missile, a top attack warhead will be miniaturized. Thus, a smaller and lighter warhead may be used to pierce top armour vertically. The missile becomes small enough to be carried in clusters or groups. These are showered down from suitable aircraft canisters which can be delivered by craft or missile.

Thus an advancing armoured force may be attacked by hundreds of shaped-charge bomblets dropped directly onto the tops of the armoured vehicles.



weapon designer. He can control the speed of the missile, the composition, mass, density and also speed of detonation of the warhead, and finally he can control the time of pre-detonation by changing the length of the stand-off probe.

The designer can modify any of these parameters to produce plasma jets which will defeat the thickest armour, and it is not unknown for the heaviest warhead jets to be capable of piercing one side of a fighting vehicle, and then continuing straight through to pierce the opposite



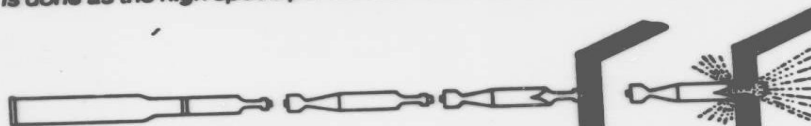
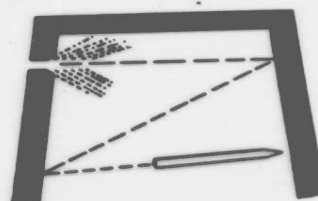
TANK KILLERS

The U.S. Army now favors the 120 mm smoothbore gun for its main battle tank, replacing the rifled 105 mm. (The Soviets use a smoothbore 125 mm.) The shift from rifled to smoothbore came about chiefly because spinning the round is no longer advantageous. In the days of stubby, full-bore rounds, the projectile behaved much like a rifle bullet and spin stabilization was essential. Today's modern rounds behave poorly when spun. The shaped-charge round does a better job if the warhead has minimum spin when it hits the target. The penetrator of the kinetic energy round now has a such a long length to diameter ratio, (about 18 to 1), that spinning causes it to wobble and lose stability. Instead, rounds are fin stabilized; small vanes are exposed after the round is fired to keep the projectile on course.



In a kinetic-energy round, the penetrator does the damage. It is made of a high-density material.

Before the round is fired, the penetrator is held by a sabot which falls away while the projectile is in flight. The sabot allows the full power of a large diameter round to boost the small-diameter projectile. When the penetrator hits the target, its energy drives it through the armor. Once through, it contributes to the destruction by spalling metal from the armor it has penetrated. Most of the damage is done as the high speed penetrator ricochets around inside the tank.



The high explosive round flies under fin stabilization until the tip hits a target. On impact, the shaped charge within the round ignites and begins to play a stream of plasma on the target. Each shaped charge configuration has an optimum distance from the target where the cutting power of the plasma cone is greatest. This detonation distance is established by the length of the warhead tip. The plasma cone burns through the armor and spray molten particles into the tank at speeds of 30,000 fps.

composite armor standard. It consists of soft and hard materials in alternating spaces. The densification of the armor is critical to its success. armor is made is cret. Even knowle material being t enemy a good i much protection vides against spe

Composite armor is the subject of many research projects, particularly metal armor. This family of armor has exceptional strength to weight and breakthroughs in

How armor is designed for the tank is another matter, and the amount of armor protect is a tricky question. tionally, the tank is protected along the forward arc, using armor section to defeat threats, this armor is positioned. Sloped armor deflects small arms fire. new high velocity rounds are a recent trend, but as many sections as possible. The "boxy" tank designers

Most heavy armor is in the form of an armored skirt. The skirt protects the tank from the sides and can be broken up by forces reaching the tank. Ideally, the skirt should be able to slant and spray harmlessly in the direction of the penetrator or start to reach the tank. One of the



COVER STORY

If nuclear weapons really are negotiated out of Europe, what will NATO do to offset the Soviets' 2-to-1 edge in conventional firepower? The answer may lie in the one technological trump card America still holds: Sophisticated microelectronics in "smart" weapons that find their own targets—with deadly accuracy

One shot, one kill: A new era of 'smart' weapons

Viewed from the ground, it looks more curious than threatening: A paint can dangling from a tiny parachute, slowly fluttering to earth. But suddenly, with a crack and a brilliant white flash, the "paint can" spits out a molten metal slug that crashes at 5,000 miles per hour directly through the engine of the Soviet tank below.

In the distance, a flock of tiny parachutes drops onto the countryside. Their lethal cargo: A portable mine field that will stay in place until acoustic sensors detect passing Soviet armor. Then they, too, come alive with a barrage of hypervelocity slugs.

Behind the Soviet lines, model-airplane-like drones buzz overhead, relaying high-resolution TV pictures of massing Soviet divisions to the NATO command center hundreds of miles away.

And along the seven railroad lines that the Soviet high command has or-

viding armies with unprecedented mobility. Medieval knights feared the killing potential of the crossbow so much that at the Lateran Council of 1139 it was outlawed as "un-Christian." The invention of gunpowder, the cannon, the breech-loading rifle—each in turn revolutionized warfare. In 1862, Richard Gatling's machine gun introduced a grim new reality to the battlefield. During World War I, the mobility, firepower and armor of the tank began changing the strategy of static and horribly bloody trench warfare.

Yet none of history's revolutionary new weapons and technologies changed one basic fact about war: It has always taken hundreds or thousands of rocks, arrows, bullets, artillery shells or bombs to wipe out a single target. In the end, it has usually been numbers, skill and courage, not technology, that have prevailed on the battlefield.



U.S. AIR FORCE SYSTEMS COMMAND

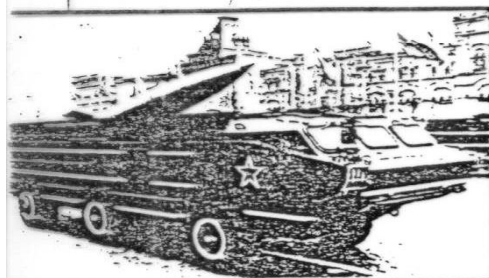
RFIGHTER FOCUSED.

SMART WEAPONS

THE KREMLIN'S CATCH-UP PLAN

Invest now, build later

Lagging behind in critical computer and sensor technologies, the Soviets aren't trying to match U.S. smart weaponry gadget for gadget. At least not right away. Instead, they are gambling that the Gorbachev economic reforms eventually will so strengthen Moscow's technological base that it can compete both commercially and militarily with the United States. Moreover, some Soviet military theoreticians have been quicker than many of their Western counterparts to grasp the potential of smart weapons.



Conventionally armed Soviet SS-21s threaten NATO airfields

Writing in a Soviet military journal, Marshal Nikolai Ogarkov has observed that "automated search-and-destroy complexes, long-range high-accuracy terminally guided combat systems, unmanned flying machines and qualitatively new electronic-control systems make it possible to sharply increase the destructive potential of conventional weapons, bringing them closer to

Historically, Soviet weapons are made "soldierproof," suitable to the skills of soldiers who receive little technical training. The aim is summed up by reported orders of helicopter designer Mikhail Mil to his engineers: "Make it simple, make it rugged, make it reliable, make it work." Argues Christopher Donnelly, a British Soviet expert: "In some respects, by use of good engineering techniques and clever design, the Russians produce better weapons systems than we do with high technology."

The Soviets are also good at coming up with simple fixes to offset the enemy's high-tech weapons. For example, Soviet "reactive" armor seeks to undo the direct-hit capability of smart antitank munitions. When hit by a warhead, an explosive layer sandwiched inside the armor goes off, deflecting the blast to save the tank.

Already the Soviets lead the U.S. in some kinds of laser research, and a Pentagon analysis says they have caught up in six technology areas, including aerodynamics, explosives and optics. They are at work on radar-evading Stealth aircraft, and one smart helicopter antitank missile, the AT-6 Spiral, is said to have antijamming devices and heat sensors that give it a 90 percent kill probability.

"They already have quantity, and now are looking for better quality" that includes computer-chip technology on MiG-29 and MiG-31 fighters and computerized artillery fire-control centers, says

TECHNOLOGY DRIVEN. WARFIGHTER FOCUSED.

Misnomers

- “On impact, the shaped charge within the round ignites and begins to play a stream of plasma on the target. Each shaped charge configuration has an optimum distance from the target where the cutting power of the plasma cone is greatest. This detonation distance is established by the length of the warhead tip. The plasma cone burns through the armor and sprays molten particles into the tank at speeds of 30,000 fps.”

More Misnomers

- “A shaped charge detonates on impact, liquefying metal, which melts the tanks armor.”
- “The jet is a high temperature plasma (about 20,000 C)”
- “The jet reaches a density several times that of steel, and the armor becomes plastic and yields whilst the jet torch assists by melting and burning the armor metal”

 **PDF Complete**

*Your complimentary
use period has ended.
Thank you for using
PDF Complete.*

[Click Here to upgrade to
Unlimited Pages and Expanded Features](#)

Shaped Charge Jet in Air



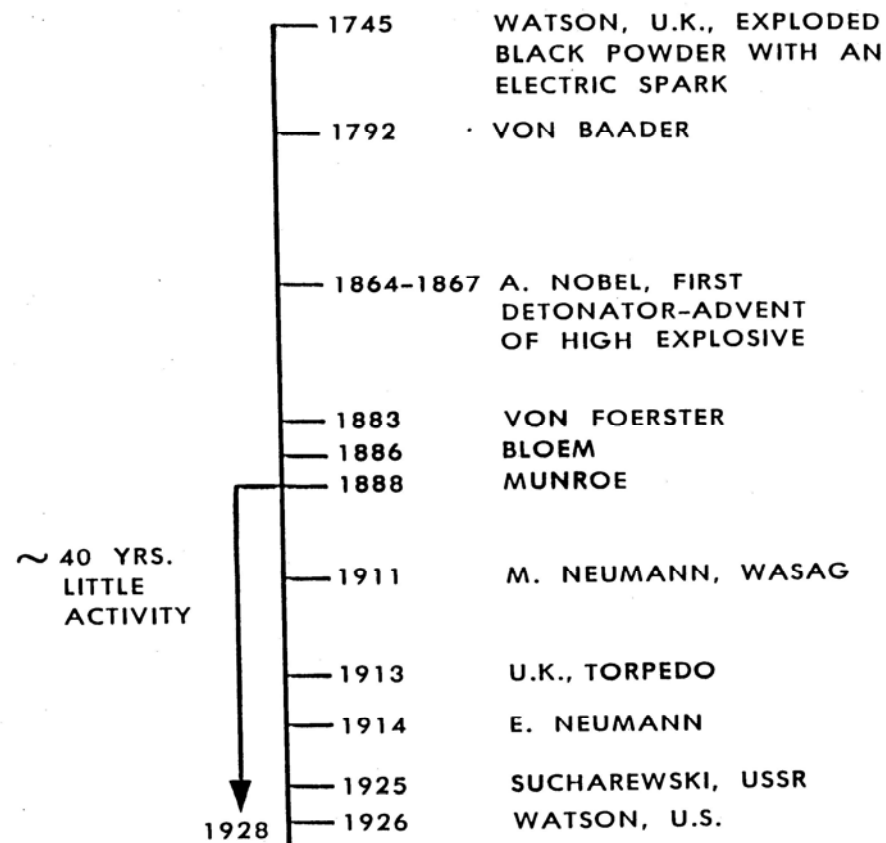
TECHNOLOGY DRIVEN. WARFIGHTER FOCUSED.

HISTORY OF SHAPED CHARGES

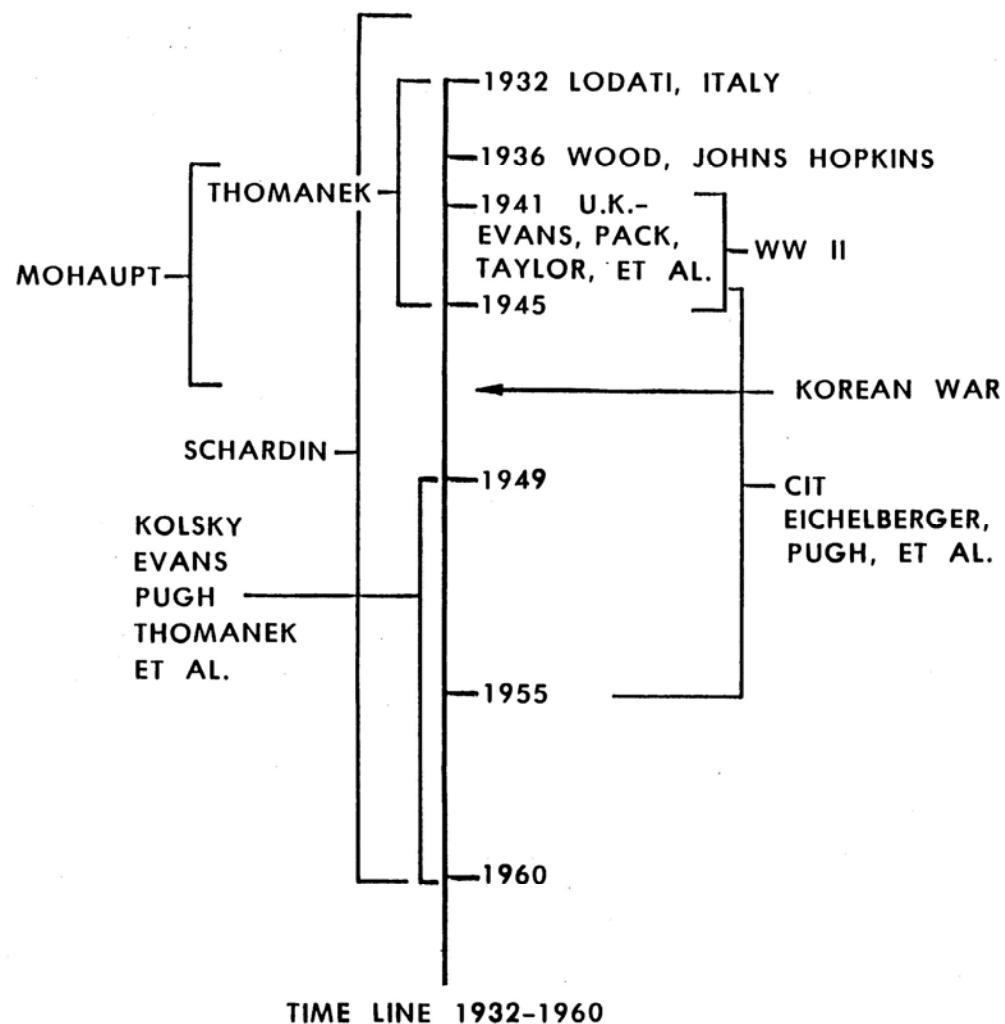
THE EARLY HISTORY



" von Baader	1792	M. Neumann	1911
" Nobel	1867	Sukharevskii	1925
" von Foerster	1883	Lodati	1932
" Bloem	1886	Wood	1936
" C. Monroe	1888	Thomanek	1935
" Lepidi	1891	Mohaupt	1939



TIME LINE 1745-1928



1960

U.S., GERMANY, U.K.,
FRANCE, U.S.S.R.
(GOVERNMENT AND
INDUSTRY) CONTINUAL
RESEARCH

**Former Soviet
Union and
other countries**

1988

TIME LINE 1960-TO DATE

IGHTER FOCUSED.

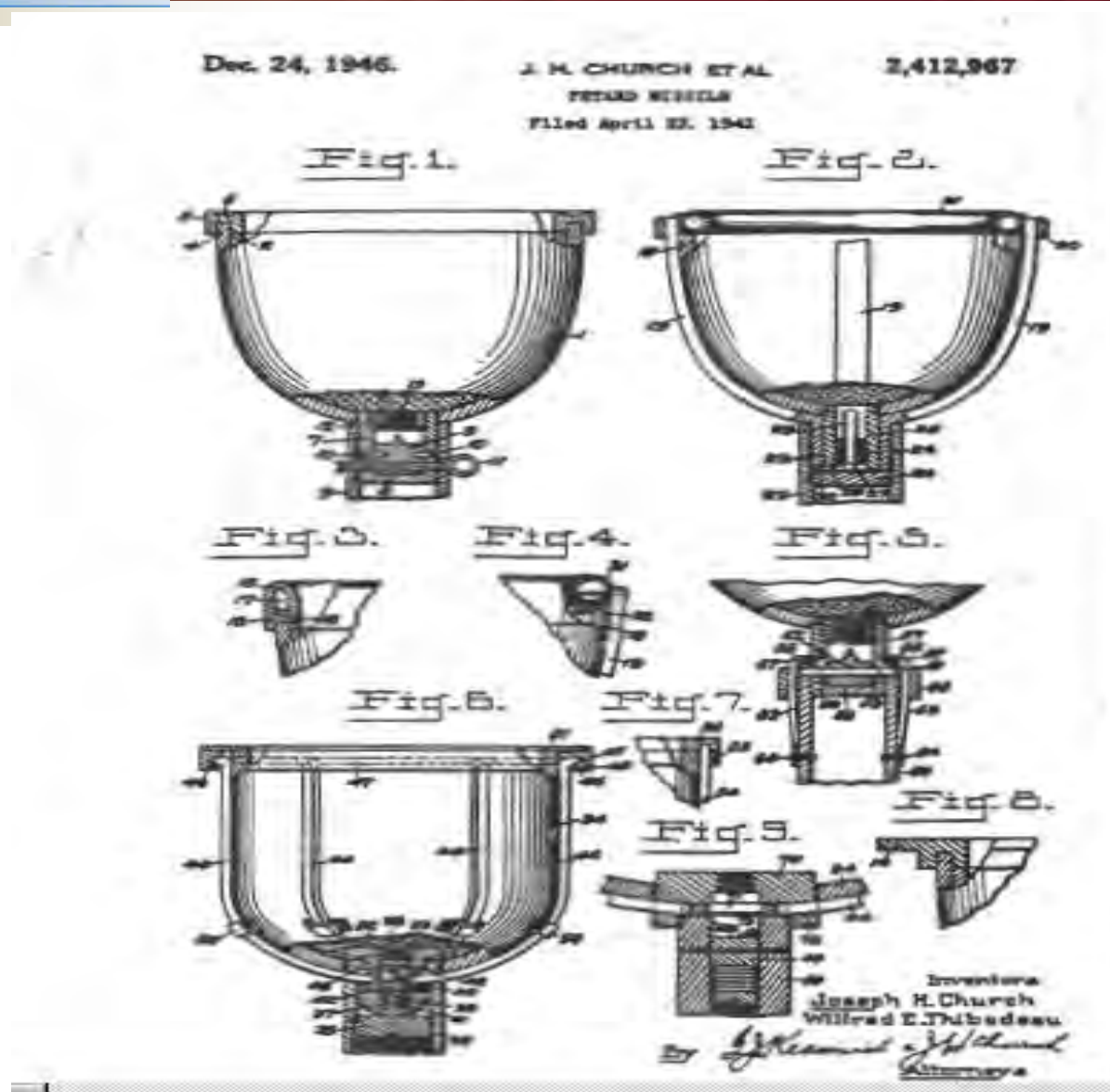
IN ABOUT 100 YEARS, THE US PARTICIPATION
IN SHAPED CHARGE TECHNOLOGY WENT FROM
THE DISCOVERY BY MONROE; 40 YEARS OF
LITTLE ACTIVITY UNTIL THE INTRODUCTION TO
WEAPONS TECHNOLOGY BY MOHAUPT ABOUT
1940; AND CONTINUOUS RESEARCH TO DATE.

PETARDS



The petard or shaped charge of those times, relates M. F. Massey of the Office, Chief of Ordnance, Washington, D.C., in his history of hollow charges, consisted of a cast or wrought iron case of various shapes. This case was filled with powder moistened with good wine, and pressed or pounded into the case as firmly as possible, care being taken not to crack a grain of the powder, as flowers were expensive even then and funerals consume time far better spent in other pursuits. The case was then closed with a wooden plug and paper well beaten in and painted with hot tar. A quick match or a fuse ignited the charge through a hole in the top.

Years came and went and in 1825, one James Cutbush, Professor of pyrotechnology at West Point, recommended a further improvement in the petard by substituting brandy for wine. That recipe is still in use by makers of consolidated charges and cased telescoped ammunition, except that they use aqueous solutions of industrial grade alcohol, not brandy. The petard is by no means dead, as US patent 2,412,967, filed in 1943 attests.



Explosives with Lined Cavities*

Garnett Bostower, Duncan P. MacInerney, Emerson M. Price, and Sam Gu

(Received January 18, 1948)

Explosives detonated in contact with thick steel plates produce much deeper holes in the steel when there is a cavity in the explosive in contact with the plate. While this phenomenon has been known for more than 150 years, the enormous increase in penetrating power that can be produced by lining the explosive cavity with thin metal has been discovered only recently. During the war a number of light, low-velocity, antitank weapons (e.g., the rocket-propelled Flakpistol) were developed which made use of this phenomenon to perforate thick armor plate.

A fairly complete mathematical theory of this essentially new phenomenon is presented together with some of

the experimental data that aid testing of the theory. The process is best, the formation of a long thin jet (traveling lengthwise) (10,000 ft. sec.) and, on the target material by the extra million atoms produced by the jet.

The theories of both of these classical hydrodynamics of perfect fluids because the strength of the neglected at the high pressures

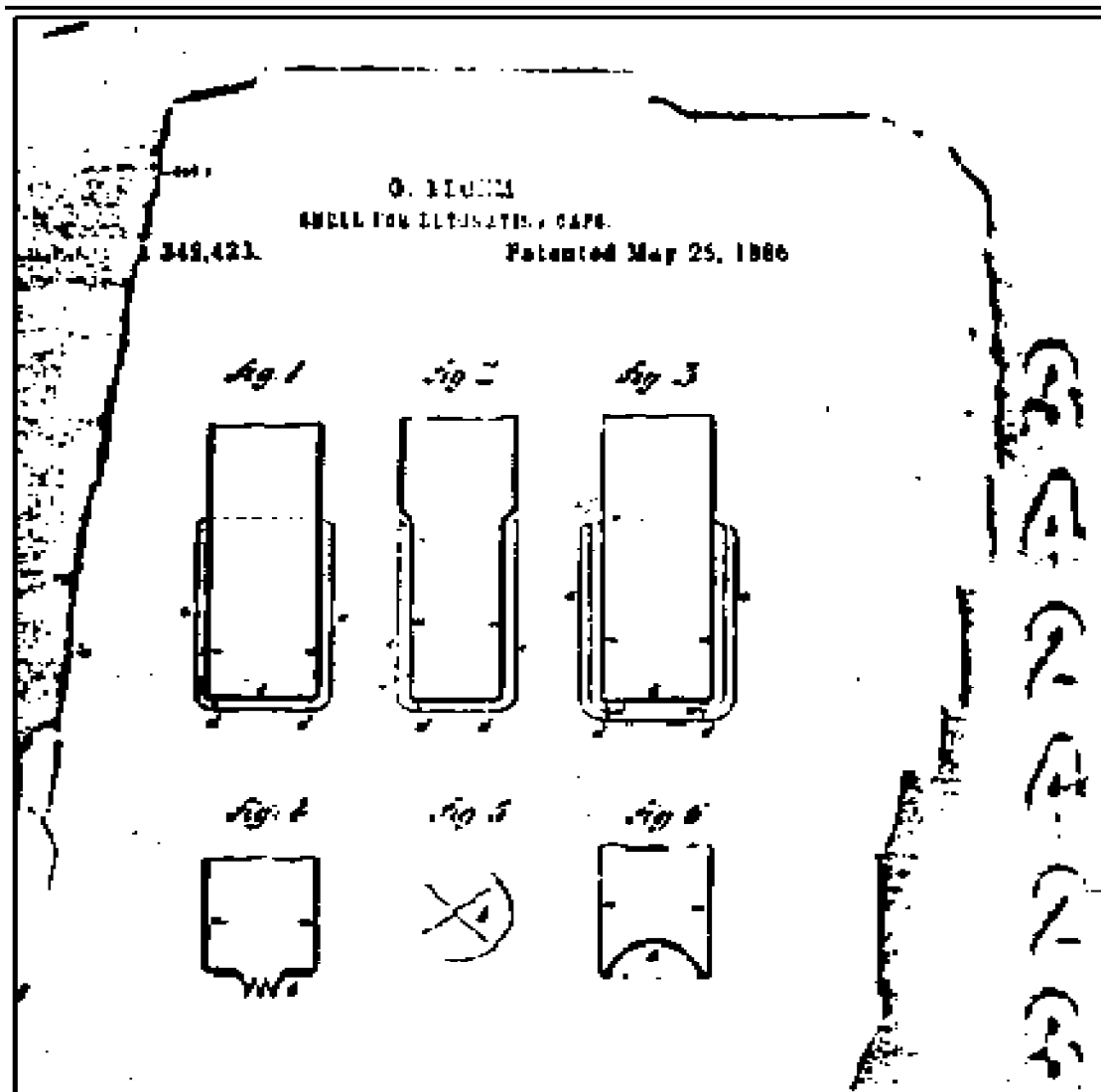
JAP, JUNE 1948

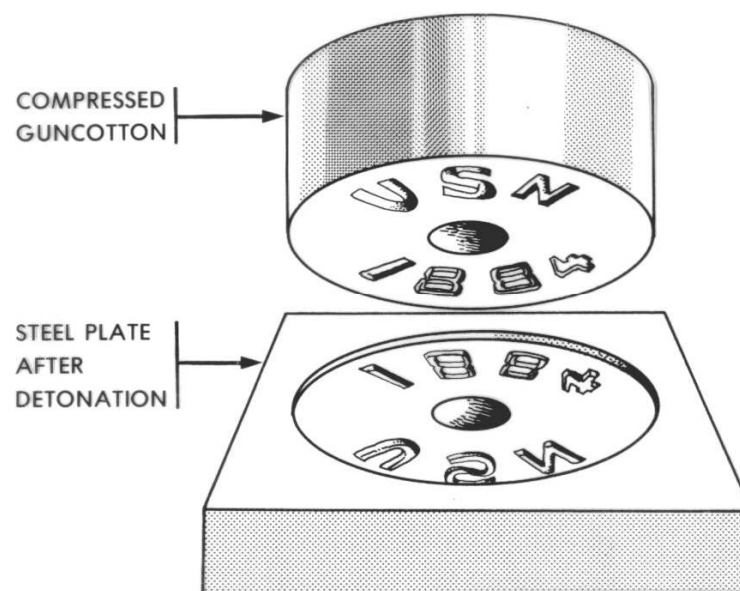
FOR over a century mining engineers have known that some of the force of an explosive charge could be concentrated on a small area by hollowing out the charge opposite to the area ("hollow charge principle"). The earliest known reference to this is 1792; a popular account appeared in von Neumann's Magazine in 1844. The effect became known as the Munroe effect in England and the United States, and as the Neumann effect in Germany, in honor of later workers (1895, 1911).

Early in the recent war a large number of new weapons, based on an important modification of this principle, appeared almost simultaneously in the armed forces of the major combatants. It had been discovered that by lining the hollow with a thin metal liner it became possible to perforate armor plate, concrete walls, or other structures with a surprisingly small weight of

explosive charge. Very often took the form of a projectile charge in the nose. So advantage over the ordinary in that their ability to pierce independent of their strike head placed and static charges are at least as effective as armor as those used in projectile impact.

This fact led to a variety of the hollow charges to the known method was the use employed in the American which were very effective; they had striking velocity the ordinary antitank and American tanks could be by individual infantrymen





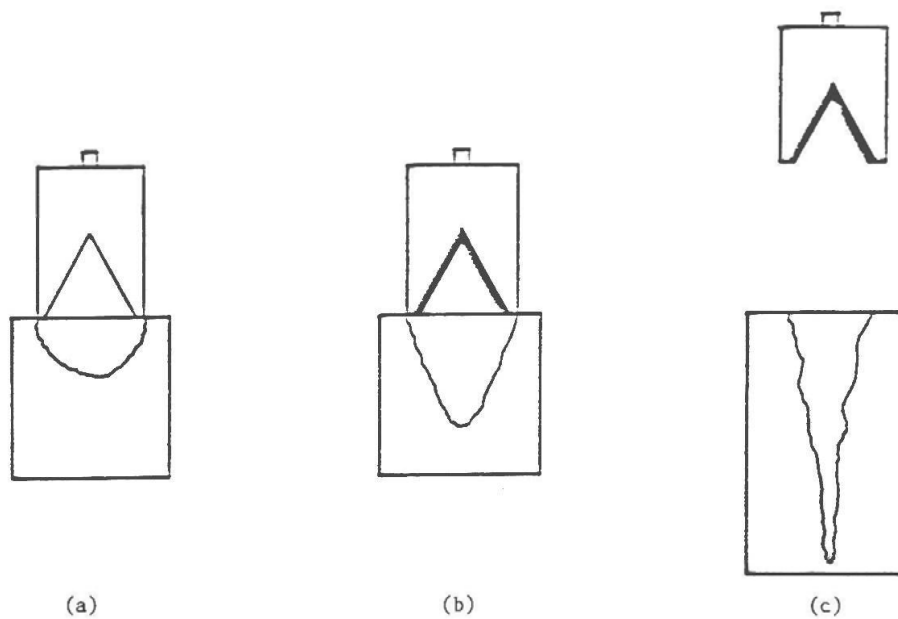


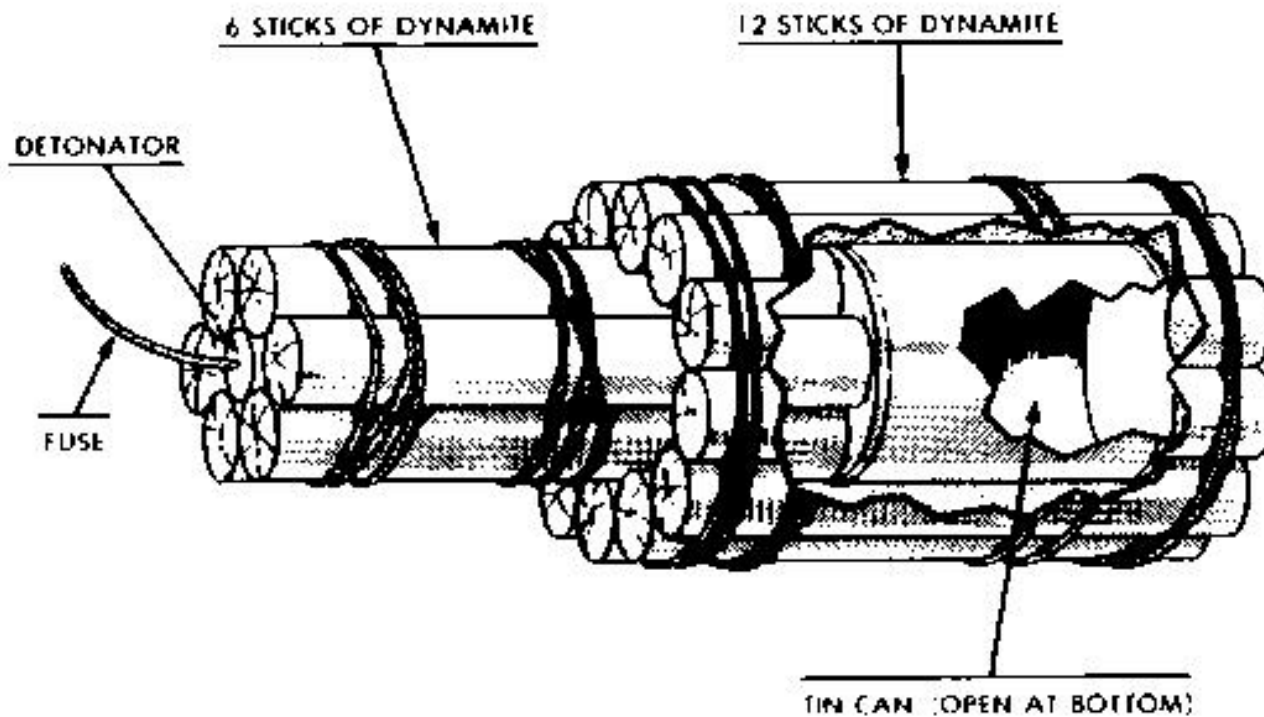
Figure 4. The Lined Cavity Effect



PDF
Complete

*Your complimentary
use period has ended.
Thank you for using
PDF Complete.*

[Click Here to upgrade to
Unlimited Pages and Expanded Features](#)



TECHNOLOGY DRIVEN. WARFIGHTER FOCUSED.



TECHNOLOGY DRIVEN. WARFIGHTER FOCUSED.

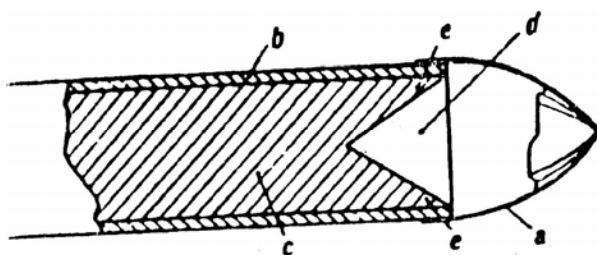


Fig. 2

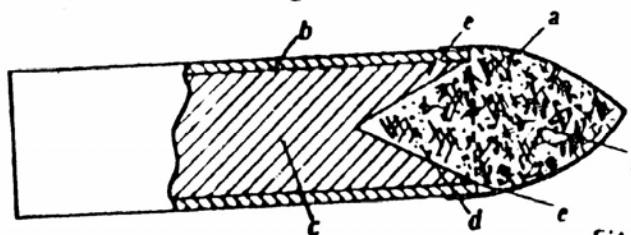
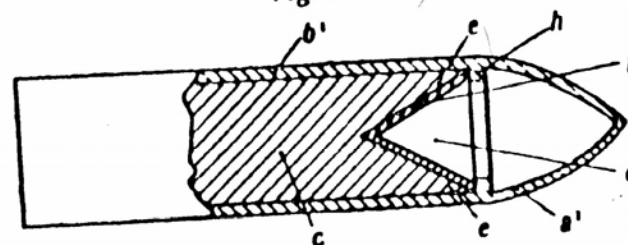


Fig. 3



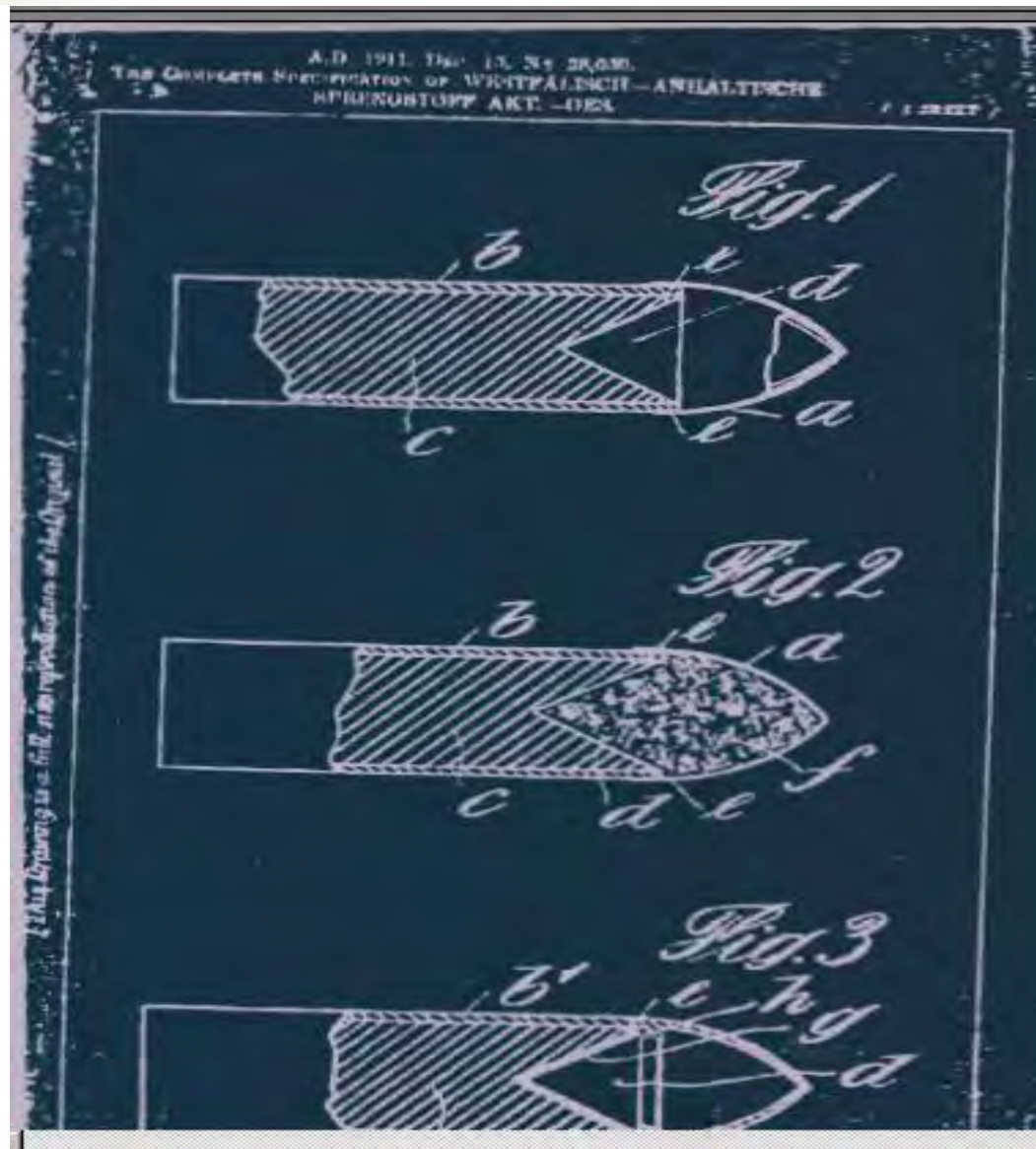
Projectiles with Hollow Charges
(Note liner (g) in Fig. 3)
(WASAG patent, 1911)



PDF
Complete

Your complimentary
use period has ended.
Thank you for using
PDF Complete.

[Click Here to upgrade to
Unlimited Pages and Expanded Features](#)



TECHNOLOGY DRIVEN. WARFIGHTER FOCUSED.

84 SARRAU et VIEILLE
mettent au point la poudre B
von DUTTENHOFER fabrique
poudre gélatinisée en grain à
Roßweil (D)

85

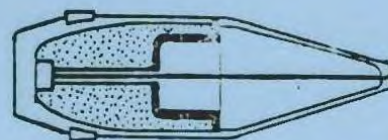
86

87 NOBEL invente la « balistite »,
poudre à base de nitrate de m.

91 Eclat avec les autorités françaises,
NOBEL quitte Paris.

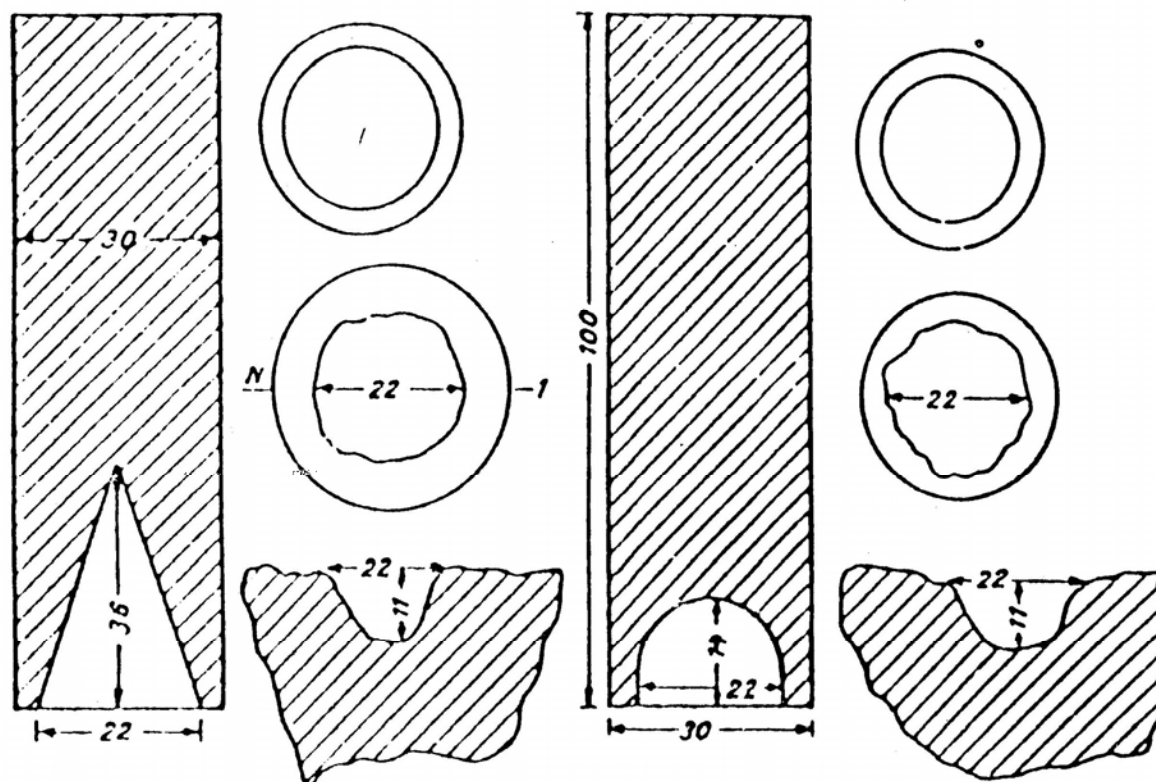
TURPIN détecte à Paris la
détonabilité de l'acide picrique.
Fabrication de la mélinite en France.
Adoption générale pour les charges
d'obus. Les études des « canons
dynamite » s'arrêtent.

LEPIDI étudie un obus à charge
creuse (« Obus chambré ») au Bouchet.
Il détecte l'effet du revêtement et de la
distance d'action, mais a à abandonner
l'étude quand un tube de canon éclate.

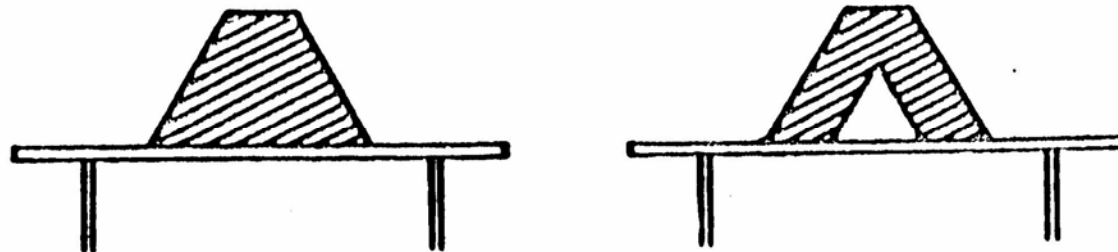


Obus chambré de Lepidi

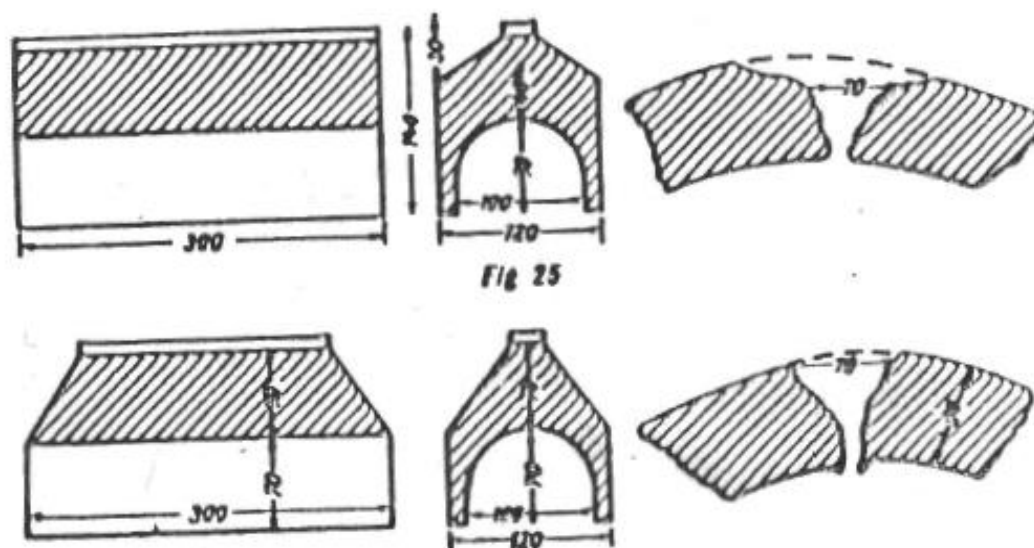
"The most advanced state in the history of shaped-charge was undoubtedly achieved in France. In the gun-powder factory situated in Le Bouchet during the period 1891-1893, a certain captain named LEPIDI worked on a project named "obus chambré", which was nothing other than a HEAT(shaped-charge) shell with a cylindrical liner. During this period, LEPIDI performed a static study of the influence of the liner thickness, of the standoff distance and of the liner material and he was able to statically perforate 140 mm of armor with a 155 mm shell. The final construction of a nearly modern antitank shell failed at that time, only due to troubles with the initiation system. Because of the use of an inadequate time-fuse device, a gun exploded and therefore the experiments were stopped and the results sunk in forgetfulness"



Hollow Charges with Increased Explosive Head
(M. Sukharevskii, 1926)



Setup to Compare Solid and Hollow Conical Charges
set on steel plate



Linear (Unlined) Shaped Charges
(M. Sukharevskii, 1926)

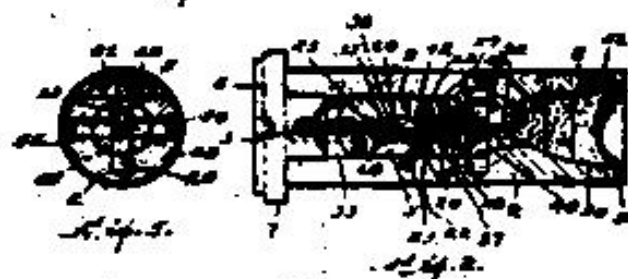
The Watson Fuze

April 14, 1922.

G. P. WATSON
Inventor
Filed Sept. 20, 1919

1,824,811

2 Sheets-Sheet 1



Inventor
Charles W. Watson

By John S. Hender

Poulter's Device

June 3, 1964 T. C. POULTER 3,136,249
SHEARED CHARGE EXPLOSIVE ONLY AND LINER SHEARFOR
Filed June 10, 1961

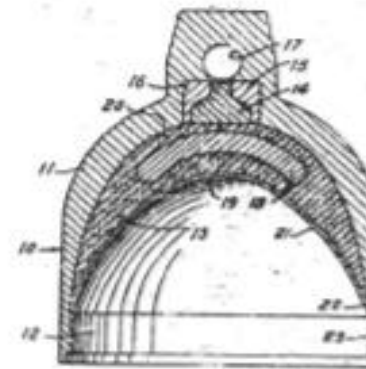


Fig. 1



Fig. 2

INVENTOR
Thomas C. Poulter

BY *John C. Lewis, Jr.*
ATTORNEY

Fig. 30 Poulter wave sheared oil well charge, U.S. Patent 3,136,249

Optical and Physical Effects of High Explosives

By R. W. WOOD, For. Mem. R.S., Professor of Experimental Physics,
Johns Hopkins University

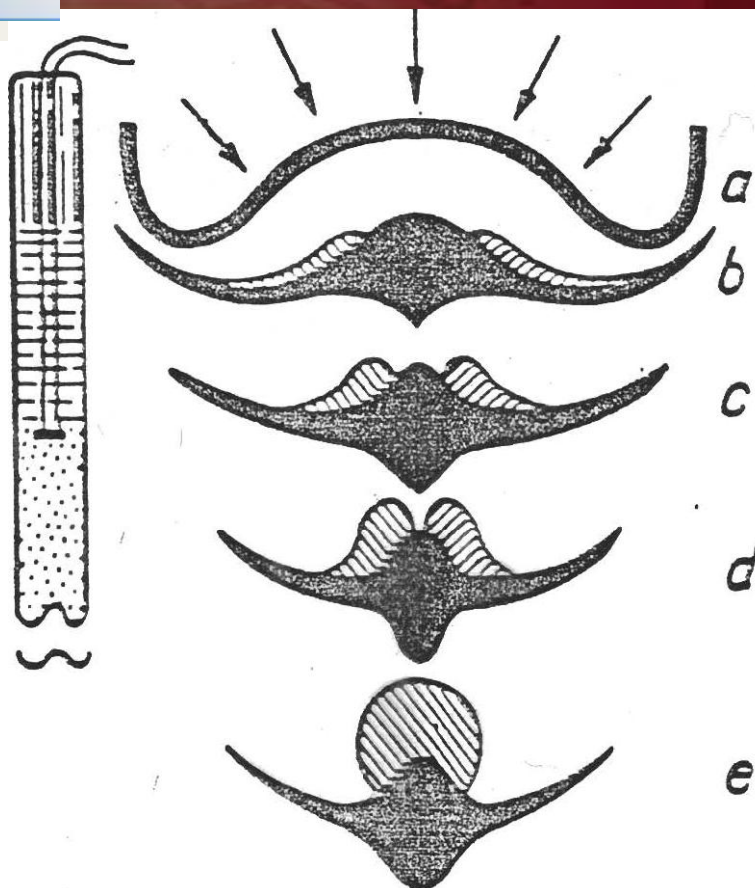
(Received 25 June, 1936)

[PLATES 7 AND 8]

I—PLASTIC FLOW OF METALS

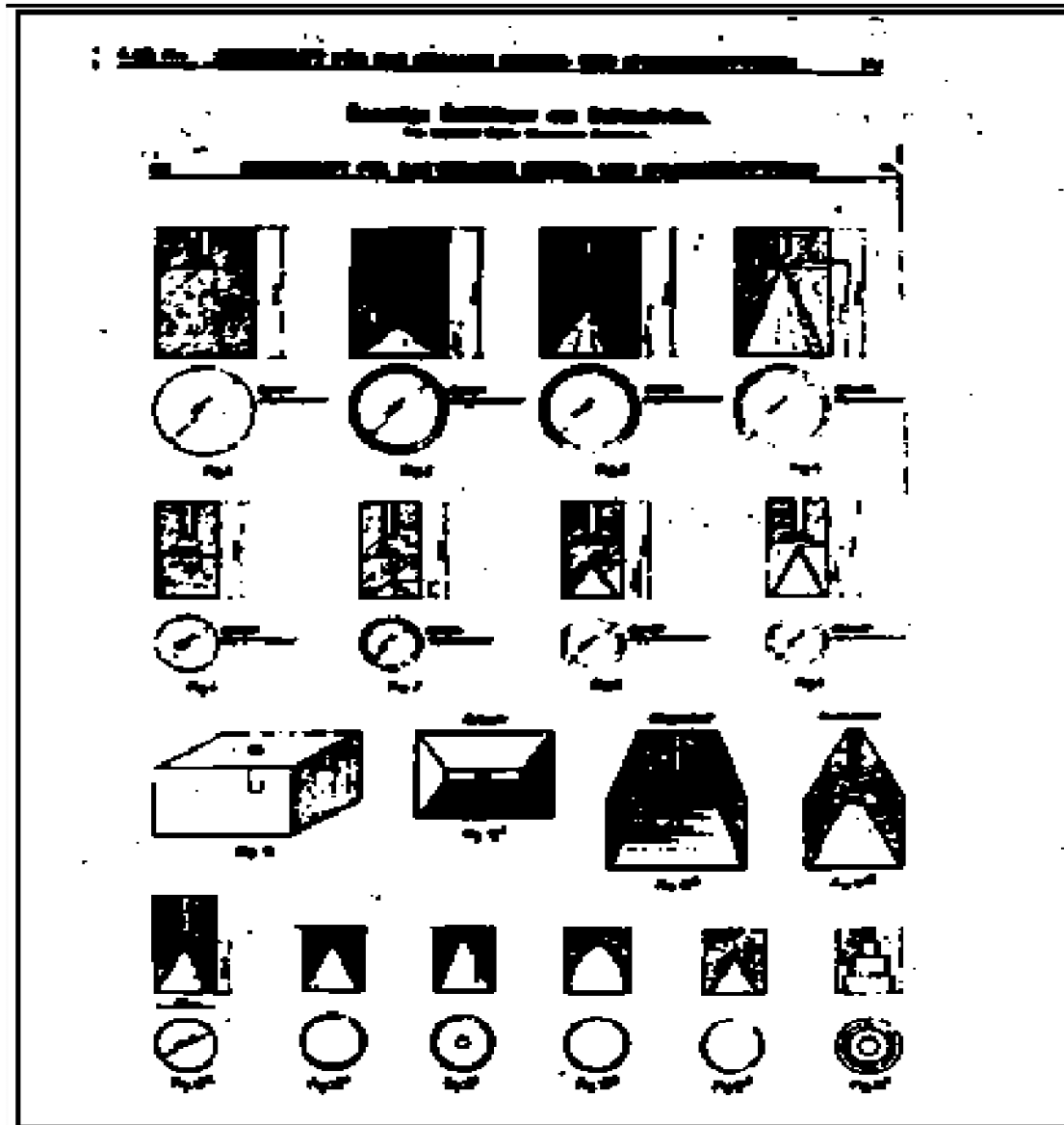
My interest in the study of the effects produced by high explosives originated in the investigation of "evidence" in a number of murders by bomb, and more especially in connexion with a most unfortunate and unusual accident which resulted in the almost instant death of a young woman who, on opening the door of the house furnace to see if the fire was burning properly, was struck by a small particle of metal which flew out of the fire and penetrated the breast bone, slitting a large artery and causing death in 2 or 3 minutes from internal haemorrhage. The particle, which was not much larger than a pin-head, was submitted to me for identification, and though its form resembled nothing with which I was familiar, I surmised that it was probably a part of a dynamite-cap or "detonator" used for exploding the dynamite charges in the mines, which, by some carelessness on the part of a miner, had been delivered intact with the coal.

These detonators are spun from very thin sheet copper and consist of



Blasting Cap and Postulated Transformation of Lined
Bottom following Detonation
(R. W. Wood, 1937)

Liner Shapes



ITER FOCUSED.

DEVELOPMENT OF HOLLOW CHARGES (1942) [From (54)]

Historical Survey:

- | | |
|------|--|
| 1883 | Work by Foerster (hollow charge effect; use in projectiles) |
| 1910 | WASAG hollow charge for blasting charges of all types patented. Sheet metal liner used without knowledge of effect |
| 1914 | Neumann, "Investigation Into Hollow Charges Without Liner" (also acute angle cone hollow charge) |
| 1926 | Hollow charge investigations at inspection of arms and equipment |

- 1935/36** Development of armor-piercing projectile by WA A with hollow charge (patent Capt. Wimmer)
- Late 1935** Demonstration of anti-tank rifle by Thomanek in presence of Hilter and WA A . No results.
- June 1937** Determination of favorable effect of standoff detonation with hemispherical liner (WA F)
- Nov/Dec 1938** Proposed introduction of shells with hollow charge and aluminum liner (no increase in effect) by WA Pruf 1

**Jun 1938-
May 1939**

Work by Thomanek (employed by Luftwaffe - Gatow); evacuated hollow charge (no improvement); recognition of liner effect by Prof. Schardin; disagreement between Thomanek and Schardin.

15 Feb 1939

Final report by WA Pruf 5 on hollow charge tests; realization of increased effect (independent of Gatow) through solid liner

June 1939

Introduction of 7.5cm projectile with hollow charge and aluminum liner.

**Dec 1939 -
Jan 1940**

**Test results presented by Thomanek to
Research Institute Gatow (WA Pruf 1)**

May 1940

**Use of hollow charge detonations without
reinforced liner on Liege fortifications, after
development by WA Pruf 5**

May 1940

**Explosive Experiment Company given green
light by WA Pruf 5 for development**

Most Significant Results:

Casing device for hollow charges (patent applied for 10 August 1940).

Acute angle cone and liner with wall thickness for armor-piercing projectiles (patent applied for 9 September 1940).

Diaphragm-like liner for hollow charge, 6 November 1940.

Hollow charge for rifle anti-tank land mine, 29 May 1941.

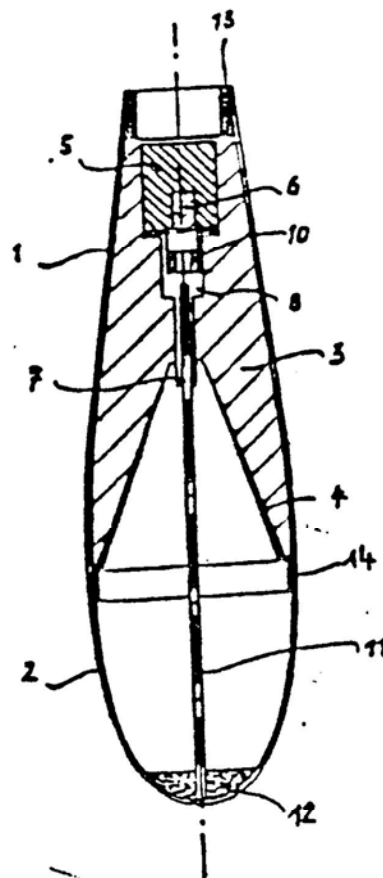
7 Sep 1940 Detonation tests by WA F (without Thomanek) with satisfactory results with acute angle cone hollow charge (solid sheet metal liner) and standoff detonation (cast charge).

- | | |
|---------------------------|--|
| 20-30 Sep
1940 | First demonstration of anti-tank rifle grenade (WASAG). Hollow charge with thin liner. |
| Late 1940 | Completion of construction of hollow charge 15 (hollow charge with heavy liner) in Gatow. |
| March 1941 | Testing of hollow charge 15 on Maginot Line forts. |
| 9 May 1941 | Delivery of 450 rifle grenades by WASAG for use on Crete. |

Steel liners (0.5 to 1 mm thick) were found to be superior to gray-iron casting (June 1940). Hollow charges with conical liners (up to 1.5 mm and with angles between 20 - 45 degrees) and proper standoff (25 - 30 mm) would effect perforation of 15 mm armor plate. The charges used were cast. An increase of the diameter of the blast hole was made possible by the use of a bell-shaped hollow charge which would also permit fewer irregularities than with the acute cone. The diameter was 1 cm (of the charge).

The idea of firing a hollow charge shell from the shoulder was first conceived in 1937 (i.e., a rifle grenade).

NOTES: WA A is an abbreviation for *Waffenamt* (Army Weapons Office) which had a department designated WA Pruf for the proof testing of weapons. WA Pruf is an abbreviation for *Waffenamt Prüfwesen* (Offices of Weapons Proof and Development). WA F means *Waffen Forschung* (weapons research) and worked with shaped charges under the direction of Dr. Schumann. The *Technische Akademie der Luftwaffe* or TAL (Technical Academy of the Air Force) was headquartered at Berlin – Gatow and headed by Dr. Schardin. It was roughly a World War II counterpart of BRL. For additional organizational details see Simon (57).



Rifle Grenade (German Patent 975,806)
(F. R. Thomanek, 1941, assigned to WASAG)

1947

FIGURE III

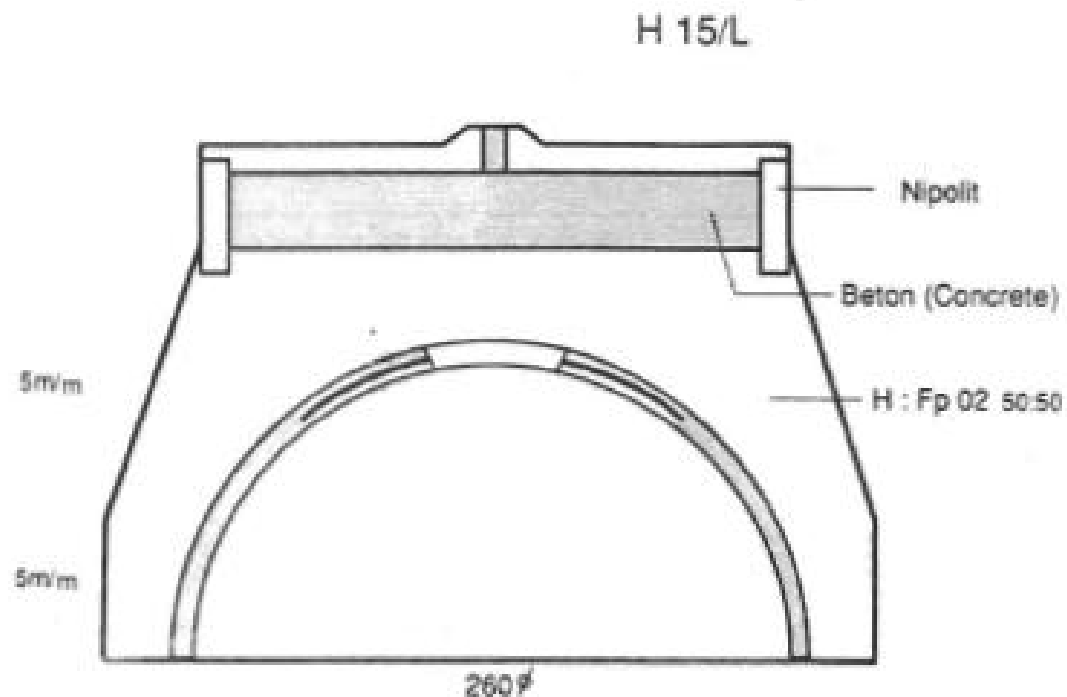
Source
 Ordnance Department, U.S. Army
 "The Shaped Charge" lecture by
 L.E. Erikson 4 April 1947
 Technical Division, Picatinny Arsenal

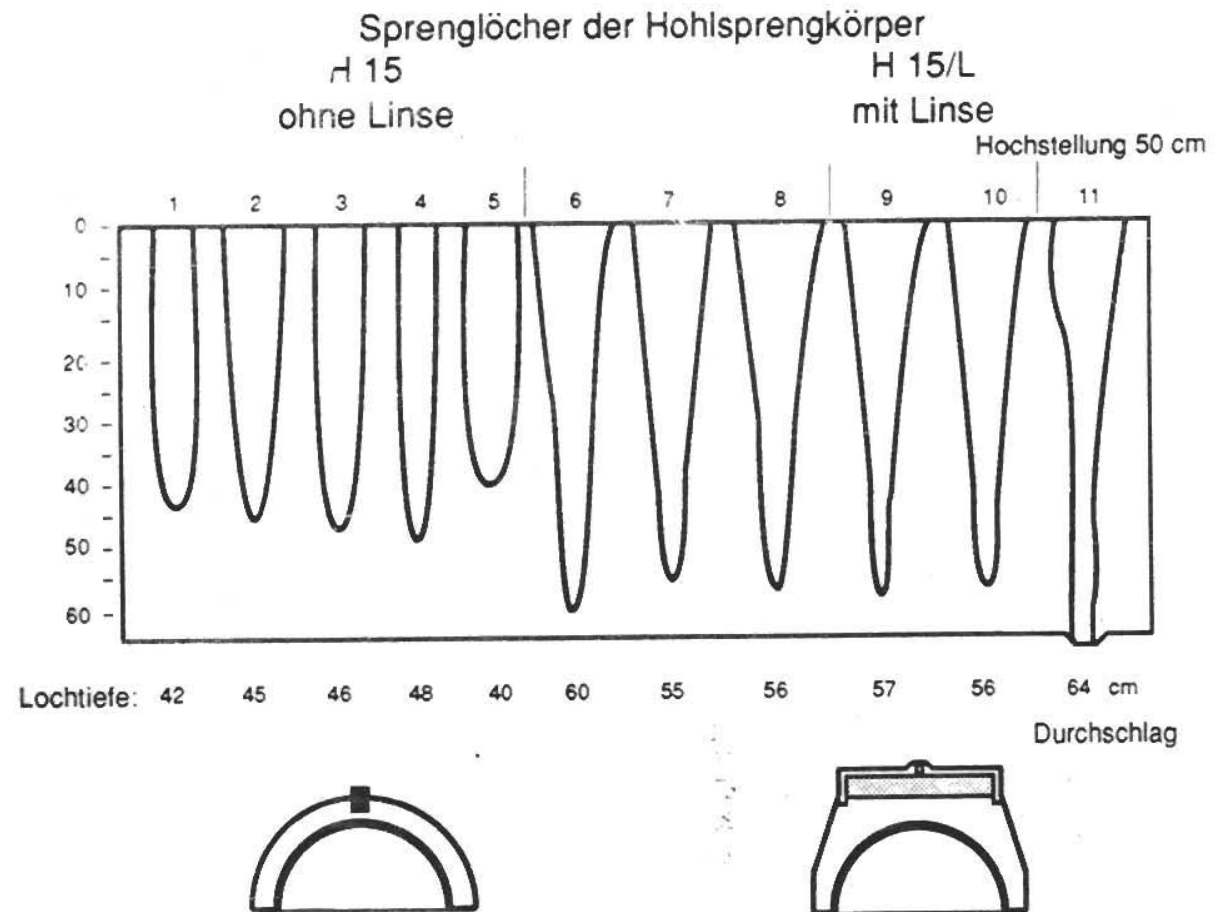
SECTIONAL VIEW OF A SHAPED CHARGE



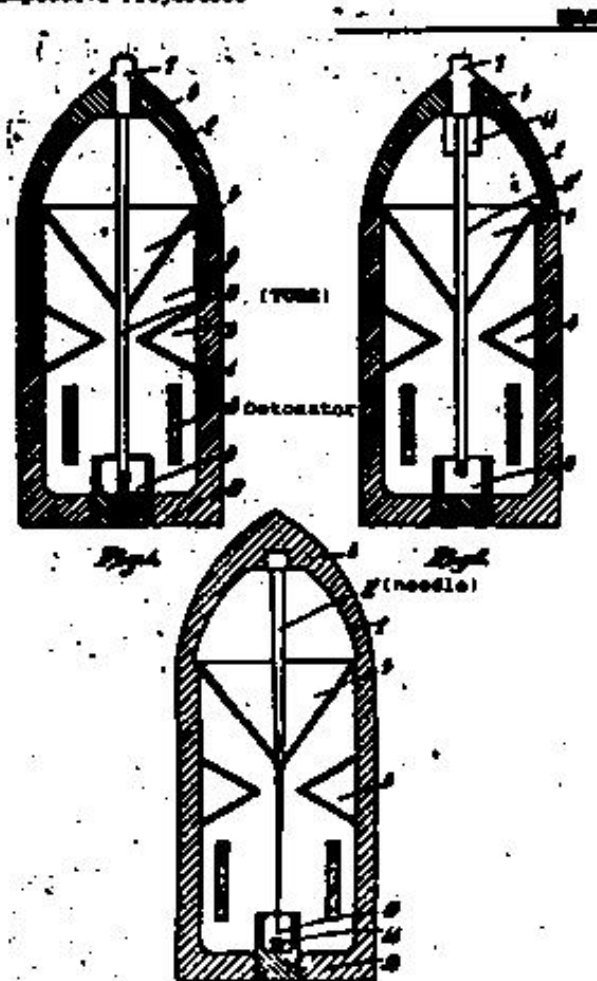
Figure 4

1943 German paper "Preliminary Information report about the enhanced performance of hollowcharge bodies by directed initiation (lenses)"
von Prof. Dr. Erich Schumann u. Dr. Gerd Hinrichs





Invention data claimed: Applicant: Sager, Societe Anonyme de Gestion
France 9 Nov 1939 et d'Exploitation de Brevets
Assignees: Barthold Haupt, Henry Haupt,
Australia 14 Aug 1941 Erich Loenders, et France.
"An Improved Explosive Projectile"



April 22, 1947.

U. S. PATENT

2,419,414

REPEATING
FIRE ARMS

Filed Oct. 2, 1945



Fig. 1



Fig. 2



Fig. 3



Fig. 4

By *Harry M. Thompson*

Attorney

TECHNOLOGY DRIVEN. WARFIGHTER FOCUSED.

1942

FIGURE 23

March 14, 1941

H. W. HERRMANN

2,974,806

PIRATES

Original Filed Dec. 28, 1940



Fig. 1.



Fig. 3.



Fig. 2.



Fig. 5.

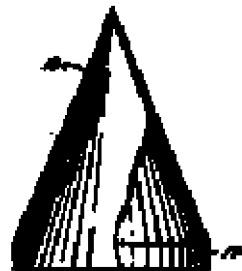


Fig. 4.

H. W. HERRMANN

INVENTOR

H. W. Herrmann

ATTORNEY

TECHNOLOGY DRIVEN. WARFIGHTER FOCUSED.

Sept. 9, 1947.

J. C. GRAY ET AL

2,426,997

PROVISIONAL

Filed March 10, 1945

Fig. 1

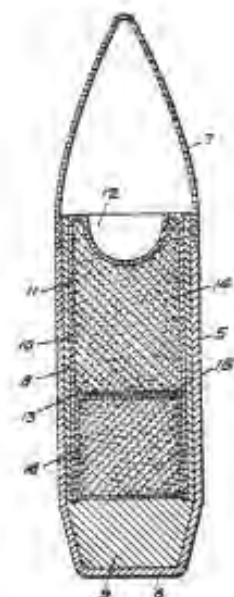


Fig. 2

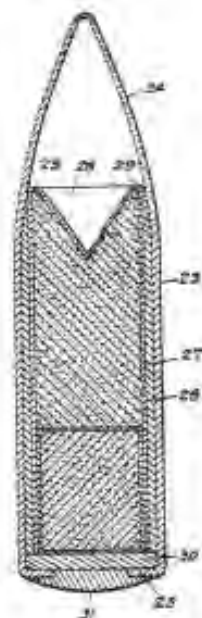
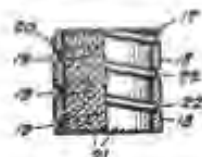
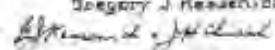


Fig. 3



Inventors
John C. Gray
Wilfred E. Thibodeau
Joseph M. Church
Gregory J. Kessenich
By  Attorneys

Point-to-point distance	6.00 m
Point-to-line distance	5.50 m
Line width	1.00 m
Point-to-line distance	6.50 m, 0.00-6.00 m
Line curvature	0.00-0.01 (curvature = $1/\text{radius}$)
Line intersection	Light shaded
Endpoints	0.00-0.25 pixels
Endpoint change length	1.00 m
Endpoint change weight	1.00 m
Branch length	0.00 m
Branch weight	200 kg

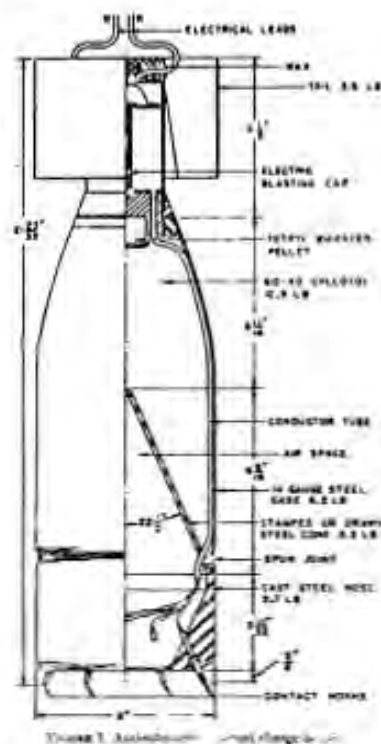


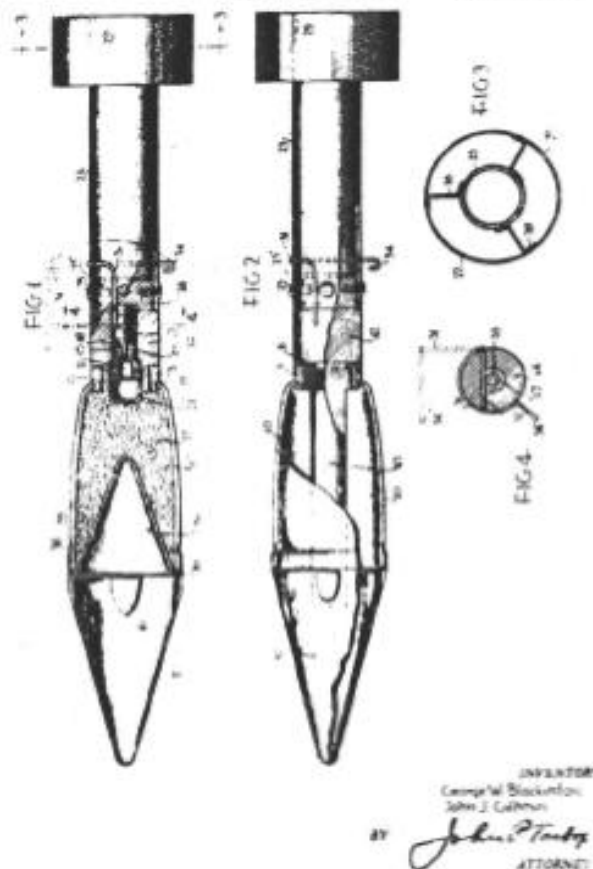
Fig. 30 Antisubmarine HEAT Scatterbomb, U.S. Navy, WWII, ca. 1945

May 11, 1948. G. W. BLACKINTON ET AL. 2,441,388

PROJECTILE

Filed Aug. 19, 1942

2 Sheets-Sheet 1



Oct. 15, 1957

S. A. MOSES

2,809,585

PROJECTILE FOR SHAPED CHARGES
Filed Nov. 16, 1949

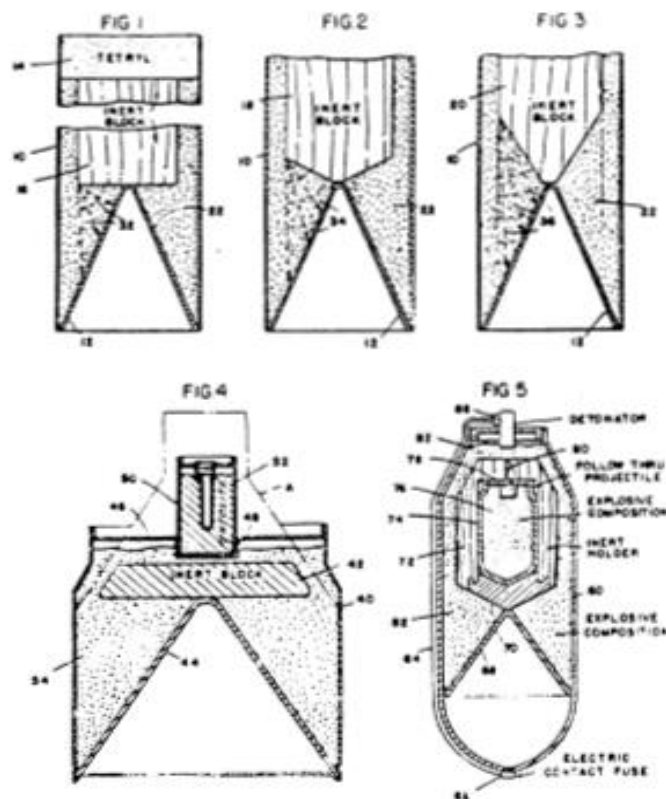
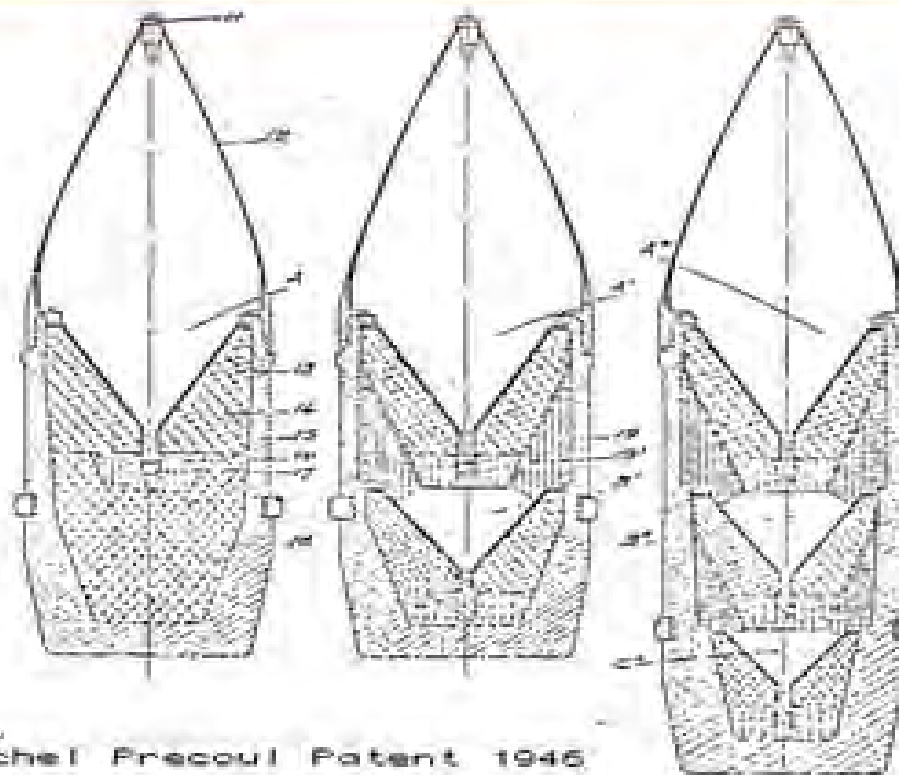


Fig. 38 Moses patent wave shapers, follow through U.S. 1949

103

dem Shaped Charge



Michel Precoul Patent 1946

Societe' Technique de Recherches
Industrielles et Mecaniques

TECHNOLOGY DRIVEN. WARFIGHTER FOCUSED.

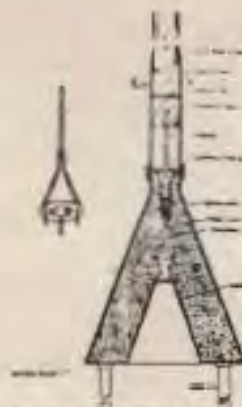
ANTITANK "LUNGE" MINE

The antitank mine, an armless device used by German troops, consists of a conical shaped explosive charge enclosed in a steel container, and a wooden handle. Three legs equally spaced around the base of the charge provide proper support. A well in the apex of the charge contains the detonator.

The firing mechanism, quite simple in construction, consisting of a 5440R 1724 trigger, a shear pin, and a safety pin, is located in a metal sleeve. This sleeve, which holds the mine and the handle 1 1/2 inches apart, slips over the end of the handle and is held in place by the shear pin and safety pin. It is attached to the body of the mine by a threaded connecting ring.

To operate the mine, the soldier must first remove the safety pin, and then, using bayonet action, lunge forward, striking the mine squarely against the tank. When the legs of the mine strike the target, the handle is driven forward breaking the shear pin, and the trigger is driven into the detonator, causing explosion of the mine.

The mine will penetrate 3 inches of steel plate, with impact at a 90° angle, and plates of approximately 4 inches can be penetrated.



SPECIFICATIONS	
Weight of mine body (without legs)	12 lbs.
Weight of mine (with legs)	15 lbs.
Length of handle	30 in.
Weight of handle	1 1/2 lbs.
Weight of explosive charge	17 1/2 lbs.
Weight of mine	30 lbs.
Weight of mine (with legs)	33 1/2 lbs.



1944. 10/10. 10/10. 10/10. 10/10. 10/10. 10/10. 10/10. 10/10. 10/10. 10/10.

A two meter diameter shaped charge



TECHNOLOGY DRIVEN. WARFIGHTER FOCUSED.

NUMERICAL ANALYSIS OF BI-METALLIC EXPLOSIVE SHOCK-LOADING AND RELEASE EXPERIMENTS (Wave Interaction)

Jeremy Kleiser, Brian Plunkett, and Lalit Chhabildas
Air Force Research Laboratory – Munitions Directorate – Eglin AFB

September 2008



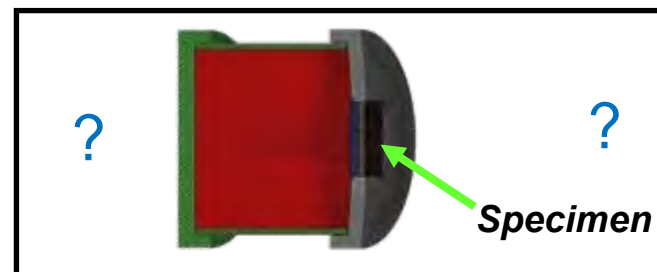
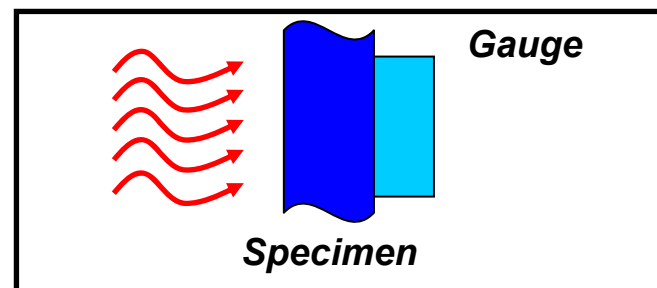
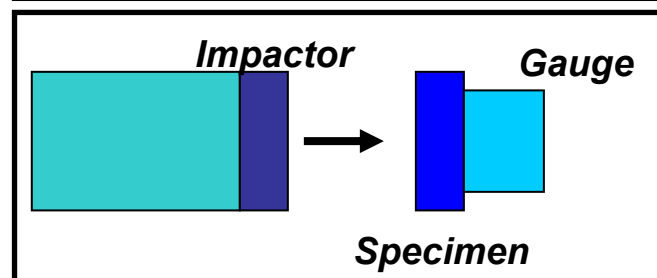
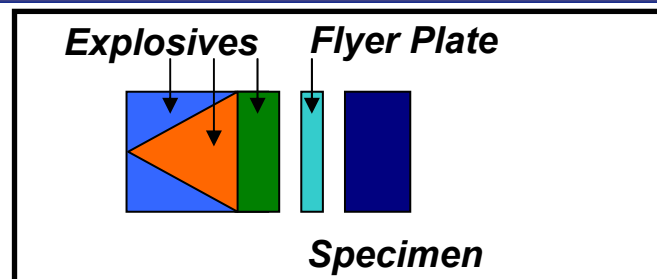
DISTRIBUTION A: Approved for public release; distribution unlimited.
Approval Confirmation 96 ABW/PA No. 07-03-08-312



Shock Loading Techniques

Established Techniques

- **Explosive Loading**
 1. Plane wave lens
 2. Explosively-driven flyers
- **Smooth-bore guns**
 1. Single-stage compressed gas
 2. Propellant
 3. Two-stage light gas
 4. Rail guns
 5. Three-stage light gas
- **Radiation**
 1. Electron beams
 2. Nuclear explosions
 3. Laser beams
 4. Z machine (X- rays, magnetic flux)



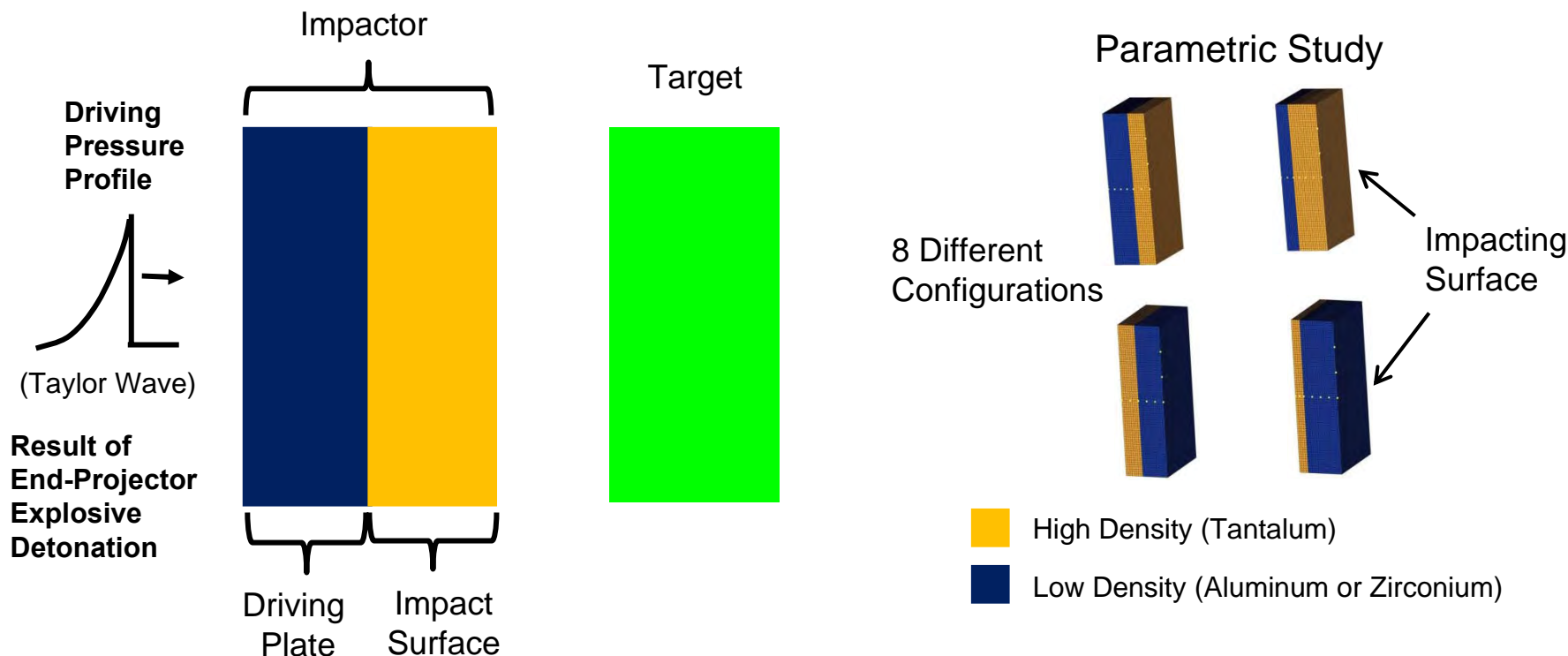
Evaluate Explosive End-Projector
In-house capability but not
an established technique



Objective

Effects of the End-Projector on Terminal Velocity

Evaluate loading conditions and its effects (pressure, velocity, strain) through the bonded plates using the End-Projector, and its effects on terminal velocity





Equation of State & Constitutive Parameters

Used to Simulate Material Response - EPIC Hydrocode

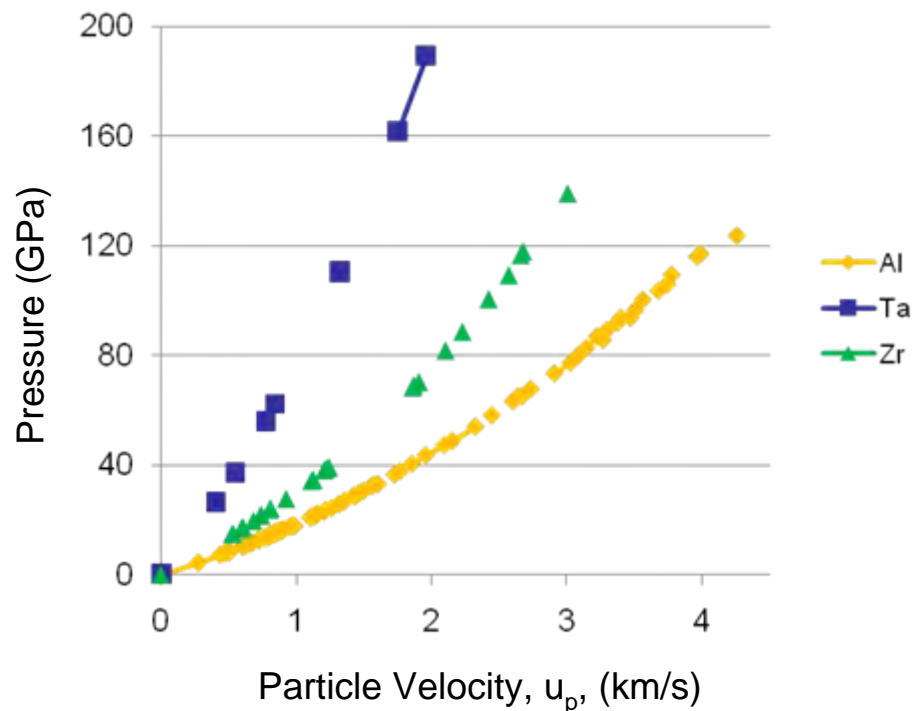


Materials:

- Aluminum – Al
- Tantalum – Ta
- Zirconium - Zr

Property	Al	Ta	Zr
Density, ρ_0 (g/cm ³)	2.78	16.6	6.65
Yield Stress (GPa)	0.310	0.170	0.230
Poisson Ratio	0.33	0.34	0.34
Bulk Sound Velocity, C_s (km/s)	5.328	3.414	3.757
U_s / u_p Slope (S)	1.338	1.201	1.271
Spall Strength (GPa)	1.7	6.5	2.16
Impedance, $Z = \rho_0 U_s$	14.8	56.7	25.0

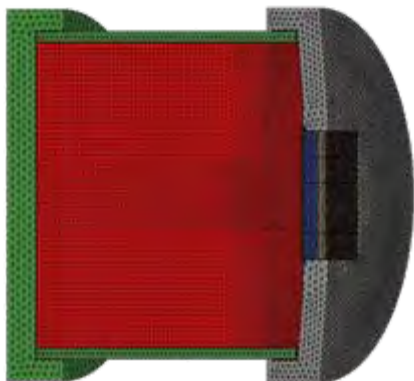
Strength Properties: Johnson-Cook Model
EOS: Mie-Gruneisen Model 2



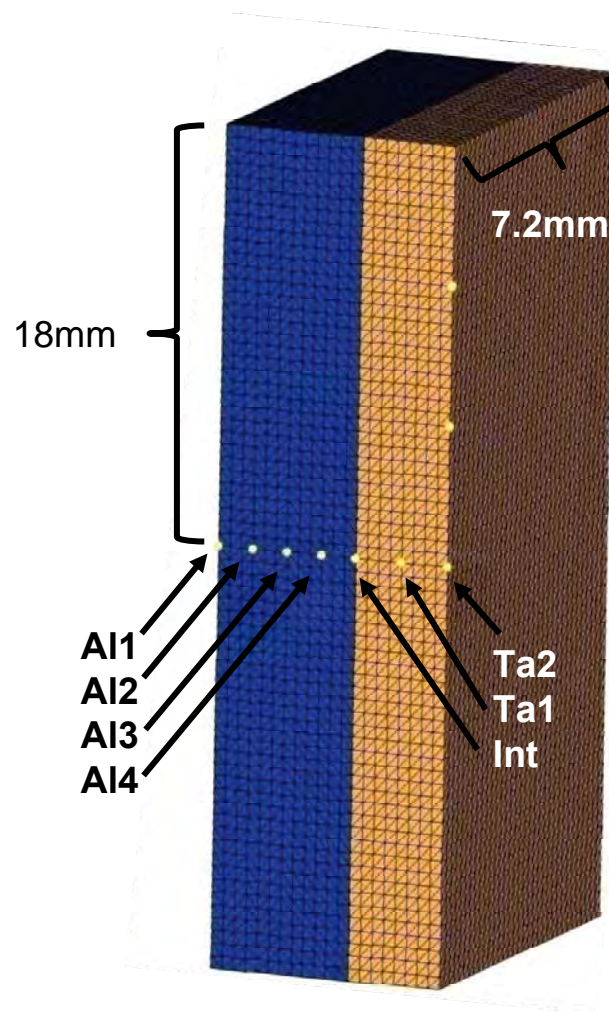
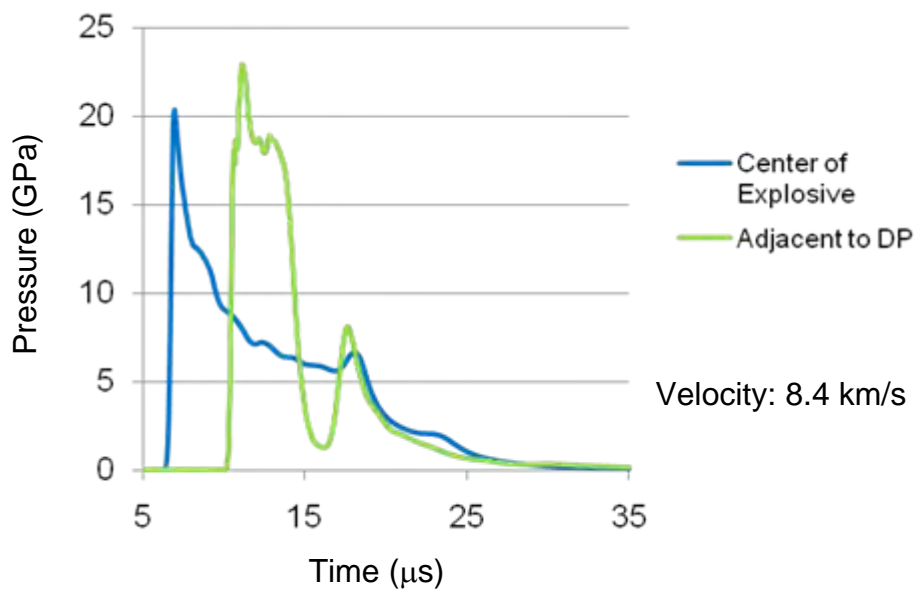


Numerical Configuration

Monitor Through-thickness and Lateral Dimensions



Driving Pressure Profile

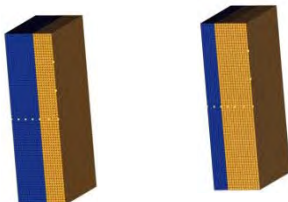
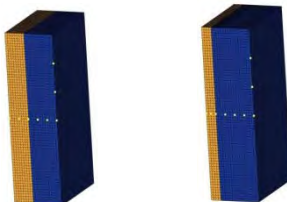


Code: EPIC; 1.1 Million Constant-strain Tetrahedral Elements

Approved for public release; Distribution Unlimited. Approval Confirmation 96 ABW/PA No. 07-03-08-312

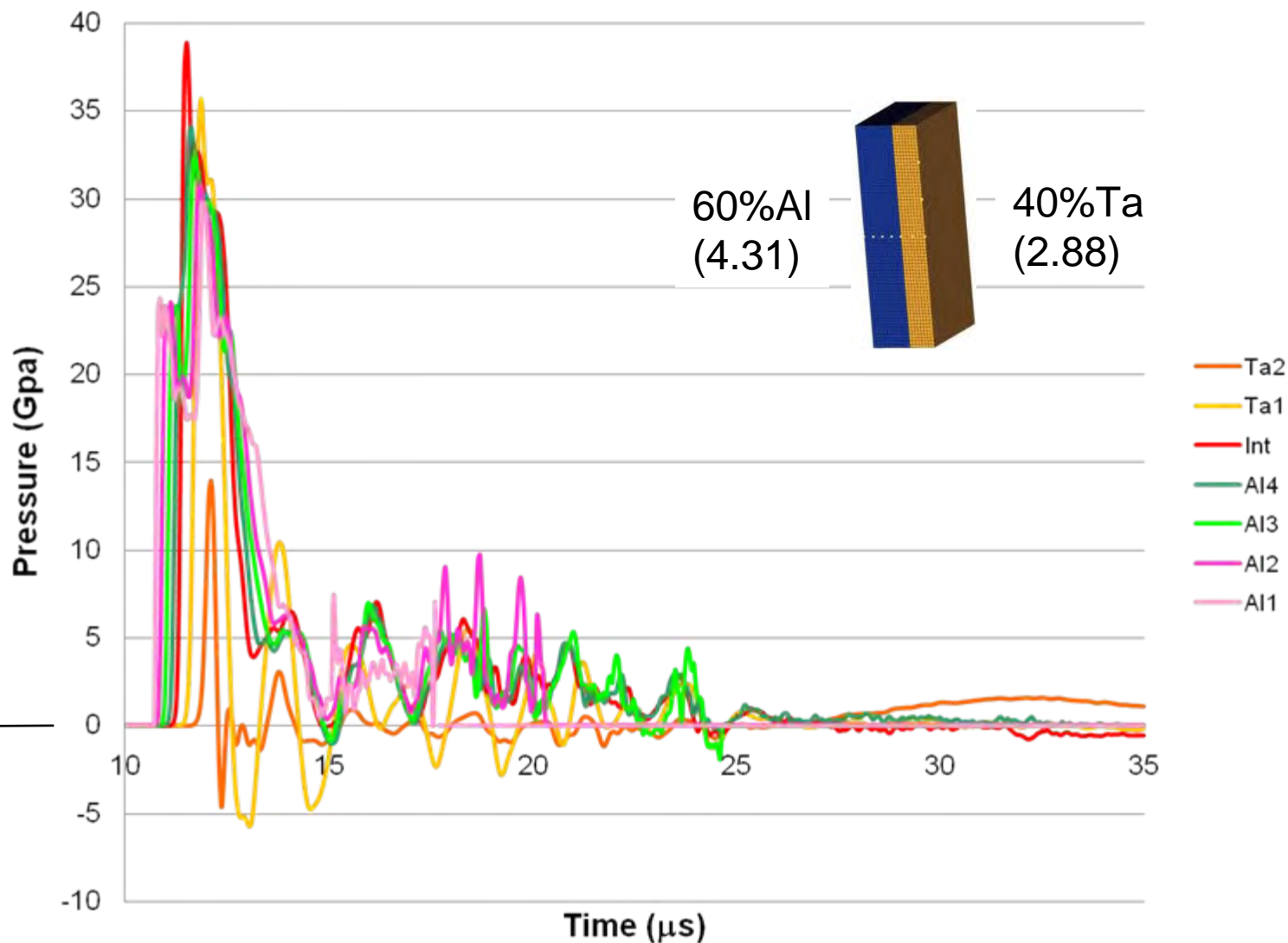


Bimetallic Plate Configuration

Configuration	1	2	3	4	5	6	7	8
Driver Plate Material (Explosive Surface)	Al	Al	Zr	Zr	Ta	Ta	Ta	Ta
Driver Plate Material Thickness (mm)	4.31	2.16	4.31	2.16	2.88	1.44	2.88	1.44
Impactor Surface Material	Ta	Ta	Ta	Ta	Al	Al	Zr	Zr
Impactor Surface Material Thickness (mm)	2.88	5.03	2.88	5.03	4.31	5.75	4.31	5.75
Type	Shock / Release				Shock / Reshock			
<div><div></div> High Density (Tantalum)</div> <div><div></div> Low Density (Aluminum or Zirconium)</div>								

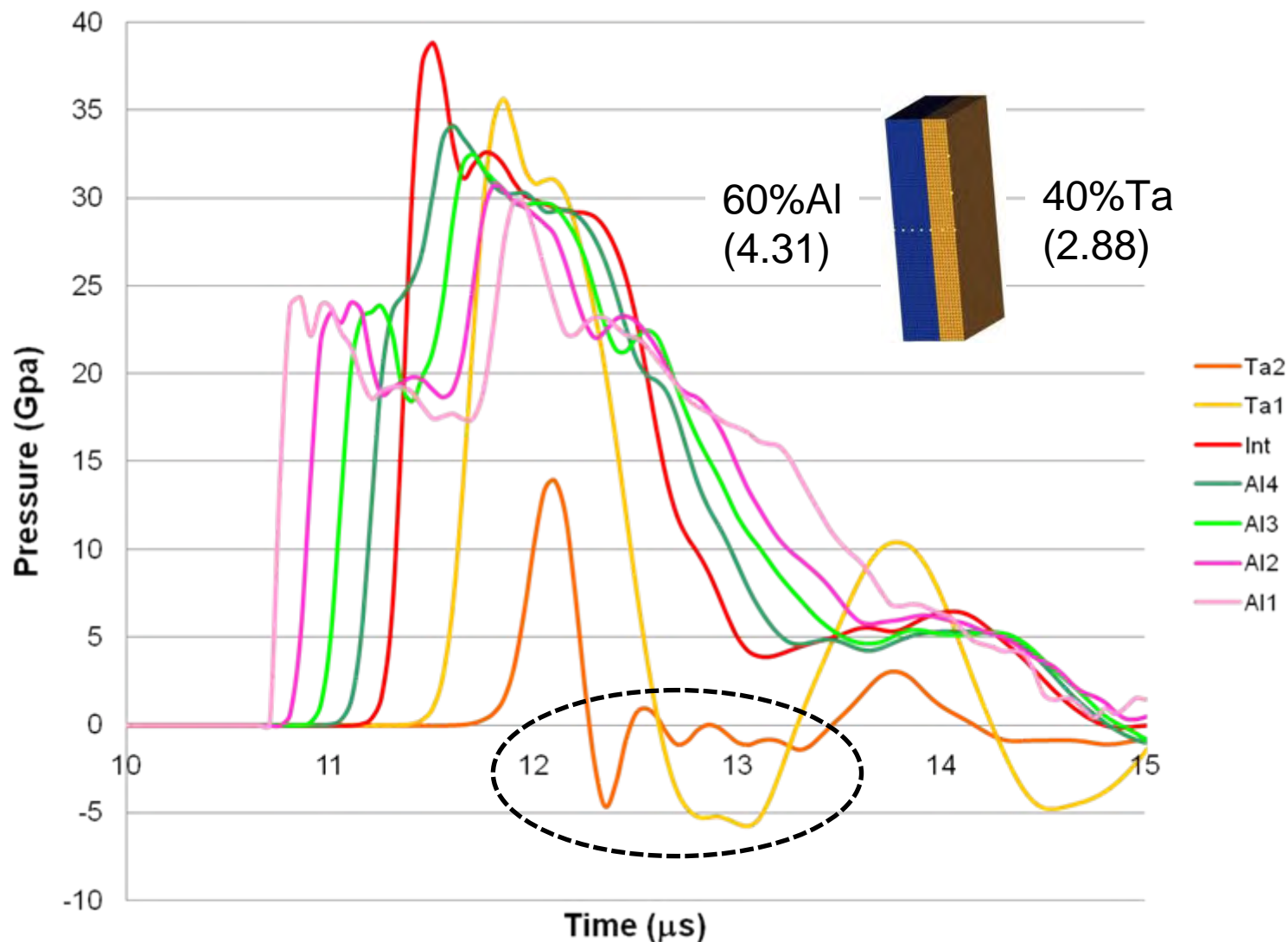


Through Thickness Pressure (Configuration 1)



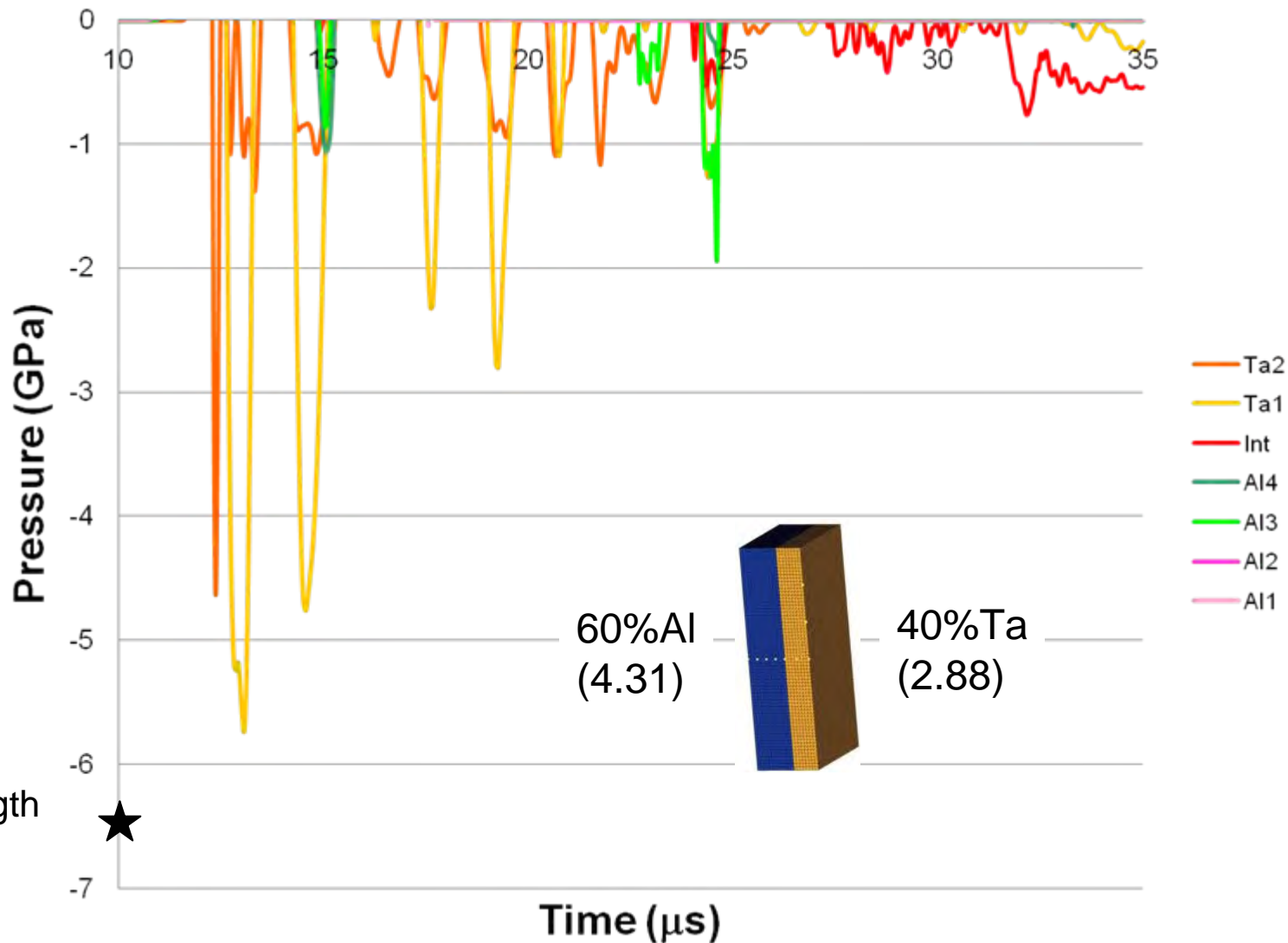


Through Thickness Pressure (Configuration 1)





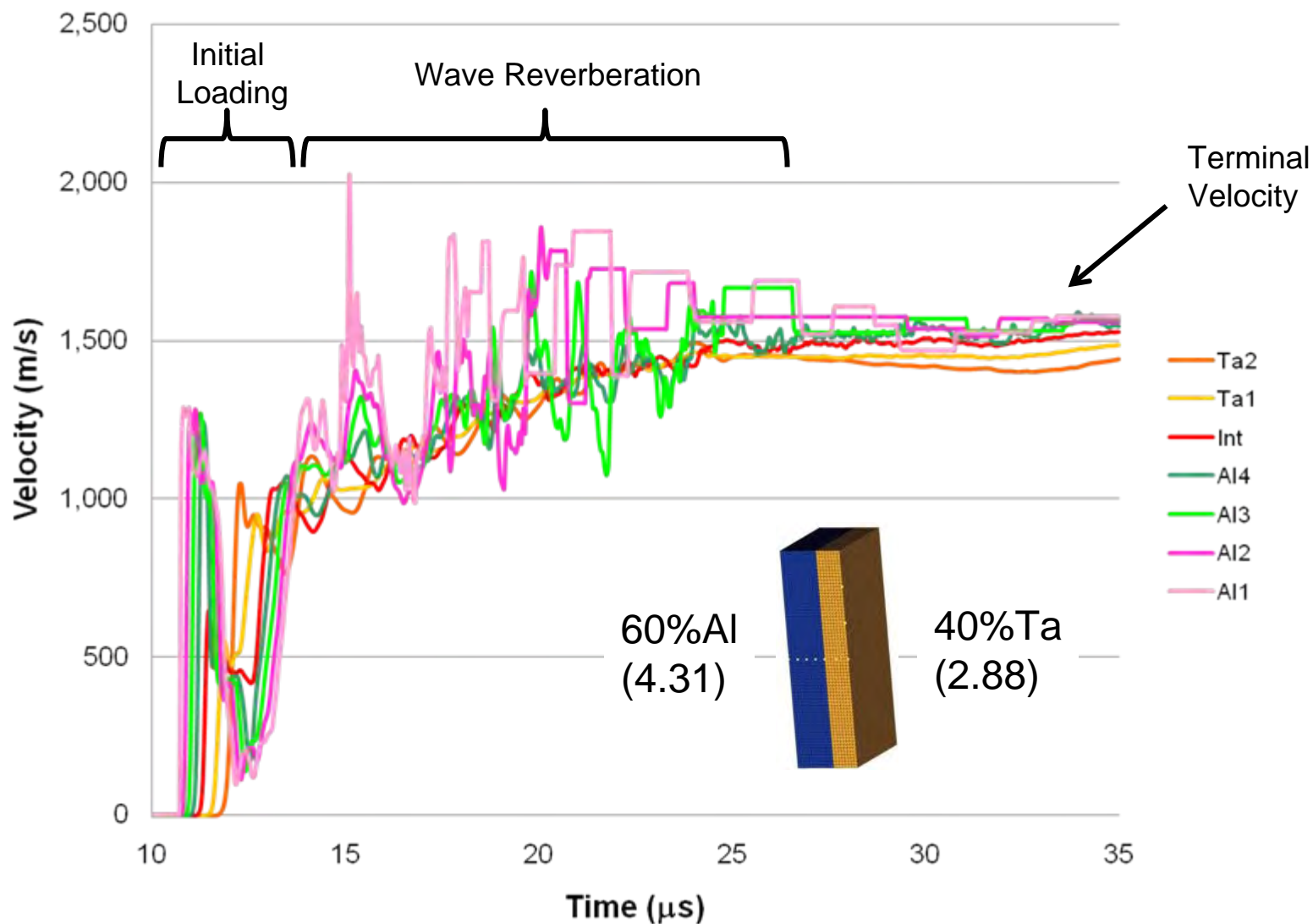
Through Thickness Tension (Configuration 1)



~Spall Strength
of Tantalum

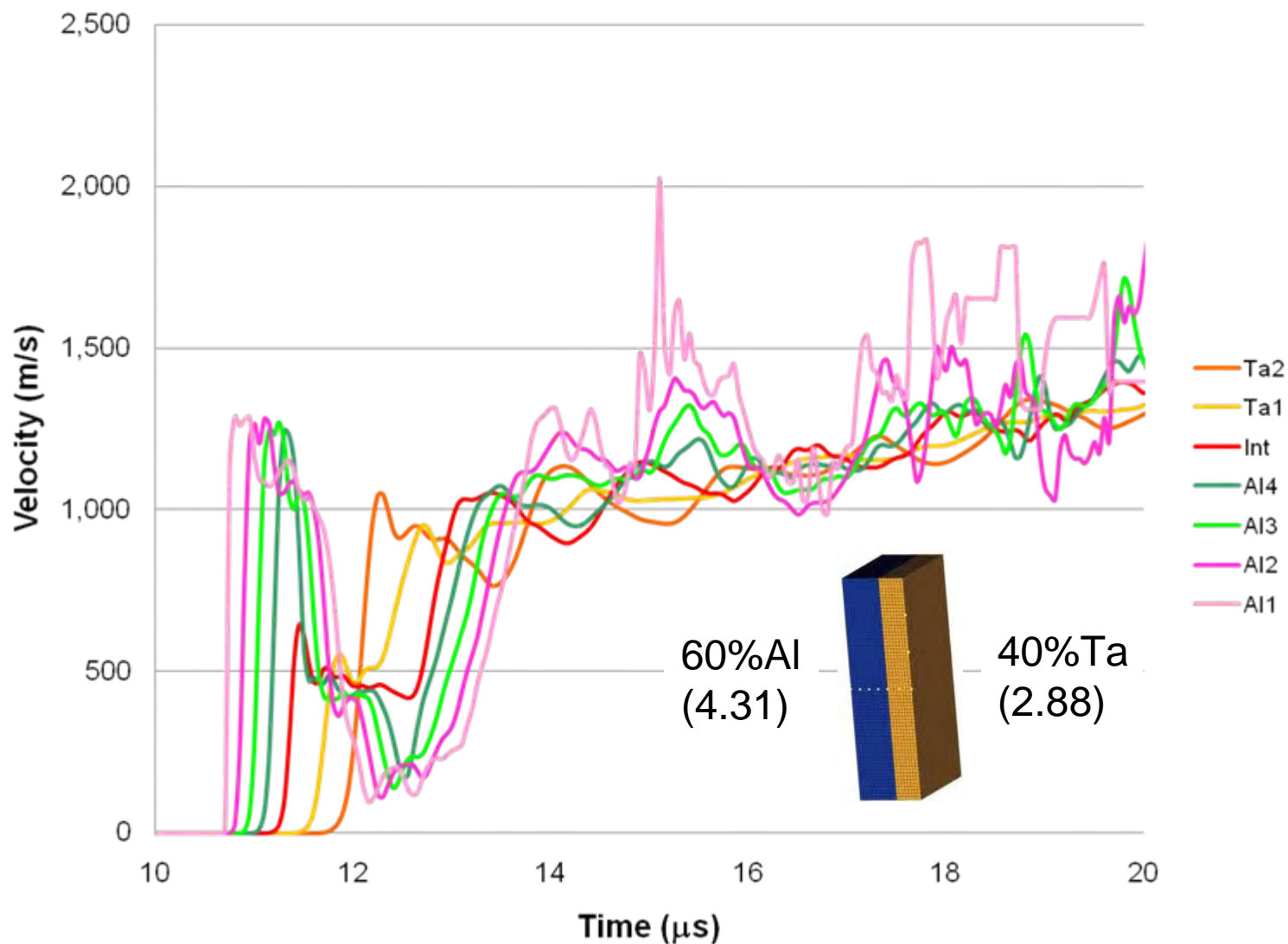


Through Thickness Velocity (Configuration 1)



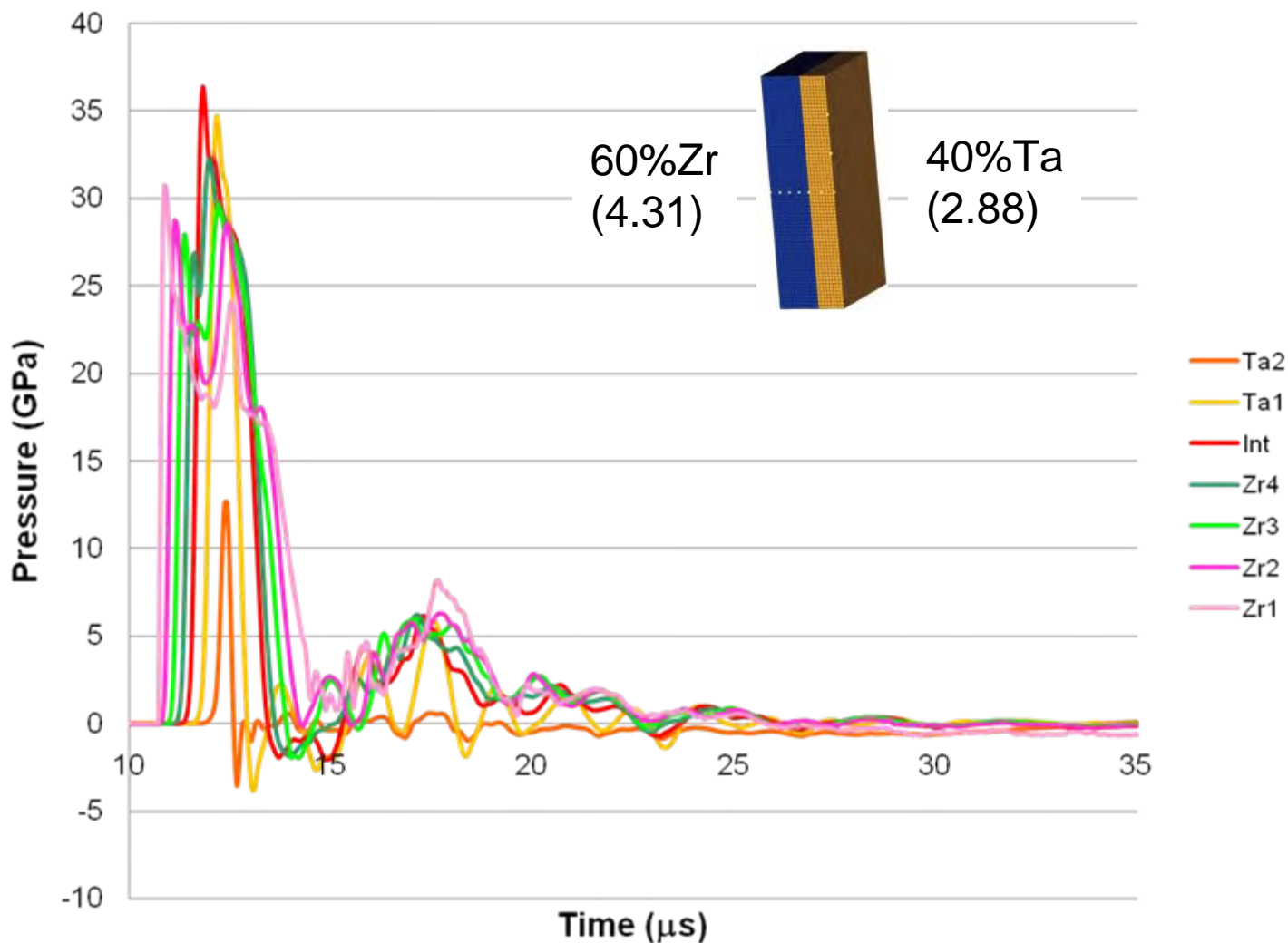


Through Thickness Velocity (Configuration 1)



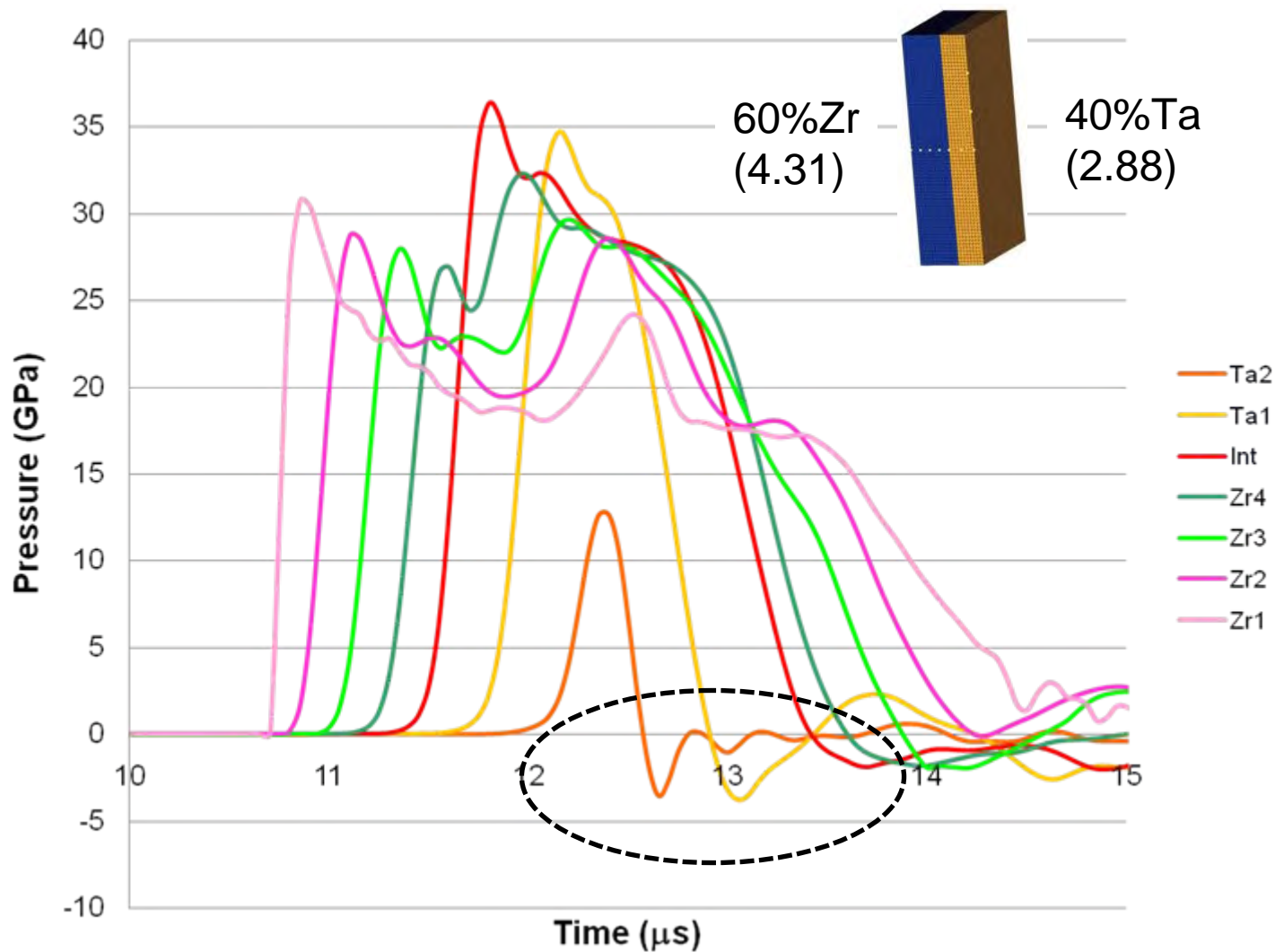


Through Thickness Pressure (Configuration 3)



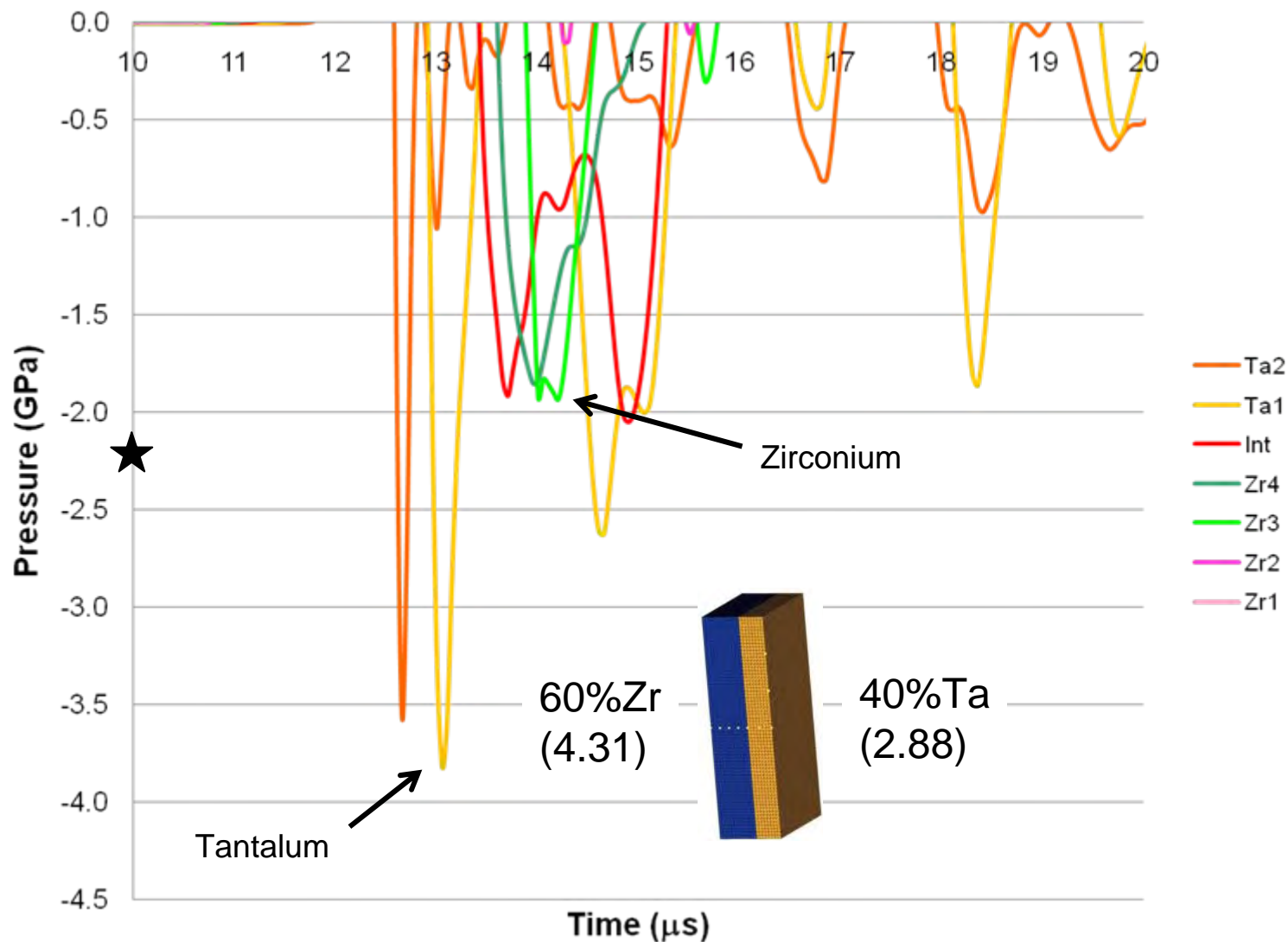


Through Thickness Pressure (Configuration 3)



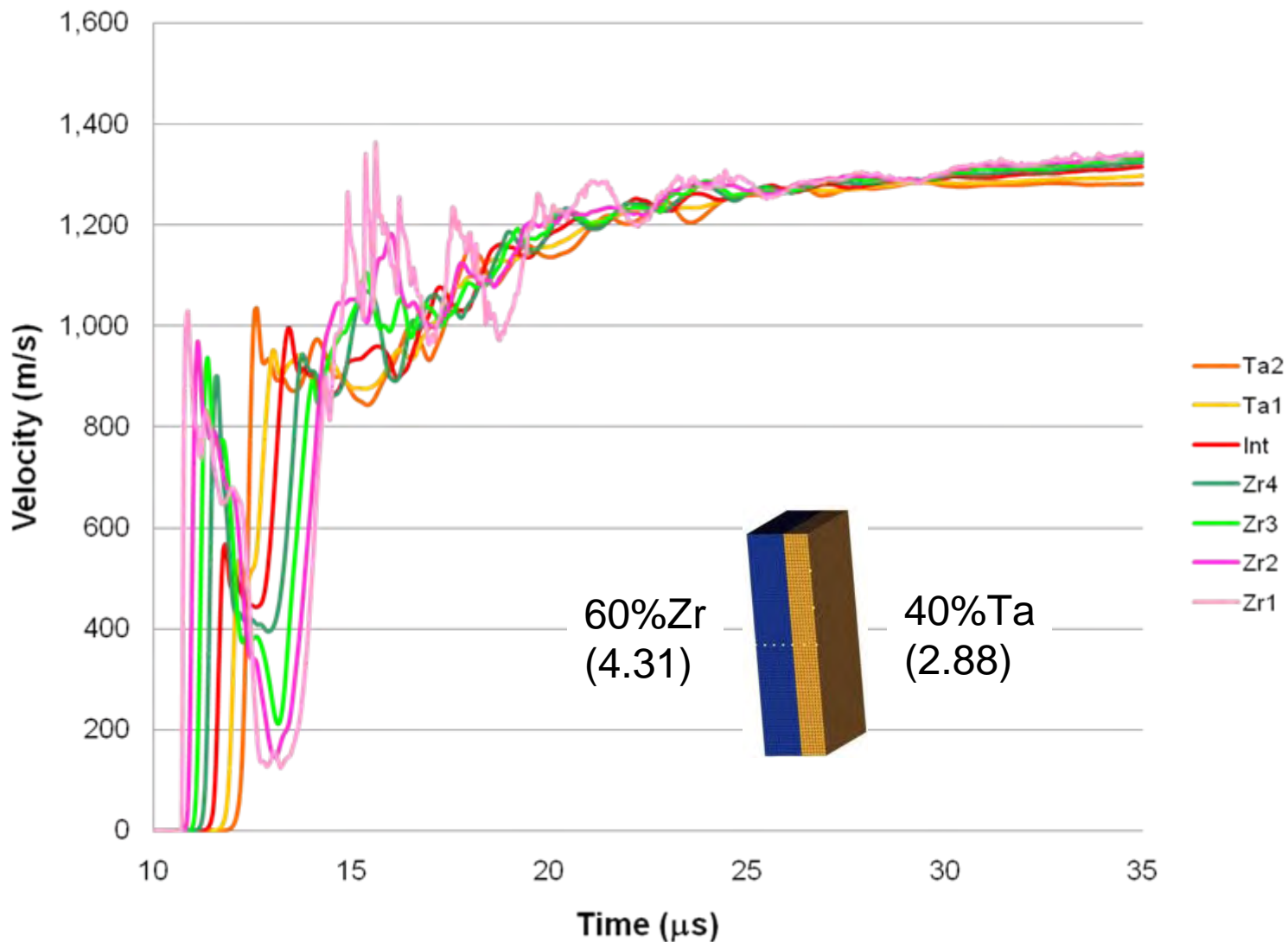


Through Thickness Pressure (Configuration 3)



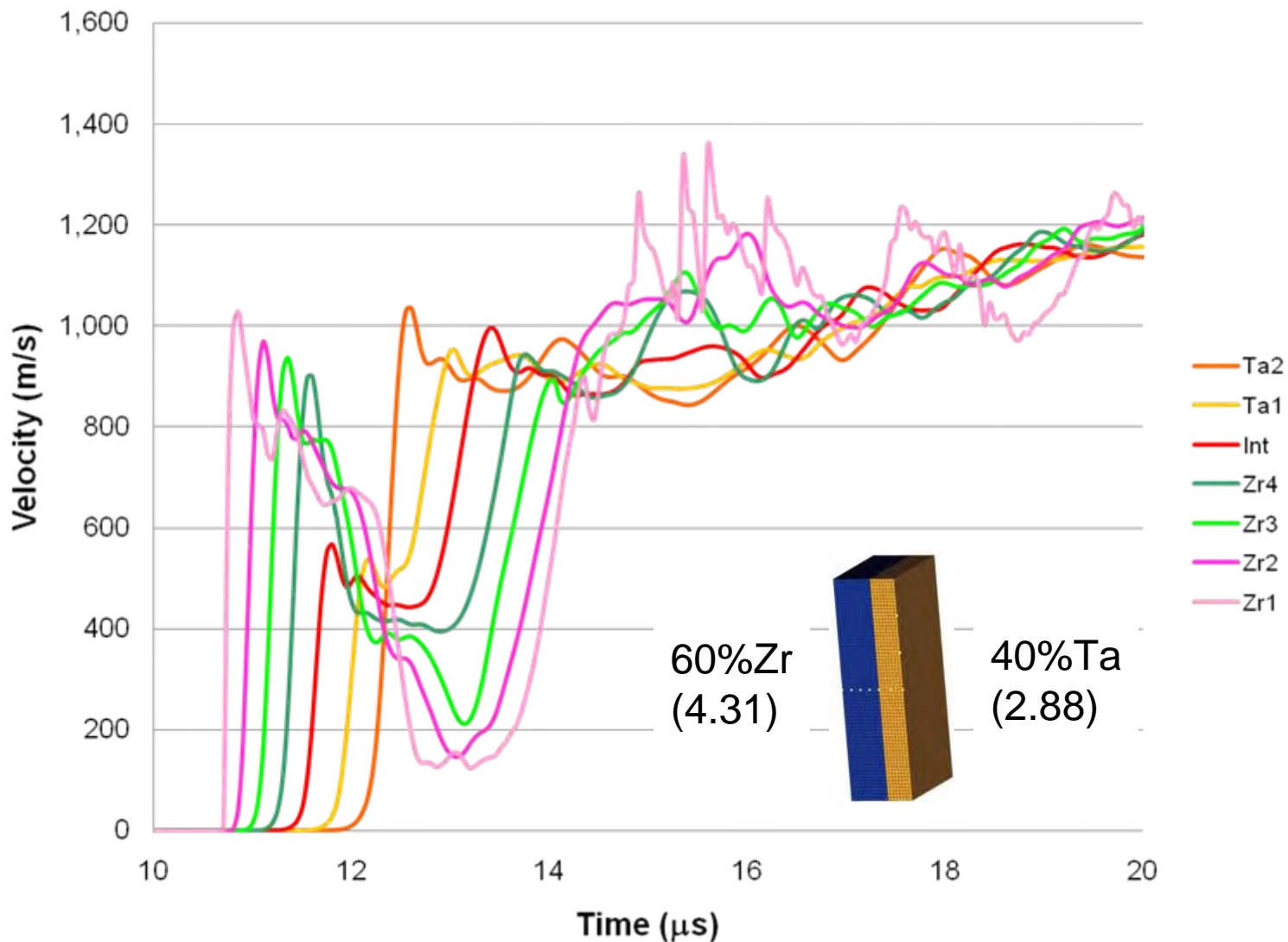


Through Thickness Velocity (Configuration 3)



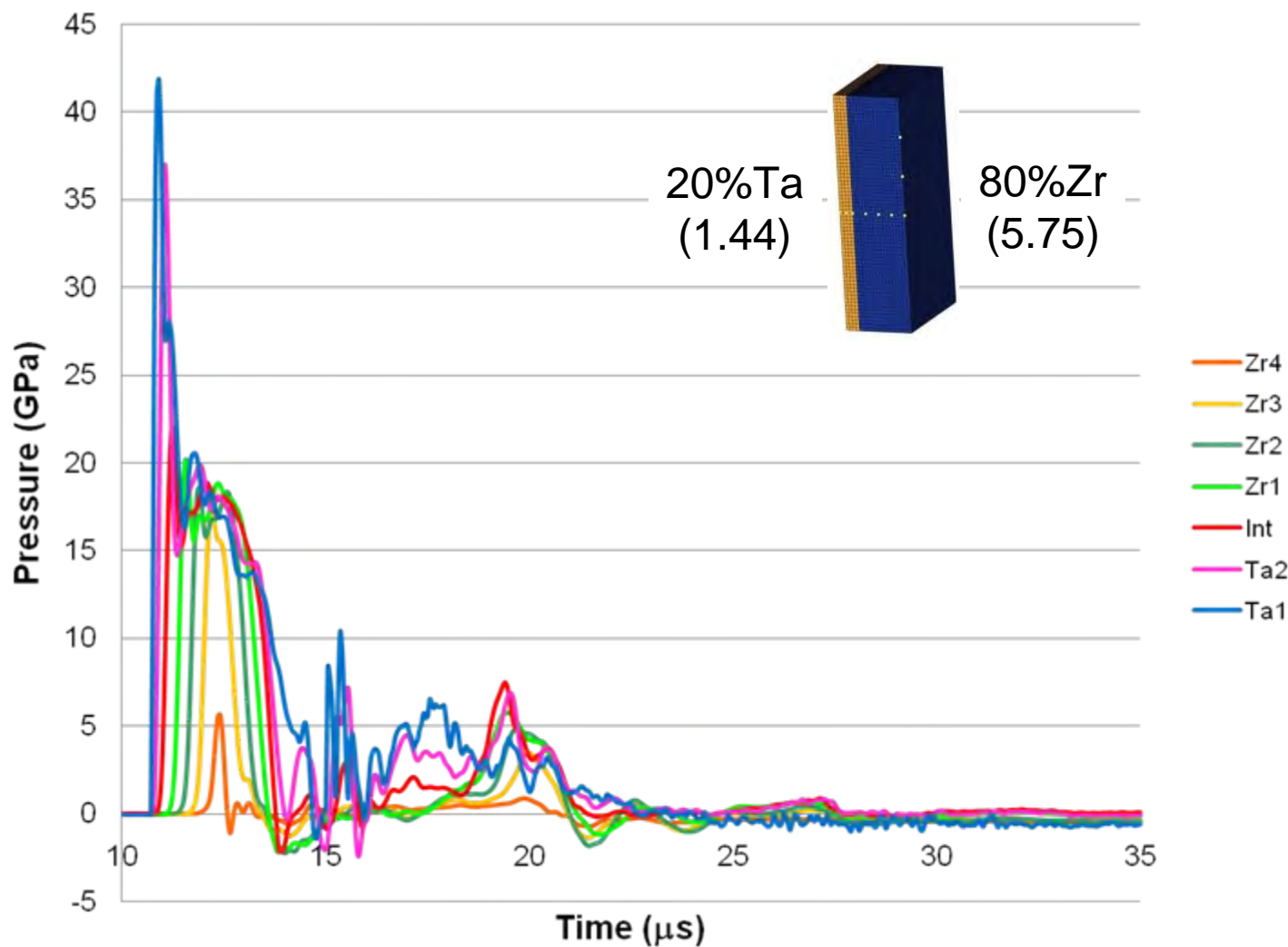


Through Thickness Velocity (Configuration 3)



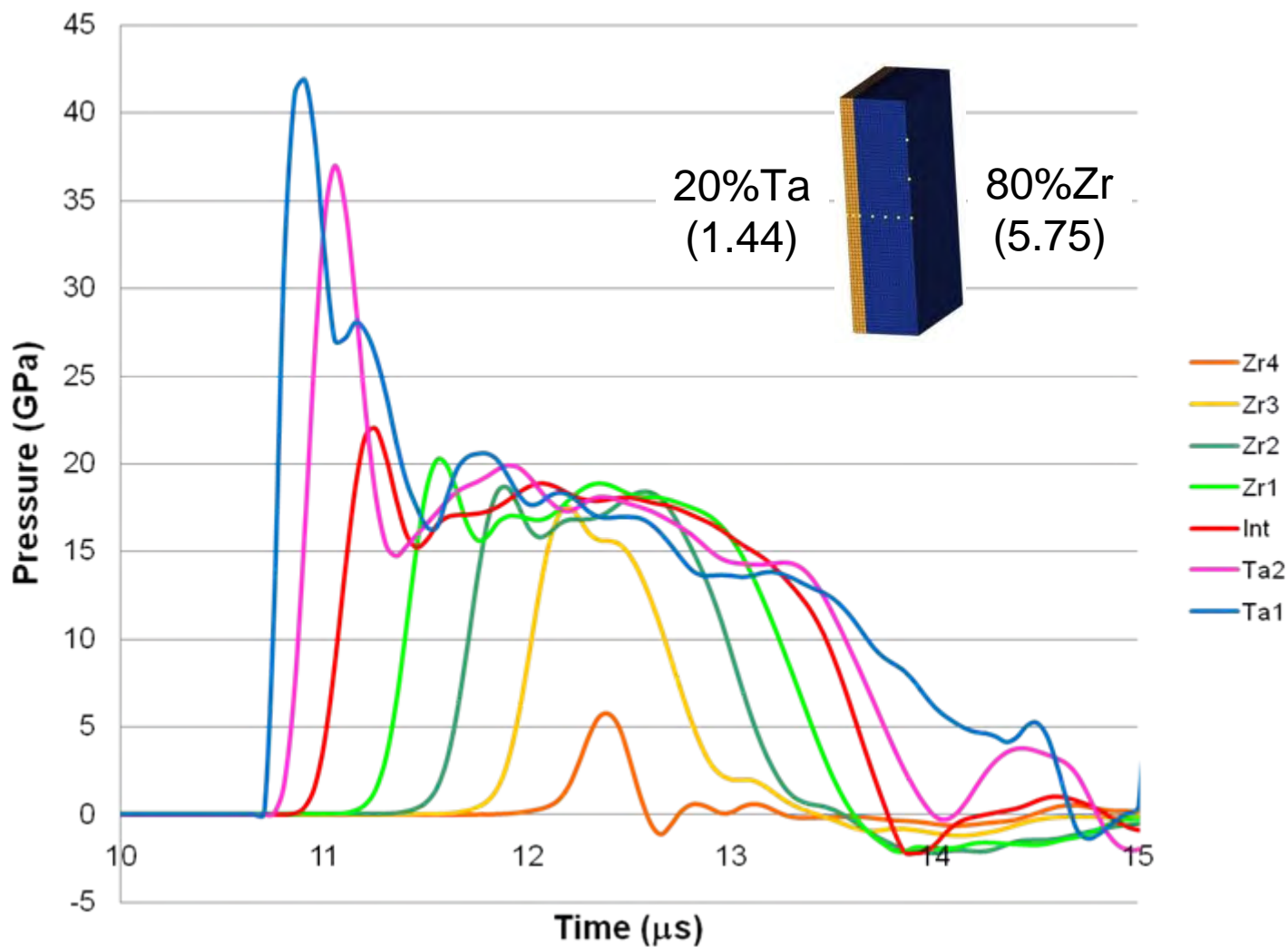


Through Thickness Pressure (Configuration 8)



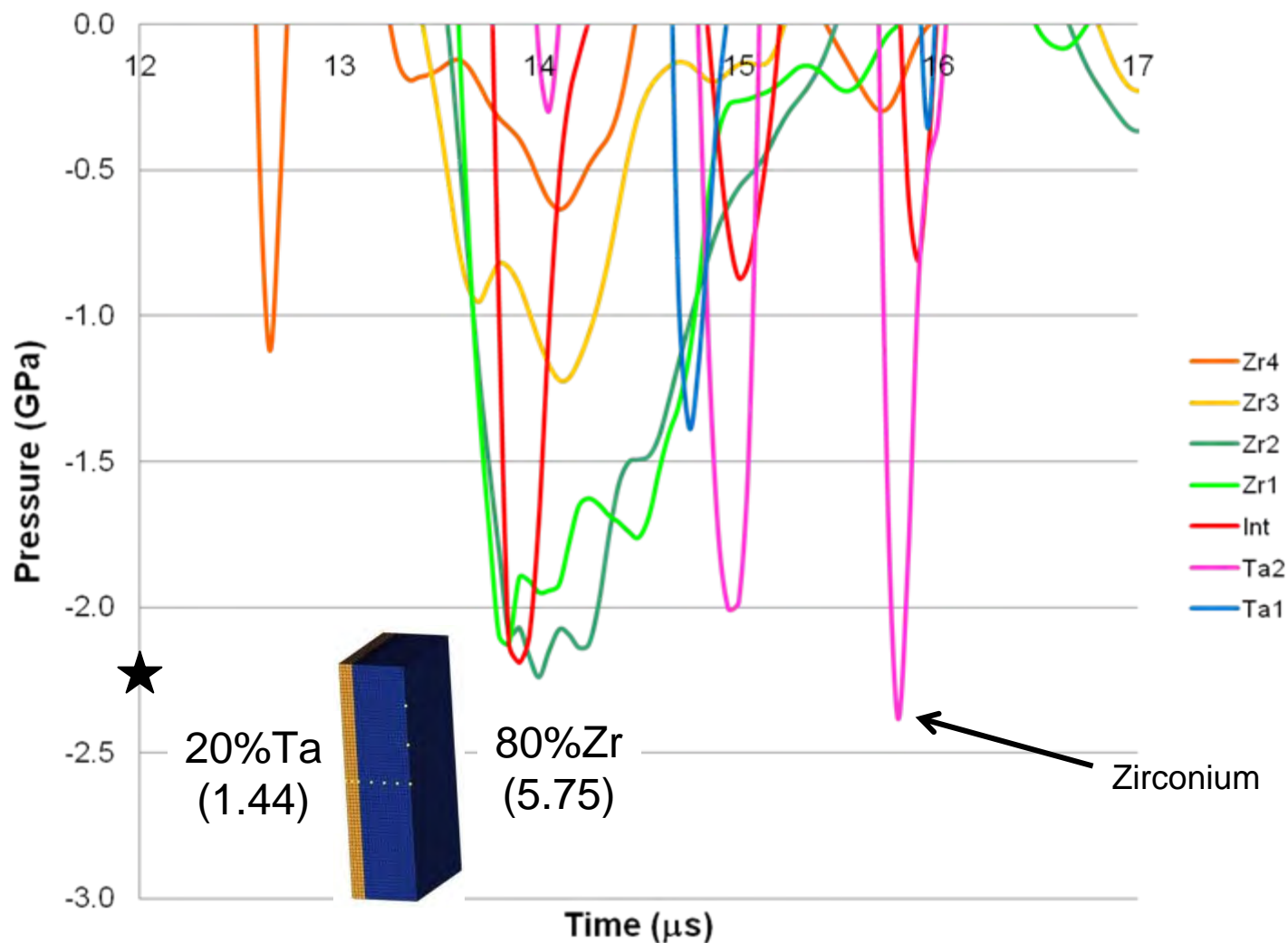


Through Thickness Pressure (Configuration 8)





Through Thickness Pressure (Configuration 8)



~Spall Strength
of Zirconium

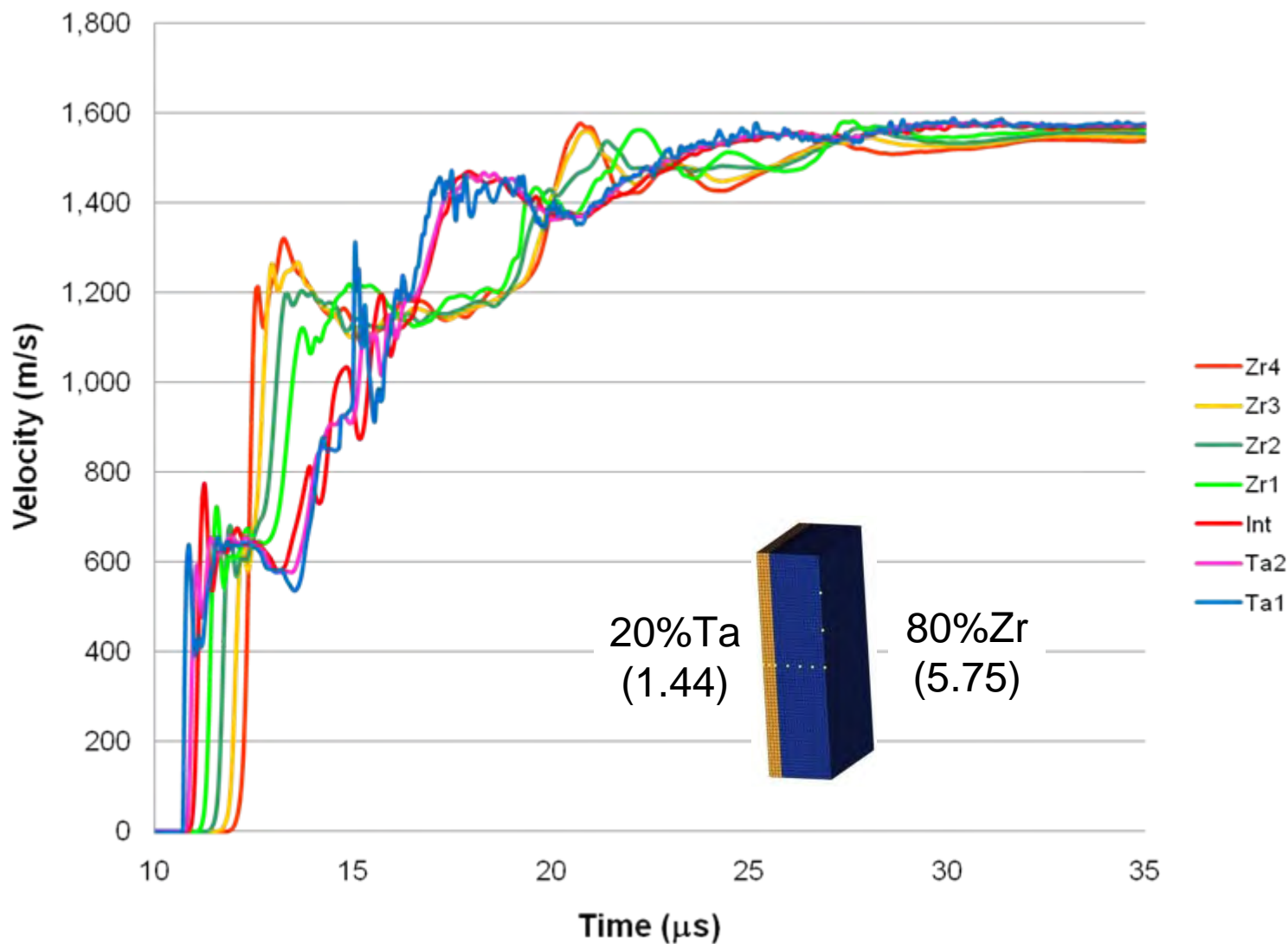
20%Ta
(1.44)

80%Zr
(5.75)

Zirconium

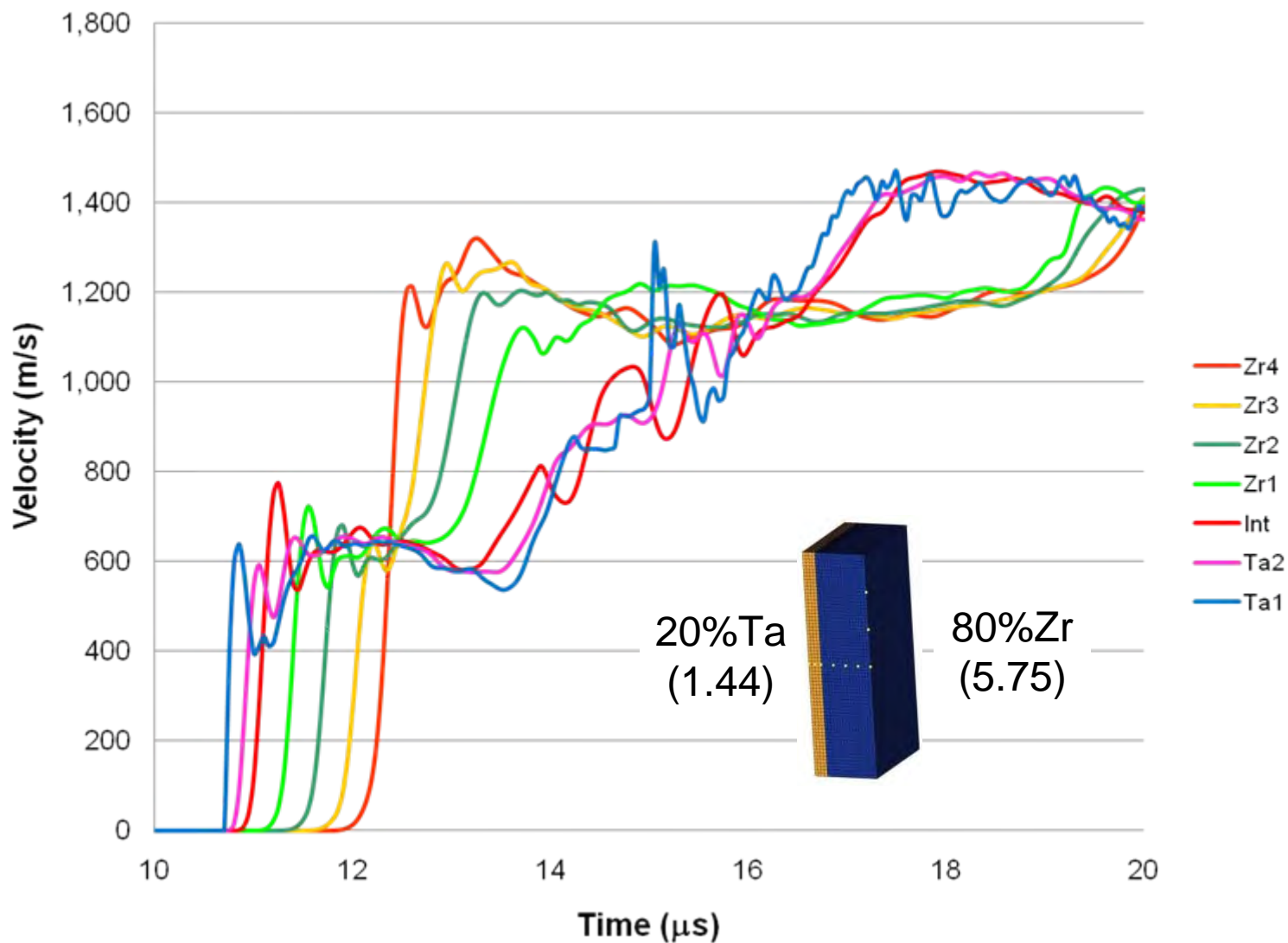


Through Thickness Velocity (Configuration 8)





Through Thickness Velocity (Configuration 8)





Summary

Configuration	1	2	3	4	5	6	7	8
Driver Plate Material (Explosive Surface)	Al	Al	Zr	Zr	Ta	Ta	Ta	Ta
Max Compression (GPa)	32.5	35.5	32.2	34.1	41.9	41.9	41.9	41.9
Max Tension (GPa)	1.88	0.76	1.93	0.83	5.90	4.56	4.26	2.38
Impactor Surface Material	Ta	Ta	Ta	Ta	Al	Al	Zr	Zr
Max Compression (GPa)	35.7	38.8	34.7	37.9	13.3	14.8	18.5	20.2
Max Tension (GPa)	5.7	7.15	3.82	6.86	3.74	4.22	1.51	2.23
Interface								
Max Compression (GPa)	38.9	41.2	36.4	39.8	14.5	15.7	20.4	22.0
Max Tension (GPa)	0.76	1.21	2.05	0.21	5.13	4.08	2.19	2.19
Velocity								
Terminal Velocity (m/s)	1500	1150	1300	1050	1575	2150	1300	1575

■ Anticipated Spall



Conclusions

- Good potential for explosively launched bimetallic plates regarding shock loading experiments
- As expected, material choice and dimensions play a key role in the survivability of launching the bonded plates. Lower impedance mismatches reduce spall susceptibility but at expense of reshock
- Shock / Re-shock experiments are more susceptible to spall and thus more challenging to design
- Additional system features may be introduced such as an air gap between the explosive and driver plate which would result in a lower driving pressure and therefore reduced susceptibility to spall.
- It is encouraging that these initial studies are quite promising. Further studies should include using an optimization routine which would include controlling the dimensions of the air gap, and the relative thicknesses of the driver plate and impactor plate.



U.S. Army Tactical Wheeled Vehicle Vulnerability Test and Evaluation Methodology

Presented at the 24th NDIA
International Symposium on
Ballistics

Presented by Stephanie K. Koch
U.S. Army Evaluation Center

Approved for public release;
distribution is unlimited.

Any TWV T&E Methodology

Introduction

Traditional Ballistic Vulnerability Candidates



Heavily Armored Combat Vehicles

OEF/OIF Ballistic Vulnerability Candidates



Unarmored TWV\$

ny TWV T&E Methodology

Agenda

- Phase 1: Coupon Testing
- Phase 2: Component/Subsystem Testing
- Phase 3: Exploitation Testing
- Phase 4: System Level Testing



Army TWV T&E Methodology

Phase 1: Coupon Testing

Coupon testing provides a quick and cost effective means to determine the capabilities of an armor solution.

- A coupon is a 2 x 2 foot piece of the complete armor recipe.
- A coupon test involves testing against various ballistic threats.
- Three phases of coupon testing.
 - V_{50}
 - Requirement
 - Armor Characterization





ny TWV T&E Methodology

Phase 1: Coupon Testing

V_{50} coupon testing determines whether or not an armor recipe is worthy of further investigation.

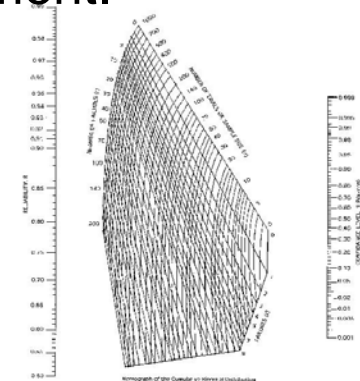
- A V_{50} is the velocity where a complete penetration and partial penetration are equally likely for the threat under consideration.
- The V_{50} is calculated by taking the mean of an equal number of highest partial and lowest complete penetrations.
- The V_{50} for a certain armor recipe is compared to other recipes to determine the performance capabilities.

Army TWV T&E Methodology

Phase 1: Coupon Testing

Requirements coupon testing determines whether or not an armor recipe meets specific requirements.

- Example requirement: The armor must provide an X% probability of protection against a threat fired at a velocity with a Y% confidence level.
- The cumulative binomial distribution is used to determine the number of partial impacts required to meet the requirement.
- Coupon testing is then conducted.





ny TWV T&E Methodology

Phase 1: Coupon Testing

Armor characterization coupon testing primarily supports modeling and simulation efforts.

- Penetration Algorithm Development
- Behind Armor Debris (BAD) Characterization



ny TWV T&E Methodology

Phase 2: Component/Subsystem Testing

Component/Subsystem testing determines the affect of certain system components/subsystems on the survivability of the crew.

- Typical combat vehicle evaluations focused heavily on component/subsystem testing to determine the survivability of the system as a whole.
- TWVs are only required to provide crew protection so those components/subsystem that could affect the survivability of the crew are tested.
 - Fuel Cells
 - Automatic Fire Extinguishing Systems (AFES)



ny TWV T&E Methodology

Phase 3: Exploitation Testing

Exploitation testing determines the ballistic vulnerabilities of the integrated armor.

- Exploitation testing addresses the ability of certain projectiles to penetrate vulnerable areas of the armor package as installed on the cab.



Any TWV T&E Methodology

Phase 4: System Level Testing

System level testing determines the overall protection provided to the crew of the vehicle under consideration.

- System level testing focuses on addressing crew vulnerabilities against threats that can not be addressed in the other three phases.
 - Typically focuses on blast-type threats.
- System level testing also provides insight into battle damage and repair capabilities.

Event	Location	Test Condition
1. Mine	Under Wheel	Running vehicle, Stowage, <u>Heated Fuel</u>
2. Mine	Underbody	Running vehicle, Stowage, <u>Heated Fuel</u>
3. Fragmenting Round	Side of Vehicle	Not Running, Stowage, <u>Simulated Fuel Tank Weight</u>



ny TWV T&E Methodology

Conclusion

The TWV ballistic vulnerability methodology is a detailed, flexible, and judicious building block approach to test and evaluation.

- Phase 1: Coupon Testing
- Phase 2: Component/Subsystem Testing
- Phase 3: Exploitation Testing
- Phase 4: System Level Testing

any TWV T&E Methodology



Questions



Warhead Filling and Casing Interactions affect the Blast Field performance

**Authors: Paul Locking – BAE Systems (Land)
Dennis Flynn – BAE Systems (Land)
Jim Dunnett – Fluid Gravity Engineering**

g effects on Blast

ACKNOWLEDGEMENTS

This work was funded by the Weapon & Platform Effectors (WPE) Domain of the UK MoD Research Acquisition Office (RAO) and contracted through QinetiQ, the Prime Contractor.

The authors are grateful for their kind permission to publish this work. RAO has since become the Defence Technology Innovation Centre (DTIC).

resentation Outline

- “ Objectives
- “ Historical Background
- “ Recent Trials
- “ Analysis
- “ Conclusions

g effects on Blast

Errata

I would like to apologise for one typographical error that got through the proof reading:

~~Al~~uminium Alloy 6086T6q

should read

~~Al~~uminium Alloy 6082 to Condition T6q

Objectives

- “ Currently Engineering models predict Blast output from cased warheads use experimentally derived algorithms, e.g. Fano and Fisher curves
- “ Such curves are typically based upon TNT explosive with the cast iron or steel cases
- “ Review Historical Data
- “ Investigate
 - . Ideal and Non-Ideal explosives
 - . Brittle and Ductile case materials
- “ Integrated Trials and EDEN hydrocode Modelling to assess these Engineering models
- “ Establish a preferred model and its fit parameters with applicability for each case

Engineering Models

Fisher	$EBC = C \times [0.2 + 0.8/(1 + M/C)]$
Modified Fisher	$EBC = \{C + C \times [0.2 + 0.8/(1 + M/C)]\}/2$
Fano	$EBC = C \times [0.2 + 0.8/(1 + 2 \times M/C)]$
Modified Fano	$EBC = C \times [0.6 + 0.4/(1 + 2 \times M/C)]$
Warren	$EBC = C \times [0.4 + 0.6/(1 + 2 \times M/C)]$
US for Pressure	$EBC = 1.19 \times C \times [1 + M/C \times (1 - M_c)/(1 + M/C)]$
US for Impulse	$EBC = C \times [1 + M/C \times (1 - M_c)/(1 + M/C)]$

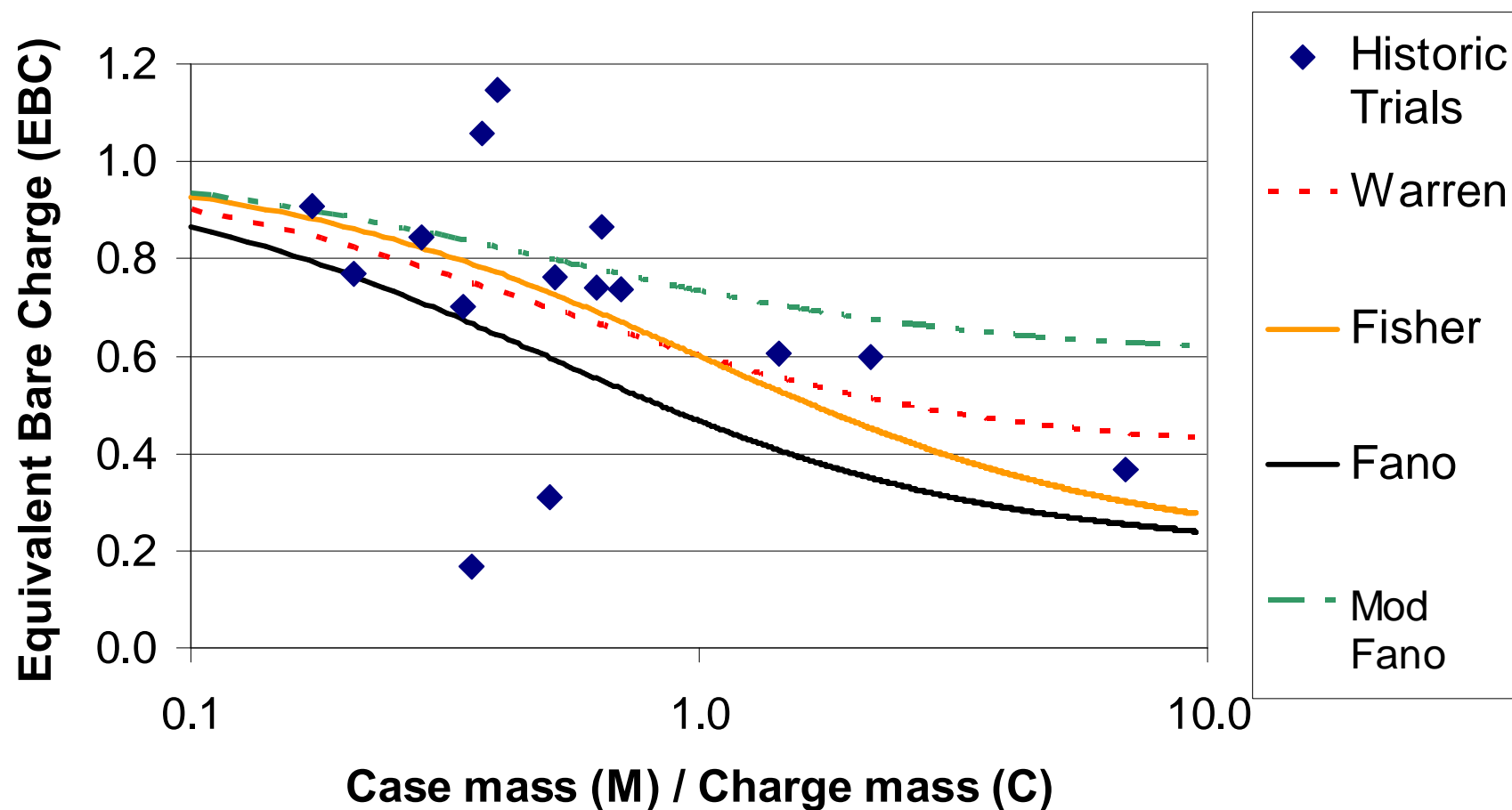
EBC = Equivalent Bare Charge

C = Charge mass

M = Mass of metal (in parallel section)

$M_c = M/C$ if $M/C \leq 1.0$ or 1.0 otherwise

for Steel Casings



ing Case Effects on Blast

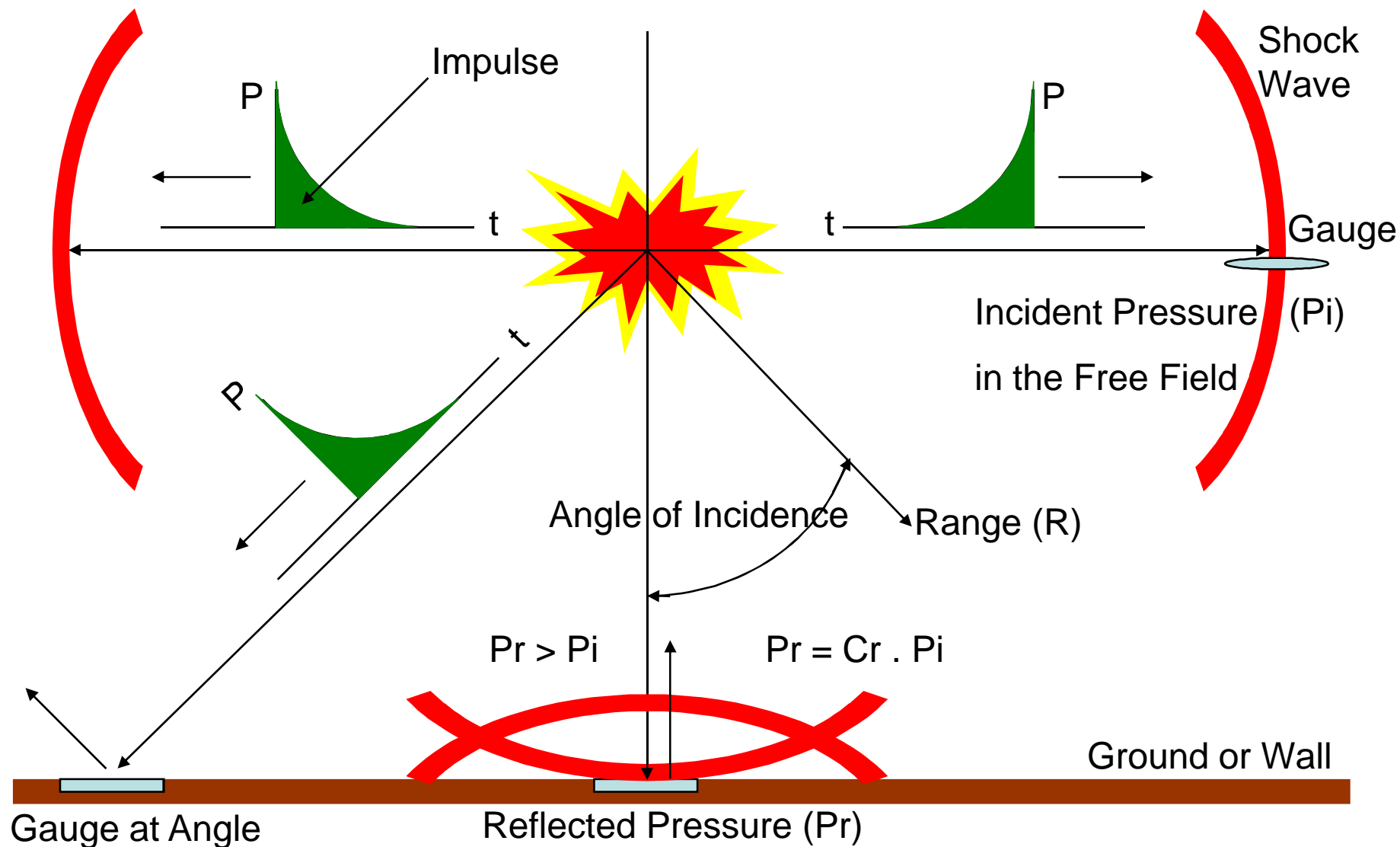
- Limited understanding of case effects
- Large scatter of trials data
- Wide choice of 'Engineering Models'
- Limited data
- Need for updated trials with purpose made hardware and extensive instrumentation
- With experimental controls
- Integrated EDEN hydrocode modelling
- Trials designed specifically for the hydrocode modelling

Limitations / Unknowns

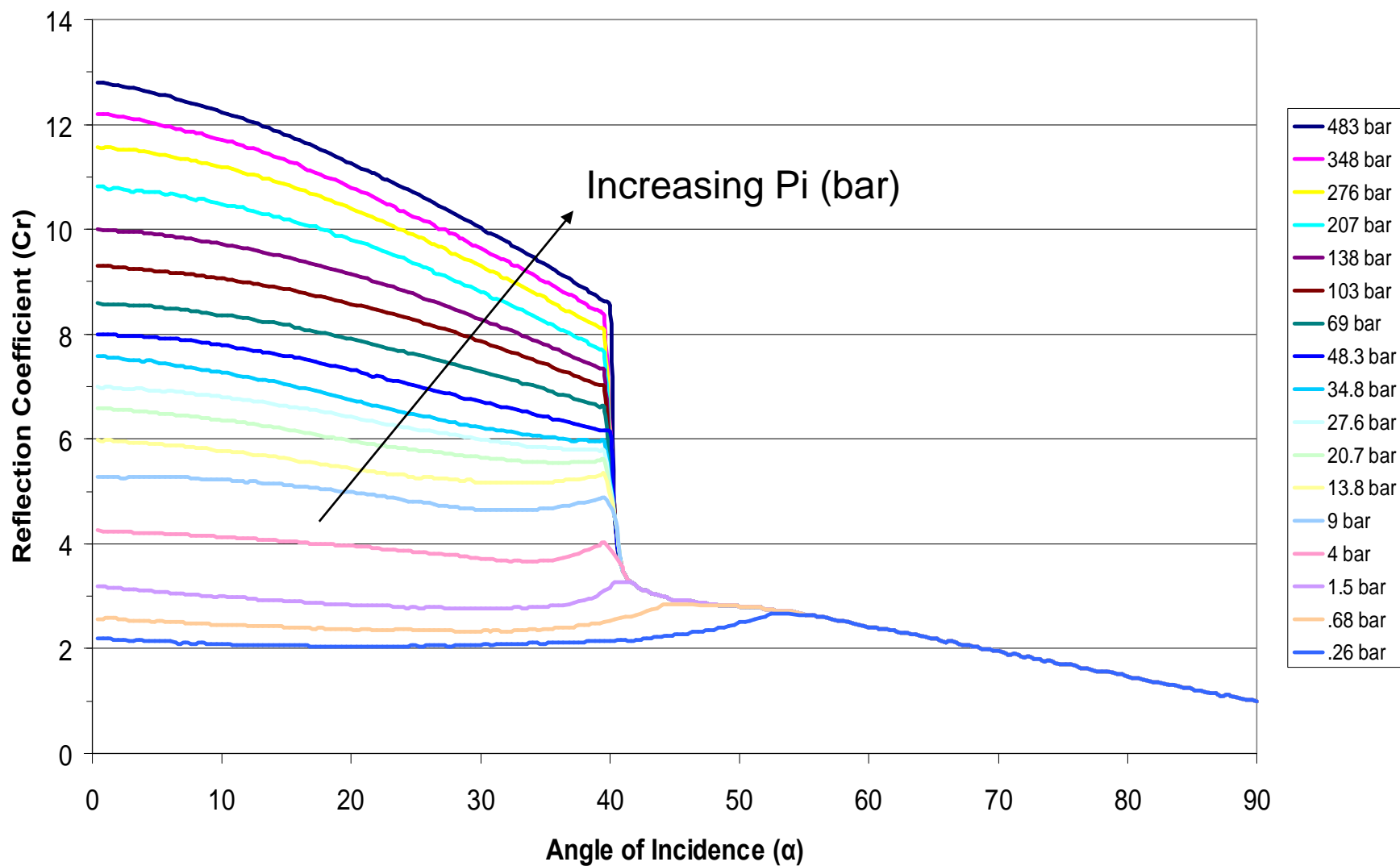
- ” Explosive Type
- ” Casing Material
- ” Fragmentation Mechanism (Natural / Pre-fragmented)
- ” Pressure or Impulse
- ” Pressure Considered (Incident / Reflected)
- ” Ground / Air
- ” Shape (Spherical / Cylindrical)
- ” Scaling
- ” Confinement (Uniformly / Heavy Nose)
- ” Initiation (Central / End)
- ” Position / Aspect - **Best historic trials gauge positions undefined**

Typical Issues that Arise

Record Reflected (P_r) pressure, but need to correct to get Incident (P_i) pressure, but it's both Angle () and Pressure dependent



Reflection Coefficient vs Angle of Incidence with Pressure



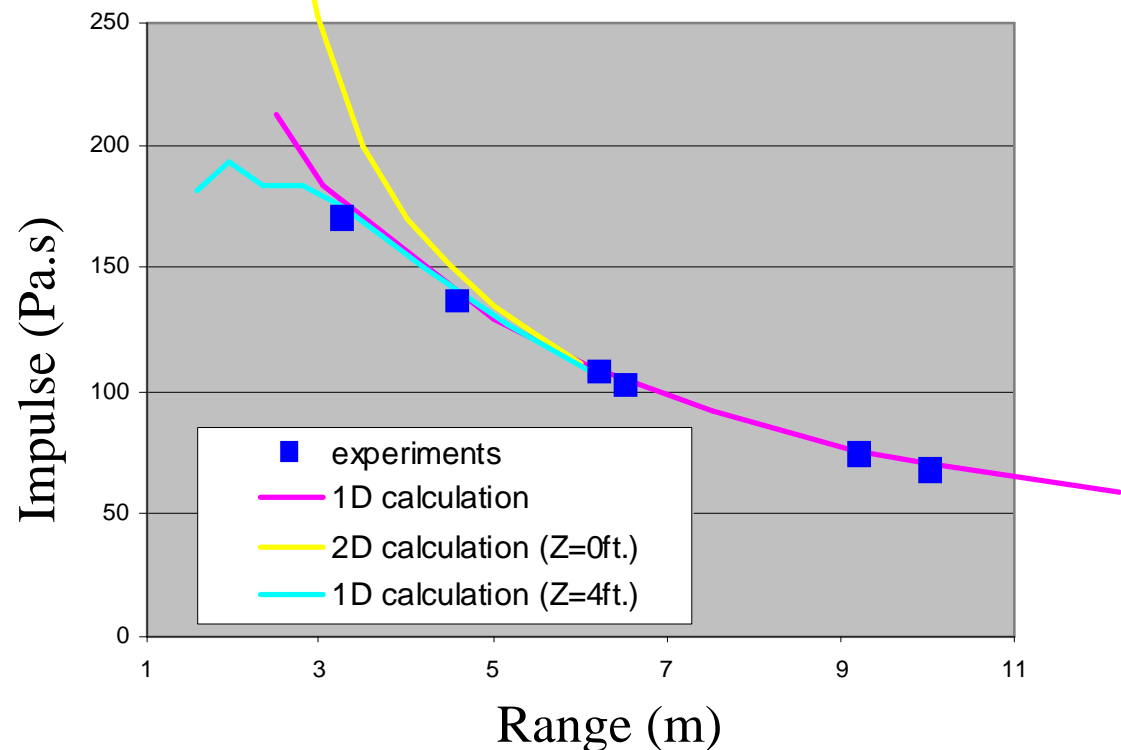
Sheard Analysis

(Royal Society, V187, 1944)

BAE SYSTEMS

Grime and Sheard experiments were found to provide sufficient data about the trial arrangement to attempt to reproduce using the FGE - EDEN hydrocode

- " Explosive = Comp-B
- " $L / D = 2 / 1$
- " Material = Brass or Steel
- " Charge / Weight =
 - 84.4%
 - 62%
 - 25%
 - 5.4%
- " End initiated
- " End plates similar
thickness to case



" Gauge positions are not clearly defined. The assumed positions match the reported data.

ow Trials

43 Experimental Firings over 3 years

“ Three explosive types:

- . Rx1100 (Ideal) (RDX/Binder 88/12)
- . Rx1400 (Non-Ideal) (RDX/Al/Binder 66/22/12)
- . PBX N109 (RDX/Al/Binder 64/20/16)

“ Two case materials:

- . Steel EN24
- . Aluminium 6082T6

“ Varying Case mass / Charge mass Ratios (0, 0.5, 2, 5, 10)

for All Series 1, 2 & 3

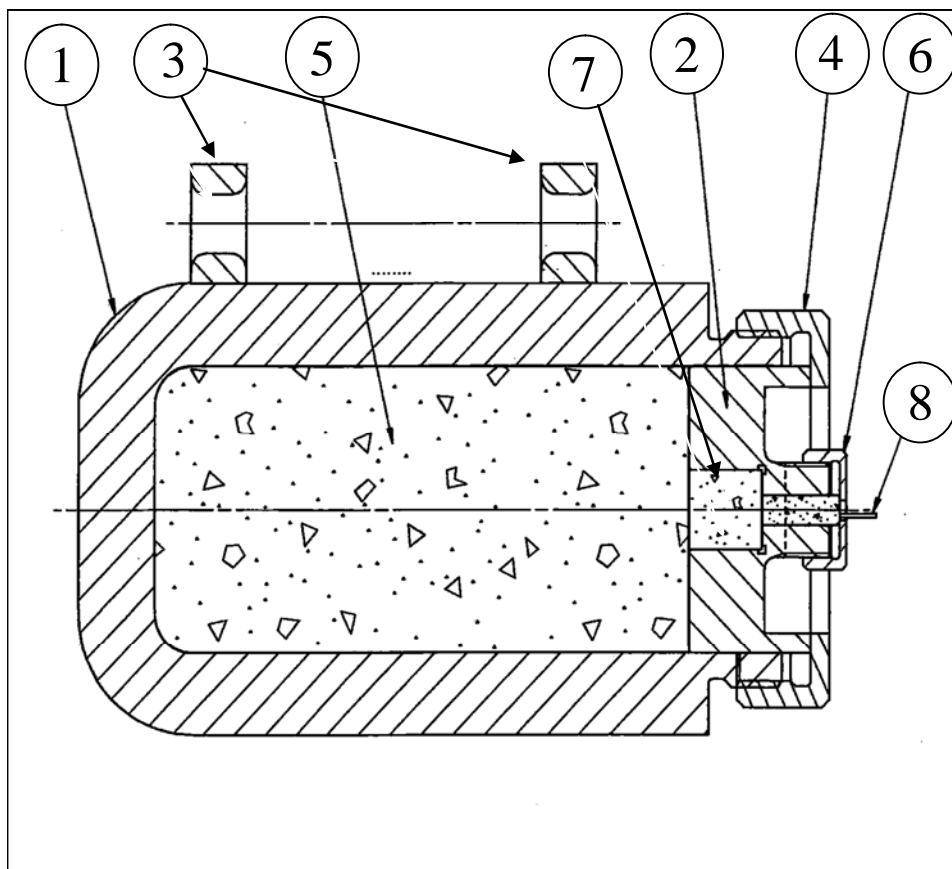
Matrix of Trials – All Series 1, 2 & 3									
Configuration		Case mass (M) to charge mass (C) ratio						Total	
Explosive	Case	0	0.5	2	5	8.46	10		
Rx1100	Bare	3						3	17
	Steel		2	2	2		2	8	
	Al		2	2		2		6	
Rx1400	Bare	3						3	17
	Steel		2	2	2		2	8	
	Al		2	2		2		6	
PBX N109	Bare	3						3	9
	Steel		2		2		2	6	
Total		9	10	8	6	4	6	43	

~~I~~deal Rx1100 - RDX /Binder 88/12

~~N~~on-Ideal Rx1400 - RDX/Al/Binder 66/22/12

PBX N109 - RDX/Al/Binder 64/20/16

Charge Configuration



Key

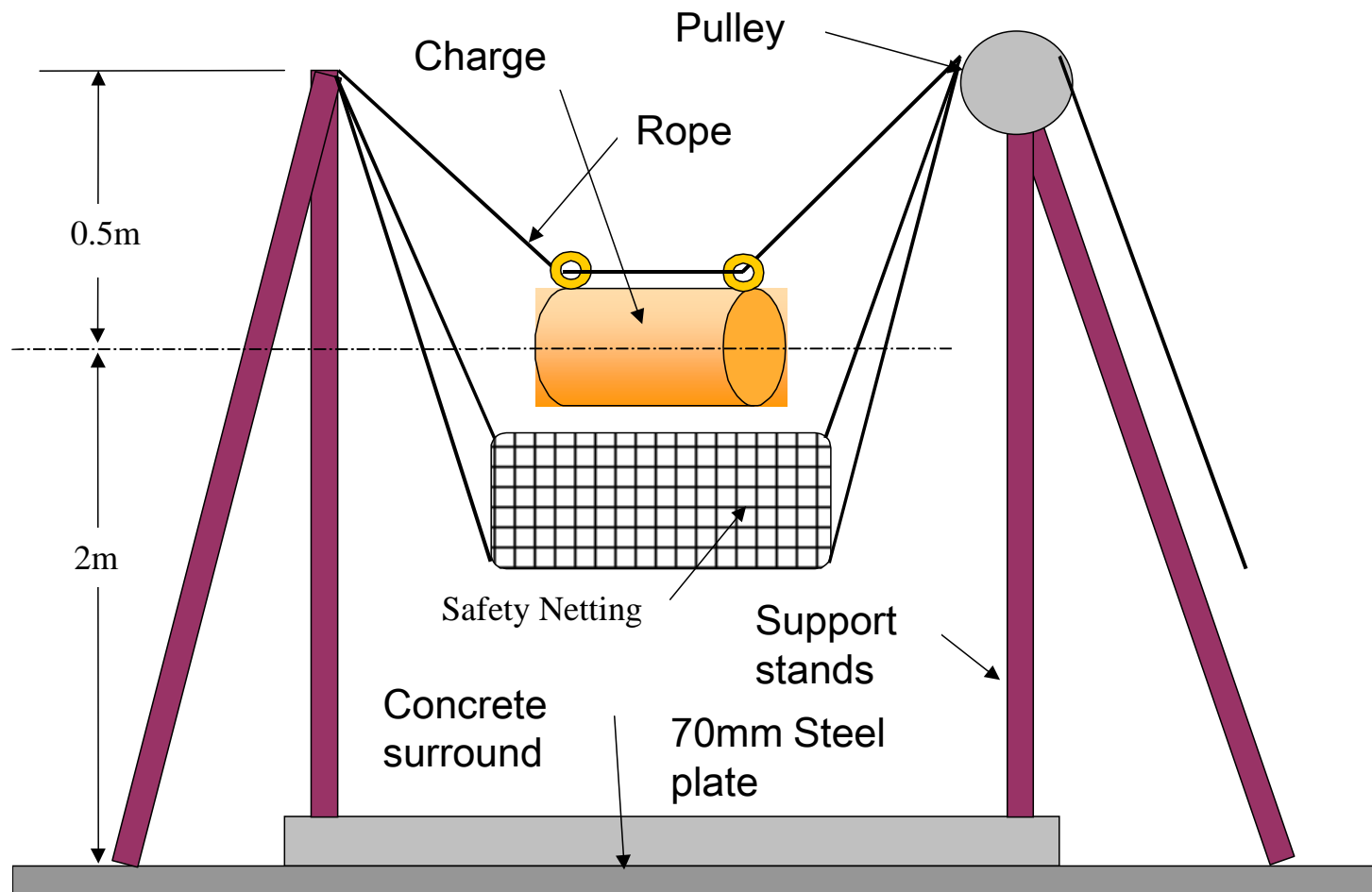
- 1 . Fragmenting case (Cylindrical)
- 2 . Charge closure
- 3 . Lifting eyelets
- 4 . Clamp ring
- 5 . Charge (1kg nominal, L/D =2)
- 6 . Detonator clamp ring
- 7 . Booster pellet (Debrix 18AS)
- 8 . Detonator (RP 80)

Note: Case thickness chosen to achieve correct case mass (M) to charge mass (C) ratio

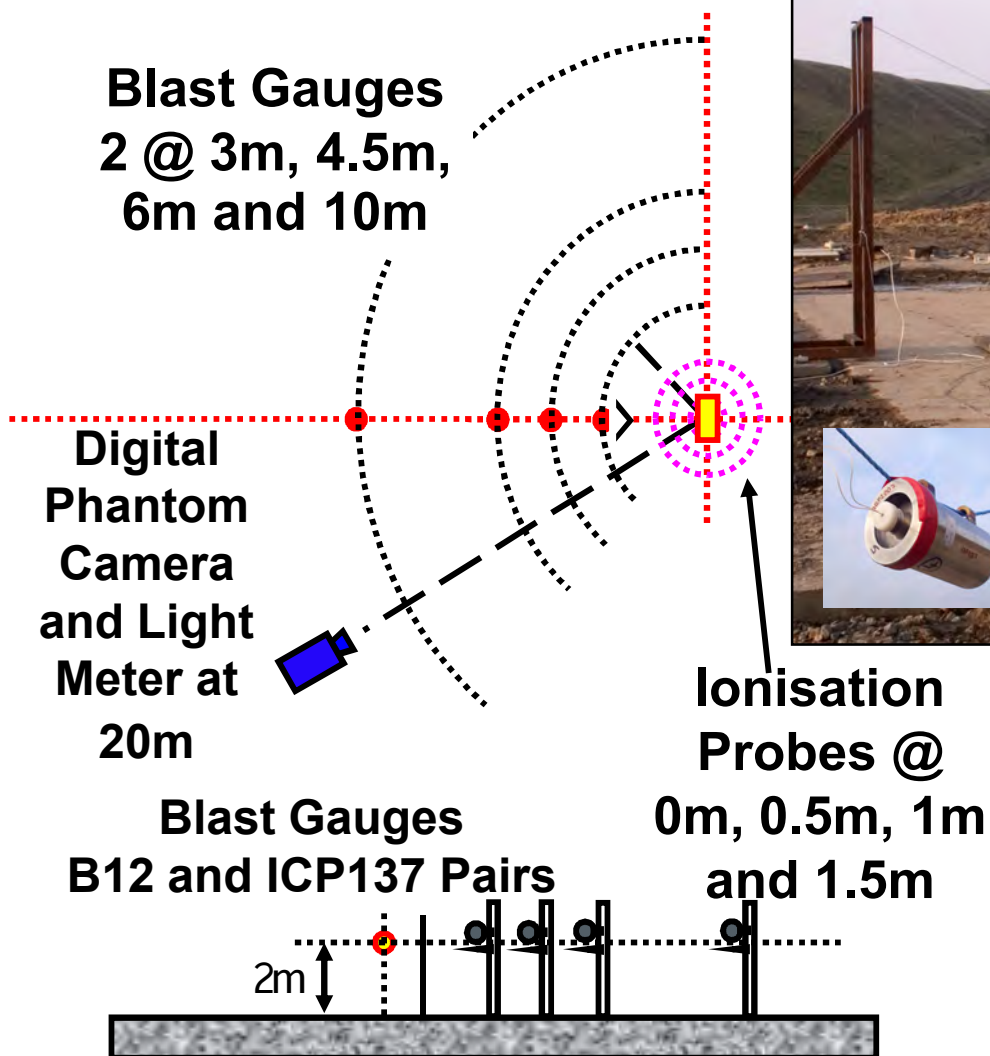
Mass - Series 1, 2 & 3

Trial Series 1, 2 & 3					
Case Thickness (mm)	Case Mass to Charge Mass Ratio				
Casing	0.5	2	5	8.458	10
AL 6082T6	4.1	13.6		41.5	
Steel EN24	1.5	5.5	12.1		20.6

Tests Schematic

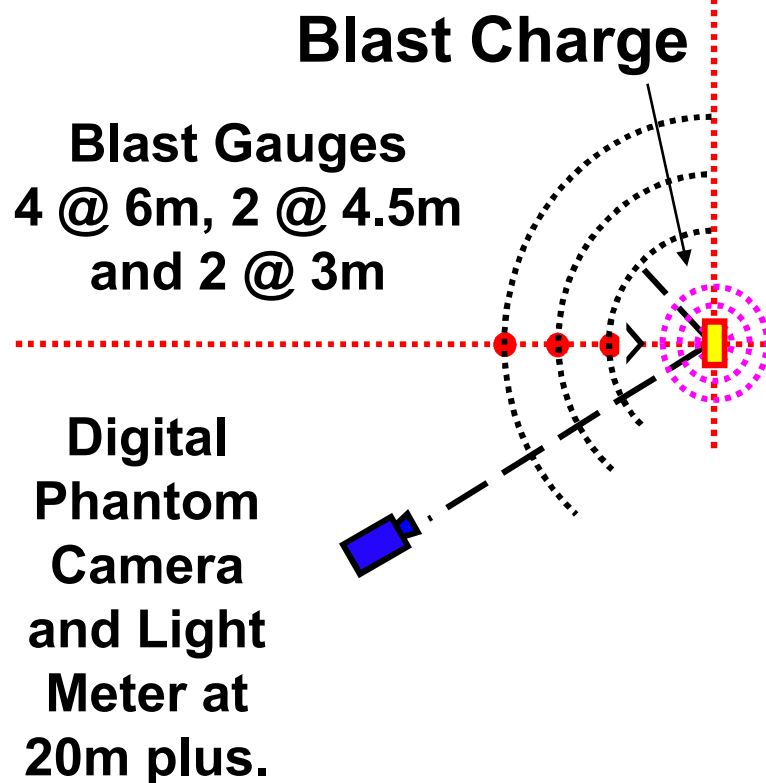


Materials Arena

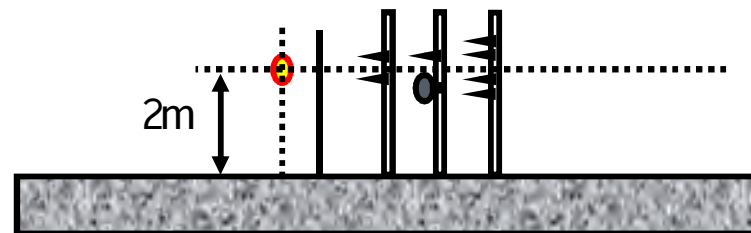


**B12 and ICP137
 @ 3m, 4.5m
 6m and 10m**

Materials Arena

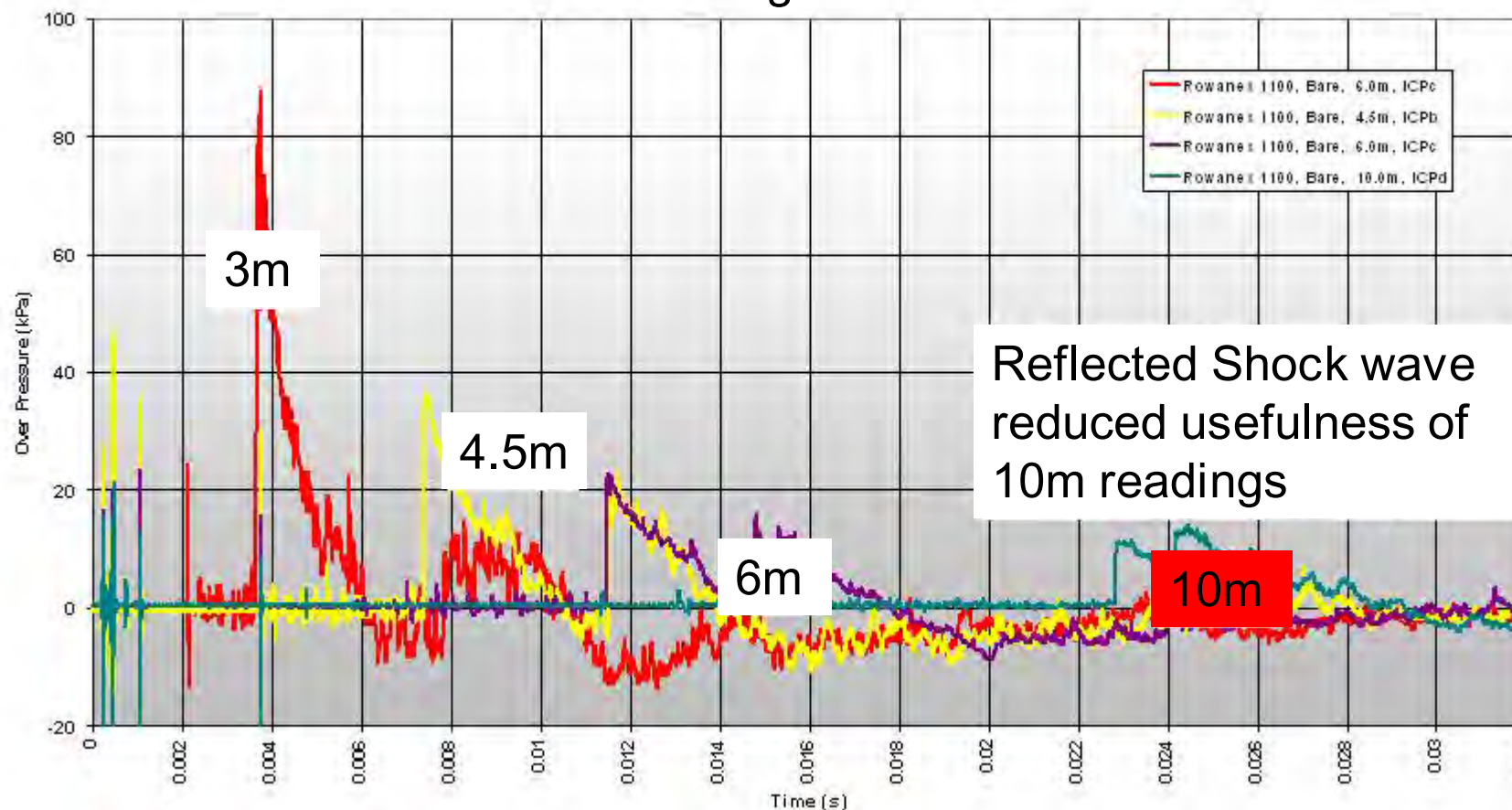


**Blast Gauges mainly ICP137 Pairs
with one B12 / ICP137 combination**



Fast Gauge Output

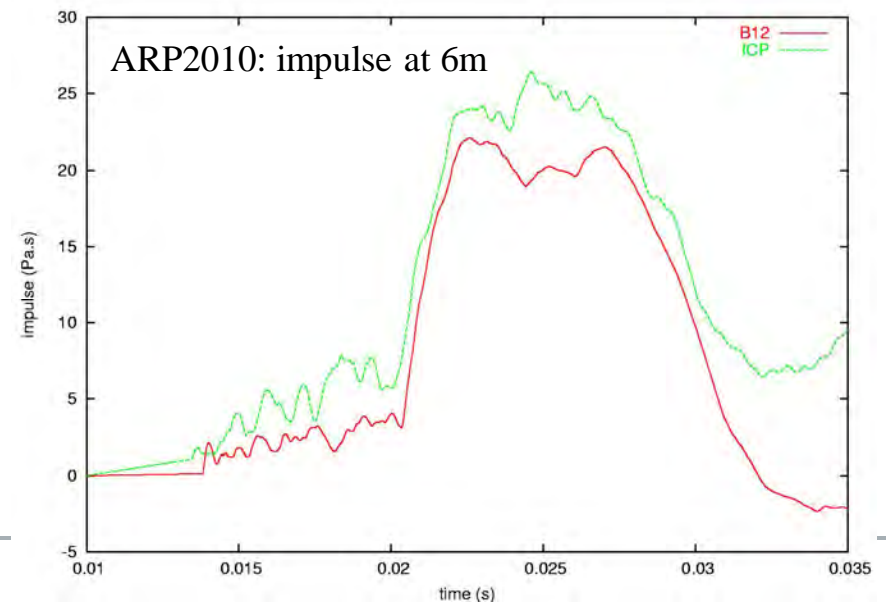
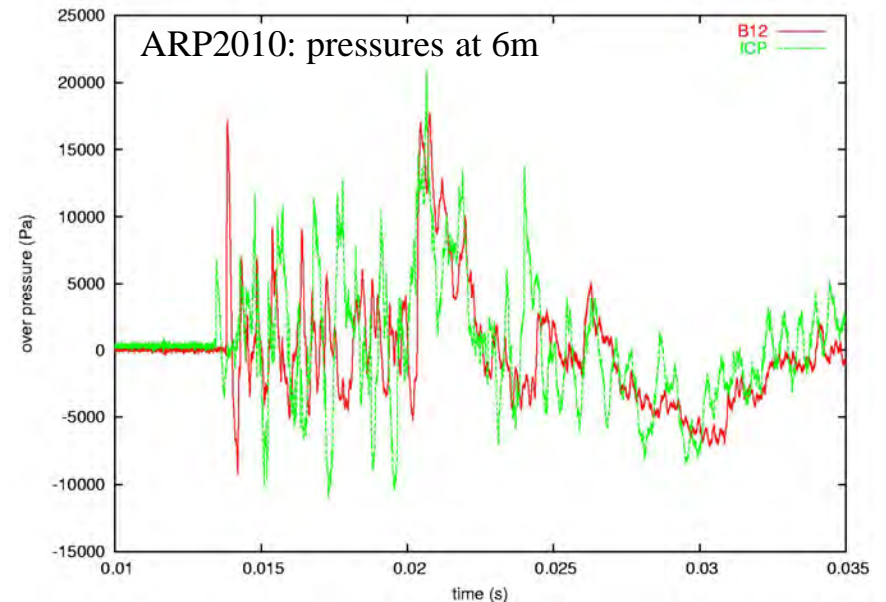
Bare charge data



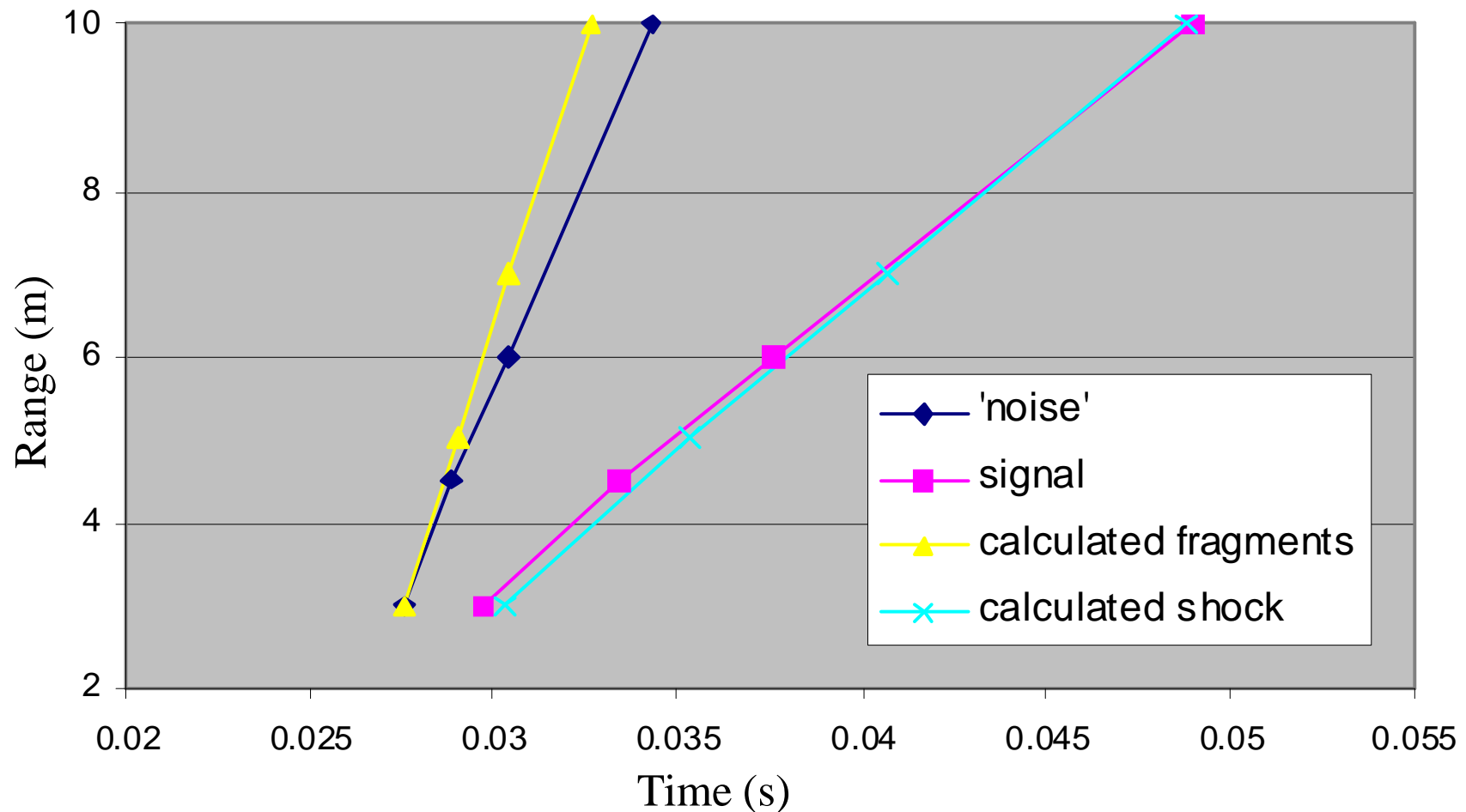
“ Impulse data is less sensitive to noise than Incident Pressure

Cased Results

- “ Very noisy
- “ Signal/noise ratio worse as:
 - . Case mass increases
 - . Increase range
- “ ICP results marginally worse than B12 gauges
- “ Little confidence in peak pressures
- “ Noise integrates to give impulse prior to arrival of signal
 - . Adjust for this in peak impulse calculation



from Cased Results



ÉNoise and Blast wave signal with predicted Shock and Fragment position

ating Case Effect

“ Use Pressure and Impulse data to compute case effects - i.e. effect case has in reducing Equivalent Bare Charge mass (EBC)

- . Convert Pressure and Impulse results to EBC masses
- . Case effect = (EBC from cased result) / (EBC for equivalent bare charge result)

“ Reference curves used to convert Impulse and Pressure results to EBC masses

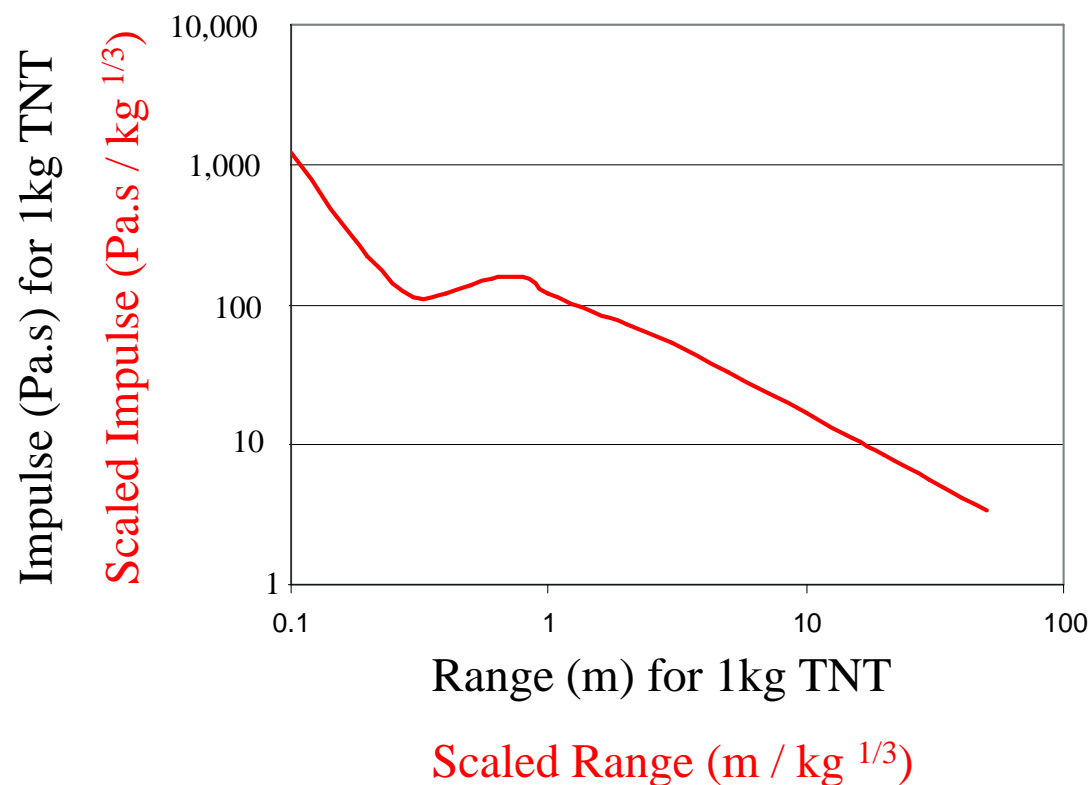
- . Use results of 1kg Spherical TNT charge calculation as reference

Impulse, for Standard 1kg Spherical TNT charge

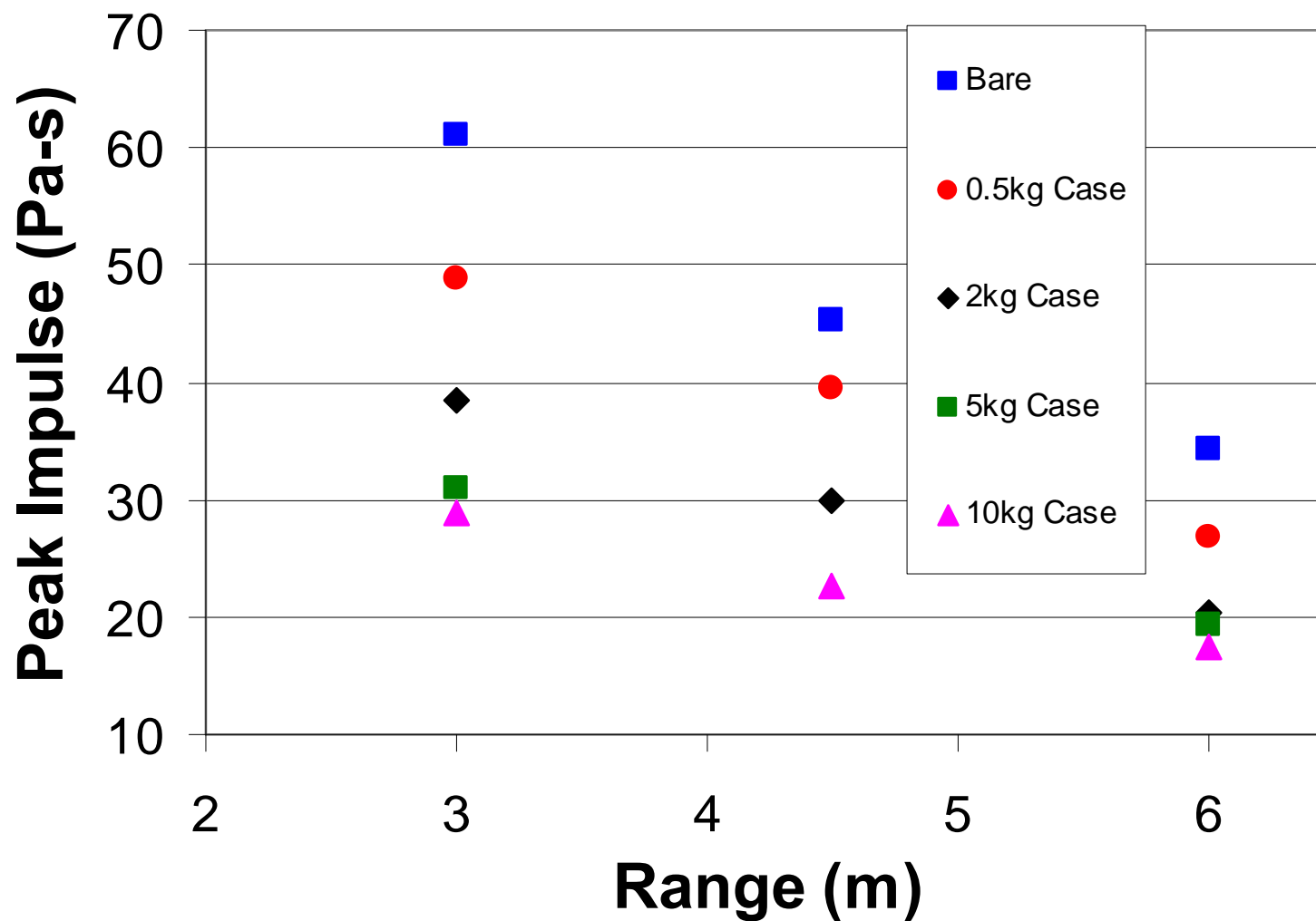
Scaled Range (R_{sc1}) and Scaled Impulse (I_{sc1}) are used to find the Equivalent bare mass of TNT:

$$R_{sc1} = R / C^{1/3}$$

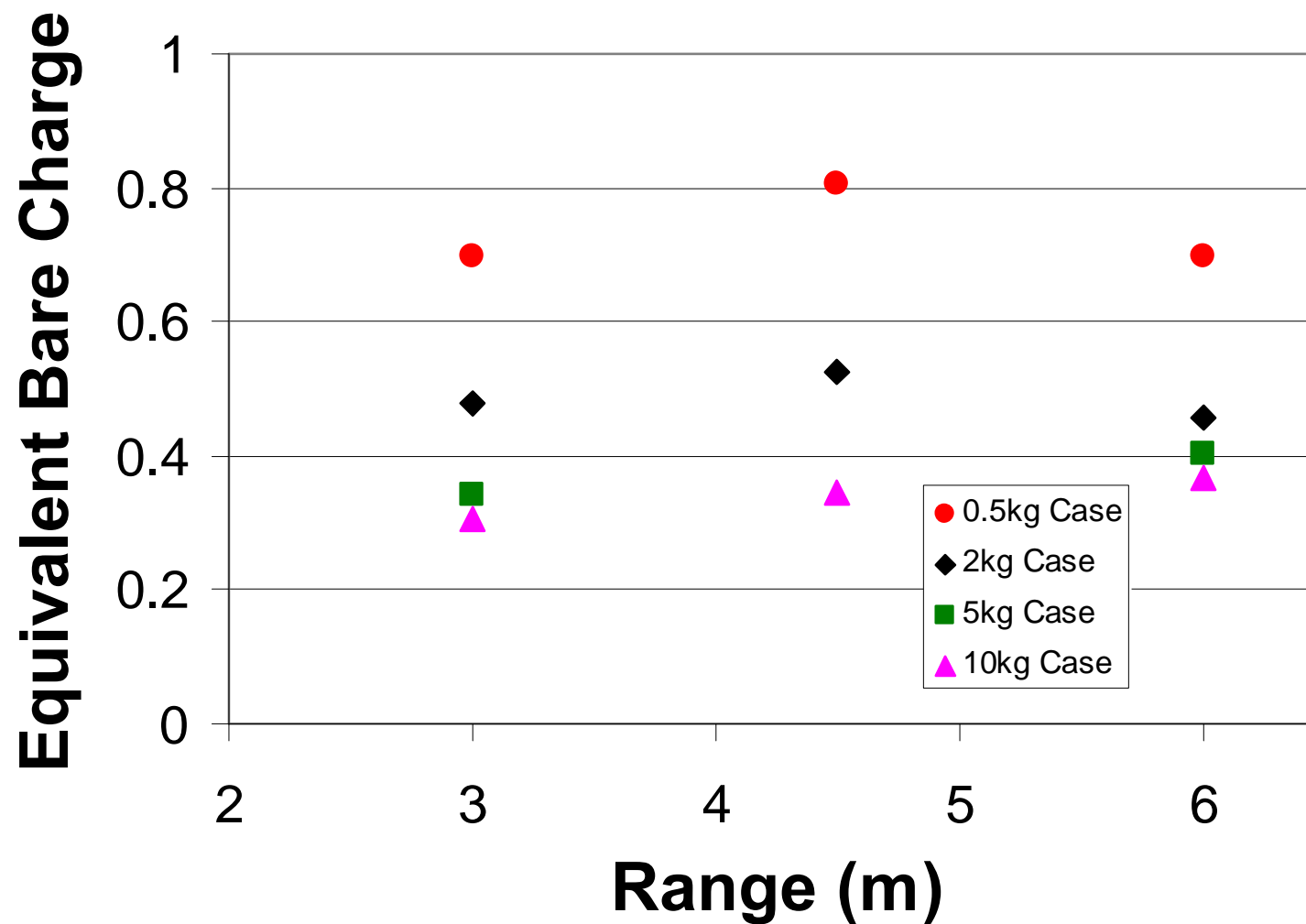
$$I_{sc1} = I / C^{1/3}$$



Range (Rx1100/Steel case)



With Range (Rx1100/Steel case)



/ Fano Equations

Historically, mainly used Fisher or Fano curves
 Fit Fisher and Fano equations to the experimental data

Fisher
 ó Fisher curve

$$\frac{EBC}{C} = 0.2 + \frac{0.8}{\left(1 + \frac{M}{C}\right)}$$

ó Modified Fisher

$$\frac{EBC}{C} = 0.6 + \frac{0.4}{\left(1 + \frac{M}{C}\right)}$$

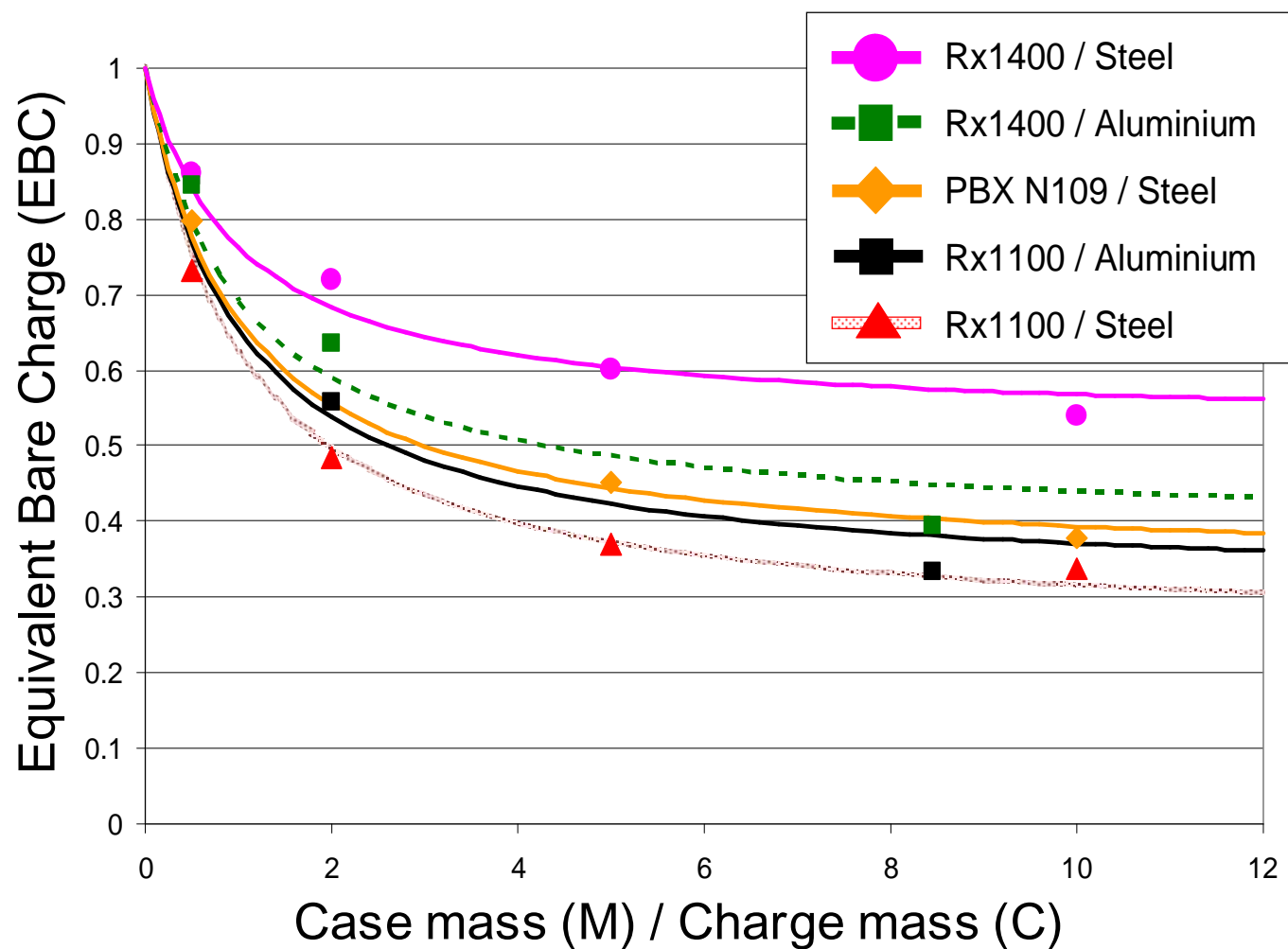
ó Generalised form

$$\frac{EBC}{C} = \alpha + \frac{1 - \alpha}{\left(1 + \frac{M}{C}\right)}$$

EBC = Equivalent Bare Charge, M = Case mass, C = Charge mass
 = Experimentally derived best fit parameter

Best fit is always the Generalised Fisher Equation rather than Fano

Equivalent Bare Charge Impulse vs. Case to Charge mass ratio



Fisher – Alpha fit for Series 1, 2 & 3

$$\frac{M_{EBC}}{C} = \alpha + \frac{(1 - \alpha)}{(1 + M / C)}$$

Trial Series 1, 2 & 3 Fitted Results		
Generalised Fisher Alpha	Casing Type	
	Steel	Aluminium
Rx 1100	0.249	0.308
Rx 1400	0.525	0.383
PBX N109	0.333	N/A

Valid for: Case Mass (M) / Charge Mass (C) up to 10:1

N.B. Historically: Standard Fisher, Alpha = 0.2

(Fisher was approximately correct for Steel cased Ideal explosives)

Results - 1

- ” Generalised Fano and Fisher models were fitted to the data. Fisher gave the best fit
 - ” Fisher used an Alpha of 0.2, whilst we predict 0.249
 - ” Consistent with his use of steel cased Ideal explosives
- ” Our results show:
 - ” a. Ideal explosive systems, Steel cases have more effect than Aluminium cases
 - ” b. Non Ideal explosive systems, Aluminium cases have the greater effect than steel cases (a great surprise)
 - ” c. Aluminium cased systems, Ideal Explosive show greater casing effects than Non Ideal explosive systems
 - ” d. Cases have a greater effect on Ideal explosive charges than on Non Ideal explosive charges
 - ” e. Case material effect is directly explosive type dependent
 - ” f. Case effects are more diverse than ever expected

Results - 2

- “ The Combined casing and explosive as a System is crucial to blast performance and which model
- “ Casings interact directly with the warhead filling during the early stages of detonation
 - “ Effects are often counter-intuitive
- “ PBX-N109 results are interesting. Although it is regarded as similar to Rx1400, we see significant differences
 - “ Case effects are significantly greater for PBX-N109, Rx1400 outperforms PBX-N109
- “ Case effects are dramatic enough to indicate that warhead fillings are often incorrect for blast performance
 - “ An optimised warhead could produce a 20% performance improvement.
Perhaps a mid life upgrade

- ” Gauge results are noisy from cased trials
 - ” Little confidence in Peak Pressure
 - ” Impulse results are reliable
 - ” Only Impulses have been used in this paper
- ” Trials have been performed to measure case effects for five different systems
 - ” Results show case effects depend on both charge type and case material
- ” Generalised Fisher equation is the best fit to data
 - ” Good fit for Steel systems, but less satisfactory for Aluminium systems
- ” The reasons for this observed charge and case material dependence is not understood
 - ” Crowley has since proposed a model in which the case effect is a function of the ratio of the case yield stress to the pressure in the unexpanded case

inally

” Thank you for listening
Any questions?

” Contact:
Paul Locking
Technical Specialist (Blast & Ballistics)
BAE Systems (Land), UK
Tel: +44-1793-78-6427
Email: paul.locking@baesystems.com



High Speed Penetration into Low Strength Concrete Target

24th International Symposium on Ballistics
September 22-26, 2008
New Orleans, LA

**V. K. Luk, J. A. Dykes, J. E. Bishop,
P. A. Taylor, J. S. Ludwigsen, and D. A. Dederman**
Sandia National Laboratories
Albuquerque, NM 87185-1160, USA

Contact: Vincent K. Luk
E-mail: vkluk@sandia.gov
Phone: 505-844-5498

Sandia is a multiprogram laboratory operated by Sandia Corporation for the United States Department of Energy's National Nuclear Security Administration under contract DE-AC04-94AL85000.



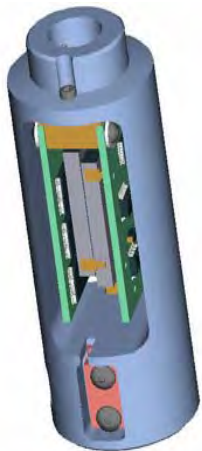
Outline

- **Phenomenon study on high speed penetration**
 - (760 - 1220 m/s, 2500 - 4000 fps)
- **High speed penetration experiments into low strength concrete targets**
 - (20.7 MPa, 3.0 Ksi)
- **Penetration simulations with Alegra/Shism, Emu, and Epic**
- **Summary – future plan**

Acknowledgment: Sponsorship from Defense Threat Reduction Agency, DTRA

High Speed Penetration Experiments

- **Goal:** to demonstrate the survivability of both the 7.62-cm jointed penetrator and the onboard instrumentation in high speed penetration events
 - Locate the appropriate gun launcher
 - Develop the launch package of petalled pusher/sabot that houses the subscale penetrator instrumented with triaxial data package, 3AMP
 - Conduct experiments at normal incidence into low strength concrete targets



3AMP





High Speed Penetration Experiments

- **Launch facility**

- A stationary 17.78-cm (7-inch) powder gun at the Energetic Materials Research and Testing Center (EMRTC) in Socorro, New Mexico

- **Penetrator design**

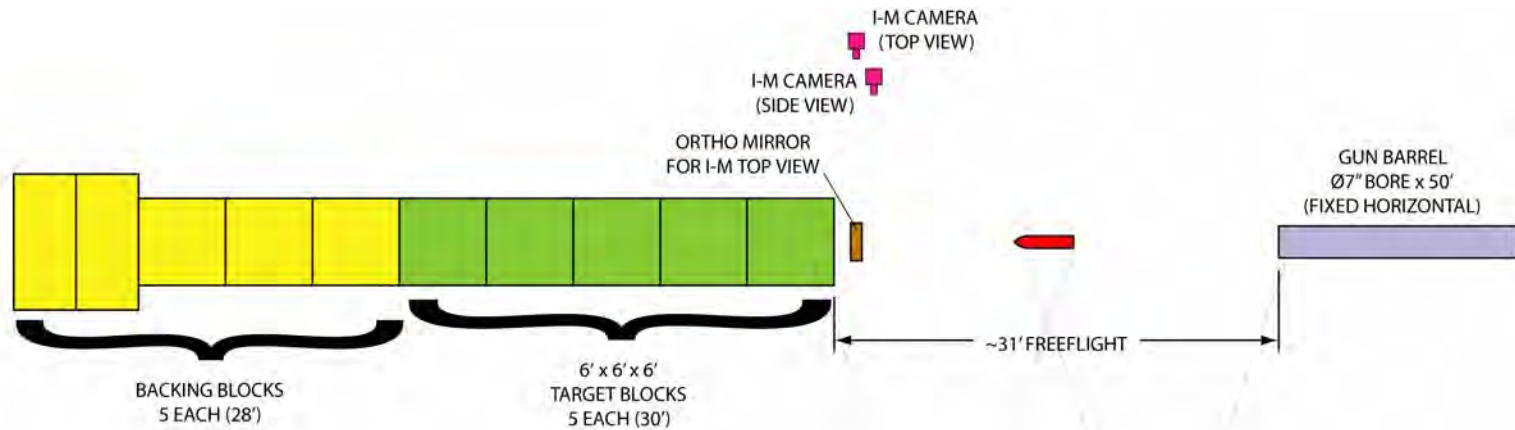
- A jointed nose of 3 CRH (Caliber Radius Head), 7.62 cm diameter, 53.1 cm long, and a weight of 13.5 Kg

- **Groutcrete target**

3 KSI Groutcrete UCS DATA			
Block	UCS (psi)		
	7 day	28 day	90 day
1	1715	2520	
2	1410	2335	
3	1335	2195	2785
4	1330	2115	2890
5	---	---	---
6	1380	2325	3040
7	1420	2365	3010
8	1370	2270	3030
9	1480	2335	3010
10	1335	2310	3130
AVERAGE	1419	2308	2985

High Speed Penetration Experiments

Experimental Layout



HIGH-SPEED
PHANTOM #2

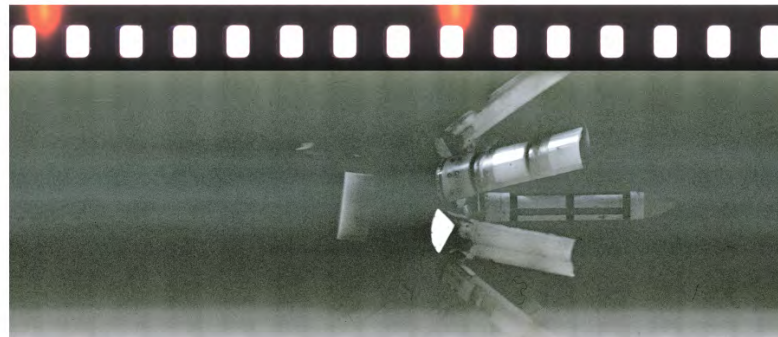
HIGH-SPEED
PHANTOM #1



Impact surface

High Speed Penetration Experiments

Results from 1st Experiment



3,637 ft/s IMPACT
SPEED - MEASURED
FROM THE I-M SIDE
VIEW FOOTAGE

- Impact condition: 1107 m/s (3636 fps) at near normal incidence
- Pusher/sabot separation occurred as designed
- Depth of penetration: 6.9 m (22.7 ft)
- 3AMP failed to record meaningful data due to high frequency accelerometer ringing during penetration event

High Speed Penetration Experiments

Results from 1st Experiment

Post-test Observations



- The penetrator and the nose joint survived
 - Nose threads free of damage and turn easily
 - Threads were hand tight after the test
- Penetrator lost 0.65 inches and 2.1 pounds (originally 20.9 inches long and 29.8 pounds)



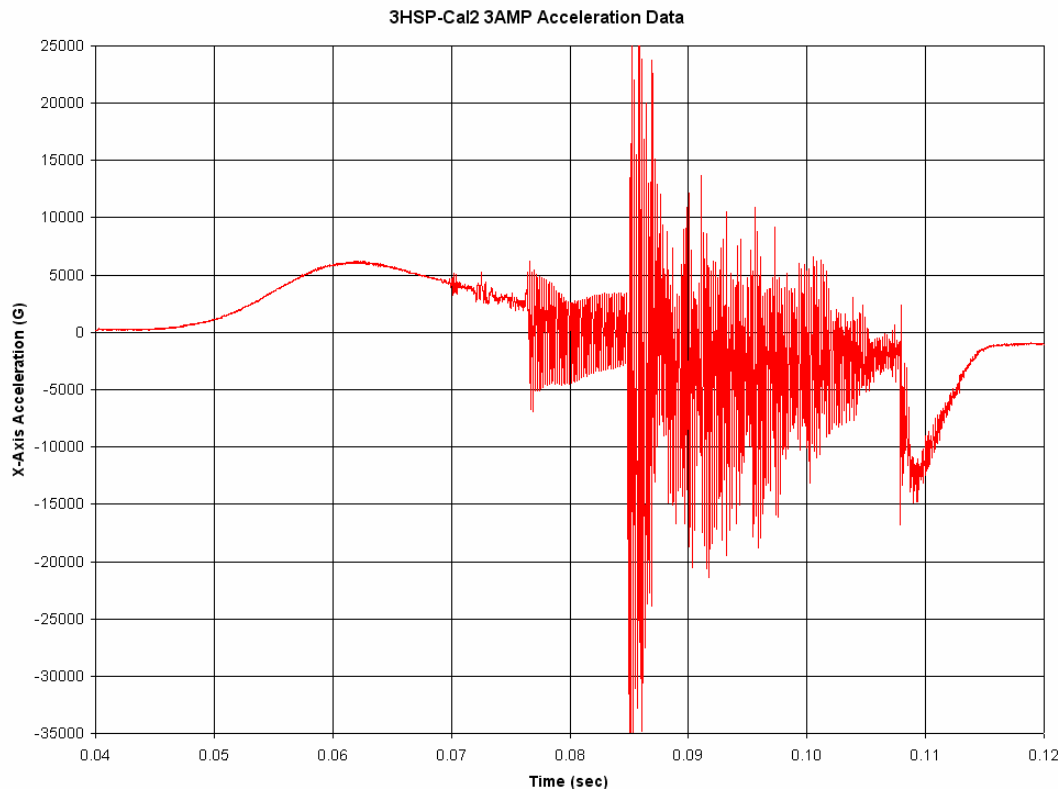
Target block 4
7 of 12

Penetrator final position

High Speed Penetration Experiments

Results from 2nd Experiment

- Impact condition: 1061 m/s (3480 fps) at near normal incidence
- Depth of penetration: 6.19 m (20.3 ft)
- 3AMP recorded meaningful deceleration data

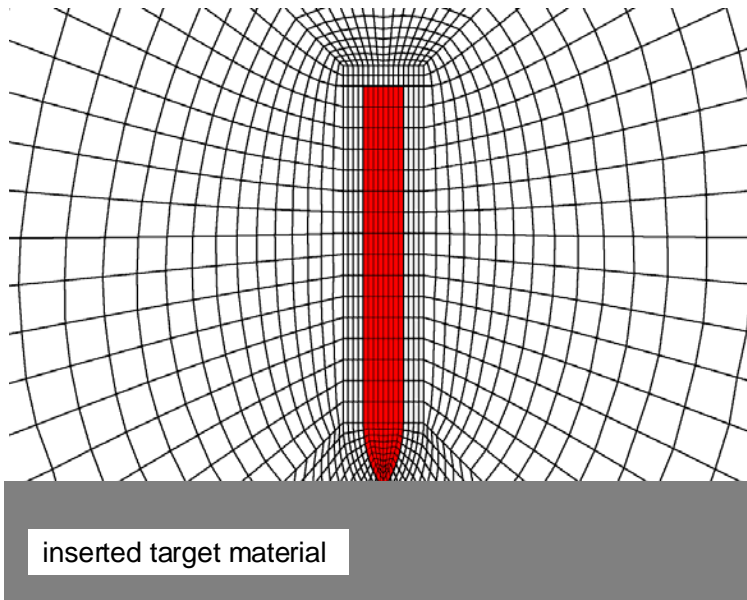


- The axial deceleration limits were recorded at +25000 g and -35000 g.
- A considerable amount of accelerometer ringing still occurred prior to impact, but it might have not affected the performance of the accelerometer.

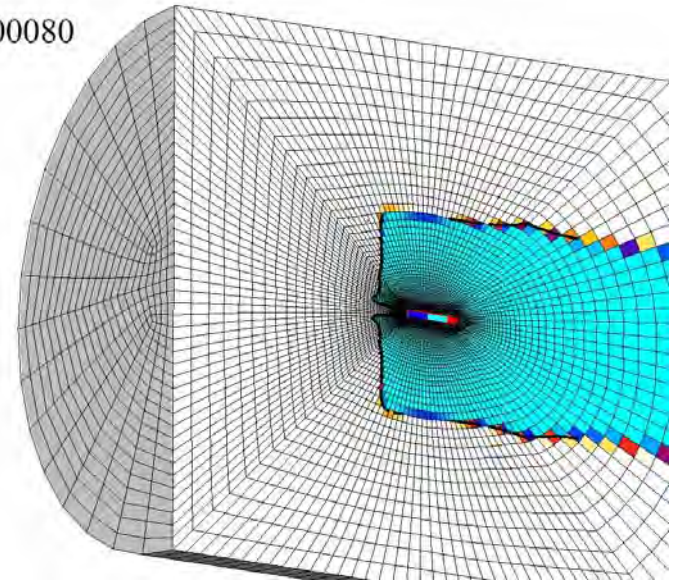
High Speed Penetration Analyses

Alegra/Shism

- Alegra/shism is a specific algorithm for soft/hard impact conditions. For penetration simulations, the Shism takes the penetrator mesh and interface to be Lagrangian and models the target region as ALE.



Time = 0.00080

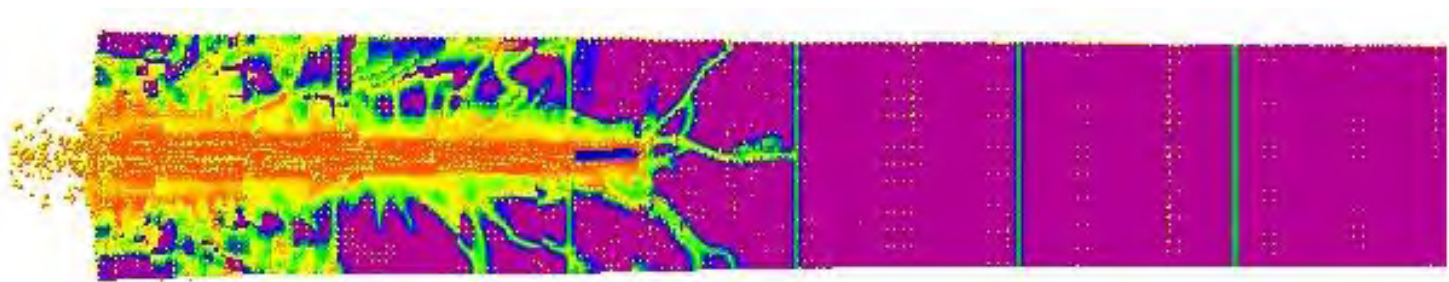


- Calculated depth of penetration = 4.6 m (Test data: 6.9 m)

High Speed Penetration Analyses

Emu

- **Emu:** A Lagrangian code, based of peridynamic theory, uses a mesh-free, particle approach to describe conservation laws in integral equations.
- In the penetration model, the concrete was modeled as a brittle elastic-plastic material, and the penetrator as a rigid projectile.
- Analysis results:
 - Depth of penetration = 4.25 m (Test data: 6.9 m)
 - Peak axial deceleration = 48500 g (Test data: 35000 g)



Final configuration of penetration event with concrete damage



High Speed Penetration Analyses

Epic

- **Epic:** a general purpose finite element code, capable of solving structural dynamic and penetration problems.
- Epic has a large library of material models for isotropic and anisotropic behavior and a selected set of failure criteria. It has a special feature to transform distorted 3D elements into meshless particles.
- In the high speed penetration model, the concrete target was modeled with 3D elements using the HJC concrete model with a 24 MPa (3.5 ksi) unconfined concrete compressive strength and a 0.34 MPa (50 psi) tensile strength.
- Calculated depth of penetration = 3.05 m (Test data: 6.9 m)



Summary

• **Penetration experiments**

- Jointed penetrator design and launch package with petalled pusher/sabot have been developed.
- Onboard 3AMP package survived and recorded deceleration data for high speed penetration experiment with normal incidence into 20.7 MPa concrete target.
- Future tasks include high speed experiments into 39 MPa concrete target.

• **Penetration analyses**

- Sandia has extensive experiences in analyzing penetration events at conventional speeds using Alegra/Shism, Emu, and Epic, and the penetration models perform well.
- However, the high speed penetration models with these codes calculate lower depth of penetration and higher decelerations → target provides much higher penetration resistance.
- New penetration models will be researched and developed to account for radial cracking resulting in material softening of concrete target.



ry Industries Ltd. (IMI)
Heavy Ammunition Division



THE APPENDIX

MEIR MAYSELESS, EITAN HIRSCH

SEPTEMBER 2008

OUTLINE

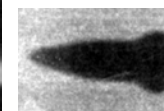
- INTRODUCTION
- EXPERIMENTAL RESULTS
- NUMERICAL MODELLING
- DISCUSSION

INTRODUCTION

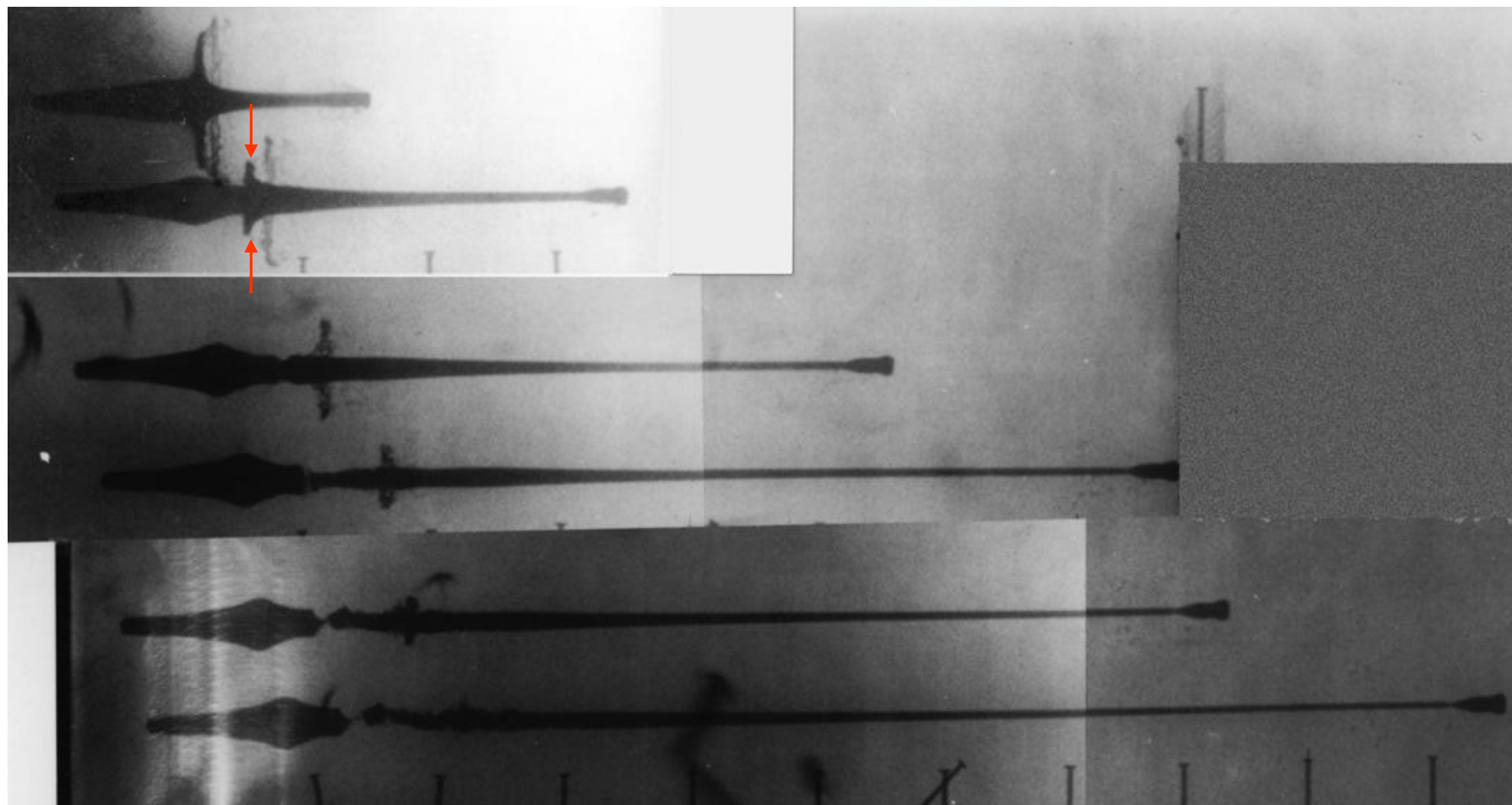
CLASSICAL PARTITION OF THE JET :

MAIN (coherent) JET

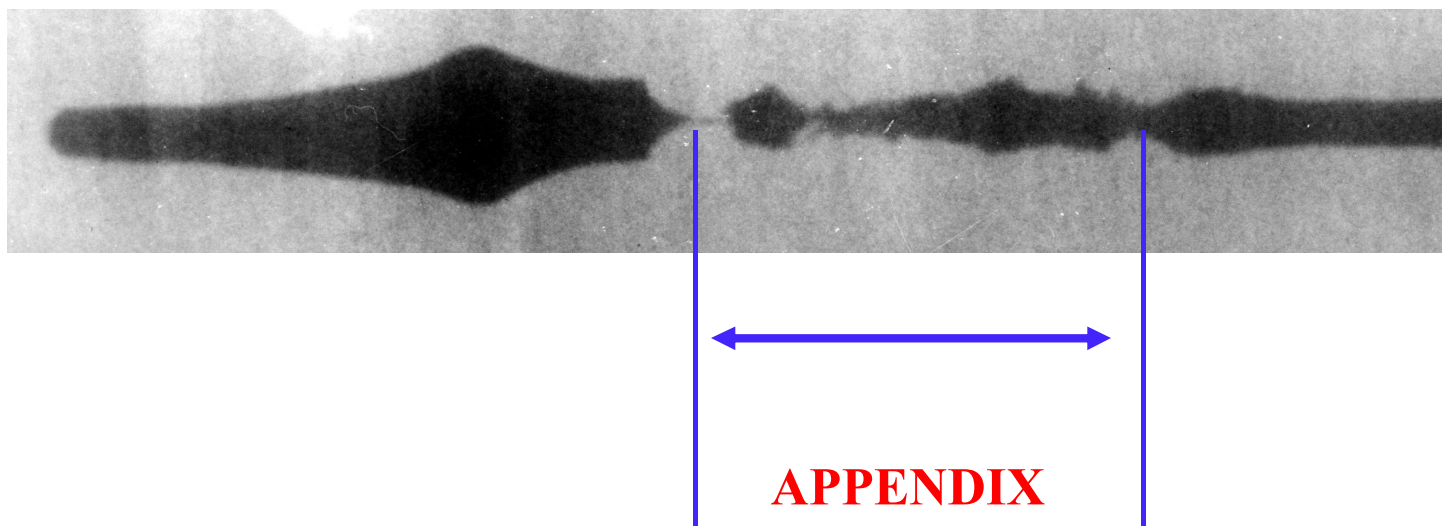
SLUG



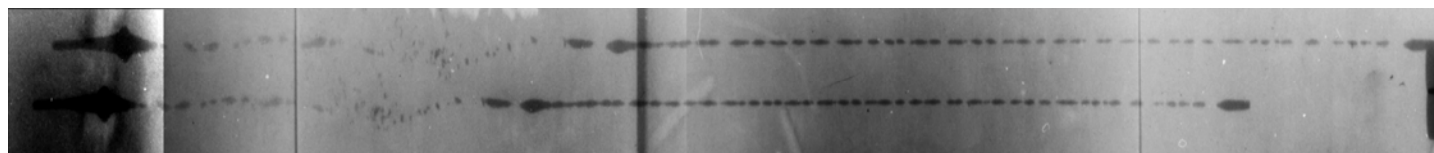
BUT IF WE LOOK CLOSER:



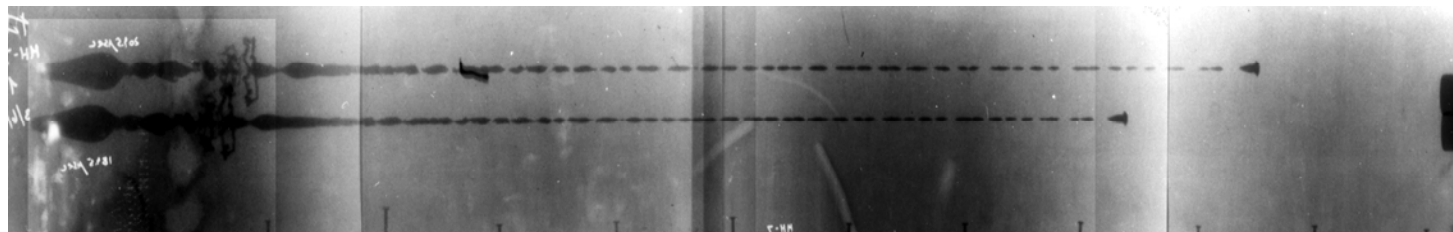
AND YET CLOSER:



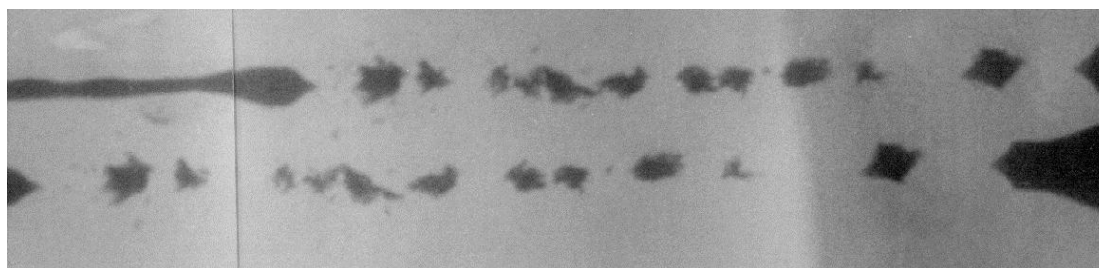
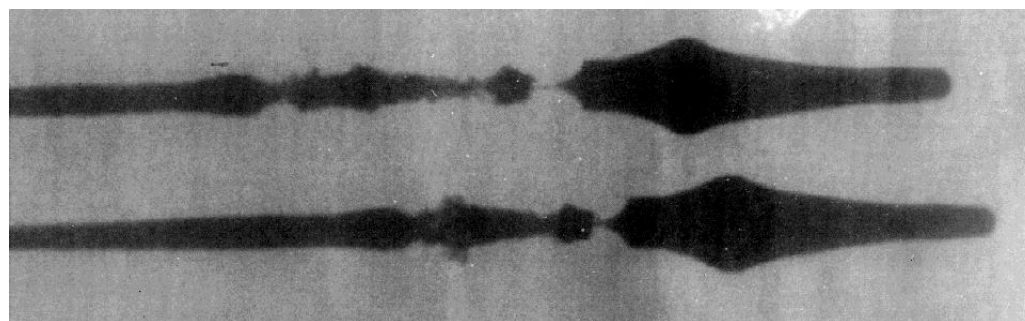
EXPERIMENTAL RESULTS



1% CD LINER



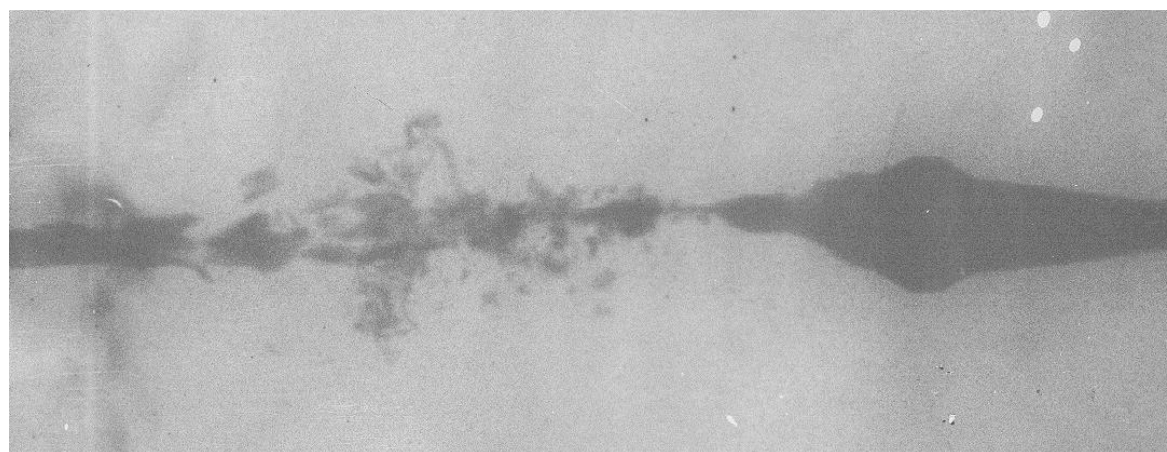
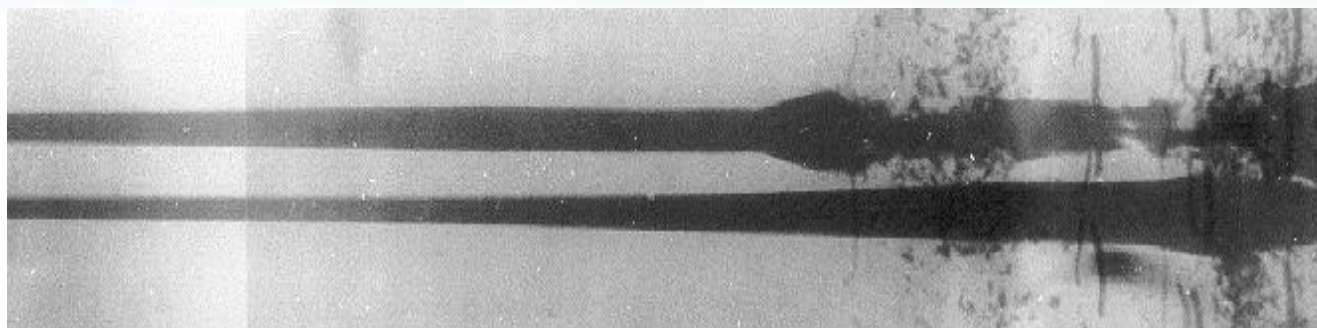
4% CD LINER



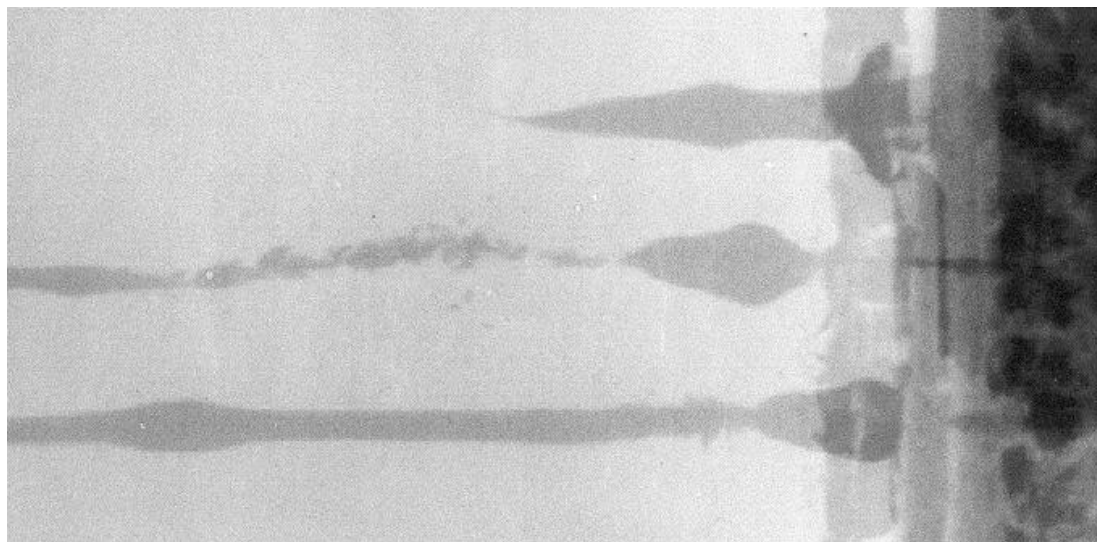
POINT INITIATED UNCONFINED



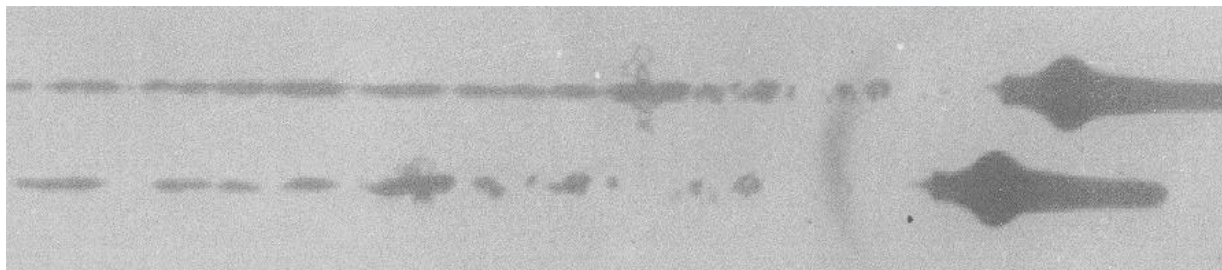
CHARGE AT 30 μ S, 45 μ S, 90 μ S, 100 μ S, 180 μ S & 200 μ S



PERIPHERALLY INITIATED CHARGES

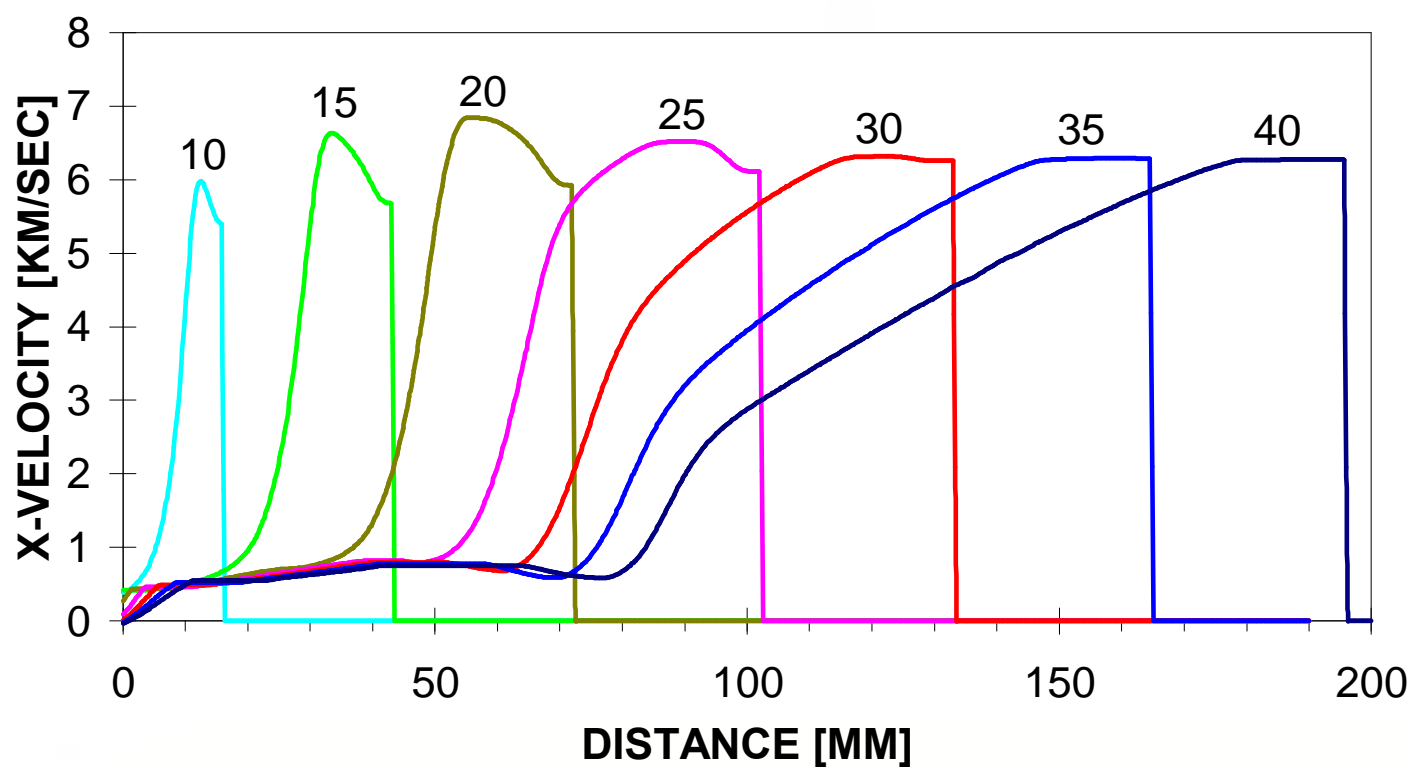


HEAVILY CONFINED HEMI SPHERICAL CHARGE AT 30 μ S, 50 μ S AND 80 μ S

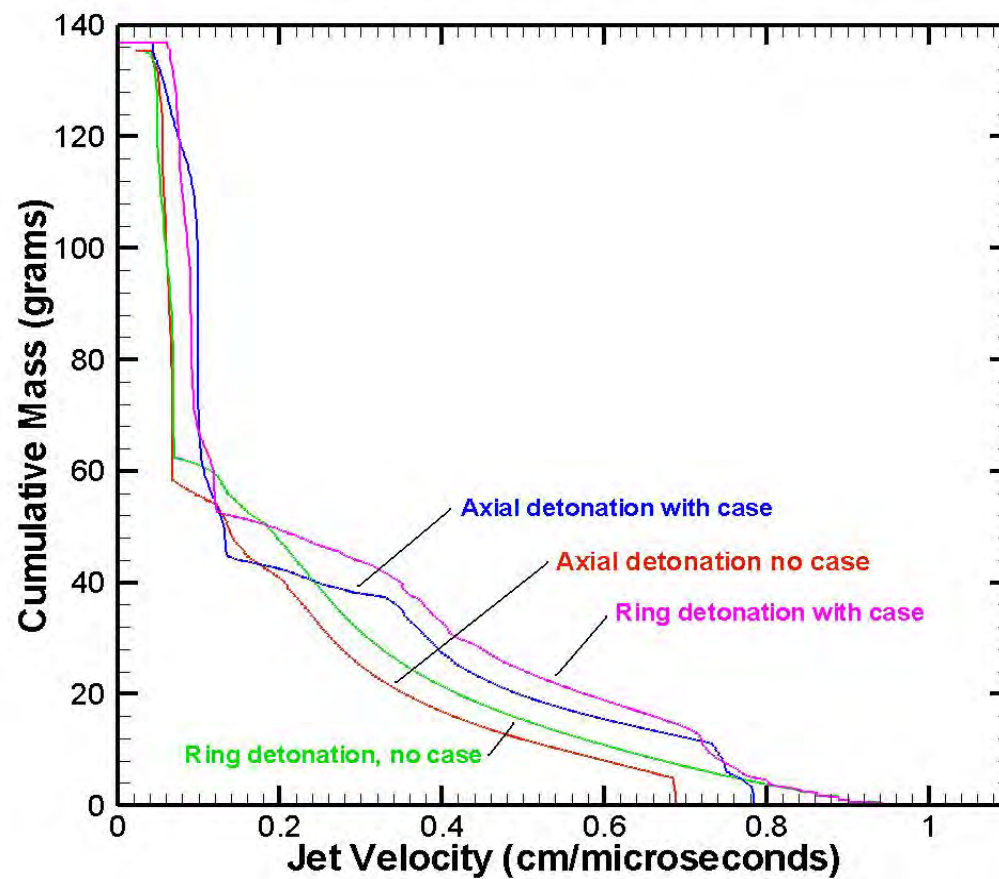


SMALL CHARGE AT 30 μ S AND 50 μ S

SIMULATED VELOCITY PROFILES FOR P.I. 2% CD LINER THICKNESS



Mass Summation vs. Velocity (t=45)



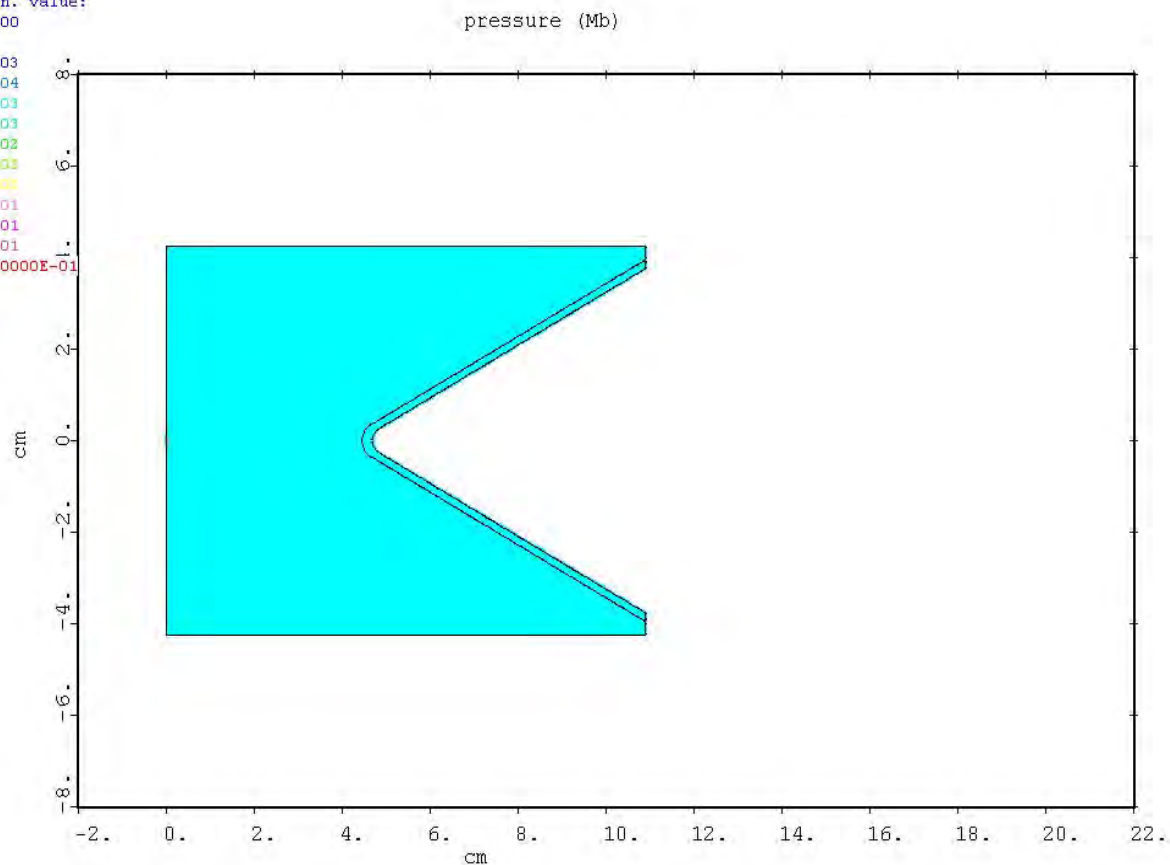
GOALS

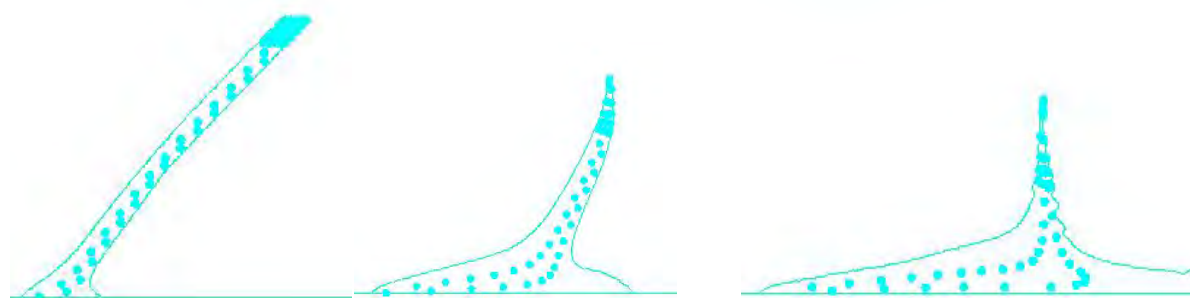
IDENTIFY THE APPENDIX

CHARACTERIZING THE APPENDIX

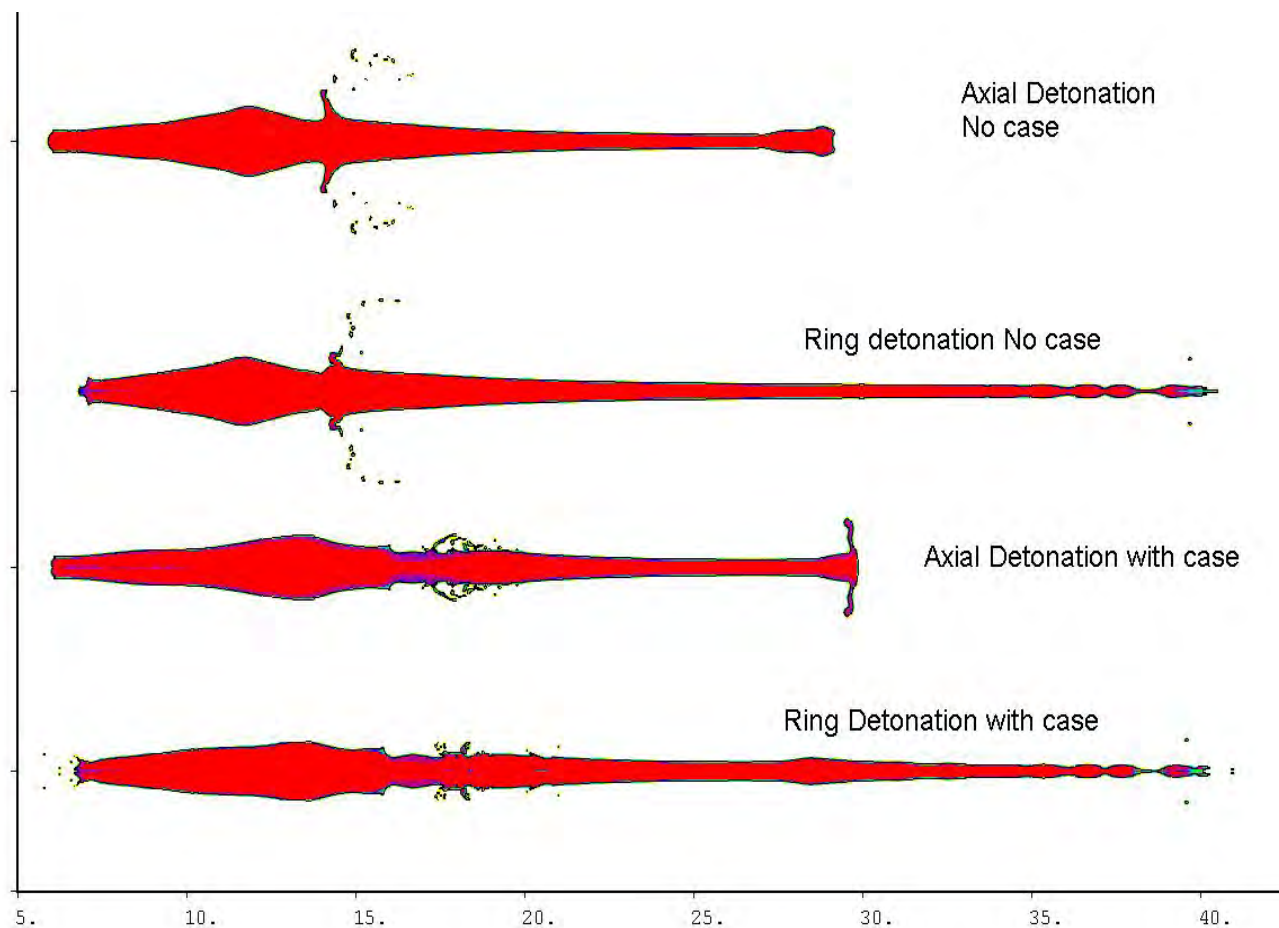
Point initiated charge

```
base line no case r=0 initiation  
time = 1.0789E-01  
global max. value:  
1.1765E-01  
global min. value:  
0.0000E+00  
values:  
-1.0000E-03  
-5.0000E-04  
1.0000E-03  
3.0000E-03  
1.0000E-02  
3.0000E-03  
5.0000E-02  
1.0000E-01  
1.5000E-01  
2.0000E-01  
above 2.0000E-01  
PRESSURE
```

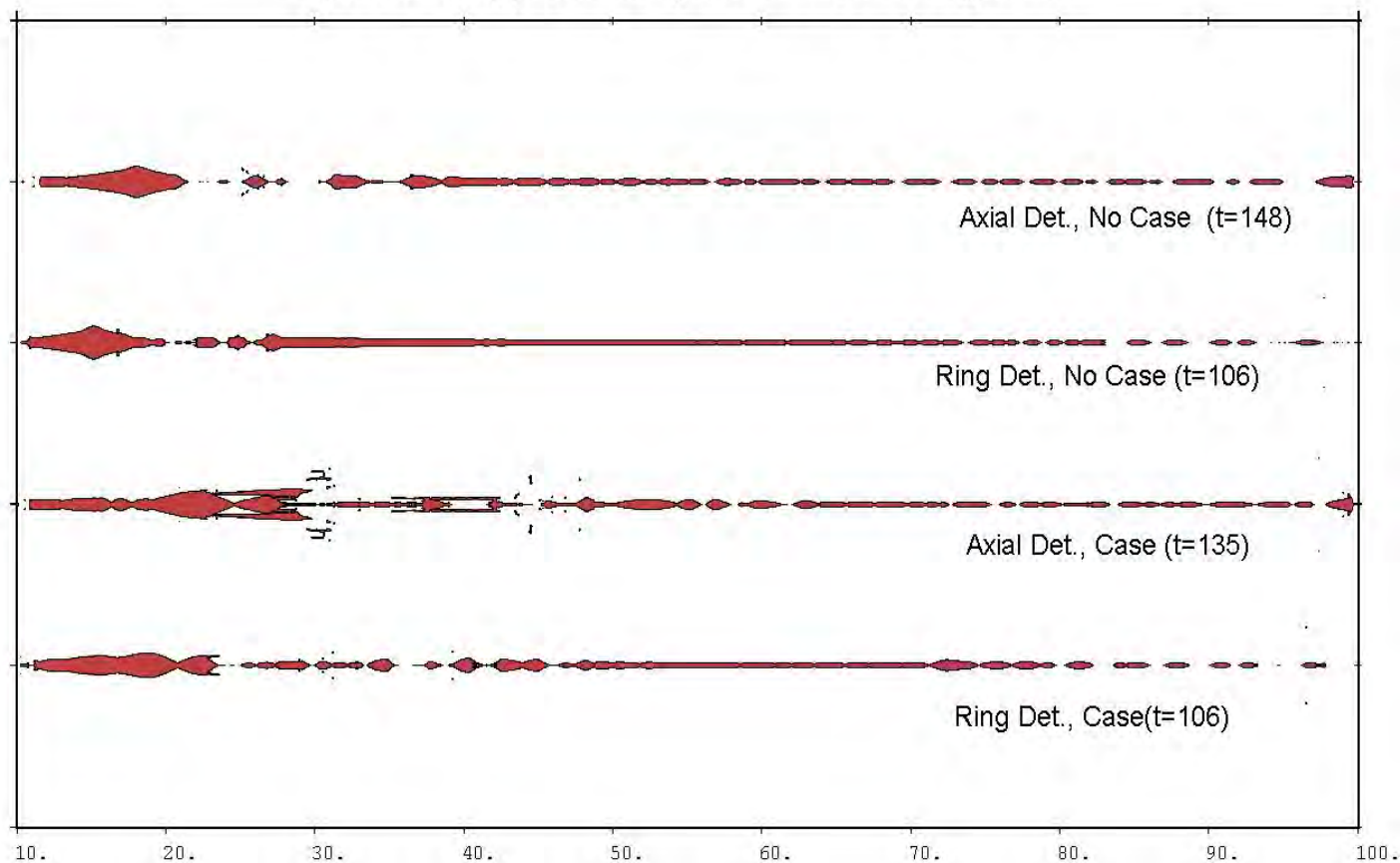




Numerical simulation results of a flow of the liner material points
in a point initiated confined charge
at 10 μs (left), 20 μs (center) and 30 μs (right), after initiation.



Tips are at approximately 90 cm from charge end.



SCAN CALCULATION FOR 1%, 2%, 4% CD LINER THICKNESS

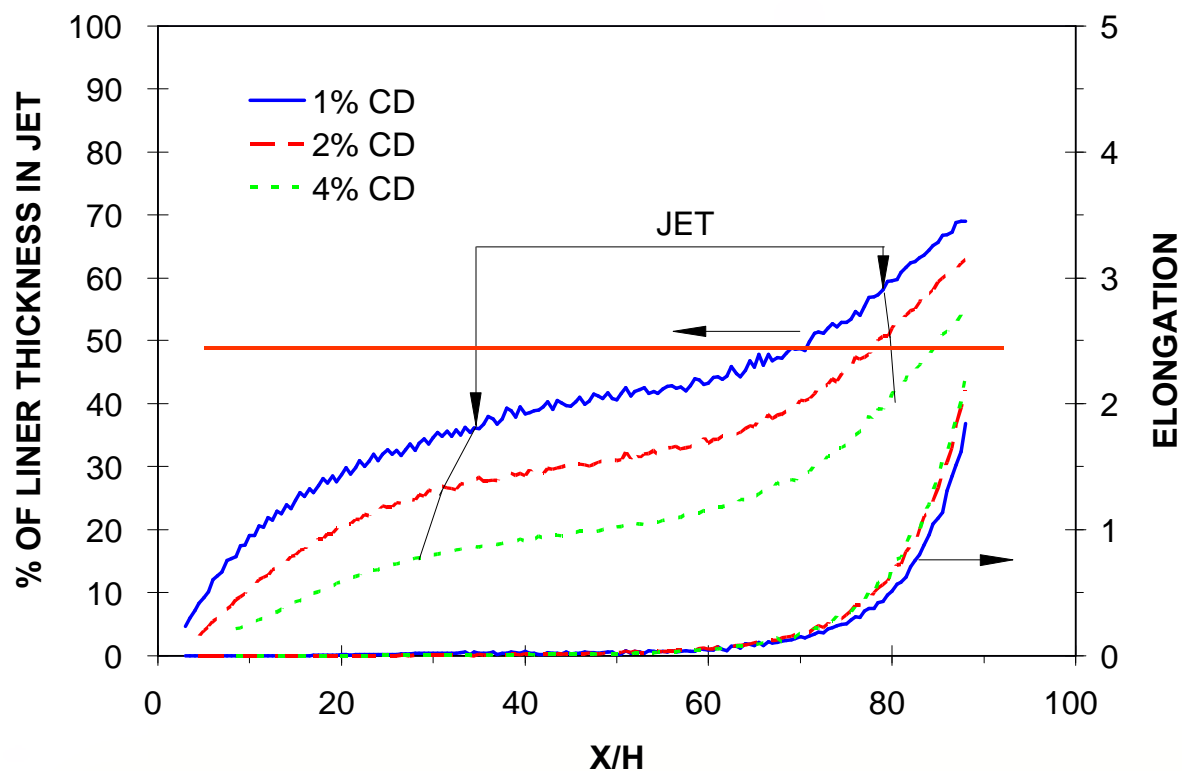




Figure 5: jet from a 72mm charge, 60°, 0.4mm (0.5%CD) thick copper

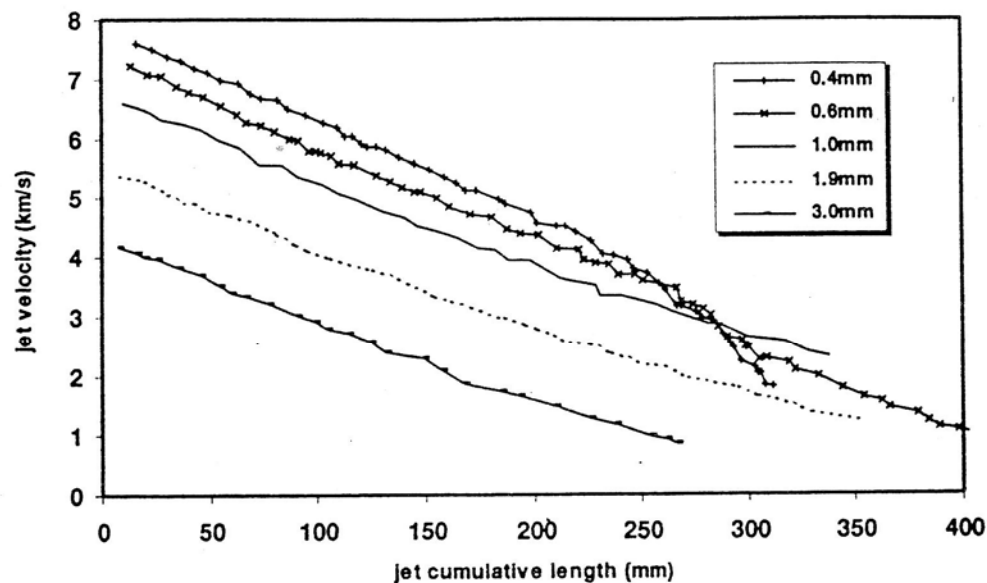


Figure 3: particulation behavior of jets from 60° copper cones with different wall thickness: experimental jet velocity vs. cumulative length from radiographs

P. Y. Chanteret and A. Lichtenberger, "About Varying Shaped Charge Liner Thickness", in Proceedings 17th Int. Symp. On Ballistics, Midrand, South-Africa, 1998.

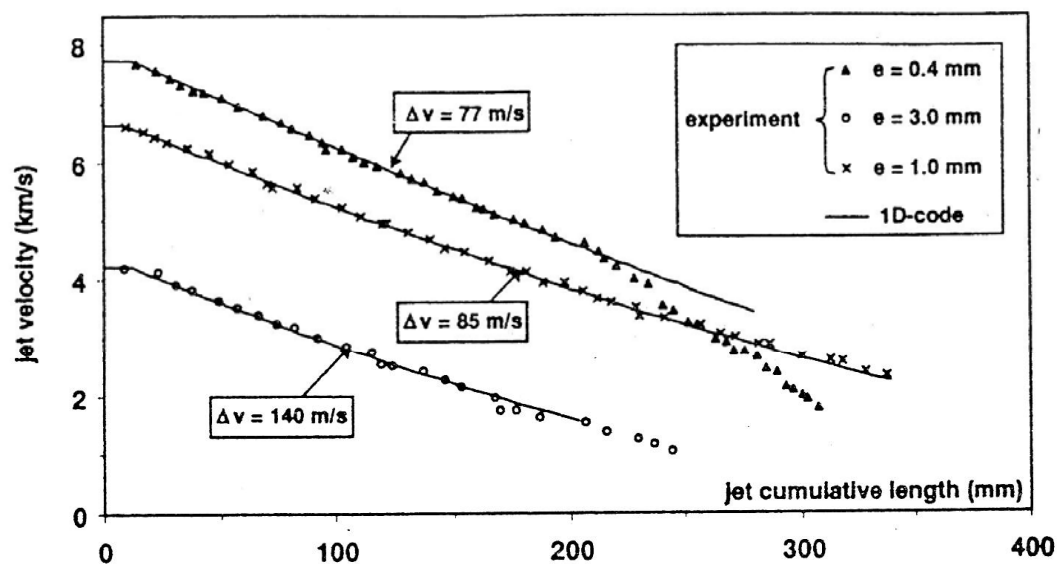


Figure 11: experimental and 1D-code calculated jet velocity vs. cumulative length;
60° copper liners with 0.9%, 2.2% and 6.7% CD liner wall thickness.

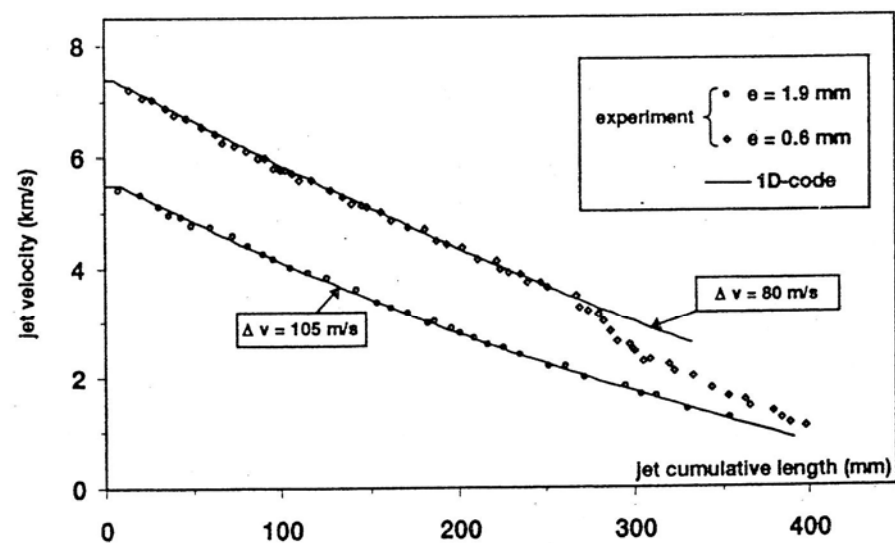
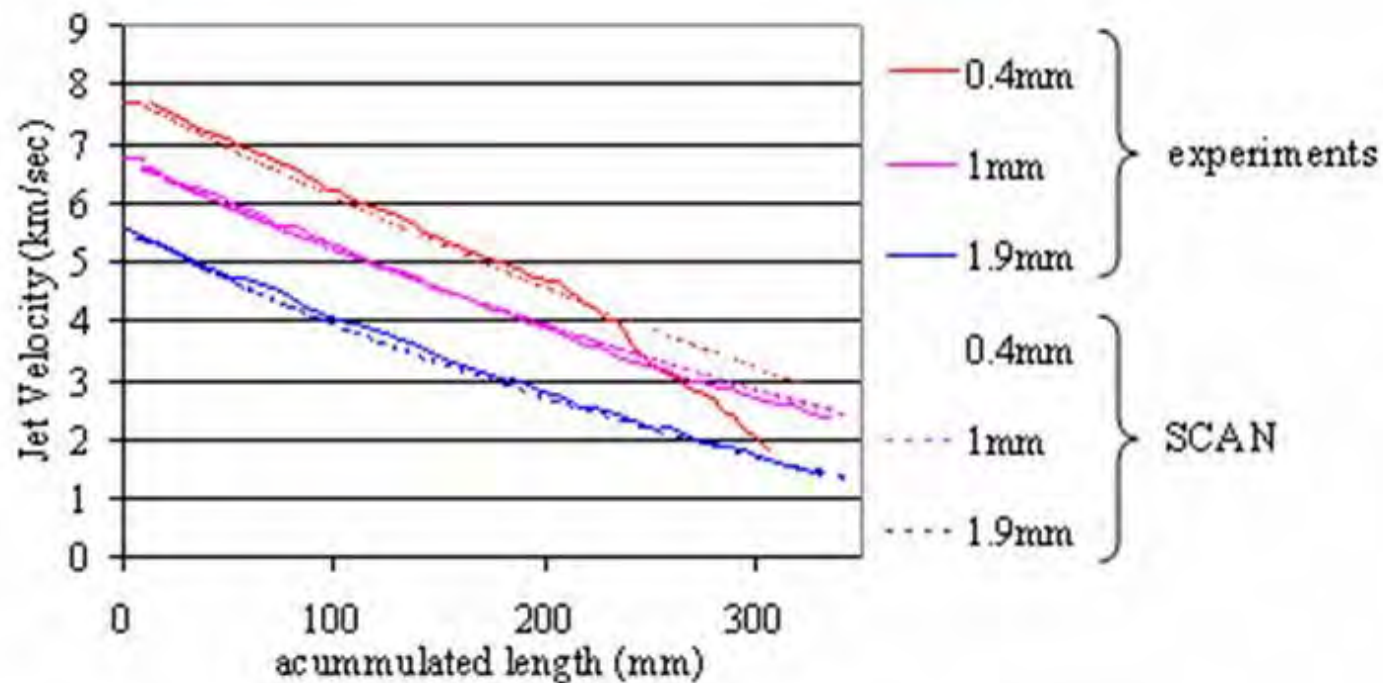
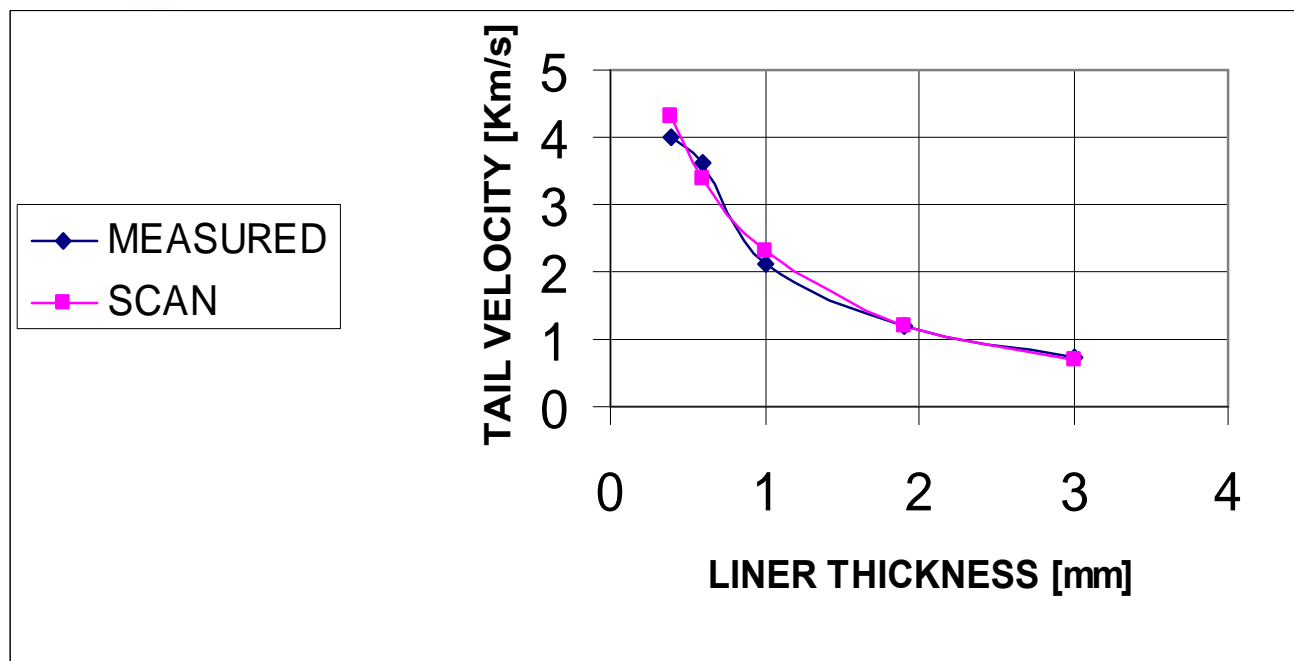


Figure 12: experimental and 1D-code calculated jet velocity vs. cumulative length; 60° copper liners with 1.3% and 4.2% CD liner wall thickness.

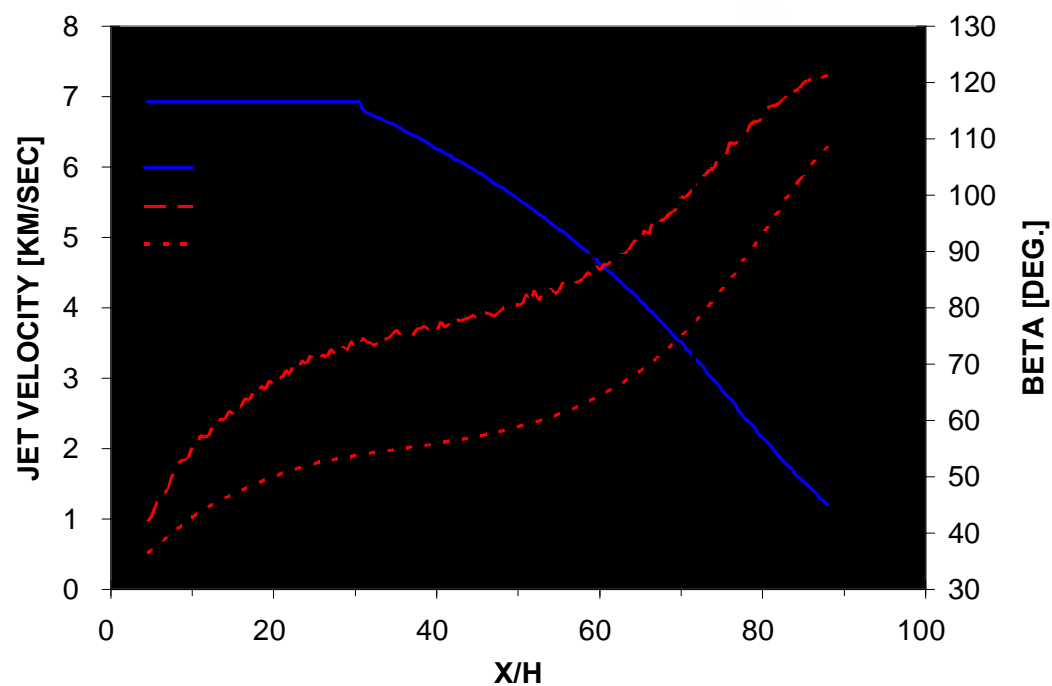


SCAN calculations compared to Chanteret and Lichtenberger experimental results. The sudden change in the slope seen in the 0.4mm liner characteristic is where the appendix begins to form in this case (it is in the process adjustment) .



Experimental results (Chanteret and Lichtenberger) of the jet velocity where the Appendix starts, as a function of the liner thickness, compared to the SCAN theoretical results.

SCAN CALCULATION FOR 2% CD LINER THICKNESS



CONCLUSIONS:

THE APPENDIX REGION WAS IDENTIFIED.

$$\beta \geq 90^\circ$$

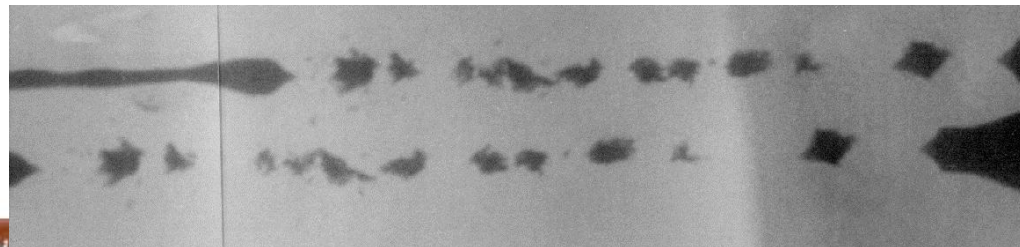
$$V_S = V_1 - V_f < 0$$

HIGH STRAIN RATE.

HIGH VELOCITY DIFFERENCE BETWEEN PARTICLES.

NON STABLE ZONE.

EFFECTIVE FOR PENETRATING SOFT TARGETS.





Numerical Simulation of Projectile Acceleration Process Using Solid/Gas Two-Phase Reacting Flow Model

Hiroaki MIURA¹, Akiko MATSUO¹ and Yuichi NAKAMURA²

¹Department of Mechanical Engineering, Keio University, JAPAN

²NOF Corporation, JAPAN

Systems Utilizing Solid Propellant

Chemical energy of
solid propellant
 $\approx 4\text{MJ/kg}$



Kinetic energy of
projectile

Gun System

Military Technology
Cannon

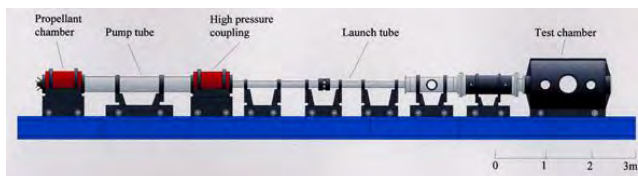


<http://www.army-technology.com/projects/crusader/crusader5.html>

Scientific Research
Ballistic Range



<http://www.knlab.msl.titech.ac.jp/>



<http://ceres.ifs.tohoku.ac.jp/~coe/facility.html>

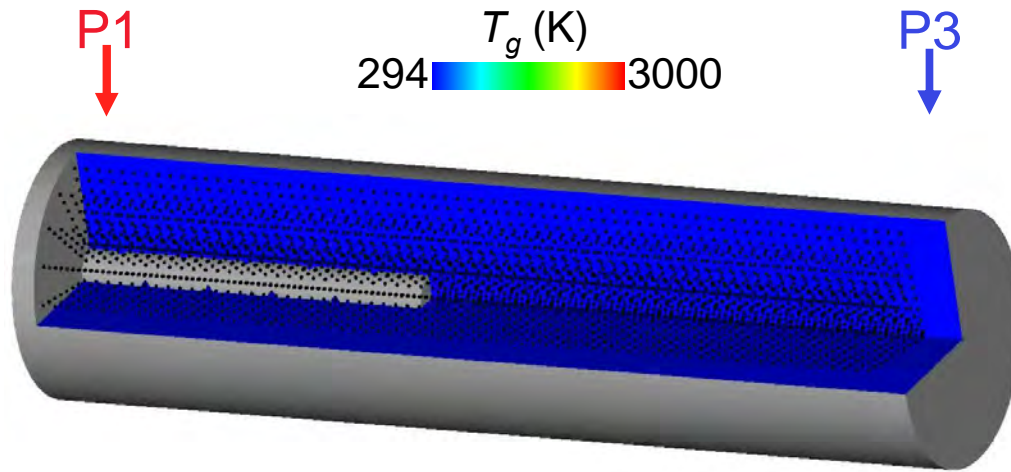
Solid Rocket

Space Propulsion
Solid Rocket Booster



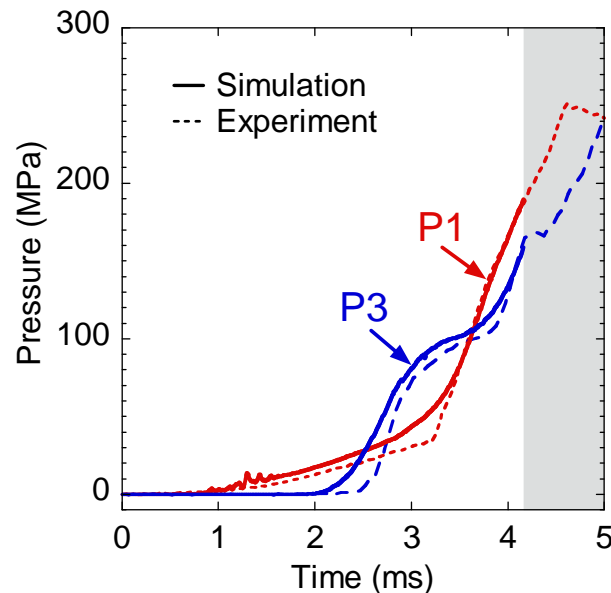
http://spaceinfo.jaxa.jp/db/kaihatu/shuttle/shuttle_g/sts-87-2.jpg

Pressure of Granular Solid Propellant



Breech

Base



H. Miura *et al.*, ISEM2008

The movement of granular solid propellant causes the chamber pressure fluctuations.



Simulation of propellant grains movement is significant to predict the destructive pressure waves generation.

bular Solid Propellant

Granular propellant

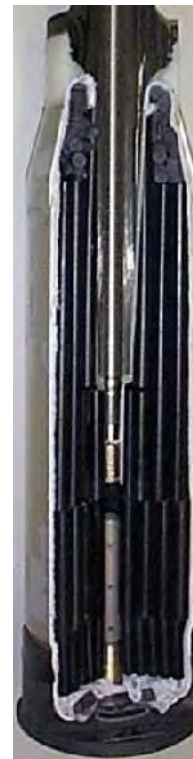


Characteristics of granular propellant

- “ Larger surface area
Rapid fire
- “ Easy adjustment
for propellant mass
- “ Problem of strong
pressure waves

FAS Military Analysis Network

Tubular propellant



Characteristics of tubular propellant

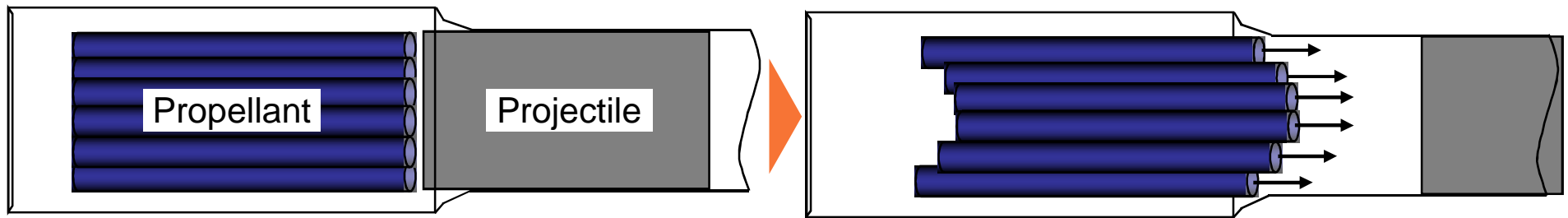
- “ Smaller surface area
Slow burning
- “ Uniform ignition and
uniform charge
concentration

Simulation technique for tubular propellant combustion should be developed.

Modeling for tubular propellant movement with burning

n of Tubular Solid Propellant

To simulate tubular propellant behavior in the chamber



Modeling for tubular propellant movement with burning

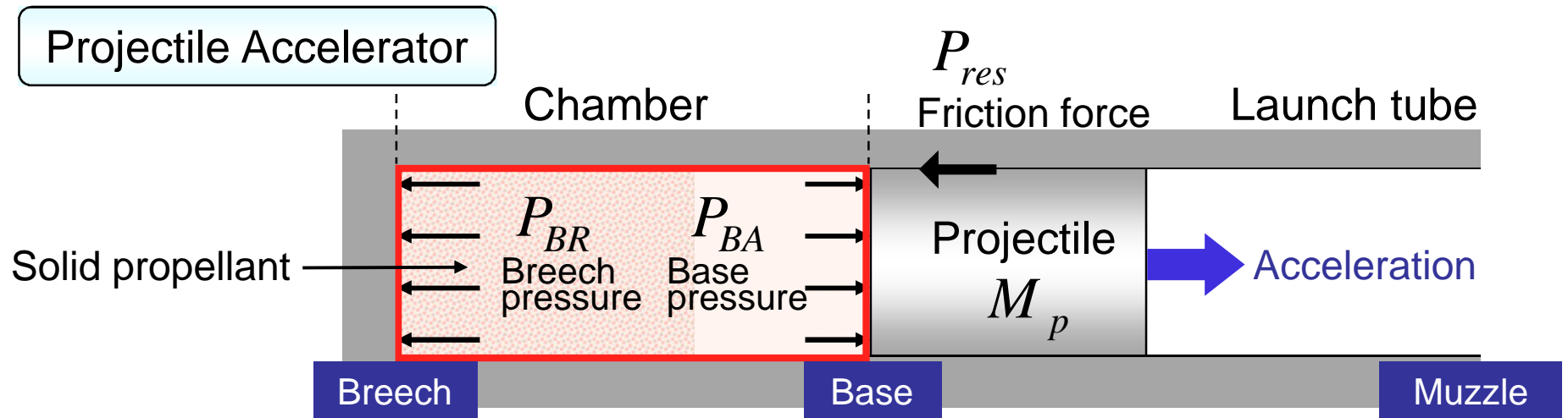
- ❑ A long tubular propellant lies in the wide range of computational domain.

Consideration of property distributions on propellant surface

- ❑ Each tubular propellant moves in the chamber.

Movement model for propellants by Lagrangian approach

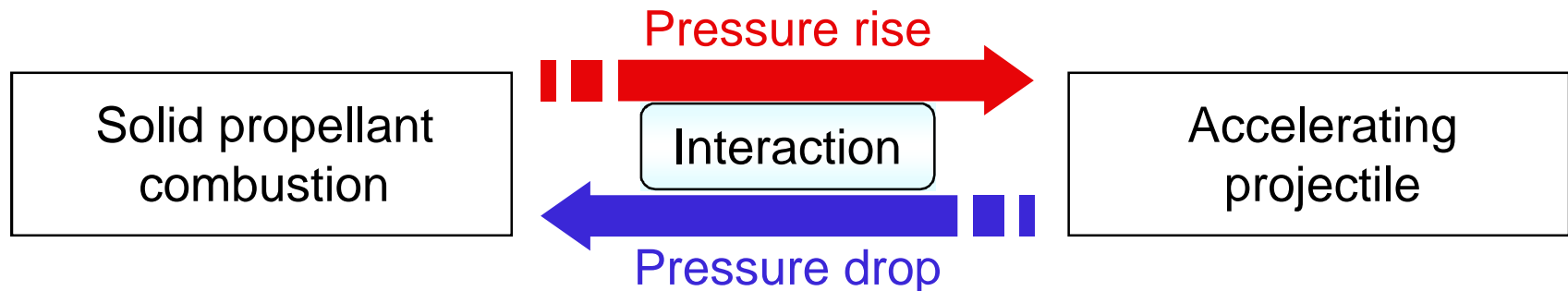
Model for Projectile Accelerator



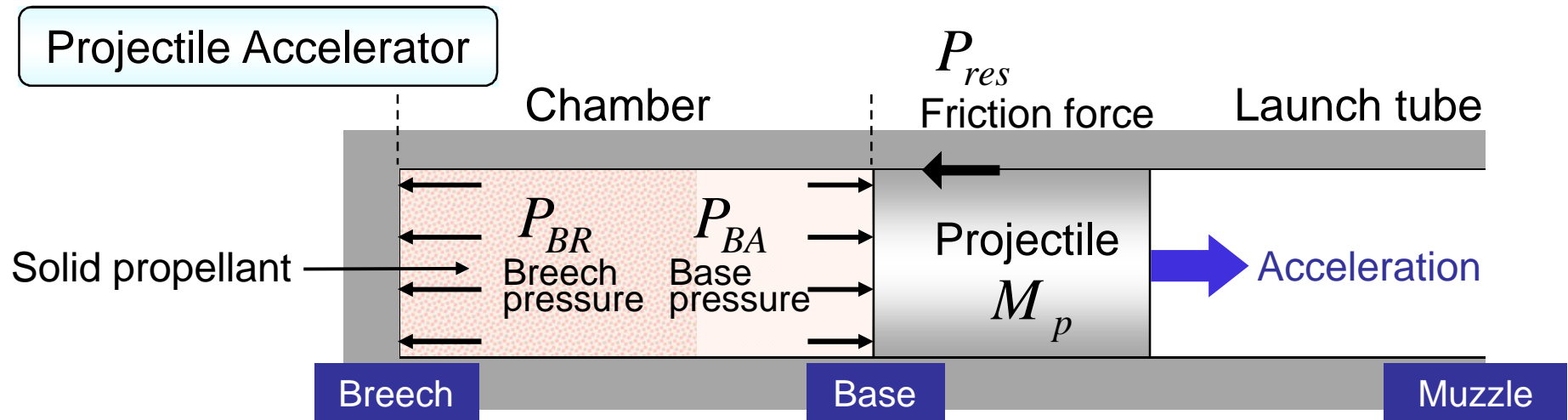
- ❑ Combustion gas and solid propellant coexist in the chamber.



- ❑ Chamber volume increases with the projectile movement.




Analysis Based on Interior Ballistics



Prediction of events in the accelerator is required.

Elements of accelerating process simulation by numerical analysis

- ☐ Solid/Gas two-phase flow
- ☐ Solid propellant combustion
 - Propellant (Solid phase)  Combustion gas (Gas phase)
- ☐ Moving boundary problem

Objective

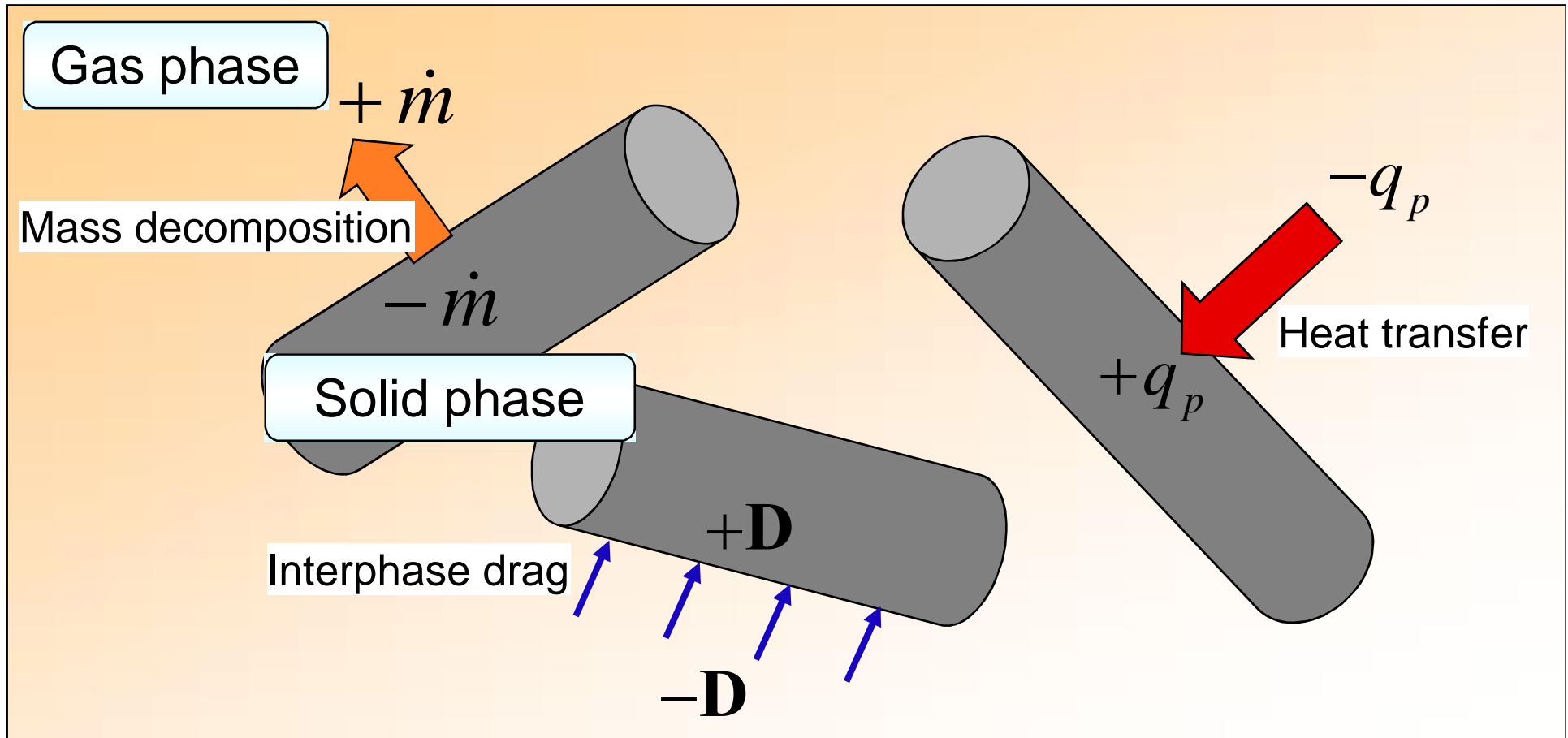
To simulate the process of accelerating a projectile by tubular solid propellant combustion in the 50mm projectile accelerator using the developed 2D axisymmetric two-phase flow code and the moving overlapped grid method.

- Simulation method is validated using experimental data.
 - “ Breech pressure history
 - “ Projectile velocity history
- Conditions of projectile mass M_p and propellant mass C are varied for the examination of those effects on the performance of gun system.
 - “ Maximum breech pressure
 - “ Projectile muzzle velocity and kinetic energy

Calculation Method for Interior Ballistics Simulation

- Two-phase Fluid Dynamics Code
- Modeling Tubular Propellant
- Modeling Projectile Movement

Interaction Between Two Phases



$$\dot{m} = \dot{m}(r) \quad r = ap^n$$

$$\mathbf{D} = \mathbf{D}(\mathbf{u}_g - \mathbf{u}_p)$$

$$q_p = q_p(T_g - T_p)$$

$$T_p \geq T_{\text{ignition}} \rightarrow \text{ignition}$$

Governing Equations

Gas-phase

$$\frac{\partial}{\partial t}(\alpha \rho) + \nabla \cdot (\alpha \rho \mathbf{u}) = \dot{m} + \dot{m}_{ig}$$

$$\frac{\partial}{\partial t}(\alpha \rho \mathbf{u}) + \nabla \cdot (\alpha \rho \mathbf{u} \mathbf{u}) = -\alpha \nabla p - \mathbf{D} + \dot{m} \mathbf{u}_p$$

$$\frac{\partial}{\partial t}(\alpha e) + \nabla \cdot (\alpha (e + p) \mathbf{u}) = -\mathbf{D} \cdot \mathbf{u}_p + \dot{m} \left(q + \frac{\mathbf{u}_p \cdot \mathbf{u}_p}{2} \right) + \dot{m}_{ig} q_{ig} - q_p$$

$$\begin{cases} \frac{\partial}{\partial t}(\alpha \rho Y_{pr}) + \nabla \cdot (\alpha \rho Y_{pr} \mathbf{u}) = \dot{m} \\ \frac{\partial}{\partial t}(\alpha \rho Y_{ig}) + \nabla \cdot (\alpha \rho Y_{ig} \mathbf{u}) = \dot{m}_{ig} \\ \frac{\partial}{\partial t}(\alpha \rho Y_a) + \nabla \cdot (\alpha \rho Y_a \mathbf{u}) = 0 \end{cases}$$

pr : propellant gas
 ig : igniter gas
 a : air

Solid-phase

$$m_{p,i} \frac{du_{p,i}}{dt} = (p_L - p_R) A_i + D_i - \dot{m}_i u_{p,i}$$

1D motion of i -th propellant

{ Gas-phase Compressible fluid
 Solid-phase Constant density

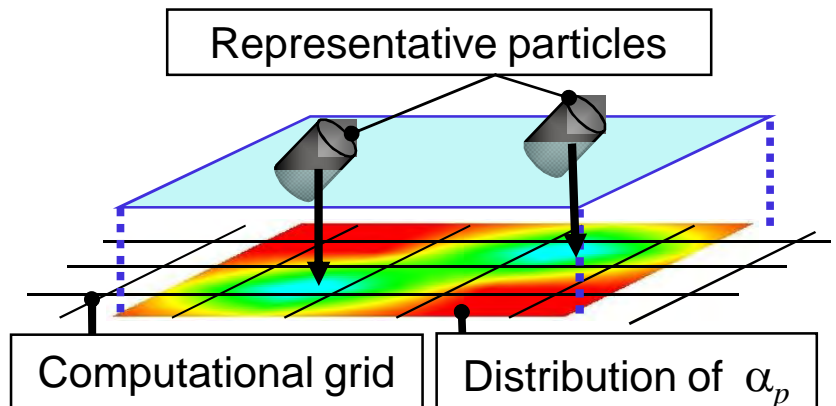
Computational volume is divided into the volume of gas and solid.

α : Volume fraction of gas-phase (porosity)

α_p : Volume fraction of solid-phase

$$\alpha = 1 - \alpha_p$$

The distribution of α_p is determined from the distribution of representative particles.



Governing Equations

$$\begin{aligned}
 \text{Gas-phase} \quad & \frac{\partial}{\partial t}(\alpha \rho) + \nabla \times (\alpha \rho \mathbf{u}) = \dot{m} + \dot{m}_{ig} \\
 & \frac{\partial}{\partial t}(\alpha \rho \mathbf{u}) + \nabla \times (\alpha \rho \mathbf{u} \mathbf{u}) = -\alpha \nabla p - \mathbf{D} + \dot{m} \mathbf{u}_p \\
 & \frac{\partial}{\partial t}(\alpha e) + \nabla \times (\alpha (e + p) \mathbf{u}) = -\mathbf{D} \cdot \mathbf{u}_p + \dot{m} \left(q + \frac{\mathbf{u}_p \cdot \mathbf{u}_p}{2} \right) + \dot{m}_{ig} q_{ig} - q_p
 \end{aligned}
 \quad
 \begin{cases}
 \frac{\partial}{\partial t}(\alpha \rho Y_{pr}) + \nabla \times (\alpha \rho Y_{pr} \mathbf{u}) = \dot{m} \\
 \frac{\partial}{\partial t}(\alpha \rho Y_{ig}) + \nabla \times (\alpha \rho Y_{ig} \mathbf{u}) = \dot{m}_{ig} \\
 \frac{\partial}{\partial t}(\alpha \rho Y_a) + \nabla \times (\alpha \rho Y_a \mathbf{u}) = 0
 \end{cases}$$

pr : propellant gas
 ig : igniter gas
 a : air

$$\text{Solid-phase} \quad m_{p,i} \frac{du_{p,i}}{dt} = (p_L - p_R) A_i + D_i - \dot{m}_i u_{p,i} \quad \text{1D motion of } i\text{-th propellant}$$

□ Gas-phase components

- Propellant combustion gas (pr)
- Igniter combustion gas (ig)
- Air (a)

□ State equation for gas-phase

$$p = \frac{RT}{(1/\rho - b)} \quad b : \text{Covolume}$$

\dot{m} : Propellant mass decomposition rate

\dot{m}_{ig} : Igniter mass decomposition rate

\mathbf{D} : The interphase drag between two-phase

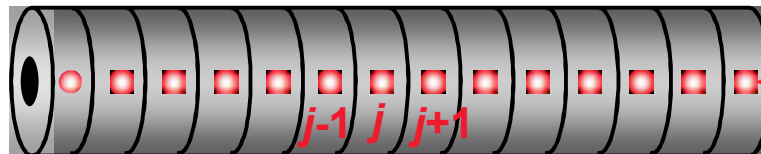
q : The combustion heat of propellant

q_{ig} : The combustion heat of igniter

q_p : Heat loss to solid phase

Representative Particle Properties

Information of propellant geometry for ***j*-th representative particle**



At the end of each tubular propellant

$$\text{Volume } V_{p,j} = (\Delta L_{p,j} - \Delta u_j) \left\{ \frac{\pi}{4} (D_p - 2\Delta u_j)^2 - \frac{\pi}{4} (d_p + 2\Delta u_j)^2 \right\}$$

$$\begin{aligned} \text{Surface area } S_{p,j} = & \pi (D_p - 2\Delta u_j) (\Delta L_p - \Delta u_j) + \pi (d_p + 2\Delta u_j) (\Delta L_{p,j} - \Delta u_j) \\ & + \left\{ \frac{\pi}{4} (D_p - 2\Delta u_j)^2 - \frac{\pi}{4} (d_p + 2\Delta u_j)^2 \right\} \end{aligned}$$

$\Delta L_{p,j}$: Divided length of tube

D_p : Outer diameter of tube

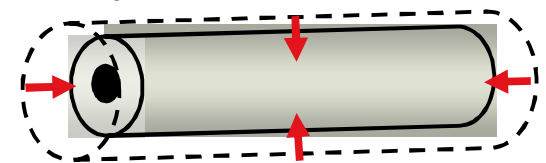
d_p : Inner diameter of tube

$$\Delta u_j = \int_0^t r dt \quad r = ap^n$$

At the other position

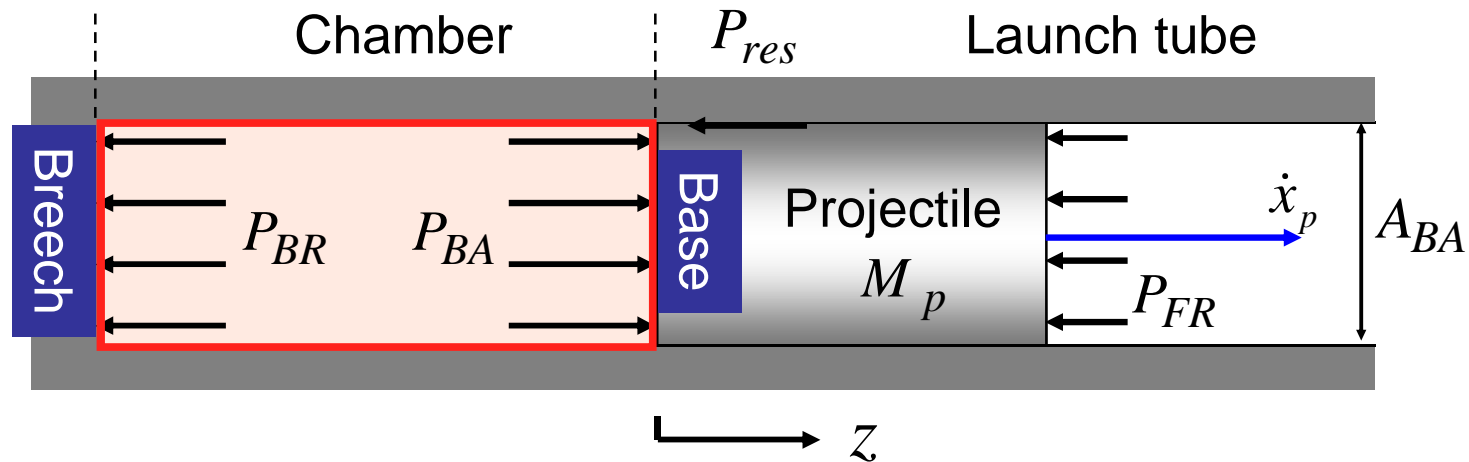
$$\text{Volume } V_{p,j} = \Delta L_{p,j} \left\{ \frac{\pi}{4} (D_p - 2\Delta u_j)^2 - \frac{\pi}{4} (d_p + 2\Delta u_j)^2 \right\}$$

$$\text{Surface area } S_{p,j} = \pi (D_p - 2\Delta u_j) \Delta L_p + \pi (d_p + 2\Delta u_j) \Delta L_{p,j}$$



Projectile Movement in Launch Tube

Kinetic model of projectile movement



P_{BR} : Breech pressure
 P_{BA} : Base pressure

P_{res} : Resistive pressure

Projectile velocity $\dot{x}_p = \int_0^t \ddot{x}_p dt = \int_0^t \left(\frac{(P_{BA} - P_{FR} - P_{res})A_{BA}}{M_p} \right) dt$



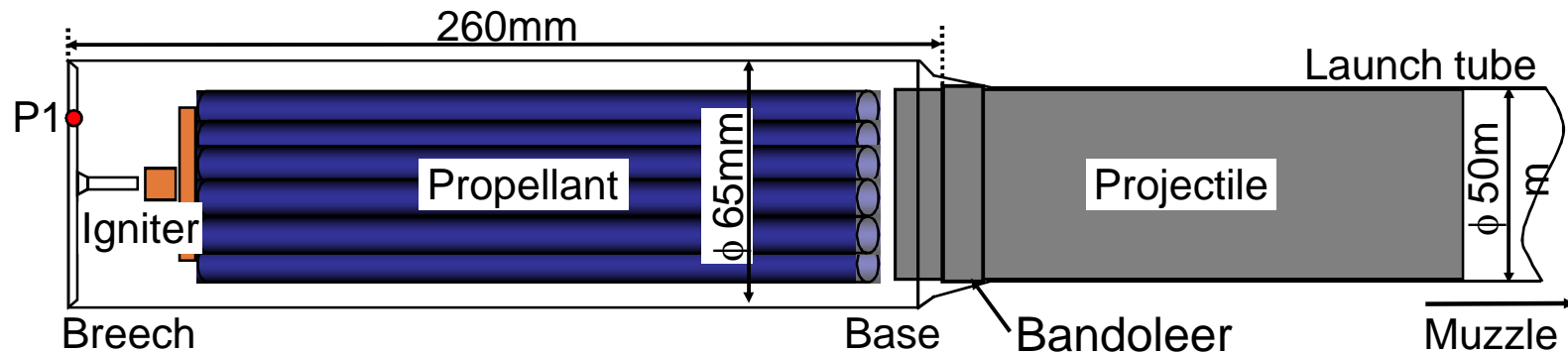
*Your complimentary
use period has ended.
Thank you for using
PDF Complete.*

[Click Here to upgrade to
Unlimited Pages and Expanded Features](#)

Interior Ballistics Simulation of 50mm Gun

Computational Model

Reproduction of the experiment of 50mm gun by NOF Corporation



The projectile velocity was recorded using an in-bore Doppler radar system.

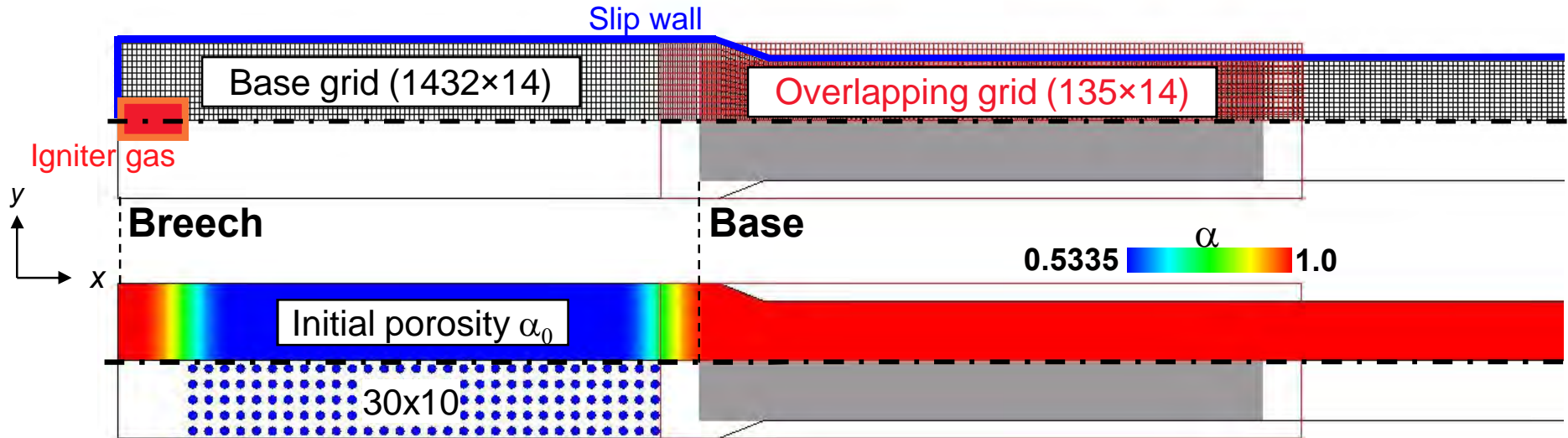
Computational data

Diameter of tube (mm)	50
Length of tube (mm)	3195
Projectile mass M_p (kg)	2.5, 3.5, 4.5
Propellant mass C (kg)	0.4, 0.5
Propellant type	Double-base
Shape of grain	Tubular (one hole)
Size of grain (mm)	$\phi 6.35 \times 200$

Propellant properties

Adiabatic flame temperature T_0 (K)	3133
Impetus F (J/g)	1036
Specific heat ratio γ	1.232
Density ρ_p (kg/m ³)	1615
Covolume b (cm ³ /kg)	993

Computational Setup



Calculation condition

Overlapping grid is movable

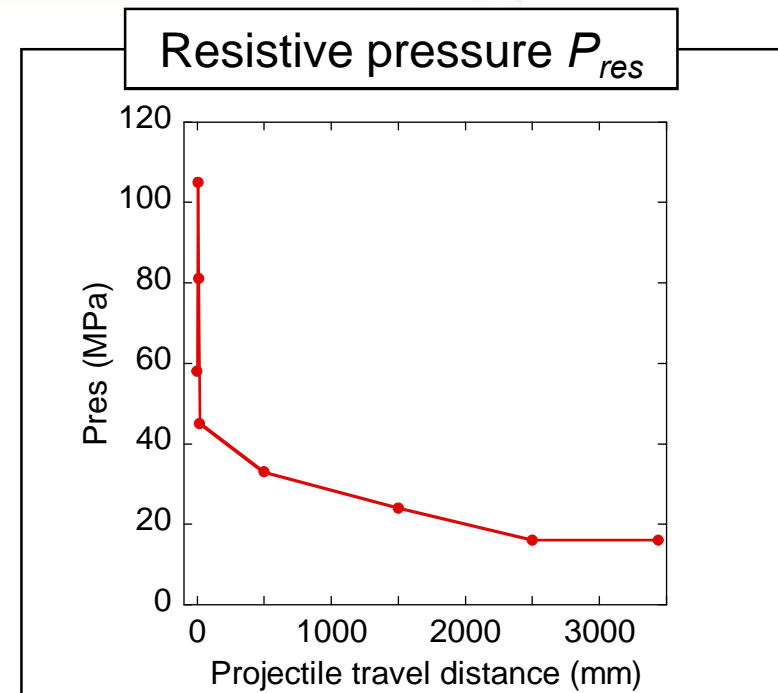
Wall condition : Adiabatic slip wall

Initial condition : 101kPa, 294K, $\gamma=1.4$

Calculation method

Discretization method of convection term
: SHUS (Shima and Jounouchi, 1995)

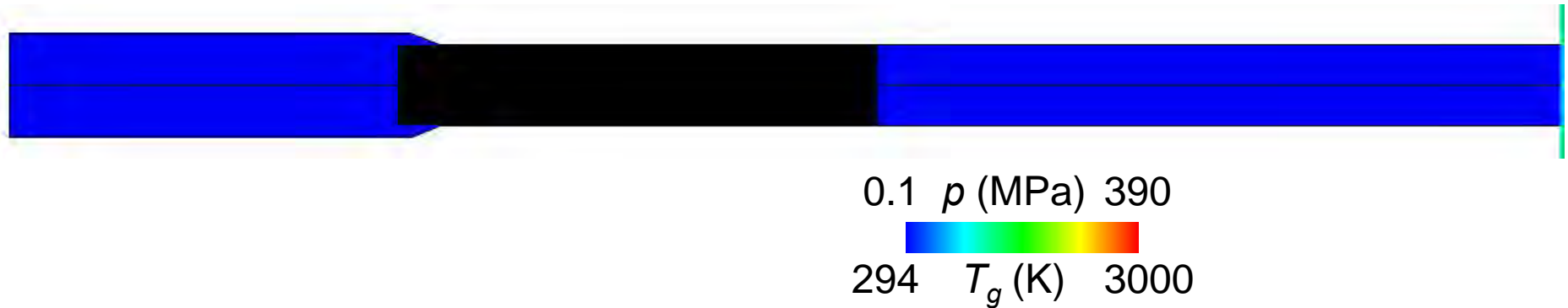
Time integration method
: 2-step Runge-Kutta method



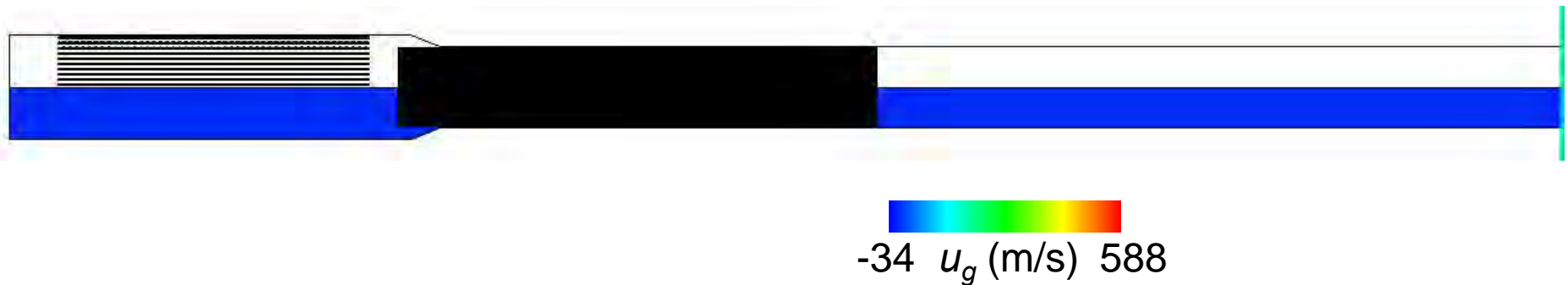
Accelerating Process

$$M_p = 4.5\text{kg and } C = 0.5\text{kg}$$

Pressure / gas temperature distribution

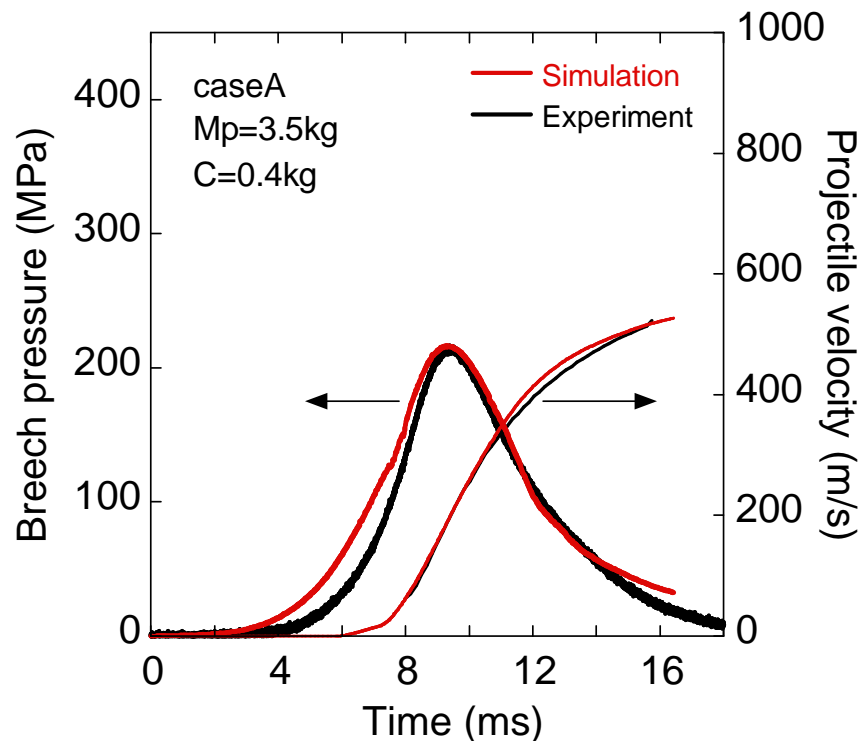


Propellant / gas velocity distribution

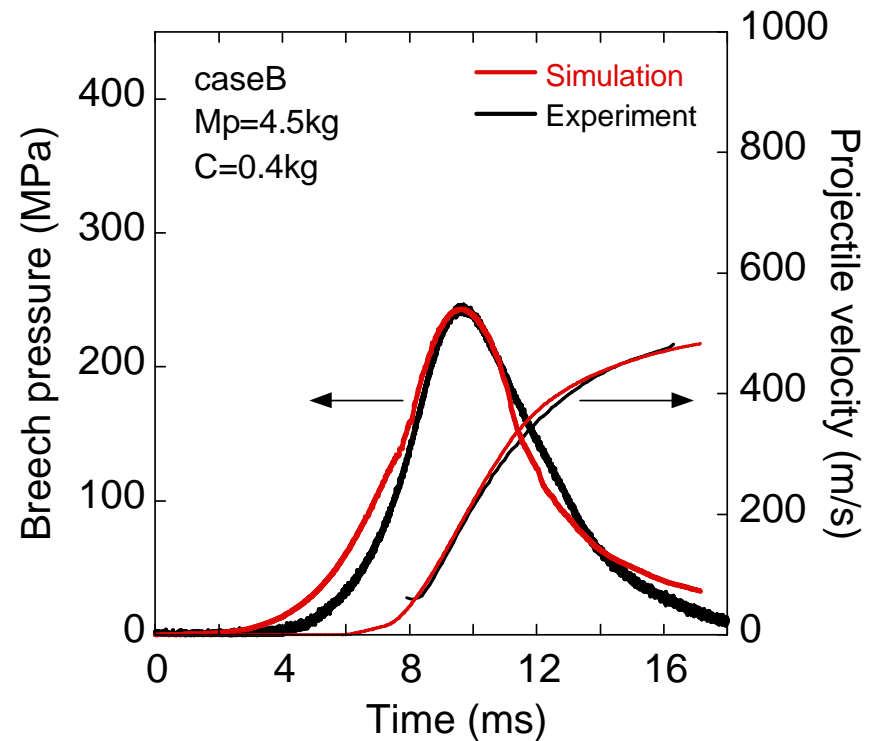


Comparison of Predicted Data with Experiment

Case A ($M_p=3.5\text{kg}$ and $C=0.4\text{kg}$)



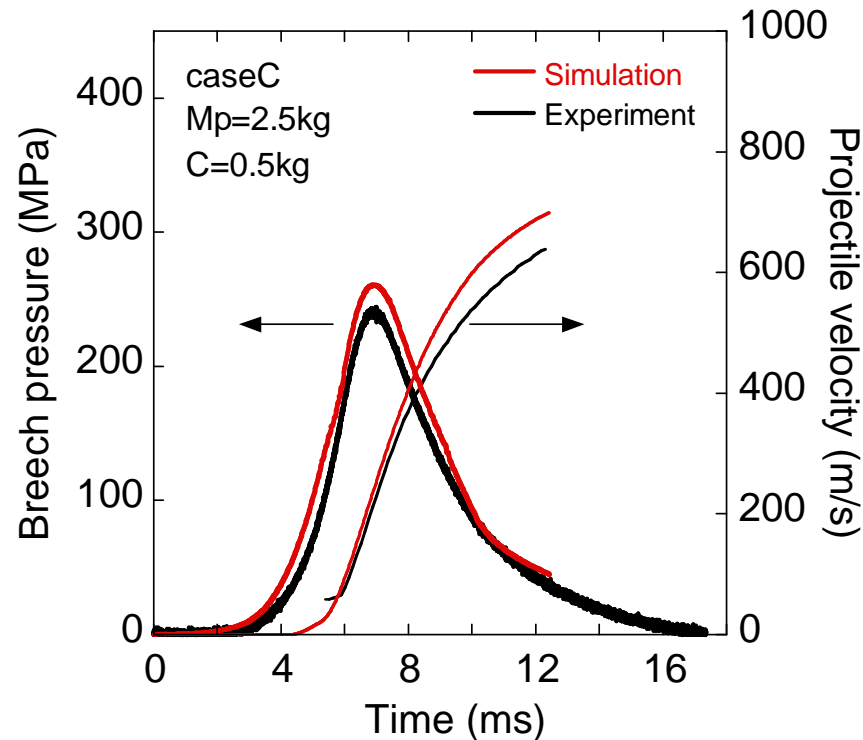
Case B ($M_p=4.5\text{kg}$ and $C=0.4\text{kg}$)



- Predicted histories of the breech pressure and the projectile velocity are in good agreement with the experimental data in the each case.

Comparison of Predicted Data with Experiment

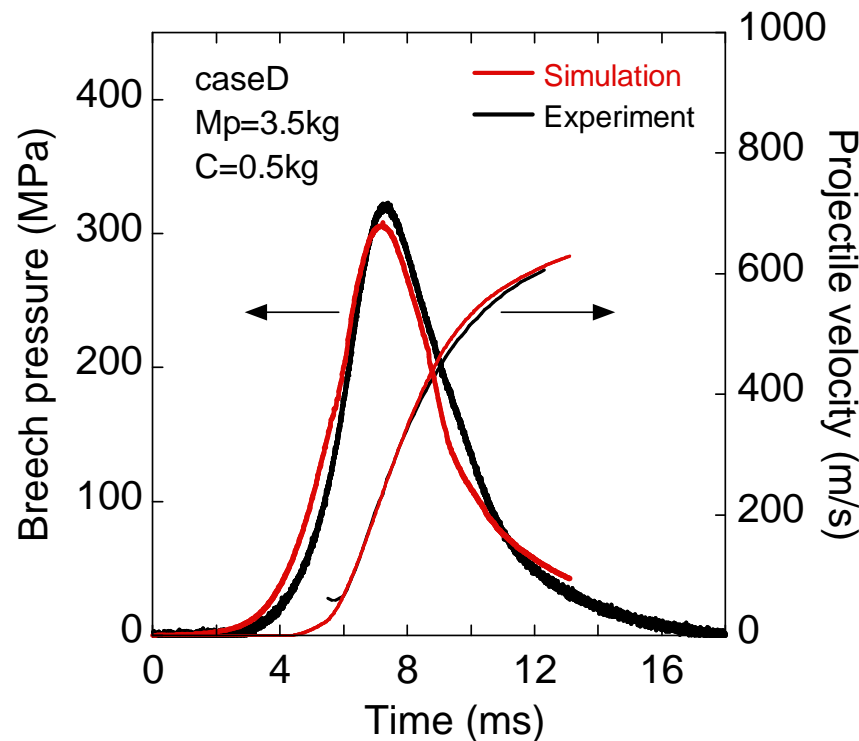
Case C ($M_p=2.5\text{kg}$ and $C=0.5\text{kg}$)



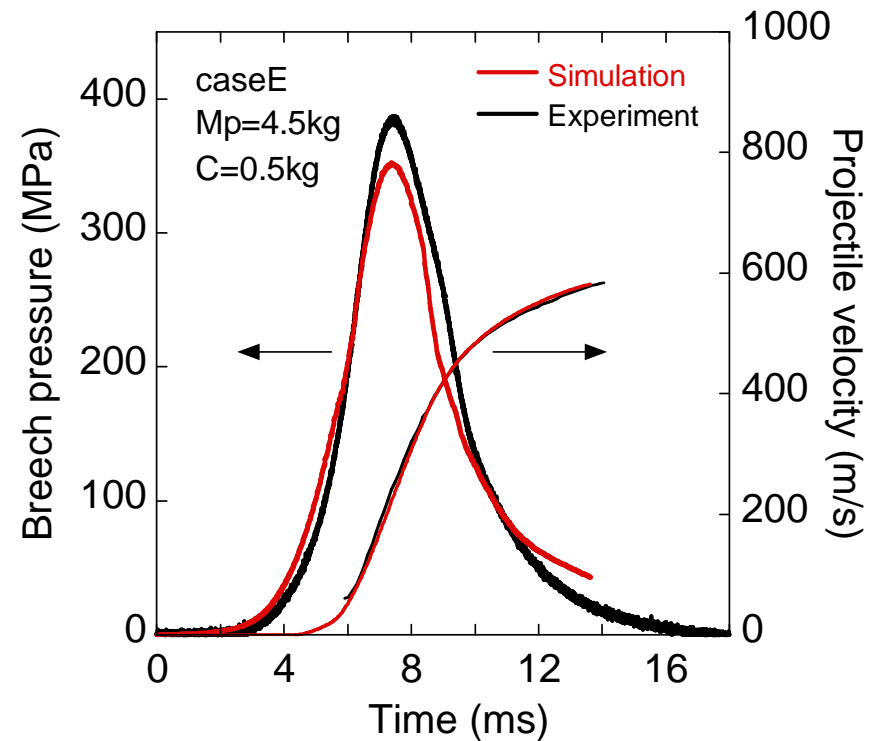
- ❑ Predicted breech pressure and projectile velocity are higher than the experimental data in this case.

Comparison of Predicted Data with Experiment

Case D ($M_p=3.5\text{kg}$ and $C=0.5\text{kg}$)



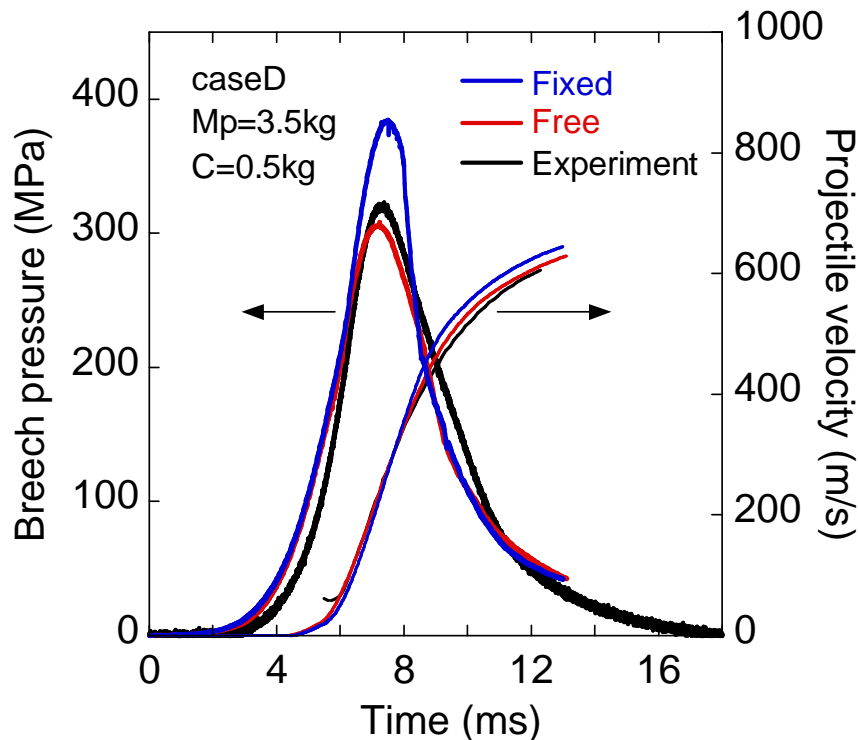
Case E ($M_p=4.5\text{kg}$ and $C=0.5\text{kg}$)



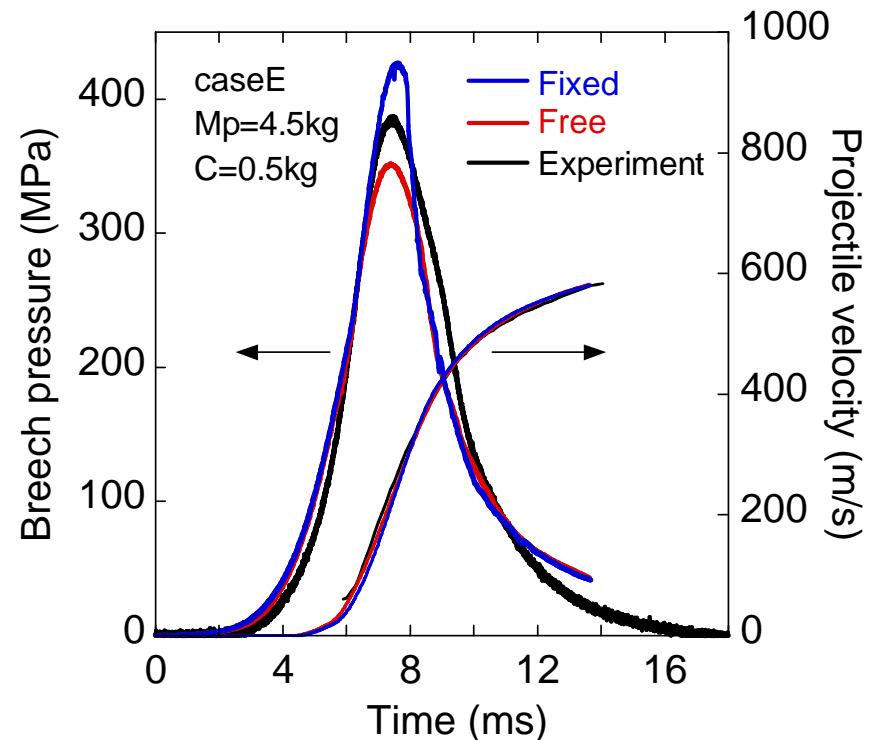
- Predicted histories of the breech pressure and the projectile velocity are in good agreement with the experimental data in the each case.

and Fixed Propellant Models

Case D ($M_p=3.5\text{kg}$ and $C=0.5\text{kg}$)



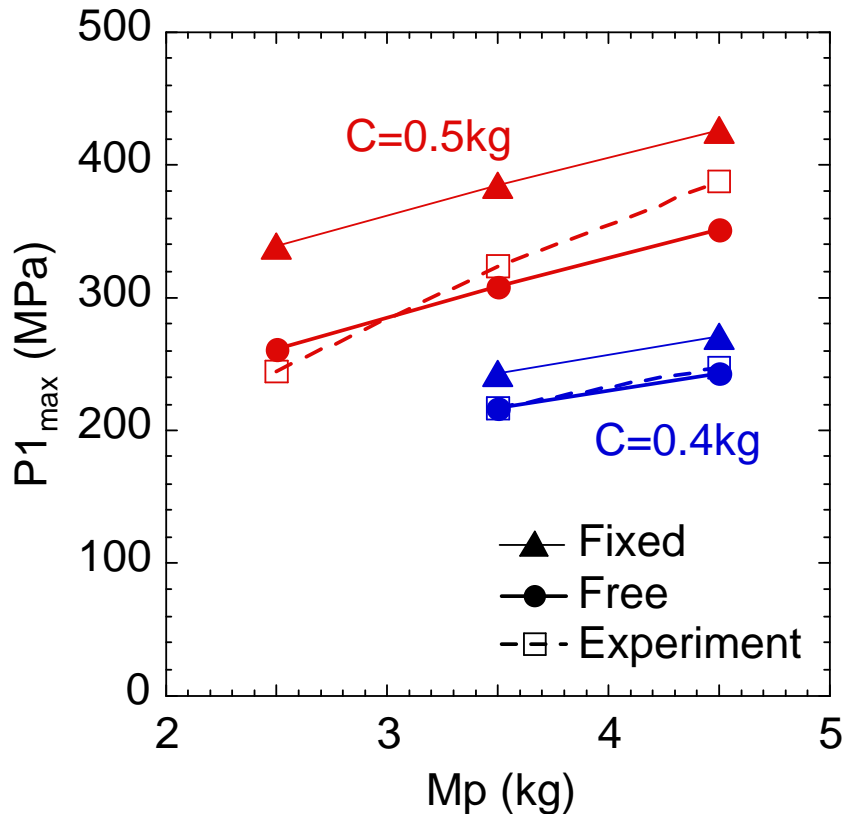
Case E ($M_p=4.5\text{kg}$ and $C=0.5\text{kg}$)



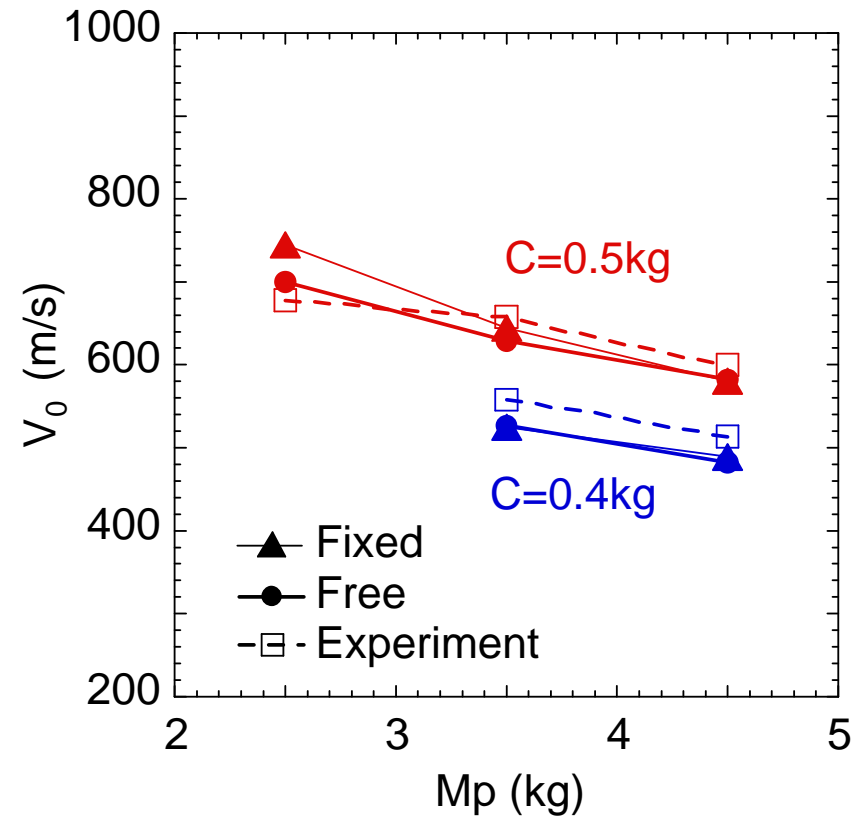
- ❑ If we use the fixed propellant model (without propellant movement), the predicted pressure becomes much higher than the free propellant model (with propellant movement).

and Fixed Propellant Models

Maximum Breech Pressure



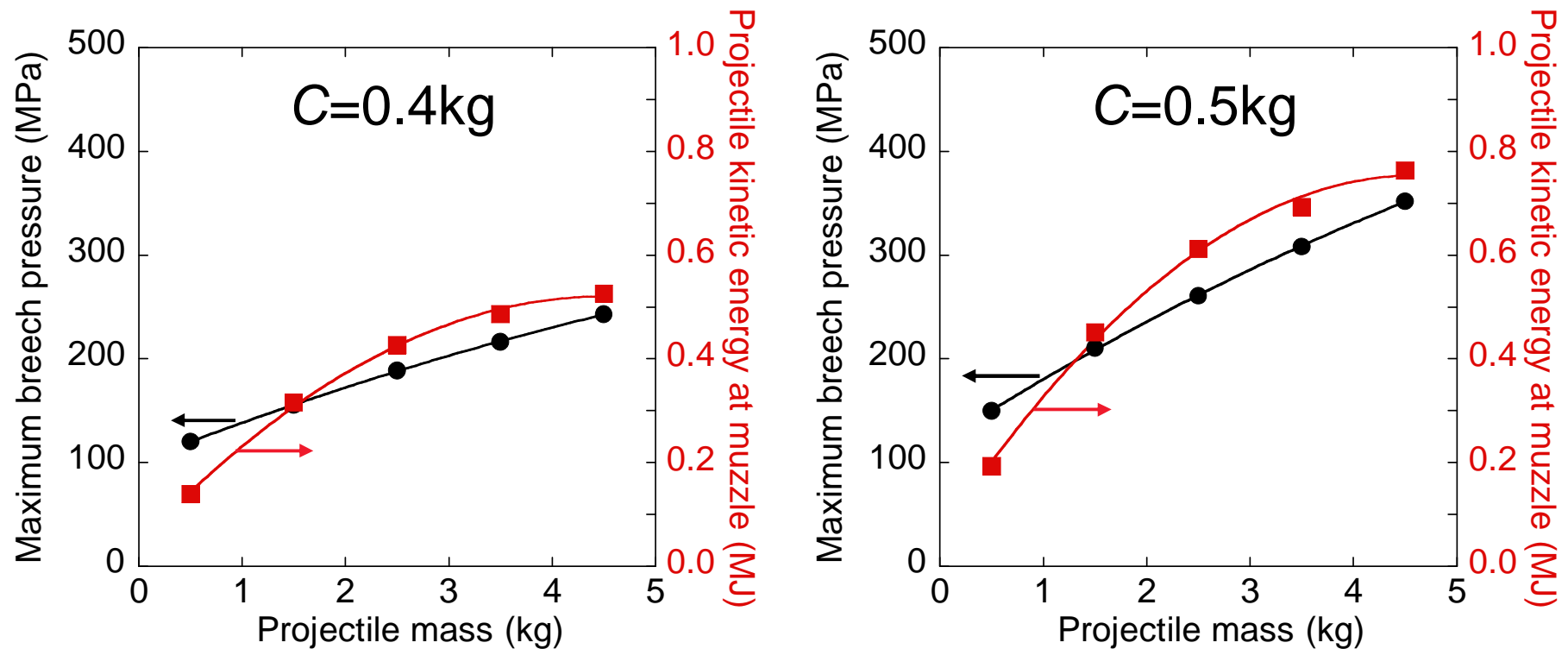
Muzzle Velocity



- ❑ The muzzle velocities of the two models were almost equivalent. However, the maximum breech pressure was overestimated by the **Fixed Model**, and the **Free Model** well reproduced the experimental maximum pressure.

ation of Projectile Mass

Simulated maximum breech pressure
and projectile kinetic energy



- ❑ The maximum chamber pressure increases linearly whereas the projectile kinetic energy converges with the projectile mass M_p .

Conclusion

The processes of accelerating a projectile by tubular solid propellant combustion in the 50mm projectile launch system were simulated for various cases using the developed 2D two-phase flow code and the moving overlapped grid method.

- ☐ In the comparison between the predicted results and the experimental data of various M_p and C condition, the results of the simulation with propellant movement showed being in good agreement with the experimental results.
- ☐ There was trade-off relation between the chamber pressure suppression and the projectile kinetic energy improvement. However, the projectile kinetic energy at the muzzle converged with increasing the projectile mass M_p .

Hiroaki MIURA

Belongs to Department of Mechanical Engineering
at Keio University in Japan

miura@mech.keio.ac.jp

dr074673@hc.cc.keio.ac.jp

Development of the NLOS-LS PAM Warhead

24th International Symposium on Ballistics

September 22 – 26, 2008
New Orleans, LA

NLOS-PAM Team



- Prime Contractor: NetFires LLC
 - Raytheon Missile Systems
 - Lockheed Martin Missiles & Fire Control



NLOS-PAM Overview

- Low cost, direct attack missile
- Provides precision fire support for the Brigade Combat Team and for USN Littoral Combat Ship



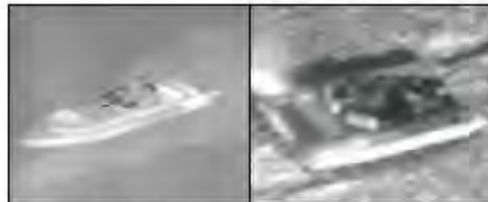


PAM System Description

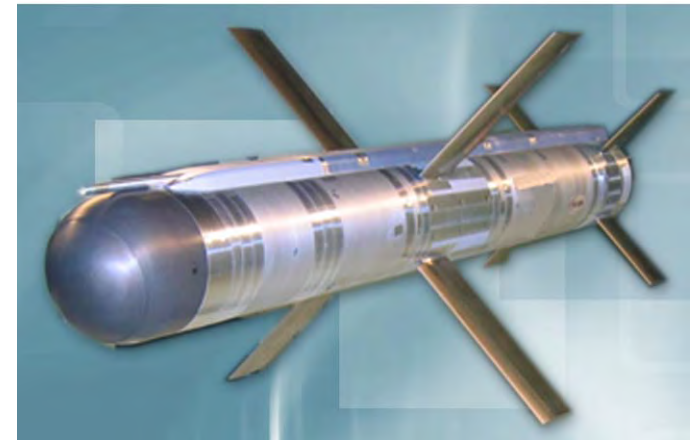
- Large multi-mode warhead
- 7-inch diameter 120 lb class
- Range 0-40 kilometers
- Effective against moving and stationary targets
- In-flight updates, retargeting and image capabilities
- Target sets
 - Light armor
 - Heavy armor
 - Bunkers
 - Fortifications



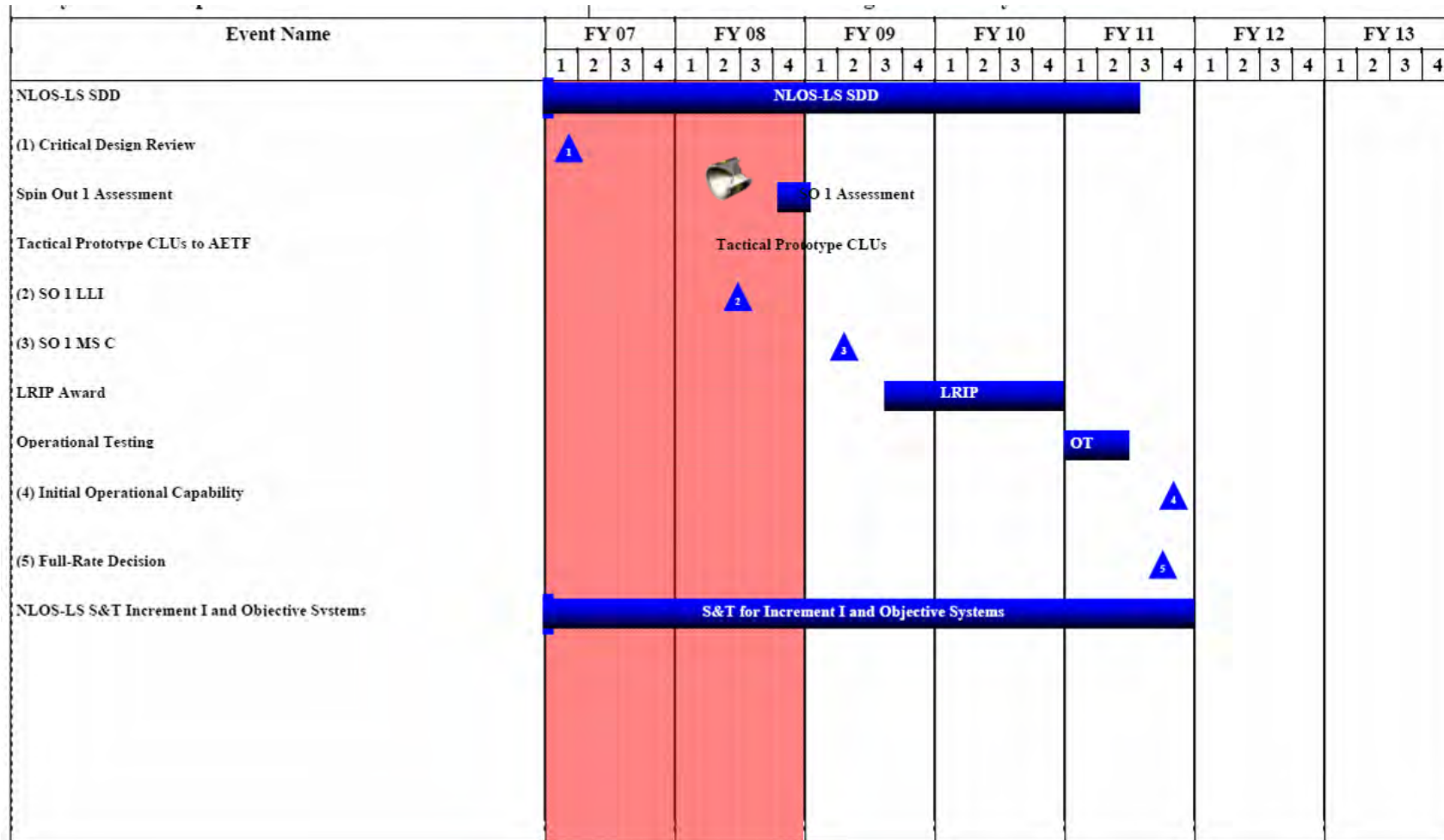
PAM Warhead Effectiveness



PAM Seeker Image of Land and Sea Targets



Program Schedule



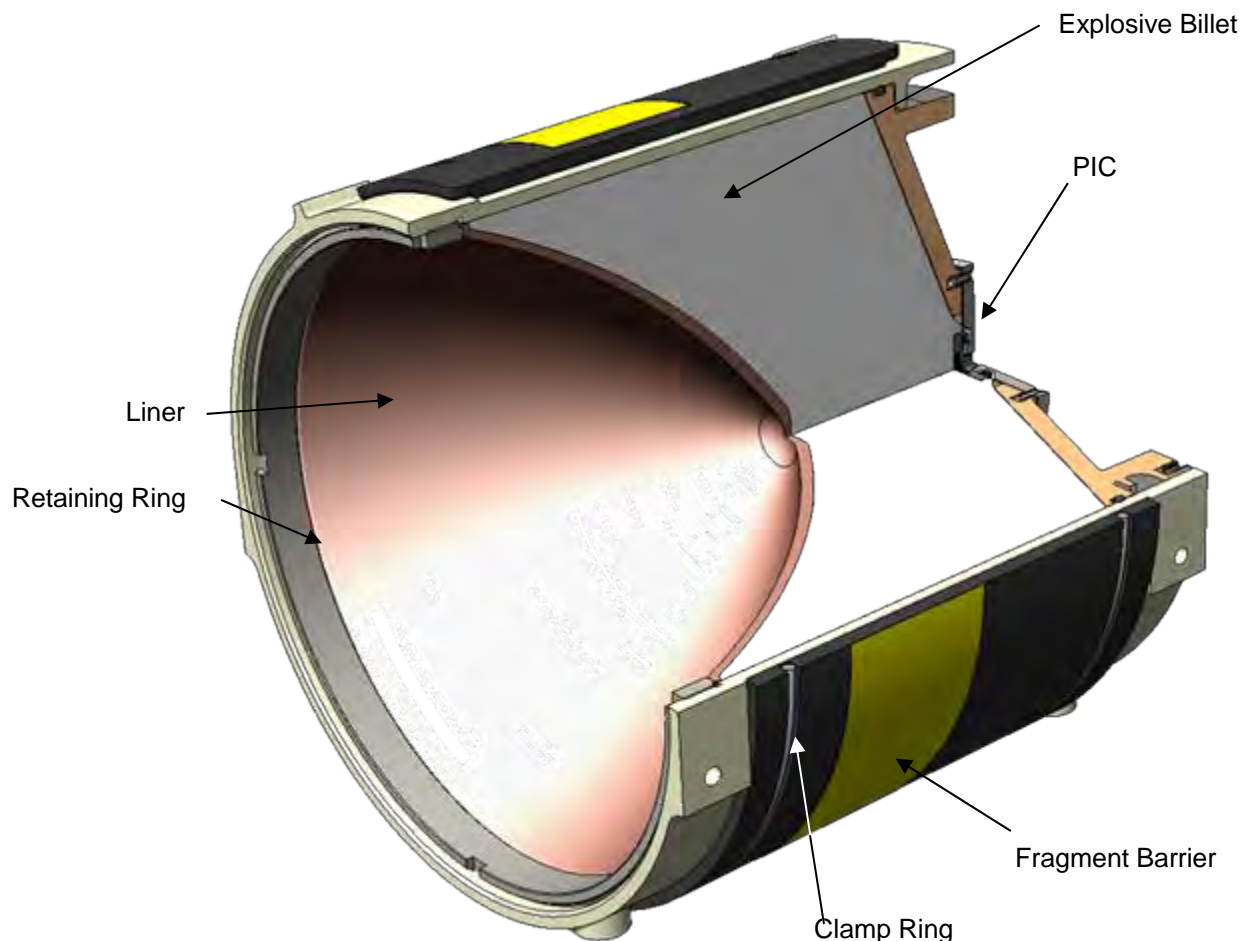
Multimode Warhead Challenges



- Short Stand-Off
- High Penetration Performance
- Strict IM requirements
- Cost as a Key Performance Characteristic
- Small Envelope
- Evolving Requirements



Warhead Overview





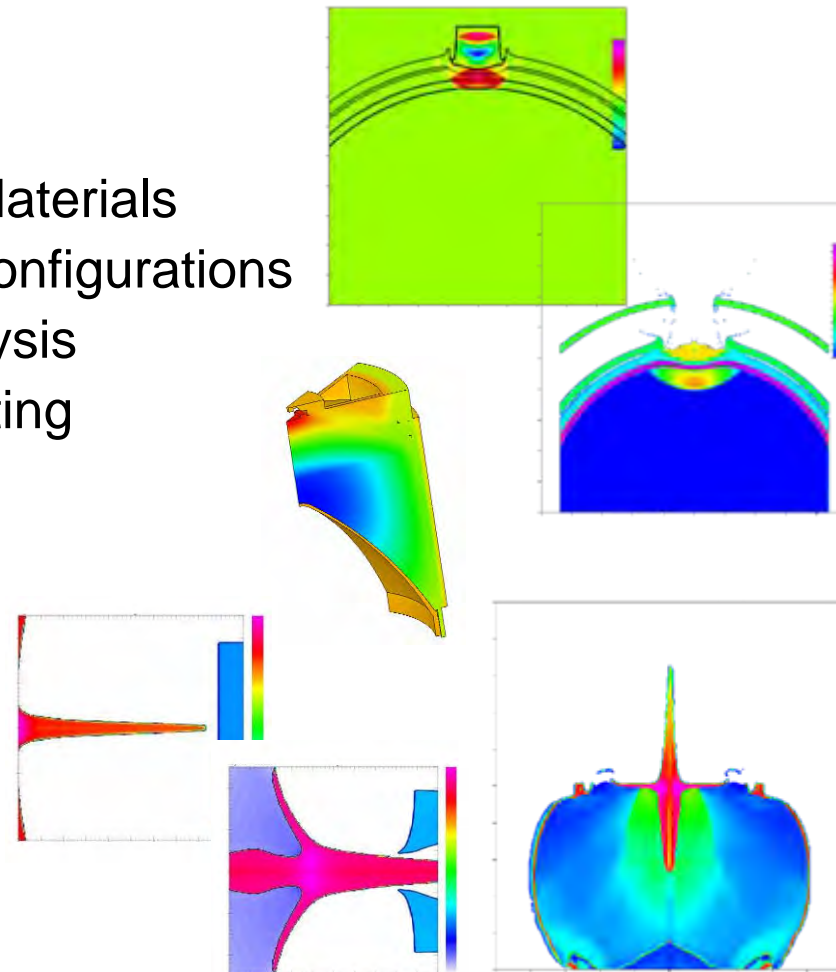
Warhead Development

- Competitive Risk Reduction Effort
 - Trade Studies
 - Explosive Material (Penetration Performance vs. IM Performance)
 - Casing Design (Materials to reduce sensitivity to Fragment Impact)
 - Liner Material Study (Penetration Performance vs. Cost)
 - Analysis
 - Penetration Performance (Hydrocode)
 - Seeker Keep Out Zone
 - Testing
 - Jet Characterization
 - RHA and Armor Targets (Penetration Performance)
 - Soft Targets (Arena and Bunker Testing)
 - Insensitive Munitions Testing (Slow Cook-Off and Fragment Impact)
- Followed by the Detail Design Phase



Modeling & Simulation

- Fragment Barrier Analysis
 - Understanding the Physics
 - Study the effects of different Materials
 - Study the effects of different configurations
- Slow Cook-Off Performance Analysis
 - Design Features to Allow Venting
 - Thermal Analysis
- Penetration Performance
 - 2D Hydrocode
 - Optimize Design
- Jet Characteristics
 - 3D Hydrocode
 - Ensure Straightness of Jet





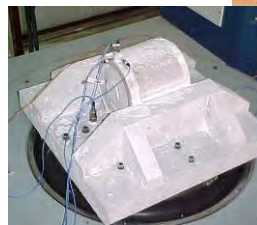
PAM Warhead Performance

Key Characteristic	Performance
Range target penetration depth	
Range target penetration diameter	
RHA penetration	
Mass	
Design to cost	



Performance Testing

- Tested 5 Different Design Variations
- Conducted over 100 Explosive Tests
 - Arena Testing
 - Jet Characterization
 - RHA Penetration
 - ERA Target Penetration
 - Environmental Testing
 - Behind Armor Debris Testing
 - Reliability (Vari-Comp)



IM Testing



Threat	Test Results
Fast Cook-off	Type V
Slow Cook-off	Type V
Bullet Impact	Type V
Fragment Impact	Type V
Sympathetic Detonation	Type V*
Shaped Charge Jet	Type I*

*=Expected



Production Readiness

- Lean Design Effort
 - Use Low Cost Materials
 - Reduction of the number of Parts
 - Incorporation of Molded Components
 - Detail tolerance stack up analysis to optimize tolerances
 - Work with each component Vendors on reducing Cost Drivers
 - Streamline Assembly Process
- Early Development of Acceptance Testing
 - Perform Lot Acceptance Tests (LAT) to Characterize Variation
- Control of Critical Characteristics
 - Characteristics that mostly control performance variation
- Pilot Production Line incorporated on Qualification Build





Design Challenges

- Striking a Balance between Low Cost and High Performance
- Integrating Production Processes early on
- Mitigating Fragment Impact and Slow Cook-Off Hazards
- Maintain Performance with Environmental Factors
- Incorporating Environmentally Compliant Processes and Products



Acknowledgements

- Raytheon Missile Systems
 - Bill Zarr
- ARDEC
 - Darin Kielsmeier



Ballistic Performance Assessment of Lightweight Body Armour Material Systems Against IED Threats

by

G. Pageau, Scientific Advisor ISSP
K. Williams, PM AMMPHS TDP, DRDC-Valcartier
D. Bourget, GL PPE Group, DRDC-Valcartier
C. Hedge & M. Cheng, Allen-Vanguard
B. Ancil, Biokinetics Ltd

24th International Symposium on Ballistics
22-26 Sept. 2008, New Orleans, LA, USA



Canada



Overview

- Background
- Goal/approach
- Threat comparison
- Protection levels options
- Test results
- Summary
- Future work
- Questions





Background

- Military **soft armors** mainly designed to defeat **lower mass/velocity fragments** from warheads detonating at large distances
- Bullet resistant **rigid armors** mainly designed to defeat standard **rifle bullets** fired at close distances, with no fragment resistance specified
- Ballistic threat spectrum wider and more complex
- PPE (soft & hard) **not designed and neither specified** to protect against blast effects and fragments impacts from **IEDs**





Goal

- Increase soldier survivability against IED threats at no extra PPE weight

Approach

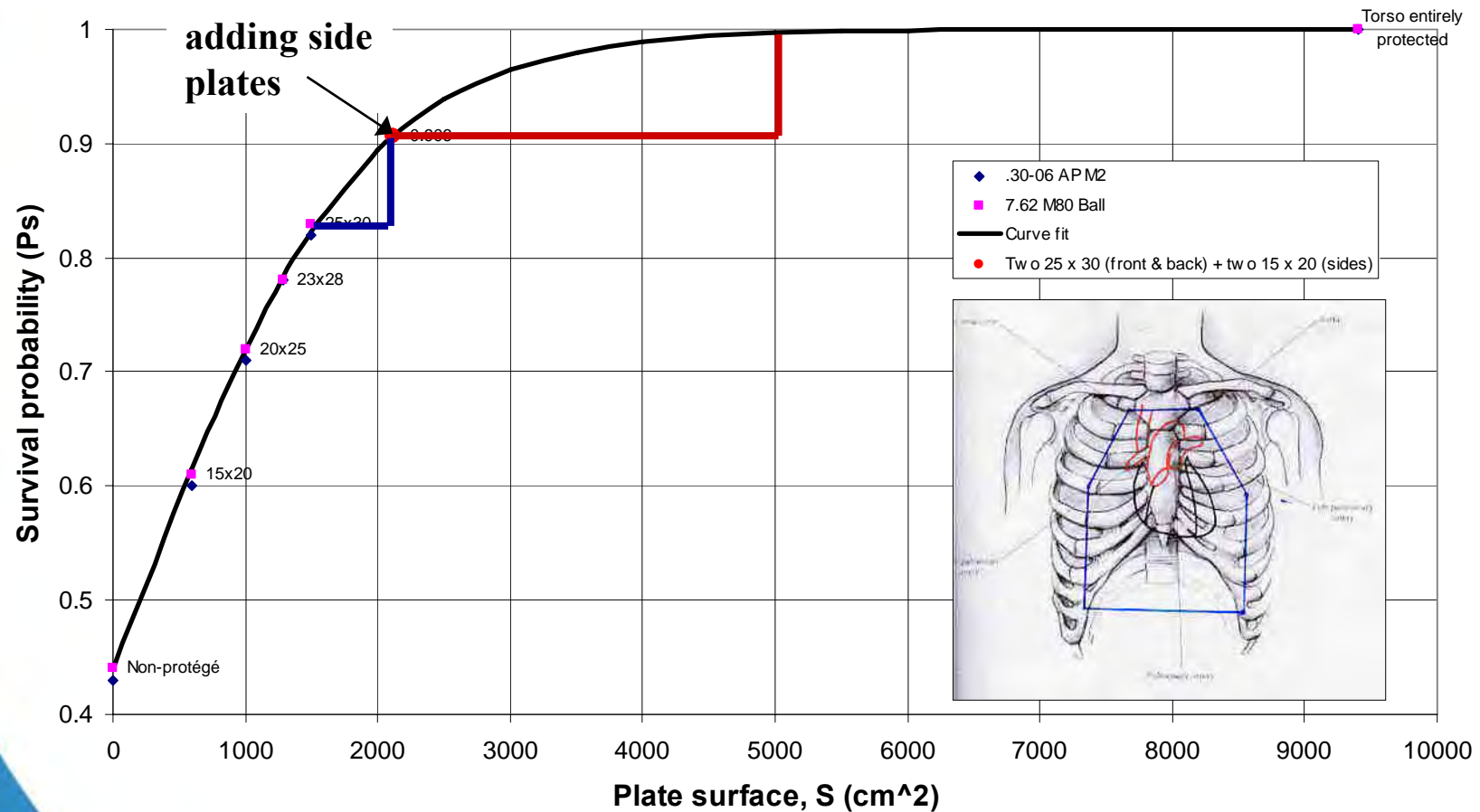
- Reduce current PPE weight:
 - Soft Armour:
 - 20% weight saving with same requirements
 - 30% weight saving with lower requirements
 - Hard Armour:
 - 20% weight saving with same requirements
 - 30% weight saving with lower requirements
- Apply weight savings to better match the threat
 - Provide novel IED specific armour components





Torso Coverage Study

- Desirable: uniform coverage of vital organs





Threat Review: Fragments

- Natural fragmenting munitions
 - Large number of fragments (7000-14000) of all sizes (0.5 to 500 gr)
 - Made of steel typically, 30 Rc hardness
 - Initial velocity from 1000 to 1800 m/s
 - L/D or shape factor variable typically 0.5 to 1.1
- Pre-formed fragmenting munitions
 - Spheres:
 - Mines: 7/32 in sphere (0.7 grams)
 - Grenades: 2.5-3.0 mm sphere (0.12 grams)
 - Cubes, steel or tungsten
- Controlled fragmentation





IED Threat Implications

- **Closer proximity from detonation**
 - Higher fragment density & velocity
 - At short range: blast arrive before fragments thus the need for live field tests
 - Fragment impact about simultaneous
 - More frequent negative impact angle
 - Larger fragment variability
 - Size, shape, material





Fragment Surrogates

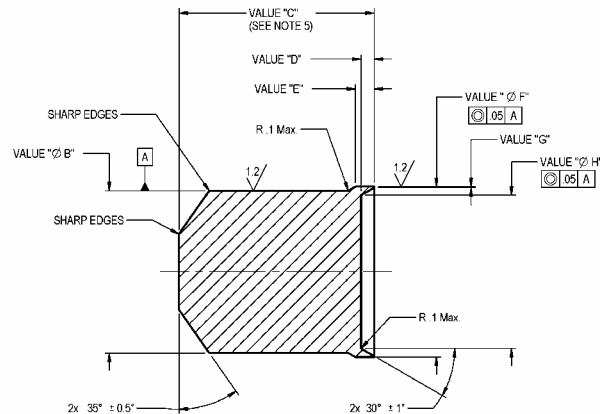
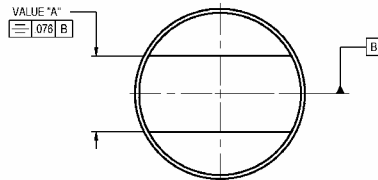
- Primary fragments:
 - FSP 1.1-g chisel nose, $L/D = 1$
(MIL-P-46593 & Stanag 2920 & 4569)
 - Skirted vs unskirted versions
 - RCC flat nose ($L/D = 1$ or $L/D < 1$)
 - Required for CRA (V_s - V_r data)
 - Std sizes: 2, 4, 16 and 64-gr, (128-gr)
 - Based on DeLuca work at AAMRC (V_s/V_r match)
- Secondary fragments:
 - Behind armor debris FSP, shorter, $L/D = 0.4$ (rarely used)
- Possible to design special size for custom threats using homogeneous scaling





Fragment Simulating Projectiles (FSP) (STANAG 4569)

Fragment Simulator	Weight (grains)	A (mm)	Ø B (mm)	C (mm)	D (mm)	E (mm)	Ø F (mm)	G (mm)	Ø H (mm)
FSP 1: 5.56 mm	17±0.5	2.54-0.3	5.46±0.02	6.52	0.4±0.05	0.6±0.05	5.72±0.05	0.08±0.04	5.0±0.1
FSP 2: 7.62 mm	44±0.5	3.45-0.3	7.52±0.02	9.30	0.73±0.05	0.86±0.05	7.87±0.05	0.12 max	6.93±0.25
FSP 3: 9 mm	64±0.5	4.03-0.3	8.69±0.05	9.17	0.4±0.05	0.6±0.05	9.04±0.05	0.12 max	8.42±0.05
FSP 4: 12.7 mm	207±2	5.69-0.4	12.83±0.05	15.24	1.15±0.05	1.47±0.05	12.75±0.08	0.13 max	11.43±0.05
FSP 5: 14.5 mm*	322±2	655-0.4	14.40±0.05	18.00	1.36±0.05	1.68±0.05	15.01±0.08	0.15 max	13.25±0.12
FSP 6: 20 mm	830±4	9.27-0.4	19.89±0.05	24.00	1.62±0.05	2.31±0.05	20.83±0.08	0.2 max	18.80±0.12





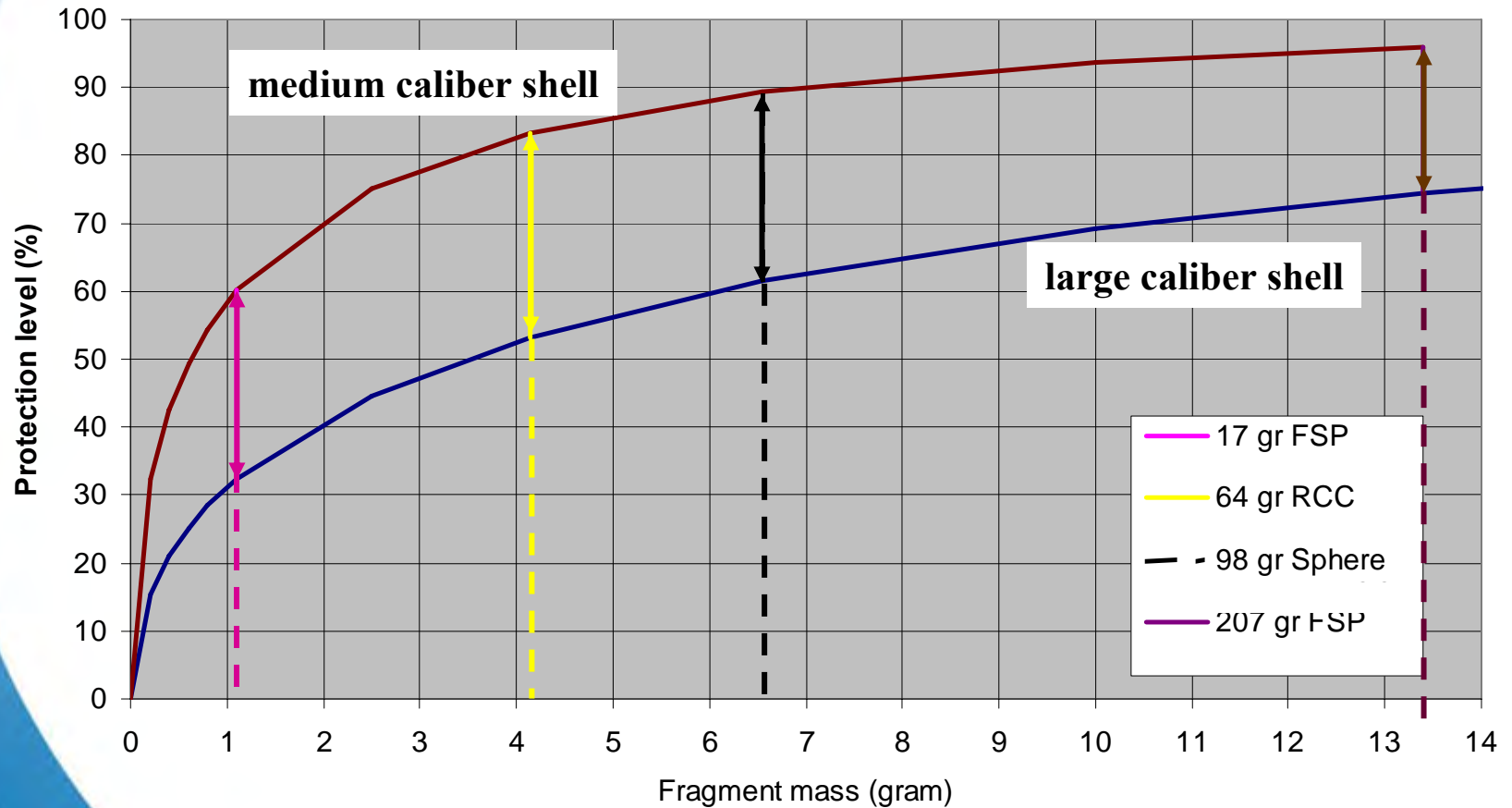
96-gr Sphere Fragment

- 11.5 mm diameter, steel HRC 60
- Dimensions, shape & weight very consistent
- Easily available at low cost
- Easily launchable, i.e.: no issues with:
 - sharp edges & hardness
 - flight stability (no yaw)
- More relevant to IEDs & controlled fragment munitions:
- Fill weight gap between 64 gr RCC & 207 gr FSP



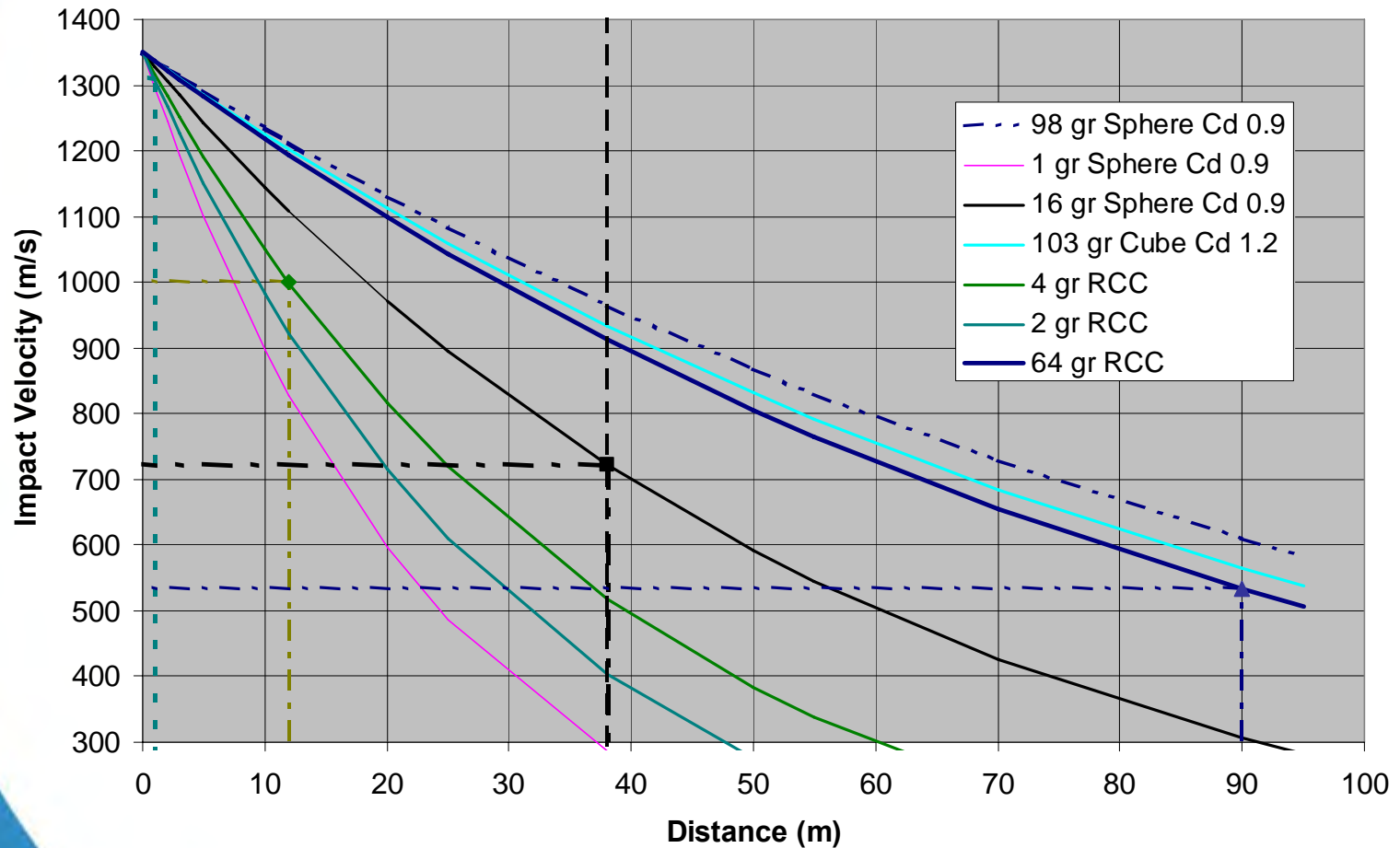


Protection Level vs Fragment Size



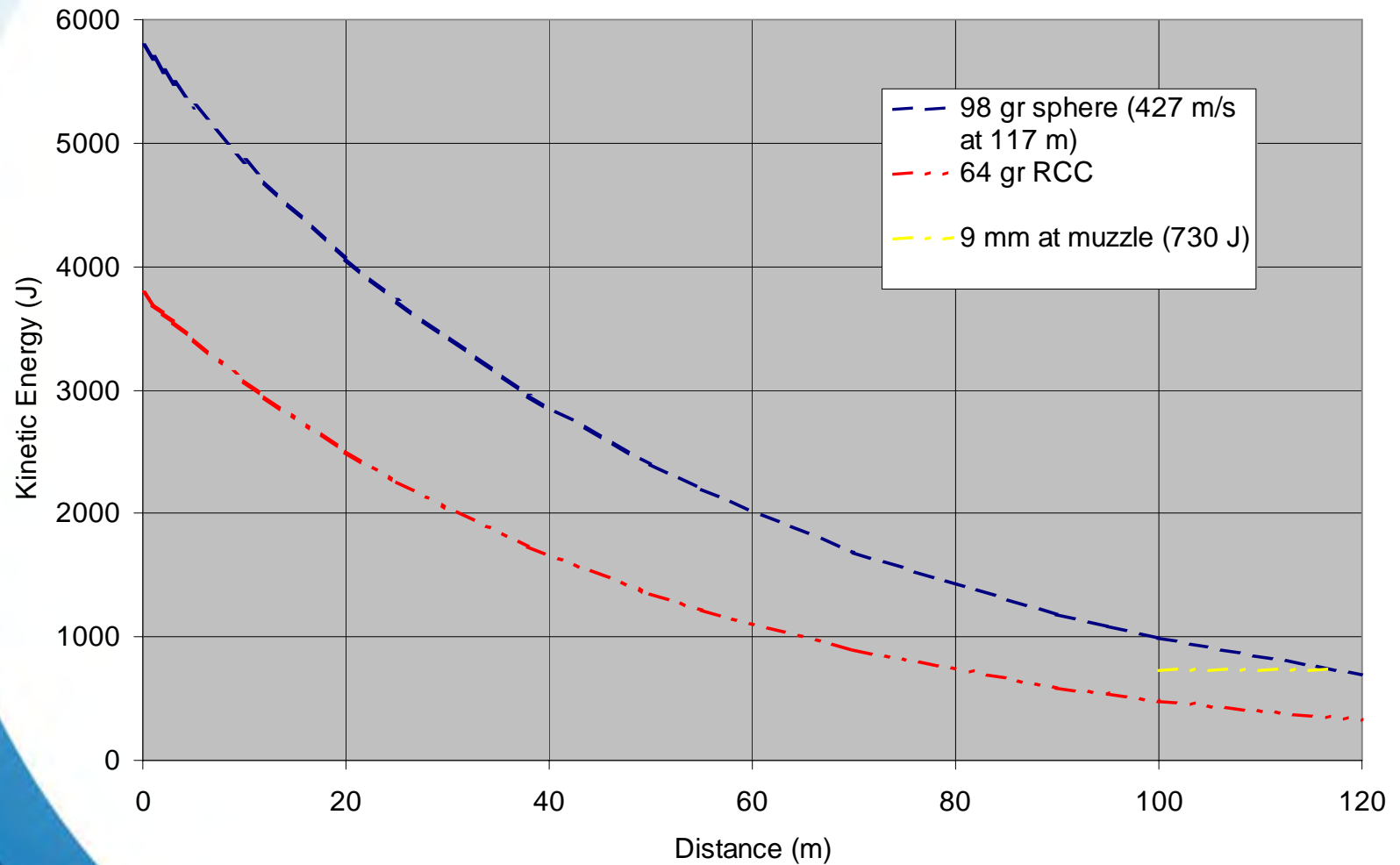


Velocity Decay vs Fragment Mass & Shape



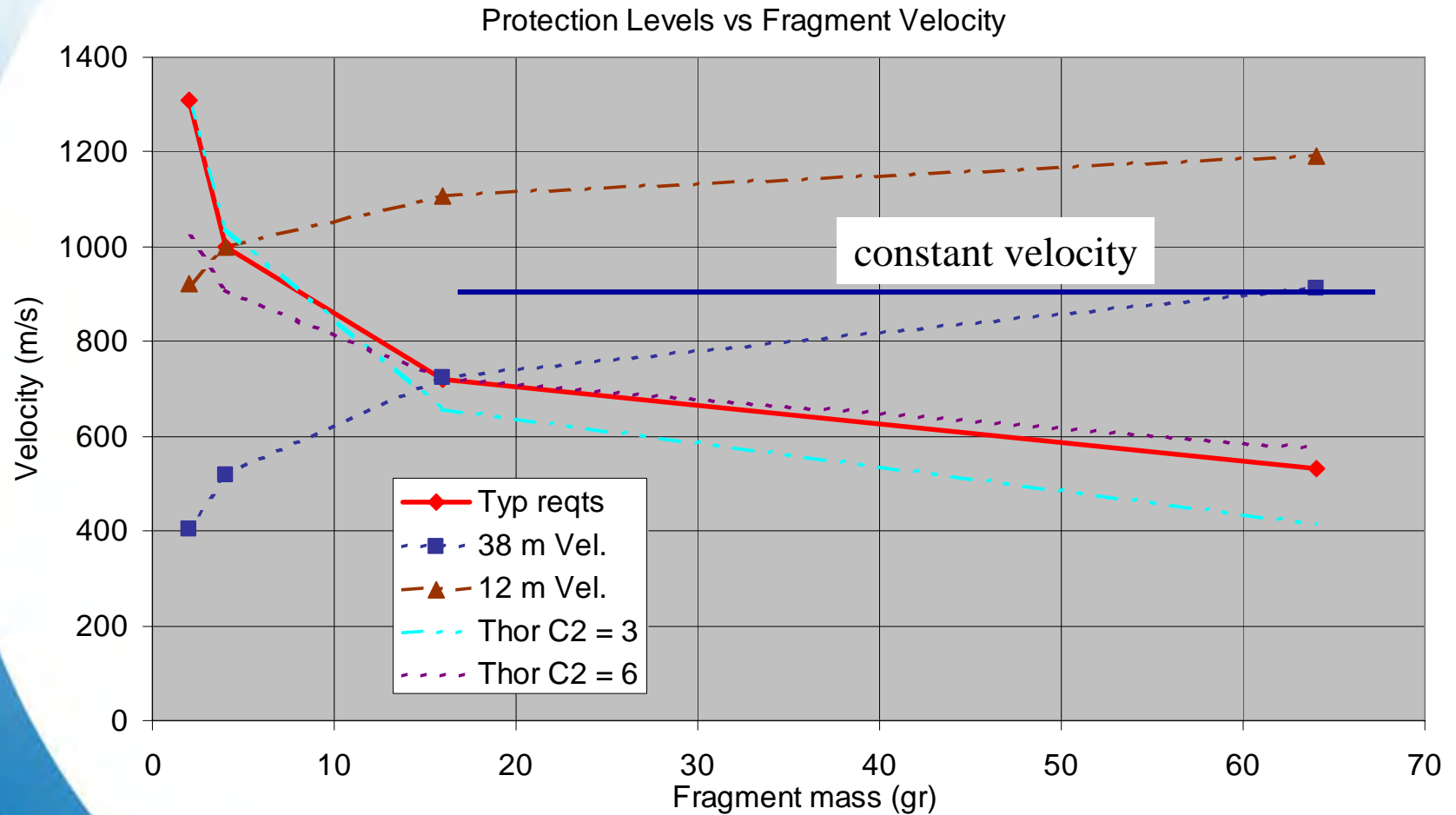


Kinetic Energy Comparison





Threat Velocity Specifications





Test Projectiles

- **Fragments:**
 - 16 gr sphere
 - 96 gr sphere 1000 m/s
 - 17 gr FSP
 - (207 gr FSP)
- **Bullets:**
 - 9 mm FMJ NIJ level 2
 - 5.56x45 SS109 STANAG level 1
 - 7.62x51 M80 NIJ level 3





Soft Armor Targets (AD 2.5 kg/m²)

- Polyethylene (PE) felt
- Aramid fabrics
 - K129
 - KM2
 - Special
- Hybrids



Typical samples photos



Hard Armor Targets (AD 20 kg/m²)

- Metallic
 - Aluminum (6061 & 7075-T6)
 - Magnesium (AZ31B-H24)
 - Titanium (Ti-6Al-4V)
- Polyethylene unidirectional composites (PEA, PEB, PEC)
- Metallic/composite
- Ceramic/composite (Plates)
- Hybrid (S-Glass, PE, Aramid + Ti & Al)



Metallic plate ans 2008



Aluminum (front)



Magnesium (back)



Test Conditions

- 38 x 38 cm samples
- Rigid armour targets tested stand-alone
- Some combinations tested in conjunction with soft armour
- Limited tests done at obliquity

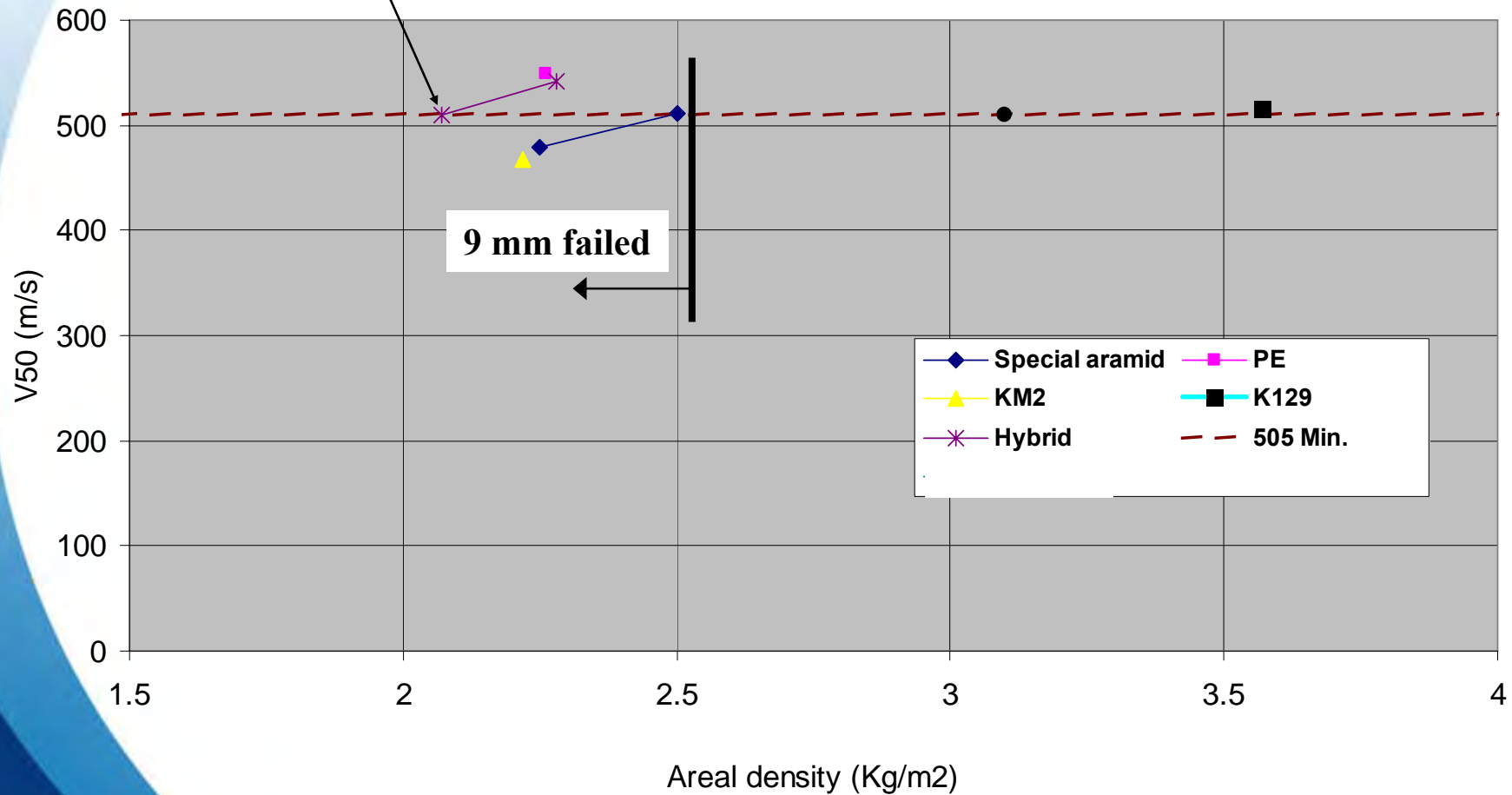
Test Types

- V50 (6 shots)
- Teta 50
- Vproof and backface
- Targets supported on Minicell foam support except for Vbfs using plastilina block



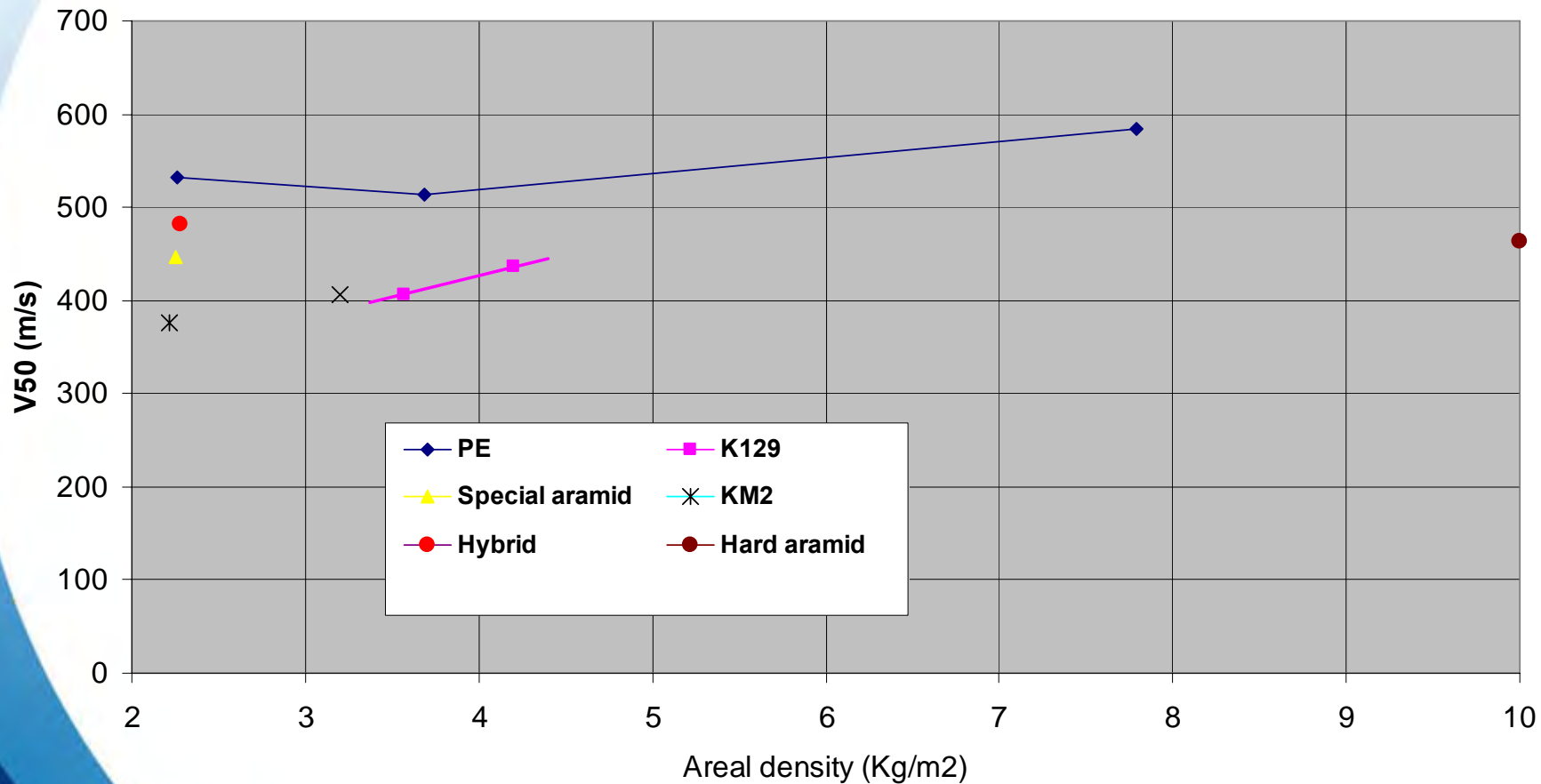
Soft Armor Performance (17-gr FSP)

Lightest solution
meeting 17 gr reqts



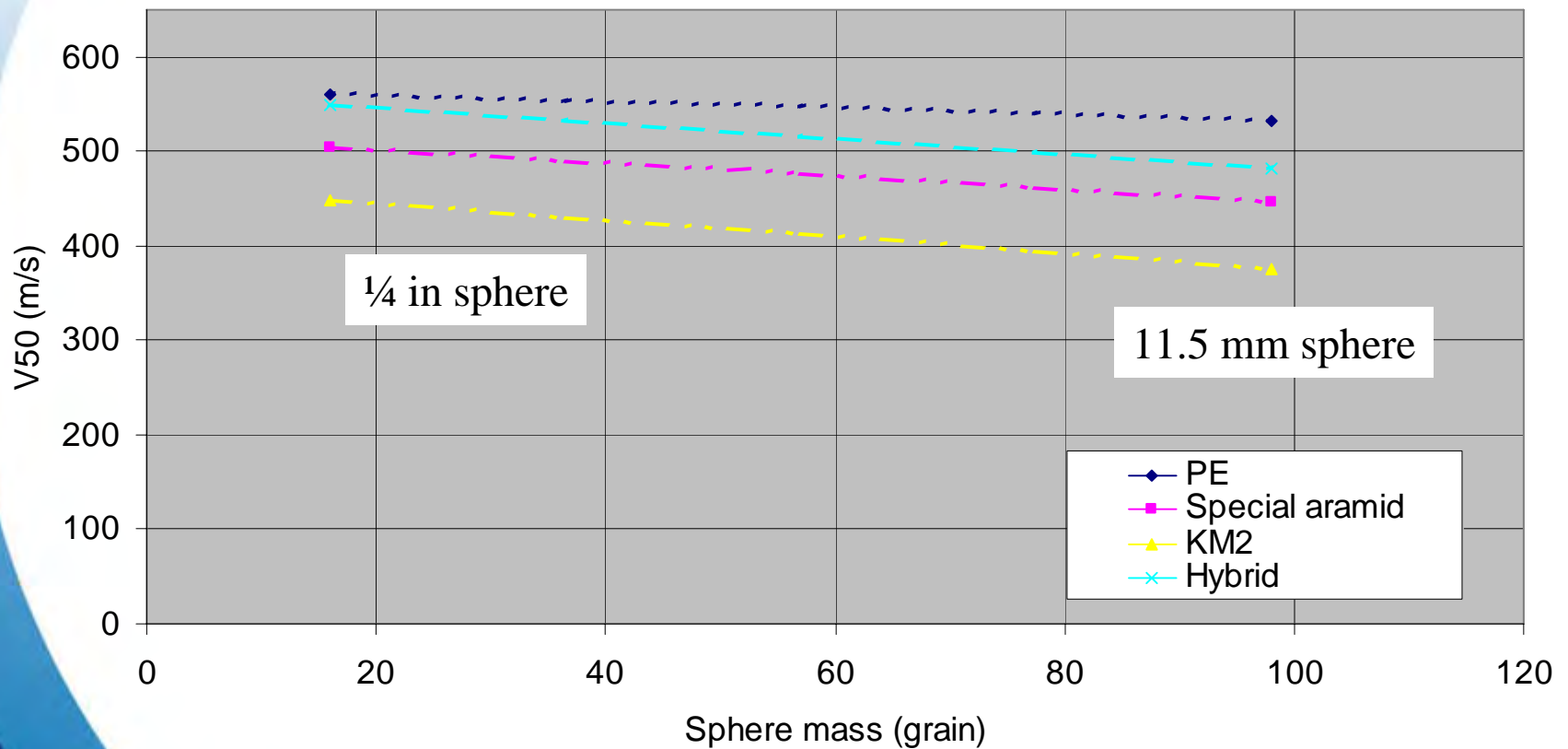


Soft Armor Performance (96-gr Sphere)



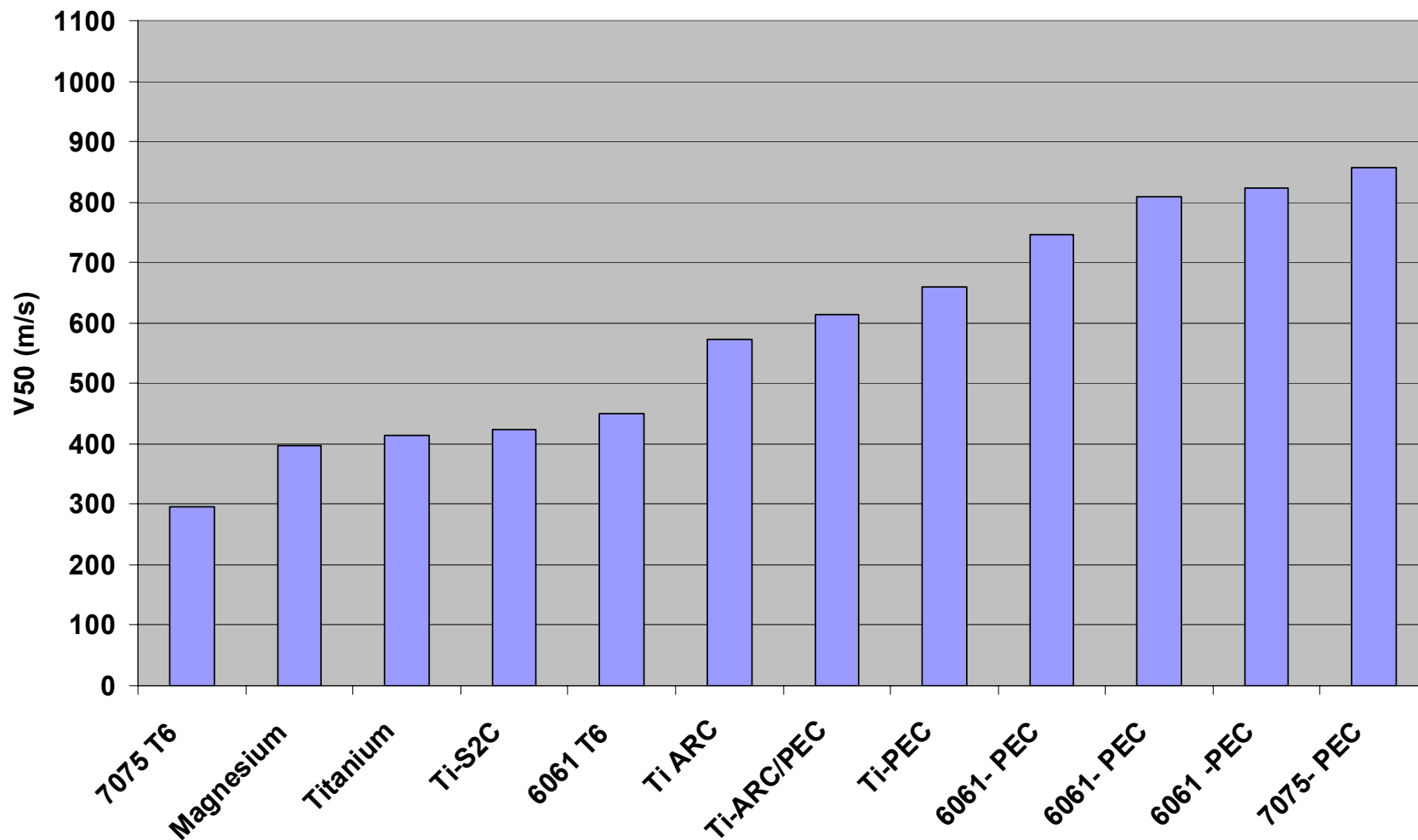


Soft Armors Results vs Sphere Mass



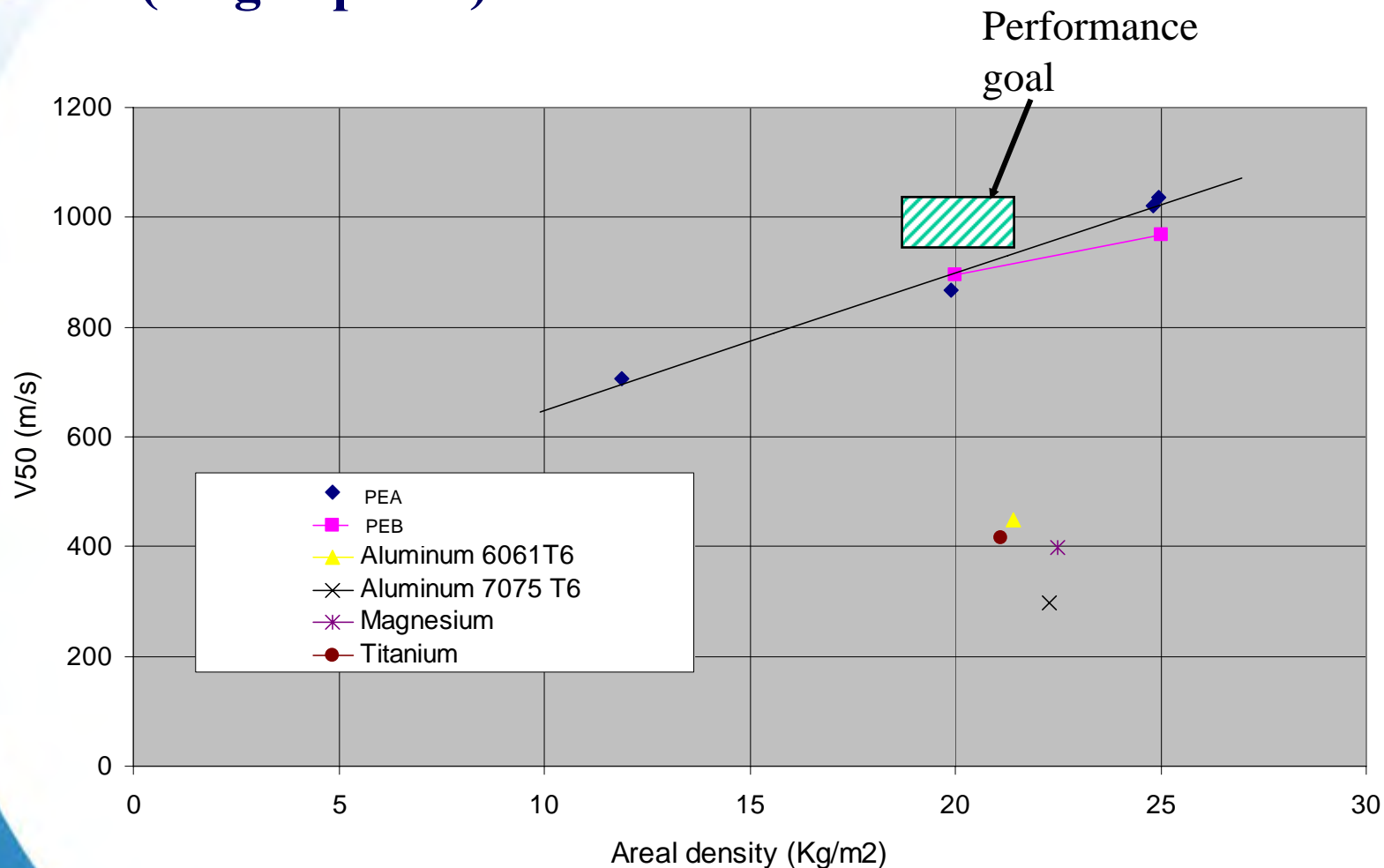


Hard Armor Performance Comparison (AD 20 Kg/m²)



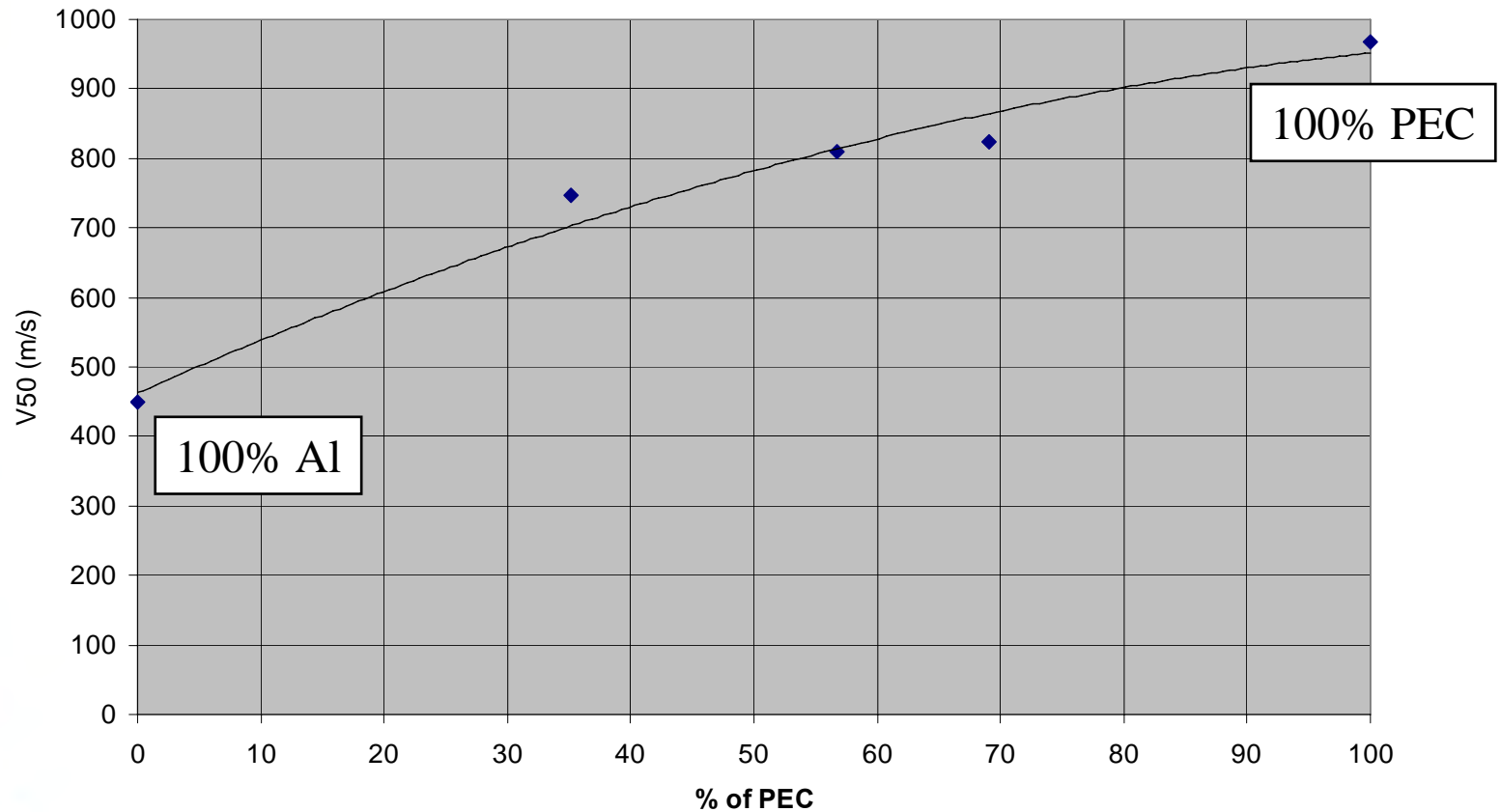


Hard Armour Performance (96-gr Sphere)



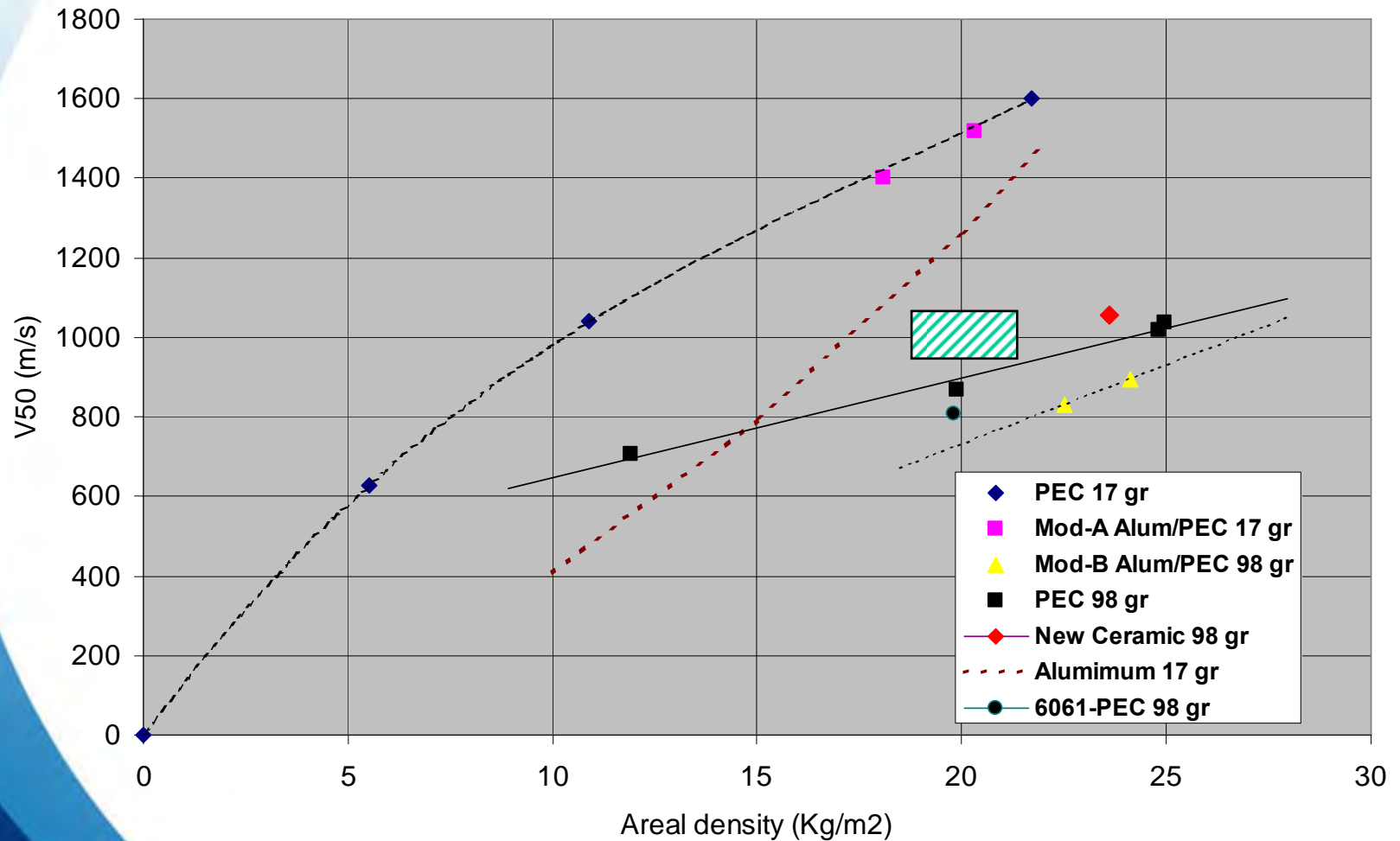


Aluminum/PEC Ratio Study (96-gr sphere)



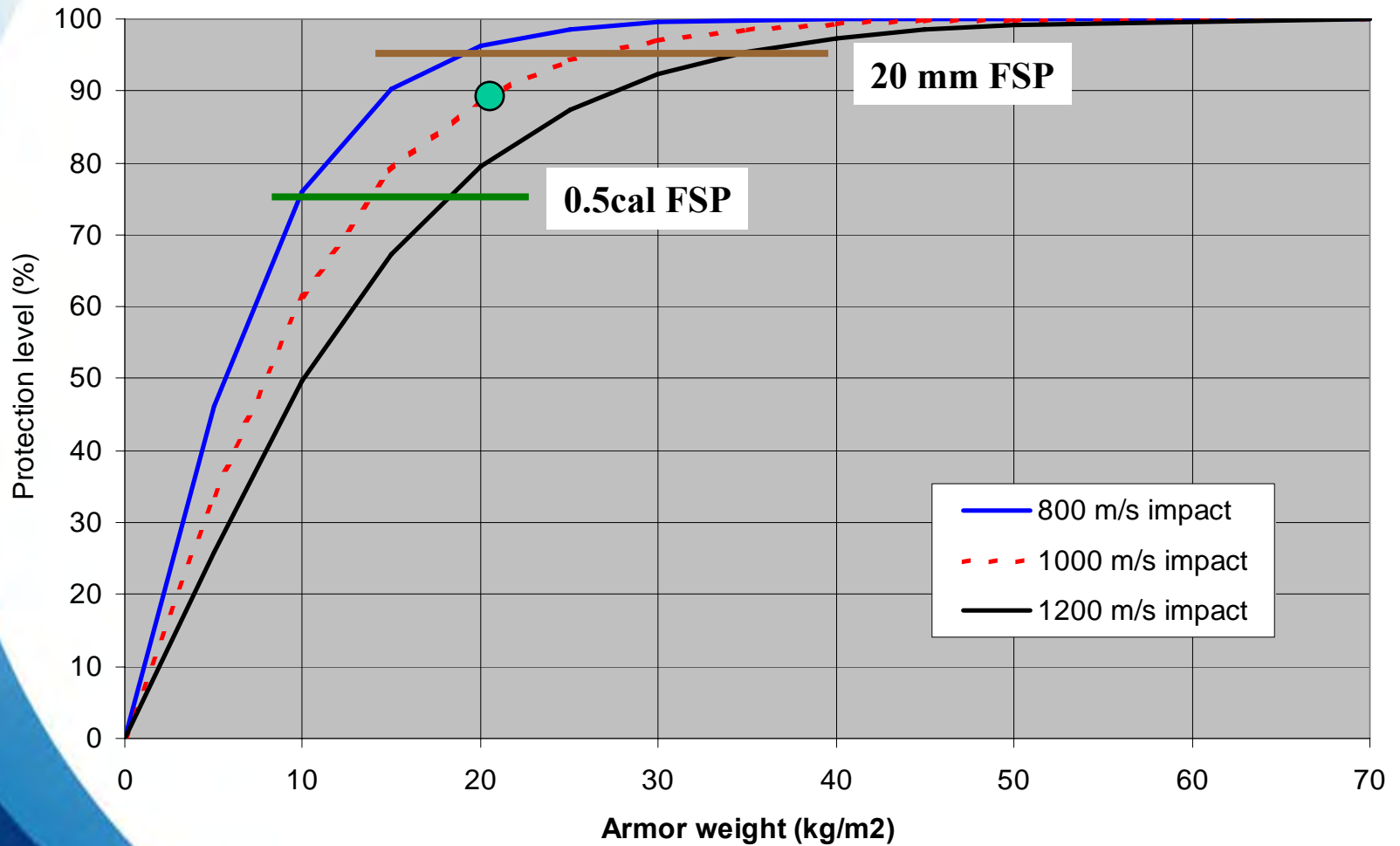


Special Hard Armor Configurations (17-gr and 96-gr fragments)





Protection Level vs Weight & Velocity





Summary

- The 96-gr sphere demonstrated as a viable IED laboratory fragment
- Promising results obtained with some novel armor systems
- Large effects of protection level selected on resulting armour weight
- Level 3+ plate performed quite well vs. fragments & bullets
- Lighter material solutions needed for allowing greater armor coverage & higher protection with no weight penalties
- Trade-off analysis not trivial as many parameters involved





Future work

- Validate performance goals & metrics
 - threat parameters
 - protection/survivability level(s)
 - body coverage
- Conduct detailed trade-off analysis (integrated vs modular vs scaleable)
- Study resulting blast mitigation capabilities
- Further explore new materials and concepts
- ...



Key Performance Parameter: Soldier Acceptance

Questions?





24th ISB New Orleans 2008

Defence R&D Canada (DRDC) • R & D pour la défense Canada (RDDC)



Biography

Mr. Pageau joined Defence R&D Canada in 1981. He graduated from University of British Columbia with a master degree in Materials Science. He currently works as the scientific advisor for the Integrated Soldier Systems Project within the Directorate of Soldier Systems Program Management in Ottawa. He was exchange scientist at the Natick Soldier Center for two years.



 **PDF Complete**
Your complimentary
use period has ended.
Thank you for using
PDF Complete.
[Click Here to upgrade to
Unlimited Pages and Expanded Features](#)

's First University Affiliated Research Center



The Effect of Velocity on Jacketed Rod Efficiency

Brad Pedersen, Stephan Bless, Robert Fromm
24th International Symposium on Ballistics
New Orleans, Louisiana
September 2008

Objective

The objective of this work was to determine the penetration performance of steel jacketed rods against armor steel (RHA) targets at velocities above 2.2 km/s.

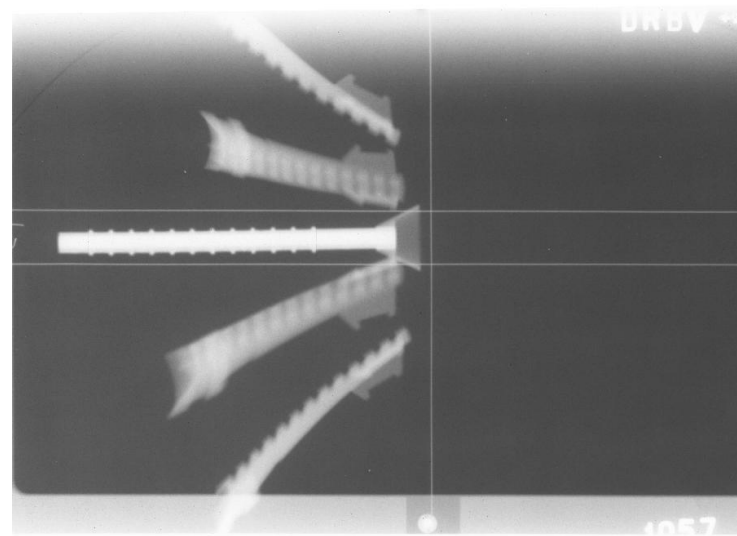
This effort sought to extend the velocity range above the previously considered 2.2 km/s in an attempt to reach the penetration performance of tungsten rods.

Introduction

This study consisted of hypervelocity experiments and supporting numerical simulations. Steel jacketed rods with core to jacket diameter ratios (μ) of 0.6 and 0.4 were investigated at nominal velocities of 2.6 and 2.8 km/s.

The results of the experiments were compared to the simulations for resultant crater size and normalized penetration (P/L).

Penetrators



Materials:

W-Ni-Co Core rod

4340 Steel Jacket

Co-based brazing alloy for bond

ID/OD Ratios (μ): 0.6, 0.4

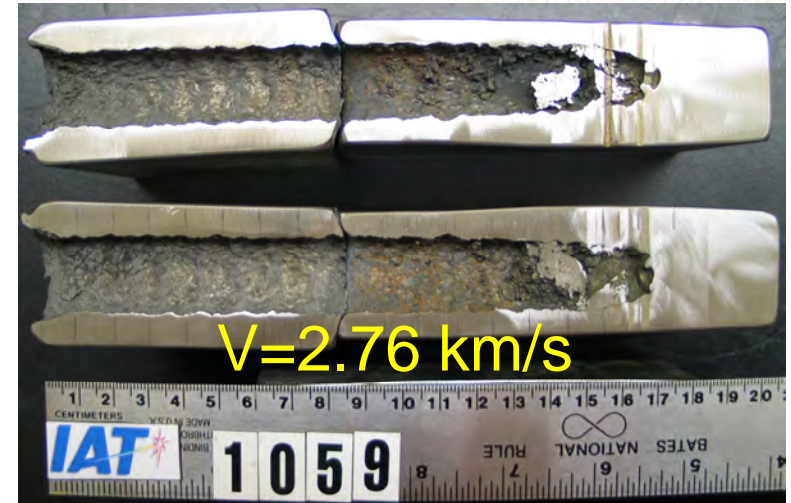
L/D = 15

Rod mass and length were constant

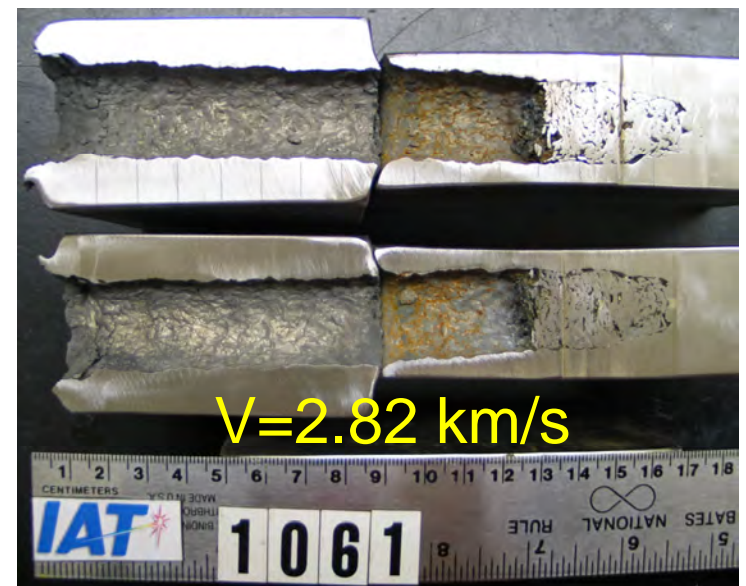
Velocities: ~2.6 and 2.8 km/s

Penetration Channels

$\mu=0.6$



$\mu=0.4$



In general, the $\mu=0.6$ craters were deeper but the $\mu=0.4$ had larger crater diameters and more material in the bottom.

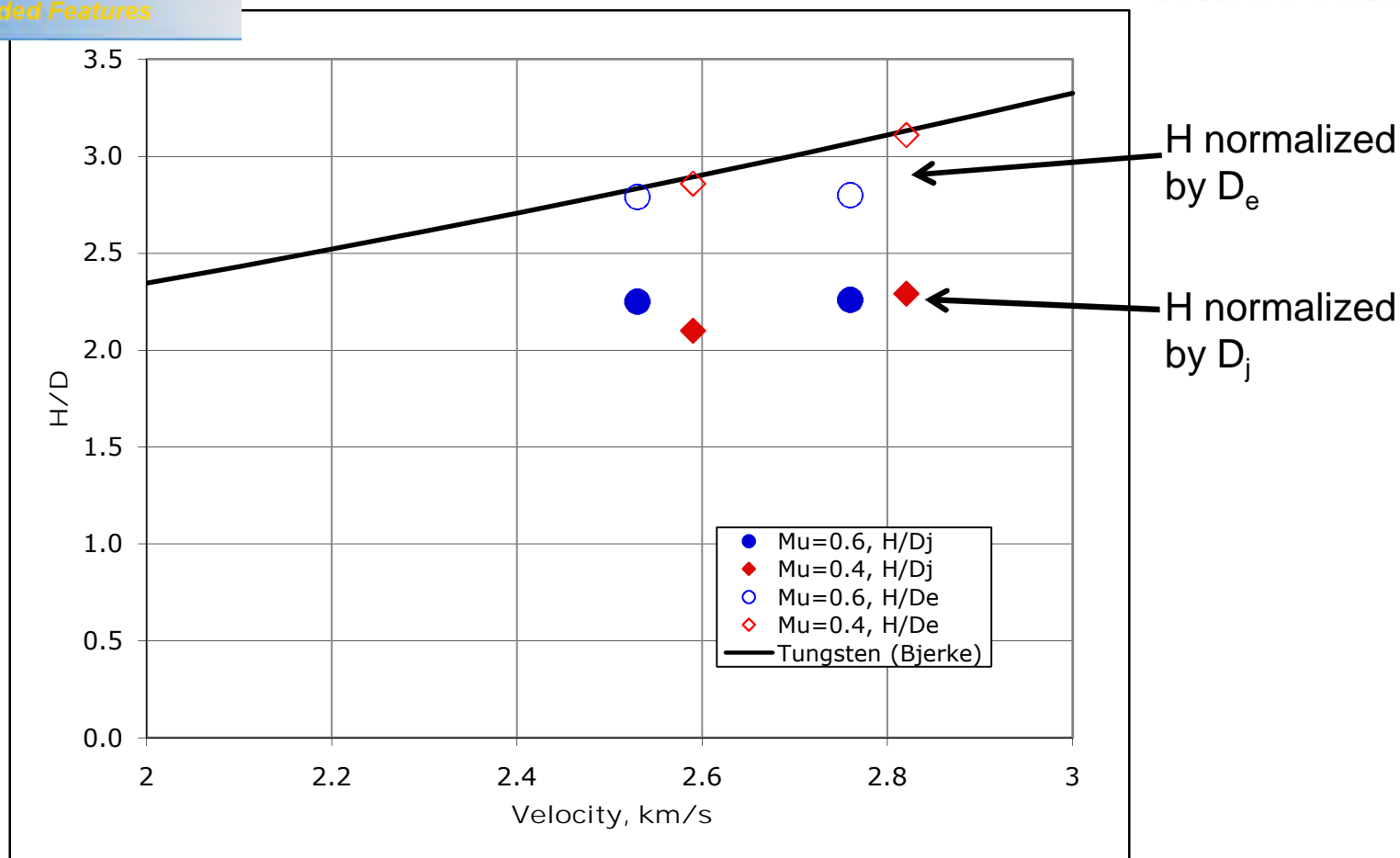
Normalized Crater Diameter

A comparison of the normalized crater diameter (H/D) from the jacketed rod tests to the Bjerke* relation for tungsten rods was made. For the jacketed rod data, the crater diameter (H) was normalized by the jacketed rod diameter (D_j) and the diameter of an equal mass and length tungsten rod (D_e).

$$D_e = \left[D_c^2 \underbrace{\left(\left(\frac{1}{\mu^2} - 1 \right) \frac{\rho_j}{\rho_w} + 1 \right)}_{\text{Average density}} \right]^{1/2}$$

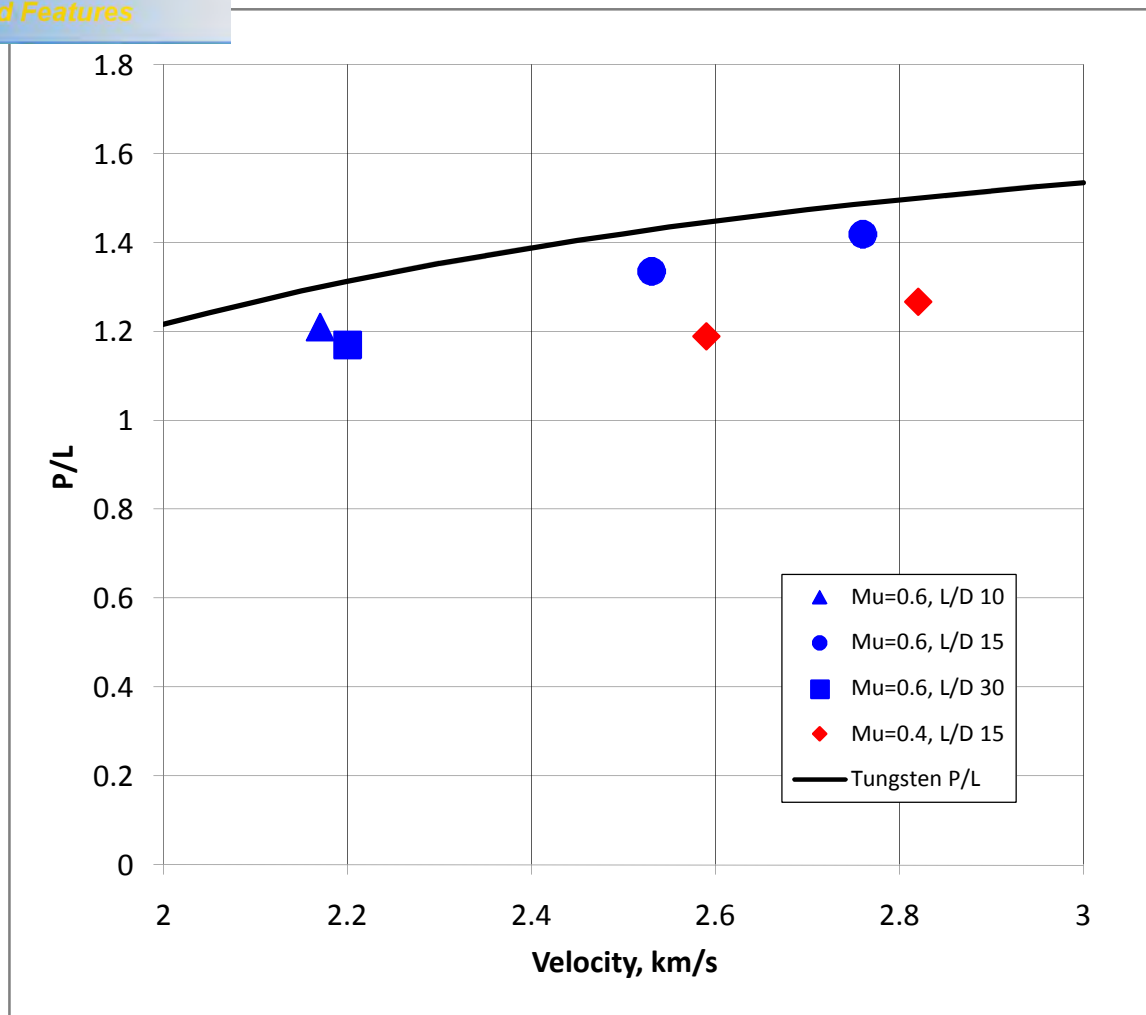
* Bjerke, Int. J. Impact Engineering **12**, 281-292, 1992

Normalized Crater Diameter



The crater diameter appears to scale as the square root of the average density.

Penetration Results



P/L does not depend on L/D at 2.2 km/s (10-30).

Jacketed rods never penetrate as well as all-tungsten rods but closely approach the performance as velocity increases.

Numerical Modeling

2D axis-symmetric
AUTODYN
Lagrangian solver.

Simulated tungsten
rods, and Mu=0.4
and 0.6 jacketed
rods at V=2.2, 2.6,
2.8 km/s.

AUTODYN-2D v6.1 from Century Dynamics

Material Location

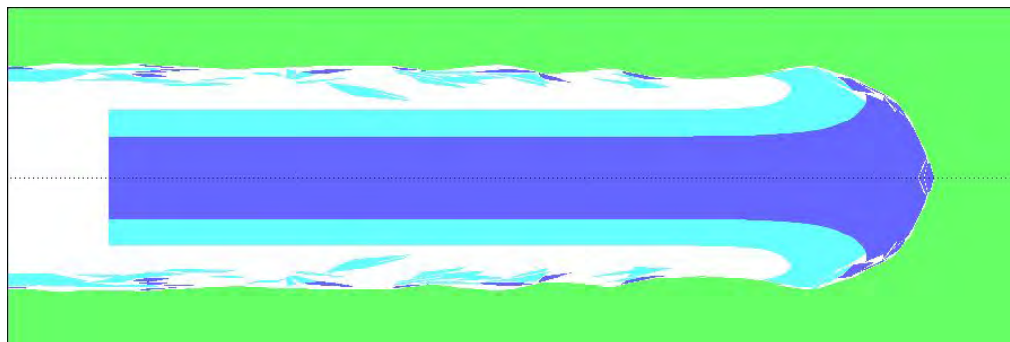
TUNGSTEN

RHA

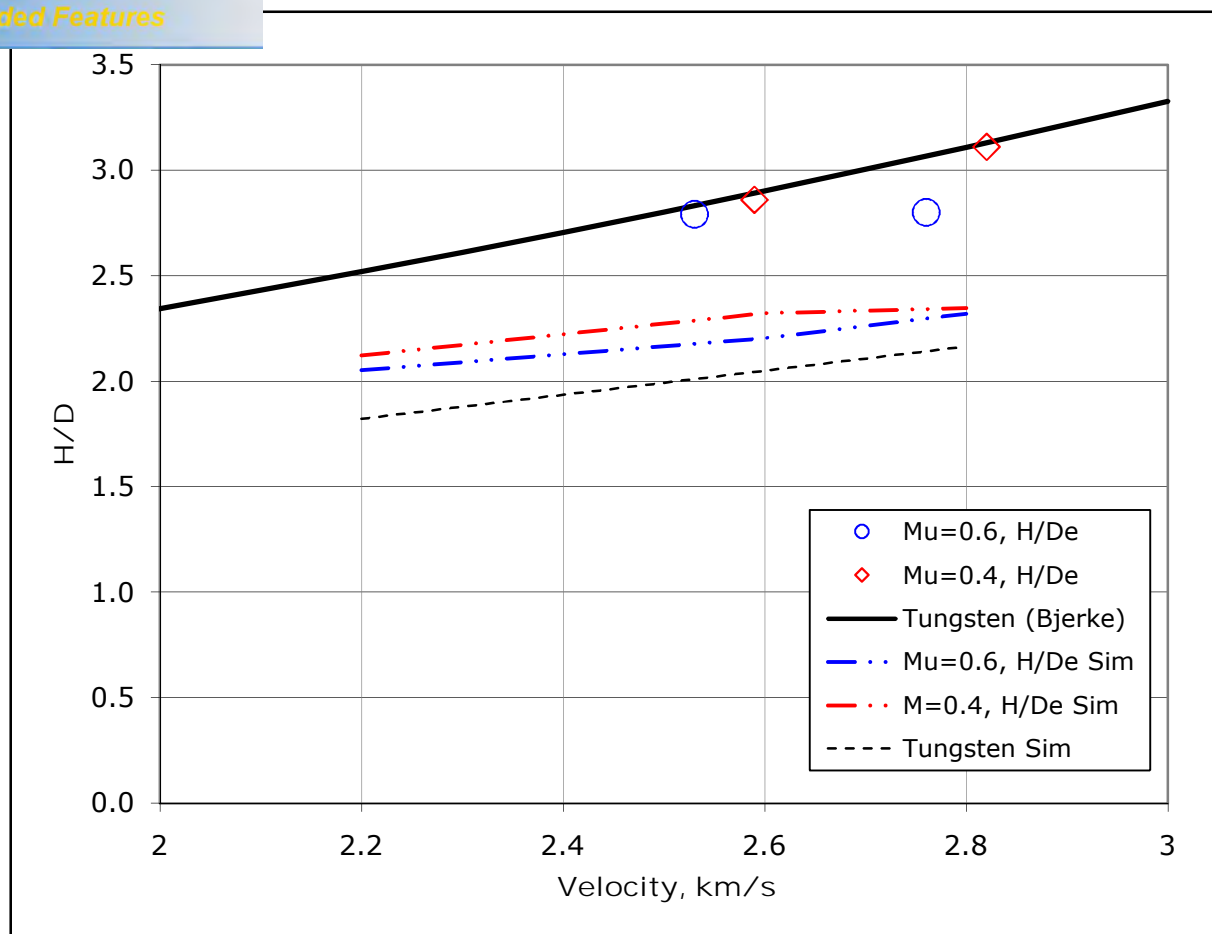
STEEL 4340



ratio-Bvel-2-8
Cycle 0
Time 0.000E+000 ms
Units mm, mg, ms
Axial symmetry

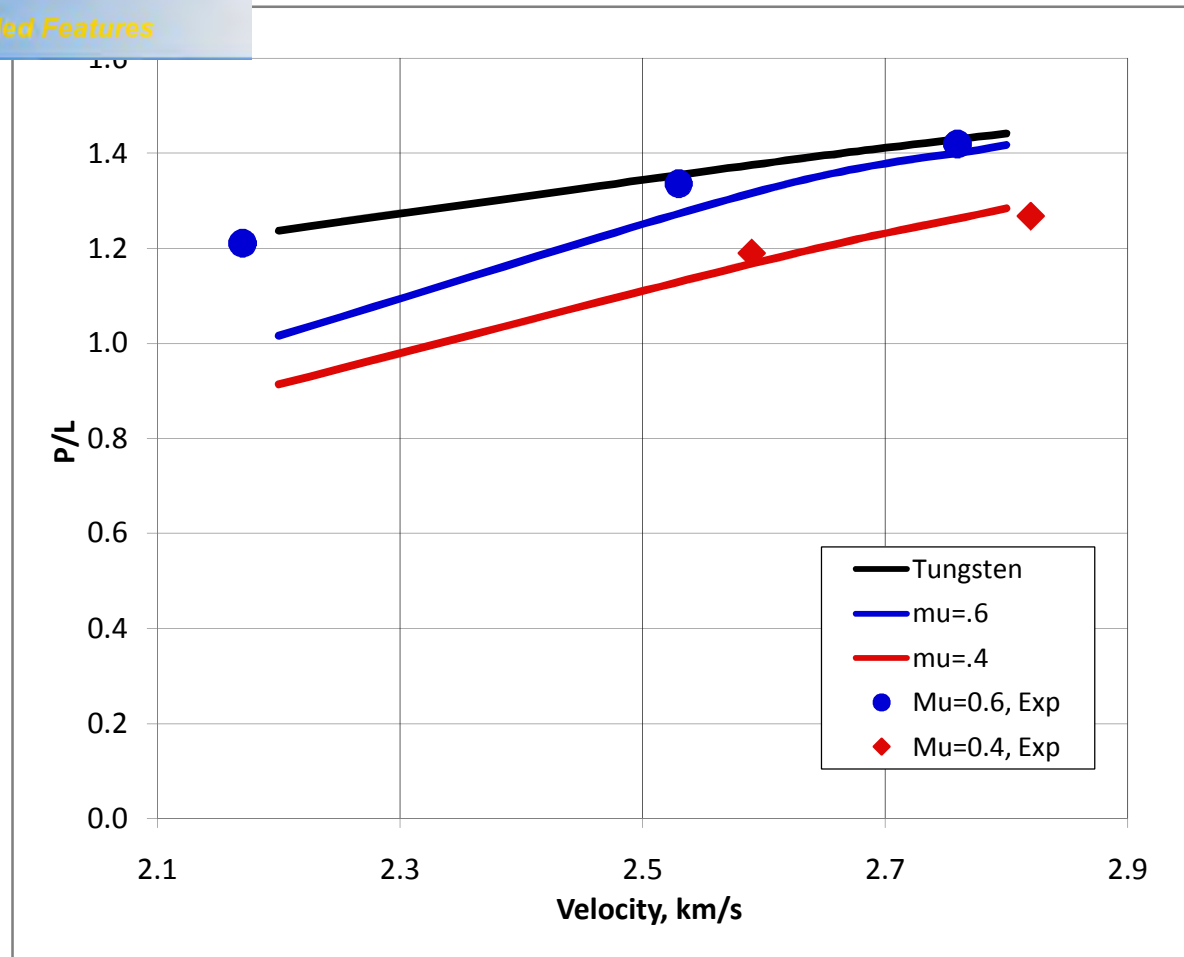


Crater Modeling – Crater Size



The simulated crater size is significantly less experimental data.
In the simulations, craters from tungsten rods are smaller than craters from jacketed rods, which is not correct.
AUTODYN is not accurately modeling the crater growth.

Physical Modeling - Penetration



Despite the inaccuracies of the crater size, at high velocity, the simulations agree well with the normalized penetration from the experiments. At 2.2 km/s, the simulations do not agree with the data. This is likely because in that calculation the crater is not large enough to allow the jacket material to flow freely after it erodes.

Conclusions

For $\mu=0.6$, jacketed rods approach but never attain the penetration of tungsten rods.

The penetration of $\mu=0.4$ rods is less than $\mu=0.6$ rods.

The simulations matched the penetration for velocities above 2.6 km/s, but under-predicted penetration at 2.2 km/s.

For these jacketed rods, the crater diameter scales as the square root of the average density.

The simulations under-predicted the crater diameters for both jacketed and tungsten rods.



24th International Symposium on Ballistics
New Orleans, LA

Mine Countermeasure Dart Dispense Modeling & Simulation

Gary Prybyla
Naval Surface Warfare Center
Indian Head Division

23 September 08



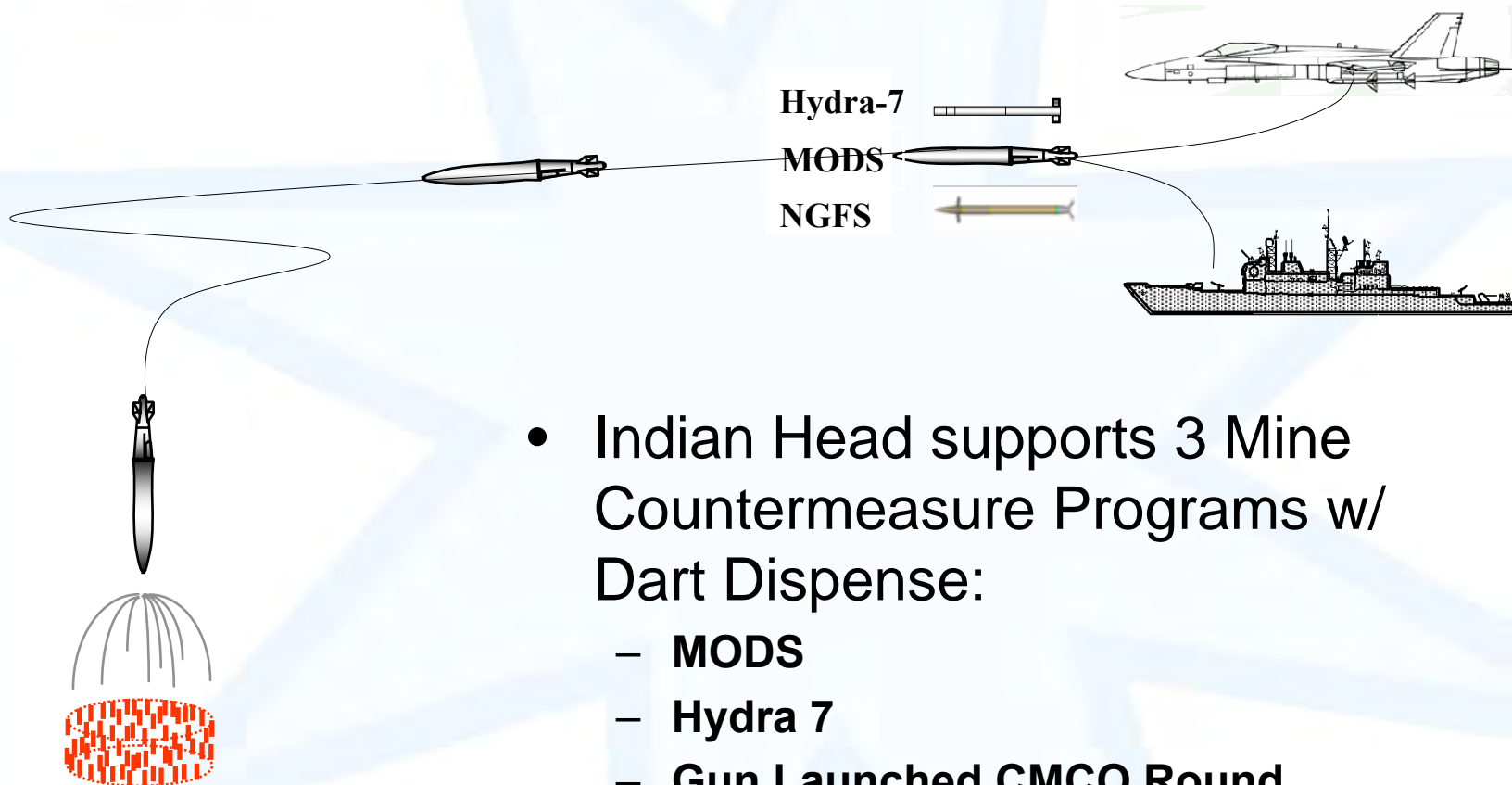
Contributors/Co-authors

- Digital Fusion, Inc.
 - William Dietz
 - James Baltar
 - Kevin Losser
- NSWC Panama City
 - Dr. Michael Neaves

Outline

- Description of Mine Countermeasure Darts
- Background of Dart Dispense Working Group
- Simulation Matrix
- Model Results
- Discussion

Navy Mine Countermeasure Programs

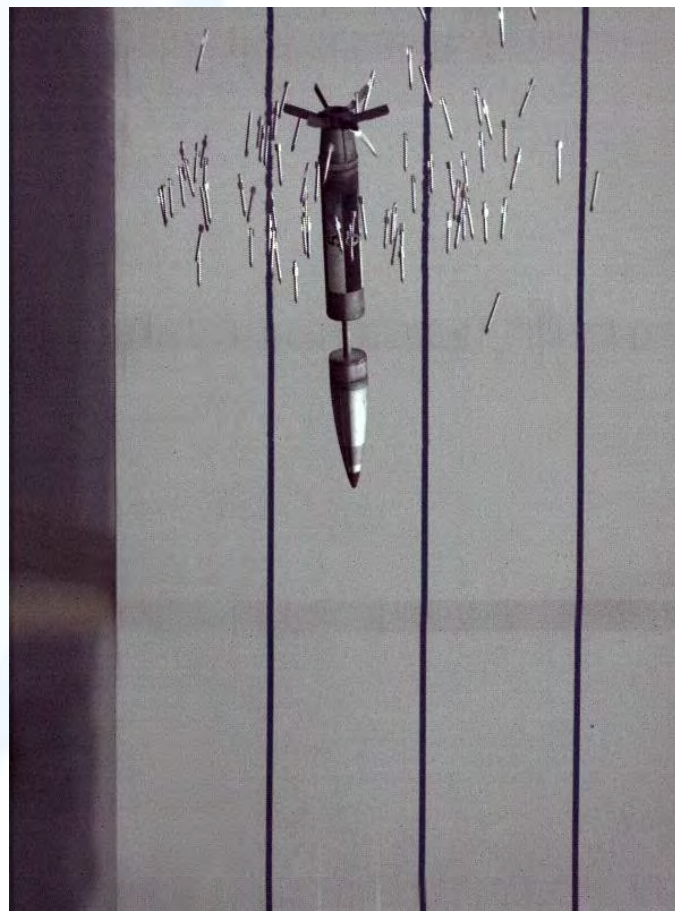
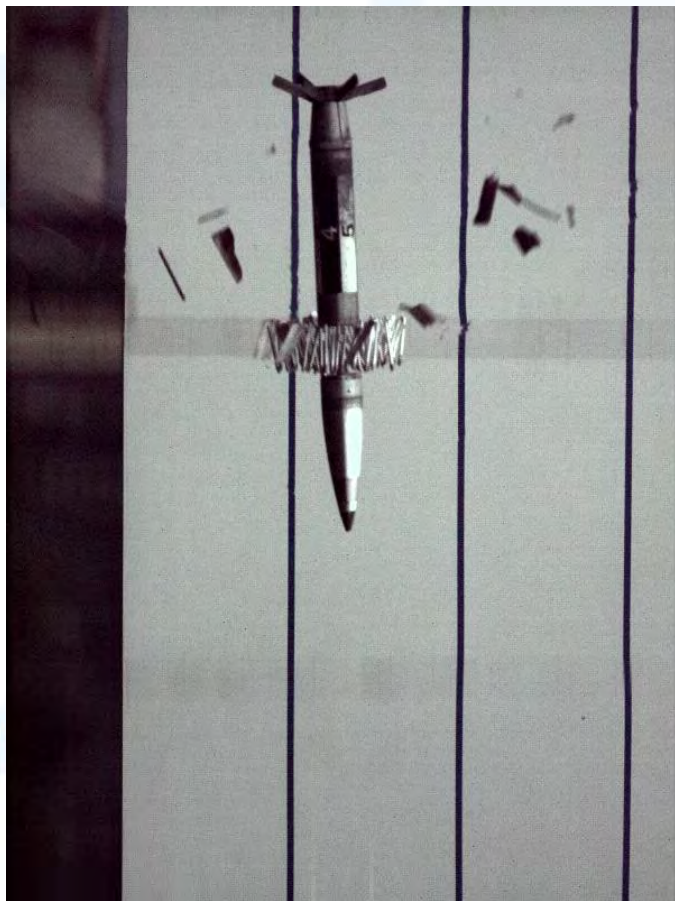


- Indian Head supports 3 Mine Countermeasure Programs w/ Dart Dispense:
 - **MODS**
 - **Hydra 7**
 - **Gun Launched CMCO Round**

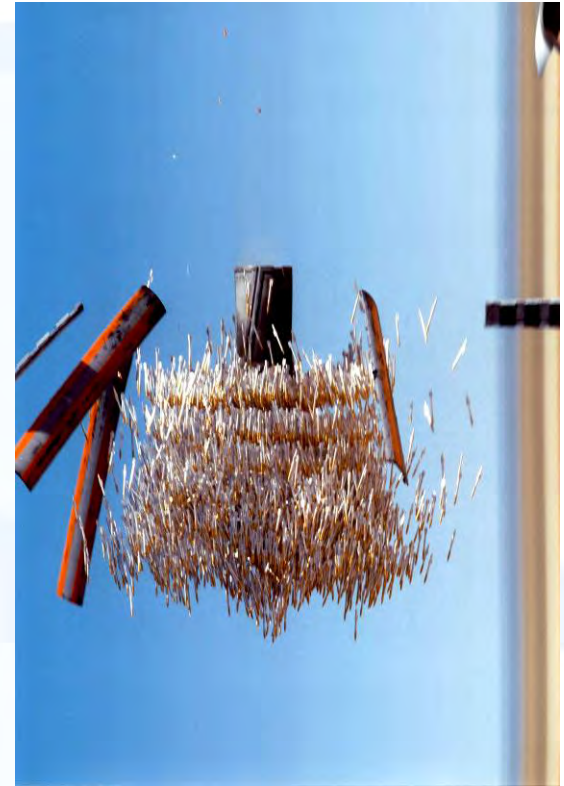
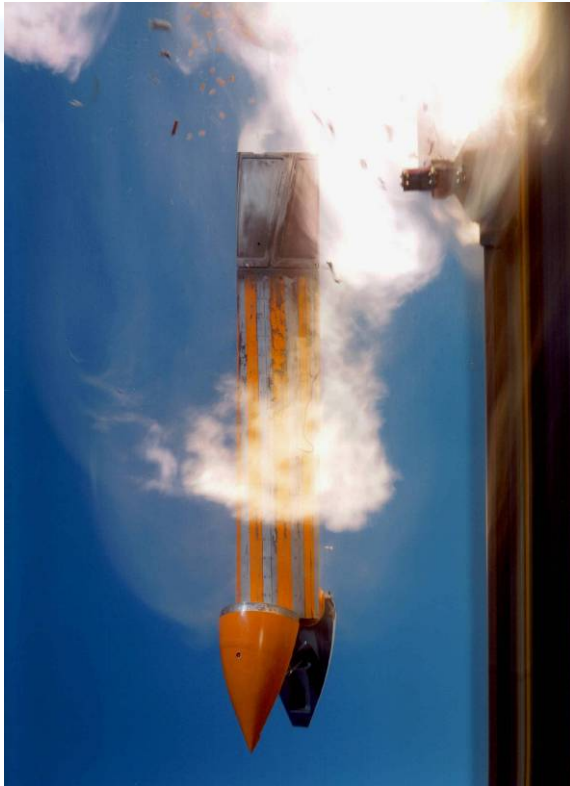


Venom Penetrator Dart

- Naval Gun Fire System CounterMine CounterObstacle Dispense



- MODS Dispense of 6000+ darts



- **History of Dart Dispense M&S Working Group**
 - **Initial Dispensing Technology Workshop, coordinated by Mr. Brian Almquist, Office of Naval Research, held in February 2002**
 - **Working Group formed – kickoff meeting in June 2002**
 - **Team Members:**
 - ONR
 - NSWC/Indian Head
 - NSWC/Panama City
 - Army Aeroflightdynamics Directorate, Ames Research Center
 - NASA/Langley
 - NEAR, Inc.
 - Digital Fusion
 - **DoD High Performance Computer Project “Modeling of Mine Countermeasure Dart Dispense” initiated FY2003**
 - **Challenge Project Status awarded during 2007 & 2008 (1,000,000+ CPU hours per year)**



Objectives of Working Group



- Enhance state-of-the-art techniques for predicting dart aerodynamics during dispense
- Transition techniques to 6-DOF models to predict multiple dart trajectories and impact patterns
- Enhance 6-DOF tools used in Analysis of Alternatives

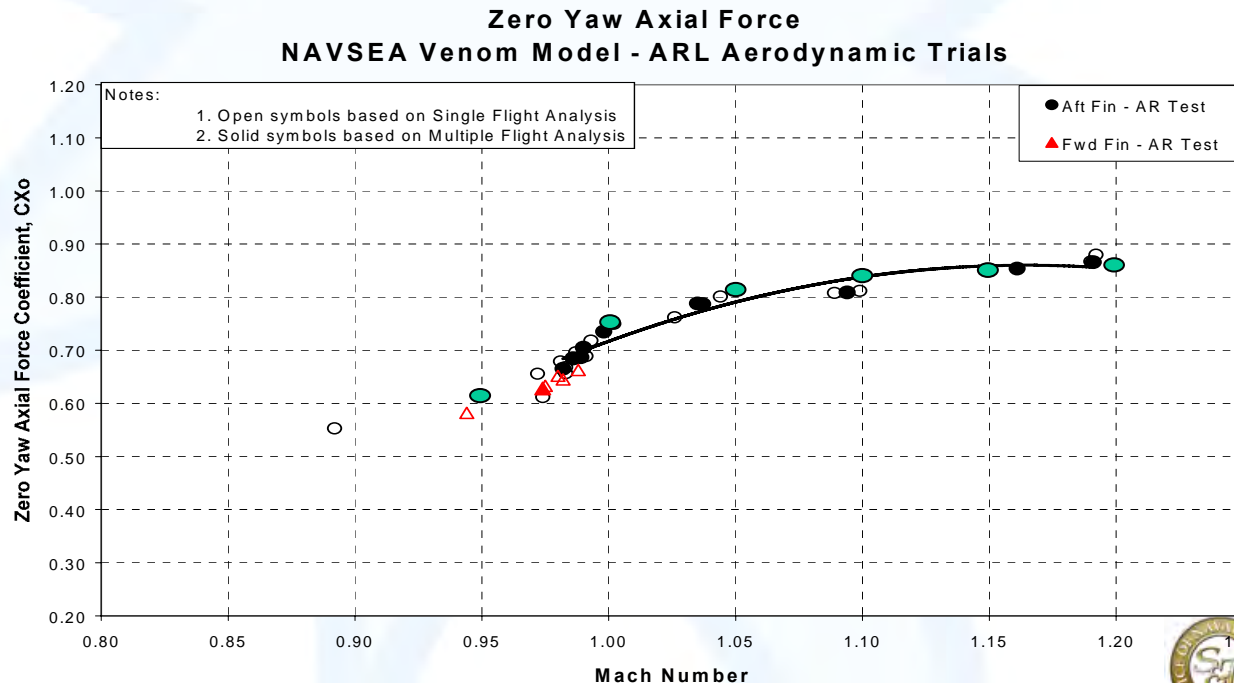


The Challenge !!

- Accurately model the dispense of multiple darts, approaching a full MODS payload: Multiple-Body Six Degrees-of Freedom (6-DOF) Computational Fluid Dynamics (CFD) with Collisions
- Determine how many darts need to be modeled to capture the overall dispense dynamics
- Given enough memory and computing power, can we model the dispense of all 4000+ darts?

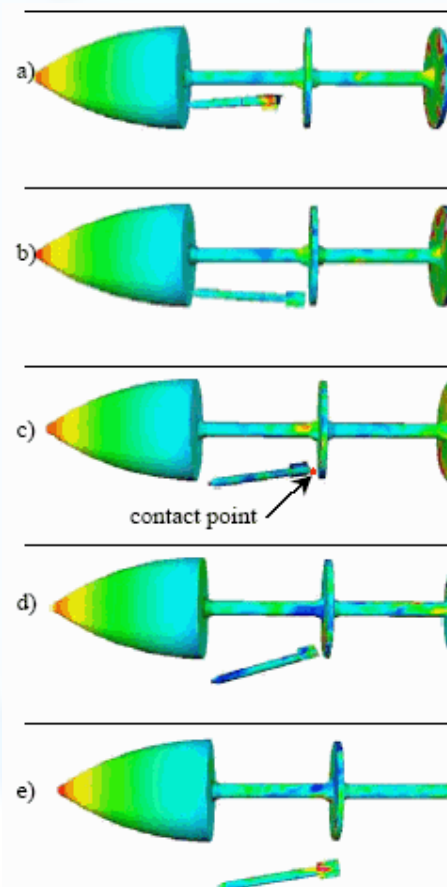
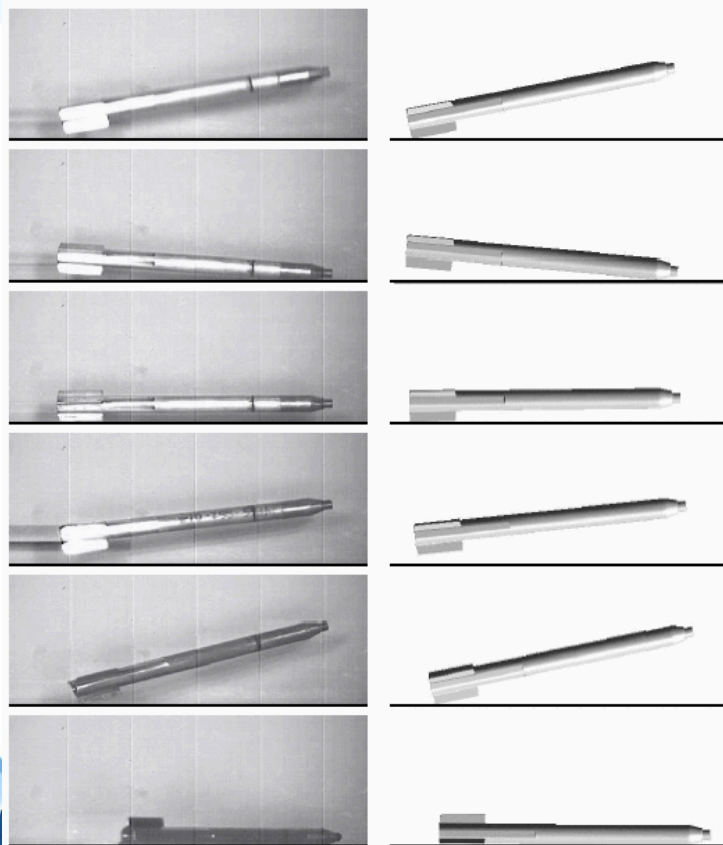
Preliminary CFD Simulations

- Evaluated several CFD codes
- Compared results of single dart simulations to Aeroballistic Test Range data (from Aberdeen and Eglin AFB)
- OVERFLOW selected as primary CFD code



Code Modifications

- Collision Module added to OVERFLOW
 - Provides for dart-to-dart and dart-to-dispenser collisions
 - Validated against single dart drop tests

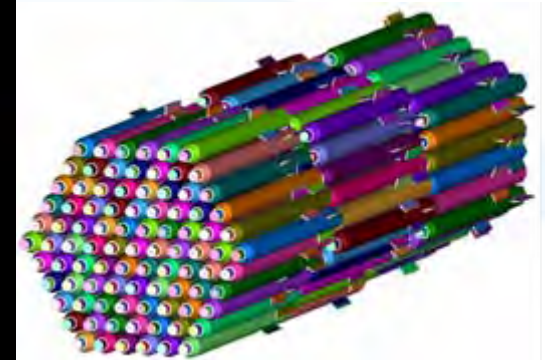
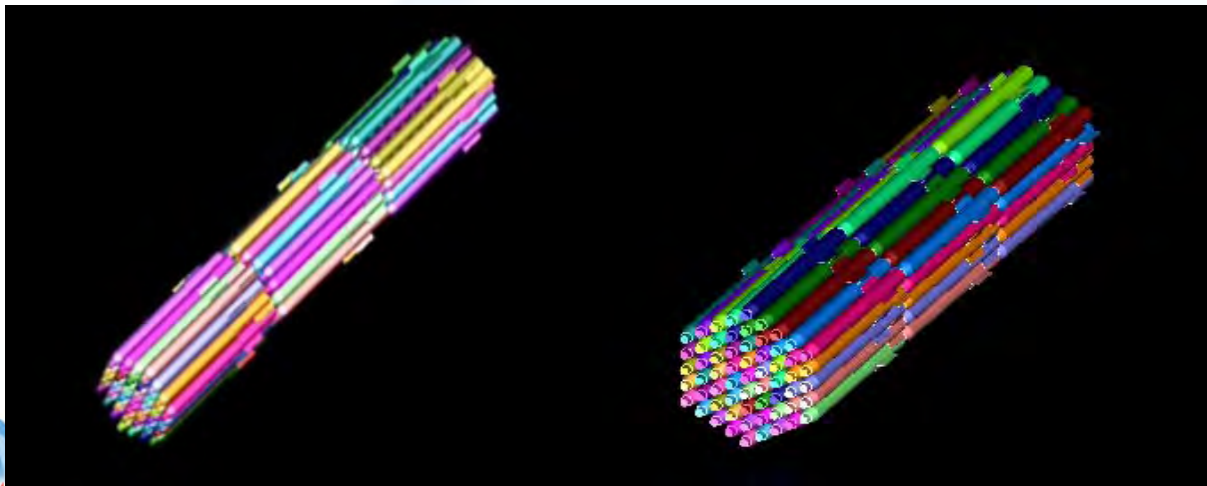


Simulation Matrix

1. 273 darts (3 axial layers x 5 radial rows), 6 Hz spin rate, Mach 1.2
2. 273 darts (3 axial layers x 5 radial rows), 12 Hz spin rate, Mach 1.2
3. 273 darts (3 axial layers x 5 radial rows), 18 Hz spin rate, Mach 1.2
4. 111 darts (3 axial layers x 3 radial rows), 12 Hz spin rate, Mach 1.2
5. 183 darts (3 axial layers x 4 radial rows), 12 Hz spin rate, Mach 1.2
6. 381 darts (3 axial layers x 6 radial rows), 12 Hz spin rate, Mach 1.2
7. 273 darts (3 axial layers x 5 radial rows), 12 Hz spin rate, Mach 1.6
8. 273 darts (3 axial layers x 5 radial rows), 12 Hz spin rate, Mach 2.0

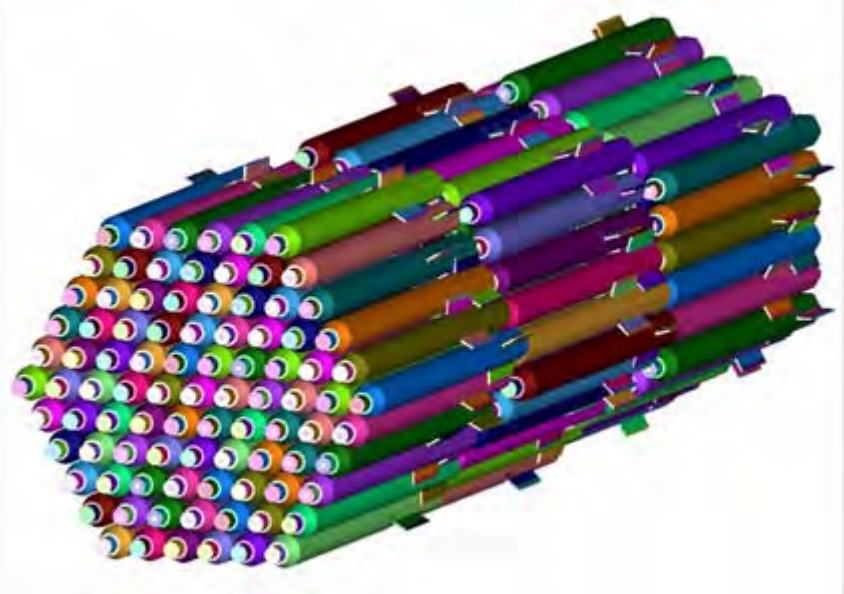
“Number of Darts” Study

- Compare Matrix runs #2, #4, #5, & #6 to determine differences in dispense behavior resulting from 111, 183, 273, & 381 dart packs
- Matrix run #6 (381 darts) has not been completed
- All runs performed at same Mach number (1.2) and Spin Rate (12 Hz)

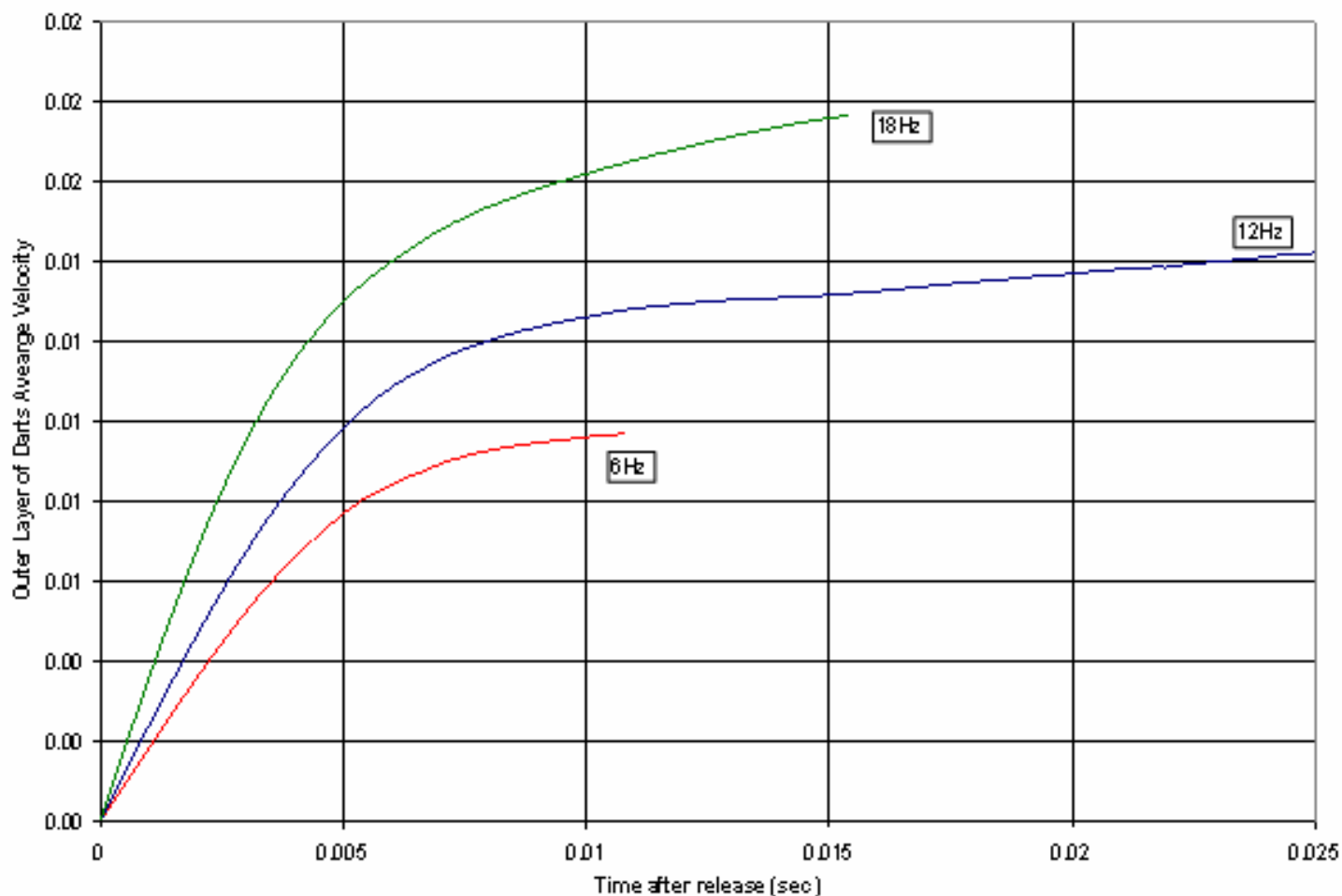


“Spin Rate Effects” Study

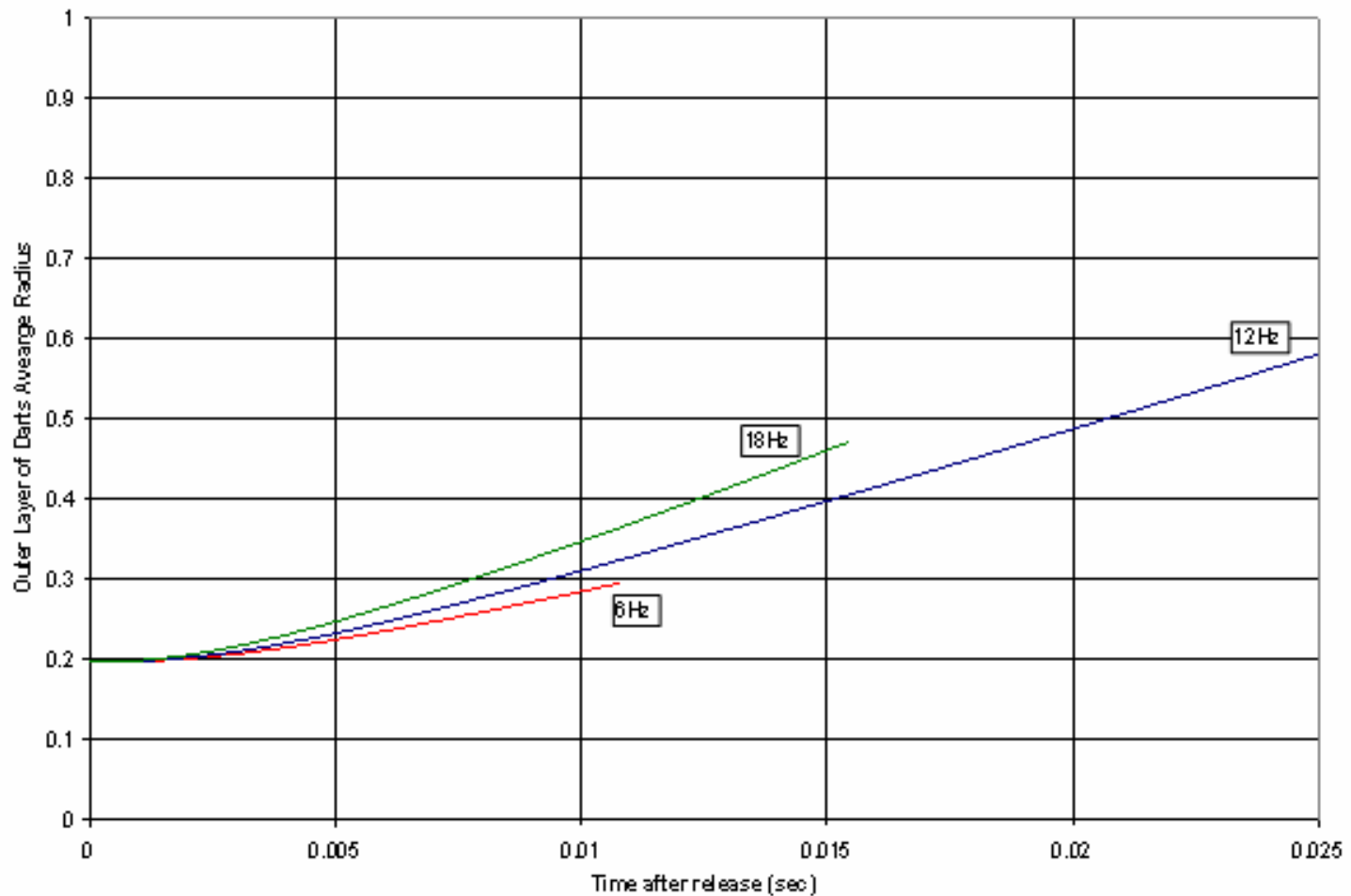
- 5 Radial Layers, 91 Darts Per Row, 3 Rows = 273 Darts
- Full 6-DOF Simulation with Collisions, Various spin rates
- ~400 Million Grid Points
- Viscous grid spacing
- Initial Spacing Factor = 1.2
- Physical Run time
 - 6 Hz = ~0.01 seconds
 - 12 Hz = ~0.025 seconds
 - 18 Hz = ~0.015 seconds
- Errors out due to bugs in OVERFLOW-2 grid adaptation feature (bugs fixed in later versions) and memory limitations



273 Darts – Average Normalized Velocity Comparison



273 Darts – Average Radius Comparison

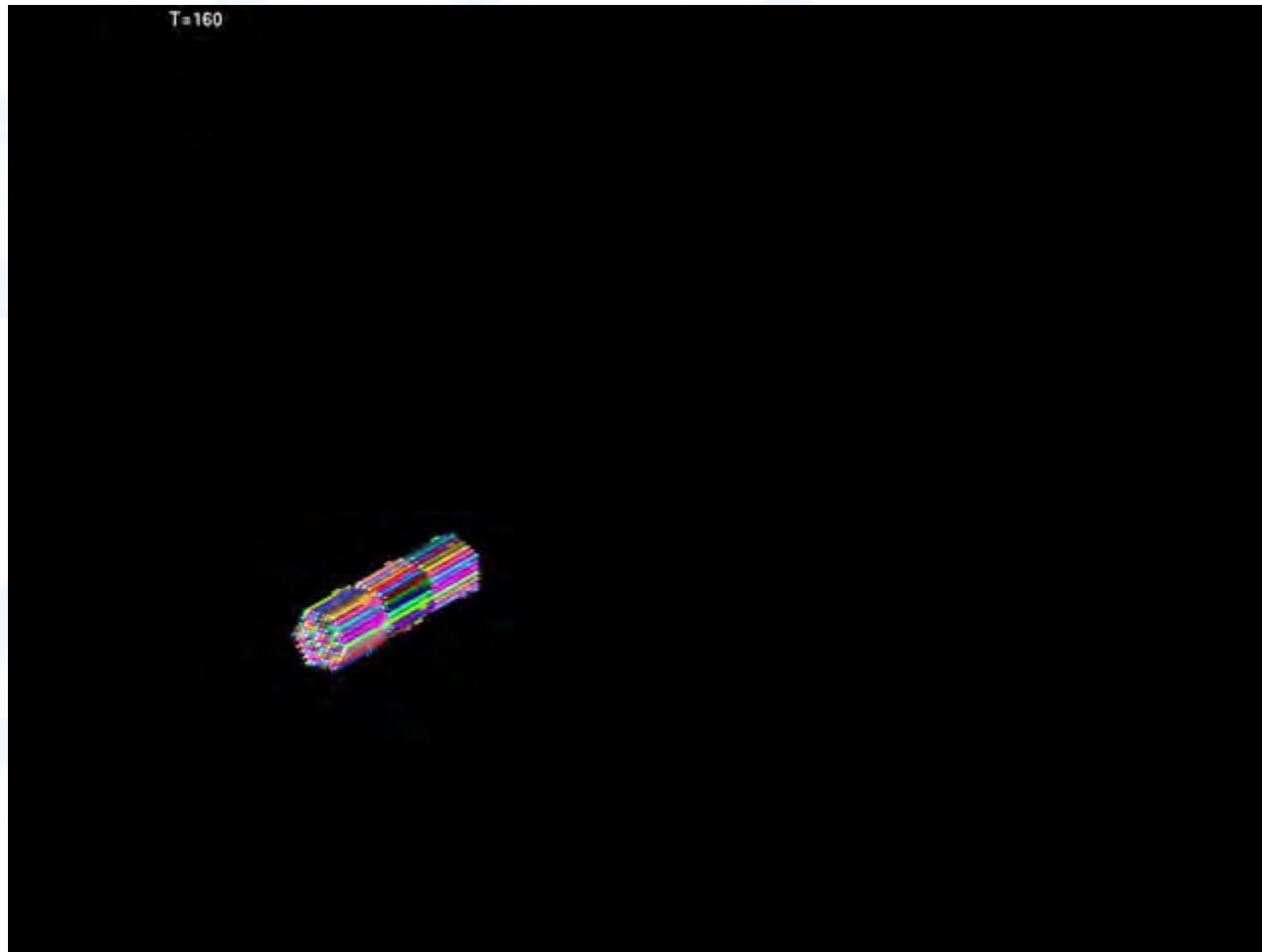


273 Darts (Longer Run Times)

- 5 Radial Layers, 91 Darts Per Row, 3 Rows = 273 Darts
- Full 6-DOF Simulation with Collisions, 12 Hz spin rate
- ~300 Million Grid Points
- Wall Function Grid, $y^+ = \sim 50$
- Initial Spacing Factor = 1.1 (previous simulations at 1.2)
- Run time ~0.1 seconds after release
- 600-840 processors
- Errors out due to one dart hitting outer boundary

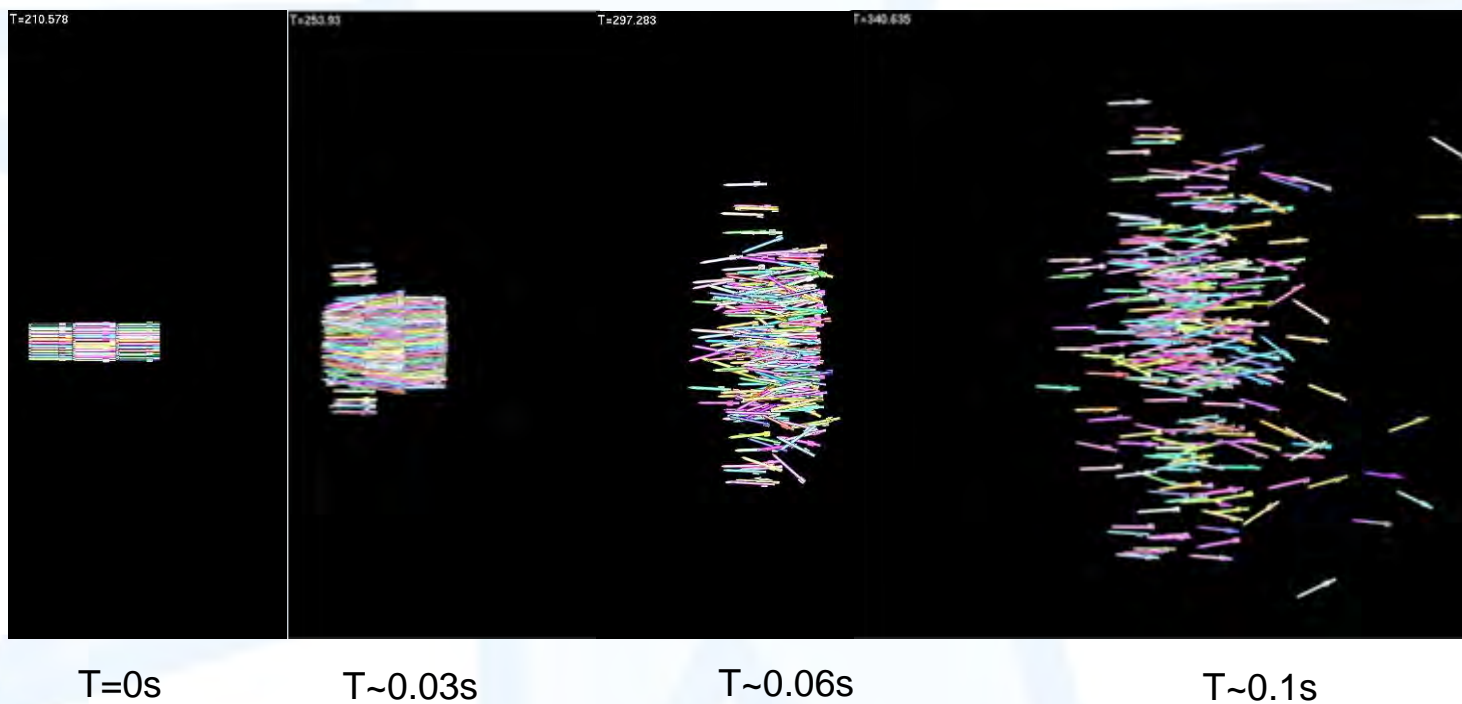
273 Darts (Longer Run Time)

Run to ~0.1 sec after release (MOVIE)
Iso View

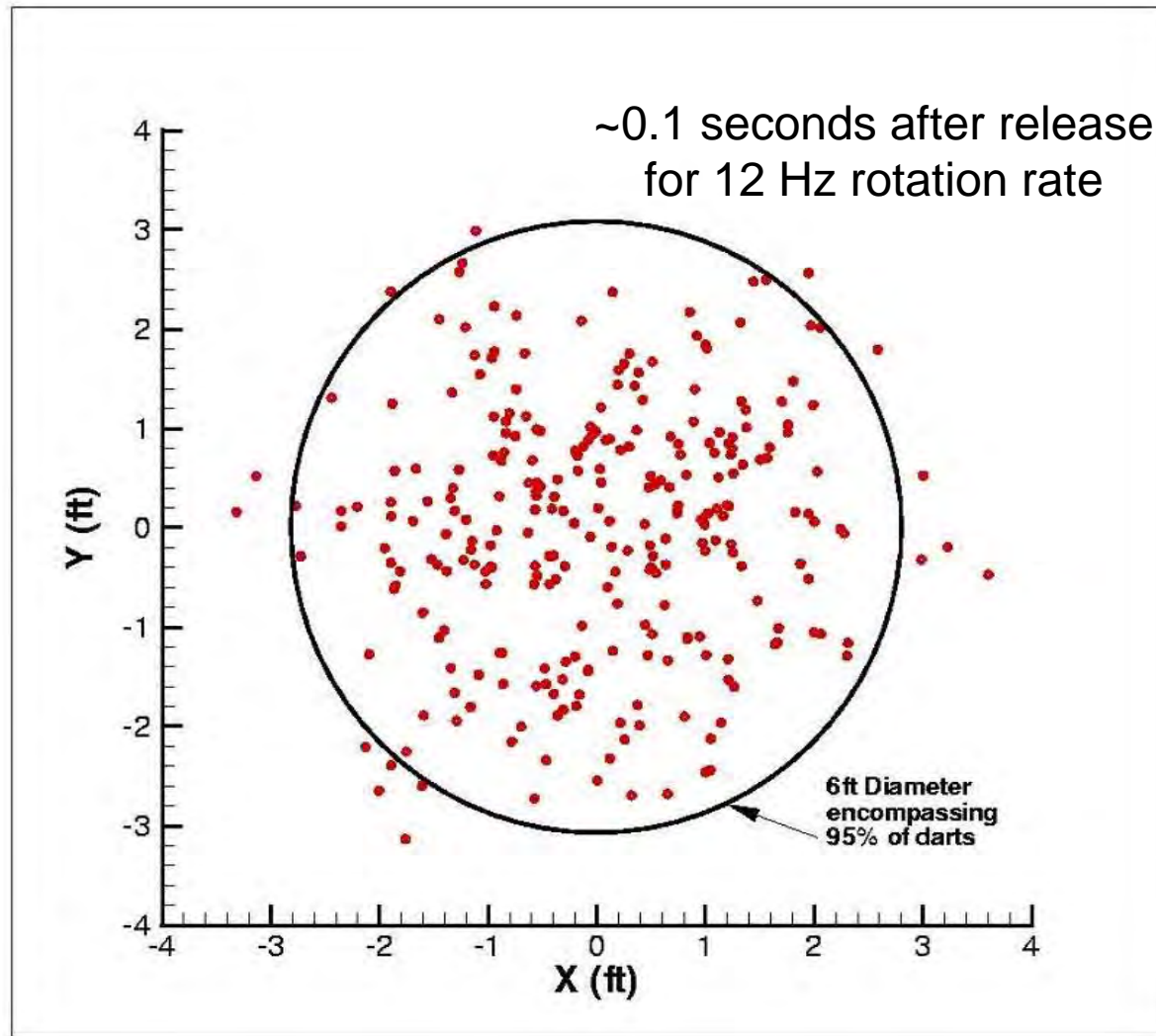


273 Darts (Longer Run Time)

Dispense sequence at Mach 1.2 with 12 Hz rotation rate



273 Darts – Spread (12 Hz)



Modeling Lessons Learned

- Wall Functions reduce point count, ease memory requirements
- File size is still a significant problem – storage and transfer
- Memory is limitation, not CPU time
- Increase processor count to get required memory
- Most CPU time spent in initialization and spin
- Graphics/post-processing is a concern

Results/Conclusions

- **“Number of Darts” Study**
 - Collisions may play big role in determining pattern size
 - Drafting effects are reduced after 3 axial layers
 - Additional axial rows of darts may fill in the “gaps” left by the first couple of rows
 - Darts are almost independent of each other after 0.1 sec for 273 dart case (small clusters)
 - Hexagonal pattern preserved, additional darts on the sides may produce more circular pattern
- **“Spin Rate Effects” Study**
 - Average Radial Dart velocities proportional to spin rates
 - Higher spin rates may produce “cleaner” patterns

Future Plans

- Additional simulations of larger dart packs are progressing (2009 Challenge Project)
- Plan to run Mach 1.6 and Mach 2.0 for 273 darts (Mach number effects study)



QUESTIONS?





Numerical Computations of Dynamic Pitch-Damping Derivatives using Time-Accurate CFD Techniques



TECHNOLOGY DRIVEN. WARFIGHTER FOCUSED.

Dr. Jubaraj Sahu,
Aerodynamics Branch
U.S. Army Research Laboratory

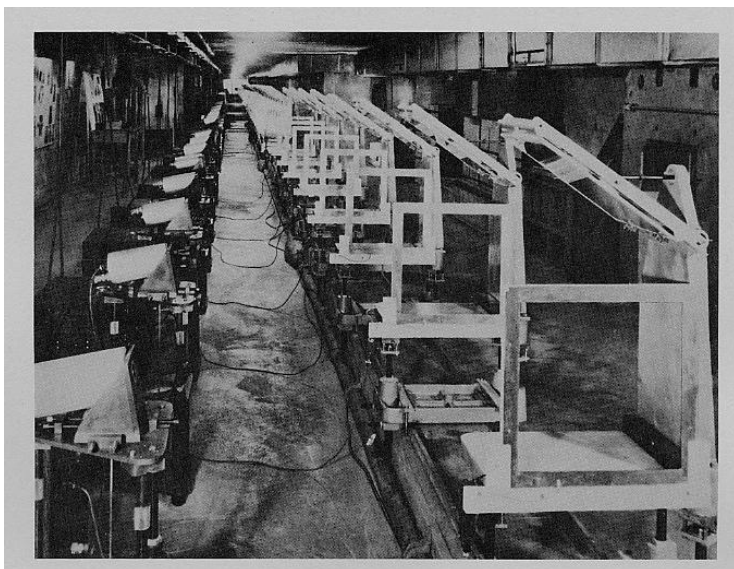
24th International Symposium on Ballistics
New Orleans, Louisiana
22 . 26 September, 2008

- **Wind Tunnel testing**
- **Actual flight testing**
 - ◆ **Experimental facilities (Aero Range, Transonic Range)**
 - ◆ **Measure the positions and orientations; get Aero from 6-DOF fits**
- **Empirical codes (AP, DATCOM, PRODAS etc.)**
- **Computational Fluid Dynamics (CFD)**
 - ◆ **Steady-State Aerodynamics**
 - ◆ **Unsteady Aerodynamics for Magnus, Roll Damping, Pitch Damping using unsteady rolling and imposed pitching motions (Virtual Wind-Tunnel Method)**
- **CFD and 6-DOF Rigid Body Dynamics Coupling for “Virtual Fly-Outs”**
 - ◆ **Simulate actual free flight (integrated unsteady aero/flight dynamics)**
 - ◆ **Extraction of aerodynamic coefficients (both static and dynamic) from virtual fly-outs**
 - ◆ **Easily extended for computation of dynamic pitch damping moment coefficient using imposed pitching motion– a special case of the virtual fly-out procedure**
 - ◆ **Roll damping and Magnus moment coefficients also are obtained from time-accurate computations of rolling motion, inherently an integral part of the virtual fly-out method**

Use of HPC in the Development of the Digital Virtual Aerodynamic Range

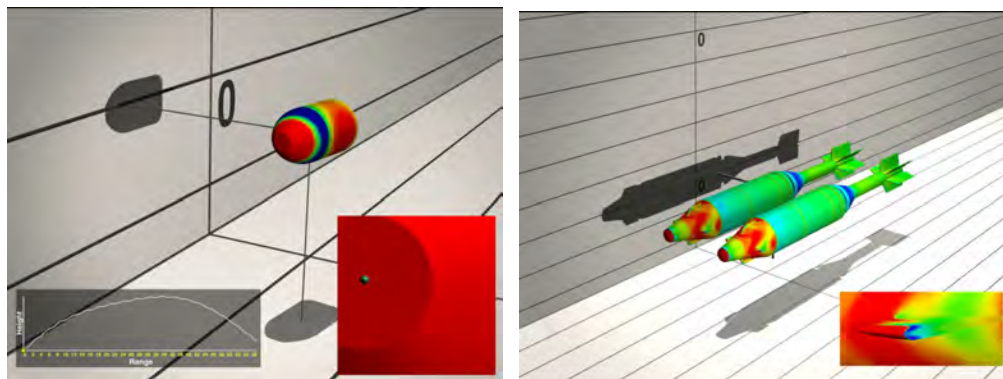


Aerodynamics Experimental Facility



- Measures projectile orientation and position only
 - Pitch, Roll, Yaw
 - X, Y, Z
 - 6DOF fit of range data
 - Limited visualization at a few stations
 - Aerodynamic coefficients determined
 - Characterize observed flight dynamics

Digital Virtual Aerodynamic Range



- Computes entire projectile state
 - Pitch, Roll, Yaw
 - X, Y, Z
 - **Linear velocities**
 - **Pitch, Roll, and Yaw Rates**
 - Unlimited flow visualization
 - Integrated Aerodynamics and Flight Dynamics
 - Predictive capability for new geometries
 - Outputs wake and pressure contours

TECHNOLOGY DRIVEN. WARFIGHTER FOCUSED.

Interdisciplinary Computational Technique



CFD Computational Technique

- 3-D Unsteady Navier-Stokes equations
- Higher order turbulence modeling including hybrid RANS/LES
- Dual Time-Stepping for transient flow computations
 - Two time-steps
 - First (outer) global or physical step –usually set to 1/100th of the period of oscillation
 - Second (inner) step – 5 to 10 inner iterations
- Grid Motion and BC:
 - Grid moves and rotates as the projectile moves and rotates
 - Free stream is preserved for arbitrary mesh and arbitrary mesh velocity

CFD/RBD COUPLING PROCEDURE

- 6-DOF equations solved at every CFD time-step
- CFD provides aerodynamic forces and moments
- 6-DOF provides the response of the body to the forces and moments
- The response is converted to translational and rotational accelerations
- Integrate the accelerations to obtain translational and rotational velocities
- Integrate once more to obtain linear position and angular orientations
- 6-DOF uses quaternions to define angular orientations
- From the dynamic response, grid point locations and velocities are set

Complete Virtual Fly-Out Procedure

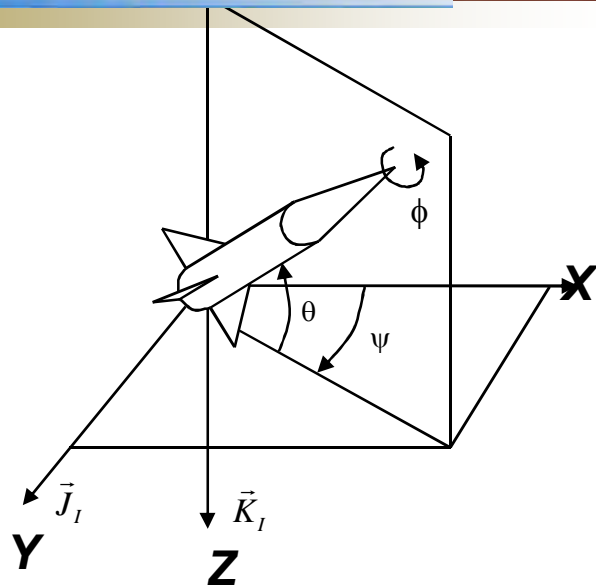
- **STEP 1:**
 - “Steady-state” mode
 - Grid velocities account only for translational motion
 - Initial conditions also include the angular orientations
- **STEP 2:**
 - “Uncoupled” mode (Kinematics)
 - Add rotational component in X (spin, p)
 - Compute for a few spin cycles until solution converges
- **STEP 3:**
 - “Coupled mode”
 - Add the other rotational components (q and r)
 - Full dynamic calculations

Time-Accurate CFD Procedure for Dynamic Derivatives

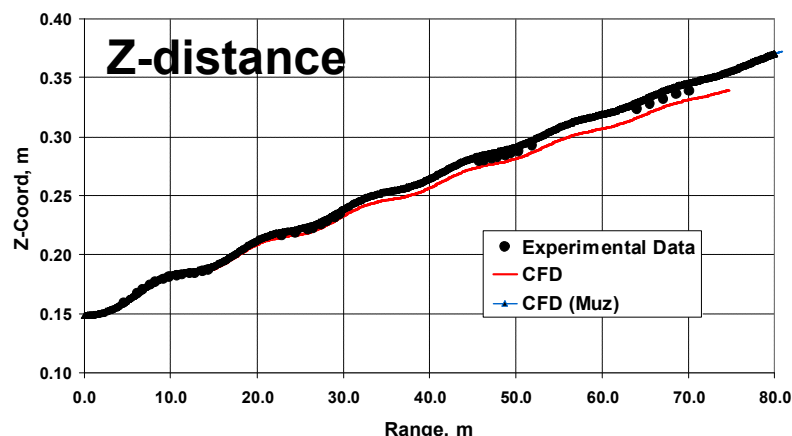
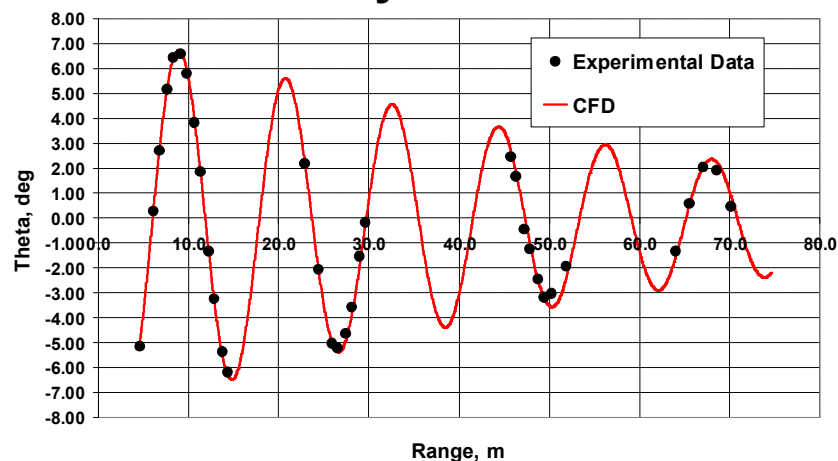
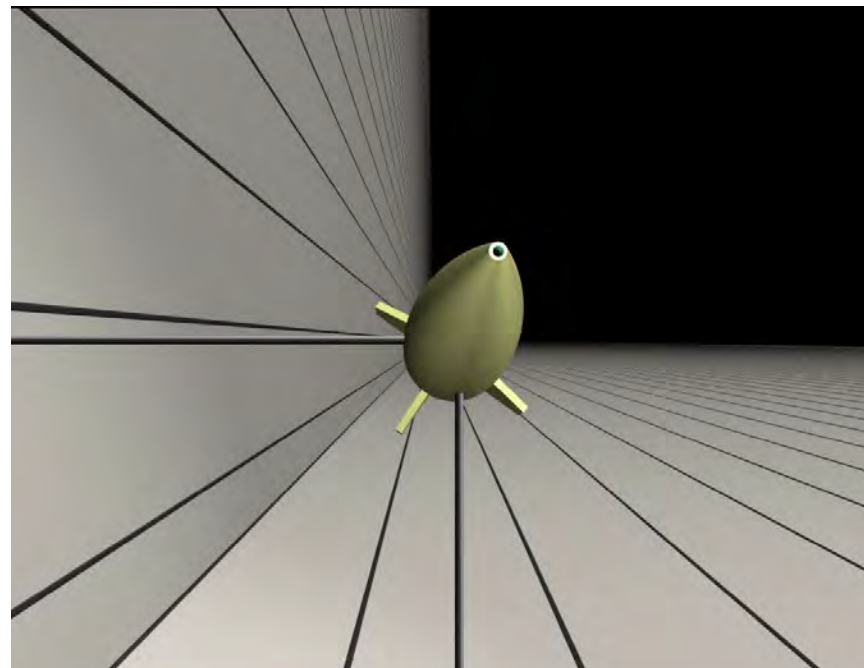
- **STEP 1:**
 - “Steady-state” mode
 - No translation motion
- **STEP 2:**
 - “Uncoupled” mode (Rolling Motion)
 - Add rotational component (spin, p)
 - Compute for a few spin cycles until solution converges
- **STEP 2:**
 - “Uncoupled” mode (Pitching Motion)
 - Add the other rotational component (q)
i.e. impose pitching motion
 - Pitching motion can be sinusoidal

Ballistic Fly-out of a Finned Projectile

Initial Velocity, Mach = 3 (Supersonic)

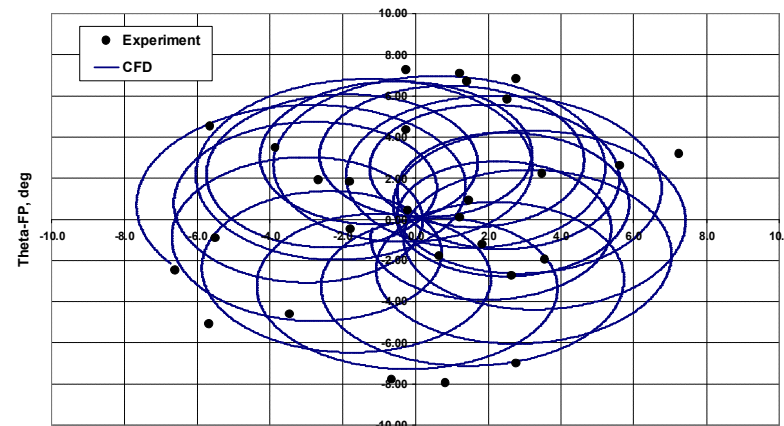
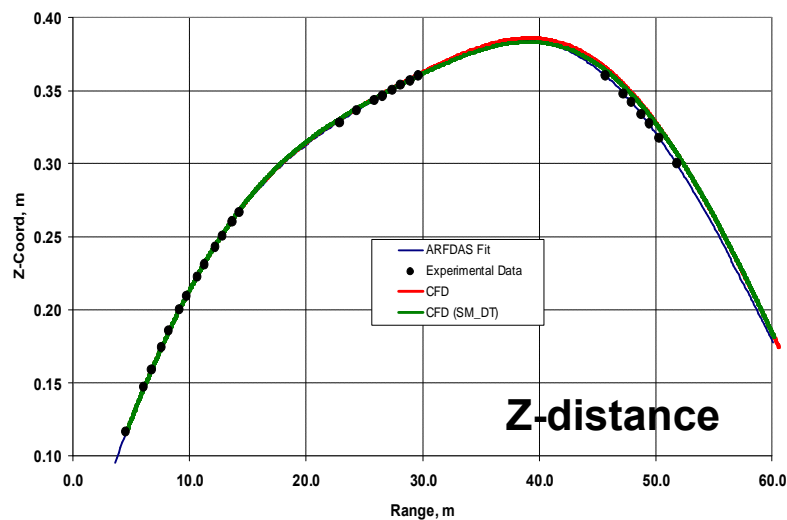
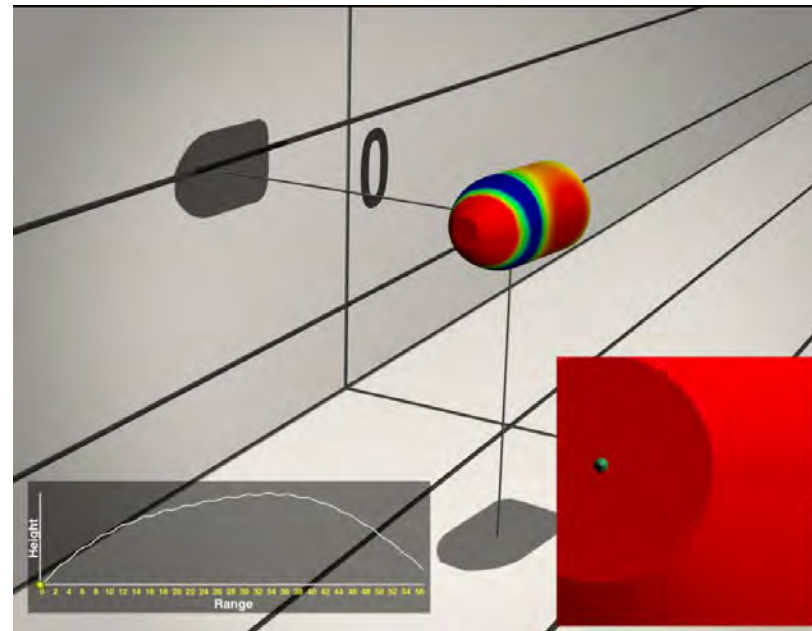
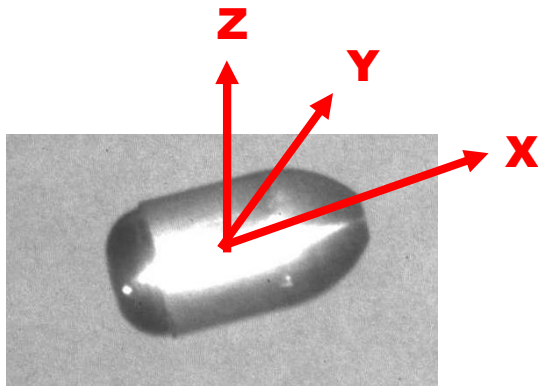


6-DOF system



Computed positions and orientations (Euler angles) of the projectile match very well with the data measured in actual free flight tests. **TECHNOLOGY DRIVEN. WARFIGHTER FOCUSED.**

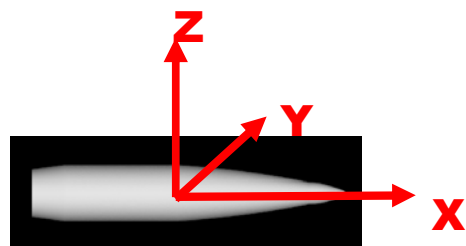
Another Example: Spinning Projectile Initial Mach = 0.4 (Subsonic Flight)



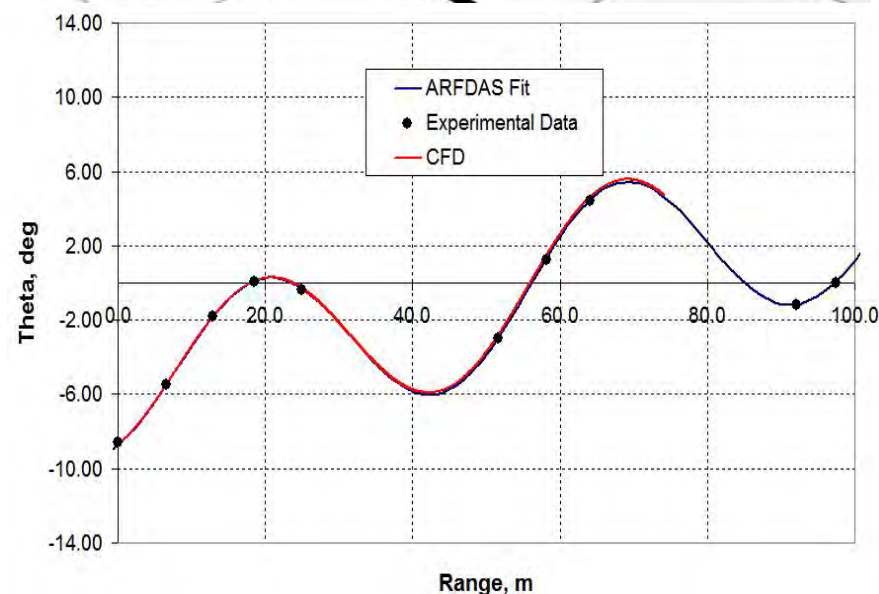
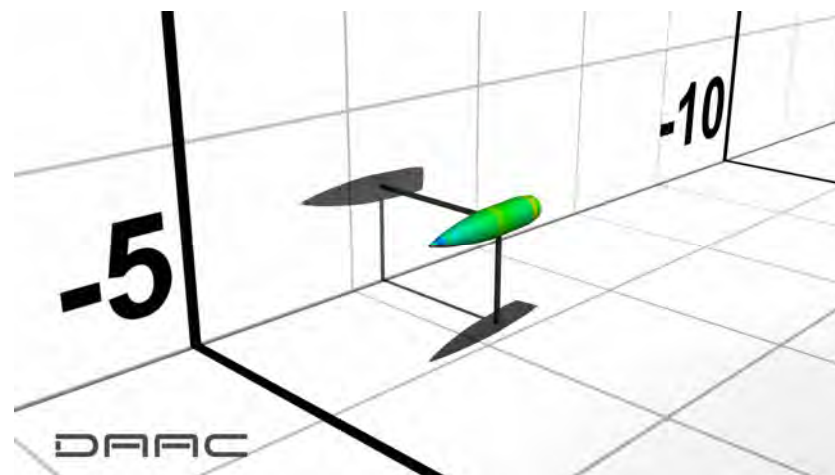
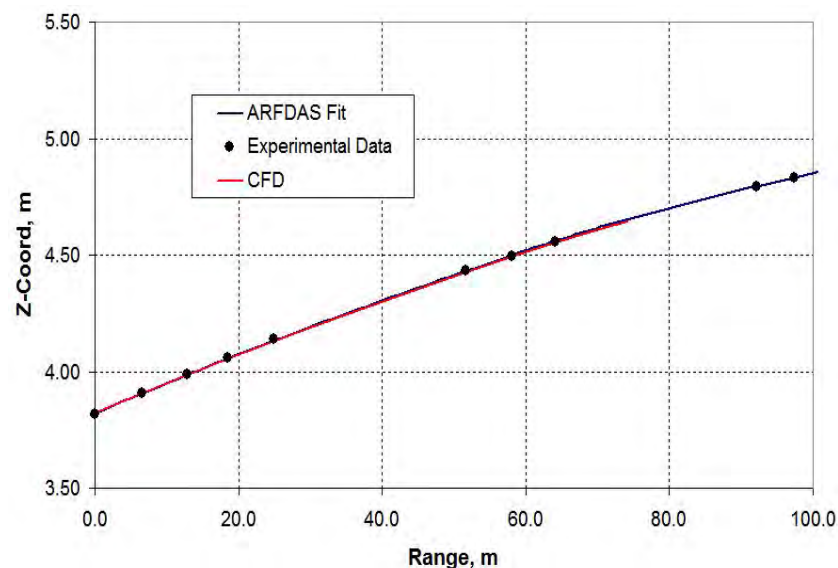
Virtual fly-out technique computes the trajectory of an in-flight spinning projectile; computed results match well with the flight test data

TECHNOLOGY DRIVEN. WARFIGHTER FOCUSED.

Virtual Fly-Out of a Spinning Projectile Initial Mach = 1.1 (Transonic Flight)



Z-distance



Virtual fly-out technique computes the trajectory of an in-flight spinning projectile; computed results match well with the flight test data.

TECHNOLOGY DRIVEN. WARFIGHTER FOCUSED.

Extraction of Aerodynamic Coefficients from Virtual Fly-Out Simulations



Spinning Projectile

raction of All Aerodynamic Coefficients



Pitch-Damping Moment Coeff.

Virtual fly-outs simulations require only the total aerodynamic forces and moments to fly the projectile.

How do we extract the aerodynamic force and moment coefficients from the virtual fly-out simulations? How good are they?

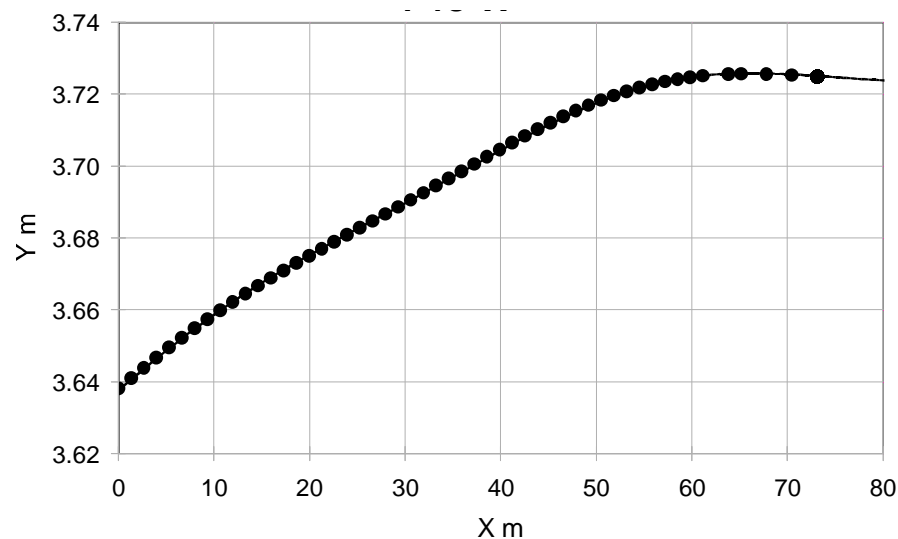
Different Approaches:

1. Aerodynamic coefficients extracted from CFD/RBD virtual fly-out solutions using range reduction software (ARFDAS, for example).
2. PACE - Simple fitting procedure that require a set of short time-histories (virtual fly-outs) at different Mach numbers.

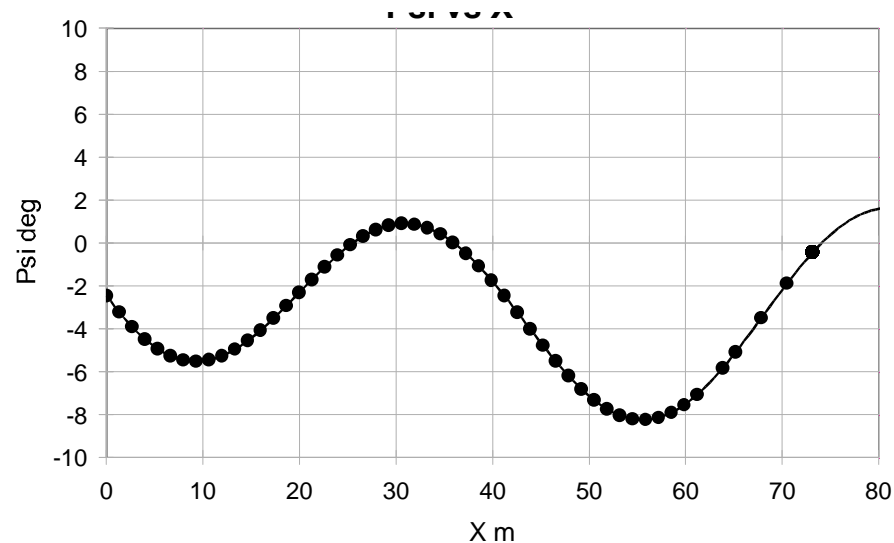
ARFDAS Fit of CFD Generated data Initial M = 1.1



1. Aerodynamic coefficients extracted from CFD using range reduction software, ARFDAS using the virtual fly-out solutions
2. Position (x,y,z) and the orientation (three Euler angles) of the projectile, obtained from the virtual fly-out simulations were provided as input to ARFDAS. ***Same procedure is used for actual flight measured data.***



Y-distance



Euler roll angle

Extracted force and moment coefficients (static and dynamic) from virtual fly-out simulation

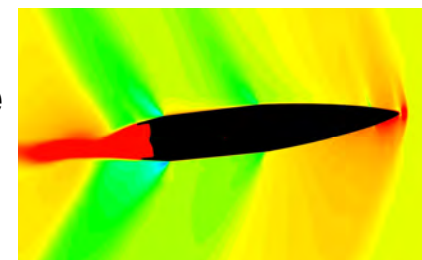


Data Source	Zero-Yaw Axial Force Coeff., C_{D_0}	Normal Force Coeff. Deriv., C_{N_α}	Pitching Moment Coeff. Deriv., C_{m_α}	Pitch Damping Moment Coeff., C_{m_q}	Magnus moment Coeff. Deriv., $C_{n_{p_\alpha}}$	Roll Damping Moment Coeff., C_{l_p}
Spark Range	0.359	2.081	4.209	-25.3	1.05	-0.019
CFD	0.335	2.362	4.283	-22.9	0.93	-0.019

Aerodynamic coefficients extracted
 from the virtual fly-out method
 matches very well with those
 obtained from free flight tests.



Validate using separate
 unsteady CFD
 (Virtual wind tunnel
 method)



Pitch Damping Moment



$$\text{Pitch Damping Moment} = \frac{1}{2} \rho V^2 S d \left(\frac{q d}{2V} \right) (C_{m_q} + C_{m_{\dot{\alpha}}})$$

Pitching motion imposed:

$$\alpha = \alpha_m + \alpha_0 \sin(\omega t)$$

Here,

C_{m_q} = pitch damping moment coefficient due to q

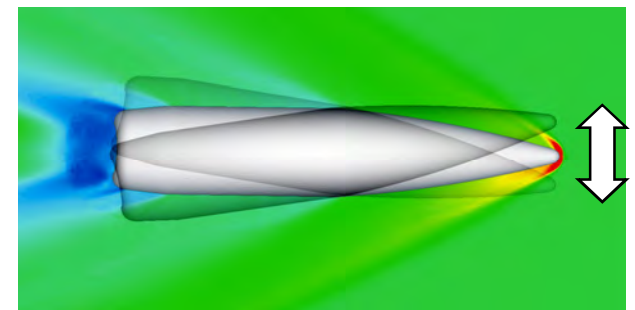
$C_{m_{\dot{\alpha}}}$ = pitch damping moment coefficient due to $\dot{\alpha}$

α = instantaneous angle of attack

α_m = mean angle of attack

α_0 = pitch amplitude

ω = pitch frequency, related to reduced frequency ($k = qd/2V$)

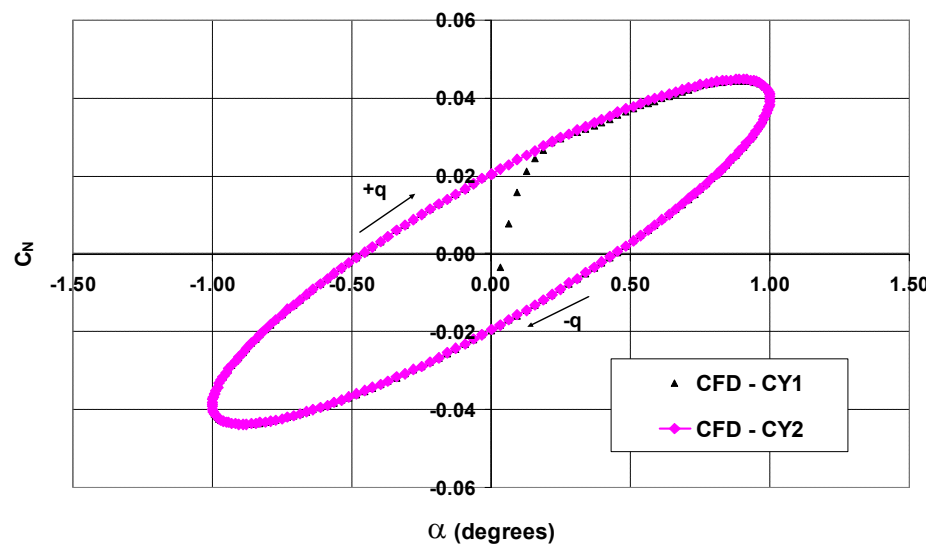


**Virtual wind tunnel method
(Imposed pitching motion)**

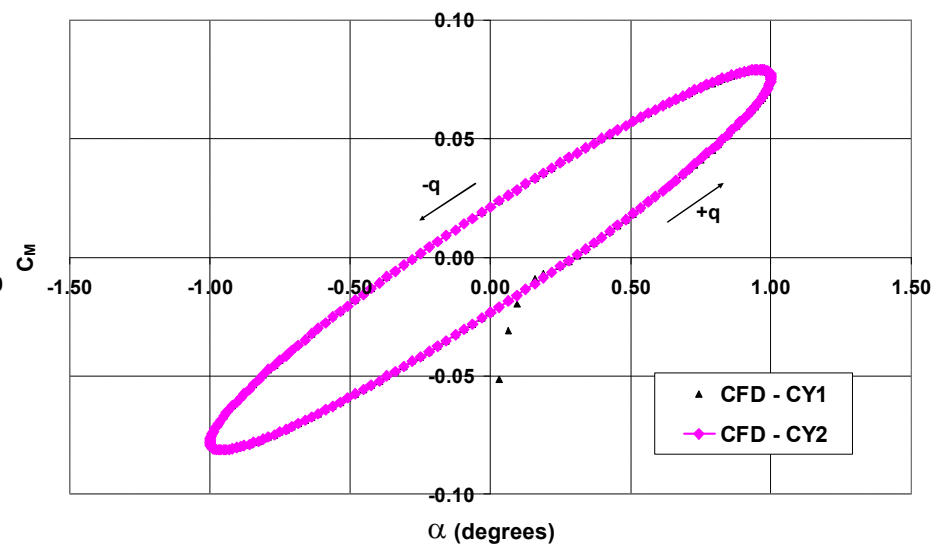
Time-Histories of Normal Force and Pitching Moment coefficients



Mach = 1.1
 $\alpha_0 = 1.0$, $k = 0.1$



Normal force



Pitching moment


Pitch damping moment is obtained directly from the time-history plot of the pitching moment coefficient resulting from the imposed pitching motion.

Extracted force and moment coefficients from virtual fly-out

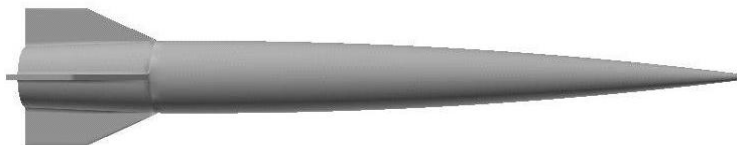


Data Source	Zero-Yaw Axial Force Coeff., C_{D_0}	Normal Force Coeff. Deriv., C_{N_α}	Pitching Moment Coeff. Deriv., C_{m_α}	Pitch Damping Moment Coeff., C_{m_q}	Magnus moment Coeff. Deriv., $C_{n_{p_\alpha}}$	Roll Damping Moment Coeff., C_{l_p}
Spark Range	0.359	2.081	4.209	-25.3	1.05	-0.019
CFD	0.335	2.362	4.283	-22.9	0.93	-0.019

Pitch damping moment extracted from the virtual fly-out method matches very well with that obtained by a separate unsteady CFD approach with prescribed pitching motion.


Computed
 $C_{Mq} = -24.0$ using virtual wind-tunnel approach

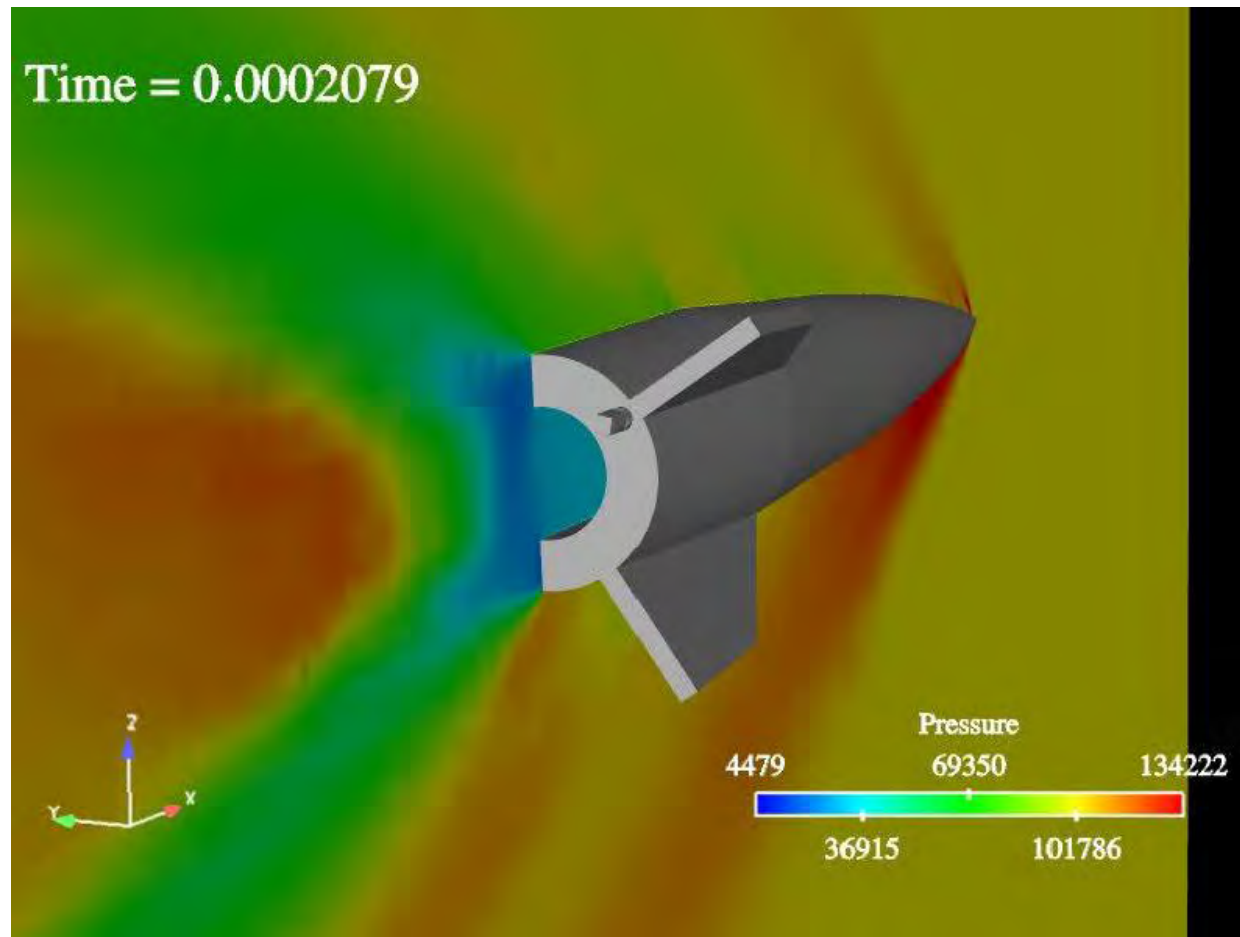
Extraction of Aerodynamic Coefficients from Virtual Fly-Out Simulations



Finned Projectile

Initial Fly-out of a Finned Projectile

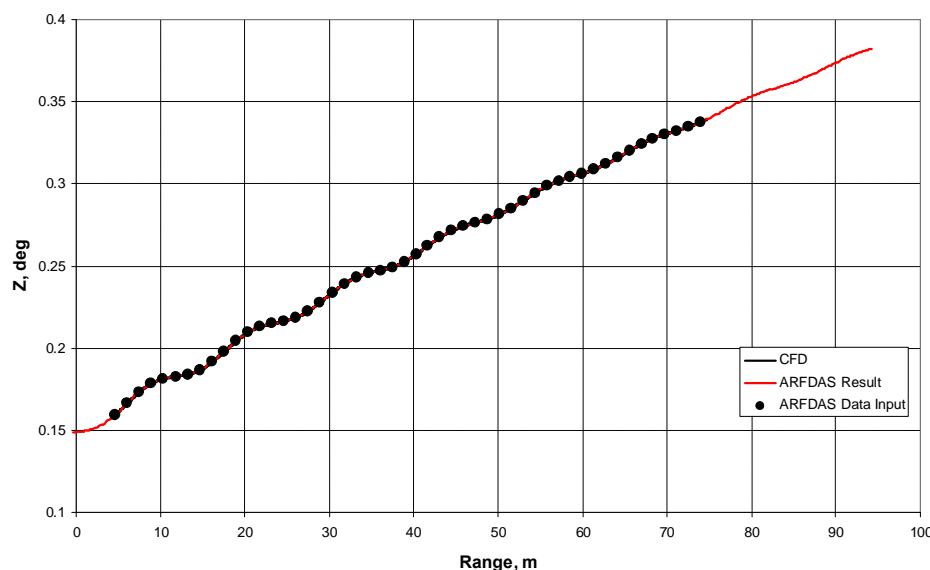
Initial Velocity, Mach = 3 (Supersonic)



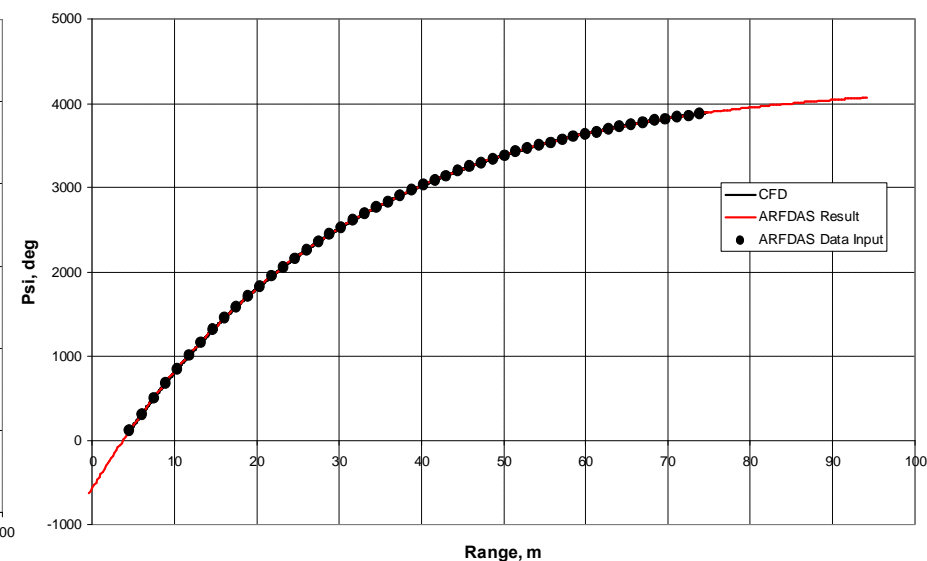
ARFDAS Fit of CFD Generated data Initial M = 3.0



1. Aerodynamic coefficients extracted from CFD using range reduction software, ARFDAS using the virtual fly-out solutions
2. Position (x,y,z) and the orientation (three Euler angles) of the projectile, obtained from the virtual fly-out simulations, were provided as input to ARFDAS. ***Same procedure is used for actual flight measured data.***



Z-distance



Euler roll angle

Extracted Aerodynamic Coefficients from Virtual Fly-Out Simulation



Data Source	Mach No.	CXo	CNa	Cma	Cmq	Clp
Spark Range	3.0	0.221	5.83	-12.60	-196	-2.71
CFD	3.0	0.253	5.88	-12.46	-172	-3.24



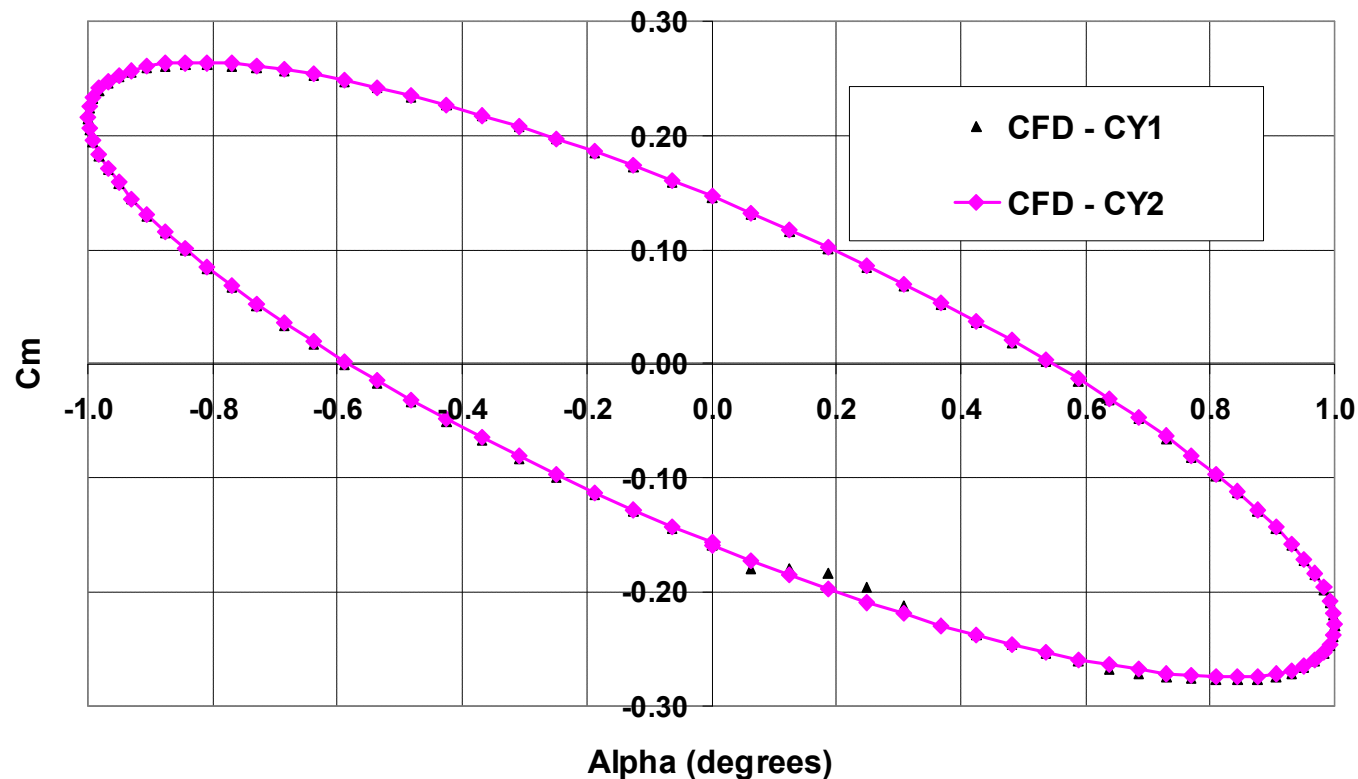
Pitch-Damping Moment Coefficient

Time-history of the Pitching Moment with Angle of Attack



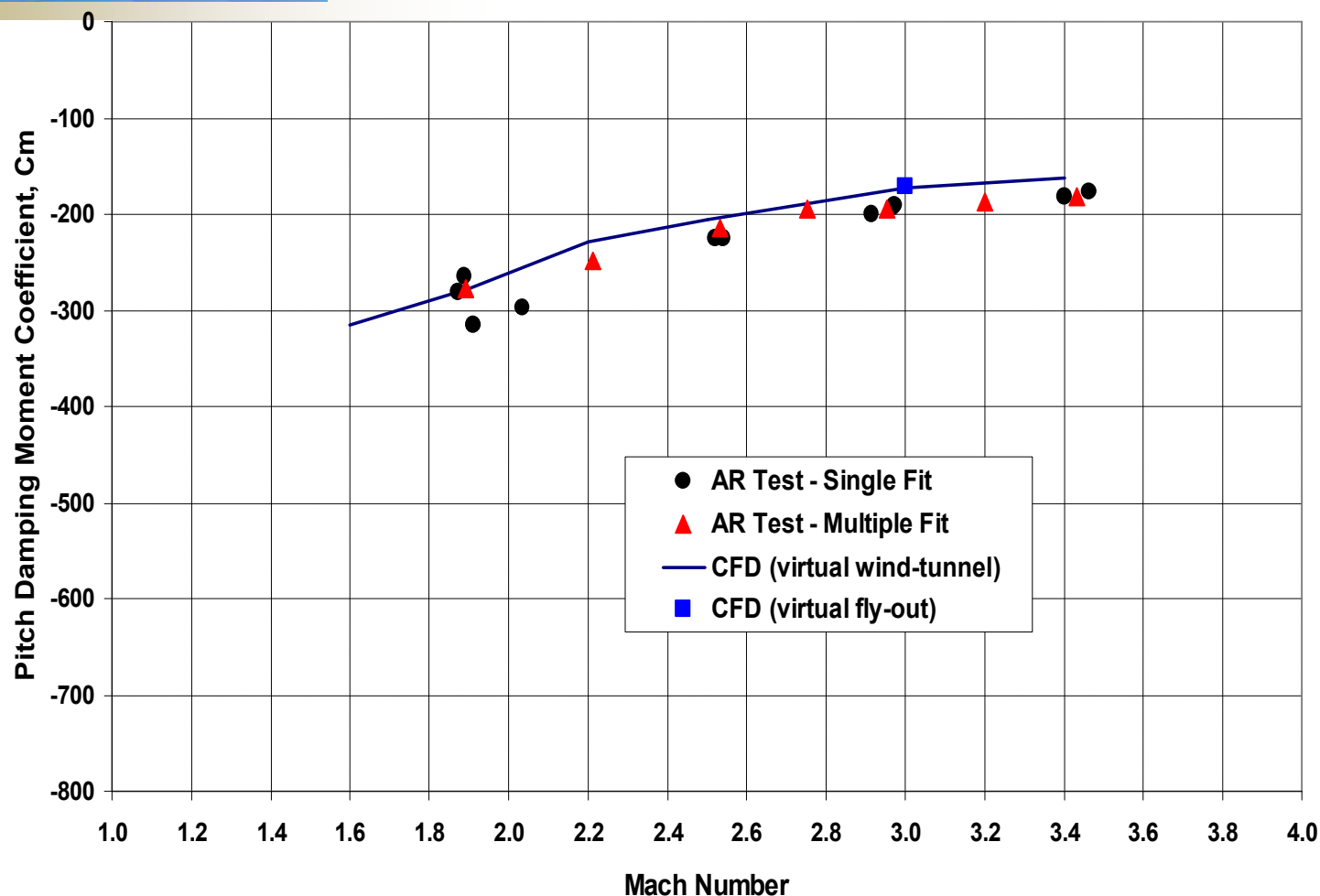
Mach = 3.0

Virtual Wind Tunnel Method



Pitch damping moment is obtained directly from the time-history plot of the pitching moment coefficient resulting from the imposed pitching motion.

Computed Pitch-Damping Moment Coefficient as a function of Mach number



- Computed pitch-damping moment coefficients match fairly well with the data obtained from free flight tests.
- Almost identical prediction by both virtual fly-out and virtual wind-tunnel techniques.

TECHNOLOGY DRIVEN. WARFIGHTER FOCUSED.

Concluding Remarks



- **Multidisciplinary CFD/Rigid Body Dynamics Coupling for Virtual Fly-Outs**
 - **Integrated unsteady aerodynamics and flight dynamics**
 - **All aerodynamic coefficients (static and dynamic) can be easily extracted from the same virtual fly-out solution**
 - **Technique easily reduces to the virtual wind tunnel approach for computation of dynamic pitch damping derivatives**
- **Aerodynamic coefficients extracted (both static and dynamic) match fairly well with the data obtained from free flight tests**
- **Both virtual fly-out and virtual wind-tunnel methods essentially predict the same dynamic pitch damping moment coefficients**

A large, faint, circular seal of the Institute for Advanced Technology is centered in the background. The seal features the text "INSTITUTE FOR ADVANCED TECHNOLOGY" around the top and "AUSTIN • TEXAS" around the bottom. In the center, there is a stylized atomic or orbital diagram with the Latin phrase "aspira ad astra" (aspires to the stars) below it.

A Comparative Study of Penetration Codes for Brittle Materials

Dr. Sikhanda Satapathy, Anthony Dawson, Dr. Gregory Rodin
International Ballistics Symposium
New Orleans, Louisiana
September 23, 2008

Objective

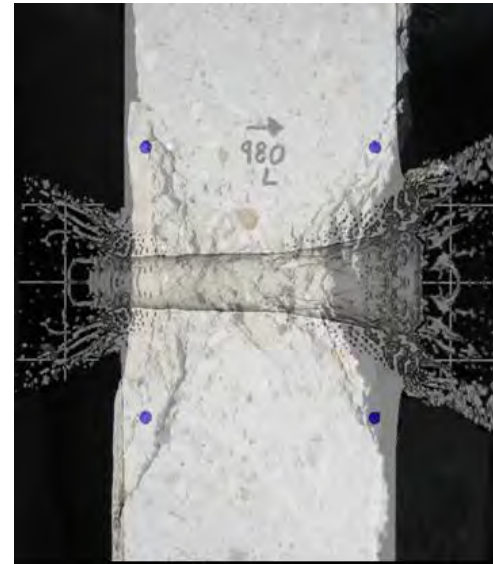
- Identify and exercise computational tools for modeling penetration of concrete targets, and compare with IAT experiments

Back Ground

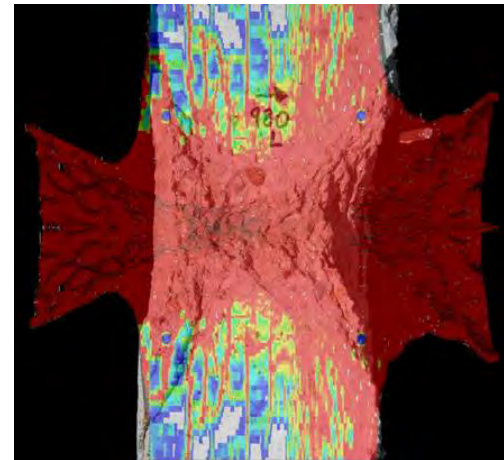
- Earlier comparisons (reported in 2007 HVIS) were not satisfactory
- A non-local peridynamic approach (EMU) was identified for comparison with continuum method (CTH.)

Approach

- Evaluate peridynamics as an alternative approach and compare with CTH's BFK and HJC models.
- Benchmark CTH and EMU with Cavity Expansion Analysis
- Validate with low velocity deceleration data

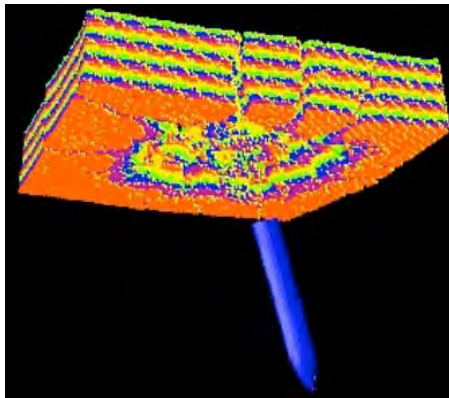
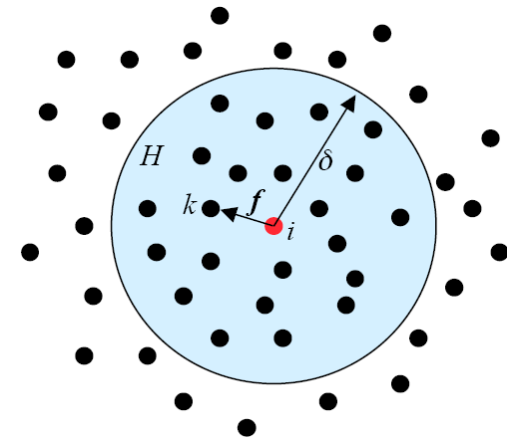
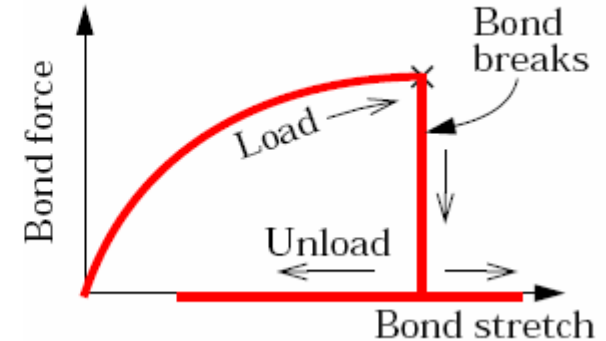


CTH (BFK) model compared with experiment



CTH (HJC) model compared with experiment

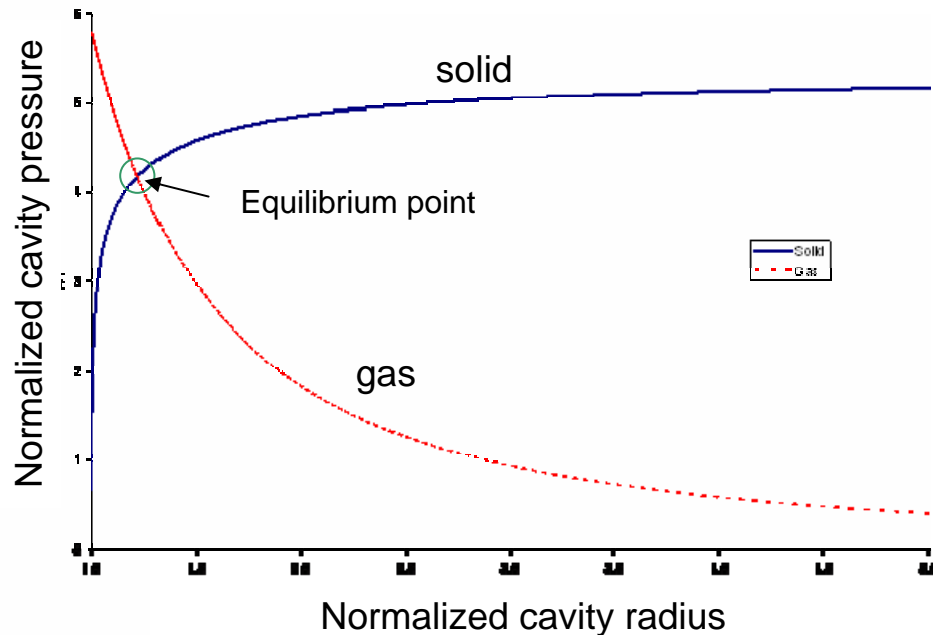
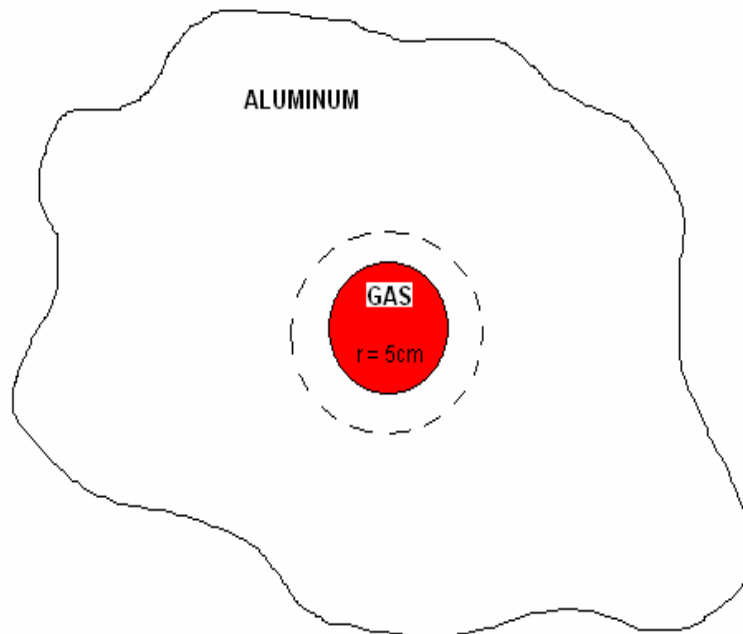
- Classical Continuum Mechanics uses partial differential equations. However, spatial derivatives may not exist everywhere in the body (i.e. fractures)
- Peridynamic method* uses integral equations which hold everywhere in the body, regardless of any discontinuities
- Cracks form by breaking bonds irreversibly.
- Meshless Lagrangian method

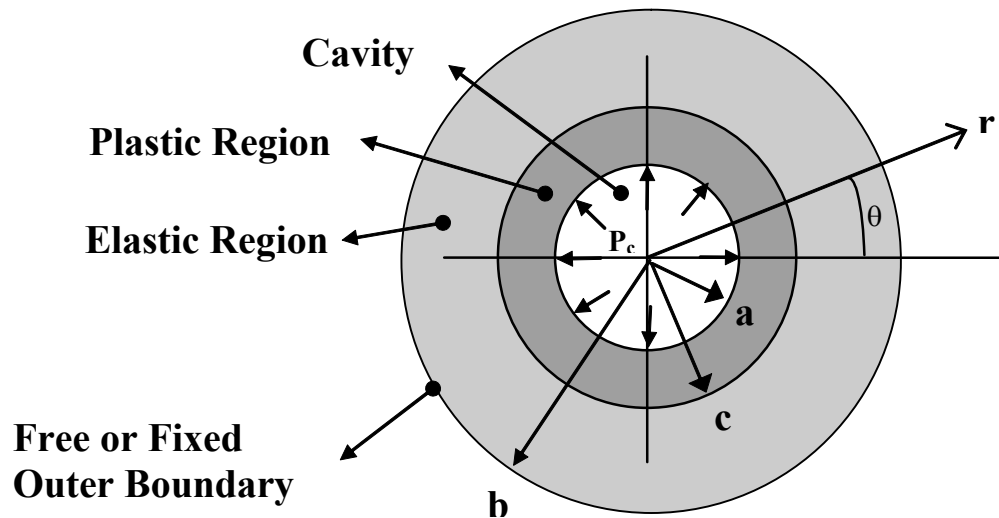


$$\rho \ddot{u}_i^n = \sum_{k \in H} f(u_k^n - u_i^n, \mathbf{x}_k - \mathbf{x}_i) \Delta V_i + b(\mathbf{x}_i, t)$$

* Ref. Silling and Askari, Comp. Struct., 2005

- Cavity expansion problem was chosen for verification purposes.
- Since traction boundary conditions couldn't be imposed easily neither in CTH nor in EMU, a surrogate problem was chosen
- Cavity was filled with high pressure gas that expanded in an infinite body of aluminum until it reached equilibrium.





Cavity Expansion Pressure

$$\frac{P_c}{Y} = \int_0^{\infty} \frac{f(X)}{\exp(3X/2) - 1} dX$$

$P < 2Y/3$:

Elastic stress field ($r > a$)

$$s_r = -P \frac{a_0^3}{r^3} \text{ and } u_r = \frac{Pa_0^3}{4\pi r^2}$$

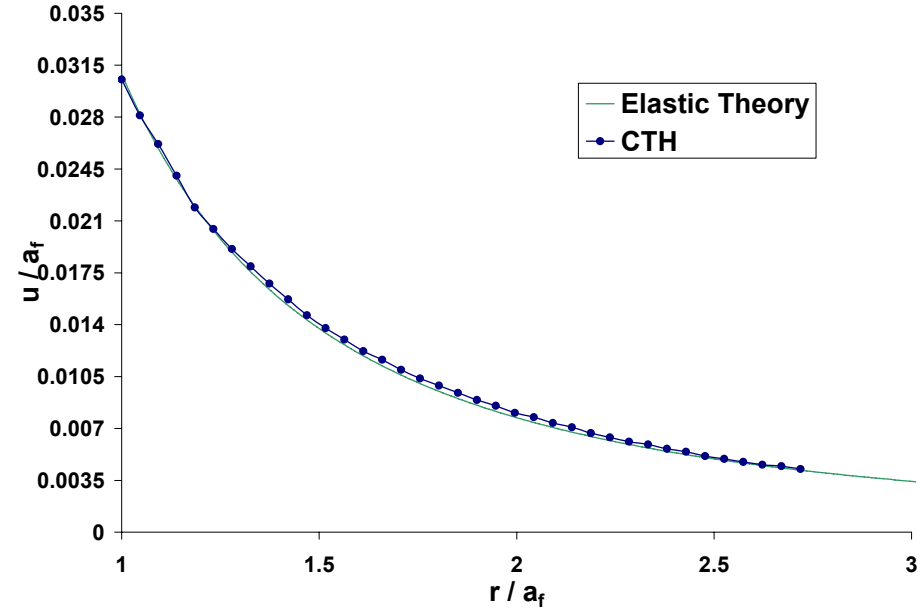
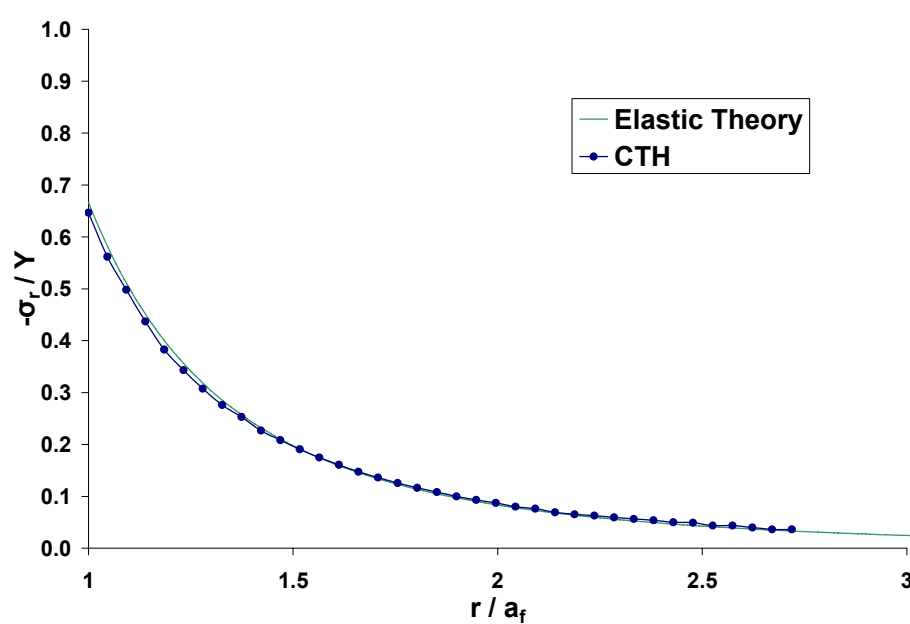
$P > 2Y/3$:

Elastic field ($r > c$)

$$\sigma_r = -\left[\frac{2Y}{3} \left(\frac{c}{r} \right)^3 \right] \text{ and } u_r = \frac{Yc^3}{6\pi r^2}$$

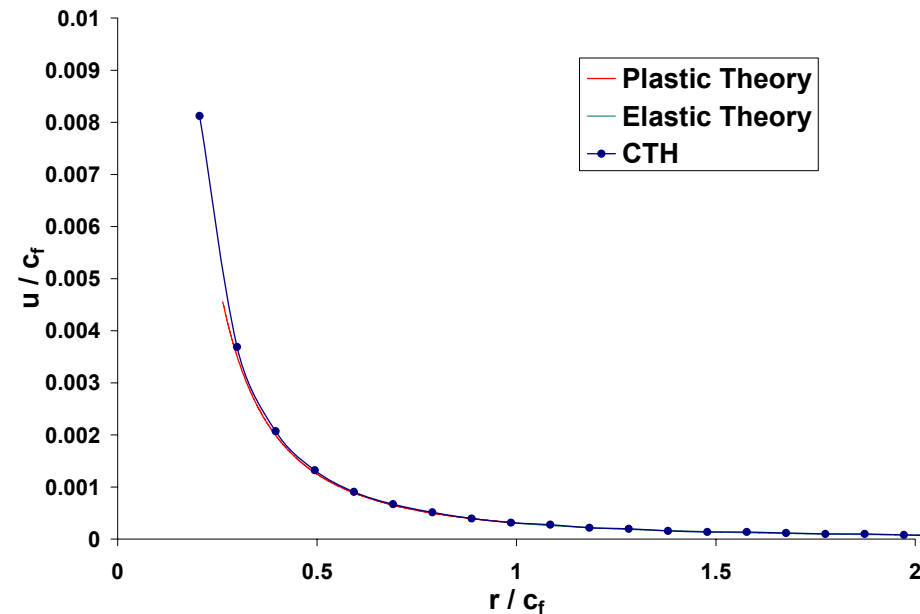
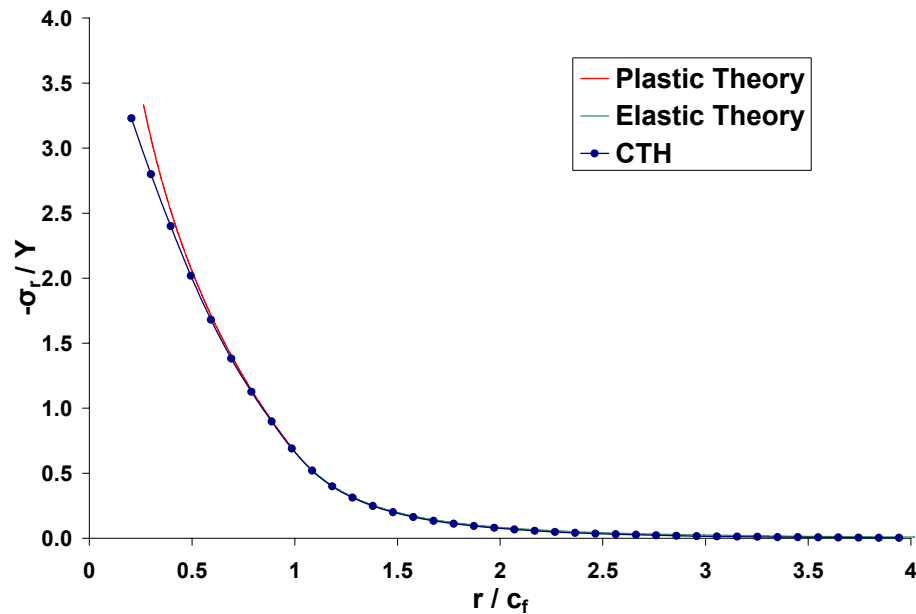
Plastic field ($a < r < c$)

$$\sigma_r = -\left[\frac{2Y}{3} + 2Y \ln \left(\frac{c}{r} \right) \right] \text{ and } u_r = r \left\{ 1 - \left[1 - \left(\frac{c}{r} \right)^3 \left(1 - e^{\frac{-Y}{2\mu}} \right) \right]^{\frac{1}{3}} \right\}$$



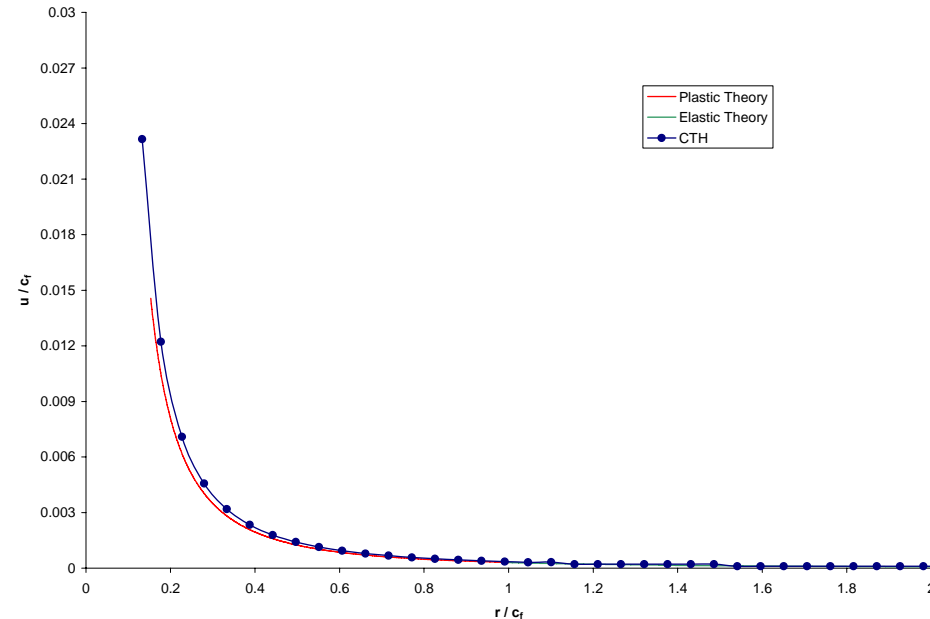
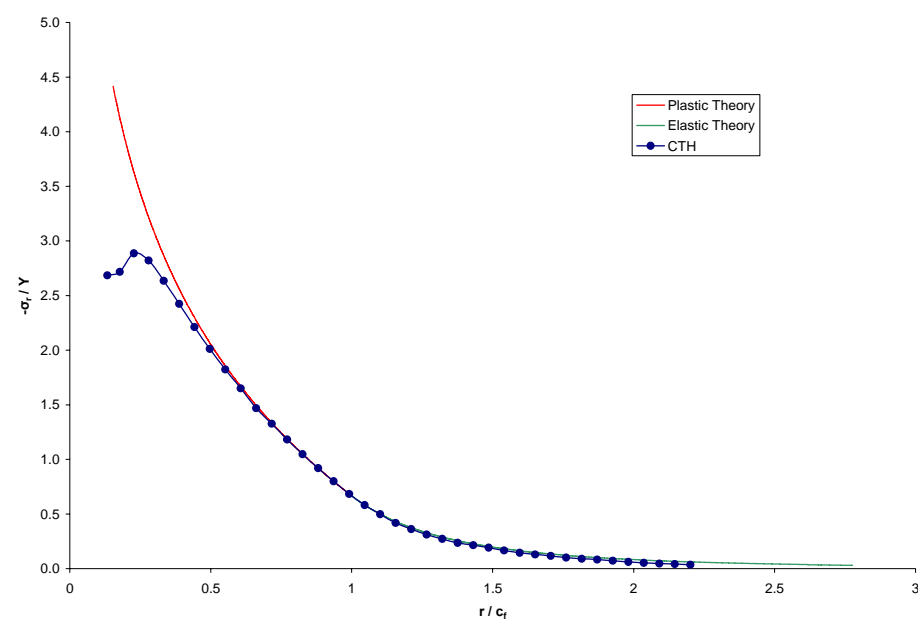
Radial stress and Displacement vs. radius for nominally elastic case

CTH calculation used a linear equation of state and an elastic-plastic strength model



Radial stress and Displacement vs. radius for nominally elastic-plastic case.

Notice the departure of numerical solution from theory near the cavity wall.



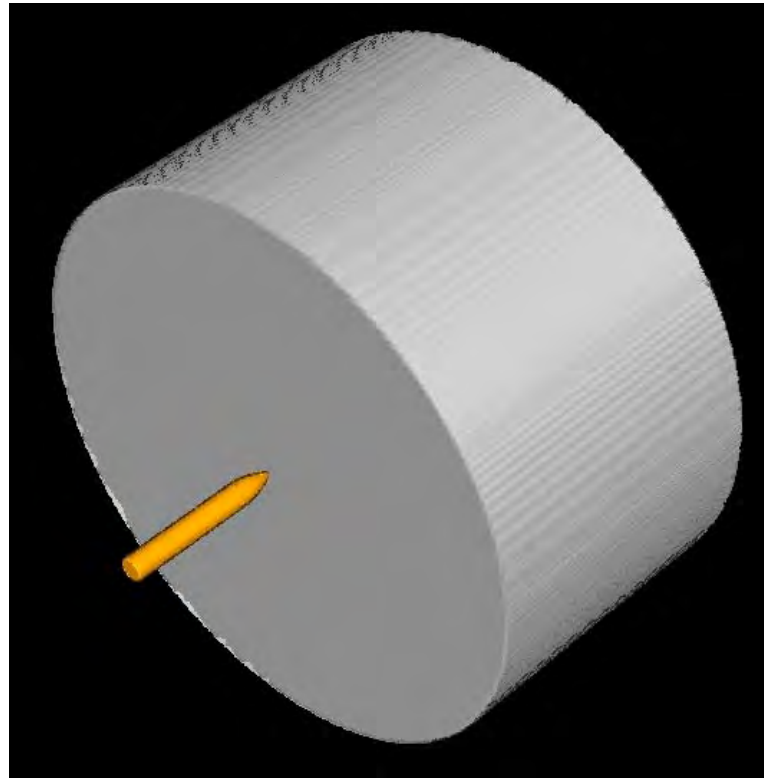
Radial stress and Displacement vs. radius for significant plastic yielding case.

Notice the departure of numerical solution from theory near the cavity wall.

Dynamic Cavity Expansion:
$$P_0 \frac{a_0}{c_a} \frac{\ddot{a}}{\dot{a}} - \frac{2Y}{3} + 2Y \ln \frac{a}{a_0} = b_2 \dot{a} + b_1 a$$

- CTH produced satisfactory results when dynamic effects were not significant.
- EMU implementation did not produce the desired solution since gas diffusion into solid couldn't be prevented.
- Code modification needed to complete the verification process for EMU.

- Rigid penetration into Concrete (1.83 m radius, 23 MPa f'_c)
- Steel Penetrator of 80 mm dia, 13 kg at 380 m/s
- Penetration depth and deceleration measurements taken with accelerometer



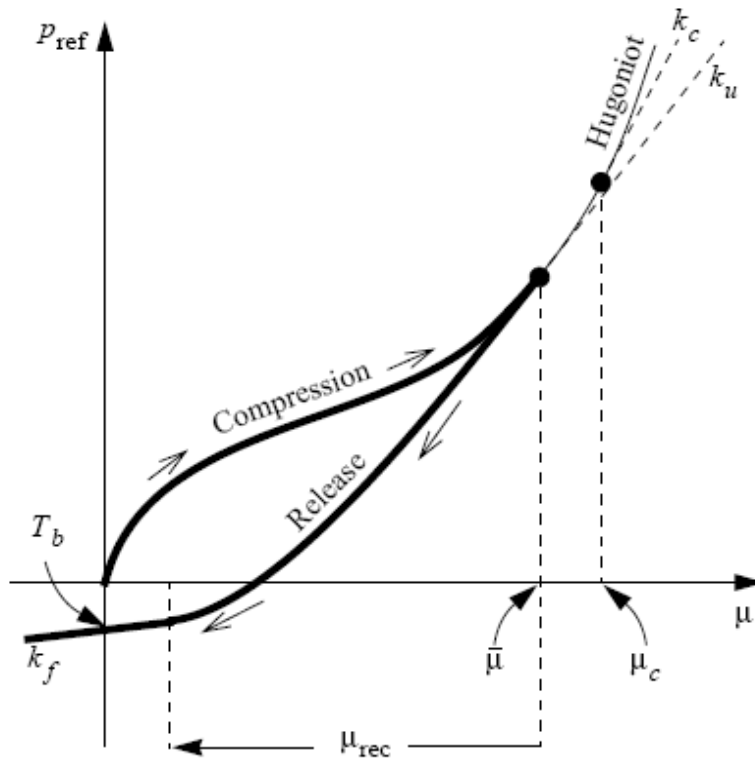


Figure 2.2. Compression (loading) followed by release (unloading) along a reference curve. (Not all the void space is crushed out in this path, $\bar{v} > v_c$.)

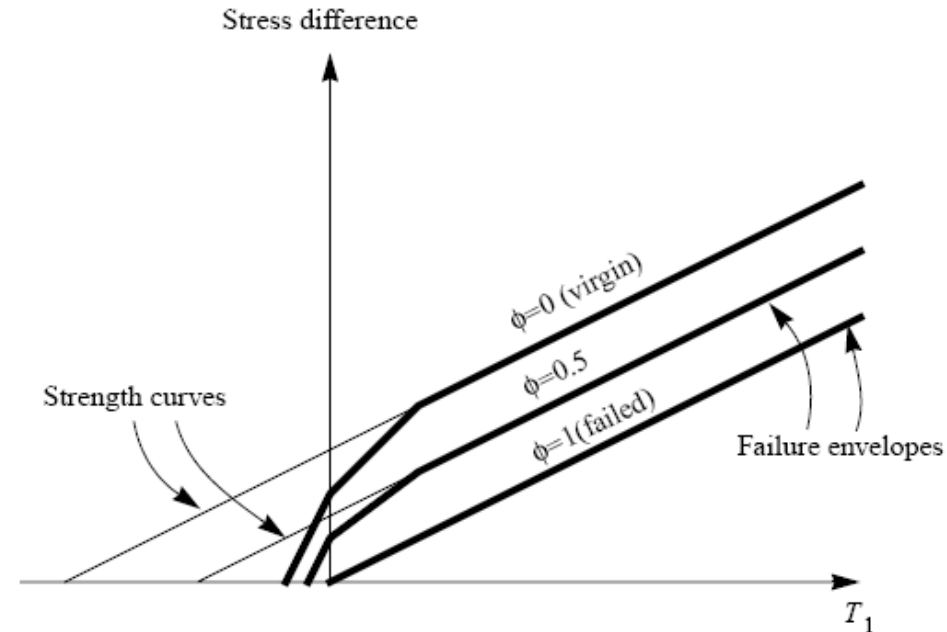
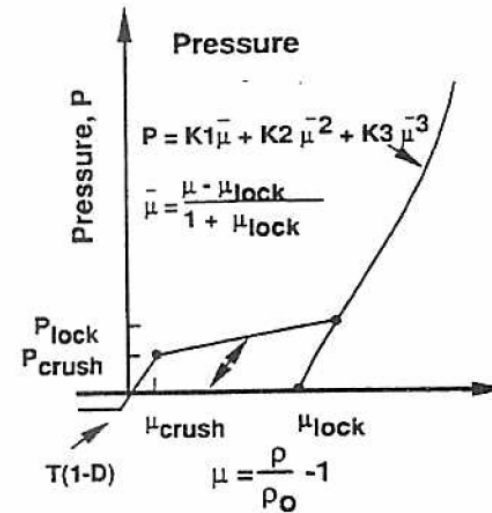
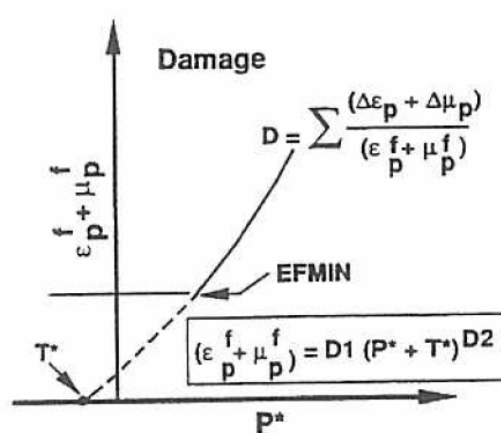
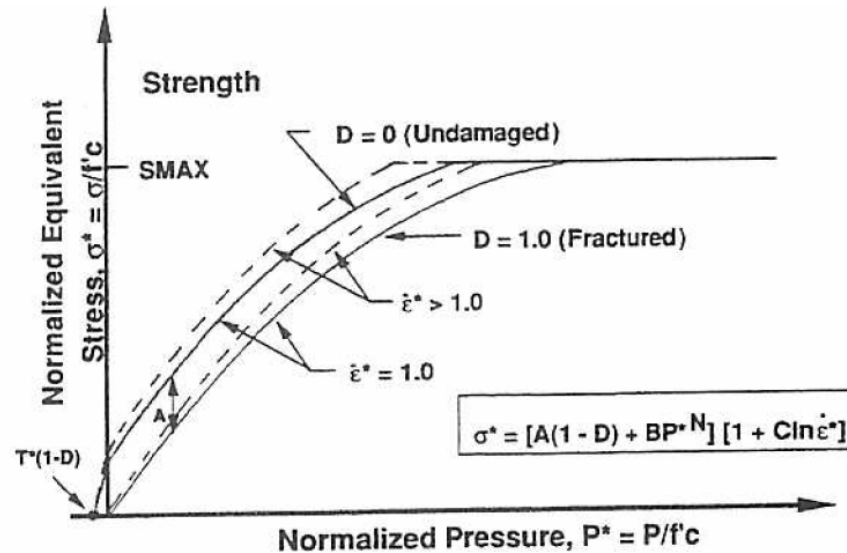
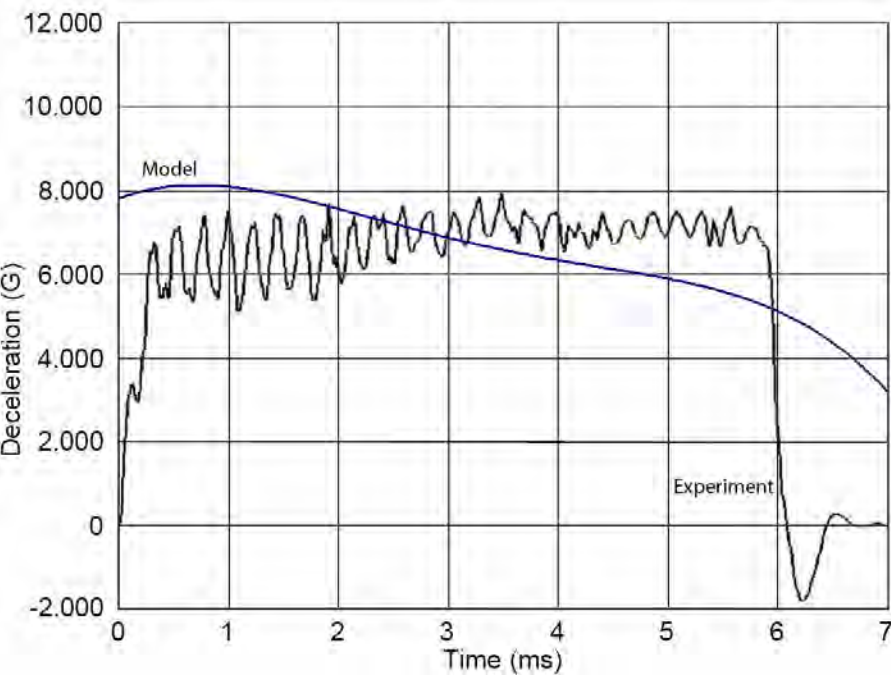


Figure 2.5. Evolution of the failure envelope.

- Scalar damage model explicitly dependent on time
- Damage has three components: brittle, ductile and compressive

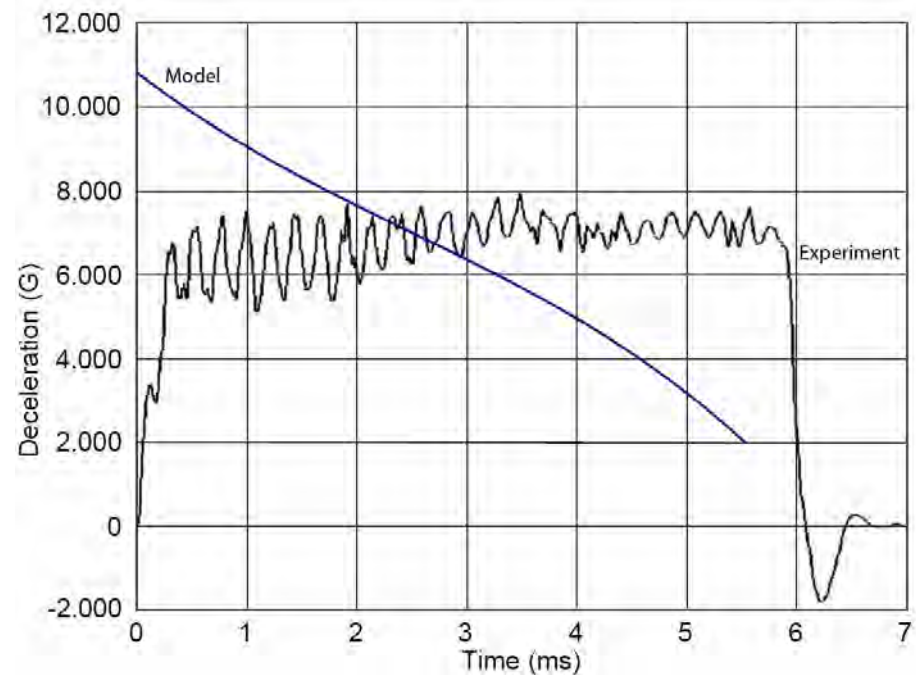


- Damage accumulated from both equivalent plastic strain and plastic volumetric strain (majority from EPS)



BFK

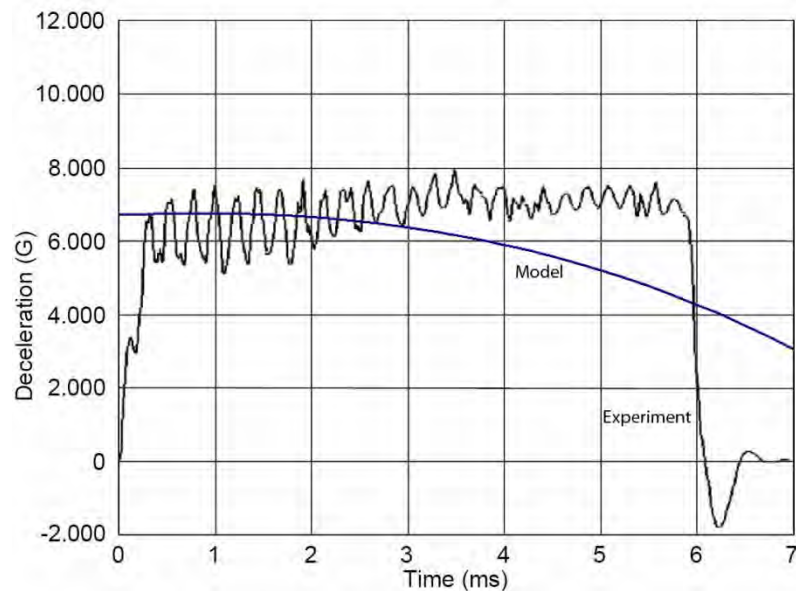
Depth Under-predicted by 5.1%



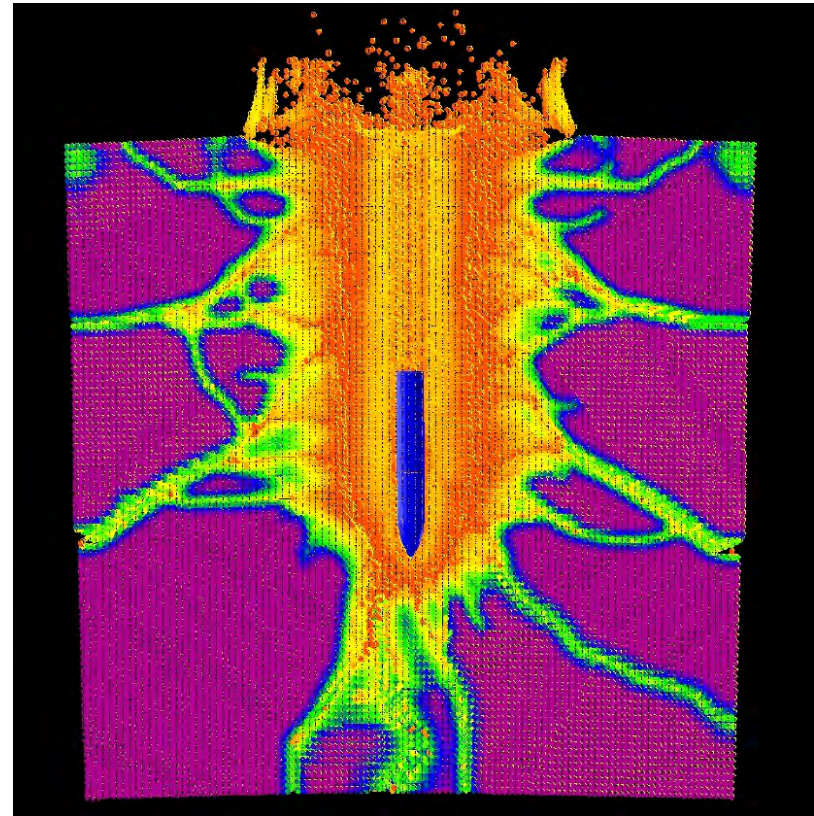
HJC

Depth Under-predicted by 23%

BFK simulation is in much closer agreement with test results than HJC simulation.

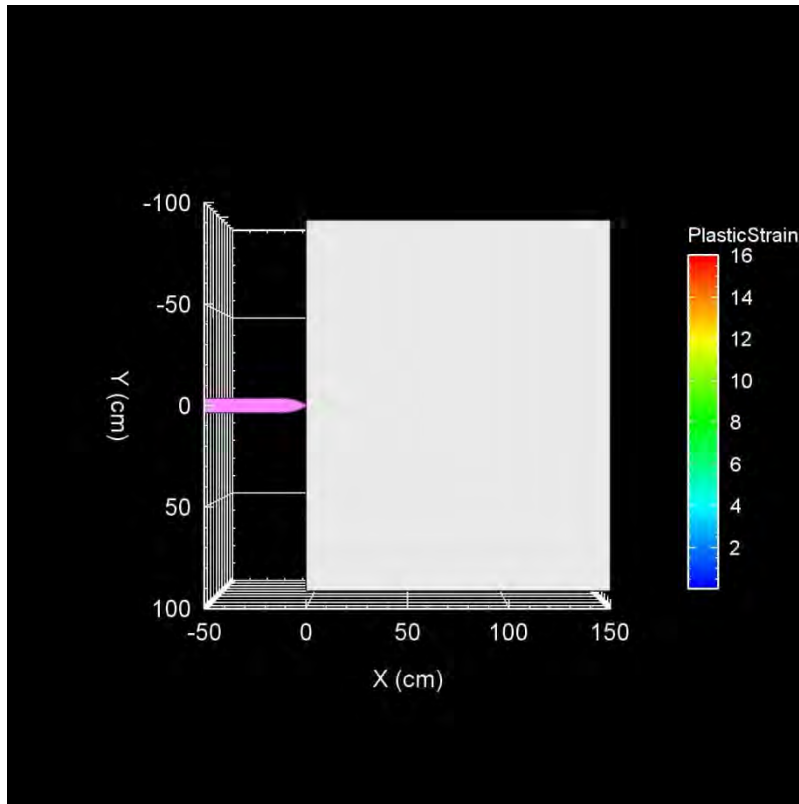


Depth Over-predicted by 0.5%

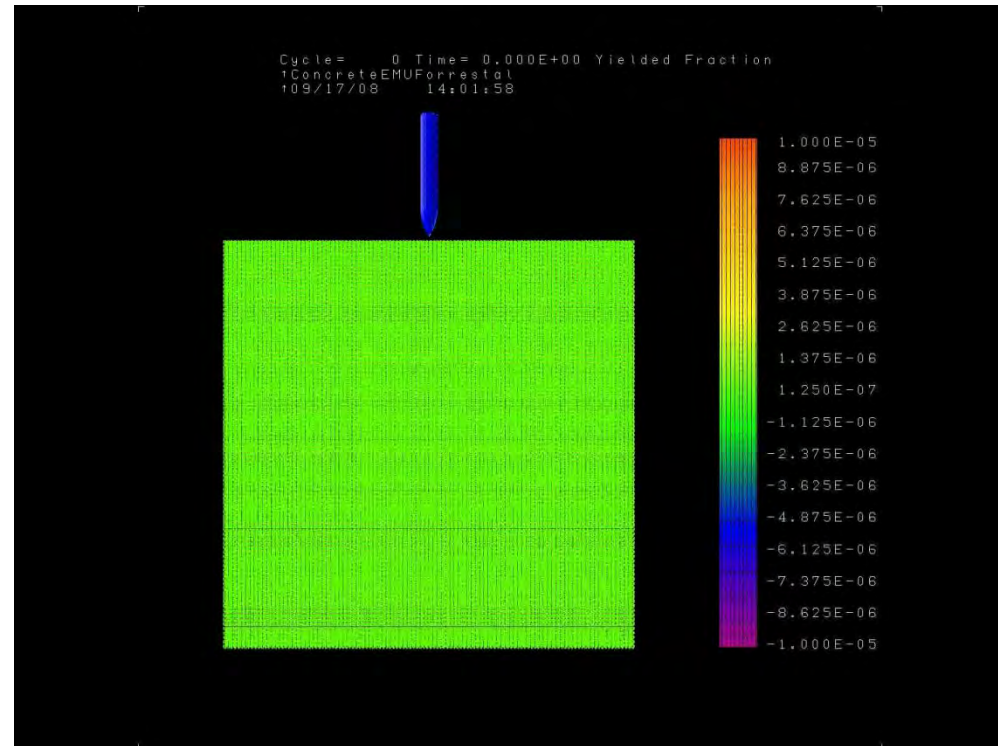


EMU accurately modeled the deceleration

Cracks in target were similar to experimental observations



CTH



EMU

- CTH verification with cavity expansion solution for elastic-plastic materials was satisfactory when dynamic effects were not significant.
- CTH-BFK model produced reasonable agreement with deceleration data.
- EMU verification couldn't be completed due to code limitations.
- EMU agreed with deceleration data very well.
- EMU produced fracture patterns similar to that observed in experiments.

Questions?



RDECOM

**THE MECHANICS OF PROJECTILE ARREST FOR
COMPLIANT CROSS PLIED UNIDIRECTIONAL
LAMINATES**

Brian Scott
Bryan Cheeseman
ARL, APG MD

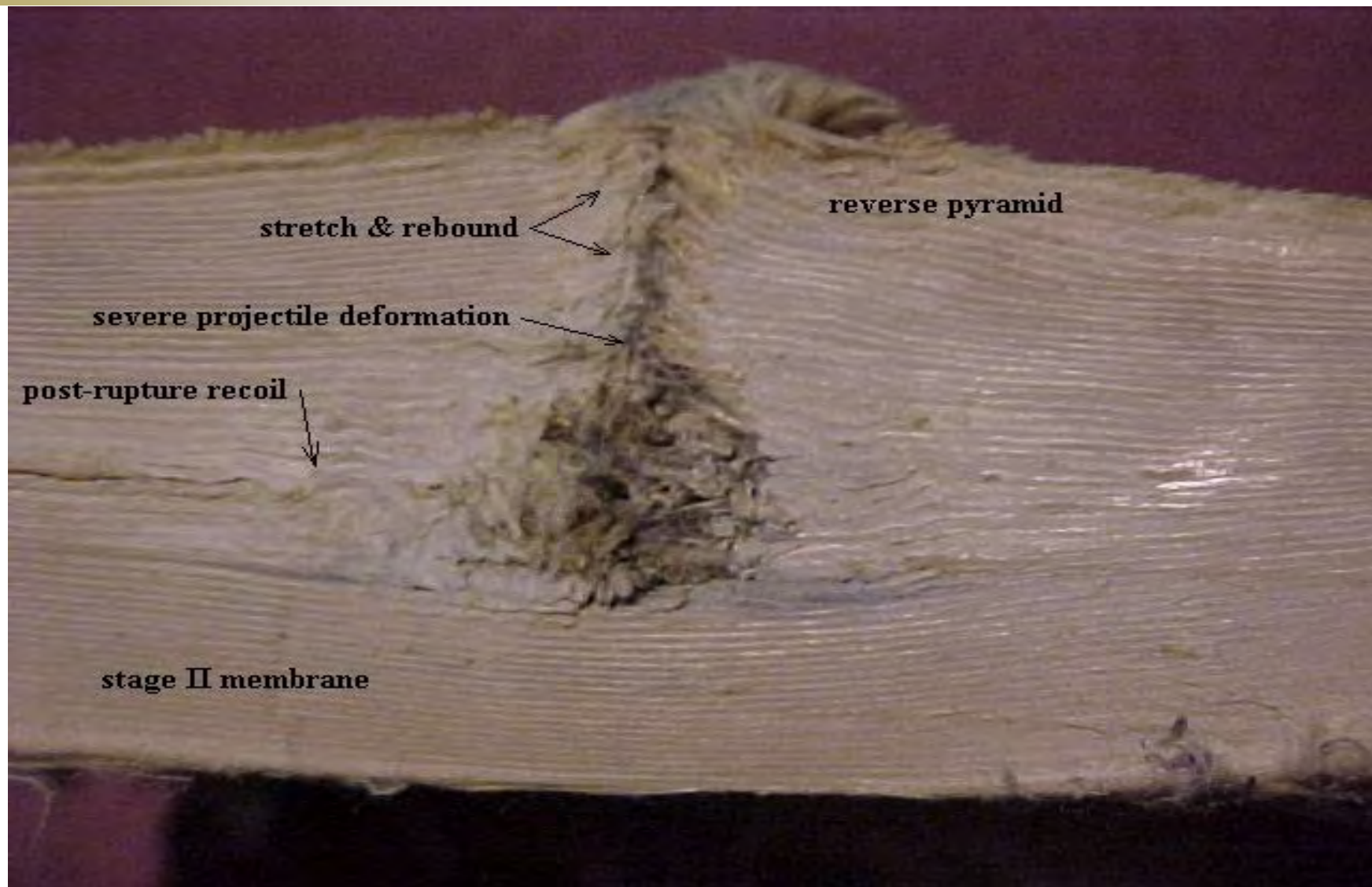


TECHNOLOGY DRIVEN. WARFIGHTER FOCUSED.

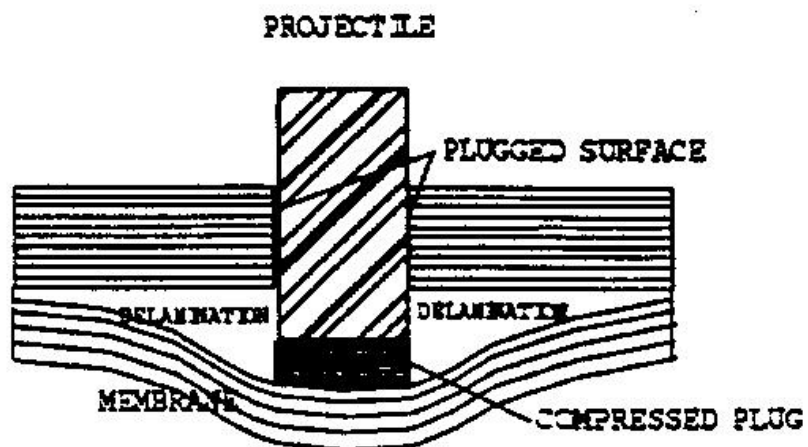
**International Symposium on Ballistics
New Orleans, LA
26 September 2008**

- Experimental observations
- Mechanics hypothesis
- Numerical simulations
- Conclusion

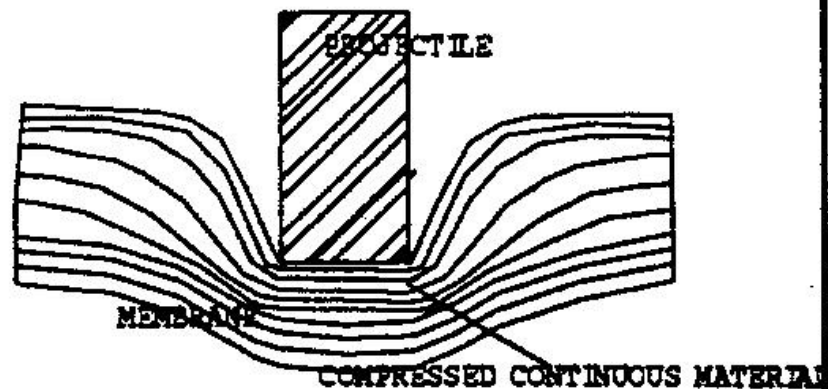
- Penetration of Kevlar Laminate by Long Rods and Jets, Scott, B and Walters, W., 12th ISB, San Antonio, 1990
- Good performance with woven architectures of high strength fibers with 20% phenolic matrix
- Better performance is obtained with:
 - Cross ply unidirectional layup
 - Finer ply architecture
 - Higher strength reinforcements
 - Elastomer (thermoplastic or thermoset) matrices
 - Lower resin content laminates



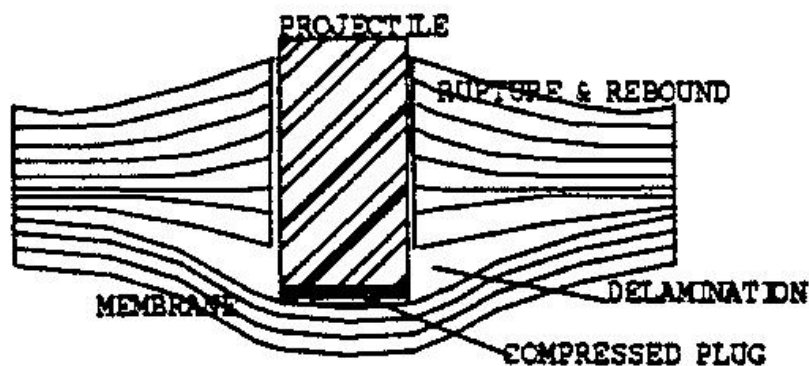
- **Video observations:**
 - Uni structures exhibit global extension and displacement (first inward, then outward)
 - Woven structures exhibit more localized ruptures with less of the far field deformation
- **Evidence of fiber stretching prior to tensile rupture**
- **Thru thickness compression of underlying layers**
- **Aramids exhibit little evidence of transverse shear failure**
- **UHMWPE difficult to discern due to localized melting of fiber ends**
 - Presumably due to passage of or contact with hot projectile
- **Tensile fiber strength: > 500ksi**
- **Transverse fabric shear strength 3 – 5 ksi (aramid or UHMWPE) ASTM D732**
- **Transverse compression strength ? Not well defined yield point (behaves like elastomer)**
- **UHMWPE 20% thicker than aramid laminate at equal areal density**



Classical Plug & Membrane Behavior



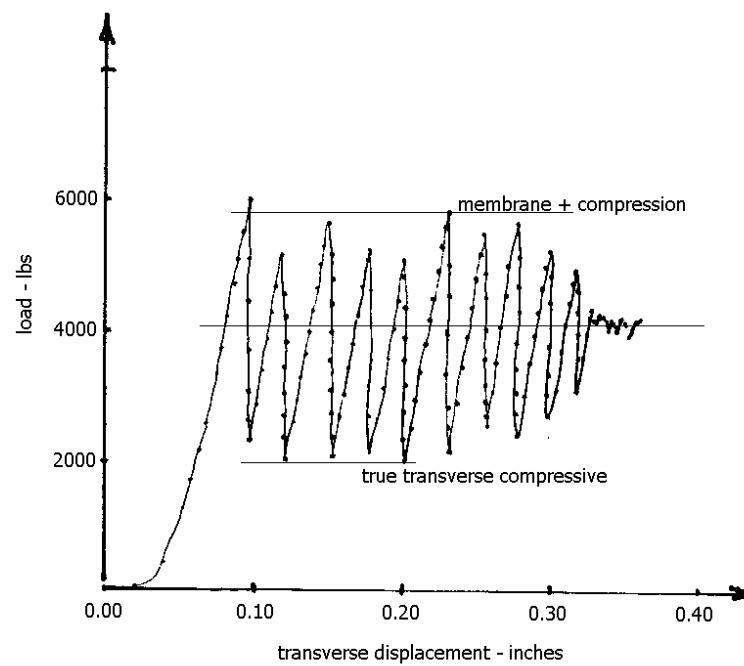
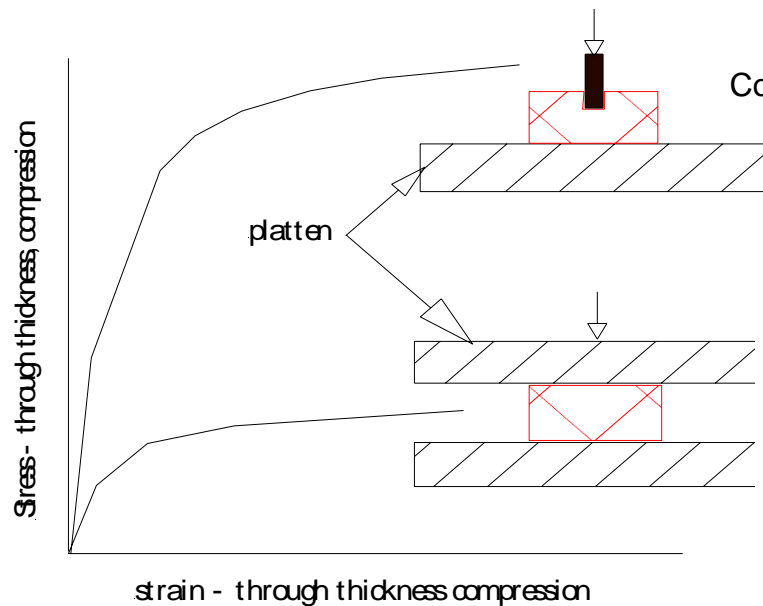
Stage I - Prior to front layer rupture

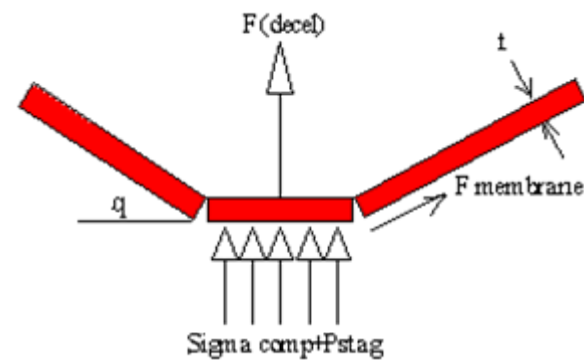
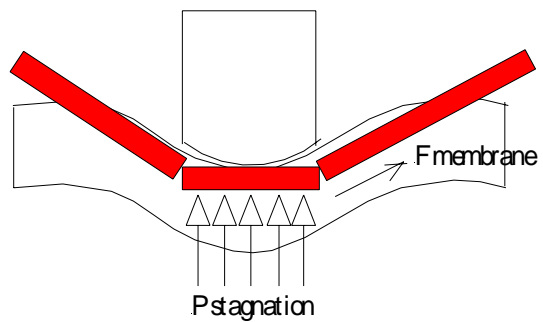


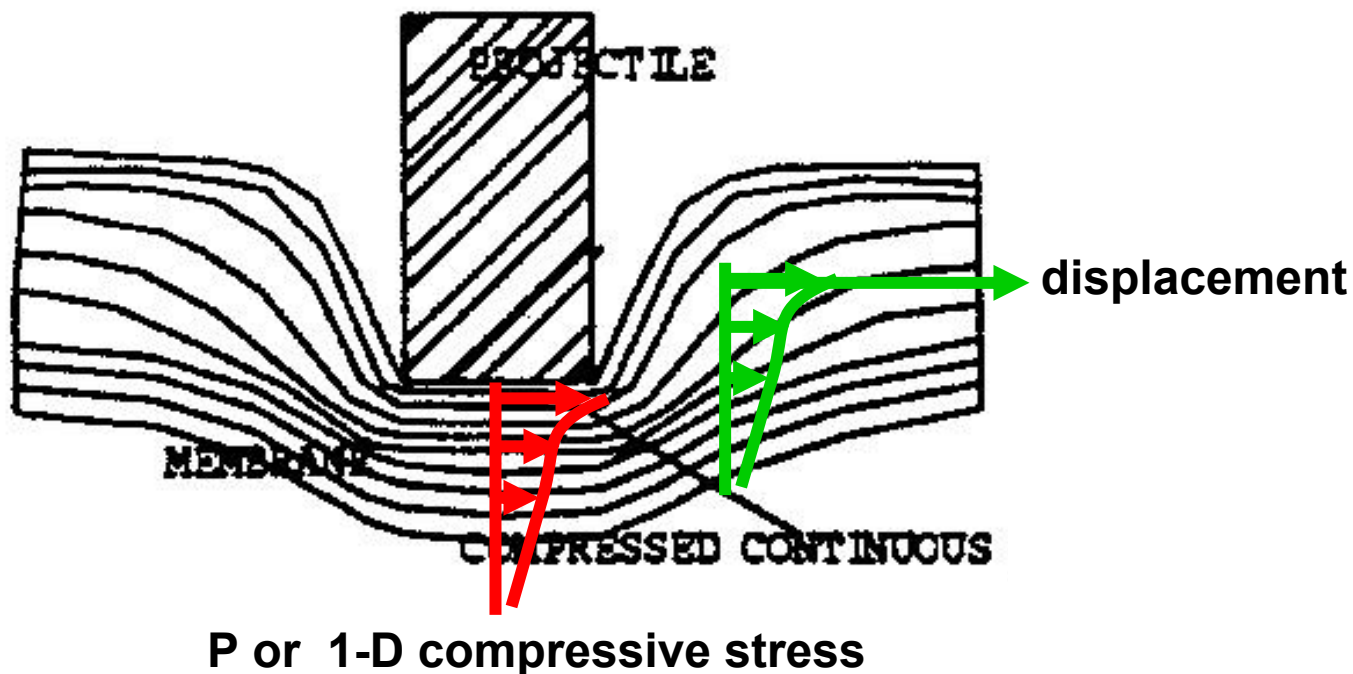
Stage II - Post front layer rupture

Constrained Compression Test

Composites Engineering, Vol 4, No. 3, Woodward, et al, 1994







Surface fibers impacted

Material cannot flow until fibers rupture (approx. 4%)

Surface fibers are compressed transversly and forced into underlying layers

“Self-Confined” material develops large comp stress or hydrostatic pressure

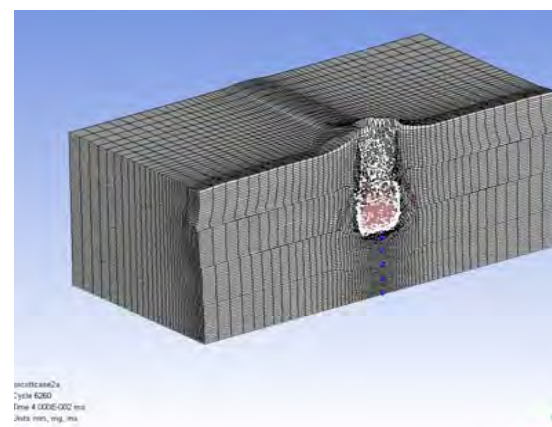
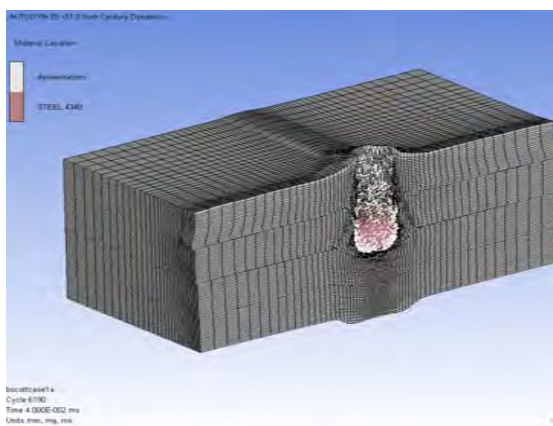
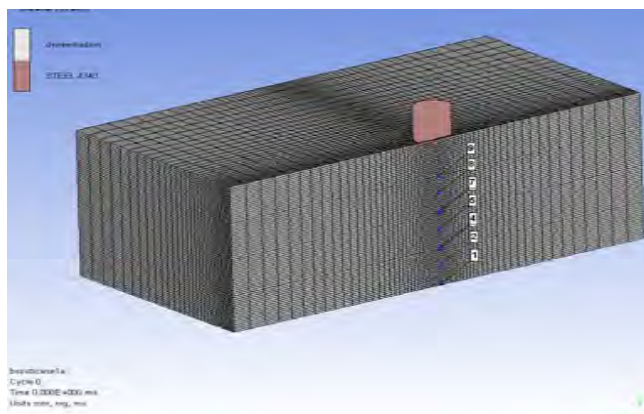
Large compressive stresses decelerate projectile

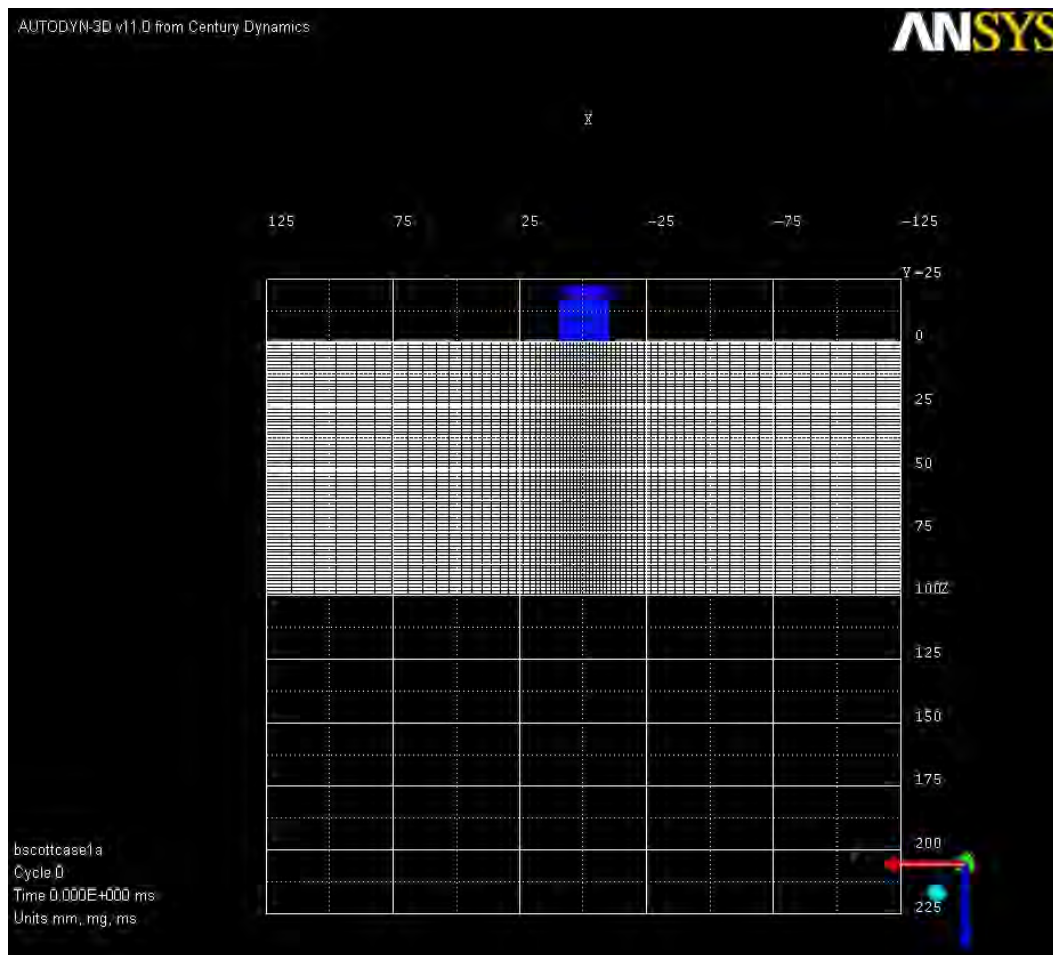
Ansys Autodyn

Dyneema HB2

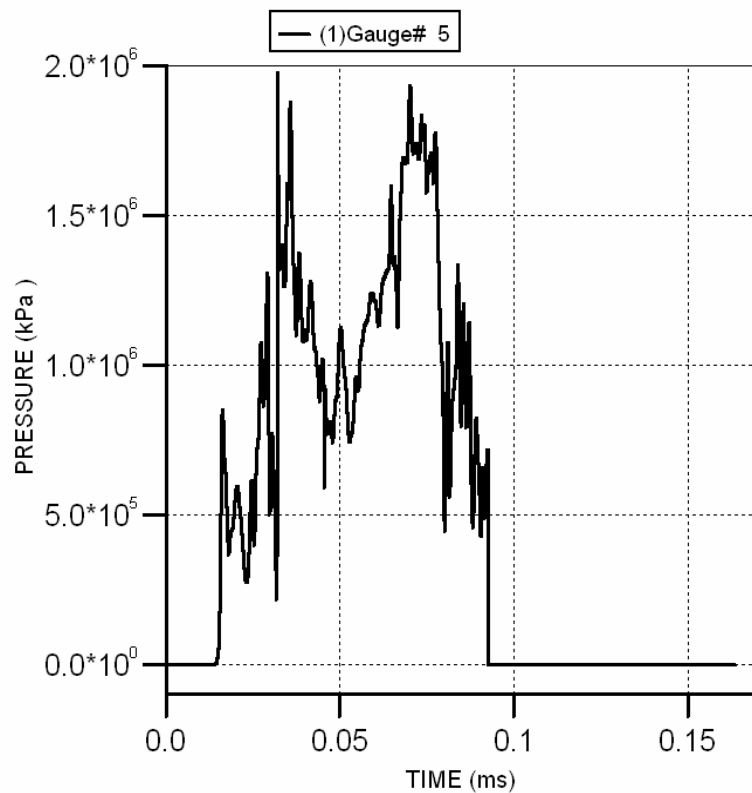
- O'Donoghue, P.E., Anderson, C.E., Jr., Friesenhahn, G. J. and Parr, C. H. 1992. "A Constitutive Formulation for Anisotropic Materials Suitable for Wave Propagation Computer Programs," *J.Comp. Materls.*, p.p. 26(13), 1860-1884.
- Anderson, C.E., Jr., Cox, P. A., Johnson, G. R. and P.J. Maudlin, P.J. 1994. "A Constitutive Formulation for Anisotropic Materials Suitable for Wave-Propagation Computer Programs 2," *Computational Mechanics*, 15(3), 201-223.
- Hiermaier, S., Riedel, W., Clayhurst, C.J., Clegg, R.A. and Wentzel, C.M. 2003. "AMMHIS Advanced Material Models for Hypervelocity Impact Simulations," EMI Report No. 175/03, Freiburg, Germany.
- Riedel, W., Harwick, W., White, D.M. and Clegg, R.A. 2003. "ADAMMO Advanced Material Damage Models for Numerical Simulation Codes," EMI Report No. 175/03, Freiburg, Germany.
- Stijnman, P.W.A., 1995. "Determination of the elastic constants of some composite by using ultrasonic velocity measurements," *Composites*, 26, 597-604.
- Hayhurst, C., Leahy, J., van der Jagt-Deutekom, M., Jacobs, M. and Kelly, P. 2000. "Development of Material Models for Numerical Simulation of Ballistic Impact onto Polyethylene Fibrous Armour," *Proceeding of the Personal Armour Systems Symposium, Colchester, U.K.*
- "Data used to model the ballistic behaviour of HB25 in ADAMMO model of Autodyn," Oct. 17 2006. *DSM Dyneema*, Urmond, The Netherlands.

20 mm diameter 50 gram 4340 steel cylinder
2.0 km/s impact velocity
100 mm thick initial 40 microseconds
Two b.c. Rigid backing / simple frame



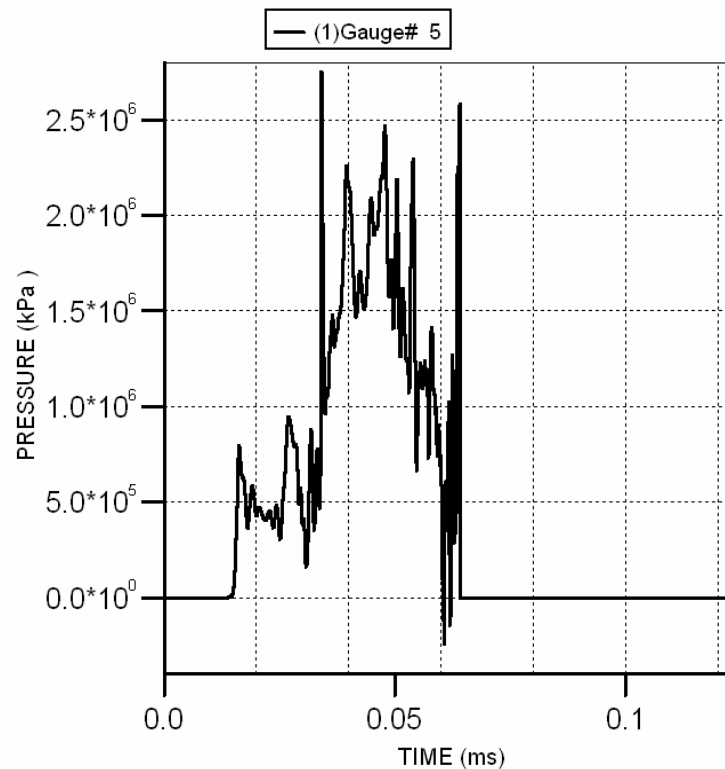


Gauge History (bscottcase1a)

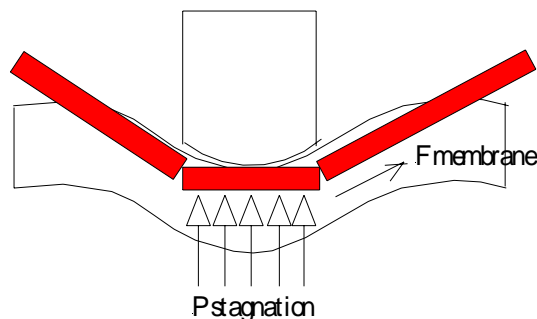


Simple frame b.c.

Gauge History (bscottcase2a)



Rigid backing b.c.



$$\int F \cdot dt = \delta(mv)$$

assume: penetration rate: $u = v / (1 + \sqrt{\rho_t / \rho_p})$
 target thickness: 10.0 cm
 impact velocity: 2000 m/s
 projectile diameter 1.0 cm
 projectile mass 5.0 gm
 $\sqrt{\rho_t / \rho_p}$.35
 linear f(t)

Initial axial momentum: 100 kg m/s

Pressure from simulation: 2M kPa (300 ksi)

Assume uniform over cross-section

First 40 microseconds: 25 kg m/s

- Hypothesis of self-constrained compression leading to extraordinary axial retardation stresses is confirmed by transient simulations
- Comparing two distinct boundary conditions, we identify the benefit of higher thru thickness pressures with the rigid backing case
- The high pressures account for a large fraction of the impulse delivered to the projectile
- The failure modes involving fiber axial tensile strength and transverse compressive strength appear to be uncoupled
- Uni construction allows for more global extension prior to rupture than woven architecture
- Compliant matrix and elastomeric transverse compressive behavior of fibers may be most important

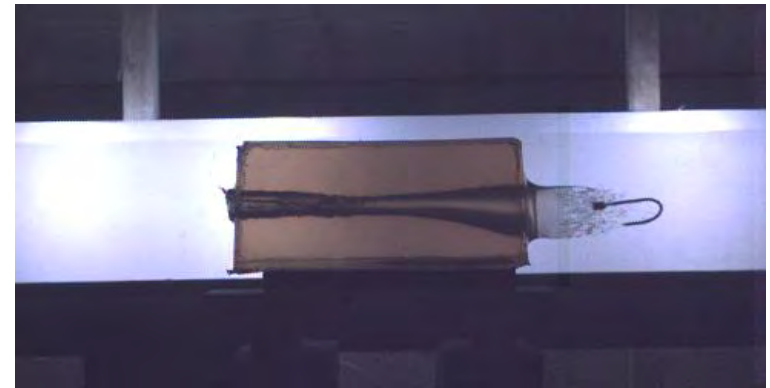
Experiments with Gun Launched Penetrators into Gelatin Target Materials

J. Stubberfield, C. Woodley, N. Lynch and A. Hepper
A presentation to: The 24th International Symposium
on Ballistics

25th September 2008

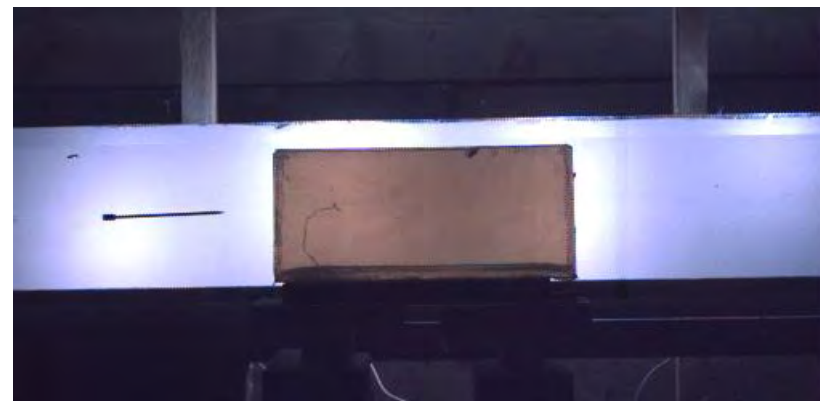


- 01 Penetrator and Launch Package Design
- 02 Interior Ballistic Modelling
- 03 Choice of Gun System
- 04 Instrumentation
- 05 Experimental Set Up
- 06 Target Before Penetrator Interaction
- 07 The Effects of Pitch at Impact
- 08 Targets After Penetrator Interaction
- 09 Conclusions
- 10 Questions



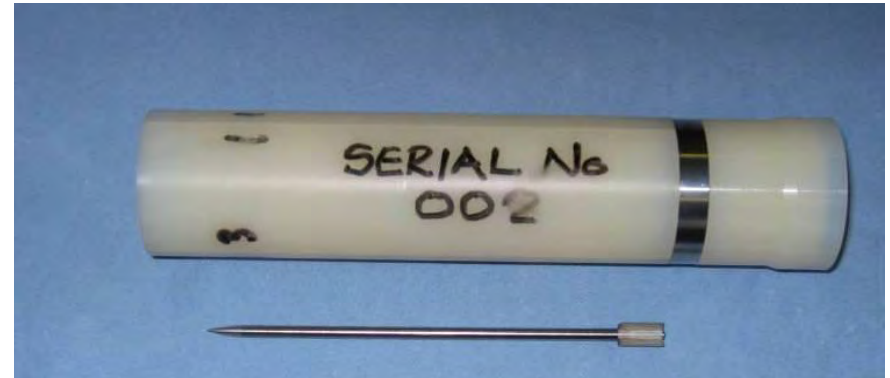
01

Penetrator and Launch Package Design



Launch Package Design

- “ Successful launch of unthreaded, high Length to Diameter (L/D) ratio penetrator requires careful design
- “ Need a light-weight launch package which fully supports the penetrator within the sabot
- “ Close fitting engineering tolerances to eliminate balloting in-bore
- “ Light-weight base pushed launch package
- “ Prevents penetrator buckling in-bore and flexing during its flight to the target



02

Interior Ballistic Modelling



Modelling

- “ Selection of the correct Interior Ballistic (IB) solution critical for success
- “ One dimensional codes can predict muzzle velocities, maximum peak chamber pressures, maximum shot base pressures and other critical characteristics
- “ Codes identify efficient charge designs to avoid catastrophic effects to the gun system
- “ The parameters within the code can be used to condition a launch package in-bore, over the longest possible distance and thus creates what is described as a soft launch phenomena
- “ The QinetiQ Internal Ballistics Simulation (QIBS) version 2.7 was used to predict the IB solution.

03

Choice of Gun System



System

- “ 40mm calibre long barrel, smooth bore powder gun system
- “ Muzzle velocities from $\sim 300\text{m/s}$ to $\sim 2700\text{m/s}$ can be achieved.
- “ Gun system is a three section, smooth bore barrel system with an overall length of 10 meters
- “ The barrel is supported over its length with three tripods
- “ One-piece ammunition system and a modified Bofors 40/70 cartridge case



04 Instrumentation



- “ High speed video techniques enabled the study of penetrator interactions and penetrator impact and residual velocity data
- “ Penetrator pitch at impact and at exit and the related cavity formation determined
- “ Lighting techniques using a diffuser screen and sequential flash bulbs enabled a long capture duration to be used

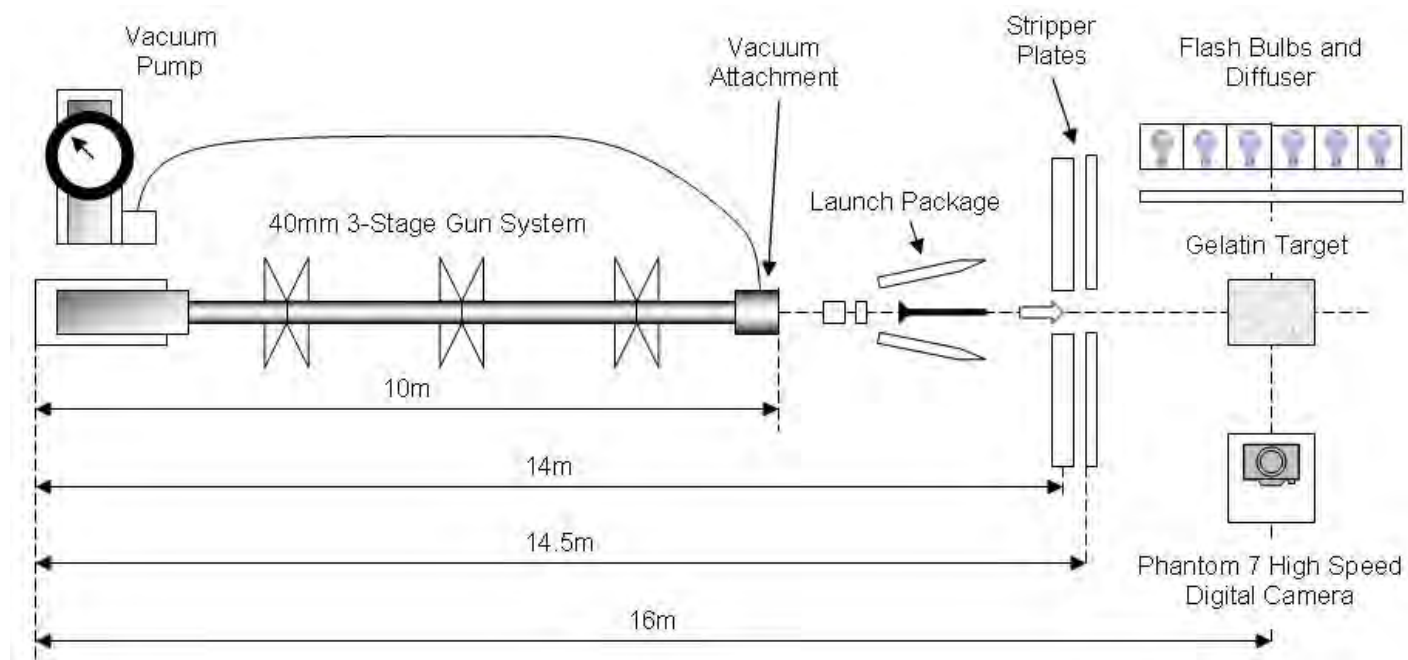


05 Experimental Set Up



Set Up

- Outline diagram showing the overall set up used for the experiments



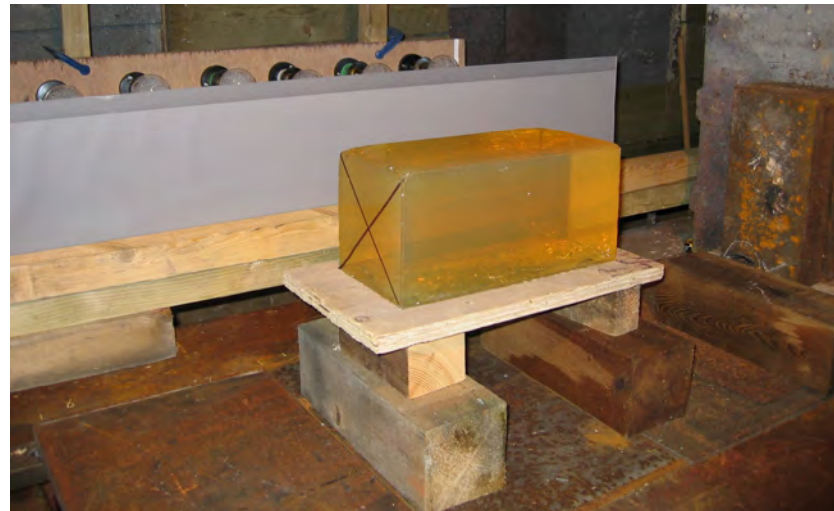
06

Target Before Penetrator Interaction



Penetrator Interaction

- “ Targets mounted on a wood platform as the Gelatin target material tends to be mobile in nature
- “ Target rear illuminated to observe the penetrator interaction and cavity formation through the opaque Gelatin material
- “ Diffuser screen mounted between the flash bulb array and the target



07

The Effects of Pitch at Impact

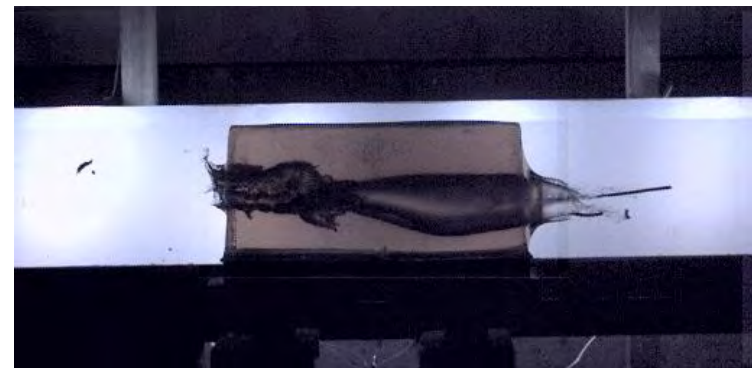


Negative Pitch at Impact

- “ Low negative pitch error: Penetrator exits the target in a severely bent condition
- “ High negative pitch error: Penetrator exits the target in a broken condition, breaking occurs during interaction with the target



High Speed video of a low
negative pitch impact



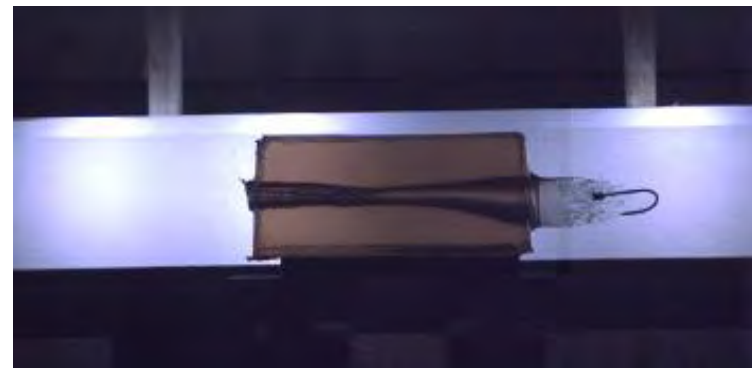
High speed video of a high
negative pitch impact

Very Low Negative Pitch at Impact

- “ Low and Very low negative pitch: Penetrator exits the target in a severely bent condition
- “ In both cases the bending is seen to be progressive during the interaction process and at exit with the target
- “ The severity of bending is linked to the impact error condition



High Speed video of a very low negative pitch impact



High speed video of a very low negative pitch impact

Positive Pitch at Impact

- “ Positive pitch at impact: Penetrator again exits the target in a broken condition breaking-up during interaction with the target



High Speed video of a
positive pitch impact

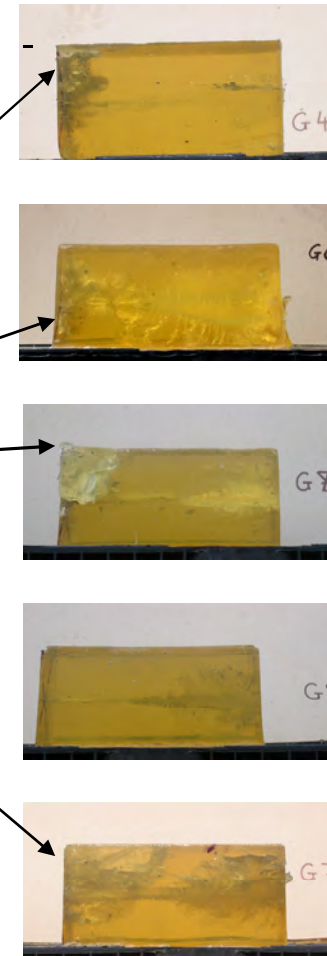
8

Targets After Penetrator Interaction



Penetrator Interaction

- “ With base pushed launch package designs, it can be difficult to eliminate residual material from interaction with the target
- “ Stripper plate removes majority of sabot petal component
- “ This residual material interacts with the Gelatin targets post penetration
- “ In most cases this was limited to the rear of the target and not considered detrimental to the formations of the observed cavities



9 Conclusions



- “ Unthreaded and high L/D ratio penetrators can be launched successfully
- “ Base pushed launch package designs can be used to launch these penetrators providing close fitting engineering tolerances are applied to the design
- “ IB modelling is an essential tool which identifies the correct design solutions
- “ Long barrel gun systems can be used to create soft launch phenomena
- “ High speed video techniques capture the penetrator performance at relatively low cost
- “ Low and very low negative pitch at target impact can produce a penetrator which is severely bent at exit from the target
- “ Higher pitch error at target impact can produce a penetrator which is broken into two or more pieces at exit from the target
- “ Impact condition is a contributing factor to projectile exit condition and cavity formation

10 Questions?



 *Your complimentary
use period has ended.
Thank you for using
PDF Complete.*

[Click Here to upgrade to
Unlimited Pages and Expanded Features](#)

QinetiQ

The Global Defence and Security Experts

QinetiQ

[dstl]

www.QinetiQ.com

© Copyright QinetiQ Limited 2008



LOADING MECHANISMS from SHALLOW BURIED EXPLOSIVES

**Leslie C. Taylor
William L. Fournery, Ulrich Leiste
Bryan Cheeseman
23 Sept 2008**





Acknowledgements



Sponsor
TARDEC

Richard Goetz
David Fox





Team Members



Tim Hennessey

NSWC/IH

Sean Tidwell

NSWC/IH

William Szymczak

NRL

Andrew Wardlaw

ATR Inc.



U of MD Tasks

Using Small-Scale Tests

- Understand interaction between charge and target
- Support development of computational tools
- Explore technology and concepts to mitigate effect of flush & buried charges
- Explore scaling rules
- Measure pressure distribution over face of target as function of time
- Develop total impulse data
- Explore effect of target shape on loading
 - Non-deforming targets
 - Vees, pyramids,
 - Others
 - Deforming targets



Loading Mechanisms

Interaction Between Shallow Buried Charge & Target Takes Place in Near Field Of Explosion

- Details Are Important, e.g.:
 - Charge Shape & Detonator Location
 - Charge – Target Geometry
 - Local Soil Properties
 - Including Smoothness of Surface
 - Etc.



Test Charges



PENTOLITE CHARGES ($H/D = \sim 3$)

Provided by NSWC/IH

Pressed Pentolite

Explosive Mass: 0.8g 4.4g 8.0g

Detonator – Reynolds RP-87 (0.069g RDX & PETN)

PETN CHARGES ($H/D = \sim 3$)

DETA Sheet – 63% PETN 37% Binder

Explosive Mass: 0.5g 0.636g 4.4g 8.0g

DETA Mass: 0.68g 0.90g 6.875g 12.59g

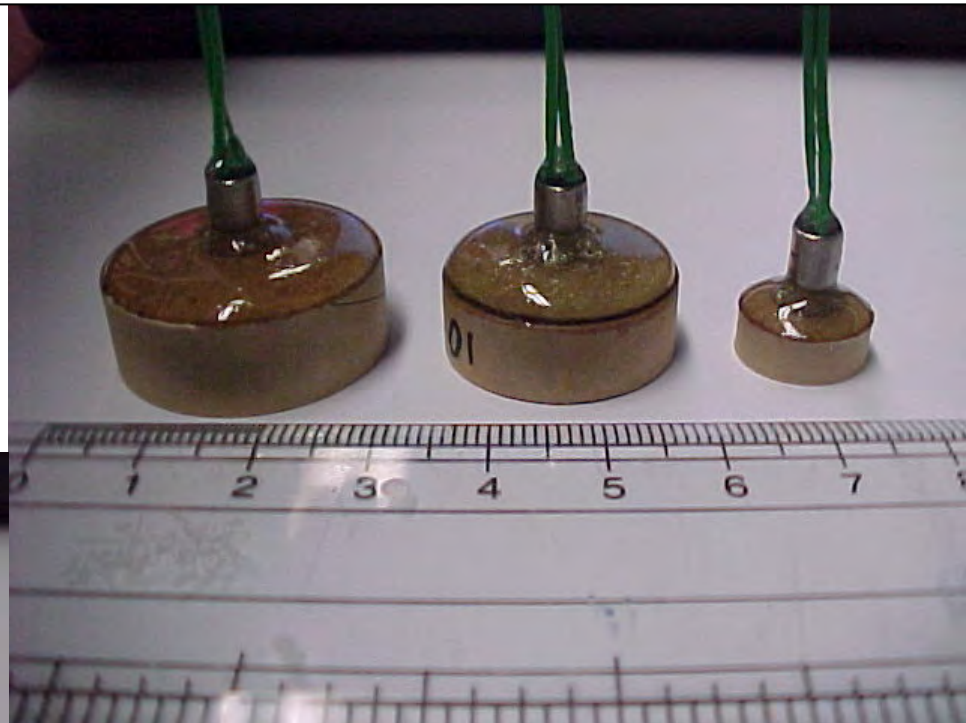
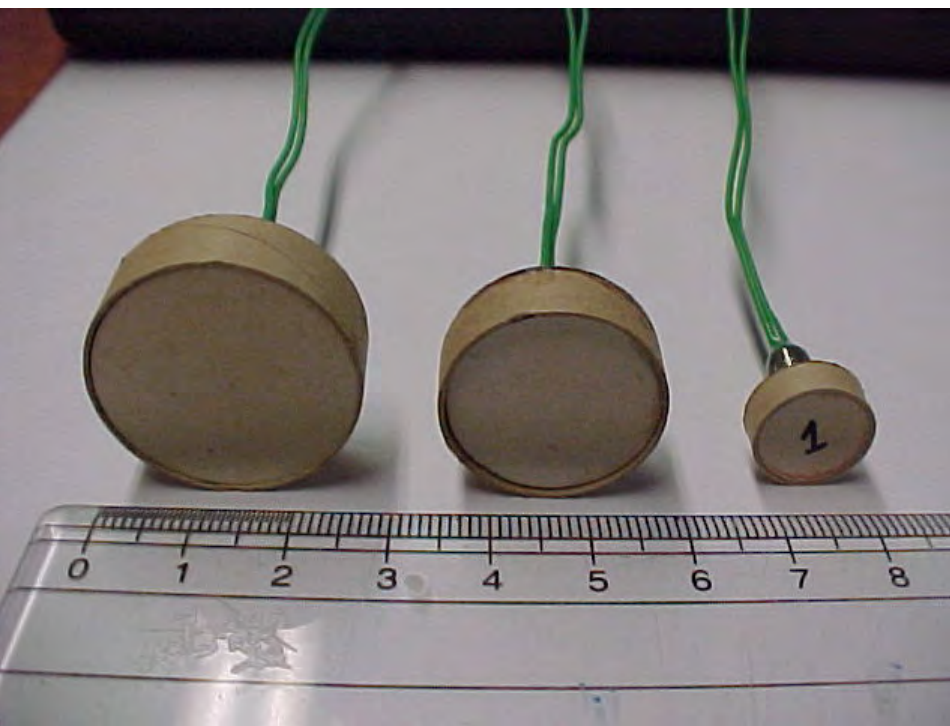
Detonator – Reynolds RP-87 (0.069g RDX & PETN)

Explosive Mass Always Includes Detonator Explosive

Pentolite Charges

Charge size
(Wt includes RP-87 Det)

Wt.	D(mm)	H(mm)
0.8g	12.0	4.0
4.4g	21.8	7.3
8.0g	26.6	8.9

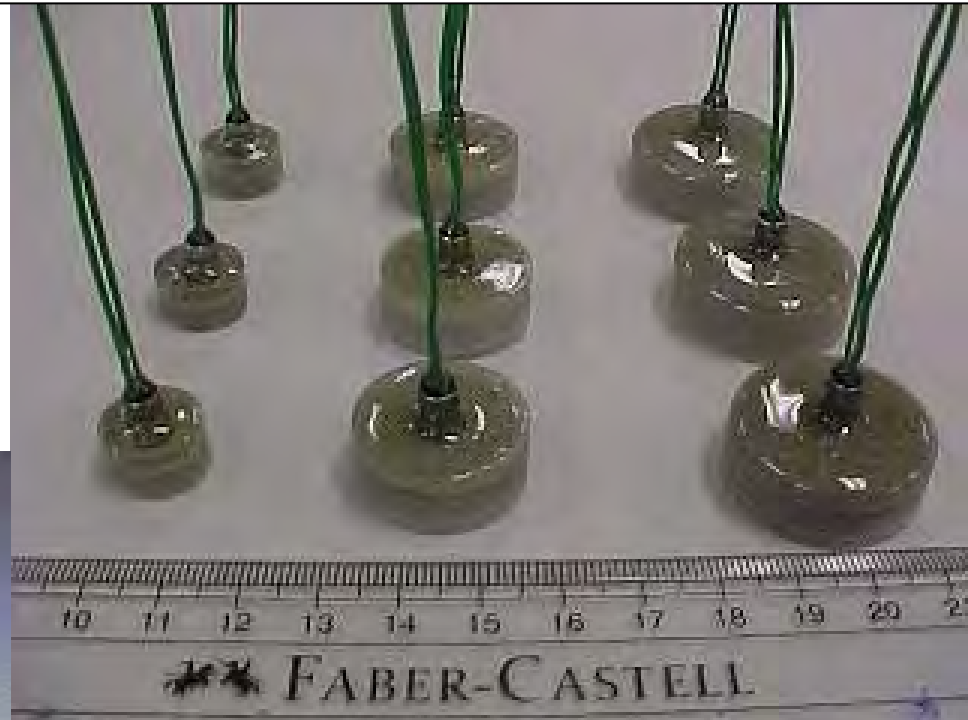


RP-87 contains .069g explosive

DETASHEET Charges

Charge size
(Explosive Weight)
(Wt includes RP-87 Det)

Wt.	D(mm)	H(mm)
0.5g	12.0	2.7
2.5g	21.0	4.6
5.0g	26.0	5.8



Weight given above is weight of PETN
plus RP-87 Det (.069g)
DETASHEET is 63% PETN
Total charge wt – about 1.59 times larger



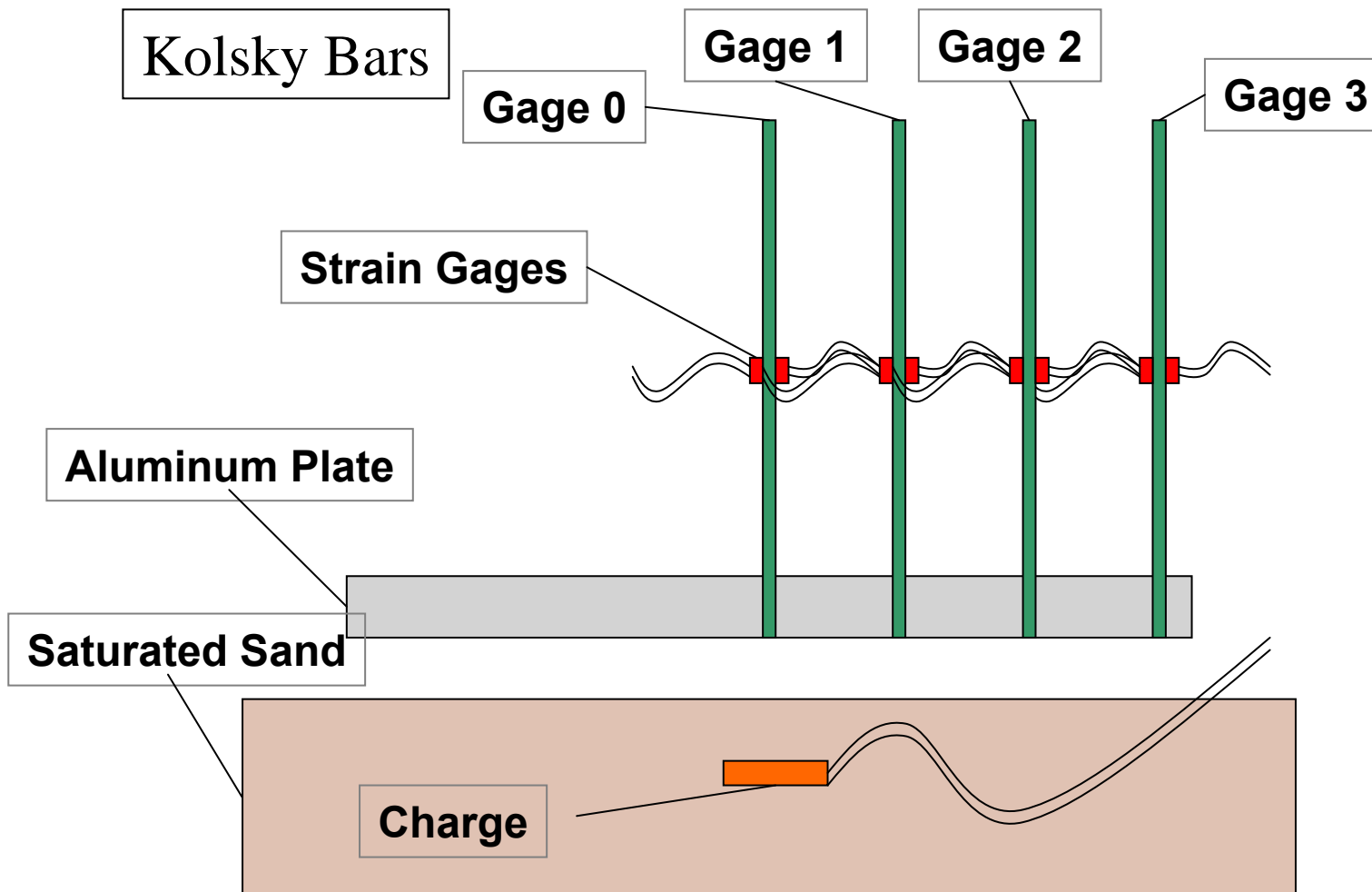
Pressure



- Pressure at Any Point on Target as Function of Time is Load on Target at That Point
- Pressure Has Proved Very Hard to Measure Accurately
- Substitutes Have Been Used: Integrated Values
 - Impulse Distribution
 - Total Vertical Impulse

Pressure Test

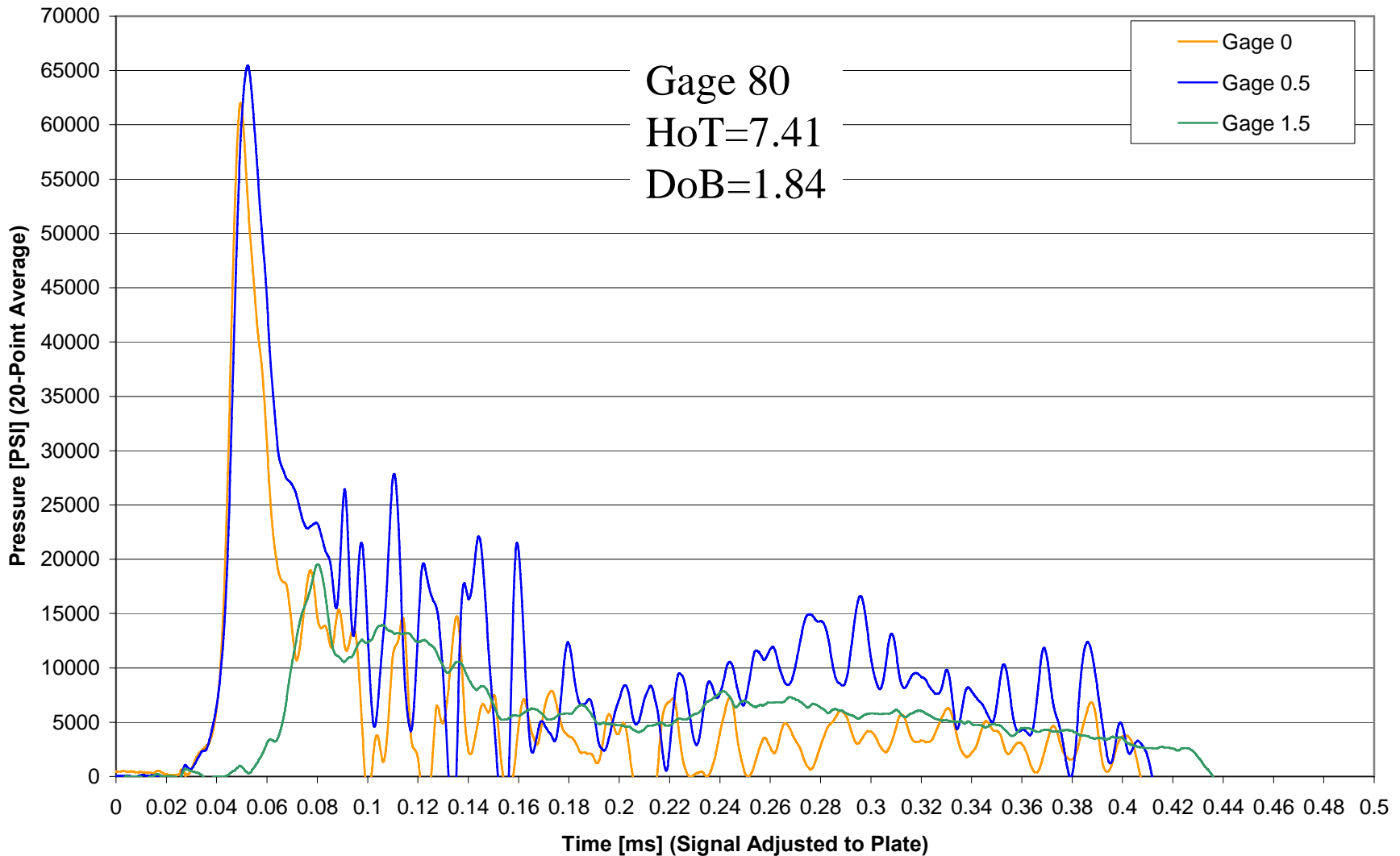
Fixed Plate Pressure Test





Pressure Test

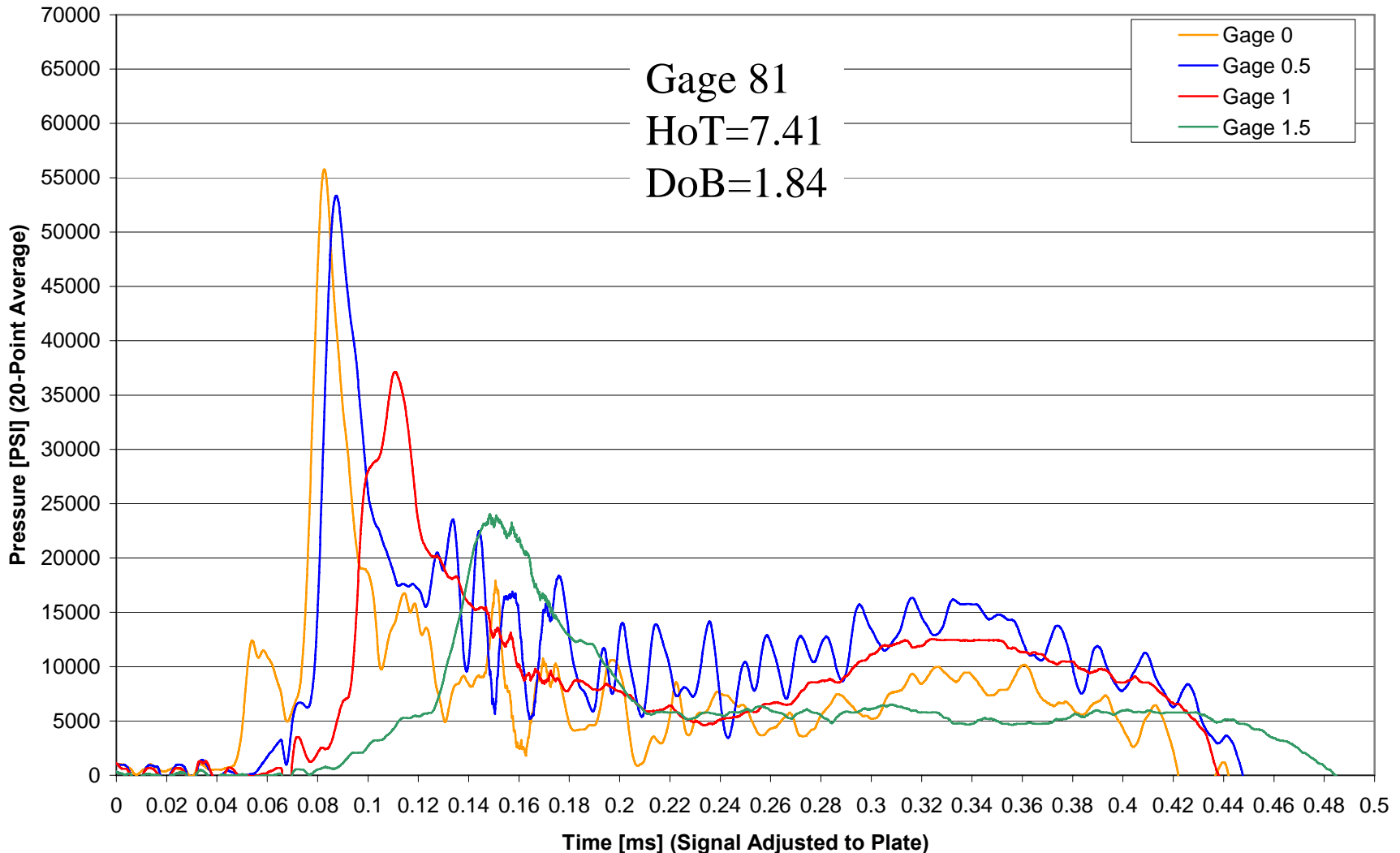
Navy 1+6 Scaling Factor 9.7 DOB 0.41" SOD 1.65"
Data Sheet 5.0g 1xRP-87 Booster



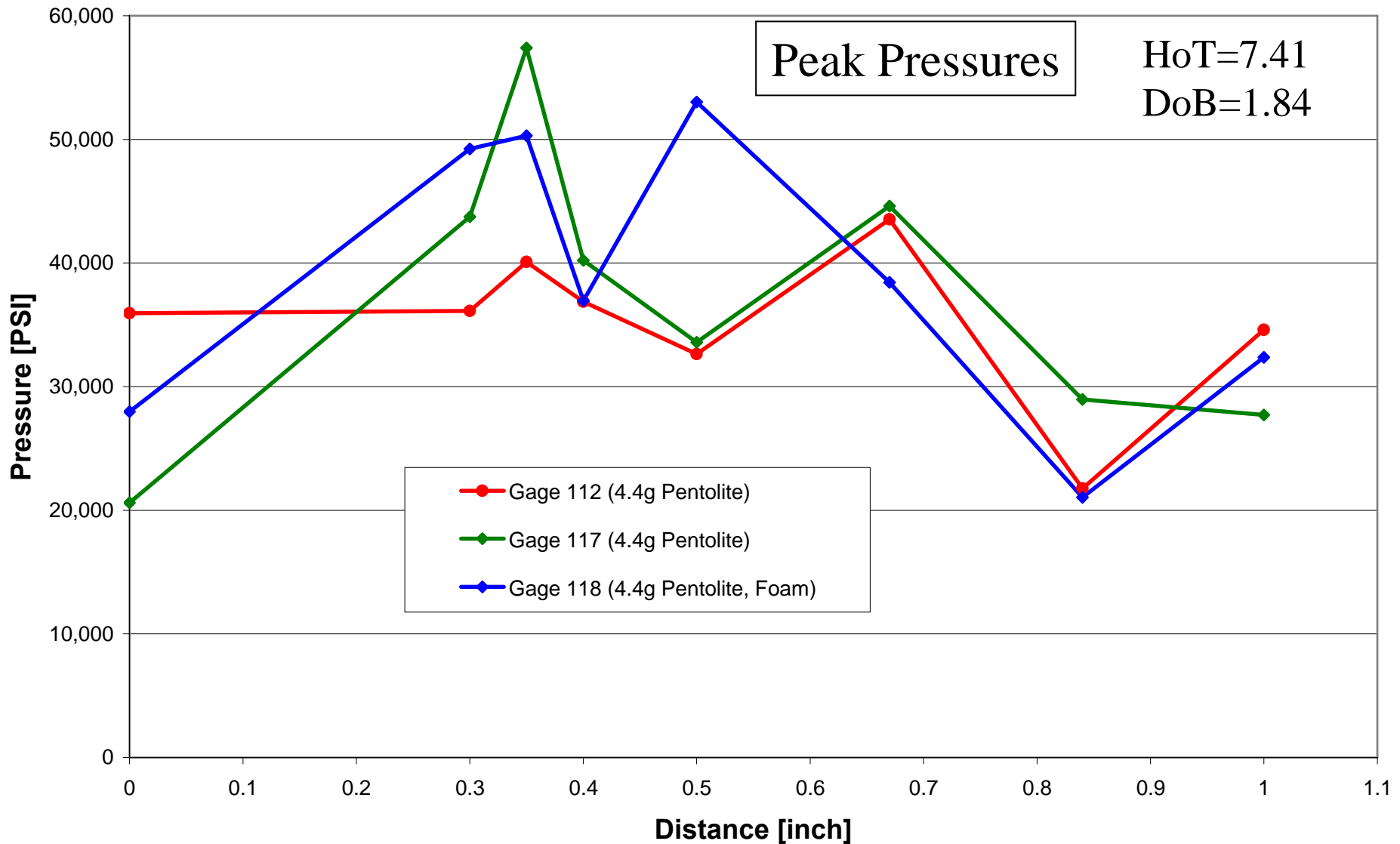


Pressure Test

Navy 1+6 Scaling Factor 9.7 DOB 0.41" SOD 1.65"
Deta Sheet 5.0g 1xRP-87 Booster



Pressure Test

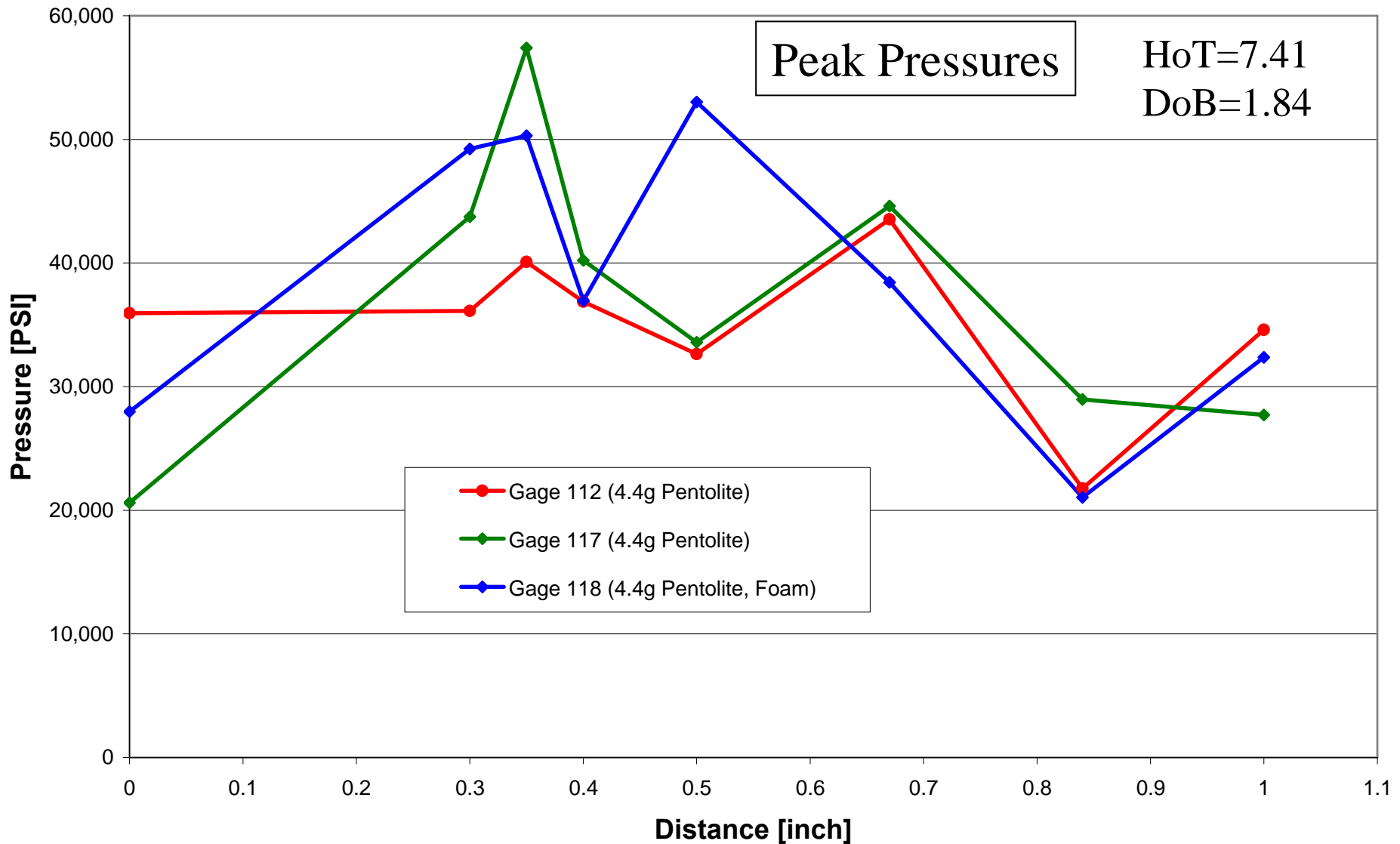


Pressure Test

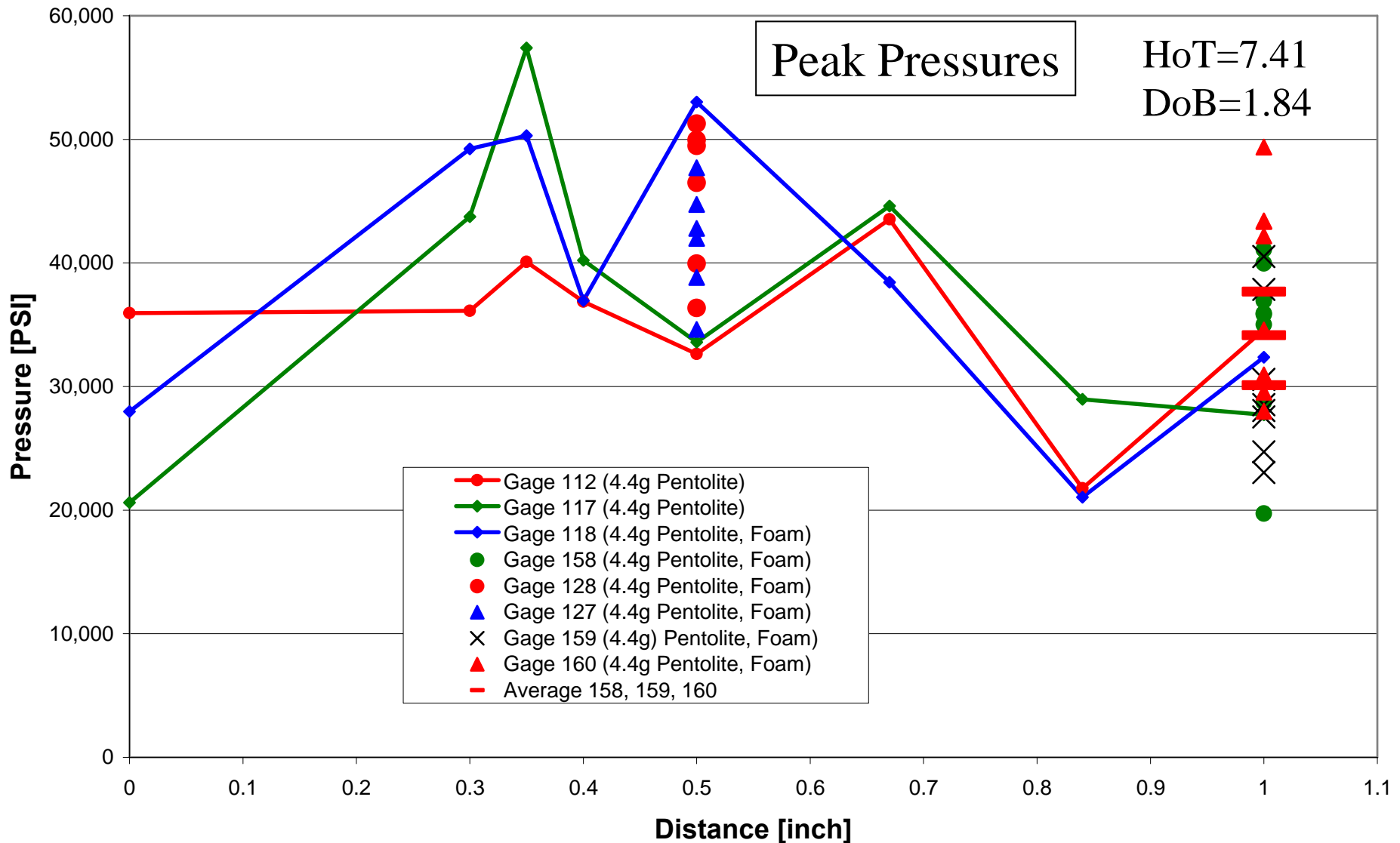


Eight Kolsky Bars in Circle

Pressure Test



Pressure Test





Loading Mechanisms

- Target Loaded by Soil Driven Against Target by Gas Bubble
- Target Loading Not Truly Impulsive
- Occurs Over Finite Time Appropriate to Bubble Processes
 - Generally Millisec Rather Than Microsec
- Target Loading Depends Upon
 - Charge Size & Shape
 - Charge – Target Geometry,
 - Etc.



Loading Mechanisms

Shallow Buried Explosive

- Shockwave does not play *direct* role in target loading
 - Unless target in contact with surface
- Shockwave plays *indirect* role in target loading



Loading Mechanisms

- Target Loaded by Soil Driven Against Target by Gas Bubble
- Soil Cap Directly Over Charge Major Contributor to Load
 - Properties Of This Material When it Hits Target
Important
 - They Are Not *In Situ* Properties
 - Properties & Configuration of Soil Modified
by Shockwave
- Shockwave Important for What it Does to Soil Not to Target

Early Time Effects

When Charge Detonates

- Emits Shockwave
 - Essentially Parallel to Top of Charge, Because of Charge Shape

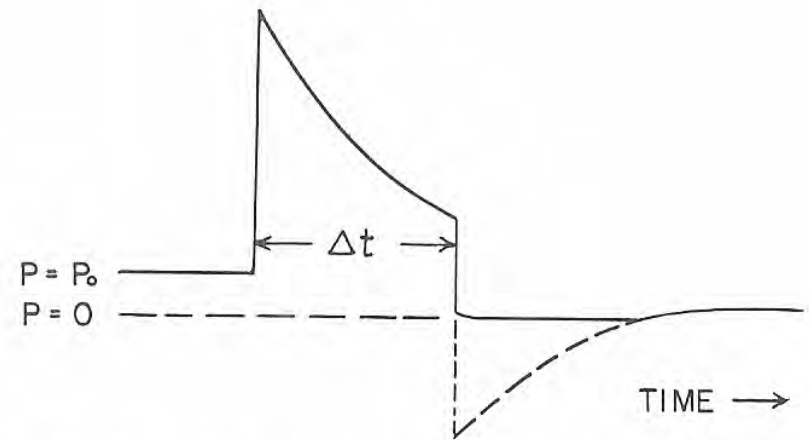


Fig. 7.21 Gauge pressure as a result of surface reflection.

Underwater Explosions, Cole, 1948

- At Surface, Shock Mostly Reflected as Relief Wave in Soil
 - Impedance Mismatch Between Saturated Soil & Air

Early Time Effects

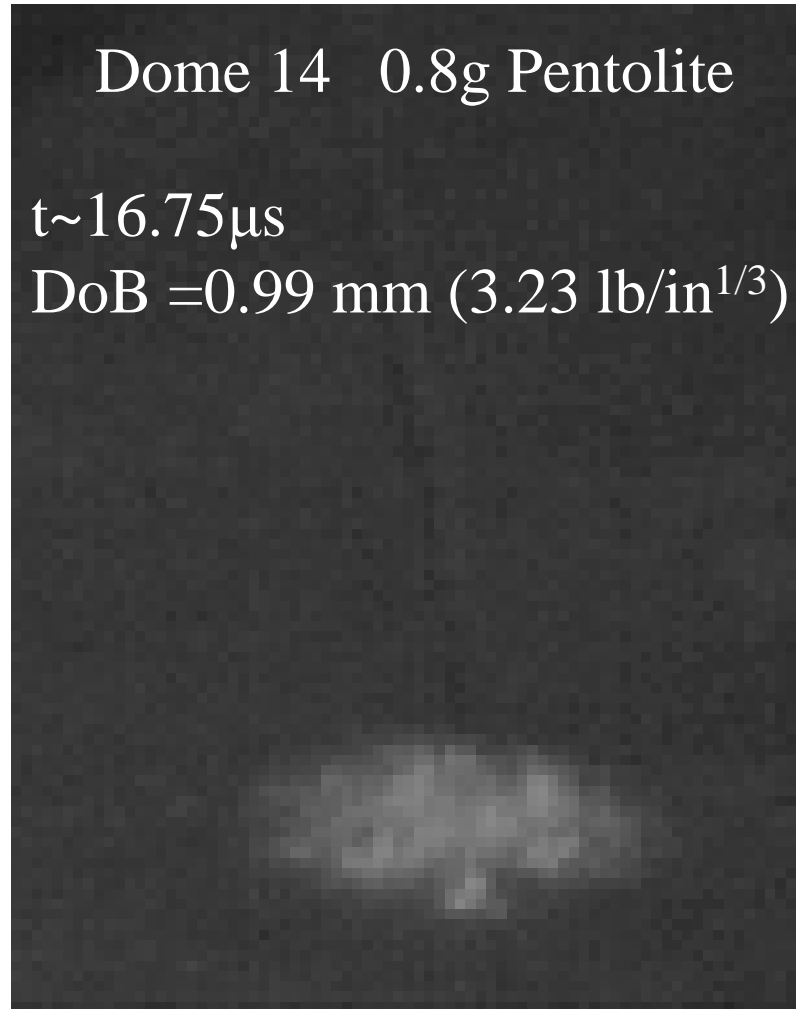
When Charge Detonates

- Not all shock energy reflected
 - Weak shock sent into air
 - Spray thrown up

Dome 14 0.8g Pentolite

$t \sim 16.75 \mu\text{s}$

DoB = 0.99 mm (3.23 lb/in^{1/3})





Early Time Effects

Bulk Cavitation

- Negative Pressure in Relief Wave Interacts With Pressure in Soil Cap
 - Tries To Go Negative
- Water & Saturated Soil Cannot Support Tension – Cavitates
- Bulk Cavitation Creates Three Layers
 - High Density, Low Density, High Density
- If Cavitated Region Present When Soil Cap Hits Target
 - Pressure Rise Interrupted

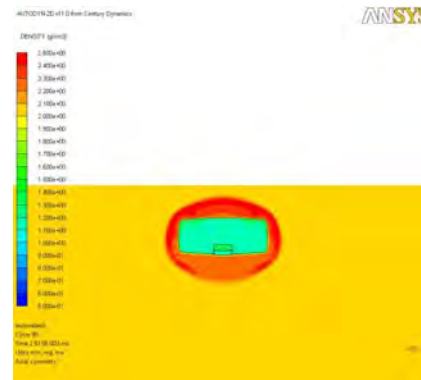
Early Time Effects

Bulk Cavitation

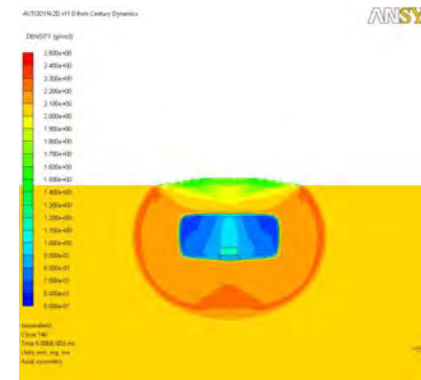
4.4g Pentolite Charge



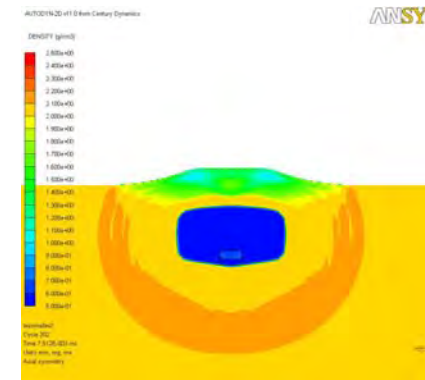
$t=0 \mu s$



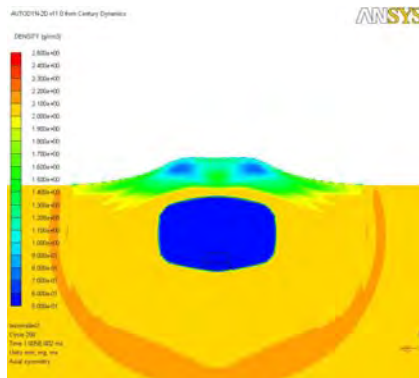
$t=2.5 \mu s$



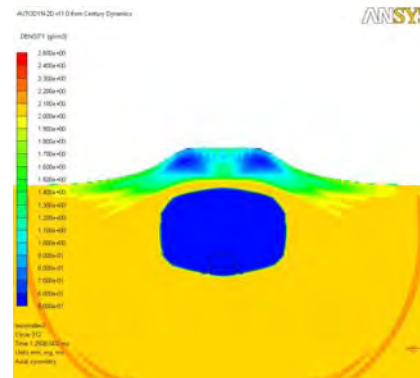
$t=5.0 \mu s$



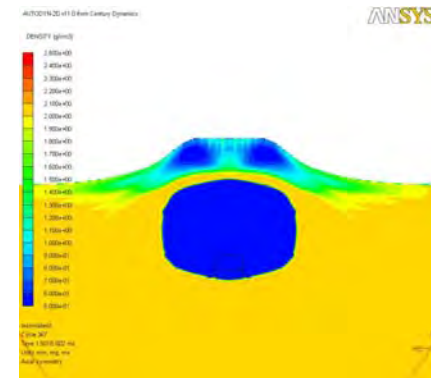
$t=7.5 \mu s$



$t=10.0 \mu s$



$t=12.5 \mu s$



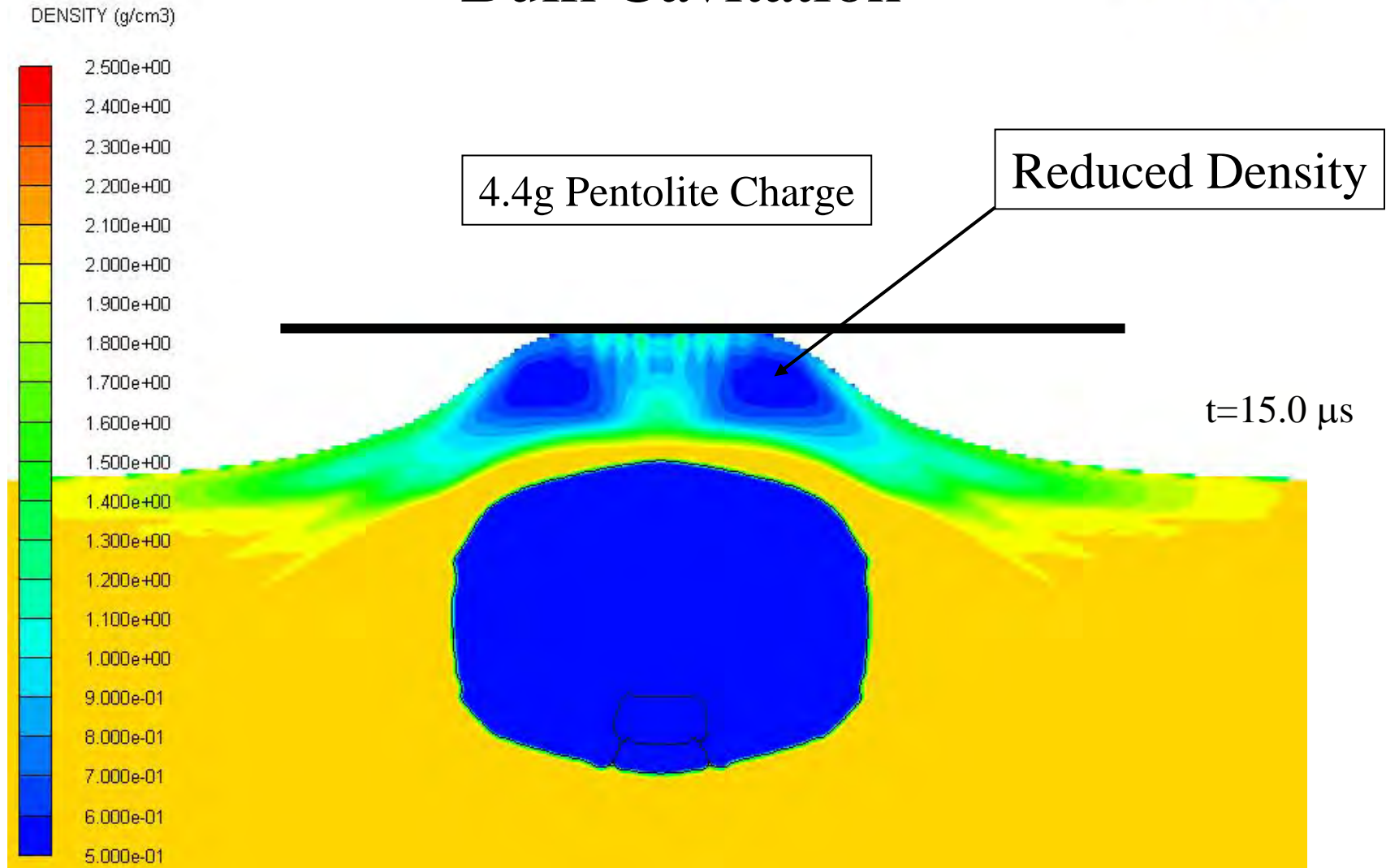
$t=15.0 \mu s$

Early Time Effects

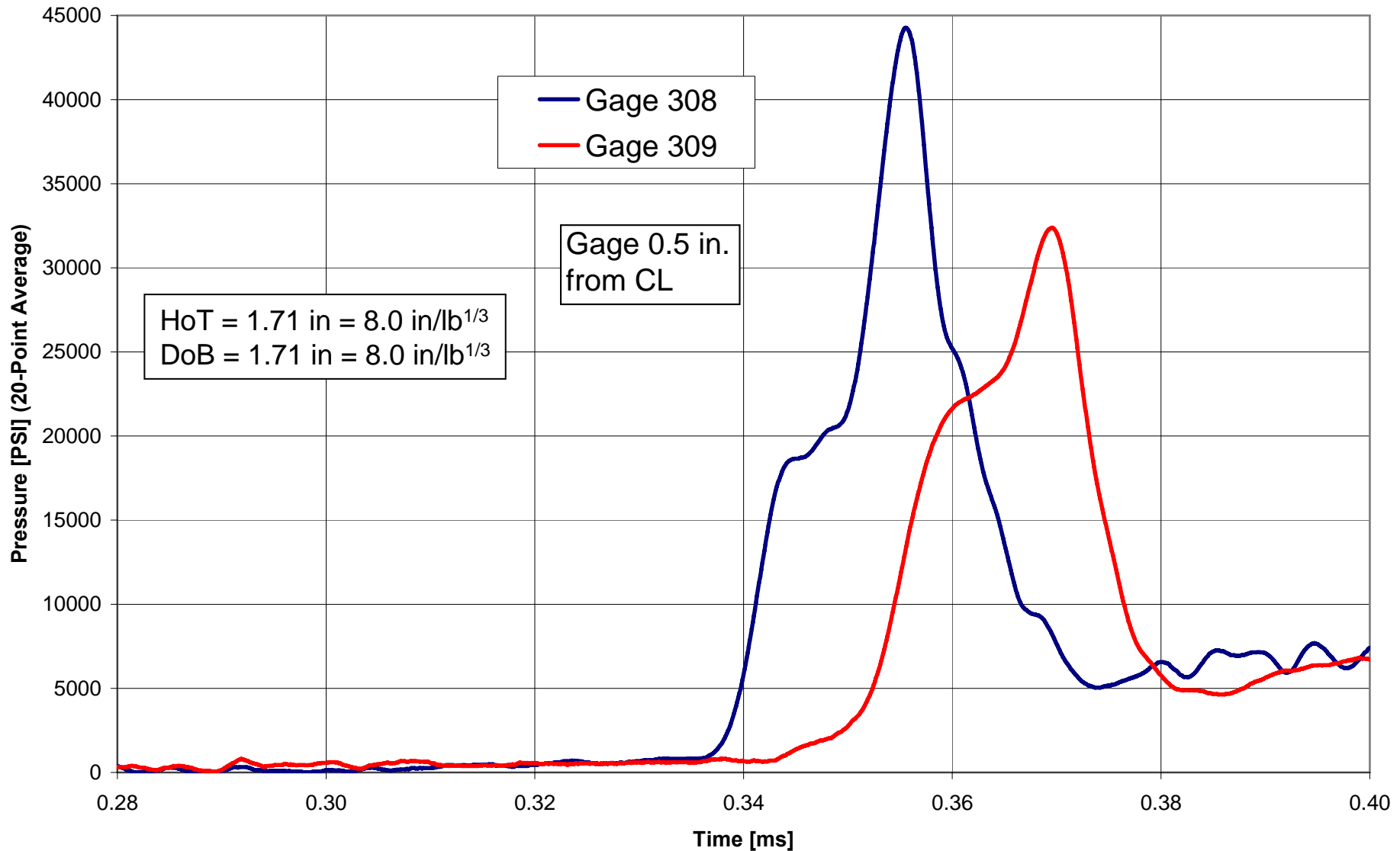
AUTODYN-2D v11.0 from Century Dynamics

ANSYS

Bulk Cavitation



Early Time Effects





Early Time Effects

Richtmyer-Meshkov Instability (RMI)

Occurs when interface between fluids of differing density is impulsively accelerated, e.g. by the passage of shock wave

Development of instability begins with small amplitude perturbations which initially grow linearly with time

Followed by nonlinear regime with spikes appearing in the case of heavy fluid penetrating light fluid

A chaotic regime eventually reached and the two fluids mix

RMI can be considered impulsive-acceleration limit of Rayleigh–Taylor instability.



Early Time Effects

Richtmyer-Meshkov Instability (RMI)

- Our Event Over (Target Hit) Before Chaotic Mixing Phase
- Our Interest – Amplification Of Initial Perturbations
 - Interface Between Soil And Air is Never Smooth
- RMI Origin of Spikes (Fingers) of Material That Move Faster Than Bulk of Soil Cap

Early Time Effects

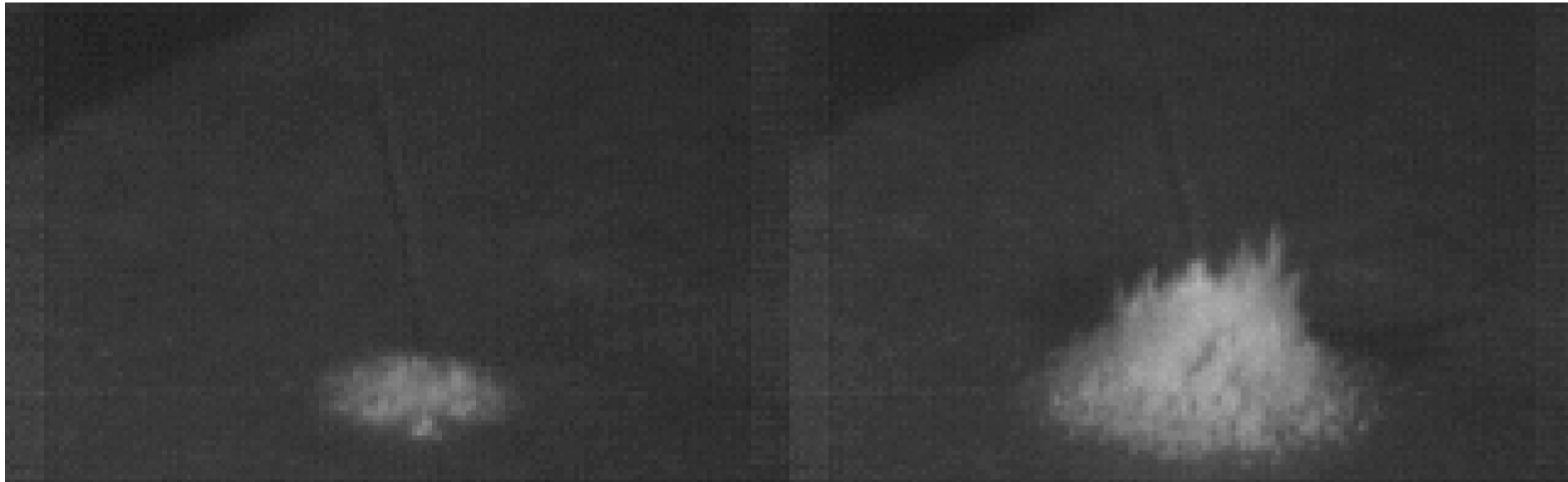
Richtmyer-Meshkov Instability (RMI)

Dome 14 0.8g Pentolite

DoB = 0.99 mm (3.23 lb/in^{1/3})

$t \sim 16.75 \mu\text{s}$

$t = 33.5 \mu\text{s}$ later

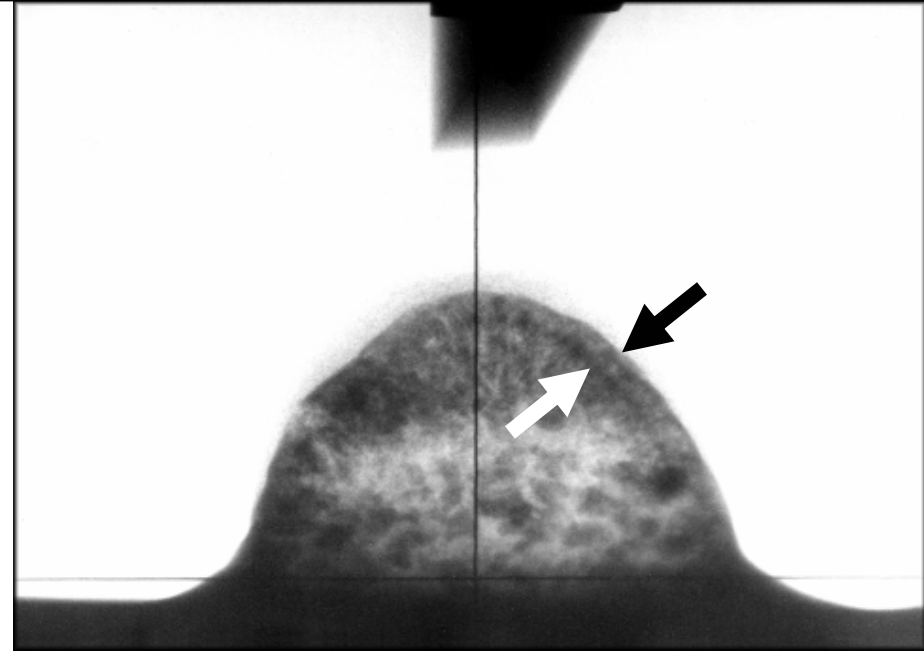


- Since Soil Surface Chaotic, Distribution Of Fingers Chaotic
 - Leads Directly To Difficulty In Measuring Pressure

Early Time Effects

Spherical Spreading

- Soil Cap Quickly Assumes Shape of Rough Hollow Dome
- Soil Cap Thins as Material Above Charge Spreads Over Surface of Dome
- Thinning Shortens Peak Loading Duration



Flash X-Ray

Shot 17-1. 125.9 μ s Fairly Dry Sand

Bergeron, Walker & Coffey, DRES-SR-668, April 1998

Wt = 106 g

DoB = 30 mm

D = 62mm

T = 22mm

t = 0.1259 ms

If W = 4.4 g

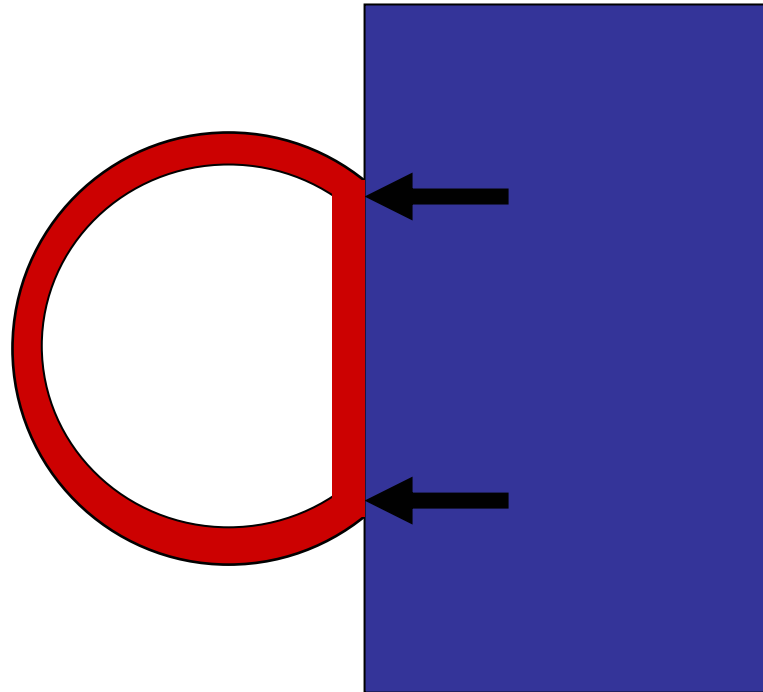
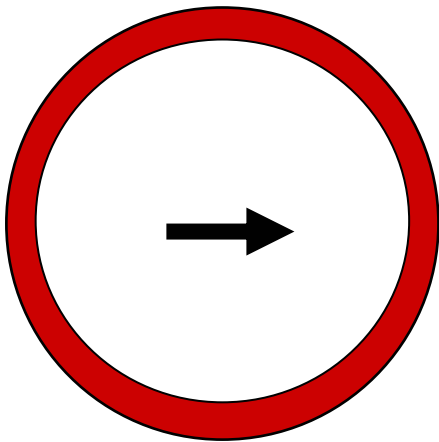
DoB = 10.4 mm

t = 0.0436 ms

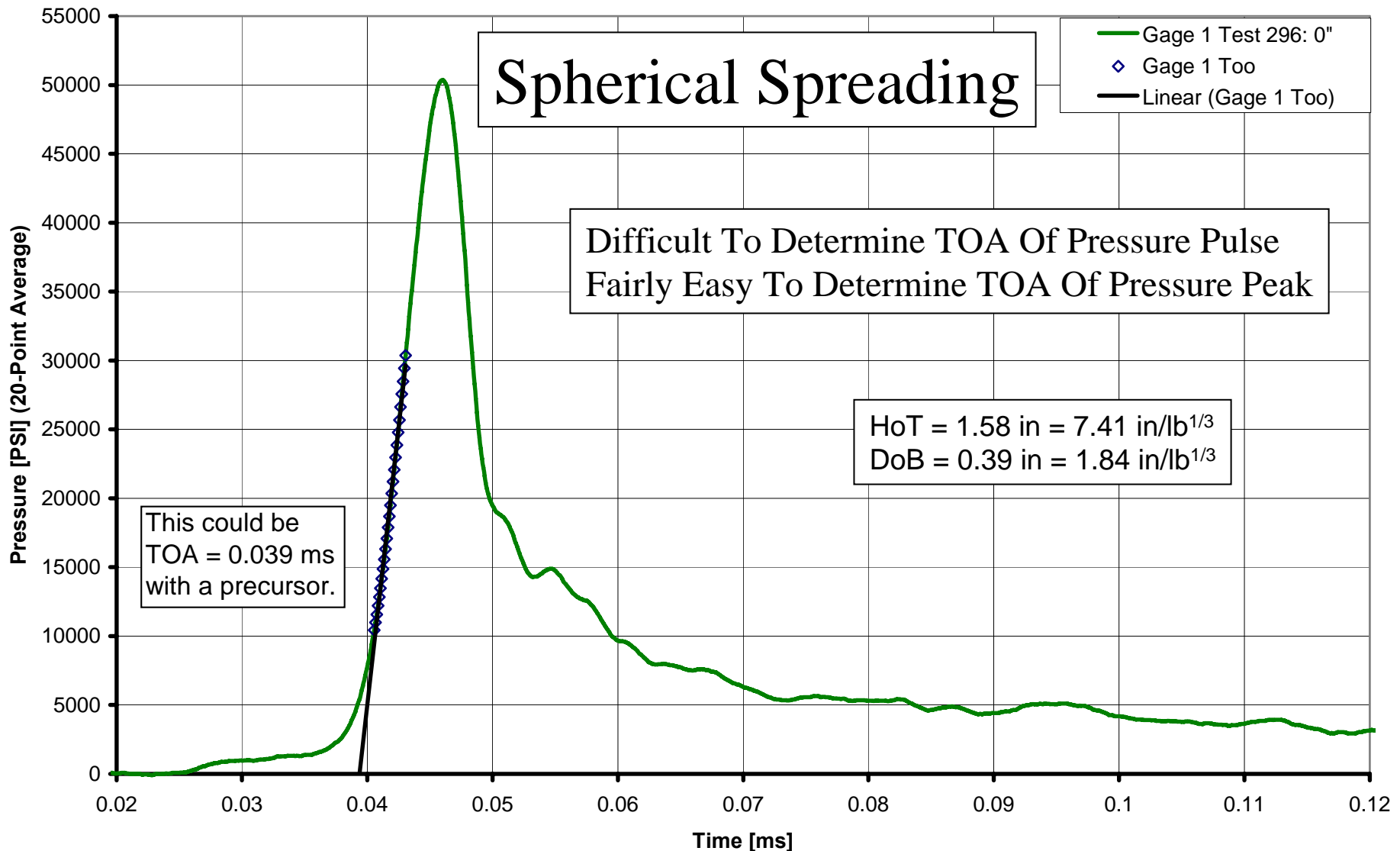
Early Time Effects

Spherical Spreading

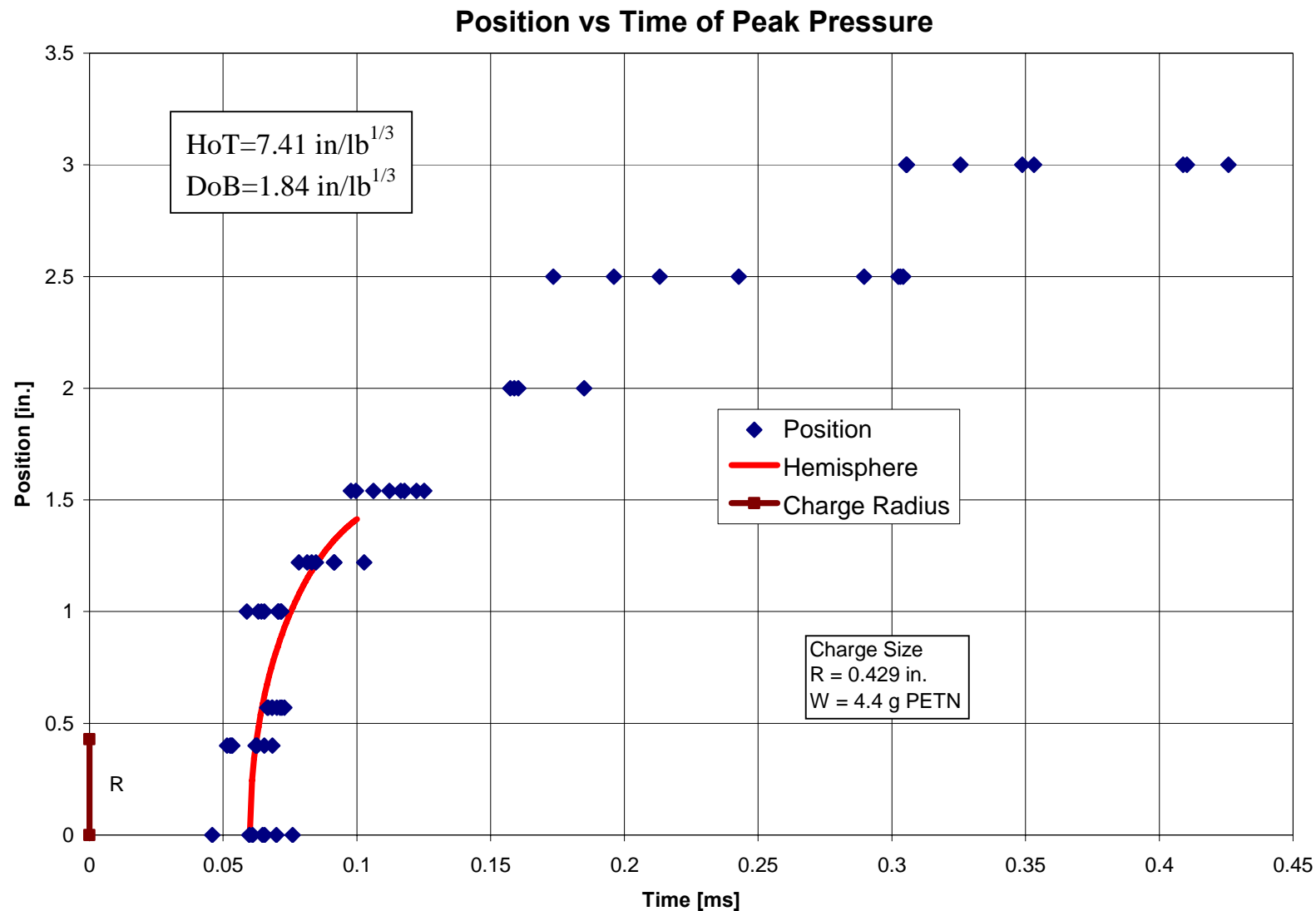
Consider Dome as Hollow Ball Hitting a Plane Target



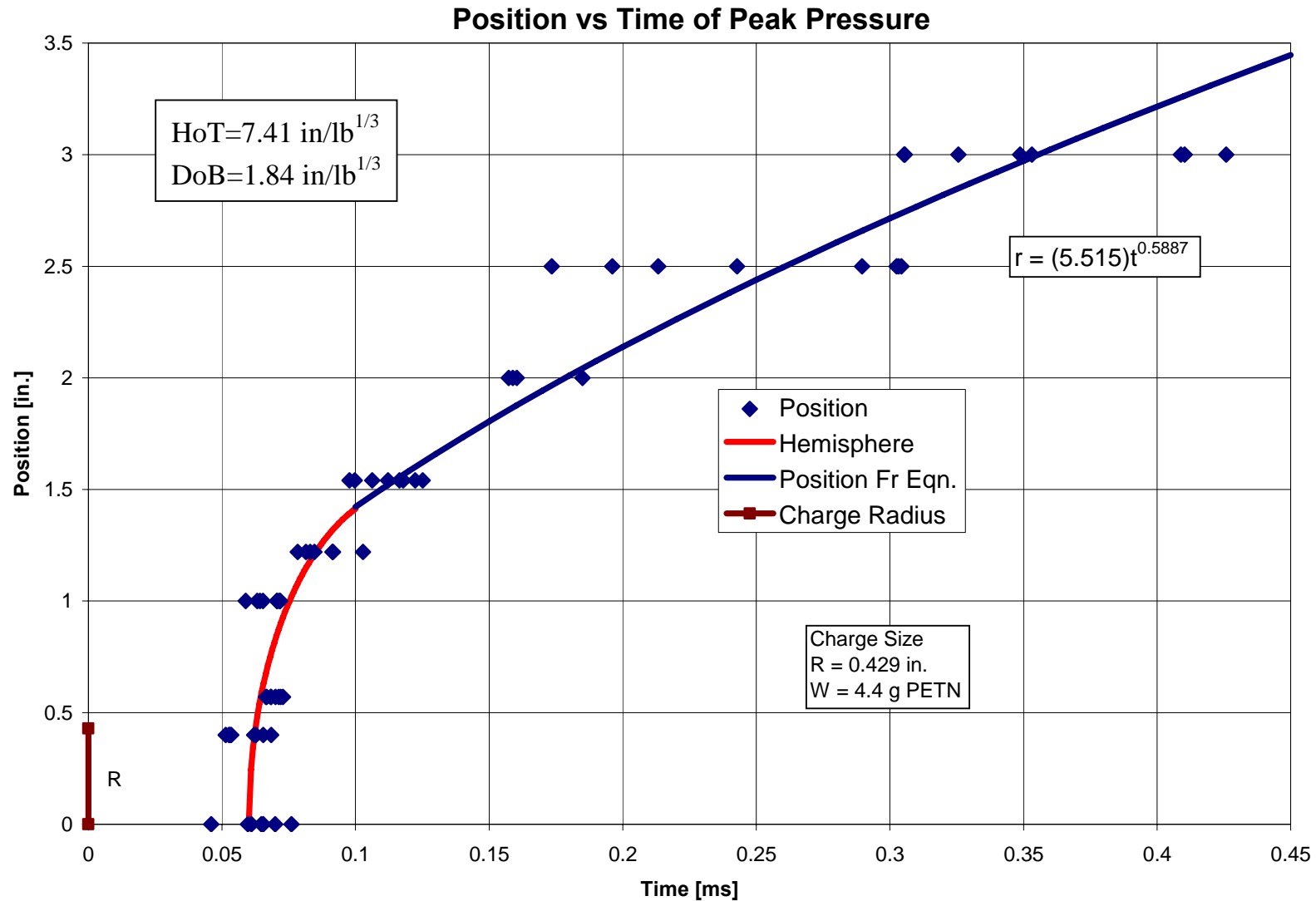
Early Time Effects



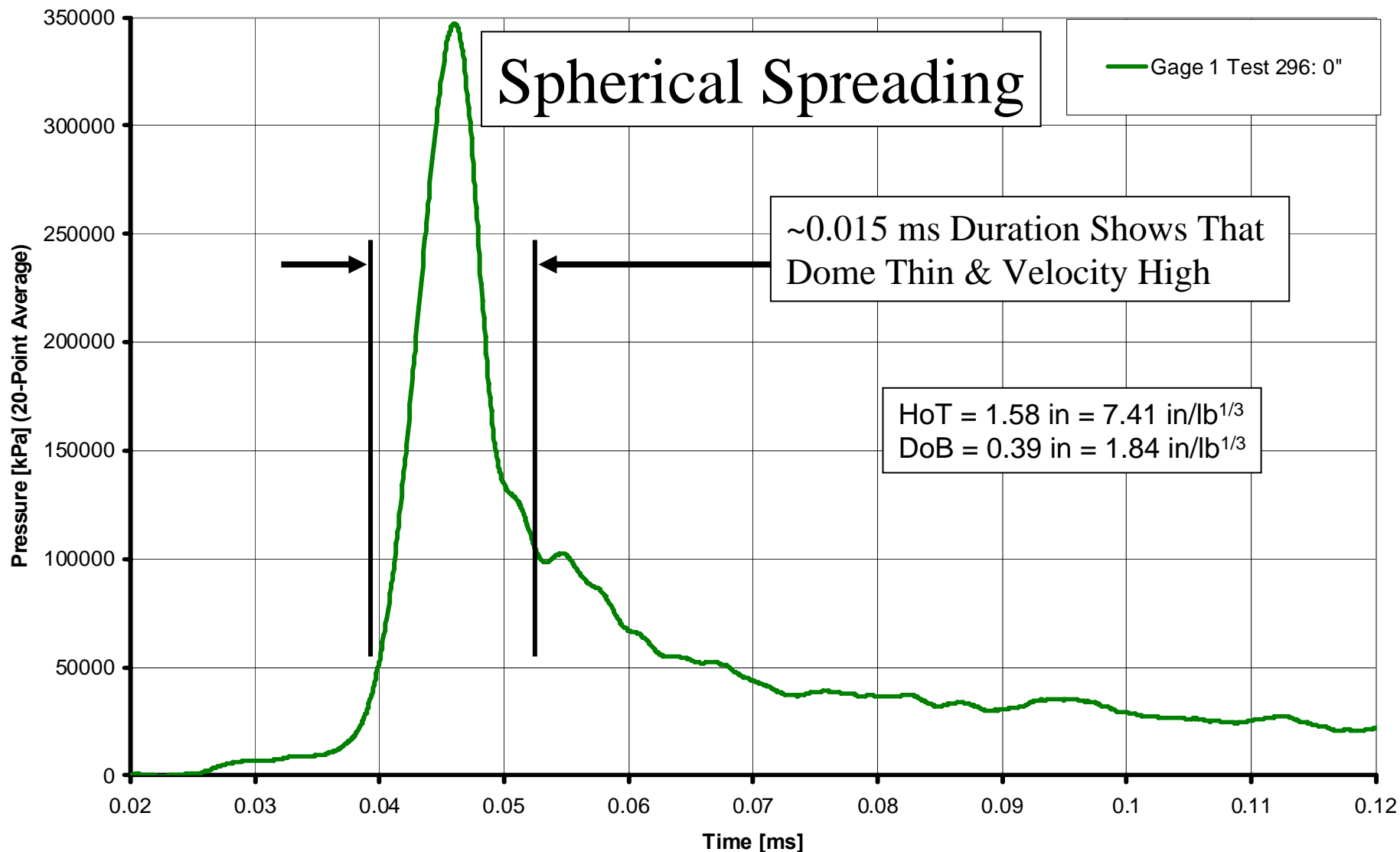
Spherical Spreading



Spherical Spreading



Early Time Effects



Early Time Effects

- Residual Shock in Air & Spray Hitting Target
 - Pressure Precursors
- Cavitation in Soil Cap
 - Variability in Pressure Rise Rate
- Richtmyer-Meshkov Instability
 - Variability in Value & Time of Peak Pressure
- Spherical Spreading & Dome Hitting Target
 - Rapid Initial Pressure Rise & Fall
- All Happens In Very Short Time - e.g. at 4.4 g Scale
 - First 0.1 ms After $t = 0$
(Scales to 1ms for 10 lb (4.5 kg) Charge)
- Effect Confined to ~ 3.5 Times Charge Radius
- Not The Whole Story

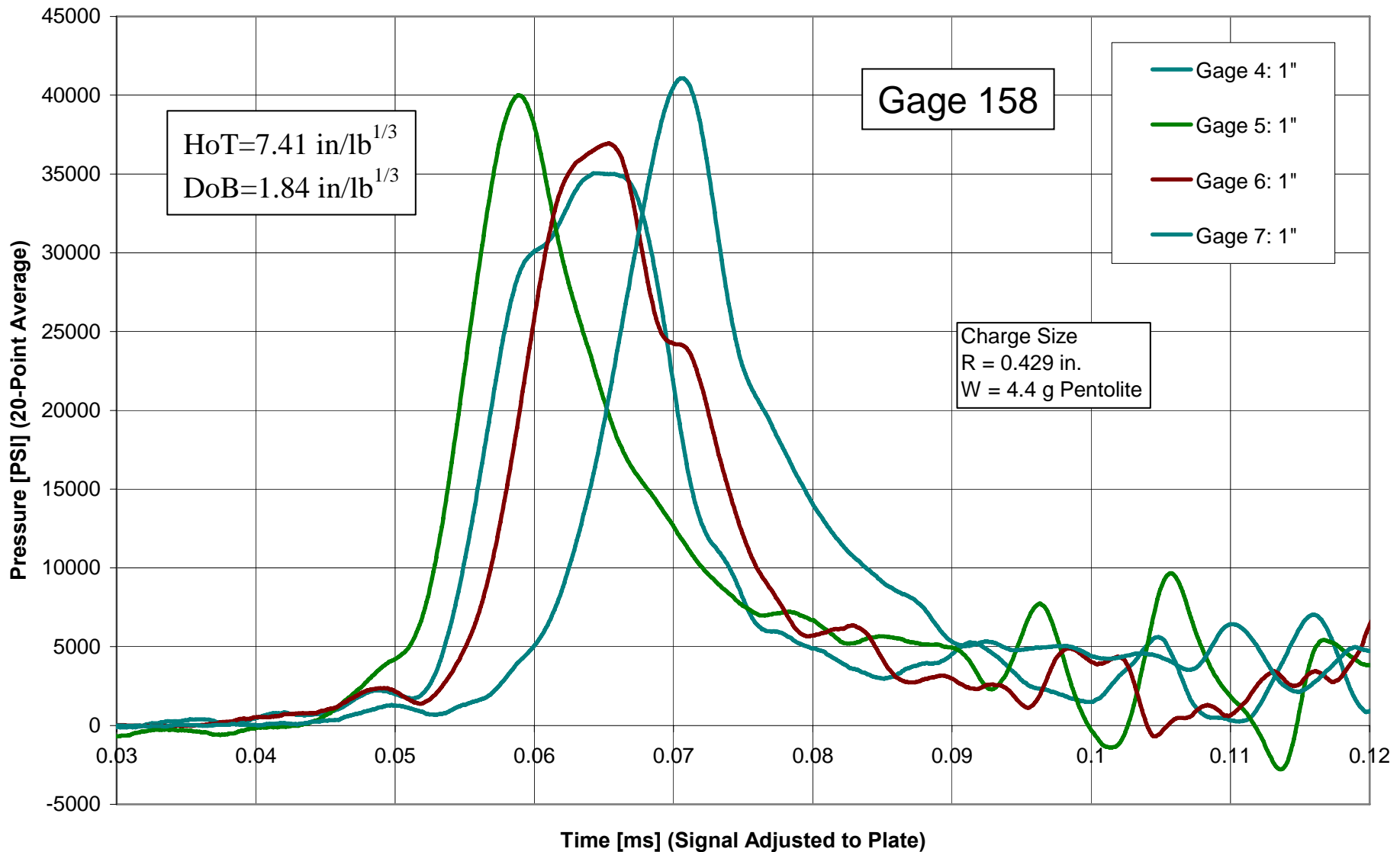


Late Time Effects

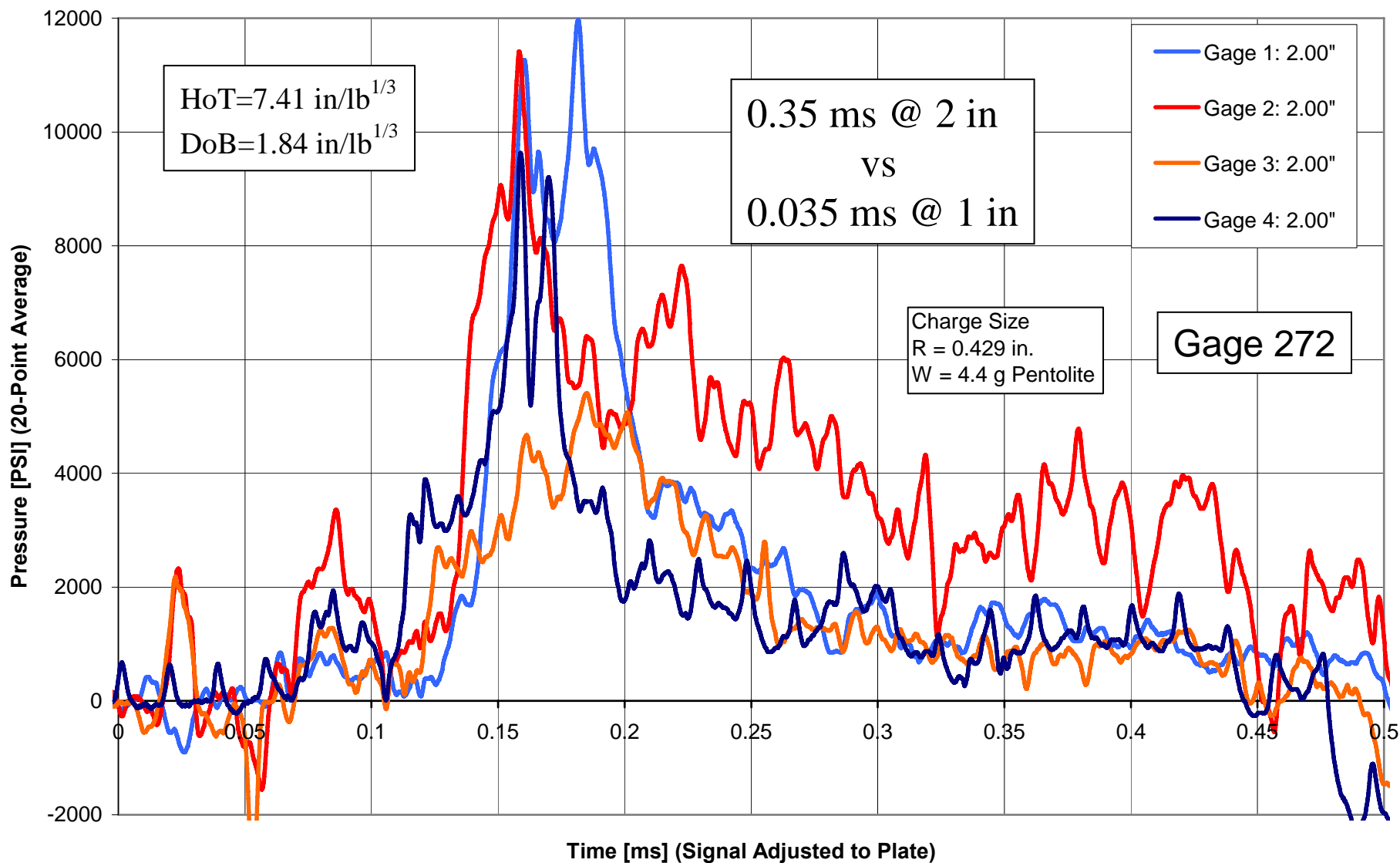
Two Additional Processes

- Material Outside Soil Cap Scooped Out of Crater by Explosive Gas
- Gas Pressure on Bottom of Target Trapped by Material Coming Out of Crater
- Pressures Much Lower
 - Act Over Much Longer Time
 - Act Over Much Greater Area

Late Time Effects



Late Time Effects

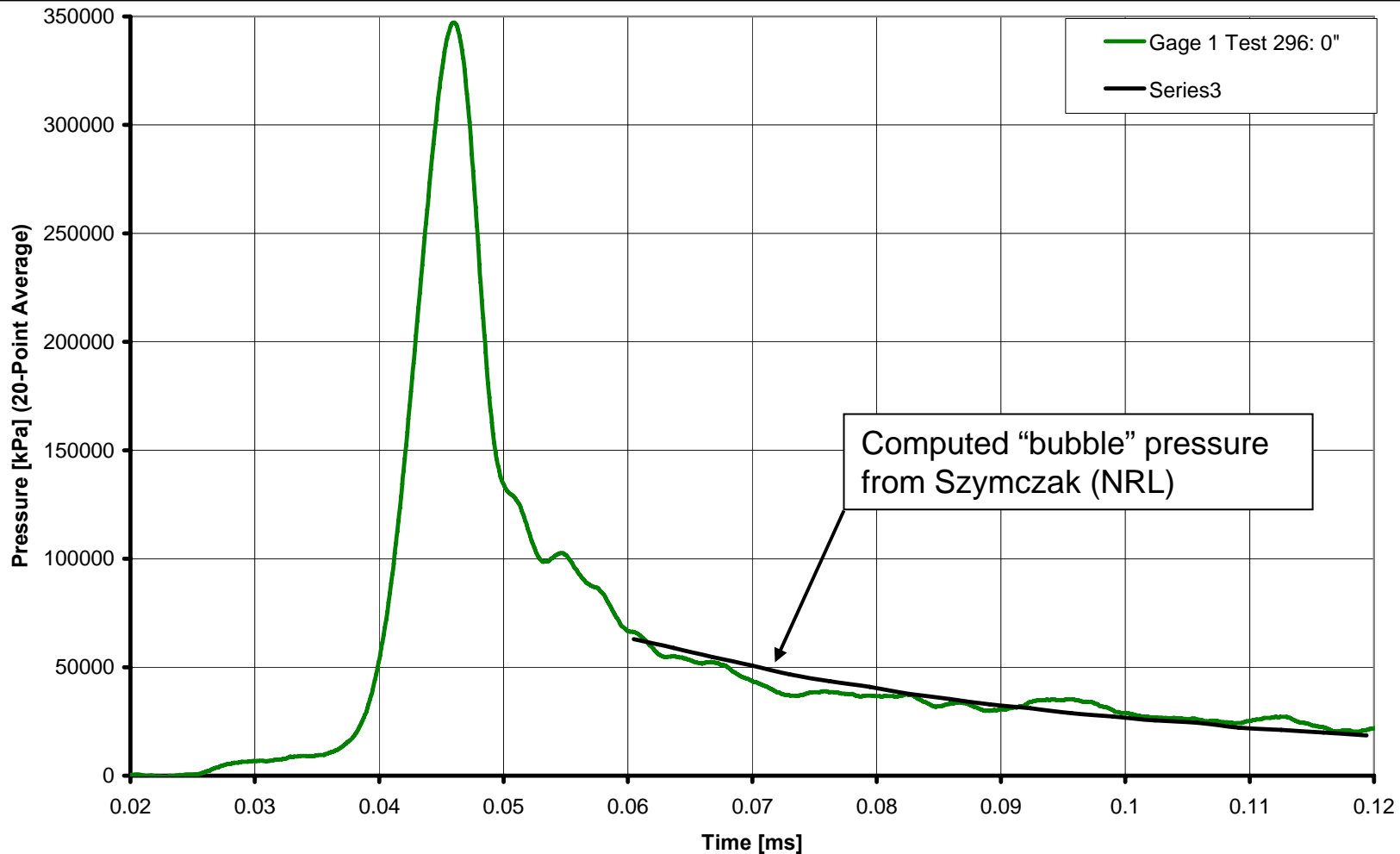




Late Time Effects

- Material Streaming Out Of Crater & Hitting Target
 - Travels Parallel To Wall Of Crater
 - Ring-shaped Stagnation Region on Target
 - Thickness Of Region Increases Rapidly
 - Vertical & Radial Velocities Comparable
- Lower Pressures & Longer Duration
 - $t = 0.35 \text{ ms @ } 50.8 \text{ mm vs } 0.035 \text{ ms @ } 25.4 \text{ mm}$
 - $p_{\text{max}} = 12,000 \text{ psi @ } 50.8 \text{ mm vs } 40,000 \text{ psi @ } 25.4 \text{ mm}$

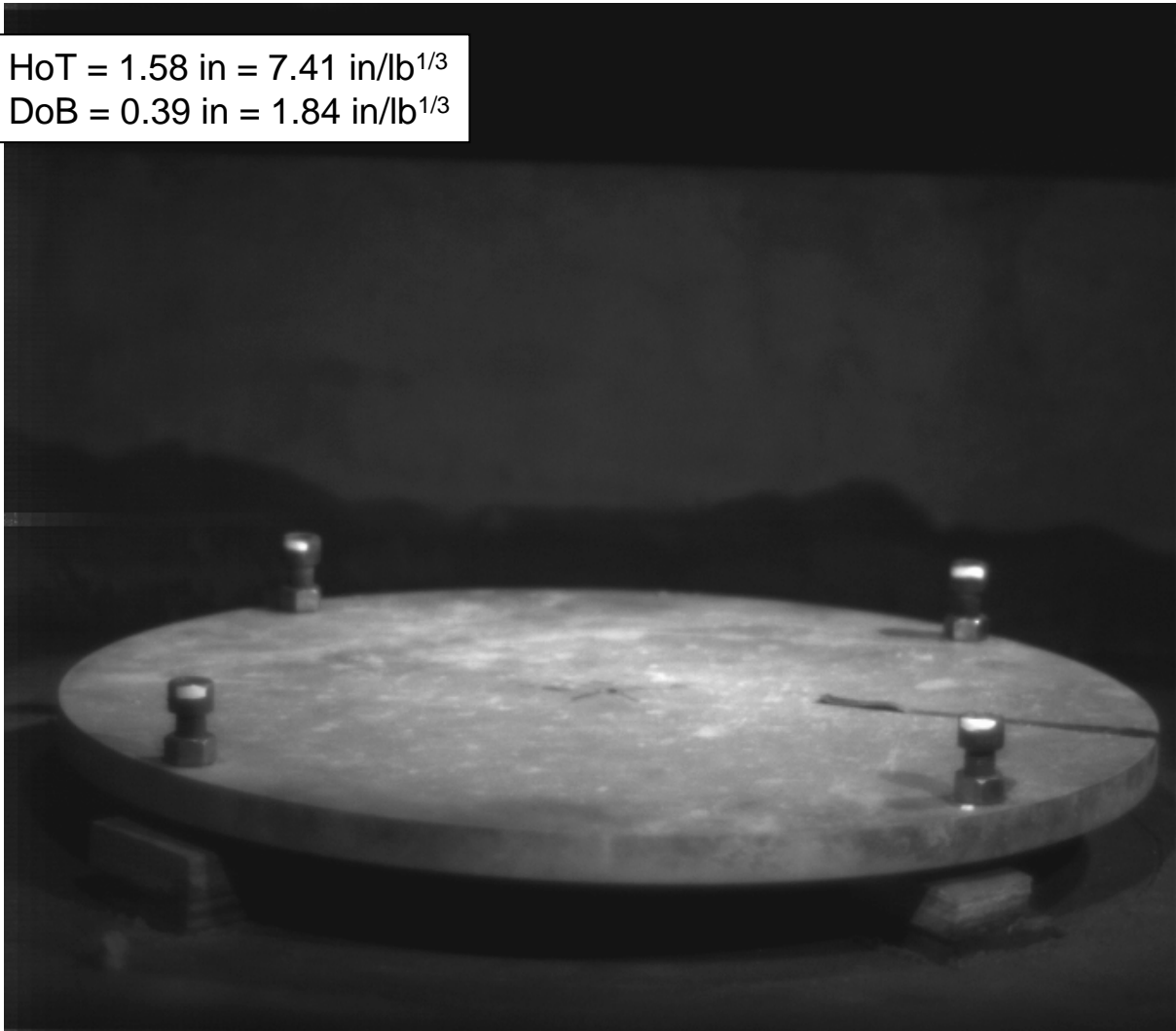
Late Time Effects



- Annular Jet of Saturated Soil Provides Confinement for Explosive Gas Pressure in "Tail" of Pressure – Time Curve

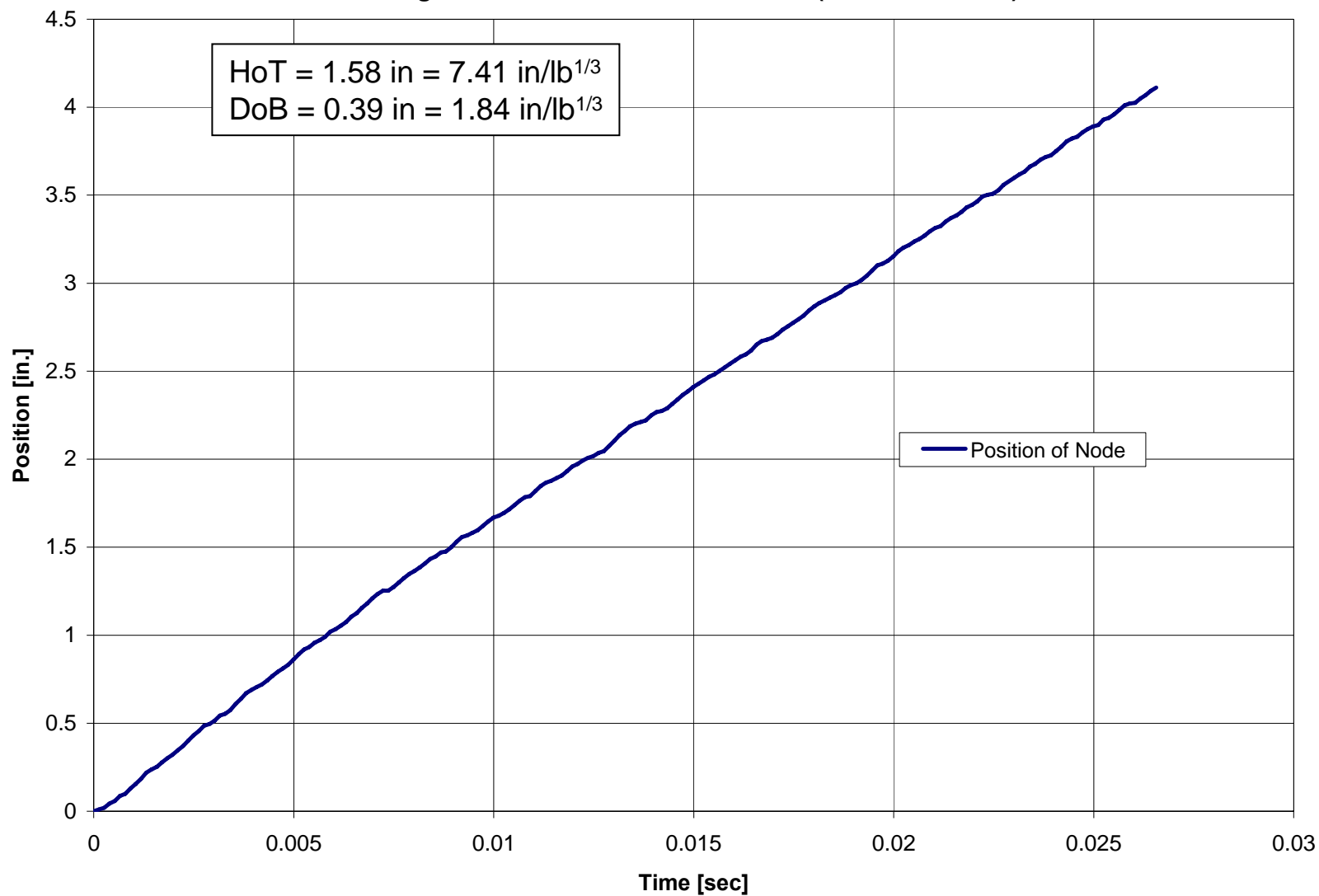
Late Time Effects

HoT = 1.58 in = 7.41 in/lb^{1/3}
DoB = 0.39 in = 1.84 in/lb^{1/3}



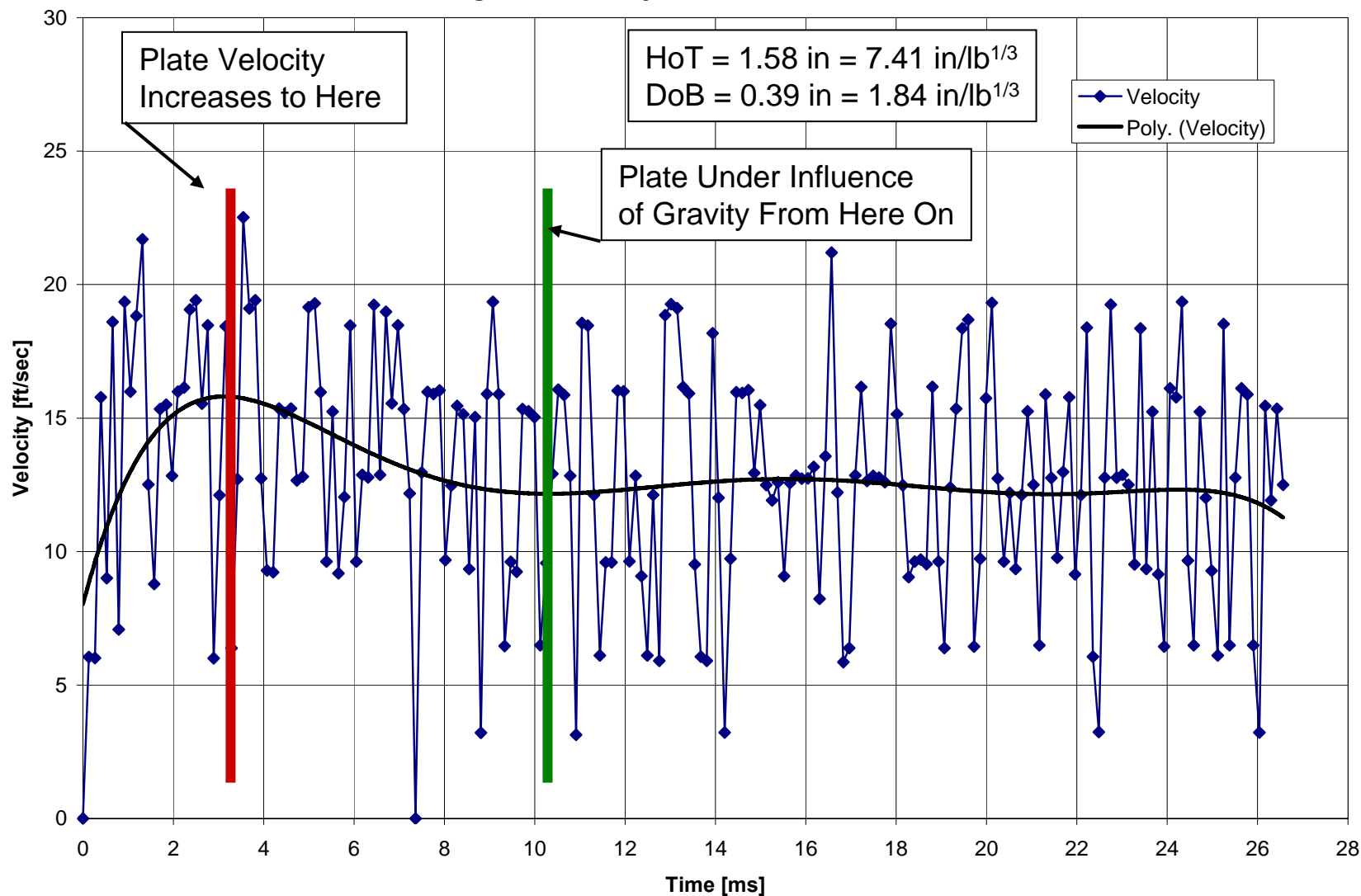
Late Time Effects

Gage 314 Position of Node vs Time (Smoothed Data)



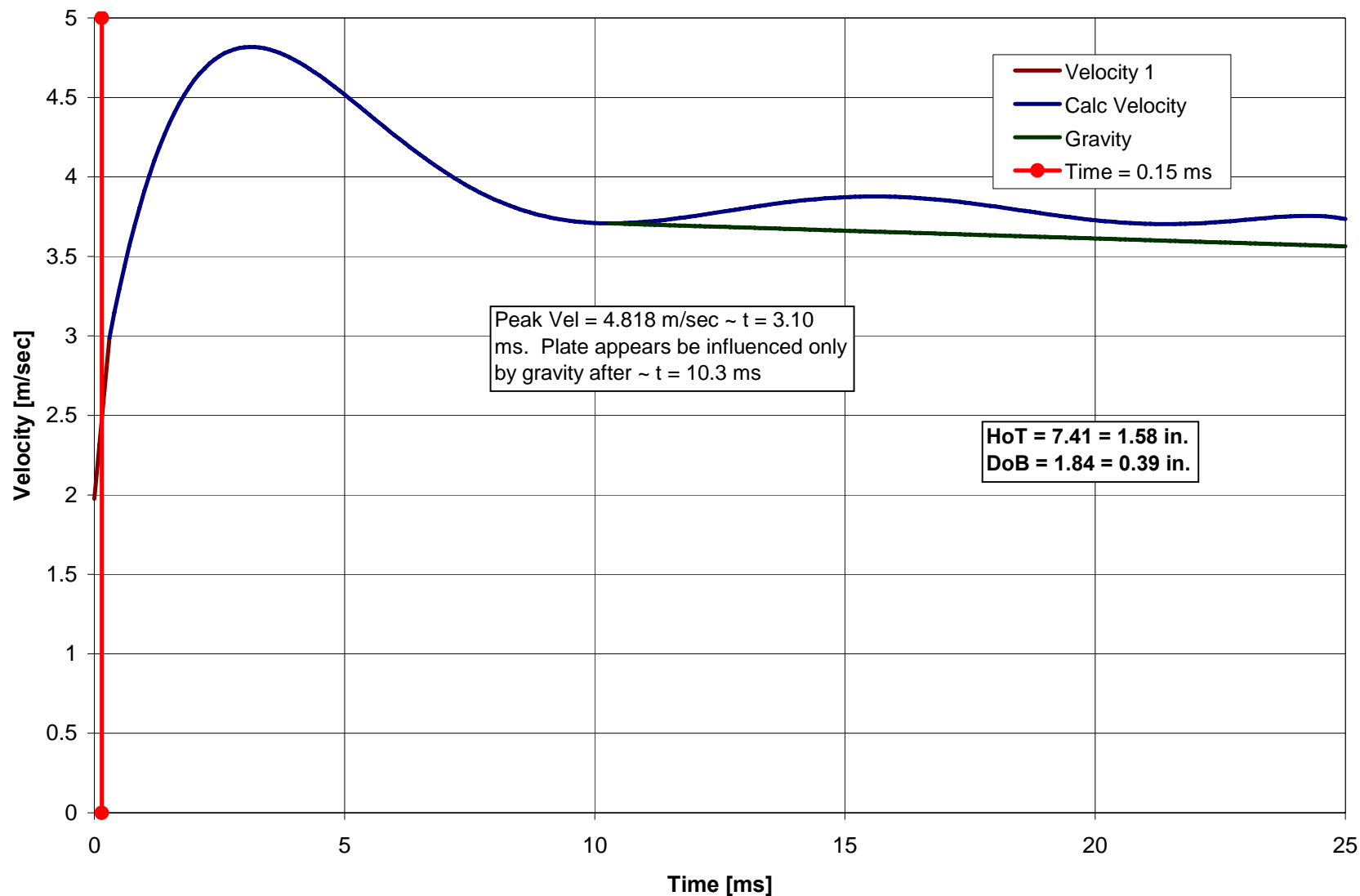
Late Time Effects

Gage 314 Velocity - Smoothed Position Data



Late Time Effects

Gage 314 Velocity - Smoothed Data





Late Time Effects

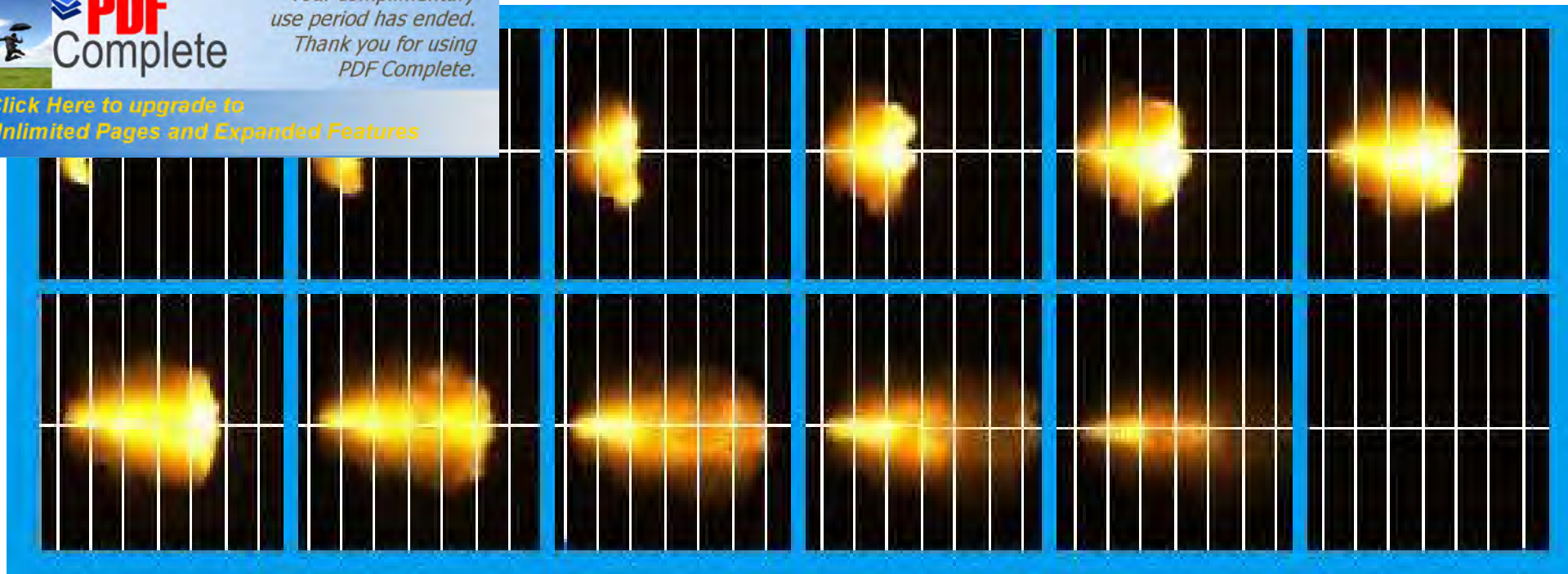
- In Spite of Lower Pressures Resulting From
 - Impact of Material From Crater
 - Pressure of Trapped Gas
- Late Time Processes Make Major Contribution to Impulse
- Target Plate Gained Velocity for ~ 3 ms
- Increase After ~ 0.15 ms Due to Late Time Processes
- Also Notice:
 - Plate Slows at Greater Than 1g Until $t \sim 10$ ms
 - Gas Bubble Can Over-Expand & Slow Plate



Summary

- Primary Loading Mechanism
 - Soil Driven Into Target by Expanding Gas Bubble
- First Phase
 - Complex, Modulated by Shockwave
 - Very Brief
 - Acts on Small Portion of Target
 - Provides About Half Total Vertical Impulse
- Second Phase
 - Dominated By Crater Excavation Processes
 - Pressures Lower
 - Order of Magnitude Greater Duration
 - Much Larger Area of Application
 - Provides About Half Total Vertical Impulse

Leslie C. Taylor
Ph: 301/405-5339
University of Maryland
Paper: ISB 277-2008

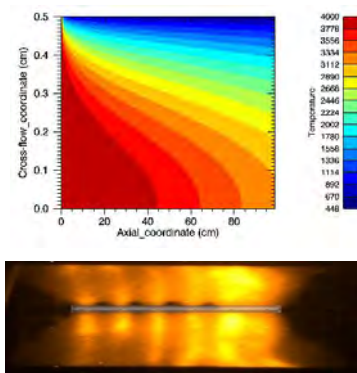


Consideration of the Ignition Delay of Gun Propellants

M. J. Taylor, C. R. Woodley, S. R. Fuller, S. Gilbert, J. I. Gransden

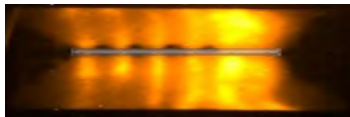
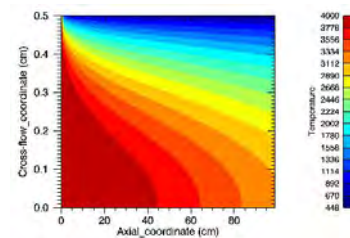
A presentation to: 24th International Symposium on Ballistics, New Orleans,
Louisiana September 22-26, 2008

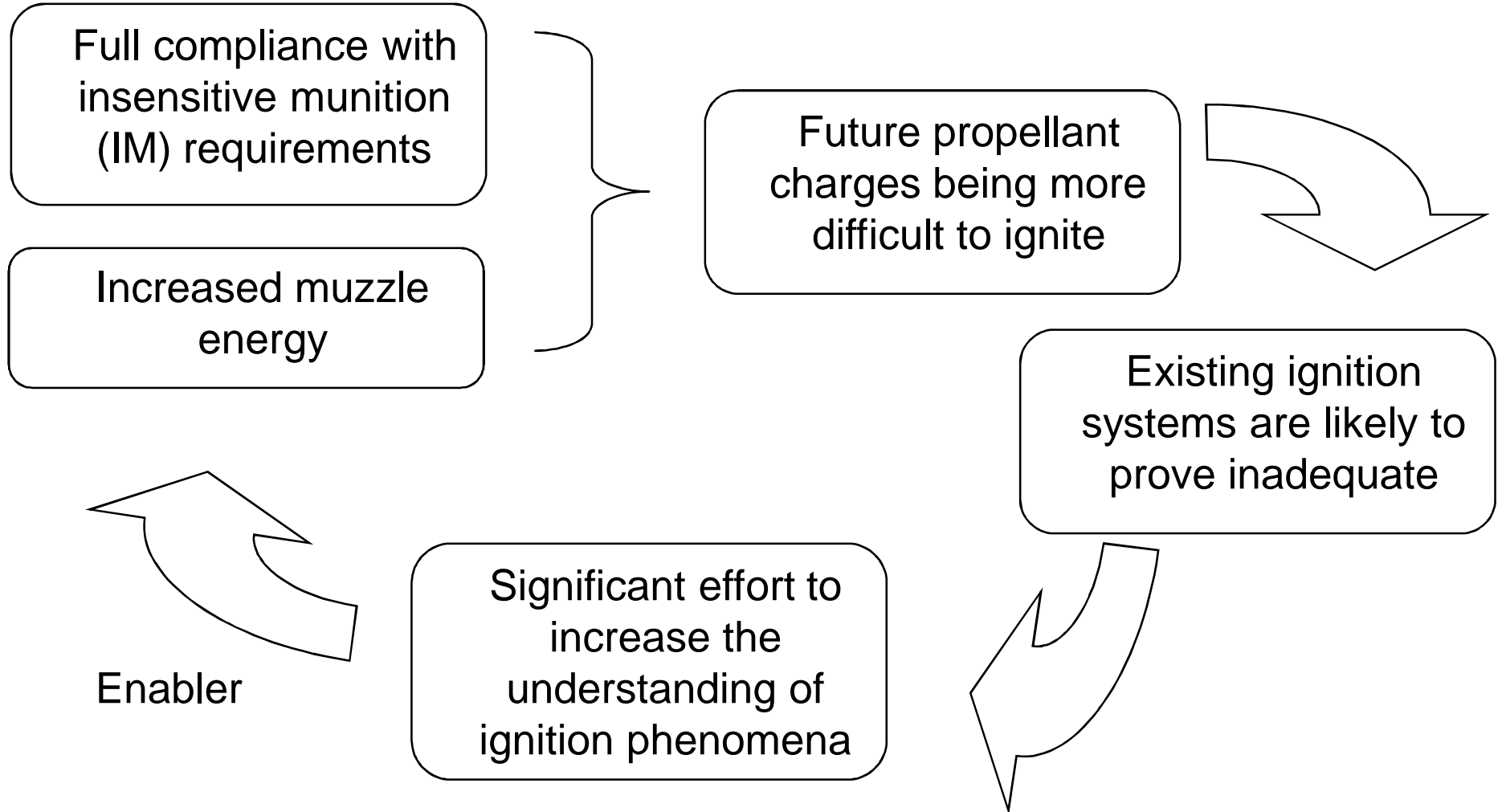
- 01 Background
- 02 Empirical Expression for Ignition Delay
- 03 The Ablation Coefficient
- 04 Analytical Treatment of Ignition Delay
- 05 Conclusions



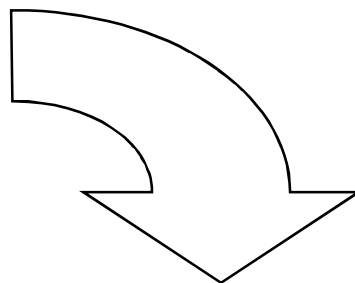
01

Background



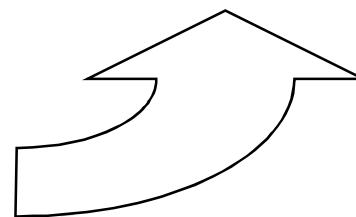


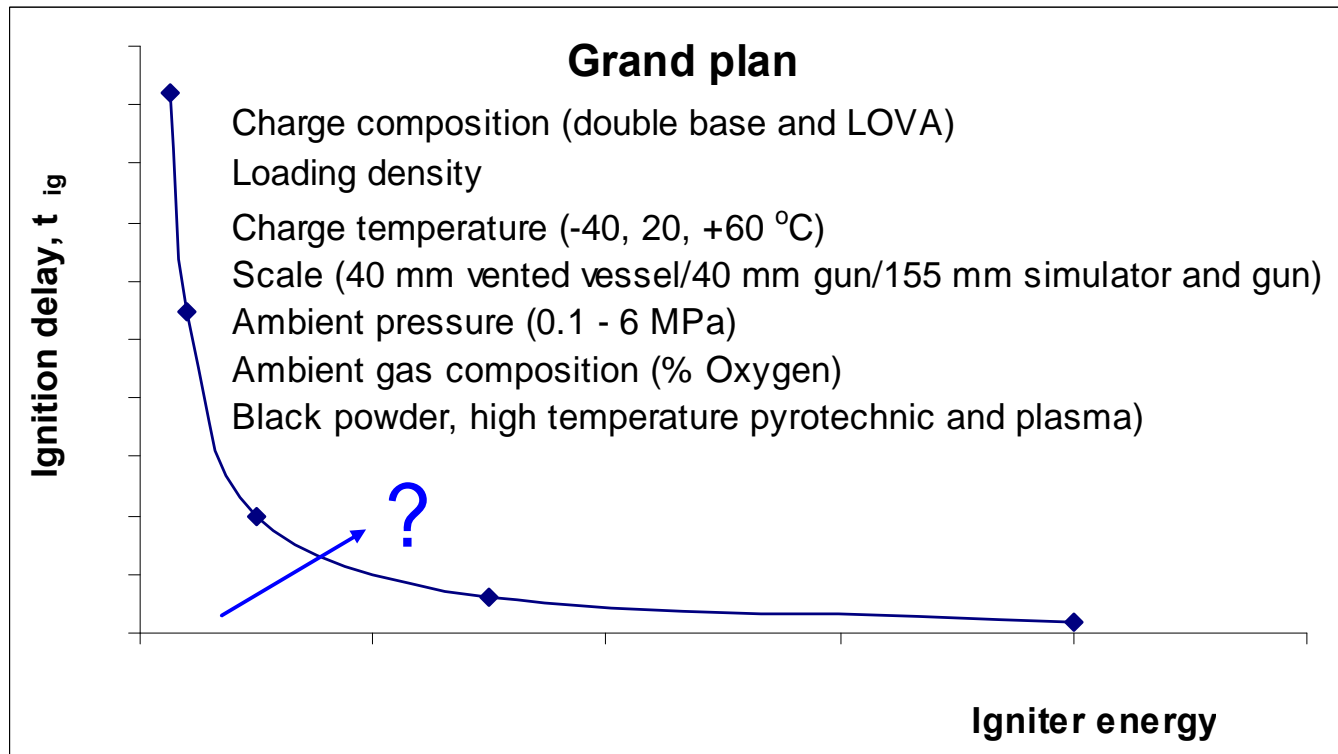
A MOD DTIC
programme
designed to address
this need



Includes the UK component of
the EUROPA Ignition
Phenomena TA between
French, German, Swedish and
the UK Govn~~ds~~

Aimed at increasing the depth
of understanding of ignition by
experiment and encapsulate
in computer modelling





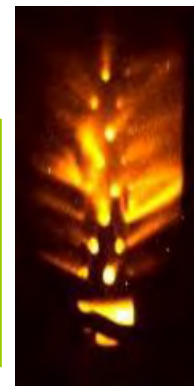
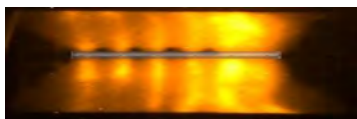
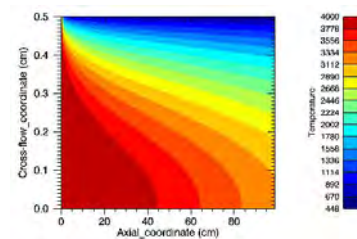
“ Ignition delay is an important and sensitive measurand

Over-ignition leads to pressure waves: **modelled with reasonable confidence**

Under-ignition leads to long ignition delays: **cannot be predictively modelled**

02

Empirical Expression for Ignition Delay

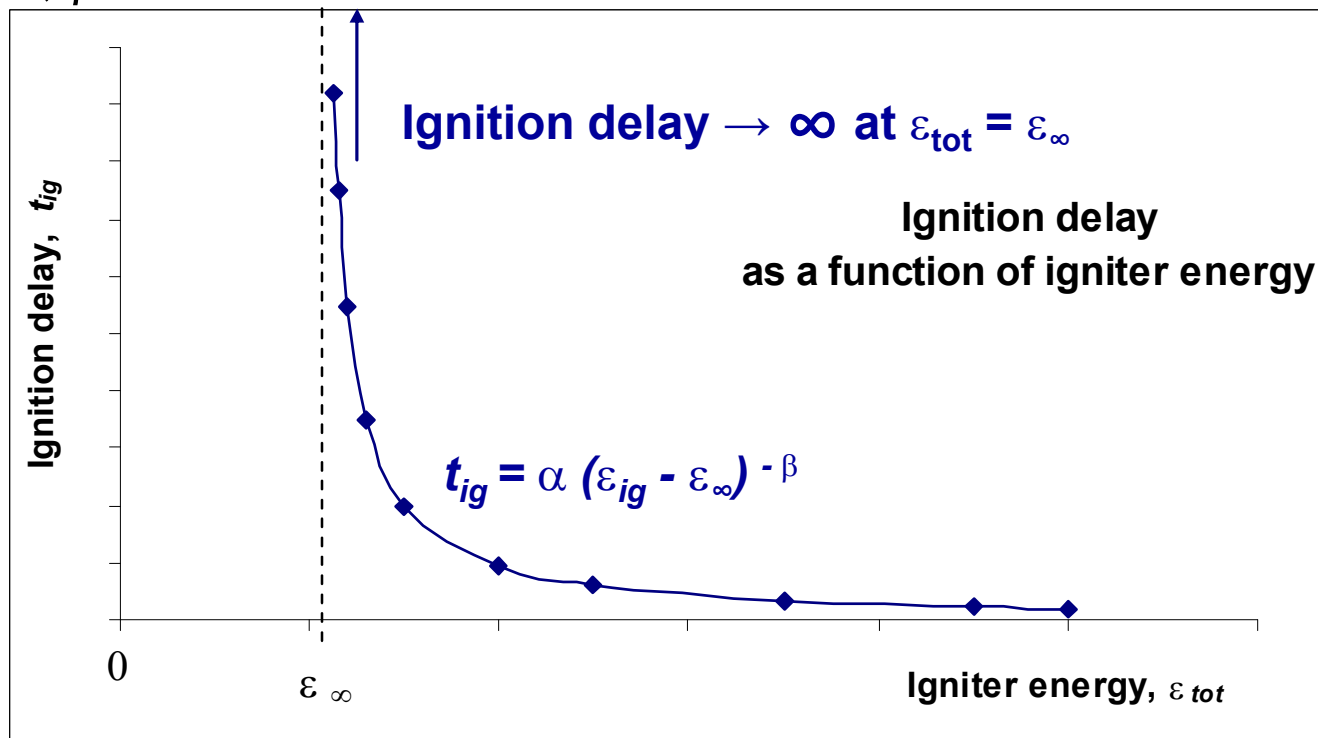


Equation for Ignition Delay

$$t_{ig} = \alpha (\varepsilon_{ig} - \varepsilon_{\infty})^{-\beta} \quad (1)$$

where ε_{∞} is the energy leading to mis-fire ($t_{ig} = \infty$ when $\varepsilon_{ig} - \varepsilon_{\infty} = 0$);

α, β are constants



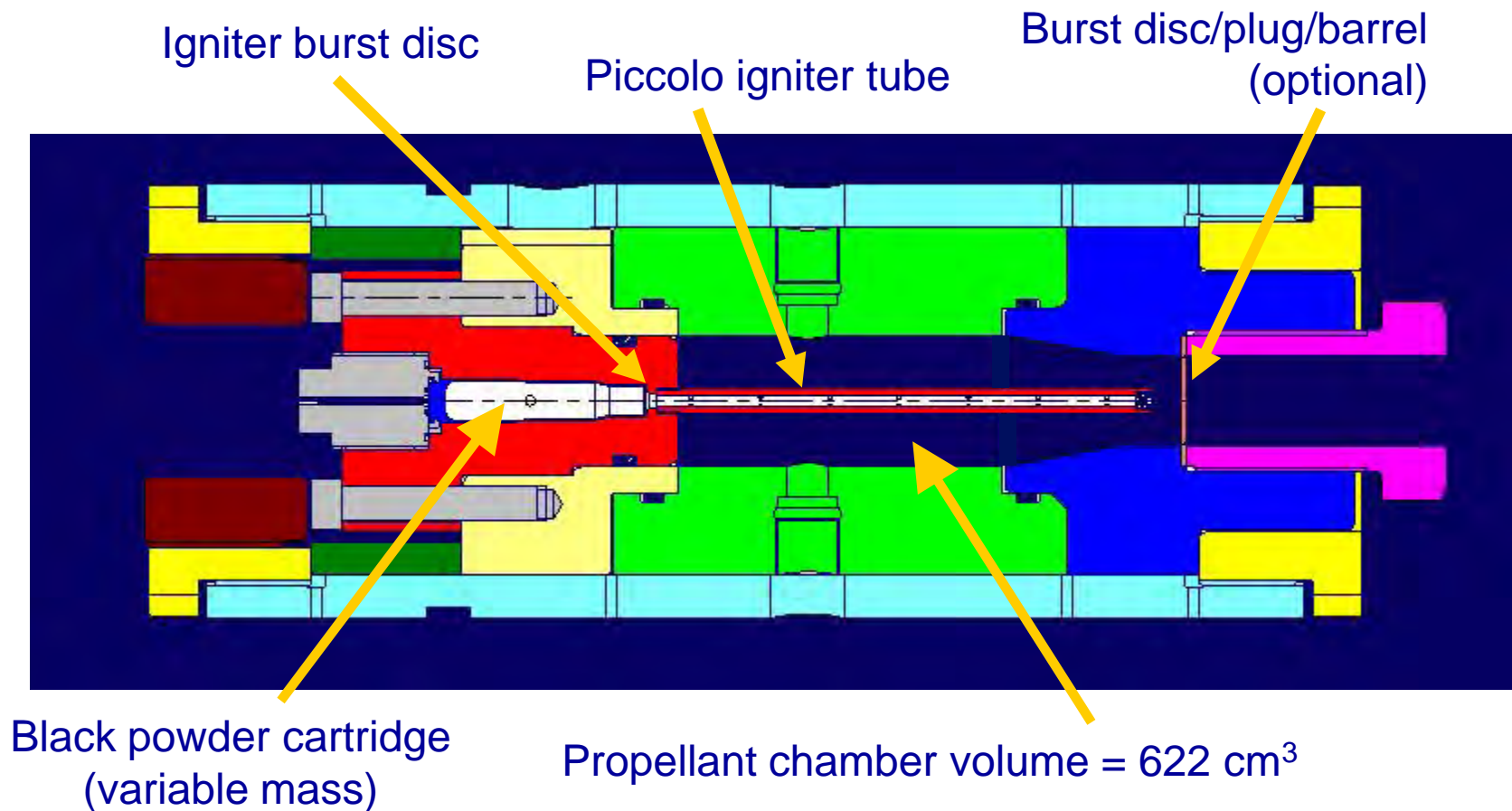
Aims:

Determine function coefficients for propellant ignition for a range of parameters

Use data for ignition model validation and model development

Session for Ignition Delay

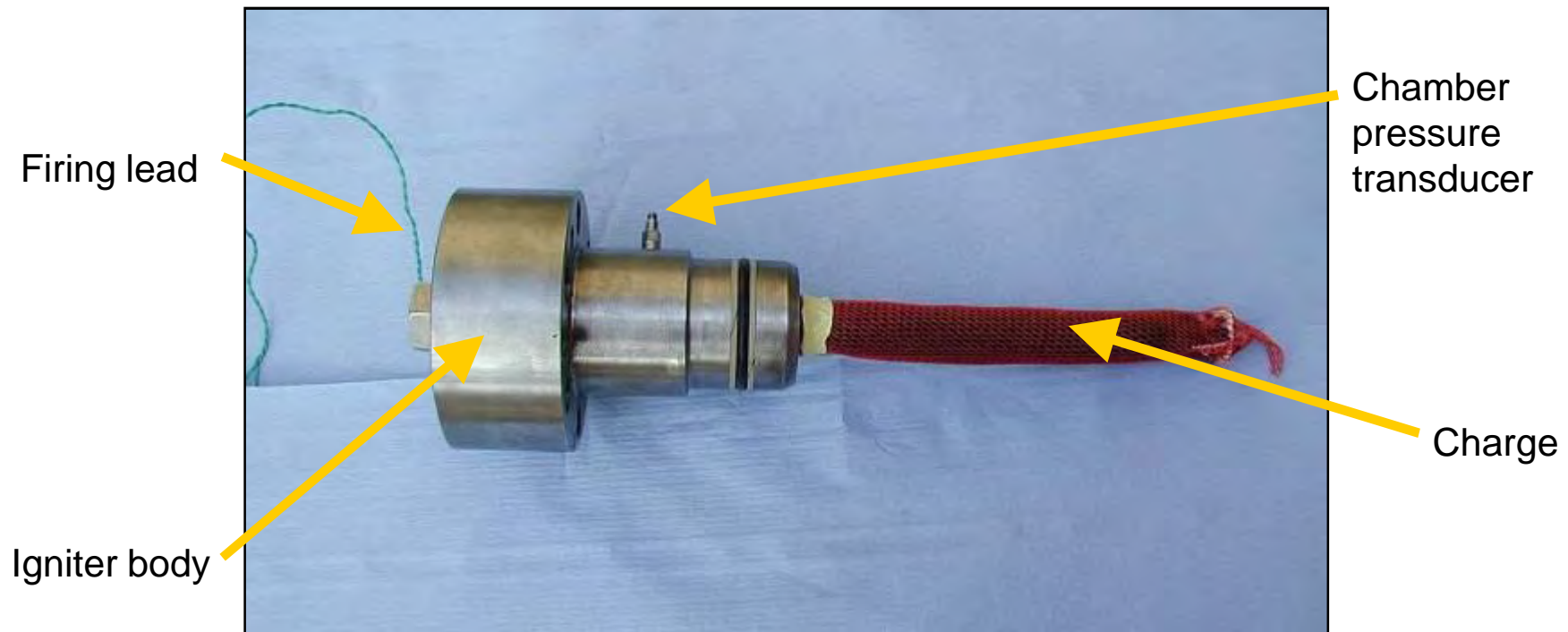
Instrumented 40 mm black powder igniter and vessel



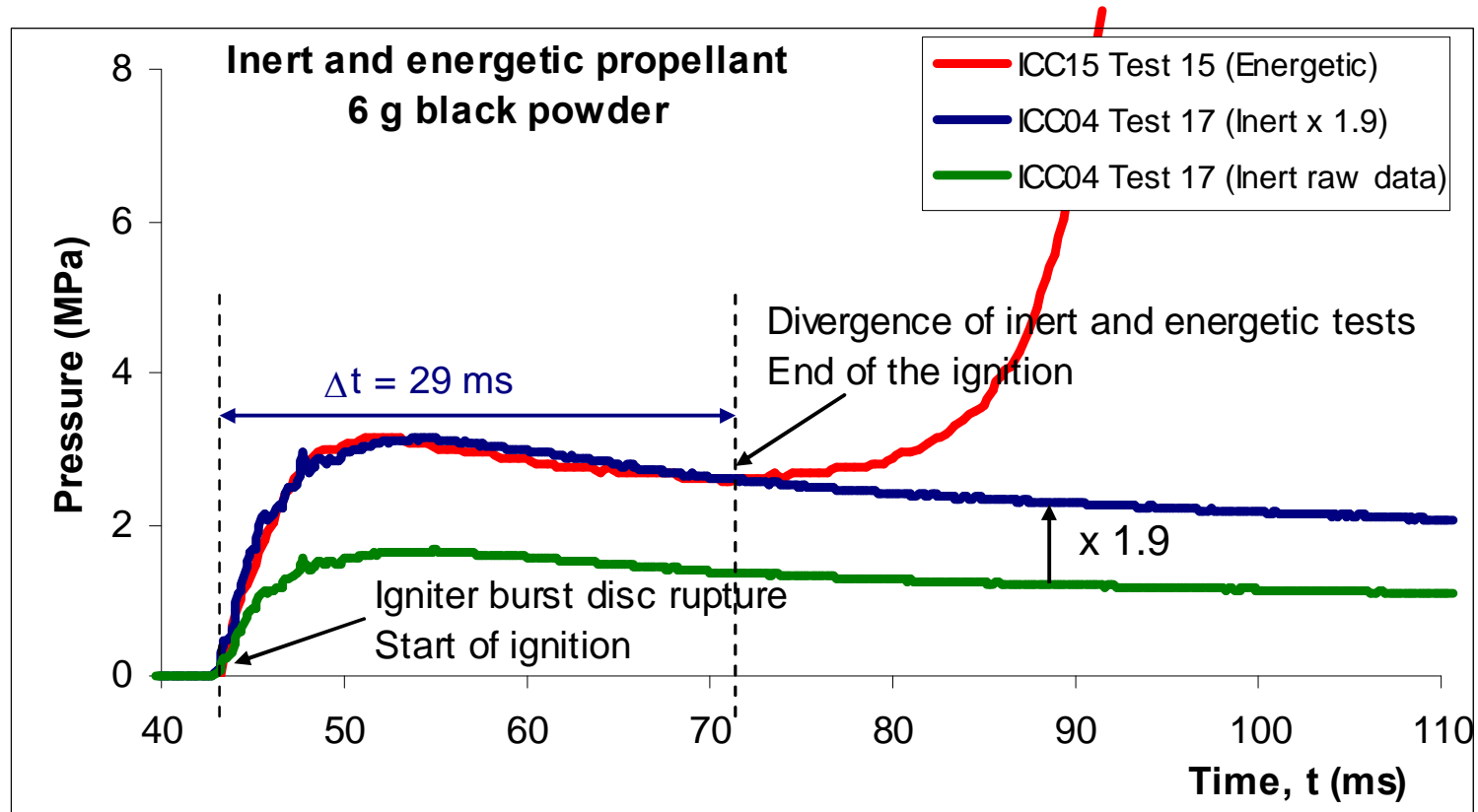
Session for Ignition Delay

The propellant charge is made around the piccolo tube

Loading density is adjusted by radial (as opposed to longitudinal) adjustment

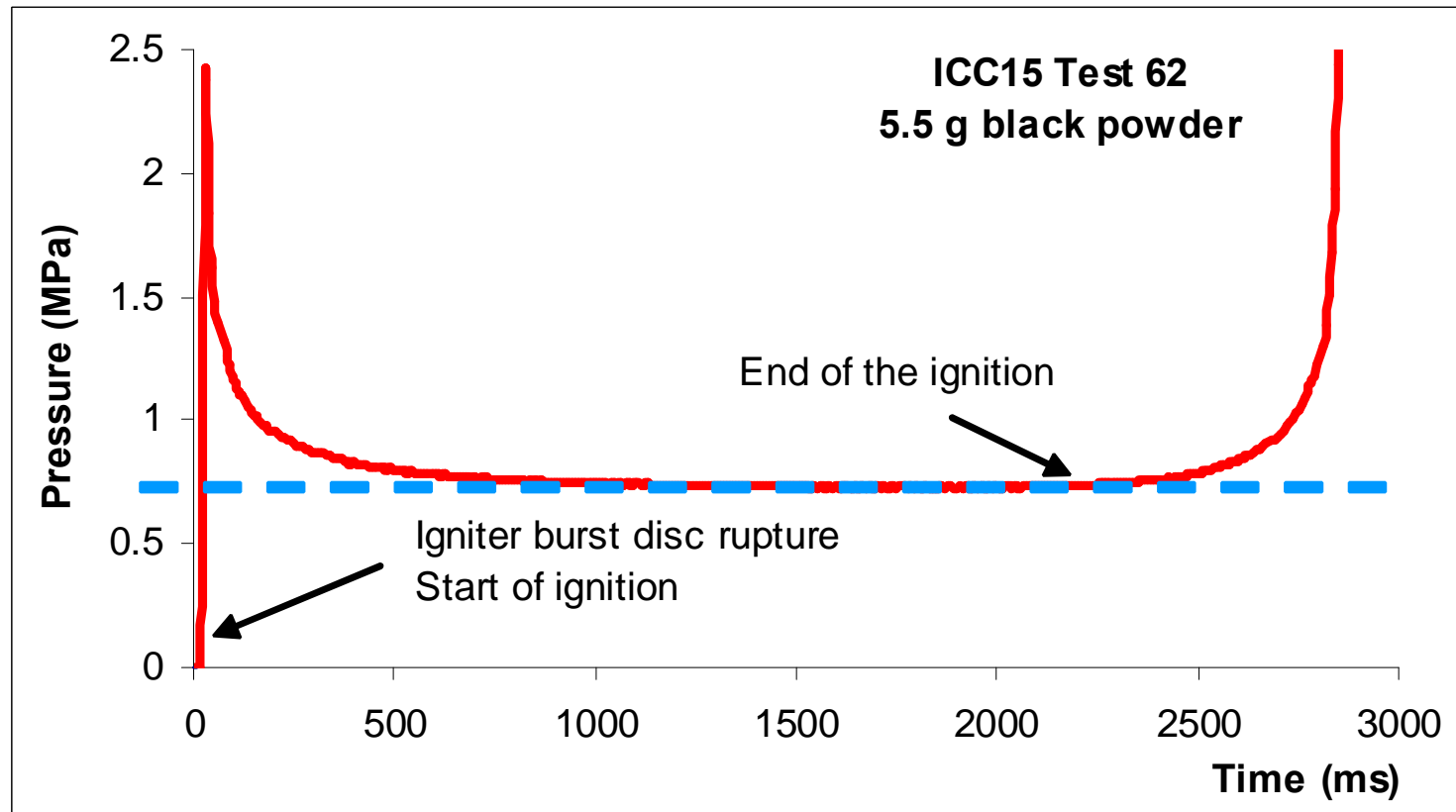


Session for Ignition Delay



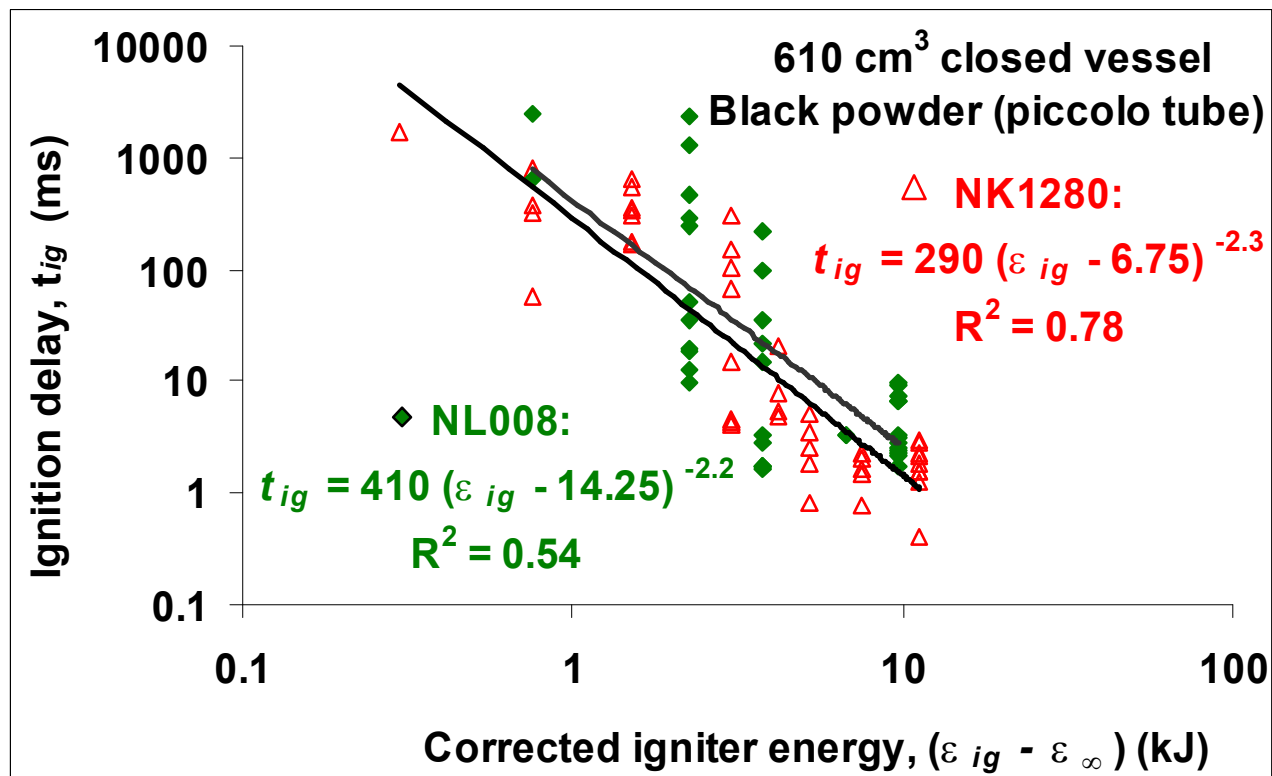
Energetic tests generated up to 4 times more pressure than inert tests

Session for Ignition Delay



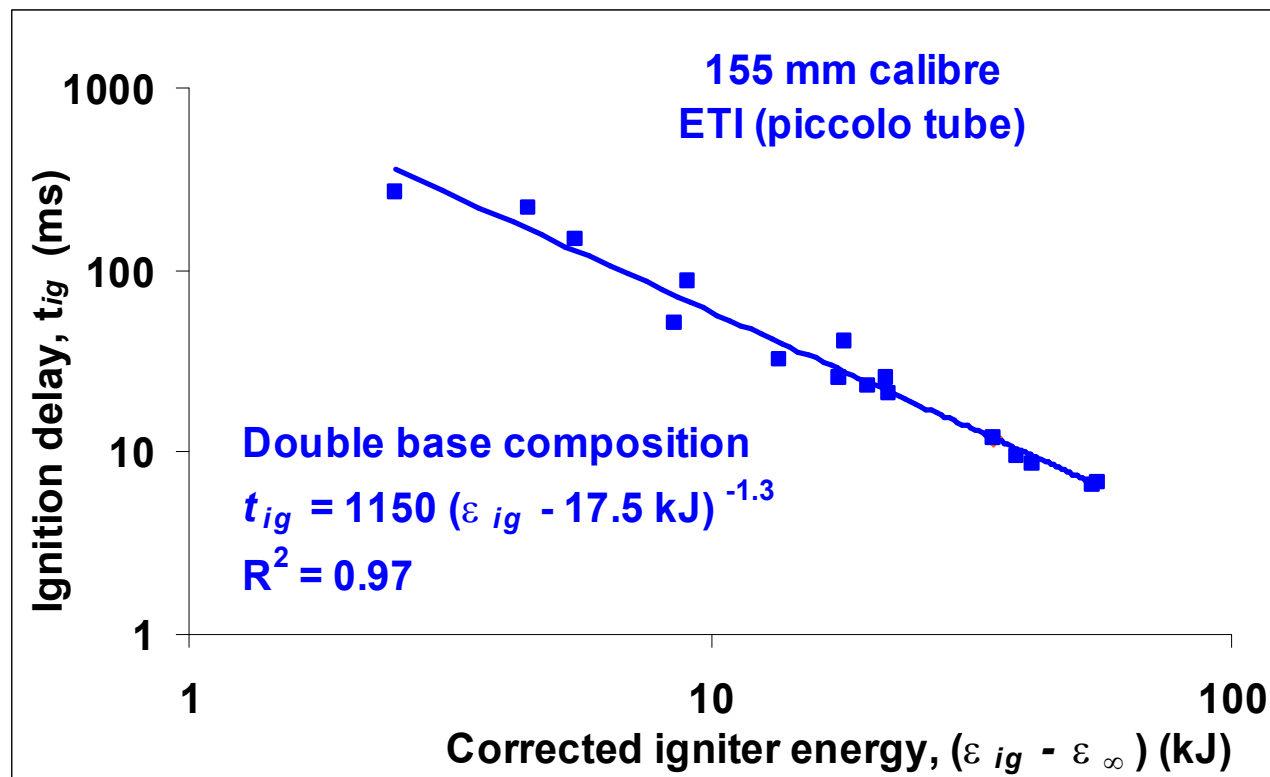
End of ignition can be defined by change in dp/dt

Equation for Ignition Delay



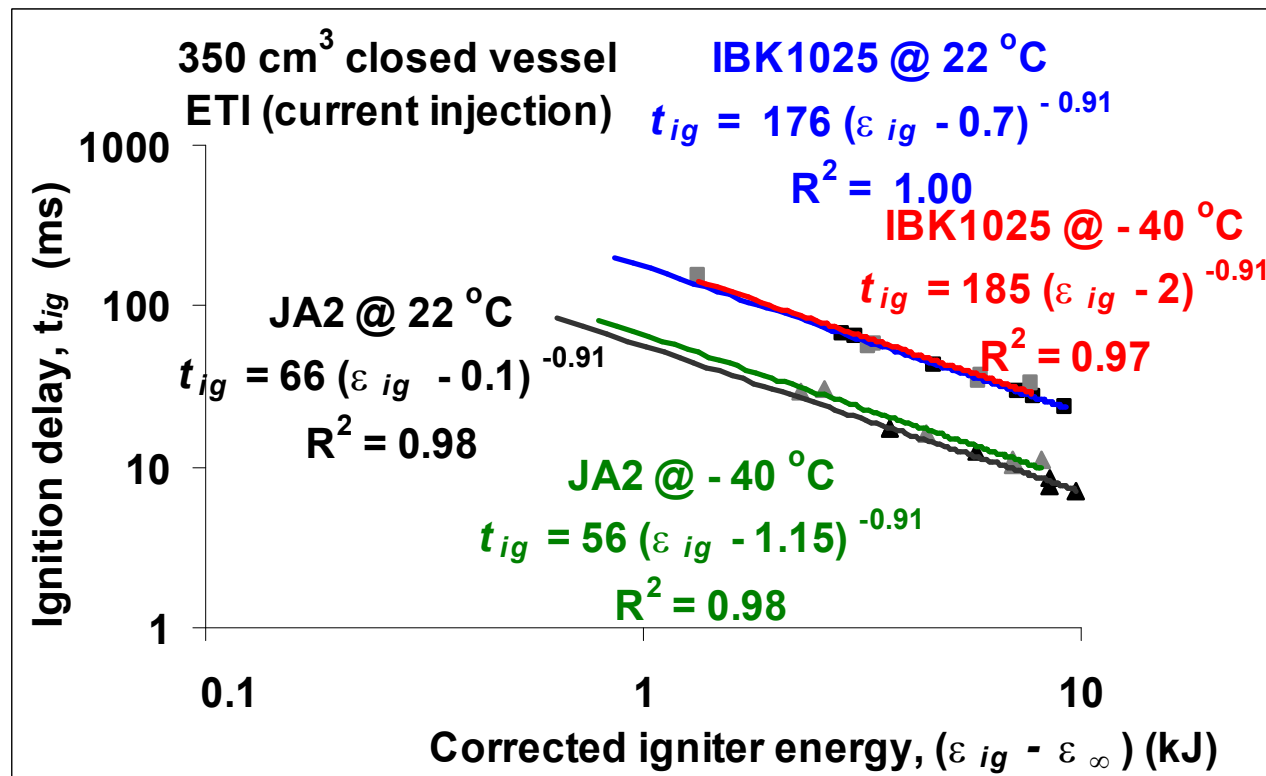
Ignition using a piccolo igniter with black powder . poor repeatability at cannon calibre

Equation for Ignition Delay



Ignition using a piccolo igniter with black powder . good repeatability at 155 mm calibre

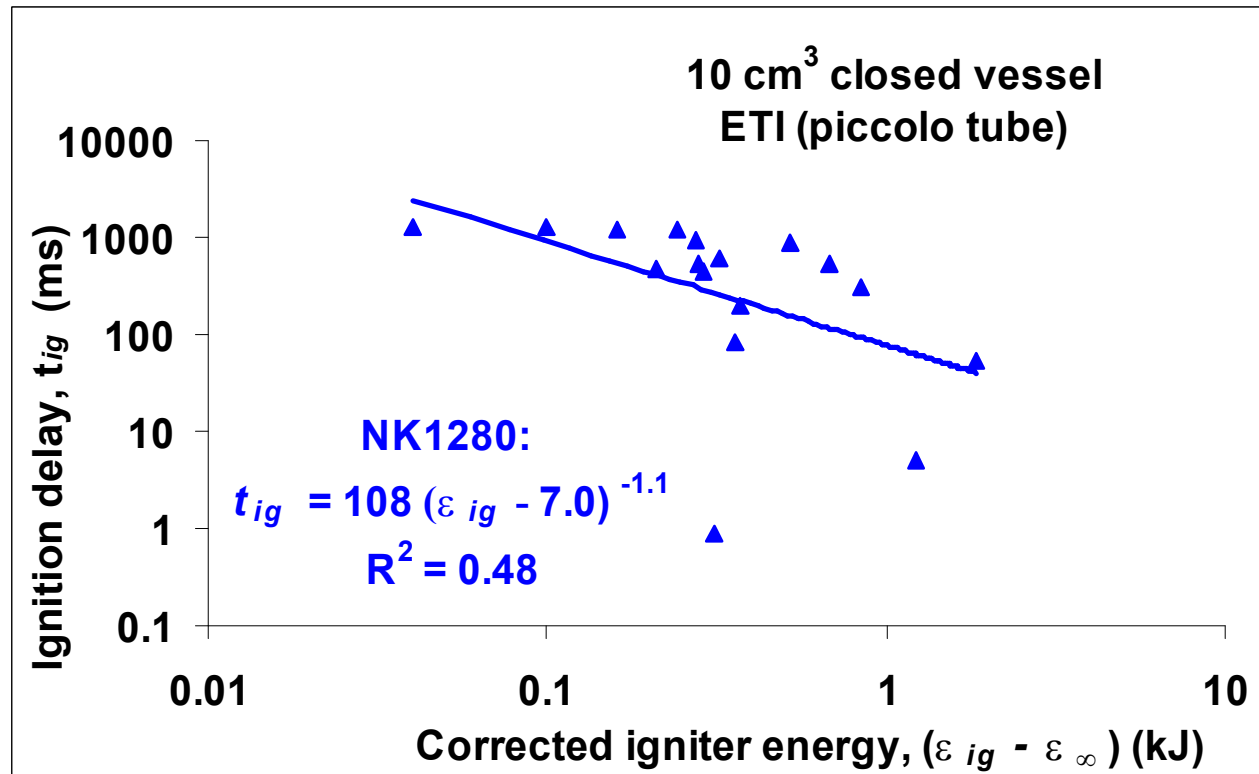
Equation for Ignition Delay



Ignition using a current injection igniter with ETI . good repeatability at cannon calibre

Results courtesy of TNO - M. Bakker, C. Schoolderman, C. van Driel and E. Folgering, WTC Ignition of LOVA Gun Propellants, 37th Int. Annual Conference of ICT, Karlsruhe, Germany, 27th June - 30th June, 2006

Regression for Ignition Delay

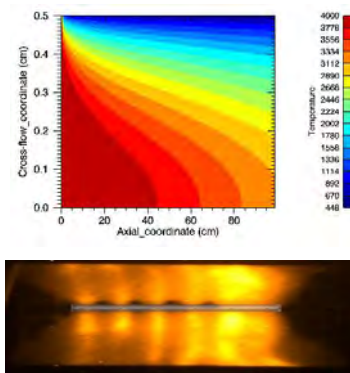


Ignition using a
piccolo igniter with
ETI . poor
repeatability at
cannon calibre

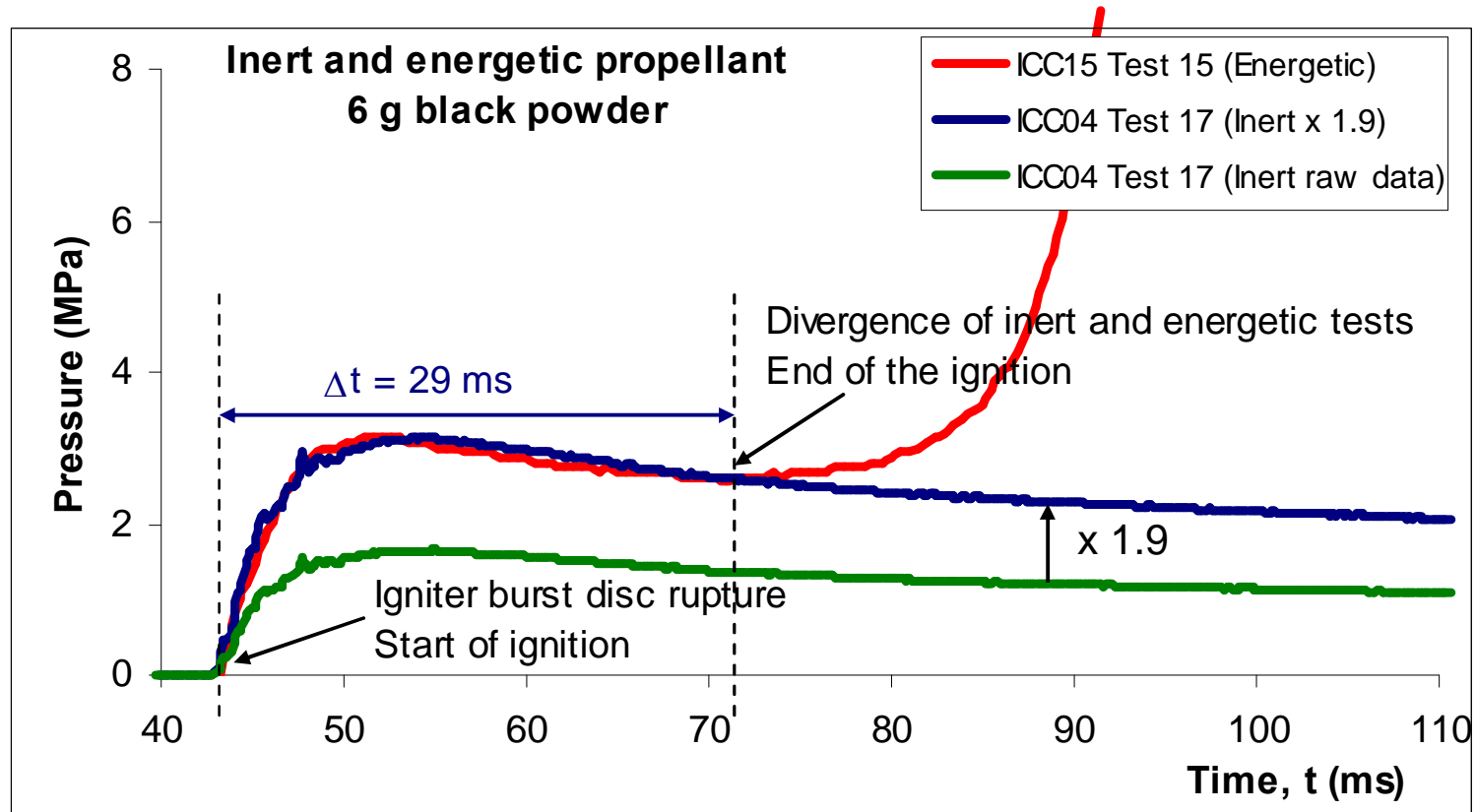
Consistent poor repeatability at cannon calibre with piccolo igniter.

03

The Ablation Coefficient



oefficient



Energetic tests generated up to 4 times more pressure than inert tests

coefficient

- “ It is proposed that erosive burning (ablation) of the propellant is caused by the discharging igniter

This adds energy and pressure to the system during the ignition phase

$$t_{ig} = \alpha (\varepsilon_{ig} + ap - \varepsilon_{\infty})^{-\beta} \quad (2)$$

- “ Variability in ignition delay caused by variability in ablation coefficient, a

The factor, a , slightly varies from test to test

- “ The factor, a , greatly varies with test conditions

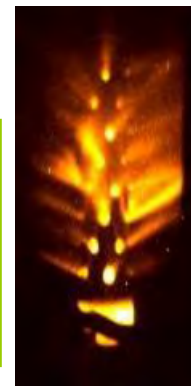
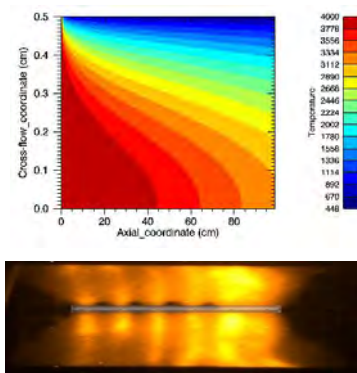
Cannon calibre ETI using a piccolo igniter gives the largest factor

Highly brisant (hard) igniter

Cannon calibre ETI using current injection gives the least factor

Low brisance (soft) igniter

04 Analytical Treatment of Ignition Delay



ment of Ignition Delay

“ The time to ignition can also be described by:

$$t_{ig} \sim \frac{1}{4} \pi \lambda \rho c_p T_p^2 I^{-2} + t_{stab} \quad (2)$$

where

λ is the propellant heat conductivity

ρ is the propellant density

c_p is the propellant specific heat

T_p is the propellant pyrolysis temperature

I is the heat flux

“ t_{stab} is the time required for initiation and stabilisation of gas phase reactions and is only significant during over-ignition when the heat flux is large and I^{-2} diminishes (i.e. when ignition delays are small)

tment of Ignition Delay

- “ The expressions for ignition delay, equations (2) and (3), are obviously describing the same event but from empirical and theoretical perspectives

The theory considers the rate of heat transfer and the experiment considers the time-integrated energy

- “ However, these expressions can be equated by substituting for heat flux with time-integrated energy in equation (3)

Development of Ignition Delay

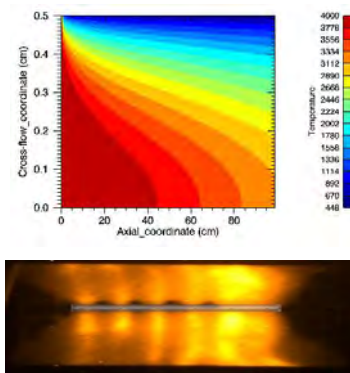
- “ If the rate of energy transfer is assumed to be constant then, for relatively long ignition delays:

$$t_{ig} = \alpha (\varepsilon_{ig} + ap - \varepsilon_{\infty})^{-\beta} = \frac{1}{4} \pi \lambda \rho c_p T_p^2 t^2 A^2 \varepsilon^{-2} \quad (4)$$

where ε is the igniter energy transferred to the propellant, t is the time to transfer ε and A is the surface area over which ε is transferred

- “ This comparison gives a useful platform from which to understand and compare the various values of the igniter coefficients

05 Conclusions



- “ Studies have investigated ignition delay of gun propellant
 - An empirical treatment of the relationship between ignition delay and igniter energy agrees in form with an analytical expression
 - The correlation between experiment and theory is excellent under some conditions, but appears to be poor under others
 - An hypothesis to explain this has been put forward, that some igniter designs produce excessive ablation of propellant
- “ Some of the main assumptions in the theoretical treatment are invalidated, but the comparison between the experiment and theory has been surprisingly successful
- “ Efforts to understand the physical and chemical processes occurring during the long ignition delays are planned



*Your complimentary
use period has ended.
Thank you for using
PDF Complete.*

[Click Here to upgrade to
Unlimited Pages and Expanded Features](#)

QinetiQ

The Global Defence and Security Experts

www.QinetiQ.com

© Copyright QinetiQ limited 2006

Jacketed penetrators having different thickness

Penetrator performance and production

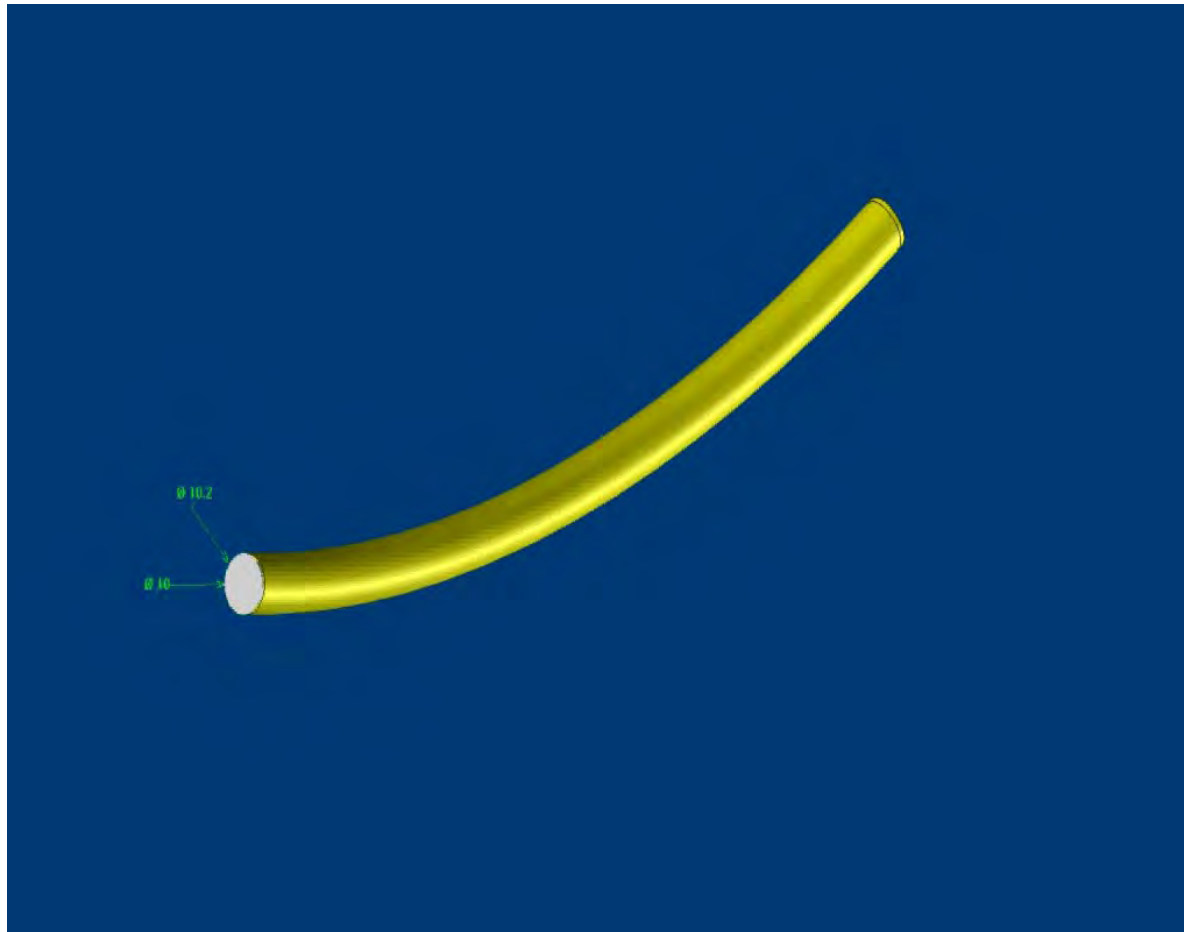
TNO | Knowledge for business



Contributors to this work:

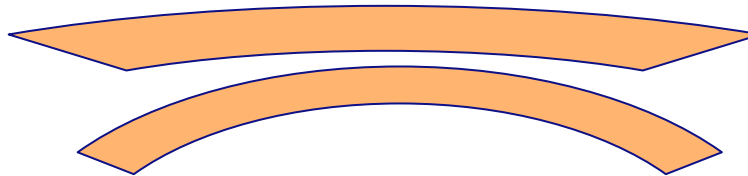
- Dr. Erik Carton
- Dr. Marianne Stuivinga
- Mark Dijkstra, Msc
- Dr. Niels van der Meer
 - TNO Defence, Security and Safety
 - Lange Kleiweg 137, 2280 AA Rijswijk, The Netherlands
 - Phone: +31 15 2843581
 - Fax: +31 15 2843939
 - Email: niels.vandermeer@tno.nl

Increasing the jacket thickness make the penetrator stiffer

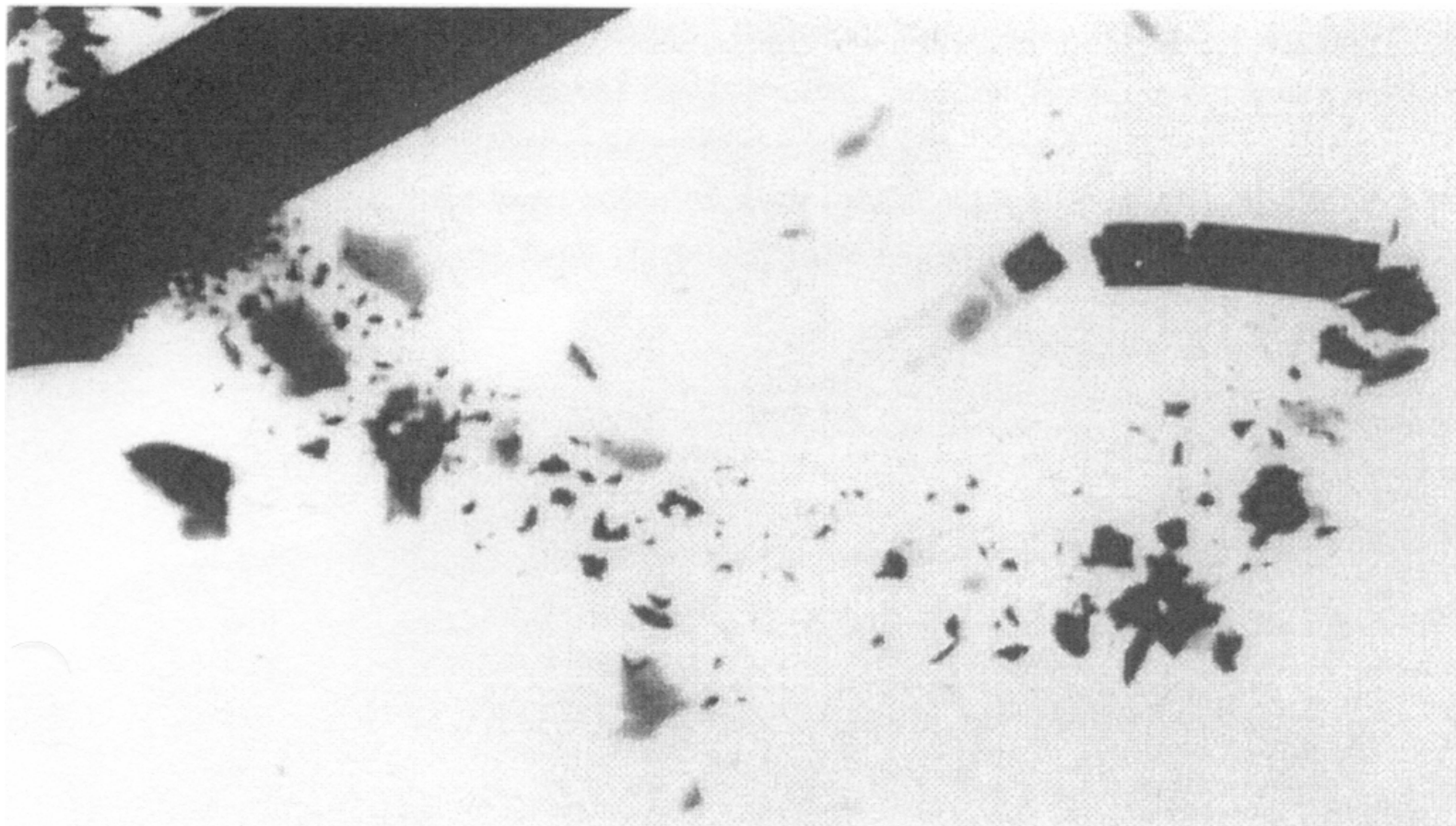


Content of presentation

- Join technique of jacket and core: explosive cladding
- Propellant production and light weight sabot
- Experiments with and results for jacket penetrators
- Conclusions



Limit fragmentation.....



Jacketed penetrators obtain higher flexural rigidity with increasing jacket thickness

- Flexural rigidity of a rod $\propto E \times R^4$ (Youngs modulus x radius⁴)
- Penetrator mass increase as well $\propto R^{2/3} \times \rho$ (radius^{2/3} x mass density)
- Use high Young's modulus, low mass density material for the jacket
- Large radius of low density jacket will reduce penetration capacity of jacketed penetrator
- Commercially available metals (tubes) have been used for jackets

Focus

- Most published work is focussed on the important penetrator depth of penetration (DOP)
- This work is focussed on penetrator condition after perforating spaced/layered thin targets
- Reduced DOP of an intact jacketed penetrator is sometimes preferred over hardly any DOP of a broken penetrator

Under what circumstances can a jacket be useful?

- Thick target plates cause probably too high lateral forces on the penetrator

A jacket could be of advantage in case of:

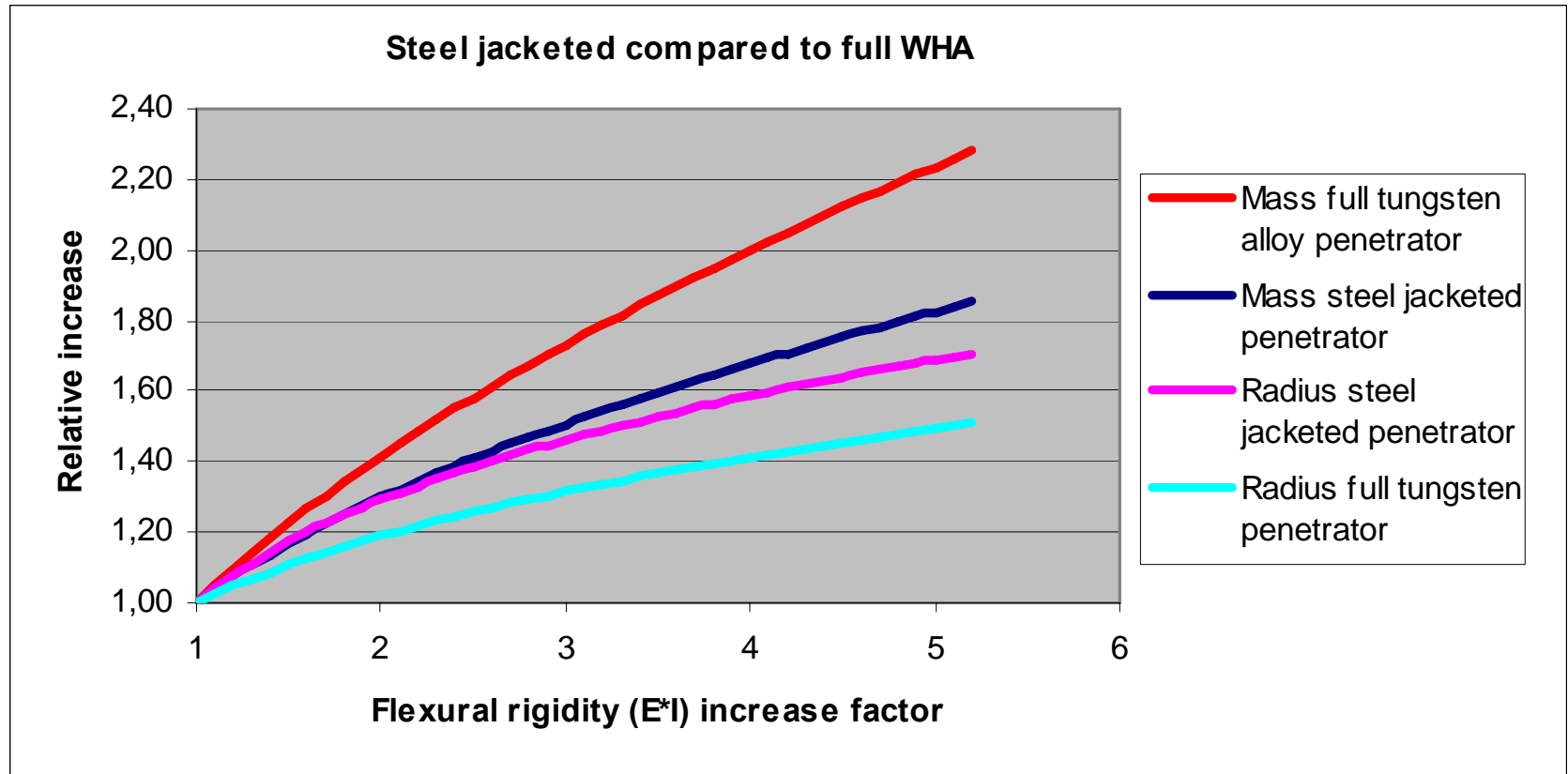
- Spaced target
- Layered target

.....both consisting of relatively thin plates

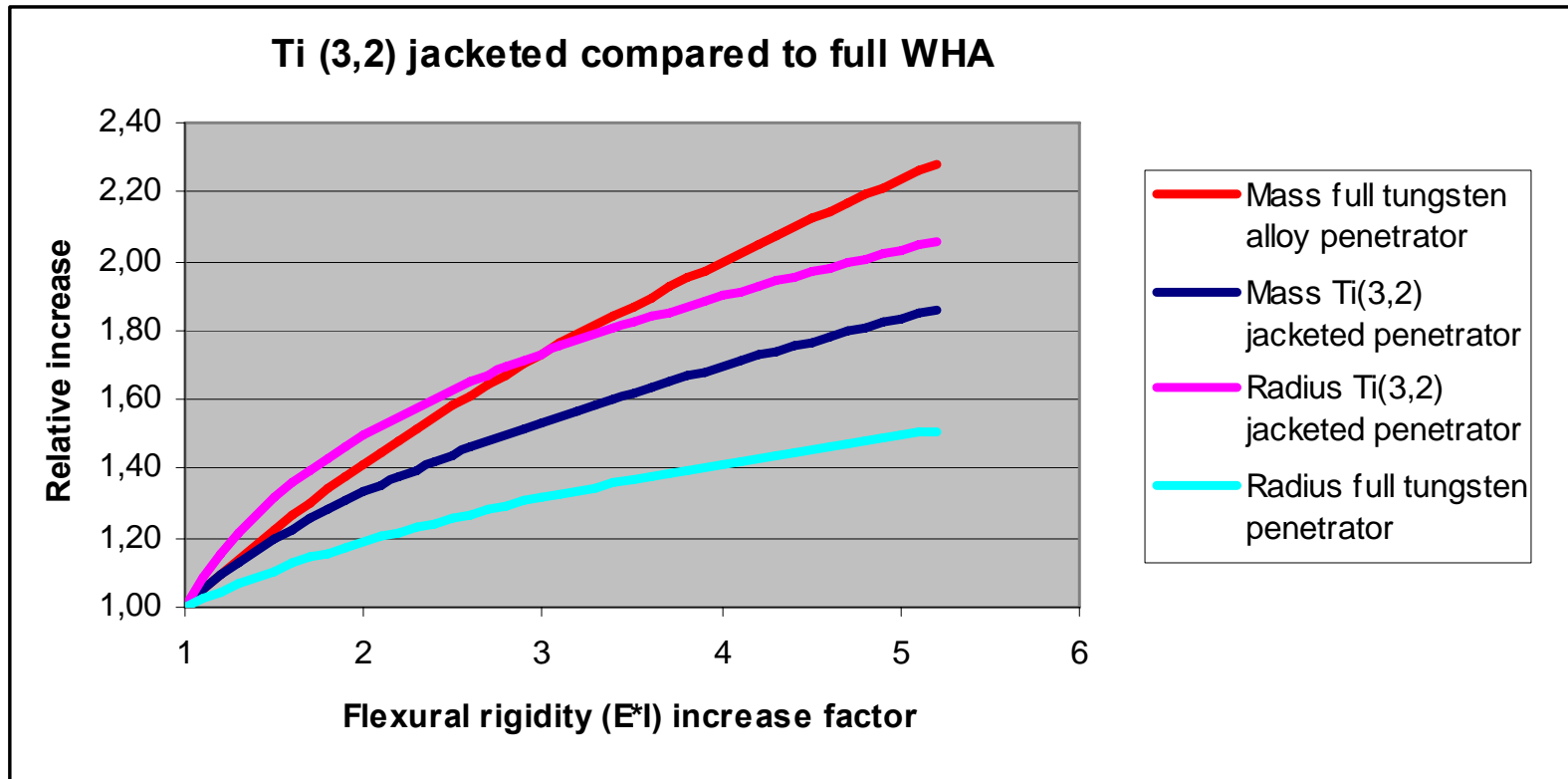
Results of published work

<i>Type of work</i>	D_c/D_j	V_{impact}	<i>Ref/year</i>
Computer code	> 0.9	1700 m/s	[2]/1994
Experiment	> 0.8	1800 m/s	[4]/1996
Experiment	> 0.6	2200 m/s	[3]/2001
Experiment	> 0.7	1500 m/s	[5]/2005
Experiment	0.5 – 0.8	1100 – 1300 m/s	this work

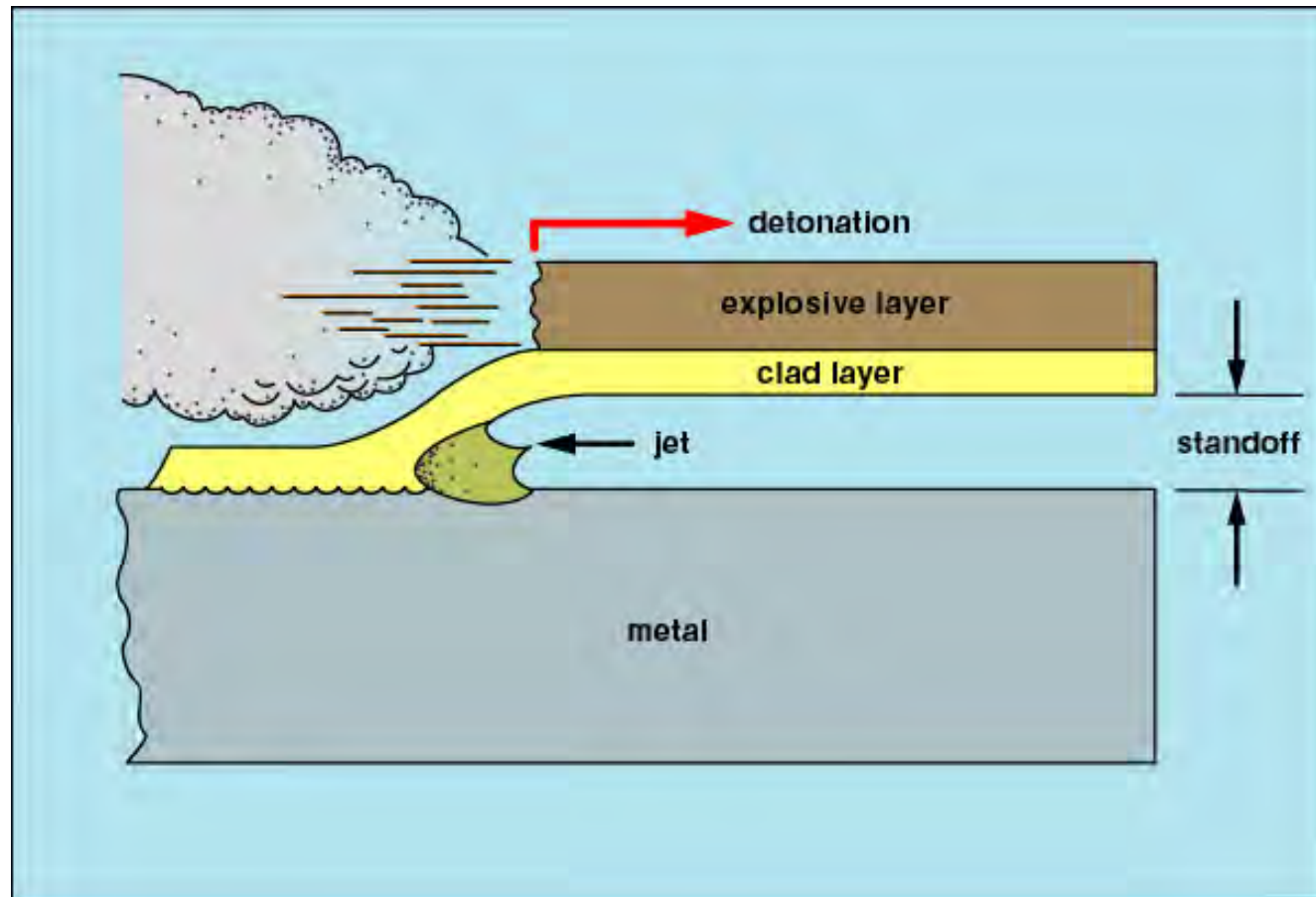
Relative mass and radius increase (1)



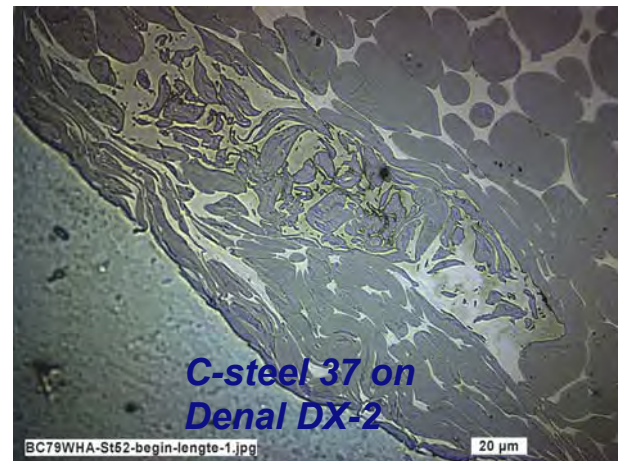
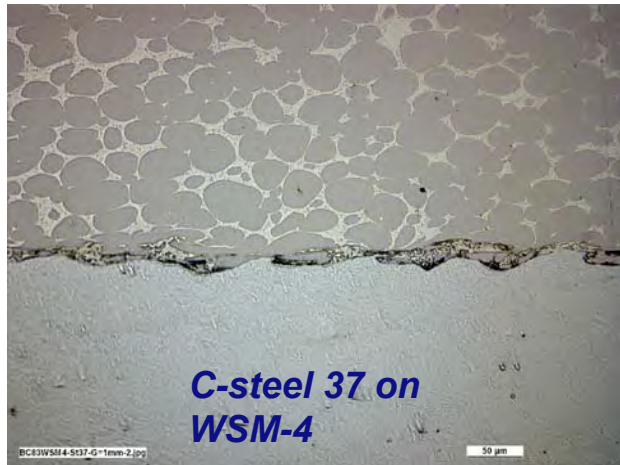
Relative mass and radius increase (2)



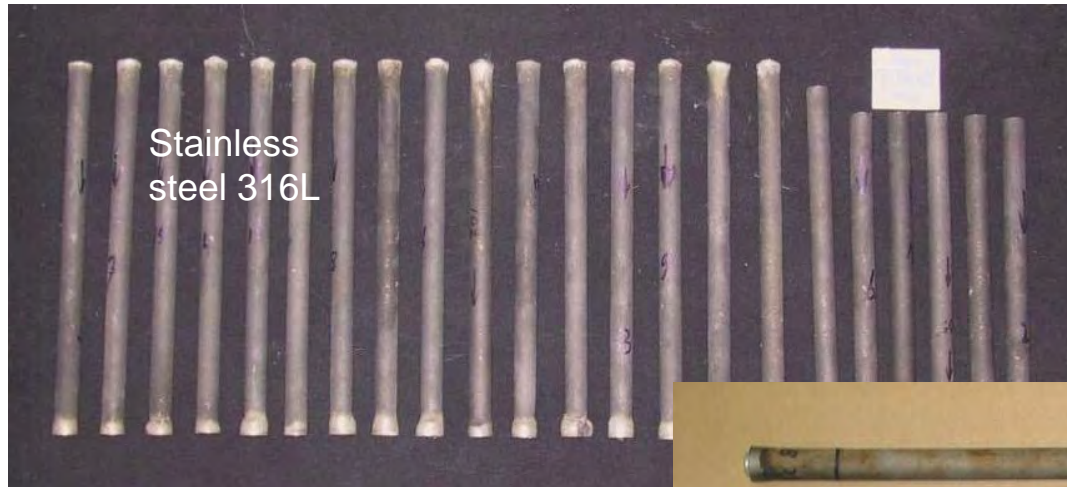
Explosive cladding



WHA – metal interface



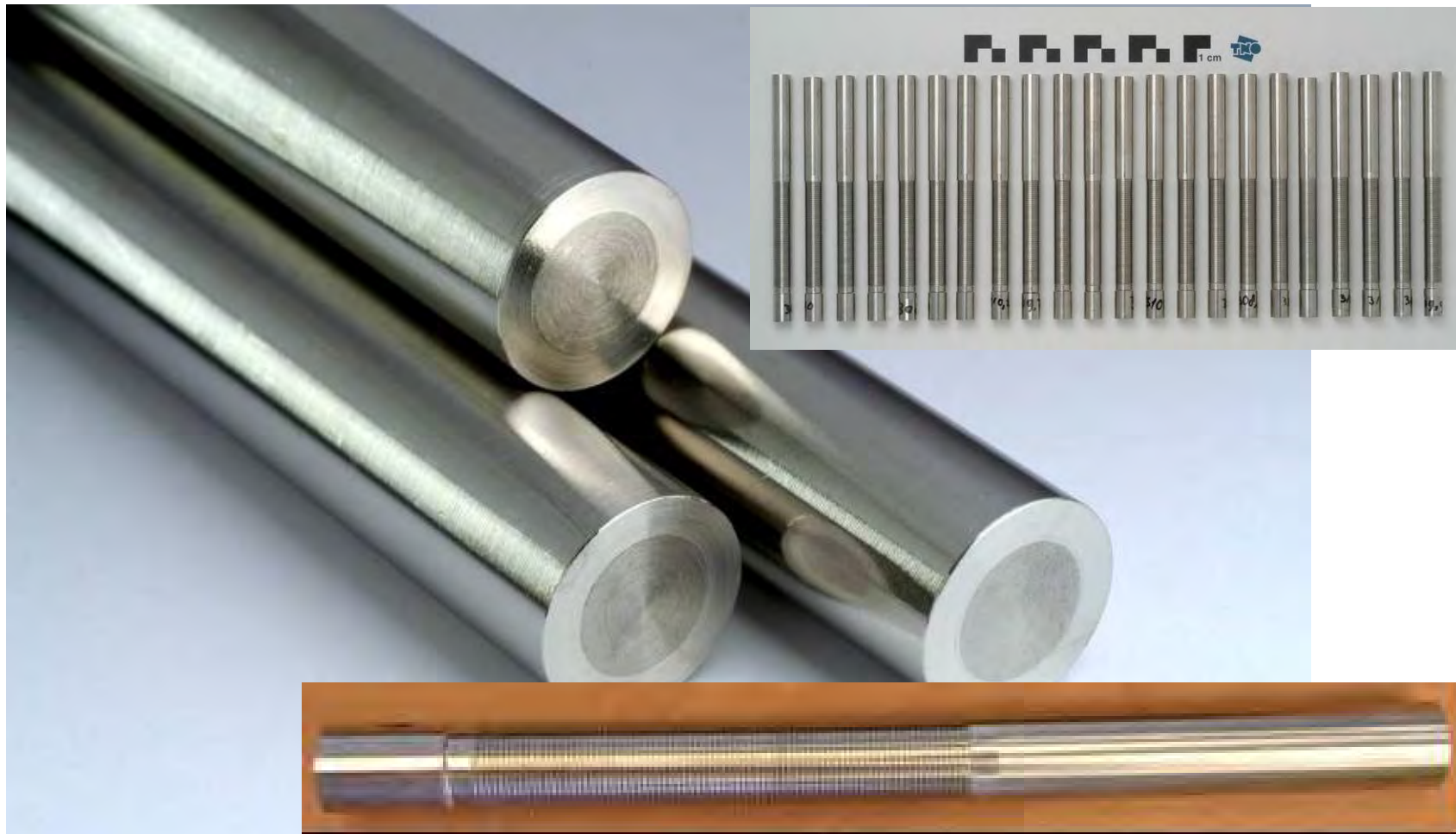
Explosively clad metals on WHA rods



Shear strength data of jacket - core interface

Jacket material	WSM-4 rod diameter (mm)	Jacket thickness (mm)	Shear strength (MPa)
Titanium (3,2)	10	1.2	156
Titanium pure grade 2	15.2	1	159
C-steel-37	14.9	1.3	65

Stainless steel 316L clad on WSM-4 rod



Penetrators having screw thread on the jacket instead in the jacket



Penetrators, sabot and propellant casing



Light weight sabot



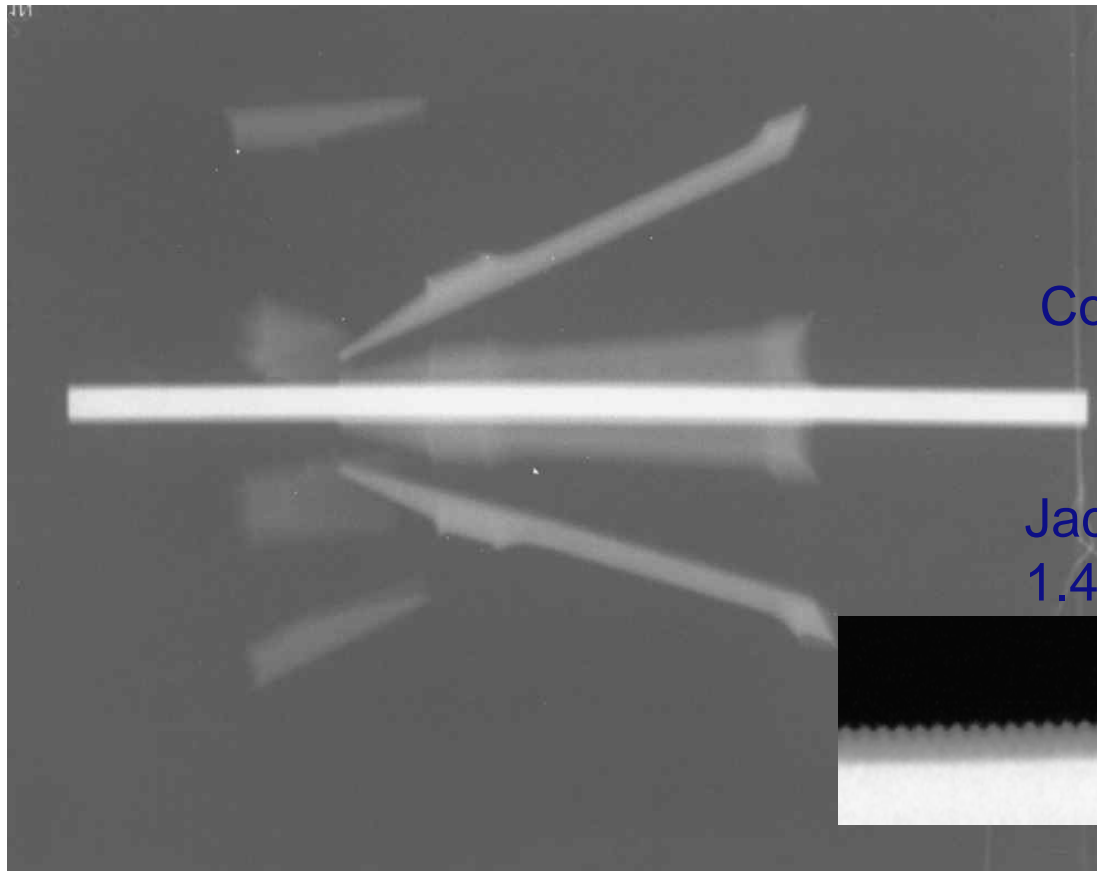
Propellant production facility: extruder



Experimental arrangement



Pure Titanium (grade 2) jacketed penetrator prior to impact (thin jackets)

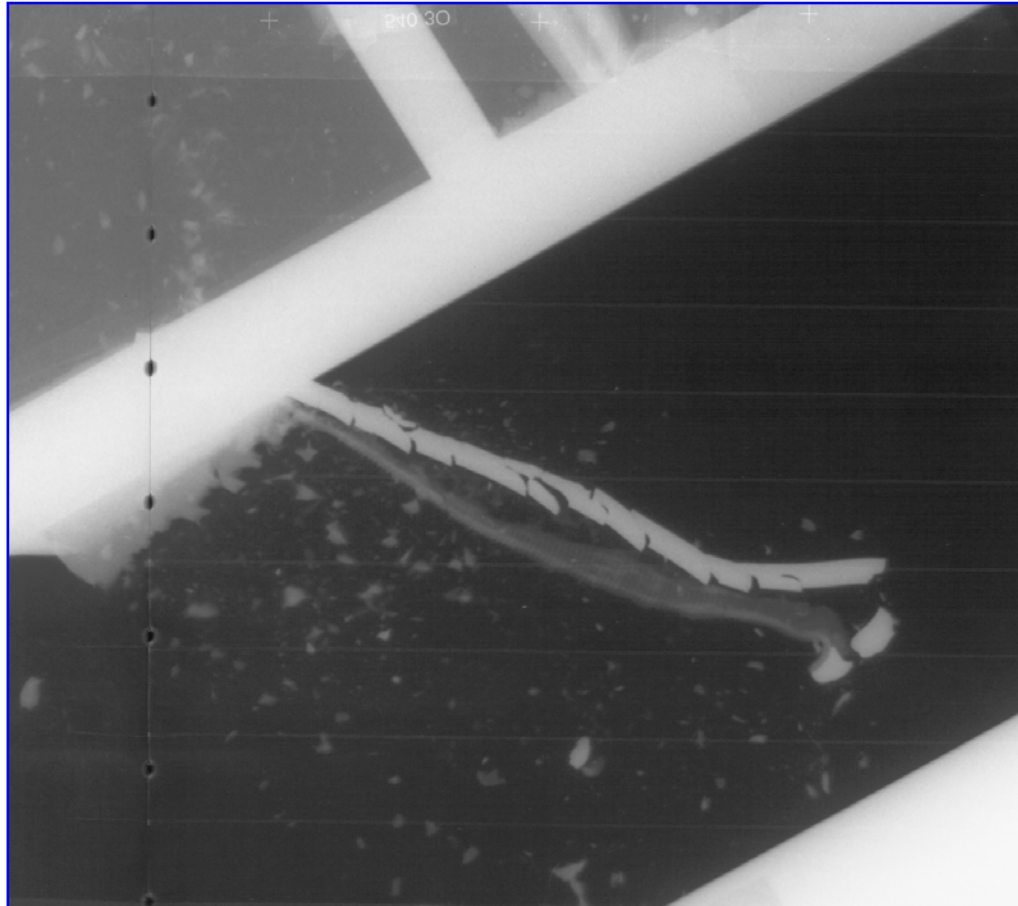


Core diameter: 6.3 mm

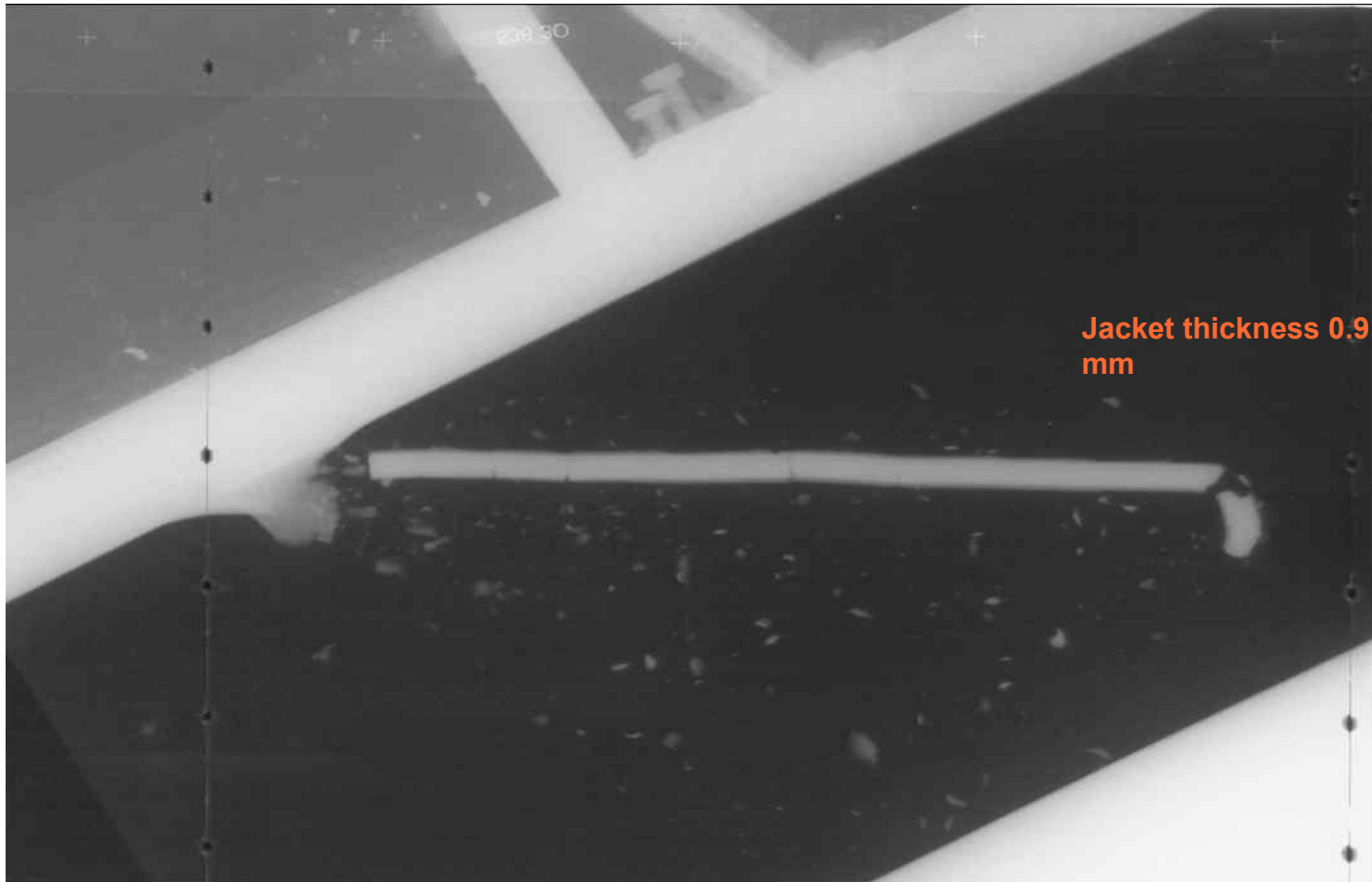
Jacket thickness
1.45 mm



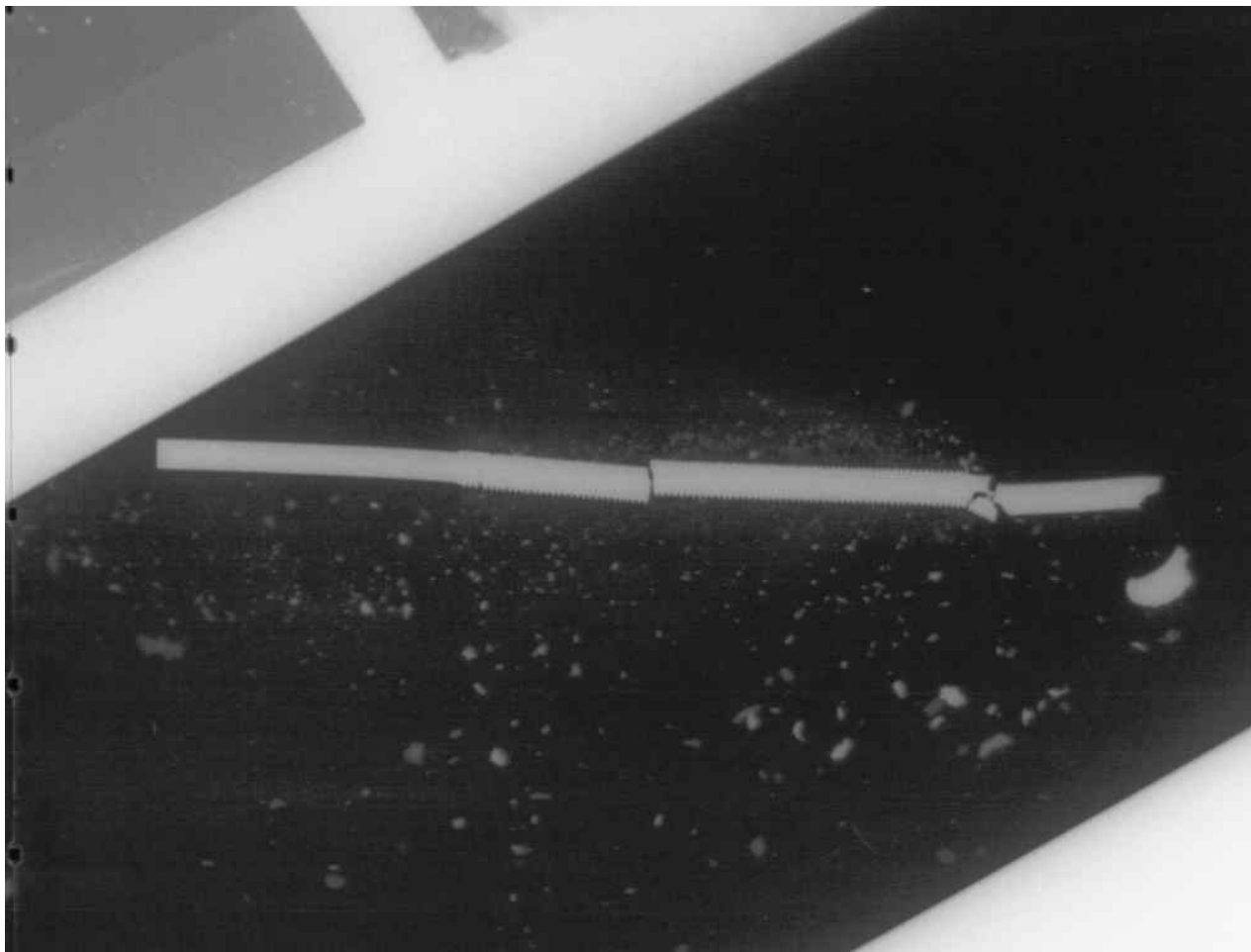
Pure Titanium (grade 2) jacketed penetrator (Denal DX2) after impact of layered steel/rubber/steel target



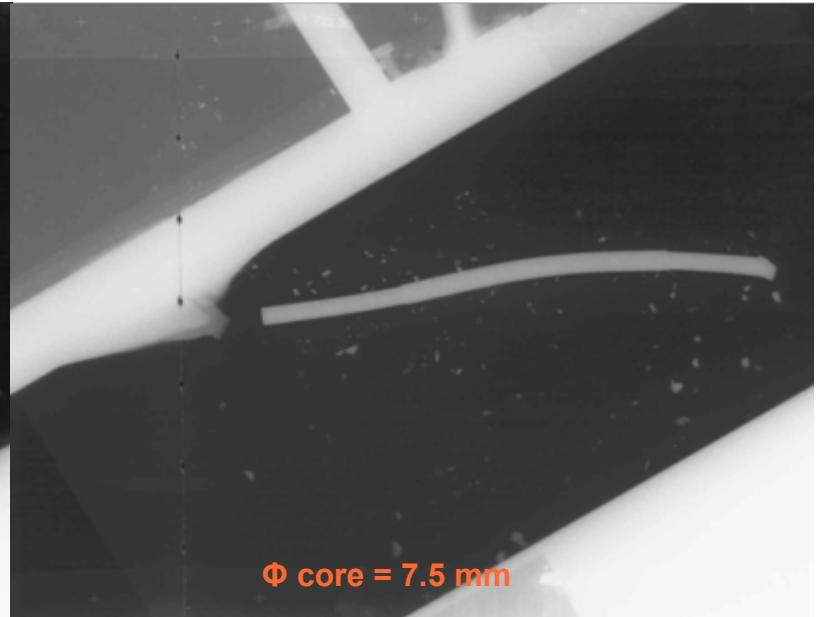
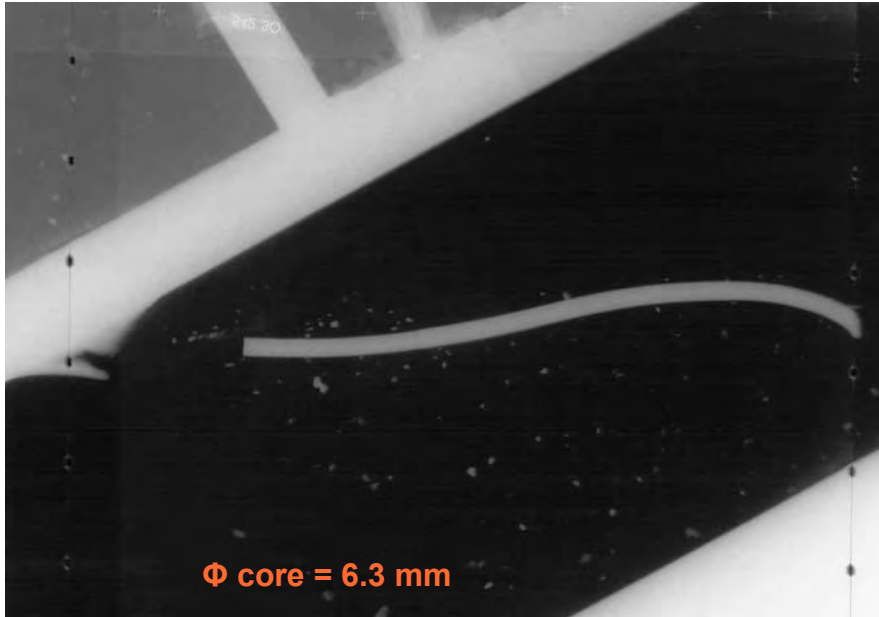
C-steel-37 jacketed penetrator (core: Denal DX 2)



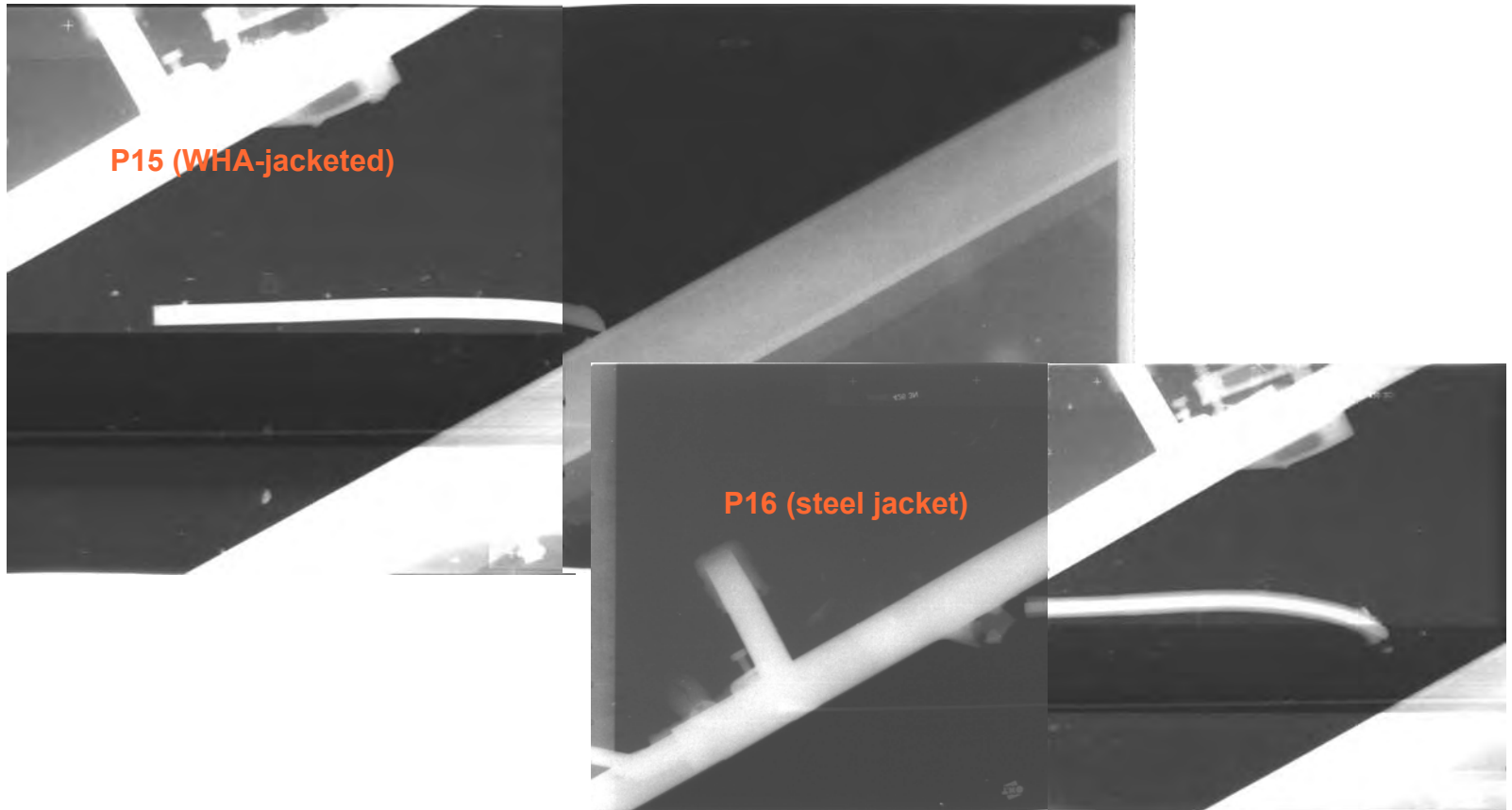
Denal DX 2 penetrator without a jacket



WSM-4 and WSM-4 “jacket”



Thick jackets: WHA “jackets” compared to steel jacketed (core: WSM-4)



DOP reduction

Penetrator	Jacket material	DOP (mm)
423/P15 $\mu = 0.64$	WHA	118
425/P16P $\mu = 0.5$	Steel-37	68

Steel jacketed penetrator

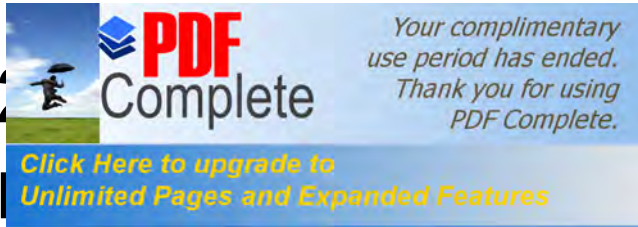


Penetration of stainless steel jacketed penetrator into RHA



Conclusions:

- Jackets can be clad on WHA rods and withstand acceleration forces for muzzle velocities up 1300 m/s (and very likely higher)
- At moderate velocities 1100 -1300 m/s:
 - Jackets can be of advantage:
 - against thin layered targets
 - in case projectile mass is a limiting factor for a firing system;
- Thicker jackets ($\mu \approx 0.5$) jackets reduce “DOP” in semi-infinite RHA-target
- At higher impact velocities, thicker jackets may give advantages as well



Symposium on Ballistics

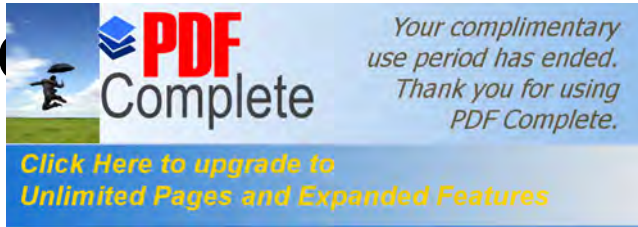
October 22-26, 2008

Numerical Simulation of Muzzle Exit and Separation Process for Sabot-Guided Projectiles in Supersonic Flight

Dr.-Ing. Jörn van Keuk, Dr.-Ing. Arno Klomfass



Fraunhofer Institut
Kurzzeitdynamik
Ernst-Mach-Institut



- **Introduction / Motivation**
- **Physical Aspects of the Firing Process**
- **Strategies for the Numerical Simulation / Proposed Procedure for the Study**
- **Results for Sabot Separation Simulations**
- **Conclusions / Future Work**

Innovation

of Sabot Separation Processes

Sabot Separation: Coupled Problem of Aerodynamics and Structure Dynamics

Sabot Function:

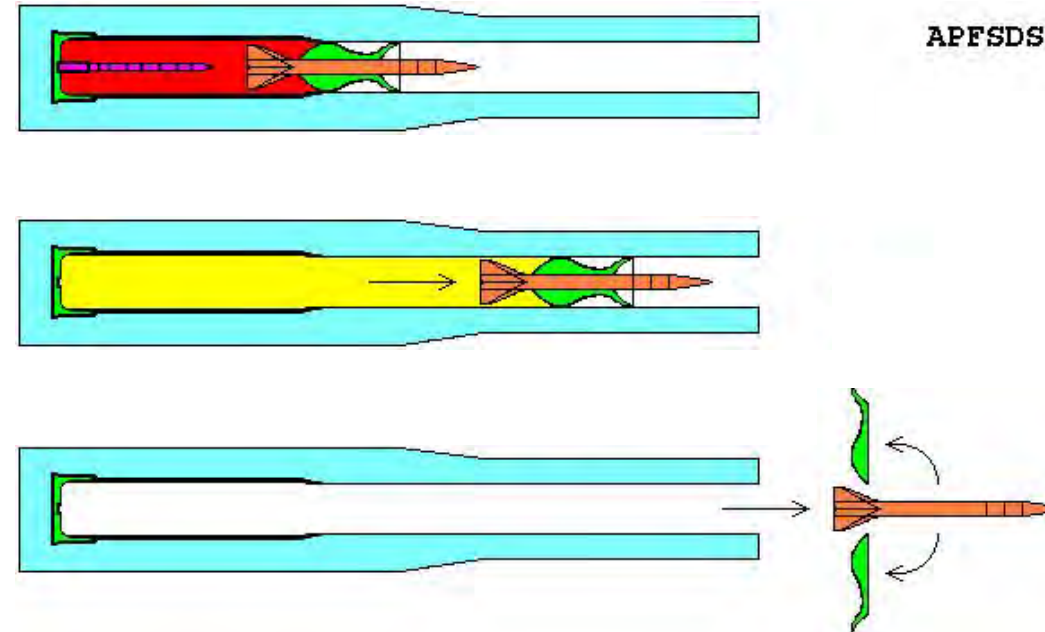
- Guidance of Sub-Caliber Munition

Design Tasks:

- Stability Against Mechanical Loading
- Undisturbed Separation Process
- **Minimum Weight**

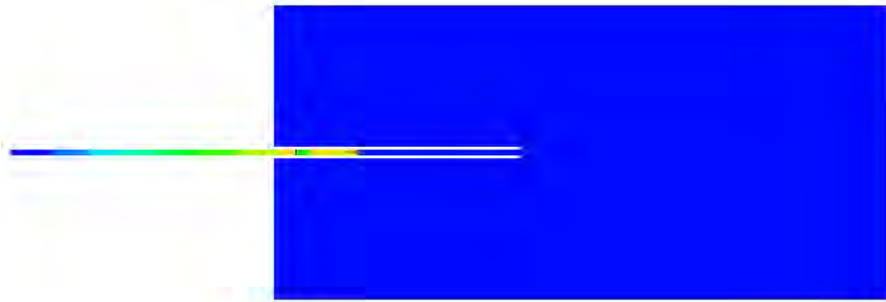
Challenges for the Numerical Simulation:

- Highly Unsteady Problem
- Relatively Moving Bodies
- Material Failure Modelling



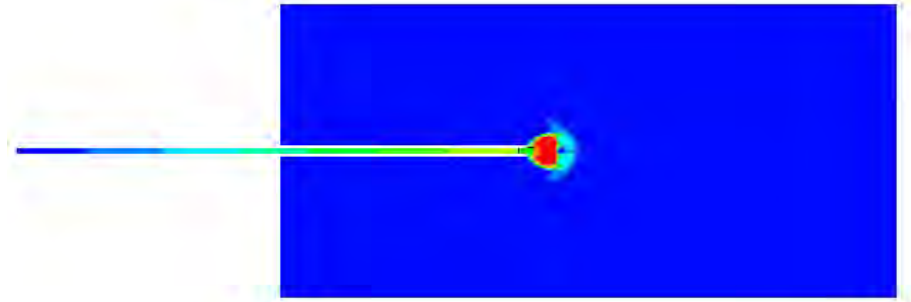
of the Firing Process

ndrical sProjectile%(Autodyn)



Phase 1: Interior Ballistics

- $t_0 < t < t_1$
- Compressed Air Ahead of Projectile
- Interaction: Projectile-Gas-Barrel
- **Not Subject of the Presentation**



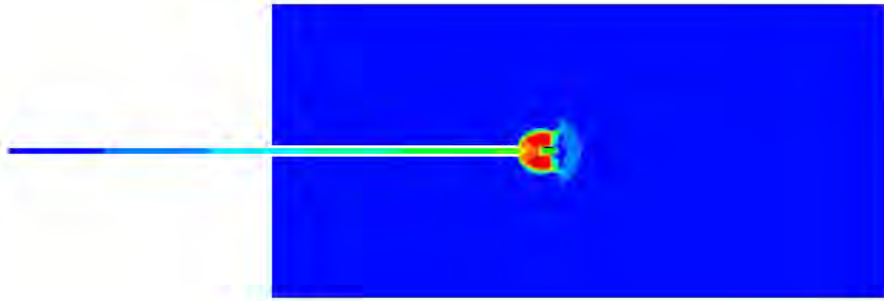
Phase 2: Muzzle Exit Ballistics

- $t_1 < t < t_2$
- Front of Projectile Outside the Muzzle
- Risk of Canting / Fracture

[movie1.avi](#)

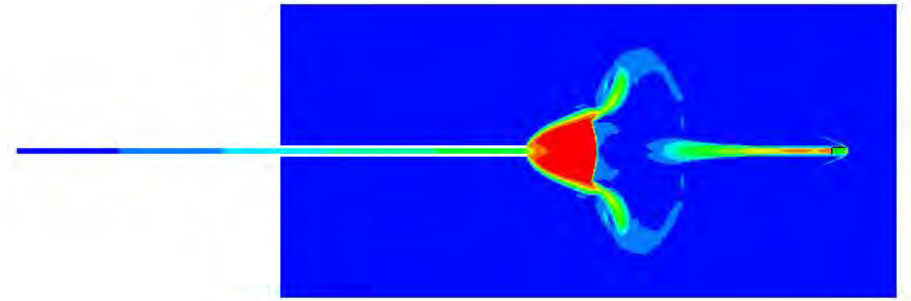
of the Firing Process

ndrical sProjectile% (Autodyn)



Phase 3: Muzzle Exit Ballistics

- $t_2 < t < t_3$
- Projectile Completely Outside the Muzzle
- Significant Incident Flow from Behind

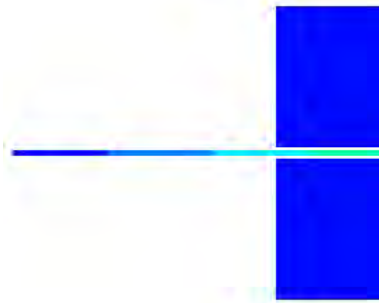


Phase 4: Exterior Ballistics

- $t_3 < t < t_4$
- No Interaction with Propellant Gas / Barrel
- Flight Through Undisturbed Atmosphere

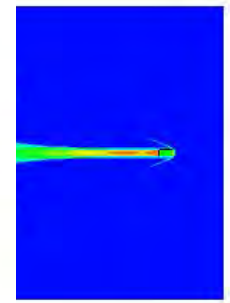
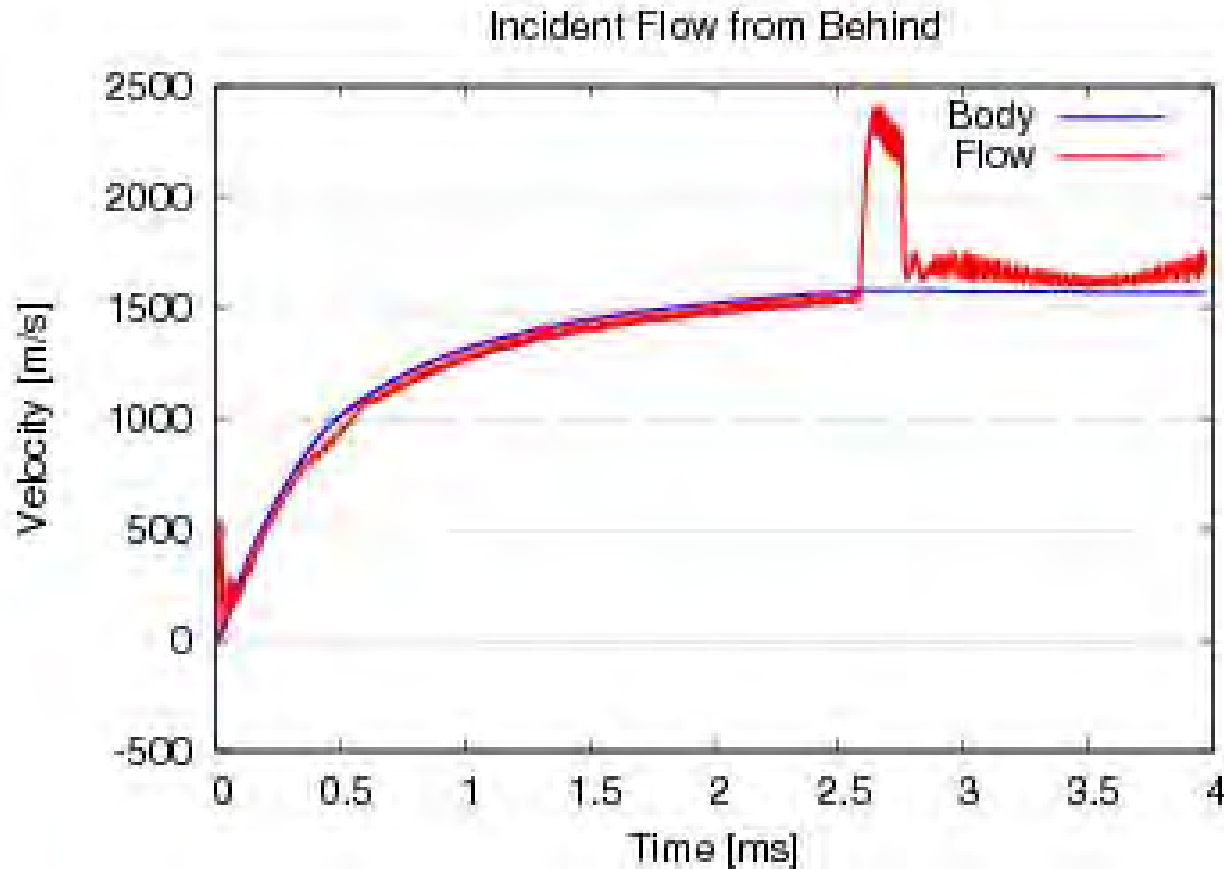
of the Firing Process

ndrical sProjectile%(Autodyn)



Phase 3: Muzzle

- $t_2 < t < t_3$
- Projectile Comp
- Significant Incic

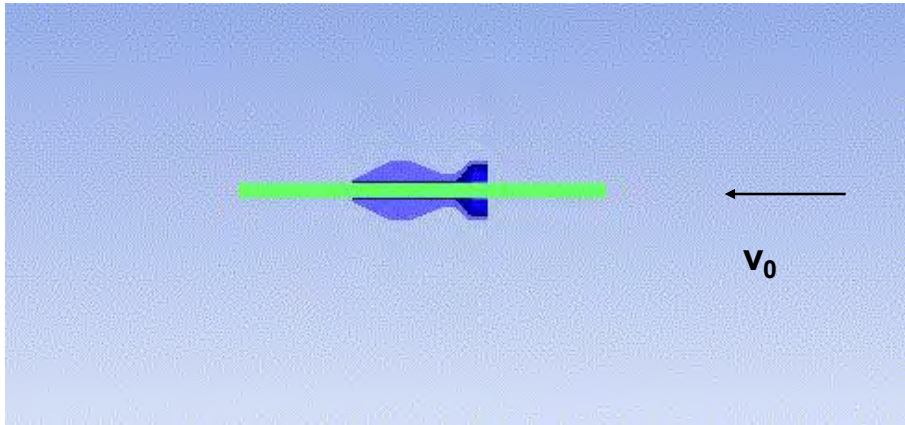


ics

ellant

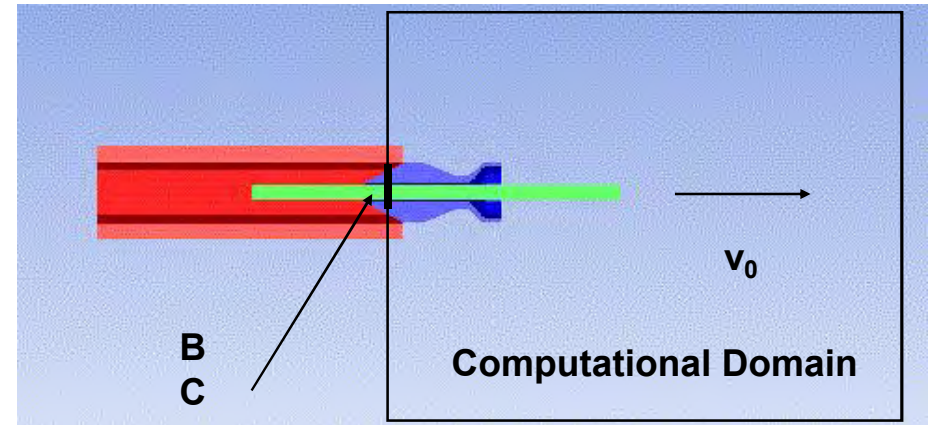
ed Atmosphere

Numerical Simulation



Concept A

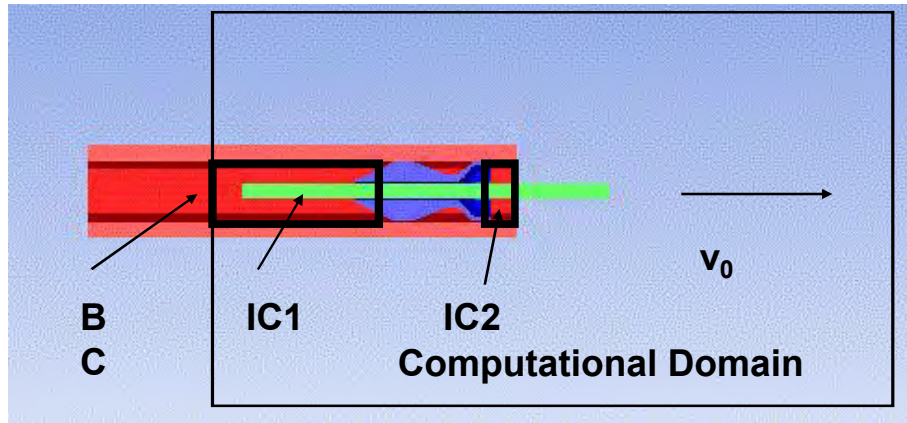
- Moving Observer
- Instantaneous Inflow



Concept B

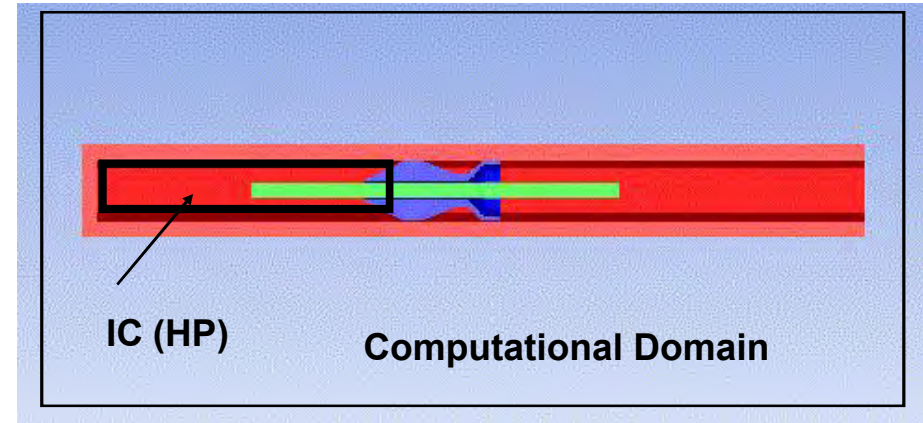
- Earth-Fixed Observer
- Boundary Condition at Muzzle Exit

Numerical Simulation



Concept C

- Earth-Fixed Observer
- Initial and Boundary Conditions Inside the Barrel

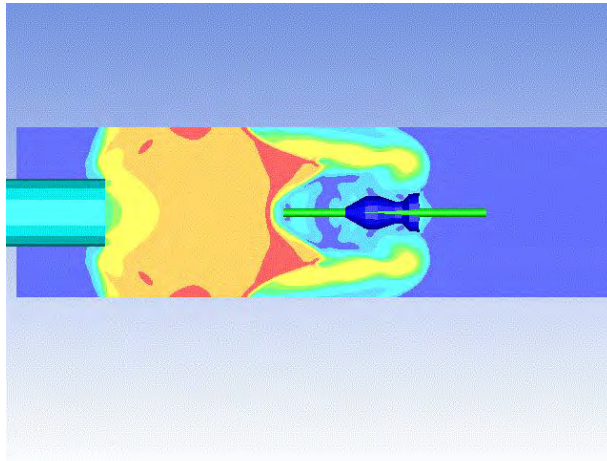


Concept D

- Earth-Fixed Observer
- Initial Condition Inside the Barrel (High Pressure)
- **Estimation of Required Gridpoints**
~ 90.000.000 → Very Expensive

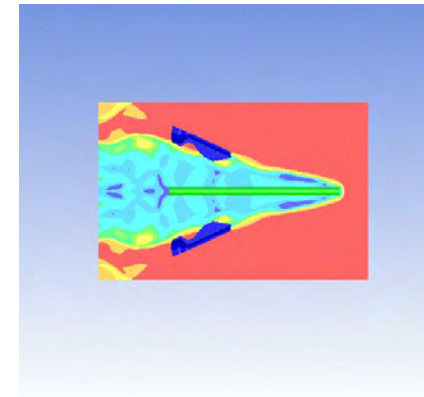
Pre for the Study

pts A und C)



Phase 1:

Earth-Fixed Observer (Concept C)



Phase 2:

Moving Observer (Concept A)



Switch of Coordinate System!

Point of Time: $t = t_3$

Separation Simulations

Coordinate Switch (Sim. EMI, Concept C+A)

Discretization: Air (1.000.000 Points), Sabot (3.900 Points)



Pressure

t = 0.00 ms



Abs. Velocity

Separation Simulations

Coordinate Switch (Sim. EMI, Concept C+A)

Discretization: Air (1.000.000 Points), Sabot (3.900 Points)



Pressure

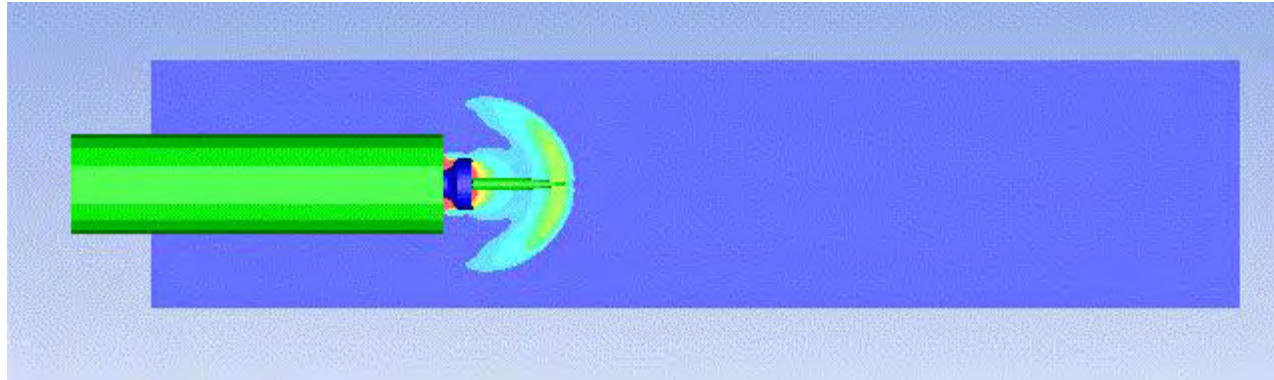
t = 0.00 ms



Abs. Velocity

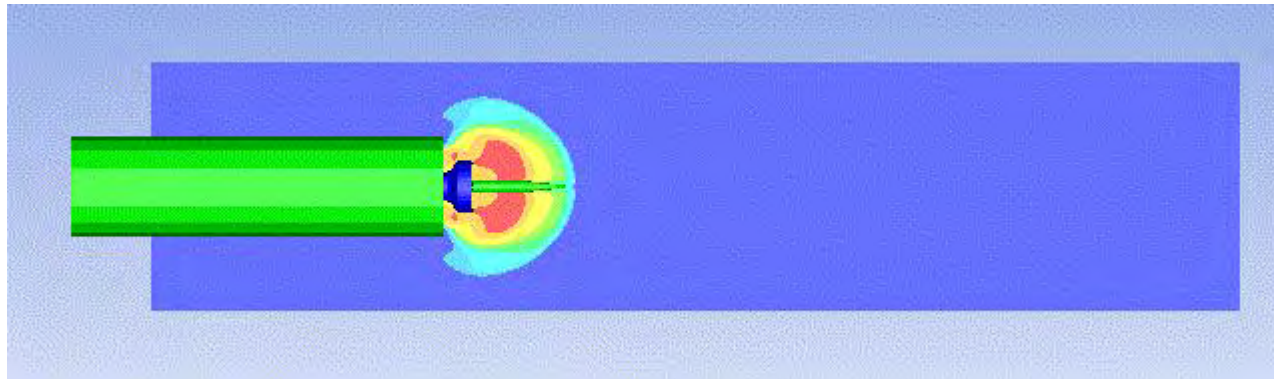
Separation Simulations

Coordinate Switch (Sim. EMI, Concept C+A)



Pressure

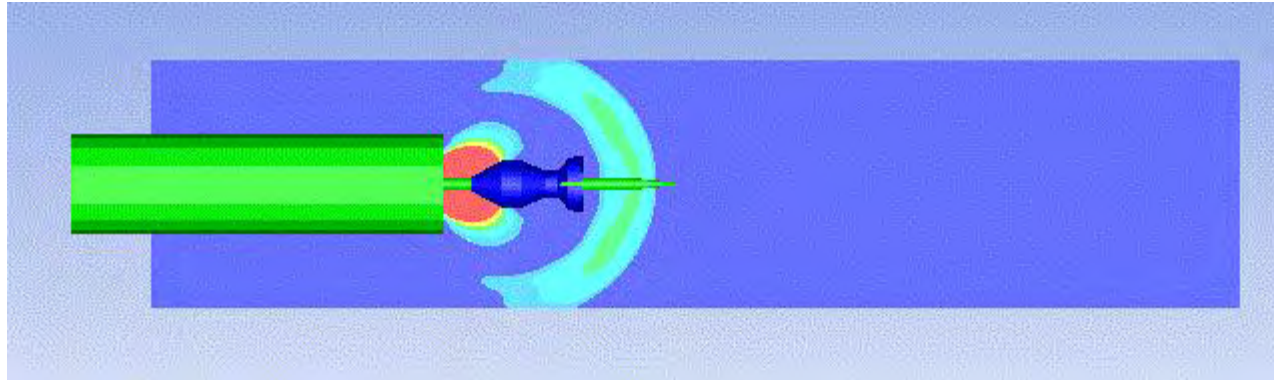
$t = 0.06 \text{ ms}$



Abs. Velocity

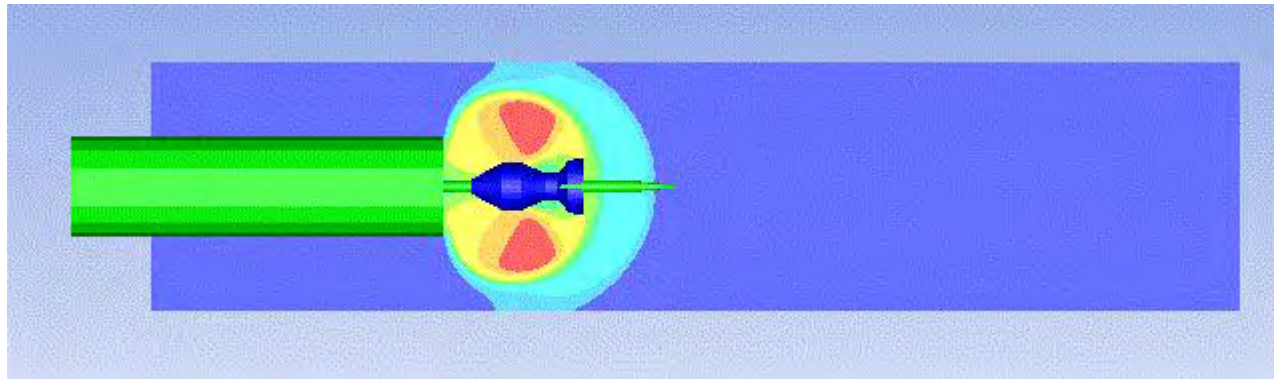
Separation Simulations

Coordinate Switch (Sim. EMI, Concept C+A)



Pressure

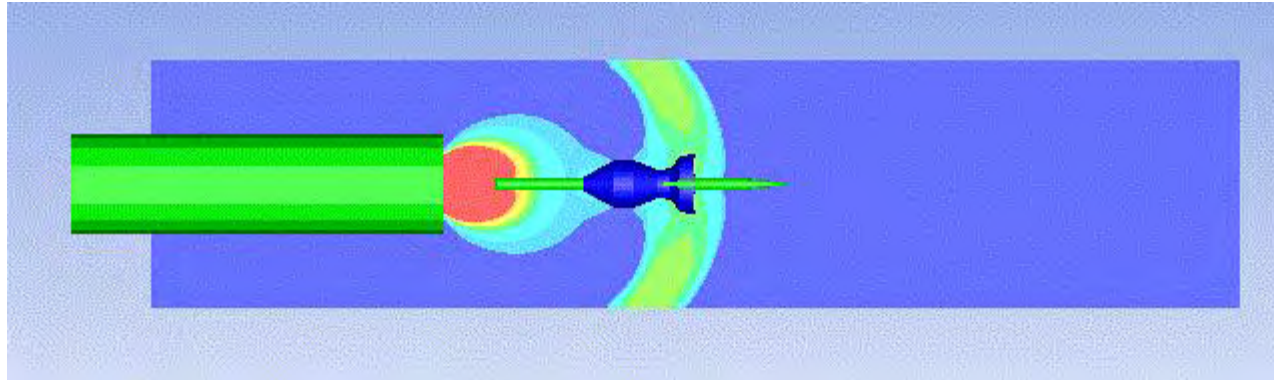
$t = 0.12$ ms



Abs. Velocity

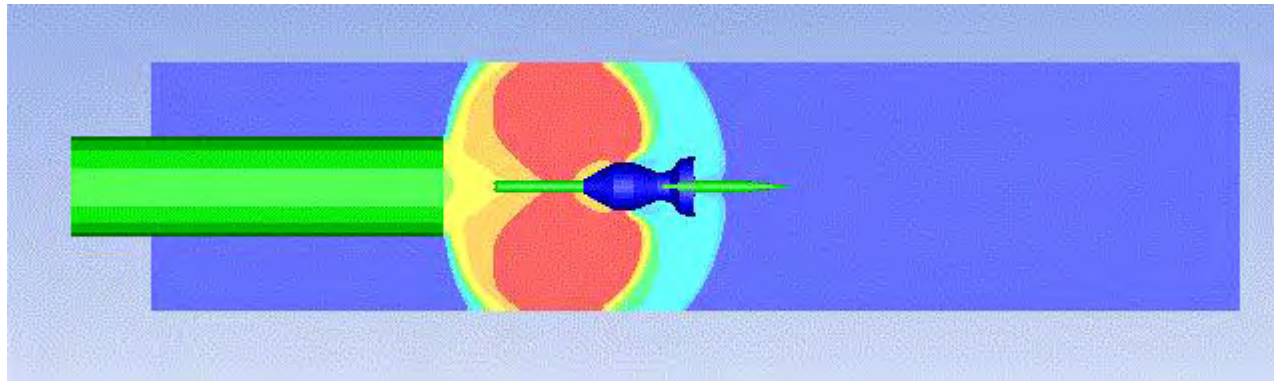
Separation Simulations

Coordinate Switch (Sim. EMI, Concept C+A)



Pressure

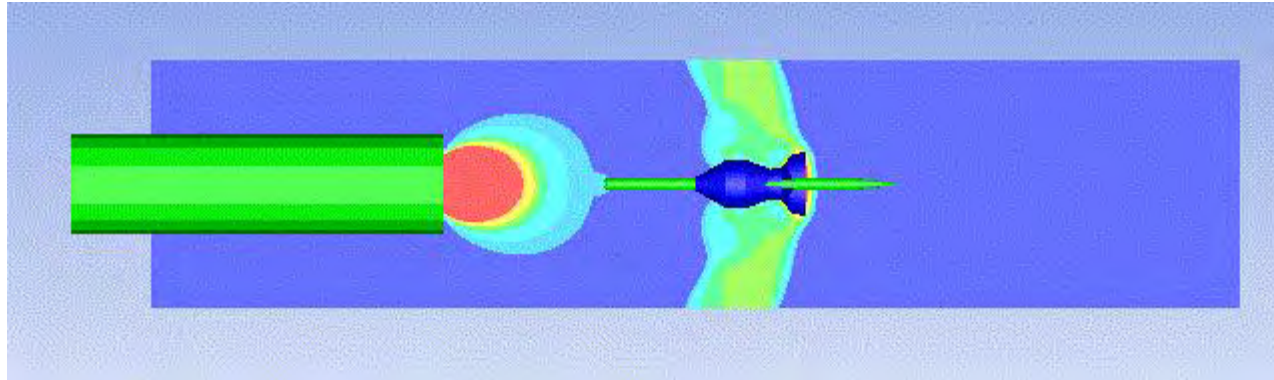
$t = 0.18 \text{ ms}$



Abs. Velocity

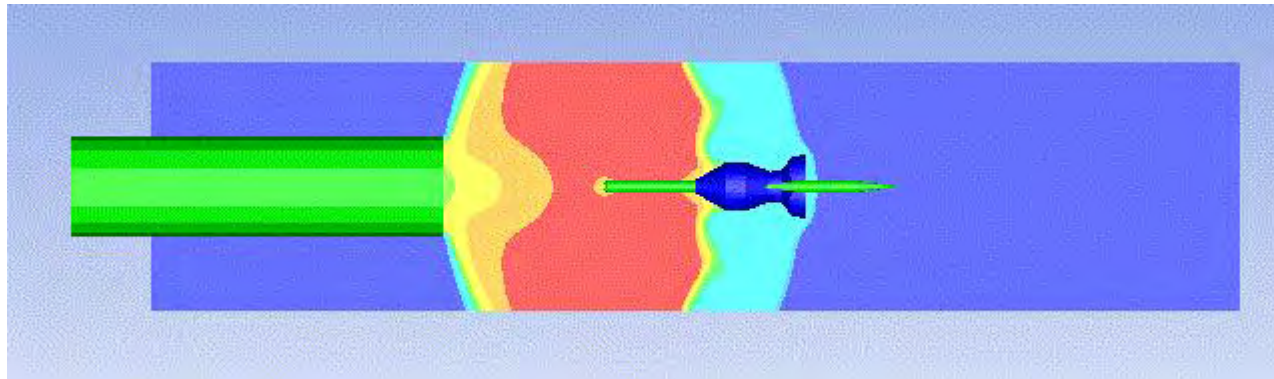
Separation Simulations

Coordinate Switch (Sim. EMI, Concept C+A)



Pressure

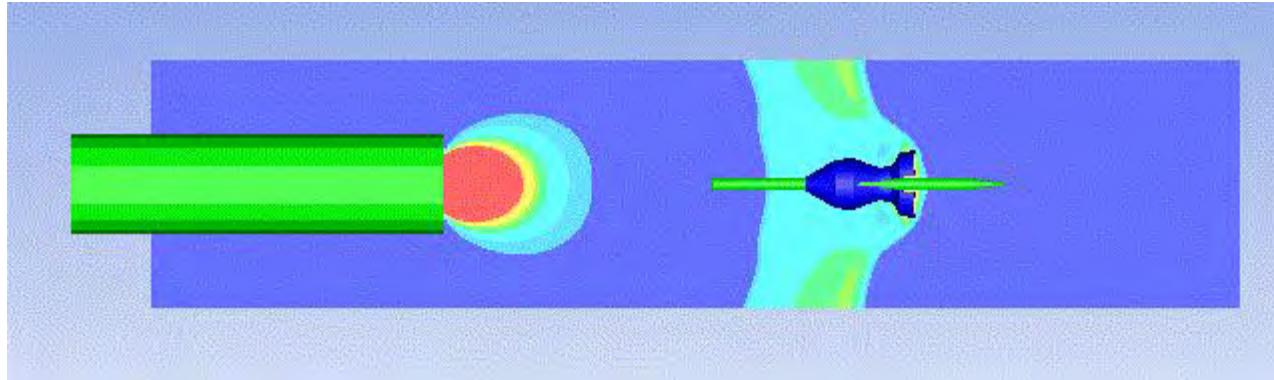
t = 0.23 ms



Abs. Velocity

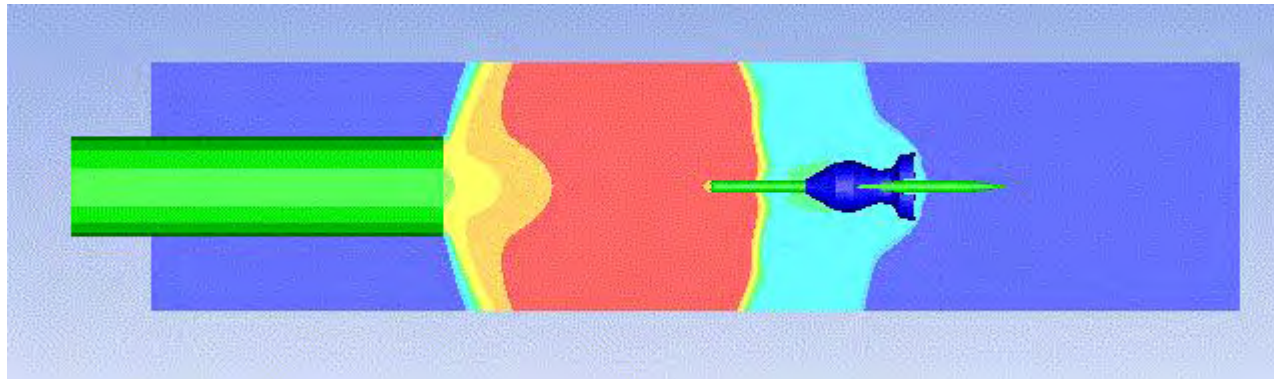
Separation Simulations

Coordinate Switch (Sim. EMI, Concept C+A)



Pressure

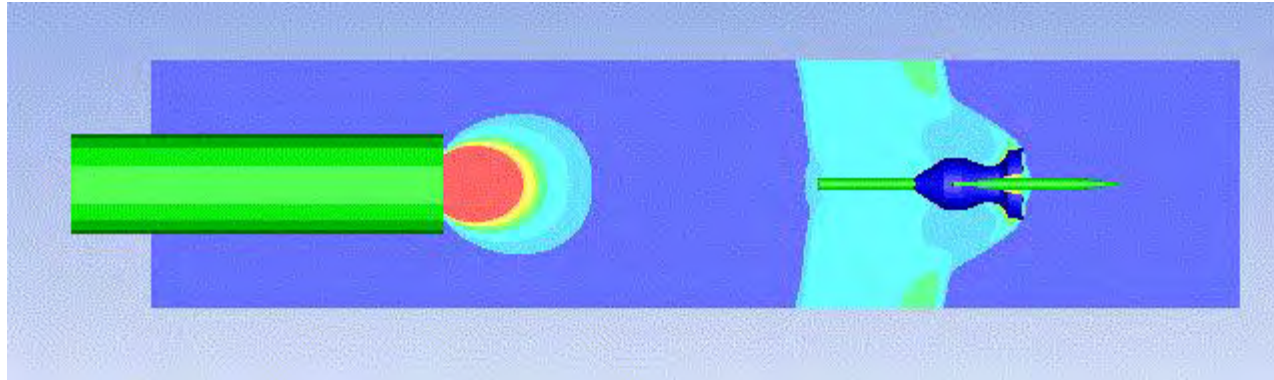
$t = 0.29 \text{ ms}$



Abs. Velocity

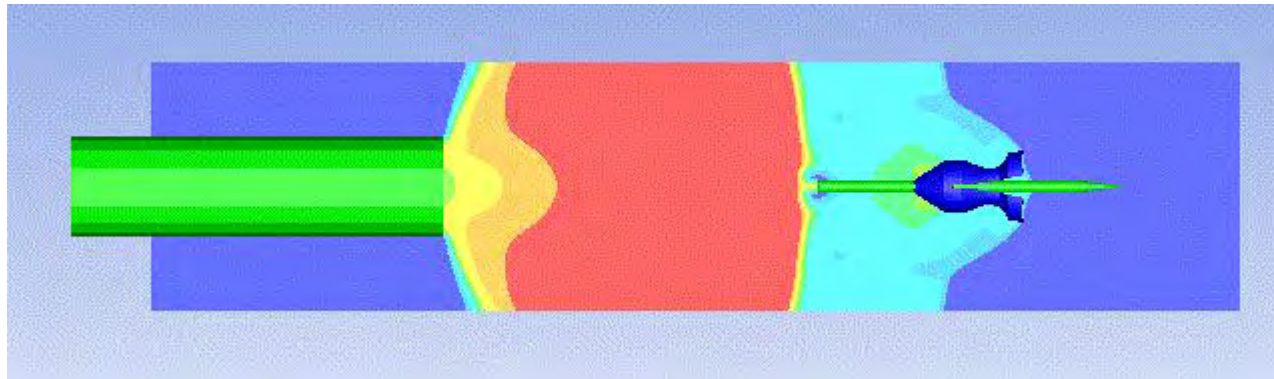
Separation Simulations

Coordinate Switch (Sim. EMI, Concept C+A)



Pressure

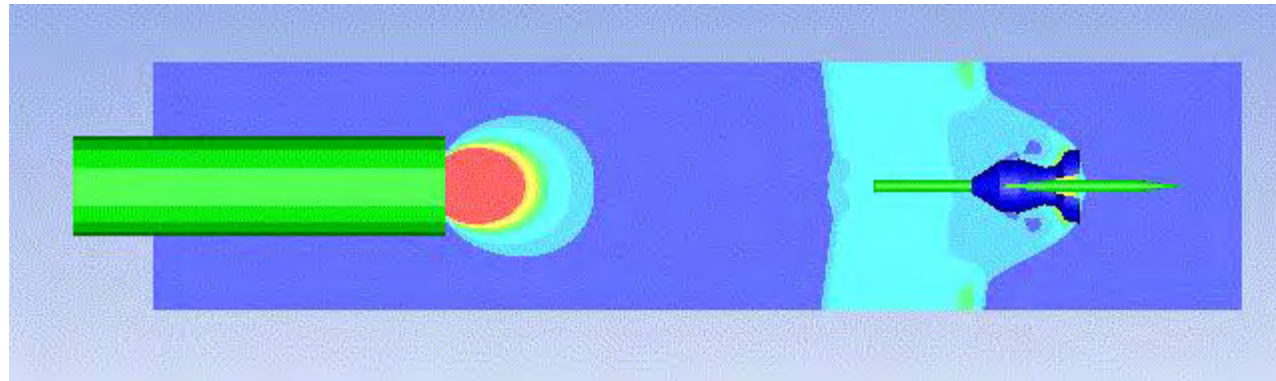
$t = 0.35 \text{ ms}$



Abs. Velocity

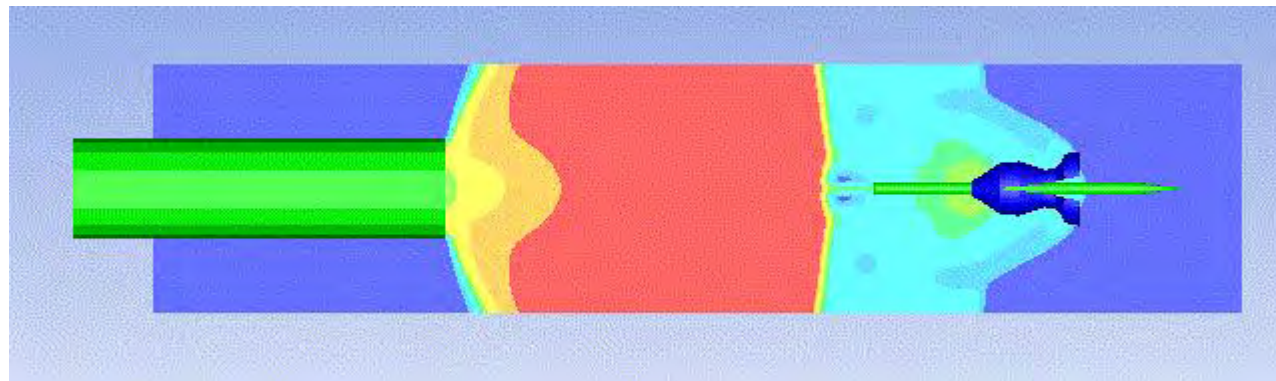
Separation Simulations

Coordinate Switch (Sim. EMI, Concept C+A)



Pressure

t = 0.38 ms

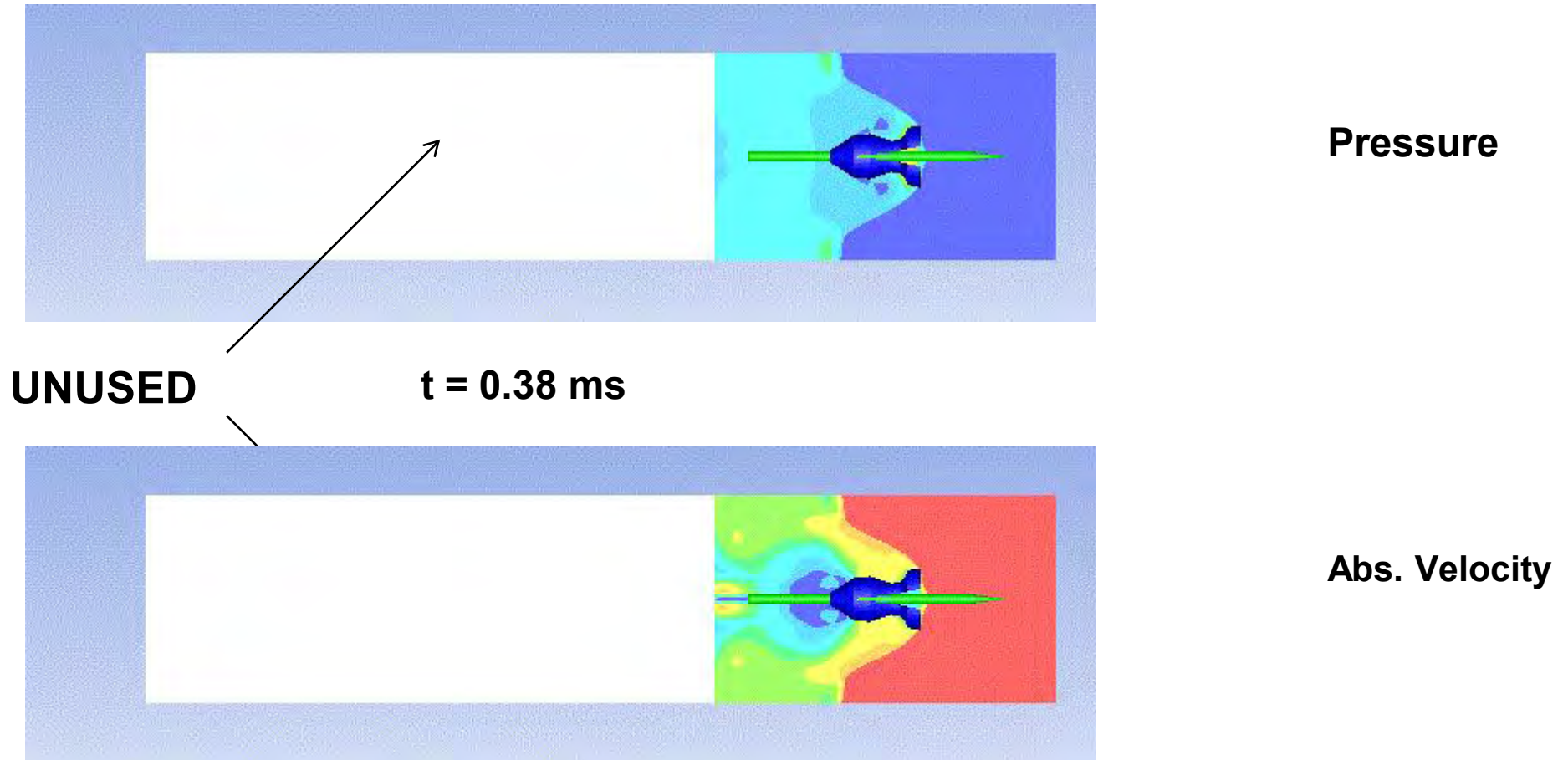


Abs. Velocity

Separation Simulations

Coordinate Switch (Sim. EMI, Concept C+A)

SWITCH



Separation Simulations

Coordinate Switch (Sim. EMI, Concept C+A)



Pressure

$t = 0.71 \text{ ms}$



Abs. Velocity

Separation Simulations

Coordinate Switch (Sim. EMI, Concept C+A)



Pressure

t = 1.05 ms



Abs. Velocity

Separation Simulations

Coordinate Switch (Sim. EMI, Concept C+A)



Pressure

t = 1.39 ms



Abs. Velocity

Experimental Results (ISL)

Penetrator: 10 mm Caliber, 240 mm Length

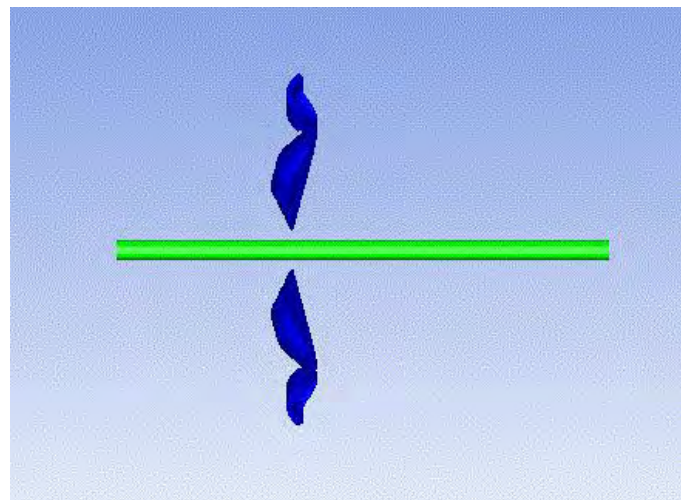
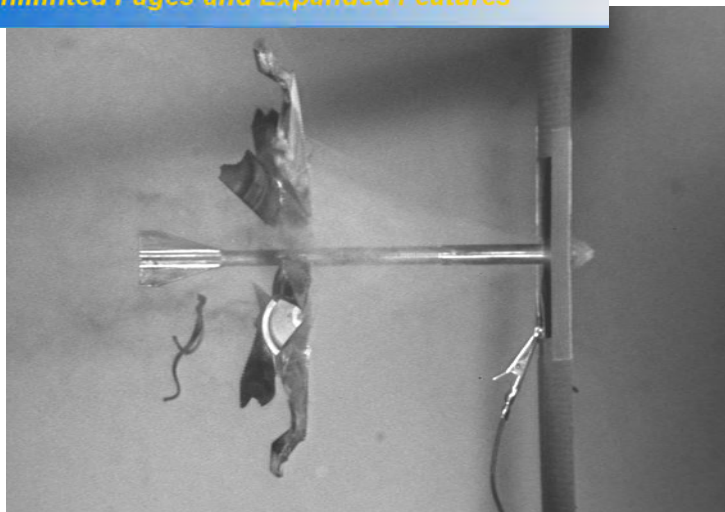
Sabot: 40 mm Caliber, Magnesium (Magnesium Alloys)

4 Parts → Two-Plane Symmetry

Parameter	Condition A [Schirm, ISL, 2005]	Condition B [Schirm, ISL, 2008]
Material Density Sabot	1.78 g/cm ³ (Mg)	1.52 g/cm ³ (Mg Al3 Li9)
Propellant Mass	0.38 kg	0.40 kg
Maximum Gas Pressure	341.2 MPa	380.3 MPa
Muzzle Velocity	1510 m/s	1633 m/s
Acceleration	794008 m/s ²	897000 m/s ²

Separation Simulations

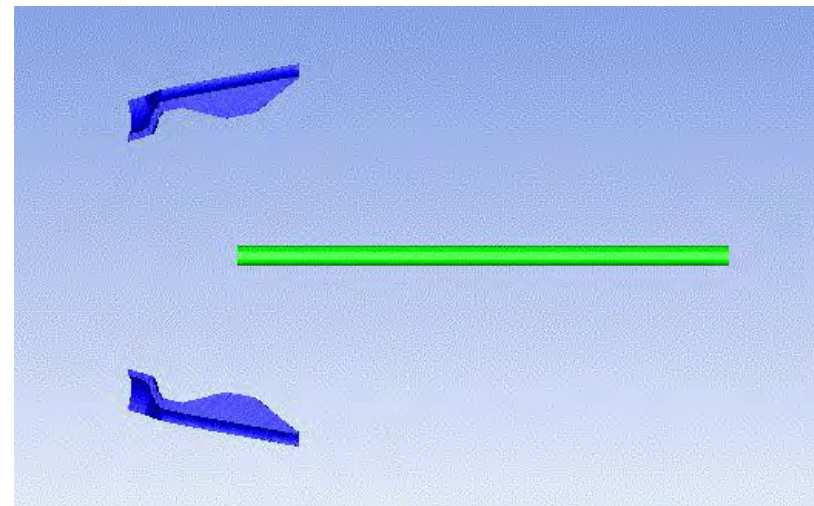
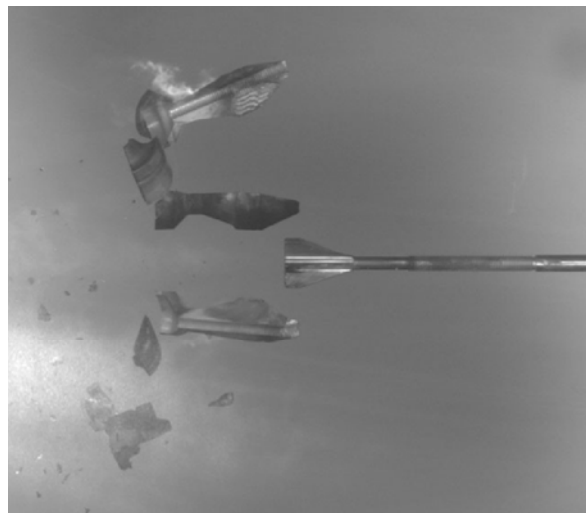
n: Exp. (ISL) / Sim. (EMI, Condition B)



2.0m Behind
Muzzle Exit

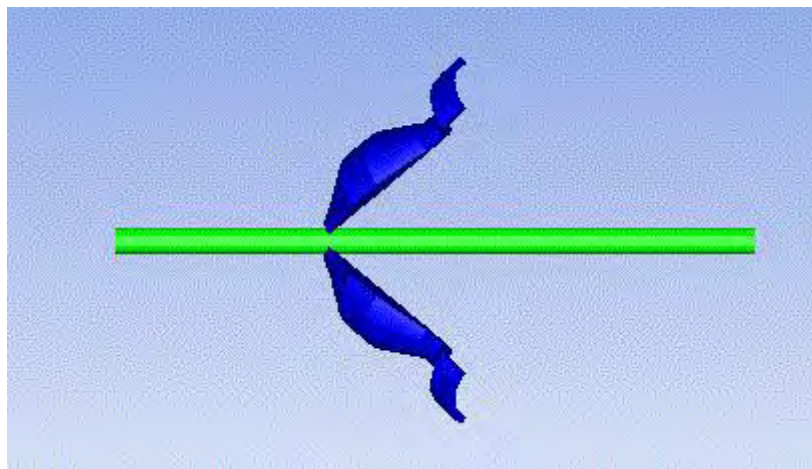
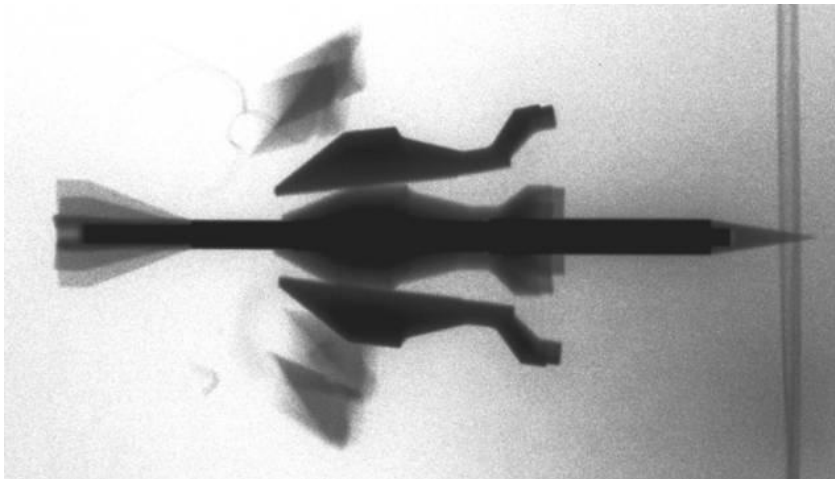
3.25m Behind
Muzzle Exit

Experiment (ISL)



Separation Simulations

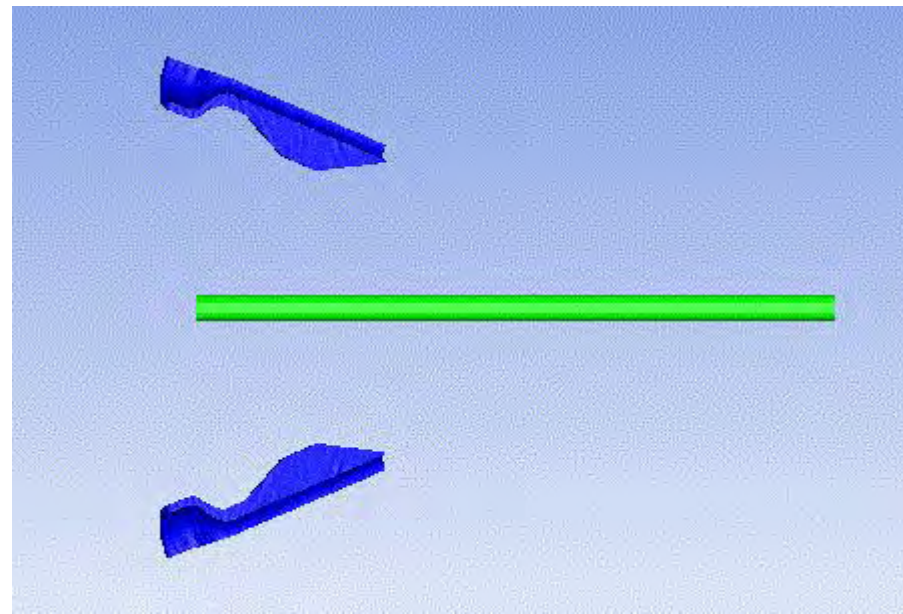
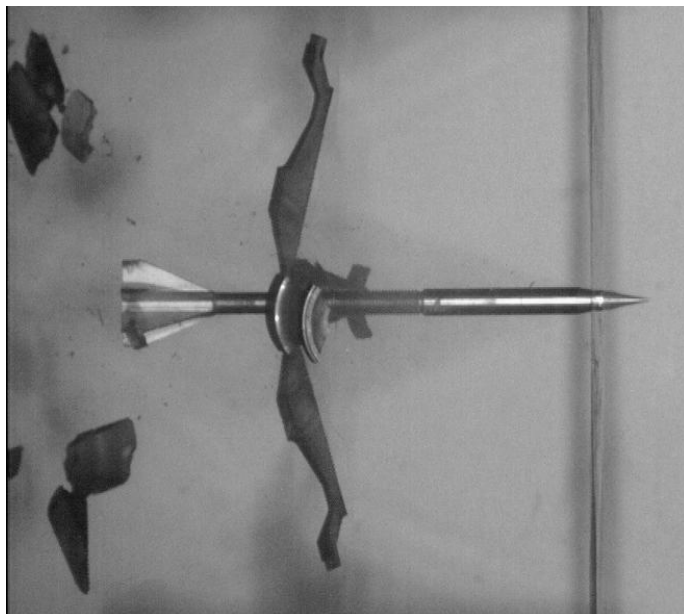
n: Exp. (ISL) / Sim. (EMI, Condition A)



1.8m Behind
Muzzle Exit

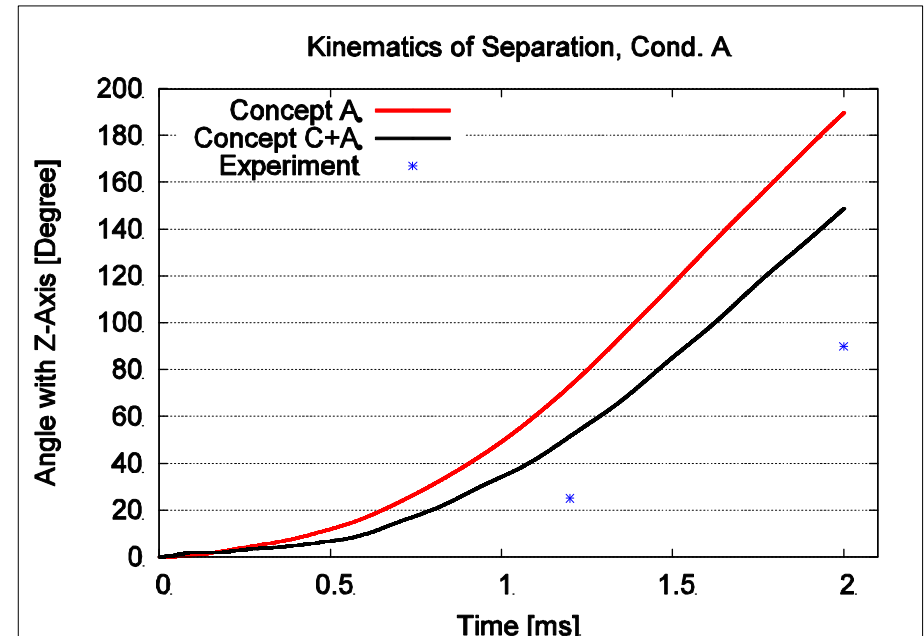
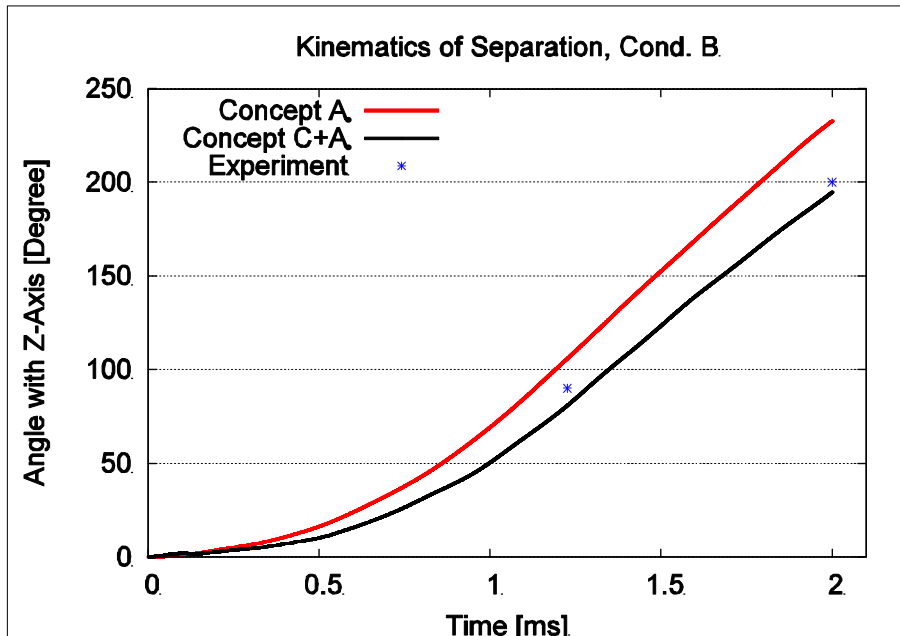
3.0m Behind
Muzzle Exit

Experiment (ISL)



Separation Simulations

Kinematics of Separation (Different Strategies)



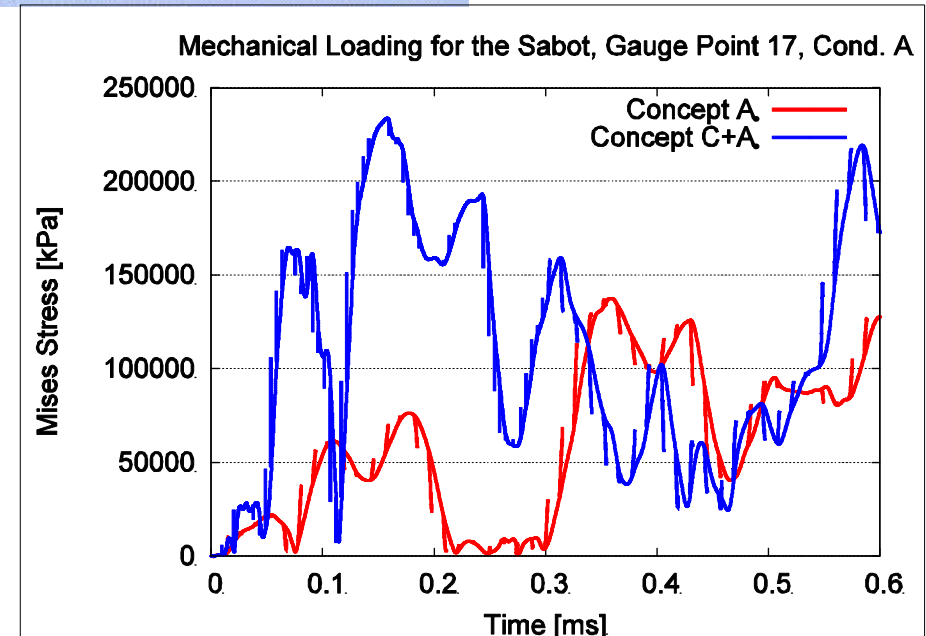
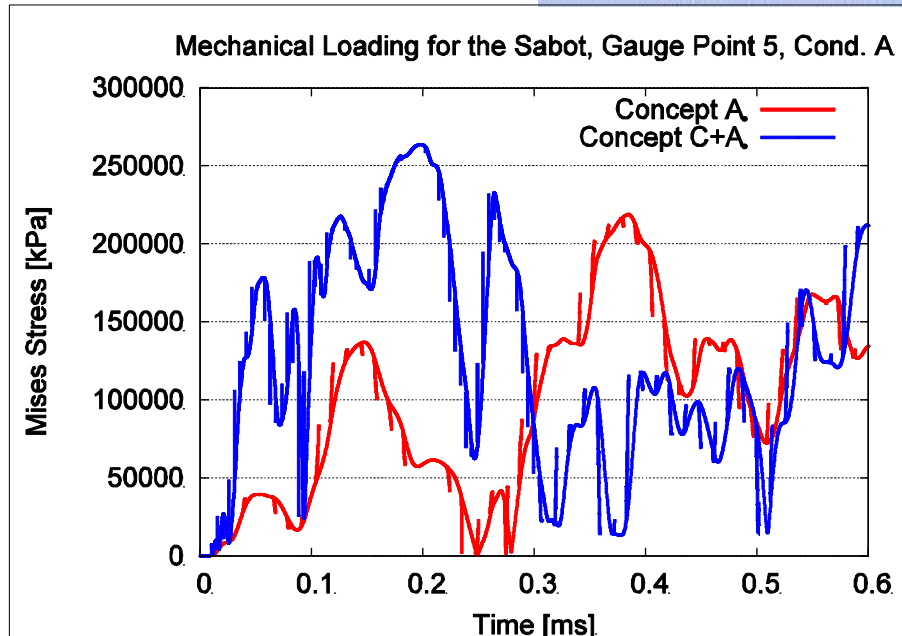
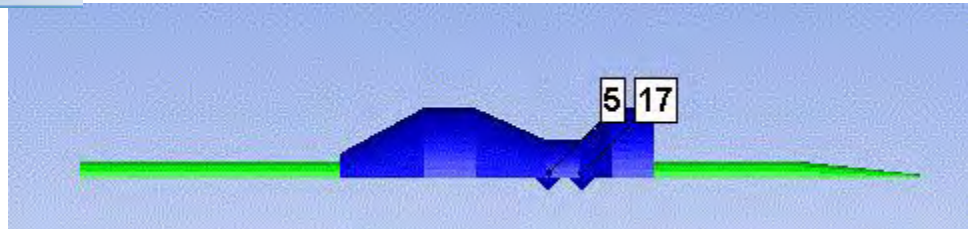
Effects of Muzzle Exit have to be Considered (Both Conditions)

Problem of Numerical Capturing (Tracking) of the Penetrator Nose (Geom. Singularity)

Additional Uncertainties in the Experiments

Separation Simulations

for the Structure (Different Strategies)



Effects of Muzzle Exit Result in Significantly Higher Structure Loads

[movie2.avi](#)

- **Numerical Simulations for Sabot Separation Processes with Different Approaches**
- **Ability for Simulation of Muzzle Exit- and Exterior Ballistics by Coordinate Switching**
- **Future Work:**
 - **Numerical Investigation of Effects of Experimental Uncertainties (Mass, Geometry, Muzzle Exit Velocity / Angle of Attack)**
 - **Influence of the Penetrator Nose / Fins**
 - **Sabot Design Optimization**
 - **„Loading History“ for Separated Structural Calculations**

Funded by: Bundeswehr Research Institute for Materials, Explosives, Fuels and Lubricants

Assessment of potential blunt trauma under ballistic helmets

Celia Watson, φAnnette Webb, Ian Horsfall

Impact and Armour Group, Cranfield University Shrivenham, UK.

φ Land Engineering Agency, Australian Department of Defence,
Melbourne, Australia

c.h.watson@cranfield.ac.uk



Aims:

To investigate force measurement techniques

Measure head contact loads from non-penetrating ballistic impact on helmets.

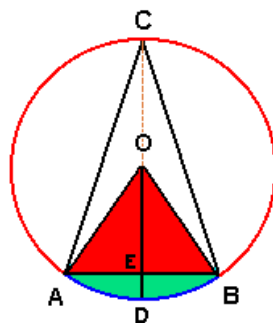
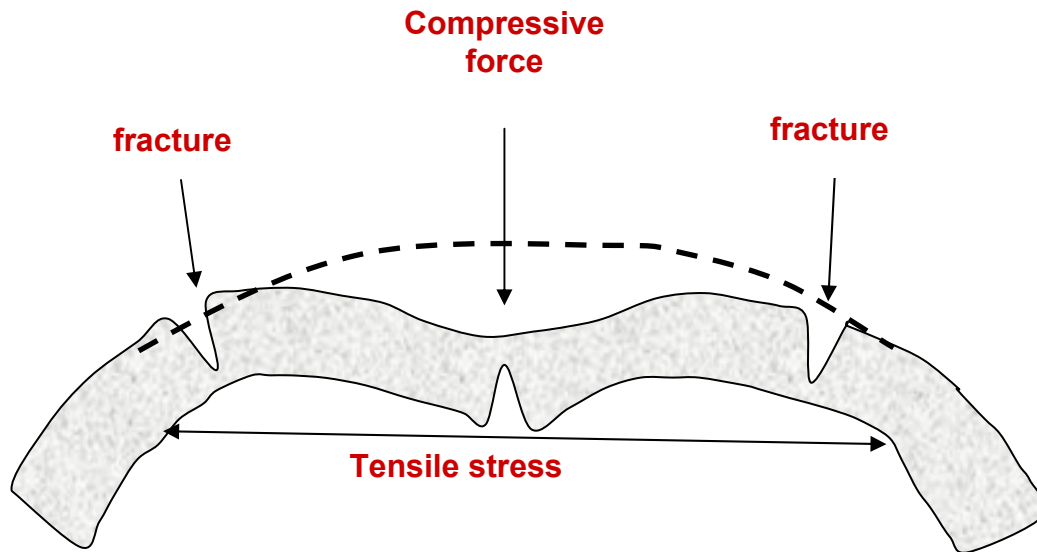
Use the force information to develop a simple method of force measurement for helmet testing.



Forensic analysis

Wilber related the size and shape of fracture damage

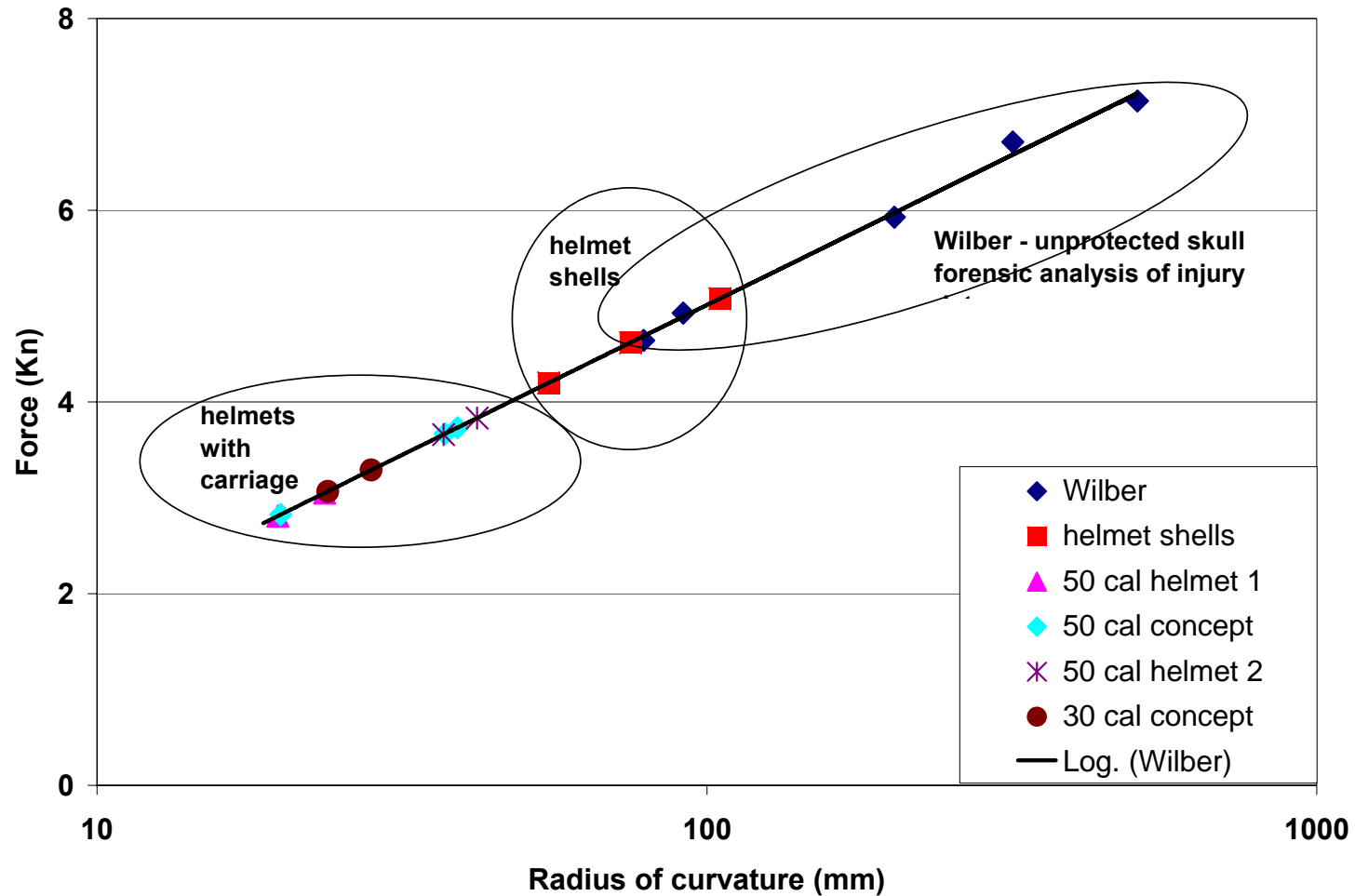
To the radius of curvature of the impacting weapon.

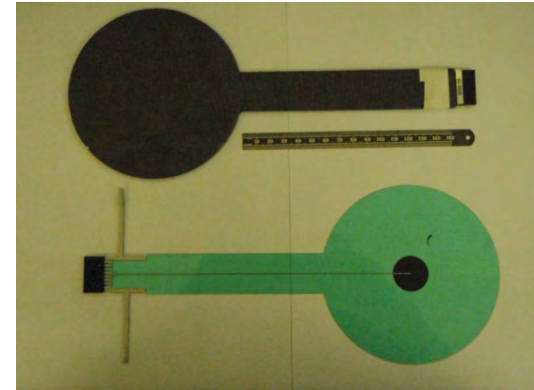
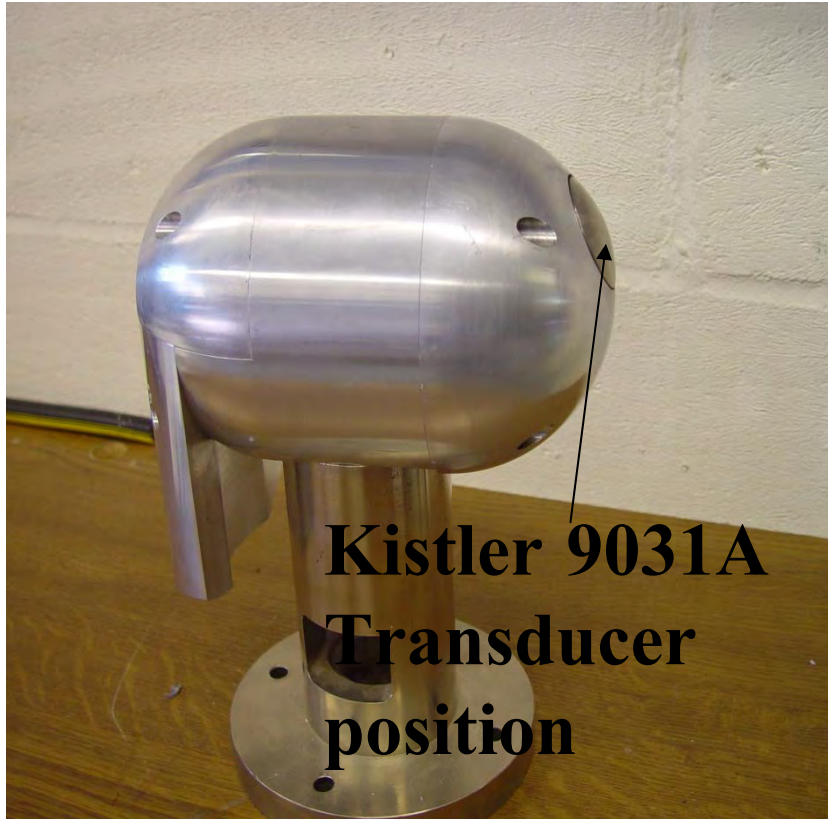


intersecting chord theorem



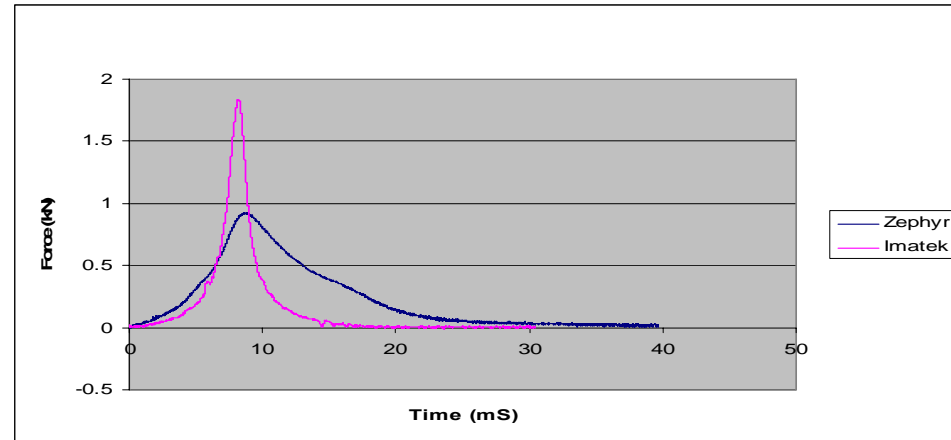
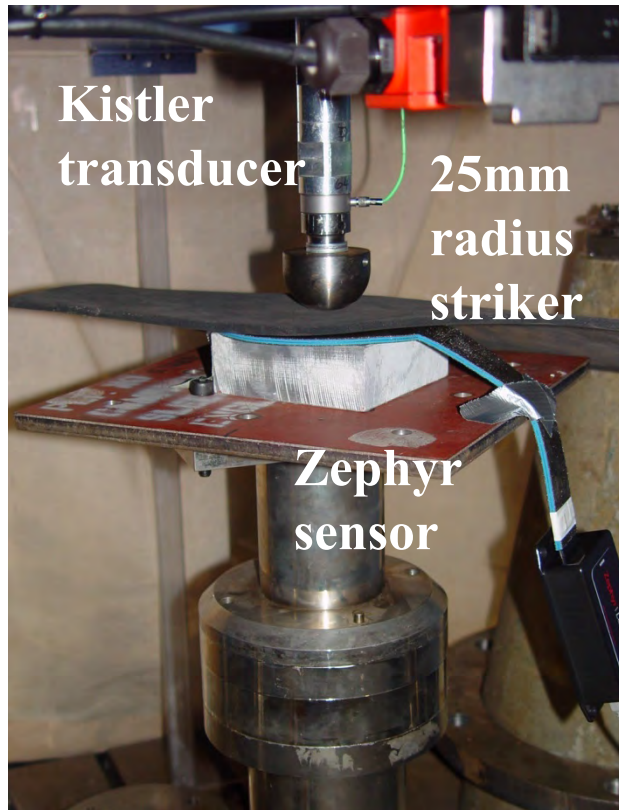
Force vs Radius of Curvature for Skull Fractures



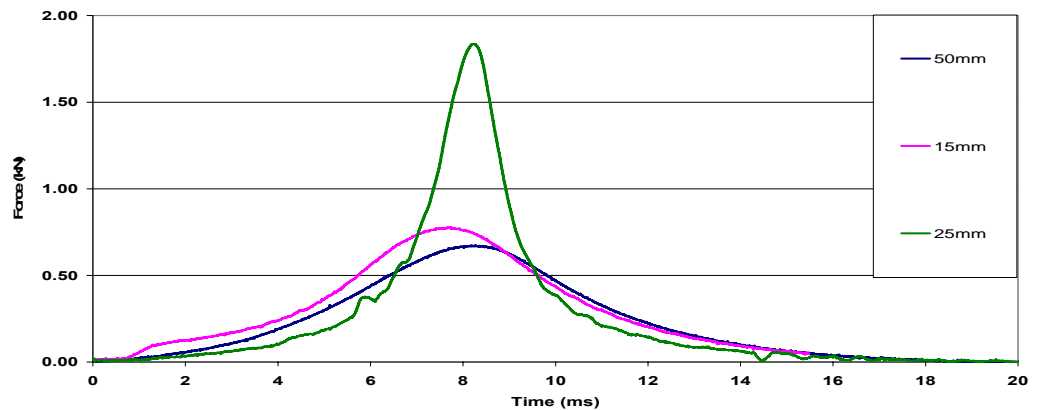


**Zephyr® film
sensor pads**



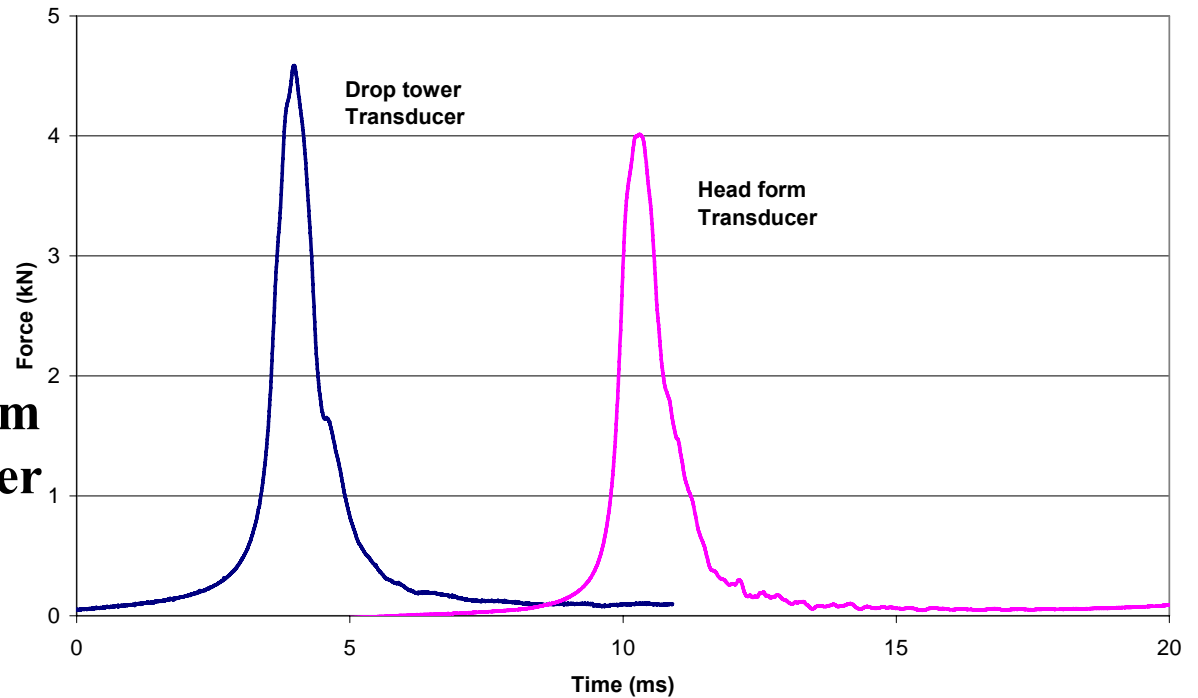
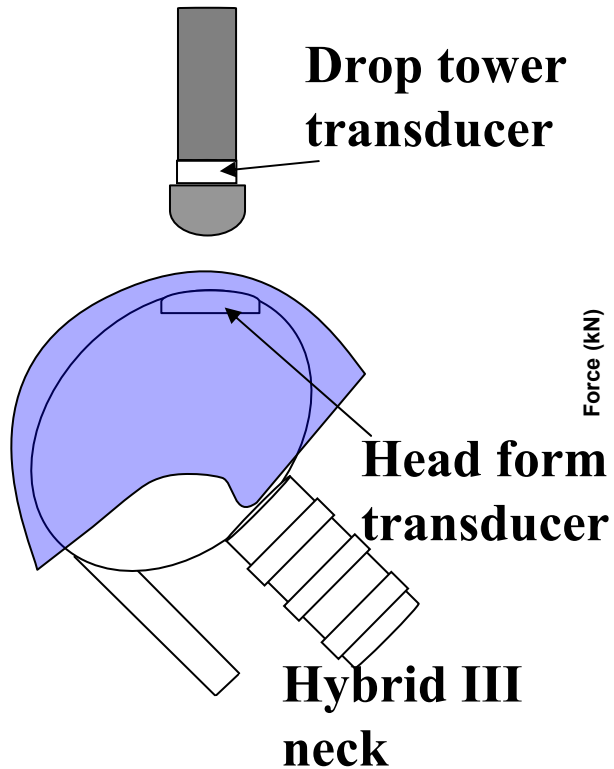


Force output from 9031A Kistler® load cell compared with Zephyr® sensors



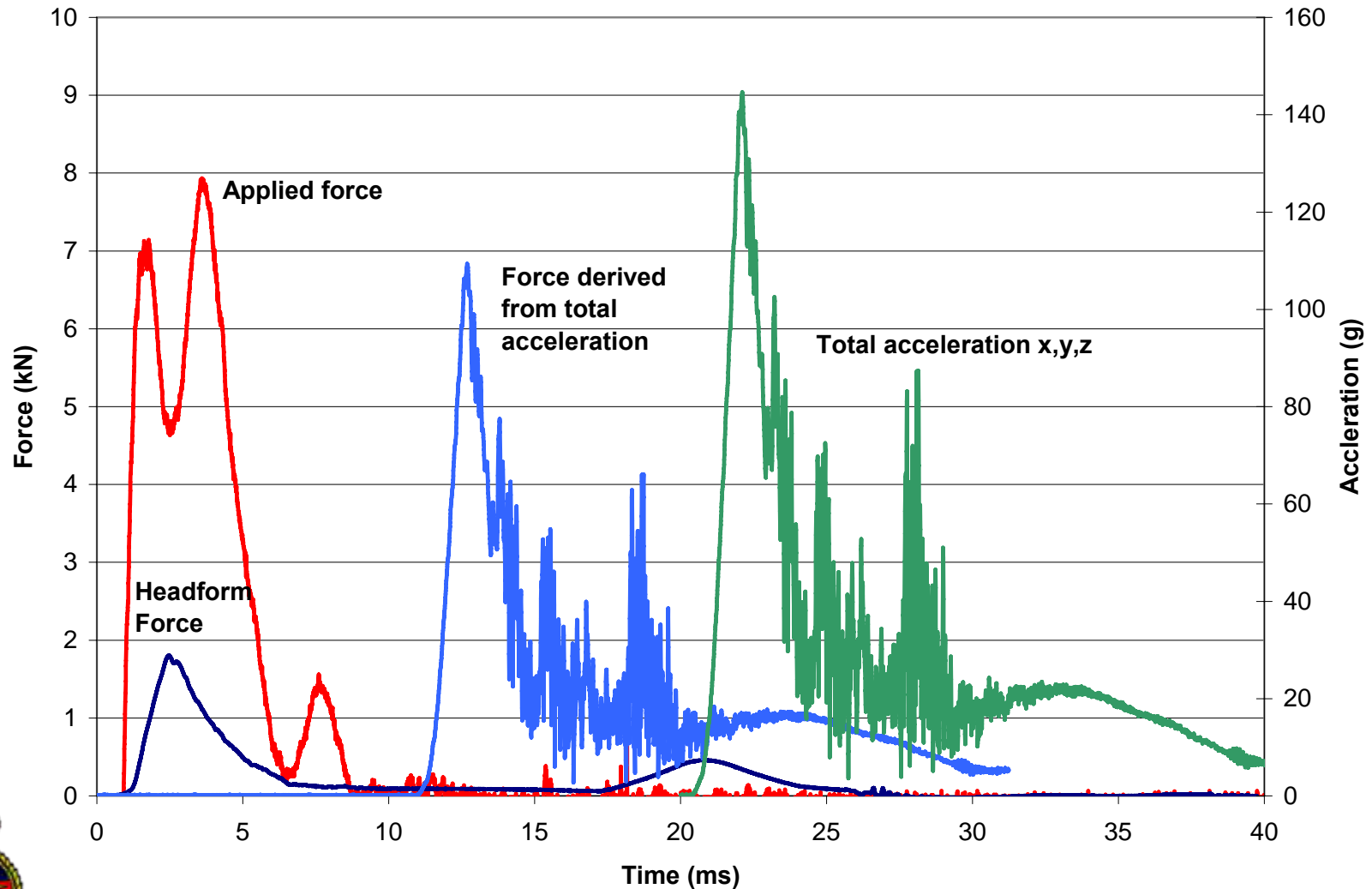
Effect of radius of different strikers





Force vs time - comparison of
transducer outputs





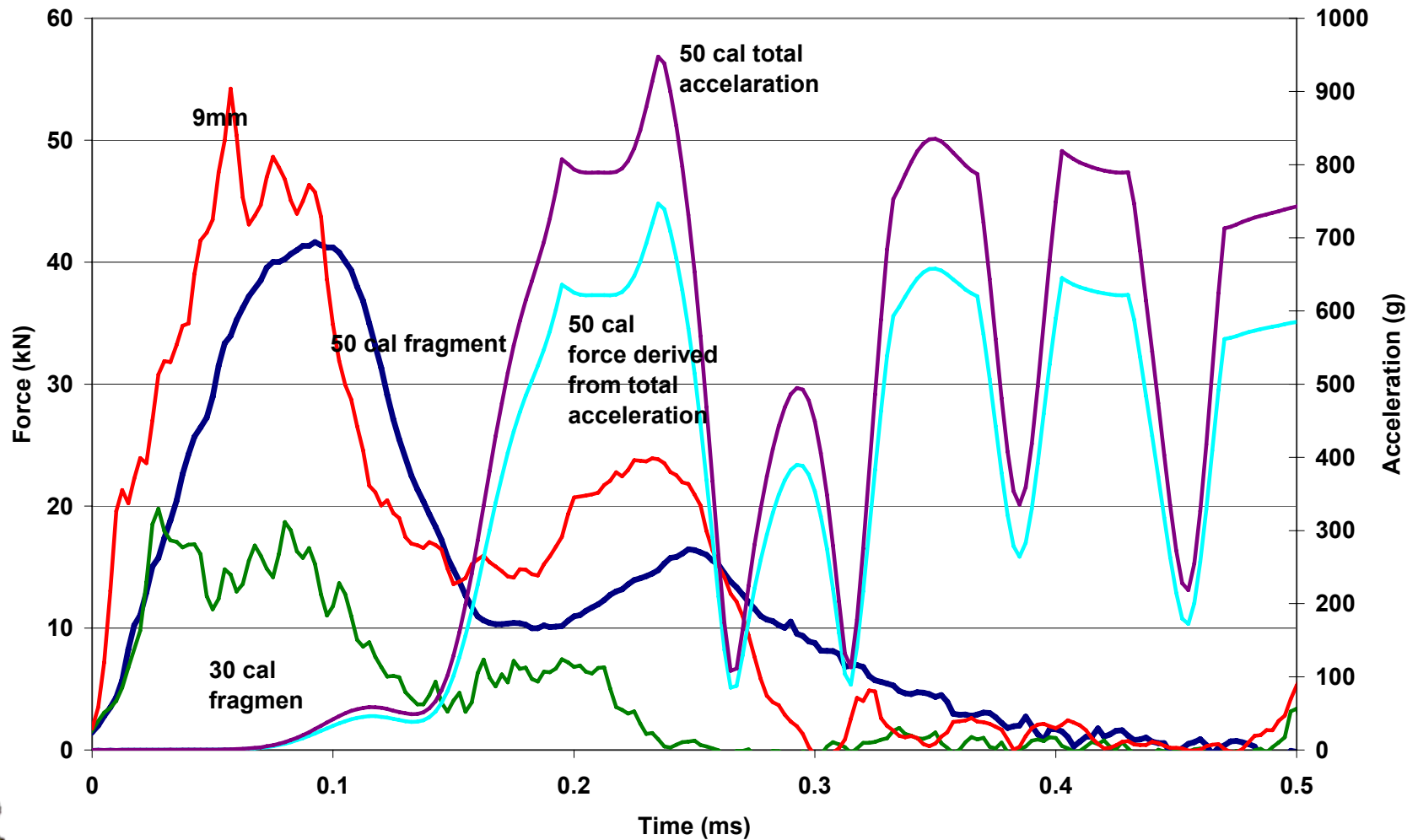


Shots loaded the centre of
Film sensors

No standoff other than the
mitigation allowed by the
carriage system

Kevlar helmet shell with carriage system
showing position of Zephyr sensor on
Aluminium head form and Hybrid III neck.





9mm impact on helmet

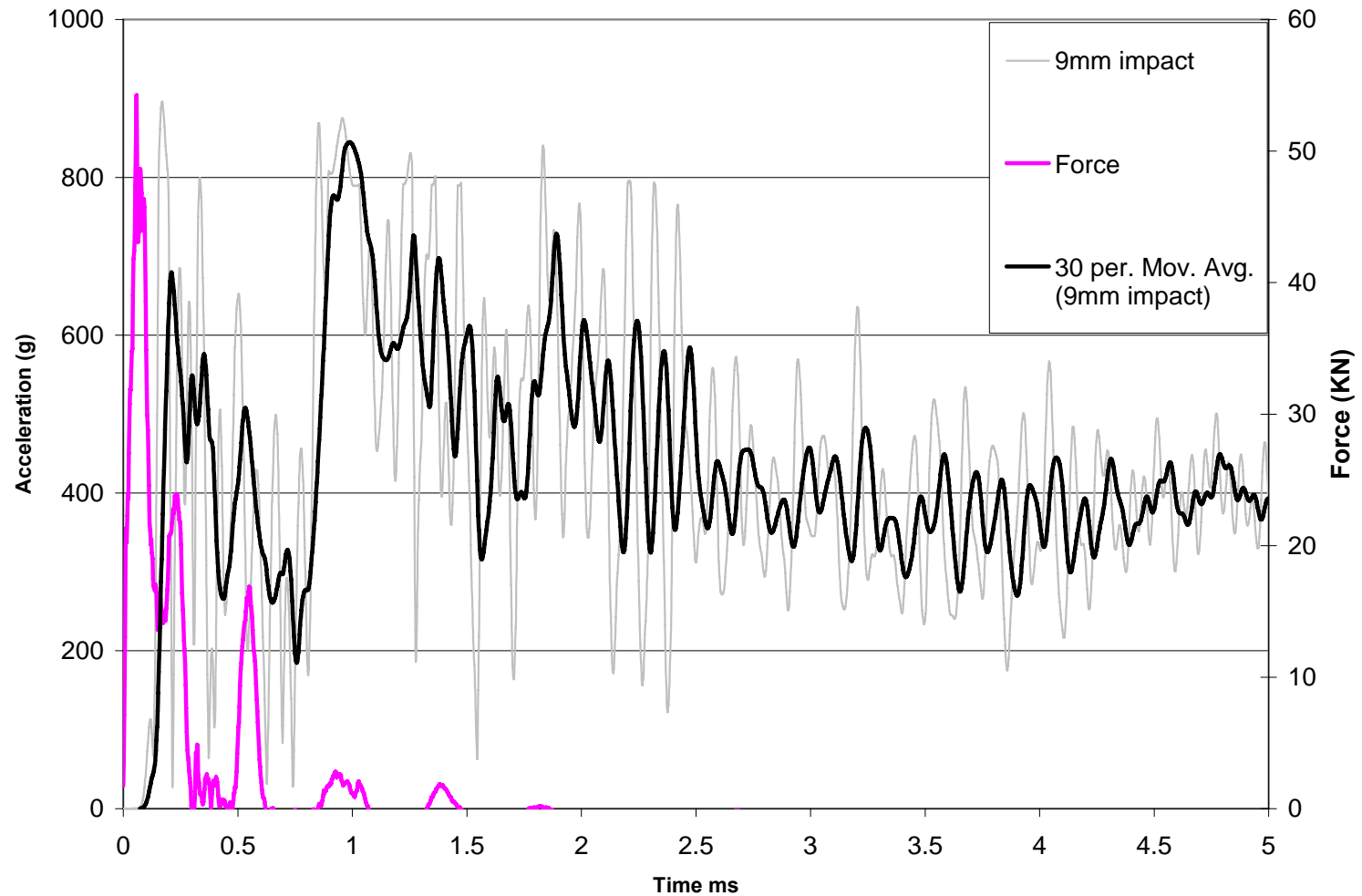


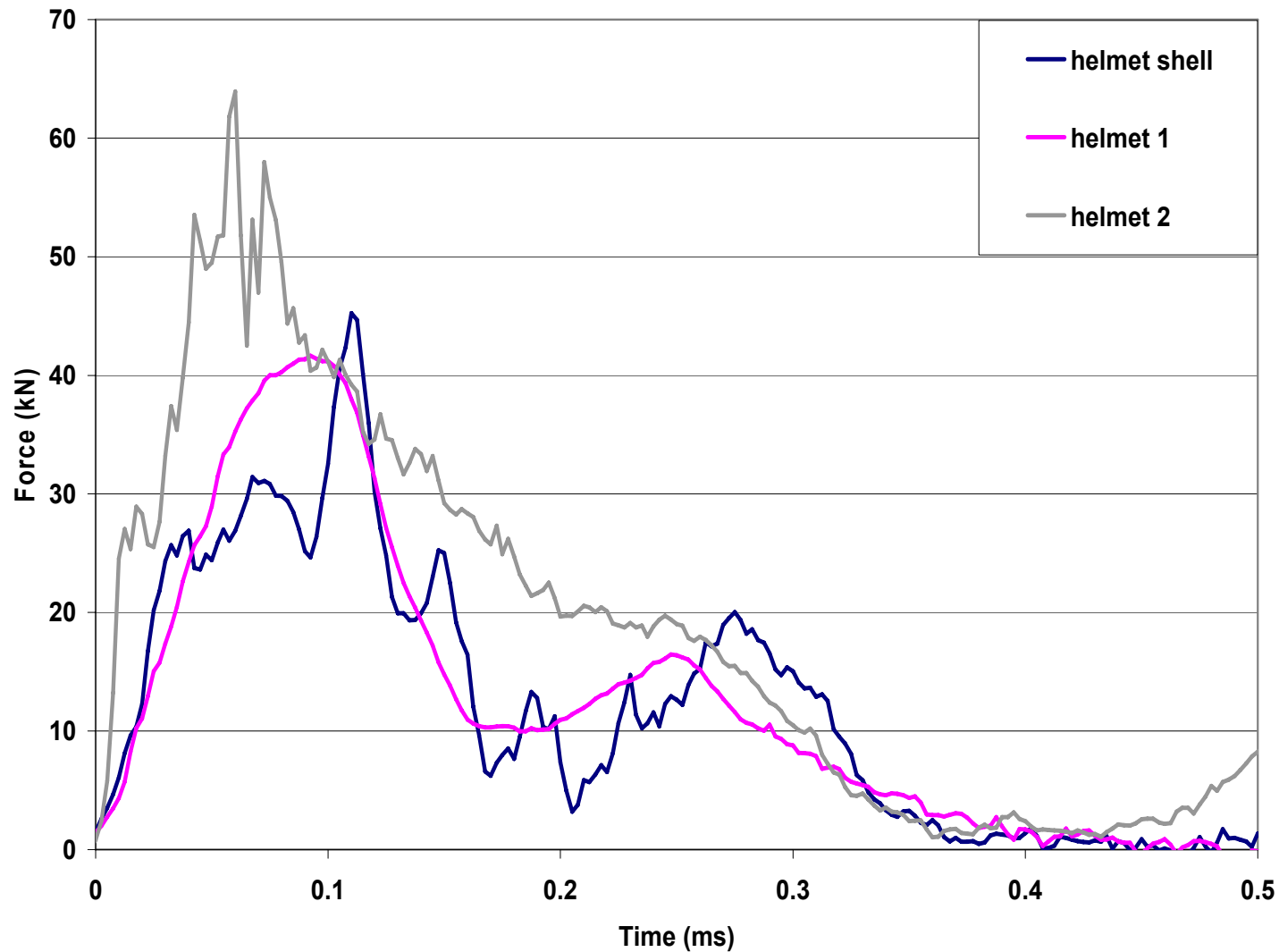
Initial impact

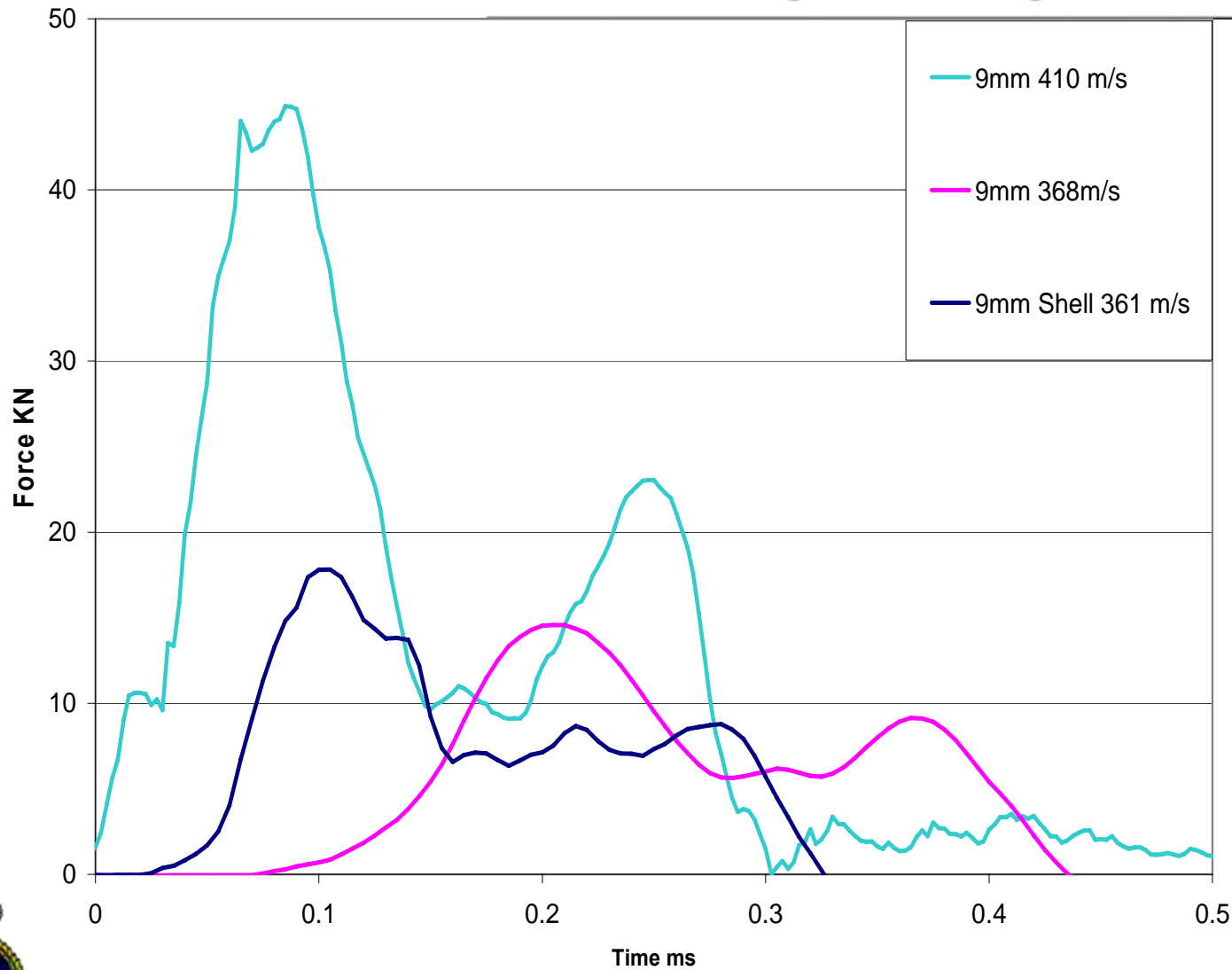


Complete impact motion









Summary

The head form was robust

Peak force results were repeatable.

Time histories of Force and acceleration correlated with high speed video and similar work by other researchers

0.05ms duration of the peak force from ballistic impact is a higher rate than the 15.0ms duration rate accepted as suitable for the HIC

Head form not bio-fidelic and compliance issues will be investigated in further work.



Film sensors show promise but need further development



Trajectory Deflection of Fin- and Spin-Stabilized Projectiles Using Paired Lateral Impulses

Pierre Wey

Pierre.Wey@isl.eu

Daniel Corriveau

Daniel.Corriveau@drdc-rddc.gc.ca



DEFENCE



DÉFENSE

Presentation Overview



- Objective
- Effect of a Lateral Impulse
- Basic Mathematical Model and Analytical Solution
- Pairing the Impulses
- Examples
- Conclusions



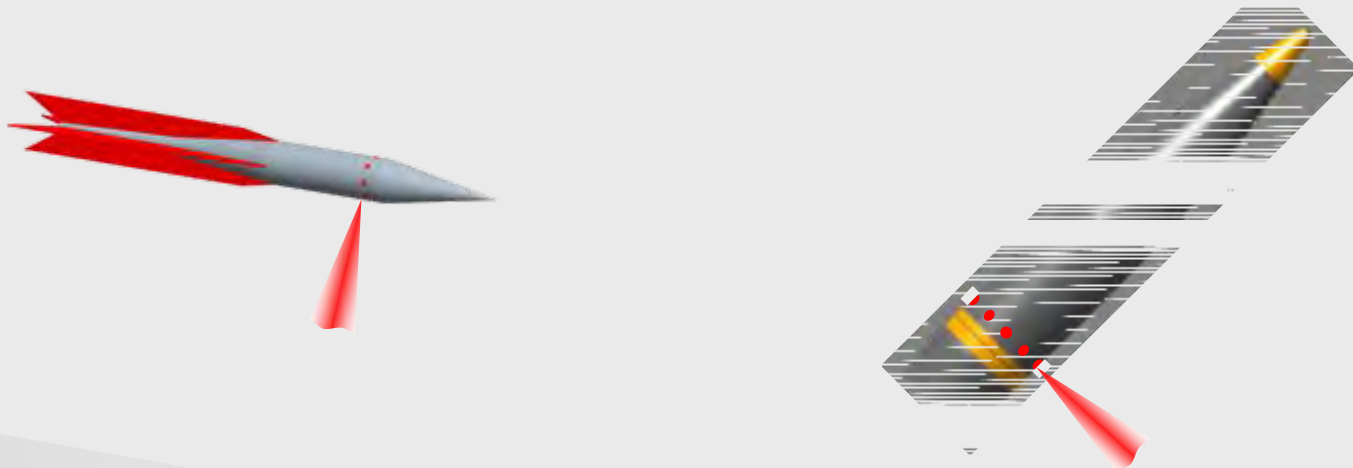
DEFENCE



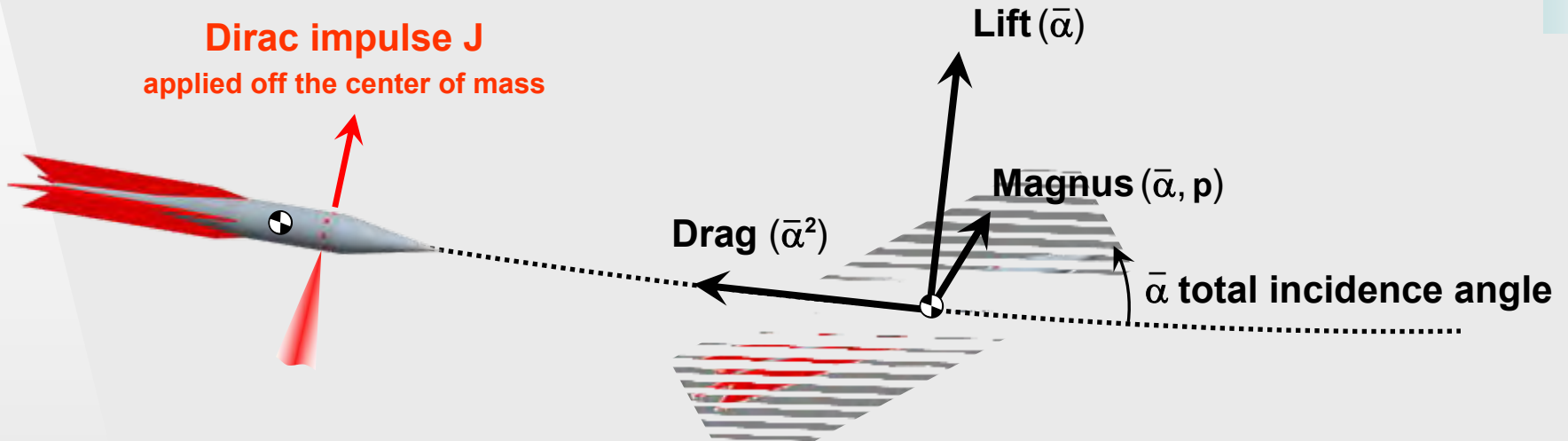
DÉFENSE

Objective

- To develop a well defined procedure for using paired impulses on fin- and spin-stabilized projectiles in order to achieve enhanced drift corrections



Effect of a Lateral Impulse ^(1/2)



Trajectory deflection: total lateral impulse = $J + J_L + J_Y$

$$\begin{aligned} & \int \text{Magnus } (\bar{\alpha}) \, dt \\ & \int \text{Lift } (\bar{\alpha}) \, dt \end{aligned}$$

Additional velocity decrease: axial impulse = J_{D2}

$$\int \text{Drag } (\bar{\alpha}^2) \, dt$$

More challenging to implement properly



DEFENCE



DÉFENSE

Effect of a Lateral Impulse ^(2/2)

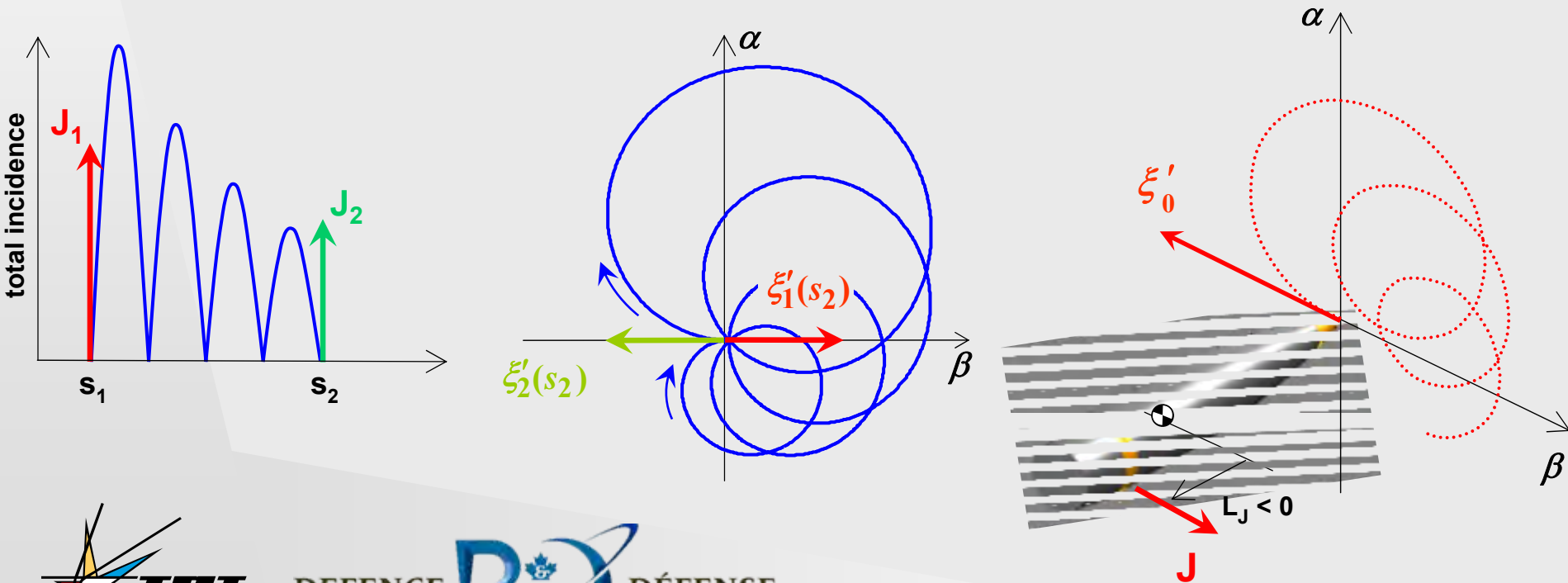
Pairing lateral impulses off the center of mass

Basic idea:

- J_1 triggers the angular motion at s_1
- J_2 stops the angular motion at s_2

Advantages:

- the lateral correction is enhanced by the lift impulse resulting from the angular motion
- the range lost is minimized by stopping the angular motion



DEFENCE



DÉFENSE

Basic Mathematical Model (1/4)

Linearized equation of the complex incidence motion:

$$\xi'' + (H - iP) \xi' - (M + iPT) \xi = \xi'_0 \delta(s)$$

Dirac impulse

Magnus moment
+ vel. change

$$T = \frac{\rho A d}{2m} \left(C_{L\alpha} + \frac{md^2}{I_x} C_{np\alpha} \right)$$

Overtuning moment
(restoring or destabilizing)

$$M = \frac{\rho A d^3}{2I_y} C_{m\alpha}$$

Gyroscopic effect $P = \frac{I_x}{I_y} \frac{pd}{V}$

Damping factor
+ vel. change

$$H = \frac{\rho A d}{2m} \left(C_{L\alpha} - C_D - \frac{md^2}{I_y} C_{mq} \right)$$



DEFENCE



DÉFENSE

Basic Mathematical Model (2/4)



Motion = sum of two rotating arms:

$$\xi = K_{F0} e^{i\phi_{F0}} e^{(\lambda_F + i\phi'_F)s} + K_{S0} e^{i\phi_{S0}} e^{(\lambda_S + i\phi'_S)s}$$

Angular frequencies

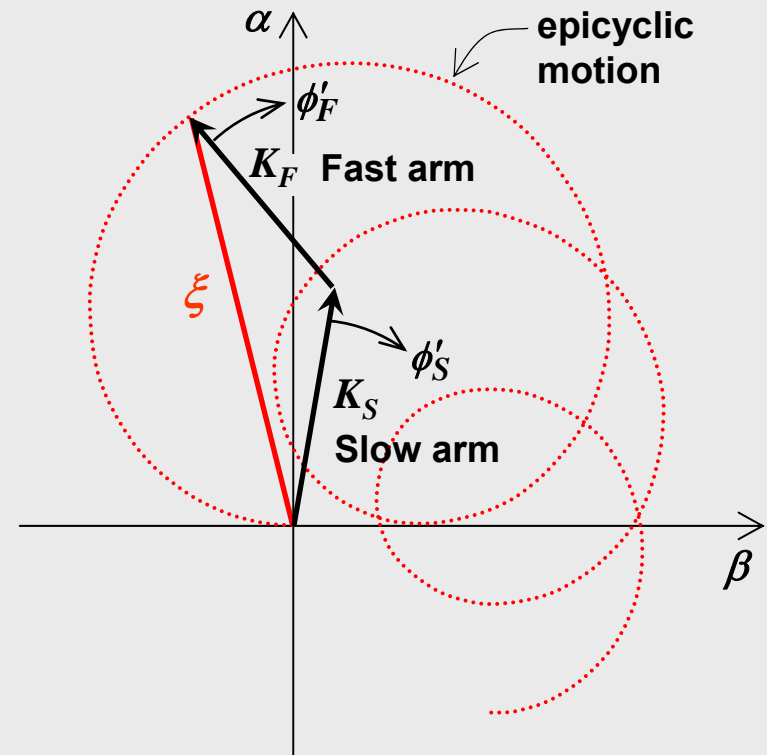
$$\phi'_F = \frac{1}{2} \left(P + \sqrt{P^2 - 4M} \right) \quad \phi'_S = \frac{1}{2} \left(P - \sqrt{P^2 - 4M} \right)$$

Damping factors

$$\lambda_F = -\frac{1}{2} \left(H - \frac{P(2T-H)}{\sqrt{P^2 - 4M}} \right) \quad \lambda_S = -\frac{1}{2} \left(H + \frac{P(2T-H)}{\sqrt{P^2 - 4M}} \right)$$

Initial arms

$$K_{F0} e^{i\phi_{F0}} = -\frac{i\xi'_0 + \phi'_S \xi_0}{\phi'_F - \phi'_S} \quad K_{S0} e^{i\phi_{S0}} = \frac{i\xi'_0 + \phi'_F \xi_0}{\phi'_F - \phi'_S}$$



DEFENCE



DÉFENSE

Basic Mathematical Model (3/4)

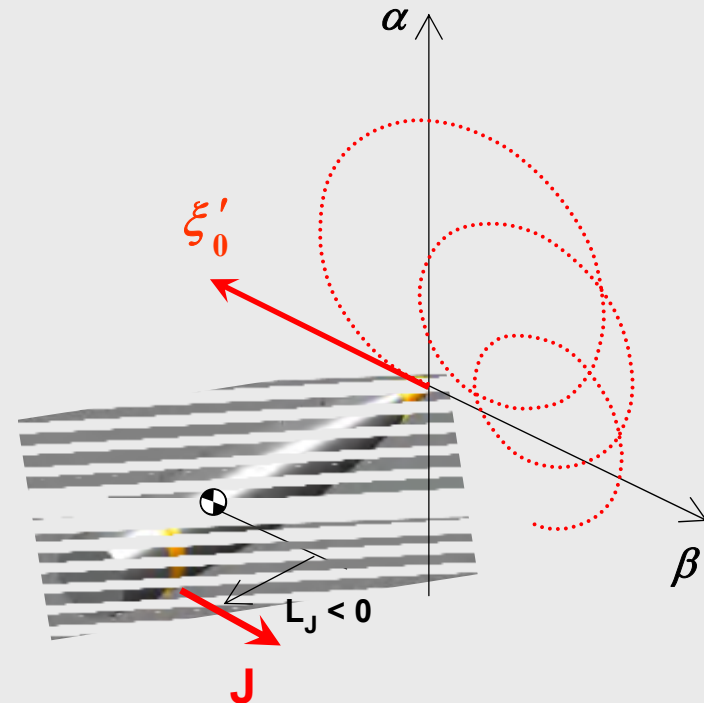
Initial conditions forced by the Dirac impulse:

$$\xi_0 = -\frac{J}{mV}$$

└─> negligible in supersonic mode

$$\xi'_0 = \frac{J L_J d^2}{I_y V}$$

└─> main cause of angular motion
(unless $L_J \rightarrow 0$)



DEFENCE



DÉFENSE

Basic Mathematical Model (4/4)



Lateral impulses: Lift + Magnus

$$J_L = \int_0^{\infty} L(t) dt$$

$$J_L = \frac{1}{2} \rho A V d C_{L\alpha} \int_0^{\infty} \xi ds$$

$$\int_0^{\infty} \xi ds = -\frac{K_{F0} e^{i\phi_{F0}}}{\lambda_F + i\phi'_F} - \frac{K_{S0} e^{i\phi_{S0}}}{\lambda_S + i\phi'_S}$$

$$J_Y = \int_0^{\infty} Y(t) dt$$

$$J_Y = i \frac{C_{Yp\alpha}}{C_{L\alpha}} \frac{p d}{V} J_L$$

Axial impulse: additional Drag

$$J_{D_2} = \int_0^{\infty} D_2(t) dt$$

$$C_D = C_{D0} + C_{D2} \sin^2 \bar{\alpha}$$

$$J_{D_2} = \frac{1}{2} \rho A V d C_{D2} \int_0^{\infty} |\xi|^2 ds$$

$$\int_0^{\infty} |\xi|^2 ds = -\frac{K_{F0}^2}{2\lambda_F} - \frac{K_{S0}^2}{2\lambda_S} - \frac{2 K_{F0} K_{S0} \left[(\lambda_F + \lambda_S) \cos(\phi_{F0} - \phi_{S0}) + (\phi'_F - \phi'_S) \sin(\phi_{F0} - \phi_{S0}) \right]}{(\lambda_F + \lambda_S)^2 + (\phi'_F - \phi'_S)^2}$$



DEFENCE

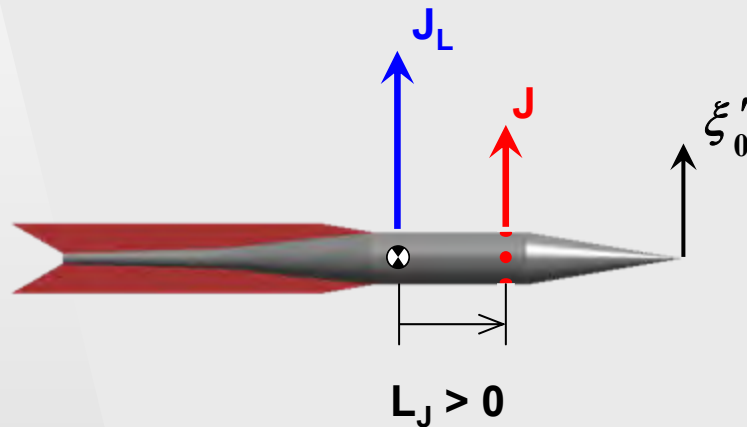


DÉFENSE

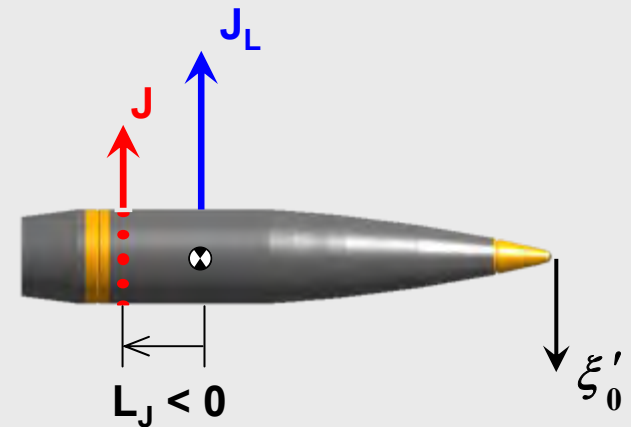
Pairing the Impulses: Location ^(1/2)

Goal: maximizing $J + J_L$

Fin-stabilized projectile



Spin-stabilized projectile



Rule #1: the lateral impulse must be applied

- ahead of the center of mass for fin-stab. shells
- behind the center of mass for spin-stab. shells

$$J_L = -J L_J \frac{C_{L\alpha}}{C_{m\alpha}} e^{i\Delta\phi}$$



DEFENCE

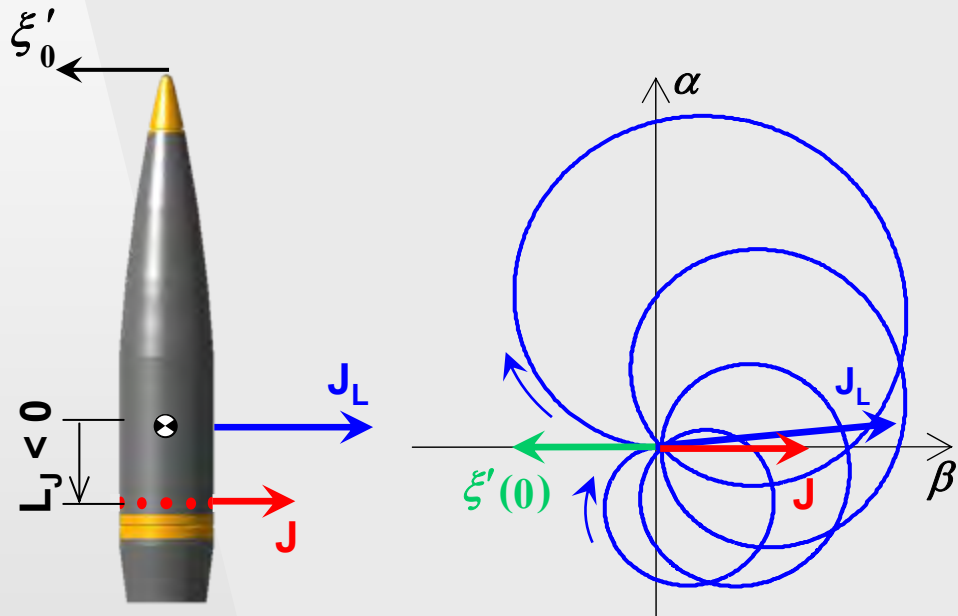


DÉFENSE

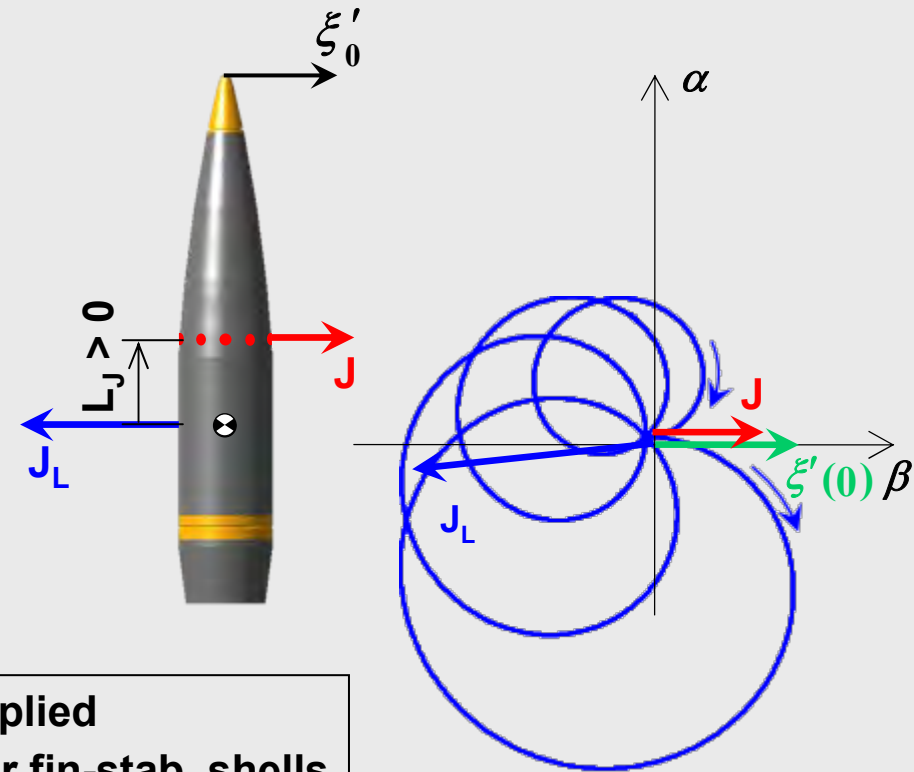
Pairing the Impulses: Location ^(2/2)

Goal: maximizing $J + J_L$ for spin-stabilized projectile

How to do it:

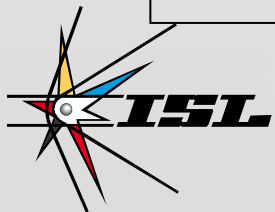


How not to do it:



Rule #1: the lateral impulse must be applied

- ahead of the center of mass for fin-stab. shells
- behind the center of mass for spin-stab. shells

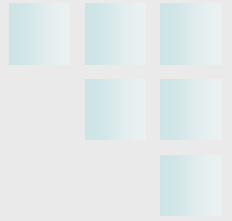


DEFENCE



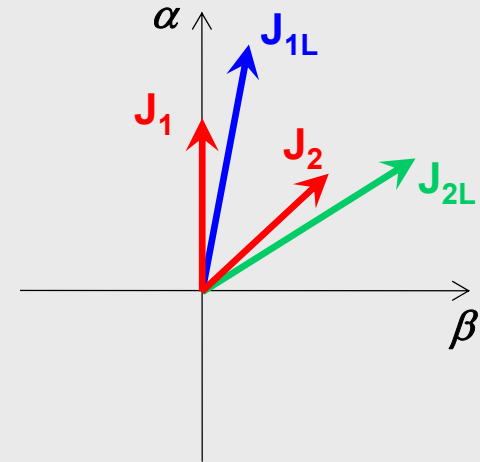
DÉFENSE

Pairing the Impulses: Orientation



Total lateral impulse = $(J_1 + J_{1L}) + (J_2 + J_{2L})$

- independent of $(s_2 - s_1)$
- maximum if J_1 and J_2 are aligned



Rule #2: J_1 and J_2 must be triggered at the same roll angle

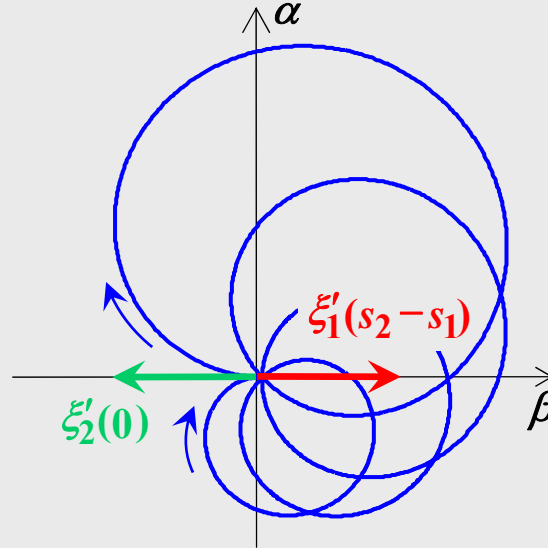
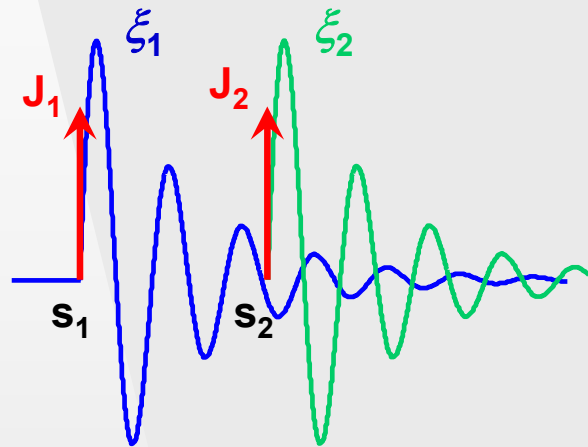


DEFENCE



DÉFENSE

Pairing the Impulses: Timing



Linearized equation of motion:

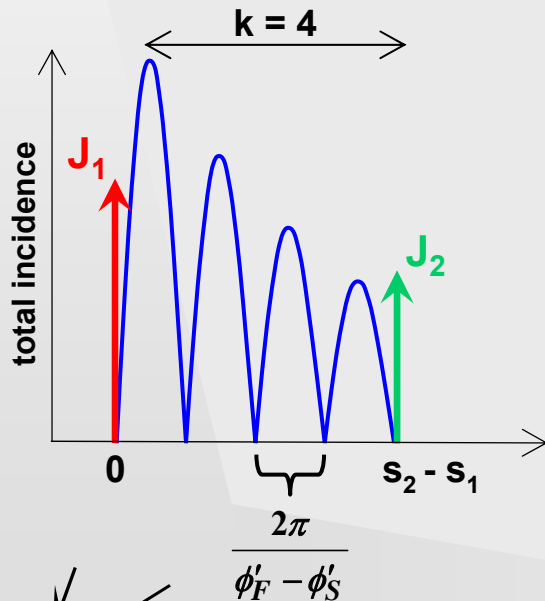
$$\xi = \xi_1 + \xi_2$$

$$\forall s \geq s_2, \xi_1(s) + \xi_2(s) = 0$$

Motion strictly opposed if:

$$\xi_1(s_2 - s_1) = \xi_2(0) = 0$$

$$\xi'_1(s_2 - s_1) = -\xi'_2(0)$$



Rule #3:

$$s_2 - s_1 = k \frac{2\pi}{\phi'_F - \phi'_S}$$

$$k = \text{nearest integer to } \frac{\text{sign}(\phi'_S)}{2} \left(\frac{\phi'_F}{\phi'_S} - 1 \right)$$

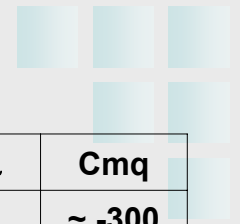


DEFENCE



DÉFENSE

Example: GSP Shell



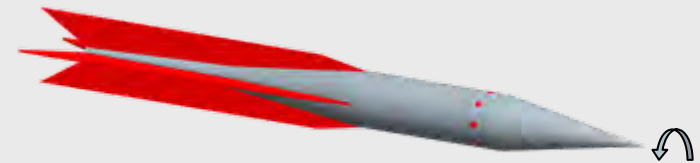
d	m	I_y	Mach	p	CD_0	$CL\alpha$	$CYp\alpha$	$Cm\alpha$	Cmq
30 mm	0.7 kg	$5.04e-3 \text{ kgm}^2$	3.5	22 Hz	0.19	7.6	~ 0	-5.3	~ -300

(actual)

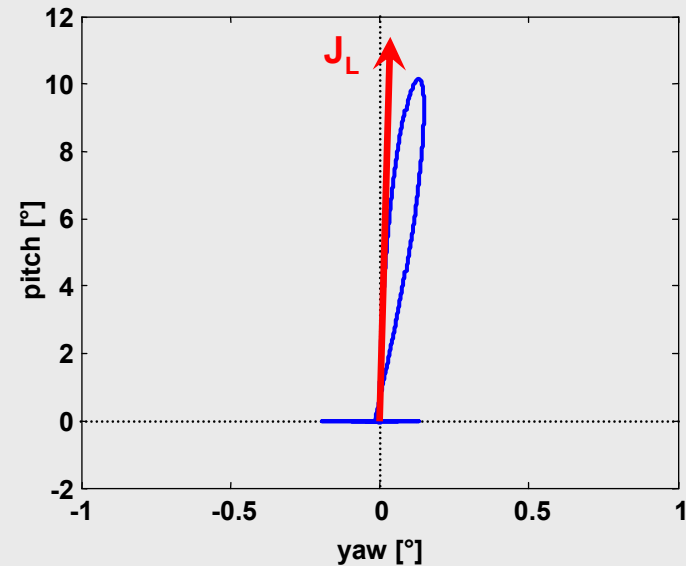
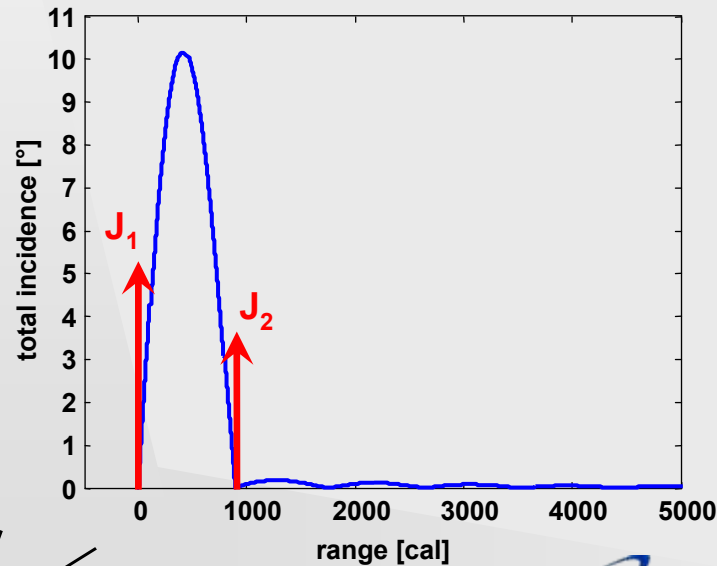
L_J	2.5 cal
J_1	2.0 N·s
J_2	1.4 N·s
$s_2 - s_1$	885 cal
$\bar{\alpha}_{\max}$	10.1°

V_J	4.75 m/s
V_L	16.63 m/s
$\Delta\phi$	0.09°
V_Y	0 m/s
V_{D2}	3.98 m/s

GAIN 3.48



(26.5 m or 22.3 ms)



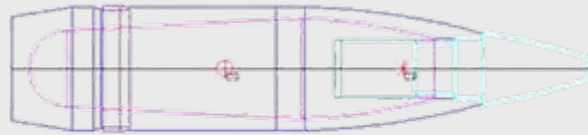
DEFENCE



DÉFENSE

Example: 105 mm Artillery Shell ^(1/2)

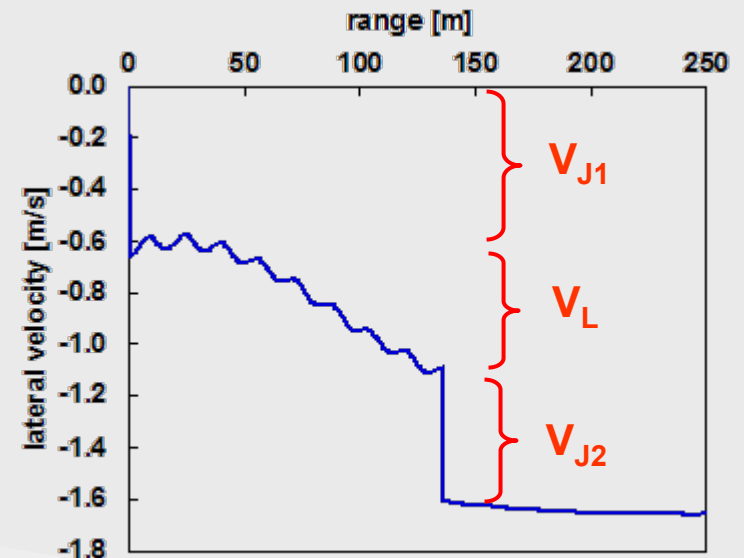
d	m	I_y	Mach	p	CD_0	CL_α	$CY_{p\alpha}$	Cm_α	Cm_q
105 mm	15.05 kg	$2.19e-1 \text{ kgm}^2$	1.5	310 Hz	0.375	2.12	-0.8	3.6	-17



L_J	-0.51 cal
J_1	10 N·s
J_2	7.83 N·s
$s_2 - s_1$	1293 cal
$\bar{\alpha}_{\max}$	1.5°

(135.6 m)

V_J	1.18 m/s
V_L	0.36 m/s
$\Delta\phi$	-3.5°
V_Y	0.05 m/s



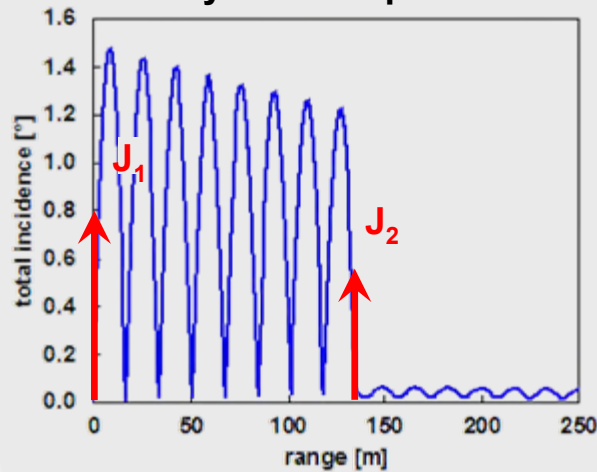
DEFENCE



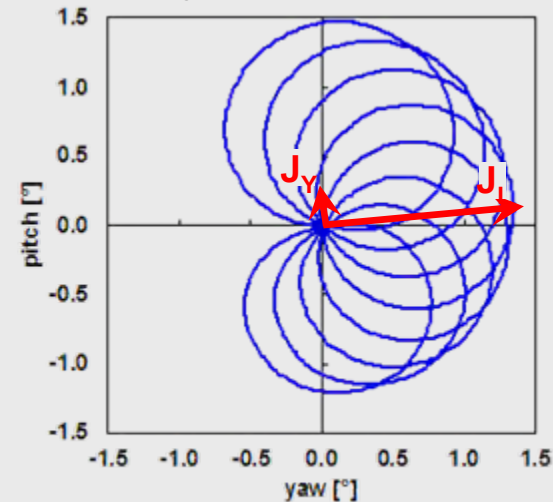
DÉFENSE

Example: 105 mm Artillery Shell^(2/2)

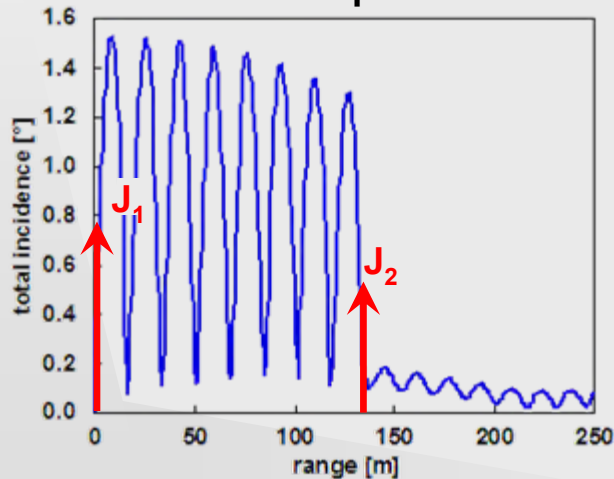
Analytical computations



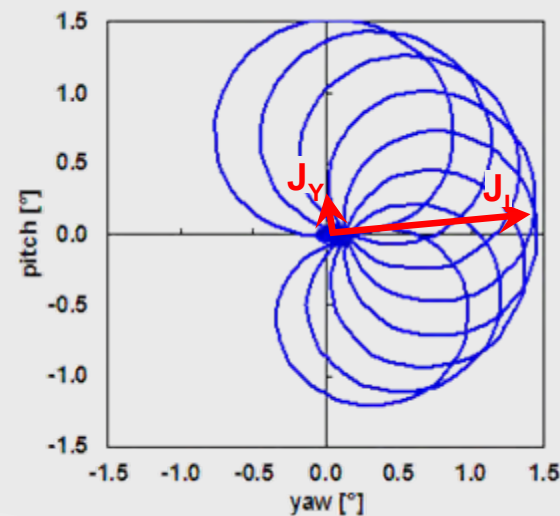
Analytical computations



6-DOF computations



6-DOF computations



DEFENCE



DÉFENSE

Conclusions



- An analytical model was developed to predict the angular motion of a projectile subjected to impulse thrusters
- The analytical model predicts the projectile's angular motion very well
- A procedure to properly paired impulses in order to minimize the drag while maximizing the lateral velocity was developed
- The gain in lateral velocity obtained from the induced angular motion is significant



DEFENCE



DÉFENSE

Multiple Effects Warheads for Defeat of Urban Structures and Armour

Anthony J Whelan
24th ISB presentation (New Orleans)

23rd September 2008



Contents

01 Background

- Defeat of Armour and Structures
- Lethal Mechanisms
- Supporting Technologies
- Combining Technologies

02 Design Study

- Break-in-Charge
- Main warhead
- Tandem Interaction

03 Firing Programme

- Break-in-Charge
- Main warhead

04 Conclusions



Images courtesy of Jane's Information Group

01 Background - Defeat of Armour and Structures

Example Targets

- Heavy armour
 - MBT
- Medium armour
 - MRT, SPG, LAFV
- Light armour
 - Logistics, Improvised carrier (Pick-up)
- Urban structures
 - Double skin brick – sand bag fortified
 - Concrete panel – double steel reinforcement

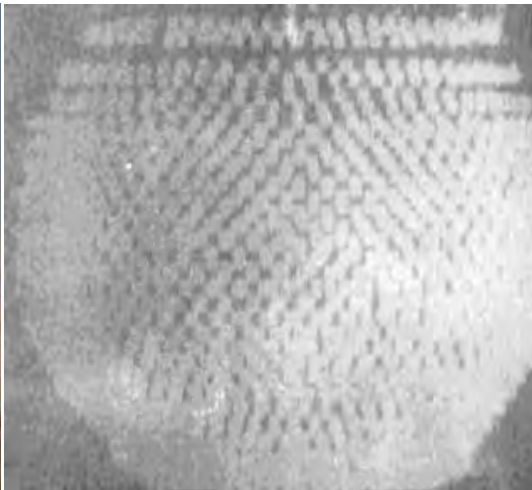


Images courtesy of Jane's Information Group

01 Background - Lethal Mechanisms

Several lethal mechanisms required to achieve defeat across the target spectrum

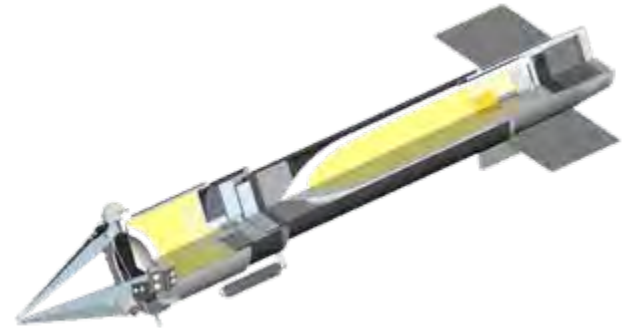
- Blast
- Fragmentation
- Chemical energy – shaped charge, EFP or Slow Stretching Jet (stretching EFP)



01 Background – Supporting Technologies

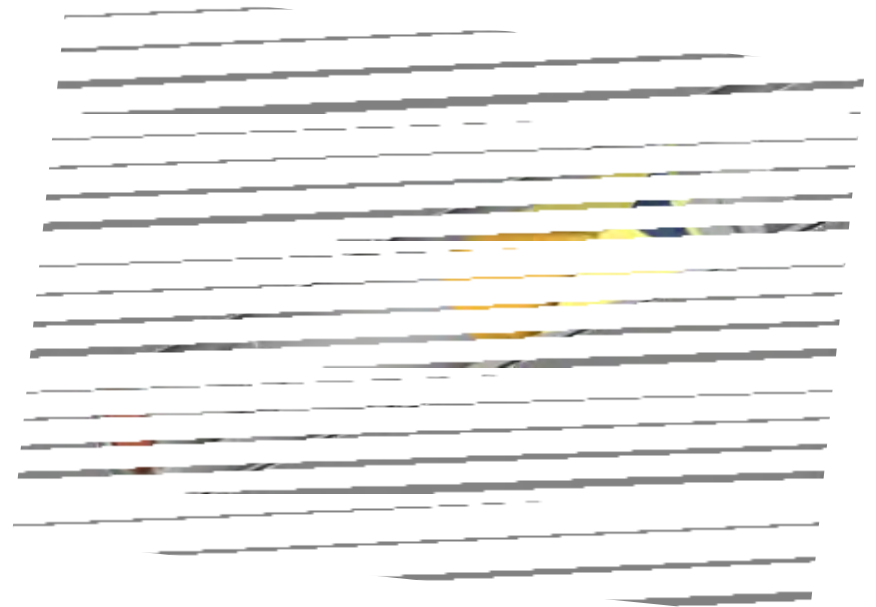
Urban Assault Weapon Programme

- Focussed on structures defeat
 - Utility against light/medium armour
 - Man portable – shoulder launched



High Performance Shaped Charge

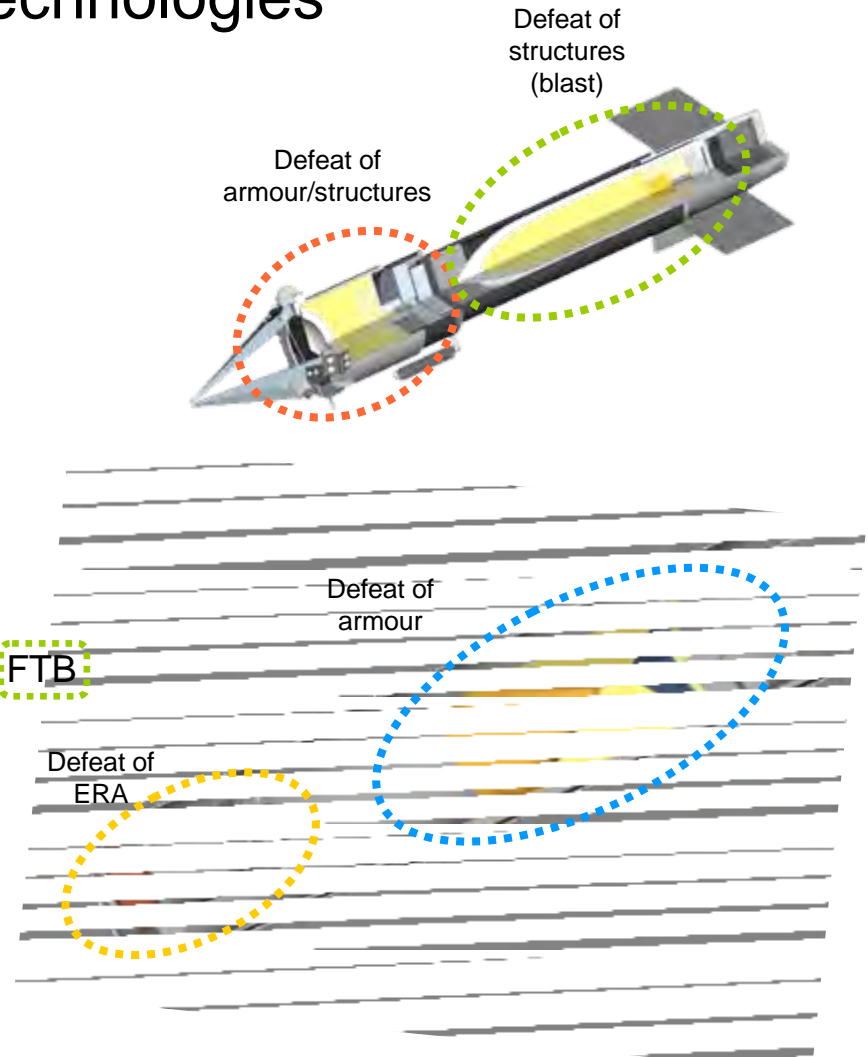
- Focussed on heavy armour defeat
 - Tandem shaped charge
 - Crew portable and Air launched



01 Background – Combining Technologies

Enable defeat of armour and structures

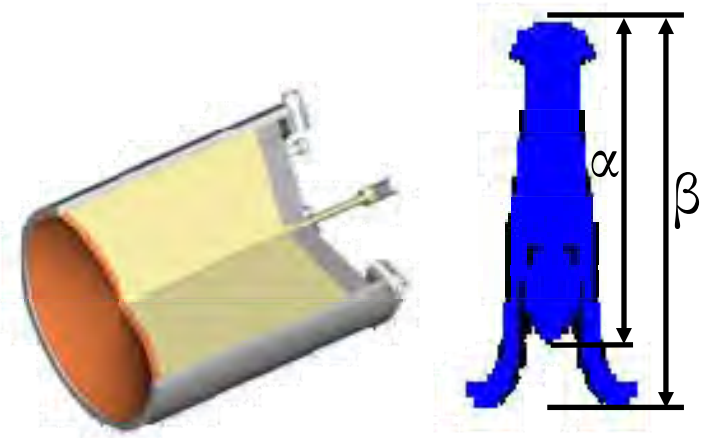
- Precursor
 - Combine traditional precursor and BiC warhead functionality
- Main Charge
 - Combine high performance shaped charge with FTB function



02 Design Study – Break-in-Charge

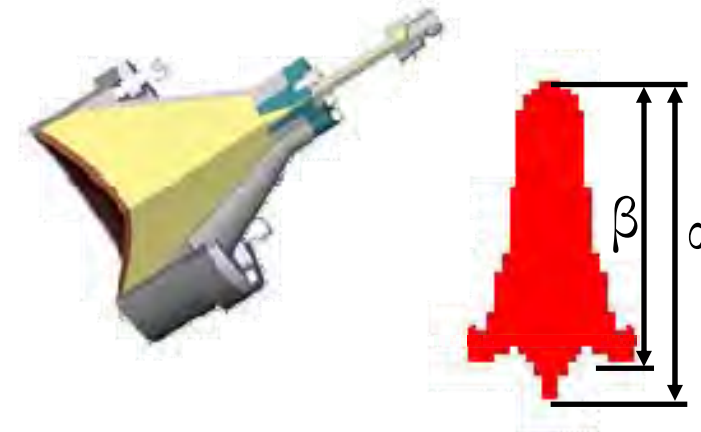
Baseline BiC - SSJ

- EDC1s filled warhead design



MEW BiC - CSSJ

- PBX filled warhead design
 - PBX replacement – aiding IM compliance
 - Use of PBX reduced CJ pressure by ~7%



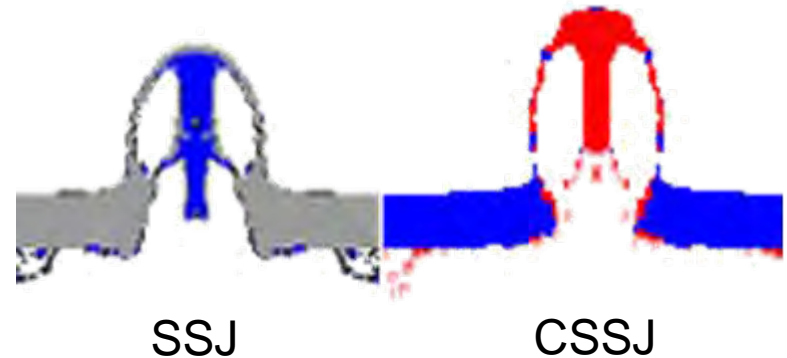
Warhead design

- GRIM 2D hydrocode
 - Mass reduced by 30%
 - Volume reduced by 35%
 - 4% reduction in length of central portion of projectile (α)

02 Design Study - Break-in-Charge

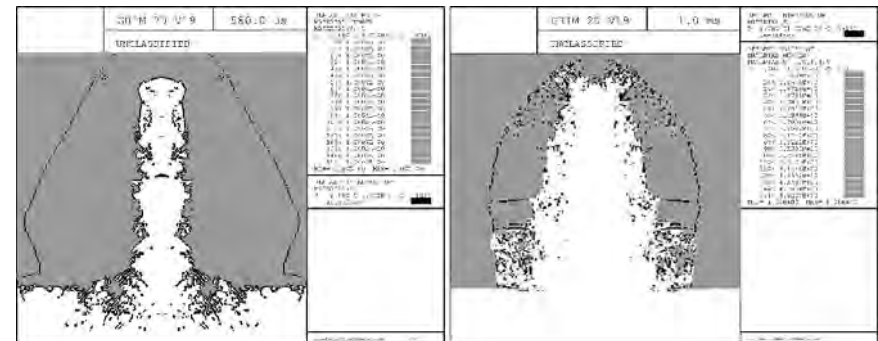
Target defeat modelling

- RHA perforation – hole diameter
 - CSSJ 82% of Baseline hole diameter



- Concrete penetration

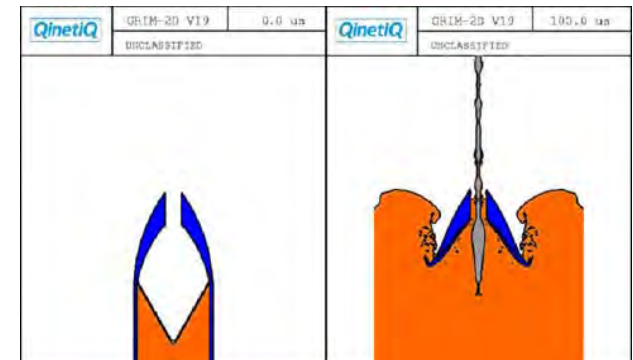
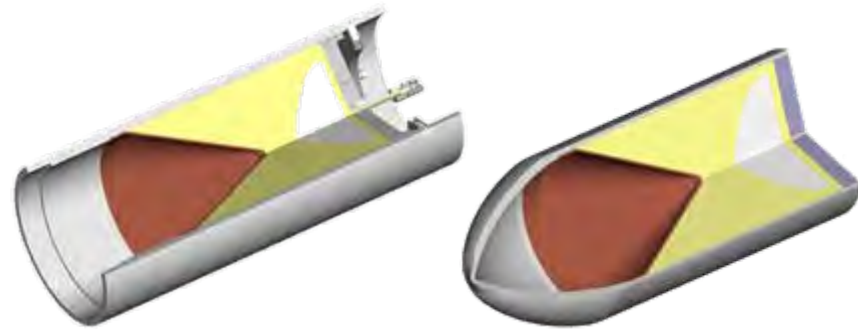
Whd Type	Stand-off (CD)	Bore Depth	Minimum Bore Diameter (CD)	Throat Diameter (CD)
SSJ	1	100%	100%	100%
CSSJ	1	98%	181%	211%



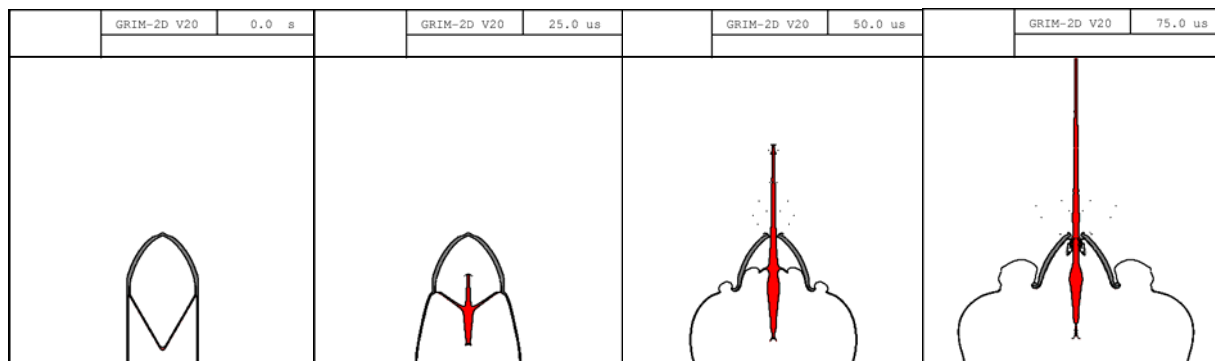
02 Design Study – Main Warhead

Hydrocode modelling study

- Changes made in several areas
 - Casing material – Aluminium to Steel
 - Casing geometry – inclusion of Ogive
 - Initiation geometry – increase in initiation angle
 - Explosive fill – EDC1s to PBXN-110



Initial design - heavy Ogive

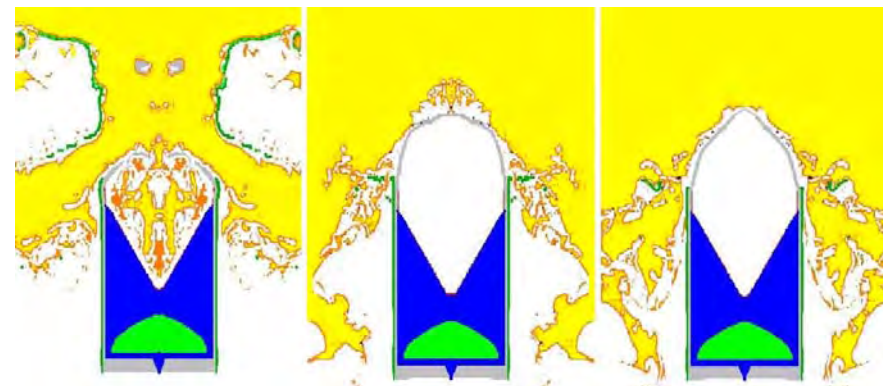
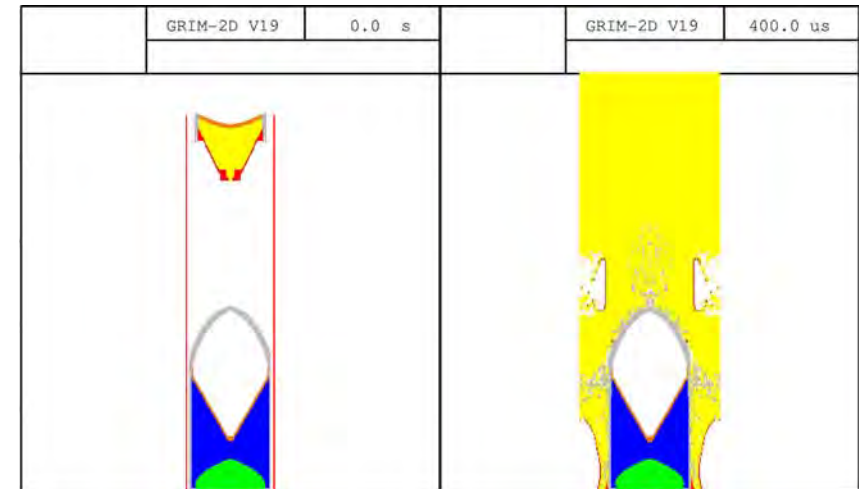


Final design – light Ogive

02 Design Study – Tandem Interaction

Hydrocode modelling study

- Fixed inter-charge spacing
 - Commensurate with in-service ATGWs
 - No inter-charge barrier
- Several iterations
 - Ogive profile
 - Main warhead casing material – Aluminium to Steel
 - Precursor warhead – Polymer composite rear half of casing
- Survival of main charge



03 Firing Programme - Break-in-Charge

BiC warhead Trials

- Anti-structures trial
 - Fortified domestic target
 - Municipal C40 concrete
 - Double steel reinforcement (1/2" bar) to front and rear of target
- Trial Results
 - Increase in hole diameter noted
 - Performance level maintained
 - Defeat of targets at normal and 45° obliquities



Double skin
brick wall



Sandbag
reinforcement to
rear of brick wall



Steel
reinforced
concrete wall



1.5 CD



2 CD

90° attack



4.5 CD



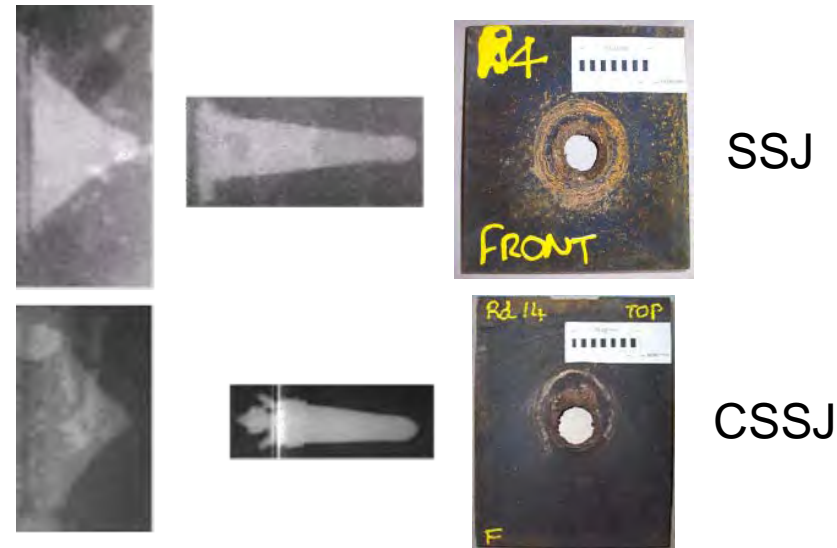
2.5 CD

45° attack

03 Firing Programme - Break-in-Charge

BiC warhead Trials

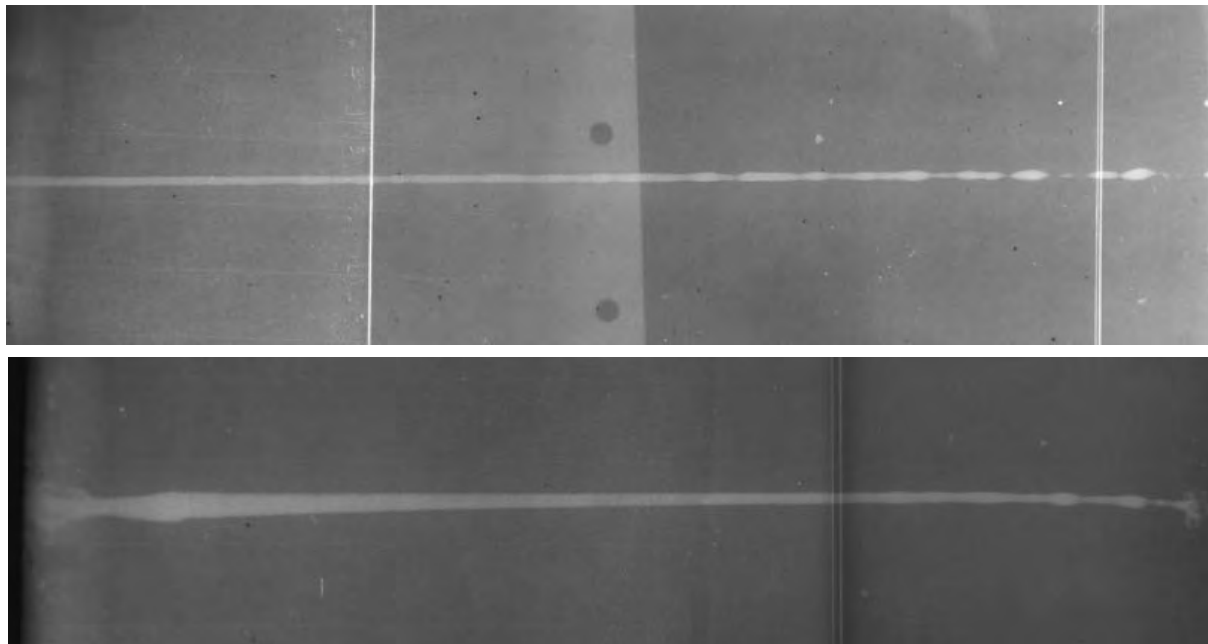
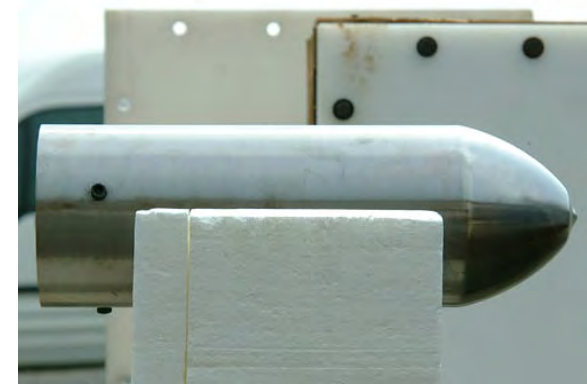
- Anti-armour trial
 - RHA plate
 - MBT heavy ERA
- Performance levels
 - Baseline BiC
 - 0.4 CD through hole
 - MEW BiC
 - 0.4 CD through hole
 - Defeat of heavy ERA targets



03 Firing Programme – Main Warhead

Static main warhead trial

- Variability in warhead performance observed

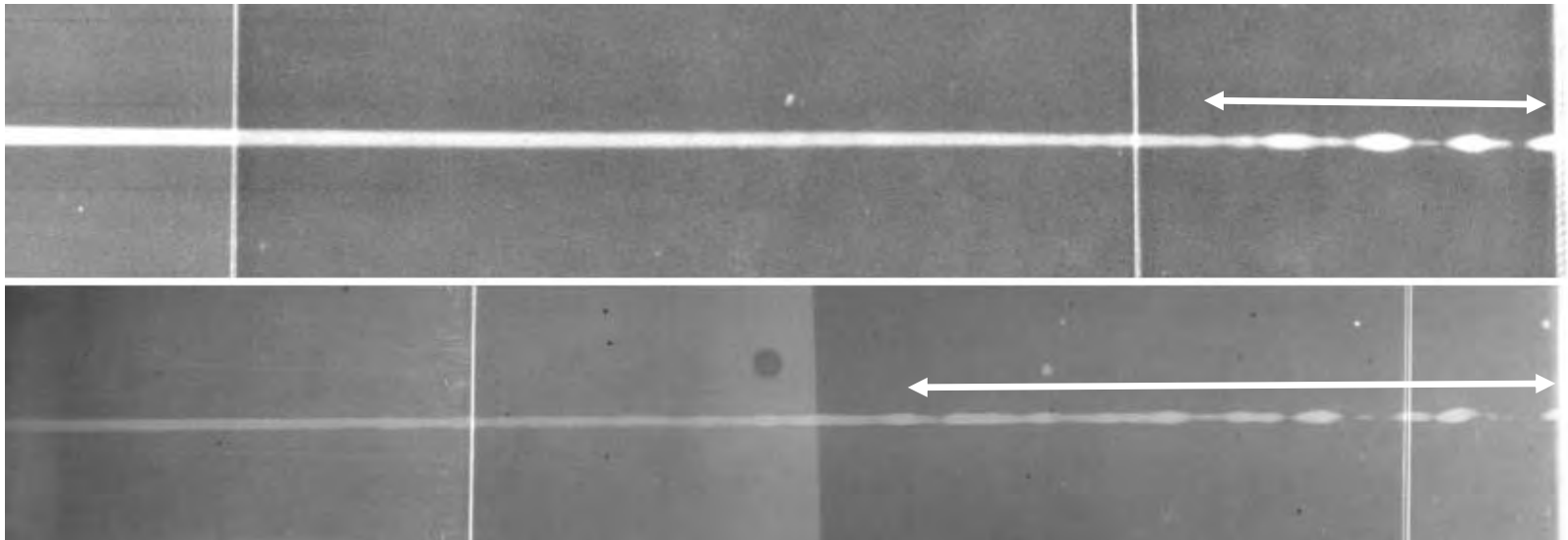


Radiography of two separate FTB/MC firings, (from top) at 100 μ s, and 170 μ s

03 Firing Programme – Main Warhead

Comparative break-up characteristics

- On-set of break-up occurs earlier
 - Ogive interaction most probable cause



PBXN-110 filled D2 warhead with no ogive (top) PBXN-110 filled FTB/MC (bottom)

03 Firing Programme – Main Warhead

Eight main warheads fired

- Firings against RHA
 - Def-Stan 95-13 RHA
 - Various stand-offs
- Large reduction in penetration
 - Jet curvature main cause

Warhead #	Stand-off (CD)	*Average Penetration Reduction (%)	Notes
1	8	19	Jet curvature observed, Jet velocity 8.5mm/μs
2	4	N/A	
3	4	N/A	
4	5	N/A	Jet curvature observed on radiography
5	5	N/A	Curvature at front of jet, jet tip unusual geometry
6	10	17	Target key-holed, jet particulation appears advanced
7	8	19	Jet curvature observed on radiography
8	8	19	Jet velocity 8.65mm/μs

*Average values are those of PBXN-110 filled precision shaped charge

04 Conclusions

BiC Warhead

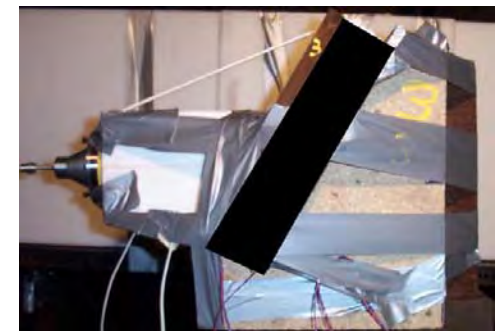
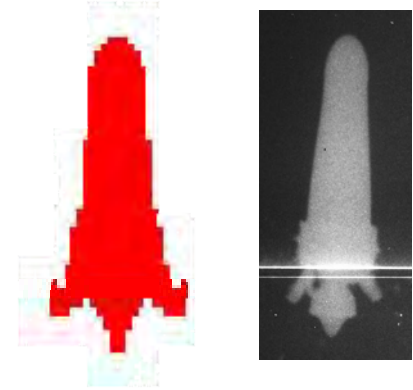
- Performance level maintained
 - More IM compliant explosive
 - Reduced overall mass and volume

Main Warhead

- Reasonable level of RHA penetration
 - Jet curvature through initiation inaccuracies – major loss in performance
 - Ogive – jet interaction

Tandem Interaction

- Hydrocode modelling
 - Main charge appears unaffected by BiC 400 μ s after detonation



04 Conclusions

Overall concept

- Tandem interaction must be observed
 - Current research work is investigating this issue
- Design for production
 - Minor changes required to accommodate through life issues
 - Expansion/contraction of explosive fill under service environment
 - FCO/SCO design features
- Compliancy with system mass/centre of gravity constraints
 - Use in crew portable system
 - Requires re-engineering of warhead solution
 - Use in air launched system
 - No major changes envisaged



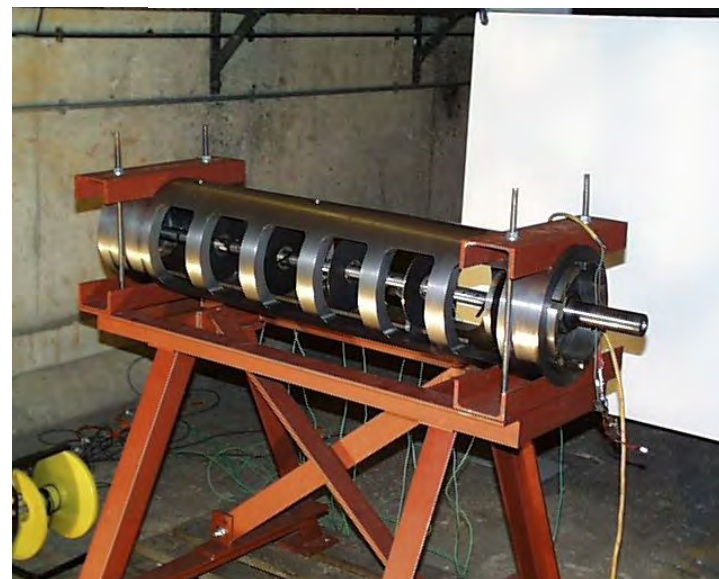
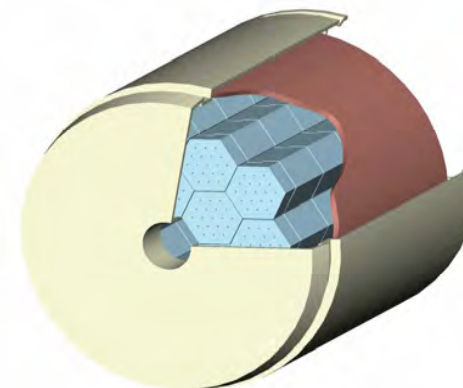
Independent expertise where it matters most.

Two-dimensional modelling of modular charge gun firings

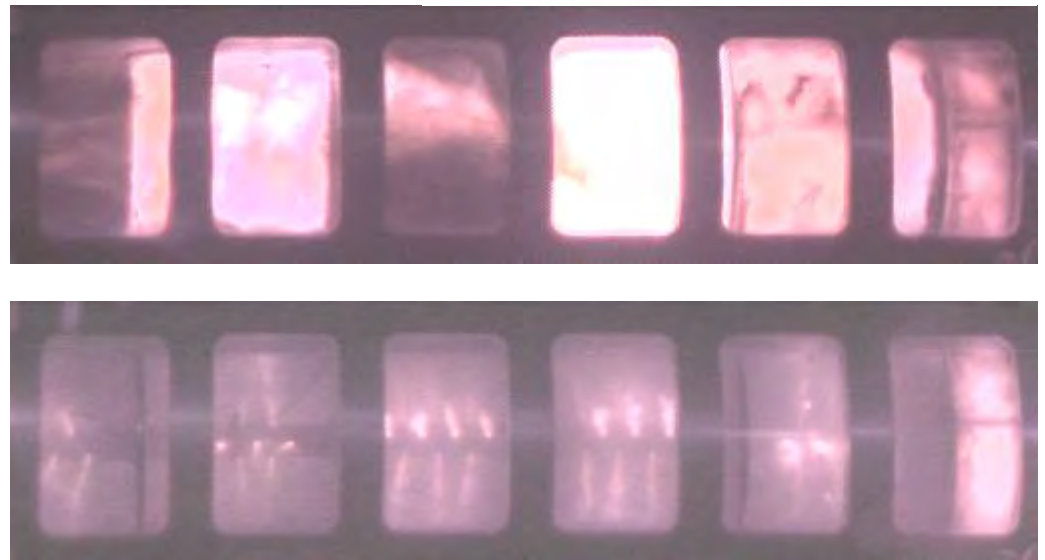
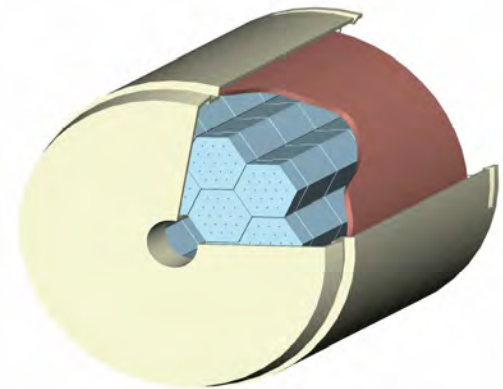
Clive Woodley, Steve Fuller

A presentation to: 24th International Symposium on Ballistics

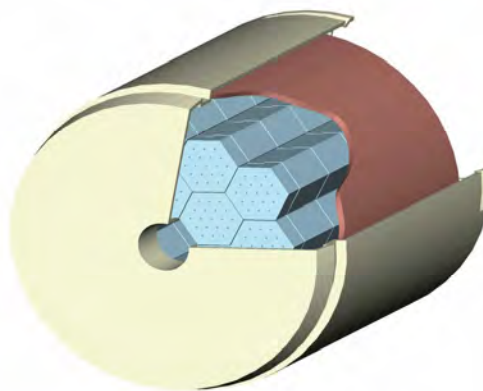
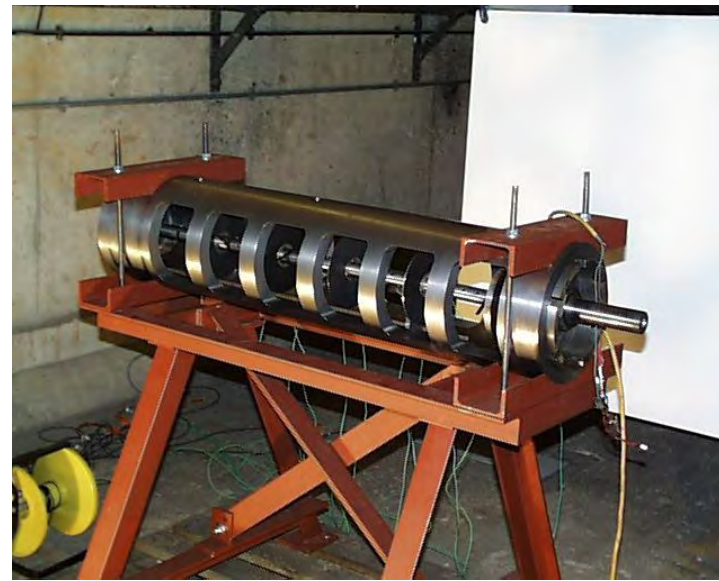
September 2008



- 01 Description of UPCS2
- 02 Description of QIMIBS
- 03 IB modelling of UPCS2

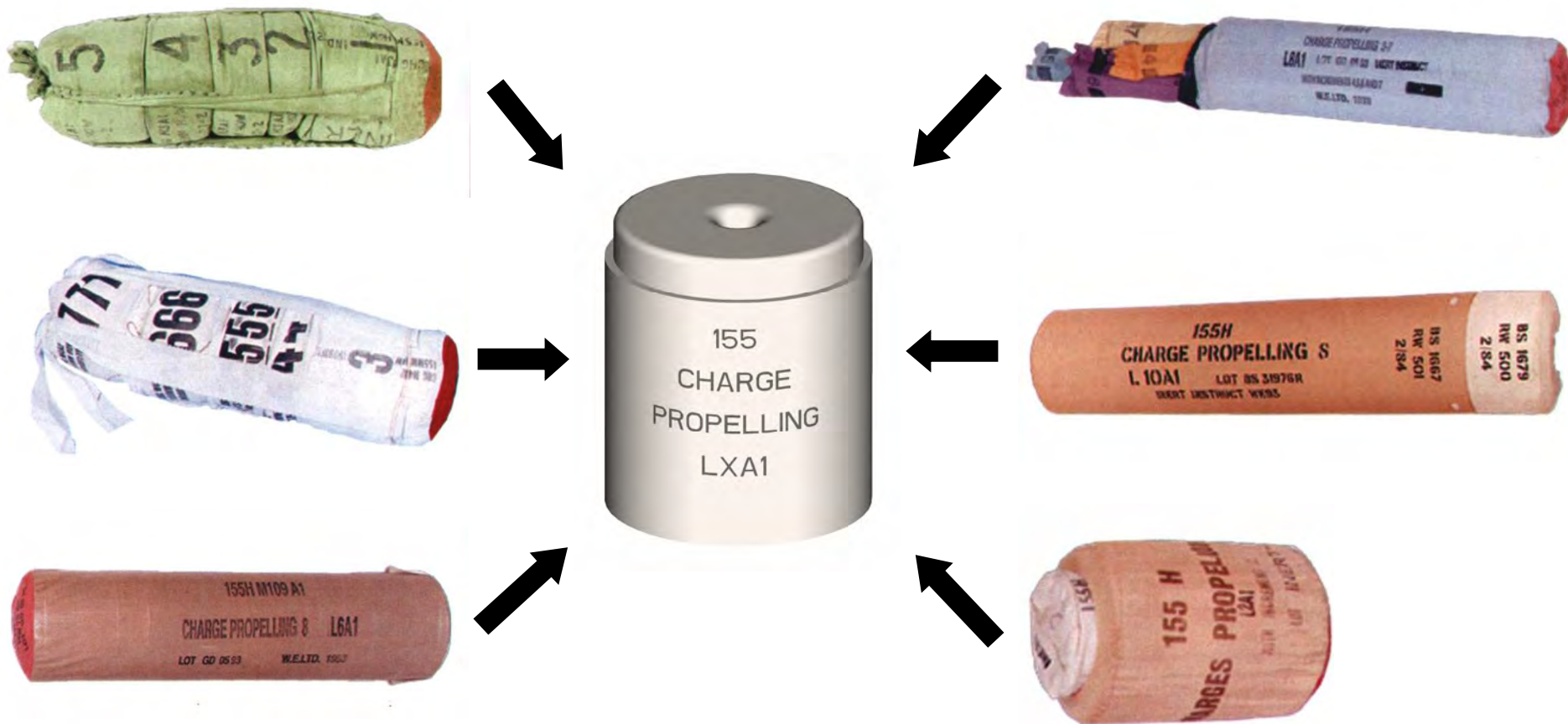


01 Description of UPCS2



S?

Existing 155mm charge inventory replaced with 1 module



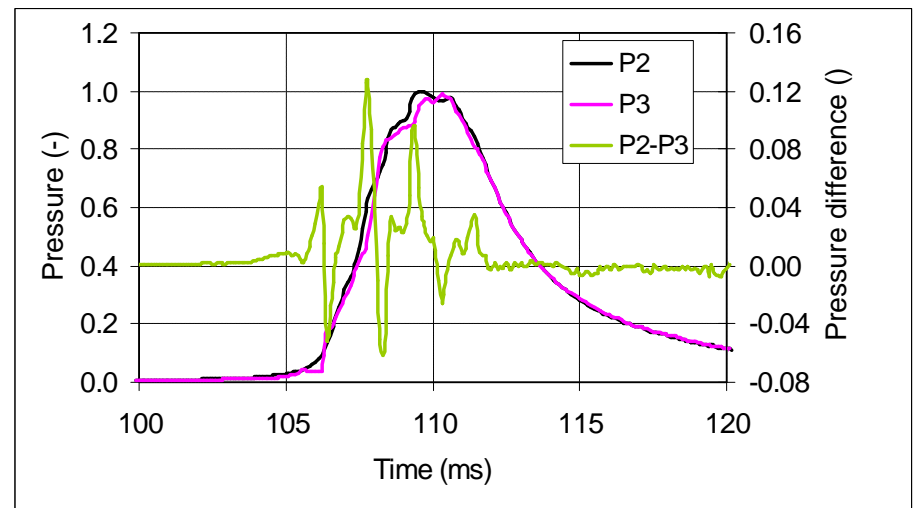
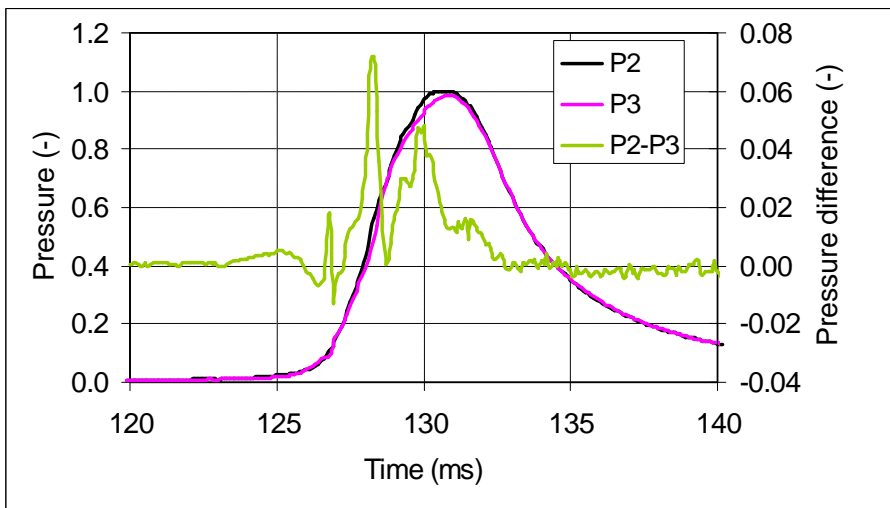
Objectives

- “ To determine temperature coefficient data for experimental propellant under gun firing conditions
- “ To determine top zone performance for experimental propellant
- “ To determine low zone performance for experimental propellant
- “ **To investigate the performance of the ignition system**

some results

- Smooth pressure-time profiles were recorded for Z2 and Z3 charges.
- A smooth pressure time profile at zone 4 (+21°C) was also observed

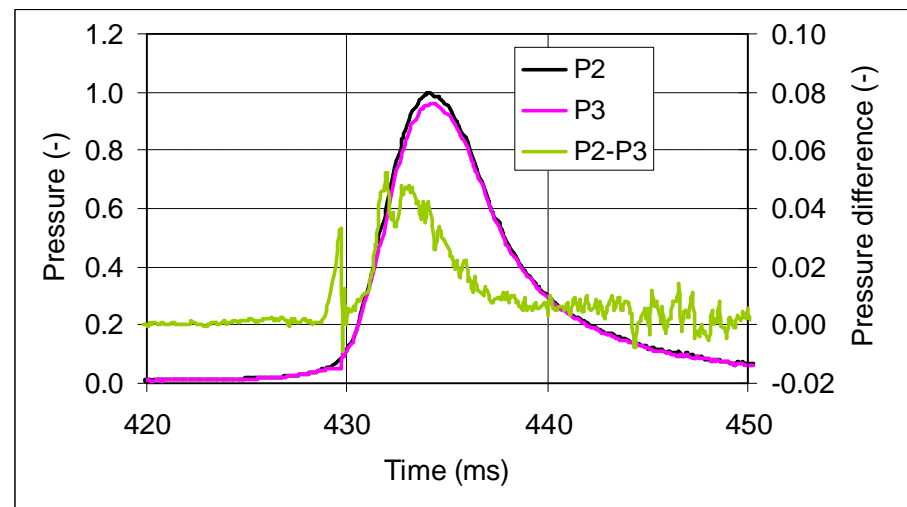
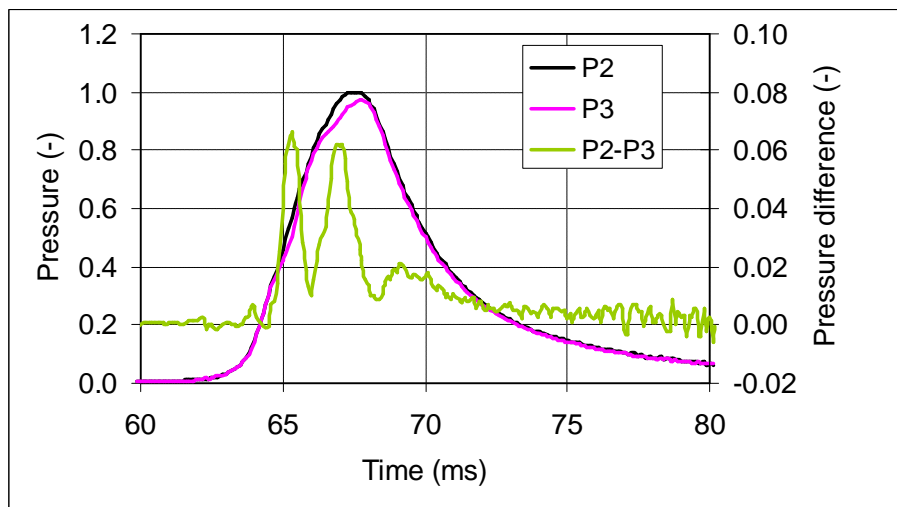
- But so was a not so smooth curveq



some results

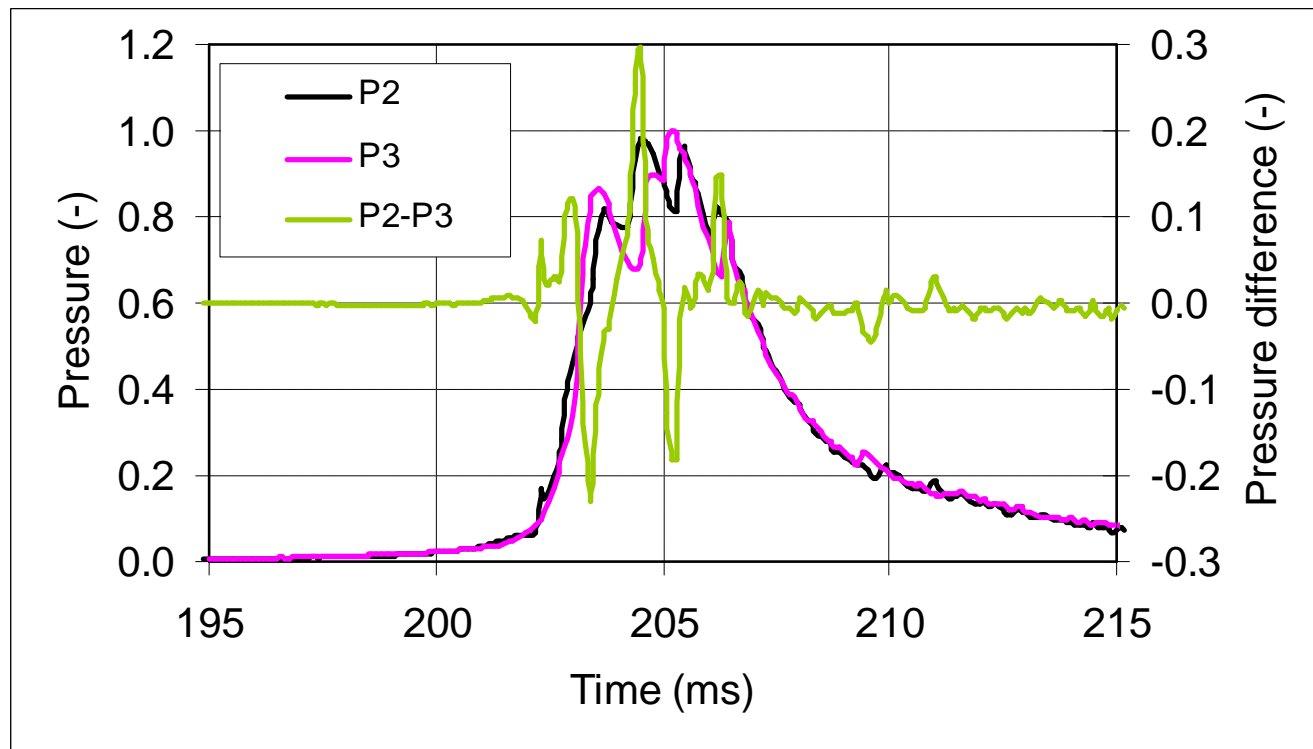
Results at zone 4 at 63°C

and -33°C were acceptable



some results

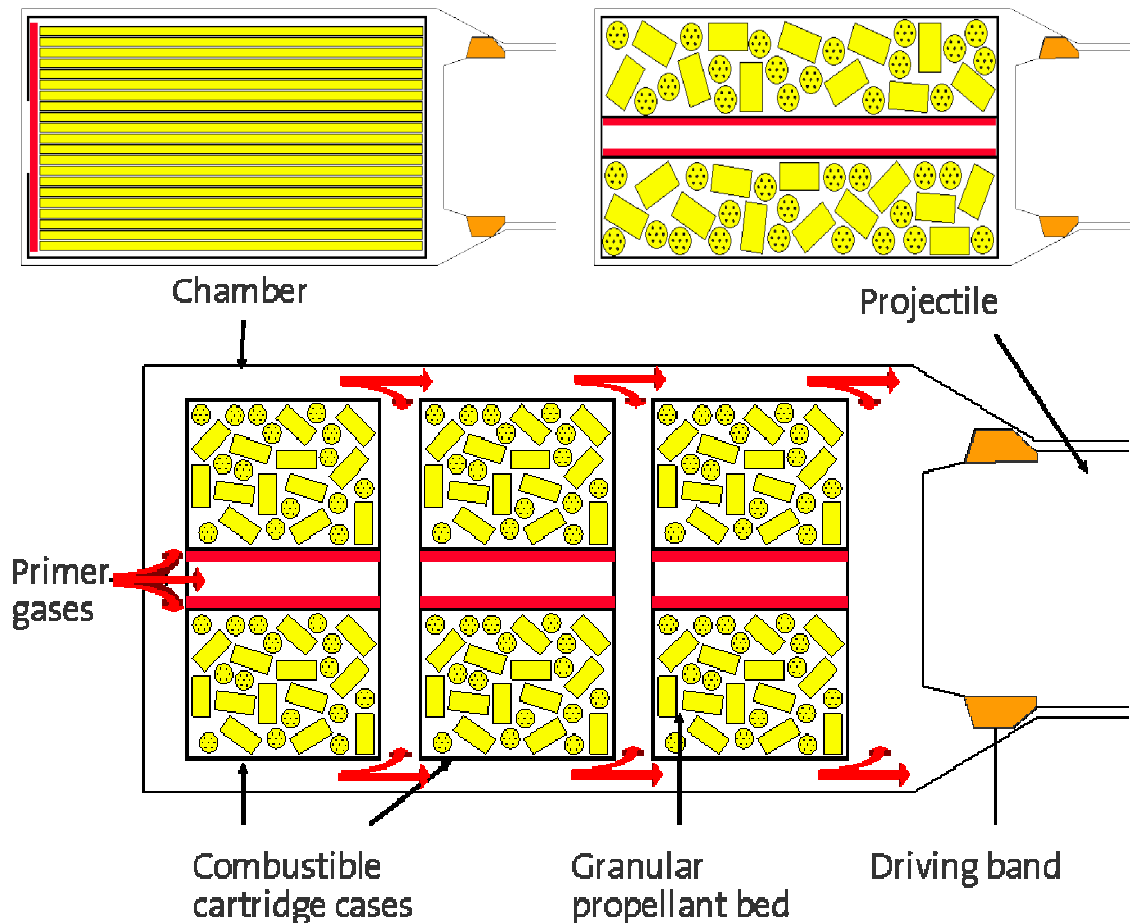
- “ 4.5 modules at -33C gave bad results!
- “ The firing mechanism was forcibly ejected from the gun breech with a substantial velocity



Background

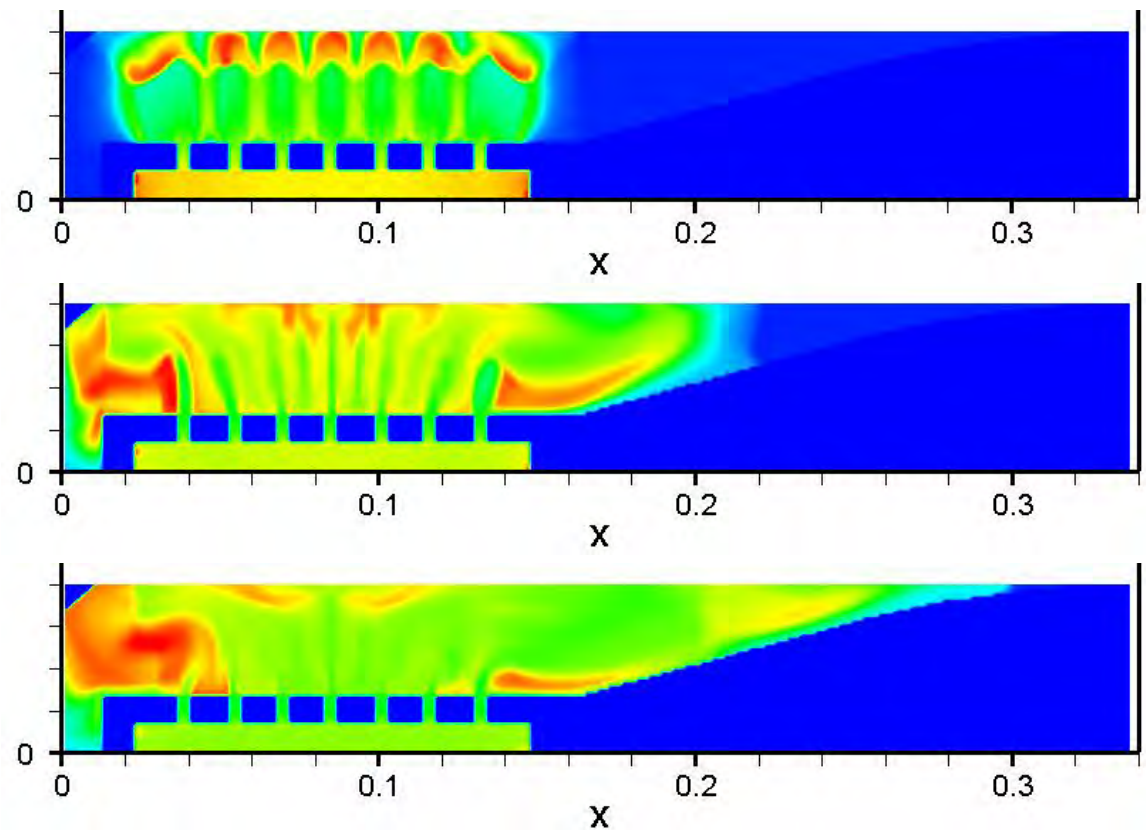
Safety & performance are important requirements . linked to ignition

- “ More conventional charges, comprising stick and granular propellant, can be modelled
- “ Want any pressure waves to be eliminated or minimised and consistent
- “ Want simultaneous ignition along length of charge
- “ Combustible cartridge cases present barrier to flamespread along the propellant bed
- “ Modules act as projectiles!



02

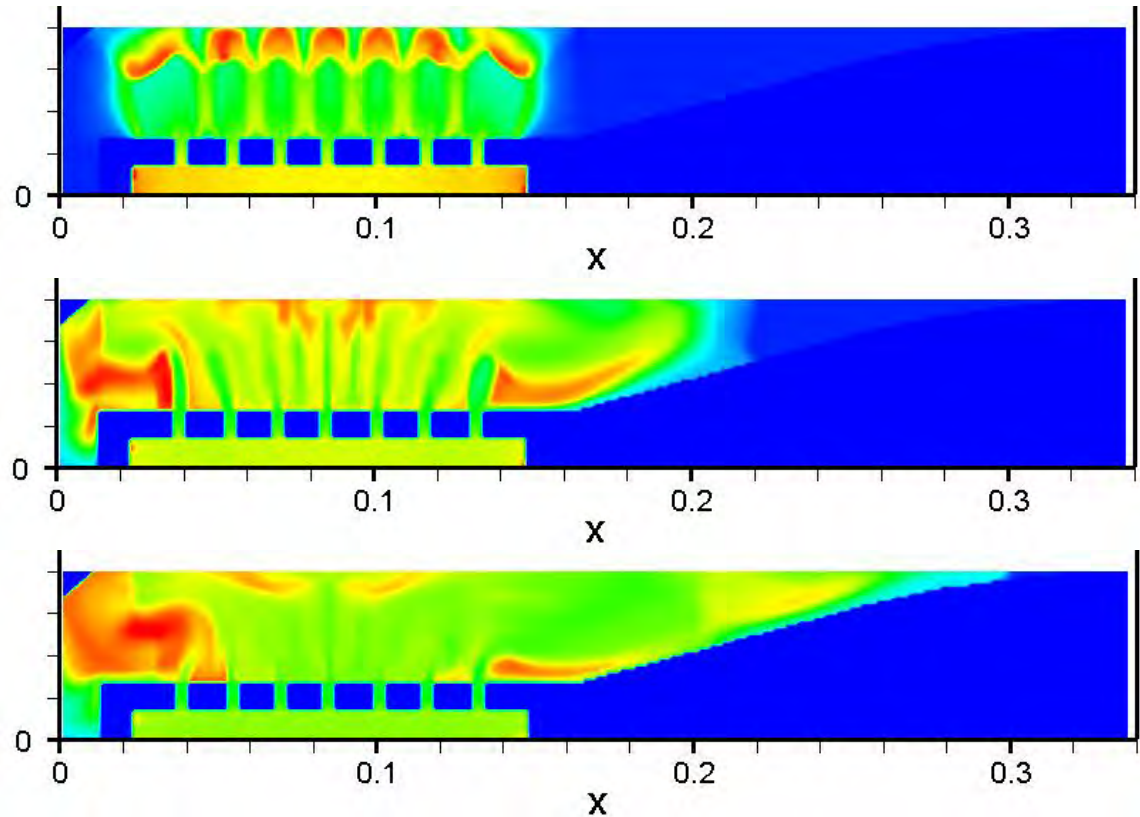
Description of QIMIBS



Background

2D mortar code

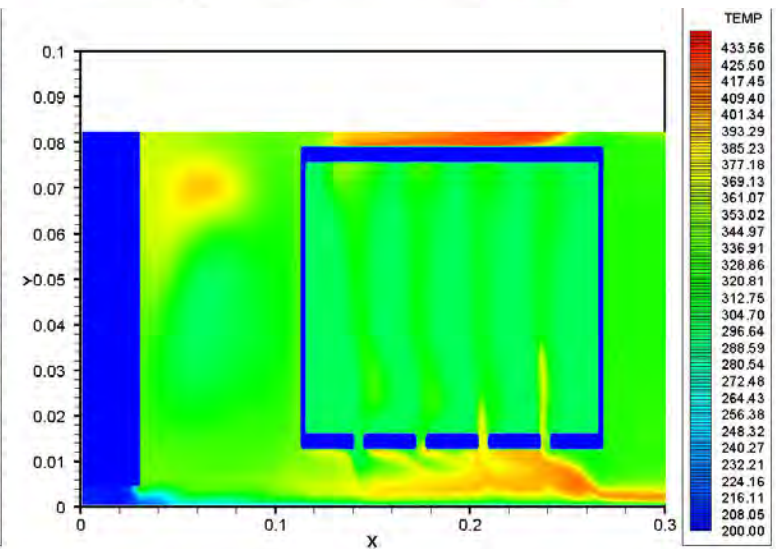
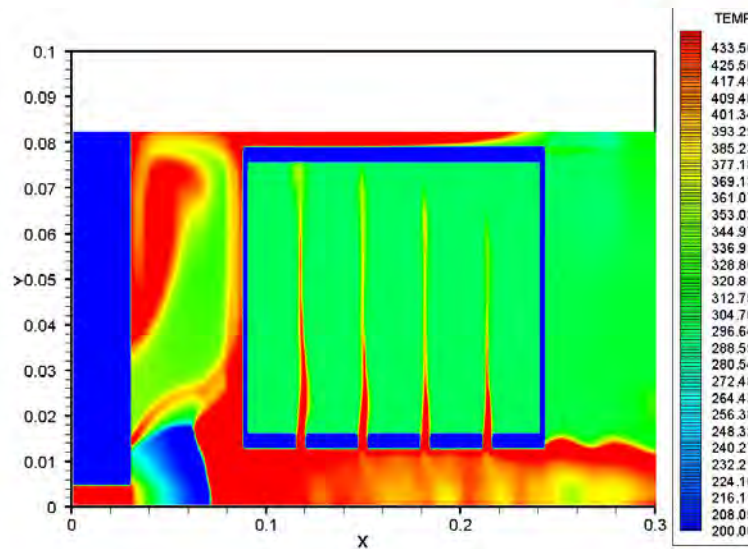
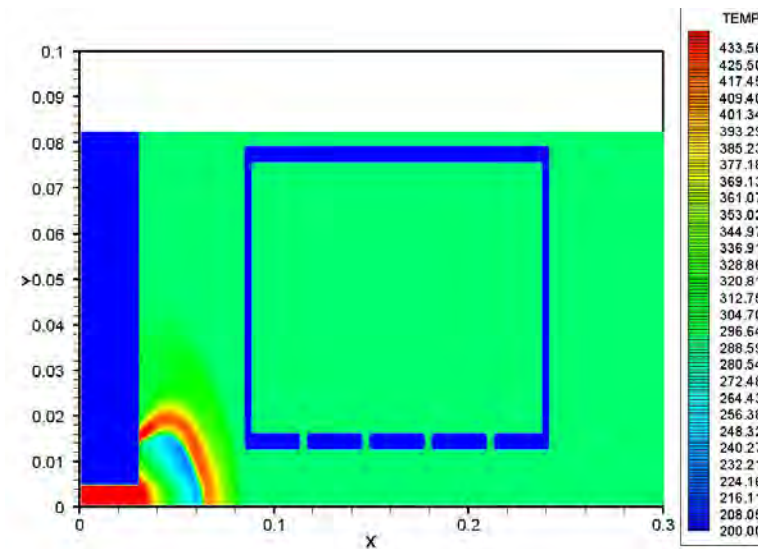
- “ Developed initially with MOD funding
- “ Developed further using QinetiQ funding
- “ Details presented at 22nd International Symposium on Ballistics
- “ Ability to represent internal solid boundaries and burst discs
- “ Modified for CTA, MCS & other applications



base flow equations

$$\begin{aligned}
 \frac{\partial}{\partial t}(\rho \epsilon) + \frac{\partial}{\partial z}(\rho \epsilon u) + \frac{\partial}{\partial r}(\rho \epsilon v) &= -\frac{\epsilon \rho v}{r} + \dot{m}_{ig} + \sum_{k=1}^n \dot{m}^k \\
 \frac{\partial}{\partial t}(\rho \epsilon u) + \frac{\partial}{\partial z}[\epsilon(\rho u^2 + p)] + \frac{\partial}{\partial r}(\rho \epsilon uv) &= -\frac{\epsilon \rho uv}{r} + p \frac{\partial \epsilon}{\partial z} + \sum_{k=1}^n (\dot{m}^k u^k - f_z^k) \\
 \frac{\partial}{\partial t}(\rho \epsilon v) + \frac{\partial}{\partial z}(\epsilon \rho uv) + \frac{\partial}{\partial r}[\epsilon(\rho v^2 + p)] &= -\frac{\epsilon \rho v^2}{r} + p \frac{\partial \epsilon}{\partial r} + \sum_{k=1}^n (\dot{m}^k v^k - f_r^k) \\
 \frac{\partial}{\partial t}(\rho \epsilon E) + \frac{\partial}{\partial z}[\epsilon \rho u(E + p/\rho)] + \frac{\partial}{\partial r}[\rho \epsilon v(E + p/\rho)] &= -\frac{\epsilon \rho v}{r}(E + p/\rho) + \dot{m}_{ig} Q_{ig} \\
 &\quad - W + E_E + \sum_{k=1}^n [\dot{m}^k (Q_p^k + \kappa^k) - p \left(\frac{\partial(\epsilon^k u^k)}{\partial z} + \frac{\partial(\epsilon^k v^k)}{\partial r} \right) - u^k f_z^k - v^k f_r^k - q^k N^k S^k] \\
 \frac{\partial}{\partial t}(\rho^k \epsilon^k) + \frac{\partial}{\partial z}(\rho^k \epsilon^k u^k) + \frac{\partial}{\partial r}(\rho^k \epsilon^k v^k) &= -\dot{m}^k - \frac{\epsilon^k \rho^k u^k}{r} \\
 \frac{\partial}{\partial t}(\rho^k \epsilon^k u^k) + \frac{\partial}{\partial z}[\epsilon^k(\rho^k (u^k)^2 + p + p_{is}^k)] + \frac{\partial}{\partial r}(\rho^k \epsilon^k u^k v^k) &= p \frac{\partial \epsilon^k}{\partial z} - \frac{\epsilon^k \rho^k u^k v^k}{r} - \dot{m}^k u^k + f_z^k \\
 \frac{\partial}{\partial t}(\rho^k \epsilon^k v^k) + \frac{\partial}{\partial z}(\epsilon^k \rho^k u^k v^k) + \frac{\partial}{\partial r}[\epsilon^k(\rho^k (v^k)^2 + p + p_{is}^k)] &= p \frac{\partial \epsilon^k}{\partial r} - \frac{\epsilon^k \rho^k (v^k)^2}{r} - \dot{m}^k v^k + f_r^k \\
 \frac{\partial}{\partial t}(N^k) + \frac{\partial}{\partial z}(N^k u^k) + \frac{\partial}{\partial r}(N^k v^k) &= -\frac{v^k N^k}{r}
 \end{aligned}$$

03 IB Modelling of UPCS2



modelling strategy

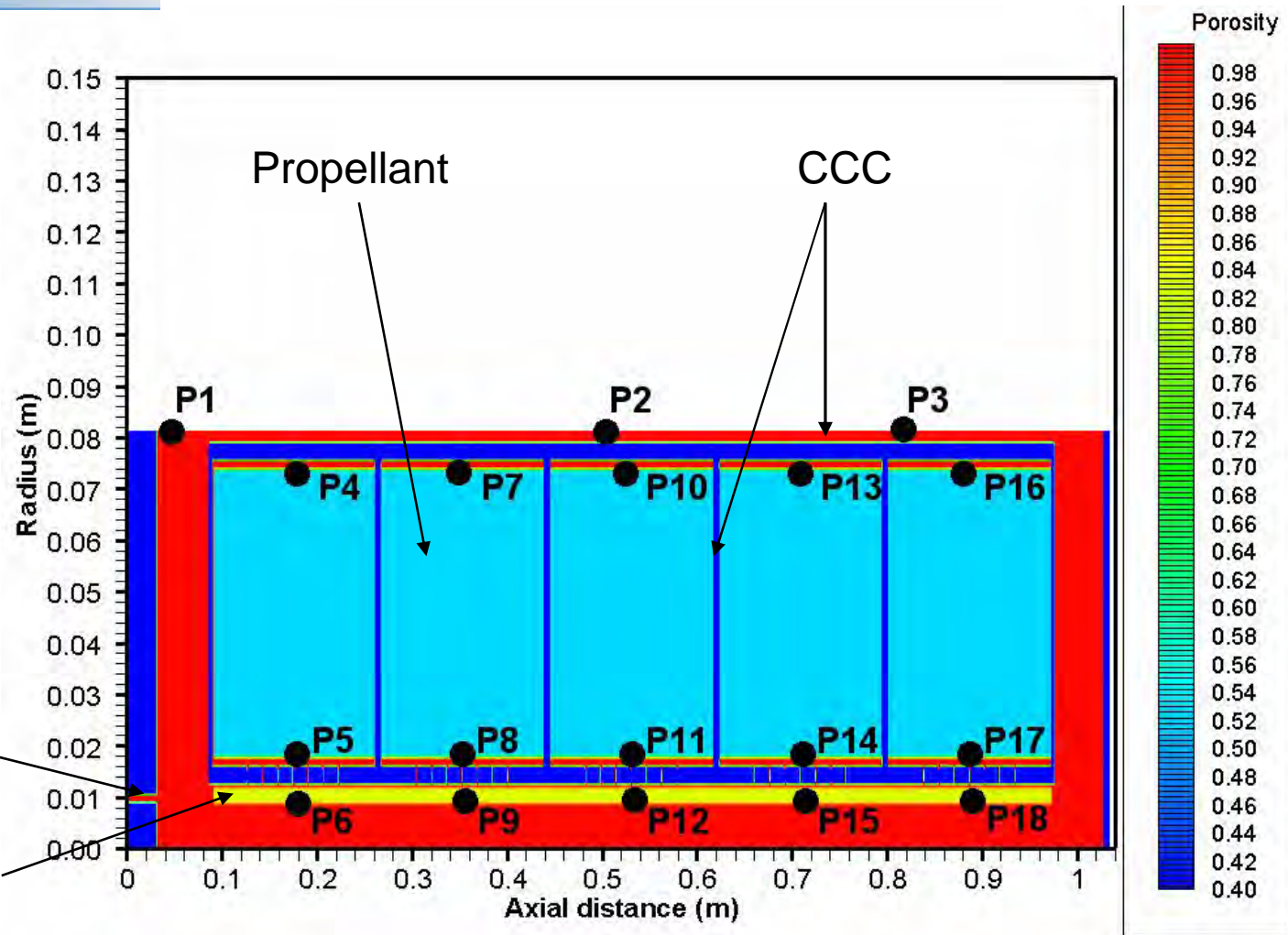
- “ No single code available that can model all details
- “ Various ignition scenarios were investigated using QIMIBS
 - Prediction of ignition time for each module
 - Ignition at breech
 - Ignition at projectile
 - Ignition at mid-chamber
- “ Estimated ignition delays were input to QIBS (1D code)
 - Predicted pressure profiles compared with experiment
- “ Ignition at breech and mid-chamber did not produce pressure profiles of desired shape
- “ Most likely ignition scenario was ignition adjacent to projectile

Initial geometry for modelling

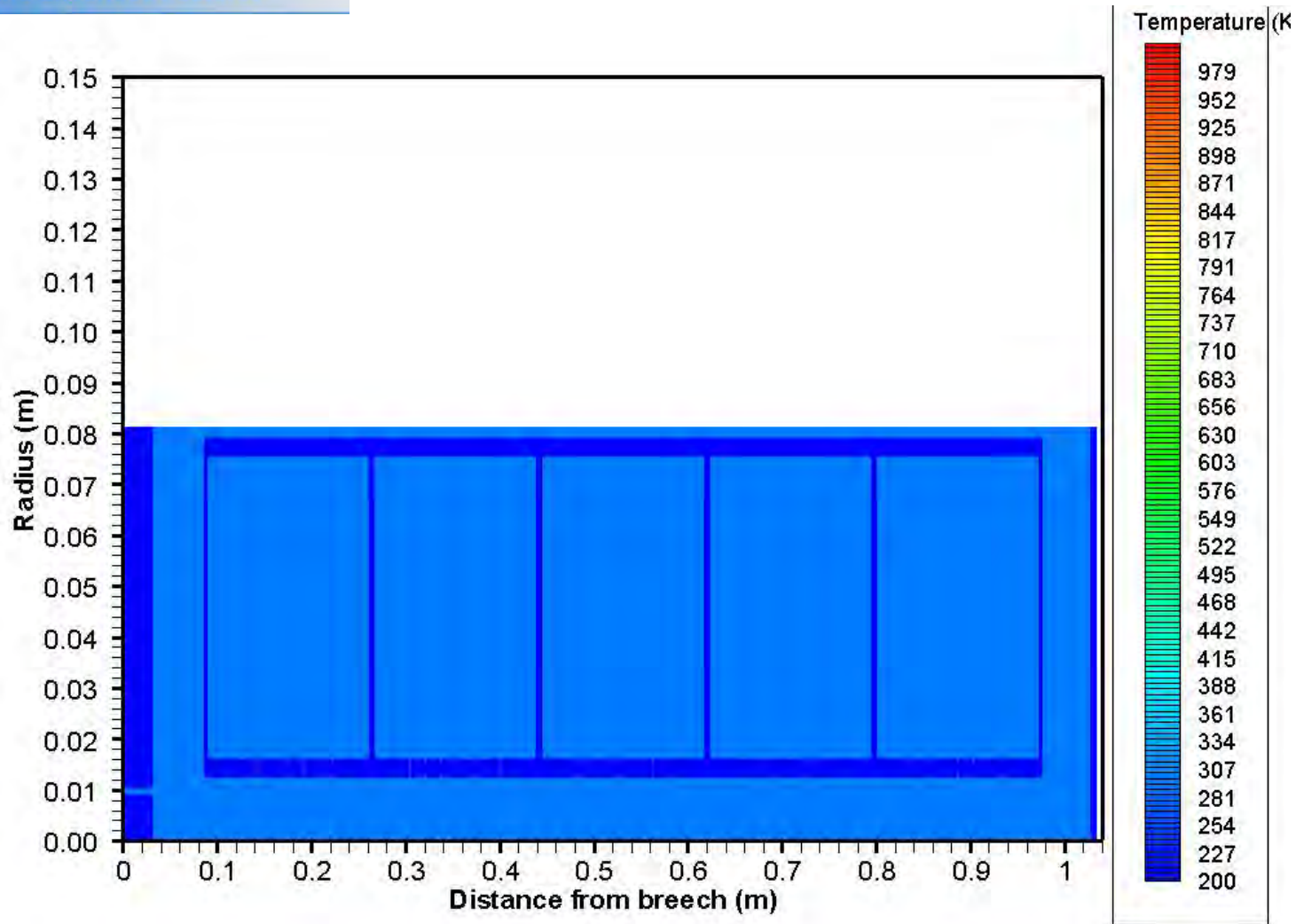
P1-P18 are fictitious pressure gauges

Primer

Igniter

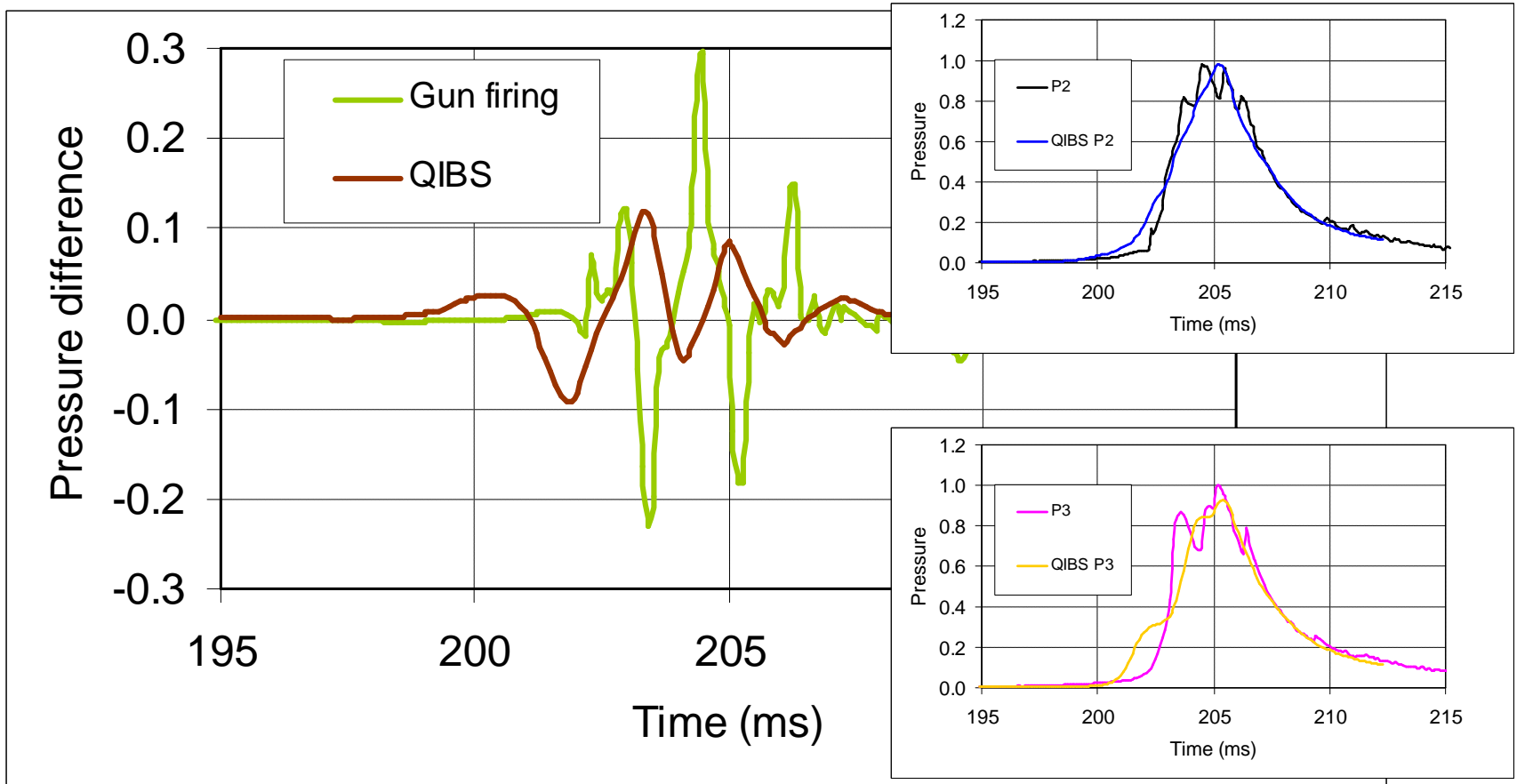


QIMIBS simulation



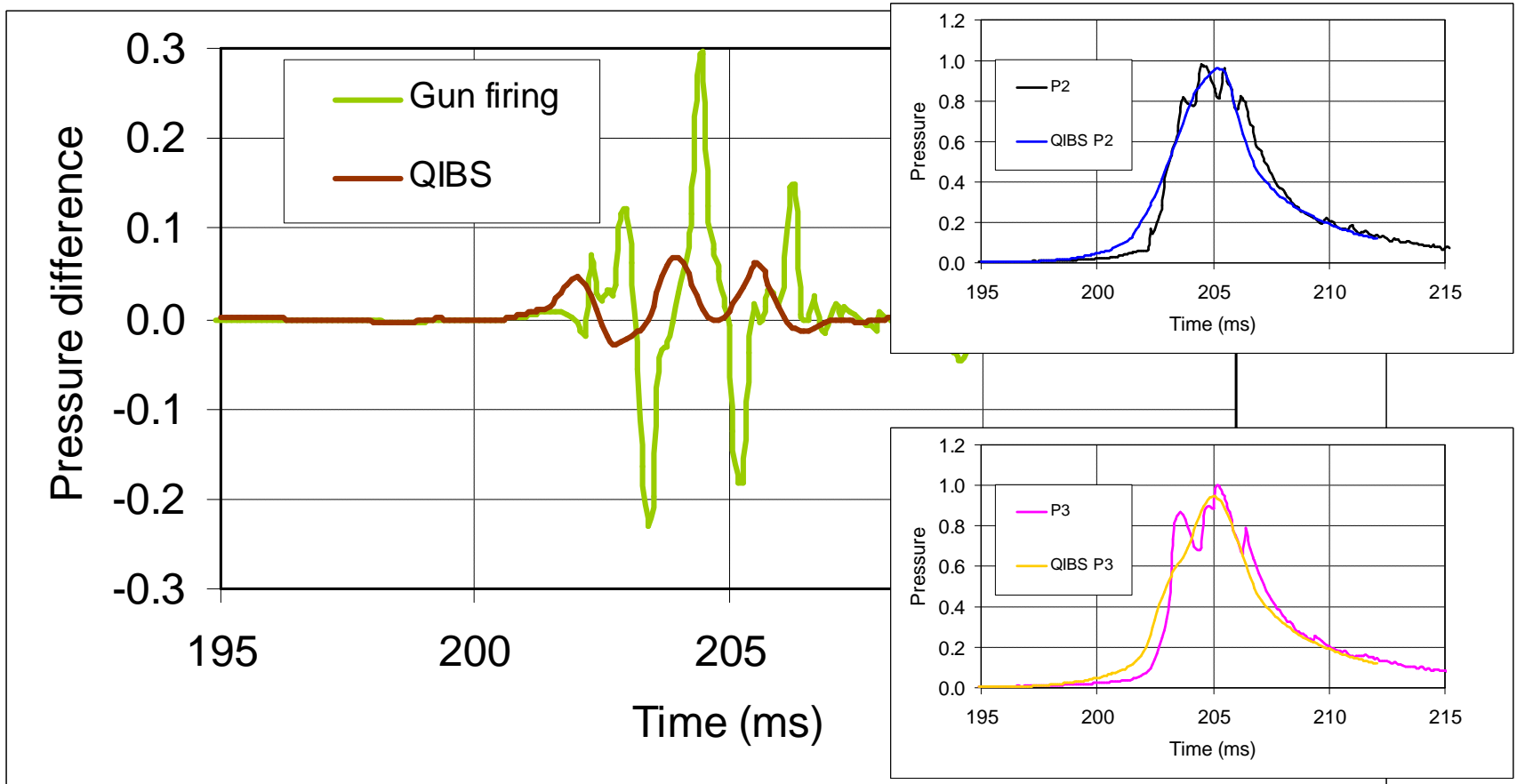
example . breech ignition

- “ Predicted and measured pressure differences are out of phase



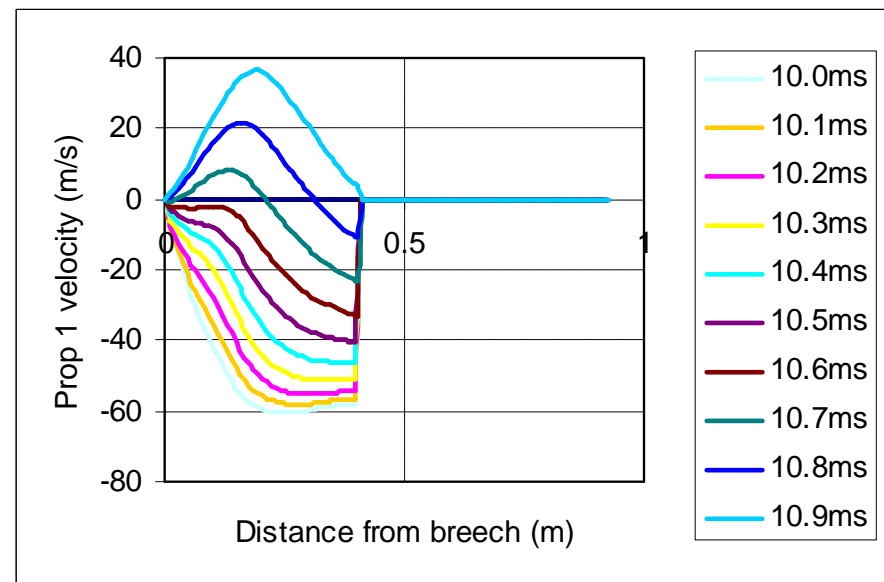
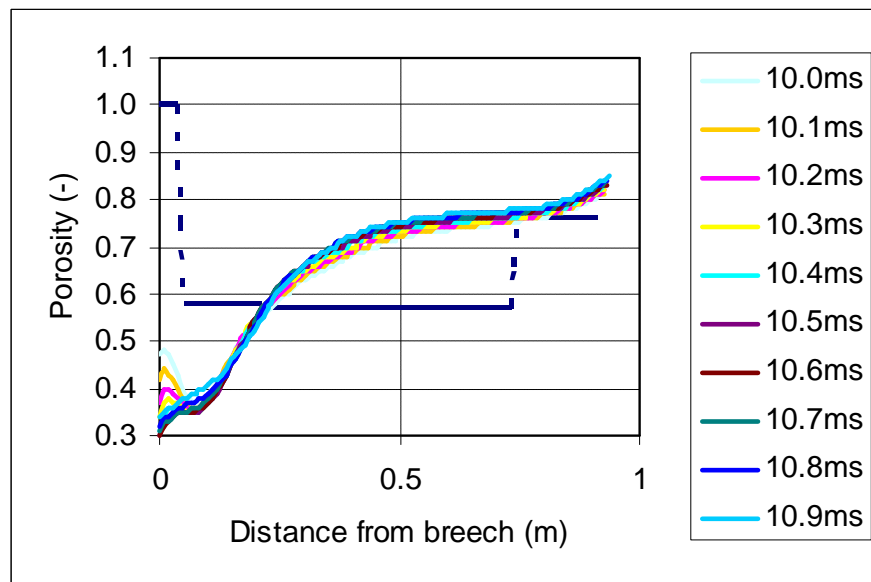
example . ignition at projectile

- “ Predicted and measured pressure differences are slightly out of phase



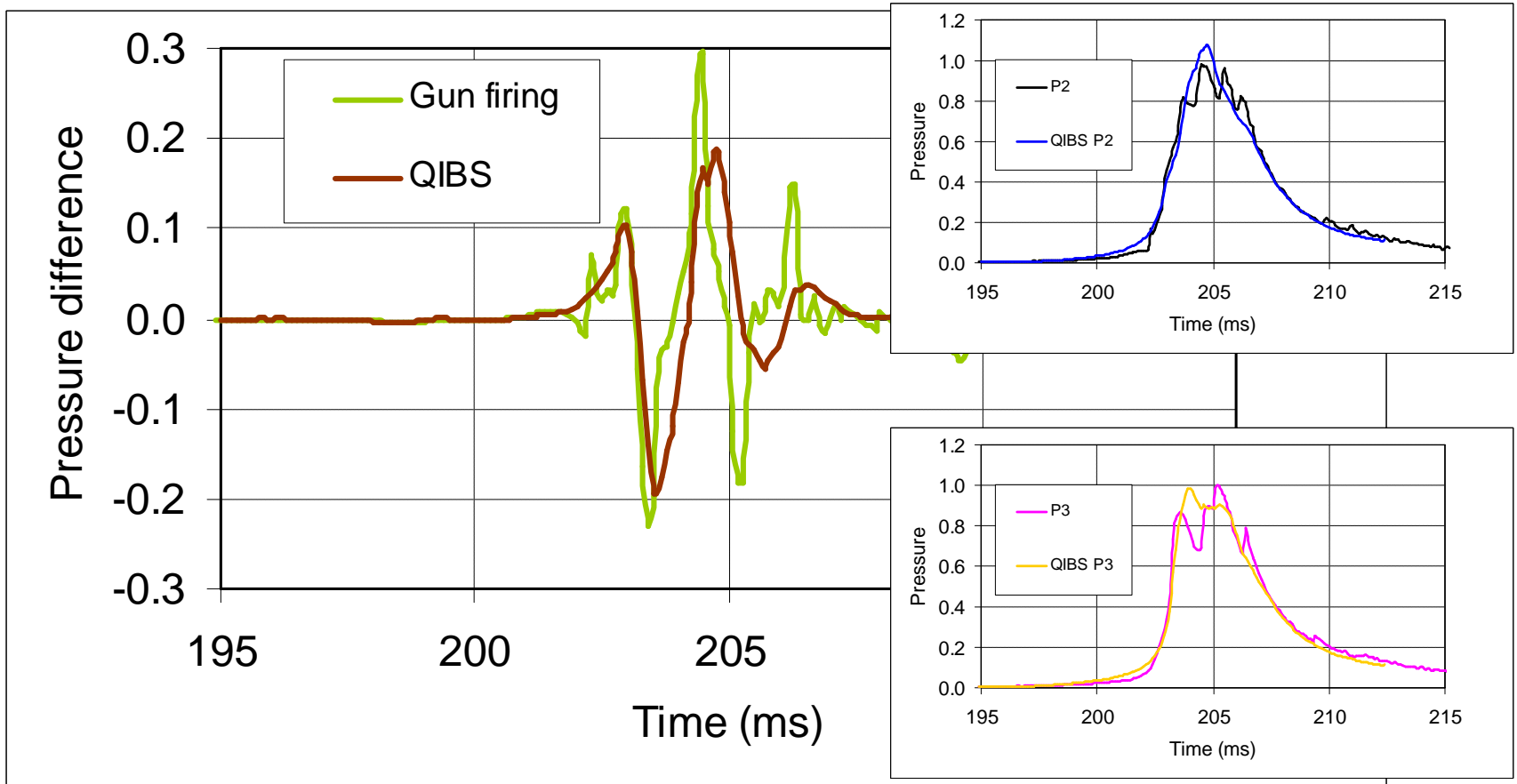
Ignition at projectile

- Analysis of QIBS simulation showed
 - Compression of propellant bed for module 1 propellant at breech
 - Significant rearward propellant velocity
 - Propellant shatter likely



Ignition at projectile . final simulation

- Excellent agreement up to maximum pressure



- “ The quantity of gun powder in the flash tubes was marginal for simultaneous ignition
- “ The charge appears to have been ignited at the projectile end with the modules closer to the breech then being subsequently ignited in turn
- “ Ignition at the projectile end then drove the charge towards the breech at over 100 mph and caused shatter of propellant in the module nearest to the breech
- “ The ensuing pressure wave drove the charge back towards the projectile at over 200 mph and shattered yet more propellant
- “ Subsequent simulations indicate that gun powder should also be present on the outside of the flash tube (in contact with the propellant) to improve the ignition train
- “ Future work - better representation of CCC to allow simulation of full IB cycle



*Your complimentary
use period has ended.
Thank you for using
PDF Complete.*

[Click Here to upgrade to
Unlimited Pages and Expanded Features](#)

QinetiQ

The Global Defence and Security Experts

www.QinetiQ.com

© Copyright QinetiQ limited 2008

Launch Dynamics Environment of a Water Piercing Missile Launcher

Jon J. Yagla

DTI Associates, Dahlgren, VA

John Basic, Samuel Koski, Brian Myruski

NSWC Dahlgren Division, Engagement Systems Department, Dahlgren, VA

Chris Weiland and Pavlos Vlachos

Virginia Tech College of Engineering, Blacksburg, VA

INTRODUCTION

The Water Piercing Missile Launcher (WPML) is based on the Concentric Canister Launcher (CCL). The launcher uses the gas jet emitted from the CCL to pierce the ambient water above a submarine or other submerged platform. The missile is then released and flies through the gas column to the surface. The launcher has the potential to eliminate pyrotechnic gas generators and pumps as the means of expelling missiles from submarines, and also has the potential for eliminating complex and noisy pressure balancing systems. Each WPML is a complete launching system, which houses the missile during transport, guides the missile during its initial flight, provides self-contained gas management, and contains all of the necessary electronics to launch a missile [1]. Costs may also be reduced as compared to existing systems that employ pyrotechnic gas generators and complex pressure balancing systems.

The CCL is composed of two concentric tubes joined by longerons running the length of the tubes and spaced at 90-degree intervals, Figure 1. The longerons provide structural support for the CCL. The missile is housed in the inner cylinder. The rocket motor nozzle end of the launcher is capped by a hemisphere, with a radius equal to the outer cylinder radius. Thrust augmentation (gun effect) is controlled by a port near the motor nozzle exit. Exhaust gases from the rocket motor strike the hemispherical end-cap and are re-routed 180-degrees through the annular region between the two cylinders, exiting at the tip of the launcher. Thus, the exhaust gases are safely re-directed along the line of fire, Figure 2.

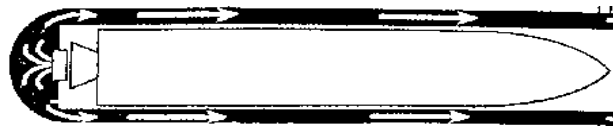


Figure 1. Concentric Canister Launcher

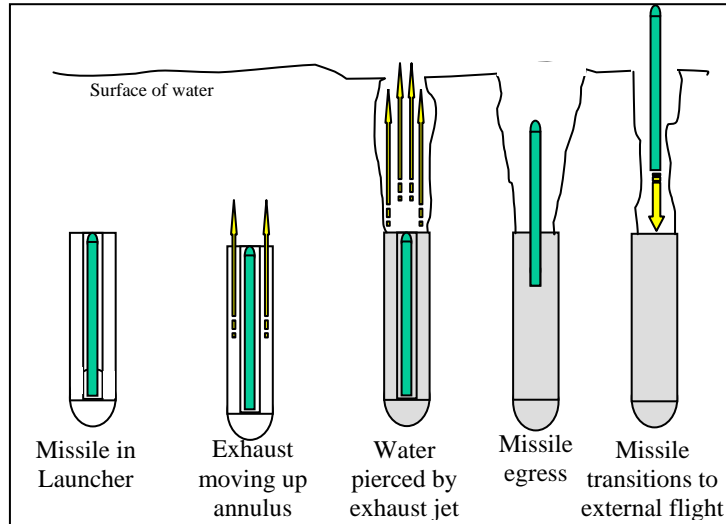


Figure 2. Water Piercing Missile Launcher Concept.

A two-dimensional Navier-Stokes calculation was performed to simulate the effects of 21-inch diameter booster motor inside a submerged CCL. The computer code used was CFDLIB, which was developed by Los Alamos National Laboratory. The water is represented as Lagrangian mass points, related to each other through stress-strain constitutive equations. The stress in the fluid is caused by relative motion of individual particles. An inflow boundary condition of rocket-motor exhaust was located at the exit plane of the CCL. The boundary condition at the exit was calculated using an in-house semi-empirical code called LAX. Figure 3 shows the volume fraction contours for three different time steps using CFDLIB. Superimposed on the contours is an uncoupled rigid-body dynamics solution of a cruise missile exiting the CCL and flying through the missile exhaust. The color fringes are blue for water, red for exhaust gas, and intermediate colors for a mixture of gas and water.

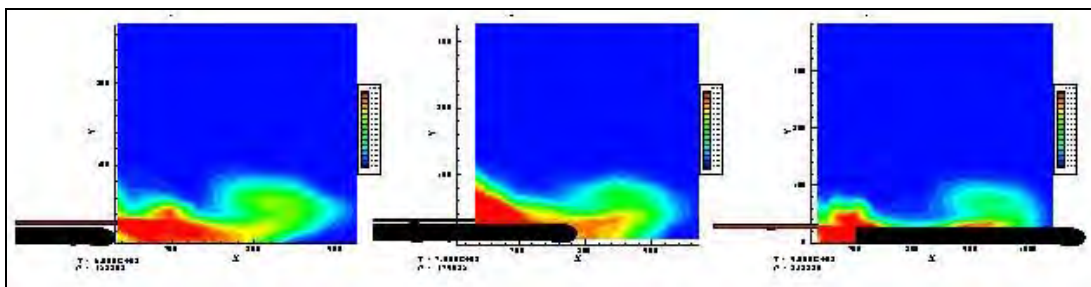


Figure 3. Computer Simulation of Water Piercing Effect and Motion of Missile

Sub scale launchers were built and tested in aquariums. A missile propelled by a 2.75-inch rocket motor was launched and recovered dry from a submerged CCL, Figure 4. Following the favorable result with the 2.75-inch rocket motor, the scale was then doubled and an ~ 8' long x 300 lb. missile propelled by a 5" JATO motor was launched with 20' of water over the launcher, Figures 5 and 6. The figure on the right is a composite view using video camera data for the top half and underwater video for the bottom. The two flashes in the bottom are pyrotechnics fired to release the missile at the right time for it to arrive at the surface at exactly the same time as the jet tip.



Figure 4. Flight Of A Missile Propelled By A 2.75 MK66 Rocket Motor
(The Bright Spot On The Left, Over The Tank, Is The Exhaust).

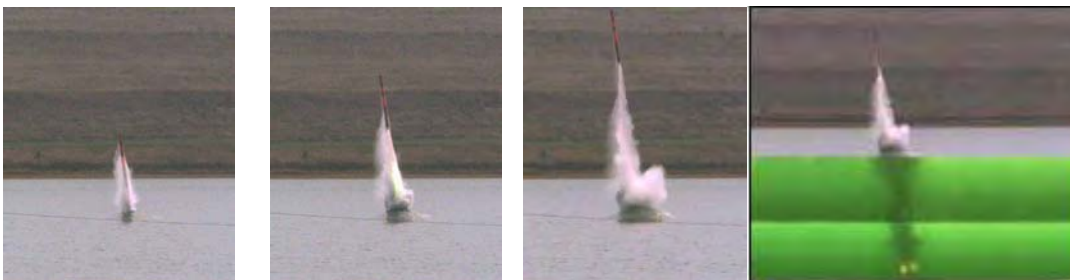


Figure 5. 5-Inch Diameter, 8- Foot Long Missile Propelled By A MK117 JATO Motor.

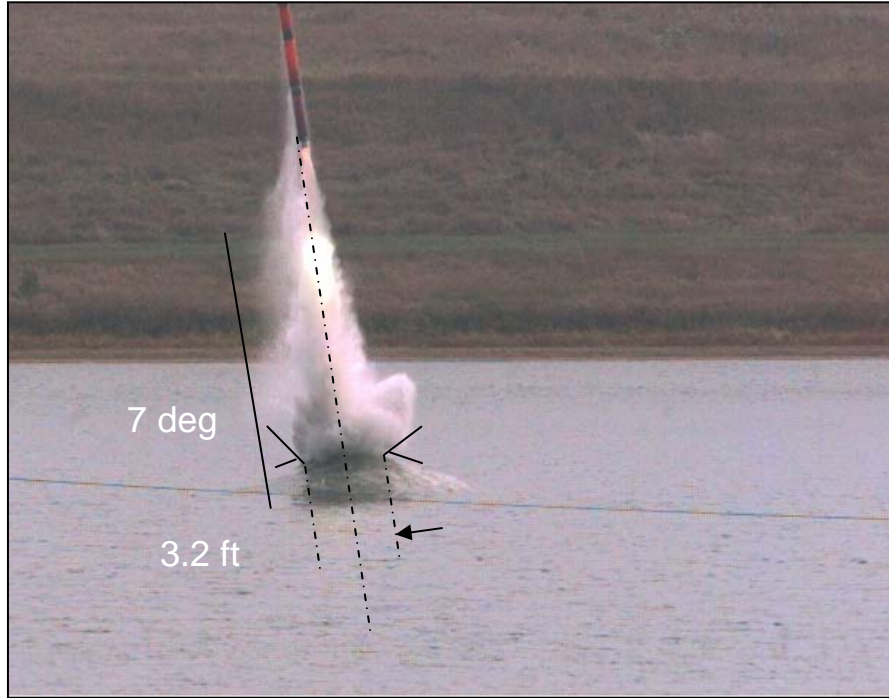


Figure 6. Details The 5-Inch Diameter Missile Transition To Atmospheric Flight.

The remainder of the paper discusses the jet motion and the underwater launch environment. There is very little literature on the formation and initial propagation of transient gas jets in water. Practically all of the literature is about steady jets. Further, there is ample information about water jets in water, and some information about gas jets in air, but very little about gas jets in water.

JET MOTION

The space – time trajectories of the jet tip have been measured for many WPMLs of sizes ranging from 1” to 27” in diameter [2]. The trajectories approximately obey a scaling law, Figure 7. Here the nondimensional jet tip height above the launcher exit plane is plotted against nondimensional time. The jet tip height is nondimensionalized by dividing the observed height by the jet momentum length, L_m , [3]. The nondimensional time is the observed time divided by L_m/V , where V is the jet velocity at the exit plane.

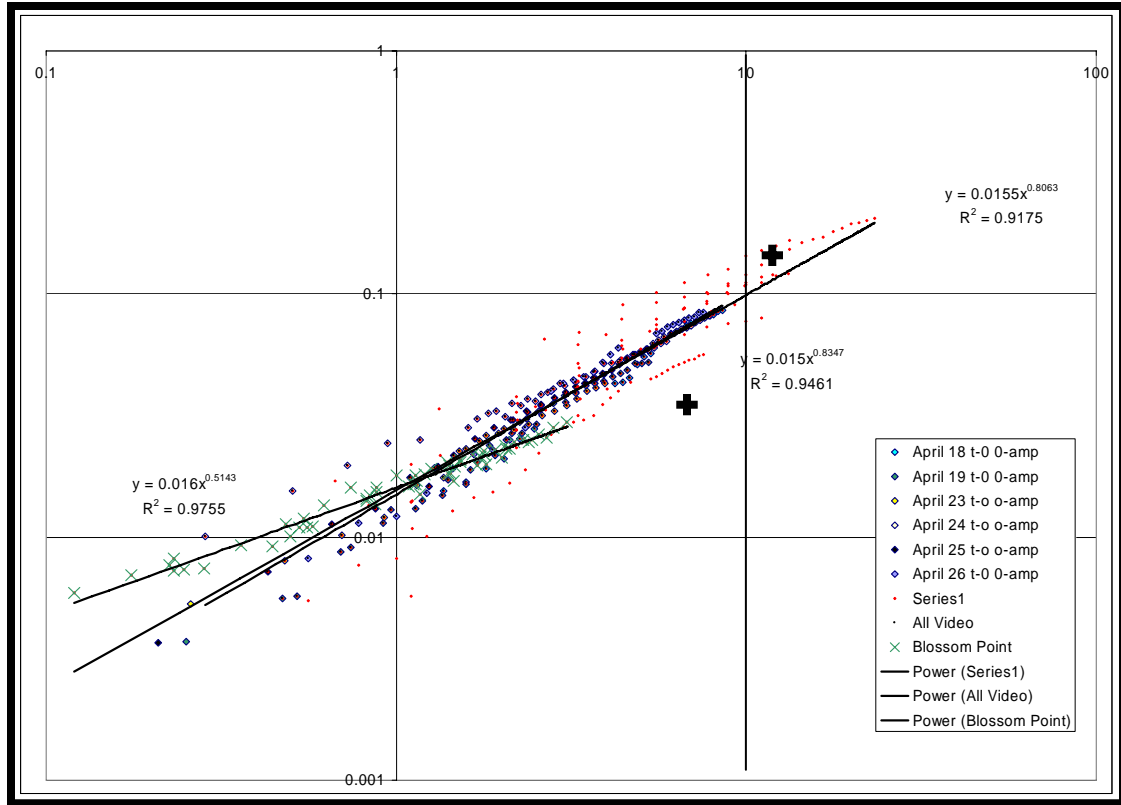


Figure 7. Jet Tip Trajectory Scaled Distance (Ordinate) Versus Scaled Time (Abscissa) Using Data From Mk 66 (2.75-Inch), JATO (5-Inch), And Zuni (5-Inch) Motors At Depths From 6 To 42 Ft. The Mk 66 Motors Were Fired In An 8-Ft Diameter Tank At Blossom Point.

To prepare for the flyout test using the JATO Motor, a preliminary static test with the same launcher was conducted at a depth of 20 ft with only the motor and no missile present. Figure 8 is the space-time trajectory of the JATO at 20 ft depth as determined using an underwater acoustic camera. The formula for the jet tip trajectory is on the upper right corner:

$$y = -6.2508 t^2 + 24.061 t + 0.235 \quad (1)$$

The formula can be differentiated with respect to time to obtain the jet tip velocity:

$$V = -12.5 t + 24.06 \quad (2)$$

These formulae are sufficient to determine the time to release missile in order for it to arrive at the surface at the same time as the jet tip reaches the surface. However they do not provide any details on the internal structure of the jet.

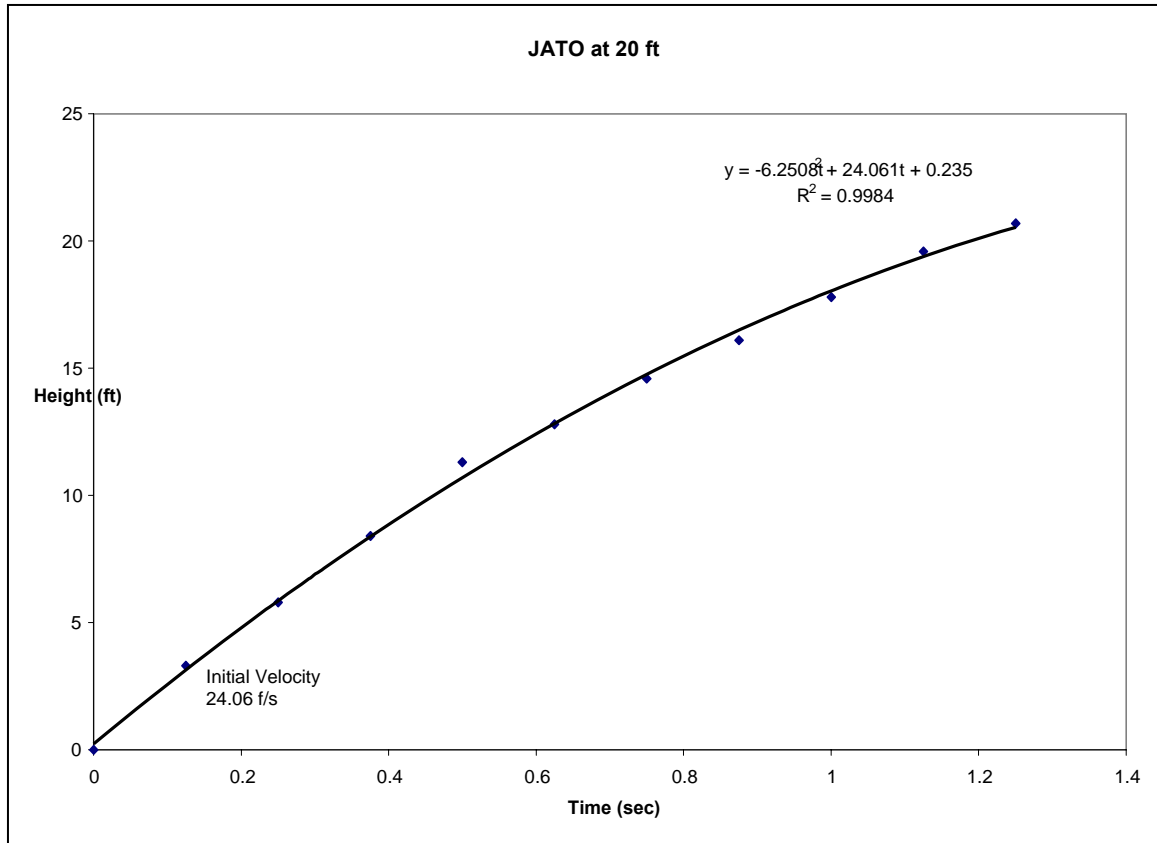


Figure 8. Space-Time Trajectory Of Jet Tip Using JATO Motor And 20 Ft Of Water Over The Launcher.

An assumption that was used to work out the jet flow over the missile is that the jet gas velocity is everywhere the same in the jet and the same as the jet tip: like blowing up a long skinny balloon. There is a high velocity in the filler neck of the balloon, but it fills slowly, so the tip velocity is small by comparison. Equation 2 was used for the jet tip velocity. We consider this a very low order approximation to the launch environment. Better data is now available. However, the launch dynamics were accurately computed with the simple model. There is a considerable effort in the laboratory to refine the launch environment properties using CFD and semi-empirical methods.

JET CHARACTERISTICS

Jet Basics

Figure 9 shows the basic geometry of a steady turbulent round jet [4]. The zone of flow establishment is the region in which the exit geometry is important to the detailed structure of the jet. Beyond this zone the exit geometry doesn't matter, and the profiles of velocity $u(x,r)$ and concentration of entrained materials $c(x,r)$ take

the Gaussian shape as shown in the figure. For the WPML, the outlet is an annulus, so the zone of flow establishment can be determined from the equivalent diameter of the annulus. The equivalent diameter is $(4A/\pi)^{1/2}$, where A is the free area of the annulus. For the JATO launcher the free area is 0.599 sq. ft. and the equivalent diameter is 0.87 ft. Therefore the zone of flow establishment should end 5.4 ft above the launcher.

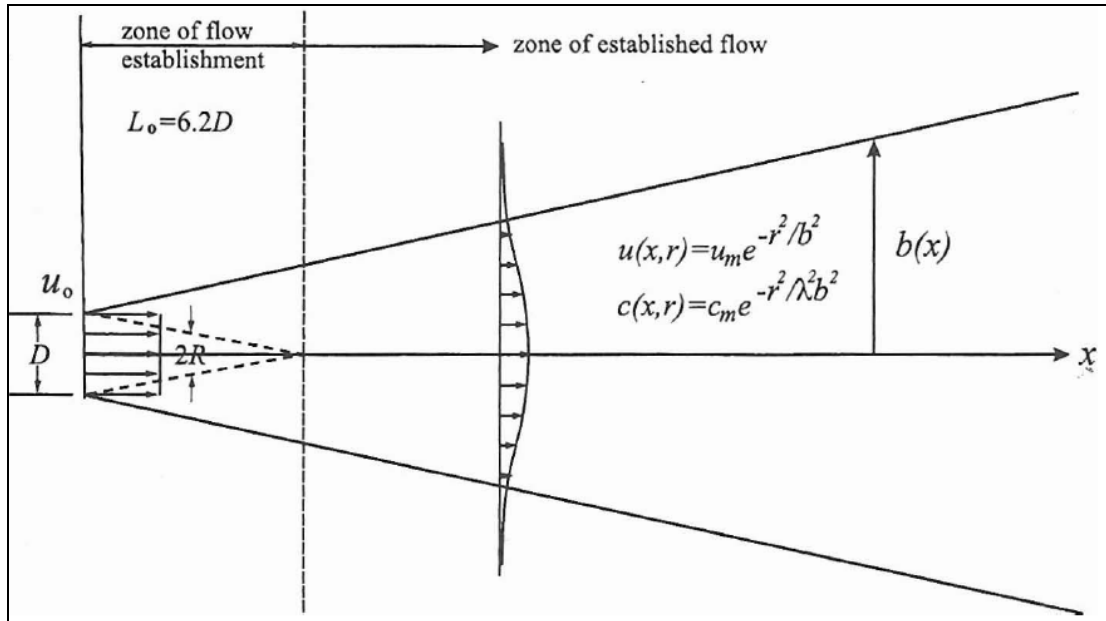


Figure 9. Basic Geometry Of A Turbulent Round Jet.

The data in references 3 and 4 are mainly from water jets discharging into water. For these jets $b(x) = 0.12x$. Here $b(x)$ is the jet radius. The half angle of the cone is 6.8 degrees. For rocket exhaust jets discharging into air, the jets are broader. Figure 10 shows rocket exhaust jets in air for three cases spanning many orders of magnitude in size. The spreading rate is $b(x) = 0.26x$ and the half angle is 13.7 degrees.

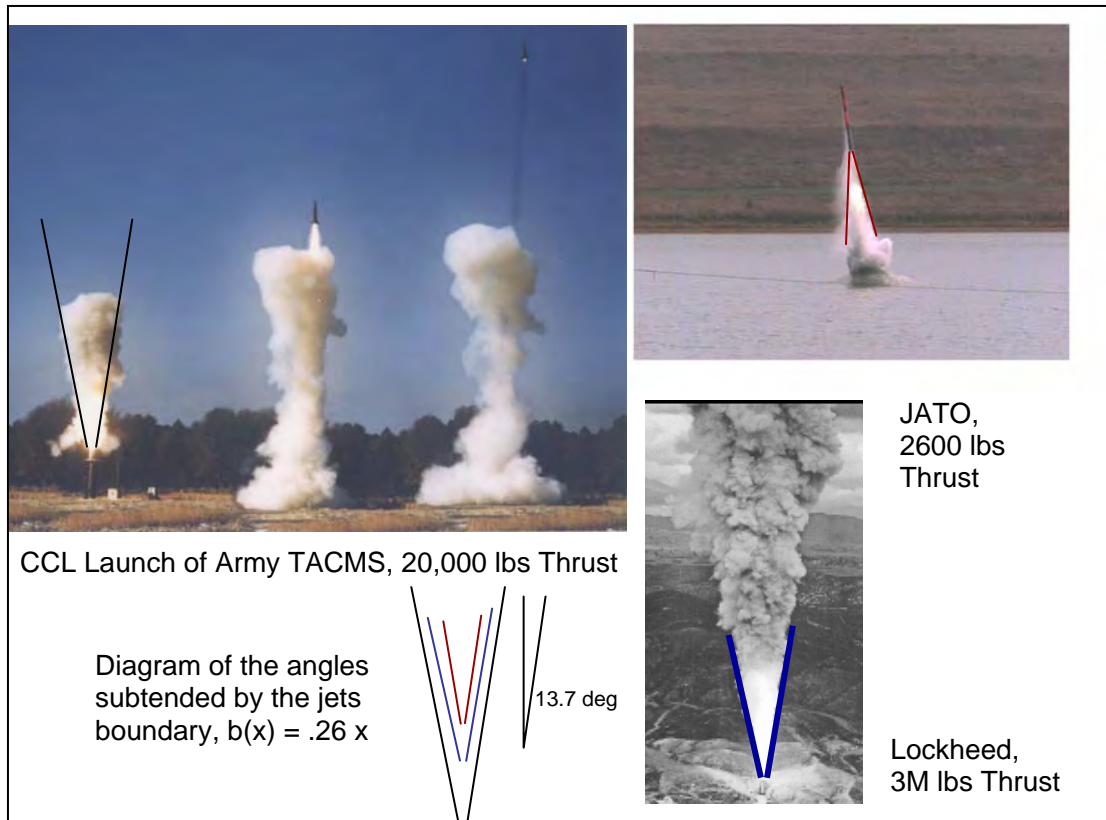


Figure 10. Rocket Exhaust Jets In Air Over A Wide Range Of Motor Sizes.

There is very little data for gas jets discharging into water. Intuition suggests the spreading rate should be insensitive to the exhaust chemical composition and somewhere between the two cases above. A jet from a MK66 motor fired with 10 ft of water over a 7-in diameter CCL is shown in Figure 11. This shows $b(x) = 0.13 x$ and a half angle of 7.4 degrees. The extent to which the cylindrical boundary just four feet from the jet centerline influenced the jet diameter is not known.

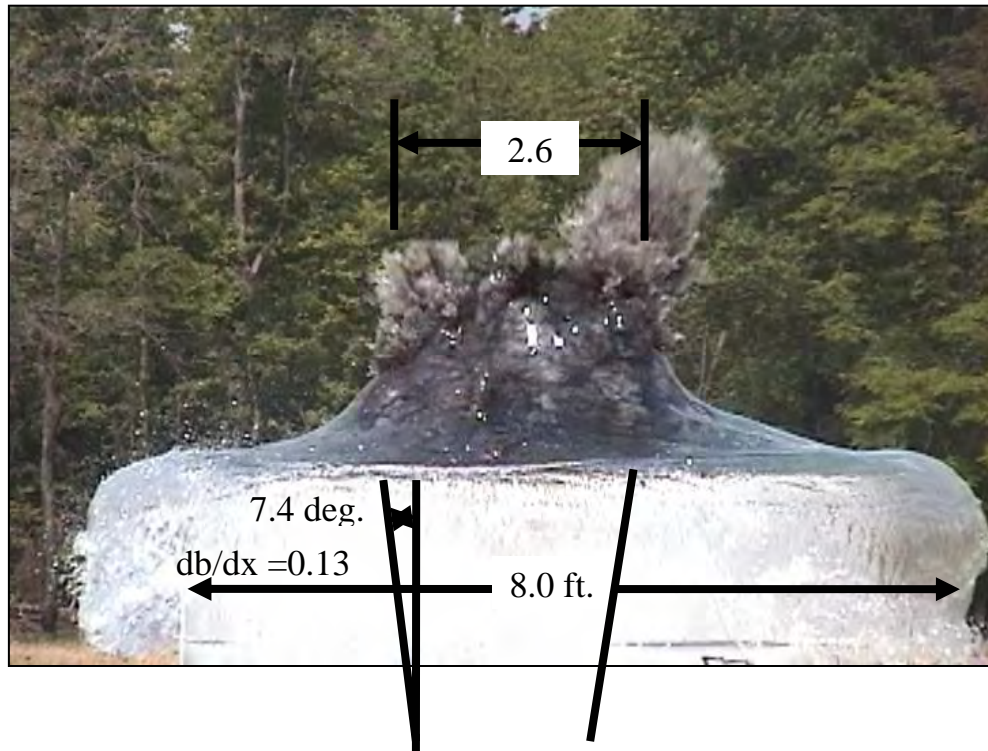


Figure 11. Water Piercing Jet From MK66 Motor At A Depth Of 10 Ft.

The data of Loth and Faeth, [5] for a steady air jet discharging into water show a zone of flow establishment ending at 8 diameters, with a jet width of $.5x$ starting at 8 diameters and diminishing to $.4x$ at 40 diameters, for a broad range of exit conditions from subsonic $M \sim 0.6$ to supersonic with $M > 2$. Their jet width is defined as twice the radius at which the air/water ratio is 0.5. The slope db/dx would be 0.25 decreasing to 0.2. Their data show at $M \sim 0.6$, the centerline of the jet out to 20 diameters is pure air. For $M = 1$ the centerline is pure air out to 30 diameters. As the Mach number was increased, penetration of pure air out to 60 diameters along the centerline was observed. Their data also shows that a region of 90% air at least 4 exit diameters in diameter extends out to 80 diameters for $M = 0.8$ and $M = 1.0$ jets, and even broader and farther for higher Mach numbers. The centerline dynamic pressure is constant at the gas outlet value for 6 diameters, then diminishes very rapidly. The dynamic pressure is down to 10% of the outlet value at 30 diameters. Although greatly diminished, the cross section dynamic pressure profiles are broad enough to affect a missile out to 70 diameters where the diameter of the profile is about 20 exit diameters.

We have been able to obtain sonogram type images, Figure 12, of jets from water piercing missile launchers. They show a nearly constant jet diameter of 0.15 the value of x at the surface. The images show a distinct interface, but the gas/air fraction at the image boundary is not known.

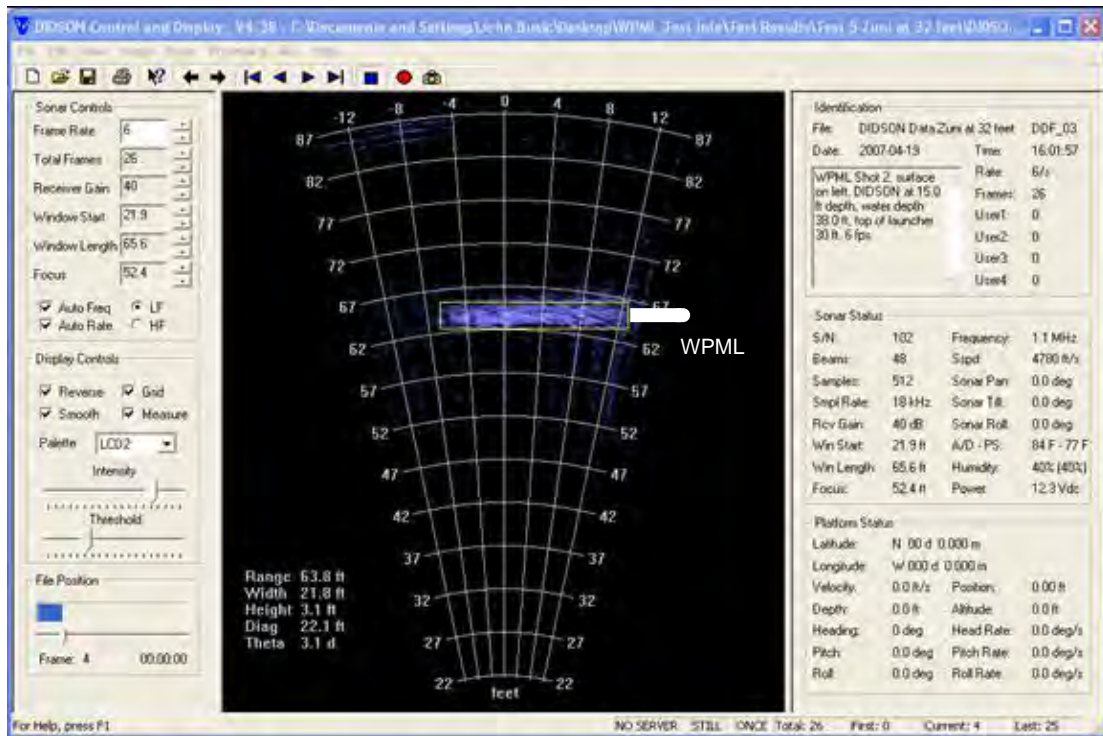


Figure 12. Image Of A Vertical Exhaust Jet From A Water Piercing Missile Launcher From An Acoustic Camera (Rotated 90-Deg, WPML Sketch Added).

LAUNCHER EXIT PLANE PROPERTIES

Computation of the Jet Exit Properties

The jet from a MK117 JATO motor is pure gas as it exits the rocket nozzle and travels up the annular space between the concentric cylinders of the gas management system. The gas properties are computed using the propellant chemical composition and nozzle geometry and an equilibrium thermochemical computer program. The MK 117 JATO motor has properties shown in Table 1. The left side of the table shows the physical properties and the right side shows the thermodynamic state and velocity at the exit. These properties are computed using a one-dimensional CFD program that expands the exhaust into the launcher hemihead and computes wave motion in the annular space. The exit plane ambient pressure depends on the depth over the launcher. The hydrostatic pressure of the water is the exit plane pressure boundary condition for the CFD analysis. This causes the gas to expand to the indicated Mach number. More powerful motors can cause the gas to expand to unity Mach number (choked flow). Notice from the table the sensitivity of the exit condition to the depth.

Table 1. Rocket Exhaust Properties

JATO		
Pressure	psi	1800
Temp	deg K	2377
Mol. Wt.	g-mol	23.23
R	$\text{ft}^2/(\text{s}^2 \text{ R})$	2140
Cv	$\text{ft}^2/(\text{s}^2 \text{ R})$	9369
Cp	$\text{ft}^2/(\text{s}^2 \text{ R})$	11510
Gamma		1.2284

Depth	ft.	10.0	20.0
P	psia	19.1	23.6
V	f/s	1982	1630
Rho	lb/in ³	7.50E-06	9.10E-06
Mach		0.680	0.560

The water provides lateral confinement of the jet, so the spreading rate is less than in air. As the jet moves up and away from the launcher, several processes take place. First is turbulent mixing. The jet has a high Reynold's number and is inherently unstable. Eddies form on the interface between the jet and the water. Water eddies are entrained by the jet, and gas eddies are decelerated and enter the water. This is called turbulent mixing and causes the velocity of the gas to decrease and the entire ambient water medium to be set in motion, with streamlines leading in laterally from afar and turning upward and becoming nearly parallel to the jet in the vicinity of the jet boundary. Momentum is conserved. Momentum gained by the entrained water is equal to momentum lost by the jet. This causes the jet to slow down and broaden with height. Figure 5 shows the jet at the time it reaches the surface. The light flashes from the release pyrotechnics are approximately one diameter apart, so the broadening is apparent.

SUFRACE INTERACTION, CROSS FLOW, AND BUOYANCY

Jet Broadening at the Surface and Cross Flow

There are actually two stages of broadening, the first being normal jet broadening due to turbulent mixing, and a second stage of much more rapid broadening immediately near the surface. Figure 13 shows the time averaged shape of the stagnation edge of air jets from a CCL in the water tunnel at Virginia Tech [6]. The cross flow is from right to left. Jet exit Mach numbers in the range of 0.28 to 1.9 are shown. For Mach numbers greater than 0.6 the jet stands up against the cross flow very well. The shape is the same for $.6 < M < 1.67$. Thus a vertical jet from a WPML has the same cross section as a golf tee, i.e. long and slender with a gradual increase of diameter and then a flaring out near the top. Photographs of the jet taken from above the surface are somewhat misleading in that they do not show the diameter of the jet at all, but the flared out diameter which is much larger. Also notice the exaggeration of the horizontal axis.

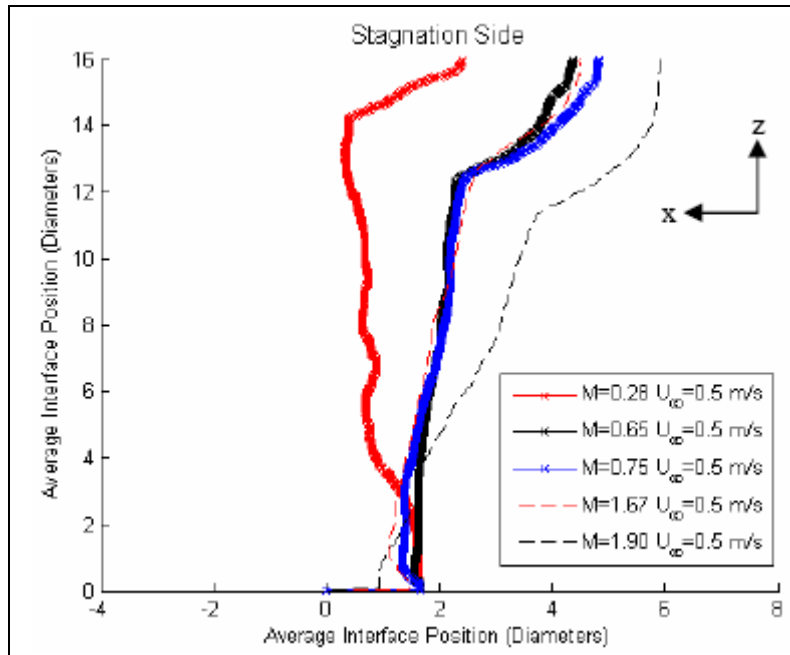


Figure 13. Time average interface position of an air jet in cross flow of .5 m/s (0.96 knot)

For the jets $0.6 < M < 1.67$ the spreading rate $db/dx = 0.186$ and the half angle is 10.5 degrees. This is a little broader than the tank test result at Blossom Point (7.4 degrees), but much narrower than rocket exhaust in air (13.7 degrees) and broader than water jets in water (6.8 degrees). For the $M = 1.67$ jet, the values are the same into cross flow as into still water. For jets with Mach numbers less than about .5, they “pinch off” shortly after reaching the surface and do not stand up very well against a cross flow.

Jet Buoyancy

As the jets slow, buoyancy becomes more important and the rate of mixing and spreading change accordingly. Momentum in the jet can be augmented by the buoyant forces and the jet can even be accelerated. For water jets in water the expansion rate is $0.105x$ in the buoyant region. The “momentum length” of a jet as obtained from dimensional analysis is the distance at which momentum gives way to buoyancy as the dominant mechanism. This has been amply confirmed for water jets in water, where jets inclined relative to vertical bend upward at this distance. The momentum length was used to nondimensionalize the jet trajectory data in Figure 7 above. For the JATO jet at 20 ft depth the momentum length is 240 ft, so buoyancy should not be important. There is no apparent buoyant effect in Figure 5. However, we have some data that show the distance for transition from momentum dominance to buoyancy dominance may be much less than the momentum length for rocket exhaust into water than water jets in water.

The trajectory for the jet tip from a MK-117 JATO motor fired at a depth of 42 ft. is shown in Figure 14. There is a pronounced change in speed at a height of 27 ft. at time 1.8 seconds. The exponent in the trajectory equation obtained from curve fitting shifts from 0.526 to 0.947. The momentum length is 190 ft. for the JATO at 42 ft. depth. From the figure it can be seen flow persists as a jet 0.45 seconds after motor burn out, and then becomes a buoyant plume. The scaled distance at the transition to buoyancy is 0.142 and the scaled time is 11.7. This point is at the upper cross on Figure 7.

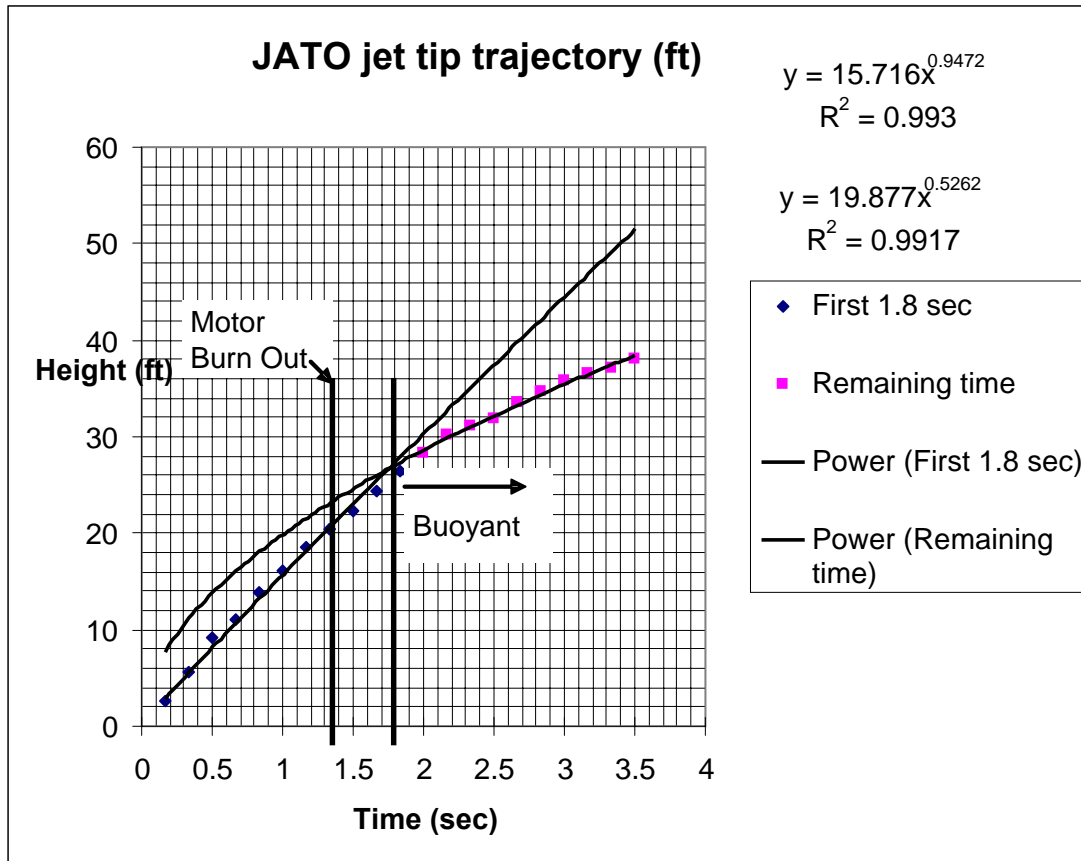


Figure 14. Jet Tip Trajectory For MK117 JATO Fired At A Depth Of 42 Ft.

We fired a SR-121 rocket motor at an inclination of 74.5 degrees to the horizontal (90 degrees is up) at a depth of 30ft. and found the jet turned upward at a distance of 11.5 ft. at time 1.28 seconds. Figure 15 shows the jet transition to a buoyant plume. When the jet got to the surface the time was 2.34 seconds and the knee in the trajectory curve was at 13.8 ft. The theoretical momentum length for this motor fired at 30 ft. is 339 ft. The scaled distance when the jet first turned upward was therefore 0.0339 and the scaled time was 6.79. This point is shown as the lower cross on Figure 7. When the jet arrived at the surface the knee was at a scaled

distance of 0.0407 and the scaled time was 12.45. Even though the momentum length for the SR-121 was greater than the MK-117 JATO, the transition to becoming a plume was closer to the launcher exit. Evidently momentum length is not a good predictor of the transition distance for gas jets in water.

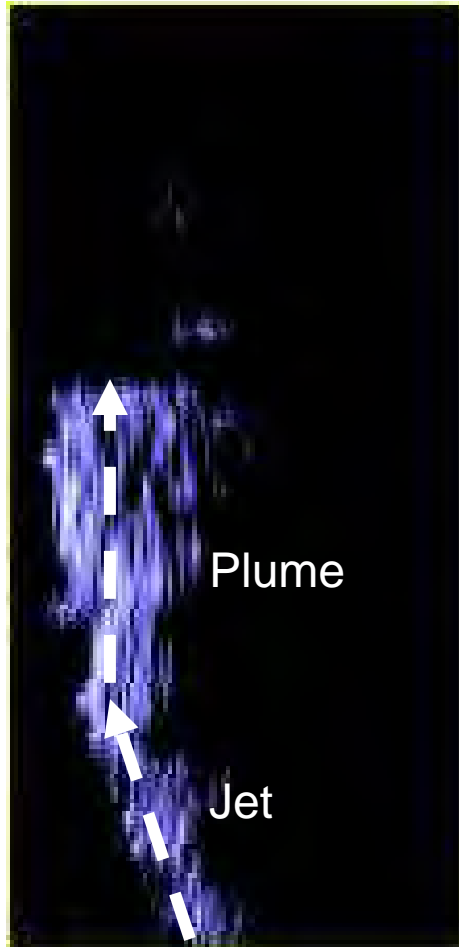


Figure 15. Inclined Jet From SR-121 Rocket Motor Transitioning To Become A Buoyant Plume.

JET INTERNAL STRUCTURE

Jet Cross Sectional Properties and Turbulence

The cross section through the jet at any given height shows nearly Gaussian distributions of the jet density, velocity and other properties. CFD results computed at NSWC are shown at the time the jet tip reaches the surface in Figures 16 and 17. The contours are for pressure and density, with embedded velocity profiles. The contours become Gaussian beyond the zone of flow establishment, which ends at 60 inches on the vertical axis. This distance is 6.6 equivalent diameters, which agrees with the zone of flow establishment ending at 6.2 diameters in Figure 9. For positions closer to the exit plane than 30 inches (3.3 equivalent diameters) the

velocity distribution is doughnut shaped. The approximately 7th power velocity distribution of internal flow in the annular space broadens, flattens, and becomes parabolic. At $x = 18$ (2 equivalent diameters) the parabolic distributions merge. The jet boundary angles from Figure 10, where $db(x)/dx$ is 0.26, are shown in Figure 17.

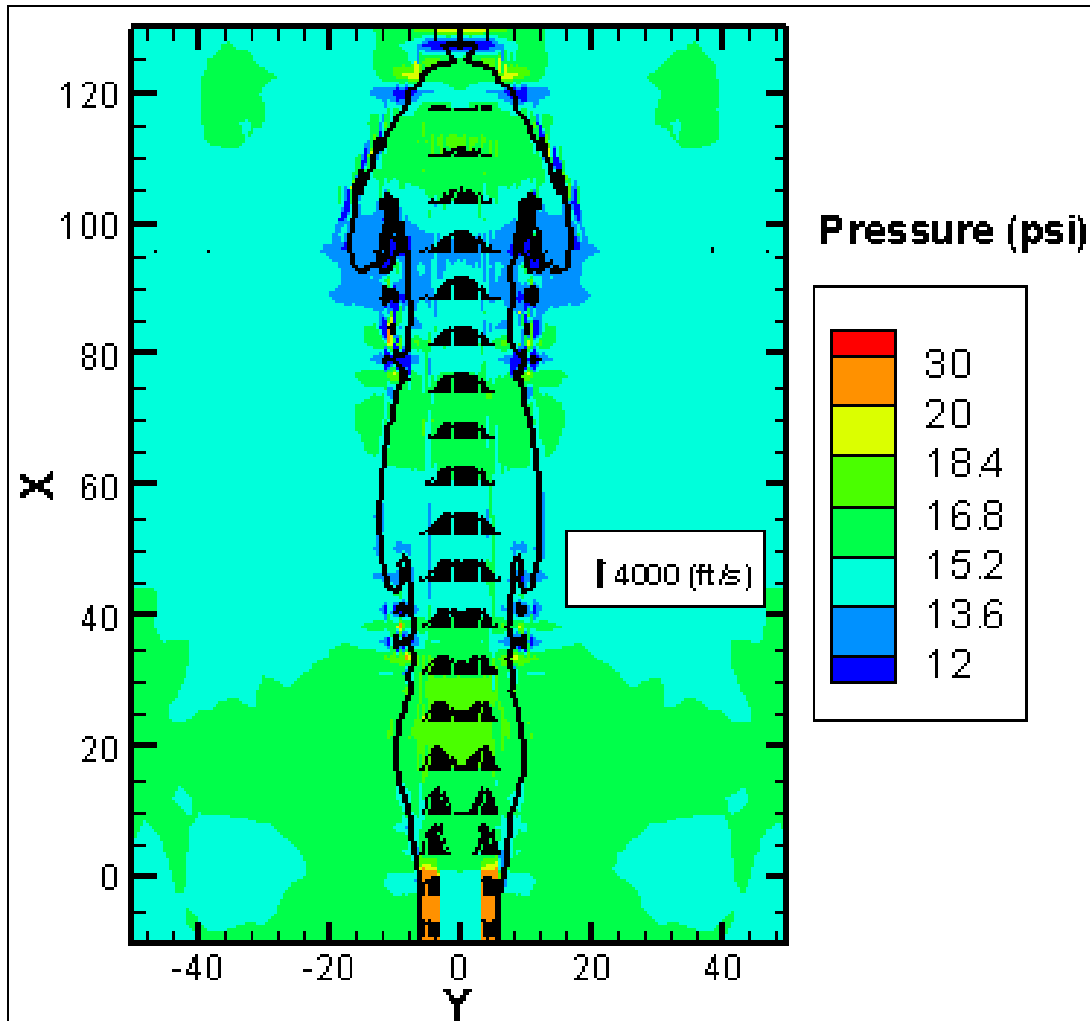


Figure 16. Pressure Contours For Jet. Length Scales Are In Inches.

The contours on Figure 17 show a sudden, near discontinuous change in density. The colors in the range 5 to 35 lb/ft³ are bunched into a solid line. The dark blue region is hot gas with some entrained water. The colors green through red are mainly water with some entrained gas. The computer results are in approximate agreement with the data of Loth and Faeth [5], even though the computer results are for a transient jet that has not reached steady state. The 0.5 air/water region which defines the jet diameter in [5] would be in the middle of the green region, which does not show on the plot because it is in the region of rapid change in the jet boundary.

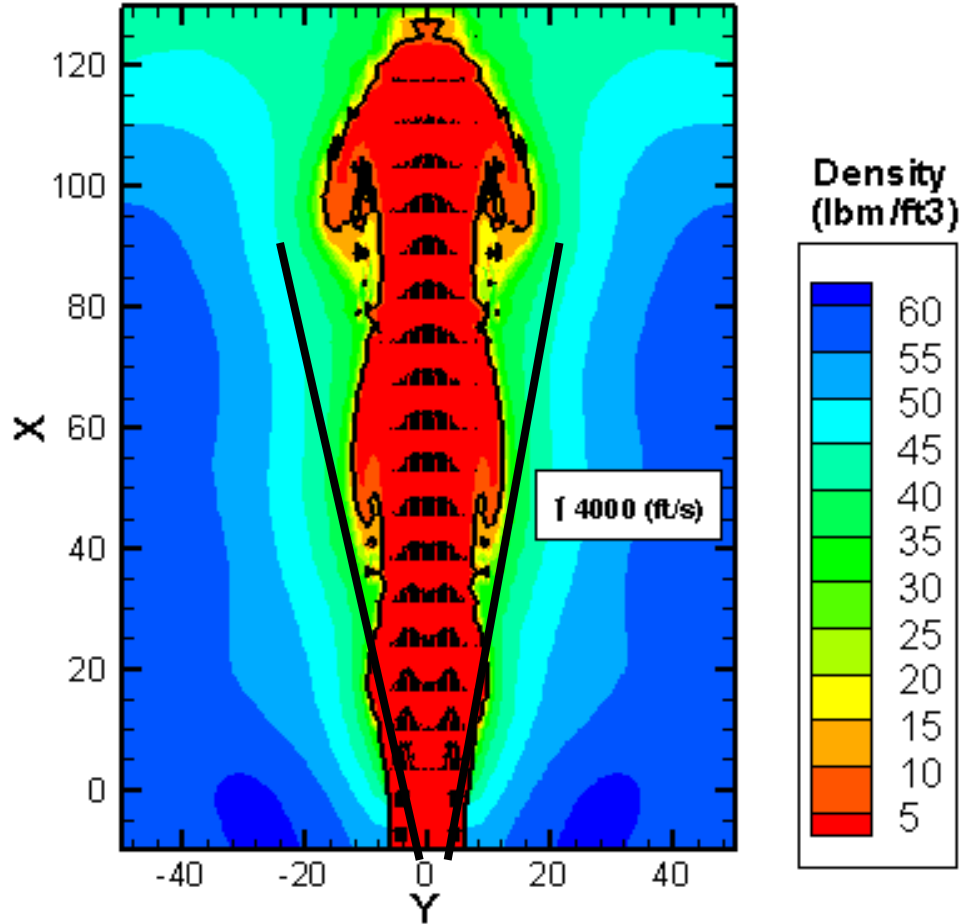


Figure 17. Density Contours For Jet. Length Scales Are In Inches. The Solid Lines Are From Figure 10, Where $B(X) = .26 X$.

Figure 18 (3.6 in [5]), shows a broad flat contour of turbulent rms intensities of 20-25% of the mean spanning the jet cross section. In the jet the fluctuations are most severe at the interface between the jet and the ambient, and the intensity profile shows two peaks. After the jet slows and becomes a plume, the shear at the interface between the jet and the ambient is less and the profiles show peak intensities along the centerline.

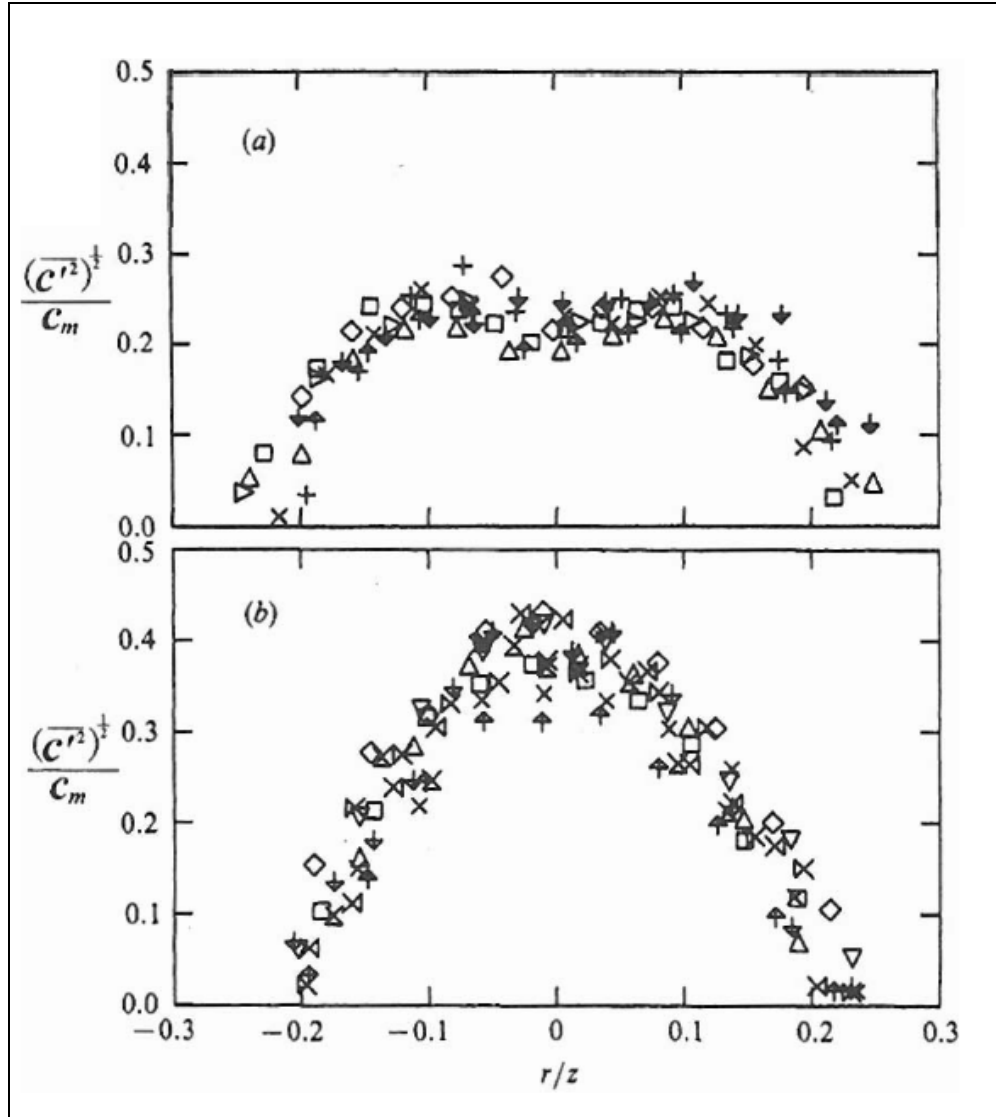


Figure 18. Turbulent Fluctuations Across A Jet (Top) And Plume (Below). The Fluctuations Are Rms Values.

The plots in Figures 16 and 17 show a jet with very high velocities in the core. Even though the core velocity is several thousand feet per second, the jet tip moves much slower. Differentiation of the trajectory equation on Figure 14 with respect to time yields a speed of 14.9 ft. per sec. over most of the burn time. The interface between the jet tip and water is Taylor unstable: a fluid trying to accelerate a second fluid of much higher density. The interface becomes highly irregular and turbulent. The high velocity gas core mixes with water at the jet tip and loses momentum very quickly in the mixing zone. This doesn't seem to cause much of a pressure disturbance in the mixing zone, but the density and velocity fields change very rapidly.

Approximate “low order” models of turbulent jets have been used extensively in civil and environmental engineering. Practically all the models are for steady flow. One example is the “top hat” model, which considers the properties to be uniform across the jet with the value being the average of the more accurate Gaussian distribution. For many problems in civil engineering the top hat model provides nearly the same result for broadening, mixing, and dilution as the Gaussian model, with much simplified calculations. The model used in our first try at the launch dynamics problem used a low order balloon filling model discussed above. It is a simple top hat model for nonsteady flow. As more data is obtained and the accuracy of CFD methods is confirmed, CFD will replace the low order semiempirical models.

SUMMARY

Turbulent rocket exhaust jets in water are similar in structure to water jets in water and gas jets in gas. Each case is characterized by a turbulent jet interface region that entrains the surrounding medium. The spreading rate db/dx and the half angle seems invariant with regard to scale and velocity, and unique to the phase of the medium and jet. They seem insensitive to the details of chemical composition. Methods for predicting the exhaust velocity and Mach number were discussed. Water depth is important, as increasing hydrostatic pressure decreases the exit Mach number and velocity. Gas jets can penetrate a considerable distance in water, and maintain a gas column out to at least 80 diameters. As the Mach number of gas jets in water approaches 0.6, the jet has the ability to penetrate a cross flow for a considerable distance. This makes the Water Piercing Missile Launcher plausible for moving platforms. Efforts are under way to develop low order semi-empirical models and computer fluid dynamics approaches to predicting detailed jet structures.

REFERENCES

1. J. Yagla, “Concentric Canister Launcher,” Naval Engineers Journal, May 1997, pages 313-330.
2. Yagla, Jon, Keith deLoach and Chris Weiland “The Water Piercing Missile Launcher,” 21st International Ballistics Symposium, Adelaide Australia
3. Fischer, H., List, J., Koh, R., Imberger, J., and Brooks, N. **Mixing in Inland and Coastal Waters**, Academic Press, New York, 1979.
4. Lee, J.H.W. and V.H. Chu **Turbulent Jets and Plumes**, Kluwer Academic Publishers, Norwell Massachusetts.
5. Loth, E. and G.M. Faeth “Structure of Underexpanded Round Air Jets Submerged in Water” International Journal of Multiphase Flow, Vol. 15, No. 4, pp 589-603, 1989.
6. Weiland, Chris, Jon J. Yagla, and Pavlos Vlachos “Experimental Study of the Stability of a High-Speed Gas Jet Under the Influence of Liquid Cross-Flow” Proceedings of FEDSM2007 5th Joint ASME/JSME Fluids Engineering

Conference, July 30-August 2, 2007 San Diego, CA.



Experimental Validation of a Kevlar Fabric Model for Ballistic Impact

Chian-Fong Yen

Tusit Weerasooriya

Paul Moy

Brian Scott

Bryan Cheeseman

ARL, APG MD



TECHNOLOGY DRIVEN. WARFIGHTER FOCUSED.

International Symposium on Ballistics

New Orleans, LA

26 September 2008

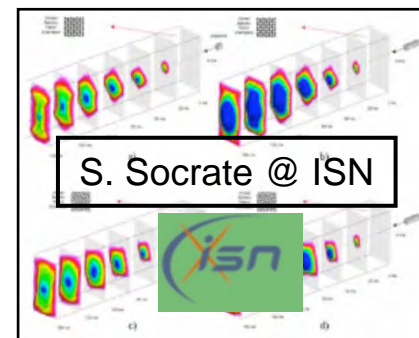
- Experimental Studies
 - Ballistic impact of single layer fabric
- Fabric Modeling
 - Yarn level model
 - Sub-yarn level model*
- Conclusions

* Including results reported in the poster #198 entitled: “**Developing Simulation Capabilities to Link Textile Manufacturing to Ballistic Performance**” by B.A. Cheeseman*, C.F. Yen, B.R. Scott, B. LaMattina, Y. Miao and Y. Wang

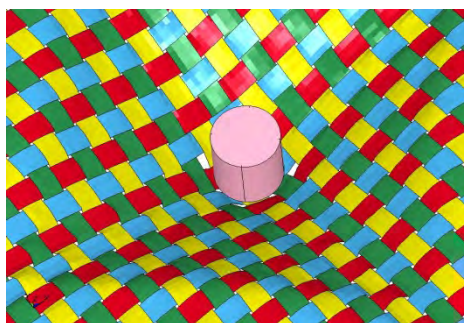
- Assess current state-of-the-art modeling capabilities and determine the most suitable numerical analysis techniques
- Develop and implement the identified analyses techniques
- Validate analyses techniques with high resolution experiments. Refine modeling capabilities as necessary to ensure the accuracy of the simulation when compared to the experiment

Fabric as a continuum

From Simons, J.W.,
Erlich, D.C. and
Shockey, D.A. 20th Int.
Symp. Ballistics, Nov.
2001



Yarn as a continuum



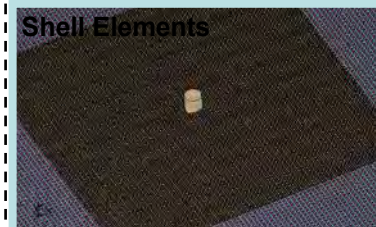
Solid Elements

M. Keefe @ UDel

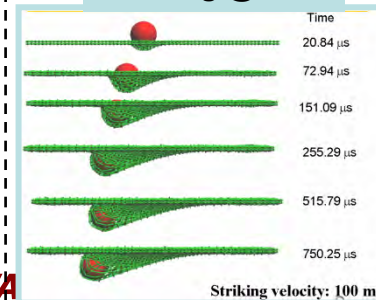


C. Yen

Shell Elements



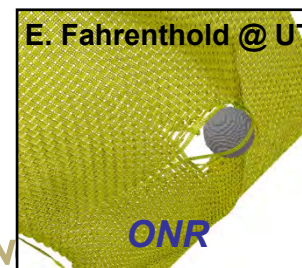
Y. Wang @ KSU



Filament as a continuum

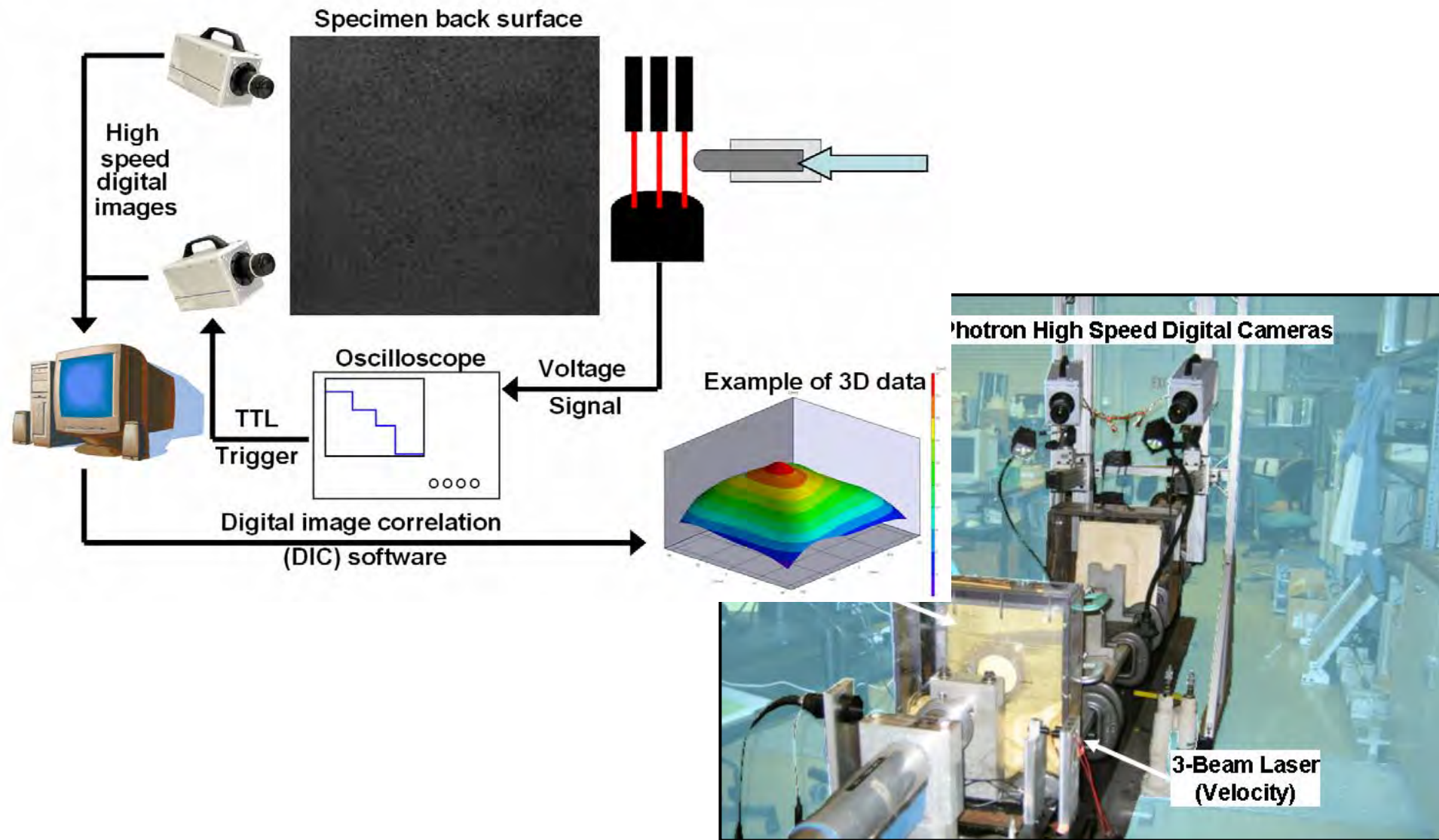


E. Fahrenthold @ UT



“...the ballistic response of the textile structure depends on the response of the fiber with which it is woven as well as the structural geometry itself.” D. Roylance, *Text. Res. J.* 1973.

RDECOM Fabric Impact Testing: Experimental Setup with High Speed Digital Cameras **ARL**



TECHNOLOGY DRIVEN. WARFIGHTER FOCUSED.

Experimental Results:

May, 2007

Tusit Weerasooriya

ARL

Target:

Hexcel Style 706

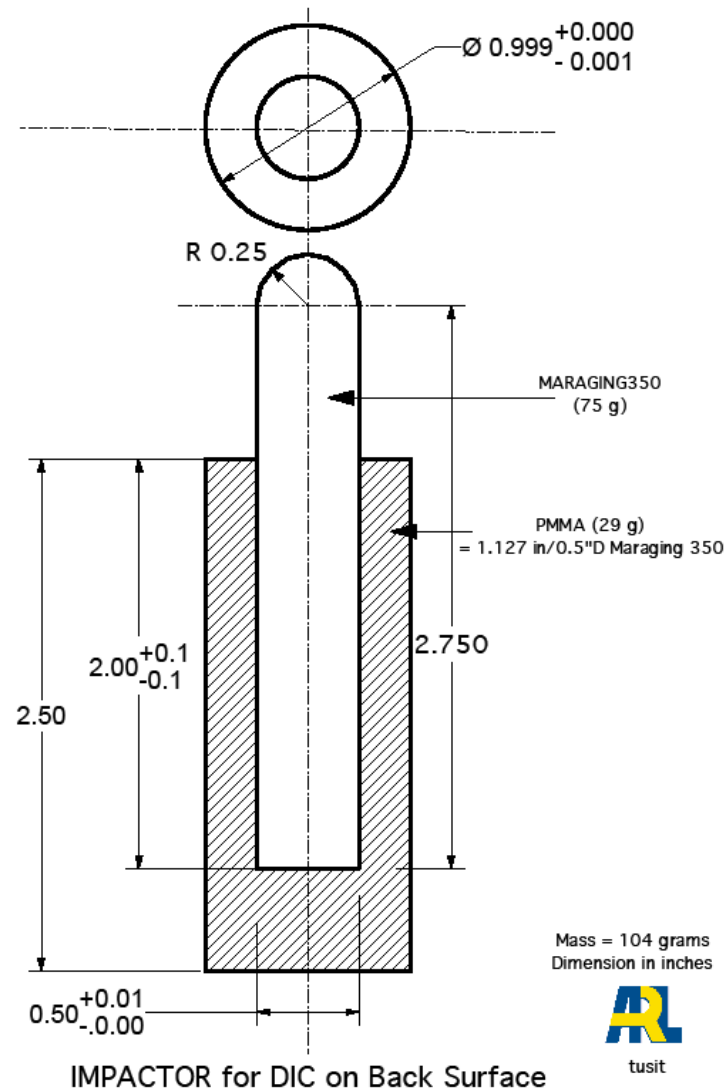
Single Layer

Square & Circular Shapes

10"x10" & Diameter = 10"

Fixed boundary

Impact Speed: 22.2m/s



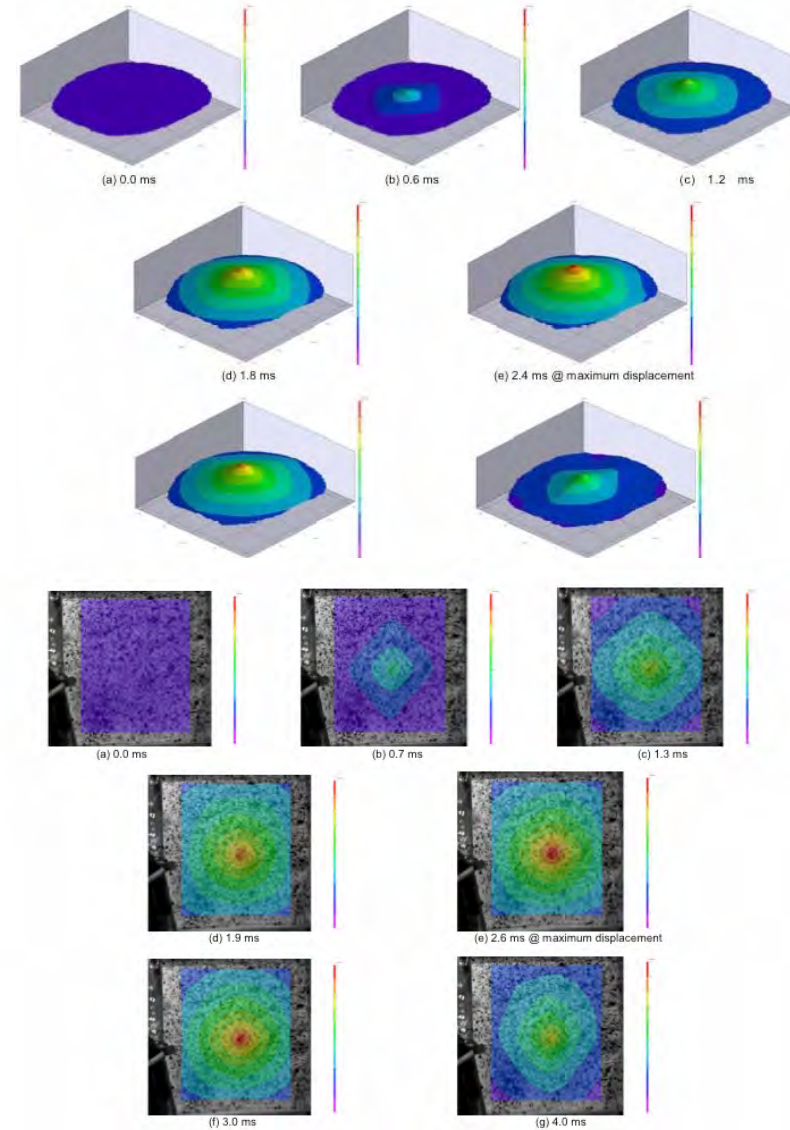
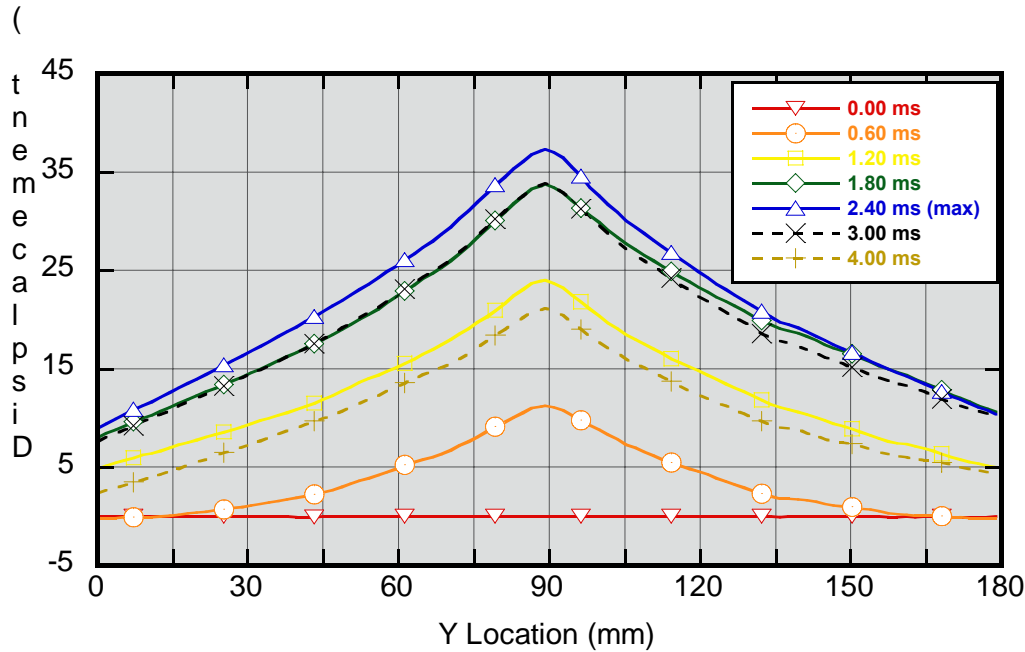
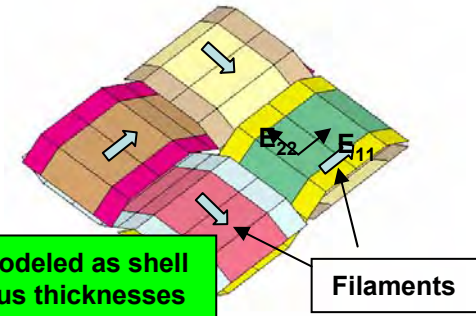
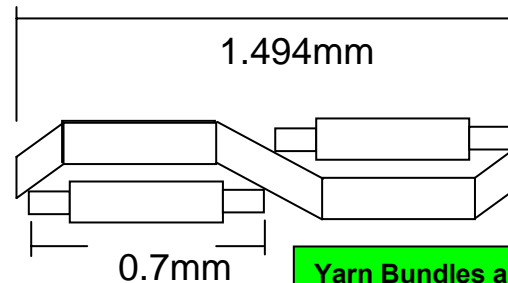
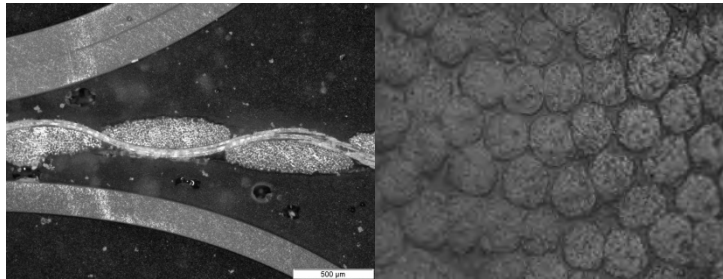
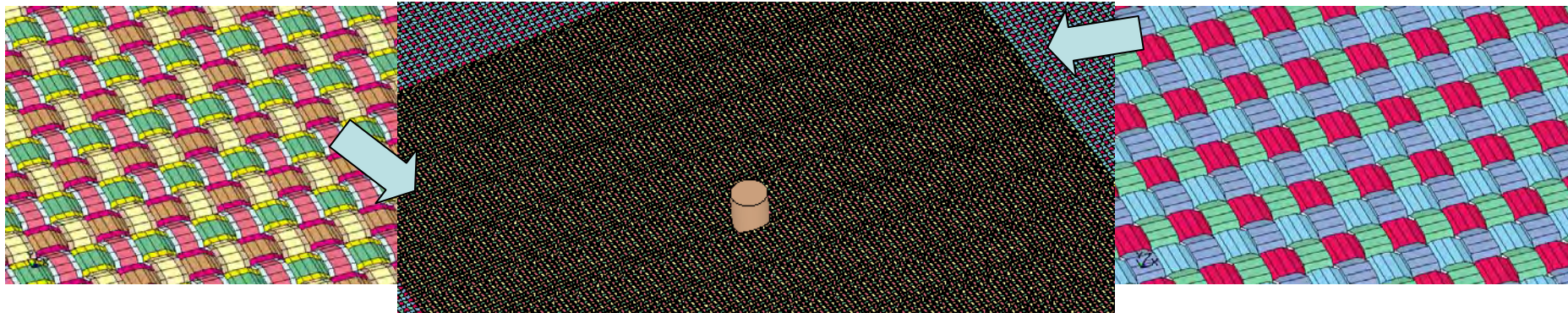


Figure 10. 2D Contour Plot from DIC of Kevlar KM2 on a Square Frame Configuration

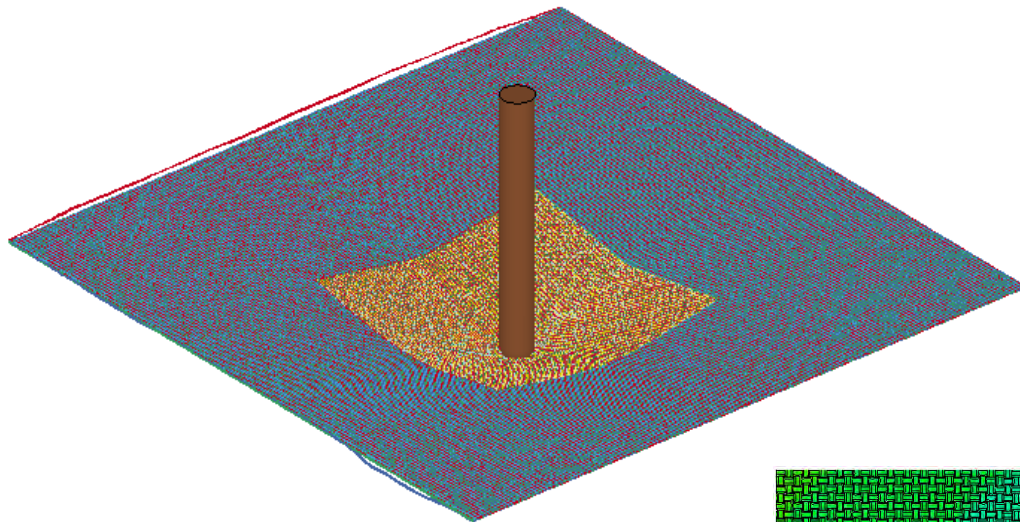
- Improved the accuracy of yarn bundle shape and dimensions in a woven structure.
- Obtained micrographs in order to get more accurate measurements.



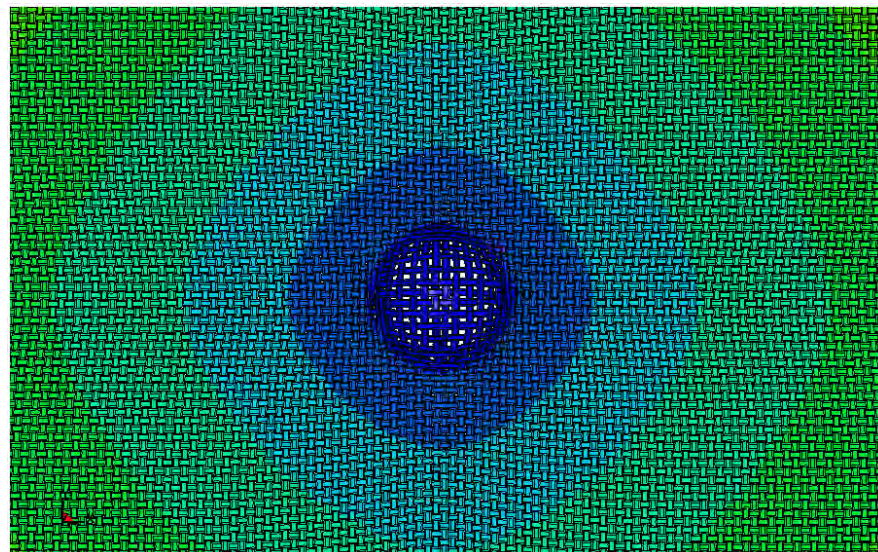
- Improved computational efficiency for shorter run times.
- Utilized refined mesh in region of impact; less refined elsewhere.

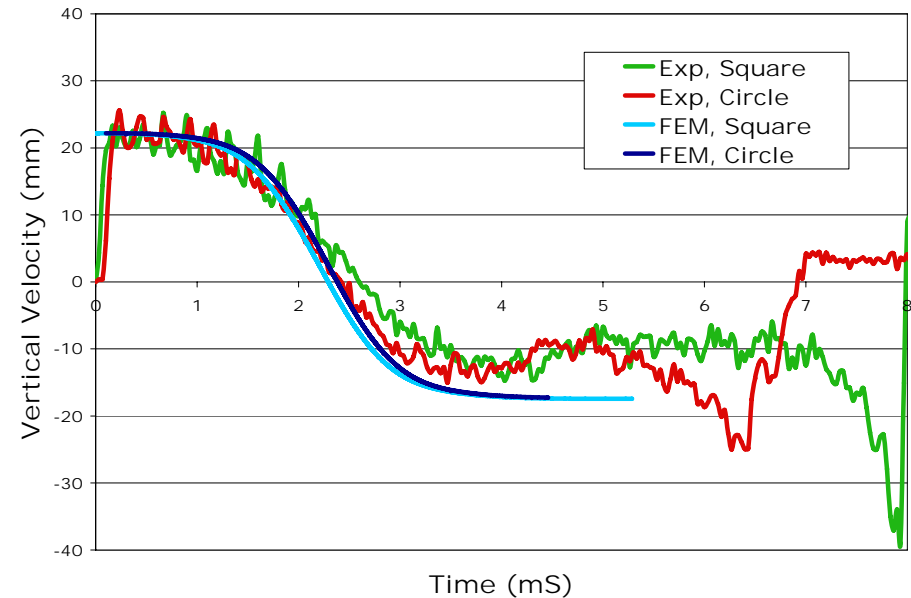
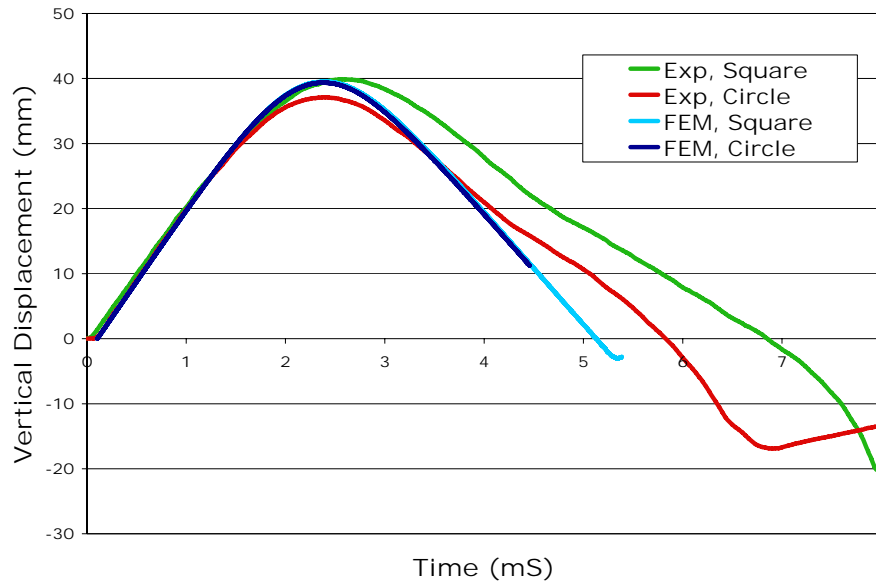


- Using one intg. pt. through bundle thickness to eliminate bundle bending rigidity
- High mesh density in center impact region



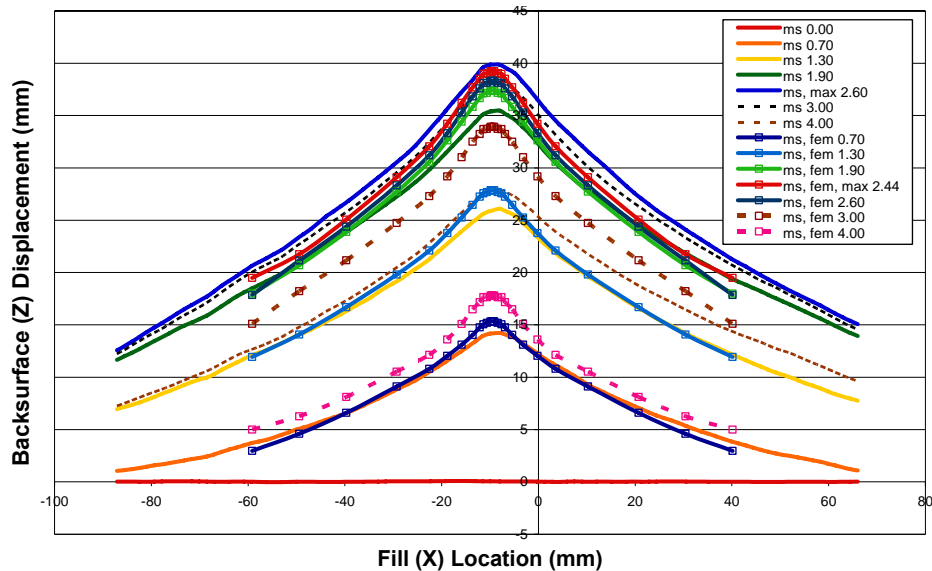
- Deformed mesh of a 34x34 Kevlar fabric layer computed at the peak deflection time of 2.3 msec



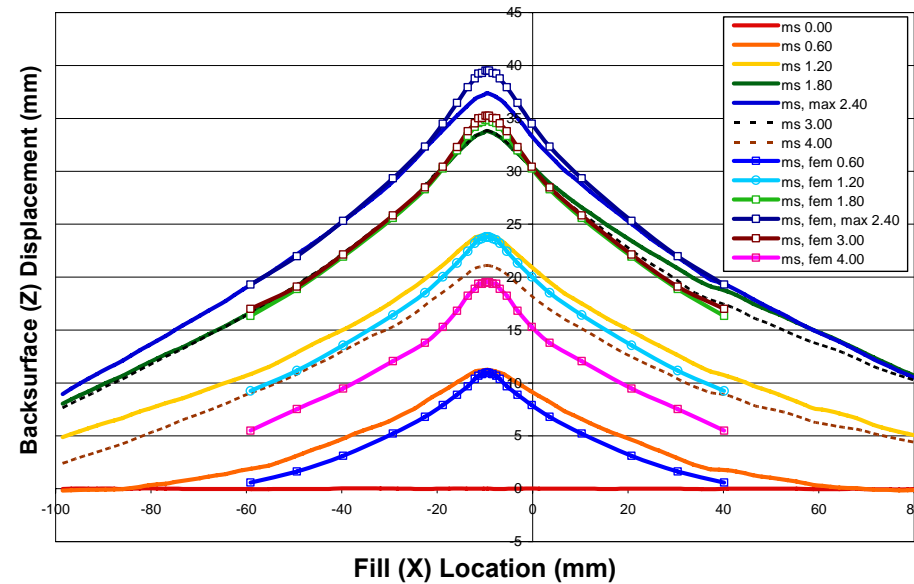


- Displacement -time and velocity – time plots of Kevlar KM2 yarn in weft (x) direction for square support and circular support through the impact point

Square Fixture

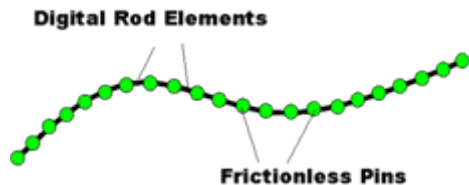


Circular Fixture



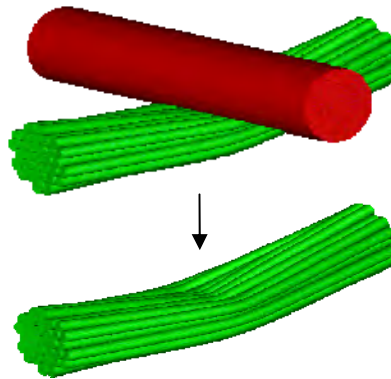
- Displacement profile of Kevlar KM2 yarn in fill direction for square and circular frame configurations through the impact point

'Filament'



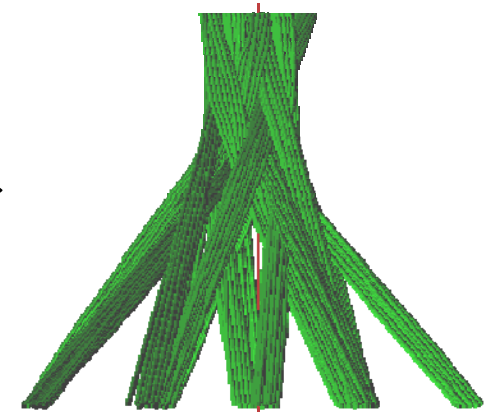
Represented as a series of
rod elements connected with
frictionless pins = 'digital
chain'

Yarn



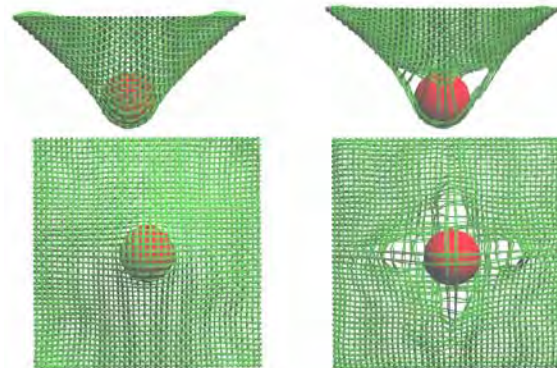
Multi-Digital Chain Yarn Model
(Here, each yarn contains 32
digital chains)

Weave or Braid



Yarns utilized to simulate
textile manufacturing process

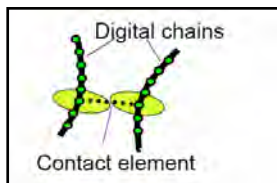
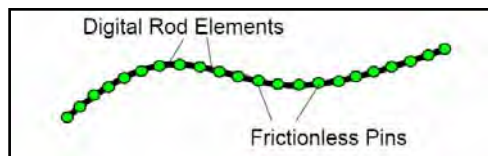
Extended textile
manufacturing
simulation program to
ballistic impact



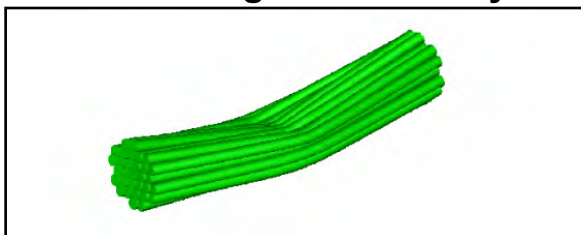
The resulting analysis tool
could provide the *critical
link* between textile
manufacturing and
ballistic performance
prediction for textile
protection systems.

- Textile manufacturing simulation taking computing time

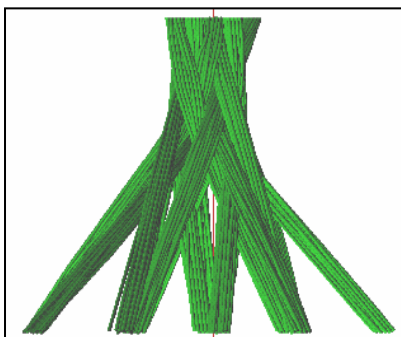
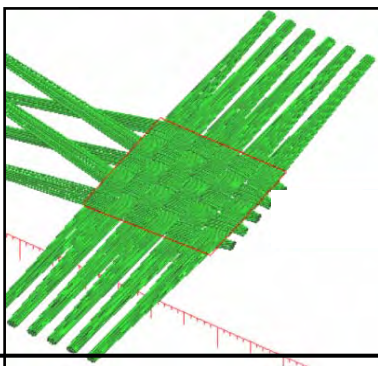
'Digital Elements (chains)' = Filaments



Assemble digital chains = yarn



Yarns utilized in textile manufacturing simulation



- Develop explicit formulation for manufacturing process



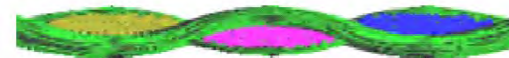
Microscopic picture



19 chain yarn model



37 chain yarn model



52 chain yarn model



67 chain yarn model



Microscopic picture

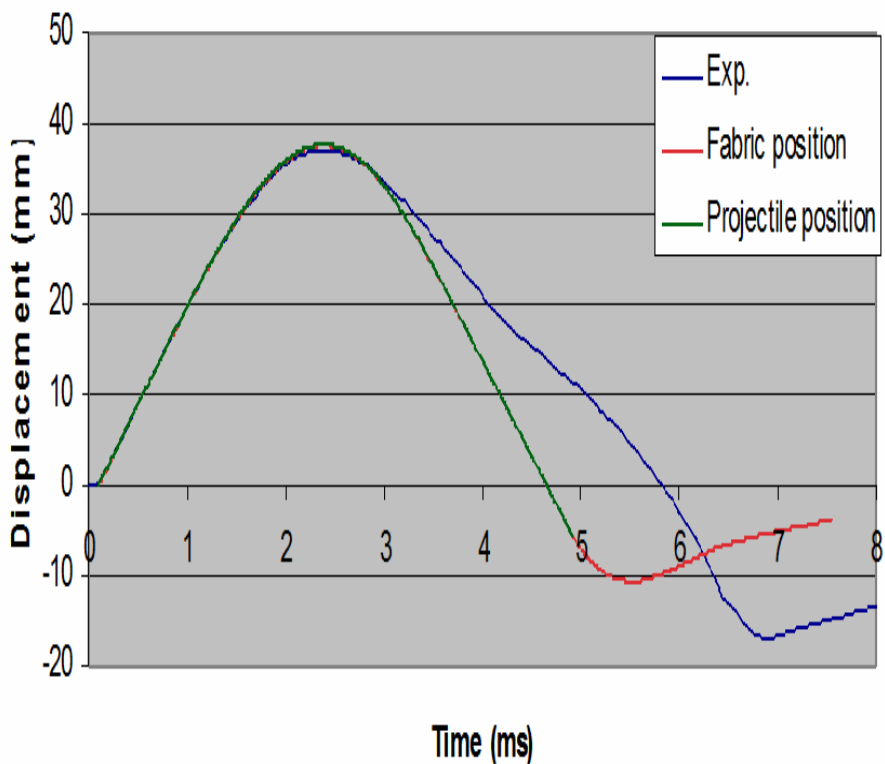


19 chain yarn model

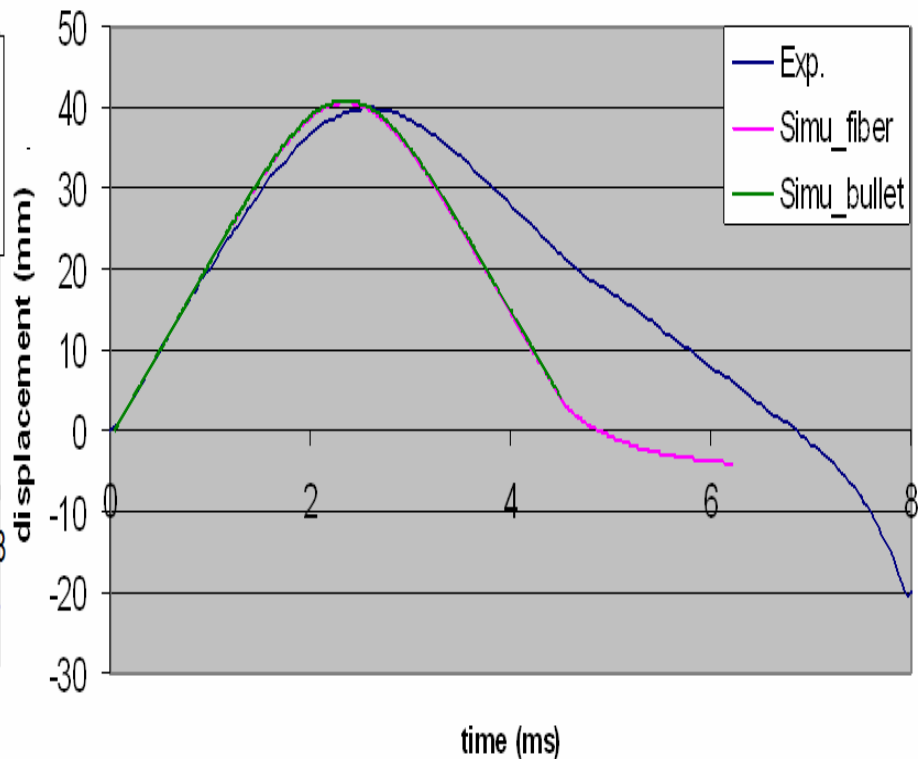
Results reported out at the Army Science Conference, Fiber Society Meeting and two Journal papers

TECHNOLOGY DRIVEN. WARFIGHTER FOCUSED.

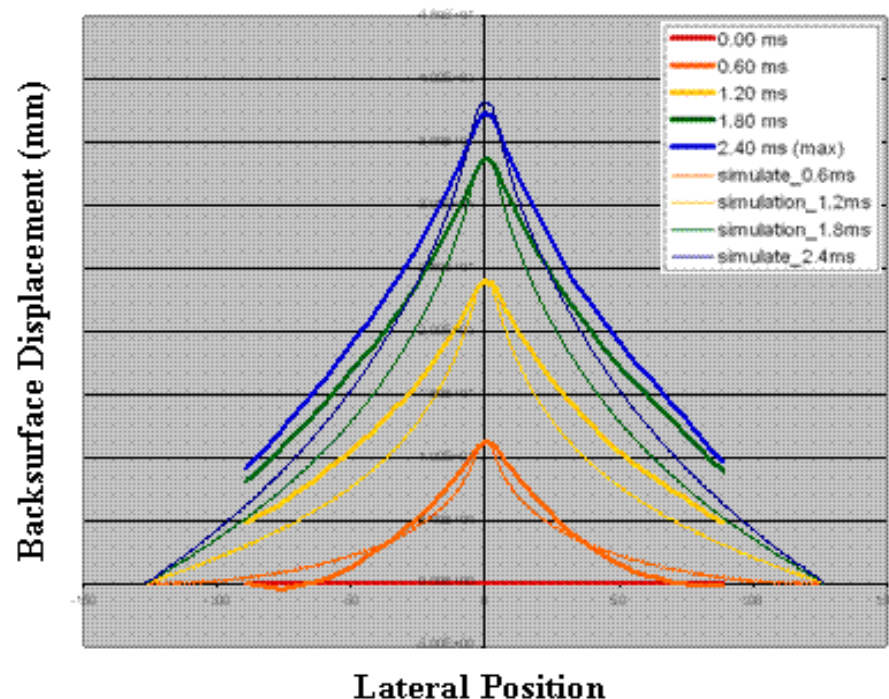
Circular Fixture



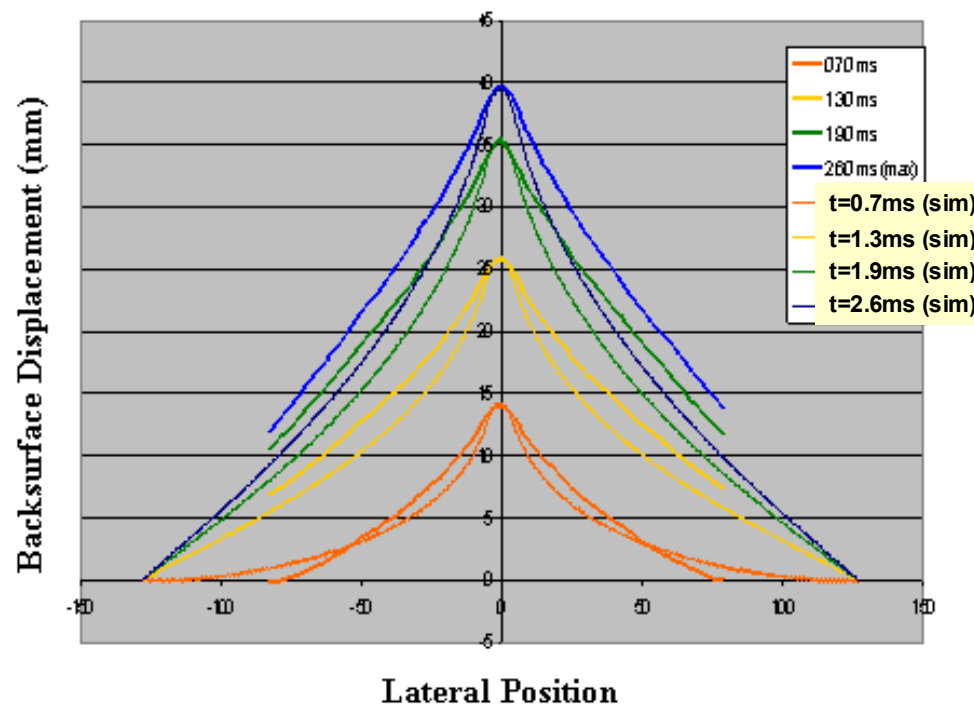
Square Fixture

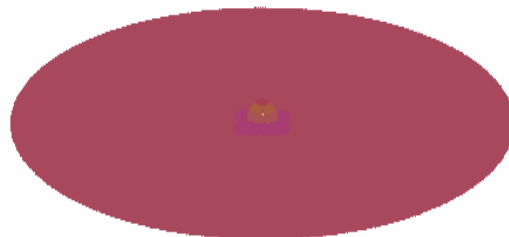


Circular Fixture



Square Fixture

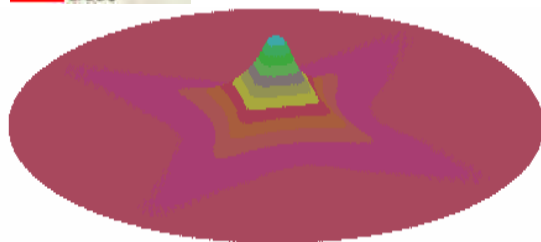




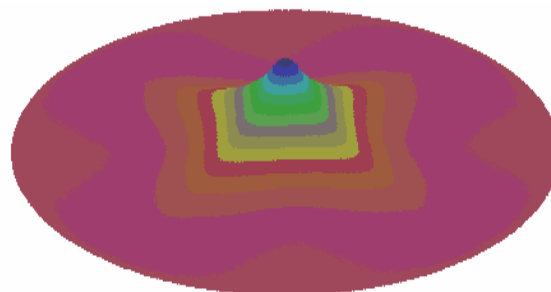
$t=0.407$ ms



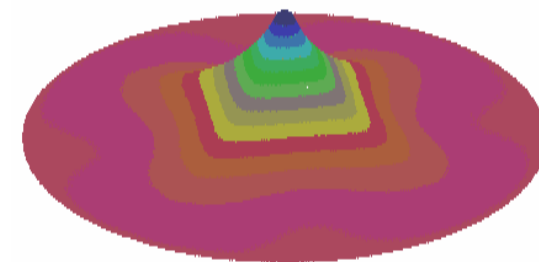
$t=0.934$ ms



$t=0.135$ ms



$t=0.187$ ms



$t=0.208$ ms

- **Two computational approaches have been developed to simulate ballistic impact and penetration of the textile fabric**
 - Yarn level model
 - Digital Element model with almost filament level resolution
- **Limited validation of the simulation with experiments has been conducted**
 - Current results indicate good agreement
 - Further validation is being performed.
- **Additional failure mode (filament shearing) and statistical fiber strengths are being incorporated in both models for ballistic modeling**
- **The developed simulation capabilities would allow a material-by-design approach to textile protection systems**
 - Yarn-level model provides computational efficiency on modeling and designing multi-layer fabric protection
 - Sub-yarn-level model by using digital element approach provides
 - Capability of linking the manufacture of a textile to its ballistic performance
 - Quantifying the effect of filament-level parameters such as inter-yarn friction, yarn twisting and pre-yarn tension on the textile fabric ballistic protection efficiency
- **When matured and validated, these fabric modeling technologies will allow rapid screening of advanced, novel, hybridized textile systems incorporating differing textile architectures and will enhance our capability for adapting to new threats and integrating new materials as they become available.**

Half scale experiments with rig for measuring structural deformation and impulse transfer from land mines

Björn Zakrisson – BAE

Bengt Wikman – BAE

Bo Johansson – FOI

Cooperation during 2007-2008 between:

BAE Systems Hägglunds AB

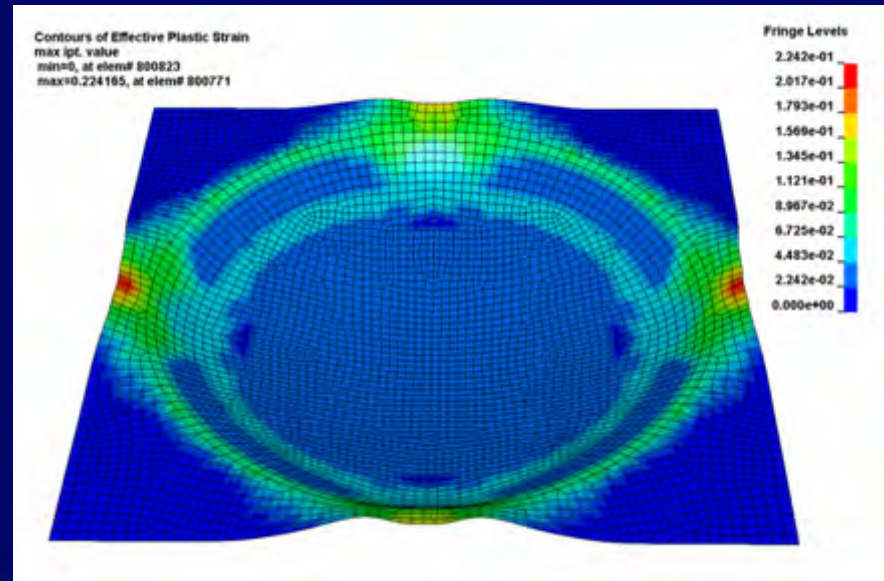
FOI, Swedish Defence Research Agency

PhD-project PROTECT

In collaboration between :

BAE Systems Hägglunds
Luleå University of Technology

Björn Zakrisson





Luleå University of Technology

BAE Systems Hägglunds AB
(Örnsköldsvik, Sweden)

FOI
Swedish Defence Research Agency
(Grindsjön, Tumba, Sweden)

Scope of work

- Experiments with land mine buried in ground
 - Performed in half scale
- Test parameters:
 - Explosive placed in steel pot or sand
 - Depth of Burial (DOB) in sand 0, 50 och 150 mm
 - Wet or dry sand
- Conditions:
 - Swedish military plastic explosive m/46
 - 86 % PETN 14 % fuel oil
 - Cylindrical with Diameter to Height ratio 3
 - 0.750 kg
 - 0.25 m stand-off distance
- Objective:
 - Detect effects of different test parameters
 - Use test results for validation of numerical model



Experimental Setup

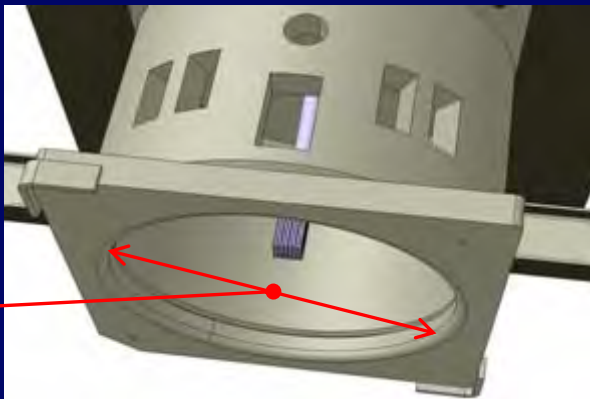
*Test module viewed
from underneath*

Plate holder

Weldox 700E
600x600 mm
t=8mm



Diameter
500 mm



Spring-
damper
system

Test
module

Sand box /
Steel pot

Measurements

- Maximum vertical jump of the test module
 - Impulse transfer to test module

$$I = m \cdot v_{\max} \approx m \cdot \sqrt{2 \cdot g \cdot z_{\max}}$$

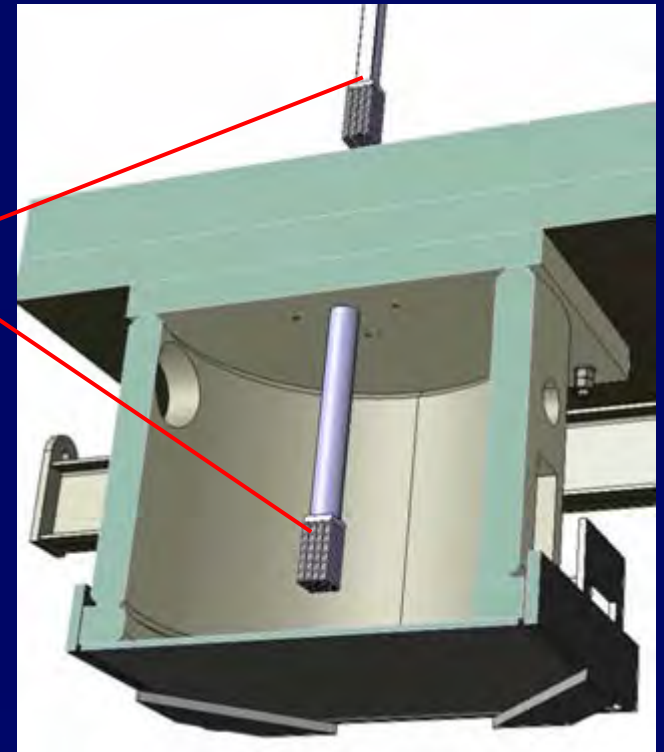
- Maximum dynamic plate deformation
- Residual plate deformation

Measurements (cont.)



Position
sensor

Aluminum
Honeycomb

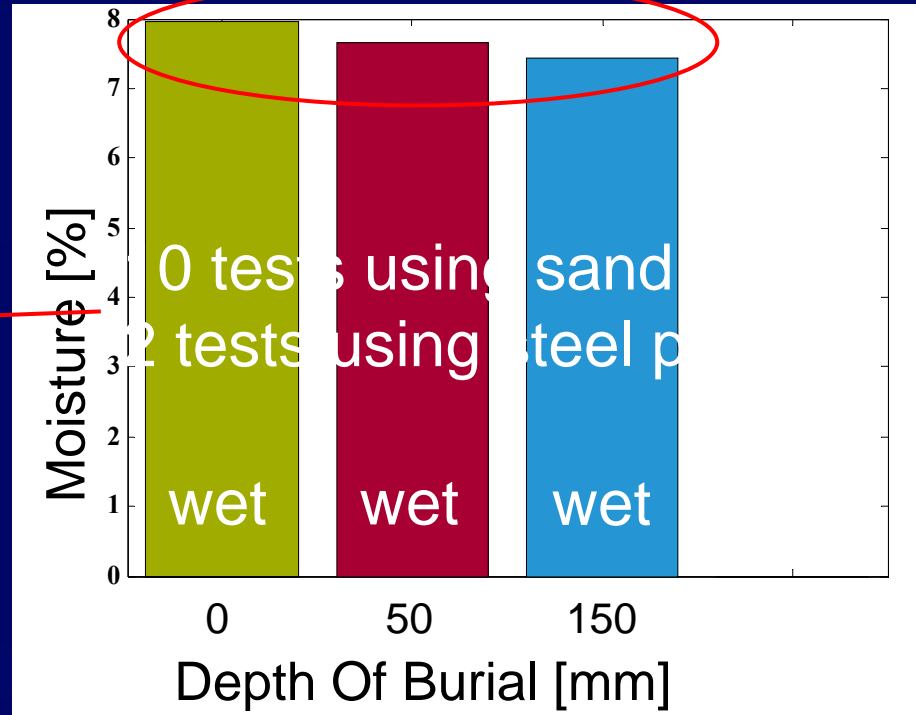
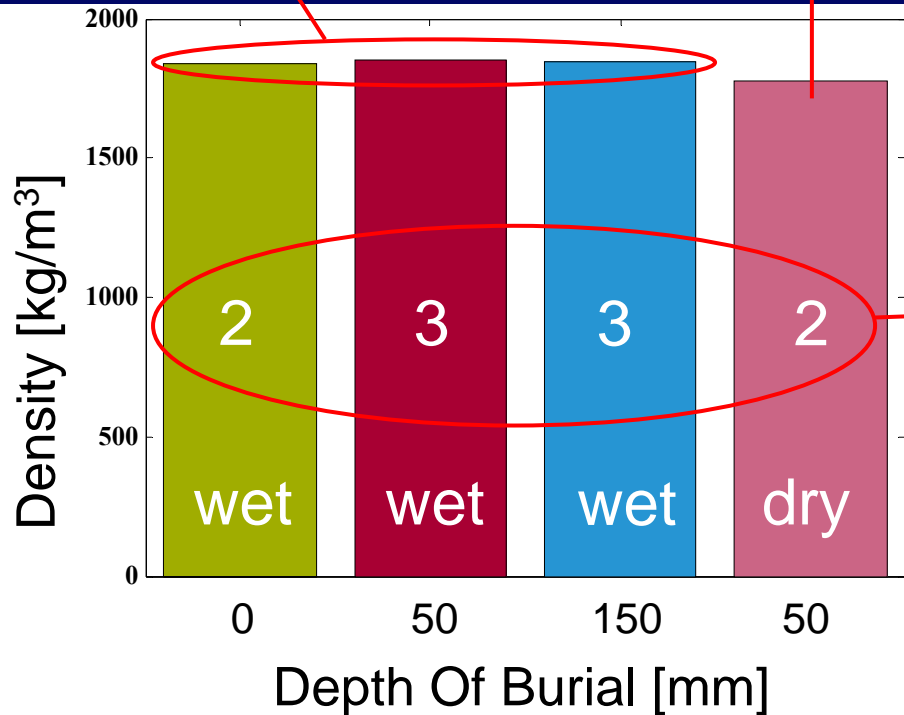


Sand properties

Mean "wet"
density
 1845 kg/m^3

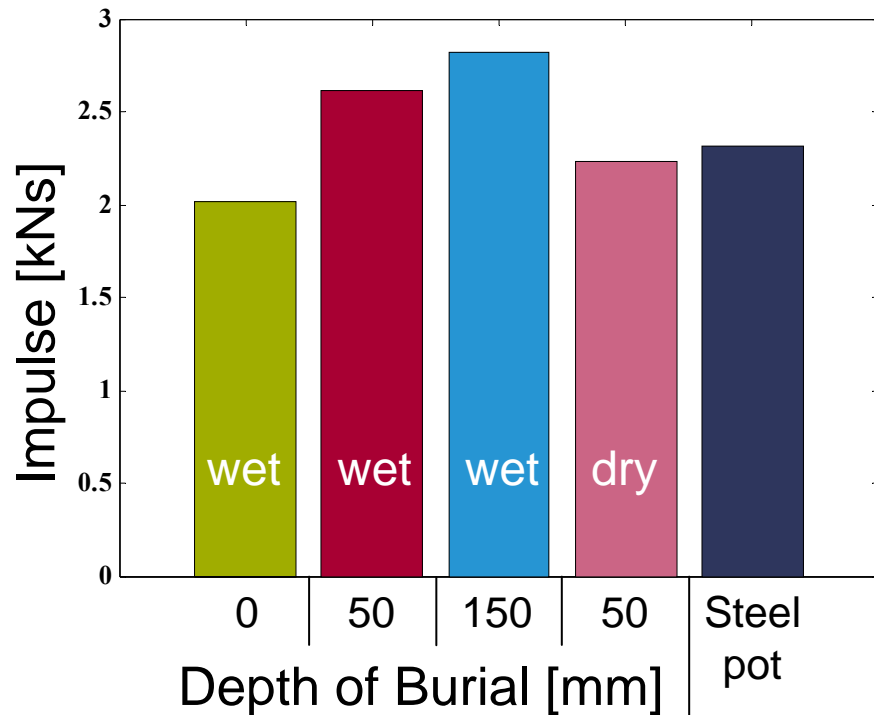
Dry density
 1771 kg/m^3

Mean
moisture
7.7 %

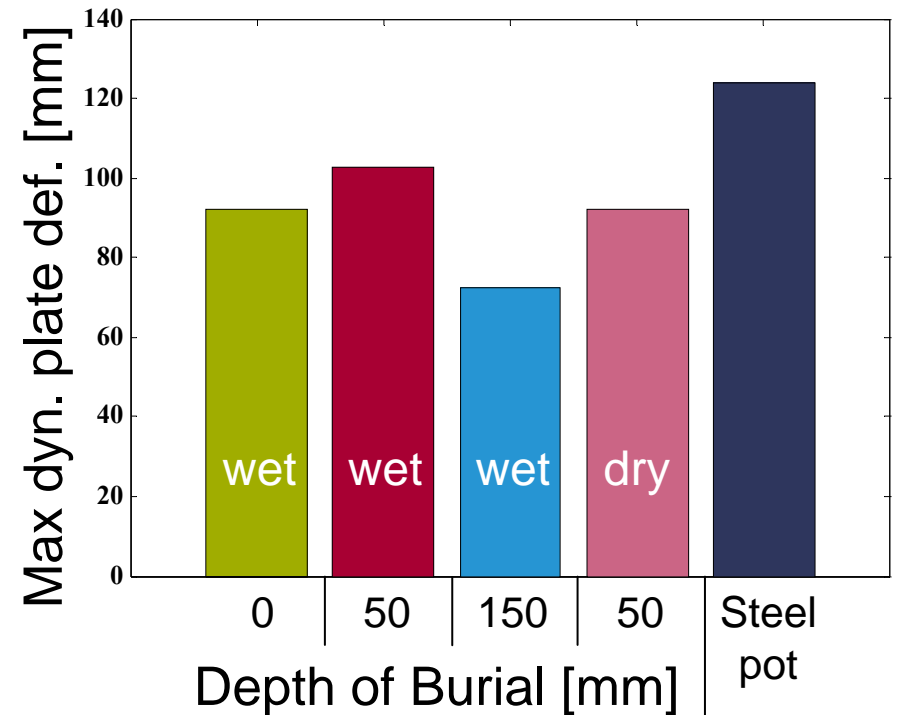


Experimental Results

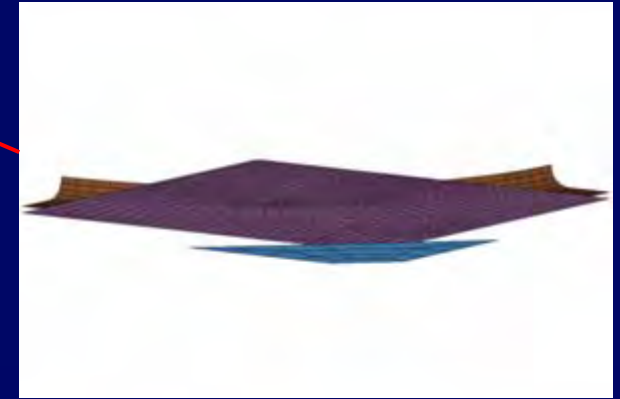
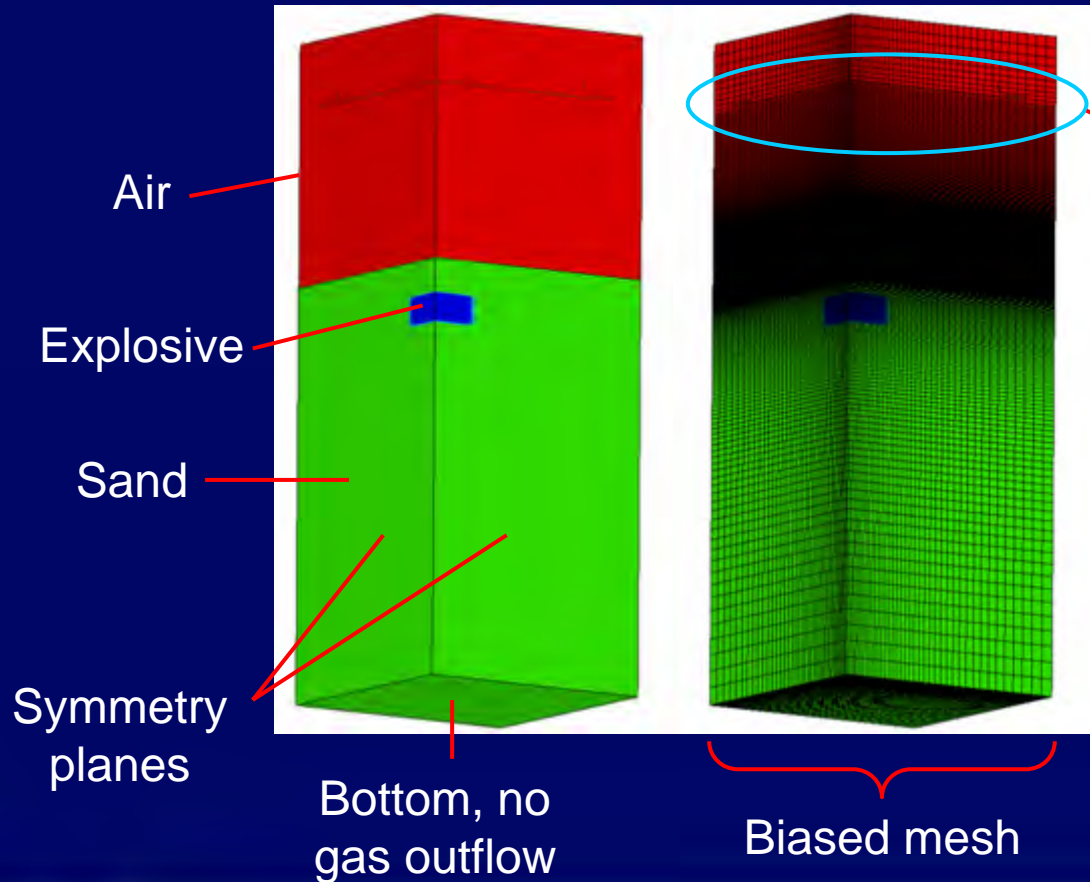
Impulse transfer to test module



Maximum dynamic plate deformation



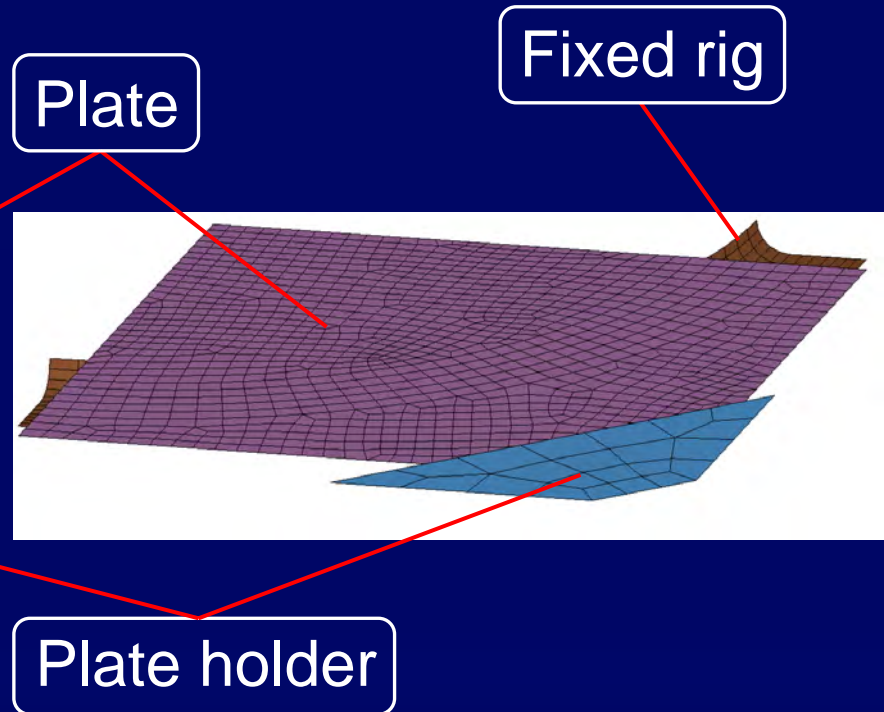
Numerical model LS-DYNA



- Symmetry model 1/4
- Sand, Air and Explosive modeled with ~536000 Euler elements
- Fluid Structure Interaction couple state variables from gas to structure

Numerical model (cont.)

LS-DYNA



Numerical model (cont.)

Materials

Sand

- Properties presented by Laine and Sandvik
 - Moisture content 6.57%
 - *Laine L., Sandvik A., "Derivation of mechanical properties for sand", 4th Silos, CI-Premier LTD, p 361-367.*
- Material model
 - Mohr-Coulomb yield surface
 - Tabulated Equation of State
 - ✓ Gives pressure-density relation
 - Initial density set to 1835 kg/m³

Steel Weldox 700E

- Johnson-Cook model

Explosive m/46

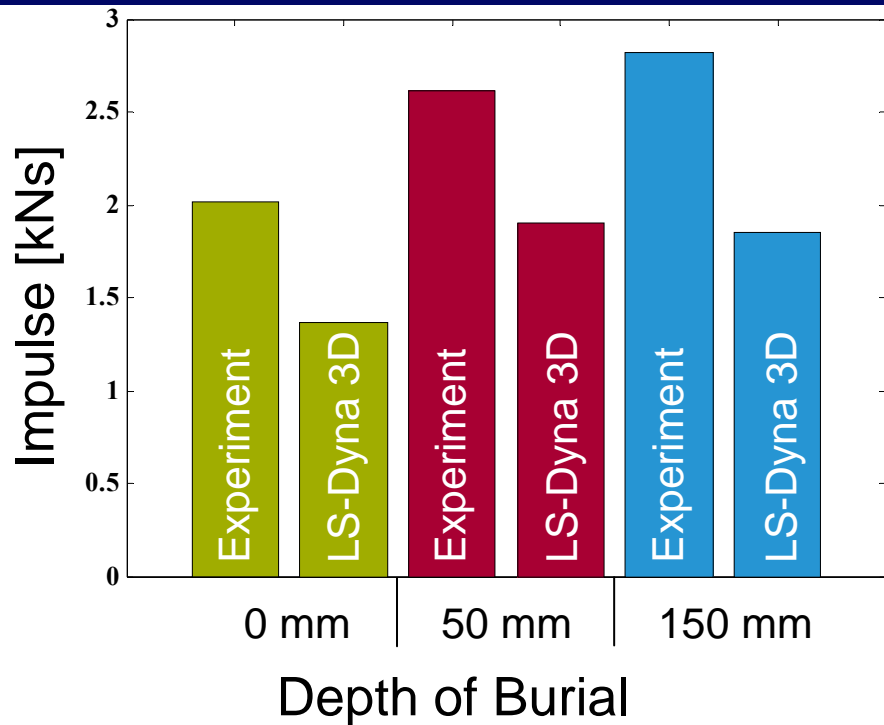
- High Explosive material
 - Equation of state JWL (Jones-Wilkins-Lee)

Air

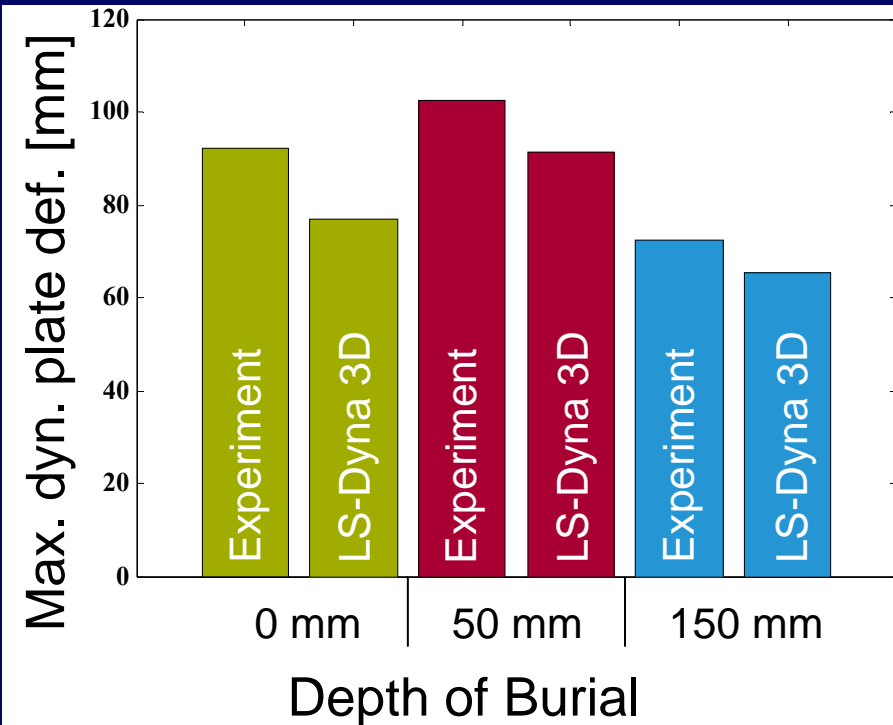
- Ideal gas

Numerical Results

Impulse transfer to test module



Maximum dynamic plate deformation



Conclusions

- Transferred impulse increases with the tested DOB in sand
- Measurement methods for test module jump give comparable results
- Wet sand results in larger impulse and plate deformation than dry sand
- Plate deformation increases with DOB up to a limit, decays thereafter
 - Indicates load localization
- Plate deformation largest when using steel pot
- Numerical simulations describe measured trends
 - General underestimation relative measurements
 - Further refinement and investigation needed

Questions?



Half scale experiments with rig for measuring structural deformation and impulse transfer from land mines

Name : Björn Zakrisson
Phone : +46 660 80824
Company: BAE Systems Hägglunds AB
E-mail: bjorn.zakrisson@baesystems.se